JAEA-Conf 2015-002
KEK Proceedings 2015-7
DOI:10.11484/jaea-conf-2015-002

Proceedings of the 21st Meeting of the International Collaboration on Advanced Neutron Sources

ICANS XXI

"Dawn of High Power Neutron Sources and Science Applications"

Sep. 29 – Oct. 3 2014

hosted by J-PARC Center, KEK, CROSS

Ibaraki Prefectural Culture Center, Mito, Japan

February 2016

Japan Atomic Energy Agency

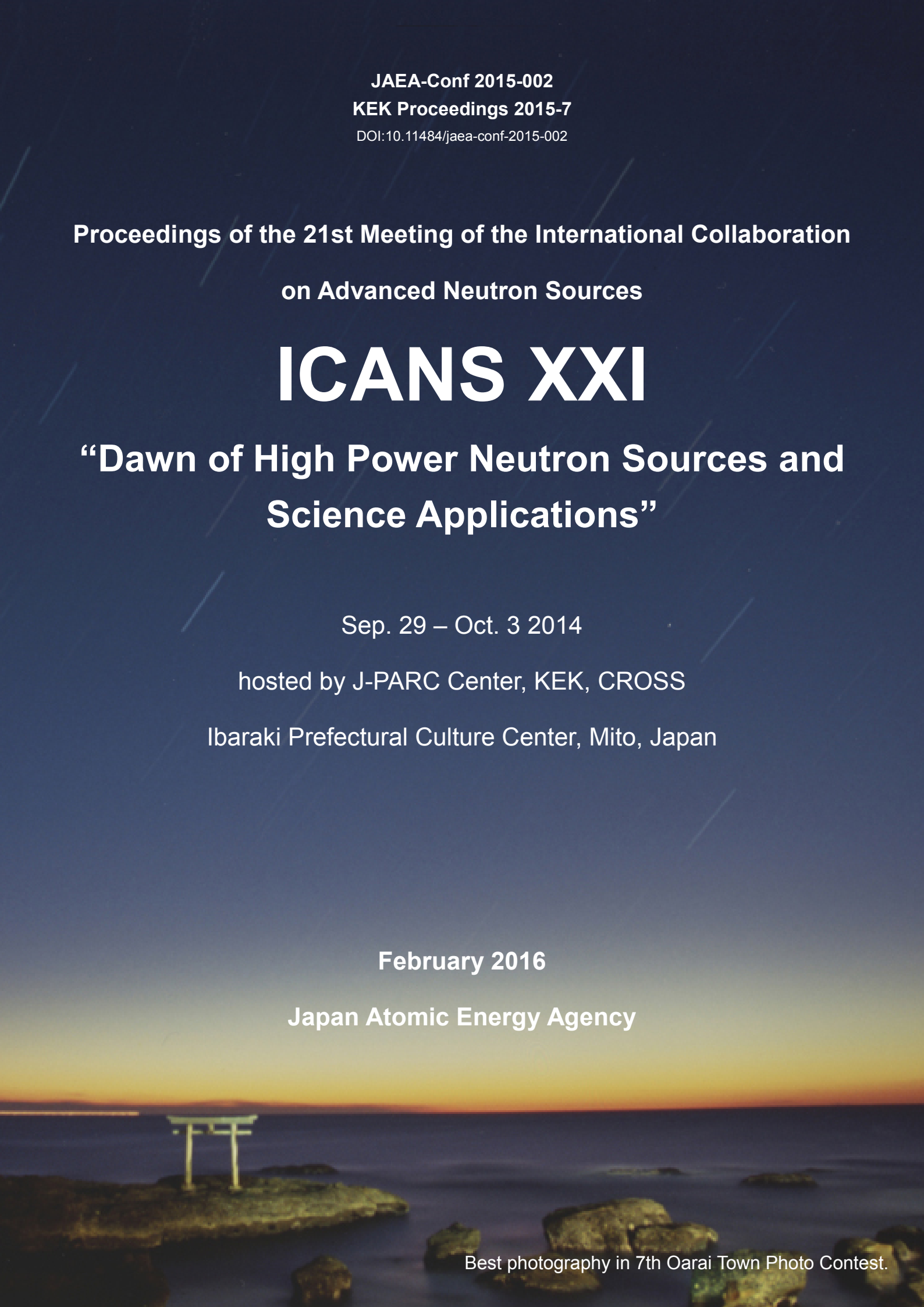

Best photography in 7th Oarai Town Photo Contest.

本レポートは国立研究開発法人日本原子力研究開発機構が不定期に発行する成果報告書です。
本レポートの入手並びに著作権利用に関するお問い合わせは、下記あてにお問い合わせ下さい。
なお、本レポートの全文は日本原子力研究開発機構ホームページ（http://www.jaea.go.jp）
より発信されています。

国立研究開発法人日本原子力研究開発機構 研究連携成果展開部 研究成果管理課
〒319-1195 茨城県那珂郡東海村大字白方 2 番地4
電話 029-282-6387, Fax 029-282-5920, E-mail:ird-support@jaea.go.jp

This report is issued irregularly by Japan Atomic Energy Agency.
Inquiries about availability and/or copyright of this report should be addressed to
Institutional Repository Section,
Intellectual Resources Management and R&D Collaboration Department,
Japan Atomic Energy Agency.
2-4 Shirakata, Tokai-mura, Naka-gun, Ibaraki-ken 319-1195 Japan
Tel +81-29-282-6387, Fax +81-29-282-5920, E-mail:ird-support@jaea.go.jp

Proceedings of

the 21st Meeting of the International Collaboration on Advanced Neutron Sources

ICANS XXI

"Dawn of High Power Neutron Sources and Science Applications"

Sep. 29 – Oct. 3 2014

Ibaraki Prefectural Culture Center, Mito, Japan

Edited by T. Oku, M. Nakamura, K. Sakai, M. Teshigawara,

H. Tatsumoto, M. Yonemura, J. Suzuki and M. Arai

(February, 2016)

This is a blank page.

JAEA-Conf 2015-002
KEK Proceedings 2015-7

Proceedings of the 21st Meeting of the International Collaboration on Advanced Neutron Sources ICANS-XXI

Sep. 29 - Oct. 3 2014, Ibaraki Prefectural Culture Center, Mito, Japan

(Eds.) Takayuki OKU, Mitsutaka NAKAMURA, Kenji SAKAI, Makoto TESHIGAWARA, Hideki TATSUMOTO[*1], Masao YONEMURA[*2], Jun-ichi SUZUKI[*3] and Masatoshi ARAI[*4]

J-PARC Center, Sector of Nuclear Science Research
Japan Atomic Energy Agency
Tokai-mura, Naka-gun, Ibaraki-ken

(Received November 10, 2015)

The twenty first meeting of the International Collaboration on Advanced Neutron Source (ICANS-XXI) was held at Ibaraki Prefectural Culture Center in Mito from 29 September to 3 October 2014. It was hosted by Japan Atomic Energy Agency (JAEA), High Energy Accelerator Research Organization (KEK) and Comprehensive Research Organization for Science and Society (CROSS). In the meeting, new science and technology in the new era with the high power pulsed neuron sources were discussed in mostly "workshop style" sessions. In each session, various kinds of issues related to not only the hardware, but also the software and even radiation safety were discussed with the keyword of "INTERFACE". More than 200 papers were presented in the meeting and 73 contributed papers are compiled in the proceedings.

Keywords : Neutron Scattering, Pulsed Neurons, Target, Moderator, Accelerator

*1 Michigan State University (J-PARC Center until September 2015)
*2 High Energy Accelerator Research Organization
*3 Comprehensive Research Organization for Science and Society
*4 European Spallation Source (ESS) AB (J-PARC Center until March 2015)

JAEA-Conf 2015-002
KEK Proceedings 2015-7

第 21 回「先端的中性子源に関する国際協力」会議（ICANS-XXI）
2014 年 9 月 29 日～10 月 3 日、茨城県立県民文化センター、水戸市

日本原子力研究開発機構
J-PARC センター

（編）奥　隆之、中村　充孝、酒井　健二、勅使河原　誠、
達本　衡輝[*1]、米村　雅雄[*2]、鈴木　淳市[*3]、新井　正敏[*4]

（2015 年 11 月 10 日受理）

第 21 回「先端的中性子源に関する国際協力」会議（ICANS-XXI）が 2014 年 9 月 29 日から 10 月 3 日に、茨城県立県民文化センター（水戸市）において開催された。この会議は日本原子力研究開発機構、高エネルギー加速器研究機構、総合科学研究機構により共催されたものである。会議では、大強度パルス中性子源を用いた新時代のサイエンスや応用研究の展開について、ワークショップ形式のセッションを主体として、ハードウェアからソフトウェア、そして放射線安全に至るまで、"インターフェイス"をキーワードに、さまざまな課題に関する活発な討論がなされた。会議では 200 件以上の発表がなされ、本報文集はその内 73 件の論文をまとめたものである。

J-PARC センター：〒319-1195　茨城県那珂郡東海村大字白方 2-4
*1　ミシガン州立大学（2015 年 9 月迄　J-PARC センター）
*2　大学共同利用機関法人 高エネルギー加速器研究機構 物質構造科学研究所
*3　一般財団法人 総合科学研究機構 東海事業センター
*4　欧州核破砕中性子源有限責任公社 (ESS AB)（2015 年 3 月迄　J-PARC センター）

Contents

目　次

This is a blank page.

Preface to the Proceedings of ICANS XXI.

Since the 1st ICANS meeting was held in 1977 at Argonne National Laboratory in the day of dawn of spallation neutron technique, ICANS has been continuously held already 20 times alternatively among three regions, Europe, America and Asia. The 21st meeting was held at Mito, Japan on 29th September to 3rd October in 2014 in a beautiful autumn weather with more than 250 participants from all over the world.

In the meeting we mostly took “workshop style” session, which is an original and traditional way of ICANS. Actually 2/3 of topics were discussed in the workshop sessions, which were essentially organized/lead by the workshop chairs. Plenary session shows overall issues in a relevant workshop, whose details were talked/discussed in the workshop.

We tried a new challenge in the meeting, and we had two panel discussion sessions. Those were the Integrated Interface session and the Blue Sky session.
In the Integrated Interface session, we had a plenary session in the first morning to show how interface between each component is important to optimize the facility/source. One fault at a single interface can easily degrade the performance of the whole system. There is no unique way to achieve a total optimization, since it depends on different circumstances in the different facility. It is not only the matter of hardware, but software aspects, even radiation safety aspect, can give a constraint/condition to an achievable reality. Therefore, it is quite useful to hear a lesson leant in each facility. In the whole meeting we chose “Interface” as the keyword to take in mind in each workshop.
In the Blue Sky session, we made a brain storming with a free panel discussion. Now the construction cost and operation cost for a spallation source has become enormous, similar to a large high energy experimental facility. Only a large number of general proposals cannot justify the financial burden paid by tax payers, and it is becoming more and more important to show an obvious return/results to the society. It is also important to save energy to effectively produce neutrons by means of any other innovative method. The session participants enjoyed the discussion.

The sector of the spallation neutron is very active in these years. Two on-going construction at ESS and CSNS, new facilities at SNS, J-PARC/MLF and ISIS-TS2, renovation at JINR and rapid progress in compact neutron sources and stable operation at PSI. Although there was an unfortunate shutdown for the user program at Lujan Center, LANSCE, whole community is rapidly growing in the world. Therefore, it was very much informative to have an enhanced facility session.
Last December, we lost very important person, who was one of ICANS initiator, Günter Bauer. His devotion to the development of the spallation source worldwide is extremely appreciated. We all give our sincerest condolence to his passing-away and gratitude for his life-time indispensable contribution to the world neutron science community.

Apart from meeting, the participants enjoyed cultural communication. The venue of the meeting was Mito city, where the 2nd Shogun Family lived for a long period of time during Edo era from 17th to 19th century, when the Tokugawa shogunate ruled the country. There is Kairakuen park by Senba Lake, which is one of the three most famous traditional parks of Japan. Especially plum blossoms in early spring are very famous. The meeting was held in autumn and the sky was very transparently blue, as seen in the group photo, therefore participants enjoyed not only the meeting but after-meeting time.
In the excursion people enjoyed seining, caught a lot of fish and enjoyed BBQ, although the early weather during the event was not preferable for seaside business. Banquet was started with an opening Sake-barrel ceremony followed by Japanese fine foods, Sake and a great Japanese drumming performance. Everyone has very much enjoyed.

At last, here, we extremely appreciate the International Advisory Committee members and the Program Committee members, with whom we made really very intensive communication to build up the scientific program. In one hand, the Local Organizing committee members spent a lot of time to prepare enjoyment, comfort, convenience for participants. We hope those were achieved very well and the participants enjoyed the stay in ICANS-XXI.

27 February 2015
The Chair of ICANS-XXI,
Masa Arai

ORGANIZATION

CHAIRS

Honorary Chair: Noboru Watanabe
Chair: Masatoshi Arai (J-PARC)

ORGANIZERS

J-PARC Center
High Energy Accelerator Research Organization (KEK)
Comprehensive Research Organization for Science and Society (CROSS)

SUPPORTING ORGANIZERS

Atomic Energy Society of Japan
Ibaraki Prefecture
J-PARC/MLF Users Society
Japanese Society for Neutron Science
Particle Accelerator Society of Japan

COMMITTEE

ADIVISORY COMMITTEE

Mark Bourke	(LANSCE)
Colin Carlile	(SVS)
Jack Carpenter	(ANL)
Kurt N. Clausen	(PSI)
Rolando Granada	(CNEA/CONICET)
Alexander Ioffe	(JCNS)
Yoshiaki Kiyanagi	(Nagoya University)
Chun Loong	(ANL)
Robert J. McQueeney	(ORNL)
Feri Mezei	(ESS)
Roger Pynn	(LENS)
Andrew Taylor	(ISIS)
Wagner Werner	(PSI)
Jim Yeck	(ESS)

PROGRAM COMMITTEE

Ken Andersen	(ESS)
Masatoshi Arai	(J-PARC)
Dimitri Argyriou	(ESS)
Dave Baxter	(LENS)
Sasha Belushkin	(JINR)
J. Bermejo	(ESS Bilbao)
Bertrand Blau	(PSI)
Hesheng Chen	(CSNS)
Michihiro Furusaka	(Hokkaido University)

Masatoshi Futakawa	(J-PARC)
Kevin Jones	(ORNL)
Robert McGreevy	(ISIS)
Guenter Muhrer	(ESS)
Toshiya Otomo	(KEK)
Eric Pitcher	(ESS)
Jorg Voigt	(Jeulich)

LOCAL ORGANIZING COMMITTEE

Chair: Masatoshi Arai (J-PARC)
Conference Secretaries: Masatoshi Futakawa (J-PARC) (Chief)
Shinichi Itoh (KEK)
Takashi Kamiyama (KEK)
Shin-ichiro Meigo (J-PARC)
Kenji Nakajima (J-PARC)
Takayuki Oku (J-PARC)
Kenji Sakai (J-PARC)
Kaoru Sakasai (J-PARC)
Hideki Seto (KEK)
Jun-ich Suzuki (CROSS)
Kentaro Suzuya (J-PARC)
Hiroshi Takada (J-PARC)
Makoto Teshigawara (J-PARC)

The 21st Meeting of the International Collaboration on Advanced Neutron Source (ICANS-XXI) from 29 Sep. to 3 Oct. 2014

This is a blank page.

1. Panel Session Reports

This is a blank page.

Blue Sky Session

Panellist; Dimitri Argyriou, Jack Carpenter, Roger Pynn, Henrik Ronnow, Feri Mezei and Andrew Tylor(The Chair)

International advisory committee had discussion that Blue Sky Session is a good idea to have a brain storming discussion.

Colin Carlile; Probably a bigger source after ESS cannot have consensus from funding authority and tax payer, if we go with the same political and technical strategy as what it is. We need one voice to the outside world, especially governments and funding authorities. This is a sort of mandated task for the neutron community.

Roger Pynn; The above process becomes increasingly important now that we have a number of expensive sources that are serving diverse science communities and politicians want to see "results".

Therefore, we chose the people above as panelists moderated by Andrew Taylor and have started discussion with the following items;

Andrew Taylor; We should aim to stimulate discussion over a wide range of topics including (say):

- *(un)realisable future sources;*
- *desirable instrumentation;*
- *exotic sample environments;*
- *challenges and constrains posed by complementary probes;*
- *ultimate scientific perspectives;*
- *affordable facilities*

with each of us being prepared to take a lead on one or more topic.

Colin; As a first suggestion, following an invitation to CERN last month to give a talk "A 50-year perspective on Accelerator needs for neutron sources", it might be useful for ICANS to include such a "blue-skies" session at Mito. It was part of the process that CERN is involved in developing an accelerator strategy for Europe. They are mandated to do that whereas neutrons have no such body. As a community we need to look well ahead and speak with one voice to the outside world, especially governments and funding authorities. All other big science disciplines do this energetically and we in neutrons should do the same.

Roger; I agree with Colin that it would be a good idea for the community to debate how it sees future sources. As Colin says, other scientific fields that depend on large facilities do this so that they can speak with one voice to funding agencies. This becomes increasingly important now that we have a number of new, expensive sources that are serving diverse science communities and politicians want to see "results". It is not easy to deliver an elevator speech that convinces politicians that neutron scattering is important (you can't mention everything in 15 seconds or less).

Günter; With regards to Colin's input about a vision for the future of neutron sources, I perfectly agree that this is a necessity. However, I also sympathize with your and Jack's view that it is unlikely that the present path of going to higher and higher power dedicated sources can be carried any further. This seems unlikely not only for political reasons but also because of the penalty in efficiency one would have to pay. It appears to me that the most important thing one needs is a communicable science concept, which is what has taken high energy accelerators forward in the past and will (hopefully) continue to do so in the future. Of course, as Roger says, it is difficult to convey the importance of neutrons to politicians because of the diversity of fields they are used in. However, this is exactly the point the community has to work on. A thorough discussion about the scientific goals and the needs or viable routes to get there is, therefore, of prime importance. Also, there is nothing as sexy as success, which is why we need to find ways to communicate what has been and is being achieved. Politicians want to see a return for investment! Much of this may be beyond the traditional scope of ICANS, but we should deal with it anyhow.

A photo of the Blue Sky Session

Kurt;
1) The science case is essential even for continued operation of our existing facilities.
2) In order to maintain the "volume" of access necessary to support a sustainable science programme with neutrons, we need to think about cost effective ways of replacing ageing facilities.

Robert; There are many important issues to be discussed about the future of neutrons on a 20 year time scale. We are moving towards having a smaller number of facilities. How do we operate to maintain the size and scope of the user community? Energy costs are becoming prohibitive - what does this mean for future strategy (e.g. high power or low power)? What about completely new technologies, e.g. laser induced wakefield? Why not have a few short presentations (5 minutes) to raise the issues and provoke discussion?

Roger; An issue that cuts across many of the issues you have raised is the following: various governments around the world have ponied up very large sums of money for neutrons over the past decade or so, to the point where the investment is beginning to look comparable to that on high-energy physics. So where is our Higgs boson or, put another way, how are we going to justify to the tax payers of the planet their investment? And the answer had better not be "by getting more users" or any of a variety of other metrics that we tend to use.

Masa; As we discussed above in the meeting and through e-mails, spallation neutron facility is becoming one of the biggest investments not only scientifically but also nationally, regionally and even economically. This dramatic development was fortunately realized probably because of effort by each individual, development of the neutron community, acknowledgement on neutron science, and acceptance by the public. It is, however, very important for neutron scientists not to behave with hubris, and to be faithful to the society, creating innovative scientific achievements and contributions to society as one of responsible tax-payer. The Blue Sky Session was the first demonstration of this kind in the long history of ICANS, and the panelists and audiences were attracted by their own discussion. Although we could not make any unified consensus from the discussions, however, we, the ICANS members, could fairly observe and redefine our present situation in the society and in the world.
We hope this kind of initiative will be continuously pursued in the coming ICANS meetings too.

Integrated Interface Panel Session

A spallation neutron source is similar to a series circuit; the components are connected in series with interfaces between them in a familiar pattern;
Accelerator-Target-Modrator-BeamTransport-Instrument-Detector-Analysis-outcomes.

Any single fault makes a bottleneck and degrades the performance as a whole. Optimization should be done holistically, even though there is no unique solution/way and in each case the result depends on constraints that apply to the facility or region. Therefore, it is a worth studying the lessons learned in each facility (such as ISIS, SNS and J-PARC/MLF) which could help on-going projects such as ESS and CSNS avoid pitfalls that have already been discovered.

We, IAC and program committee, had intensive discussion through internet and we decided the keyword in the coming ICANS should be ***interface***, which should be always kept in mind for each workshops. The session started as a plenary session as the first session in the ICANS-XXI to motivate/stimulate participants with the above concept. But this session was continued by a follow up session in the evening in the same day. Therefore, the program was started in the morning session;

<Morning session on 29 Sep. 930-1030>
Introduction and Provocation; 10min each without question.

1. Roger Pynn presented the past experiences and lessons learned.
2. Feri Mezei presented the past experiences and lessons learned.
3. Sean Langridge gave a short summary of the approach and lessons learned from ISIS-TS2.
4. Ken Andersen summarized the ESS moderator-instruments interfaces and how to best handle these.
5. Garrett Granroth presented instruments - advanced modeling of neutron scattering data at SNS and SNS-TS2, approaching on moderator-instruments interfaces.
6. Hiroshi Takada presented the experiences in J-PARC/MLF.

And the follow up free discussion session in the evening was;

<Evening session on 29 Sep. 1830-2030 >
A panel discussion session
Moderator; Roger
Panelist ; Feri Mezei, Sean Langridge , Ken Andersen, Dimitry Argryou, Robert McGreevy, Garett Granroth, Masa Arai

<Message from the Panel moderator Roger Pynn>

Here are some of the points I raised:

Construction and operation of neutron facilities are both complex activities and have grown more complex over the past decade or so. Because they cost so much to build and to run, it is hard to imagine budgets going up much in the near future -- funding agencies already think they are spending enough on neutrons. To justify this huge expenditure, we need to be very efficient and we cannot afford to take a "not invented here" attitude -- we must collaborate between facilities and leverage our strengths. This is beginning to happen with projects such as Mantid but there are many more opportunities. Industry has long recognized that inefficient interfaces between organizational subunits result in duplication of effort, conflicts and power struggles, groups hiding information, poor customer service and much more. These things are evident in every neutron facility I know to a greater or lesser extent. Industry and the public sector have generated a vast literature on the solution of these types of problems (for example
http://www.commonwealthfund.org/~/media/Files/Publications/Case%20Study/2011/Jul/1528_Edwards_achieving_efficiency_synthesis_four_top_hosps_v3.pdf)
and, as far as I can tell, we are not using it (at least not to any great extent).

Just from my own career in neutrons I have seen many examples: fights over data formats; two electronics groups sabotaging each other's efforts; conflicting cultures between nuclear scientists, accelerator scientists and neutron scatterers; safety bureaucracy that breeds a lack of attention to real safety; direct reports hiding information from their boss. I have selected examples that are sufficiently far in the past that no individuals should feel threatened, but it would be easy to find many further examples. The problems that cause these inefficient behaviors are all fairly typical human foibles. Studies show that ALL employees believe that their own organization performs well and that inefficiency occurs because of poor execution by other departments. The issue always turns out to be communication -- often the illusion that communication has occurred when it really hasn't. While an industrial company’s profit may be affected by lack of communication between, for example, engineers and salespeople, neutron sources simply change the names of the competing groups to things like "target engineers" and "instrument scientists" and replace "profit" with "scientific output". It's time for us to make use of the industrial knowledge about these issues and to become more efficient.

<Messages from Garrett Granroth>

There are a few good examples where collaboration between various neutron sources has worked well. One is the efforts on liquid Hg targets, another is the collaborative work on moderators, and a third is the Mantid software collaboration. All three of these efforts benefit multiple facilities and the work done for each is more than could be done at a single facility. Such collaboration should be the

model for solving problems of critical need to the whole community, like developing non He-3 based detectors.

A few points take away points from my presentation bear repeating.

1) Beware of Panacea solutions. In software, claims are frequently made that a code will do everything. This rarely ends up to be the truth. However, if the code makes life easier, it is better than not having it. So the net goal should be maximize one's return on software work, rather than expecting perfect returns.

2) Insulate against changing hardware infrastructure as much as possible. As a community we relied heavily on DEC hardware and software until about 2000. However it was clear from the mid 80s on, that PCs would become the dominant platform.

3) Avoid the, "this is how it has always been done", syndrome. Our facilities are all about science and innovation, but staying locked into an established way of work can stifle innovation. For example, sticking to histogram data seemed like a prudent idea, because it allowed the use of legacy software. However, moving to event data has enabled new types of experiments and is fostering new thoughts yet.

<Short memo of the discussion and consensus in the Morning and Evening session>

Summarised by Dr. Sean Langridge.

- Holistic, optimised science driven design
    - Strong community involvement
    - Early & strong scientist-engineer-operational interactions
- Active and engaged project management
- International partnerships
    - Proactive
- Software – a key integration technology
- Pipelines
- Importance of staged delivery
    - Instrument delivery into the programme
    - Importance of commissioning plans
- Early engagement with stakeholders

<Conclusion>

We held this kind of panel discussion in ICANS for the first time. We were not aiming to have a consensus from ICANS colleagues, but to have a brain storming on given issues recognized in the community and have a good chance to foster communication and collaboration among participants and facilities. We could have intensive discussion not only among panelists but also with audiences.

We should keep this kind of opportunity even in the coming ICANS meetings to keep the community sincere, vital and active.

This is a blank page.

2. Günter Bauer Memorial

This is a blank page.

IN MEMORIAM GÜNTER BAUER

Our colleague and friend, Günter Siegfried Bauer, died December 13, 2013, 72 years old. It is fitting to remember him here, today, as one of the most respected, beloved, stalwart, influential leaders of our ICANS community.

Günter Bauer during the Cold Moderator Conference at Argonne in 1997.

Günter earned his PhD in Physics at University of Bochum in 1975, spent some time at Oak Ridge National Laboratory, and then joined the scientific staff of Kernforschungszentrum, Jülich (KFZ). There, he undertook work on the Spallation Neutronen Quelle, SNQ, conceived as a 5-MW 1.1-GeV proton linac-compressor-ring neutron source, a joint project of KFZ and KfA (Karlsruhe) pursued from 1980 and presented in 1985. Günter led the target station work, based on a water-cooled rotating target. A prototype tested (without protons) successfully for 1000 hours, which he proudly showed me once, still stands on display.

He moved to the Paul Scherrer Institute (PSI) in the late 1980s, where he took up work on the target for the SINQ neutron scattering facility, an upwardly incidence system based on the steady beam of protons from the 600-MeV sector-focused synchrocyclotron. The SINQ target system was built under his scientific leadership. A steady progression of successively more aggressive target arrangements, accompanied by materials irradiation tests, led to the present “cannelloni” Pb target, which now operates at about 1.5 MW proton beam power. Later, in support of rising

interest in accelerator-driven “energy amplifier” systems, Günter pushed the MEGAPIE developments. The liquid Pb-Bi eutectic target operated successfully at MW power in SINQ for several months.

Günter’s avid interest in liquid metal targets led him to advocate liquid mercury targets for the SNS at ORNL (1.4 MW so far) and for the Material and Life Sciences facility in JPARC (1 MW to come), which are operating successfully. The problem of cavitation erosion in the pulsed source gradually became evident, and Günter worked diligently with others to develop solutions. Progress in that work continues. He took a prominent part in special interest meetings devoted to development of high-power accelerator-based neutron targets.

He tended not only to spallation target questions, but also to moderator questions, especially those of cold moderators. Günter took part in all the international meetings devoted to cold moderators and stimulated development and testing, promoting the building and use of a mockup pulsed source at the COSY synchrotron at Jülich.

Günter did not sit still at home. In early years, he traveled, sometimes with me, to spread the word for accelerator-driven neuron sources. Later, with others of us, Günter served, usually as chairman, on technical advisory committees on all of the accelerator-based neutron source projects, and some of the advanced reactor projects, some of which have been built, others not but not for want of good advice. In those sessions, he guided discussions most effectively, using his broad knowledge of the physics and engineering of sources. If other committee members failed to contribute to committee reports, he himself did the job. In these ways, Günter was a member of the ubiquitous “group of five,” with Tim Broome, Gary Russell, Noboru Watanabe, and me. We of ICANS know of all this, because Günter attended all of the ICANS meetings after 1980, and reported there.

Günter was devoted to his family: wife Gitti, Axel and Karin. When he moved to PSI, he designed and built, doing much of the work himself, a magnificent house on a hillside in Waldshut, Germany, across the Rhine from Switzerland. He equipped his Mercedes camper van with all the needed amenities for off-the-grid living and they traveled a lot. He and his family enjoyed cruising the canals of France, and included Rhonda, my wife, and me on one week-long travel in Alsace; he took patient glee watching me poorly guide our boat through the narrow waterways. Günter was fluent in English and French, and in German, of course, and perhaps also Chinese, whose country he loved and traveled extensively.

Günter was an exceptionally kind person, not only in relation to people, but also to Nature’s wild creatures. “Why did you do that?” he asked me once when I tried to kill a wasp that threatened us once in the PSI guesthouse. I felt ashamed.

And Günter had immense charm. It was almost always Günter who thanked, and arranged flowers, for the hosts and assistants at our meetings.

Now it is our turn to express our admiration and gratitude to Günter, for his long and invaluable service to the neutron science community.

THANK YOU, GÜNTER!

J. M. Carpenter

3. Orals & Posters

This is a blank page.

3-1. Facility Session

This is a blank page.

3.1.1

Progress of the Materials & Life Science Facility of J-PARC

Masatoshi Arai*, Masatoshi Futakawa, Hiroshi Takada, Katsuhiro Haga, Shin-ichiro Meigo, Yasuhiro Miyake[1], Masahide Harada, Kenji Nakajima, Ryoichi Kajimoto, Mitsutaka Nakamura, Kentaro Suzuya, Kaoru Shibata, Jun-ichi Suzuki[2], Shinichi Takata, Takeshi Nakatani, Yasuhiro Inamura, Tatsuya Nakamura, Takayuki Oku, Kazuya Aizawa, Kazuhiko Soyama, Yukinobu Kawakita

Materials & Life Science Experimental Facility, J-PARC Center, Japan Atomic Energy Agency (JAEA), Tokai, Ibaraki, Japan

[1]High Energy Accelerator Research Organization (KEK), Oho, Tsukuba, Japan,

[2]Comprehensive Research Organization for Science and Society (CROSS), Tokai, Ibaraki, Japan

E-mail: masatoshi.arai@j-parc.jp

Abstract. The facility has resumed since 17th February 2014 after reformation of operation safety system required from the new regulation because of the accident in the Hadron Facility occurred in May 2013. During eight-month shutdown period various hardware components have been improved; such as installation of additional RFQs in Linac to increase its energy to achieve higher power, repairing and replacement on the mercury(Hg) cooling loops of the neutron target, improvement on the cryogenic system for stable operation, etc. In order to mitigate the pitting damage on the Hg-target container we have been injecting helium micro bubbles in the target. The Laser Doppler vibrometory showed us that vibration amplitude on the proton bombardment has been drastically reduced by the injection.

Twenty one instruments have been already installed. Eighteen instruments are operated for user program and three instruments are under either commissioning or construction. Now the experimental hall is almost full with instruments, leaving only 2 ports available for the future use. Operational time for user program in JFY2014 was about 170 days, and we received more than 700 general experimental proposals from users.

World-class scientific outputs have been being created in various scientific fields, ranging from Li-battery science to bio-molecular science. Since J-PARC is internationally open for users, we have got experimental proposals from abroad more than 15% of the whole proposals. More than 10% of proposals have come from industries and a half of them are proprietary use. This fact has revealed a new horizon has come in the neutron scattering science in the 21 century.

1. Introduction

The J-PARC facility was funded by the Ministry of Education, Culture, Sports, Science and Technology (MEXT), and was jointly constructed by the High Energy Accelerator Research Organization and the Japan Atomic Energy Agency. J-PARC Materials & Life Science Experimental Facility (MLF) is a spallation pulsed neutron and muon facility, whose final power will be 1MW, operated at 25Hz. It ran at 300kW until before the summer shutdown since it resumed on 17 February 2014 from the shutdown due to the accident in the Hadron Facility occurred in May, 2013. MLF is a user facility for not only domestic but international users and even for industrial researchers. Unique user's number will be exceeded more than 1000 in JTY2014 with steady increase every year. Operation cycle is about 170days in a year and call for proposal is announced twice a year. We have received more than 700 general proposals in JFY2014.

2. Target Improvement for High Power

Fig.1 The Mercury target station of MLF.

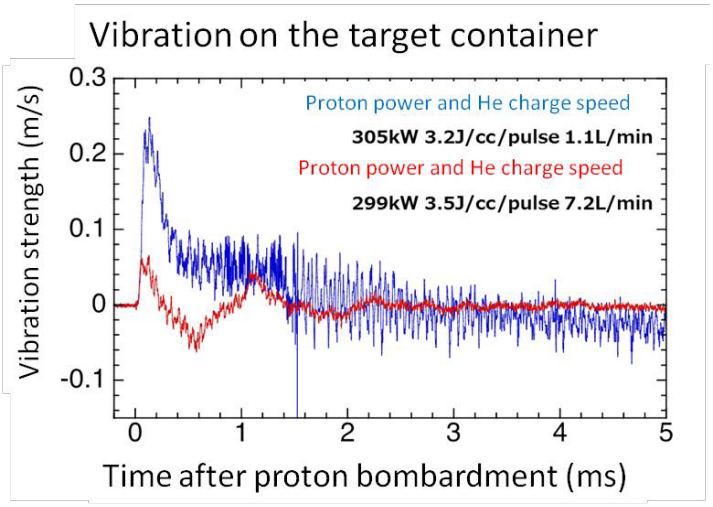

Fig.2 Vibration intensity at the target container with helium gas bubbling in a different charging speed.

2.1 Helium Bubble Injection

As it is a well known problem, "Pitting Problem", on the mercury target container is still a key issue to be settled down before ramping up the accelerator power. (Fig.1). High power proton bombardment creates cavitation in the mercury target followed by an instantaneous shock wave, which makes a serious damage on the internal surface of the target container, so called the pitting damage. In order to mitigate this problem, we have injected helium gas bubbles in the mercury flow [1]. The helium gas goes through a swirler making a mercury flow turbulence, which breaks the gas into small segments and makes micro bubbles, 100 μ in diameter. We have monitored the behavior of the container with a laser Doppler vibrometry method and found a drastic reduction of a vibration of the container on the proton bombardment. Figure 2 shows the observed vibration amplitude on the target container. There is a clear decrease for a higher gas density (charging speed).

Fig. 3 Octapole magnet installation for flattening the beam

In order to confirm the actual status of the pitting damage, we cut out the top portion of the target container during the summer shutdown, which experienced 2000MWh proton bombardment. We observed that the internal surface of the container does not have any obvious pitting damage although the exposed cumulated power is closing to the expected life time estimated from the radiation damage[2].

2.2 Installation of an Octupole Magnet

In order to reduce peak heat deposition in the target we have installed an octupole magnet which flattens the proton beam profile and can reduce the peak power as shown in Fig.3 [3]. Proton beam profile monitor has shown a flattened profile or a plateau shape profile modified from the original Gaussian profile by the magnet. We are now planning to estimate the effect from the flattened profile on the neutronics performance by a calculation code PHITS.

2.3 History of Beam Power at MLF

Figure 4 shows the history of the beam power at MLF since it started its operation in 2008. The beam power has been ramped up in step wise and reached at 300kW although there were two long shutdowns due to the disaster in 2011 and the accident in 2013. We have replaced the target two times to study the pitting damage during each long shutdown. We have started the gas injection since the end of 2012 when the power increased to 300 kW. We ran with 532 kW but for a very short period in 2012 to test an intrinsic ability of the accelerator, and it was successful.

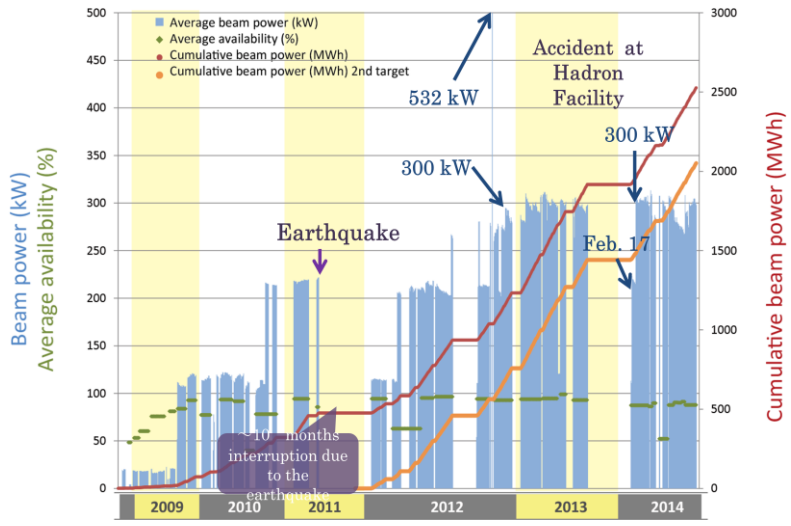

Fig.4 The history of the beam power at MLF.

3. Instrument Suite at MLF

3.1 Status of Instruments

MLF has 23 neutron beam ports and four muon ports [4]. Now 21 neutron instruments have been installed. 18 are in use for user program. Two instruments are under construction. Those are a spin echo instrument at BL06 and a polarized neutron instrument at BL23. One, an imaging instrument at BL22, is under commissioning. Two beam ports are empty and available for a future use, BL07 (poisoned decouple moderator), and BL13 (coupled moderator). Currently one muon beam port is in use for user program and three ports are under construction. Those are an ultra-slow muon channel, a surface muon channel and a high momentum muon channel.

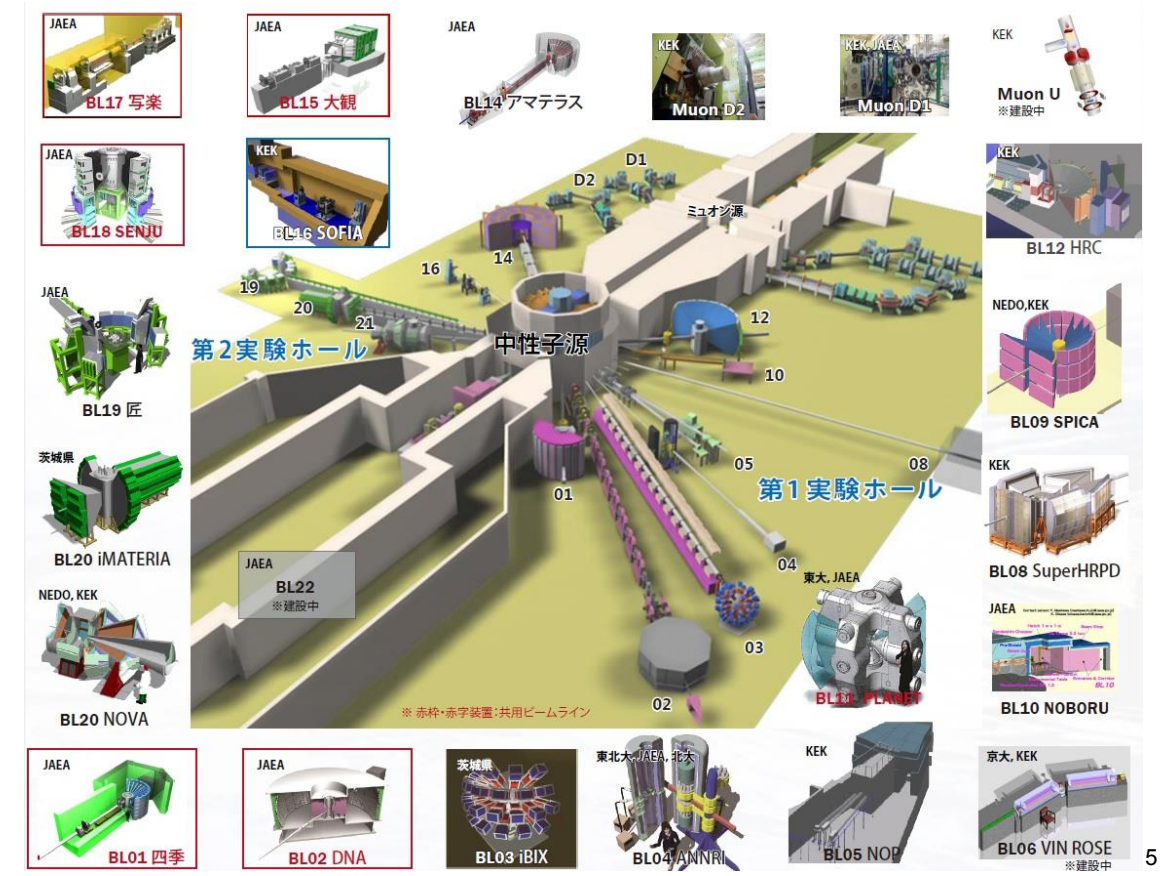

Fig. 5 Instrument arrangement in MLF

Figure 5 shows instrument arrangement in the facility. The instrument suite has been selected and constructed according to a requirement of the neutron community. All of the instrument were proposed and reviewed by the instrument selection panel. There are four organizations to operate those instruments. Those are KEK, JAEA and Ibaraki Pref., which is the local municipality, and CROSS. User program of the public beam lines are operated by a registered institution to the government (CROSS). The public beam line was built and owned by JAEA under the legislation for promoting user support/program of MLF, and its user support is done by the registered institution, CROSS. Ibaraki Prefecture owns two instruments, BL03 and BL20, to facilitate industrial use of neutrons. Two instruments, BL09 and BL20, were built by the Ministry of Economy, Trade and Industry to promote an intensive battery study and fuel cell study. Those are, however, opened for general users now. Table I summarizes the neutron instrument suit of MLF.

All of muon ports have been constructed by the KEK muon group and in use for inter-university program, and the general user program is operated as the MLF user program. This situation is the same as that of KEK owned neutron instruments. Currently only one port for decay muon channel is available for users. It is either D1(μ^+) or D2(μ^-) channel with an energy range of 30 MeV. Now Ultra-slow muon (μ^+) channel is under commissioning, which can provide very low energy muons in a rage from 50 eV to 60 keV to study surface magnetism. S-line is a new beam line under construction for the surface μ^+. H-line will be used for fundamental/nuclear physics experiment and under construction. Table II summarizes the muon channels of MLF [5].

Table I Neutron beam lines of MLF

BL no.	name		Owner	
BL01	4SEASONS	Fermi chopper instrument	JAEA	Public BL
BL02	DNA	Back scattering instrument	JAEA	Public BL
BL03	iBIX	Protein crystal diffractometer	Ibaraki Pref.	
BL04	ANNRI	Neutron cross section measurement instrument	JAEA	
BL05	NOP	Fundamental physics instrument	KEK	
BL06	VIN-ROSE	Spin echo instrument	KEK	
BL07	Empty			
BL08	SHRPD	High resolution powder diffractometer	KEK	
BL09	SPICA	Powder diffractometer dedicated for battery study	KEK	
BL10	NOBORU	Test port	JAEA	
BL11	PLANET	High pressure diffractometer	JAEA	Public BL
BL12	HRC	High resolution chopper instrument	KEK	
BL13	Empty			
BL14	AMATERAS	Cold disc chopper instrument	JAEA	
BL15	TAIKAN	Small and wide angle diffractomenter	JAEA	Public BL
BL16	SOPFIA	Horizontal surface reflectometer	KEK	
BL17	SHARAKU	Vertical surface polarized neutron reflectometer	JAEA	Public BL
BL18	SENJU	Single crystal diffractometer	JAEA	Public BL
BL19	TAKUMI	Engineering diffractometer	JAEA	
BL20	iMATERIA	High intensity powder diffractometer	Ibaraki Pref.	
BL21	NOVA	Liquid-amorphous diffractometer	KEK	
BL22	RADEN	Energy resolved imaging station	JAEA	Public BL
BL23	POLANO	Polarized neutron inelastic scattering instrument	KEK	

Table II Muon beam channels of MLF

Name		Owner
D1, D2 lines	Decay muon-channel	KEK
U-line	Ultra slow muon channel	KEK
S-line	Surface muon channel	KEK
H-line	High momentum muon channel	KEK

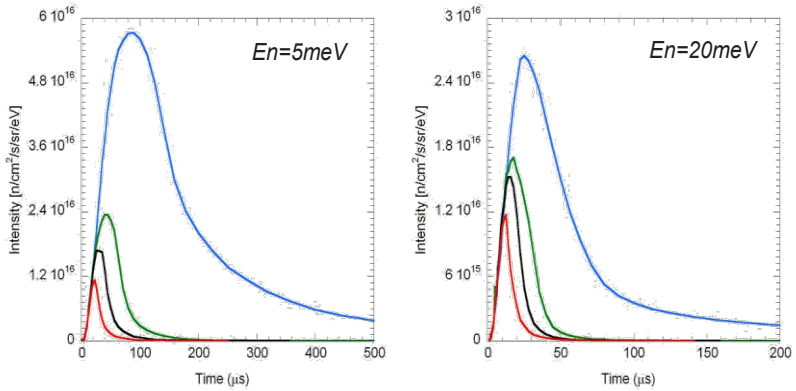

Fig. 6 Pulse peak structure at 5 and 20meV for Coupled moderator; blue, decoupled moderator; green, poisoned decoupled moderator; black and red (font and back surface)

3.2 Some Performance of Instruments [6]

The target station has three kinds of moderators as shown in Fig.6. The coupled moderator is very intensive, but has a broad peak structure. Decoupled one is good for high resolution instrument with sharp pulse structure but sacrificing intensity. Poisoned decoupled moderator has a sharper pulse structure and less intensity, and it is used for extremely high resolution instrument such as very high resolution powder diffractometer [7]. The energy of neutron is commonly analyzed by the time-of-flight of neutrons going through a flight path in a pulsed neutron source. Hence it is a natural consequence that a sharp pulse structure of neutron with a long flight path for instrument is necessary to realize a high resolution instrument. However, this traditional concept has been dramatically improved in the design work for instruments in MLF.

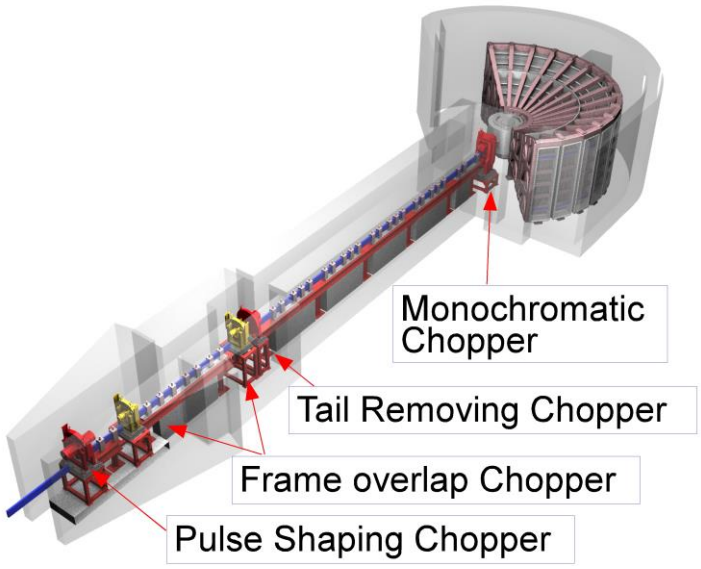

Fig. 7 Illustration of AMATERAS. Pulse shaping chopper cut out an intensive peak from a broad pulse of a coupled moderator.

One of good examples has been demonstrated in AMATERAS [8], in which a pulse shaping chopper has been implemented to cut out an intensive peak portion from the broad peak from the coupled moderator. This innovative concept has been firstly demonstrated by Feri Mezei group [9] and becomes a world trend for cold disk chopper instrument such as CNCS [10] at SNS and LET [11] in ISIS. Figure 7 shows an illustration of AMATERAS. A pulse shaping chopper makes a sharp and symmetrical shape pulse, and behaves as a virtual pulsed source instead of the actual moderator. A monochromatic chopper makes energy selection. Frame overlap choppers and a tail removing chopper suppress unwanted neutrons. Energy resolution can be tunable by choosing a pulse width at not only the monochromatic chopper but also the pulse shaping chopper, hence instrument becomes very much flexible on the resolution and intensity adjustable for various kind of measurements. A similar technique has been also adopted for the DNA instrument (Fig.8). DNA is a

backscattering spectrometer and scattered neutron energy is analyzed by a crystal. An observed example is depicted in Fig. 9, in which tunneling spectrum obtained from γ-Picoline is depicted for two different conditions with or without pulse shaping chopper operation. It is clearly shown that the energy resolution can be also flexibly tunable in a measurement.

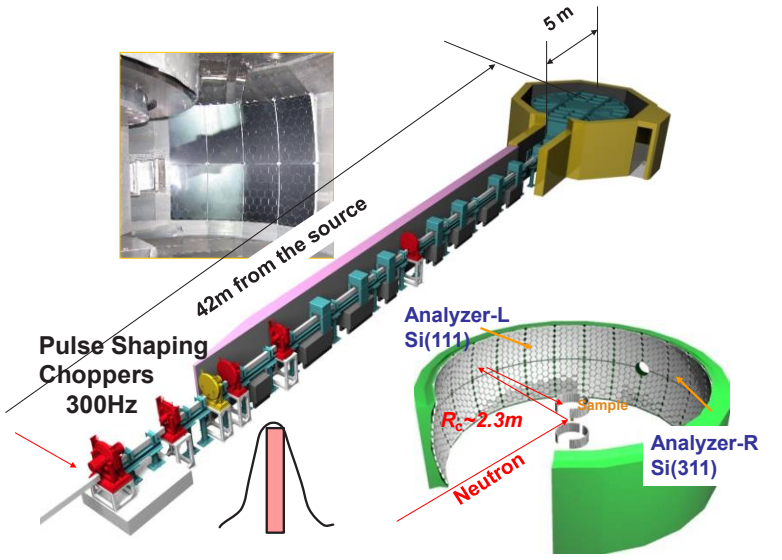

Fig. 8 DNA spectrometer. Pulse shaping chopper cut out a sharp peak band and the scattered neutron is analysed by a Si-crystal in the back-scattering geometry.

We have also developed so called multi-Ei method, in which multiple incident energies can be utilized in one time for a set-up for an inelastic scattering experiment. Therefore, spectrum observed with several different incident energies are automatically obtained. The method is very effective to make a survey in the different energy scales to find an unknown phenomena [12].

At pulsed neutron source we can utilize white beam and the neutron energy is analyzed by the time-of-flight method. Therefore, we do not need to scan scattered neutrons by moving detector angle. Instead detector can be fixed at angles. Therefore we can arrange detector banks at various scattering angle as much as we can afford as shown in Fig. 10 as an example for TAIKAN. With this detector arrangement TAIKAN can cover a very wide coverage in the momentum space from a small angle region to 20 $Å^{-1}$ in one measurement. An example on glassy carbon is depicted in Fig.11. The result shows from the small angle region to diffraction range with a very reasonable agreement with a result from APS in the absolute intensity [13].

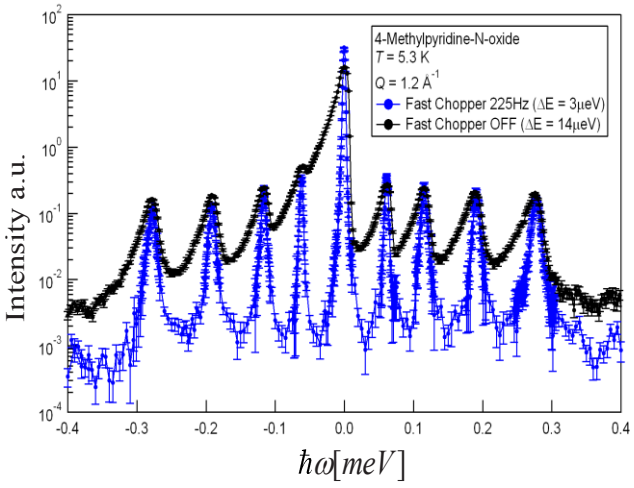

Fig. 9 Tunnelling spectrum form γ-Picoline with/without pulse shaping chopper. The resolution is about 3μeV/15μeV for each case.

NOVA also showed a very quick measurement on a SiO_2 glass sample. S(Q) ranging from 0.2 to 40 $Å^{-1}$ can be obtained in one second with a good statistics at 100kW in the accelerator power.

MLF has introduced an event recording data acquisition system as the standard system for the first time as a neutron facility [14]. In this system, neutron is counted/recorded with information when, where and

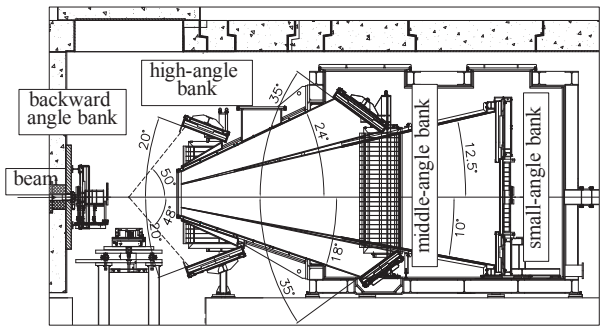

Fig.10 Detector arrangement of TAIKAN, small and wide angle diffractometer.

how the neutron was recorded one by one with relevant information such as temperature of sample, goniometer angle, even a rotation phase of a chopper system. Hence one event record contains many relevant information altogether. Once those information is recorded with neutron event, therefore, experiment can be done even with a continuous temperature scan, continuous goniometer rotation, etc. Data analysis can be done after experiment by choosing the data, which exist within required conditional limits such as sample temperature, goniometer angle, etc. As an extension, we can make a real time measurement of a transient phenomenon or an in-situ experiment as a routine experiment in any instrument in MLF.

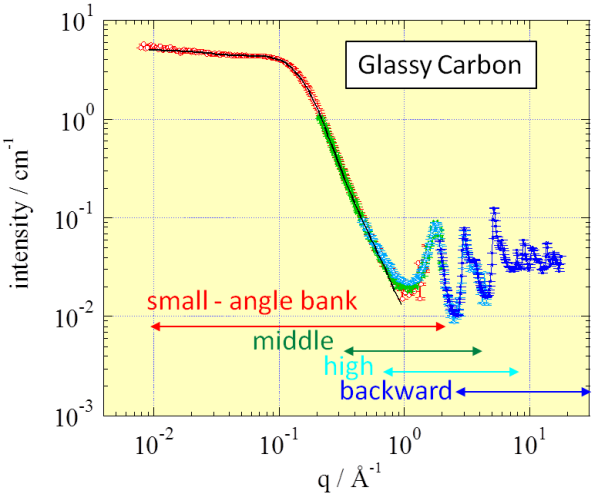

Fig. 11 Example of data of Glassy Carbon observed on TAIKAN. The data is comparable in the absolut scale with that obtained in APS.

4. Research and Development on Devices

4.1 Detector Development at MLF

We have been developing scintillation detectors since before starting the construction of the facility. One of the most intensively developed systems is a wave-length-shift-Fiber system (WLSF).

This type of scintillation detector can have a two dimensional array of light guides, which shift the wave length of initially created scintillation light on the neutron absorber, and the shifted light can easily transmit along the fiber to photo-multiplier-tube (PMT) effectively. The spatial resolution can be mainly determined by the separation of the light guide so that the resolution can be easily tunable and can have good resolution less than 1mm [15, 16]. The event position is determined by using a direct encoding technique with multi-anode PMT's. Newly developed sintered ceramic scintillator material, $ZnS/^{10}B_2O_3$, improved detecting efficiency, gamma sensitivity and afterglow at the same time [17]

We are now implemented those detectors in iBIX(1.2mm resolution) [18], SENJU(4mm resolution) [19] and SHARAKU (4mm resolution) [20] as shown in Fig.12

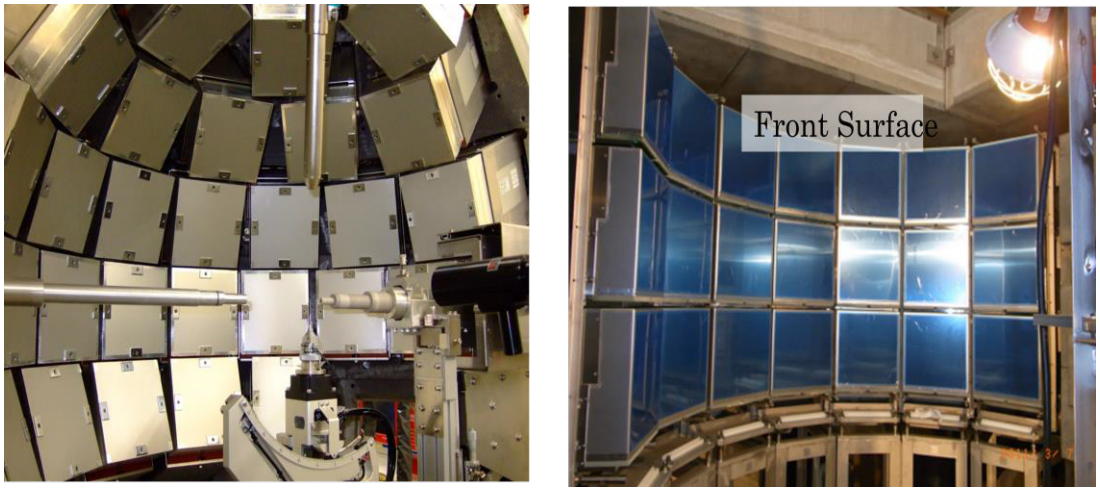

Fig.12 WLSF Detector system of iBIX V(1.2mm resolution) and SENJU (4mm resolution).

4.2 ^{3}He Spin Filter Development

We are developing a ^{3}He Spin Filter by utilizing the spin exchange optical pumping method (SEOP) [21]. Our development on the spin polarization was far behind from other facilities in the past, however, we have recently developed a very compact setup with a compact laser-optical system, and the ^{3}He polarization has exceeded more than 70%. Hence, the equipments are now good enough for a practical use in experiment. We have already tested them on TAIKAN and SHARAKU and obtained a very reasonable performance in the experiments.

5. Scientific outcomes

5.1 General Proposals to MLF

We call for general proposals twice a year. Since we had disaster and accident, we could operate the facility stably only in 2012. In Fig. 13 we show a statistics of proposals each half year. The number of the proposals is steadily increasing each year regardless the difficult situation in 2011 and 2013. Total number of proposals in 2014 is closing to 700. The trend of the increase of the proposal almost follows the increase in the accelerator power and we expect that proposal will be 1500 when we can have 1MW in the accelerator power with more than 2000 unique users number. Proposals from universities are about 45%, 16% from abroad, 10% from industries in 2014. The over subscription rate is about 1.7. This is a healthy competition rate, although a specific instrument has a very high rate more than 3.0.

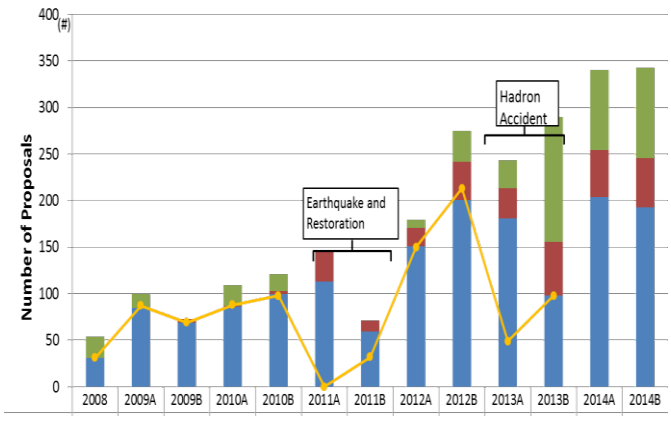

Fig.13 History of the general proposals to MLF. Blue; accepted, Brown; Reserved, Green; not accepted, Yellow; executed proposals.

The number of published papers for each instrument is depicted in Fig.14. The number is not high enough in

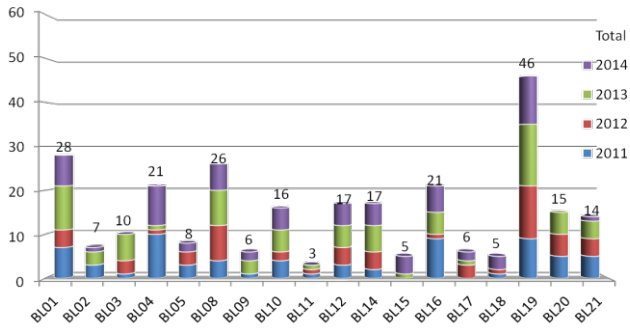

Fig.14 Number of publication for each instrument through year

comparison with a benchmark in the world class facilities yet, and further effort is necessary to catch up with them.

6. Conclusion

The MLF facility has been well developed regardless of the disaster and accident, and is well in use for a user program. The ability of the facility is steadily increasing in accordance with the improvement of the accelerator power. MLF has already reached in a world class level, although further efforts will be definitely necessary.

Acknowledgments

We acknowledge all of the MLF staffs to keep the facility operation stable and effective for the user program. This report is an extended version of a proceedings paper on J-PARC symposium held on July 2014, Tsukuba [22]

References

[1] Masatoshi FUTAKAWA, Hiroyuki KOGAWA, Shoichi HASEGAWA, et al.,
Journal of NUCLEAR SCIENCE and TECHNOLOGY, Vol. 45, No. 10, p. 1041–1048 (2008)
Masatoshi Futakawa , Katsuhiro Haga, Takashi Wakui, Hiroyuki Kogawa, Takasahi Naoe
Nuclear Instruments and Methods in Physics Research A 600 (2009) 18–21
[2] JAEA-Tech 2004-001/ KEK Report 2004-03 (2004) in Japanese.
[3] S. Meigo, M. Ooi, K. Ikezaki, A.Akutsu and H. Fujimori,
MOPRI116, Proc IPAC2014 Dresden, Germany (2014).
[4] *http://j-parc.jp/researcher/MatLife/en/instrumentation/ns.html*
[5] Y. Miyake, K. Shimomura, N. Kawamura, P. Strasser, A. Koda, S. Makimura, H. Fujimori, et al.,
Physics Procedia 30 (2012) 46–49.
[6] Masatoshi Arai, Ryoichi Kajimoto, Mitsutaka Nakamura, Yasuhiro Inamura, et al.,
J. Phys. Soc. Jpn. 82 (2013) SA024 (14 pages)
[7] Tetsuya Kai, Masahide Harada, Makoto Teshigawara, Noboru Watanabe, Yujiro Ikeda
Nuclear Instruments and Methods in Physics Research A 523 (2004) 398–414
[8] Kenji Nakajima, Seiko Ohira-Kawamura, Tatsuya Kikuchi et al.,
J. Phys. Soc. Jpn. 80, SB028 (2011)
[9] M. Russina, Gy.Kali, Zs.Santa, F.Mezei
Nucl. Inst. Meth. Phys. Res. A 654 (2011) 383-389
[10] G. Ehlers, A. A. Podlesnyak, J. L. Niedziela, E. B. Iverson, and P. E. Sokol:
Rev. Sci. Instrum. 82 (2011) 085108.
[11] R. I. Bewley, J. W. Taylor, and S.M. Bennington:
Nucl. Instrum. Methods Phys. Res., Sect. A 637 (2011) 128
[12] Mitsutaka Nakamura, Ryoichi Kajimoto, Yasuhiro Inamura et al.,

Journal of Physical Society of Japan, 78 (2009) 093002-1 – 093002-4,
[13] Shin-ichi TAKATA, Jun-ichi SUZUKI, Takenao SHINOHARA, Takayuki OKU, et al., Proceedings of the J-PARC Symposium 2014 (JPS Conference Proceedings)
[14] T. Nakatani, Y. Inamura, T. Ito, K. Moriyama and T. Otomo: JPS Conf. Proc. 1, 014010 (2014)
[15] M. Katagiri, et al., Nucl. Instr. & Meth. A, 529 (2004) 313
[16] T. Nakamura, et al., Nucl. Instr. & Meth A, 600, 164-166 (2009)
[17] T. Nakamura, et al., J. Phys.: Conf. Ser., 528, 012043 (2014)
[18] I. Tanaka, et al., Proc. ICANS-XVII, 17th Meeting of the International Collaboration on Advanced Neutron Sources, April 25-29, 2005, Santa Fe, New Mexico, LA-UR-3904 (ICANS-XVII proc.),937-945 (2006),
T. Hosoya, et al. Nucl. Instr. & Meth. A, 600 (2009) 217.
[19] I. Tamura, K. Oikawa, T. Kawasaki, T. Ohhara et al., Journal of Physics: Conference Series, 340 (2012) 4 ,
T. Kawasaki, et al., Nucl. Instr. & Meth. A, 735, 444-451 (2014)
[20] Masayasu Takeda et al., Chinese J.of Phys. Vol.50, 2012, 161-170
[21] Takayuki OKU, Hirotoshi HAYASHIDA, Hiroshi KIRA, Kenji SAKAI, et al., Proceedings of the J-PARC Symposium 2014 (JPS Conference Proceedings)
[22] M.Arai et al., Proceedings of the J-PARC Symposium 2014 (JPS Conference Proceedings)

3.1.2

New Sorgentina Fusion Source (NSFS) experimental facility supporting materials research

P. Console Camprini[1], P. Agostini[1], D. Bernardi[1], M. Angelone[2], M. Frisoni[3], A. Pietropaolo[2], M. Pillon[2], A. Pizzuto[2]

1 ENEA Brasimone Research Center, 40032, Camugnano (BO), Italy
2 ENEA Frascati Research Center, via E. Fermi 45, 00044 Frascati (Roma), Italy
3 ENEA Bologna, via Martiri di Monte Sole 4, 40129 (BO), Italy

***Corresponding author**: antonino.pietropaolo@enea.it

Abstract. Within the framework of fusion technology research and development, a neutron source has long been considered a key facility to perform irradiation tests aiming at populating materials engineering database – supporting DEMO reactor design and licensing. New Sorgentina Fusion Source (NSFS) has been proposed taking advantage of well-established D-T neutron generators technology, scaled in order to attain a bright source of about 10^{15} n/sec. The provision of an actual 14 MeV neutron spectrum, resembling that of a D-T fusion machined, is a relevant feature. In this contribution, the main facility characteristics are provided, together with a brief discussion on target thermal and mechanical issues.

1. Introduction

Materials testing with fusion relevant neutron source is essential to DEMO design in order to cope with technical (nuclear damage) and regulatory (licensing) issues. In the European roadmap to fusion energy [1-2], testing of materials are scheduled by 2026 up to the following radiation levels: damage of 30 dpa for structural steels, 10 dpa for copper and tungsten. On the other hand, nuclear materials testing is required for a broad range of components e.g. those for auxiliaries and diagnostic.

In this context, the NSFS project provides a potentially unique tool. Indeed, the 14 MeV neutron spectrum offered by Sorgentina facility will closely resemble that of a fusion machine like DEMO, thus providing a very important tool to calibrate and validate displacement per atom (dpa) accumulated in other irradiations facilities such as more readily available fission and accelerator-based facilities. These unique features strengthen strategic relevance for Sorgentina proposal, even within the framework of future powerful plants offering fusion-like spectrum but not exactly DT fusion 14 MeV neutron flux spectrum. The envisaged DT neutron flux spectrum of Sorgentina indeed aims at allowing the study of the influence of nuclear transmutation on the electric characteristics of ceramic insulators, optical fibers, window materials and superconducting cables, selection and test of low activation materials, populating nuclear database and damage cross-section data as well as validation of numerical model simulations. Moreover it will enable to carry out basic studies on neutron damage to materials irradiated with 14 MeV neutrons to validate damage calculation codes and provide a neutron field where damage cross-sections can be tested and/or measured. It would furnish reliable data about the radiation hardness of materials to be used for diagnostics and produce neutron flux and

spectra similar to that expected in a tokamak in order to allow for 1) nuclear diagnostics calibration under real spectra, 2) reliable test of electronics equipment and components to be used for diagnostics, remote handling etc. The intense 14 MeV neutron flux will allow to investigate tritium production assessing the behavior of breeding materials working under reactor-like condition as well as methods for tritium handling, extraction and on-line measurement.
Neutron flux spectra and intensities required for materials irradiation must be sufficient to study material damage process. In fact, degradation phenomena such as irradiation creep, volumetric swelling and phase instabilities approach saturation at damage levels above 10 dpa [3].
Material embrittlement onset is more difficult to define. Displacement cascade - consisting in the migration of vacancies and interstitials – produce segregation phenomena, micro-structural evolution, dislocation climb and voids creation. All these processes induce irradiation hardening and embrittlement at relatively low temperatures. By contrast, creation of voids and dislocation climbing produce swelling and irradiation creep – which occurs for doses higher than 10 dpa at higher temperatures.
With a proper design and optimization of the layout, other possible activities of interest in other fields are, for example, irradiation of electronics chips and frontend electronics, neutron imaging (with proper moderation of source neutrons), materials neutron activation studies as well as tests on components for sources large scale neutron facilities.

2. NSFS main components

Sorgentina main design and key feature is the strategy of matching a well-proven neutron source type with existing technology, in an innovative plant concept which makes this source much brighter compared to previously realized facilities [4]. Deuterium-Tritium fusion reaction is currently used in industrial neutron generators in which ion source and accelerator are coupled to a D-T enriched target which turns out to be a planar 14 MeV fusion neutron spectrum source. Sorgentina design concept relies upon ion source and accelerator stages from neutral beam injector devices already utilized at large experimental tokamaks [5] together with a properly scaled rotating target technology. Twofold water-cooled rotating target of about 2 m radius is operated at rotational speed of about 1000 rpm. Inlet fluid flow of some 110 lit/sec is inserted at about 50°C bulk temperature, 8 MW thermal power per target has to be removed – 16 MW total power being deposited onto the whole target. D & T ion beams are delivered to two rotating targets facing each other. Total ion current per each target is about 40A, 20A from deuterium and 20A from tritium. Beam energy is about 200 keV to optimize fusion reaction probability following the reaction $D + T \rightarrow {}^{4}He + n + 17.6MeV$. Ion beams impinge on both sides of a double wheel target where 14 MeV neutrons are generated. The schematic of Sorgentina is sketched in Figure 1. Three irradiation volumes are foreseen to accommodate: small specimens (0.5 l) at high flux; small material/components samples (1.2 l) at intermediate flux; larger volume (several litres) for small mock ups at lower flux.

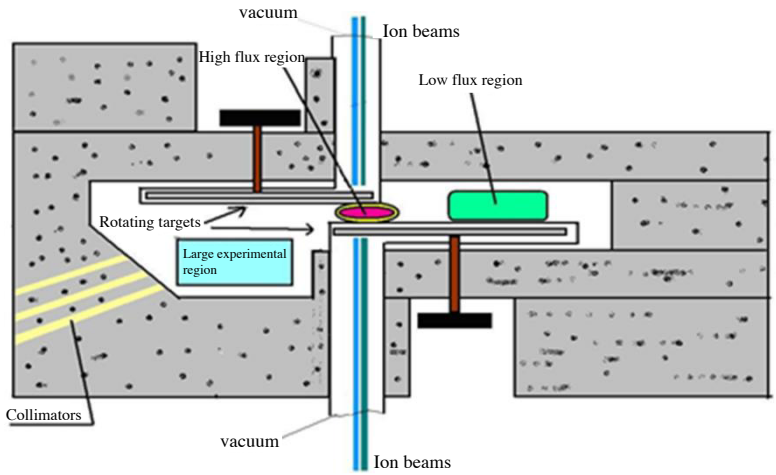

Figure 1: *Layout of double-plate target showing: ion beams on both sides, 0.5 litres irradiation volume in-between and larger irradiation volumes*

Gap between neutron source plates is intended to measure about 3 cm. Irradiation rigs are designed to accommodate specimens in about 2 cm accounting for rotation and mechanical fabrication uncertainty sizes. Sorgentina design results in a very compact layout. In Figure 2, the assembly of the Sorgentina system is shown.

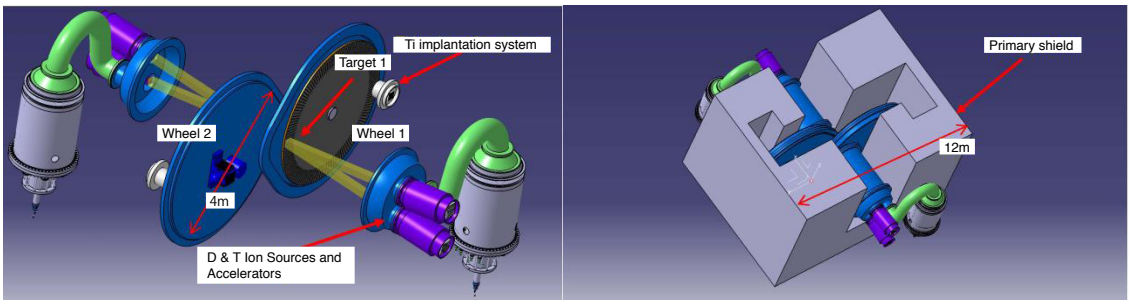

Figure 2: *(a) Layout of double targets showing: ion beams on sides; (b) Sorgentina embedded in the primary neutron shield.*

2.1 Thermal and Mechanical Design

Preliminarily thermomechanical evaluation of target performances were carried out analysing a slice of the interacting plate - using a 2D plain strain finite element (FE) model implemented through the free software package CALCULIX [6]. Only one half of a single tube was modelled due to periodic and symmetry conditions. The heat power deposited by the beam into the metal hydride layer was simulated by imposing a pulsed heat flux on the exposed face with a maximum value of 400 MW/m^2. A water coolant pressure of about 30 MPa was applied on the tube internal surface, corresponding to the maximum pressure induced by the centrifugal forces at the top of the plate (assuming a height of 250 mm) plus the hydraulic head of the circulation pump. A conservative value of 40 kW/m^2/°C for the coolant heat transfer coefficient was adopted. Table 1 summarizes the geometric and operating design parameters. The material properties of CuCrZr-IG specified in the ITER Structural Design Criteria for In-Vessel component (SDC-IC) [7] were used in the analysis. The presence of the hydride layer was properly taken into account in the model.

Table 1: *Geometric and operating parameters of the target*

Heat flux	400 MW/m^2
Rotational Speed Water pressure	1000 rpm 30 MPa
Wheel radius	2 m
Plate height	250 mm
Tube diameter	2 mm
Rotation period	60 ms
Beam-plate interaction time	0.48 ms
Heat transfer coefficient	40 kW/m^2 °C
Inlet water temperature	10 °C

Starting from the initial condition, a certain number of beam pulses were applied until the temperature history repeated identically at every cycle. The hydride temperature evolution within the cycle once that equilibrium condition was reached is shown in Figure 3. A maximum value < 300 °C, well below the critical value of 400 °C, is found. It is acceptable from the point of view of hydride stability and tritium retention.

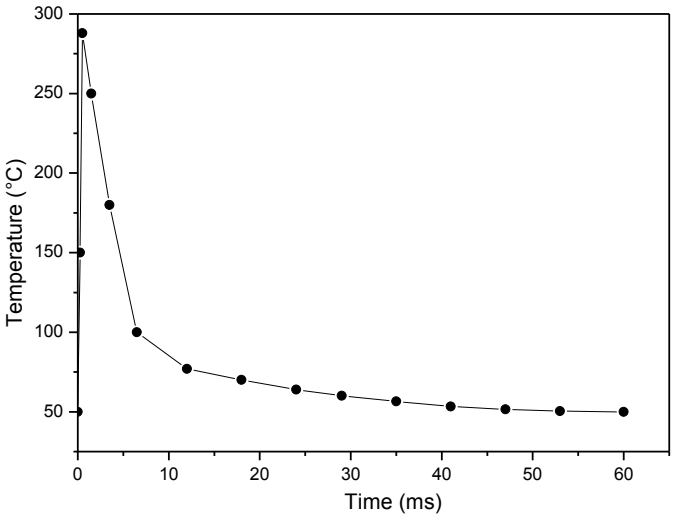

Figure 3: *Hydride temperature evolution within the cycle*

The maximum Tresca stress in the tube area is around 66 MPa (Figure 4), which is safely lower than the minimum allowable stress of the material at the temperature experienced by the tube (~110 MPa at 180 °C), thus proving that the global structural integrity of the plate is assured.

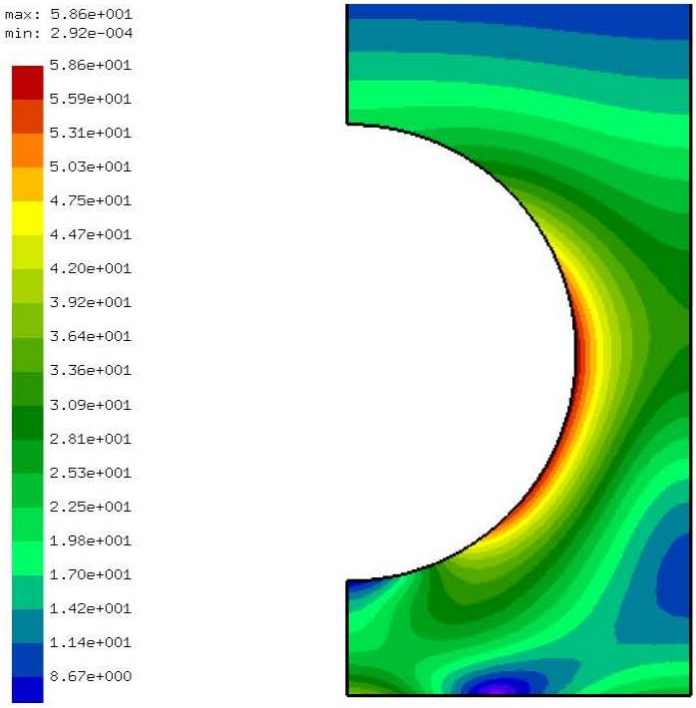

Figure 4: *Tresca equivalent stress in the tube area*

A specific design with a conical structure of the surface exposed to the beam was adopted in order to reduce thermal fatigue effects. The calculated Tresca stress amplitudes at various positions of the considered structure are shown in Figure 5. These values must be compared with the CuCrZr fatigue limit that can be taken around 200 MPa [8] at Sorgentina relevant number of cycles/year (~5x10^8). It is seen that fatigue limits are verified for the operating conditions considered. Thus, it can be stated that the Sorgentina target appears to be feasible and mechanically reliable, even under a conservative analysis.

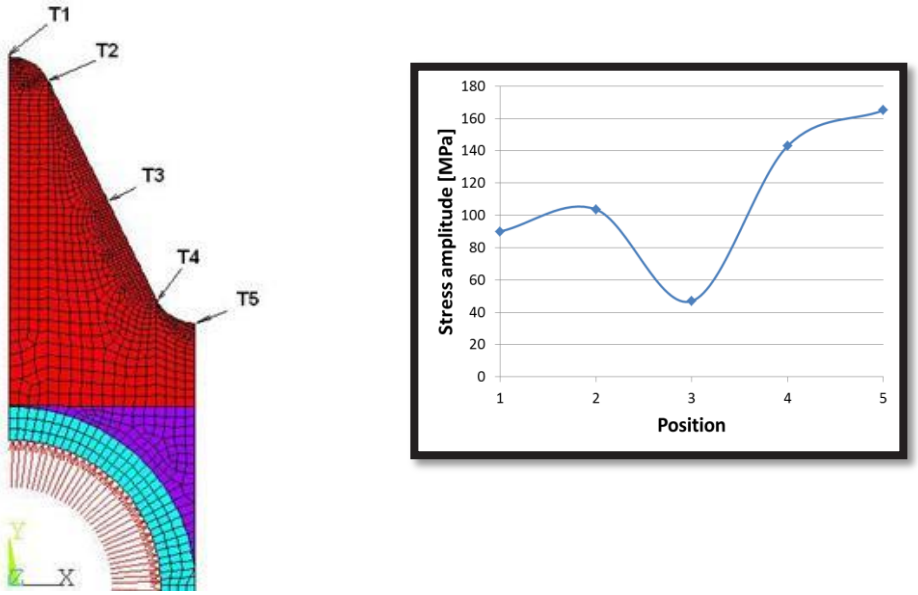

Figure 5: *Tresca stress amplitude (right) at various positions (left) of the exposed surface*

2.2 *Irradiation performance*

Sorgentina irradiation capability is attained through two surface-emitting sources of about 20x10 cm^2 that are ion beams footprints on the rotating target (see Figure 2). Neutron production rate and then source evaluation is related to beam characteristics and lattice properties of the metal in which hydrogen isotopes are implanted. In fact, ions beam energy enhances fusion probability up to reaching a plateau . Different molecular and triatomic species are generated in the ion source and accelerated to the target as well. Neutron yield is calculated starting from design parameters: beam energy, total current, beam composition (monoatomic, molecular and triatomic), metal hydride [9].

Calculated neutron yield assumes 50% deuterium and 50% tritium beams, of monatomic composition (D^+,T^+), impinging on different target coating layers. Calculations reported hereafter considered ion source monoatomic production of about 100% efficiency. Actual ion sources attain performances higher than 95% [10]. Hydrogen-to-metal atomic ratio is taken into account - as a comparison – depending on hydride stoichiometric saturation. Provided implantation regime and saturation achieved, titanium could attain hydrogen loading of about 2 – a conservative hydrogen loading factor which corresponds to no on-line implantation configuration – namely 1.8 for titanium [11].

Neutron transport calculations were performed using the MCNP5-1.6 Monte Carlo code [12]. Each target is hit by the ions beam within a rectangular area which is 20 cm long on target radius and 10 cm in direction of angular rotation. Irradiation volume thickness within rotating targets is taken 3 cm in the present design in order to maximize source flux overlapping.

In the MCNP model, neutrons before reaching the irradiation volume travel through some material layers accounting for both copper-chromium-zirconium alloy as piping and finally water as coolant, as reported in Figure 6.

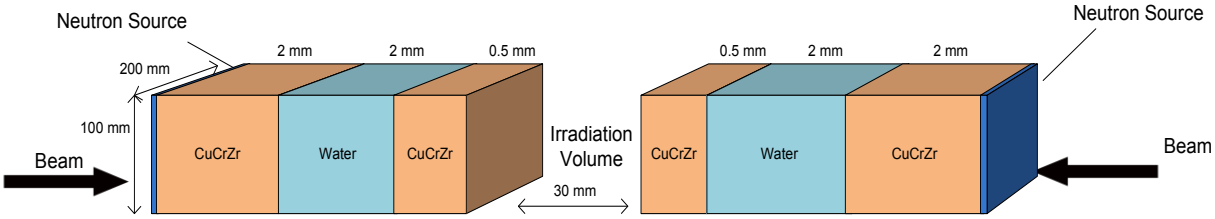

Figure 6: *Monte Carlo model for neutron irradiation evaluations*

Metallic structure gives mechanical frame and contains hydraulic pressure inside cooling pipes. Neutron flux and materials irradiation damage have been evaluated inside the gap by means of neutron cross section data according to FENDL-3 Starter Library, release 4, FENDL-3/SLIB4 [13]. Present nuclear data set is currently considered a robust approach by international agencies and research institutions. The Norgett, Robinson and Torrens (NRT) model [14] has been applied to calculate the dpa rate. Neutron flux (n/cm^2/s) and displacement per atom (dpa /fpy) have been calculated in several irradiation volumes and these values are listed in Table 2. Small gradients for neutron flux and dpa rate occur inside irradiation volume as it can be also noticed in the iso-flux maps shown in figure 7. This means a quite homogeneous irradiation field according to experimental purposes. This is perceived a relevant feature of present source design, aiming at homogeneous irradiation of samples for a solid analysis of future results. Materials irradiation through high energy neutrons gives rise to nuclear reactions (n,p), (n,α), (n,d) etc. which are not triggered in case of low energy neutrons. In fact, 14 MeV neutron flux spectrum has an impact also in the "real" formation of hydrogen and helium atoms which, moving throughout the material lattice yield charged particles reactions, a not negligible problem for materials exposed to energetic and intense neutron flux. Furthermore, presently used theoretical models to predict this effect have never been validated with 14 MeV neutrons. This is another important goal achievable with Sorgentina as the validation of Predictive Tools for DEMO is a fundamental task of the present design.

Table-2 : *Neutron flux and dpa /fpy for candidate layer hydrides*

Titanium hydride layer		
Test Volume [cm^3]	Neutron flux [n/cm^2/s]	dpa/fpy
10	2.14 10^{13}	2.00
25	2.1 2 10^{13}	1.90
50	2.09 10^{13}	1.87
100	2.04 10^{13}	1.84
150	2.00 10^{13}	1.82
250	1.89 10^{13}	1.77
500	1.54 10^{13}	1.60

As a matter of fact, the mechanical properties of irradiated sample are strongly modified by both helium and hydrogen production rates and Sorgentina has to provide irradiation consistent with fusion machine environments.

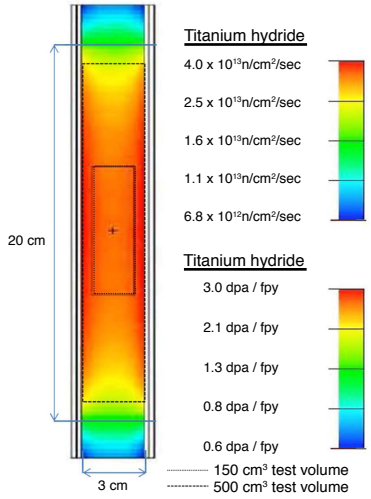

Figure 7: *Neutron flux distribution in test chamber*

Irradiation dpa/fpy values are strictly dependent on the damage energy cross sections contained in the available data libraries. In order to optimize the values of dpa, some parametric calculations have been performed by introducing different external reflectors, with the aim to increase the overall number of neutrons in the irradiation volumes. Materials considered for the reflector calculation were lead, beryllium, graphite, tungsten and depleted uranium. Calculations have been performed considering reflectors with different thickness. Only small differences on the dpa/fpy values as a function of the considered materials were found. The introduction of a reflector determines an increase of the total neutron flux in the irradiation zones that doesn't give an analogous increase in the dpa. This is due to the fact that reflected neutrons have an energy spectrum degrading toward low energy.

Achievable irradiation performances, related dpa rates and available testing volume are satisfactory designed features for Sorgentina, according to experimental capacity envisaged and technological needs for research and development activities.

2.3 Ion Source and accelerator

Sorgentina performances are accomplished through energetic deuterium and tritium ion beams. Deuterium ion beam of 20 A impinges on the target together with 20 A tritium ion beam – yielding a 40 A total current on each plate. Let remember that two rotating plates, facing each other, are forming the twofold rotating target. Power delivered on each target is 8 MW – 16 MW in total. Both deuterium and tritium beam energy is 200 keV in order to induce an optimal fusion reaction rate. High yield monoatomic ion source is required as well. Large-area, multiple-aperture ion sources are currently or have been utilized in main fusion experimental facilities like JET in Europe and JT-60U in Japan. Sorgentina design is meant to utilize powerful positive ion sources developed for JET tokamak. Plasma heating at JET is achieved by means of Neutral Injection Boxes (NIB) in which Positive Ions Neutral Injectors (PINI) are installed to feed plasma through D-T ion neutralized beams. Positive hydrogen ions are produced in a filament driven discharge in PINI ion source and accelerated using a multi-aperture electrostatic accelerator. Acceleration grids are placed within vacuum enclosures; ion source is located on high voltage side of this extraction part. PINI ion source is magnetically confined bucket type with magnetic filter to enhance proton yield. Sorgentina ion source is intended for neutron generation through monoatomic yield enhancement and then PINI technology is expected to be considered in supercusp magnetic field configuration [15]. Radiofrequency driven arc formation is planned to be implemented as well, in order to improve both monoatomic yield of the source and continuous source operation lifetime, reducing maintenance [16]. PINI sources have been successfully operated both with deuterium and tritium ions, provided some dedicated gas loops and insertion flow mechanism modification. Minor design changes concerned use of all-metal seals and provision of pumped interspaces. Conversely, most extensive change regarded installation of a Tritium and Deuterium Gas Introduction System (TDGIS) supplied by a proper active gas handling system that share a secondary containment envelope [1719]. Assuming 200 kV the beam energy, grid gaps are optimized in order to reach current design levels fulfilling best beam perveance. Horizontal and vertical focal lengths may be optimized properly tuning aperture steering off set - in present evaluations they are considered as 10 m and 14 m respectively, as in JET standard configuration. In this regard, JET PINI injectors are currently operated at performances quite close to Sorgentina design parameters. In fact since 2003, octant 4 NBI has been operated with 6 tetrode 80kV/52-58A beam lines, 130 kV/60A and 140 kV/30A triode beam lines. Conversely, NBI at octant 8 has been operated with 8 triode PINIs at 130 kV/60A [1820]. Within the framework of EFDA-JET upgrade programs to increase neutral power injected to plasma, all beam lines are planned to be replaced with triode 125kV/65A PINIs. The reported performances are for the neutral ions injected in the torus. Long pulse beam is a major concern impacting Sorgentina loading factor as well as all neutral heating systems at experimental tokamaks. EFDA reports advances in PINI technology as far as pulse duration is concerned. In fact injection time has been extended from 10 sec to 20 sec and at half power from 20 sec to 40 sec. Studies for next enhancements proved technical feasibility of longer pulses. Critical heat removal reduces global availability impacting several JET PINI beam-line components as neutralizer, ion dumps and beam scrapers. Conversely, in Sorgentina configuration only intermediate grids failure may induce plant performance reduction. Upgrade to continuous pulse is then considered feasible provided a minimum R&D phase. PINI devices are referred to as established technology since installation availability is globally considered very high. PINI operational reports regard also high system reliability that is above 90%, taking advantage of some decades experience. Table 3 reports the main ion source parameters.

Table 3: *Parameters for a single ion source and accelerator*

Parameter	Value
Extraction voltage	200 kV
Extraction current	20 A (per beam)
Current density	0.1 A/cm^2
Current pulse duration	continuous
Ion species	D^+, D_2^+, D_3^+ / T^+, T_2^+, T_3^+
Ion species yield (RF)	~100:0:0
Operational pressure	0.3 Pa
Gas consumption	0.8 Pa m^3 /sec
Focal length in horizontal plane	10 m
Focal length in vertical plane	14 m
Beam divergence	0.5°

For sake of brevity, the reader is referred to a forthcoming paper devoted to the thorough and detailed description of the facility [19].

3. Conclusions

Sorgentina is conceived to contribute in a valuable way to solve the issues of materials development and characterization. 14 MeV neutron irradiation represents a mandatory step in the path towards the understanding of the material damage mechanism in order to validate database derived from different neutron spectra. Also the possibility to make a screening of materials damage up to DEMO relevant dpa in few years from now gives to Sorgentina a great added value.

The design activity made so far demonstrates the soundness of Sorgentina proposal. A considerable neutron generation of about 10^{15} n/sec is expected to be attained and irradiation performances up to about 2 dpa/fpy are possible inside a test volume of about 500 cm^3.

Limited specific R&D activities are deemed necessary to fix and properly validate all design elements. Particularly, continuous RF plasma production has to be demonstrated. All basic technology is anyway well established and proven since it is successfully utilized in other industrial and research frameworks. Rotating target seems adequate to the scope; fatigue lifetime of the substrate will be tested. Operational reliability is then intended to be proved through ad-hoc experimental campaigns on small mock-ups. Tritium reloading of titanium hydride - by means of implantation – does not present in principle any difficulty since it is successfully experimented in sealed-tube neutron sources. Calculations and test performed at JET show that necessary D-T concentration in hydride layer may be achieved, on average, during target thermal cycle.

Preliminary safety analysis has demonstrated the inherent safety of Sorgentina and, therefore, no particular difficulties are expected in finding a suitable site. Moreover, the 14 MeV neutrons allow Sorgentina to provide a source for calibration irradiation and reference material damage tests.

Sorgentina is then proposed as a strategic infrastructure within the European framework to support R&D roadmap towards development of a reliable exploitation of fusion energy.

Indeed NSFS envisaged activity could be devoted to:(a) carry-out basic studies on 14 MeV neutrons induced damage into irradiated materials in turn validating damage calculation codes;(b) verify the influence of nuclear transmutation on the electric characteristics of ceramic insulators, optical fibers and window materials;(c) provide a neutron field were damage cross sections can be tested and/or measured;(d) address basic experimental information for the selection of low activation materials; and(e) furnish reliable data about the radiation hardness of materials to be used for diagnostics. A proper design of the layout and the use of moderators may be useful to obtain intense fluxes of thermal

neutrons enabling the test beam lines to be conceived for support in R&D on neutron instrumentation for large scale neutron facilities.

References

[1] EFDA, Fusion Electricity, A roadmap to the realization of fusion energy, 2012
[2] Eurofusion, Work Program, 2014
[3] E. Gaganidze and Jarir Aktaa, Fus. Eng. Des., 88, 2013, 118-218
[4] M. Martone, Feasibility Study of a 14-MeV Neutron Source, ENEA Tech. Report, 1990
[5] L.R. Grisham et al., Operations with Tritium Neutral Beams on the Tokamak Fusion Test Reactor, Nuclear Instruments and Methods in Physics Research B, 99, (1995), 353-356
[6] G. Dhondt, CalculiX CrunchiX USER'S MANUAL version 2.6.1 (2013)
[7] SDC-IC, Appendix A – Materials Design Limit Data, ITER G 74 MA 8 01-05-28 W0.2 (2004)
[8] S. Heikkinen, Thermally induced ultra high cycle fatigue of copper alloys of the high gradient accelerating structures, Doctoral Thesis, Helsinki University of Technology, TKK-ME-DIS-10 (2010)
[9] J. Kim et al., Nuclear Instruments and Methods, 145 (1977), 9
[10] IAEA Tecdoc, Neutron Generators for Analytical Purposes, IAEA 12-00724
[11] M. Martone, High flux, high energy deuterium ion implantation in high temperature titanium, ENEA Tech. Report, 1992
[12] X5 Monte Carlo Team "MCNP-v5", LANL Report LA-CP-03-0245 April 2003
[13] Fusion Evaluated Nuclear Data Library FENDL-3.0 Starter Library (Release 4)
[14] M.J. Norgett, M.T. Robinson and I.M. Torrens, A proposed method of calculating displacement dose rate, Nucl. Eng. Des. 33 (1975) 50-54
[15] E. Surrey et al., Properties of the JET 130kV/60A Positive Ion Neutral Injector, EFDA-JET-CP(02)04-02
[16] E. Speth et al., Development of Powerful RF Plasma Sources for Present and Future NBI Systems, Plasma Sciences and Technology, 6 (2004)
[17] T.T.C Jones et al., Tritium Operation of the JET Neutral Beam System, Fus. Eng. Des., 47 (1999), 205-231
[18] R. King et al., A Review of JET Neutral Beam System Performances from 1994 to 2003, EFDA-JET-CP(04)06-24
[19] P. Console Camprini et al., Optimized Design for Sorgentina Fusion Source, Nuclear Instruments and Methods (ongoing), (2015)

This is a blank page.

3-2. Target and Moderator Development

This is a blank page.

3.2.1

Implementation of pressure wave mitigation and in-situ diagnostic of structural integrity for mercury target at MLF/ J-PARC

Masatoshi Futakawa, Katsuhiro Haga, Hiroyuki Kogawa, Takashi Naoe, Takashi Wakui, Makoto Teshigawara, Hiroshi Takada

J-PARC Center, Tokai-mura, Naka-gun, Ibaraki, 319-1195, Japan

futakawa.masatoshi@jaea.go.jp

Abstract. A liquid-mercury target system for a pulsed high power spallation neutron source is installed at at the MLF (Materials and Life science experimental Facility) in the J-PARC (Japan Proton Accelerator Research Complex). The moment the proton beams bombard the mercury target, pressure waves are generated in the mercury by thermally shocked heat deposition, which affects the structural integrity. The damage, so-called pitting damage, which is induced by the cavitation due to pressure wave propagation in mercury, is a critical issue to determine the lifetime and increase the acceptable proton beam power. Aggressive R&D has been carried out to understand and mitigate this phenomenon. As a result, a microbubbling system is recognized to be one of the most expectable techniques for the mitigation. In parallel, an in-situ diagnostic system is developed to evaluate the structural integrity. The vibrations of target vessel induced by the pressure waves were measured and the microbubbling was confirmed to be effective to mitigate the pressure waves.

1. Introduction

Neutrons are used for the innovative research that will bring about breakthrough in scientific and engineering research fields, i.e. fuel cell, hydrogen embrittlement, protein structure, medicine, etc. Mercury has the benefits for spallation neutron sources because of the high neutron yielding efficiency and usage as a coolant, and is available as target materials to produce neutrons by spallation reaction that is caused by the high-energy protons bombardment in mercury. The pulsed spallation neutron sources are being operated at the MLF (Materials and Life science experimental Facility) in the J-PARC (Japan Proton Accelerator Research Complex) in Japan [1] and SNS (Spallation Neutron Source) in US [2], which are standing on the way to increase the power up to MW-class. As increasing the proton beam power, the structural degradation due to fatigue and cavitation associated with the impulsive structural behavior is enhanced and gets to be a crucial issue: *i.e.* at the moment that the proton beam bombards in the mercury, thermal shock is generated in the mercury and the pressure waves are induced, whose amplitude is dependent on the proton beam power. On the process of the pressure wave propagation, aggressive cavitation generates in the mercury and imposes damage repeatedly on the solid wall of the target vessel. Therefore, the structural integrity is affected by the fatigue damage combined with cavitation. Theoretical and experimental investigations were carried out to understand the relationship between pressure wave conditions, mercury cavitation aggressiveness and fatigue damage growth behaviors on solid materials [3,4].

The in-situ diagnostic system on the structural integrity evaluation has been developed, which consists of a laser Doppler vibrometor, an impulsive sound microphone and a radioactive products detector. The laser Doppler vibrometor and the microphone were installed to investigate the dynamic responses of the target vessel [5]. The pressure waves excite the mercury target vessel and negative pressure that may cause cavitation along the vessel wall. The radiation detector is used to find pinholes resulting from the accumulated damage of fatigue combined with cavitation [6].

Gas-bubbles are injected into the flowing mercury to mitigate the pressure waves and suppress the cavitation inception [7]. The injected gas-bubble conditions were examined and the effects were predicted experimentally and theoretically from the viewpoints of microscopic and macroscopic time-scales, *i.e.* in the former is essential the pressure wave propagation process at the onset of proton beam injection, and in the later is dominant the interaction between the structural vibration and the pressure in mercury [8]. The relationship among the proton beam, the bubbling conditions and the pressure waves, which is very strongly related to the structural integrity of the target vessel, was investigated by the in-situ diagnostic system. Additionally, the numerical simulation on the dynamic response was carried out using LS-DYNA FEM code and compared with measured results.

2. Pressure wave and structural degradation

Figure 1 shows the target vessel for the spallation neutron source at the MLF/J-PARC. Mercury, which has high atomic number and is liquid at room temperature, has the benefits for pulse spallation neutron sources because of the high neutron yielding efficiency and usage as a coolant. The mercury target system consists of the target vessel and the mercury circulator which are installed on the target trolley [9]. The target vessel is filled with mercury circulating at *ca.*1m/s as flowing along by the beam window. The spallation reaction is induced when accelerated protons (1 MW, 3 GeV, 25 Hz, and 1 μs pulse duration) are bombarded in mercury and approximately a half of the power is dissipated for rapidly heating in mercury [10]. As a result, thermal shock occurs and generates the pressure waves in mercury. Temperature rising ΔT in mercury is given by

$$\Delta T = \frac{\Delta Q}{\rho c_v} \quad , \tag{1}$$

where T is temperature, Q is heat density, c_v is specific heat capacity, ρ is density of mercury.
Pressure rising ΔP is given by

$$\Delta P = \beta_p K_T \Delta T \quad , \tag{2}$$

where P is pressure, β_p is thermal expansion, K_T is bulk modulus.

Nuclear heat distributions ΔQ in the mercury target is very dependent on the proton beam profiles

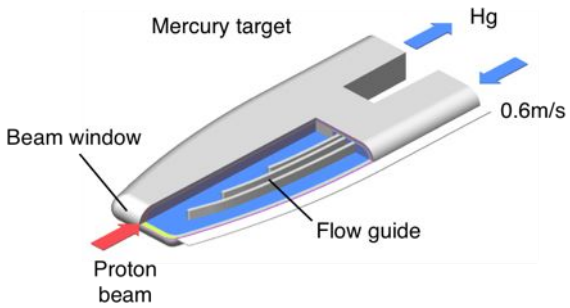

Figure 1 Mercury target at MLF/J-PARC. The drawing illustrates the inner wall of target vessel: *i.e.* the vessel consists of multi-wall structure to protect from the mercury leakage into the outside of vessel.

and the maximum peak pressure attributes to a peak heat deposition of beam profile. In order to investigate the pressure propagation and the dependency of pressure waves on the beam profiles, FEM analyses were carried out using an explicit code LS-DYNA [11]. Table 1 shows the element types and numbers used in the model consisting of the target vessel and mercury. The cut-off pressure model is applied to mercury to simulate the mercury failure due to cavitation. In the cut-off pressure model, a relationship between volumetric strain and pressure is assumed to be linear elastic when the pressure larger than the threshold, *i.e.* so-called the Blake threshold, whereas the mercury has no stiffness when the pressure is less than it. Actually, the threshold, *i.e.* liquid tensile strength, should be varied according to pressure rate as taking account of cavitation core growth that is dependent on the spinodal phenomena for phase changes between vapor and liquid [12]. Nevertheless, the cut-off pressure was assumed to be –0.15 MPa constant independently of the pressure rate as taking account of the numerical simulation efficiency. The boundary condition along the interface between solid wall and liquid mercury was tied.

Figure 2 shows the pressure time responses in liquid mercury nearby the beam window and the stresses imposed on the beam window under 1 MW power beam condition at the MLF/J-PARC. Nearby the window, the maximum pressure larger than 30 MPa is caused immediately after the proton beam injection with 1 μs pulse duration, and the longest period of negative pressure is 6 ms approximately as shown in Fig.2 (a), and then the pressure increases gradually after 8 ms. The negative pressure with a relatively long period is induced by the interaction between the solid wall and the presurre in mercury. The stresses imposing on the proton beam window are increased directly by the pressure wave collision agaist the beam window and excited by the interaction between the vessel

Table 1 Elements in FEM model of mercury target.

Structure	Element type	No. of elements	Material model
Mercury	8-node hexahedral solid	640,500	Bilinear with cut-off pressure
Target vessel	4-node tetragonal shell 8-node hexahedral solid	102,004	Linear elastic

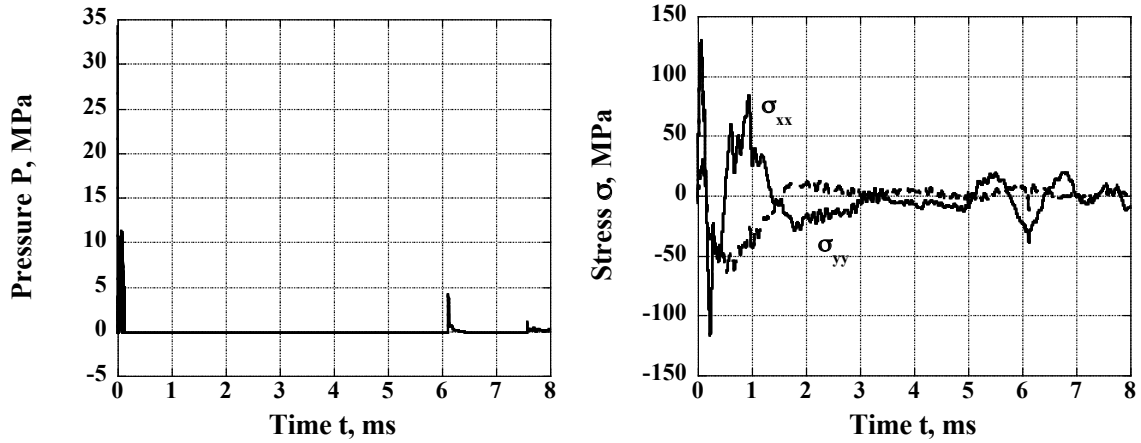

(a) Time response of pressure (b) Time response of stresses

Figure 2 Time responses of pressure nearby the beam window and imposed stress on beam window.

wall and the mercury. The structural degradation due to the fatigue damage up to giga-cycles has to be considered, because the proton beams are injected into the target at 25 Hz throughout the lifetime of 5000 h which is defined in the target vessel design.

The other degradation factor related with pressure responses is cavitation damage, which is dependent on the cavitation bubble growth and collapse behaviors affected by the pressure wave time-response. The cavitation inception needs a certain negative pressure to grow the cavitation bubbles. The fatigue and cavitation damages are accumulated on the proton beam window which is a relatively thin wall structure and a critical part for the structural integrity. In fact, the radiation damage was taken into account to decide the lifetime in the target design: *i.e.* the steel ductility is likely to be degradaed by the accumulated radiartion dose that can be estimated by the radiation time and the proton beam intensity and energy. However, after reconizing the cavitation damage induced by the pressure waves, the fatigue combined by the cavitation got to be the most critical issue to realize the high power mercury target [14]. Therefore, in order to evaluate the structural integrity and keep the soundness, we developed the mitigation technique and the in-situ diagnostic system for the pressure waves.

3. Pressure wave mitigation by microbubbles

We are trying to inject microbubbles into the mercury to reduce the pressure waves and the imposed stresses and to suppress the cavitation bubble inception and growth [7] : *i.e.* the initial compressive pressure wave is reduced by absorption of the thermal expansion in mercury due to the contraction of microbubbles at the heat deposited area and at the onset of pressure wave propagation; during the wave propagation, the microbubbles can reduce the amplitude of the compressive pressure waves through attenuation of the pressure waves due to the thermal dissipation of kinetic energy and the dispersion. The cavitation inception is not dependent on the compressive pressure itself, and needs a certain negative pressure to grow the cavitation bubbles, *i.e.* so-called the Blake threshold. As assuming that the cavitation intensity is associated to the bubble size, the negative pressure period is essential to predict the damage. It is deduced numerically that the magnitude and the period of negative pressures resulting from the interaction between the intensive compressive pressure and the vessel wall and the inertia effect followed by the propagation of intensive compressive pressure waves are reduced effectively by the suitable bubble condition [14].

A bubbling element to establish the suitable bubble condition in flowing mercury; 50 μm in radius and 10^{-3} to 10^{-5} in void fraction, was developed and installed to the mercury vessel as illustrated in Fig. 3. The installed location was determined as taking account of the bubble distribution under flowing mercury, which was predicted by numerical simulation and experiments [15].

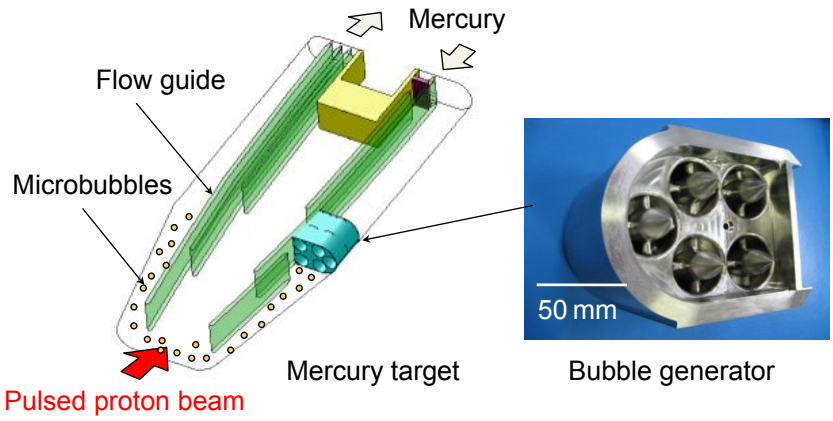

Figure 3 Pressure wave mitigation technique with microbubbles in merucry target.

4. In-situ diagnostic system

The in-situ diagnostic system in terms of the structural integrity of the mercury target for the high power spallation neutron source at the target station in the MLF/J-PARC consists of three different concepts to add redundancy and enhance reliability: *i.e.* a laser Doppler vibrometor, a sound measurement and a radioactive products detector.

The laser Doppler system installed in MLF/J-PARC consists of the He-Ne laser generator (wavelength: 632.8 nm, power: 1.2 mW), the optical fiber (30 m), the X-Y stage, the mirror assembly, the reflexive mirror, etc. As illustrated in Fig.4, the laser beam was travelled through the optical fiber up to the X-Y stage fixed at the top of the reflector plug in the core vessel. The laser beam travels in the distance of 5 m through He gas atmosphere under high radioactive condition from the X-Y stage to the reflexive mirror fixed on the target vessel in the core vessel. The reflexive mirror was fabricated from a gold plate as taking account of radiation resistance and laser reflectance. The mirror surface was machined by using an advanced micro-machining technique to achieve a sufficient reflective efficiency. The micro-cutting reflexive mirror is shown in Fig.4 as well. The side of pyramid shape is 100 μm with a sharp corner, so that the reflection efficiency is more than 90 %, in the range that the allowable angle of the injected laser beam on the reflexive mirror surface is within ca 30 degree: *i.e.* the intensity of reflected laser beam is sufficient to measure the Doppler shift, even if the injection laser beam is inclined at 30 degree against the reflexive mirror surface.

A microphone with the frequency range DC to 20 kHz for the sound measuring system is installed around the position with about 5 m far from the target vessel. Because of the high radiation environment, there are the shielding blocks between the microphone and the target vessel to protect from radiation damage on the microphone. The atmosphere is filled with helium gas at a room temperature.

Additionally, the detection system for a pinhole-type failure due to accumulated cavitation and fatigue damages was developed as taking account of radioactive products in mercury. Two kinds of nuclei, ^{88}Kr and ^{122}Xe, that are originated in radioactive mercury and the most sensitive and distinguishable from the other radioactive products in terms of the steel vessel wall or the other components, were selected to detect the target failure with the pinhole-type failure penetrating through the vessel wall at the very early stage [6].

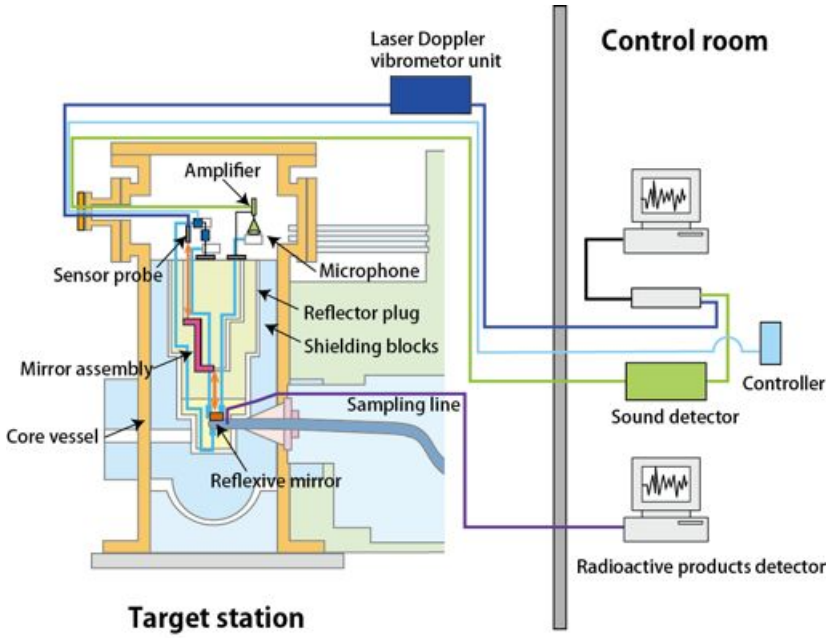

(a) Schematic drawing of in-situ diagnostic system on structural integrity of mercury target.

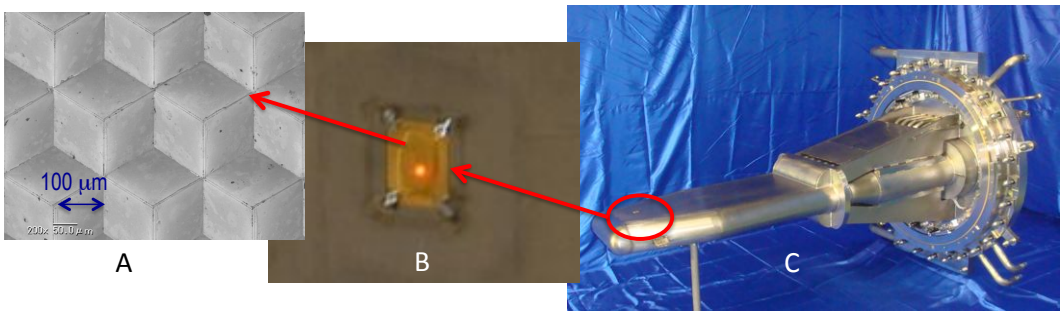

(b) Mercury target with reflexive mirror

Figure 4 In-situ diagnostic system of a pulsed high power neutron source at the MLF/J-PARC.

5. In-situ diagnostic system

Figure 5 shows the time-responses of displacement velocity measured at the upper wall of target vessel. The dynamic responses under various proton beam conditions were successfully measured under even high radiation condition by using remotely measuring system with the laser Doppler vibrometor. The relationship between the proton beam condition and dynamic responses was summarized as shown in Fig.6. The peak heat deposition was varied at 2, 4, and 5 J/cc by changing the beam profile. It was recognized that the dynamic behaviour is strongly associated with the proton beam power. The trend was confirmed numerically as shown in Fig. 7, which exhibits an adequate agreement with the experiment result shown in Fig.5. The most important part of the target vessel is the beam window because of the relatively thin wall, 2.5 mm in thickness, and severe loading conditions: combined static pressure with dynamic pressure due to pressure wave and thermal load due to proton beam heating. Figure 8 shows the relationship between the peak amplitude of displacement velocity at the upper wall and the imposed stress on the beam window. It is seen that there is the linear

relationship between the velocity v at the upper wall and the imposed stress σ_d (Mises stress) on the beam window, and is described by the following equation:

$$\sigma_d = C\, v \qquad (3)$$

Note that the velocity is associated with the proton beam condition: *i.e.* energy, total power, beam profile, etc. Needless to say, C is dependent on the target vessel structure: $C=160$ *MPa/(m/s)* in the MLF/J-PARC target vessel. We can estimate the stress at the beam window readily by using Eq(3) and the in-situ measured velocity.

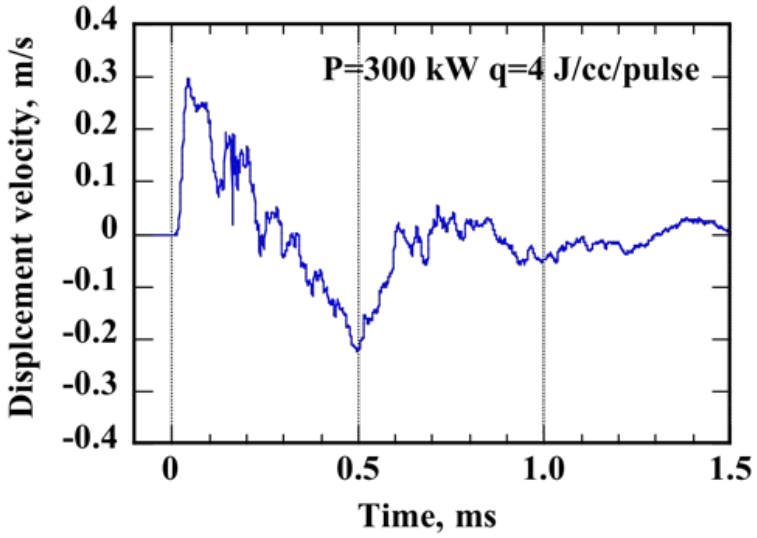

Figure 5 Time-responses of displacement velocity measured at the upper wall of target vessel.

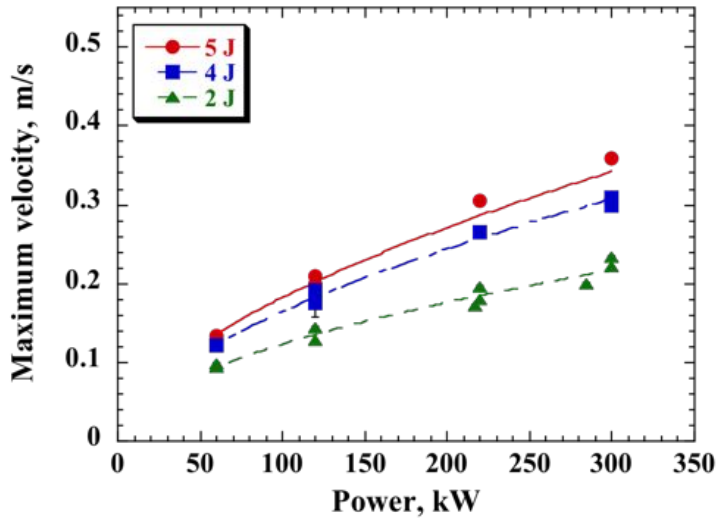

Figure 6 Relationship between the proton beam condition and dynamic responses.

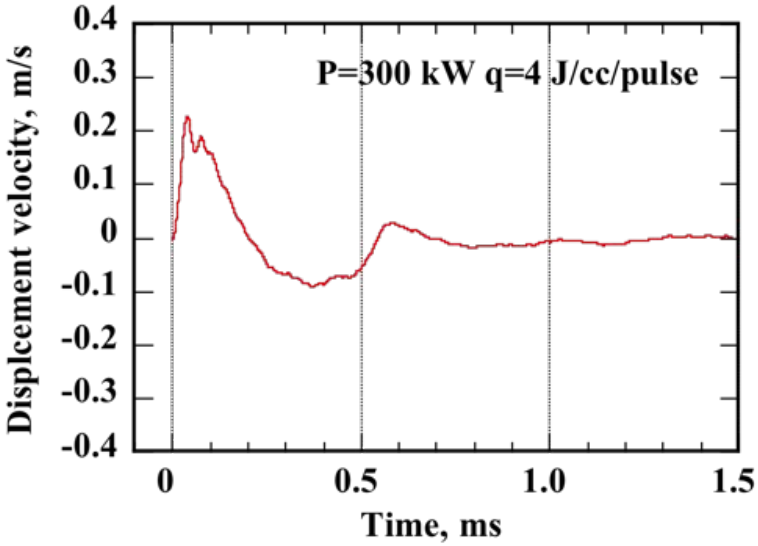

Figure 7 Numerically simulated dynamic response.

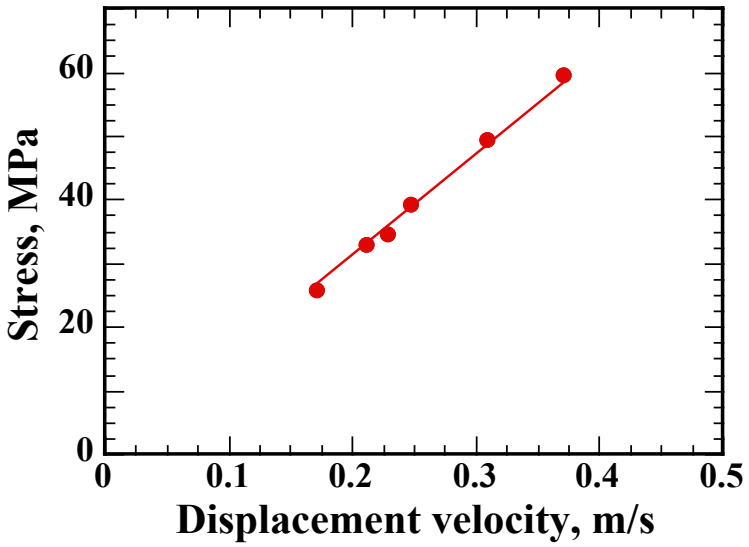

Figure 8 Relationship between displacement velocity and imposed stress on the beam window.

The stress increases definitely with the proton beam power and is estimated to be beyond the allowable design stress under 1 MW proton beam power with certain beam profiles [16]. In order to realize 1 MW power operation, R&Ds were carried out under international collaboration to mitigate the pressure wave imposing dynamic stress on the beam window. One of the most expectable technique is to inject micro-bubbles into the flowing mercury. Figure 9 shows the effect of microbubbles on mitigation of the displacement velocity, *i.e.* the pressure wave and the structural dynamic response were reduced by microbubbles. The amplitude with microbubbles gets to be less than a half of one without microbubbles. It can be said that the imposed stress on the beam window under the 1 MW operation is estimated to be lower than the allowable stress and the steady operation might be possible even under 1 MW beam power from the viewpoint of stresses evaluation if the microbubbles are injected into the flowing mercury continuously. It is found from the comparison between wavelet analyses on the velocities with and without microbubbles that the high frequency components beyond 20 kHz were damped immediately by the microbubbles. Cavitation bubble collapsing brings about excitation with high frequency components [7]. The cavitation damage is not unambiguous yet until the post irradiation examination, PIE will be carried out to look into the inside wall surface of the proton beam window. It is, however, expected that the cavitation damage is mitigated effectively because the pressure waves and the high frequency components are reduced certainly.

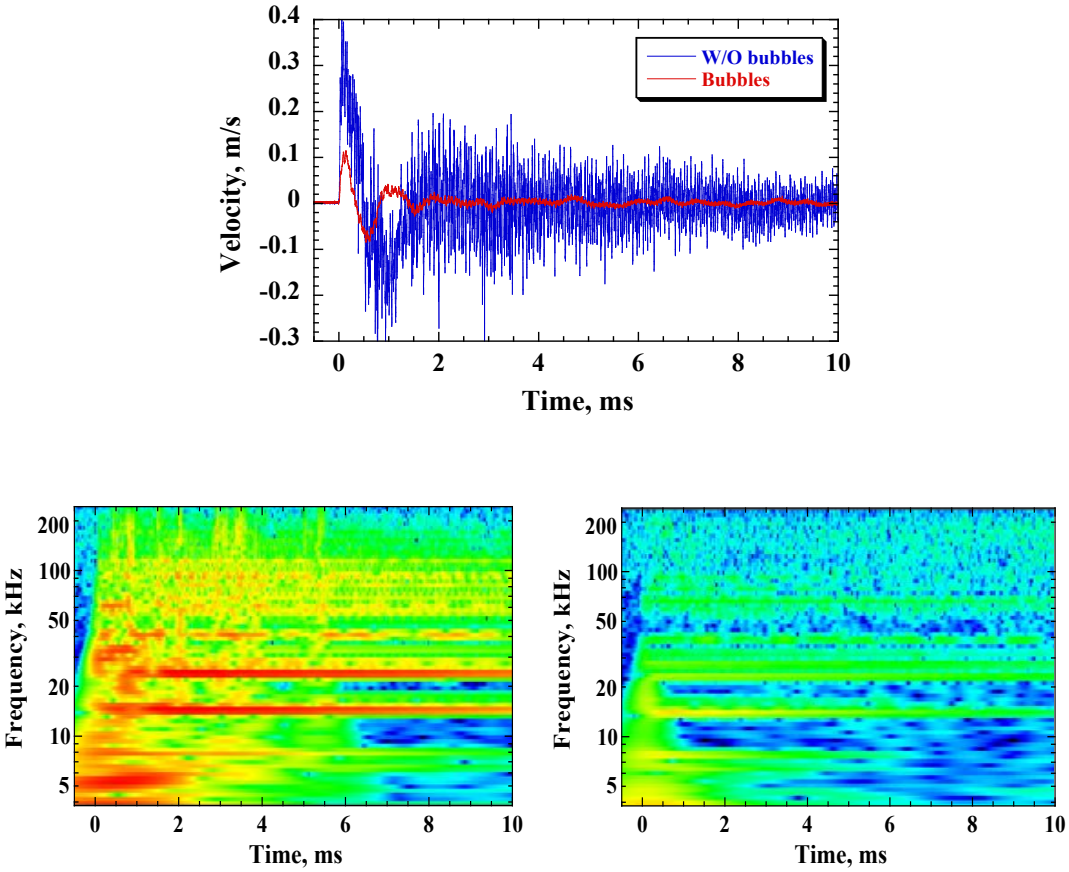

Figure 9 Effect of microbubble mitigation on pressure waves: time responses and wavelet analyses of displacement velocity under the condition with and without microbubbles.

Figure 10 shows the time responses and the wevelet analyses of sound measured under the condition with and without microbubbles. The bubbling effect is understandable clearly: *i.e.* the sound response induced by the proton beam injection was suppressed and the sound damping was enhanced by the microbubbles. The structural vibration affects the sound, which corresponds to the displacement velocity measured at the target vessel wall. The developed diagnostic evaluation technique based on the laser Doppler vibrometor and sound measuring system is suitable to detect the structural integrity related to the pressure waves which are induced by the high intense proton beams in the mercury target for the neutron source. The technique might be applied as the in-situ diagnostic system for structural integrity evaluation under ultimate environments in nuclear reactors and/or space station, etc.

The background of radiation is being evaluated to recognize the radioactive products originating from mercury throughout the operation. The data is being accumulated to detect the pinhole-type failure. Fortunately, up to now the signal related to the failure has not been recognized.

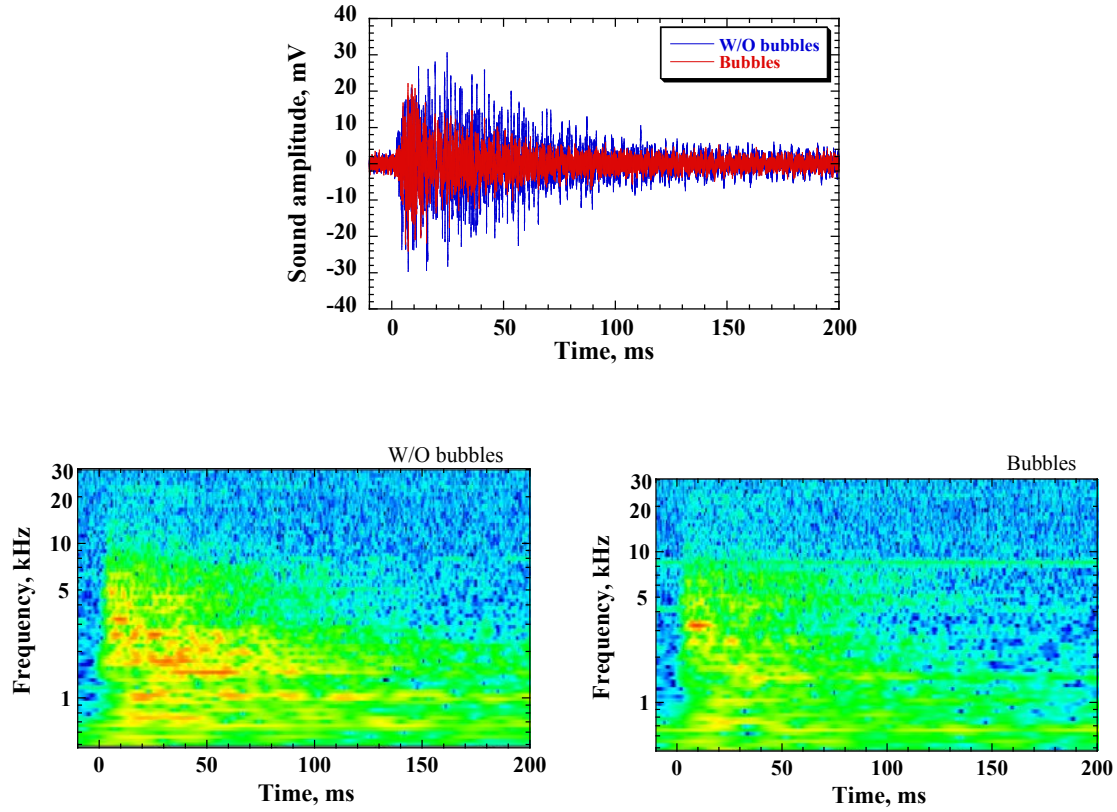

Figure 10 Effect of microbubble mitigation on pressure waves: time responses and wavelet analyses of sound under the condition with and without microbubbles.

6. Conclusion

A liquid-mercury target system for a pulsed high power spallation neutron source was installed at the MLF/J-PARC. The in-situ diagnostic system is embedded to evaluate the structural integrity related with the pressure waves induced by the high intensive proton beam bombardment. The system consists of the laser Doppler vibrometor, the sound measuring microphone and the radioactive products detector. The structural integrity is very dependent on excitation due to the pressure waves. Microbubbles are injected into the flowing mercury to mitigate the pressure waves and the mitigation effect was successfully confirmed by using the in-situ diagnostic system. The imposed stresses on the beam window under the condition with microbubbles were estimated to be lower than a half of ones without microbubbles. The developed in-situ diagnostic system is very useful to evaluate the structural integrity of the target vessel operating under extremely high radiation environments.

Acknowledgements

The authors gratefully acknowledge the funding by the Japan Society for the Promotion of Science through a Grant-in-Aid for Scintific Research (No. 20360090 and No. 23360088).

References

[1] http://j-parc.jp/MatLife/en/
[2] http://sns.gov/facilities/SNS/
[3] Futakawa, M., Naoe, T., Kogawa, H., Tsai C., Ikeda, Y., Pitting damage formation up to over 10 million cycles -off-line test by MIMTM-, J. Nucl. Sci. Techol., 2003, 40, p. 895-904.
[4] Futakawa, M., Naoe, T., Tsai, C.C., Kogawa, H., Ishikura, S., Ikeda, Y., Soyama, H., Date, H., Pitting damage by pressure waves in a mercury target, J. Nucl. Mater., 2005, 343, p. 70-80.
[5] Teshigawara, M., Wakui, T., Naoe, T., Kogawa, H., Maekawa, F., Futakawa, M., Kikuchi, K., Development of JSNS target vessel diagnosis system using laser Doppler method, J. Nucl. Mater., 2010, p. 238-243.
[6] Kasugai. Y, Otsu, K., Kai, T., monitoring system of mercury target failure using radioactivity measurement, ICANS XIX, 2010, Grindelwald, Switzerland.
[7] Futakawa, M., Kogawa, H., Hasegawa, S., Naoe, T., Ida, M., Haga, K., Wakui, T., Tanaka, N., Matsumoto, Y., Ikeda, Y., Mitigation technologies for damage induced by pressure waves in high-power mercury spallation neutron sources(II), J. Nucl. Sci. Technol., 2008,45, p.1041-1048.
[8] Futakawa, M., Naoe, T., Kogawa, H., Haga, K., Okita, K., Cavitation erosion induced by proton beam bombarding mercury target for high power spallation neutron source, Proc. of the 8th int. symp. on cavitation CAV2012, 2012, No.290.
[9] Neutron Section Section/J-PARC center, Technical Design Report of Spallation Neutron Source Facility in J-PARC, JAEA-Technology 2011-035, 2011.
[10] Futakawa, M., Kikuchi, K., Conrad, H., Stechemesser H., Pressure and stress waves in a spallation neutron source mercury target generated by high-power proton pulses, Nucl. Instrum. Methods Phys. Res., 2000, Sect. A, 439, 1-7.
[11] Kogawa, H. Hasegawa, S., Futakawa, M., Riemer, B., Wendel, M., Haines, J., Numerical study on pressure wave propagation in mercury loop, J. Nucl. Mater., 2008, 377, 195-200.
[12] e.g. Brennen, C.E., Caviation and bubble dynamics, Oxford Univ. Press. 1995.
[13] Futakawa, M., Wakui, T., Kogawa, H., Ikeda, Y., Pressure wave issues in high power mercury target, Nucl. Instrum. Methods Phys. Res., 2006, Sect. A 562, 676-679.
[14] Okita, K., Matsumoto, Y. and Takagi, S., Propagation of pressure waves, caused by a thermal shock, in liquid metals containing gas bubbles, Proc. FEDSM2005-77397, 2005.
[15] Haga, K., Naoe, T., Kogawa, H., Kinoshita, H., Ida, M., Futakawa, M., Riemer,B., Wendel, M., Felde, D., Abdou, A., Distribution of microbubble sizes and behavior of laser bubbles in mercury flow in a mockup target model of J-PARC, J. Nucl. Sci. Technol., 2010, 47, p.849-852.
[16] Kogawa, H., Ishikura, S., Sato, H., Harada, M., Takatama, S., Futakawa, M., Haga, K., Hino, R., Meigo, S., Maekawa, F., Ikeda, Y., Effect of proton beam profile on stress in JSNS target vessel, J. Nucl. Mater., 2005, 343, 178-183.

3.2.2

Progress of the ESS monolith design and engineering solutions for target and moderator systems

Rikard Linander, Daniel Lyngh, Ulf Odén

European Spallation Source, P.O Box 176, SE-221 00 Lund, Sweden

rikard.linander@esss.se

Abstract. The on-going project for construction of the European Spallation Source (ESS), the 5 MW long-pulsed neutron research facility in Lund, Sweden, has entered the phase in which design work and development are focused on realising solutions that shall satisfy well-defined requirements. The Target Station, which converts the pulsed proton beam delivered by the linear accelerator to cold and thermal neutron beams tailored for neutron science applications, consists of several systems. Each of these elements offers unique design challenges for the engineering teams both in terms of providing the necessary primary function and in satisfying complex requirements for physical and functional interfaces between systems. The monolith, which houses the target, the moderators and several other essential systems, shall provide sufficient radiation shielding and retain the internal helium atmosphere properties within specified limits. Some of the associated engineering challenges are to define and meet support and alignment requirements; to find solutions for safe, robust and efficient replacement of components; to choose appropriate yet cost effective materials for the shielding structures; and to create a design that allows the construction to respect a tight installation plan. Within the monolith, the moderator and target systems, whose optimal performance is critical to the overall performance of the facility, present similarly complex design challenges. This paper presents the progress and status of the design work for the ESS target monolith as well as summarising the engineering solutions adopted for the target, moderators and other components and parts of the monolith.

1. Introduction

1.1. Brief description of the ESS project context

The ESS target station, being one of the main parts of the facility, is managed as a project within the ESS programme. Starting with the site decision in 2009, a suite of dedicated sub-projects were executed which through the so called Target Station Design Update (TSDU) project resulted in the description of the target station in the ESS Technical Design Report (TDR) [1], by April 2013. After extensive planning efforts the construction project started in the beginning of 2014 aiming at finalising the facility for delivery of the first neutrons to instruments in 2019.

1.2. General description of the ESS target station [1]

The function of the target station is to convert the intense proton beam from the accelerator into several intense neutron beams, for use by neutron science instruments. This conversion is achieved by the interplay of a number of basic functions. In the heavy metal target the impinging proton beam radiation from the accelerator is converted via the spallation process into fast neutrons as the useful

product, while generating a large amount of heat, radioactive isotopes and prompt radiation as unavoidable by-products. The moderator-reflector assembly surrounding the target transforms the fast neutrons emitted by the target into slow neutrons, which are the final form of useful radiation provided by the neutron source, while further radioactive waste is produced by the absorption of neutrons by various target structures. These two neutronically active systems are surrounded by a radiation shielding system of approximately 7000 tons of steel, in order to contain the extreme level of highly penetrating gamma and fast neutron radiation created in the target and its vicinity. The beam extraction system provides intense slow neutron beams through beam guides, which traverse the target shielding. These neutron beam guides are accessible at the surface of the shielding, for delivery to and use at the neutron-scattering instruments facing the beam ports at variable distances. The proton beam window separates the high vacuum in the accelerator from the atmospheric-pressure inert helium gas inside a large container vessel, in which all of these systems are housed. They form, together with the tight container, the target monolith, which takes the shape of an 11 m diameter and 8 m high cylinder.

At ESS, the proton beam will deliver 5 MW power in the form of kinetic energy. About 10% of this energy is converted to mass through the nuclear reactions in the spallation process that produces neutrons, other nuclear fragments, isotopes and gamma radiation. The energy of these particles makes up the remaining 90% of the proton beam energy, and it is almost all deposited within a distance of 1 m from the site of proton beam impact in the target. Different cooling circuits in the target monolith remove this large amount of heat from the target itself (3 MW), from the moderator-reflector assembly (1.2 MW) and from the monolith shielding (0.3 MW). The proton beam window is directly heated by the traversing beam and requires cooling of about 6 kW, though this value is strongly dependent on window design details.

Radiation damage and fatigue limit the lifetime of the three most strongly affected systems: the target, the reflector-moderator assembly and the proton beam window. All of these systems will need to be changed multiple times during the lifetime of the facility, with frequencies ranging between 6 months and 5 years, as conservatively estimated on the basis of available experience at spallation sources. The removed used components represent a considerable amount of radioactive waste. The other part of the radioactive waste consists of gases, volatiles and airborne particles, which will be continuously captured by a variety of efficient filters and traps.

2. Progress in engineering and evolution of the system design

The following subsections describes the current progress and evolution of the design of the monolith systems, the target systems and the moderator and reflector systems, compared to the design concepts for these systems set forth in the TDR [1]. The paper reflects the status of the engineering designs of the systems during the initial phases of the construction project in the autumn of 2014. It should be acknowledged that it is a phase of continuous development towards the preliminary design and further on the final design and construction of the facility.

2.1. Modifications to the monolith systems and choice of concepts

The main functions of the monolith can be summarized as providing shielding sufficient for personal protection and for reduction of signal background for the neutron science instruments as well as confining radioactive inventory both during normal operation and in off-normal situations. In order to satisfactorily perform these main functions several additional supporting functions have to be defined and assigned to the monolith systems. The most important supporting functions are to remove excess heat deposited in the monolith structures during operation, to provide structural support for intrinsic components, plugs and shielding blocks with appropriate and repeatable alignment precision and to allow access for maintenance and replacement in accordance with expected lifetime and reliability of each component and part.

Figure 1 shows the layout and configuration of the monolith systems and the intrinsic target components that were presented in the TDR [1]. This previous design concept featured, so called, light shutters internal to the a large confinement vessel. These internal shutters were envisaged to be

operated with drives located on top of the monolith via pull rods penetrating the confinement vessel. The large confinement vessel was also equipped with many other covers and penetrations, separately for each main internal components. Notably the target drive was to be contained in a quite tight housing located very near the cover above the moderator and reflector plug.

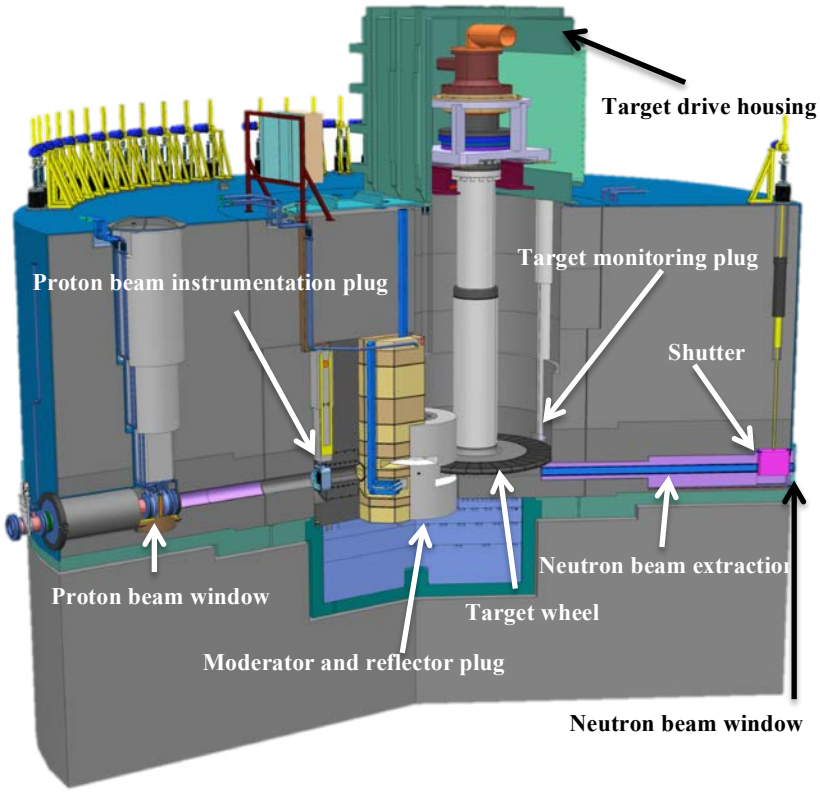

Figure 1. Layout of the monolith as presented in the TDR [1], April 2013.

2.1.1. *Important modifications of the confinement system*. The large diameter of the confinement vessel was found to be inconvenient during the initial planning of the installation since it was located very close to the building concrete structures. In order for the monolith installation to become independent from the building construction works to a larger extent it was decided to consider a smaller diameter for the confinement vessel. The decision to decrease the diameter of the confinement vessel is coupled to the choice of making the light shutters external to the vessel. At the same time it was concluded to be advantageous to merge most of the covers and penetrations into a larger dome with one common vessel head and a cylinder wall with permanent penetrations for pipes, cables and optical paths. The diameter finally chosen for the confinement vessel is approximately 6 m, see the light blue structure in figure 2.

2.1.2. *Shielding system changes*. The most significant evolution of the shielding system, i.e. the steel shielding blocks and parts is the introduction of a lower support cylinder structures for supporting the mass of the upper monolith parts and distributing the forces down to the concrete foundation and base slab. It was decided to pursue an engineering design with well defined steel structures in order to be able to sufficiently predict the behaviour and qualify all parts for all events and load cases, such as installation and test loads, normal operation loads as well as extreme conditions like seismic events.

The introduction of the three support cylinders, together with the central column, as can be seen in figure 2 leads to a significant advantage in that the permanent bulk shielding in between these

cylinders does not need to provide any load bearing function. The bulk shielding can therefore be optimized from both a shielding and cost perspective.

An additional advantage of the decrease of the confinement vessel diameter is that requirements on cleanliness and corrosion resistance can be somewhat relaxed for the upper outer parts of the monolith, which is a quite large fraction of the permanent bulk shielding.

Finally, after further and more detailed shielding calculations it was concluded that the optimal diameter of the monolith steel shielding is 11 m, complemented by half a metre of concrete.

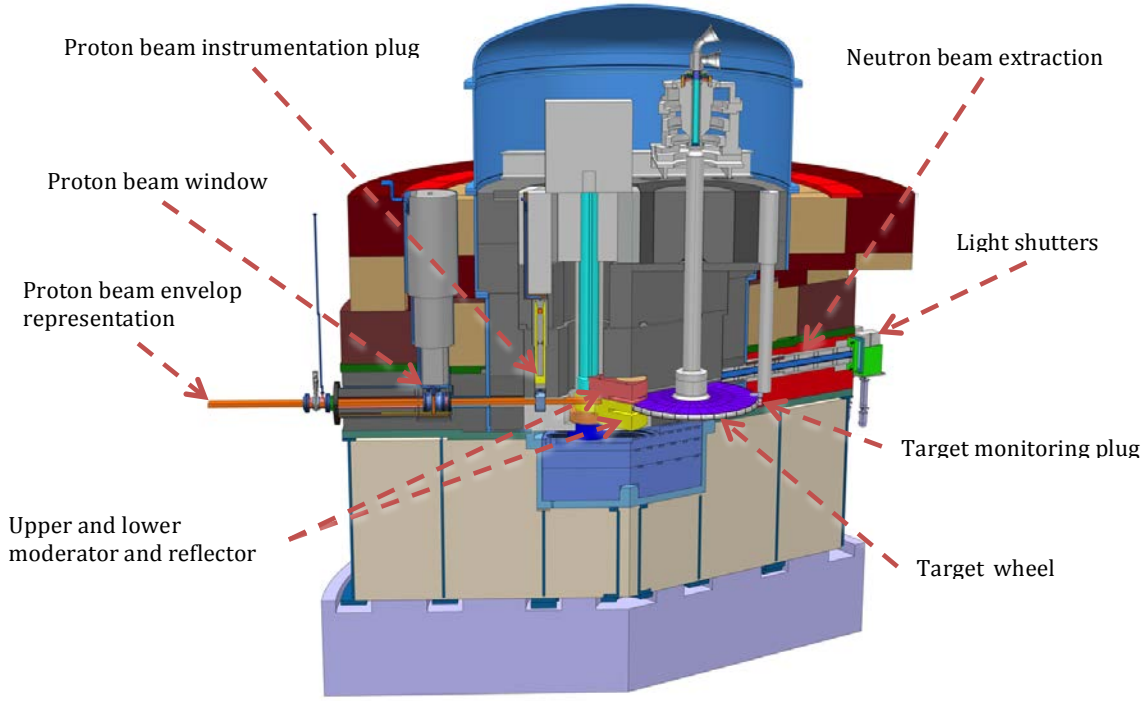

Figure 2. Status snapshot of the monolith layout during autumn of 2014.

2.1.3. *Development status for the monolith systems*. All changes and modifications of the monolith systems, gathered together, have resulted in a much simpler and robust design. It provides high flexibility and is more adapted for instance to the modified MR configuration, addressed later in this paper. A very big advantage and in fact a driver for some of the changes is that the presented monolith layout makes provisions for an installation sequence that will be as independent as possible on the concrete construction works. As a whole the modifications, especially the relaxation of requirements on permanent bulk shielding parts, are in fact part of the strategy to mitigate risks related steel cost variation.

2.2. Important changes to the target systems

The target systems at ESS comprises two main parts. The first part is the target wheel unit which is a rotating disc containing tungsten as spallation material, a long shaft, a motor drive and bearings. Secondly the target primary cooling system that circulates helium for removal of the heat deposited in the wheel unit by the impinging proton beam.

The design of the target systems have not been significantly modified compared to the TDR [1] description of the technical concept, but the target wheel unit as well as the target primary cooling system has been taken to the next level of details. In the beginning of the autumn of 2014 the cooling system passed the preliminary design review tollgate. Likewise, the preliminary design review for the target wheel unit was planned for late 2014. This means that both systems were taken to detailed design by the end of 2014.

The main change for the target systems was the decision to increase the pressure of the helium coolant from 0.35 MPa to 1.0 MPa. The advantages and drawbacks are described below and as a conclusion the benefits of the change of the pressure that has been taken credit for are summarized.

2.2.1. *Advantages of an increased helium coolant pressure*. The most significant advantages with a higher gas pressure is that the power consumption of the helium circulator will be reduced. It also means that the volume flow of helium becomes lower which can be taken credit for either as lower fluid velocities, i.e. lower pressure loss, in the piping system and components or as smaller dimensions of the pipes and components.

2.2.2. *Drawbacks of an increased helium coolant pressure*. The main disadvantages of an increased gas pressure that the static primary stresses of the target vessel will be higher which puts higher demands on the design of the target wheel unit. Also leakage rates in shaft seals, flanges and joints will increase. A minor drawback is that the helium inventory will be larger.

2.2.3. *Credited benefits of increased helium coolant pressure*. The current technical solutions for the target wheel unit as well as for the target primary cooling system, i.e. the solution that have passed the preliminary design review, are effectuating the following advantages of increasing the operating pressure from 0.35 MPa to 1.0 MPa. The circulator will consume considerably less power and the size and cost of the circulator will be significantly smaller. It actually means that there will be more possible suppliers of the circulator since a more conventional product can be chosen.

Also smaller pipes, fittings and other components will be used in the system, keeping the total pressure loss at the same level as for the previous system layout for a lower pressure.

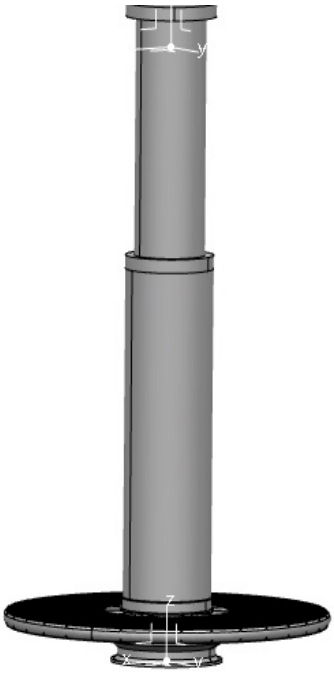

Figure 3. Picture showing the previous size of the target shaft as presented in the TDR [1], April 2013. Total mass of the component was approximately 17 tons.

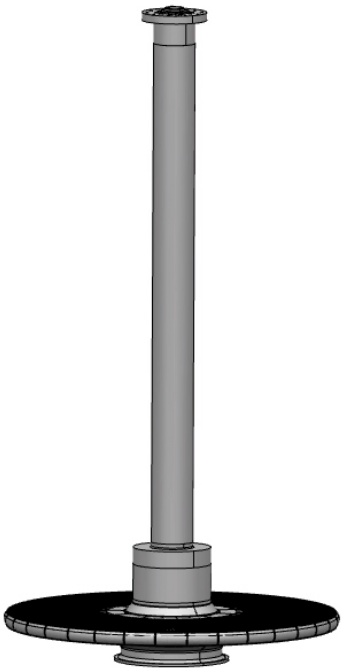

Figure 4. Picture of the current design of the target wheel featuring a smaller size shaft, decreasing the total mass to 11 tons.

The effect on the target wheel unit is, as mentioned, that the design of the pressure sustaining parts like the vessel and connection flanges will have higher design requirements. However, the increased pressure also makes provisions for making the long shaft much slimmer as can be seen in figures 3 and 4. This means that the mass of this component, meaning the entire target wheel unit, can be decreased from 17 to 11 tons which is a big advantage for handling and disposal of a spent target wheel.

For more information on the design changes for the target systems, see [2].

2.3. Evolution of the moderator and reflector systems

Original design and configuration of the ESS moderators and reflectors. The previous MR configuration had two identical "volume" moderators in one single plug. For neutronic performance reasons the viewing angles of each of the two sets of moderators were limited to two opposite 60° sectors. A picture of the original TDR [1] design of the MR plug is shown in figure 5. Figure 6 indicates its position inside the monolith relative to the target wheel. The total mass of the complete MR plug was as high as 24 tons.

Extraction of a double MR plug from its operational position, for replacement, included a horizontal shift of about 1 m followed by a vertical lift. Especially the horizontal shift was considered being a risky step in the handling procedure.

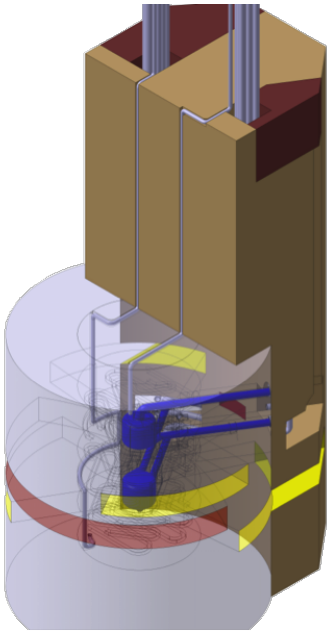

Figure 5. Double MR unit with two integrated identical volume type moderators as presented in the TDR [1], April 2013.

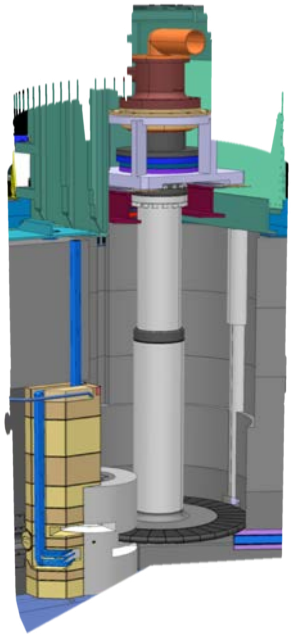

Figure 6. Location of the double MR unit and its configuration with the target wheel inside the monolith.

2.3.1. *The flat moderator concept*. During the neutronic optimization phase of the project following the release of the TDR a concept with a flat moderator was studied and concluded to be worth pursuing for use at ESS. Such a flat type moderator can serve a much larger sector than a volume type moderator. Thus it became an option to either use only one moderator for all instruments or to employ two different types of moderators above and below the target wheel. In any case it was concluded to be beneficial to structurally separate the upper and the lower MR assemblies.

During the spring of 2014 the design team for the ESS target station focused on developing a good engineering solution for a flat moderator. These efforts have resulted in a preliminary design proposal that is depicted in figure 7.

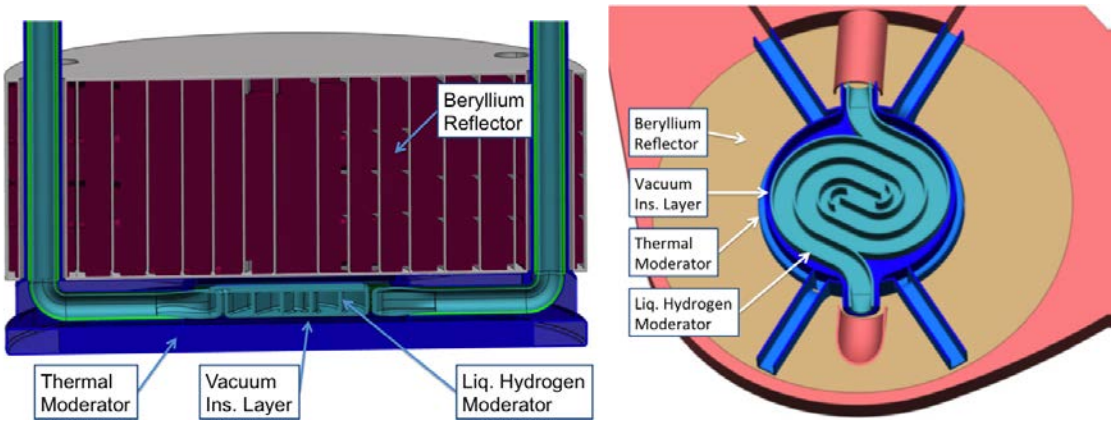

Figure 7. Final preliminary design proposal for a flat moderator, with a central cylindrical cold hydrogen moderator and thermal water moderator wings.

2.3.2. *Flat moderator impact on the MR plug configuration and design*. As indicated above, the decision to change one of the MR assemblies to a flat type moderator led to the need of redesigning the MR plug(s) to be structurally decoupled and possible to handle and replace independently. In fact, it was concluded to be practically impossible to open up as large openings in the reflector structure of the previous double MR plug.

A handful of configuration and design alternatives with separate upper and lower MR plugs/assemblies were studied during the summer of 2014. Several of these studied solution candidates included a simpler, only vertically handled (lifted), upper MR plug together with a lower MR plug with different access path and handling concept. Some of the alternatives that was finally discarded assumed horizontal insertion from one of the experimental halls, inclined insertion from an upstream basement room, vertical insertion to a position upstream the target wheel but offset the spallation hot spot and a wheel like structure that enabled the lower moderator to be rotated from its operational position to a replacement position.

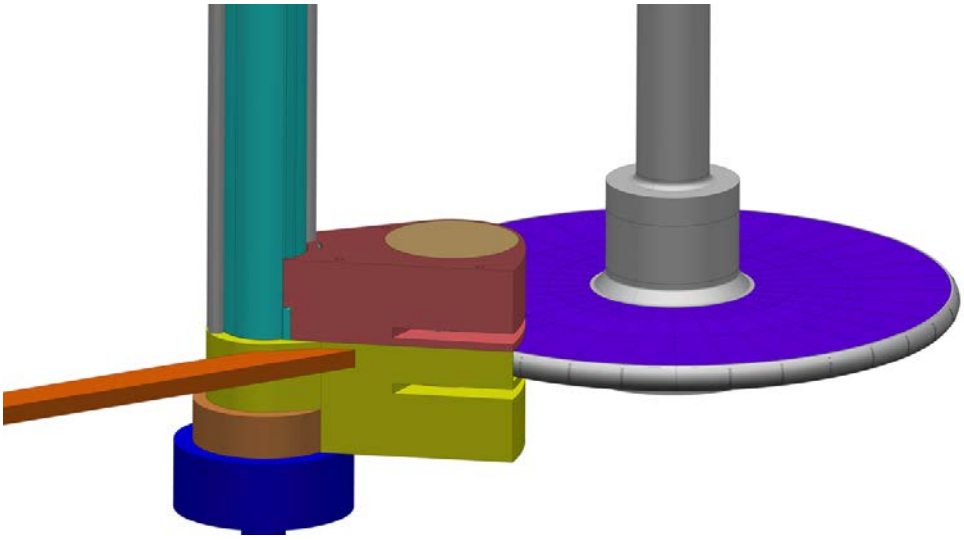

Figure 8. The chosen configuration and design concept for moderators and reflectors, designated with the working name “the double twister”.

Figure 8 shows the configuration and design concept for the separated MR plugs that was finally chosen and decided. It features the same replacement and handling scheme for both the upper and the lower MR assemblies with a rotation around a common stationary axis followed by a vertical lift. The

upper MR unit (magenta) is connected to the outer annular shaft (turquoise) while the lower MR unit (yellow) is attached to the inner annular shaft (brown).

Further details on the preliminary design for the MR plugs and the handling concept can be found in [3].

References

[1] S Peggs, "ESS Technical Design Report", ISBN 978-91-980173-2-8.

[2] R Linander, U Odén, "Status update on the ESS Target systems development", ICANS XXI paper, TM-P04

[3] D Lyngh, R Linander, "Engineering developments of the ESS Moderator and Reflector systems" ICANS XXI paper, TM-P12

3.2.3

Thermal hydraulic design of a double-walled mercury target vessel by simulations and water experiments

K Haga, T Naoe, T Wakui, H Kogawa, H Kinoshita and M Futakawa

J-PARC Center, JAEA, Tokai, Ibaraki 319-1195, Japan.

E-mail: haga.katsuhiro@jaea.go.jp

Abstract. To mitigate the cavitation damage of the mercury target vessel operating at the spallation neutron source of J-PARC, a double-walled structure for the target vessel was investigated and designed by numerical simulation. It was found that rapid mercury flow in the narrow channel at the beam window and sufficient cooling performance of the target wall were attained. Moreover, the rapid mercury flow might be maintained even in the case of an inner-wall fracture. These results were found to be consistent with the water experiments in the case of small damage of the inner wall.

1. Introduction

In the mercury target of the pulsed spallation neutron source of J-PARC, injections of high-power (1 MW) pulsed proton beam induce pressure waves in the mercury and cause cavitation damage to the target vessel wall, which is a crucial issue for stable system operation [1]. To mitigate cavitation damage, a microbubble injection technique, which reduces the intensity of the pressure waves, has been developed. A microbubble generator, also called a bubbler, was developed to generate microbubbles with a diameter less than 100 μm in the mercury; it has been used in the mercury target system of J-PARC since October 2012. Using a Laser-Doppler vibrometer, it was found that the displacement velocity of the target vessel was reduced to 1/3 on average at the proton beam power of less than 300 kW, which showed the efficacy of the microbubble injection.

For the further development of the high-power target, we focused on the mercury flow effect to mitigate the cavitation damage. So far, the analytical and experimental studies [2,3,4] and the operational experiences of Spallation Neutron Source (SNS) [5] suggest that rapid mercury flow can mitigate the cavitation damage. To include these effects in the target design of J-PARC, we developed a double-walled structure and applied it to the beam window, which is the forefront tip of the target vessel. The mercury flow channel, with a narrow gap of 2 mm, was made by adding an inner wall just inside the beam window.

In this report, thermal hydraulic design of the double-walled target by simulations and the results of the water experiments using the mock-up model are presented, including the case of failure of the inner wall.

2. Double Wall Concept to Extend the Lifetime of the Beam Window

Figure 1 shows a schematic of the structure of the double-walled target vessel (top view). Based on experimental data [6], though it is under the stagnant condition, the effect of pitting damage mitigation becomes better as the channel gap is smaller, because the channel walls can disturb the inflation of

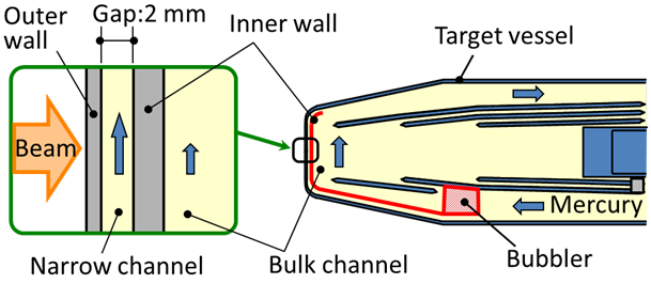

Figure 1. Structure of the double-walled target and the magnified view of the beam window

cavitation bubbles before they fully expand. Moreover, the effect of the fast mercury flow to deform the cavitation bubbles will reinforce the performance of the narrow channel to mitigate the pitting damage. On the other hand, the channel gap should be decided considering the manufacturing tolerance. Considering these conditions, the gap of the narrow channel was decided to be 2 mm at the beam window.

The mercury flow is separated into two channels at the bubbler, i.e., the narrow channel and the bulk channel, and they join again downstream of the beam window. Although the narrow channel is a straightforward channel with no obstacles, the bulk channel is equipped with the bubbler, which is the primary flow-resistant component in the target vessel. The maximum pressure drop at the bubbler is assumed to be 0.2 MPa considering the mercury pump performance. The mercury velocity in the narrow channel increases until the pressure drop becomes the same as that in the bulk channel, which makes the mercury velocity in the narrow channel faster than that in the bulk channel.

The merit of the double-walled structure is that the inner wall is not the mercury containment boundary, and enough cooling efficiency is expected because both sides of the inner wall are cooled by the mercury flow. This merit expands the freedom of the inner wall design for applying technologies in order to mitigate the cavitation damage on the inner surface of the inner wall. Furthermore, sufficient cooling efficiency of the inner wall enables the wall thickness to be increased, which has the advantage of enabling an increase in the erosion allowance. In the present design, the thickness of the outer wall is 3 mm and that of the inner wall is 5 mm. All these merits lead to a longer lifetime for the target vessel.

3. Target Design by Simulation

3.1. Design requirements and concerns

The design requirements for the thermal hydraulic design of the double-walled mercury target are as follows:

- A high-velocity flow field throughout the narrow channel to achieve the pitting damage mitigation effect.
  - --- In the experiences of SNS target operation, serious damages were not observed on the inner surface of the beam window cooling channel where the mercury flows at 3 m/s at maximum. Based on this fact, the design criterion for the minimum mercury velocity in the narrow channel was set at 3 m/s.
- Sufficient cooling performance which causes no serious temperature rise throughout the mercury target vessel.
  - --- The maximum temperature of the target in the past design was around 200 °C. The temperature of the target in new design should not exceed this value so much.

There are also concerns for the fabrication and the operation of the target vessel as follows:

- Influence of fabrication tolerance on the flow velocity in the narrow channel.
- Influence of inner wall failure to the mercury flow and the wall cooling.

Evaluation results of these items are shown in the following sections.

3.2 Simulation model and conditions

The commercial base thermal hydraulic code—ANSYS FLUENT—was used to analyze the time-averaged thermal hydraulics in the target model. The analytical model was a three-dimensional full model. The cell shape was tetrahedral and the total cell number was 22 million. The turbulence model was realizable k–ε model and the wall boundary condition was the law-of-the-wall.

The inlet mercury temperature was set to 50 °C. Based on experimental data, the pressure drop coefficient of the bubbler was set to 8.1, which led to a mercury velocity at the model inlet of 1.025 m/s in order to make the pressure drop at the bubbler 0.2 MPa. The volumetric heat generation was considered under the condition of the proton beam energy and power of 3 GeV and 1 MW, respectively. The proton beam profile was assumed to be Gaussian, and the maximum heat density was 430 W/cm^3 in the mercury near the beam window. The thermal condition at the outer wall boundary was set to adiabatic. The buoyancy of mercury was not considered in this analysis, because in a forced convection flow with a high Reynolds number, which is on the order of 10^5 in this case, inertial force is the dominant factor to determine the flow field and the effect of buoyancy is considered to be negligible. The turbulent Prandtl number was set to 1.5. The temperature dependency of the physical properties of mercury and stainless steel was considered.

3.3 Mercury flow field and temperature distribution

Figure 2 and Figure 3 show the simulation results of the flow field and the temperature distribution at the horizontal cross section. While the mercury velocity is ca. 1.5 m/s in the bulk channel, it is almost 4 m/s in the narrow channel at the beam window. The maximum wall temperature is 157 °C at the outer surface of the outer wall, which is not high enough to cause any problems. The maximum temperature of the inner wall, though it is somewhat thicker, is lower than that of the outer wall because it is cooled on both sides. The mercury temperature is around 60 °C in the area near the beam window and increases to 120 °C at 500 mm in the X position. Figure 4 shows the mercury flow velocity distribution in the narrow channel, which is in the vertical cross section at the center position of the beam window. Looking at the angle from −80° to 80°, we found that the flow velocity is fast (>3.5 m/s) at the center of the beam window, where rapid velocity is specially needed for the cavitation damage mitigation. The flow velocity decreases sharply at −90° and 90°. The intensity of the cavitation is assumed to be relatively weak in these regions. The flow velocity deductions seen at −30° and 30° are caused by the wake flow of the reinforcement ribs fixed in the entrance region of the

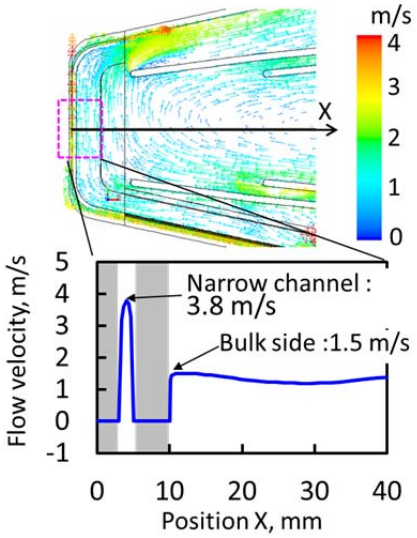

Figure 2. Mercury flow field near the beam window on the horizontal cross section

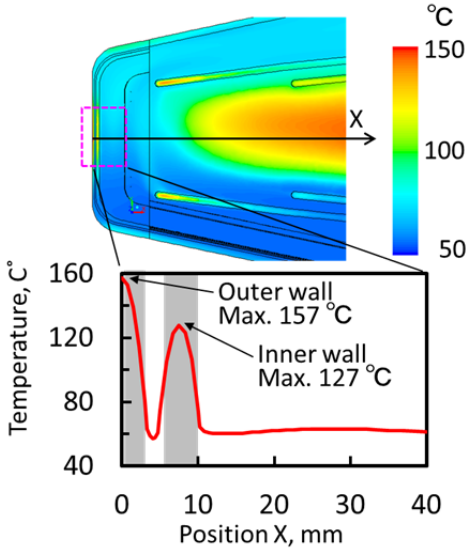

Figure 3. Temperature distribution on the horizontal cross section

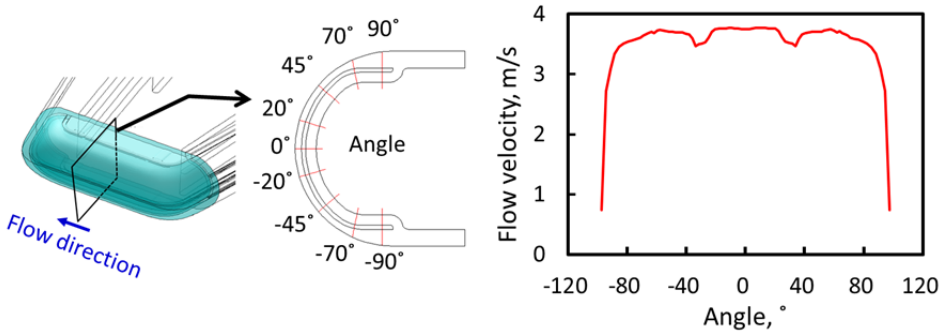

Figure 4. Mercury flow velocity distribution in the narrow channel in the vertical cross section at the center position of the beam window

narrow channel.

These results show that the design requirements of the double-walled target are fulfilled.

3.4 Influence of the fabrication tolerance of the narrow channel on the flow distribution

Because the target vessel is fabricated by welding many stainless steel parts, deformation due to the welding heat have to be considered. Because the gap of the narrow channel is small, 2 mm, the influence of the fabrication tolerance on the flow distribution should be evaluated in advance. Figure 5 shows the evaluated cases and the results. The angle in the horizontal axis of the graph has the same meaning as shown in Figure 4. In the simulation, two types of deformations were assumed, i.e., the forward and downward deformation. The models of these deformation patterns are such that the inner wall moved forward and downward respectively as shown in the upper figures in Figure 5. The channel gaps assumed in these cases are also shown in Figure 5. The flow velocity distributions in the vertical cross sections at three different positions were evaluated: the beam window center and 35 mm upstream and downstream from the center. Note that only the beam window region of the target vessel was modeled in this simulation to save the simulation cost, but the flow velocity distribution is well simulated, which can be understood by comparing Figure 4 and Figure 5 (a).

In the case of no deformation, the flow velocity distributions are fairly uniform at all cross sections

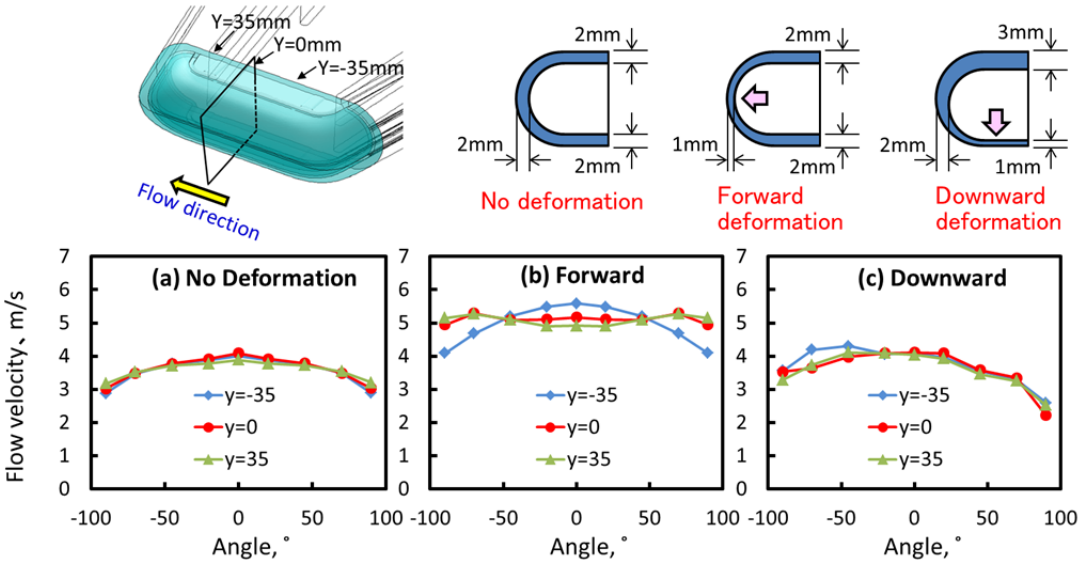

Figure 5. Deformation patterns of the inner wall and their influence on the flow distribution in the narrow channel

and are faster than 3 m/s. In the case of forward deformation, the average flow velocity increases at all cross sections because of the reduction in the cross sectional area of the flow channel. This result is advantageous for the cavitation damage mitigation. In the case of downward deformation, the flow velocity at the bottom side increased somewhat compared with the case of no deformation, but at the top side, where the channel gap increased to 3 mm, the flow velocity decreased to 2 m/s at all cross sections. This result indicates that special attention should be paid to the deformation that makes the channel gap broader, because it leads to reduction in the flow velocity.

3.5 Influence of inner wall fracture on the flow field

Because the efficacy of micro-bubbles to mitigate the cavitation damage has not yet been confirmed quantitatively in the actual mercury target, the possibility of inner wall fracture has to be considered. The inner wall fracture was modeled by a circular hole in the inner wall at the center of the beam window, and the influence of the hole on the flow fields in the narrow and bulk channels was evaluated. The hole diameter was assumed to be 10 mm and 30 mm. Figure 6 shows the simulation results. Surprisingly, the mercury flow velocity in the narrow channel at the center of the beam window does not decrease much, and the velocity is kept well over 3 m/s even in the case of a 30-mm hole diameter. The ratio of the amount of mercury flow outgoing to the bulk channel from the narrow channel, which is called the branch flow, is only 0.2% and 2.7% for the 10-mm and 30-mm holes, respectively.

Figure 7 shows the pressure distribution at the center axis of the hole. For the 10–mm hole, the pressure difference in the narrow and the bulk channel is very small near the region of the hole, which suppresses the branch flow. For the 30–mm hole, there is a pressure gradient descending to the bulk channel from the narrow channel, which causes the branch flow of 2.7%.

These results indicate that the effect of rapid mercury flow in the narrow channel to mitigate the cavitation damage is kept even if a damage hole penetrates the inner wall at the beam window. Of course, the shape of the damage hole and edge might influence the flow field in the narrow channel, but as a matter of fact, it was observed at SNS that the outer wall of the narrow channel was not damaged, and the inner wall had damages penetrating throughout the wall thickness. Thus, there is a possibility of double-walled target structure having a hole originally at the center of the beam window of the inner wall.

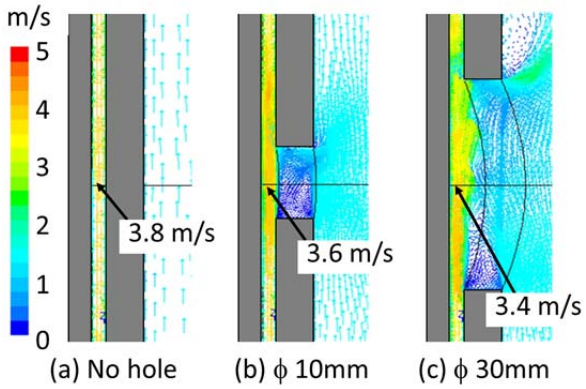

Figure 6. Mercury flow fields in the case of inner wall fracture. The fracture was modelled by a circular hole at the center of the beam window.

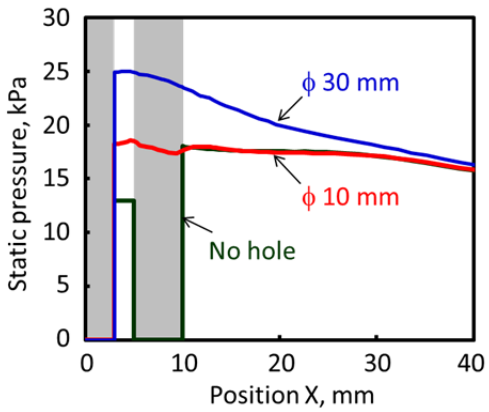

Figure 7. Pressure distribution along the center axis of the beam window (x axis is the same as Figure 1 and Figure 2).

4. Water experiments using a mock-up model

4.1. Experimental setup

In order to verify the simulation results shown above, water experiments using the mock-up model of the double walled target were carried out. The model was made of transparent acrylic resin to be used for the visualization experiment. The inner structure and the size were the same with the actual target, but the wall thickness was much thicker to ensure the structural strength against the inner pressure of around 0.2 MPa. The target model was set horizontally and the water flow velocity in the narrow channel of the double wall was measured by processing the images taken by the high speed video camera. Bubbles of ca. 0.5 mm in diameter were injected at the upstream of the narrow channel as the seeding particles to measure the water flow velocity by image processing. The high speed video camera was set at the upper side of the model to get clear image of bubbles as shown in Figure 8. The water flow velocities were measured at the areas of upstream and downstream of the beam window center to investigate the influence of the hole at the beam window simulating the inner wall fracture. The field of view was square with the dimensions of 50 mm x 50 mm.

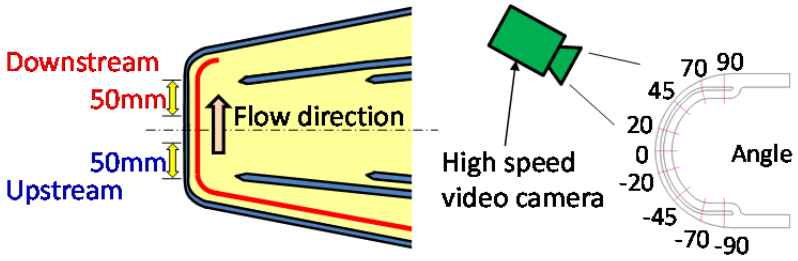

Figure 8. Focused area of video camera on the water experimental model

4.2. Experimental results

When the water velocity is very high, which is more than 10 m/s, the clear image of the bubble flow cannot be obtained even if the flame rate of the video camera is maximized. Thus, the experiments were carried out with the water flow velocity of around 6 m/s in the narrow channel, which corresponds to the water flow rate of 1050 L/min at the inlet of the target model. The water flow velocity was 1.85 m/s and the Reynolds number at the target inlet was 213000, which is 1/5 of mercury flow condition in actual target. Just the same way as the simulation, the fracture of the inner wall was modelled by a circular hole at the center of the beam window. Three cases were measured, which are no hole, 10 mm and 30 mm in diameter.

Figure 9 shows the results of the water experiments. In the case of no hole, the flow velocity is fairly

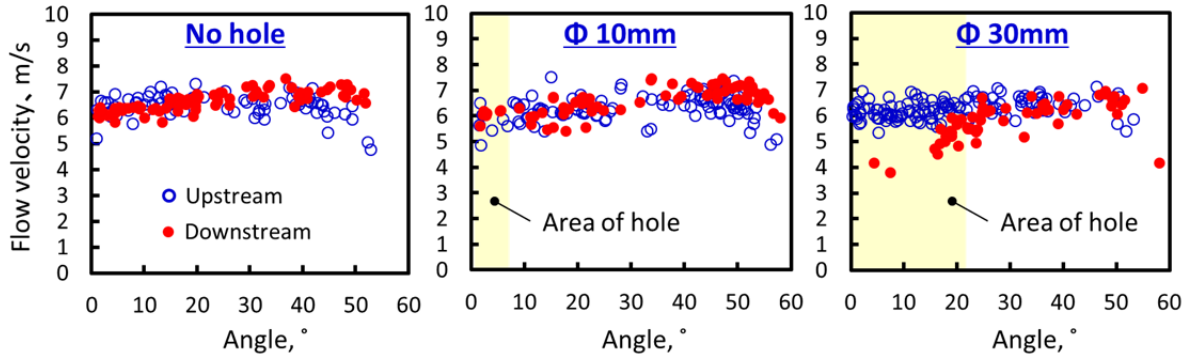

Figure 9. Results of the water experiments
(Water flow rate at model inlet : 1050 L/min)

uniform across the angle position. In the case of 10 mm, no obvious flow velocity change was detected at both the upstream and the downstream, which indicates that the inner wall fracture of 10 mm in diameter does not disturb the flow field in the narrow channel so much. These results are consistent with the simulation results shown in the former chapter. But in the case of 30 mm, the flow velocity decreased by 30 % at downstream of the modelled hole. The velocity reduction is larger than that evaluated by the simulation and the cause of the difference will be investigated by water simulation. It was found that the flow velocity in the narrow channel is not disturbed by the small damage of the inner wall, which suggests that the effect of cavitation damage mitigation can be maintained.

5. Summary

Evaluation of the thermal hydraulic design of a double-walled target vessel was performed by numerical simulations, and the items shown below were found:

1) A rapid mercury flow velocity of almost 4 m/s in the narrow channel was attained at the beam window, which might lead to the damage mitigation of the wall.
2) The effect of the double-walled structure to promote the cooling performance of the target vessel was confirmed, making it possible to increase the inner wall thickness.
3) When setting the fabrication tolerance of the narrow channel, special attention should be paid to the deformation that makes the channel gap broader, thereby leading to the reduction in the flow velocity.
4) Fast flow velocity in the narrow channel is maintained even at a fractured place open to the bulk channel, and the amount of mercury flowing out of the narrow channel to the bulk side is very small.

The water experiments were carried out to verify the simulation results with the Raynolds number of 1/5 of the actual mercury target, and the items shown below were found:

5) The flow velocity is fairly uniform across the angle position.
6) The inner wall fracture of 10 mm in diameter does not disturb the flow field in the narrow channel so much. These results are consistent with the simulation results.

6. References

[1] M. Futakawa, et.al.: Nucl. Instr. and Meth., A 562 (2006) p.676.
[2] M. Futakawa, et.al.: J. Nucl. Sci. Technol., Vol. 45 (2008) No. 10, p.1041.
[3] B. Riemer, et al.: J. Nucl. Mater., 377(2008) p.162.
[4] B. Riemer, et al.: J. Nucl. Mater., 398 (2010) p.207.
[5] D. McClintock, et al.: J. Nucl. Mater., 431(2012) p.147.
[6] T. Naoe, et.al.: Transactions of the JSME, Vol. 80 (2014) No. 810, fe0025. (in Japanese.)

3.2.4

Pressure wave reduction due to gas microbubbles injection in mercury target of J-PARC

H Kogawa, T Naoe, T Wakui, K Haga, M Futakawa and H Takada
J-PARC Center, JAEA, Tokai, Ibaraki 319-1195, Japan.

E-mail: kogawa.hiroyuki@jaea.go.jp

Abstract. We have developed a helium gas microbubbles injection system to reduce the pressure waves in mercury target of pulsed spallation neutron source of J-PARC (the Japan Proton Accelerator Research Complex). The reduction effect with the microbubbles injection was investigated to measure the displacement velocity of the target vessel with a novel diagnostic system using laser Doppler vibrometer. The measurement was carried out under the conditions that the proton beam power was from 60 kW to 300 kW and the injected gas fraction, β (ratio of injected gas flow rate to mercury flow rate), was from 0 to 4×10^{-3}. As results, we confirmed the pressure waves measured with bubbles injection of $\beta=4\times10^{-3}$ reduced to 1/4 of those without the microbubbles injection.

1. Introduction

At the Japan spallation neutron source (JSNS) of the J-PARC (Japan Proton Accelerator Research Complex) a mercury target system has been operated by bombarding pulsed proton beam to produce neutron beams for promoting not only researches of materials science, life sciences, etc. but also industrial applications [1]. The pulse duration and the repetition rate of proton beam are 1 μs and 25Hz, respectively. Hence the beam energy is 40 kJ/pulse in the rated beam power of 1 MW. Since the time duration is very short, mercury is rapidly heated and pressure waves are generated in mercury. They impose on the mercury target vessel which is made of Type 316L stainless steel, deforming it. Hence the reduction of pressure waves is important to reduce fatigue damage in the vessel. Furthermore, the deformation and inertia due to pressure wave propagation induce negative pressure at the vicinity of the target vessel, which causes cavitation. The cavitation induces erosion on the target vessel, shortening its lifetime significantly [2, 3]. At the spallation neutron source in US (SNS), the target vessel was damaged by cavitation induced erosion. As comparing the operational conditions between the JSNS and SNS, the repetition rates are 25 and 60 Hz, respectively. Therefore, since the energy of one proton beam pulse in the JSNS is 2.4 times higher, the target vessel in the JSNS receives higher pressure waves than those in SNS when the proton beam power is same.

We have been developing a microbubbles injection technique to reduce the pressure waves which cause cavitation erosion and fatigue damages on the mercury target vessel. Microbubbles in the mercury target are oscillated by the pressure waves and this oscillation dissipates the energy of pressure waves by changing kinetic energy to thermal energy. The bubble oscillation depends on the increasing time of pressure and bubble size. That is, the smaller bubbles are favorable to reduce the pressure waves which rapidly increase its amplitude. Numerical calculation showed that the microbubbles of 100 μm in radius mitigated efficiently the pressure wave in the mercury target [4].

A microbubble generator [5] was installed into the mercury target system of J-PARC and the

operation of the real target system with bubbling has been started since October 2012, which is the first operation in the world. During the operation, the proton beam power and beam profile, which change strength of pressure waves generated in mercury, and the bubbling condition were varied to estimate the effect under high power condition. In this report, the effect of bubble injection on pressure wave reduction is presented under the various proton beam and bubbling conditions.

2. Mercury target system in JSNS

Figure 1 shows schematic of the mercury target vessel of JSNS. Proton beam bombards at nose of the target vessel which is called as a beam window. The mercury target vessel consists of a mercury vessel and surrounding safety hull to prevent the mercury spill to the outside if the mercury vessel is broken. Figure 2 shows the heat density distribution for the 1 MW beam injection calculated with the Particle and Heavy Ion Transport code System (PHITS) [6, 7]. At present, the beam power has been reached to 300 kW. The beam power, the peak heat density and the distributions of heat density in x- and y-direction in mercury as shown in Figure 2 were changed to investigate the effect of beam condition on the generated pressure waves. To remove efficiently the generated heat, there are flow guide inside of the mercury target vessel as show in Figure 1 (a). These flow guides have roles of not only controlling mercury flow pattern in the vessel but also has restriction of a deformation of the vessel due to the pressure wave. Mercury comes into an inlet pipe, and then it flows perpendicularly to the proton beam injecting direction as its flow rate is distributed to much the heat density distribution by a flow guides. In the case of the beam condition as shown in Figure 2, pressure of ca. 40 MPa and stress of 150 MPa will be generated at the peak heat position and the beam window, respectively.

The pressure waves could be measured indirectly by the deformation of the target vessel in the JSNS. A laser Doppler vibrometer (LDV) was installed in the JSNS. The LDV measures the displacement velocity in the direction of the laser beam injection. The reflective mirror is set on the top of the target vessel to reflect the laser beam efficiently as show in Figure 1 (b). The mercury vessel and the safety hull are connected by the ribs and the mirror set on the rib, so that the mirror can follow the vibration of the mercury vessel due to the pressure.

Bubble generator is set in the target vessel, which injects microbubbles to mercury. The bubble generator was set in the inlet pipe at 450 mm apart from the beam window to realize both of many bubbles passing near the peak heat position and the beam window and the structural integrity of the bubble generator against the thermal stress due to the temperature rise in the bubble generator itself. This bubble generator generates microbubbles of 90 μm in radius. In this study, not only the beam condition but also the bubbling condition was changed to investigate the effect of the bubbles on the pressure wave reduction. Actually we were troubled on that injected gas could not be increased up to summer in 2013 because mercury came into a gas supplying line and injected gas fraction, β, which is defined as the value of the injected gas flow rate, Q_{He}, divided by the mercury flow rate, Q_{Hg}, was 9×10^{-4} in user operation. In summer shutdown 2013, a liquid-gas separator was installed and the injected gas fraction could be increased to 4×10^{-3}.

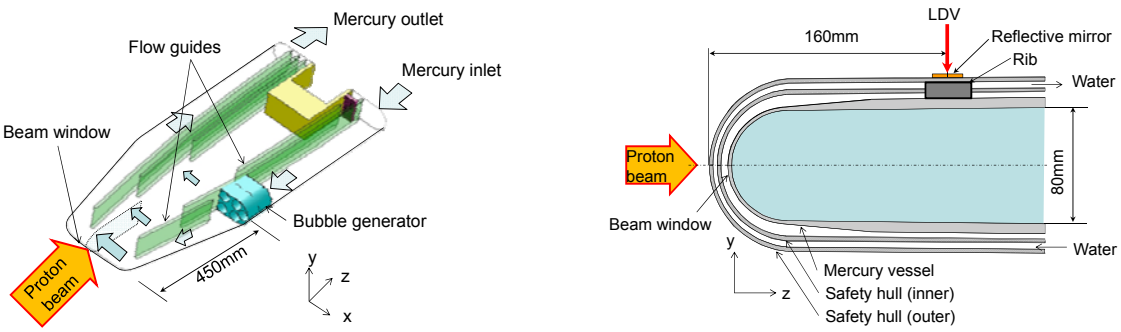

(a) Mercury vessel (Bird view) (b) Target vessel (cross sectional view)

Figure 1. Schematic of mercury target vessel.

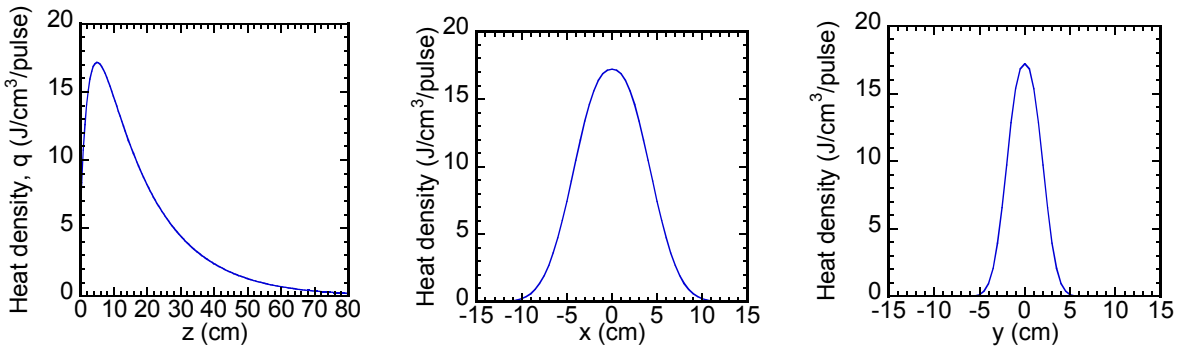

(a) (b) (c)

Figure 2. Distribution of heat density in mercury under 1 MW proton beam condition;(a) Along the beam injection direction (z) at x=y=0 cm, (b) Along x-direction aty=0 cm z=4 cm, (c) Along x-direction at x=0 cm z=4 cm.

3. Reduction of pressure wave by bubbling

Figure 3 compares time history of displacement velocity between the cases without and with bubbling under the beam condition of 300 kW and 3.0 J/cm^3/pulse. With bubbles injection, the maximum velocity decreased to 1/3 of the case without bubbling. And high frequency components caused by the shaking of the mirror, which appears in the case without bubble, was attenuated by the injecting bubbles. Figure 4 compares the maximum velocity among various beam conditions and with or without bubbling. Comparing with the cases without bubbling, the maximum velocity has lager variation in the case with bubbling. This is caused by the variation of the injected gas amount. In the same power, the maximum velocity increases with the heat density. The averaged maximum velocity generated in the bubbling condition is ca.2/3 of that in without bubble.

Reduction of the pressure waves depends not only on the injected bubble size but also amount of the injected gas [4]. The injected gas fraction was changed. Figure 5 shows the reduction of the maximum velocity as a function of the amount of injected gas fraction. The vertical axis represents the averaged maximum velocity obtained with the bubbling condition, which is normalized by that obtained under the same proton beam condition without bubbling. It is noted that the results shown in Figures 3 and 4 are obtained when the injected gas fraction is ca. 9×10^{-4}. The normalized maximum velocity decreased with increase of the injected gas fraction. The normalized velocity was reduced by increasing the injected gas fraction. When the injected gas fraction was increased to 1.7×10^{-3} and 4×10^{-3}, the averaged maximum velocity reduced to 1/3 and 1/4 of that without bubbling, respectively.

4. Discussion –Estimation of bubbling effect under the high power condition-

As shown in Figures 4 and 5, the maximum velocity induced by the pressure wave depends on the beam condition and the injected gas fraction. Since the beam power will be increased from 300 kW to 1MW, we estimated the velocity for high-power beam-condition.

As shown in Figures 4, the maximum velocity, V_{max}, increases as a function of the maximum heat density q_{max},

$$V_{max} = A \times q_{max}^{B} \quad (1)$$

where, A is the constant depending on the beam power and B the constant depending on the bubbling condition. Furthermore, the constant A increases as follow;

$$A = C \times W^{D} \quad (2)$$

where, W [kW] is the beam power in 25 Hz operation. Table 1 shows the B, C and D values obtained from Figure 4.

At present, operation is possible with the injected gas fraction, β, of 4×10^{-3}. Supposing that the

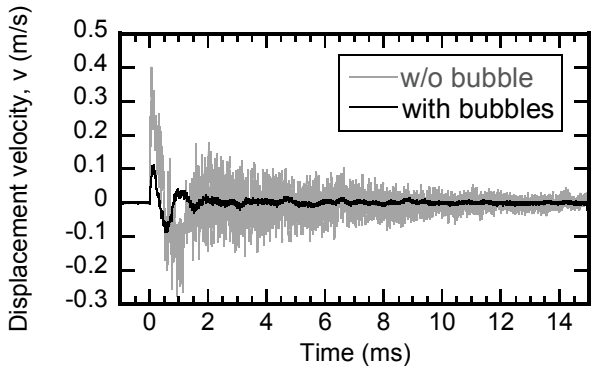

Figure 3. Comparison of the time history of the displacement velocity between cases without bubbling and with bubbling under the 300 kW and 3.0 J/cm^3/pulse.

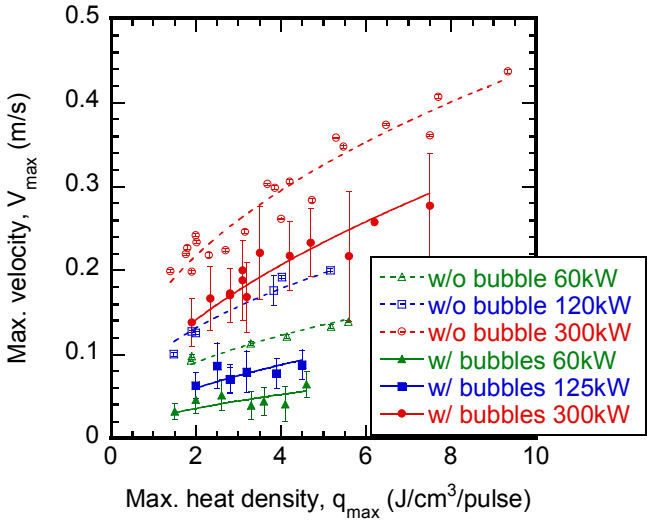

Figure 4. Comparison of the maximum velocity between the bubbling condition (β=9×10^{-4}) and without bubble.

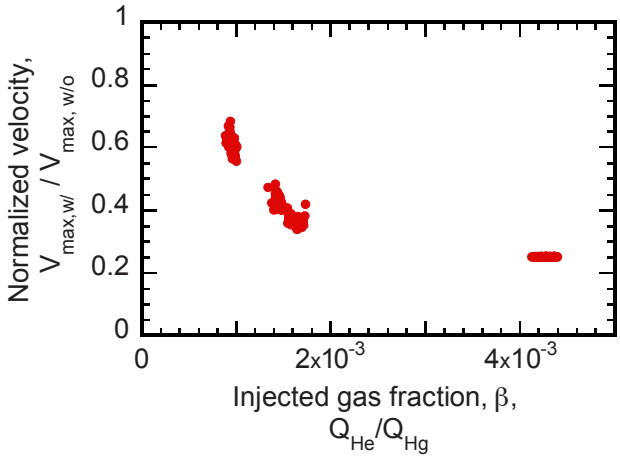

Figure 5. Effect of the injected gas fraction on the reduction of the maximum velocity (W=300 kW).

maximum heat density, q_{max}, will be 0.011×W [J/cm^3/pulse] in the future operation for the user program, the maximum velocity estimated by using the equations (1), (2) and Figure 5 is shown in Figure 6. In the case of $\beta=4\times10^{-3}$, the maximum velocity under 1 MW beam condition is estimated to be 0.33 m/s which corresponds to 315 kW beam condition without bubble. This is expected to mitigate the cavitation induced erosion on mercury vessel. The effect of bubble injection on mitigation of cavitation induced erosion will be evaluated by observing the target vessel cut after its service operation.

Table 1 *B* and *C* values for equations (1) and (2)

	B	***C***	***D***
Without bubble	0.44	0.0075	0.56
With bubbles ($\beta=9\times10^{-4}$)	0.55	0.00096	0.8

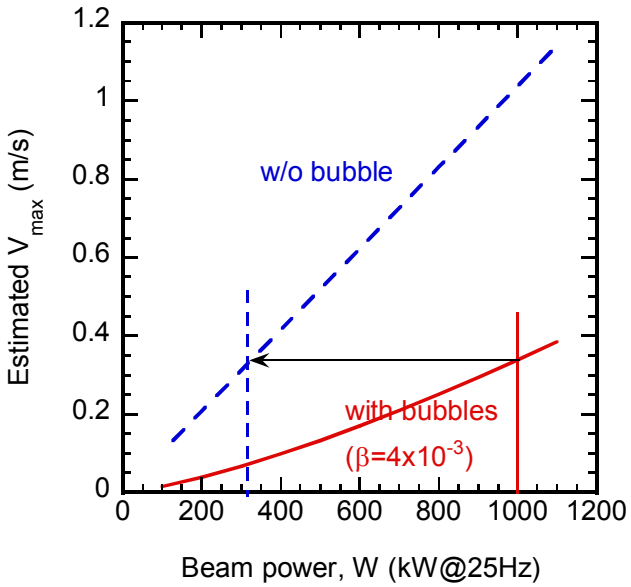

Figure 6. Estimated maximum velocity comparing the bubbling case to the case without bubble.

5. Summary

The effect of the bubble injection on reduction of the pressure waves was confirmed by the test operation in the JSNS, J-PARC. The bubble generator installed into the JSNS mercury target generates the microbubbles of 90 μm in radius. The injected gas fraction, β, was varied from 9×10^{-4} to 4×10^{-3} comparing with the case without bubble injection. To estimate the bubble effect under high-power proton-bema condition, the proton beam power bombarding the mercury target was changed from 60 kW to 300 kW and the displacement velocity which indicates the strength of the pressure wave of target vessel was measured with novel diagnostic system using the laser Doppler vibrometer.

In the case of $\beta=9\times10^{-4}$, the maximum velocity of the target vessel was reduced to 1/3 of that without bubbling in the best case. The averaged result shows the velocity reduction of 2/3. The averaged maximum velocity was reduced by the increase of the injected gas fraction. That is, when the injected gas fraction was increased to 1.7×10^{-3} and 4×10^{-3}, the averaged maximum velocity reduced to 1/3 and 1/4 of that without bubbling, respectively.

Effect of bubble injection on the pressure wave reduction under high-power proton-beam condition was estimated based on the measured result. The estimation indicated that the maximum displacement velocity generated in 1 MW beam operation with bubbles of $\beta=4\times10^{-3}$ corresponds to that in 315 kW operation without bubbles. This is expected to mitigate the cavitation induced erosion on mercury

vessel to prolong its lifetime. The effect of bubble injection on mitigation of cavitation induced erosion will be evaluated by observing the target vessel cut after its service operation.

References

[1] Information on http://j-parc.jp/index-e.html
[2] Futakawa M, Naoe T, Kogawa H, Tsai C C and Ikeda Y 2003 *J. Nucl. Sci. Technol.* **40** 895
[3] Futakawa M, Naoe T, Tsai C C, Kogawa H, Ishikura S, Ikeda Y, Soyama H and Date H 2005 *J. Nucl. Mat.* **343** 70
[4] Okita K, Takagi S and Matsumoto Y 2008 *J. Fluid Sci. Technol.* **3** 116
[5] Kogawa H, Haga K, Naoe T, Kinoshita H, Ida M and Futakawa M 2010 *Proc. ICANS XIX* (Grindelwald: Switzerland)
[6] Harada M, Maekawa F, Teshigawara M, Kato T and Watanabe N 2008 *Proc. ICANS-XVIII* (Dongguan: China), p 616
[7] Harada M, Maekawa F, Oikawa K, Meigo S, Takada H 2011 *Progress in NUCLEAR SCIENCE and TECHNOLOGY*, **2**, pp 872-878

3.2.5

In-situ structural integrity evaluation for high-power pulsed spallation neutron source by using a laser Doppler method

T. Wan, T. Naoe, T. Wakui, K. Haga, H. Kogawa and M. Futakawa

J-PARC Center, 2-4 Shirane Shirakata, Tokai-mura, Ibaraki 319-1195, Japan

wan.tao@jaea.go.jp

Abstract. High-power pulsed spallation neutron sources are being developed in the world. Mercury is used as a target material to produce neutrons. At the moment of the proton beams bombard the mercury target, the mercury target vessel is impulsively excited resulting from the interaction between mercury and solid wall due to the pressure waves. The vibrational velocity on the outer surface of the target vessel was measured by a laser Doppler vibrometer to diagnose the structural integrity of the vessel. Measured vibrational signals, were applied for evaluating the damage inside the target vessel that is induced by the cyclic loading and cavitation bubble collapsing due to the pressure waves. A technique, the Wavelet Differential Analysis (WDA), was applied to clearly indicate the effects of damages on the impulsive vibration behavior. Moreover, in order to reduce the effects of superimposed noise on the vibration signals on the WDA, the statistical methods, the Analysis of Variance (ANOVA) and the Analysis of Covariance (ANCOVA), were applied. The lab-experimental results, numerical simulation results with manually added random noise, and field data were analysed by the statistic methods. The results demonstrated that the established in-situ diagnostic technique can effectively evaluate the structural integrity.

Nomenclature

WDA	Wavelet Differential Analysis	
WDI	Wavelet Differential Image	
Img	Wavelet Image	
f	frequency	Hz
t	time	s
I_a	average intensity of WDI	
D	diameter of damage	mm
$V(t,f)$	value of intensity of the WDI at time t and frequency f	dB
SS_T	total sum of square	
n	total number of samples	
y_{ij}	*jth* sample value of the *ith* group	
M	sample mean of all samples	
h	number of samples in each group	
$\bar{y}_i$	sample mean of the *ith* group	

X	factor X that affects the vibration behavior
Y	factor Y that affects the vibration behavior
SS_b	sum of square between groups of samples
SS_e	sum of square within groups of samples
SS_X	sum of square due to factor X
SS_Y	sum of square due to factor Y
D_X	degree of freedom of factor X
D_e	degree of freedom of within groups of samples
F	calculation value of F-test
SS_{noise}	sum of square due to noise
$SS_{residual}$	sum of square excluding noise
$D_{e'}$	degree of freedom of modified within groups of samples
$SS_{b'}$	modified sum of square between groups of samples
$SS_{e'}$	modified sum of square within groups of samples
F'	modified calculation value of F-test
T	calculation value of t-test
$\bar{y}_k$, $\bar{y}_l$	modified sample mean of the *kth* and *lth* group
$S_{\bar{y}_k - \bar{y}_l}$	standard error of the modified sample mean
$f(x)$	random function of noise amplitude
A,-A	maximum amplitude value of noise
c, d	constants

1. Introduction

High-power pulsed spallation neutron sources are being developed in the world. In the Japan Spallation Neutron Source (JSNS), pulsed proton beams (25 Hz, 1 μs pulse duration) are injected into a mercury target to produce neutrons for the innovative materials and life science research. The mercury target vessel is a triple walled structure consisted of water shroud, helium vessel, and mercury vessel. The proton beam window of mercury vessel has a double-walled structure consists of inner and outer walls with a mercury narrow channel. However, various kinds of damages, such as cavitation, cyclic fatigue and proton and neutron irradiation damage, are imposed on the target vessel during its operation. Especially the cavitation damage caused by the pressure waves is a critical issue for the target vessel. Pressure waves are generated in the mercury due to rapid heat deposition resulting from the proton beam injection [1, 2]. The pressure waves propagate to the target vessel and impose cavitation damage on the inner wall, especially at the beam window portion [3]. Meanwhile, the pressure waves give rise to the vibration of the target vessel.

The cavitation damage remarkably reduces the life-time of the target vessel [4, 5]. To solve this issue, the micro bubbles injection technique is being developed by Japan Atomic Energy Agency (JAEA) to mitigate the pressure waves [6~11]. On the other hand, it is also important to establish the structure integrity evaluation technique for the target vessel, which is strongly expected from the viewpoint of estimating the lifetime of the target and keeping stable operation.

The dynamic responses of the target vessel vibration caused by the pressure waves were focused on to develop the structure integrity evaluation technique. A laser Doppler vibrometer (LDV) was installed as an in-situ diagnostic system with the advantage of providing an entirely remote and non-contact technique, which prevents the sensor from the radiation damage [12]. This diagnostic technique can be applied to the structural integrity diagnosis for not only the nuclear facilities but also extreme environments where a human activity is extremely limited, such as in the space and the oceans.

In the case of numerous cavitation damage imposed on the inner wall of the target vessel, the vessel might be easily deformed by the thermal stress because the thickness of wall is reduced, and the gap of the window channel would be possibly reduced due to the deformation. The cavitation damage is accumulated on the inner wall and if it was severe enough, the inner wall would be broken and a

penetrated damage would be formed on it. The vibration signals will be affected by the deformation of inner wall and the penetrated cavitation damage, as shown in Fig.1.

In a previous study, penetrated cavitation damage was assumed on the inner wall of target vessel [13]. The dependency of dynamic responses of double-walled target vessel on cavitation damage was investigated through the numerical simulation. The diagnostic technique, Wavelet Differential Analysis (WDA), was developed to clearly observe the differences of vibration signals that are dependent on cavitation damage.

Nevertheless, the damage dependency is usually covered by the noise that appears in the lab-scale experimental and real system of field data which was obtained by the LDV during the operation of the real target. In the present study, on basis of the WDA technique, the statistical methods referred to as Analysis of Variance (ANOVA) and Analysis of Covariance (ANCOVA) were used to reduce the noise effect on the impulsive vibration behavior.

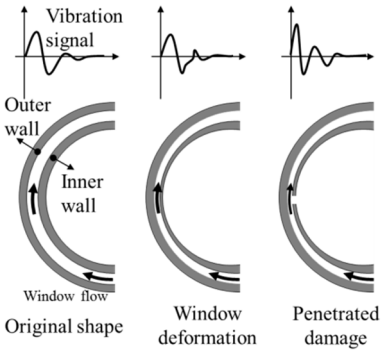

Figure 1. Schematic drawing of window deformation, damage scenarios and target vessel vibration.

2. Experiments

To experimentally investigate the dependency of vibration behavior on damage, an electro-Magnetic IMpact Testing Machine (MIMTM) was used to simulate the double-walled structure of the target vessel. Figure 2 shows the schematic of detection setup of MIMTM vibration. An electro-magnetically driven striker impulsively impacted the mercury, which was filled in a chamber with a size of Φ100×15 mm^3, to impose the pressure waves on type 316L stainless steel plate specimen (60×60×2.5t mm^3), which is the same material as the mercury vessel was fixed into the chamber by bolts. The gap between the specimen and the upper wall of MIMTM was fixed to 2.3 mm. In order to moderate the penetrated cavitation damage on the inner wall, penetrated holes with diameters of 1, 2, 5, and 10 mm were made at the center of the specimens, respectively. Impulsive pressure signals were induced in mercury at a power of 560W/pulse with a repetition rate of 1 Hz. The cavitation damage occurred under such a condition in the MIMTM was roughly similar to that of the MW-class proton beam injection [14].

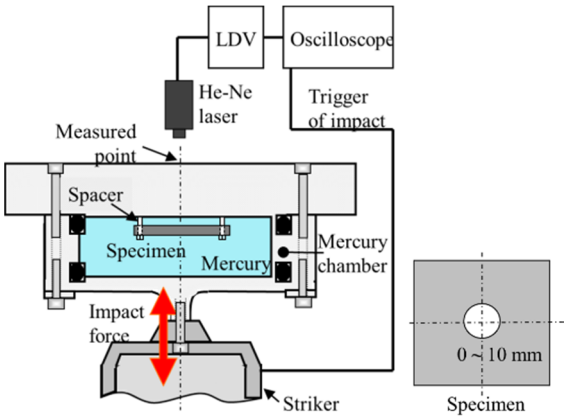

Figure 2. Schematic drawing of measuring system of MIMTM vibration.

The vibration of MIMTM was subsequently detected by a He-Ne laser Doppler vibrometer (Onosokki, LV1710). The laser (wavelength: 633 nm) was illuminated onto the center of the upper rid of the mercury chamber. The detectable frequency range was from 1 Hz to 3 MHz with a sensitivity of 0.01 (m/s)/v. The detected vibration velocity signals were saved in an oscilloscope with a sampling rate of 1.25 MHz. The oscilloscope was triggered by the drive signal of the electromagnetic coil. Each signal was obtained by averaging 100 impacts in order to reduce the background noise.

3. Numerical simulations

In order to investigate the dependency of dynamic responses of the double-walled target vessel on damage under conditions of various proton beam powers, FEM analyses were carried out using a conventional code LS-DYNA [13, 15]. A half model (Figure 3) for the double-walled target vessel of JSNS was established. The gap between the outer and the inner walls was set 2 mm. Structures and the mercury were meshed as a half model by the shell and solid elements, respectively. Numbers of shell and solid elements were 95052 and 1758852, respectively. The boundary of Z-direction of the bottom of the vessel was kept fixed, and that of the end of the mercury was set to be non-reflecting.

Penetrated damage holes with diameters of 1, 5, 10, 20 and 40 mm were assumed on the inner wall of the target vessel at the center of the beam incident area, as shown in Figure 4. This position is most likely to be damaged [3]. The output node position, measuring point, is the same as the LDV measurement point on the real target vessel. In this simulation, helium vessel and water shroud was ignored, because the effects of helium vessel and water shroud on vibration signals have been checked and the results are unremarkable.

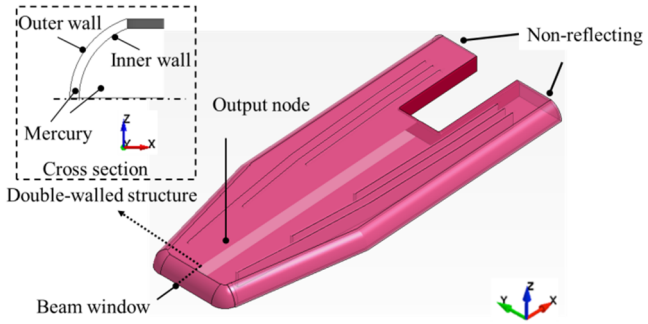

Figure 3. Geometrical model of mercury vessel.

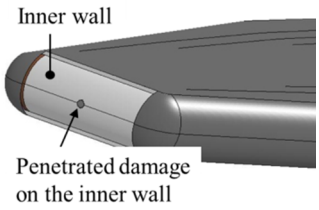

Figure 4. Damage location.

4. Analysis methods and calculation procedure

4.1. Wavelet differential analysis [13]

In order to clearly and quantitatively indicate the differences caused by damage, first, the wavelet differential process for the time responses of vibration velocity was carried out; the process is described by Eq. (1):

$$WDI_D = |Img_D - Img_0| \,/\, |Img_0| \,, \tag{1}$$

where *WDI* is the wavelet differential image, *Img* is the wavelet image of vibration signal, and the subscripts *D* represents the damage with a diameter of *D* mm, whereas the subscript *0* implies no damage. Then, the average intensity (I_a) of the wavelet differential image (*WDI*) could be calculated through equations (2) – (4).

$$I_a = \int^{\Delta f} \int^{\Delta t} V(t,f)dtdf \,, \tag{2}$$

$$\Delta f = f_2 - f_1 \,, \tag{3}$$

$$\Delta t = t_2 - t_1 \,, \tag{4}$$

where measuring frequency ranges from f_1 to f_2 (in hertz), and measuring time ranges from t_1 to t_2 (in seconds); $V(t, f)$ is the value of the intensity of the WDI at time t and frequency f (in decibels), and I_a is the average intensity of the differential image.

4.2. Applied statistical methods

4.2.1. *Analysis of variance* In the present study, we are very interested in the differences of vibrational signals caused by damage. In order to analyse the differences of groups of WDI results, the statistic method referred to as the ANOVA was applied. In ANOVA, the total variation of data is portioned into several components [16-18]. The total variation of the system, defined by the total sum of squares term, SS_T:

$$SS_T = \sum_{ij}(y_{ij} - M)^2 \quad for\, i, j = 1, 2, 3, \cdots, p, \tag{5}$$

$$M = \frac{1}{n}\sum y_{ij} \ , \tag{6}$$

where n represents the total number of samples; y_{ij} represents the *jth* sample value in the *ith* group; M is the sample mean of all samples.

Experimental studies contain certain test error, and so it is necessary to calculate the error variance in ANOVA. The total sum of square can be divided into the sum of square between groups of samples, SS_b, and sum of square within groups of samples (caused by error), SS_e:

$$SS_T = SS_b + SS_e \ , \tag{7}$$

$$SS_b = \sum_i h(\bar{y}_i - M)^2 \ , \tag{8}$$

$$SS_e = \sum_{ij}(y_{ij} - \bar{y}_i)^2 \ , \tag{9}$$

where h is the number of samples in each group, $\bar{y}_i$ is the sample mean of the *ith* group.

If there are two main factors that affect the results and the two factors have no mutual interactions with each other, then the total sum of square can be expressed as:

$$SS_T = SS_X + SS_Y + SS_e \ , \tag{10}$$

where SS_X and SS_Y represent variations due to factor X and Y, respectively.

Degrees of freedom need also to be considered together with each sum of squares whilst performing ANOVA calculations. Subsequently, the obtained data are used to calculate the value F of F-test. The value of F for factor X can be expressed as following:

$$F = \frac{SS_X/D_X}{SS_e/D_e} \ , \tag{11}$$

where D_X and D_e are the degree of freedom of factor X and within groups of samples, respectively. The value of F for factor Y can be calculated as the same way.

The value F represents the difference degree between the groups of samples. Larger F value means there are more obvious differences between groups of samples.

4.2.2. *Analysis of covariance* ANCOVA is a statistic method that combined regression and ANOVA [16]. When the noise level is considerable high, it might have significant effects on the vibration analysis. The damage dependency might be masked by the noise. So it is necessary to remove the noise effects from the results. In ANCOVA, the total sum of square, SS_T, can be divided into the sum of square of noise, SS_{noise}, and that of excluding noise, $SS_{residual}$, which is shown as:

$$SS_T = SS_{noise} + SS_{residual} \ , \tag{12}$$

The former part at the right hand of the equation can be removed by a regression analysis. The sample mean of each group is modified by the regression. The sum of square of residual part consists

of modified sum of square between groups of samples, $SS_{b\prime}$, and modified sum of square within one group of samples, $SS_{e\prime}$. It can be expressed that:

$$SS_{residual} = SS_{b\prime} + SS_{e\prime}, \tag{13}$$

Subsequently, F-test was carried out (taking factor X as an example):

$$F' = \frac{SS_{b\prime}/D_X}{SS_{e\prime}/D_{e\prime}}, \tag{14}$$

where $D_{e\prime}$ represents the degree of freedoms of modified within groups of samples. The F' factor is considered to be able of indicating the differences more exactly because the noise effect is taken into consideration.

Finally, t-test was carried out for multiple comparisons between the modified groups of samples. It can be expressed as the following:

$$T = \frac{\bar{y}_k - \bar{y}_l}{S_{\bar{y}_k - \bar{y}_l}}, \tag{15}$$

where $\bar{y}_k$ and $\bar{y}_l$ are the modified sample mean of the *kth* and *lth* group; $S_{\bar{y}_k - \bar{y}_l}$ is the standard error of the modified sample mean. Similar with the *F* factor, the *T* value represents the difference degree between the groups of data.

4.3. Calculation procedure

In order to reduce the noise effects on the results, the WDA, ANOVA and ANCOVA were applied to raw data analysis, by the following calculation procedure.

Many parameters, such as damage size, beam power, bubble condition, etc., may impose effects on the target vessel vibration results. At first we are very interested in the damage size effects on the vibration behaviours of target vessel. In the following text of this sub-section, damage size is selected as the parameter to introduce the calculation procedure under the condition of fixing other parameters.

Figure 5 shows the flow chart of calculation procedure. First, one reference raw data should be selected, which is usually the time response of vibration signals with minimum damage among the raw data which needed to be analysed. The raw data should be classified into different groups, and each group represents one level of damage degree. The number of samples in one group, *h*, is the same in each group. Subsequently the wavelet differential images were obtained between the data in each group and the reference data, and then the I_a of each *WDI* was calculated. Through the above calculations, I_a of *WDIs* was got in each group with a number of *h*. The simple average value and error bar for the I_a of *WDIs* in each group can be calculated. After that, group number one that with the minimum damage is set as the reference group. The ANOVA and ANCOVA are carried out by using I_a of *WDIs* between other groups and group number one, respectively. The *F* factor of ANOVA and *T* factor of the ANCOVA can be obtained to indicate the degree of difference between other groups and group number one. Larger value of *F* or *T* indicates more significant differences between groups.

5. Results and discussions

5.1. MIMTM vibration

Figure 6 shows the time responses of MIMTM vibration velocity. It can be seen that the differences between the dynamic responses without damage and that with damage is obvious. To quantify the penetrated damage size dependency, the I_a *of WDI* was calculated. Figure 7 shows the I_a *of WDI* as a function of the damage size. The average vale of I_a *of WDI* is dependent on the damage size, however, the tendency of I_a *of WDI* is unobvious, and error bar is large for each group of twelve data. This is because experimental results contain noise and the I_a of *WDI* is sensitive to noise. Therefore, the dependency of I_a of *WDI* on damage is influenced by noise. Subsequently ANOVA was carried out. The data was grouped by damage size. The noise in each data is different. The group of data without

damage was set as the reference group. Figure 8 shows normalized *F* factor of ANOVA as a function of the penetrated damage size. The damage dependency is clearly recognized by using *F* factor of ANOVA. The *F* factor increases steadily when the damage size trends larger. The differences between the time responses of vibration velocity with damage and those without damage trend much more obvious with increasing the damage size. From the results, it is learned that larger damage size imposes more significant effects on the vessel vibration. If a penetrating damage forms on the inner wall of the target vessel, pressure waves propagate through the damage to vibrate the outer wall of target vessel. When the damage trends larger, more energy will be carried by the waves to impact the outer wall, and thus stronger vibration of the target vessel is aroused.

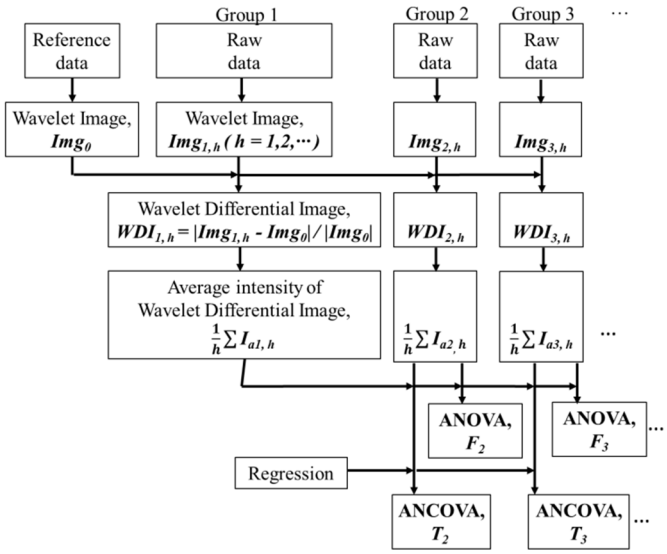

Figure 5. Flow chart of calculation procedure.

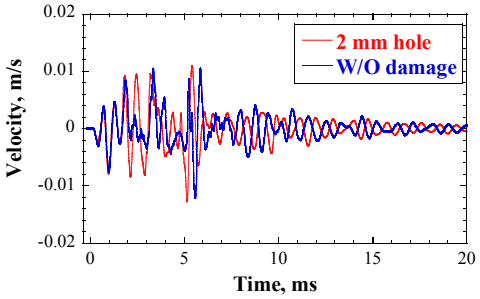

Figure 6. Time responses of vibration velocity of MIMTM.

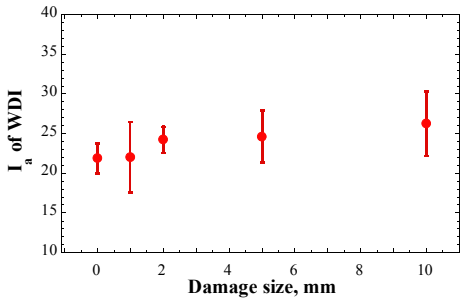

Figure 7. Average intensity of wavelet differential image as a function of damage size of penetrated cavitation damage for MIMTM vibration.

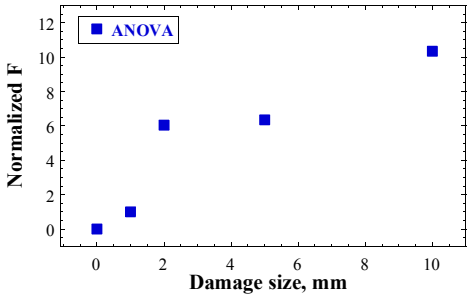

Figure 8. Normalized F factor of ANOVA as a function of the size of penetrated cavitation damage.

5.2. Target vessel vibration

5.2.1. *Beam power: 1MW* The size of target vessel is much larger than that of MIMTM, and thus the frequency components of the time responses of vibration are different. Besides the MIMTM study, the target vessel vibration also should be investigated. The damage size was controlled in the numerical simulations, and the numerical simulation results were used to analyse the dependency of target vessel vibration on damage. Random noise was manually added into the vibration signals that obtained by the

numerical simulations. The evaluation procedure was then applied to such vibration signals with noise. The noise was added by a random function that can be expressed as:

$$f(x) \in (-A, A), \tag{16}$$

where A represents the maximum amplitude of the noise and can be selected manually. Noise with amplitude $|A|$ could be added to the vibration signals by using this random function. For each damage condition, twelve data were obtained by adding the random noise.

Firstly, noise with maximum amplitude of about 7% of the maximum vibration velocity amplitude, was added to the numerical simulation signals (beam power: 1 MW). Figure 9 shows an example of time responses of vibration velocity for target vessel and the corresponding wavelet images before and after adding the noise. The wavelet image was significantly changed after adding the noise, especially in the relatively higher frequency range. The average value of I_a of *WDI* as a function of the penetrated damage size was shown in Figure 10. The absolute value of error bar is similar with the MIMTM case. Obviously, compared with results obtained by the numerical simulation [13], the added noise changed the value of I_a of *WDI* and induced large error bar. However, though the dependency of I_a of *WDI* on damage size was unobvious, the trend was not changed by the noise. Figure 11 shows the normalized F factor of ANOVA as a function of the penetrated damage size. By applying the ANOVA, the damage dependency was enhanced. It illustrates that ANOVA is effective to enhance the effect of damage on vibration signals for the low noise level.

When the noise level is not strong enough to change the trend of damage dependency, the effects of noise on the vibrational signals is not significant and can be reduced through applying ANOVA for analysing the I_a of *WDIs*.

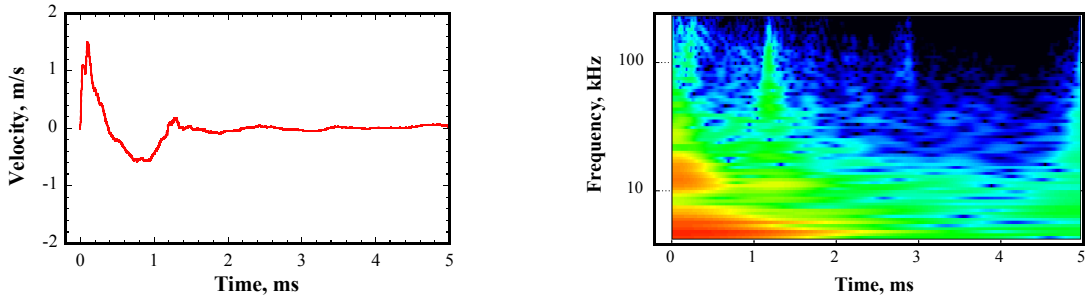

(a) Numerical simulation signals [13]; 1 MW, without damage

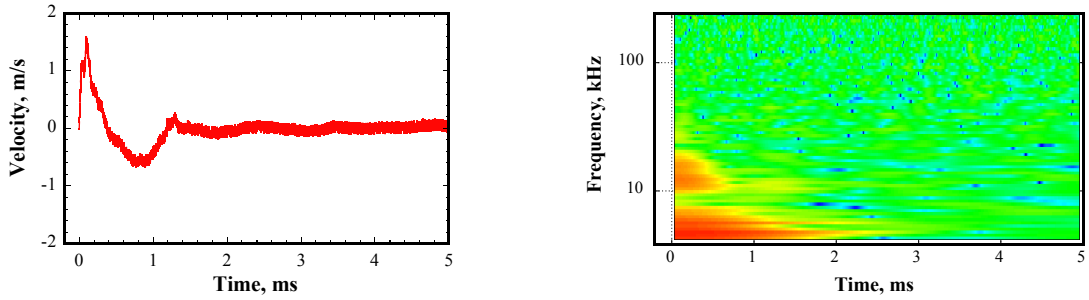

(b) Add 7% noise to the numerical simulation signals

Figure 9. Time responses of vibration velocity for target vessel and the corresponding wavelet images; numerical simulation and add 7% noise.

5.2.2. *Beam power: 100 kW* Figure 12 shows one vibration signal obtained from the real target. The proton beam power is 100 kW. Strong noise could be viewed in the vibration signal. To investigate the damage dependency under such a beam power condition, numerical simulations were carried out. Average intensity of wavelet differential image was plotted as a function of the damage size, as shown in Figure 13. Independent of the beam power, the average intensity of wavelet differential image is

proportional to the damage size. The comparative increments of energy, which is carried by the waves that penetrate the damage hole to excite the outer wall of target vessel, trends larger when the damage size becomes larger.

Figure 14(a) shows an example of vibration signal obtained by the numerical simulation. The beam power is 100 kW without damage. To simulate the noise level of the field data, the maximum amplitude of added noise was increased to about 30% of the maximum amplitude of the vibration signal. Figure 14(b) shows the vibration signal with manually added noise. The noise level is comparable to the field data that obtained from the real target. Then such vibration signals with manually added noise were used for the analysis.

Figure 15 shows the average value of I_a of *WDI*, *F* factor of ANOVA and *T* factor of ANCOVA as a function of the penetrated cavitation damage size. The error bar of I_a of *WDI* becomes much larger relative to the lower noise situation due to a much stronger noise level. The trend of damage dependency changes due to the strong noise level. In this case, the *F* factor of ANOVA fails to indicate the damage size dependency due to the strong noise. Therefore, the noise effects should be taken into consideration and be moved. Thereafter, the ANCOVA was applied to analyse the data. The dependency of *T* factor on damage size can be fairly observed. ANCOVA effectively reveals the damage dependency even in case of a strong noise level.

Figure 16 shows the damage size as a function of normalized *T* factor for the experimental and numerical simulation results. The trends showed by the experimental and numerical simulation results are similar with each other, which is coincidence with the variation trend showed in Figure 13. The correlation between damage size and *T* factor could be given by:

$$D = c \times T^d \,, \tag{17}$$

where *D* is the size of penetrated damage, unit is mm; *c, d* are constants related to the material property, structure geometry, etc.

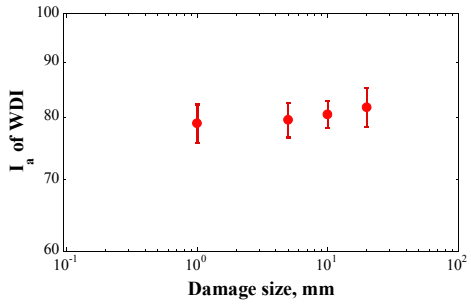

Figure 10. Average intensity of wavelet differential images as a function of the size of penetrated cavitation damage; add 7% noise to the numerical simulation signals.

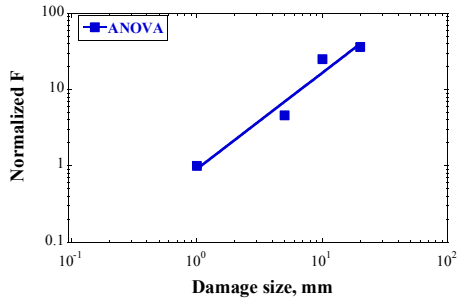

Figure 11. Normalized F factor of ANOVA as a function of the size of penetrated cavitation damage; add 7% noise to the numerical simulation signals.

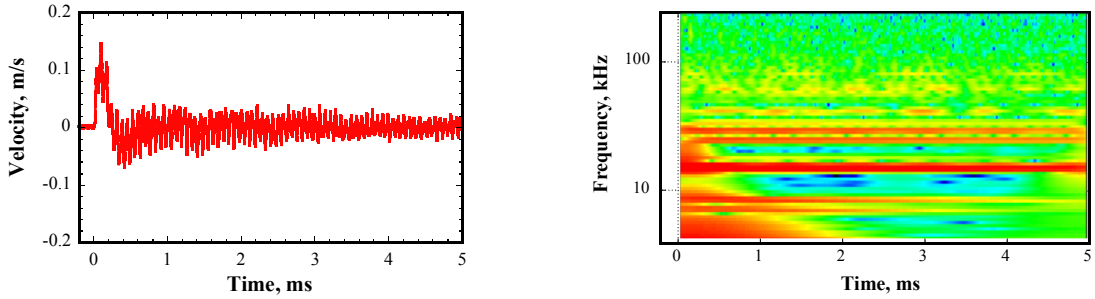

Figure 12. Field data obtained from the real target and the corresponding wavelet image; beam power: 100 kW.

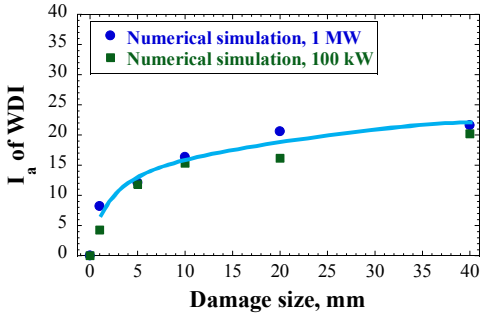

Figure 13. Average intensity of wavelet differential image as a function of damage size.

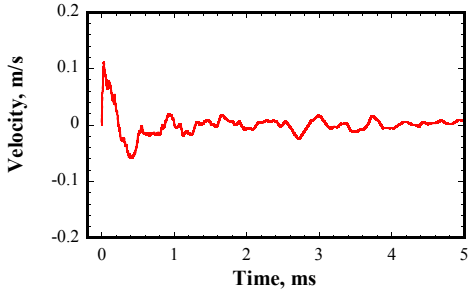

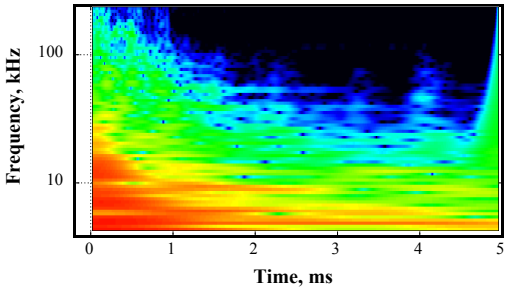

(a) Numerical simulation signal and the corresponding wavelet image; 100 kW, without damage

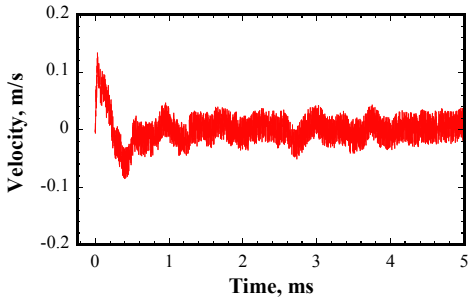

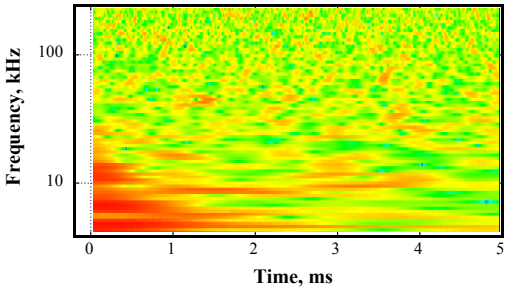

(b) Add 30% noise to the numerical simulation signal and the corresponding wavelet image

Figure 14. Time responses of vibration velocity for target vessel and the corresponding wavelet images; numerical simulation and add 30% noise.

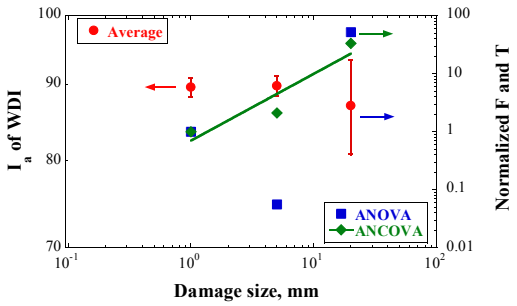

Figure 15. I_a of WDI, normalized F of ANOVA, and normalized T of ANCOVA as a function of the penetrated cavitation damage size; add 30% noise to the numerical simulation signals.

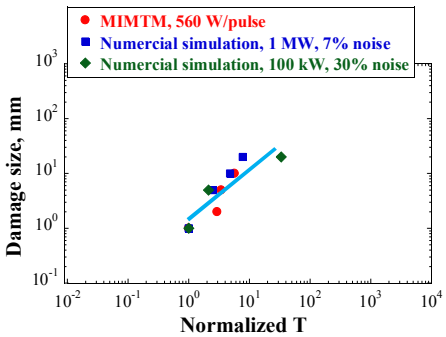

Figure 16. Damage size as a function of the normalized T factor.

5.3. Field application

As introduced previously, in the JSNS mercury target, Helium gas is injected into the target vessel to form micro-bubbles in mercury to mitigate the pressure waves [7]. The microbubbles-induced void fraction in the mercury is controlled by the flow rate of gas injection. The vibration behavior of the target vessel is closely related to the void fraction of liquid mercury [8]. ANCOVA was applied for analyzing the vibration signals obtained from the real target with various flow rate of gas injection.

The vibration signals were acquired from the real target at a certain time in several different days. The beam power and damage degree during the data acquisition period could be considered the same. Figure 17 shows an example of field data detected from the real target. The noise level is considerably high. The corresponding noise signal was obtained by each field vibration signal minus the averaged vibration signal of one day. Figure 18 shows the I_a and T factor as a function of the data acquisition date. The I_a fluctuates slightly, whereas the T factor firstly increases quickly and then fluctuates slightly. It is considered that the variation trend of T factor is related to the absolute differential He flow rate. To check this, the absolute differential He flow rate and normalized T factor was plotted as a function of the data acquisition date, as shown in Figure 19. Obviously, the variation trend of the absolute differential flow rate and normalized T factor fits well to each other. ANCOVA effectively reduced the effect of noise and revealed the gas flow rate dependency.

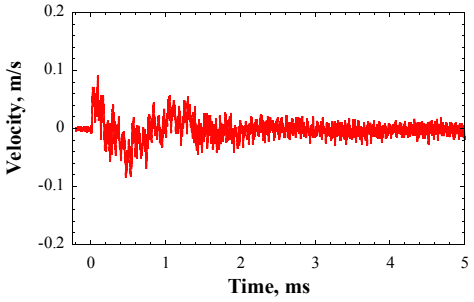

Figure 17. Field data obtained from the real target; with micro bubbles injection.

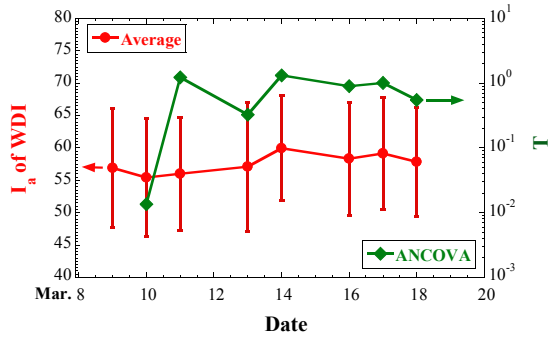

Figure 18. I_a of WDI and T factor of ANCOVA as a function of data acquisition date.

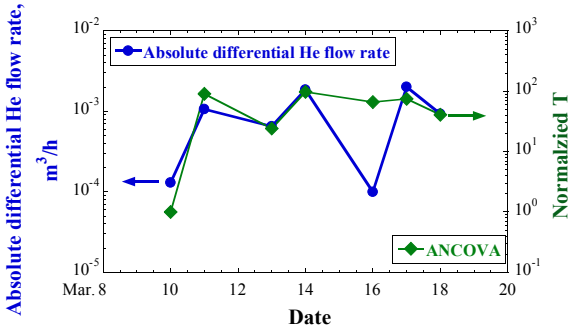

Figure 19. Absolute differential He flow rate and normalized T factor of ANCOVA as a function of data acquisition date.

6. Conclusion

A laser Doppler vibrometer method for monitoring the target vessel vibration was employed to establish the in-situ structure integrity evaluation technique for the JSNS mercury target:

1) Wavelet Differential Analysis (WDA) technique was developed to enhance the differences between vibrational signals. The vibration behavior of target vessel is very dependent on the damage size.
2) Analysis of covariance (ANCOVA) was applied to reduce the noise effects on the vibrational signals, and the T factor of ANCOVA clearly indicated the damage dependency on the vibrational

signals.

3) The combination of the WDA and ANCOVA could be possibly used to evaluate other parameters that are related to the structural vibration.

The established in-situ diagnostic technique proposes a possible way for in noncontact and remotely structure integrity evaluation.

Acknowledgement

This work was partly supported by the Japan Society for the Promotion of Science through a Grant-in-Aid for Scientific Research C (No. 23360088).

References

[1] Futakawa M, Kogawa H, Hino R 2000 *J. Phys. VI France* **10** 237.
[2] Futakawa M, Kikuchi K, Conrad H, Stechemesser H 2000 *Nucl. Instrum. Meth. A* **439** 1.
[3] McClintock D A, Riemer B W, Ferguson P D, Carroll A J, Dayton M J 2012 *J. Nucl. Mater.* **431** 147.
[4] Futakawa M, Kogawa H, Hasegawa S, Ikeda Y, Riemer B, Wendel M, Haines J, Naoe T, Tanaka N, Okita K, Fujiwara A, Matsumoto Y 2006 *Sixth International Symposium on Cavitation* 1.
[5] Futakawa M, Kogawa H, Hasegawa S, Ikeda Y, Riemer B, Wendel M, Haines J, Bauer G, Naoe T, Okita K, Fujiwara A, Matsumoto Y, Tanaka N 2008 *J. Nucl. Mater* **377** 182.
[6] Kogawa H, Shobu T, Futakawa M, Bucheeri A, Haga K, Naoe T 2008 *J. Nucl. Mater* **377** 189.
[7] Futakawa M, Kogawa H, Hasegawa S, Naoe T, Ida M, Haga K, Wakui T, Tanaka N, Matsumoto Yand Ikeda Y 2008 *J. Nucl. Sci. Technol.* **45** 1041.
[8] Naoe T, Kogawa H, Futakawa M, Ida M 2011 *J. Nucl. Sci. Technol.* **48** 865.
[9] Naoe T, Ida M, Futakwa M 2008 *Nucl. Instrum. Meth. A* **586** 382.
[10] Naoe T, Hasegawa S, Bucheeri A, Futakawa M 2008 *J. Nucl. Sci. Technol.* **45** 1233.
[11] Riemer B W, Wendel M W, Felde D K, Abdou A A, McClintock D A 2012 *J. Nucl. Mater.* **431** 160.
[12] Teshigawara M, Wakui T, Naoe T, Kogawa H, Maekawa F, Futakawa M, Kikuchi K 2010 *J. Nucl. Mater.* **398** 238.
[13] Wan T, Wakui T, Naoe T, Futakawa M, Maekawa K 2014 *Appl. Mech. Mater.* **566** 629.
[14] Futakawa M, Naoe T, Kogawa H, Tsai C C, Ikeda Y 2003 *J. Nucl. Sci. Technol.* **40** 895.
[15] Hallquist J O 2006 *LS-DYNA Theory Manual* (USA: Livermore Software Technology Corporation).
[16] Rutherford A 2012 *Introducing Anova and Ancova: A GLM Approach* (Hoboken John: Wiley & Sons, Inc.).
[17] Gopalsamy B M, Mondal B, Ghosh S 2009 *Int. J.Adv. Manuf. Tech.* **45** 1068.
[18] Zahid A K, Arshad N S 2012 *Int. J.Mater. Prod. Tec.* **43** 2.

3.2.6

Effects of strain rate and temperature on fatigue strength of the mercury target vessel structural material

Xiong Zhihong[1], Takashi Naoe[2], Masatoshi Futakawa[2], Katsuhiro Maekawa[1]
[1]Graduate School of Science and Engineering, Ibaraki University, Hitachi, Ibaraki 316-8511, Japan.
[2]J-PARC Center, JAEA, Tokai, Ibaraki 319-1195, Japan.

E-mail:13nd208n@hcs.ibaraki.ac.jp

Abstract. In the present study, ultrasonic fatigue tests were conducted with controlling specimen surface temperature to investigate the effects of strain rate, temperature and work hardening on very high-cycle fatigue strength of 316L SS. Also, the micro-hardness change due to cyclic fatigue was investigated. The experimental results indicated that the fatigue strengths of solution annealed (SA) and cold worked (CW) at 250 ºC were reduced about 10% and 30% than that of at room temperature, and the fatigue strength was enhanced by the high strain rate. The cyclic hardening occurred in the region of very high-cycle fatigue in the case of SA 316L. In contrast, in the case of 10% CW 316L, cyclic softening occurred when the number of cycles is below 10^6 and followed by cyclic hardening. In the case of 20% CW 316L, the cyclic softening was observed when the number of cycles is below 10^7, while the cyclic hardening occurred subsequently. Furthermore, the sharp increase of the surface temperature was observed in both SA and CW specimens just before the fatigue failure.

1. Introduction

A high-power pulsed spallation neutron source, Japan Spallation Neutron Source (JSNS), is installed at the Materials and Life science experimental Facility (MLF), in the Japan Proton Accelerator Research Complex (J-PARC). High-power pulsed proton beams with an energy of 3 GeV and a power of 1 MW are injected into the liquid mercury to produce spallation neutrons [1]. An enclosure vessel of liquid mercury, a so-called target vessel as shown in figure 1, is made of type 316L austenitic stainless steel (316L SS), which has been widely used in the nuclear industry because of its excellent ductility, corrosion resistance, and irradiation performance. The target vessel is suffered from the cyclic loading due to the proton beam-induced pressure waves [1]. In the case of the JSNS, the repeated proton injection frequency is 25 Hz, and the lifetime is designed to be 2500 hours from the viewpoint of the radiation damage. Therefore, the number of loading cycles will achieve beyond 10^8 cycles, very high-cycles throughout the expected lifetime. The fatigue limit of the 316L SS stainless steel has decreased about 40% by the peak-peak roughness of the pitting damaged surface when the

[1] Graduate School of Science and Engineering, Ibaraki University, Hitachi, Ibaraki 316-8511, Japan.

number of loading cycles gets to be 10^8 [2]. It is reported that the very high-cycle fatigue degradation is different from the conventional fatigue up to million cycles, and the fatigue crack initiation due to internal flaw and/or inclusion becomes dominant in very high-cycle fatigue [3]. The strain rate at the beam window portion of the target vessel is estimated to be 50 1/s at the maximum (as shown in figure 2), which is relatively higher than that of the conventional fatigues. The fatigue strength is affected by the strain rate, i.e., the increase of fatigue lifetime with increasing strain rate [4, 5]. Furthermore, the temperature at the beam window will reach up to 250 ºC due to heat deposit at 1MW operation.

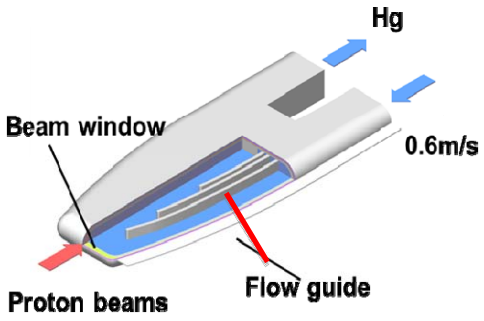

Figure 1. Mercury target vessel at the JSNS

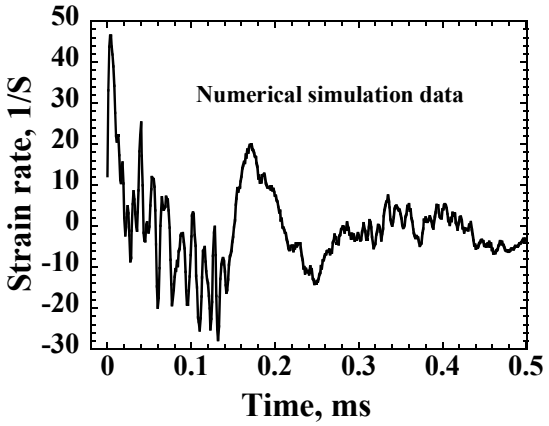

Figure 2. Time response of strain rate at the center part of the beam window

The mercury target vessel is exposed to intense fluxes of protons and spallation neutrons. Irradiation induced defects (frank loops essentially) act as dispersed barriers to dislocation motion, and are responsible for the observed increase in yield stress and the ductility loss. Simultaneously, grain boundaries can be weakened by irradiation, and radiation-embrittlement can lead to crack formation when an irradiated material is subject to cyclic stress loading [6].

Additionally, Liquid Metal Embrittlement (LME) due to mercury immersion is concerned for the mercury target vessels, and is investigated through micro-hardness measurement and bending fatigue testing [7-9]. It was reported that the surface of 316L SS got to be harder and the crack propagation rate was accelerated caused by mercury immersion.

The mechanical properties including high-cycle fatigue behavior and deformation mechanisms of type 316L have been reported in detail [9-11]. There are few researches on the fatigue behavior of type 316L in very high-cycle fatigue region. In the present study, in order to investigate the fatigue strength of the type 316L in high-strain rate, very high-cycle fatigue tests were conducted by using an ultrasonic fatigue-testing machine. Also, the fatigue strength at the temperature of 250 ºC was investigated.

2. Experimental procedure

2.1. Specimen

The type 316L austenitic stainless steel was used for the very high-cycle fatigue test. A part of the as-received materials, which were heat-treated at 1055 ºC for 6 min with water quench (referred to SA), were subjected to different cold-rolled levels, i.e., 10% and 20% reduction of thickness (referred to 10% CW and 20% CW).

An hourglass shape specimen was selected for the test as shown in figure 3. In order to obtain the resonance frequency of the specimen at 20 kHz, the lengths of l and L were selected as 22.7 mm and 40 mm, respectively.

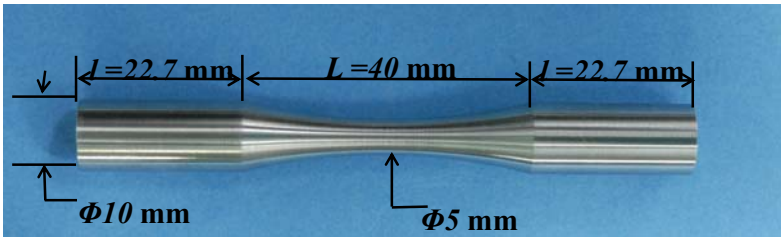

Figure 3. Photograph of the fatigue specimen

2.2. Fatigue test

Load-controlled fatigue tests were conducted by using an ultrasonic fatigue testing system (Shimadzu, USF-2000) as shown in figure 4. The specimen was loaded in tension-compression (the ratio of stress $R = \sigma_{max} / \sigma_{min}$ was -1) with a resonance frequency of 20 kHz. Fatigue failure of the specimen was defined as the resonance frequency exceeded to ±500 Hz of the initial state due to the occurrence of micro-crack. This means that the specimen is not completely broken after the fatigue test. The maximum number of load cycles in this experiment was set to 10^9. More detailed information for the ultrasonic fatigue test is reported elsewhere [12].

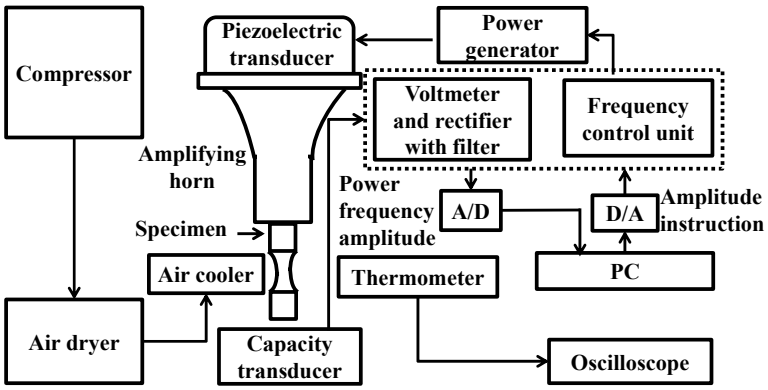

Figure 4. Schematic of ultrasonic fatigue testing machine

In order to prevent an increase of specimen temperature caused by the internal heat generation together with high-speed deformation, loading/arresting intervals were controlled during the test in addition to the air-cooling of the specimen surface. The temperature rise of the center portion of the specimen surface was monitored by using an infrared radiation thermometer (KEYENCE, IT2-02), with a spot diameter of ca. 1.2 mm.

In this research, the self-heating of the specimen during the ultrasonic fatigue test was used for increasing specimen-temperature in order to perform the fatigue test at the temperature of approximately 250 ºC. The fatigue test was carried out as follows: 1) starting the ultrasonic fatigue test without cooling and with the intermittent loading, where the loading time and arresting time were selected according to the stress amplitude; 2) applying the air cooler when the specimen temperature is reach up to about 260 ºC; and 3) adjusting the flow rate of the cold air to maintain the specimen temperature around 250 ºC.

2.3. Micro-hardness measurement

In order to investigate changes in mechanical properties by cyclic loading, the cross-sectional hardness was measured by using a micro hardness tester with a Berkovich tip (Shimadzu, DUH-W201S). The fatigue-failed specimen was cut in a longitudinal direction, and a center part was used for hardness

measurement. The cut specimens were mounted and polished to a mirror surface by using the colloidal silica liquid abrasive with the particle diameter of 0.06 μm. The universal hardness is defined as the quotient of the test load and the surface area of the indentation under an applied test load, which is obtained by [13]

$$H_u = \frac{L_{\max}}{26.43 D^2_{\max}}, \quad (1)$$

where D_{max} is the maximum depth, and L_{max} is the maximum load.

3. Results and discussion

3.1. Specimen temperature during ultrasonic fatigue test

Figure 5 shows the time histories of the surface temperatures of the specimens during the ultrasonic fatigue test under a constant loading time 0.11 s and arresting time 5.0 s. It is observed that the specimen failed at 7.4×10^6 cycles under 260 MPa for SA and 1.05×10^6 cycles under stress amplitude of 380 MPa for 10% CW, respectively. It can be seen that, in the case of SA, the temperatures of specimen was kept at about 13.5 °C at the maximum. On the other hand, the temperature of the 10% CW gradually increased because of the capacity of air cooler was not enough. Figure 6 shows the time histories of the surface temperatures of the specimens during the ultrasonic fatigue test under the loading time 0.11 s and arresting time 0.99 s for SA and the loading time 0.11 s and arresting time 0.22 s for 10% CW, respectively. The specimens failed at 1.22×10^7cycles under the stress amplitude of 180 MPa for SA and 1.29×10^7 cycles under the stress amplitude of 380 MPa for 10% CW, respectively. It can be seen that the temperature at the surface of specimens was kept at about 250 °C.

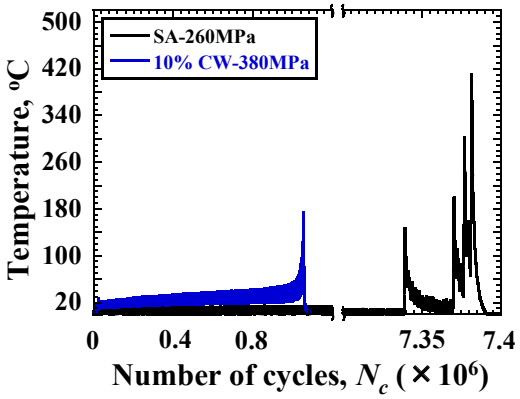

Figure 5. Temperature histories of the specimens tested at room temperature

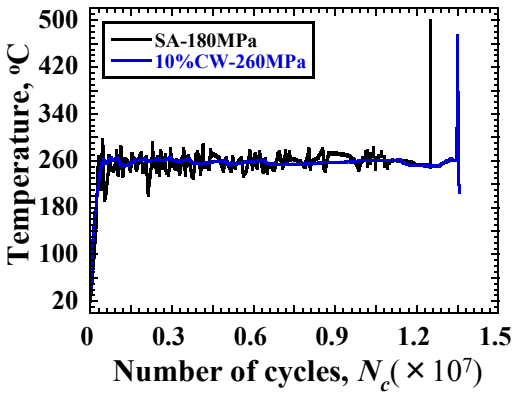

Figure 6. Temperature histories of the specimens tested at 250 °C

At the beginning of the fatigue test around 250 ºC, the temperature rising process (from 0 ºC to 250 ºC) is much less than 1% of the total lifetime. The sharp increases of the surface temperature were noted in both SA and CW specimens just before fatigue failure takes place regardless of the testing temperature. This trend might be utilized to detect the failure just before it. This phenomenon has also been reported in the steels and aluminum alloys [14]. It was suggested that this sudden increase of the temperature allows determining the number of cycles at crack initiation, and more than 90% of the total life that is devoted to crack initiation. In the case of 316L SS, the temperature increase might be enhanced as compared with that of the other metals because of the low thermal conductivity [15].

3.2. Effect of cord work on fatigue strength

The applied stress amplitude as a function of the number of cycles to failure (*S-N*) of SA, 10% CW and 20% CW are shown in figure 7. The fatigue data were fitted according to the Wöhler's approach as follows,

$$\log N_f = a - b\log\sigma_a \tag{2}$$

where σ_a is the stress amplitude, and a and b are constants.

The fatigue failure occurred beyond 10^7 cycles, i.e. in the very high-cycle fatigue regime for the SA, 10% CW and 20% CW. A continuous decline, which is usually observed in the very high-cycle fatigue regime for carbon steels [3, 16], is observed in the 316L regardless of the degree of cold working. That is, the conventional fatigue limit disappears, and the fatigue limit only exists at a given number of cycles. The fatigue strengths of SA, 10% CW and 20% CW at the number of cycles of 10^9 are about 190 MPa, 340 MPa and 390 MPa, respectively. The fatigue strength of 20% CW is higher than that of SA and 10% CW, and the fatigue strength increases with increasing CW level under the stress-controlled fatigue. It was suggested that the dislocation density was increased with the CW level [17]. Increments in dislocation density cause the increase of the tensile strength, which will enhance the fatigue strength. The fatigue degradation rates, defined as the slope of the S-N curve above the fatigue limit, are 1/24, 1/36 and 1/117 for SA, 10% CW and 20% CW, respectively; i.e. the fatigue degradation rate decreases with CW level.

3.3. Effect of strain rate on fatigue strength

In order to investigate the effect of strain rate on the fatigue strength of SA, the fatigue data was compared with the reference data [10, 11, 18]. The experiments of references and the ultrasonic fatigue test were conducted with strain rate magnitude from 10^{-3} to 10^{-1} 1/s and 10^2 1/s, respectively. It can be seen in figure 8 that there are almost no differences in the fatigue lifetime when the frequency is increased from 0.2 Hz to 20Hz (equivalent strain rates from 10^{-3} 1/s to 10^{-1} 1/s). In contrast, the fatigue lifetime exhibits a great increase when the strain rate is increased up to 10^2 1/s. Besides, the effect of strain rate on fatigue limit gets to be more pronounced at high strain rate around 10^2 1/s.

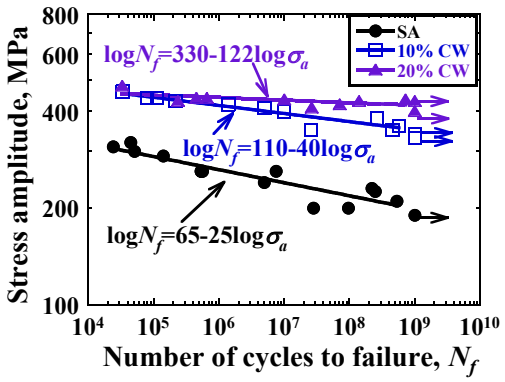

Figure 7. S-N curves of SA, 10% CW and 20%CW

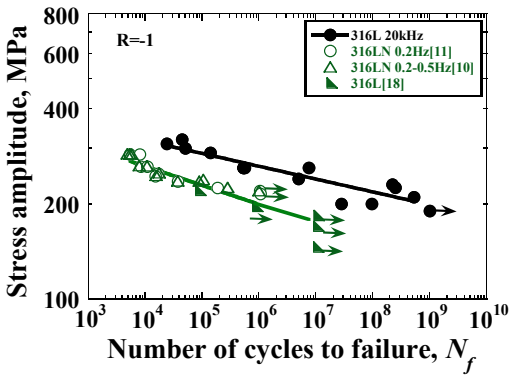

Figure 8. S-N curves of the type 316 SS with different strain rate [10, 11, 18]

Other researchers have reported similar results. In the study on 50CrMo4 [19], the fatigue lifetime increased with the increasing strain rate was also observed. In 316L austenitic stainless steel [20], the decrease of the fatigue lifetime in the low strain rate was considered due to the higher crack density and the decrease in crack propagation rate or cracks initiation life caused by the more pronounced dynamic strain aging at the low strain rate. Moreover, the dynamic strain aging range of the austenitic stainless steel has been proved from 200 °C to 800 °C [21]. Therefore, the increment in fatigue lifetime in the present research should be independent of the dynamic strain aging. Some researchers

suggested that the strength is enhanced at high strain rate [22, 23], which causes the increase of the fatigue strength. Some other researchers [23, 24] considered that the reason of the longer fatigue lifetime at the high strain rate is the slower fatigue crack propagation rate. From this viewpoint, the following model summarized from many experimental data for various materials is used to describe the effect of the testing loading frequency on the fatigue crack propagation rate as follows [24]:

$$\frac{da}{dN} = C_0 f^{-\lambda} (\Delta K)^n \tag{3}$$

where f is the loading frequency, n and C_0 are constants related to the combination of material, temperature and environment, $\triangle K$ is the range of stress intensity factor. From this model, it can be seen that the fatigue crack propagation rate decreases with increasing loading frequency. In the study of 304 austenitic stainless steel [23], the increment in fatigue lifetime is considered due to the deceleration of the fatigue crack propagation and the delay of the crack initiation. Basing on the SEM observation, the striation spacing, which corresponds to the macroscopic crack propagation rate, decreased with increasing strain rate [23].

3.4. Fatigue strength at 250 °C

The applied stress amplitude as a function of the number of cycles to failure (*S-N*) of SA, 10% CW and 20% CW under room temperature (referred to RT) and 250 °C (referred to HT) are shown in figure 9. It can be seen that the fatigue failure occurred beyond 10^7, i.e. in the very high-cycle fatigue regime independent of the testing temperature. The fatigue strengths of SA and 10% CW at 250 ºC were reduced about 10% and 30% than that of at RT, respectively.

It is well known that the fatigue strength of metals and alloys depends on their mechanical properties, such as ultimate tensile strength (UTS). In general, the decreasing in ultimate tensile strength will lead to the decreasing of fatigue strength. Figure 10 shows changes in engineering UTS of SA and 17% CW as a function of temperature [25]. It was indicated that the engineering UTS decreases with increasing temperature. Therefore, the decreasing of fatigue strength at 250 °C is due to the decreasing engineering UTS.

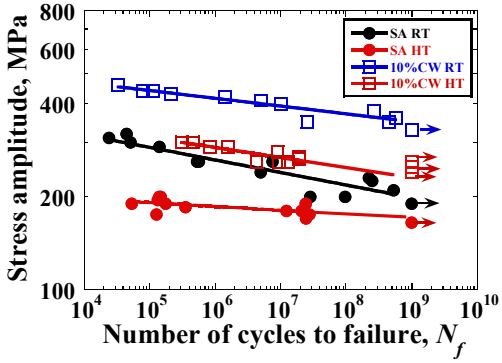

Figure 9. S-N curves of SA and 10% CW under room temperature and 250 °C

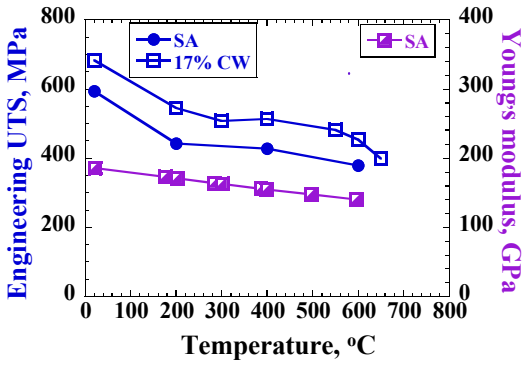

Figure 10. Relationship between engineering UTS, young's modulus and temperature [23, 26]

It has been reported that the reduction of fatigue lifetime at the temperature around 250 °C was attributed to the effect of dynamic strain aging, which occurs in the range from 200 °C to 800 °C in the case of austenitic stainless steel [21, 25, 26]. There are two ways of the dynamic strain aging effect on the fatigue resistance. One is that the dynamic strain aging induces inhomogeneity of deformation lead to the multiple crack initiation, which causes the reduction of the crack initiation life, that is, the fatigue resistance decreases in the crack initiation stage [21]. Another is that dynamic strain aging induced embrittlement can cause a large stress concentration at the crack tip, which will enhance the

crack propagation rate. That is, the fatigue resistance decreases in the crack propagation stage [25]. Kim et al. [27] have also noted that the increasing of crack propagation rate of 316L stainless steel in the dynamic strain-aging regime. In conclusion, the reduced crack initiation life and propagation life caused by the dynamic strain aging lead to the decrease of the fatigue resistance in the regime of dynamic strain aging. Srinivasan et al. [26] have suggested that the effect of the oxidation of the specimen will enhance the crack nucleation at slip steps. The fatigue resistant of 316L in the air was proved to be weaker than that of in the vacuum [28]. However, in the present research, the oxidation of the specimen during the fatigue tests at around 250 °C is hardly observed. Hence, the effect of the oxidation of the specimen on fatigue strength can be negligible.

During the fatigue test at 250 °C, the frequency decreases with increasing temperature until it reach up to 250 °C, as shown in figure 11. The reduction of resonance frequency induced by the temperature of 250 °C is about 400Hz, which is very small compared with that of 20 kHz at room temperature. Therefore, the effect of the resonance frequency caused by the testing temperature should not be considered. The decreasing in resonance frequency can be attributed to the decreasing in Young's modulus, which has been reported that the Young's modulus decreases with increasing temperature [28], as shown in figure 10.

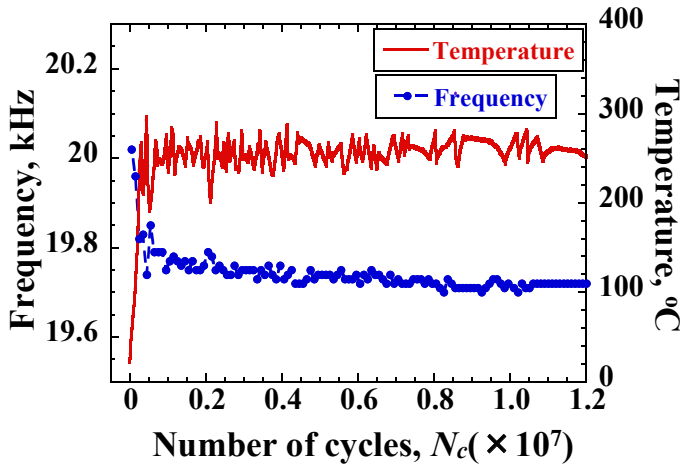

Figure 11. Frequency and specimen temperature of SA during fatigue test at 180MPa

3.5. Micro-hardness change during fatigue test

Changes in universal hardness of fatigue-failed specimens with the different number of cycles are indicated in figure 12. In the case of SA, the universal hardness shows an increase with the number of cycles: that is, a so-called cyclic hardening is recognized. In contrast, the hardness and residual strength of 10% CW show the negative relation with the number of cycles in the region below 10^6: a so-called cyclic softening is recognized, and thereafter the cyclic hardening occurs. Furthermore, in the case of 20% CW, there exists the negative relationship between the universal hardness and the number of cycles when the number of cycles is below about 10^7, i.e. cyclic softening occurs, followed by cyclic hardening. A similar tendency of the universal hardness can be seen in 10% CW, but the break point, i.e. the number of cycles when the cyclic hardening transit from cyclic softening, seems to shift to 10^7 cycles approximately.

The cyclic hardening for annealed materials [29, 30] and cyclic softening for the pre-strained materials [20, 21] in the low cycle strain-controlled fatigue have been observed. It was supposed that the cyclic behavior, i.e. cyclic hardening or softening, is related to the interaction between the plastic deformation induced by dislocation generation rate and annihilation rate [31, 32]. When the

annihilation rate of dislocation is lower than the generation rate, the dislocation density will increase, and the cyclic hardening takes place. Otherwise, cyclic softening occurs.

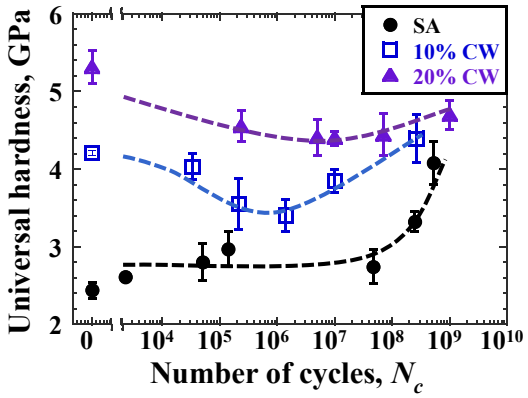

Figure 12. Relationship between hardness and the number of cycles

4. Summary

The followings are summarized from the ultrasonic fatigue tests on 316L SS:

1) The fatigue failure occurred beyond 10^7 cycles, i.e. in the very high-cycle regime, independent of the testing temperature.

2) The fatigue strength increases with the cold work level.

3) The fatigue limit at a high strain rate (10^2 1/s) is higher than that of the lower strain rate (10^{-3} 1/s to 10^{-1} 1/s).

4) The fatigue strengths of SA and 10% CW of 250 ºC were reduced about 10% and 30% from that of room temperature, respectively.

5) The cyclic behavior of the materials is dependent on their initial state, pre-strained or not. In the case of solution annealed (SA) 316L, the universal hardness showed a positive relation with the number of cycles: i.e. cyclic hardening occurred. On the contrary, in the case of cold worked (CW) 316L, the universal hardness showed a negative relation with the number of cycles, followed by cyclic softening when the number of cycles smaller than a critical value. The critical number of cycles is about 10^6 for 10% CW and 10^7 for 20% CW.

6) A sharp increase of the surface temperature was observed in both SA and CW specimens just before fatigue failure regardless of the testing temperature. This phenomenon can be applied to detect fatigue failure.

5. Acknowledgments

This research was partly supported by Japan Society for the Promotion of Science through a Grant-in-Aid for Scientific Research (No. 23360088 and 26820016).

References

[1] Futakawa M, Haga K, Wakui T, Kogawa H and Naoe T 2009 *Nucl. Instr. Meth. Phys. Res. A*. **600** 18-21
[2] Futakawa M, Wakui T, Kogawa H and Ikeda Y 2006 *Nucl. Instr. Meth. Phys. Res. A*. **562** 676-79
[3] Li X 2012 *J. Int. Mater. Rev.* **57** 92-110
[4] Wu J, Lin C 2005 *J. Mater. Sci. Eng. A*. **390** 291-98
[5] Hong S, Lee S 2005 *J. Nucl. Mater.* **340** 307-14
[6] Mansur L 2006 *Nucl. Instr. Meth. Phys. Res. A*. **562** 666-75
[7] Naoe T, Yamaguchi Y, Futakawa M 2012 *J. Nucl. Mater.* **431** 133-39

[8] Futakawa M, Wakui T, Kogawa H, Date H 2002 *Int. Conf. on Materials and processing* **Vol 1** (Honolulu: Hawaii) pp538-563
[9] Strizak J P, Mansur L K 2003 *J. Nucl. Mater.* **318** 151-56.
[10] Strizak J P, Tian H, Liaw P k, Mansur L K 2005 *J. Nucl. Mater.* **343** 134-44.
[11] Tian H, Liaw P k, Strizak J, Mansur L 2003 *J. Nucl. Mater.* **318** 157-66.
[12] Xiong Z H, Futakawa M, Naoe T, Maekawa K 2014 Adv. Mater. Res. **891-892** 536-541.
[13] Weiler W 1992 Atalanta *The proceedings of the 79th AESF annual technical conference* AESF Inc. pp 277-284
[14] Wagner D, Ranc N, Bathias C, Paris P C 2009 *Fatigue Fract. Engng. Mater. Struct.* **33** 12-21
[15] Akai A, Shiozawa D, Sakagami T 2013 *J. Soc. Mate. Sci.* **62** 554-64 (In Japanese)
[16] Sakai T, 2009 *J. Solid Mech. Mater. Eng.* **3** 425-39
[17] Ohtani T, Ogi H, Hirao M 2005 *Metall. Mater. Trans A.* **36** 411-20
[18] Huang J Y, Yeh J J, Jeng S L, Chen C Y, Kuo R C 2006 *Materials Transactions* 47 409-17
[19] Schneider N, Pyttel B, Berger C and Oechsner M, 2014, *Adv. Mater. Res.* **891-892** 1430-35
[20] Hong S G, Lee K O, and Lee S B, 2005, *Int.J. Fatigue* **27** 1420-24
[21] Hong S G, Lee S B, 2005, *J. Nucl. Mater.* **340** 307-14
[22] Schneider N, Pyttel B, Berger C, Oechsner M, 2014 Adv. Mater. Res. **891-892** 1430-35
[23] Kawata K, Miyamoto I, Itabashi M 1987 proceeding of IMPACT`87 **Vol 1** (Bremen, Germany) pp349-56
[24] Poulain T, Mendez J, Henaff G, Baglion L D, *2014 Adv. Mater. Res.* **891-892** 1420-26
[25] Shih Y S, Chen J J, 1999 *Nucl. Eng. Design* **191** 225-30
[26] Hong S G, Yoon S, and Lee S B, 2003, *Int.J. Fatigue* **25** 1293-300
[27] Srinivasan V S, Sandhya R, Bhanu Sankara Rao K, Mannan S L, Raghavan K S 1991 *Int.J. Fatigue*, 13(1991) 471-78.
[28] Kim D W, Kim W G, Ryu W S, 2003 *Int.J. Fatigue* **25** 1203-07
[29] Alain R, Violan P, Mendez J, 1997 Mater. Sci. Eng. A **229** 87-94
[30] Yu D, An K, Chen Y, Chen X, 2014, *Scripta Mater.* **89** 45-48
[31] Mughrabi H, 1978 *Mater. Sci. Eng.* **33** 207-23
[32] Stephens R I, Fatemi A, R. Stephens R, Fuchs H O 2001 *Metal Fatigue in Engineering* (New York: John Wiley & Sons) p 44
[33] Galindo-Nava E I, Sietsma J, Rivera-Díaz-del-Castillo P E J 2012, *Acta. Materialia*. **60** 2615-24.

3.2.7

Status update on the ESS Target systems development

Rikard Linander, Ulf Odén

European Spallation Source Lund Sweden

Rikard.linander@esss.se , ulf.oden@esss.se

Abstract
The on-going project for construction of the European Spallation Source (ESS), the 5 MW long-pulsed neutron research facility in Lund, Sweden, has entered the phase in which design work and development are focused on realising solutions that shall satisfy well-defined requirements. The Target Station, which converts the pulsed proton beam delivered by the linear accelerator to cold and thermal neutron beams tailored for neutron science applications, consists of several systems. Each of these elements offers unique design challenges for the engineering teams both in terms of providing the necessary primary function and in satisfying complex requirements for physical and functional interfaces between systems.

The Target systems, consisting of the tungsten target wheel, the drive, and the associated helium cooling system, have undergone optimisation and development during the preliminary design phase. Issues that have been studied include the helium coolant pressure and temperature level, internal flow paths and patterns, seal leak rates, manufacturability, integration with moderator and reflector components, remote handling strategies and waste management.

This paper is a status update on the ESS Target systems development; presenting specified parameter values, discussing chosen design solutions and addressing upcoming engineering challenges.

1. General description Target Station [1]

The function of the target station is to convert the intense proton beam from the accelerator into a number of intense neutron beams. This conversion is achieved by the interplay of a number of basic functions. In the heavy metal target the impinging proton beam radiation from the accelerator is converted via the spallation process into fast neutrons as the useful product, while generating a large amount of heat, radioactive isotopes and prompt radiation as unavoidable by-products. The moderator-reflector assembly surrounding the target transforms the fast neutrons emitted by the target into slow neutrons, which are the final form of useful radiation provided by the neutron source, while further radioactive waste is produced by the absorption of neutrons by various target structures. (Here, “fast” means neutrons with velocities in the range of 10% of the velocity of light and “slow” means velocities comparable to the speed of sound.) These two neutronically active systems are surrounded by a radiation shielding system of approximately 7000 tons of steel, in order to contain the extreme level of highly

penetrating gamma and fast neutron radiation created in the target and its vicinity. The beam extraction system provides intense slow neutron beams through beam guides, which traverse the target shielding. These neutron beam guides are accessible at the surface of the shielding, for delivery to and use at the neutron-scattering instruments facing the beam ports at variable distances. The proton beam window separates the high vacuum in the accelerator from the atmospheric-pressure inert helium gas inside a large container vessel, in which all of these systems are housed. They form, together with the tight container, the target monolith, which takes the shape of a 11 m diameter and 8 m high cylinder.

At ESS, the proton beam will deliver 5 MW power in the form of kinetic energy. About 10% of this energy is converted to mass through the nuclear reactions in the spallation process that produces neutrons, other nuclear fragments, isotopes and gamma radiation. The energy of these particles makes up the remaining 90% of the proton beam energy, and it is almost all deposited within a distance of 1 m from the site of proton beam impact in the target. Different cooling circuits in the target monolith remove this large amount of heat from the target itself (3 MW), from the moderator-reflector assembly (1.2 MW) and from the monolith shielding (0.3 MW). The proton beam window is directly heated by the traversing beam and requires cooling of about 6 kW, though this value is strongly dependent on window design details.

Radiation damage and fatigue limit the lifetime of the three most strongly affected systems: the target, the reflector-moderator assembly and the proton beam window. All of these systems will need to be changed multiple times during the lifetime of the facility, with frequencies ranging between 6 months and 5 years, as conservatively estimated on the basis of available experience at spallation sources. The removed used components represent a considerable amount of radioactive waste. The other part of the radioactive waste consists of gases, volatiles and airborne particles, which will be continuously captured by a variety of efficient filters and traps.

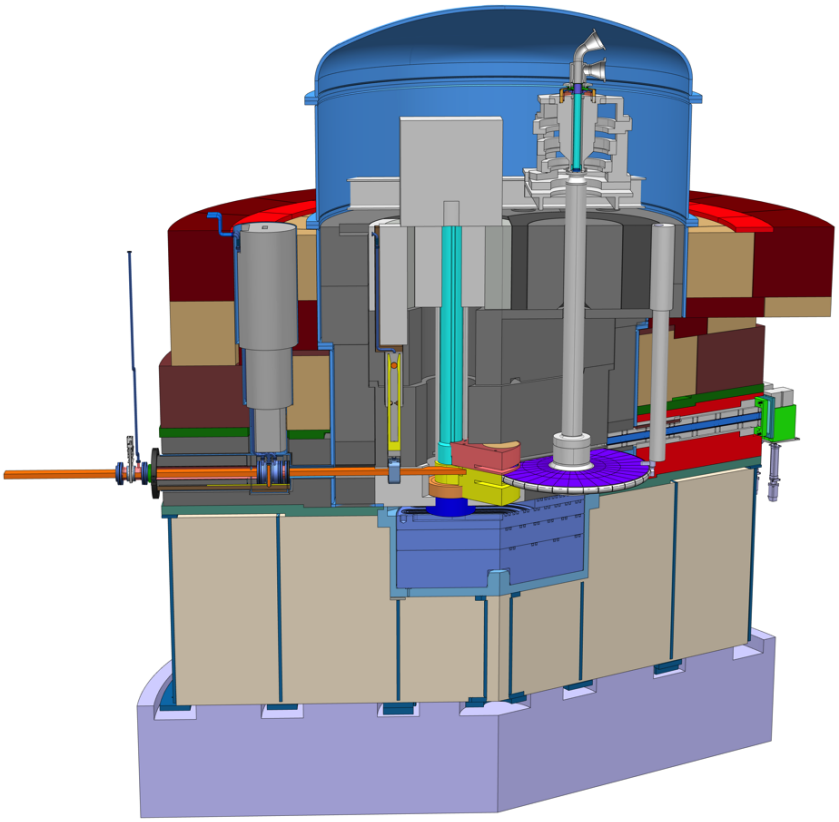

Figure 1 Monolith with target wheel and shaft inside

2. Improvements on Target Wheel, Target Shaft and Target Helium Cooling System

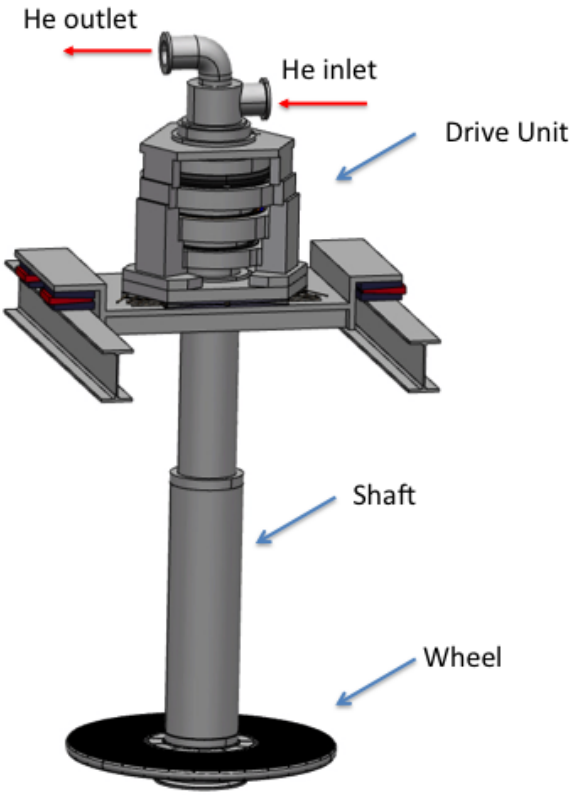

Figure 2 Target Wheel and Shaft

The Target consists of the Wheel, the Shaft, the Driving Unit and the Target Helium Cooling System. The design has been evolved since the original baseline, as described in the ESS Technical Design Report. The baseline target design calls for 33 target sectors, each made up of slabs of tungsten, the spallation material, held in place between two structural holder beams. The 33 beams delimit the target sectors and are connected to a massive central hub that makes the transition to the shaft, as shown in Figure 3

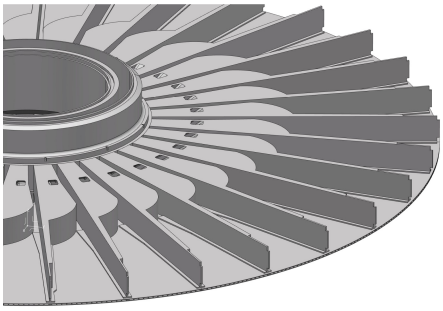

Figure 3 Central piece, beams and bottom shroud

The 33 sectors of spallation material and structural beams are contained between top and bottom ring-shaped lids welded to the periphery of the central hub, with a rim composed of the beam entrance windows and their frames. The target wheel rotates around a vertical axis. The shrouds and rim form the gas-tight target vessel, which, together with the structural beams to which it is welded, forms the target's pressure container.

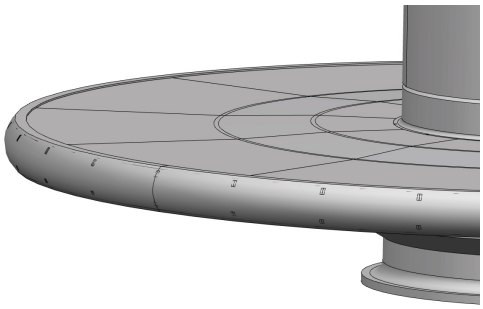

Figure 4 Target Wheel (pressure container)

To improve the cooling of the spallation material in the wheel the shroud has been redesigned. The Wheel Shroud is now built up with two plates with cooling channels in between where the helium flows from the center of the Shaft to the outer edge of the Wheel (figure 5) The helium flows both in the upper part of the shroud and the bottom.

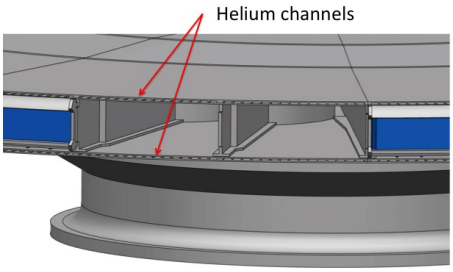

Figure 5 Target Wheel Shroud. The rim removed and the helium channels in both the upper and lower shroud plates shown.

The helium flows then back to the center of the shaft in a serpentine pattern, cooling the tungsten (figure 6).

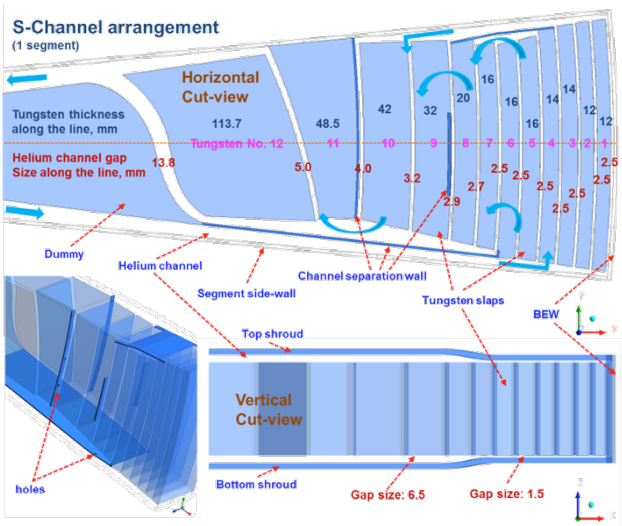

Figure 6 Spallation material arrangement. The helium flow follows in a serpentine pattern through the tungsten slabs, guided by the channel separation walls. Blue arrows indicate direction of helium flow.

A helium mass flow of 3 kg/s and an inlet temperature of 40 °C will keep the tungsten material below the critical temperature of 500°C and the Vessel including the internal structure below 400°C. These temperature limits will prevent the tungsten from oxidization in the event that air infiltrates the target vessel, and will also assure that creep behavior on the steel structure is avoided.

In the baseline design the helium operation pressure was decided to be 0,36MPa based om facts at the time. With a mass flow of 3 kg/s this pressure level leads to high helium volume flow, which puts extensive demands on the helium compressor. Critical design factors has been calculated and are compiled in a parameter diagram (figure 7)

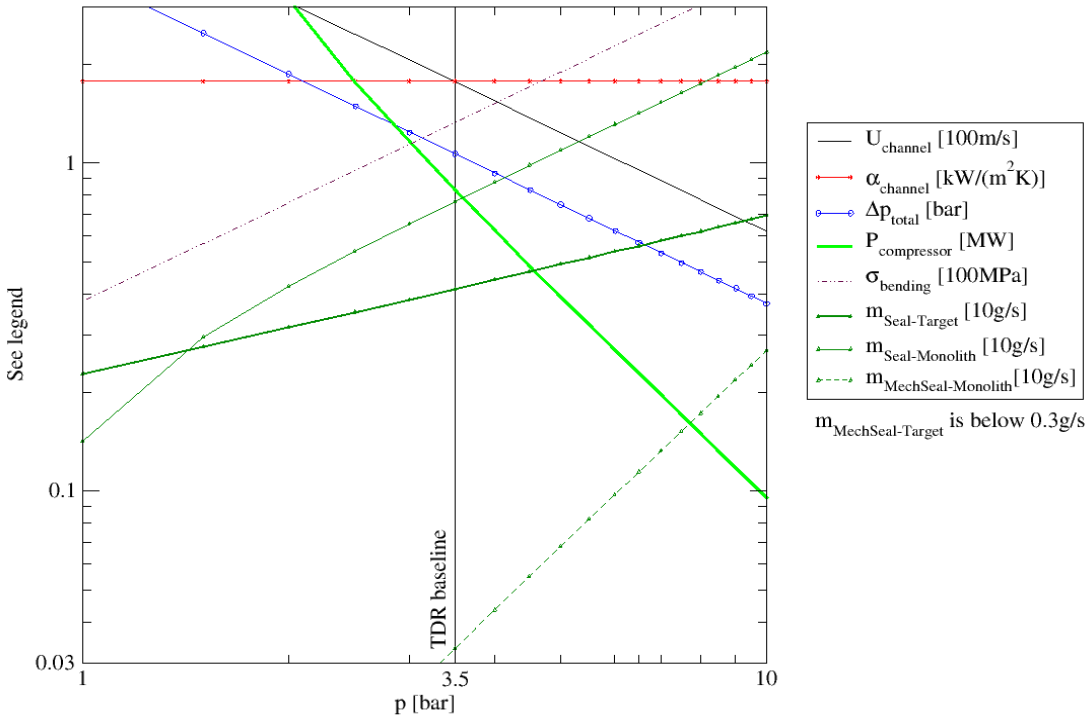

Figure 7 Critical Design Factors

The diagram shows the decreasing need of compressor power and also the reduced pressure drop, if the operation pressure is increased. Of course an increased pressure will on the other hand increase the helium leakage and also stress to the shroud.

To optimize the Target Helium Cooling System the critical design factors has been examined. The advantages to increase the operation pressure to some degree overrides drawbacks with increased stress and leakage. The operation pressure finaly was adjusted to 1,0 MPa. The Wheel has to fulfill stress criteria according to an operation pressure of 1,0 MPa. The concept design of the Wheel, composed of two plates welded together with ribs in between, forms a solid structure to meet those stress criteria. Final thermal-mechanical calculations are ongoing and minor design adjustments are foreseen.

The pressure drop in the Target Helium Cooling System is calculated to be just around 0.06 MPa. With an operation pressure of 1.0 MPa the helium compressor can by this figure be more considered as a circulator than a compressor. The increased operation pressure, from 0.36 MPa to 1.0 MPa significantly reduces the helium compressor power. A preliminary investigation of possible compressor vendors indicates that the cost for the compressor reduces significantly with these new design parameters.

A Preliminary Design Review of the Target Helium Cooling Concept Design has been performed. The result of the review was that the review committee endorsed the preliminary system design and with a few recommendations proposed that the system is ready to be progressed to its final design phase.

Regarding the Wheel and the Shaft these subsystems of the Target Station is close up to the Preliminary Design Review. The concept design of the Spallation Material is ready and also the concept design of the Wheel. The shaft is however undergoing redesign and optimization to better satisfy requirements on shielding performance and prevention of neutron streaming. The Driving Unit and the Sealing, connecting the Helium Cooling System to the rotating Shaft, also needs minor clarification of the design concept.

3. In-Kind

The construction of the ESS in Lund is strongly based on In-Kind contributions from member states. During 2014 In-Kind collaboration meetings have been performed. Institute within ESS member states were invited and the different work scopes presented. Regarding the Target Helium Cooling System and the Target Wheel and Shaft, the goal is to have an In-Kind Collaboration Agreement ready before the end of 2014.

References

[1] S. Peggs, “ESS Technical Design Report”, ISBN 978-91-980173-2-8.

3.2.8

Alternative target design for power upgrade of the TS1 target at the ISIS Neutron Facility

C Bungau[1], A Bungau[1], R Cywinski[1], T R Edgecock[1], M Fletcher[2]

[1]University of Huddersfield, Queensgate, Huddersfield, HD1 3DH, UK
[2]Ruthorford Appleton Laboratory, ISIS Neutron Facility, Didcot, OX11 0QX, UK

E-mail: C.Bungau@hud.ac.uk

Abstract. ISIS is one of the world's most powerful spallation neutron sources for the study of material structures and dynamics. Currently ISIS has two spallation targets, TS1 operating at proton beam powers of up to 200 kW, and TS2 operating to 45 kW. This paper focuses upon an upgrade study of TS1 with the goal of increasing the ultimate operating power to 0.5 MW and beyond. During this study we have taken into consideration the necessity of maintaining the spallation neutron pulse width at current values. The increased heat deposition was monitored and the target plates dimensions were modified to take this into account. Preliminary studies of an alternative molten metal target capable to cope with a higher power are also included.

1. Introduction

ISIS [1] is currently the world's most productive spallation neutron source hosting two target stations TS1 and TS2. The first target station has been operating since 1984 and over the past thirty years high quality research has been carried out at the ISIS facility at the Rutherford Appleton Laboratory in a large range of topics from physical and biological sciences to chemistry and archeology. The high demand for neutron yield and beam time for the experiments carried out at RAL led not only to the construction of a second target station TS2 but also to an upgrade of the previous target TS1, which will lead to an increased neutron flux at the instruments enabling a larger number of experiments to be carried out in a much shorter time. The TS1 target station operates at proton beam powers of up to 200 kW and the goal is to increase the operating power to 1 MW and beyond. There are many factors that could limit the performance of a high power target therefore the design of such a target presents a major technical challenge in terms of the engineering constraints of heat removal and structural radiation damage while optimising the neutron yield. Considerable efforts have been done so far for the target design and a recent study to increase the neutronic output at the TS1 target was done at ISIS [2]. This paper focuses on a target capable to cope with an increased heat deposition at 1 MW power and beyond while maintaining the spallation neutron pulse width at current values.

The ISIS accelerator has been upgraded to achieve the increased beam intensity necessary to provide a 10 pulses per second (pps) proton beam to TS2 at the same time as maintaining present intensity to TS1 where the repetition rate is reduced from 50 pps to 40 pps. The ISIS TS1 target is driven by an 800 MeV, 200 μA proton beam equivalent to almost 0.2 MW beam power.

2. The TS1 target

A schematic diagram of the ISIS target is shown in Fig. 1. It consists of a stack of 12 solid tungsten plates (105 × 80 mm) of different thicknesses (from 15 to 50 mm) enclosed in a stainless steel pressure vessel which contains heavy water for cooling the plates. The thicknesses of the tungsten target plates are shown in Table 1.

Past experiences at other neutron facilities identified water corrosion of bare tungsten as a shortcoming for neutron spallation targets. Studies of tungsten performance under flowing water at even modest temperatures have shown significant corrosion rates that are dramatically enhanced by the presence of radiolysis products induced by irradiation [3]. The slow loss of W as it is corroded will result in a drop of the delivered neutron flux to the instruments and will also facilitate the presence of radioactive tungsten isotopes in the coolant water. Irradiation embrittlement in conjunction with large scale material losses may produce drastic failures in the targets and introduce geometry variations or cracking in a manner that perturbs target temperature distributions or coolant flow beyond those anticipated in either standard operation or transient analyses [4]. All these issues degrades the operational reliability and creates safety concerns therefore the best approach to remedy these shortcomings was to clad the tungsten target with a material that is both resistant to corrosion and which also maximises the neutron yield. These two requirements suggested that heavy atomic nuclei materials like Tantalum were the solution. This approach was taken by the KYK Neutron Scirnce Laboratory (KENS) over a decade ago to overcome the limitations of bare tungsten targets [5]. At ISIS each tungsten plate is cladded in a 2 mm thick tantalum layer. The Ta/W interface must remain in close contact as developing gaps would restrict the coolant flow and create resistance to the heat evacuation generated by the target. The gaps between the plates is 2 mm and is used for cooling the plates with heavy water. The flow of heavy water is redistributed using stainless steel manifolds.

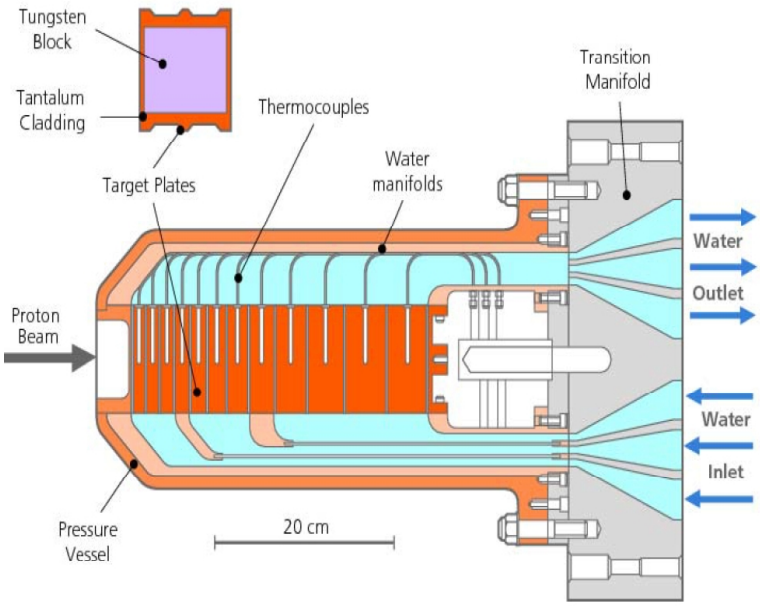

Figure 1: Layout of the ISIS-TS1 spallation target.

Four moderators are used to slow down fast neutrons escaping from the target to the lower speeds required for neutron scattering experiments. Two use water at room temperature, one uses liquid methane at 100 K and the fourth consists of liquid hydrogen at 20 K. The different temperatures result in different energy neutron beams. The moderators are small, about 0.5

Table 1: Thicknesses of the tungsten target plates.

plate no.	1	2	3	4	5	6	7	8	9	10	11	12
thickness (mm)	15	15	16	17.5	19	22	25	30	38	44	50	50

l, and are surrounded by a water-cooled beryllium reflector which scatters neutrons back into the moderators and doubles the useful flux of neutrons. Surrounding radially the reflector are the neutron channels which conduct the neutrons to the instruments for neutron scattering applications.

Based on a set of engineering drawings, the ISIS TS1 target geometry was implemented into the Geant4 Monte Carlo code [6], and Fig. 2 shows the modelling of the target and the surrounding components. In this figure, the four neutron moderators that are used to thermalize the neutrons are shown in different colours: the two water moderators (blue), the liquid methane moderator (green) and the liquid hydrogen (yellow). The two water moderators are at ambient room temperature 300 K, the liquid methane moderator operates at 100 K and the liquid hydrogen moderator at 20 K. The liquid methane moderator has curved surfaces unlike the others. The target and the moderators are embedded in a beryllium reflector shown here in grey. Also the neutron beamlines are shown (lower right) which lead the neutrons to the experimental stations.

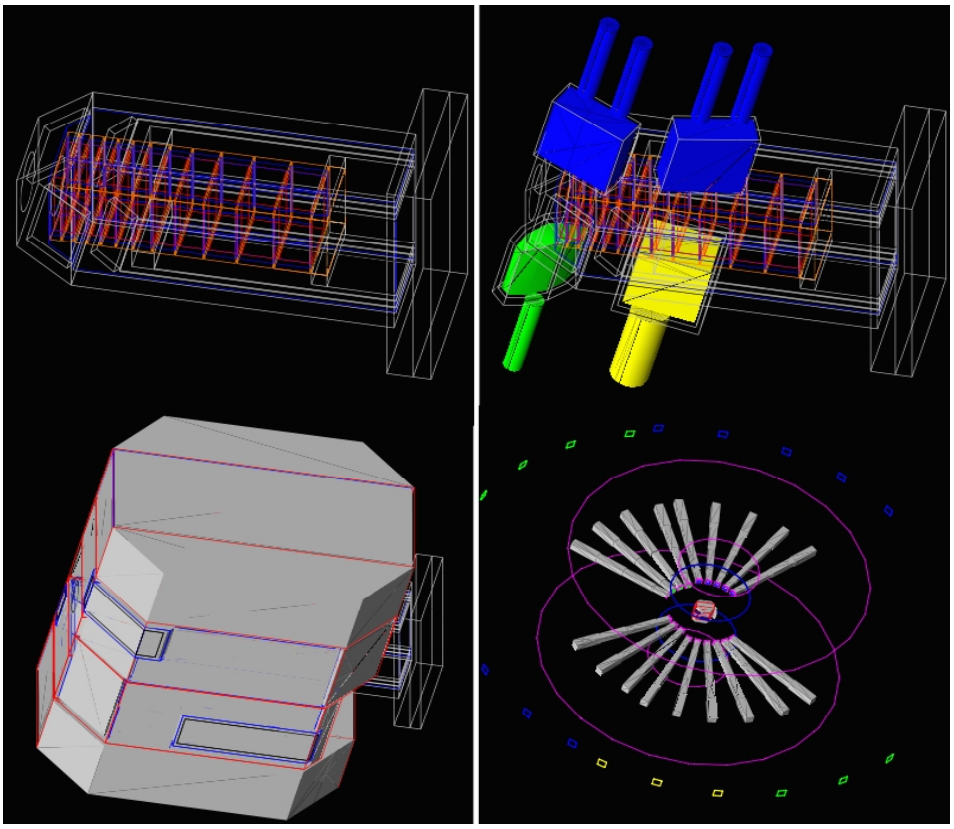

Figure 2: GEANT4 modelling of the ISIS TS1 target (upper left) , neutron moderators (upper right), reflector (lower left), shielding and instruments channels (lower right).

2.1. Heat Deposition Inside the Target

In a spallation process, as a result of the interaction of protons with target nuclei, high energy particles are produced leaving the nuclei in an excited state. They deexcite by evaporation producing more energetic particles. All these particles interact further with other nuclei in processes called nuclear cascades. The heat deposited in the target comes from the energy loss of the protons and of the nuclear recoils due to ionisation processes and is proportional to the beam current. Considering a beam current of 200 μA, the total heat rate deposition in the target plates is shown in Fig. 3 and it can be seen that it decreases gradually along the series of plates. For this reason the first plates are made thinner than the last plates. However, the heat is deposited differently in the inner tungsten material and tantalum cladding as Fig. 4 and Fig. 5 show.

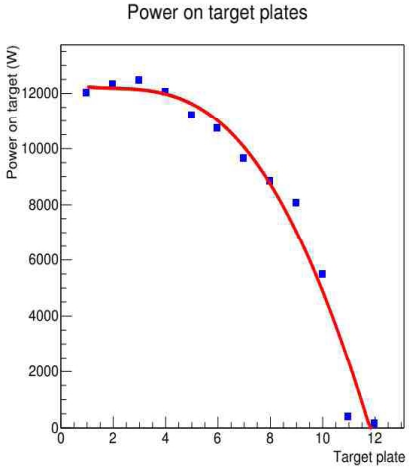

Figure 3: Energy deposition inside the target plates.

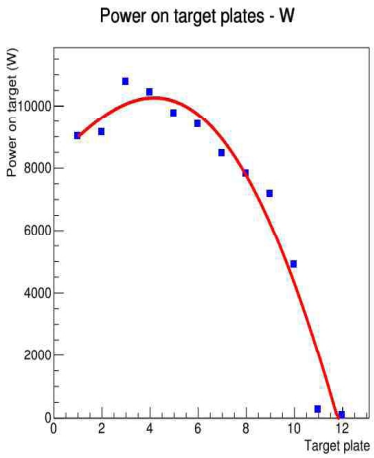

Figure 4: Energy deposition inside the inner tungsten material.

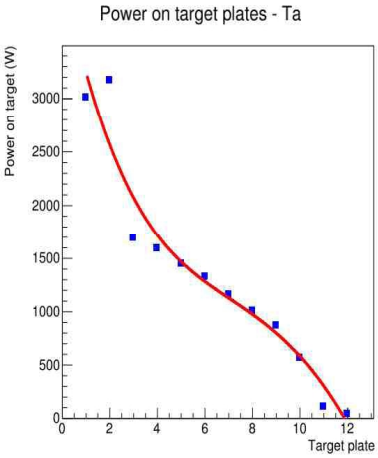

Figure 5: Energy deposition inside the tantalum cladding.

The spatial distributions of the volumetric heat deposition rates on the various target plates were calculated and the results are shown in Fig. 6. The heat deposition rates have peaks around the centre of the target plates with the maximum value being about 0.5 W/mm^3 (the bin size is 60 mm^3). These values will be used as reference values for this power upgrade study. In order to keep the fixed solid target design, more thinner plates are required to cope with the increased heat deposition due to the additional power on target. The thickness of the tungsten plate can be reduced all the way down to 5 mm, however the existing 2 mm tantalum cladding thickness can only be reduced to 1 mm due to limitations imposed by manufacturing conditions.

The neutron yields energy spectra measured at various instruments pointing to the neutron moderators are shown in Fig. 7. Because the neutron moderators operate at different temperatures the neutron spectra show a strong dependence on the moderator temperature, resulting in an increase in the number of thermal neutrons for lower operating temperatures.

3. Power upgrade to 0.5 MW and beyond

There are a number of things to consider when redesigning the target plates in order to cope with the increased proton beam power. The peak values in power on each plate should not exceed the current values. Also the maximum temperature inside the target plates should be much

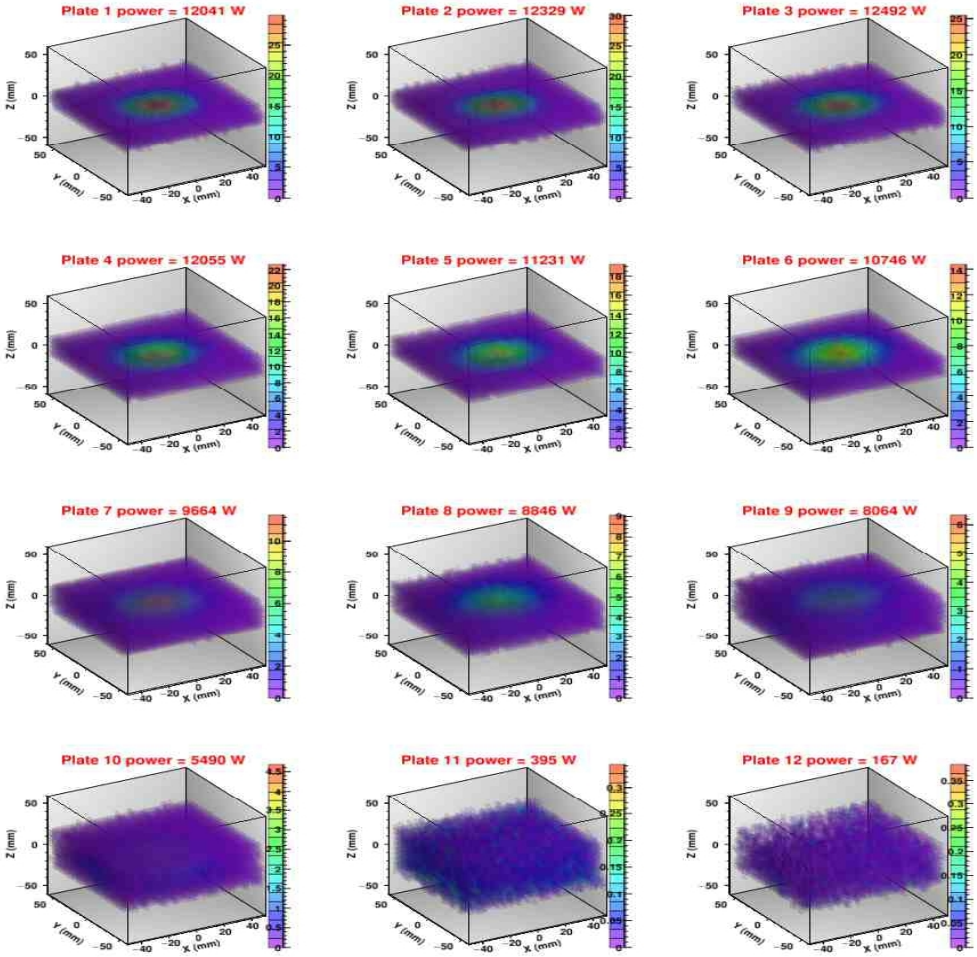

Figure 6: Spatial distribution of the volumetric heat deposition rates inside the target plates.

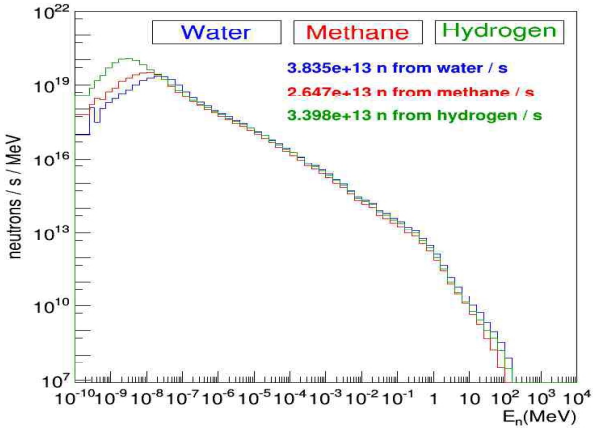

Figure 7: ISIS TS1 neutron yields for the current target plates design and a proton beam intensity of 200 μA.

lower than the melting point of the target material. There is also a limitation on the stress due to fatigue failure. Finally the water volume inside the target should not be increased too much in order to avoid slowing down the neutrons and altering the neutron pulse time distribution at the instruments. Various target plates configurations have been simulated, ending up with a new design consisting of 31 plates (instead of the current 12 plates), each plate having 1 mm Ta outer cladding on all sides.

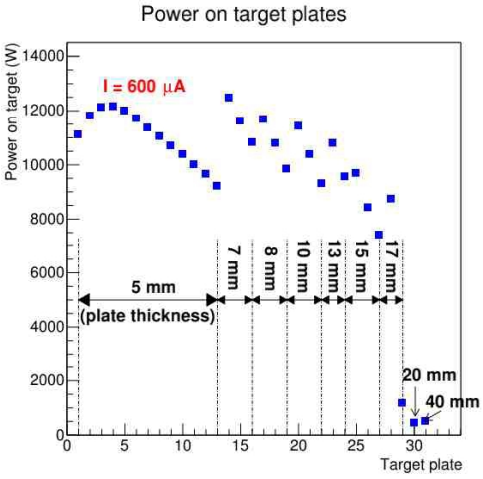

Figure 8: Total heat rate deposition inside both materials W plates and Ta cladding for a proton beam intensity of 600 μA.

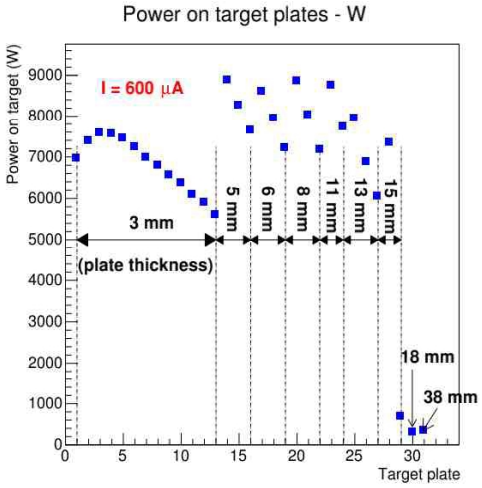

Figure 9: Total heat rate deposition inside the W plates for a proton beam intensity of 600 μA.

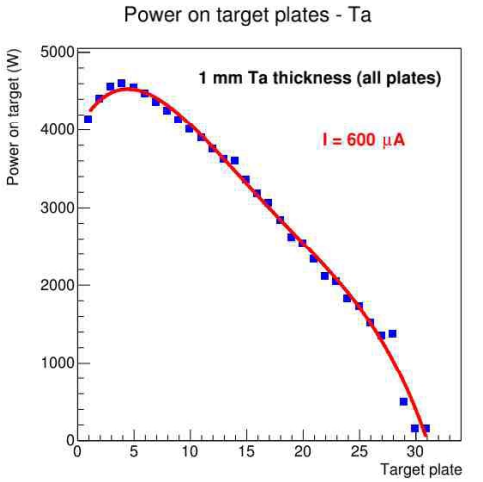

Figure 10: Total heat rate deposition inside the target plates Ta cladding for a proton beam intensity of 600 μA.

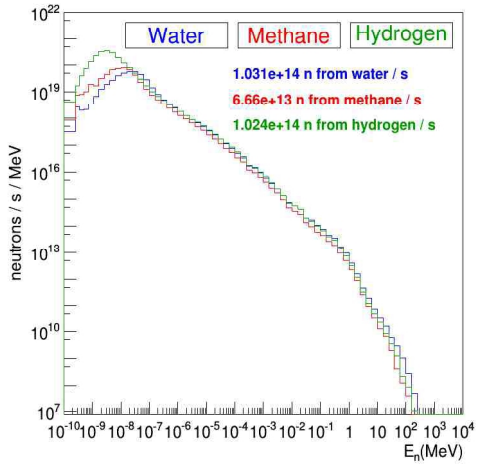

Figure 11: ISIS-TS1 neutron yields for the new thinner target plates design and a proton beam intensity of 600 μA.

The tungsten plates cladded with tantalum have an increased thickness starting from 5 mm for the first 13 plates all the way up to 40 mm for the last plate. The total power deposition on target plates is shown in Fig. 8 for all 31 target plates of different thicknesses. It can be seen

that although we increased the power on target from less than 0.2 MW to 0.5 MW, by making the plates thinner the new power on them is kept at similar values as in the current design. To avoid having a large number of thin plates, each time the power drops to a safe value, the thickness of the next plate is increased. The power deposition on plates drops to zero after the 31st plate. The power deposition inside the inner tungsten material can be seen in Fig. 9 and as expected one can see the same pattern. Although the tantalum cladding thickness was reduced by half, this being the minimum achievable thickness, the power deposition has exceeded the values in the current design. This means the new power on target of 0.5 MW is the maximum value the solid target plates can sustain. Further power increase can be achieved only by a complete redesign of the target either by having a rotating solid target or a molten metal target. The speed of rotation must be chosen such that an element of the target is fully cooled during one revolution. The design of the rotating seals and of the remote handling required are both demanding from the engineering perspective.

The neutron spectra measured at the instruments corresponding to the neutron moderators are shown in Fig. 11 for this new target design. The liquid hydrogen moderator is the most efficient in thermalizing the spallation neutrons produced inside the new target. It can be seen that there is a gain in neutron yield for the 31 target plates design. The neutron yield coming from the water and hydrogen moderator is one order magnitude higher than in the current design and for the methane moderator the neutron yield is more than twice the current value.

For a direct comparison between the new target design and the current one, the neutron yields were plotted for each moderator in the energy range of interest for the neutron instruments. The direct comparison is shown in Fig. 12 and shows that with the new target plates design the neutron yield is approximately three times higher than with the current target design.

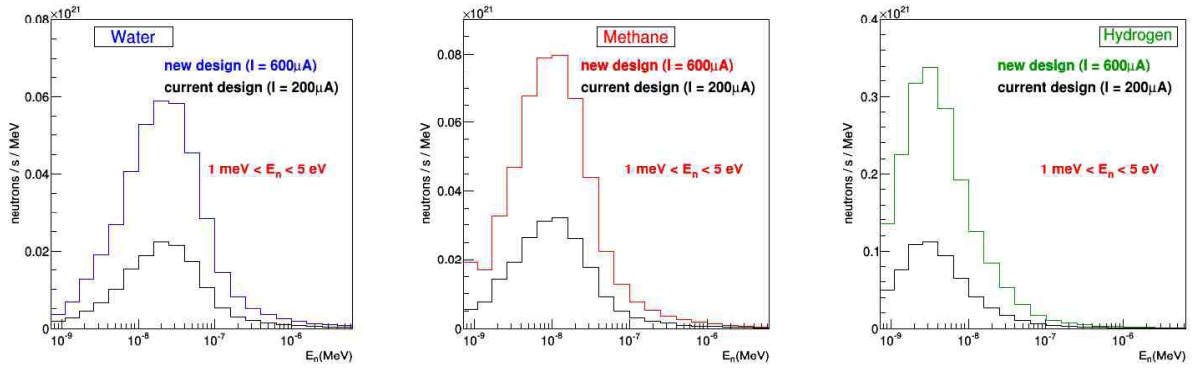

Figure 12: ISIS-TS1 neutron yields comparison between the current design and the new thinner target plates design for the neutron energy range of interest.

4. Molten target

There are a couple of advantages for having a liquid metal target. As the irradiation damage is small, the target should last long minimizing the waste disposal problem. Additionally the mean density of the liquid metal target is not diluted by a coolant because the target itself acts as the coolant with the heat being removed by convective flow. Any hazardous volatiles could be continuously extracted to reduce the potential hazard. By using an eutectic PbBi alloy containing 17% Bi the neutron production is increased twice the current ISIS values (Fig. 7) at the water and hydrogen moderators and slightly higher at the methane moderator as Fig. 13 shows. Other eutectic alloys are also being studied and show similar increase.

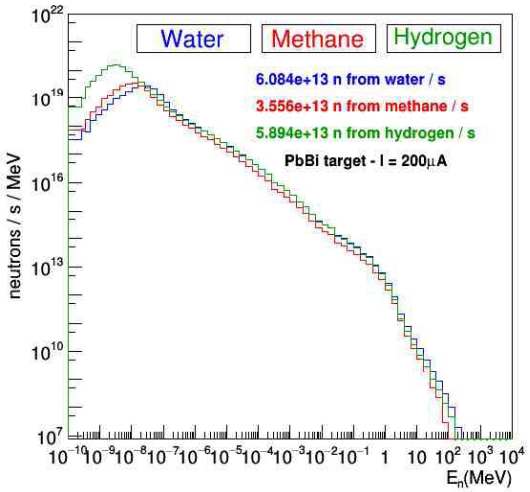

Figure 13: The neutron yield for a PbBi alloy target.

5. Conclusion

Several suggestions with varying degrees of practicality have been described above for upgrades of the TS1 target. Increasing the proton beam current from the current value of 200 μA to 600 μA requires the use of much thinner target plates, which allows the target to cope with the additional proton beam power. The goal is to increase the power on target from 0.2 MW to 0.5 MW and beyond. Several target plates configurations have been simulated and an optimum design was proposed. This consists of a set of 31 tungsten plates of increasing thickness each having a 1 mm tantalum cladding on all sides. It was found that this design copes with the additional power on target. The neutron yield increased by a factor of three compared to the current target design. Any further increase in the beam power will result in a much higher thermal stress in the Ta cladding of the target plates. A completely new design involving either a rotating solid target or a molten metal target will be required for a proton beam power above 0.5 MW.

6. Bibliography

[1] ISIS neutron spallation source, UK: http://www.isis.stfc.ac.uk
[2] S. Gallimore and C. Souza, “Proposal for ISIS Target Station 1 upgrade”, these proceedings.
[3] R.S. Lillard, D.L. Pile, D.P. Butt, Journal of Nuclear Materials, 278, (2-3), 2000, 277-289.
[4] A.T. Nelson el al., Journal of Nuclear Materials, 431, 2012, 172-184.
[5] G.S. Bauer, Journal of Fusion Energy, 8, 1989, 169-180.
[6] GEANT4 Monte Carlo code (version geant4.9.6.p03): http://geant4.cern.ch

3.2.9

Moderator performance characterization, operational experience, and plans at JSNS

M. Teshigawara[1], M. Harada, M. Ooi, H. Tatsumoto, H. Takada
J-PARC Center, JAEA, Tokai, Ibaraki 319-1195, Japan.

E-mail: teshigawara.makoto@jaea.go.jp

Abstract. By optimizing 100% para hydrogen, especially for coupled moderator, gave unique volumetric shape, such as large sized cylindrical shape coupled with water premoderator, resulting in the highest neutron intensity per pulse at 300kW. In order to confirm relationship of the measured pulse shape with the para-hydrogen fraction, para-hydrogen fraction was measured directly in the hydrogen circulation loop. The para-hydrogen fraction was almost 99.7% for off- and on- beam operation. We started to fabricate spare moderators and reflector to replace 1st moderators and reflector assembly in 2019 due to lifetime. In spare moderator, invar and Au-In-Cd alloy will be newly installed to improve moderator fabrication and reduce radioactivity.

1. Intorduction

An accelerator-based short-pulsed-spallation-neutron-source was developed to emphasize a neutron science in J-PARC. Three hydrogen moderators (coupled, decoupled and poisoned moderators) based optimization study were installed in JSNS (Japanese Spallation Neutron Source) in J-PARC. In order to characterize short-pulsed source, 100% para hydrogen, Ag-In-Cd decoupler and Cd poison sheet were applied. Especially for coupled moderator, the unique optimization, such as large sized cylindrical para hydrogen shape coupled with optimized water premoderator, gave the higher neutron intensity, which has achieved to provide the highest neutron intensity per pulse in the world at 300kW proton-beam-operation. It's on the way to upgrade the beam power, finally will be up to 1MW in 2016. In order to confirm moderator design and para-hydrogen converter performance, the combination method as a gaseous hydrogen sampling from the hydrogen circulation loop and Laser Raman spectroscopy was applied to enable the direct para hydrogen fraction measurement in the hydrogen circulation loop. On the other hand, the moderator should be replaced in every 6 MWyears due to neutron irradiation. A plan of 2nd moderator fabrication is under way. We modify the design, such as invar use to improve the moderator fabrication and Gold-Indium-Cadmium (Au-In-Cd) alloy for decoupler to reduce radioactivity. In this paper, we report these results.

2. Moderator development activity in JSNS

Since first neutron production at 2008 in JSNS, the proton beam power gradually went up to 300 kW in 2012. Last year, linac accelerator was upgraded from 180 MeV to 400MeV in the energy to increase the beam power. We will deliver 1 MW proton beam to JSNS within 2016 according to proton beam rump up schedule as shown in Fig. 1. Activity plan of moderator/reflector is shown in Fig. 2. We started to fabricate the

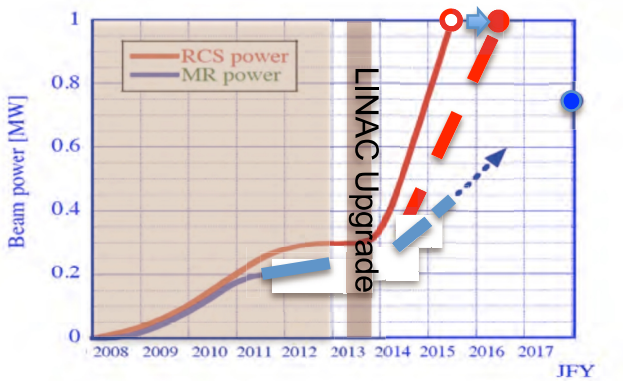

Figure 1. Accelerator rump up schedule. Linac was upgraded from 180MeV to 400MeV in the energy to increase proton beam power in 2013. Protons with 1MW beam power will be injected to JSNS in 2016

[1] Neutron source section, J-PARC Center Japan Atomic Energy Agency
Tokai-mura, Naka-gun, Ibaraki Tel:+81-29-284-3224
Teshigawara.makoto@jaea.go.jp

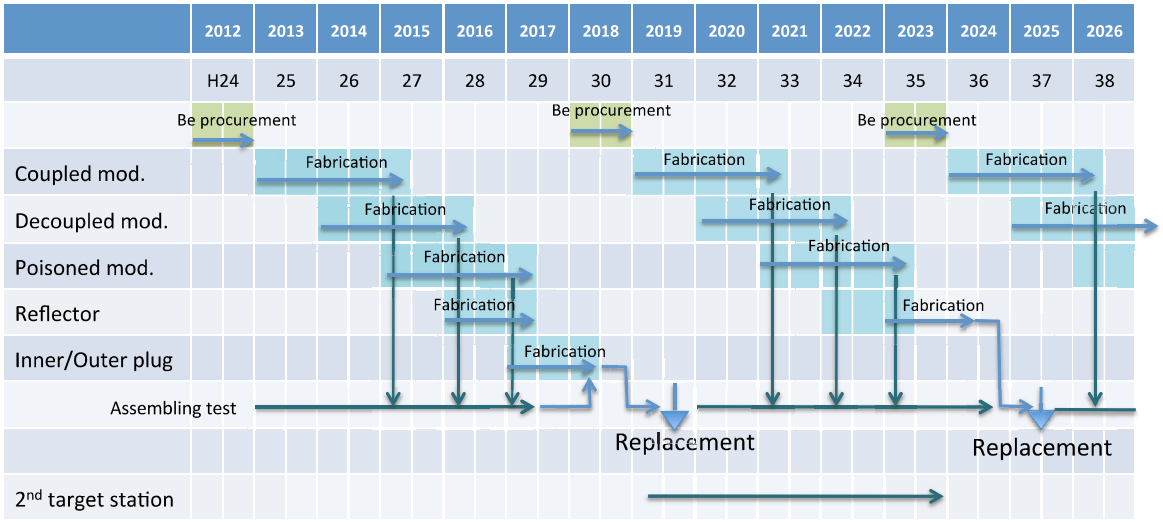

Figure 2. Activity plan of moderator/reflector. Fabrication of spare moderators and reflector is started to replace from 1st moderator and reflector assembly in 2019.

spare moderators and reflector to replace the 1st moderators and reflector assembly due to the lifetime. The lifetime was assumed to be a 20 dpa of neutron irradiation damage of aluminum alloy, which is structural material of moderator and reflector. We will estimate that the accumulated irradiation damage will reach the 20 dpa (30,000 MWhr for 1MW proton beam operation) in 2019 according to proton beam schedule. In the spare moderator, invar and Au-In-Cd alloy will be newly installed to improve the moderator fabrication and reduce the radioactivity. We also just started to consider the second target station for emphasizing the science down to very cold neutron energy region. We also are proceeding with the moderator development focusing on the high ALBEDO material, such as nano-diamonds, to intensify the blow cold neutrons under IAEA collaboration (Project No. F1216).

3. 1st moderator performance characterization in JSNS

3.1 Coupled moderator performance

A liquid hydrogen, which consists of two isomeric forms (ortho- and para- hydrogen), is only available material as the moderator for the MW-class source in terms of radiation damage. The transparent cross section of para-hydrogen, which means rapidly decrease below 14.5 meV in comparison with normal-hydrogen[1] in the total elastic scattering cross section, gives leaky neutrons from the moderator in the slowing down process, but relatively short tail in the neutron beam pulses in the cold-neutron-energy region, however, the low hydrogen density of liquid hydrogen (ca. 1/2 of solid methane) is also a weak point in the neutron moderating process. In the design, we focused on the para to ortho energy conversion in addition the pre-moderator function[2] to improve the neutron intensities in the cold-neutron-energy region for higher neutronic performance such as high peak intensity, narrow width and short tail in the "short-pulsed" neutron beam[3-11]. Especially for coupled moderator, we found the unique volumetric shape, such as large

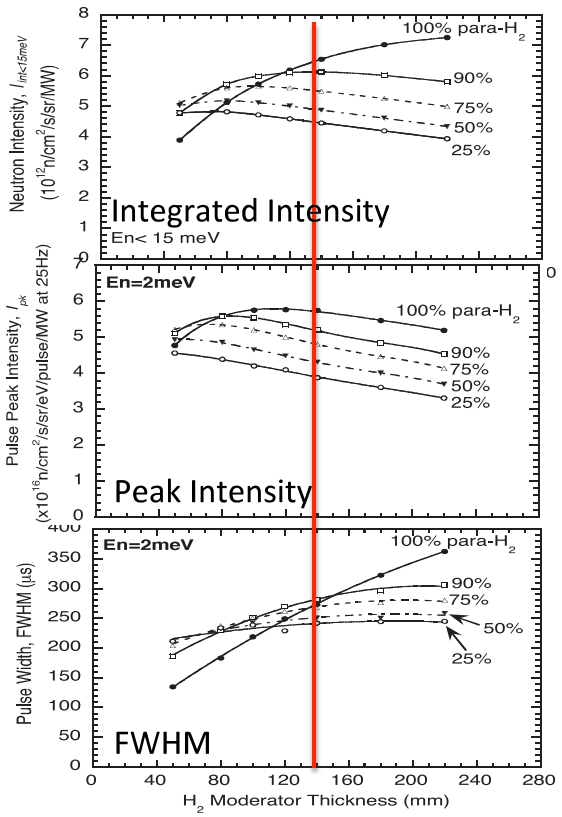

Figure 3. Hydrogen moderator thickness dependence on Pulse width (FWHM)Peak Intensity and Neutron intensity[4]

sized cylindrical para-hydrogen shape coupled with optimized water premoderator. As shown in Fig. 3, we decided the 14 cm of large moderator thickness, which gave the highest peak intensity, but somewhat sacrifice in the FWHM in pulses in the optimization study for "short-pulsed" source[4]. This coupled moderator also gave highest neutron intensity per pulse[13] in the world at 300kW proton-beam-operation in 2012. We also found that brightness area could be seen near premoderator in the spatial distribution on viewed surface of coupled moderator as shown Fig. 4. This calculation results also indicated that there was a room for the further improvement to intensify the neutrons from the different perspective, such as "long-pulsed" source design. ESS (European Spallation Source) group, which is aiming at 5 MW "long-pulsed" source, focus on increasing the brightness area in the design in order to obtain higher neutronic performance. It will be discussed somewhere.

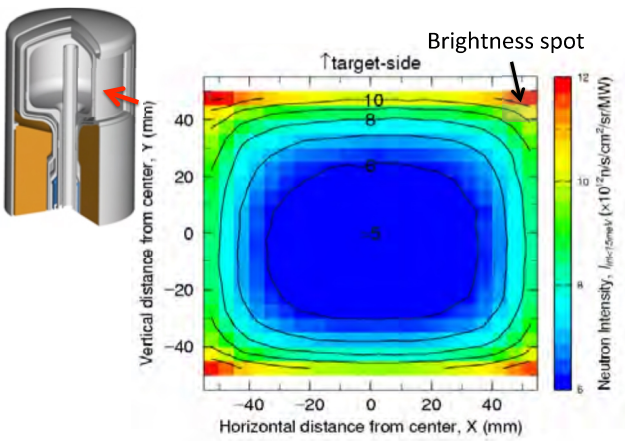

Figure 4. Spatial distribution on viewed surface of coupled moderator. Brightness spot and area can be seen near premoderator[4],

3.2 Para-hydrogen fraction measurement

In order to confirm the relationship of the measured pulse shape with the para-hydrogen fraction, it is an important to measure the para-hydrogen fraction in the hydrogen circulation loop directly. However, it is not easy to measure the para-hydrogen fraction in loop due to high pressure and cold temperature, such as supercritical hydrogen (1.5MPa and 20K) in the high power target facility. It also should be avoidable to break the stable operation of neutron source facility by accident of failure during para-hydrogen measurement process because of the open service. The combination method as gaseous hydrogen sampling from the hydrogen circulation loop and Laser Raman spectroscopy was applied in order to enable the direct para-hydrogen fraction measurement in the loop. The hydrogen sampling line was installed before / after through moderators as shown in Fig. 5. In the loop, the supercritical hydrogen (20K, 1.5MPa) was circulated. The magnetic catalyst, iron oxide hydroxide ($Fe(OH)_3$) was also installed to keep the equilibrium mixture state (99.8% para-hydrogen fraction at 20K) as shown in Fig. 5. In order to sample the gaseous hydrogen, two buffers, which consisted of small (vol.: ca. 20 ml) and large (vol.: ca. 10L) one, were con nected to hydrogen sampling line in series by the manual controlled valves. During hydrogen sampling process, it changed from supercritical state to the gaseous one. The pressure was also reduced to 1/500 (ca. 0.03MPa) by the second introduction to the large buffer. The extracted hydrogen was introduced to the glass-cells by manual valve operation as also shown in Fig. 5. Para-hydrogen fraction was measured by using Laser Raman spectroscopy (JASCO, NRS-5100) with the resolution (1 cm-1) and range (50 to 8000 cm-1) after extracted hydrogen in the glass-cell. We finally measured the para-hydrogen fraction extracted from the hydrogen circulation loop in the 300kW proton beam power. The measured Laser Raman spectrums are shown in Fig. 6 for off- and on- beam operation. The para-hydrogen fraction was almost 99.7% for off- and on- beam operation cases.

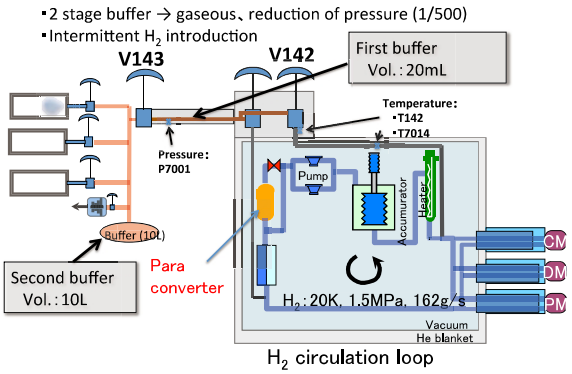

Figure 5. Hydrogen sampling from hydrogen circulation loop to measure para-hydrogen fraction.

4. Spare moderator fabrication

4.1 Introduction of invar material

In the first design, in order to make the moderator vessel and the hydrogen transfer line, as a material combination, aluminum alloy (A6061-T6) and stainless steel (SS316L) were adopted[14, 15]. However, some troubles such as welding leak, deformation and contact with other pipes, etc, were occurred in the actual fabrication process[16] due to the thermal shrinkage measure in the hydrogen transfer line. We had a plan to adopt the invar alloy to make the 2nd moderator fabrication because of very low thermal expansion. The thermal expansion of invar is one order of magnitude lower than that of aluminum alloy or stainless steel. It is also used for many specific applications, especially in cryogenic application, such as LNG (liquefied natural gas) carriers, transfer pipes, etc.

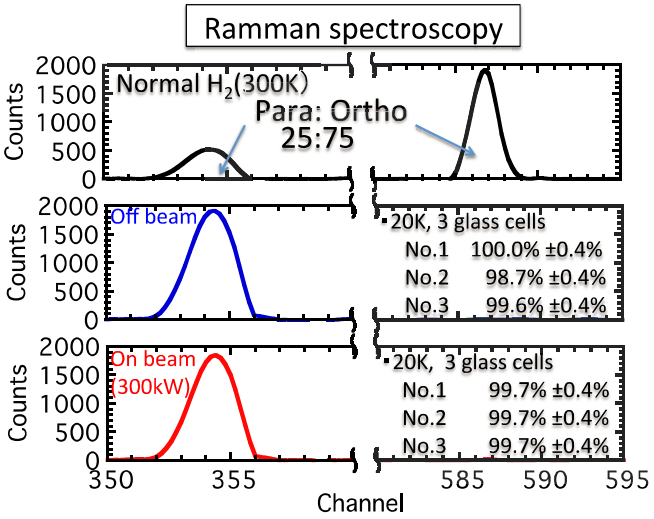

Figure 6. Measured Ramman spectroscopy for off- and on- beam operation. For the reference, normal hydrogen case is shown in upper.

Recently, it was also utilized to make the H_2 transfer line in SNS Ornl[17]. It will give more easily manufacture in the moderator fabrication process. We developed the invar-joints for the conversion of invar alloy to aluminum alloy and stainless steel and evaluated the mechanical strength of invar-joints[18, 19], which was also requirement for the Japanese High Pressure Gas Safety Law. These results were reflected the hydrogen transfer line design. Figure 7 shows the drawing of hydrogen transfer line, which is including the invar and invar joint. The thermal shrinkage could be reduced from 20 mm to 2 mm, resulting in no need asymmetrical setting in fabrication. Just now, we are starting to fabricate the spare coupled moderator based on this drawing.

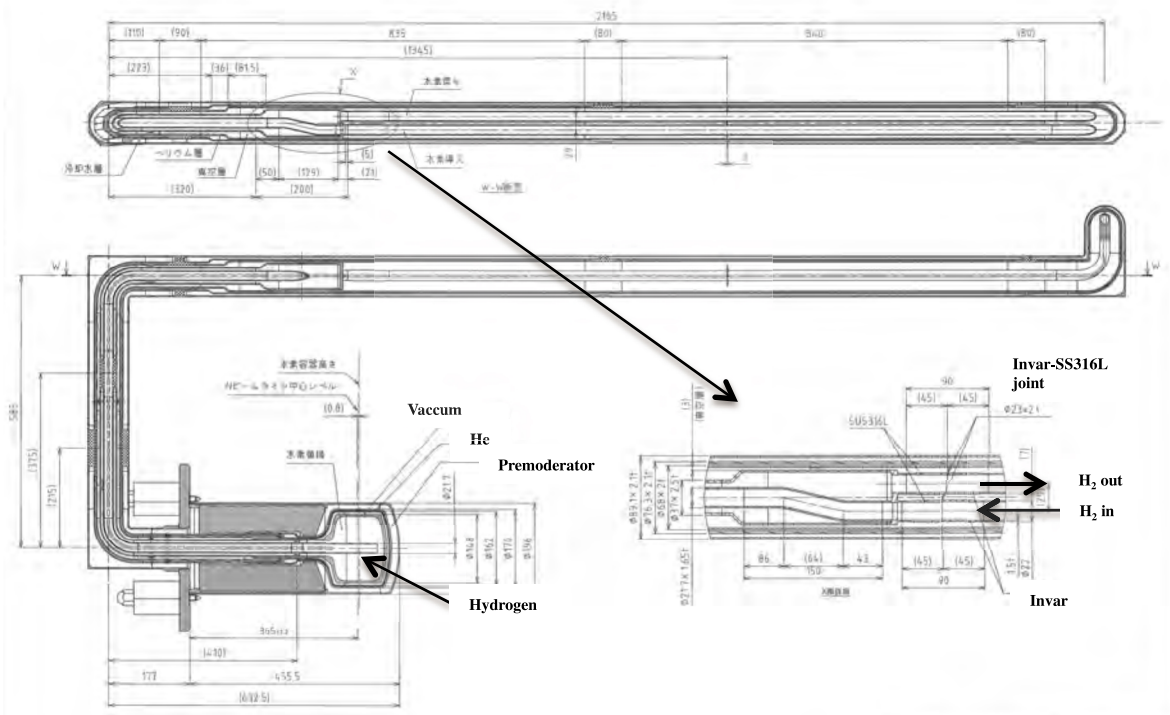

Figure 7. Drawing of coupled moderator

4.2 Au-In-Cd alloy for decoupled moderator

A thermal-neutron-absorber, called decoupler, is adopted to obtain a neutron beam pulse with narrow width and fast decay (short tail) for the decoupled and poisoned moderator. The higher cut-off energy (decoupling energy) gives shorter tail in the beam pulse. For the first moderator, we developed a Ag-In-Cd decoupler which uses a combination of the resonance absorption cross sections [20-24], resulting in reaching 1 eV of decoupling energy effectively. However, the Ag-In-Cd decoupler has a disadvantage in view of high residual radioactivity, for example, owing to ^{108m}Ag (half life of 418 years).

We have focused on the development of a low activated decoupler for the next generation decoupled moderator. A combination of Au, In and Cd was selected as the candidate decoupler material, resulting in the low induced residual radioactivity in comparison with Ag-In-Cd decoupler by three orders of magnitude without sacrificing the neutronic performance in the pulse shape. In order to utilize the Au-In-Cd decoupler, it is necessary to develop the alloying of Au-In-Cd and to make the bonding between Au-In-Cd and aluminum alloy (A5083) in terms of the heat removal and thermal stress. The required design bonding strength due to the thermal stress was estimated over 30 MPa. A Hot Isostatic Pressing (HIP) technique is applied to obtain the bonding the Au-In-Cd alloy to the A5083. This technique is also available for the bonding to unique shape, such as curved shape. In case of manufacturing of Au-In-Cd, we have already succeeded to make a homogeneous ternary Au-In-Cd alloy [25]. We also found the HIPing condision (Temp: 535℃, Holding time: 1hr) to obtain the required bonding strength between Au-In-Cd and A5083 for small sized sample[26]. We are going to next step to utilize the Au-In-Cd alloy to the actual moderator fabrication. As shown in Fig. 8, Au-In-Cd alloy ingot (Weight: C.A 1kg) is just prepared by ourselves for the actual sized HIPing test.

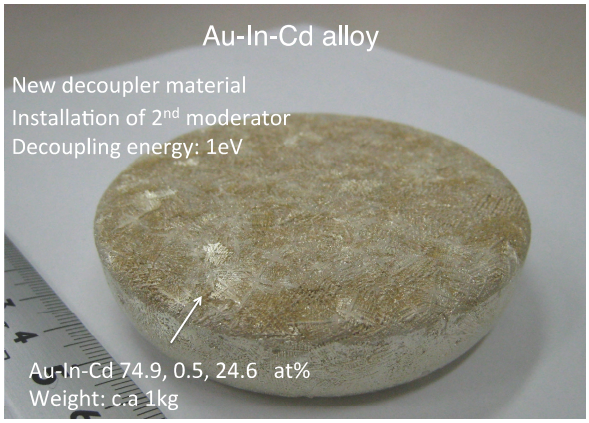

Figure 8. Au-In-Cd alloy ingot. We prepared Au-In-Cd alloy ingot for HIPing test for Au-In-Cd alloy and A5083.

5. Summery

Activity plan of moderator / reflector is described. We started to fabricate the spare moderators and reflector to replace the 1st moderators and reflector assembly in 2019 due to the lifetime. In the spare moderator, invar and Au-In-Cd alloy will be newly installed to improve the moderator fabrication and reduce the radioactivity. We also just started to consider the second target station for emphasizing the science down to very cold neutron energy region. We also are proceeding with the moderator development focusing on the high ALBEDO material, such as nano-diamonds, to intensify below cold neutrons under IAEA collaboration. By optimizing 100% para hydrogen, especially for the coupled moderator, gave the unique volumetric shape, such as large sized cylindrical shape coupled with water premoderator, resulting in the highest neutron intensity per pulse at 300kW.

In order to confirm the relationship of the measured pulse shape with the para-hydrogen fraction, para-hydrogen fraction was measured directly in the hydrogen circulation loop. The para-hydrogen fraction was almost 99.7% for off- and on- beam operation cases.

References

[1] R. E. MacFarlane, D. W. Muir, Los Alamos National Laboratory Report LA-12639-MS (ENDF356) 1994
[2] Y. Kiyanagi et al., Nucl. Instr. and Meth. in Phys. Res. A 343 1994 558-562
[3] T. Kai et al., J. of Nucl. Science and Technology Tokyo 39(2) (2002) 120-128
[4] M. Harada et al., J. of Nucl. Science and Technology Tokyo 39(8) (2002) 827-837
[5] N. Watanabe et al., J. of Neutron Research, 11 (2003) 13-23
[6] M. Harada et al., Proc. of ICANS XVI, May 12-15, 2003, Zeughaus, Germany, (2003) 697-706
[7] T. Kai et al., NIM A 523 (2004) 398-414
[8] T. Kai et al., NIM A 550 (2005) 329-342

[9] T. Kai et al., Proc. of ICANS XVI, May 12-15, 2003, Zeughaus, Germany, (2003) 657-666
[10] M. Harada et al., NIM A 539 (2005) 345-362
[11] M. Harada et al., NIM A 574 (2007) 407-419
[13] F. Maekawa et al., NIM A 620 (2010) 159-165
[14] M. Teshigawara et al., Proc. ICANS-XVI, May 12-15, Dusseldorf-Neuss, Germany (2003) 601-611
[15] M. Teshigawara et al., Proc. ICANS-XVII, April 25-29, Santa Fe, NewMexico USA (2005) 365-373
[16] M. Teshigawara et al., Proc. ICANS-XVIII, April 25-29, Guangdong, China (2007) 469-475
[17] T. McManamy et al., JNM 377 (2008) 1-11
[18] M. Teshigawara et al,. J. Nucl. Mat 431 Issuees 1-3 (2012) 212-217
[19] M. Harada et al,. J. Nucl. Mat 450 Issues 1-3 (2014) 104-109
[20] M. Harada, et al., Proc. of ICANS XVI, May 12-15, 2003, Zeughaus, Germany, p.677
[21] M. Harada, et al., Proc. of ICANS XVI, May 12-15 2003, Zeughaus, Germany, P697
[22] M. Teshigawara, et al., J. Nucl. Mat. 343 (2005) 154.
[23] M. Teshigawara, et al., J. Nucl. Mat. 356 (2006), 300
[24] K. Kikuchi, et al., Material Science Forum Vol. 652 (210) p. 92 (2010)
[25] M. Ooi, et al., J. Nucl. Mat. 431 issues 1-3 (2012) 218-223
[26] M. Ooi, et al., J. Nucl. Mat. 450 issues 1-3 (2014) 117-122

3.2.10

SNS Second Target Station Moderator Studies

F. X. Gallmeier, I. Remec, W. Lu, E. B. Iverson, J.K. Zhao, K.W. Herwig

Oak Ridge National Laboratory, Oak Ridge, TN 37831, USA

E-Mail: gallmeierfz@ornl.gov

Abstract. Moderator performance studies were conducted to scope out conceptual target-moderator-reflector configurations for a second SNS target station (STS) for providing long-wavelength pulsed neutron beams with prime peak brightness. STS was assumed to receive 467 kW proton beam power at 1.3 GeV proton energy in short-pulse structure (<1 us pulse length) at 10 Hz repetition rate into a stationary compact solid tungsten target with a flat proton beam of 30 cm^2 footprint. Coupled cylindrical supercritical para-hydrogen moderators with ambient water pre-moderators with three neutron extraction ports were investigated for neutron scattering instruments needing peak intensity beams; box-shaped decoupled centrally poisoned para-hydrogen moderators were investigated for high-resolution instruments. We optimized the configurations of coupled and decoupled moderators with the square viewed areas ranging from the standard-size 10x10 cm^2 down to the smallest size of 2x2 cm^2 viewed areas to arrive at optimized cold neutron pulse peak brightness using MCNPX imbedded into global optimizer framework. With this body of information and a requirement to feed a suite of 19 STS candidate instruments we tailored a STS moderator suite to feed a suite of 19 candidate STS instruments consisting of a flat 3cm high coupled cylindrical para-hydrogen moderator, a box-type coupled para-hydrogen moderator with 5x5 cm2 cross sectional area and 10 cm depth, and a decoupled moderator unit with a cold para-hydrogen side and an ambient water side. For the coupled cold moderators, gains in peak brightness of a factor of 11-13 were demonstrated comparing to the first target station coupled moderators operated at 2 MW and 50 Hz; for the decoupled moderators the STS gains in peak brightness were a factor of 3-4.

1. Introduction

Oak Ridge National Laboratory is pursuing conceptual design work on a second target station (STS) with the goal to supplement its suite of instruments with complementary capabilities as outlined in the STS Technical Design Report [1]. The second target station is seen as an opportunity to address next-generation science challenges. Profiting from the technological progress in neutron optics developments and to adapt to the requirements of smaller samples, longer length-scales of structures and investigation of dynamic systems, our goal is to design instrumentation that exceeds the capabilities of present day instrumentation by orders of magnitude and opens the door to new science. Improvements of the instrumentation are to be harvested from the optimizing the source (target/ moderator/ reflector) through optics to detectors. The gains achievable by the source are discussed in this paper.

Earlier efforts of STS investigated the long-pulse option utilizing every third pulse of the SNS accelerator system circumventing the accumulator ring arriving at about 1MW beam power at 20 Hz repetition rate and 1 ms pulse length [2]. Considering the inferiority of such a source in comparison with ESS operated at 5 MW, and learning about the successes of the highly optimized ISIS TS2 [3] operated in the short-pulse mode, encouraged us to explore in more depth the STS short-pulse option.

2. Target Station Concepts

The source performance derives from the right material choices of target, moderators and reflector [4] and their tight coupling and the beam parameters. Building on the existing SNS accelerator that already has shown its ability to deliver a 1.4 MW proton beam at 1 GeV proton energy, 60 Hz repetition rate and 0.7 μs pulse length, we foresee a build-out of the accelerator system to 2.8 MW and 1.3 GeV beam energy. Every sixth pulse is in a pulse-stealing mode routed to STS, which hence would operator at 467 kW and 10 Hz repetition rate. The lower power will allow us to inject the beam into the target at a beam footprint area of 30 cm^2. The remainder of the pulses would drive the first target station (FTS) at 50 Hz repetition rate in a 60 Hz time structure. We also assume here that FTS is limited to 2MW power.

Building on the expertise of spallation source technologies tested and proven in facilities at IPNS, ISIS, Lujan Center, SNS and JPARC, we choose a heavy-water cooled stacked plate tungsten target as spallation target because of the superior material density and the resulting large neutron yield in a very compact neutron production zone. For coupled cold moderators, para-hydrogen pre-moderated with light water is the prime choice for highest-intensity cold beam generation at a mega-watt facility [5]. Also for a decoupled moderator, para-hydrogen is a good choice. Liquid carbon-hydrates suffer from polymerization and subsequent clogging up of supply piping and do not offer better performance. Solid carbon hydrates (mesithylene, methane) are in use at IBR2, loose their advantage of the higher hydrogen density when used in the pelletized from. In the solid monolithic form as in use at ISIS TS2, the moderator would have to be regenerated at least 10 times more frequently to avoid the violent release of accumulated energy caused by the radiation-induced breaking of molecular bonds.

For a reflector, the unanimous pick is beryllium, a good moderator of its own right and a material with good thermal and mechanical properties.

3. Moderator Performance Studies

The increasing complexity of materials being studied at photon and neutron sources are being synthesized in elaborate procedures, which result in a reduction of available sample masses and sizes for scattering experiments. Striving for unchanged instrument resolution, the neutrons from a given fixed source size cannot be focused down to a smaller sample without degradation of the experiment and are of no use in the experiment. As has been pointed out by Zhao [6] and Carpenter [7], the source size and instrument optics has to be matched to the sample size. On the other side, the neutron brightness varies greatly across the viewed moderator face dependent on the wavelength range, moderator choice but also dependent on target/moderator geometry as demonstrated by Lu [8] for the SNS FTS moderators. These findings were actually exploited by the instruments EQSANS [9] and NSE [10] and with limited moderator view to align their optics off-moderator-center to utilize higher moderator brightness and hence gain fluxes at sample of factors of 1.5. If instruments are not utilizing the full view of the moderator, the moderator size can be reduced with gains of moderator brightness (to be shown), but also result in a lower hydrogen inventory, in a smaller integral cryogenic heat load and consequently reduced construction and operations cost.

While we were exploring these options for a short-pulse system for coupled and decoupled moderators, ESS did likewise for the long-pulse target station and indeed published interesting findings of gains that match in broad terms our results [11].

Details of our principal work, optimization studies of moderators on compact tungsten targets, surrounded by beryllium reflector, involve MCNPX [12] as the tool to assess moderator performance and are described in an extensive report [13] and in a publication in preparation [14].

Without going into detail here, the findings are summarized as follows.

For cylindrical coupled para-hydrogen moderators with light water pre-moderator and neutron extraction at three ports of a given square-sized neutron extraction ports, the moderator dimensions, pre-moderator dimensions, proton beam and consequently target height at a given proton beam footprint of 30 cm^2 (flat beam distribution), and moderator position with regard to target nose were optimized with respect to a figure-of-merit emphasizing peak brightness below 5 meV of neutron

energy. Moderators with viewed areas ranging from 10x10 cm^2 to 2x2 cm^2 were investigated. For the resulting optimized configurations extended moderator performance assessments were conducted, the results of which are shown in figure 1 for peak brightness and figure 2 for brightness integrated over one pulse. The analyses for FTS and STS assumed equal energy pulses, however, the proton energies assumed 1 GeV for FTS and 1.3 GeV for STS.

The STS moderator with viewed area 10x10 cm^2 closest matches the FTS moderators, which all have viewed areas of 10 cm width and 12 cm height. In the cold neutron range below 10 meV the pulse-integrated and peak pulse gains of the STS moderator are 7 and 5. A factor of four of the STS gains for the coupled moderator can be attributed to moving the moderator at the prime neutron production zone of the target and by having a moderator depth optimized to para-hydrogen. In contrast, the FTS coupled moderators are located downstream of the decoupled moderators at a distance from the prime neutron production and were dimensioned to 5 cm depth to make them fairly insensitive to ortho-para fluctuations of the uncatalized hydrogen loop. With these choices, the FTS coupled moderators suffered greatly in performance as comparisons to the JPARC coupled moderator as indicated in Ref. [15]. The gains above four are to be attributed to the target choice, compacter proton-beam footprint and better target/moderator coupling. Additional gains of a factor of 2.5 and 3 in pulse-integrated and peak brightness, respectively, are to be had over the STS configuration with 10x10 cm^2 viewed area. It is worth mentioning that with the selection of the peak-brightness FOM, the moderator radius reduced from 7.6 cm for the 10x10 cm^2 viewed area to 3.7 cm for the 2x2cm^2 while the pre-moderator thickness increased from 1.5 cm to 2.8 cm. For a selection of a FOM favoring the pulse-integrated brightness the optimal moderator dimensions would certainly have resulted in larger radii and somewhat higher pulse-integral brightness values closer to what we found in the long-pulse studies [2].

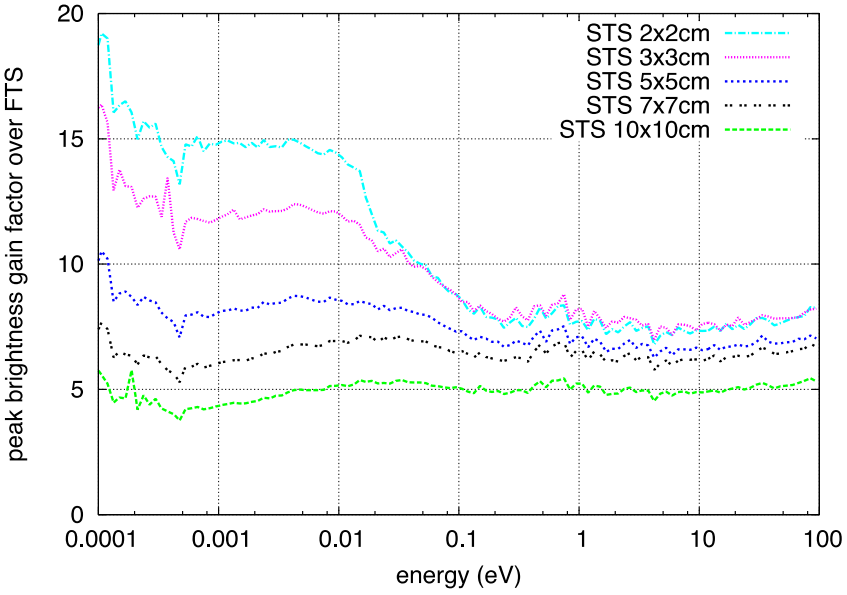

Figure 1. Peak brightness gains over the FTS coupled moderator based on equal power pulses.

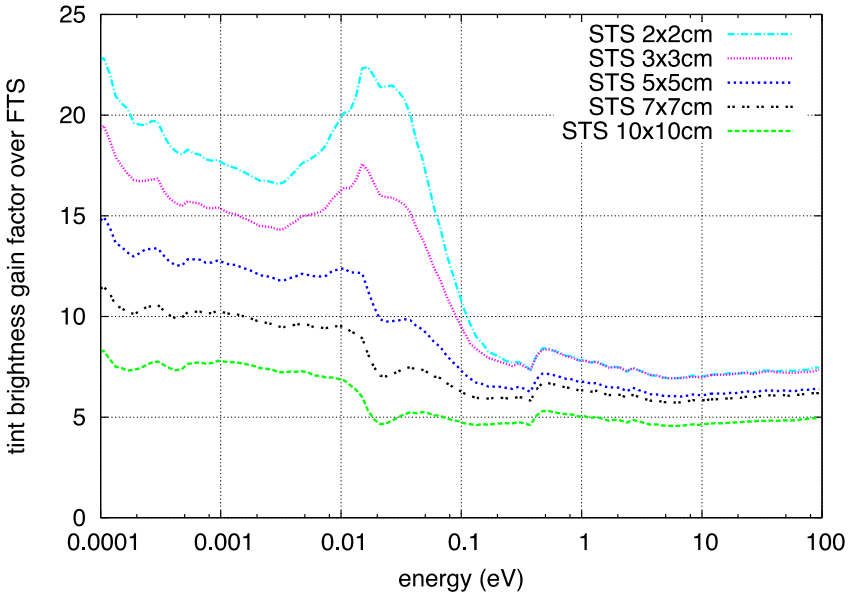

Figure 2. Pulse-integrated brightness gains over the FTS coupled moderator based on equal-energy pulses.

In a similar way, decoupled para-hydrogen moderator studies were conducted. The studied decoupled moderators were box-type moderator volumes, viewed from two opposite sides, centrally poisoned by gadolinium and decoupled from the beryllium reflector by cadmium layers around the not-viewed aluminum vessel walls and the square-sized neutron extraction ports. The optimization tuned the moderator dimensions, proton beam height at fixed proton beam area of 30 cm^2, and the moderator position with regard to the target nose. As the FOM, we used the neutron intensity below 10 meV energy within a pulse time window of energy-dependent width equivalent to the emission time FWHM value of the pulse of the FTS decoupled hydrogen moderator [8] and penalized by the neutron intensity outside of the time-window. Better-converged calculations were performed for the optimized configurations for each setting of viewed area. The moderator depths of 4.4 cm thickness obtained from the optimizations for all viewed area settings produced FWHM pulse widths that were somewhat narrower than that of the FTS moderator. For this reason the moderator thickness was increased to 5 cm for the production calculations, which arrived at better FWHM matches. The gains of peak brightness over the FTS decoupled hydrogen moderator [8] are shown in figure 3. Gains of a factor of 2.6 are obtained for cold neutrons for the STS moderator with 10x10 cm^2 viewed area. It seems that the overall smaller decoupled moderators benefit more from the small-footprint target and proton beam. The gains grow to a factor of 5 for the small STS version with 2x2 cm^2 viewed area, hence by almost a factor of 2 over the STS 10x10 cm^2 configuration.

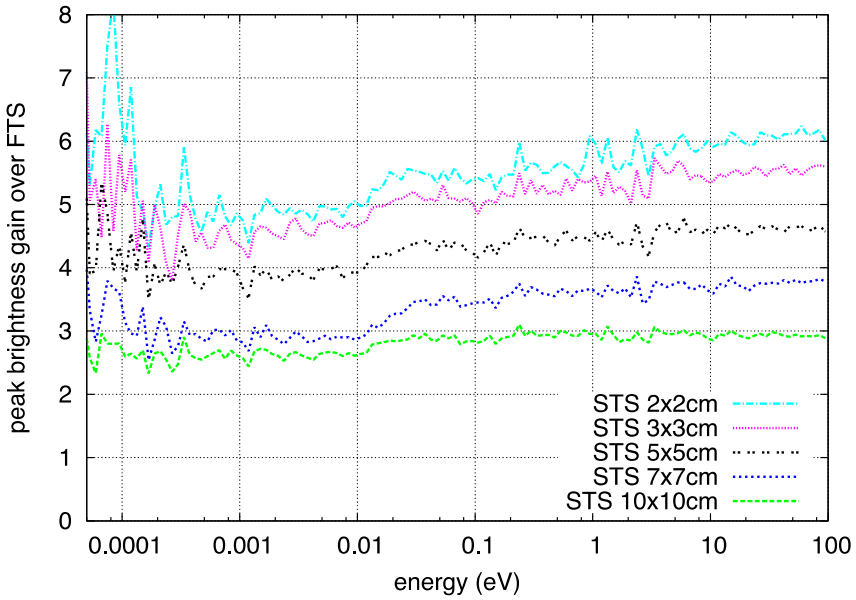

Figure 3. Peak brightness gain factors over the FTS decoupled moderator based on equal power pulses.

4. Matching STS Instrument Needs to Moderators

These model simulations described in section 3 indicate that significant gains of neutron performance are to be had at STS over FTS. In parallel to these studies, an STS candidate instrument suite of 19 instruments was developed. The instrument developers requested the preferred type of moderator (coupled/decoupled), neutron spectrum (cold/thermal) and the viewed area size as summarized in Table 1. As only three to four moderators can be realized at a target station, choices of moderators and moderator characteristics have to be made. From Table 1 we conclude that the moderator with highest request is a coupled cold moderator with viewed area of 3x3 cm^2. Configuring the cylindrical para-hydrogen moderator with two viewed ports of 3x3 cm^2 and one port with 3x6 cm^2 (height x width), we still can maintain the flat moderator design and serve 11 instruments. In addition a larger–area coupled cold moderator is requested and essential to two instruments, which requires a second cold coupled moderator. Decoupled moderators of various sizes and with thermal and cold characteristics that are best met by a back-to-back para-hydrogen/ambient water decoupled moderator of viewed areas of 7x7 cm^2.

Table 1. Moderator characteristics as requested by the proposed STS instrument suite.

Moderator type	View port size (cm)	Requested	Assigned
Cold coupled	10x10	1	0
Cold coupled	5x5	4	3
Cold coupled	3x3	7	7
Cold coupled	3x6	0	2
Cold decoupled	7x7	3	4
Cold decoupled	5x5	1	0
Thermal-cold decoupled	7x7	2	3
Thermal-cold decoupled	3x3	1	0

5. First Try STS Moderator Suite

A first effort was undertaken to cast the thoughts of the previous chapter into a moderator suite for a technical design report (TDR). In this design depicted in figure 4 the target structure was refined by a 19 tungsten plate structure, which resulted from thermal heat removal considerations. The cylindrical para-hydrogen moderator was placed at the bottom of the target (B), a box-type coupled para-hydrogen moderator at the top upstream position (TU) with 5x5 cm^2 viewed area, and a decoupled moderator unit consisting of ambient water and decoupled para-hydrogen moderators at the top downstream position (TD) each with 7x7 cm^2 viewed area. To arrive at optimal positions and dimensions, the bottom moderator was optimized first, followed by the coupled cold moderator in the top-upstream position, both using the peak cold brightness FOM mentioned above. Before putting our attention to the decoupled moderator unit, the sensitivity of the performance of the TU moderator with regard to displacement in upstream direction was assessed with the finding that a 3 cm shift cost only 5% of performance reduction. After applying the TU moderator shift, the decoupled TD moderator unit was optimized using the decoupled moderator FOM tailored to the FTS decoupled cold hydrogen and ambient water moderators, respectively. Naturally the optimizer moved the moderator as close as possible to the prime neutron production zone without interfering with the TU moderator.

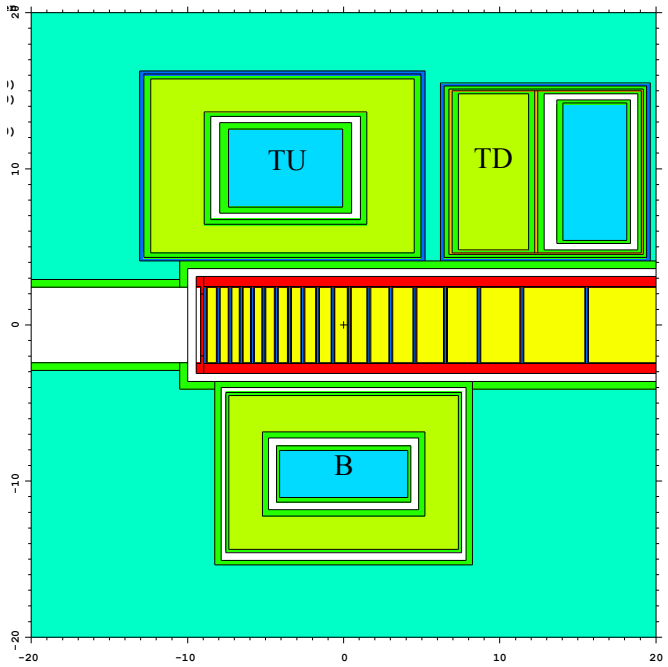

Figure 4. Arrangement of three moderators in wing configuration around the STS tungsten target.

Again a final analysis was undertaken to arrive at fully converged moderator performance data. Results of peak brightness spectra are shown in figures 5 and 6 for the coupled and decoupled moderators, respectively. We were pleased to see that the TDR moderator performance held up to the promises of the single-moderator studies. The cylindrical para-hydrogen moderator saw only a single digit percentage loss mainly by adding the detailing of the target structures including cooling channels. The TU cold coupled moderator with 5x5 cm^2 viewed area increased its peak brightness by 10% over the single moderator studies despite the 5% loss from shifting it upstream, mostly because its shape was converted from a cylindrical to a box-type moderator with tighter coupling to the pre-moderator. The decoupled para-hydrogen moderator suffered only a 25% loss over the single-moderator results.

6. Conclusions

Despite adopting conservative, but proven choices for the material and design of the target/moderator/reflector assembly, an attractive target/moderator/reflector configuration is found. Optimization of moderator and premoderator dimensions, and moderator positions with regard to the target result in a configuration with a small proton beam footprint and tightly coupled target moderator with promising STS moderator performance. Brightness increases of a factor of 2-3 by downsizing the moderator viewed areas from 10x10 cm^2 to 2x2 cm^2 were demonstrated both for coupled and decoupled moderators. Gain factors on peak brightness of a factor of 13 were shown for STS at 467 kW beam power at 10 Hz compared to FTS operated at 2 MW and 50 Hz for a 3 cm high para-hydrogen cylindrical moderator. The gain factors for the STS decoupled moderators are 3 and 4 for the cold and thermal moderators, respectively. In this round of analyses, the optimizations were driven by crude empirical quantities based on peak brightness metrics. Ultimately, we are striving to refine the optimization strategies to involve instrument specific metrics to arrive at moderators that perfectly tailored to the instruments' needs.

Acknowledgments

Research sponsored by the Laboratory Directed Research and Development Program of Oak Ridge National Laboratory, managed by UT-Battelle, LLC, for the U. S. Department of Energy. Work performed at Oak Ridge National Laboratory is managed by UT-Battelle, LLC, under contract DE-AC05-00OR22725 for the U.S. Department of Energy.

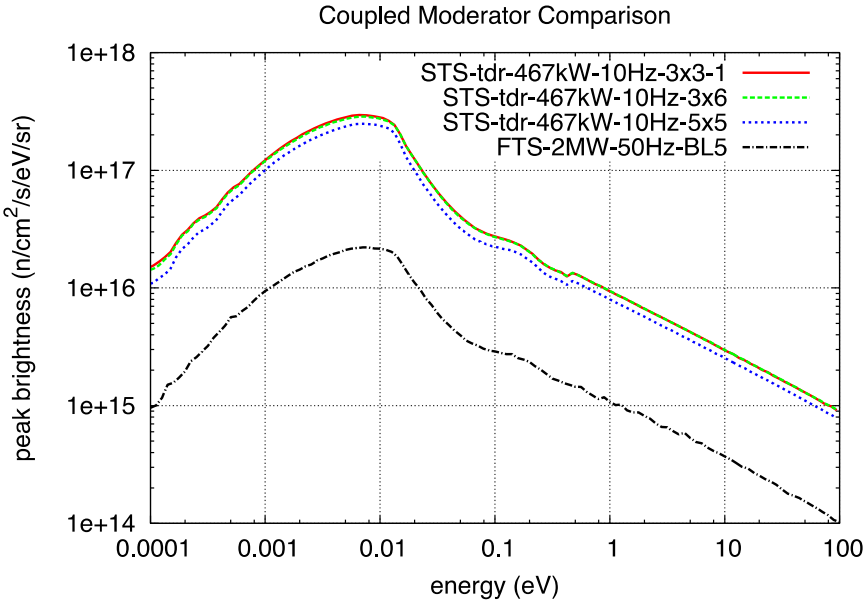

Figure 5. STS-TDR peak brightness of the coupled cold moderators compared to the FTS cold moderators.

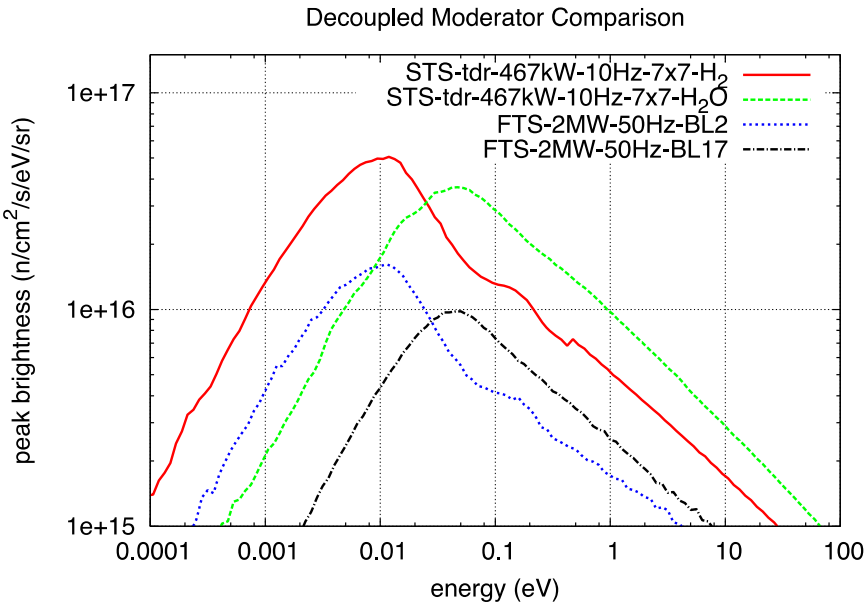

Figure 6. STS-TDR peak brightness of the decoupled cold and thermal moderators compared to the FTS moderators and compared to an optimized single STS para-hydrogen moderator.

References

[1] Technical Design Report – Second Target Station, ORNL/TM-2015/24, Oak Ridge National Laboratory, Oak Ridge, Tennessee, USA (January 2015).

[2] F. X. Gallmeier et al, "SNS Second Target Station Moderator Performance Update" 19th meeting on Collaboration of Advanced Neutron Sources, March 8 – 12, 2010, Grindelwald, Switzerland.

[3] Documentation for the ISIS Second Target Station Project, http://ts-2.isis.rl.ac.uk/.

[4] J. M. Carpenter and W. B. Yelon, "Neutron Sources," Chapter 2 in *Methods of Experimental Physics*, editors-in-chief R. Celotta and J. Levine, Volume 23 Part A, *Neutron Scattering*, editors K. Sköld and D. L. Price, Academic Press, Inc. (1986).

[5] N. Watanabe and Y. Kiyanagi, Towards a high-efficiency pulsed spallation neutron source, Physica B 189&181 (1992), pp 893-895.

[6] Zhao, J.K., Robertson, J.L., Herwig, K.W., Gallmeier, F.X. and Riemer, B.W., Optimizing moderator dimensions for neutron scattering at the spallation neutron source, Review of Scientific Instruments Vol. 84(12), pp. 125104 (2013).

[7] J.M. Carpenter and D.F.R. Mildner, Neutron Guide Tube Gain for a Remote Finite Source, Nucl. Inst. Meth. 196 91982), pp 341-348.

[8] Lu, W. et al., Improved Moderator Performance Calculations at SNS, Proceedings of the Tenth International Meeting on Nuclear Applications of Accelerators-AccApp'11, pp. 203 (2012).

[9] J.K. Zhao et al., The extended Q-range small-angle neutron scattering diffractometer at the SNS, J. Appl. Cryst. (2010). 43, pp. 1068–1077.

[10] Ohl M., Monkenbusch M., Arend N., Kozielewski T., Vehres G., Tiemann C., Butzek M., Soltner H., Giesen U., Achten R., Lindenau B., Budwig A., Kleines H., Drochnerd M., Kaemmerling P., Wagener M., Moller R., Iverson E.B., Sharp M., Richter D., The spin-echo spectrometer at the Spallation Neutron Source, SNS, *Nucl. Inst. and Meth A*, **696**, 85-99, (2012).

[11] K. Batkov et al., Unperturbed moderator brightness in pulsed neutron sources, Nucl. Instr. Meth. A 729 (2013), pp 500-505.

[12] D. P. Pellowitz, MCNPX Version 2.6.0 User's Manual, LA-CP-07-1473, Los Alamos National Laboratory, April 2008.
[13] F. X. Gallmeier, "Moderator studies for a SNS short-pulse second target station," SNS Document: STS04-41-TR0001-R00, Oak Ridge, TN, USA, 2013.
[14] F. X. Gallmeier et al, Moderator Studies for a SNS Short-pulse Second Target Station, in preparation.
[15] T. Kai et al., Neutronic performance of rectangular and cylindrical coupled hydrogen moderators in wide-angle beam extractionoflow-energyneutrons, Nucl. Inst. Meth. A 550 (2005), pp. 329-342.

3.2.11

Moderator Configuration Options for ESS

Luca Zanini[1], Konstantin Batkov[1], Esben Klinkby[1,2], Ferenc Mezei[1], Eric Pitcher[1], Troels Schönfeldt[1,2] and Alan Takibayev[1]

1) European Spallation Source ESS AB, Box 176, S-221 00 Lund, Sweden
2) DTU Nutech, Technical University of Denmark, DTU Risø Campus, Frederiksborgvej 399, DK-4000 Roskilde, Denmark

E-mail: luca.zanini@esss.se

Abstract. The current, still evolving status of the design and the optimization work for the moderator configuration for the European Spallation Source is described. The moderator design has been strongly driven by the low-dimensional moderator concept recently proposed for use in spallation neutron sources or reactors. Quasi-two dimensional, disc- or tube-shaped moderators, can provide strong brightness increase (factor of 3 or more) with respect to volume para-H_2 moderators, which constitute the reference, state-of-the-art technology for high-intensity coupled moderators. In the design process other, more conventional, principles were also considered, such as the importance of moderator positioning, of the premoderator, and beam extraction considerations.

Different design and configuration options are evaluated and compared with the reference volume moderator configuration described in the ESS Technical Design Report.

1. Introduction

The European Spallation Source (ESS), which entered the construction phase in 2013 in Lund, Sweden, aims at starting operations and delivering the first neutrons in 2019 [1]. At 5 MW time-average power, and 125 MW peak power (to be achieved by 2022), ESS will be the most powerful neutron source in the world for neutron scattering studies of condensed matter. Neutrons will be produced by a 2 GeV proton beam impinging on a target made of tungsten. ESS will be the first high-power long pulse source [2], the pulse length of the beam will be of 2.86 ms, with 14 Hz repetition rate.

A key for a highly performing neutron source is the optimisation of the configuration of the target, moderator and reflector assembly [3]. The use of tungsten as spallation material will ensure a high neutron yield per incoming proton; the high density of tungsten favours the production of neutrons in a small volume, increasing the probability that neutrons will eventually be slowed down by the moderators placed next to the target. The presence of a reflector surrounding the moderators is essential to increase the slow-neutron intensity from the moderators. For a long pulse facility such as ESS, the recommended cold moderator type is a coupled, pure para-H_2 moderator [4], because it delivers the highest brightness per proton. The coupling between moderator and reflector (i.e. the absence of any neutron absorbing material to shape the pulse length) guarantees the highest peak flux from the moderator surface; pulses are shaped in time by choppers placed in the beam lines.

An extensive effort from the ESS neutronic team has been carried out to design high-brightness moderators; the current, still evolving status of the work is described in this paper.

2. The baseline of the Technical Design Report

In April 2013 the ESS Technical Design Report (TDR) was issued[1]. The TDR design was based on the best available state-of-the-art technology, which for high intensity moderators is the J-PARC coupled volume para-H_2 moderator [4]. In the TDR baseline configuration [1], there are two volume moderators filled with pure para-H_2. The MCNPX model shown in Fig. 1 reproduces the engineering design developed during the target station design update phase. The moderators have a diameter of 16 cm and a height of 13 cm, see Fig. 1. The moderators are surrounded by light water premoderators (except for the cold neutron extraction window), of which the most important part, from the neutronic point of view, is the layer between target and moderator, which is 2 cm thick. The window surface on the cold moderators for beam extraction is of 12 × 12 cm^2. On the sides of the cold moderators, thermal moderators are placed for bispectral beam extraction. The openings in the reflector for beam extraction are of 60°, with two openings per moderator, as shown in the figure. More information is available in Ref. [5].

The absolute brightness was calculated at a distance of 10 m from the moderators, using collimators to view only the moderator surfaces. The calculated peak cold brightness is a factor of 75 larger that in ILL yellow book [6] at 4 Å, a factor of 60 larger at 6 Å, and a factor of 65 larger at 10 Å.

This paper describes the work carried out after the TDR was issued, in an attempt to improve the neutronic performance of the ESS moderators beyond best established practice.

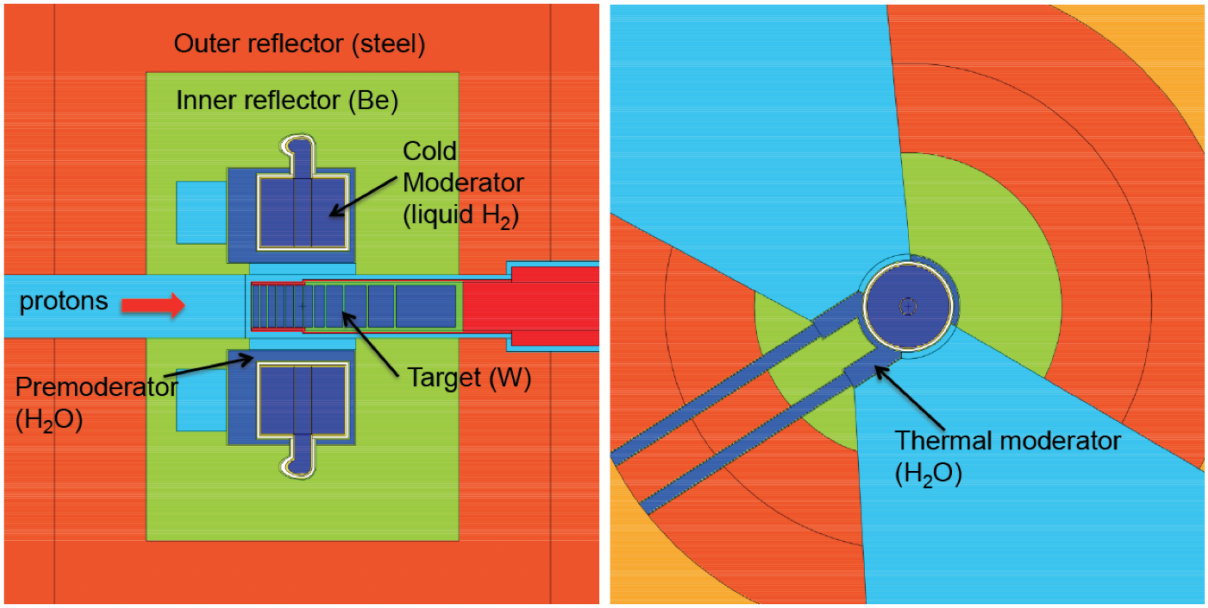

Figure 1. MCNPX[7, 8] geometry of the reference TDR moderator configuration.

3. Low-dimensional moderators

Much of the work was based on the concept of low-dimensional moderators for increased brightness, which are explained in details in Refs.[9, 10]. The basic principles of low-dimensional moderators is explained by the single-collision model [10]: the mean free path of thermal neutrons in para-H_2 is of about 1 cm, while is of about 11 cm for cold neutrons. Assuming that one collision only is needed to bring a thermal neutron to the cold regime, it is shown that the

moderator brigthness is increased for quasi two dimensional (flat) or quasi one-dimensional (tube) moderators. The brightness distribution map in the moderator face is shown in Fig. 2 for a 10 cm and a 1.5 cm tall moderator, showing the presence of regions of higher brightness in the tall moderator, while a flat moderator essentially has a single hot spot of neutron emission. In order to work, it is required that the moderators are filled with close to pure para-H_2; this can be achieved in high-power facilities by use of catalyzers.

The resulting brightness as a function of moderator height is shown in Fig. 3. Note that brigthness increase corresponds to a decrease in total neutron emission (red curve) as well as of the total heat load in the moderator. Therefore a high intensity moderator is not the brightest one; however, it is worth noting that, for the cylindrical shape used for the calculations in Fig. 3, already for 3 cm thickness the total neutron emission is about 80 % of the maximum reached at 10 cm.

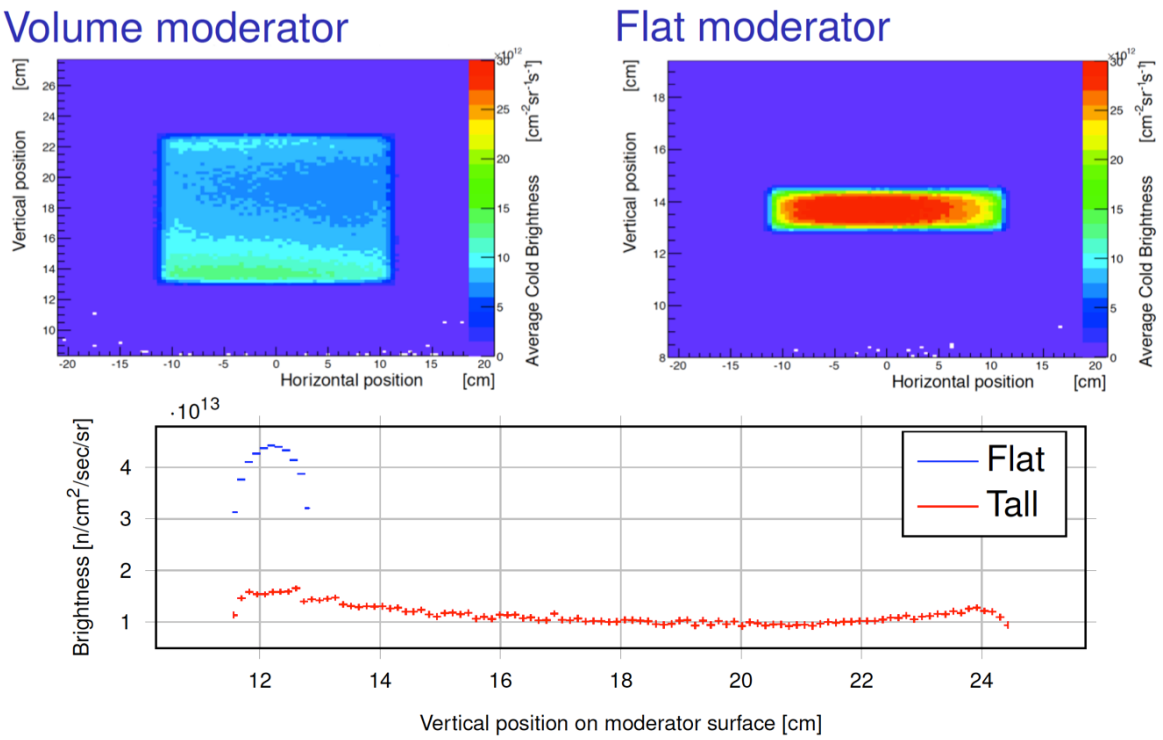

Figure 2. *Top:* Calculated brightness map from volume moderator (left) and flat moderator (right). *Bottom:* Brightness distribution along the moderator height for volume and flat moderator.

3.1. Other design principles

- Perturbation effect: in addition to the moderator shape effects, a brigthness increase is observed in low-dimensional moderators by the simple fact that being more compact, less reflector materials is removed around the moderators for beam extraction.
- Premoderator: the importance of the premoderator is well established and premoderators are widely used for cold neutron sources. The premoderator gives a spectral shaping, bringing neutron energies down from 1 MeV range to thermal. We have found that this

plays a crucial role not only for the cold moderator, but also for the thermal one (in which case the thermal moderator can be considered more as a scatterer than a moderator). As a result, we found that an extended premoderator, with dimensions practically equal to the Be reflector, and thickness of about 3 cm, gives a substantial gain in both thermal and cold moderator brightness.

- Position optimization: even though in a coupled moderator many of the neutrons reaching the moderator have been scattered by the inner reflector, we found that the positioning of the moderators close to the neutron production hotspot is quite important for brightness optimization. Additionally, it may be advantageous to place the thermal moderator above the target hotspot, rather than the cold moderator, because the thermal moderator is more compact, making it possible to place both thermal and cold moderators very close to the hotspot.
- Extraction optimization: a single moderator will not necessarily be able to serve the whole ESS instrument suite. However, we have found that in some cases this is possible; this is the case for the 3 cm pancake; if two moderators are installed, the ability to serve all the instruments by one or the other moderator is an advantage for maximum availability/flexibility.

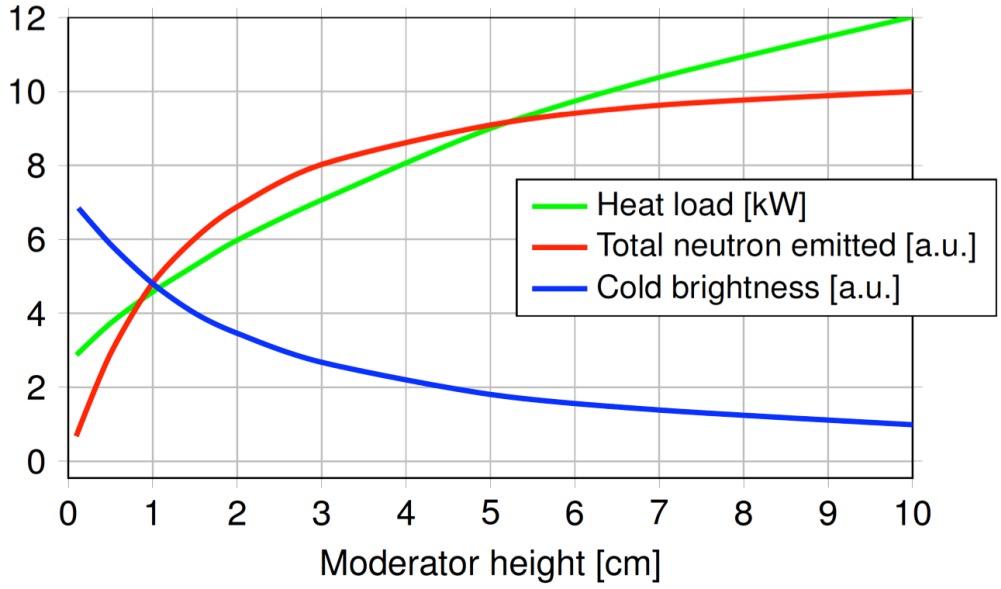

Figure 3. The integral cold brightness ($0 < E < 20$ meV) increases with decreasing height of the flat moderator (blue curve). On the contrary, the total number of emitted neutrons (brightness multiplied by the viewed area of the emitting surface) increases (red curve) with increasing moderator height, as well as the heat load (green curve).

4. The pancake moderator

The pancake design makes use of most of the concepts and findings described above. The resulting model is shown in Figure 4. The important features of this design are the following:

- 3 cm tall, 20 cm diameter cylindrical vessel containing pure para-H_2; the viewed surface can be up to 3 cm (Height) × 20 cm (Width), even though usually neutrons are extracted from a window 3 cm (H) × 6 cm (W). The choice of the diameter is considered a good balance between cold and thermal brightness, in the sense that it gives near maximum cold performance, while allowing a higher thermal brightness since the water wings are moved a bit closer to the neutron hotspot (Fig. 5).
- Neutron extraction for 2 × 120° angular openings.
- Water wings on the side of the cold moderator, for thermal neutron extraction. The viewed surface can be up to 3 cm (H) × 12 cm (W), or even more, even though usually neutrons are extracted from a window 3 cm (H) × 6 cm (W) or smaller.
- Extended premoderator between target and cold and thermal moderators, making use of findings described in section 5, for increased thermal brightness, with the additional advantage of reduction of the amount of Be close to the target.

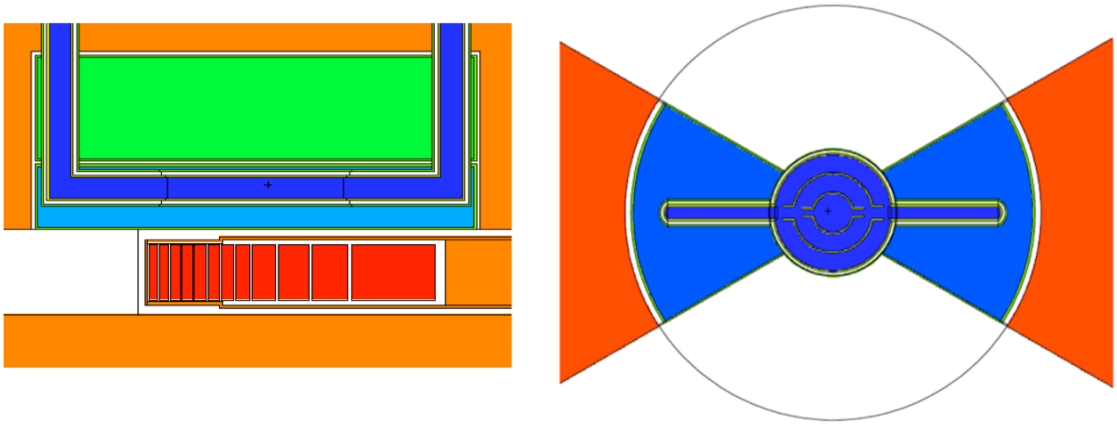

Figure 4. Reference geometry for the pancake configuration. See explanation in the text.

The pancake moderator is designed for increased cold brightness. The cold brightness is on average a factor of 2.4 the brightness delivered by the TDR moderators. For extraction of thermal neutrons, the thermal brightness is a factor of 1.5 the TDR. Thermal neutrons are extracted from the sides of the cold moderator. The thermal brightness can be increased by bringing the water closer to the neutron hotspot, but this can be obtained only at the expense of reduced cold brightness.

5. The second moderator

The pancake moderator brings not only an increased performance with respect to the TDR design, mainly in the cold brightness, and partially also in the thermal brightness, but also the fact that a flat moderator can serve the whole ESS instrument suite covering 2 × 120° beam extraction sector. This gives the opportunity to use the slot for the second moderator (the bottom moderator) to add flexibility to the facility. In other words, a second moderator can be used to supplement top pancake with either: *i*) a larger emission surface, resulting in a high intensity moderator, or *ii*) a moderator with a different overall wavelength spectrum, i.e.

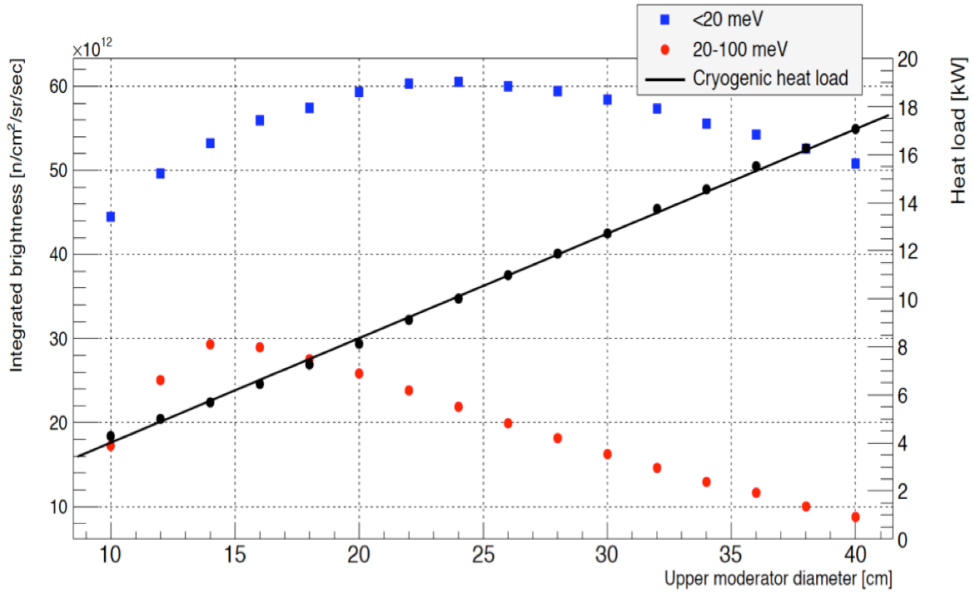

Figure 5. Integrated cold and thermal brightness for a pancake moderator, and heat load on the cryogenic parts (structure and hydrogen), as a function of the moderator diameter. The model (see Fig. (4)) includes some structure and pipes.

with increased thermal brightness with respect to the cold brightness, or *iii*) a combination of both things. The increased emission surface was discussed thoroughly. Essentially the gain in intensity with the moderator height is a balance between reduced brightness and increased area, and is seen in Figure 3; calculations for a 6 cm tall cold moderator were performed; its brightness is reduced with respect to the 3 cm pancake by about a factor of 1.5. Effort was particularly focussed on designing a moderator that would improve the thermal component of the spectrum.

6. The Optimized Thermal (OT) moderator

For maximum performance, the moderator should be placed near the hot spot of neutron production in the spallation target. In tungsten, because of its high-density, this is an area extended only a few cm starting about 10 cm from the target edge. The effect is mitigated by the presence of the Be reflector, however it is significant: the effect on vertical placement was calculated to be of about 3%/cm, while for horizontal placement is of about 1-2%/cm.

The thermal brightness can be improved if a moderator is specifically designed to improve this part of the spectrum. It was found that brightness of the thermal moderator increases if a water layer, approximately 3 cm thick, is placed between target and moderator, in a similar way to what happens to the top pancake (Fig. 6). The combination of optimal placement of the moderator with respect to the neutron production hot spot, and of the presence of this water layer, is found to give an increase up to a factor of 1.7 with respect to the brightness of the top pancake, for the same moderator height. The cold moderator next to the water moderator, shown in Fig. 6 is similar to a tube moderator and will provide high cold brightness; however it is highly directional and its brightness will decrease with the angle of beam extraction with respect to the tube axis.

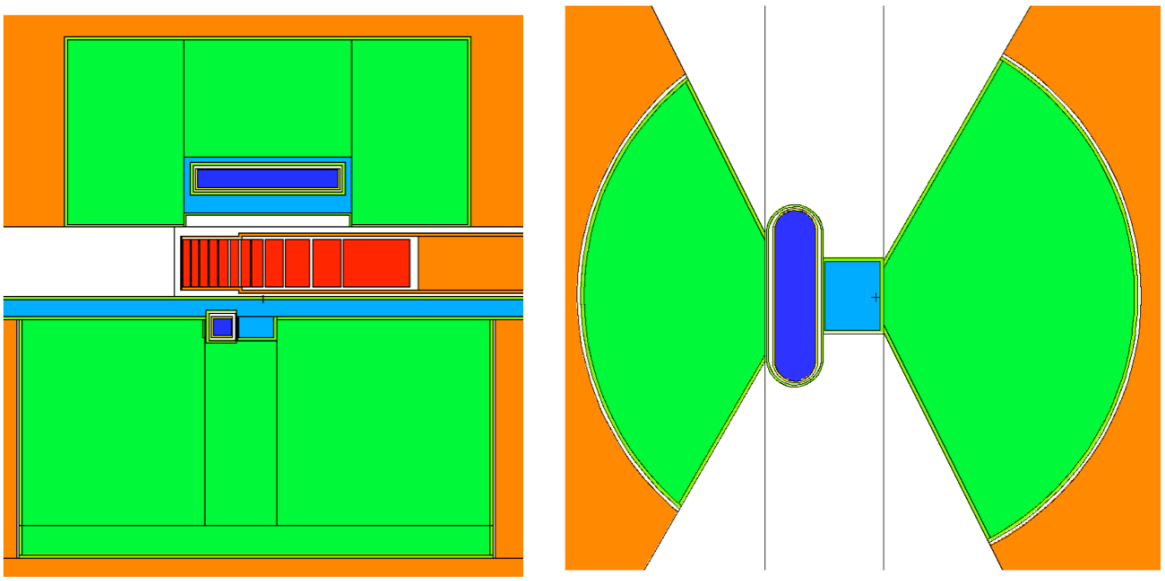

Figure 6. Geometry with a pancake 3 cm top moderator, and an optimized thermal moderator (3 cm tall) on bottom. *Left*: side view showing the 3 cm water layer between target and moderators. *Right*: top view showing the thermal moderator (light blue) and the cold moderator (dark blue), surrounded by the beryllium reflector (green).

7. Results and next steps

In Fig. 7 calculated wavelength spectra for the TDR, pancake and OT moderators are shown. Flat moderators offer a clear brightness increase with respect to the original TDR design based on volume moderators. Cylindrical pancake moderators are excellent cold moderators with a brightness about 2.5 times higher than the TDR moderators. The increase in thermal brightness is however limited, only a factor of 1.5: the thermal brightness remains the weak part of this moderator configuration. It is important to note that the TDR design suffers also from this drawback, as the peak thermal brightness is only a factor of 7 higher than the ILL yellow book, as opposed to the cold brightness which is 60 to 75 times higher than the yellow book. In an attempt to increase the thermal brightness we have developed the Optimized Thermal design. The OT is capable of delivering a thermal brightness higher than the pancake for a bigger emission surface. This increase is due to both optimal positioning of the water moderator (close to the neutron production hotspot) and to the optimal use of the extended premoderator (3 cm water layer between target and moderator). In order to deliver a good cold brightness, the OT has a cold tube moderator of its side. The resulting thermal-cold performance is enhanced (there is also come increase in cold brightness compared to the pancake). However, it is limited to a sector of about 60°, because of the strong directionality of the cold moderator, which means that this optimized thermal moderator must be used in conjunction with a top moderator.

The combination of a top pancake and an OT at the bottom, is a valid possibility for ESS. However, other possibilities are currently under consideration, and different designs are on the table exploting the design approach developed in the last two years and discussed in this paper.

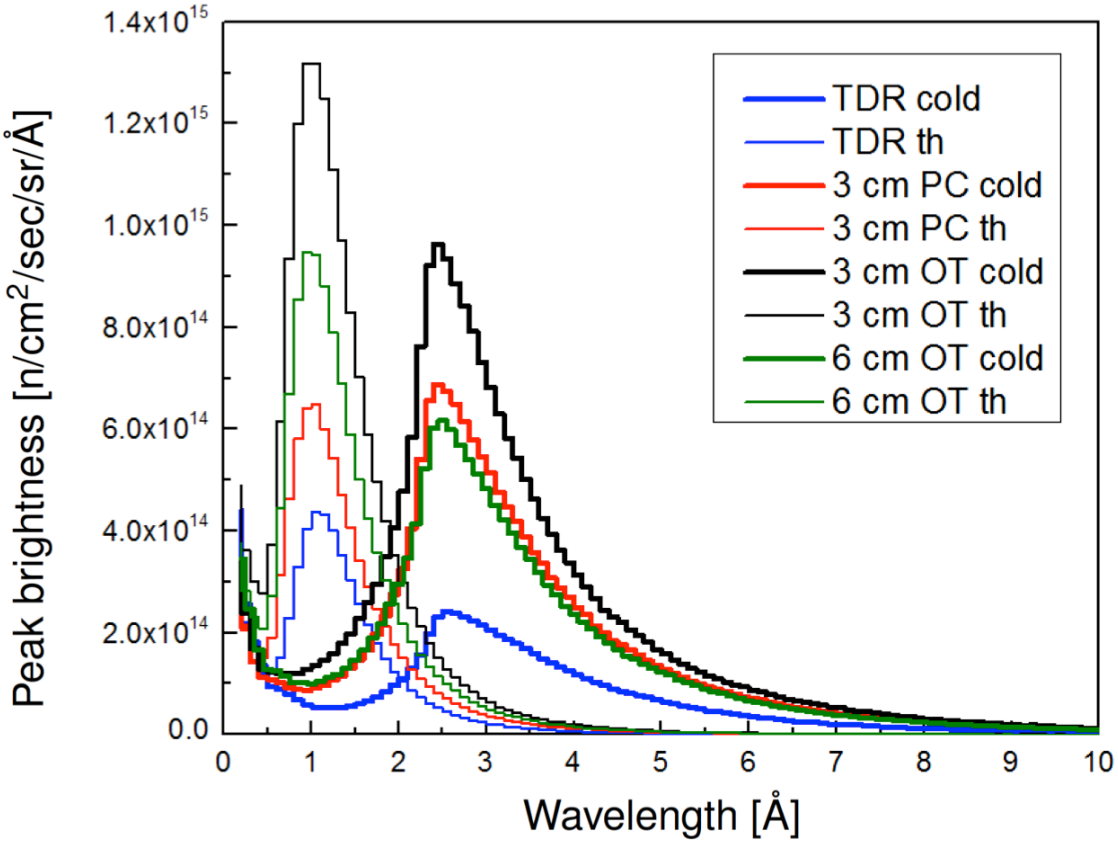

Figure 7. Calculated wavelength spectra from TDR, pancake (PC) and Optimized Thermal (OT) configurations. See explanation in the text.

Acknowledgments

The authors acknowledge Ken Andersen (ESS) for suggesting the study of a second moderator optimized for thermal neutron brightness.

References

[1] ESS Technical Design Report, S. Peggs editor, ISBN 978-91-980173-2-8, 2013, http://europeanspallationsource.se/scientific-technological-documentation
[2] F. Mezei, Long pulse spallation sources, Physica B 234-236 (1997) 1227.
[3] N. Watanabe, Neutronics of pulsed spallation neutron source, Rep. Prog. Phys. 66 (2003) 339381, and references therein.
[4] T. Kai, M. Harada, M. Teshigawara, N. Watanabe, Y. Ikeda, Nuclear Instrum. Methods A 523 (2004) 398.
[5] M. Magán et al., Neutronic analysis of the bi-spectral moderator such as that proposed for ESS Nucl. Instrum. Methods A729 (2013) 417425.
[6] Institut Laue-Langevin. 'ILL Yellow Book 2008.' http://www.ill.eu/?id=1379 , 2008.
[7] Waters L. S. et al. 2007. The MCNPX Monte Carlo radiation transport code. *AIP Conf.Proc.* **896**, 81-90.
[8] X-5 Monte Carlo Team 1987, MCNP – A General Monte Carlo N-Particle Transport Code, Version 5, *LA-UR-03-1987*.
[9] K. Batkov, A. Takibayev, L. Zanini and F. Mezei, Unperturbed moderator brightness in pulsed neutron sources, Nucl. Instrum. Methods, A729 (2013) 500.
[10] F. Mezei et al., Low dimensional neutron moderators for enhanced source brightness, Journal of Neutron Research 17 (2014) 101105 101.

3.2.12

A model for non-thermalized neutron spectra emitted from para-hydrogen

T. Schönfeldt[1,2], K. Batkov[2], E. B. Klinkby[1,2], B. Lauritzen[1], F. Mezei[2], A. Takibayev[2], P. K. Willendrup[3] ,L. Zanini[2]

1: Center for Nuclear Technologies, Technical University of Denmark, Roskilde, Denmark
2: European Spallation Source, Lund, Sweden
3: Department of Physics, Technical University of Denmark, Lyngby, Denmark

Abstract. At spallation and reactor cold neutron sources, neutrons are cooled by moderators. At high power neutron sources, such as the Japan Proton Accelerator Research Complex (J-PARC), European Spallation Source (ESS) and the Spallation Neutron Source (SNS) only few moderator materials are practical, due to the high radiation environment near the moderator and cooling demands. One of the very popular materials, used at J-PARC and planed for ESS, is the spin singlet state of H_2, para-hydrogen. This study assesses the non-Maxwellian neutron spectral structure achieved in para-hydrogen moderators, which is due to the complexity of the inelastic scattering cross section below 50 meV. The analytical description of a thermalized spectrum with slowing down components are discussed, then a formula is developed which is a good description of this non-equilibrium para-hydrogen neutron spectrum.

These analytical descriptions are fitted to the thermal and cold neutron spectra expected at the European Spallation Source according to the baseline configuration, as described in the Technical Design Report (TDR). The results of the fits have been implemented in McStas 2.0 and is used throughout the ESS instrumentation community. Though not shown here it is worth noting that the spectra for different heights of moderators in the more recent ESS geometry have also been fitted to this para-hydrogen spectrum model, the fits have been implemented and released in McStas 2.1.

1. Introduction

According to the TDR (see [1]) the European Spallation Source (ESS) will produce neutrons by spallation, driven by a 5 MW, 2.5 GeV proton beam impacting on a massive rotating tungsten target wheel. The target will be surrounded by a moderator reflector system, where the neutrons will be thermalized in an ambient temperature light water moderator and cooled further in a 20 K cylinder of liquid para-hydrogen. The moderators will be surrounded by an inner reflector made from beryllium, which in turn is surrounded by an outer reflector made of steel, as shown in Figure 1.

Neutron production and moderation is simulated via the Monte Carlo method using MCNPX [2]. From these simulations it is possible to predict the expected brightness spectrum, as shown in Figure 2.

The spectral brightnesses from the cold and thermal moderators are plotted in Figure 2. The figure also shows the overall brightness expectation from bispectral extraction, which is calculated from the cold and thermal spectrum respectively taking into account expected transmission and reflection factors [3].

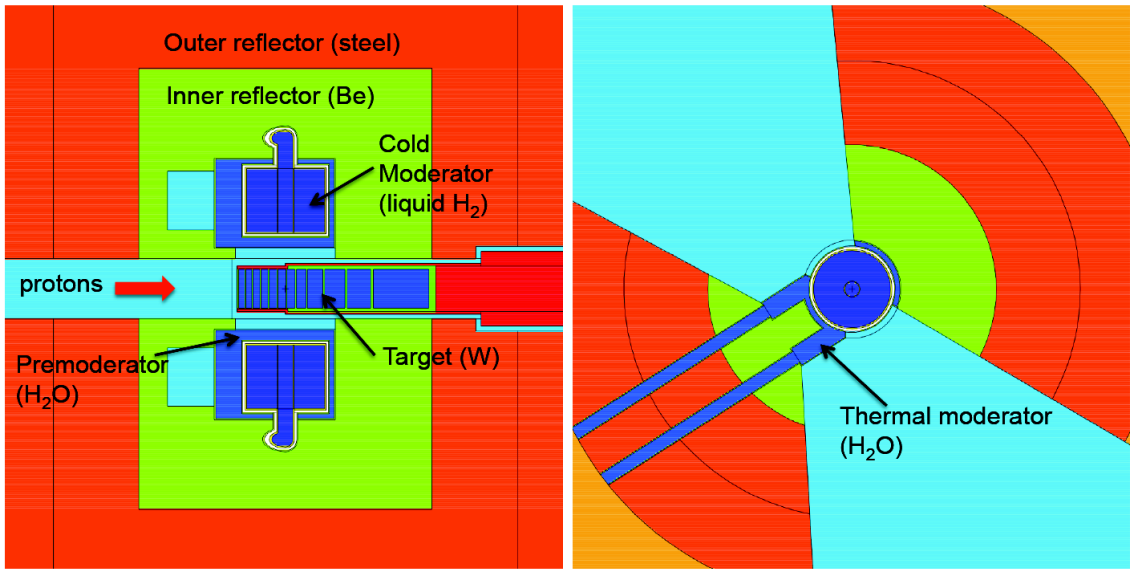

Figure 1: Target-Moderator-Reflector system, the TDR MCNPX model [1].

Supercritical para-hydrogen is a favourite material for high cold neutron brightness at high power sources. However, as the para-hydrogen cross section drops off with two orders of magnitude around 15 meV neutrons are emitted prior to thermalizing. Due to this complexity of the inelastic scattering cross section below 15 meV the resulting spectrum cannot be described by a simple Maxwellian distribution.

The goal of this study is to provide a model for the cold spectrum from the para-hydrogen moderator; additionally, an analytical description of the thermal and slowing down components of an ordinary neutron spectrum will be discussed. In this study these analytical descriptions will be fitted to the simulated spectrum from the ESS baseline design [1], while in [4] the same function have, with great success, been fitted to the expected cold brightness from different heights of flat moderators [5].

2. Model

In this section analytical expression describing the wavelength distribution of the thermal and cold ESS neutron spectrum will be constructed from parts. In the end these constructed functions will be fitted to the wavelength spectrum obtained from simulations.

2.1. Slowing down

As neutrons are slowing down, at wavelengths (λ) below the thermal energy of the medium ($\lambda < 0.5$ Å) some of them will be emitted from the moderator. In this region the distribution is expected to fall off inversely proportional to the wavelength.

This is understood by looking at the flux as a function of lethargy, $\phi(u)$ ($u \propto \log(\frac{1}{E}) \propto \log \lambda^2$), which is well known to be a flat distribution at epithermal energies. From this one can easily derive the flux as a function of wavelength: $\phi(\lambda) = \phi(u- > \lambda)\frac{du}{d\lambda} = k\frac{du}{d\lambda} \propto \frac{1}{\lambda}$. As brightness is proportional to the flux it follows that the epithermal brightness is also proportional to $\frac{1}{\lambda}$.

When the neutron energy approaches the energy of the medium, the $\frac{1}{\lambda}$ term should disappear. Historically $(1+e^{\alpha(\lambda-\lambda_{cf})})^{-1}$ has been used, where λ_{cf} and α are the parameters controlling the position and rate of the cut-off. By introducing an intensity parameter I_{SD} one can write the

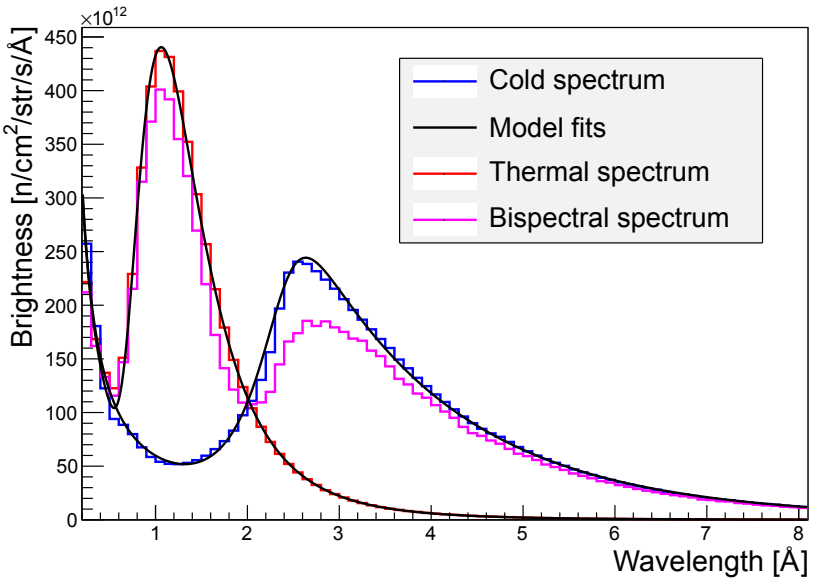

Figure 2: Expected peak brightness for cold, thermal and bi-spectral extraction, for the ESS, baseline configuration [1]. The peak brightness is calculated for the operational parameters described in the TDR: 2.5 GeV proton kinetic energy, average macro-pulse current of 50 mA, macro-pulse length of 2.857 ms, corresponding to a peak power of 125 MW and energy per pulse of 357 kJ.

full slowing down function SD as a function of wavelength:

$$SD(\lambda) = I_{SD}\frac{1}{\lambda}\frac{1}{1+e^{\alpha(\lambda-\lambda_{cf})}} \tag{1}$$

2.2. Thermalization

At low energy the neutrons will begin to equilibrate around the thermal energy of the moderating medium and the thermal spectrum can be described by a Maxwellian (M):

$$M(\lambda) = \frac{2k_{Th}^2}{T^2\lambda^5}e^{-\frac{k_{Th}}{T\lambda^2}} \tag{2}$$

Where $k_{Th} = \frac{2\pi^2\hbar^2}{m_n k_B} \approx 949$ KÅ^2 and T is the temperature. It is well known that at low energy the cross section increases with speed, hence it also increases with wavelength. As this increase is mainly due to absorption longer wavelength neutrons have lower probability of survival in a moderator, this results in a suppression of long wavelength neutrons. The most common approach is to increase the temperature parameter T of the model above that of the system. Another way of modelling this is by increasing the power of the wavelength, i.e. $\lambda^{-5} \rightarrow \lambda^{-(5+\chi)}$, where χ is often in the order of 0-1. However, in this study only the temperature increase was adopted while the later correction (the χ part) was neglected.

The full thermal moderator wavelength spectrum (S_{Th}) can now be assembled from the above pieces:

$$S_{Th}(\lambda) = I_{Th}\frac{2k_{Th}^2}{T^2\lambda^5}e^{-\frac{k_{Th}}{T\lambda^2}} + I_{SD}\frac{1}{\lambda}\frac{1}{1+e^{\alpha(\lambda-\lambda_{cf})}} \tag{3}$$

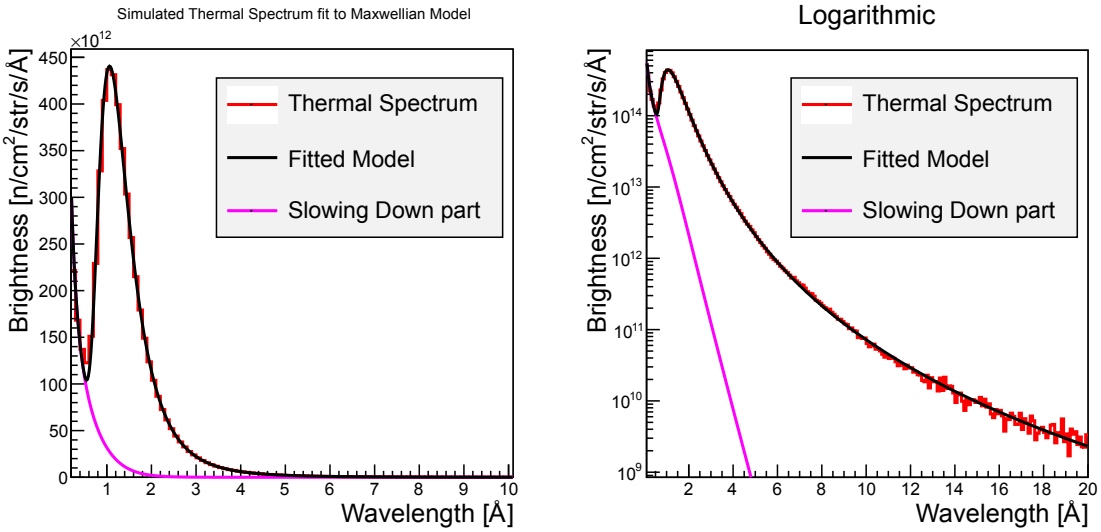

Figure 3: Expected ESS peak brightness from thermal moderator (linear left, logarithmic right), fitted to Eq. 3, parameters are shown in Table 1. The *SD* part is plotted in purple in the background.

where I_{Th} is the intensity of the thermal Maxwellian. This model (Eq. 3) have been fitted to the simulated brightness spectrum of the thermal moderator, shown in Figure 3. The obtained parameters are shown in Table 1.

Table 1: Parameters used in Figure 3; only I_{Th}, I_{SD} are fitted, the remaining parameters are fixed to the values obtained in an earlier study [6].

Parameter	Value
I_{Th}	4.35915×10^{14} cm^{-2}sr^{-1}s^{-1}
I_{SD}	7.48017×10^{13} cm^{-2}sr^{-1}s^{-1}
T	325 K
α	2.5 Å^{-1}
λ_{cf}	0.88 Å

2.3. Para-hydrogen

The cold moderator consists of 20 K pure para-hydrogen. The neutron scattering cross section drops off (with almost two orders of magnitude) near the excitation energy of the ortho (triplet) spin-state (para is the singlet state), around 15 meV. A s a result para-hydrogen becomes transparent (or translucent; cold neutrons mean free path is 10 cm to 15 cm, which is very long compared to the mean free path of a few mm for thermal neutrons) to neutrons with wavelengths longer than 2.32 Å. It should be noted that this happens before the neutrons are at thermal equilibrium (i.e. 15 meV corresponds to 174 K), hence the cold spectrum can not be described b y a Maxwellian. This is confirmed by looking at Figure 4, which amongst other things includes a fit o f a Maxwellian to the distribution. This transparency also results in a number of geometrical effects, some of which can be found in [7]. Due to this anisotropy it is worth mentioning that the spectrum fitted in this study is the neutron spectrum observed at the center of one of the four 60 ° extraction windows, directly in front of the cold para-hydrogen moderator.

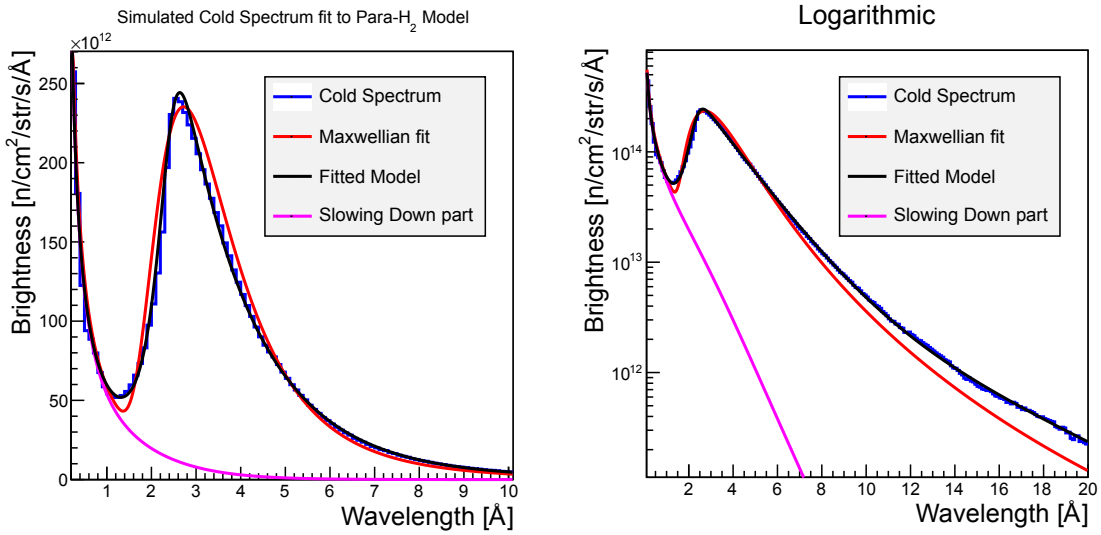

Figure 4: Expected ESS cold peak brightness (linear left, logarithmic right), fitted to Eq. 4 with parameters as shown in Table 2. The slowing down part is shown in purple and a Maxwellian fit is shown in red. Note that the Maxwellian description is inadequate both near the peak of the distribution (∼3 Å) and at long wavelengths ($\lambda > 7$ Å).

Thermal neutrons entering the cold para-hydrogen will very quickly (most often in a single scatter) be cooled below this 15 meV threshold energy and be transmitted from the moderator. This means that the spectrum from a para-hydrogen, at wavelengths above 2.3 Å will look like the spectrum of an inelastic down scatter, which on the tail can be fairly well described by an exponential.

But para-hydrogen is not fully transparent; in fact cold neutrons have 10 cm to 15 cm mean free path, which means that a few neutrons will re-scatter, even below the 15.2 meV limit. These neutrons mainly scatter on the intermolecular para-hydrogen spin state which has much lower scattering cross-section and a energy around 5 meV. These second scatters can be modelled by a second exponential with lower intensity and slower decay rate.

In summary, the tail of the para-hydrogen spectrum can be written as: $(I_1 e^{-\alpha_1 \lambda} + I_2 e^{-\alpha_2 \lambda})$, where I_1 and I_2 are intensities of the first and the second scatter respectively and α_1, α_2 are the decay rates of the primary and secondary scatter exponential respectively. Note that $I_1 >> I_2$ and $\alpha_1 >> \alpha_2$.

The two exponentials should only exist at energies larger than the transparency energy, around 15 meV, this can be described by a function growing from 0 to 1 fast enough, i.e. faster than the two exponentials fall off. A good description of this turns out to be: $(1 + e^{\alpha_l(\lambda - \lambda_l)})^{-\frac{1}{\gamma}}$, where γ and α_l governs the rate at which the transparency sets in and λ_l govern the position.

The full ESS para-hydrogen cold spectrum model (S_{cold}) becomes:

$$\begin{aligned} &S_{cold}(\lambda) = \\ &\frac{1}{(1 + e^{\alpha_l(\lambda - \lambda_l)})^{\frac{1}{\gamma}}} (I_1 e^{-\alpha_1 \lambda} + I_2 e^{-\alpha_2 \lambda}) \\ &+ I_{SD} \frac{1}{\lambda} \frac{1}{1 + e^{\alpha_{SD}(\lambda - \lambda_{SD})}} \end{aligned} \tag{4}$$

where I_{SD}, α_{SD} and λ_{SD} are the intensity, the cut off rate and cut off position of the slowing down function (similar to the one from the thermal spectrum). α_l and γ govern the rate and

Table 2: Parameters from the fit shown in Figure 4. Note that $\lambda_{SD}, \alpha_{SD}$ have been taken from [6].

Parameter	Value
I_{SD}	7.22356×10^{13} cm^{-2}s^{-1}sr^{-1}
α_{SD}	0.9 Å^{-1}
λ_{SD}	2.444 Å
α_l	-6.71404 Å^{-1}
λ_l	2.42099 Å
γ	2
I_1	1.2634×10^{15} cm^{-2}sr^{-1}s^{-1}Å^{-1}
α_1	0.617494 Å^{-1}
I_2	2.01876×10^{13} cm^{-2}sr^{-1}s^{-1}Å^{-1}
α_2	0.2237 Å^{-1}

structure of the region where the transparency sets in and λ_l relates to the position (λ_l should be in the order of 2.3 Å). Figure 4 shows a fit of Eq. 4 to the expected cold spectrum, which reveals the parameters shown in Table 2. Note that the fit uses $\gamma = 2$ corresponding to a square root, which is descriptive for a large bulk moderator as the one investigated in this study. However, further studies have shown that for more advanced moderator designs, e.g. the flat moderators described in [5], a square root is an inadequate description.

3. Conclusion

A fit of expected ESS baseline, thermal and cold, neutron spectra have been carried out. While the thermal spectrum fits nicely to a Maxwellian, it has been shown that the common Maxwellian description of the para-hydrogen neutron spectrum is inadequate. Therefore a new formula (Eq. 4) has been developed, which fits the simulated ESS para-hydrogen spectrum very accurately in the range from 0.01 Å to 20 Å. The results of the fits have been implemented in McStas 2.0 and is used throughout the ESS instrumentation community.

References

[1] S. Peggs, editor. *ESS Technical Design Report*. April 2013.
[2] L. S. Waters, G. W. McKinney, J. W. Durkee, M. L. Fensin, J. S. Hendricks et. al. The MCNPX Monte Carlo radiation transport code. *AIP Conf.Proc.*, 896:81, 2007.
[3] Mezei, F. Private communications, 2013.
[4] T. Schönfeldt et al. Phenomenological study of expected cold and thermal brightness phase-space at ESS. *In review, NIMa*, 2014.
[5] K. Batkov, A. Takibayev, L. Zanini and F. Mezei. Unperturbed moderator brightness in pulsed neutron sources. *Nucl. Inst. Meth.*, 729(0):500, 2013.
[6] Mezei, F. Internal report: Ess target - moderator performance estimates, 2010.
[7] T. Schönfeldt et. al. Optimization of cold neutron beam extraction at ESS. *AccApp Conf. Proc. (2013)*.

3.2.13

Neutronics modelling for the ISIS TS-1 upgrade

Goran Škoro and Stuart Ansell

ISIS Facility, Science and Technology Facilities Council, Rutherford Appleton Laboratory, Harwell Oxford, Didcot OX11 OQX, United Kingdom

E-mail: goran.skoro@stfc.ac.uk

Abstract. Following the successful validation of the current ISIS target station 1 (TS-1) neutronics model, the objective of this work is to re-assess the target, reflector and moderators (TRAM) assembly of the ISIS TS-1 to determine the possible improvements available by replacing these components. The goal is to deliver an upgrade model which improves the scientific output from all neutron beamlines, provides the largest collective gain, keep the instruments pulse time characteristics within the limits provided by instrument scientists, and can be built with minimum risk. A number of the MCNPX models of the TS-1 future TRAM assembly have been prepared by ISIS neutronics team. The new models have been optimized as part of the CombLayer package allowing extensive parametric and component selection without compromising the detailed engineering requirement. The upgrade models have been benchmarked against a baseline TS-1 model taking into account flux and time distribution of all existing TS-1 instruments. The best model shows that significant benefits can be achieved without modification to existing instruments, making the upgrade a low risk project.

1. Introduction

The Target Station 1 (TS-1) at ISIS operates very successfully for almost three decades. However, with the knowledge and computational tools now available it is widely believed that the neutronic output, efficiency and reliability of the TS-1 can be significantly improved. This was the reason to start a feasibility study of the potential TS-1 upgrade. Within the scope of the project, the proton beam delivered to the target is planed to be as it currently is: 800 MeV protons, beam current[1] of 180 μA and approximately double Gaussian profile with $\sigma_x = \sigma_y =$ 1.8 cm. The repetition rate is 50 Hz but every fifth pulse is delivered to the Target Station 2. Because re-configuration of the instruments (and the corresponding beamlines) is not a likely option, the project has been focused on re-assessing the TS-1 target, reflector and moderator (TRAM) assembly. In reviewing the risks, the TS-1 upgrade project has been defined as a reasonably conservative, driven by the fact that TS-1 is already operating, and compromising existing performance of the instrument suite in either flux or availability needs to be negligible [1].

The procedure for neutronics part of the project was, as a first, to create a robust, detailed neutronics model of the current TS1 (*baseline*) with idea to validate the neutronics reliability after review of simulation results and comparison with experimental results. The next step was to establish and then maintain a number of simulation models of the TS-1 zone which includes future TRAM assembly and current void vessel, beamlines, bulk shielding, etc. The

[1] There is a possibility to increase the beam current to 200 μA.

CombLayer tool [2] has been used for construction and optimisation of all these models (ultra-rapid prototype models, detailed models that establish beamline performance and selected high specification models for specialized types of calculations). The new models have been benchmarked against a baseline TS-1 model taking into account flux and time distribution of all existing TS-1 instruments. The main results of this neutronics study and TS-1 upgrade optimisation are presented in the following sections.

2. Current ISIS TS-1 model

The cross-sections of the TS-1 TRAM assembly are shown in Figure 1. The target consists of tantalum cladded tungsten plates. There is 12 tungsten plates with different thicknesses: 1.1, 1.1, 1.2, 1.35, 1.5, 1.8, 2.1, 2.6, 3.4, 4.0, 4.6 and 4.6 cm. The height of the tungsten plates is 4.0 cm and the width is 5.25 cm. The thickness of tantalum cladding is 0.2 cm. Target pressure vessel is made of stainless steel and the target is cooled with heavy water. The water channels width is 0.2 cm.

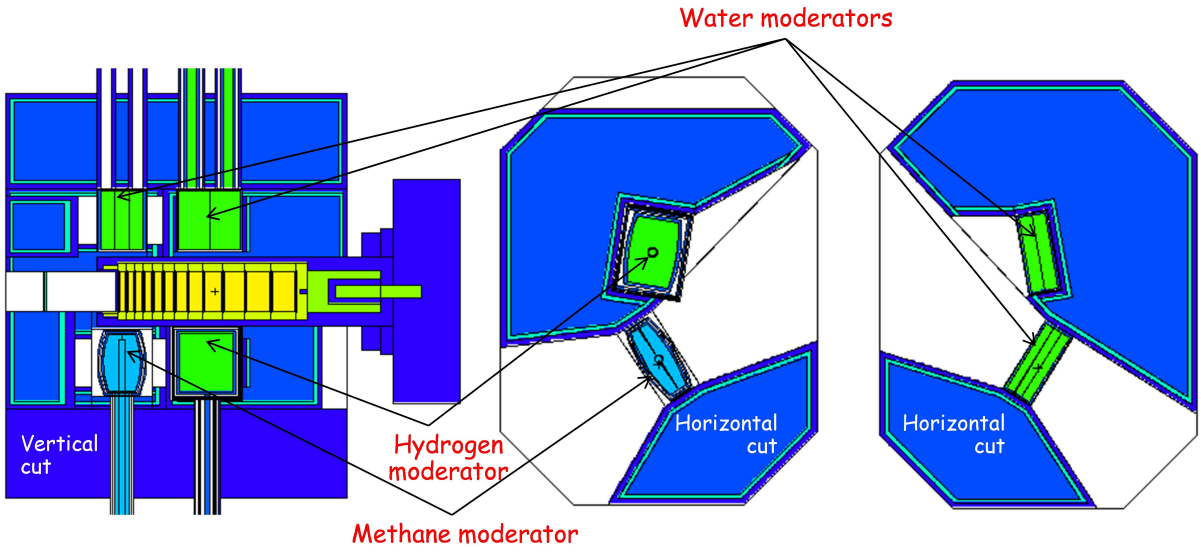

Figure 1. MCNPX model of current ISIS Target Station 1 TRAM assembly.

The reflector is made of beryllium rods cooled with heavy water (packing fraction = 90:10 by volume). The reflector size is: 83 cm (height) x 52 cm (width) x 70 cm (thickness).

Currently there are four moderators at the TS-1. Two water moderators operating at room temperature are located above the target (see Figure 1). The first water moderator has two poison (gadolinium) layers, the second one has a single poison layer. These two moderators are identical in size: 12 cm (height) x 12.5 cm (width) x 4.5 cm (thickness). The poison layer thickness is 0.005 cm. Below the target there are liquid hydrogen moderator and the liquid methane moderator (see Figure 1). Hydrogen moderator operates at 20 K with assumed composition: 80% para-hydrogen : 20% ortho-hydrogen. The hydrogen moderator size is: 12 cm (height) x 11 cm (width) x 8 cm (thickness). Liquid methane moderator operates at 110 K, and it is centrally poisoned with a single, 0.005 cm thick, gadolinium layer. The methane moderator size is: 11.5 cm (height) x 12 cm (width) x 4.5 cm (thickness). The neutron flightlines are lined with, 0.65 cm thick, boral layers. The same material is used as the moderators decoupler.

These four moderators serve 17 beamlines at ISIS target station 1 (see Figures 2 and 3) and provide neutrons for the experiments in the fields of spectroscopy (MAPS, MARI, MERLIN),

molecular spectroscopy (IRIS, OSIRIS, TOSCA, VESUVIO), large scale structures (CRISP, SURF, LOQ), diffraction (HRPD, SXD, POLARIS, GEM, PEARL), disordered materials (SANDALS), etc. These different instruments have different priorities that have to be fulfilled. For example POLARIS, TOSCA, GEM, HRPD and PEARL are sensitive to pulse width while MAPS, VESUVIO, SXD, MERLIN, SURF, CRISP, LOQ and IRIS can accept "relaxed" pulse width if this is a condition to have bigger flux gain. All these requests, of course, constrain the neutronics optimisation.

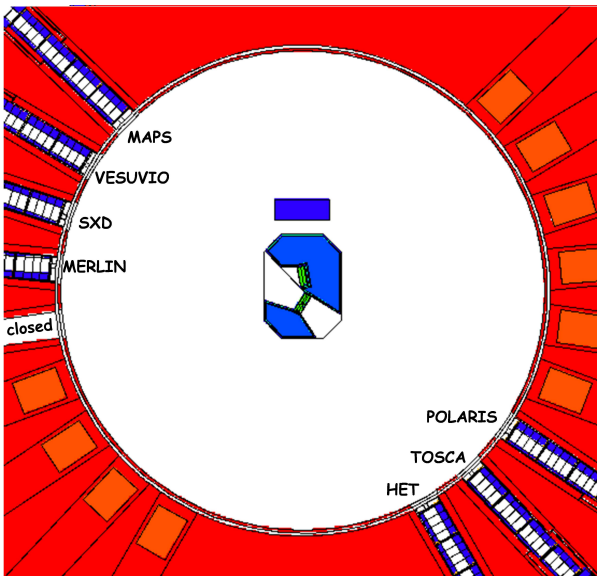

Figure 2. MCNPX model of current ISIS Target Station 1: The beamlines for water moderators.

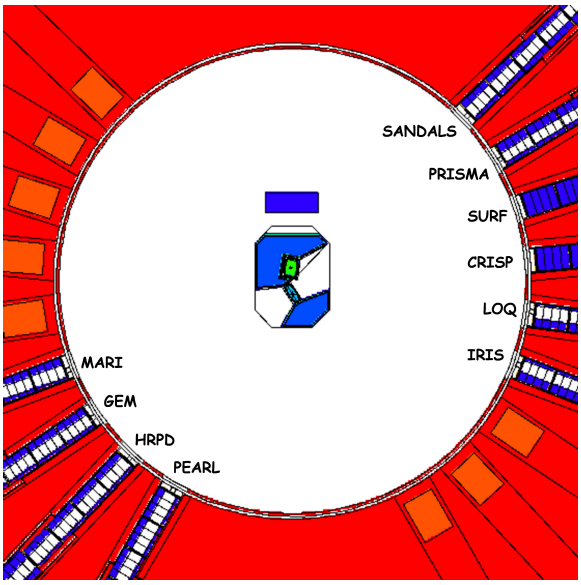

Figure 3. MCNPX model of current ISIS Target Station 1: The beamlines for cold moderators.

The CombLayer tool has been used to build MCNPX [3] model of the Target Station 1. Next step was to calculate neutron spectrum (for each beamline) using a point detector placed 10 m down each flight path, viewing the corresponding moderator through the modeled collimation within the bulk shield. It can be seen in Figures 2 and 3 that the model of the beamlines shutter inserts is very detailed. This is necessary not only for comparison with experimental data but also to allow accurate comparison with the upgrade model because the beamlines will remain the same. The CEM03 physics model [4] and ENDF/B-VII cross-section library [5] have been used in these simulations. In addition to this, the McStas [6, 7] input files have been prepared to help instrument scientists to trace down neutrons to the sample/detector positions and to compare the obtained results with experimental data. Very nice agreement between TS1 Baseline model results and experiments has been found (see [8] for more details). The comparison with the experiments helped also to resolve some issues in the knowledge of the current TS-1 performance[2].

3. The TS-1 upgrade models

The neutronics part of the TS-1 upgrade project has been driven by the idea to get a gain through a combination of (relatively) small changes in the TS-1 TRAM rather than through a single dramatic change in concept which could increase the project risk level. A number of

[2] For example, the para-hydrogen/ortho-hydrogen ratio in the hydrogen moderator has been estimated by matching the shape of the experimental time-of-flight data from the OSIRIS instrument [8].

TS-1 upgrade models have been produced using the CombLayer tool and for each model the performance is compared with the baseline model (over full TS-1 instrument suite).

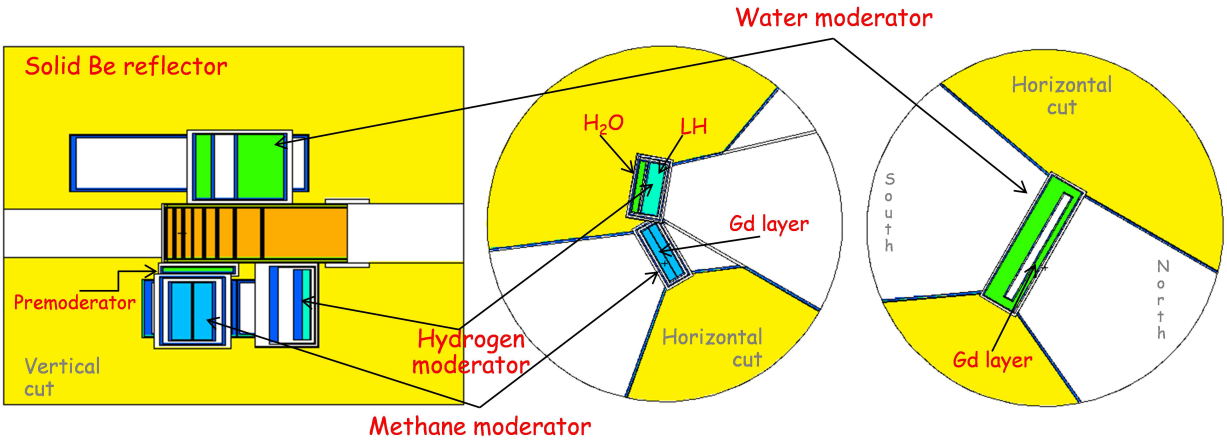

Figure 4. MCNPX model of the proposed TRAM assembly for ISIS Target Station 1.

The neutron flux ratios are calculated by taking the same tally point for each instrument and placing the different model (upgrade and baseline) in the void vessel and dividing the integrated flux. The pulse time shapes were also analysed and compared with the corresponding baseline results. The cross-sections of the final TS-1 upgrade model is shown in Figure 4 and the list of changes can be summarized as follows:

3.1. Target and reflector

The new target design is similar to current, operating TS-1 target. The main differences are that the target cross section is changed to be cylindrical (with core radius of 4.9 cm) and that target housing material is changed from stainless steel to tantalum (thickness of tantalum pressure vessel is 0.3 cm). The target is still based on tantalum-clad tungsten plates with 0.2 cm thick water (D_2O) channels between them. Tantalum cladding thickness remains 0.2 cm. The thicknesses and the number of plates have been optimised for three different beam currents: 180 (default), 240 and 300 μA. It is shown that number of plates increases with increasing beam current from 8 at 180 μA, to 10 at 240 μA and finally to 12 plates at 300 μA [9]. For the default beam current the thicknesses of eight tungsten plates are: 1, 1.1, 1.3, 1.6, 2.1, 2.8, 4.7 and 16.4 cm. The change of the reflector is based on replacing the stainless steel vessel filled with beryllium rods to a solid, edge-cooled beryllium structure. A new reflector has a cylindrical shape of 45 cm in radius and it is 70 cm high.

3.2. Cryogenic moderators

Hydrogen moderator is now a composite moderator, it has a liquid hydrogen layer backed with a water layer which serve as a pre-moderator. The liquid hydrogen part of this composite moderator operates at 20 K, with assumed para-ortho hydrogen composition of 80 : 20 to match a baseline model. Its size is 13.8 cm (height) x 14.2 cm (width) x 4 cm (thickness). The thickness of water (pre-)moderator is 1.5 cm and it operates at room temperature.

The gain factors for instruments looking at the hydrogen (composite) moderator are shown in Figure 5. The composite moderator makes gains due to the mixed LH+H_2O design. It is well known that looking into the pre-moderator of a hydrogen moderator increases the flux and this is exploited here. However, because the pulse width has to be matched, the amount of

pre-moderator has been limited, so effectively it was a study of the optimal place to put the pre-moderator.

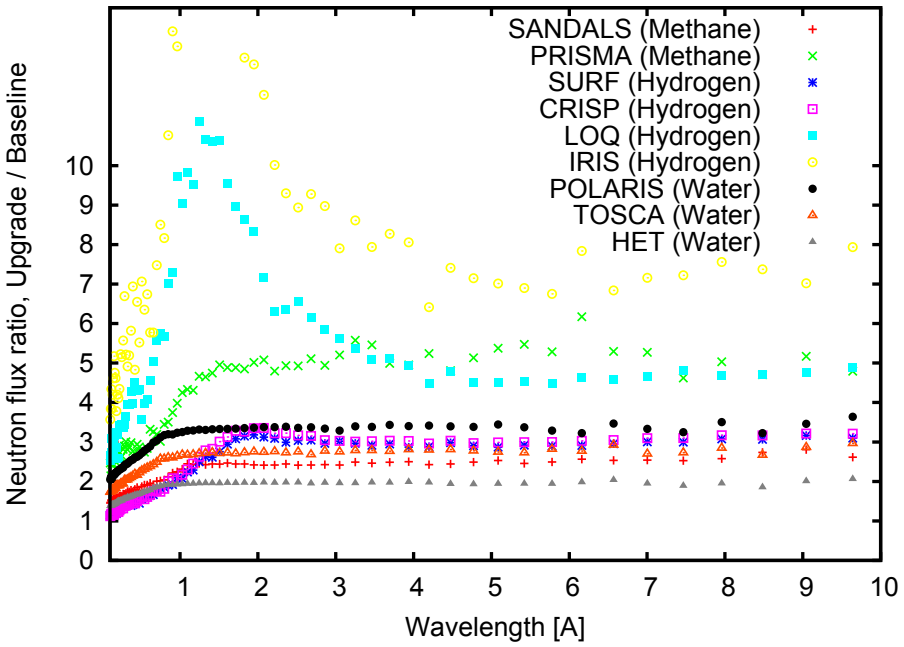

Figure 5. Gain factors for the north side beamlines/instruments.

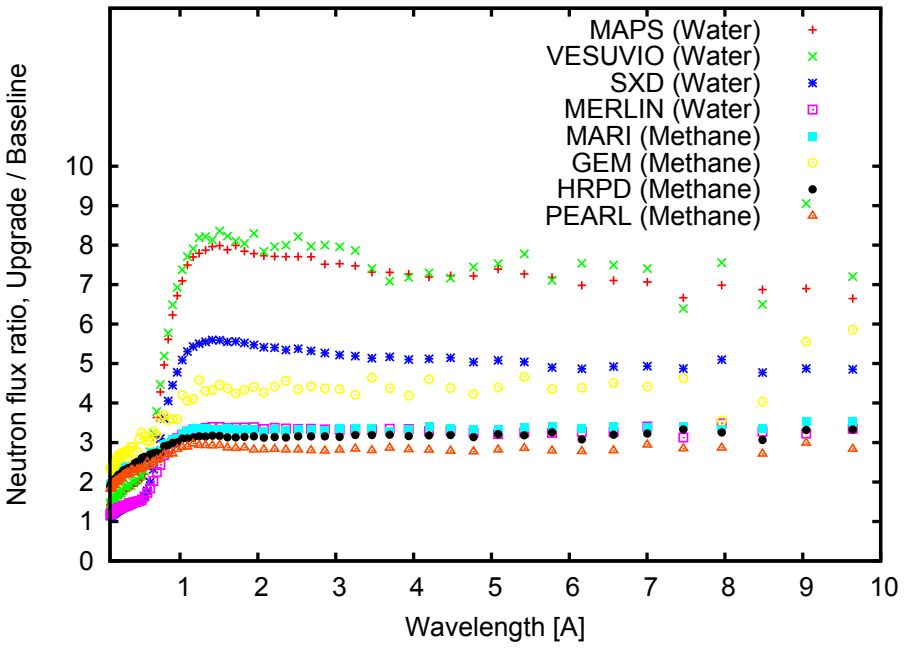

Figure 6. Gain factors for the south side beamlines/instruments.

The ratio of the pulse shape widths ('full width at half maximum' - FWHM's) for upgrade and baseline design of cryogenic moderators is shown in Figure 7 for different beamlines/instruments.

It can be seen that a significant portion of the gain in the case of a new hydrogen moderator is obtained by relaxing the pulse width by $\sim 25\%$ in the wavelength region of interest (around 6 Å). Additionally, non-negligible gains have been obtained due to the history, where originally, only two instruments were going to look at the hydrogen moderator. This is corrected here by putting the moderator in a better position for all those that view it.

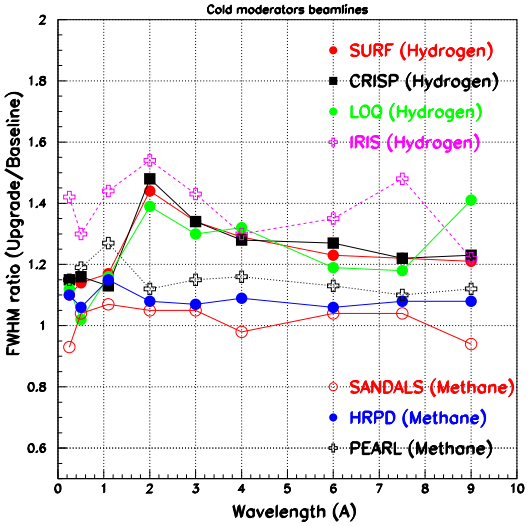

Figure 7. The ratio of the pulse shape widths (FWHM's) for upgrade and baseline design of cryogenic moderators.

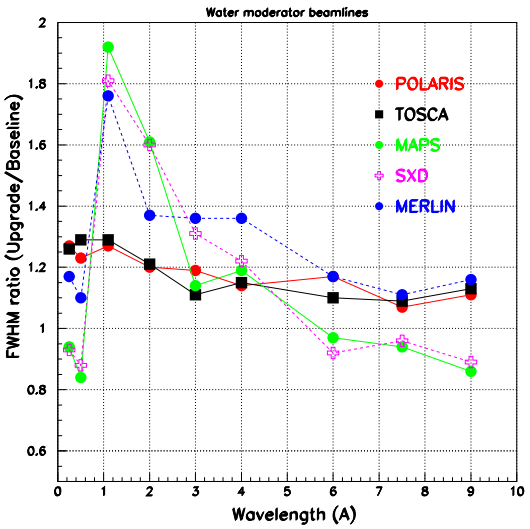

Figure 8. The ratio of the pulse shape widths (FWHM's) for upgrade and baseline design of water moderators.

Liquid methane moderator is practically identical in shape and size to the baseline methane moderator (11 cm (height) x 14 cm (width) x 4 cm (thickness)). It operates at 110 K and has a single poison (Gd) layer. However, the significant difference is that there is a 1 cm thick ambient water pre-moderator between target and liquid methane moderator. The gain factors for instruments looking at the methane moderator are shown in Figures 5 and 6. The methane moderator makes gains because of slightly better target position, the relaxation of the pulse widths for $\sim 10\%$ in the useful wavelength ranges (see Figure 7), and use of solid beryllium reflector and pre-moderator. Also, two cryogenic moderators have been moved closer to the target hot spot, allowing them to be (partially) pre-moderators to each other. In addition to these, boral liners and decouplers have been replaced with cadmium and the decouplers around the perimeter of all the moderators have been completely removed.

3.3. Water moderator

Two water moderators in current TS-1 configuration have been replaced with a single water moderator, operating at room temperature. The moderator height is 12.6 cm and width is 35.2 cm. The thickness of the water layer on south side is 4 cm and the moderator has 2 cm thick hole in the middle to partially control pulse width at south side. The instruments looking at this side of the water moderator (MAPS, SXD, MERLIN) are ready to significantly relax the pulse widths (illustrated in Figure 8) in exchange for bigger gains shown in Figure 6.

A single poison (Gd) layer has been added on the north side and the optimal thickness of the water layer on this side has been found to be 1.5 cm. The POLARIS and TOSCA instruments request that pulse widths should not be relaxed for more than $\sim 25\%$ (see Figure 8) resulted in the gain factors shown in Figure 5.

4. Conclusions

The aim of this study was to determine possible improvements of ISIS target station 1 by re-configuring the target, reflector and moderators assembly. Following the successful validation of the current TS-1 neutronics model, a number of the MCNPX models of the TS-1 future TRAM assembly has been prepared using the CombLayer tool. The neutronic output has been optimised across the existing TS-1 (and foreseeable future) instrumentation to produce the largest collective performance gain.

During the optimisation process, instrument scientists have been considered as the 'owners' of a performance metric for the neutronic output of their beamline and it is their metric which allowed ISIS neutronics team to perform optimisation of the upgrade models. For example, as one of the initial requests, most of the instrument scientists preferred to see no or limited pulse broadening within their respective useful wavelength ranges. Keeping all these constraints and requests in mind, significant gains are predicted through a combination of proposed changes (described in Section 3). Together, these changes lead to average flux gain of 3.4. It should be noted that some of the gain is a result of reduction of the amount of poisoning and decoupling while about an average factor of 2.2 (as seen by the epithermal gain) is purely due to re-configuration of the TS-1 TRAM.

The next step within the TS-1 upgrade project is to create and critically review a robust engineering analysis of the potential gains and risks involved in the upgrade scenario. It is expected that results of this process will change the gain factors. However, proposed neutronics model of the upgraded TS-1 TRAM contains sufficient engineering reality (cooling channels, clearance gaps, shutter inserts, etc.) to allow reasonably accurate prediction.

References

[1] Fletcher M 2014 Target Station 1 Upgrade Project *ICANS XXI: International Collaboration on Advanced Neutron Sources (Mito, Japan)* This proceedings.
[2] Ansell S 2014 https://github.com/SAnsell/CombLayer.
[3] MCNPX 2.7.E - Monte Carlo N-Particle Transport Code System for Multiparticle and High Energy Applications, http://mcnpx.lanl.gov/ (March 2011).
[4] Mashnik S K at al 2006 *Los Alamos National Laboratory report* LA-UR-06-1764.
[5] M.B. Chadwick M B et al 2011 *Nucl. Data Sheets* **112** 2887.
[6] Lefmann K and Nielsen K 1999 *Neutron News* **10** 20.
[7] Willendrup P, Farhi E and Lefmann K 2004 *Physica B* **350** 735.
[8] Bewley R, Ansell S and Škoro G 2014 Comparison of observed and calculated ISIS TS1 neutronic response *ICANS XXI: International Collaboration on Advanced Neutron Sources (Mito, Japan)* This proceedings.
[9] Wilcox D 2014 ISIS TS1 Upgrade: Target Plate Thickness Investigation *ISIS Internal Report.*

3.2.14

CombLayer : A fast parametric MCNP(X) model constructor

Stuart Ansell

Rutherford Appleton Labs, Chilton, Didcot OX11 0QX, U.K.

E-mail: stuart.ansell@stfc.ac.uk

Abstract.

MCNP(X) Monte Carlo neutronic modeling has now reached the level that large simulations of spallation sources starting from protons on target and recording neutrons at instrument detectors or outside biological shielding can simulated in one model. These models have the majority of the engineering aspects (e.g. pipework) described in detail. However, directly building an MCNP(X) input for a large geometry is highly time consuming and almost all the features of MCNP(X) that allow that process to be made simpler for the user (e.g. universes, lattices etc.) increase the simulation runtime by orders of magnitude.

CombLayer is a program designed to begin to overcome this problem. It ignores all the helper options in MCNP(X) and treats MCNP(X) as an assembler. Assembly-like geometry components can be rotated and repositioned, linked together, intersected and joined using a linkage system. Thus rapid production of complex MCNP(X) geometries that depend on a long list of variables and module flags, and the facilitation of tallies with appropriate variance reduction is possible.

CombLayer has built full models of facilities, with examples from ISIS TS1/TS2, SNS, ESS, Delft etc, typically with >2000 variables that can be changed within their range to carry out optimizations. Additionally, the object oriented form of all model components allows exchange of most parts to done with a simple command line flag. This facilitates "shopping list comparisons" e.g. a set of different cold moderators to be compared.

The code is publicly available at https://github.com/SAnsell/CombLayer.

1. Introduction

The Monte-Carlo MCNP(X) code [1] has been a mainstay of the neutronic community for many years and used in the design of both spallation sources such as the SNS and ISIS-TS2 as well as reactors e.g. ILL and Delft [2, 3, 4]. For the last 20 years there has been a steady increase in the realism and complexity of the models used, going from simple cubic or cylindrical moderators in a simple reflector to fully engineered moderators including pipework, pressure curvatures and corner rounds and detailed from the target to the instruments detectors. This has resulted in the number of objects and surfaces increasing from the 10s to the 100,000s. However, during the same time the mechanisms within MCNP(X) which allow the input of that geometry have not changed significantly. Surfaces are still constructed from simple quadratic infinite surfaces and the later addition of macrobodies have only added extremely primitive, non-extensible shaped surface groups e.g. the cuboid. Objects are constructed from a set of boolean operations on surfaces, the object must be completely defined and it not sufficient to allow previously defined objects to cut or overlap the new object.

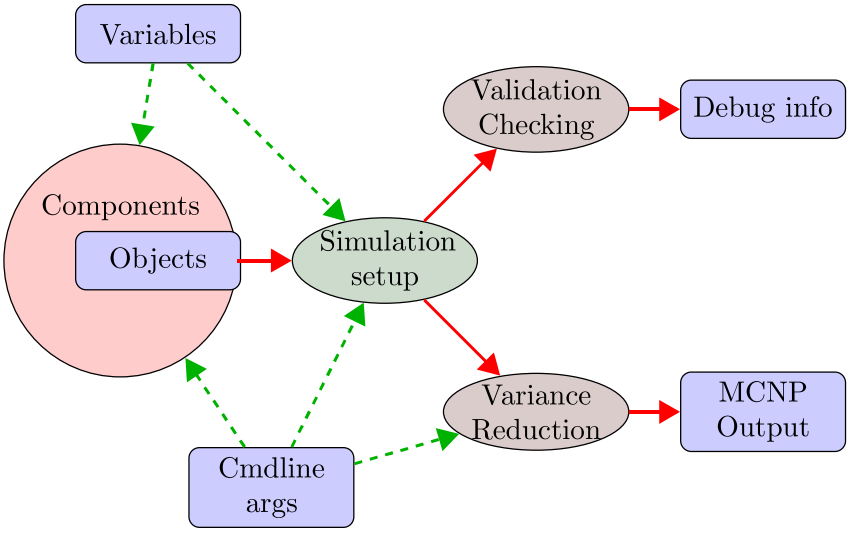

Figure 1. Diagram of the procedural flow and object construction within a CombLayer runtime execution. The green dashed arrows represent possible user input. The red solid arrows represent definitive directions of construction. First components and objects are built, simulation setup is carried out and then onwards to validity or variance reduction and output.

MCNP(X) suffers an additional problem when dealing with large assemblies, in that both the complementary operator and the universe system are not restricted. Consider three objects: A in B in C. If B is constructed using the complement of the outside of A (#A), and C is likewise constructed from B (#B), at runtime MCNP(X) needs to calculate all the surfaces in A, B and C to calculate points and lines in C. In large assemblies, this cascade dramatically reduces runtime performance or greatly increases the complexity of the modeling process.

The program CombLayer is being developed to alleviate some of these problems and in addition to be a basis program that can be extended/modified by others to be further improved.

1.1. CombLayer Architecture

The outline CombLayer architecture is shown in figure 1. The program requires users to effectively write their geometry into a C++ construction system. This is compiled into the program before running CombLayer. The output can then be influenced by a Turing complete variable system which can be set via XML files or via the command line

2. Object Construction

Volume objects within CombLayer are still constructed with a complete boolean volume description of each space in the same way that MCNP(X) treats each individual volume. Volumes are defined by combining *literals* (unique surfaces) with simple union and intersection (*operations*) to make a volume rule set. This is called a *function* within logic mathematics. All CombLayer volumes are initially pre-processed to remove non-unique surfaces and opposite plane surfaces against a global surface list. Then complementary components are expanded out.

CombLayer stores the object function as a binary tree structure. It is created by having the top node either an intersection or a union; this descends to other intersections or unions, before the leaf nodes are surface literals. The tree is partially sorted such that the minimum

number of changes of boolean type (intersection/union) occur between the head node and the surface literal, which implies that intersections and unions are gathered together. This allows the designation of two terms *surface level*, which indicates how many boolean operator changes that occur between the tree headnode and the point a surface is found, and *level object* which is the volume described by only those surface that share one particular *surface level*. The latter is commonly used for wrapping an object, finding its external surface etc.

CombLayer handles all of this internally, the only requirement from the user is to define the object either using the traditional MCNP(X) method, or as a composite object.

2.1. Object Organization

CombLayer allows the construction of objects within C++ classes that inherit from two base classes: *FixedComp* and *ContainedComp* or further derived versions of these two classes. The group of MCNP(X) objects built by this class is called a *component*.

Components are typically constructed in one class with this dual inheritance. The component is then automatically registered with the global (singleton) object register. The object register allows each component to be constructed as if it were an isolated simple MCNP(X) model. Surface numbers and objects numbers are automatically taken care, e.g. a cylinder component can be built with surfaces *1 2 -3* regardless of how many cylinder components or other components are required.

FixedComp provides an origin and an orthogonal basis set (X/Y/Z) that the geometry is being constructed with, which allows the object to be rotated and shifted in any direction, but constructed in a simple way. However, the real advantage of *FixedComp* is the provision of link points. A link point is a point on a surface which has an external axis associated with it. For example, a 4x4x4cm cube with the surface *pz 2* might have a link point on the surface at (0,0,2) with link direction (0,0,1). If the origin of the *FixedComp* is moved, or the object is rotated, these link points also follow the rotations/translations. This gives the advantage that when an new object is constructed, the new object is constructed relative to the direction and position of an existing link point. For example, a line of cubes can be created by constructing each (except the first) relative to an external link point. If the initial cube is rotated/shifted the whole line moves, but if one of the later cubes is shifted/rotated only the remaining cubes are reorientated. Further, since the link point provides a common surface interface, the cubes could be joined using this, so in the last case, the rotating cube becomes extended.

ContainedComp provides support for the external boundary of the a collection of MCNP(X) objects. It is an attempt to mitigate the cascade problem of complementary objects and universes within MCNP(X) whereby a sequence of inclusions between object A, B, C... will result in a MCNP(X) runtime degradation. The use of *ContainedComp* should give the same geometric result but not result in the runtime penalty.

When a component is built, an external boundary of surfaces is defined. The external boundary should wrap the volume of the component. In its simplest form, it can be constructed as a union of all the objects within the component, but commonly an obvious outer surface is available. For more complex object a *ContainedGroup* is available. This external boundary is not an object and does not appear within the MCNP(X) output model, but it can be used when a component could reside within another object, or if two components get so close that an intersection could take place.

ContainedComp is provided with a number of routines that make it more useful in building objects. First, if an intersection is certainly going to happen between two components (e.g. a moderator within a reflector), then the *ContainedComp* can be added directly to the containing component. Much more likely, is that the *ContainedComp* will be included in some (unknown number) of the objects that make up another component. This is carried out by using an appropriate attachSupport call, which automatically checks each of the objects within the

components to see if they overlap any part of the *ContainedComp*'s boundary. If that does happen then the full excluded boundary is added to the individual object. It is assumed that the object optimization will remove unnecessary surfaces later.

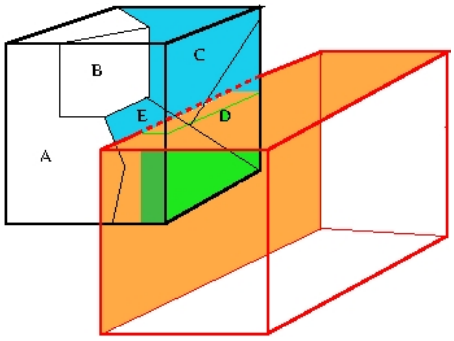

Figure 2. The intersection between an object components and a *ContainedComp*. Objects in blue (E/C/D) are the only object that get modified and they end up with only two of the surfaces (in orange) of the original ContainedComp

Figure 2 shows the consequence of the intersection of a *ContainedComp* with a different component after the object optimization process. It can be seen that *ContainedComp* are reductive, so the intersection of a ContainedComp with a component does not affect the objects own *ContainedComp*, so a sequence of component intersections are constructed, where a change to one component's composition or boundary never requires changes to another component.

The main drawback is runtime speed of building the models. In principle, it would be possible to intersect every component with every other component, but when developing models it is highly advantageous to keep the model building phase down to a few seconds. Thus a positive component-component test system is used, where the user has to state (in code) which objects are going to be tested together.

2.2. Object Optimization

During the MCNP(X) path tracking routines, the largest areas of CPU expenditure are: (i) calculating the side of a surface relative to a point, (ii) the intersection point of a line to a surface and (iii) exiting/entrance condition of a line on a surface intersection. All three of these can be dramatically reduced by reducing the number of *literals* (unique surfaces) within a volume description. If this can be achieved, both the overhead in calculating the object and number of other cells that need to be investigated when calculating the exit of a track are reduced. It is this latter overhead that can increase very dramatically as the complexity of the model is increased, with particular note to pipework and other connectible items.

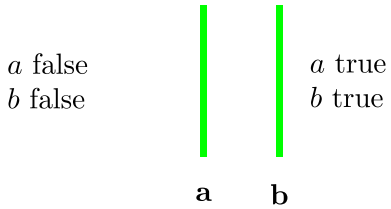

Figure 3. The planes a and b are parallel so there is an impled relation ship between them. The sense of the planes are arbitarily decided to be true towards the right.

CombLayer provides two operations for improving the number of literals; both need the pre-operational step of expanding the object function based on absolute implications. In this process, all pairs of literals (a,b) which imply the other are expanded, e.g. the two parallel planes shown in figure 3 have the property that if plane b is true, then plane a is also true, and likewise if a is false b is also false. This is expressed in standard boolean algebraic form as (using + for

union, $'$ for negation).

$$\begin{aligned} b &\implies a \equiv b' + a \\ a' &\implies b' \equiv b + a' \end{aligned} \tag{1}$$

These rules in the union form are then intersected with the existing volume object resulting in a obviously longer expression, but surprisingly because MNCP(X) calculates only those surfaces that are required for a particular condition to be determined, this expanded form results in a slightly faster executable model in MCNP(X).

This object can be further improved by removing unnecessary literals. This is done by determining the Shannon expansion for all repeated literals (regardless of +/-ve sense). The Shannon expansion of the literal a gives the logical function in the form: $a(A) + a'(B)$, where A and B are logical functions without the literal a. In the case, that $A \equiv B$, literal a can be removed from the function.

Further optimization could be carried out if 2-factor factorization and weak division of factors were available and it is expected that this capability will be added soon.

2.3. Model Variables

An essential part of geometric modeling is having control over all the parameters that make up the model which allows the user to change any parameter without the model becoming broken. CombLayer tries to ensure this via two mechanisms. The first is that there is a global database of variables which all have a type and a default value. Variables can be floating point number, integers, strings or 3D vectors. Those variables can be expressed either as values or as mathematical functions of other variables or programming constructs. Second, combined with the *FixedComp* link points and surfaces, most objects are extremely robust to change of position and size. If an object is likely to be eliminated then additional code has to be added to components to deal with this issue, but typical size change can be accommodated by standard overlap tests and exclusion on all nearby objects.

2.4. Pipework

Adding pipework to a model is such a common requirement that a specific module has been written to assist in this operation. In CombLayer a pipe is considered as a multi-layered object that follows a path through the model but has a constant shape form (e.g. cylindrical/square). The shape can change size (e.g. a pipe going from a small radius to a large radius) but the shape is considered unchanged. Additionally, the use of simple flags can turn various layers on and off at each junction.

The pipework is added by starting a pipe relative to a link point or central origin of a component. Obviously its true starting point can be offset from this link point. Then further points are defined either by another link point, or by 3D-Vector offsets until the pipe's termination point. The pipe is bent at each turn by introducing a dividing plane, even if that plane produces zero deflection. If the pipe goes through a *LayerComp* object it may be joined to each layer in turn [figure 4].

3. Post-Geometry Construction

Once the geometry has been constructed, further processing in necessary to add source terms, tallies and carry out variance reduction. CombLayer supports most tallies and some source terms, as currently written. Since CombLayer renumbers surfaces, objects and most object's final positions which are dependent on the state of many variables, it takes advantage of the *FixedComp* link points, link surfaces and the objectRegister for setting tallies. Additionally, if

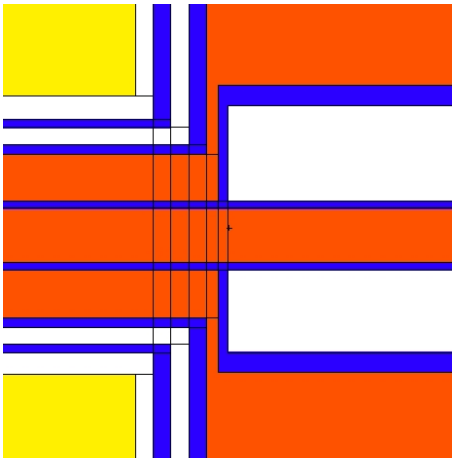

Figure 4. The pipe join with a multi-layered moderator. The requirement is that the moderator vessel is a *LayerComp* and the pipe join flag is set for each of the pipe/layer intersects. The dividing planes of each of the pipe segments can be seen within the join region.

tallies are not set via this mechanism, significant extra effort is required to set up an appropriate variance reduction mechanism.

The simplest tallies to set up are point tallies. These can be constructed as an offset 3D-vector distance from any link-point. In addition, they support area-point tallies and windowed point tallies which are common MCNP(X) modifications. Similarly surface tallies can be set up if a link-surface is required, although more difficult if not, and cell (flux/heat) tallies can be added via the objectRegister. Finally, XML tallies can be added for any other tally type or addition.

3.1. Variance Reduction

There is no complete variance reduction method in CombLayer, rather a number of enablers to construct a variance reduction system to suit the type of problem being studied. However, significant effort has been made to enable many appropriate questions to be asked of a geometric system.

Firstly, it is possible to determine an approximate *centre* of most objects and components. This is done by iterating over all the surfaces in an object to determine the triple surface intersections. Three non-parallel planes will intersect at a point; a cylinder and two planes typically intersect at two points etc. These points are then summed to a centre of mass if the point is on a true surface of the object.

The centre object points can be used in a number of ways to help with variance reductions. The first is via the cell based weight window system. For each cell it is possible to determine a biased probability to transport to any other cell based on the distance between the centres and the material in the path between the centres. Following this direct calculation of all object pairs, a Markov chain method can be used to track the cell to tally position bias for the weight window value. Different energy values can have different tracking cross sections associated with them which in turn modify the weight window result. Obviously, this is not a replacement for full adjoint variance reduction method [5], however it is very fast to use and requires minimal setup effort.

4. Conclusions

CombLayer is an extensible object-orientated system for building MCNP(X) models. Its main strength is to allow the rapid construction of complex non-repeating structures such as found in spallation sources and reactor assemblies. These structures can be linked in simple ways that allow the size and position of almost any object to change without breaking the model or having to do additional work to make the model work.

It has been used to build full assembly models from proton targets to instrument layouts in one model which could be rapidly run in a single MCNP(X) model. These models have had upto 100,000 MCNP(X) objects within them but could still be run effectively.

The code released under the GNU public license GPL3 and is available at https://github.com/SAnsell/CombLayer.

References

[1] X-5 Monte Calro team 2003 MCNP - A General Monte Carlo N-Particle Transport Code, version 5 Tech. rep. Los Alamos

[2] Gallmeier F X, Ferguson P D, Iverson E B, Popova I I and Lu W 2006 *Nuclear Instruments and Methods in Physics A* **562** 946–949

[3] Lu W, Ferguson P D, Iverson E B, Gallmeier F X and Popova I I 2008 *Journal of Nuclear Materials* **377** 268–274

[4] Ansell S 2007 *Proceedings of ICANS-XVII* pp 660–668

[5] Wagner* J C and Haghighat A 1998 *Nuclear Science and Engineering* **128** 186–208

3.2.15

ISIS Target Station 2 Reflector Modifications

Stephen Gallimore

STFC Rutherford Appleton Laboratory, Harwell oxford, Didcot, OX11 0QX, UK

E-mail: stephen.gallimore@stfc.ac.uk

Abstract. Following the successful completion of the second target station (TS2) Phase 1 project at ISIS in July 2009, the phase 2 project was initiated. This phase of the project is to deliver 4 new instruments. The design of 2 of these beam lines require modifications to be made to the TS2 reflector; a direct view of the target for ChipIR and widening the view of the coupled moderator's grooved face for the LARMOR instrument. In addition to these changes other beneficial modifications were identified and included in the new design. The modified reflector will be installation in the ISIS' long operational shutdown in 2014. This paper will provide greater detail of the changes made and report on the progress of the installation and commissioning.

1. Introduction

1.1. Background

1.1.1. *Target Station 2*. Operation since 2009, Target station 2 (TS2) typically takes a 40mA proton beam (800Mev) at a repetition rate of 10 Hz. The new target station produces extremely bright beams of low-energy neutrons enabling the ISIS science programme to expand in the key research areas of soft matter, advanced materials and bio-science.

1.1.2. *Target Station 2 Reflector*. TS2 represents a step forward in technology when compared to target station 1 (TS1) which first took beam in December 1984. One such area of advance was the design of the reflector. In TS1, the reflector is made up of beryllium rods (coated with 'Berylcoat D') housed in external stainless steel vessels that form the various parts of the full assembly. For TS2, the reflector is made from solid beryllium blocks plated in Nickel. This significantly increased the volume fraction of beryllium surrounding the target.

Another key change was the reduction in power deposited on the target and in the reflector (approximately 4kW), which meant the TS2 reflector could be cooled using light water flowing through water-cooling pads attached to the extremities of the reflector, as shown in Figure 1.

More fundamentally, operational experience from TS1 led to the reflector design incorporating a system that allowed much greater access to the target and moderators for maintenance and exchange, vastly reducing the time need to perform these operations. Figure 1 also demonstrates this 'splitting' ability.

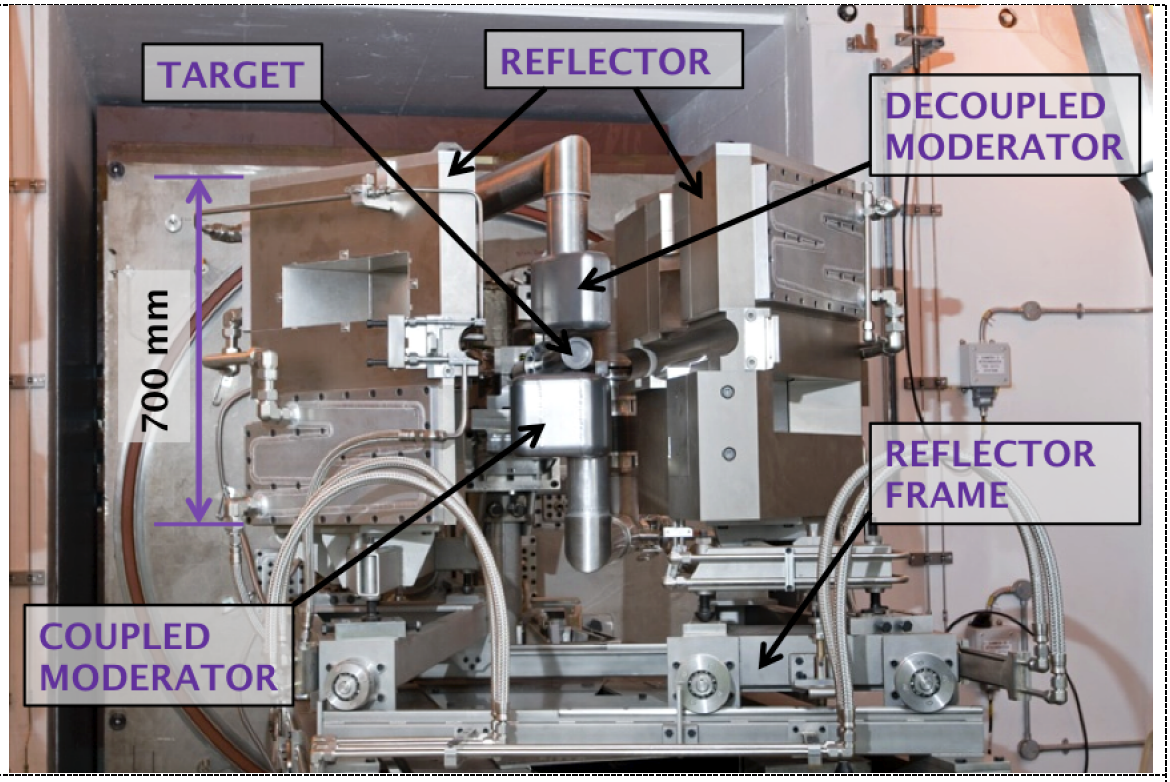

Figure 1. Labelled TS2 reflector in its 'split' state exposing the target and moderator positions

1.1.3. *Target Station 2 Instruments*. There are seven neutron instruments (see Figure 2) that are currently operational and producing research papers. In 2011, funding was made available to build four new instruments together with the necessary advanced changes to the target reflector system. These four phase II instruments (also shown in Figure 2) are currently in various stages of construction and commissioning. The instruments are:

- Chipir - A strategic facility for the aerospace and computing industries for fast neutron testing of electronics
- Zoom - Small-angle scattering instrument with polarisation for advanced materials, magnetism, environmental science, pharmacy and healthcare
- Larmor - Advanced techniques instrument for polymer science, bio-materials and food science
- Imat - Neutron imaging and materials testing for power generation, civil engineering, transportation and aerospace

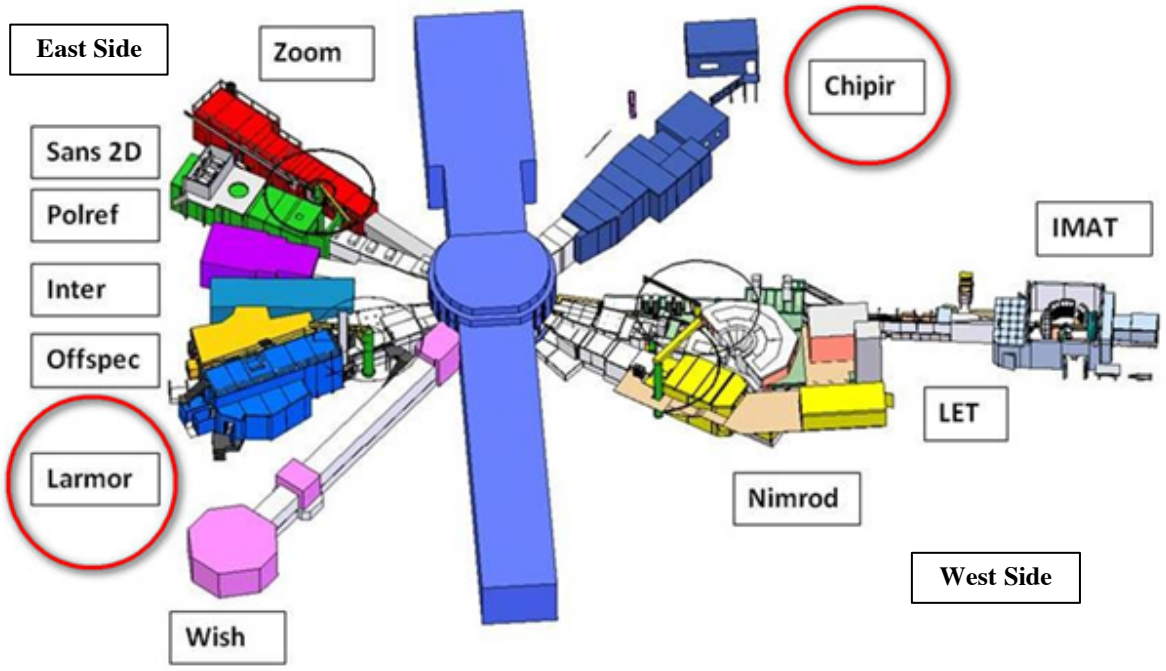

Figure 2. A schematic layout of Target Station 2 (TS2) showing the instrument suite including the phase 2 instruments and highlighting the Larmor and ChipIR beam lines.

2. Motivations to Change

2.1 Introduction

As with any project of this nature that proposes significant and costly changes, and which involves the disposal of activated components, there needs to be strong justification for doing it. The motivations for the changes made as part of RAMP2 (2nd reflector and moderator project) are broadly split into 3 sub categories, each dealt with individually below. Although the operational improvements and provision for future moderator development are worthy reasons to change, it is acknowledge that on their own they would have been insufficient to justify the cost outlay and risk to operations of the facility. It required the 2 phase II instruments in order to make the whole package of changes a viable project. Once the decision was made to change then it was prudent to try and make the other changes at the same time.

2.2 Phase II Instruments

In order to perform to their design specifications, two of the phase II instruments, Larmor and ChipIR, proposed changes to the reflector assembly. The changes required for Larmor were a consequence of the selected beam line position; the instrument selected the E6 port, which was designed to allow a view of either the upper or lower moderators. This meant that the flight line groove cut in the reflector for viewing the moderator would have to be widened. ChipIR being a unique instrument on ISIS required a completely different spectrum of neutrons in order to achieve its science and this required the instrument to have a view of target, so that it may extract the fast neutrons needed.

2.3 Future Moderator Development

As with the initial operation of any large scientific facility, the first five years of TS2 operations provided some unexpected insight, into its operational characteristics, in particular issues were experienced with the running of solid methane in the moderators. As an outcome and as part of the continued investment and development in the facility a programme was initiated to look into development of the current and future moderator concepts, both to improve operational running and potentially improve scientific output. This development and potential changes may result in changes in moderator geometry, orientation or both, plus possibly other more radical adjustments. With beryllium being a difficult and expensive material to work with and dispose of, it is far from ideal to have to discard large volumes of viable material should it need to be replaced. To gain the greatest possible flexibility with the minimum impact (loss of beryllium surrounding the moderators) on the existing instruments, the idea of exchangeable sections and 'buckets' was employed.

2.4 Operational Experience

Following initial 5 years of operation and the successful running of the day one instruments the operational experience gained from the running of the new target station highlighted some areas of potential improvement for the reflector assembly. It was also accepted that during the construction of original reflector assembly, in order to meet tight and challenging project deadlines, concessions were made in the design and construction.

One such concession was made on the original specification for the nickel-plating of the beryllium blocks, set at 50μm. At the time Materion had an issue with plating on one of the large blocks having cracked, so they were allowed dispensation to use ~20μm plating thickness instead. During commissioning of the target station water leaks were experienced in the void vessel, leading to a sub-optimal atmosphere and operational experience showed that running under these conditions that the reduced plating thickness was not enough. All new blocks for RAMP2 meet the 50μm specification.

Another such concession was made on the thickness of the cadmium decoupler for the lining of the flight-line grooves in the reflector. Due to space constraints and difficulties in manufacturing, it was not possible to achieve the 1.2mm thickness specified by the ISIS neutronics team, with 1mm being the thickest achievable. This was rectified in the design of RAMP2.

The original design of the reflector assembly was based around relatively large blocks of beryllium and there was a minor concern that should work have to be done on these in the hot cell, then they were towards to the upper limits of available space within the hot cell for several operations. This was previously decided to be an acceptable risk because of the low frequency for such work, however when the possibility came up for the reduction in size for many of the blocks as part of the project, the reduction in risk was also a supporting motivation to change.

3. Details of the Changes Made

3.1 Changes for ChipIR

ChipIR occupies the W1 beam port on the west side of TS2. To achieve the necessary spectrum of high energy neutrons it requires for its operation the RAMP2 reflector was designed to incorporate a direct line of sight to the target as shown by figure 3. Unlike any other beam line on ISIS ChipIR looks at a piece of beryllium sitting just above the target, rather than at a moderator. As can be seen from figure 3, this necessitated the design of a specially machined block featuring a smooth cylindrical bore, into the west half of the RAMP2 assembly. It is designed in such away that it could be removed and replaced in the future, maintaining a high level of flexibility and allowing for change in such

unlikely circumstances that the bore in the reflector for ChipIR has a greater impact on the other beam lines than predicted.

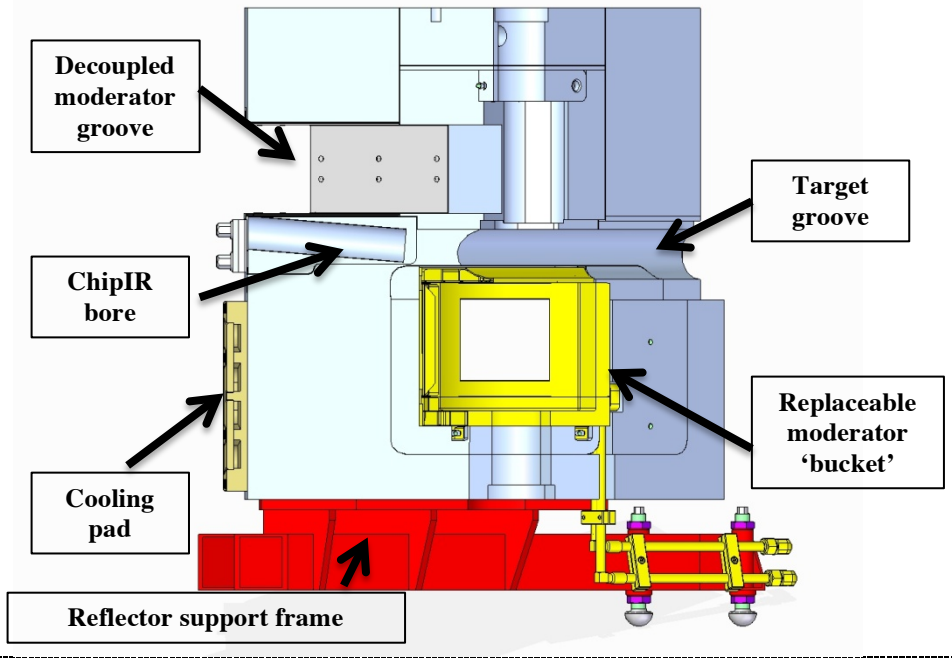

Figure 3. A section view through the west half of the reflector showing the modification made for the ChipIR beam line.

3.2 Changes for Larmor

As previously mentioned Larmor selected the E6 beam port and when this was originally installed as part of the construction of TS2 it was built with windows on the void vessel and 'torpedo tubes' such that a beam line on this port would be able to choose whether it viewed the upper (decoupled) or lower (coupled) moderators. Larmor selected to view the coupled moderator and this required the widening of the groove in the reflector from 53° to 64.4°. It also meant that the cooling pad and water piping that was located in that area needed to be modified as well, easily seen in Figure 4. The rerouting of the water piping also had the added advantage of reducing the backgrounds for the instruments facing the lower east section of the reflector assembly.

3.3 Changes for future moderator development

The basics behind the changes made in order to add flexibility to the reflector assembly for future moderator development and other geometry changes (such a flight line grooves), was to design in exchangeable sub-assemblies. The 'buckets' sitting closely around the moderators allow for dimensional and orientation changes to the moderators and on the west side there is a removable section for which will allow changes such as widening the groove for the lower couple moderator, as was done for Larmor (see above). The removable assemblies allow a much smaller amount of beryllium to be exchanged, saving time, cost and money both in the manufacture of a new piece and in the disposal of the old piece.

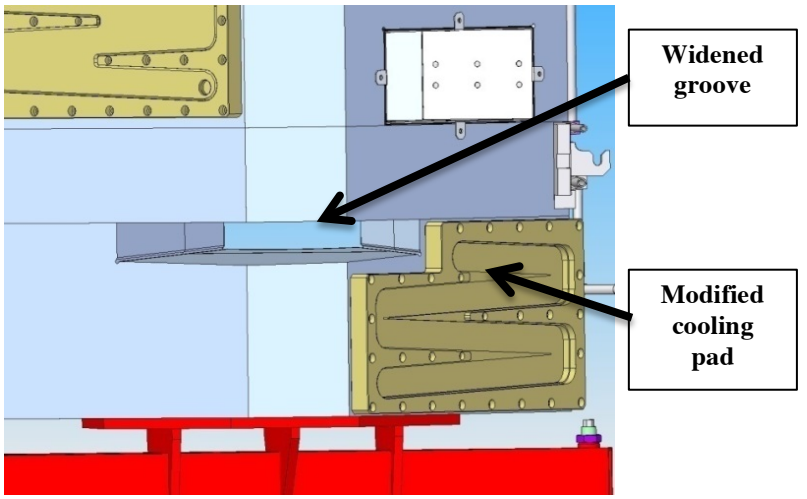

Figure 4. A CAD model view of the east half of the reflector showing the modification made for the ChipIR beam line.

3.4 Operational improvements

The original TS2 reflector featured over ten different sizes of beryllium fixings, each specialised for a specific application within the assembly. In addition, due to the relatively low ductility of the beryllium bolts (when compared to standard engineering materials) the bolting philosophy was to fix each block to the next thus keeping bolt lengths relatively short and reducing the risk of several blocks being stuck together in the event of a beryllium bolt shearing. In the new design the opportunity was taken to modify the whole fixing methodology. Firstly, the overall number of bolt sizes was reduced down to three (short, medium and long), thus reducing the remote tooling requirements and making it far easier and quicker to visually identify specific bolt types. Secondly, the way in which the assembly was fixed together was changed with long through bolts being used in the corners to connect through all the outer blocks, again reducing the total number of bolting operations required. These bolts are made from nimonic 80A due to more desirable mechanical properties and the beryllium bolts that were kept for use in more 'neutroncially sensitive' areas had their design changed to make use of the fact the beryllium is relatively brittle. The redesign added an intentional weak area just below the head of the bolt so that should the bolt fail it would do so at this location and thus always allow the two blocks bolted together to be separated.
The opportunity was taken to rectify nickel- and cadmium decoupler thicknesses. In addition, a coupled moderator also been changed as part of the work with the unused solid methane section having been removed from the internals because of operational issues and with scientists having been able to adapt to using the flux and spectrum from Liquid H_2 section of the moderator.

4. Build-up, testing and installation

Materion (formerly Brush Wellman) was selected as the supplier for the beryllium, with a British company, GSI Exotec, selected as a sub-contractor for the machining and plated of the individual blocks that make up the reflector assembly. This meant that the near net shaped beryllium blocks were shipped from the USA to the UK where they machined and plated. To ensure that the specified plating thickness was achieved for all pieces, a reference piece of accurately known prior geometry was plated with each batch and then measured to confirm the depth of nickel achieved. Unfortunately as a consequence of Materion being the main contractor and export regulations, all the finished blocks had

to be shipped back to the USA so that they could finally be sent back as the finished assembly. This meant additional time and expense.

The beryllium components were received on site 9 months before the date set for installation, thus allowing time for assembly, alignment and characterisation work. A replica supporting frame also had to be designed and built, to have the most representative conditions possible. An advantage to having such a frame is that it can also be used for training and testing purposes in the future. Time and care was taken to perform as much preparation for the installation outside of the remote handling cell.

5. Summary

To summarise, since its initial conception in 2009, the RAMP2 project has designed several important changes to the ISIS TS2 reflector assembly, in order for it to continue to best serve the operation of the facility for many years to come. The main changes made are listed below:

- Widening of the coupled moderator groove and associated changes to the water cooling pad and coupled rerouting of the water pipework for the Larmor instrument;
- A bore into the reflector to allow a specific fast neutron flux into the ChipIR instrument;
- Replaceable 'buckets' around the coupled and decoupled moderators to allow for potential future changes and moderator development;
- Improvements to the mechanical fixings within the reflector;
- Corrections to out of specification thicknesses for some nickel plating and cadmium decoupler.

The RAMP2 reflector assembly was successfully installed in the 2014/2015 long shutdown and as of writing this paper, is currently going through final checks before target operations commence again in early 2015.

6. Acknowledgements

The work presented here in this paper and in the accompanying presentation is the combination of a great deal of time and effort by a large number of ISIS' staff. I would like to acknowledge the main contributors to the project here (listed in alphabetical order); Stuart Ansell, David Bellenger, Julius Bullock, Lester Clarke, Daniel Coates, Matthew Fletcher, David Haynes, Sean Higgins, David Jenkins, Leslie Jones, Eamonn Quinn, Andy Robinson, Chris Russell, Graham Wallace & Peter Web. It is due to the dedication and commitment of its' staff such as those listed above that ISIS remains such a productive and scientifically important facility.

3.2.16

An investigation into the suitability of additive manufacturing techniques for neutron moderator vessels

S Gallimore
STFC Rutherford Appleton Laboratory, Harwell oxford, Didcot, OX11 0QX, UK

E-mail: stephen.gallimore@stfc.ac.uk

Abstract. Additive manufacturing (also known as rapid prototyping or 3D printing) techniques are increasing in popularity for several key reasons; greater freedom in possible geometry, reduced time of manufacture and connected to these are potential cost savings. ISIS has begun an investigation into the suitability of the various available techniques for the manufacture of neutron moderator vessels, in order to see if it can exploit these advantages.

It is however understood that additive manufacturing is by no means a perfect technique and part of the investigations will be to try and better understand how some of the disadvantages of the technique affect its potential application within the spallation neutron environment. Some of the main disadvantages commonly listed are; the grades of materials available/suitable for the process are limited, virtually no pre-existing material data from radiation environments, lower quality surface finish (directly from the manufacturing process), less familiarity with residual stresses in the material and questions over whether tight tolerances and consistent material thicknesses be achieved?

The work has been divided into two streams; one which utilises small samples to evaluate and compare different manufacturing and post-treatment techniques, the other that performs tests on a full-size representative moderator vessel. The complete programme of testing shall include the following tests; fundamental 'neutronic transparency', room temperature vacuum leak test, cold shock (using LN_2) and subsequent room temperature leak test, pressure cycling, a burst test, welding suitability and material data testing.

The investigations being conducted at ISIS are very much in the early stages and looking at fairly fundamental questions. Answering these will clearly guide the decision whether is it worth continuing with further investigation and development or if the currently available techniques do not produce materials that are suitable for use as moderator vessels.

This paper will present and discuss testing methodologies and results from planned tests in 2014.

1. Introduction

1.1 Additive Manufacturing

Recent years have seen the rise in popularity and number of applications of additive manufacturing (AM) techniques, which differs from traditional manufacturing techniques because material is added

as oppose to being removed by the process. The range of technologies and techniques covered by this term are also referred to as 3D printing, rapid prototyping or rapid manufacturing. The techniques first came to prominence by producing products in a range of plastics but since its conception there has been a desire to develop the techniques to be applicable with metals. They are now a wide range of companies offering production services and manufacturing equipment in this field. AM offers several potential benefits when compared to conventional subtractive manufacturing techniques and these are:

- Greater freedom in possible geometry
- Reduced time of manufacture
- Potential cost savings
- Can be produced directly from CAD data

1.1.1 Metal Manufacturing Techniques. There are several AM techniques available for the production of metal components, although following some research and a preliminary tender exercise, the selection was reduced to two main techniques. These were selective laser melting (SLM) and direct metal laser sintering (DMLS). The key difference between these two fairly similar techniques is that in SLM, the material is fully melted rather than sintered, allowing different properties (crystal structure, porosity, and so on). Both techniques work by building up fine layers of material (in the form of a powder) that uses a laser to fuse the powder grains together (see figure 1). Once one layer is complete, the excess powder is removed and a new layer is applied. This process is repeated until the required geometry is achieved. As the technique builds components layer by layer, it allows highly complex and intricate geometry to be produced. The term additive manufacture stems from the fact that material is added and not removed as with conventional machining. AM techniques offer several potential benefits when compared to the standard conventional production techniques; greater freedom in possible geometry, potentially reduced manufacture time, potential cost savings and components can be produced directly from CAD data. These are benefits that clearly would interest to any designers of moderator vessels, but particularly of interest is the additional freedom in available geometry and the novel concepts this may allow.

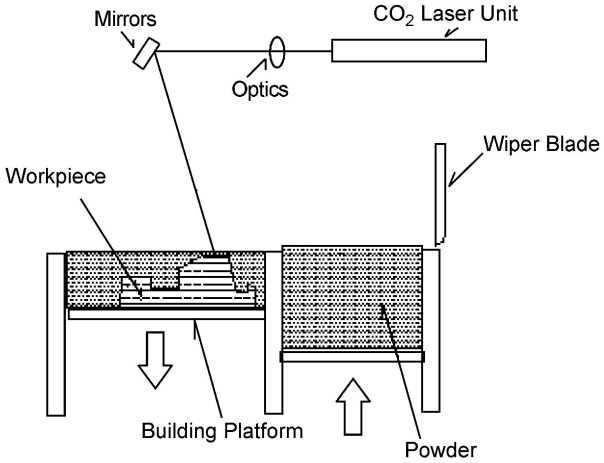

Figure 1. A schematic showing the principle behind AM techniques for the production of metal components [1]

It is however understood that AM techniques are by no means a perfect solution and part of the investigations carried out by the team at the ISIS were to try and better understand how some of the disadvantages of the techniques affect its potential application within the spallation neutron environment. Some of the main disadvantages that cause concern for moderator designers are; the

grades of materials currently commercially available as well as suitable for AM process are limited, there is virtually no pre-existing material data from radiation environments to base lifetime calculations or irradiation damage effect estimations on, AM techniques produce a lower quality surface finish (directly from the manufacturing process) when compared to machining, there is less familiarity with residual stresses in the material and there are questions over whether the tight dimensional or geometric tolerances and consistent material thicknesses often required by the design of moderators, can be achieved.

1.2 ISIS moderator vessels

The ISIS facility operates two target stations with a total of six moderators (excluding pre-moderators). As these moderators are optimised for a variety of scientific requirements they vary in geometry, size and moderating material. Target station 1 (TS1) currently features four neutron moderators; one liquid hydrogen (LH_2), one liquid methane (LCH_4) and two poisoned ambient water moderators. They are arranged in the configuration shown in figure 2, below. They are positioned above and below the TS1 target and serves a varied suite of neutron instruments. Target station 2 (TS2) operates with 2 moderators; a decoupled solid methane and a coupled liquid hydrogen moderator. These are again arranged above (decoupled) and below (coupled) the target.

ISIS has an on-going programme looking at improving operational and scientific performance of the current moderators and developing the 'next generation' of moderators for the facility. One of the driving factors in looking at AM techniques for the potential production of moderators vessels was to give the ISIS neutronics team greater geometrical freedom for their moderator concepts.

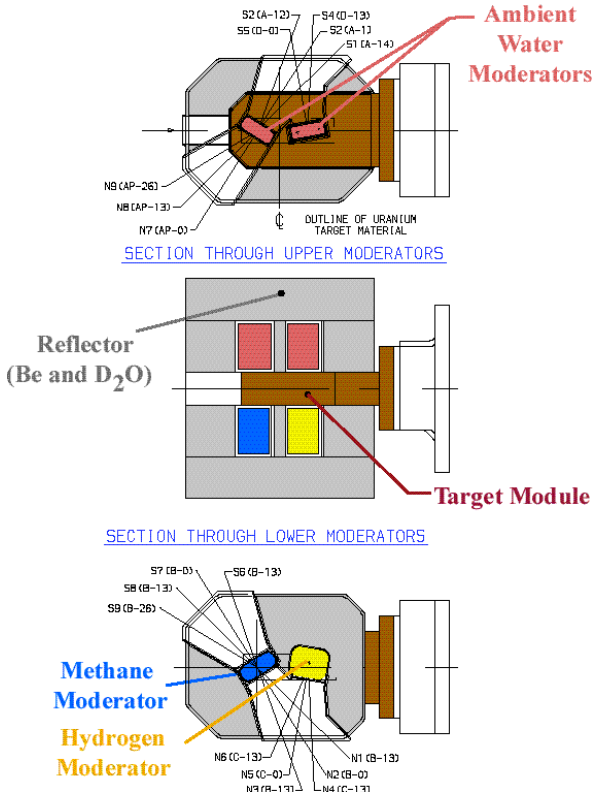

Figure 2. Showing the layout of the ISIS TS1 moderators

2. Assessing the suitability of additive manufacturing

The aim of the initial part of the investigation was to try and develop understanding of components made via AM techniques, to address some of the disadvantages listed in the introduction and to try and provide answers to some basic fundamental questions, namely, can we produce a vacuum leak tight vessel, can it withstand working pressures seen at ISIS and are the neutronic transmission and scattering characteristics of these components acceptable?

Two 'streams' of testing were pursued in parallel; one focussed more on mechanical performance and property testing and the other with a neutronic behaviour focus. These two testing streams are discussed in more detail in the paragraphs below.

2.1 Mechanical property testing

The first part of the investigation was a basic proof of technology test by having a full-scale TS2 decoupled moderator vessel (including pipe connections) manufactured (see figure 3) using an AM technique, in this case, SLS. With this successfully achieved a test procedure was drawn up. The procedure laid out the basic tests to be carried out and covered leak checks, pressure cycling, cold shock followed by a room temperature leak test, a burst test, weld tests on the samples machined out of the vessel following the burst test and mechanical property testing also carried out from sample taken from the ruptured vessel.

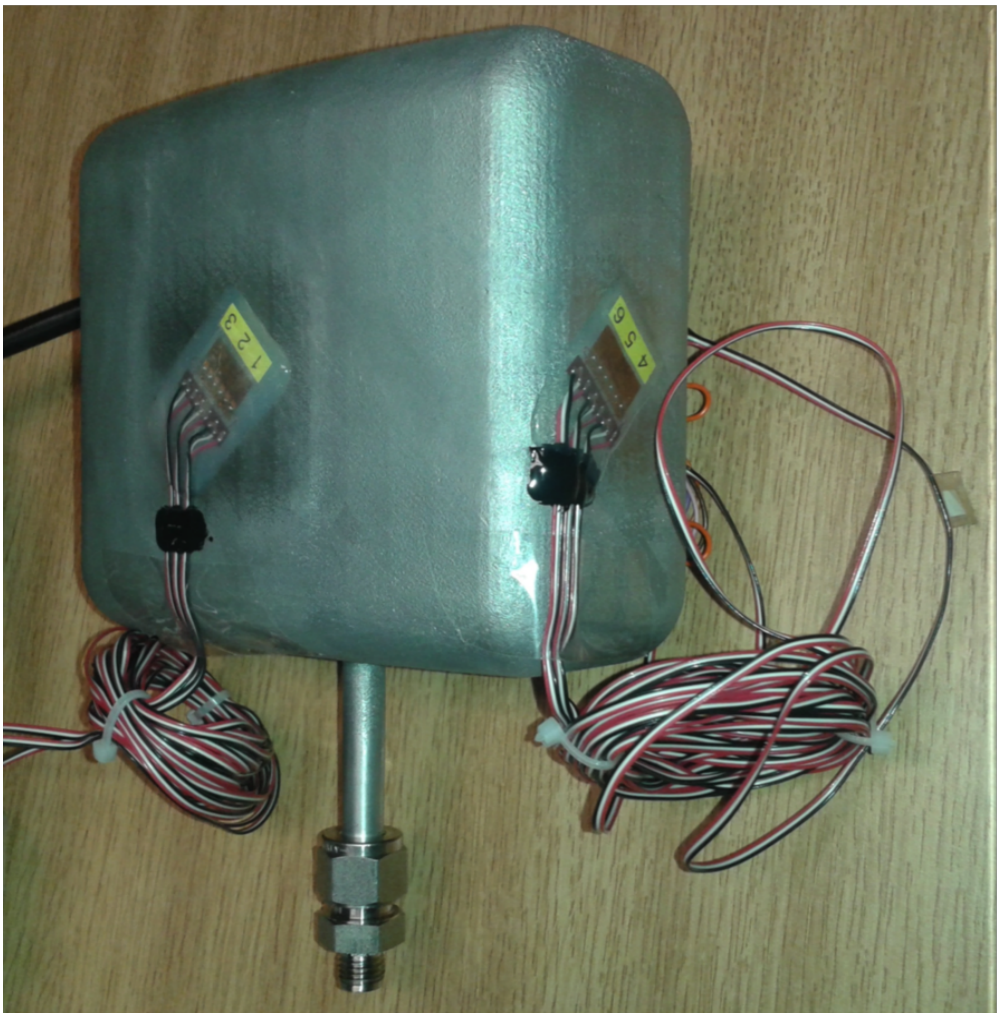

Figure 3. *Additive manufactured (AM) TS2 decoupled moderator can with strain gauges applied, before cyclic pressure testing.*

2.2 Neutronic testing

The focus of this part of the investigation was to assess the impact, if any, of the variations between aluminium vessels made by conventional techniques and those made by AM techniques. Some of the postulated differences might arise from; the material grades readily available for use with AM processes, different internal stresses generated from the manufacturing and post treatment processes the orientation of the metals grains and crystallite sizes.

A series of simple geometry samples were manufactured using both major AM techniques for metal, SLS and DMLS. Coupled with this were two variations in temperatures at which these techniques were carried out, two different post-manufacture heat treatments and two post-production surface treatments. The full list of samples and the processes applied to them is shown in Table 1. Included in the test were two samples of conventionally machined aluminium 5083 grade to act as a reference to the current material used at ISIS for the moderator vessels. The samples were provided in individual, marked bags to ensure some element of a 'blind test'. It is worth noting that compared to all the AM samples the conventional aluminium samples were very easy to spot, even by an untrained eye.

The samples measuring 20 x 20 x 4 mm were then put onto the LOQ instrument at ISIS, allowing small angle neutron scattering (SANS) measurements to be taken.

Table 1. A Table listing the information on the different AM specimens tested as part of the neutronic tests

TS-1 AM Test Samples

Sample Code	Source	Alloy	Process	Post Treatment	Surface Treatment
A	3T	AlSi10Mg	Direct Metal Laser Sintering (Hot Worked*)	None	None
B	3T	AlSi10Mg	Direct Metal Laser Sintering (Hot Worked)	None	Ceramic Blast
C	3T	AlSi10Mg	Direct Metal Laser Sintering (Cold Worked)	None	None
D (D2)	3T	AlSi10Mg	Direct Metal Laser Sintering (Cold Worked)	Stress-relieved (300C for 2 hours)	None
E	R12	5083	Machined	None	As machined (0.8)
F	R12	5083	Machined	None	As machined (0.8)
G	TWI	AlSi10Mg	Selective Laser Melting	None	None
H	TWI	AlSi10Mg	Selective Laser Melting	Stress-relieved**	None
I	3T	AlSi10Mg	Direct Metal Laser Sintering (Cold Worked)	Stress-relieved (300C for 2 hours)	Light Ceramic Blast
J (C2)	3T	AlSi10Mg	Direct Metal Laser Sintering (Cold Worked)	None	None
K	TWI	AlSi10Mg	Selective Laser Melting	Stress-relieved**	None
L	TWI	AlSi10Mg	Selective Laser Melting	Stress-relieved**	None

an anneal

*At 3T, there are two different process options. The product can be ran at 200C whilst sintering and hence, is stress relieved during the process. If cold worked, the process runs at room temperature and internal stresses are produced during sintering. 3T would then normally advise customers to have further heat treatments, like sample D.

** All TWI parts were created using the same parameters, parts 1-5 (G) are un-heat treated and parts 6-10 (H, K, & L) are heat treated. The stress relieve was **an anneal** for 2 h at 300 °C (572 °F).

3. Results

The aim of the initial part of the investigation was to try and provide answers to the questions of 'neutronic transparency' and mechanical viability.

3.1 Mechanical property testing results

A TS2 decoupled moderator vessel was successfully manufactured in aluminium using an AM technique (see figure 3) in 2012. The vessel has since been leak tested at room temperature with a mass-spectrometer to $5x10^{-8}$ mbar.litres/s, before it was subjected to a 'cold shock' test (submersion in liquid nitrogen). The leak test was then repeated, with identical results. This shows that despite some initial reservations, the AM technique was able to produce and acceptably leak tight vessel.

The vessel was twice cycled from atmosphere up to 6 bar(a) and while strain readings were taken from two strain-gauge rosettes; one positioned in the centre of one of the large faces and one positioned in the centre of a smaller side face. These data gained was used to calculate a maximum principal at the centre of the larger face (worst case) of 91MPa.

3.2 Neutronic testing results

It was felt that the easiest way to demonstrate clearly the observed differences between the various test specimens was to use the graph shown in figure 4 below.

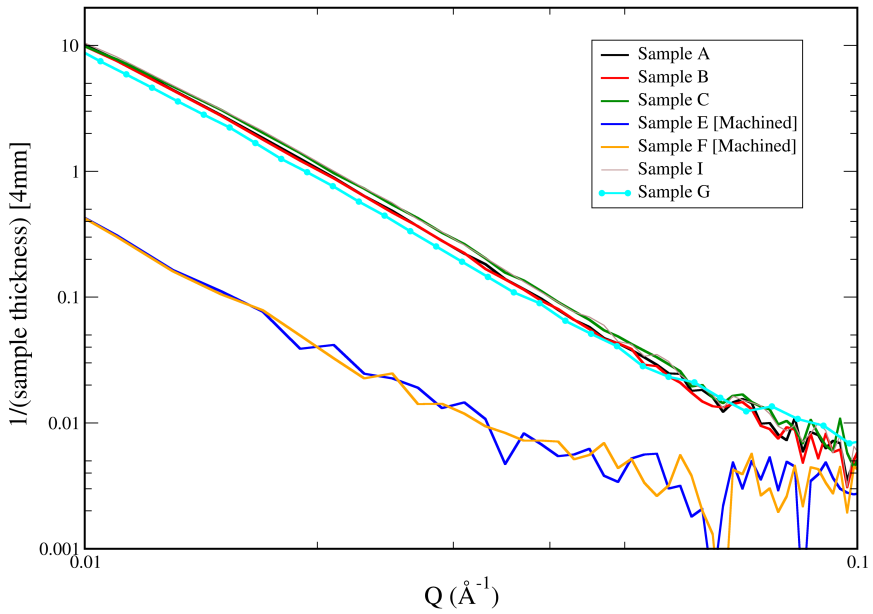

Figure 4. A graph showing the difference in small angle scattering between a representative selection of additive manufactured specimens and the standard machined aluminium reference specimens.

The graph illustrates that the AM specimens are significantly less 'transparent' to neutrons when compared to the two machine aluminium specimens. It is postulated that at least some of the observed difference may be down to composition differences between the AlSi10Mg grade used for the AM specimens and the Al5083 grade used for the machined specimens. Another postulated cause is the difference in inter-granular spacing and grain size.

Due to the log scale on the y-axis, it also shows that there is enough variation between the various specimens, to warrant further investigation (sample G can be seen to clearly sit below the lines of the other selected specimens displayed on the graph). In addition, with the postulated link to grain size

being a potential contributing factor and there being several available techniques for altering grain size in the AM specimens (both larger and smaller) the team is optimistic that further improvements can be made.

4. Future work

4.1 Correlating finite element analysis results to empirical pressure testing data

In order to provide a high level of confidence in future simulation results, a finite element analysis (FEA) model has been created and work is continuing to ensure this is robust and fully mesh independent. The model is being benchmarked against the measured data gained from the repeated pressure testing. It was decided to finish this modelling work before carrying out a burst test on the full moderator can, in case additional pressure testing could provide useful secondary results.

4.2 AM vessel burst test

It is planned for the team to carry out a recorded (using high-speed cameras) and instrumented burst test on the AM vessel. This will provide insight into the mode and position of any failures as well as the total pressure required to burst the vessel. This information can be compared with similar results from similar previous tests carried on moderator vessels produced via conventional methods.

4.3 Post-burst test mechanical testing

Once the vessel has been burst, then samples will be machined out of the remaining material and used for a variety of mechanical property (e.g tensile testing) and welding tests. Again these results can be compared back to know references. The break will also expose the structure and how it fractures (either brittle or ductile).

4.4 Continuation of neutronic behavior characterization and viability testing

At the time of writing, ISIS, is currently in a planned long operational shutdown. Therefore there is no current access to beam time in order to carry out further SANS testing. It is planned that when the facility is running again that the observed, if only slight, differences between the two AM techniques that was shown by the first round of testing , will investigated further. It is also a potential that samples could be tested on ENGIN-X to look into possible correlations between internal stresses and neutron transparency. There is also the potential to develop the AM techniques to work with more standard engineering grades of aluminium, such as Al5083 and Al6061.

5. Conclusions

It is clear that there are some strong benefits offered by AM techniques that could be exploited by moderator vessel designers. What our initial investigations have shown can be roughly concluded as follows:

- Initial indications (leak tightness and max. principle stress) show technology is mechanically viable
- The effect of the manufacturing process on neutronic performance and suitability for radiation environments is yet to be fully understood – work on-going

There is much still to learn in this interesting and rapid developing field. ISIS is very open to joint projects and collaborations, so if you are interested then please feel free to contact the author.

6. Acknowledgements

The work presented here in this paper and in the accompanying presentation is the combination of a great deal of time and effort by a large number of ISIS' staff. I would like to acknowledge some of the main contributors to the project here (listed in alphabetical order); Stuart Ansell, Sean Higgins, David Jenkins, Eamonn Quinn, Colin Souza, Stephanie Thomas and Liam Whitelegg. It is due to the

dedication and commitment of its' staff such as those listed above that ISIS remains such a productive and scientifically important facility.

7. References

[1] http://fabribles.com/community/forum/tech/49-direct-metal-laser-sintering-dlms

3.2.17

Water helium mixture for use in neutron sources as premoderator, coolant and for leak detection at the same time

Y. Beßler[1], M. Butzek[1], G. Natour[1], R. Linander[2]
[1]Forschungszentrum Jülich GmbH
[2]European Spallation Source ESS AB

E-Mail: y.bessler@fz-juelich.de

Abstract. Subject of the present report is the investigation of the feasibility of using helium as tracer gas for leak detection for a water system in close vicinity to a cryogenic surface.

In order to minimize the heat load to the hydrogen moderator, a vacuum isolation is necessary. This is achieved by adding a second vessel that surrounds the cold moderator. Due to excessive nuclear heating the second container wall has to be actively cooled. This cooling can be realized by the water used as a premoderator. A leak in any of the vessels must be possible to detect by the machine protection system and the target safety system, in order to take appropriate action to prevent further unacceptable consequences. The following scenarios are possible: In case of a big crack in one of the two vessels the vacuum would collapse and thus the situation would be detected. For capillary cracks in the moderator vessel small amounts of hydrogen will flow into the vacuum gap and vaporize. These hydrogen molecules can be detected at the vacuum pump. However, for capillary cracks in the vacuum wall small amounts of water would flow into the vacuum gap. The water would vaporize first and then freeze out as soon as it gets in contact with the cold surface of the liquid hydrogen moderator vessel. Thus, a layer of ice can build up until it forms a thermal bridge. In this case, the vacuum would not collapse and no detectable gas will reach the vacuum pump. Such a crack can therefore remain undetected. In order to handle the last mentioned case the basic idea is to mix the water of the premoderators with small amounts of helium. Thus, the helium and water mixture may be used simultaneously as a premoderator, as a coolant and as a leak detection mechanism. The ongoing studies will show whether it is feasible to inject helium into the water system, that helium will not freeze out together with the water and that it will find its way to the detection system at the vacuum pump.

1. Introduction

In the present report, some incident scenarios for the cold LH2 moderator system are considered and measures to remedy the situation are discussed. This consideration has focused on the pressure vessel of the cold source and possible leakage of the used fluids due to assumed cracks in the structure material. Such incidents can only be controlled sufficiently, if they are detected as soon as possible. Fig 1 shows a simplified horizontal section through the cold Moderator vessel including vacuum insulation and thermal Moderator.

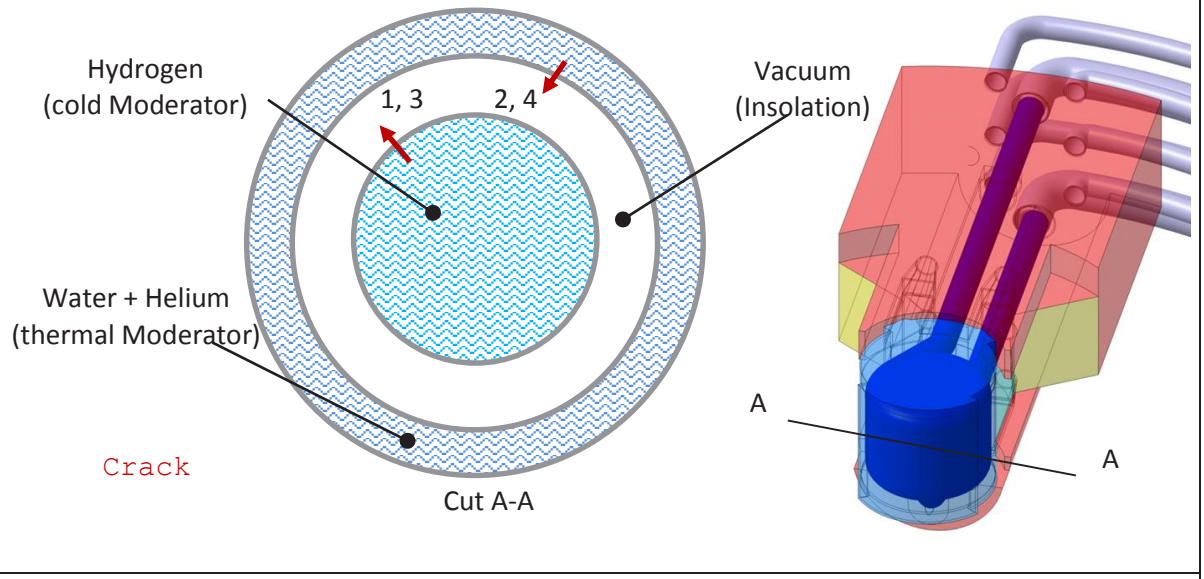

Figure 1. Simplified sectional view of the cold and thermal Moderator

We assume that the insulation vacuum is permanently pumped. At the vacuum pump measuring devices are installed which allows the detection of H_2 and He. A distinction is made between the following four incidents:

1 **Large cracks in the inner vessel wall (cold Moderator):**
A large amount of hydrogen flows into the vacuum gap. The vacuum collapses. This can be detected at the vacuum pump. Measures can be taken.

2 **Large cracks in the vacuum wall (inner wall of the thermal Moderator):**
A large amount of water flows into the vacuum gap. The vacuum collapses. This can be detected at the vacuum pump. Measures can be taken.

3 **Hairline cracks in the vessel wall (cold Moderator):**
Small amounts of hydrogen flows into the vacuum gap and evaporate. The hydrogen molecules can be detected at the vacuum pump. Measures can be taken.

4 **Hairline cracks in the vacuum wall (inner wall of the thermal Moderator):**
Small amounts of water flows into the vacuum gap. The water evaporates and freezes at contact with the cold surface of the Moderator. It forms a layer of ice, potentially building a thermal bridge. The vacuum does not collapses and no detectible gas can be found at the vacuum pump. Accordingly, measures cannot be taken.

Since incident four cannot be controlled without additional measures, in the following, a solution for this purpose is investigated. The basic idea is: Adding a gas to the water of the thermal Moderator up to the solubility limit and use it as a leak detection gas. The gas should not condense or freeze out while in contact with the cold moderator surface (20 K), so that it can be detected at the vacuum pump. The only gas fulfilling this requirement this is helium, because it is the only substance that remains a gas at the present conditions. The disadvantage is that helium has the lowest solubility of all gases (at 20°C and 1 bar are 1.5 mg helium in 1 kg water soluble). Therefore, first it should be demonstrated that the helium can be reliably and homogeneously dissolved in the water. In a second step, it has to be shown that the helium actually reaches the measuring device or if it is probably trapped by the water that freezes on the cold surface.

2. Measurement setup

Figures 2 and 3 are showing the test setup:

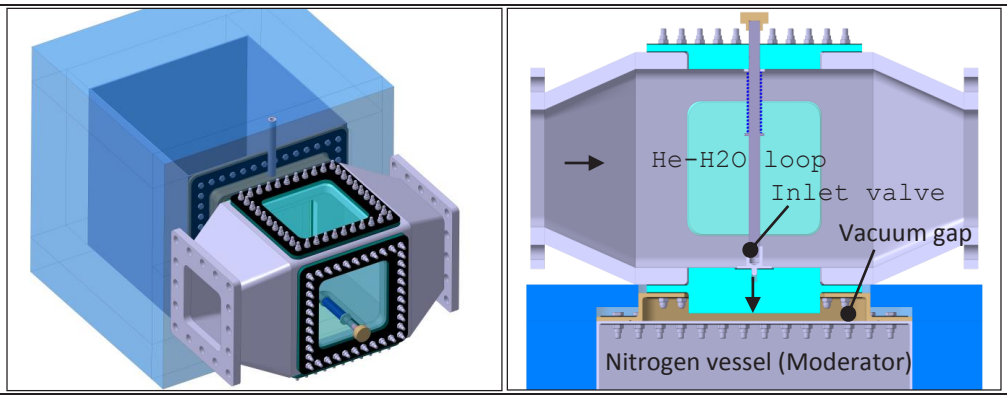

Figure 2. He leak detection test setup, left isometric CAD view, right CAD sectional view

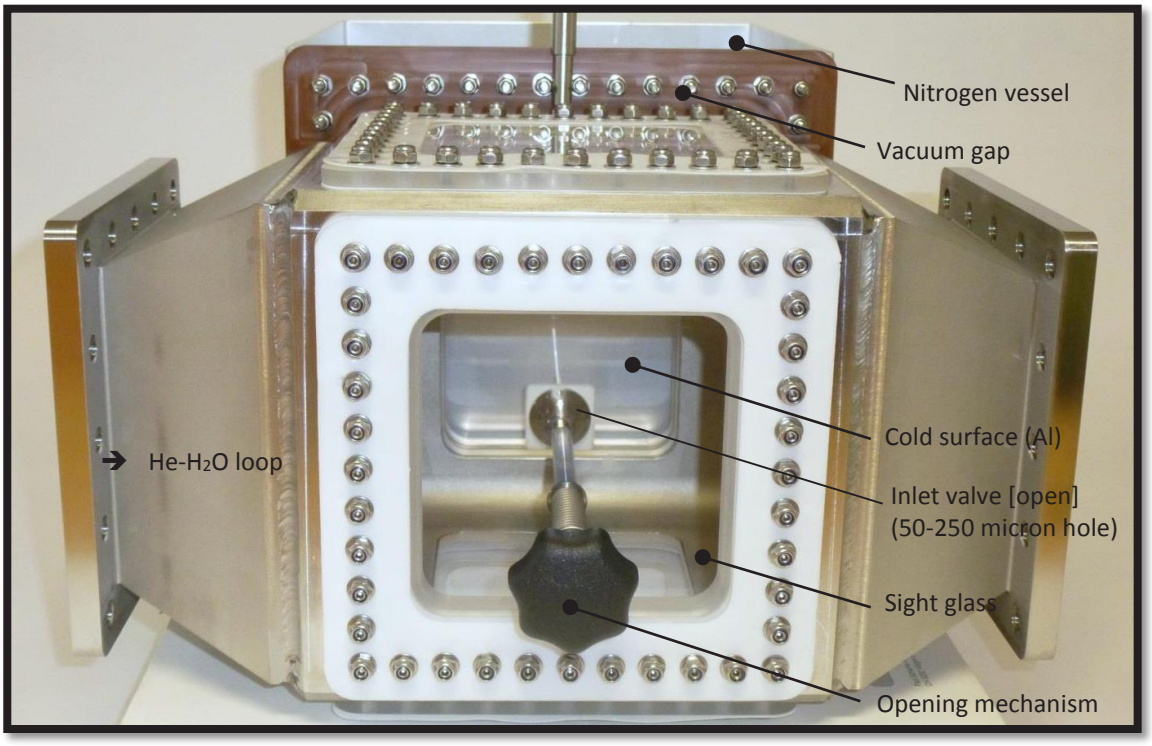

Figure 3. He-leak detection test setup during pre-assembly of the module

To simplify the test setup a liquid nitrogen filled, insulated Aluminium vessel is used as a substitute for the Moderator. The H_2O-He loop and the liquid nitrogen vessel are connected leaving a space to be pumped down simulating the 5 mm vacuum gap. The resulting space is constantly evacuated and monitored for helium gas. The rectangular channel with flowing H_2O -He mixture is equipped with an adjustable valve, which can be operated from outside the channel by a rotary knob. Cracks of various sizes (50 microns to 250 microns) are simulate by micro drilled holes in the glass wall between H2O-He and vacuum. When the valve is open, a portion of the H_2O -He mixture enters the vacuum space. To observe the behaviour of the water vapour and ice formation, the thermal Moderator loop is

equipped with quartz glass windows on all four sides. The window between the vacuum chamber and the fluid loop includes a recess for the interchangeable "cracks" that were laser cut into small quartz glass plates (see fig. 4).

Figure 4. Microscope picture of one of the "cracks" (50…250 μ m)

A mobile He injector provided by the company DELU AG is used to inject the helium. Originally, this system was developed for leak detection of underground supply lines. Helium can then be detected above ground helping to determine the location of the leak and thus reduce the amount of necessary excavations. With this system, the helium can be permanently injected and measured up to the solubility in water.

The mixture was circulated in a closed loop under a slight overpressure. The helium was injected in a bypass. Figure 5 shows the assembled test setup.

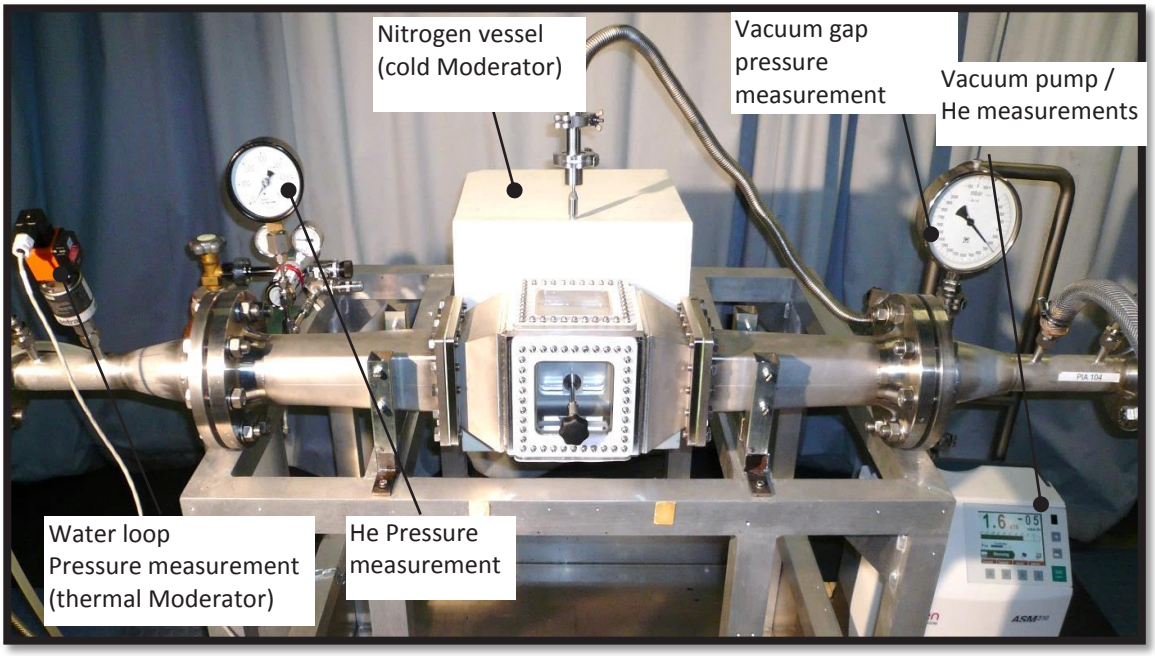

Figure 5. He- leak detection test setup with helium injector (provided by DELU AG)

3. Experimental results

The first test was performed without cold surface, i.e. the nitrogen vessel was not filled. Helium was injected up to the solubility limit in the water. After the valve is opened briefly, the mixture entered into a vacuum gap. The water is evaporated (see fig. 6) and helium could be reproducibly detected at the vacuum pump. This experiment was performed three times.

Figure 6. Incoming water helium solution evaporates due to the vacuum. Helium frees itself from the solution and can be measured

In the second test, the nitrogen vessel was filled with liquid nitrogen and cooled down to about 77 K. Helium was injected up to the solubility limit in the water. Then, the valve was opened again shortly for a few seconds. The mixture entered the vacuum chamber, the water froze immediately on the cold surface and the helium was again detected reproducibly at the vacuum pump (see fig. 7). This experiment was also repeated three times.

Figure 7. On the cold surface of the "moderator" frozen water. Helium diffuses through the ice and can be measured

In the third and last set of experiments, the nitrogen vessel was filled and cooled down. This time plain water was used instead of a H_2O-He mixture. The valve remained permanently open during this experiment. Water entered into the vacuum gap forming a large ice layer on the cold surface. After some time the ice bridged the entire 5 mm vacuum gap and consequently the leak was blocked (sealed) by the formed ice. Surprisingly this did not lead to a destruction of the glass wall from the vacuum side towards the water. After the leak was self-sealed by the freezing water, helium was injected into the water loop. Soon after this, helium was detected at the vacuum pump. This experiment showed impressively that, first, forming ice do lead to building a thermal bridge but did not lead to immediate destruction of the structure. Second, the helium was able to diffuse through the watertight ice block still allowing detection of the crack.

For conclusion figure 8 shows the so-called "soda pop" effect. As soon as the system pressure is reduced, the solubility of the helium is also decreased. Thereby helium gas bubbles are forming in the water. This is a sign for the water to be well saturated with helium. As soon as the system pressure increases again, the injector automatically feeds helium back into the water up to the solubility limit.

Figure 8. Helium fog (detection gas) results from pressure reduction

4. Summary & Outlook

The report showed that a leak detection system with the used components is possible in principle for using in the ESS facility. For secure and automated operation, it is however, necessary to make some modifications of the Helium injector used. For that, the manufacturer of the injector (DELU AG) is ready to cooperate. The following modifications are necessary for ESS:

- automation of the system, currently an operator directly at the system is necessary
- scaling of the injector, depending on the water pressure and loop volume
- definition of the circuit implementation, in the main loop or in a bypass (bypass takes longer but has lower pressure loss)

3.2.18

Engineering developments of the ESS Moderator and Reflector systems

Daniel Lyngh, Rikard Linander

European Spallation Source, P.O Box 176, SE-221 00 Lund, Sweden

daniel.lyngh@esss.se

Abstract. The on-going project for construction of the European Spallation Source (ESS), the 5 MW long-pulsed neutron research facility in Lund, Sweden, has entered the phase in which design work and development are focused on realising solutions that shall satisfy well-defined requirements. The Target Station, which converts the pulsed proton beam delivered by the linear accelerator to cold and thermal neutron beams tailored for neutron science applications, consists of several systems. Each of these elements offers unique design challenges for the engineering teams both in terms of providing the necessary primary function and in satisfying complex requirements for physical and functional interfaces between systems. The Moderator and Reflector systems are a central part of the ESS and directly impact the overall performance of the facility. These are defined as the plug holding the neutron moderators and reflectors as well as the associated cryogenic fluid and refrigeration systems. The recent development of the neutronic design of flat moderators and their application and use by the neutron scattering systems has called for a re-engineering of the moderator and reflector systems for the ESS. In addition, this novel moderator concept has a major impact on the layout of the monolith and the remote handling procedures. This paper presents the ESS Moderator and Reflector systems from the engineering perspective. Different aspects of the moderator concept chosen for ESS are addressed, focusing on the latest progress of the development work.

1. General description Target Station

The function of the target station is to convert the intense proton beam from the accelerator into a number of intense neutron beams. This conversion is achieved by the interplay of a number of basic functions. In the heavy metal target the impinging proton beam radiation from the accelerator is converted via the spallation process into fast neutrons as the useful product, while generating a large amount of heat, radioactive isotopes and prompt radiation as unavoidable by-products. The moderator-reflector assembly surrounding the target transforms the fast neutrons emitted by the target into slow neutrons, which are the final form of useful radiation provided by the neutron source, while further radioactive waste is produced by the absorption of neutrons by various target structures. (Here, “fast” means neutrons with velocities in the range of 10% of the velocity of light and “slow” means velocities comparable to the speed of sound.) These two neutronically active systems are surrounded by a radiation shielding system of approximately 7000 tons of steel, in order to contain the extreme level of highly penetrating gamma and fast neutron radiation created in the target and its vicinity. The beam extraction system provides intense slow neutron beams through beam guides, which traverse the target shielding. These neutron beam guides are accessible at the surface of the shielding, for delivery to and use at the neutron-scattering instruments facing the beam ports at variable distances. The proton

beam window separates the high vacuum in the accelerator from the atmospheric-pressure inert helium gas inside a large container vessel, in which all of these systems are housed. They form, together with the tight container, the target monolith, which takes the shape of an 11 m diameter and 8 m high cylinder.

At ESS, the proton beam will deliver 5 MW power in the form of kinetic energy. About 10% of this energy is converted to mass through the nuclear reactions in the spallation process that produces neutrons, other nuclear fragments, isotopes and gamma radiation. The energy of these particles makes up the remaining 90% of the proton beam energy, and it is almost all deposited within a distance of 1 m from the site of proton beam impact in the target. Different cooling circuits in the target monolith remove this large amount of heat from the target itself (3 MW), from the moderator-reflector assembly (1.2 MW) and from the monolith shielding (0.3 MW). The proton beam window is directly heated by the traversing beam and requires cooling of about 6 kW, though this value is strongly dependent on window design details.

Radiation damage and fatigue limit the lifetime of the three most strongly affected systems: the target, the reflector-moderator assembly and the proton beam window. All of these systems will need to be changed multiple times during the lifetime of the facility, with frequencies ranging between 6 months and 5 years, as conservatively estimated on the basis of available experience at spallation sources. The removed used components represent a considerable amount of radioactive waste. The other part of the radioactive waste consists of gases, volatiles and airborne particles, which will be continuously captured by a variety of efficient filters and traps.

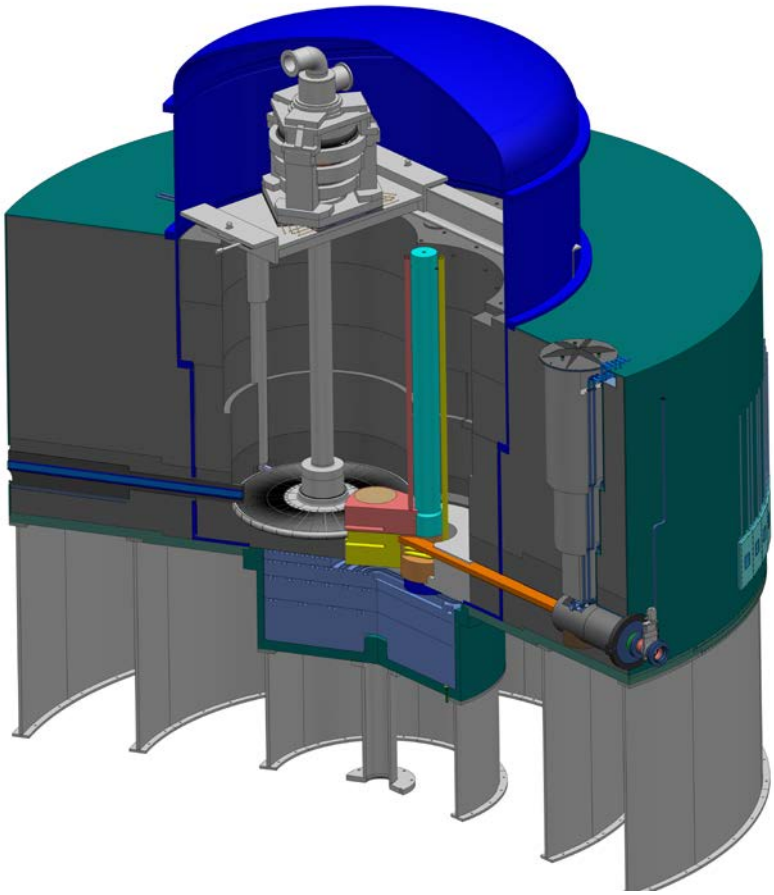

Figure 1 Monolith with Moderator & Reflector Assembly Inside

2. IMPROVEMENTS ON MODERATOR & REFLECTOR ASSEMBLIES

2.1. Flat Moderator Design

The ESS Target station has, as a result of the promising development and implementation of the Flat Moderator design, developed an engineering solution to handle the novel design significantly.

The size of the liquid hydrogen moderator is according to the current conceptual optimization at a height of 3 cm and diameter of approximately 24 cm. The cold moderator is enclosed within a vacuum chamber for insulation and placed above a flat 3 cm thick water disc acting as thermal moderator. The disc is connected to the water wings pointing out angular against the beam lines horizontally adjacent to the cold moderator allowing the instruments to align their view both the cold liquid hydrogen moderator as the well as the thermal water wings. Outside of the liquid hydrogen moderator sits a second thermal moderator flushed with water, see figure 2.

Both the outer thermal moderator and the liquid hydrogen cold moderator are designed with a serial flow pattern to allow even gradual temperature deposition through the tanks.

The reflector surrounding the moderator assembly is filled with beryllium blocks enclosed in the aluminium tank continuously flushed with cooling water.

In the concept design it is anticipated that all shells, tanks and components will be manufactured out of Al 6061-T6.

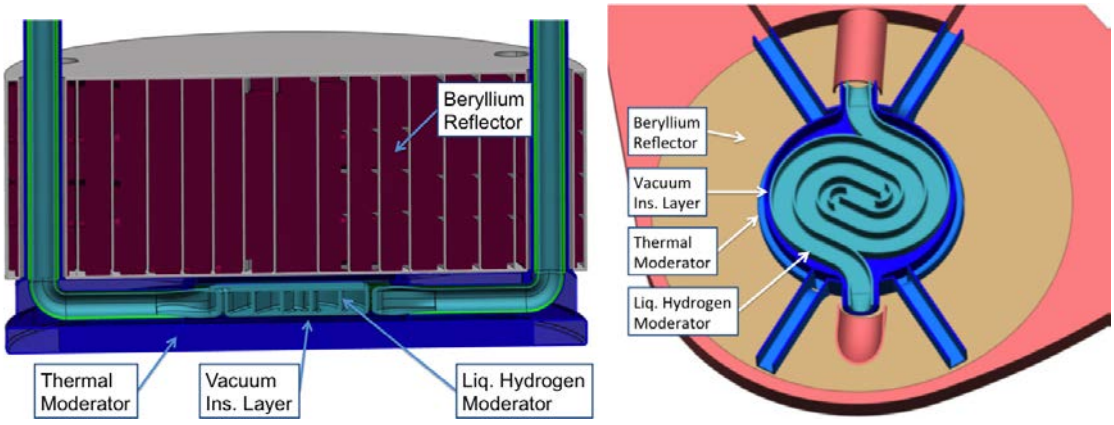

Figure 2 Flat moderator design concept

2.2. Moderator & Reflector Plug

Engineering development of the concept design has aimed towards a design of a plug that can assemble and hold a typical moderator and reflector assembly within the defined envelope, ensure a managed pipe-routing and the possibility to handle installation and removal of the plugs in/out of the monolith operational position in an effective and controlled way. Calculations have shown that a size of 70 cm for the assembly of the moderators and reflectors should be adequate still allowing changes in the detailed moderator design up to a level that could be reasonable to expect coming out of the development and experience that will be collected during commissioning and initial operations. Based on those calculations a plug was developed that could fit different combinations of moderators and reflectors of different designs and materials within this defined envelope. The plug concept thereby allows for changes in moderator type from a flat design to tube design or other moderator geometries.

The plug's design and support structure allows viewing of moderators up to 120 degrees in two directions, see figure 3, however certain moderator designs performs better with narrower viewing slots.

ESS has with the engineering design the possibility to further develop and update the moderator as neutron science progresses and new innovations are discovered without having to do major modifications of the target station. Thereby being prepared to without extensive modifications allow

implementation of new ground-breaking developments to continue to improve performance of the neutron source.

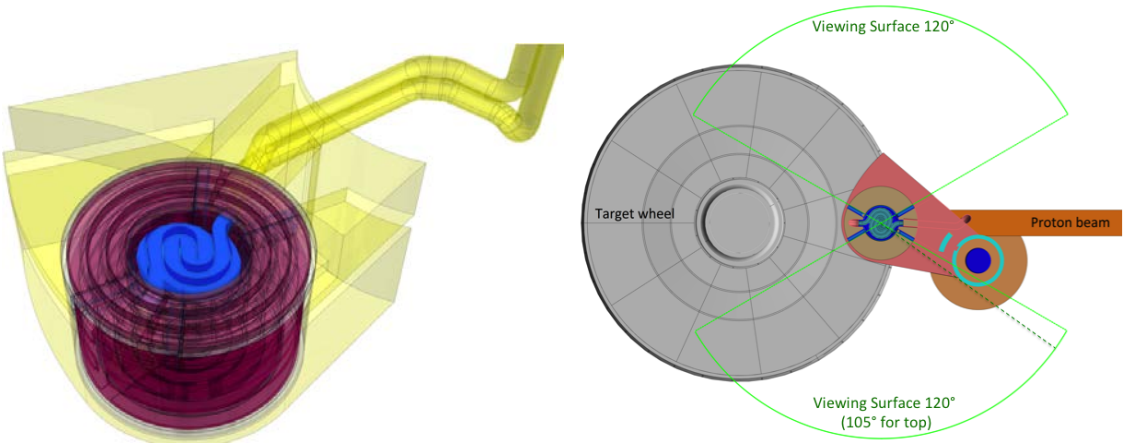

Figure 3 The lower MR assembly (left) and indicated possible viewing angles (right) for neutron science instruments

2.3. Moderator and Reflector Plug Configuration

An assembly concept design has been developed to include the new moderator and plug concept with the purpose of, being able to in a controlled and smart way of install and remove the moderator plugs, while allowing the surrounding structure and target wheel to remain in place to a large degree. The sequence of operation for replacing the moderator plugs permits exchanging them more often than the other adjacent components as the moderators will most likely be expected to have a shorter lifespan.

The two plugs can be introduced or removed independently from each other, see figure 4, by rotating the individual pipe and bracket holding each plug before attaching a custom lifting fixture that will take it of the support pipe and up into the transport cask for transfer to the hot cell. As the plugs are independently supported this allows for different exchange periods for each of the moderators enabling plugs with completely different designs i.e. lifetimes.

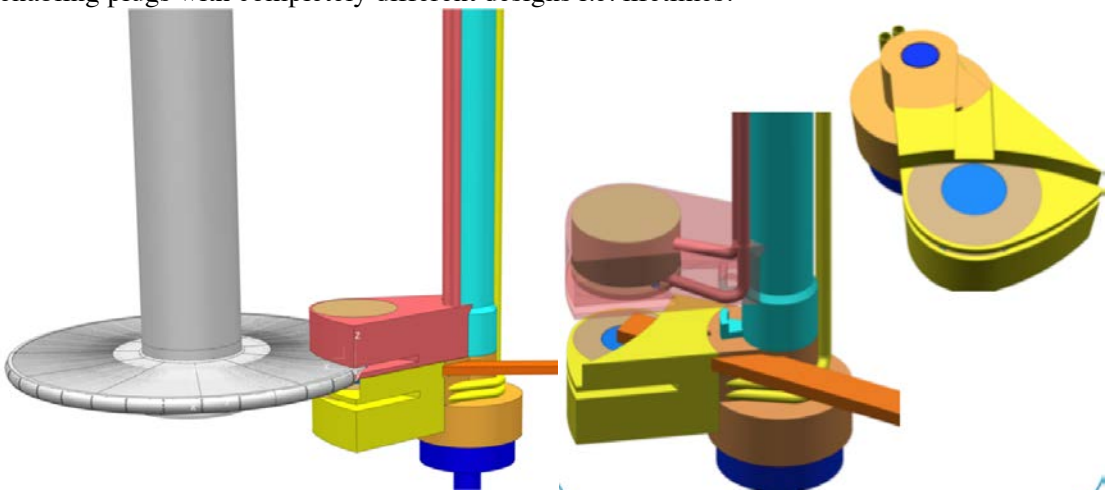

Figure 4 Configuration of the moderator and reflector plugs relative the target

2.4. MR Plug Handling System

The illustrations in figure 5 show the sequence of removing both moderators while keeping the target wheel and surround structure in place. Each of the MR Plugs is attached to a rotating support-pipe, the

two support-pipes, one for each MR plug, are supported on each other and together on a stiff axis that has its foundation into the monolith foundation.

Shielding blocks will need to be removed to let each of the plugs to be rotated from operational position into service position, and then lifted up. Pipes are permanently connected to each of the plugs and belong to the plug assembly. As the plugs are introduced or removed the pipe-bundle must be practically handled simultaneously with the plugs and when being installed connected to the supporting structure to prevent vibrations.

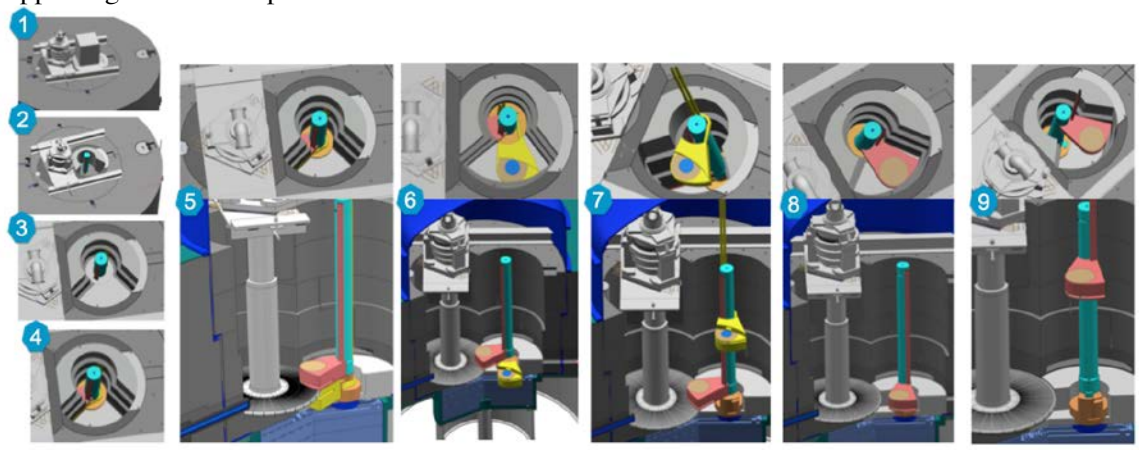

Figure 5 Handling sequence of removing both moderators

2.5. In-Kind Contribution

The construction of the ESS in Lund is strongly based on In-Kind contributions from member states. During 2014 several In-Kind collaboration meetings have been performed. Institutes within ESS member states were invited and the different work scopes presented. It is planned to reach an agreement with a European institute for taking the responsibility for the final design and delivery of several parts of the described system during first half of 2015.

References

[1] S. Peggs, “ESS Technical Design Report”, ISBN 978-91-980173-2-8.

3.2.19

Operational Experience on Utilities and Remote Handling on ISIS

David Haynes

Target Operation Group, ISIS Facility, Rutherford Appleton Laboratory

David.Haynes@stfc.ac.uk

Abstract. The ISIS Facility at RAL has been producing neutrons for science from the original Target Station (TS1 – 40/50Hz) since 1984. The second, lower power, low-repetition-rate Target Station (TS2 – 10Hz) came on line in 2008. Although the two Target Stations are different in many ways they do both have the same basic layout and the same main components:

- a moveable target, reflector and moderator (TRAM) assembly in which the neutrons are produced,
- a Remote Handling Cell (RHC) located behind the TRAM for maintenance and repair operations,
- a Target Services Area (TSA) located behind the RHC containing cooling plant and cryogenic coldboxes.

In each Target Station neutrons are produced when the proton beam from the ISIS accelerator hits a tungsten target positioned in a helium filled void vessel. Water cooling channels remove the heat generated in the target via the cooling plant located in the TSA. Moderators (ambient water, liquid CH_4, liquid H_2, solid CH_4) slow down the neutrons escaping from the target and these moderators are surrounded by water-cooled beryllium reflectors which scatter neutrons back into the moderators. In operation, all TRAM components become highly radioactive. The complete TRAM assembly (along with cooling plant, cryogenic systems and shielding plugs) is rolled back to withdraw the TRAM from the void vessel into the RHC for maintenance. The RHCs have a pair of master/slave manipulators on each side, an overhead crane which is remotely controlled, and all RHC operations are viewed through shielding windows and video cameras with zoom and focus capability. This presentation will highlight the many routine procedures such as target and moderator changes carried out over the life of ISIS, as well as more complex and unusual work such as complete reflector replacements, void vessel door seal changes, water filtration and numerous unscheduled repairs.

1. Layout and features of ISIS Target Stations.

The ISIS buildings and layout of TS1 and 2 can be seen in the aerial view in Figure 1. The ISIS 70Mev injector, synchrotron ring and building R55 (TS1) and R80 (TS2) are shown and give a clear indication of the ISIS layout.

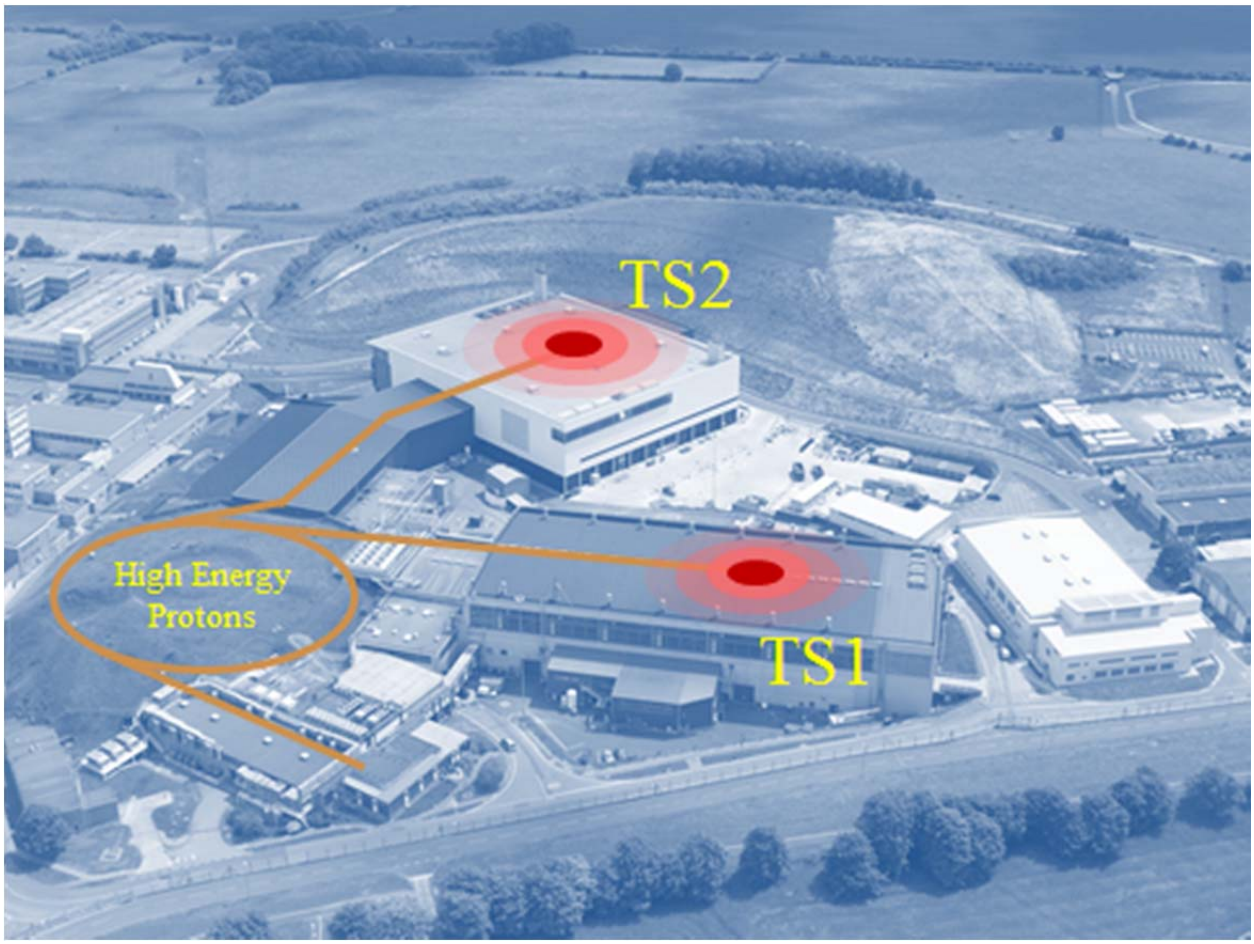

Figure 1 – ISIS Facility with TS1 & 2 Experimental Halls

The basic layout of the ISIS Target Stations is shown in Figure 2 – TS1 and 2 layouts are both the same. In each case there is a proton beam extracted from the ISIS accelerator and the beam is focused onto a Tungsten target which sits in a helium filled void vessel inside the target blockhouse and shutter array.

Neutrons produced by spallation from the target material are reflected and moderated and then pass through windows in the void vessel (nine on each side) to instruments on the ISIS beamlines.

Behind the target is a moveable shielded train with a Remote Handling Cell (RHC). There is then a secondary shield plug and then a Target Services Area (TSA) containing target cooling plant and cryogenic coldboxes for moderators, plus other equipment necessary for target operation. This arrangement allows the Target, Reflector and Moderator (TRAM) assembly to be moved back from the operating position into the maintenance position for replacement of various components using the manipulator arms in the RHC.

This basic layout and method of operation is exactly the same for TS1 and TS2.

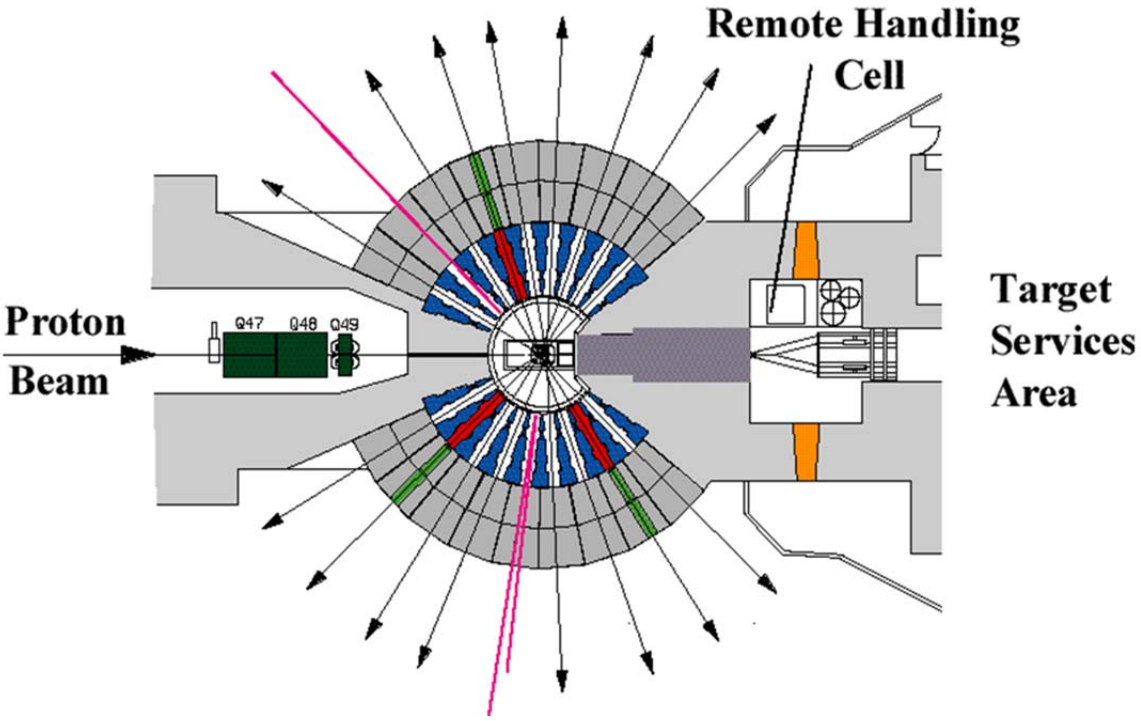

Figure 2 – Layout of ISIS Target Stations

ISIS TS1 has been in operation since 1985 and is currently operating with a target made up of 12 tungsten plates clad with a thin layer of tantalum. The ISIS Accelerator produces a 50Hz beam – 40Hz goes to TS1 and every fifth pulse from the accelerator is directed to TS2 (10Hz operation). Figure 3 shows ISIS TS1 target withdrawn into the RHC for maintenance.

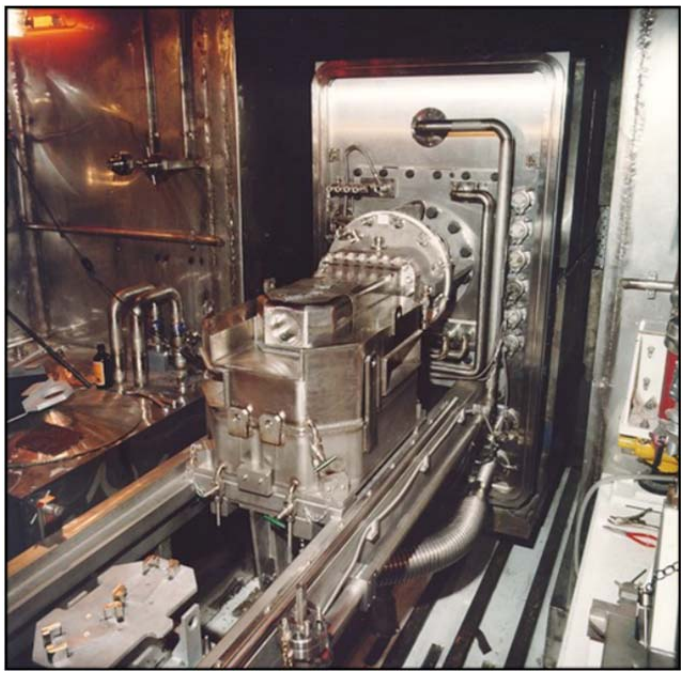

Figure 3 – TS1 TRAM Assembly in RHC

The TS1 target is cooled with D_2O. A bulk flow of 500 litres per minute is spilt between three cooling channels with more flow directed to the front target plates than to those at the rear. TS1 has four moderators, two containing H_2O at ambient temperature, one containing liquid CH_4 at 100K and one containing liquid H2 at 20K. The TS1 reflector is made up of stainless steel boxes containing beryllium rods and these rods are also cooled with D_2O.

ISIS TS2 has been operating since 2008. The TS2 target is a solid cylinder of tungsten, clad with a thin layer of tantalum and this target is cooled with H_2O. A flow of 90 liters per minute is split between two flow channels, both of which flow along the outside of the target body and across the front face where the beam hits the target. TS2 has two moderators, one containing liquid H_2 at 20K and one containing solid CH_4 at 45K. Both of these moderators are fitted with ambient water pre-moderators which sit inside the solid beryllium reflector. This reflector is edge cooled using H_2O via aluminium cooling pads clamped to the sides of each reflector half. Figure 4 shows the layout of the TS2 TRAM in the RHC with the reflector opened and rolled forward for maintenance.

Figure 4 – ISIS TS2 TRAM in maintenance position

2. A Typical Remote Handling Operation on ISIS – Removal of TS1 Target

TS1 tungsten target life is typically five years of ISIS operation. After this time the target is removed from service and stored in the ISIS Active Handling Facility (R40) prior to final disposal to Sellafield in Cumbria.

To place the target into storage it is necessary to prepare the RHC and other equipment for target removal, seal and package the target in-cell, place the packaged target into a storage flask and finally transport the flask and target to ISIS Building R40 for storage prior to final disposal. Figure 5 shows the TS1 service tunnel layout for removal of active components from the RHC.

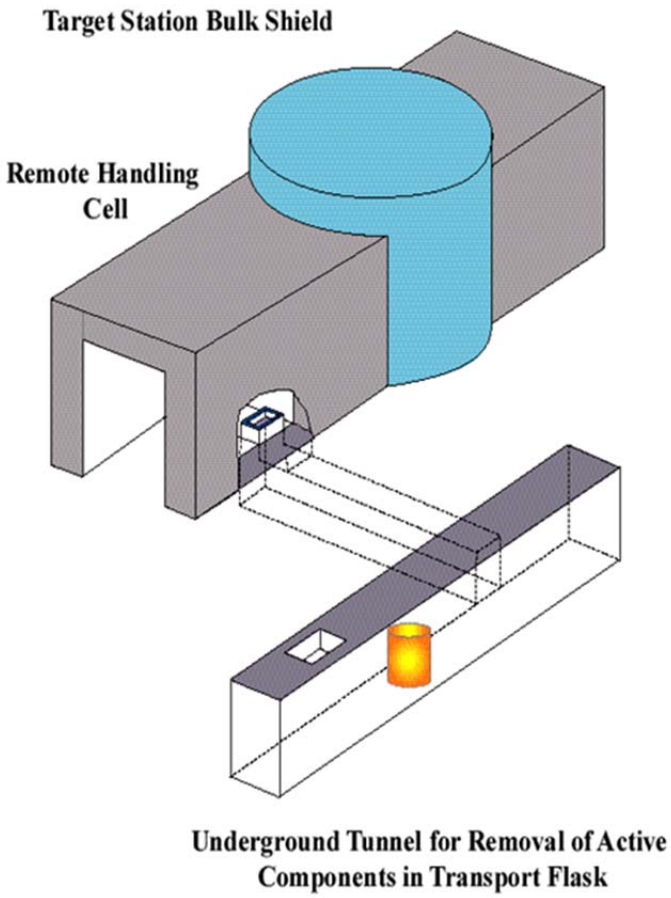

Figure 5 – TS1 Service Tunnel Layout

2.1 Preparation of Storage Flask.

A flask is prepared in R40 and is preloaded with a disposal can and flange assembly ready to be fitted to the target. The whole flask assembly is lowered onto a powered trolley in the underground service tunnel running parallel with TS1 RHC.

After positioning, the outer closure flange of the flask is removed and the flask is then transported into the cross tunnel to position it underneath the service hatch in the floor of the RHC. All operations are controlled from the TS1 Manipulator Rooms either side of the RHC.

The floor hatch is opened and the main shield plug is lifted into the RHC using the installed crane (see Figure 6 overleaf). After the shield plug has been positioned in the RHC the crane is removed and connected to an electrically driven grab mechanism that will connect with the target disposal flange. This will allow the active target package to be remotely handled for storage at ISIS and later for final disposal at Sellafield.

Figure 7 overleaf shows the grab mechanism attached to the target disposal flange and the flange/disposal can assembly being lifted into the RHC. After the assembly has been lifted in the RHC floor hatch is closed and the TRAM is withdrawn into the RHC for target removal.

Figure 6 – Storage flask shield plug being lifted into RHC

Figure 7 – Target disposal can being lifted into RHC

2.2 Removal of Target

Figure 8 below shows the TS1 target in the RHC being prepared for removal. The top section of reflector (complete with water moderators) has been rolled forward to expose the target. In the foreground of the picture is the handling frame which is used to remove and handle the target.

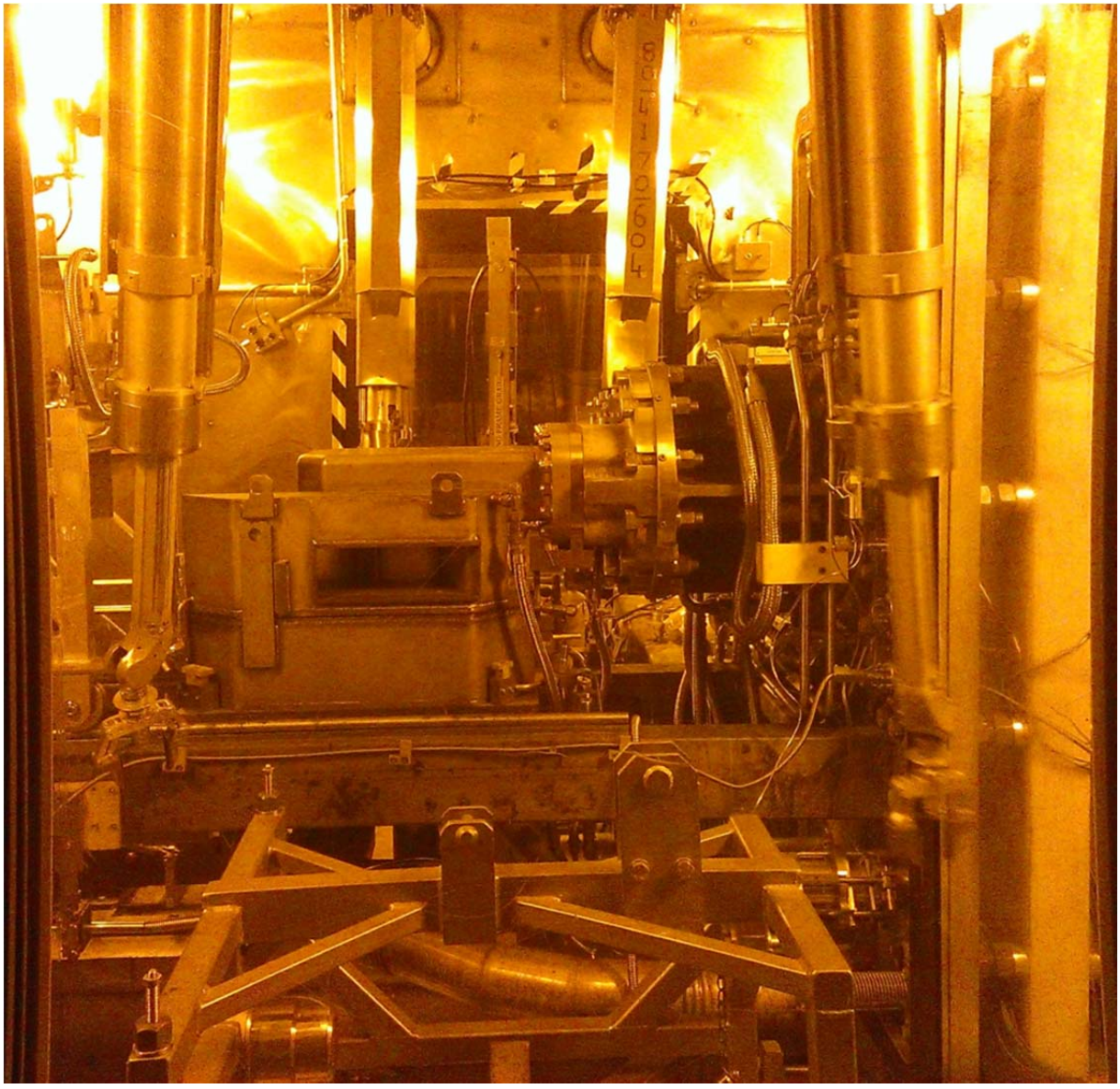

Figure 8 – ISIS TS1 Target in RHC viewed through Zinc Bromide shield window

The handling frame is lifted into position and connected to the body of the target. At this stage all D_2O in the target cooling circuits is drained and blown down into a holding tank in the service tunnel under the target station. The large flange at the rear of the target serves as a mechanical fixing to support and position the target but also seals the water connections for the cooling water for the target plates and casing circuits.

Figure 9 overleaf shows the target being lifted clear of the back door after all the bolts in this sealing flange have been released and the target umbilical connector (carrying thermocouple connections) has been disconnected.

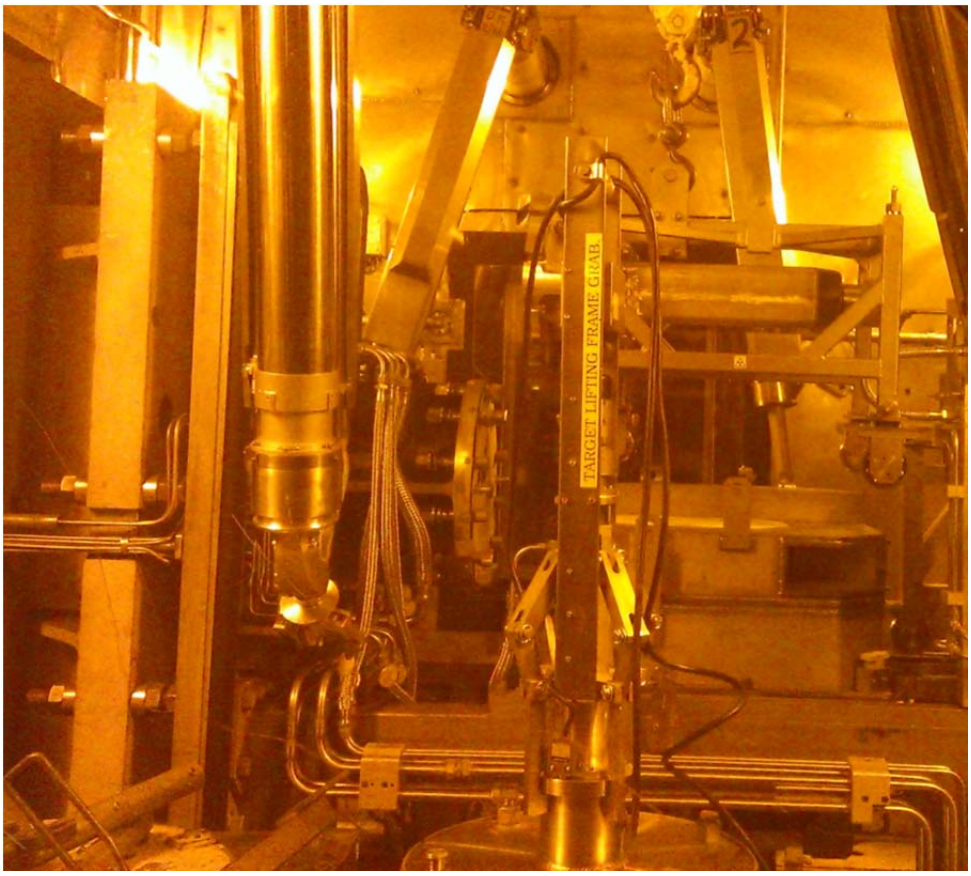

Figure 9 – Target being lifted clear of lower reflector

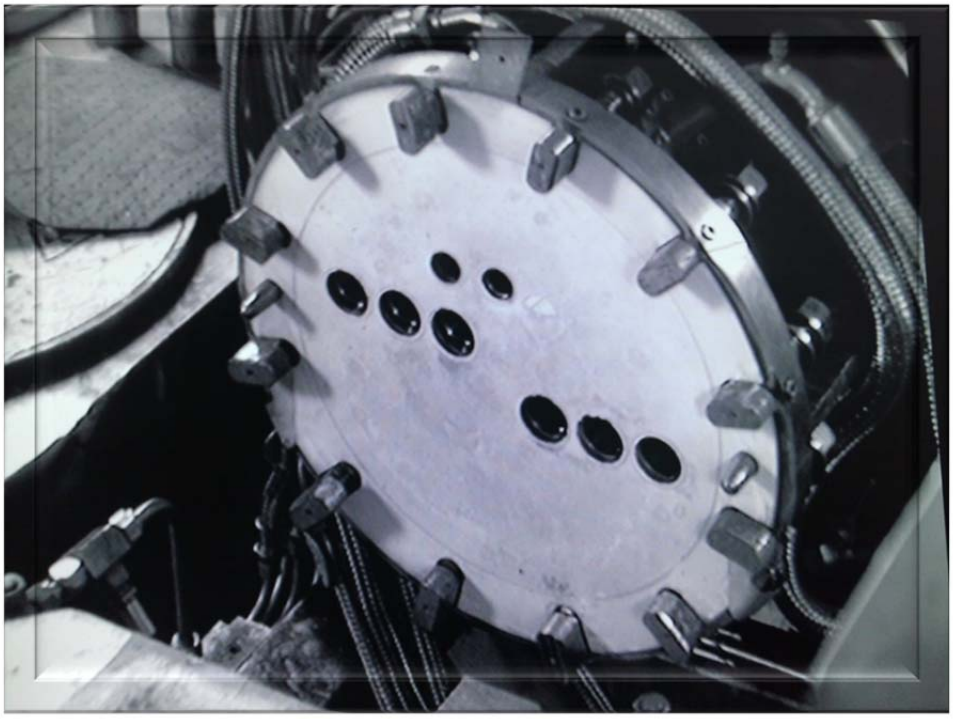

Figure 10 – Mounting flange view after target has been lifted away

2.3 Packaging Target in Preparation for Removal from RHC.
After removal the target is lifted to the north side of the RHC and placed into a rollover frame. This mechanism rotates the target into the vertical plane so that the disposal flange can be fitted. Figure 11 below shows the disposal flange being lowered onto the target (with seal in place) and figure 12 shows the nuts being tightened to clamp the flange onto the target. The flange serves a dual purpose; it seals the target in case of any Tritium release during storage and also provides a means of handling the target which is compatible with the Sellafield handling system.

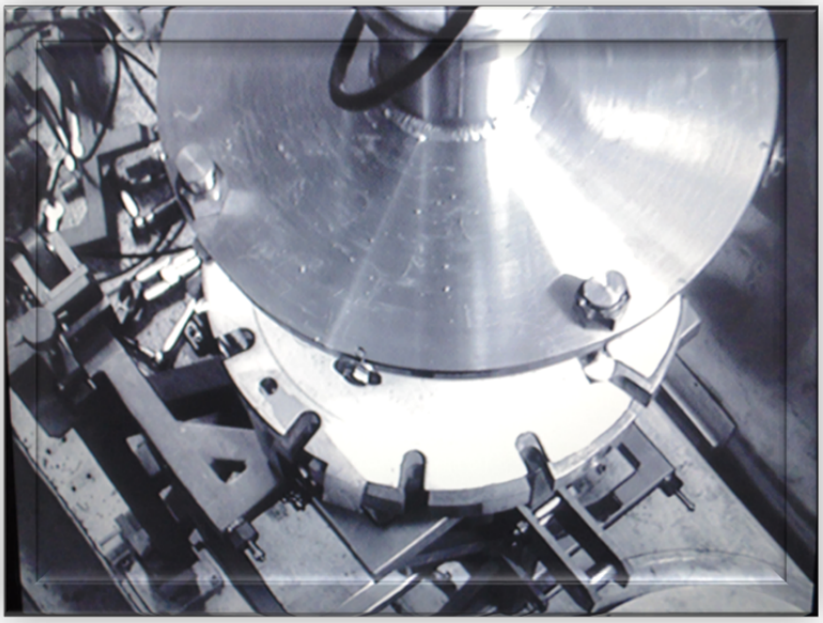

Figure 11 – Target disposal flange being lowered into place

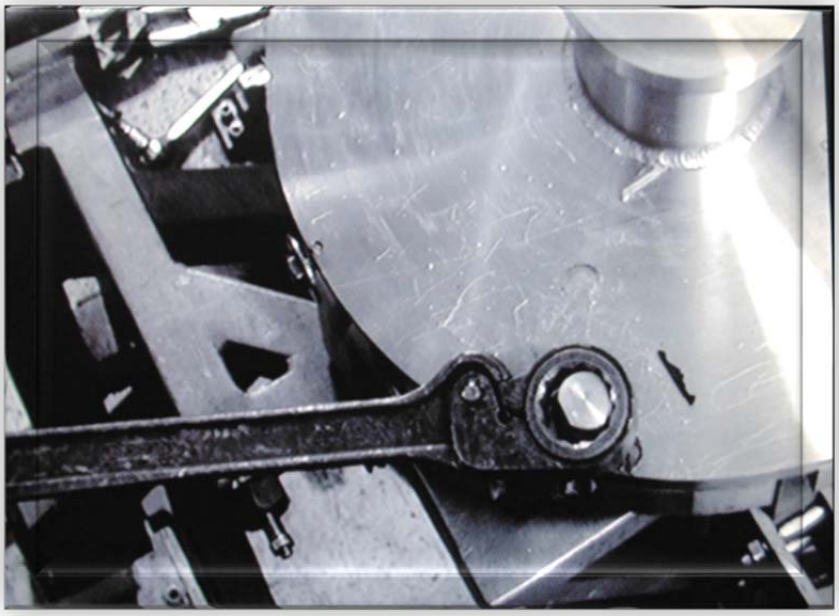

Figure 12 – Disposal flange being bolted to target

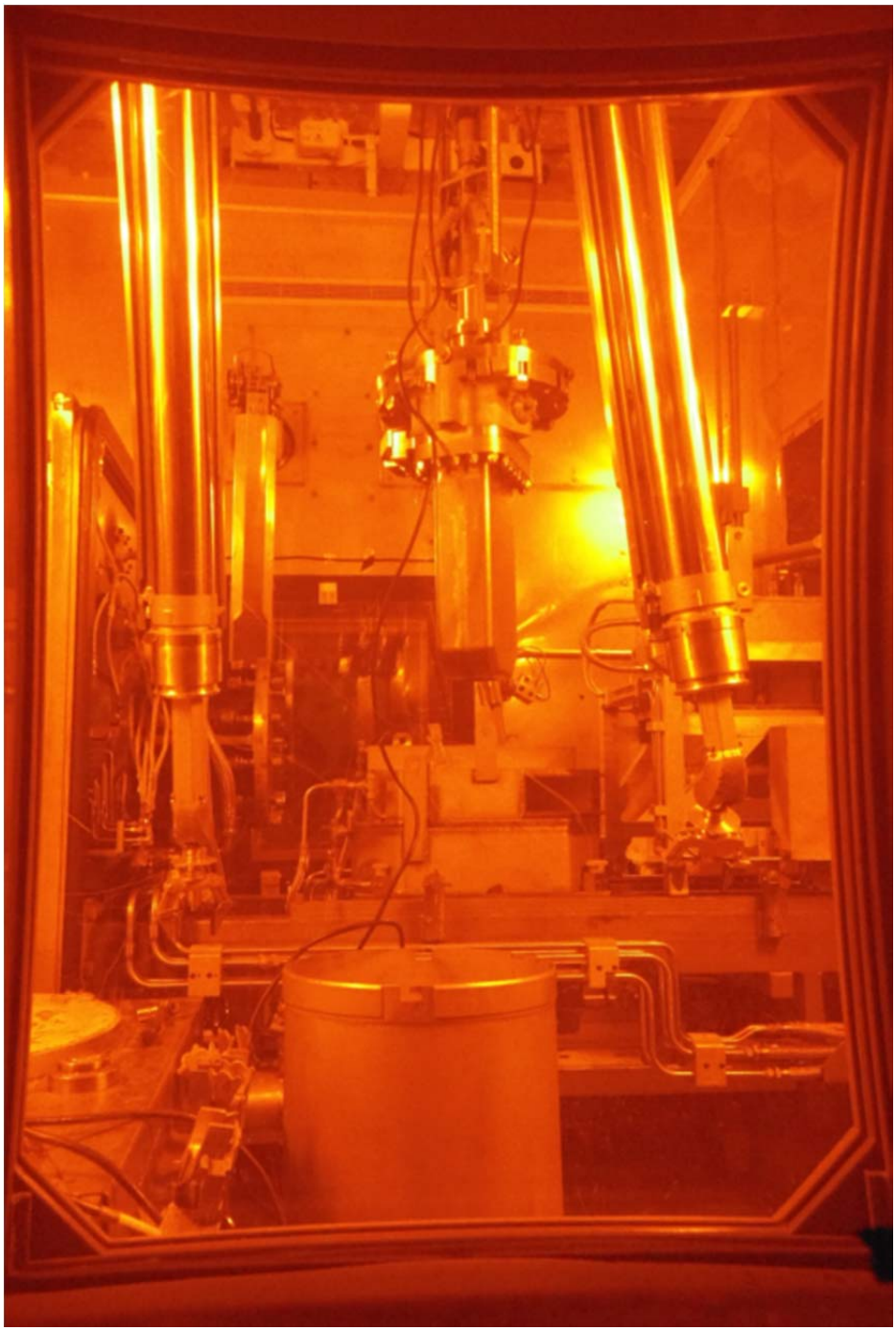

Figure 13 – Target being lifted across RHC to disposal can

In Figure 13 the target can be seen hanging vertically from the electric grab mechanism on the RHC crane. The target is being lifted across to the south side of the RHC toward the disposal can which can be seen in the foreground of this picture.

The target engages in slots the disposal can, is turned and locked in place by means of four locking bolts on the side of the disposal flange (see figure 14).

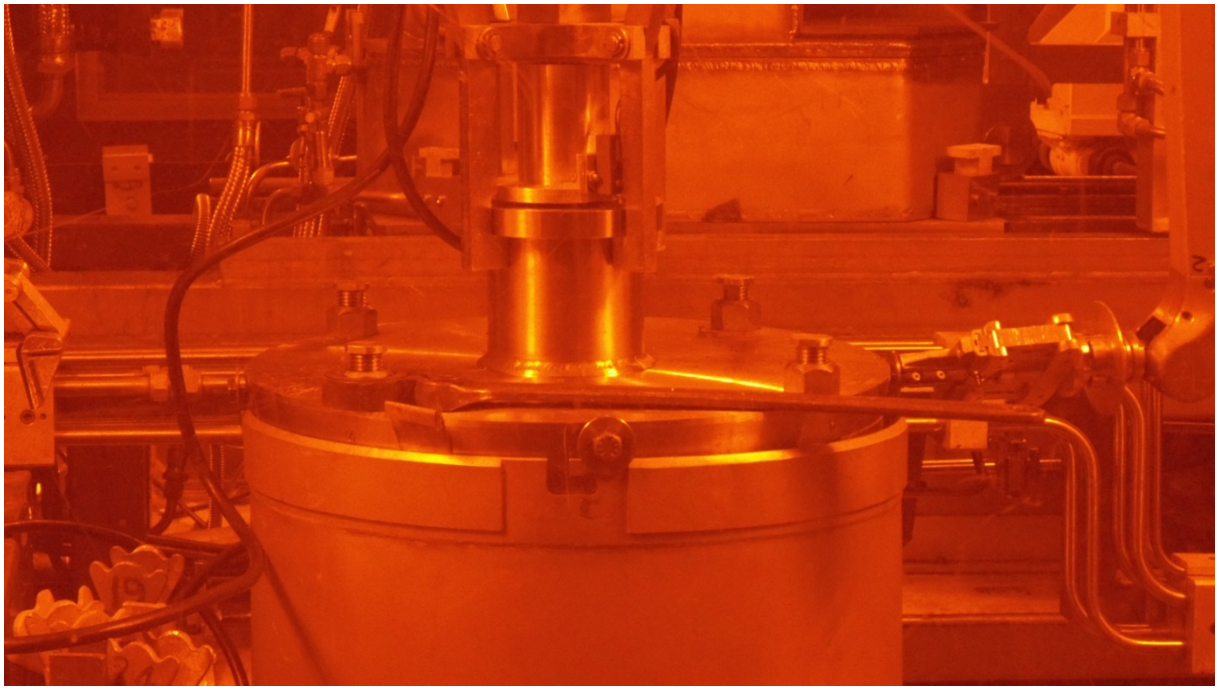

Figure 14 – Disposal flange engaging in slots in Disposal Can

2.4 Removal of Target from RHC.

After the target has been locked into the disposal can the floor hatch is opened and the complete assembly is lowered into the storage flask waiting in the cross tunnel under the RHC – see figure 15 below.

Figure 15 (left) shows target in Disposal Can being lowered into storage flask & Figure 16 (right) shows loaded flask being checked for external radiation dose

Once the target is landed in the flask the electric grab mechanism is opened and lifted back into the RHC, leaving the target in the flask. The electric grab is removed from the crane inside the RHC and the crane is connected to the flask shield plug. This shield plug is then lowered out of the hatch and placed on top of the target inside the flask. The crane is withdrawn, the hatch closed and then the flask is checked for external radiation dose and contamination.

2.5 Transportation of target to ISIS Storage Facility

After external dose rates and contamination levels have been assessed the flask can be removed from the cross tunnel ready for transportation to R40.

The closure flange is fitted to the flask and then the flask is lifted out of the service tunnel using the R55 main hall crane. The total weight of the loaded flask is approximately 9.1 Tonnes

Figure 17(Left) – Loaded flask being lifted clear of services tunnel & Figure 18 (Right) – Flask being transported to R40 for short term storage

Figure 19 – ISIS Target Transport Flask prepared for transportation to Sellafield

Figure 19 shows the target finally packaged in the ISIS Target Transport Flask. This flask is a fully licensed and registered Type B package for use on road and rail transport. This flask is used to transport spent targets from ISIS to final disposal at the Intermediate Level Beta/Gamma Waste Store (ILBGWS) at Sellafield.

3. Acknowledgements
The work presented here is the result of a large amount of preparation and organisation by many members of ISIS staff. I would like to thank my colleagues listed here for all of their hard work and dedication to making ISIS the success that it is; Andy Robinson, John Sexton, David Jenkins, Jon Chapman Chris Russell, David Baker, Gordon Burns, Gary Allen, Robin Burridge and Rajesh Gupta.

3.2.20

The ESS target station hot cell facility and associated logistics for *ICANS XXI*

Magnus Göhran[1], Lennart Åström, Paul Erterius
European Spallation Source ESS AB, ESS, Lund, P.O. Box 176, Sweden.

E-mail: Magnus.gohran@esss.se

Abstract. The European Spallation Source (ESS), Lund, Sweden will be a 5MW long pulsed neutron research facility with planned commissioning in 2019. Connected to the target station building, a hot cell facility will deal with the large, heavy and complex radioactive components as they reach their lifetime limit after service in the neutron research facility. The hot cell will be unique in its design for this specific reason. A special precondition for ESS, being a green field facility, is that there is neither a heritage nor any logistical constraints, which is often the case for existing facilities. The ESS will be operational for around 40 years once commissioned and the hot cell facility will be operative during the complete operational phase of ESS as well as being an important facility during the decommissioning phase of the ESS. This requires the design to have a very high degree of flexibility in order to adapt to changes of target station component designs as well as changes of the functional requirements for the hot cells themselves.

1. Introduction

The design of the Active Cells comprising the hot cell facility of the European Spallation Source ESS AB is in a crucial phase of preliminary design with a planned preliminary design review in mid December 2014. The layout and logistics of the Active Cells is intended to be able to treat and process spent radioactive components mainly derived from the ESS target station operation. The Active Cells facility is scheduled to be operational during the lifetime of the ESS (including decommissioning) and consideration of a flexible and versatile design is therefor crucial in order to fulfil the scheduled tasks, also taking into account that most spent components coming from the ESS operation will most likely be experiencing design updates during the ESS operation. Furthermore, the operation of the Active Cells should have little or no impact on the neutron scattering reliability and availability.

The main purpose of the treatment of the radioactive spent components is to meet the Waste Acceptance Criteria (WAC) as specified by transport, interim storage and/or final repository. As of today, the WAC is not yet known and that will have an influence on the layout and design of the Active Cells as well as on its systems and equipment.

This paper will discuss the current plans for the design of the ESS Active Cells facility and how this design take into account the uncertainties of the requirements. This also includes some degree of novelty to the design and layout both in order to be able to meet future or changed requirements once operational but also to try to address other issues when dealing with hot cells and remote handling. The later is also important due to that the ESS is a green field facility and do not rely on any heritage

[1] To whom any correspondence should be addressed.

from previous operation, this imply that the green field facility design and construction could be both a risk and an opportunity for the manufacturing of the Active Cells facility.

2. Currently planned Active Cells layout and design

In order to fulfil the requirements on receiving the spent radioactive components from the target operation as well as to treat these components to fulfil the WAC for shipping and receiving storage facility, the layout and structure of the Active Cells has been developed into 5 main areas. The *process cell* where the spent components are received, treated and loaded into waste baskets, the *maintenance cell* that functions as the logistical hub for transport of waste container as well as a location for hands on maintenance on the Active Cells equipment, the *storage pits* where waste baskets can be stored prior to offsite shipment, the *transfer area* where offsite shipment containers are loaded with waste baskets prior to shipping and the *technical galleries* from where all in-cell operations are performed and the Human Machine Interface (HMI) is located. The currently planned main features of the layout are shown in Figure 1 and the layout is further explained beneath. The inside dimensions of the hot side of the cells are roughly (30x12x15) meters (LxWxH).

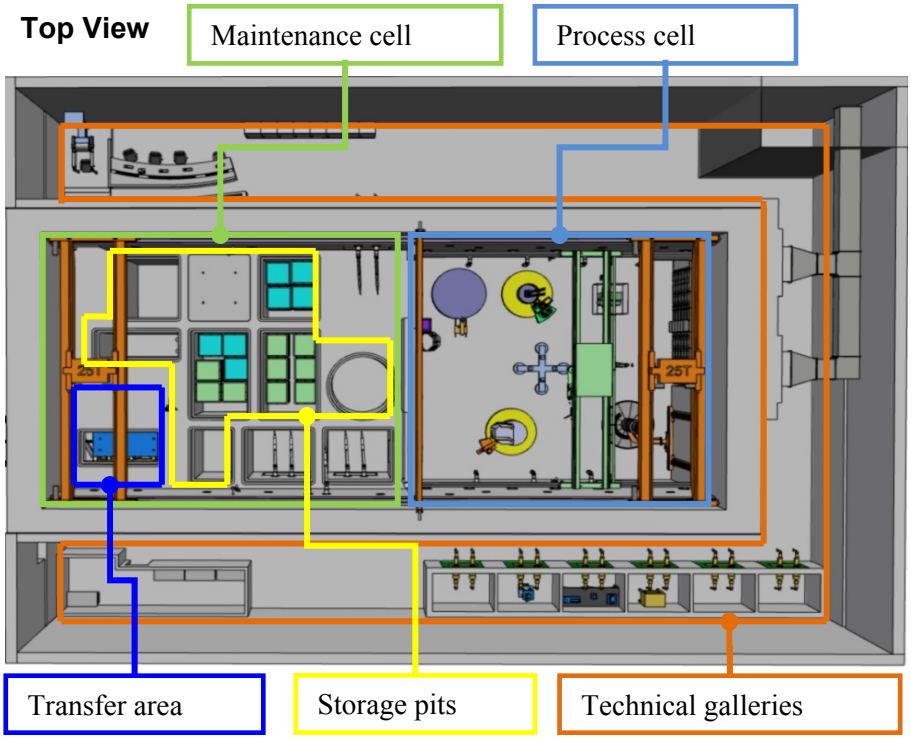

Figure 1. The Active Cells layout.

2.1. Process Cell

This part of the Active Cells has an interface to the high bay above where the radioactive spent components are loaded though a floor valve. The components are loaded to a centre position and then, depending on what component it is, moved to a certain pre-dedicated position for process and treatment. The treatment could be cutting and dismantling in order to separate materials and activation to ease and minimize risk of not fulfilling WAC for shipment and receiving facility. The waste is loaded into dedicated wastebaskets. The other structural interface is through an intra bay door that separates the process cell and the maintenance cell; here components, equipment and wastebaskets can be transported back and forth between the cells.

2.2. Maintenance Cell
The maintenance cell is dedicated for logistics of the wastebaskets transported from the process cell, either the baskets are loaded into a storage pit or through the transfer area into a shipment container. In the maintenance cell, personnel have access through an airlock to do maintenance on process and maintenance cell equipment and tools. The human access will be subjected to some preconditions as for example that the access will be done in pressure suits, the storage pit lids are in place and the intra bay door is closed.

2.3. Storage Pits
The storage pits are situated beneath the maintenance cell floor connected to the maintenance cell via hatches. The purpose of the storage pits is to provide an interim storage of waste until shipment is possible. Depending on the filling degrees, maximum weights, activity, etcetera of the wastebaskets, the storage capacity volume will hold at least 15 years of target station radioactive waste.

2.4. Transfer Area
The physical connection to offsite shipment is done through the transfer area with the possibility to transport shipment casks inside a confined area for direct top loading of wastebaskets from the storage pits (through the maintenance cell). The transfer area is designed as an airlock and the design should allow different sizes of shipment containers to be loaded.

2.5. Technical Galleries
All regular operations within the cells are performed from the technical galleries where a control board is located as well as the through wall operating equipment such as the Master Slave Manipulators (MSM). The technical galleries also house the possibility for locating smaller Post Irradiation Examination (PIE) cells.

3. The Active Cells novel design concept
For the Active Cells to be able to meet the expected performance and lifetime with many expected updates in target components as well as changes in the WAC and updates in operations in general, the design of the cells has a high focus on versatility and operational flexibility. One of the most constraining parts of a classical hot cell operation or remote handling in general is the location and performance of the HMI. For a hot cell, classically the operator would have been placed in the technical galleries in front of a shielded glass window with two manipulator arms to work with inside the cell. The drawbacks of this setup are limited view angles, high demands on in-cell lights, operator fatigue and low utilization of the manipulator arms. The ESS Active Cells is addressing these issues in a concept called the *novel design* and the concepts are further described below.

3.1. The Human Machine Interface
If the in-cell operation as well as the through wall operations is done from a central control table, the operator HMI is moved from the face of the wall to the control table. A sketch of how this interface could look like can be seen in Figure 2. This implies two things, first that the MSM´s are driven by motors instead of operator physical force and the second thing is that the operation is performed via a video feed instead of a direct view of the operation.

The motorized MSM depicted in Figure 3 is a commercial product with a tested performance with a very good feedback from operators on technical, operational and cost perspectives [1]. Since the physical extension with the motorized arm is not bound by the reachability of the operator, as a synergy, the motorized arm now has a possibility to also reach upwards. This is of course beneficial considering the size of the Active Cells.

Pursuing the placement of the operator in front of a control board, the operation inside the cells will now be done with joysticks and controls that should utilize a haptic behaviour to get the most realistic behaviour of the controls as possible. Furthermore the operation is done via cameras.

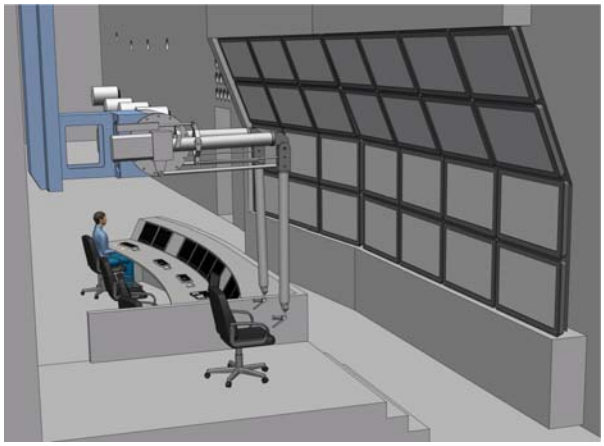

Figure 2. Sketch of a control board for running and controlling the in-cell operations.

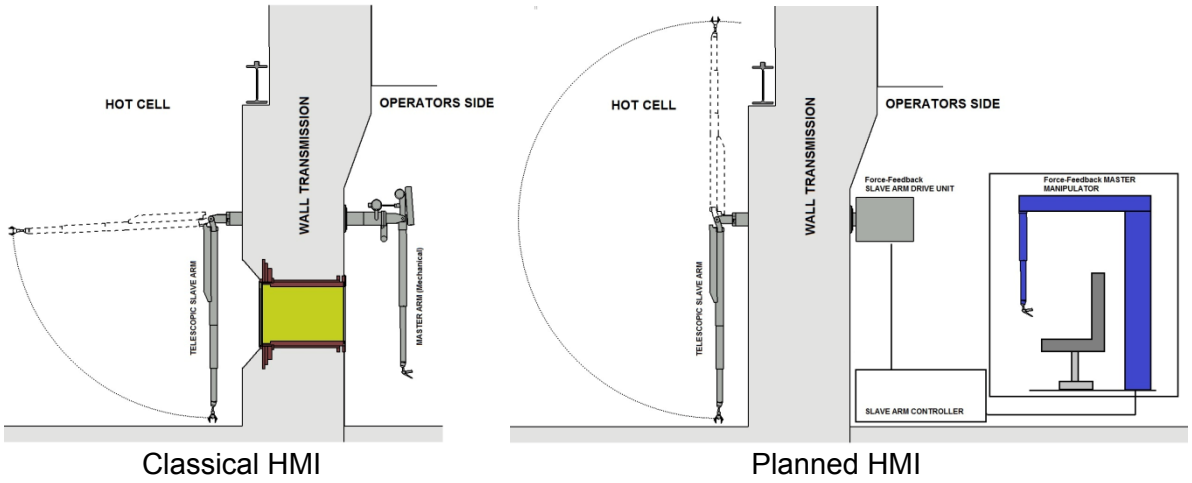

Figure 3. Difference between the manual and motorized master-slave manipulators.

3.2. Visualization

Expanding the thought on placing the operator in front of a camera feed of the cell interiors with a joystick controlling the equipment that incorporates a haptic feedback, the need for the shielding windows are no longer obvious. However there might be occasions where a window is needed and thus the project plans on incorporating at least the embedded frames for some window in the process cell and some in the maintenance cell. Excluding the windows from the day-to-day operation, the requirements on the in-cell lights is reduced significantly and there might be opportunities to use standard LED street lights for the operation.

The camera system will be the main visualization system for observing the operations and this now puts some stringent requirements on the camera system and how this system will be used. The novel concept will utilize a set of through wall plug cameras and in-cell cameras mounted on equipment and other structures. The video feed will be processed through a computer and integrated with CAD models in order for the operator to use a virtual camera position with a convenient viewing position. The viewing system is thus utilizing augmented reality [2] as a tool for the operator to get a clear view of the process inside the cells.

3.3. Master Slave Manipulator layout

The classical setup of a hot cell workstation is designed with two MSM's in front of a shielding window. By this setup, the working volume of the MSM's are very much overlapping which of course

could be both beneficial and inadequate depending on the operation that is performed. By shifting the HMI from the walls to the control board, there are no longer any need for placing the MSM's in a suitable position for the operator (in terms of height and distance between them). Working volume and overlaps, penetration heights etcetera could now be optimized for the planned work for each arm. By including a grid of plugged penetrations, the arms could then be moved to a suitable position to accommodate the changed needs including a high degree of flexibility of the future operations of the Active Cells. The difference between the working volumes of a normal hot cell set up of manipulator arms and the suggested motorized arms are displayed in Figure 4.

The penetrations used by the MSM's should be developed so that all equipment that will be routed through the walls of the cells has the same size. If so, the operation could chose if there should be a camera or a MSM or any other utility routed in a specific penetration position.

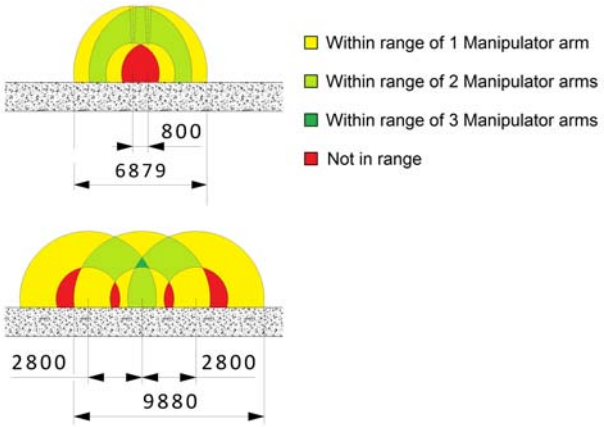

Figure 4. Top picture are describing the working volumes of a classical MSM set up and the bottom picture is a suggestion of spreading the arms out along the length of the wall, optimizing the working volume.

3.4. Mock-up testing of operation

By implementing the systems, functions and designs discussed in the sub-chapters above, placing the operator in front of a control board utilizing haptic controls and augmented reality, the mock-up testing of most operations could be performed in the same environment as the live operation. The operator will use the same controls but do the operation in a mirrored virtual reality environment instead of the actual in-cell reality.

4. Target Wheel dismantling

The wheel function and design is described in [3]. The size, weight and difference in activity of the different materials require the wheel to be dismantled prior to offsite shipment. The aim of the dismantling is to separate tungsten from stainless steel and to separate low active parts like the top of the shaft from the highly activated parts like the beam entrance window. The currently chosen method for dismantling is dry cutting utilizing a high-speed circular saw mounted on the wall. The wheel assembly is positioned on a rotating table and the saw has another 4 degrees of freedom making the cutting as flexible as possible. The saw is shown in Figure 5 where the first top part of the shaft is cut of and removed by the in-cell crane. The size and foremost the height of the target wheel assembly has a large impact on the total size of the hot parts of the Active Cells.

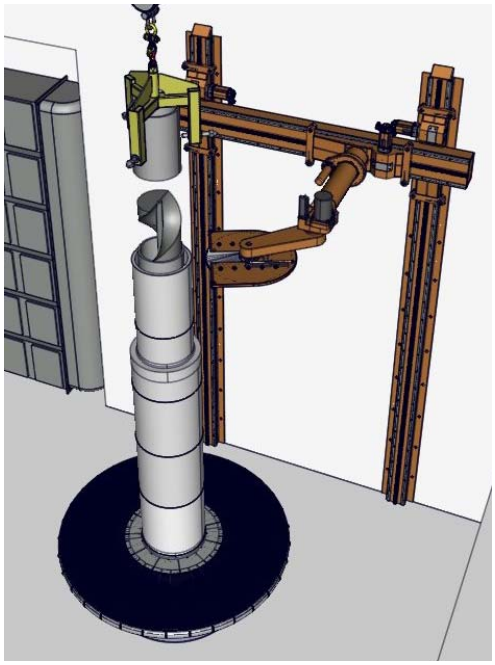

Figure 5. Detail of the target wheel disassembly. The wall mounted saw in orange and the wheel assembly in grey. The first top piece of the shaft is cut and lifted by the in-cell crane.

5. Waste logistics

Since the WAC is not yet determined and agreed with the stakeholders, the design of the Active Cells as well as the planning of the logistics for the waste should be flexible enough to accommodate a variety of offsite shipment containers. The waste should also be separated and sorted in a way so that the risk for having to re-pack and re-distribute the waste once the WAC is known should be minimized. By introducing the philosophies of flexibility to the design, the logistics will also be adoptable to future changes in the chain of transportation.

Once the WAC is known a detailed BAT (Best Available Technique) analysis will be performed that will set the parameters for the shipment. The offsite shipment itself will be under ADR-S [4] regulations.

The reference system used as the design basis is the currently used and adopted system used by some of the Swedish NPP's. An approximate number of 200 containers within this system are deployed as of today for radioactive waste storage. Depending on activity, the containers can be built with 50, 100, 150 or 200 mm wall thickness (steel).

The loading of the interim wastebaskets into the shipment container is done in the transfer area, Figure 6. This area has a connection to the transport hall where truck access is possible. The interim wastebaskets, Figure 7, are filled in the process cell and used for the interim storage in the storage pits. These baskets go through decontamination on the outer surfaces in order to avoid contamination of the inside of the shipment containers.

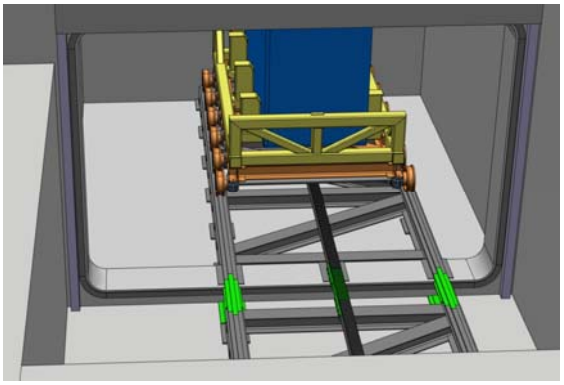

Figure 6. Waste shipment container in blue transported on rails from the transfer area to the transport hall for truck loading.

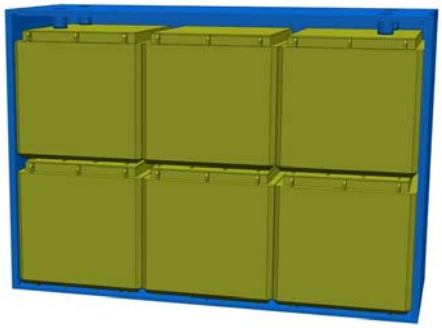

Figure 7. Detail of the waste shipment container (blue), one side omitted. The yellow wastebaskets are used as interim storage baskets that are eventually loaded inside the shipment container.

6. Conclusions

A lot of effort is currently focused at concluding on the layout and geometry of the Active Cells structural parts. Since some of the functional requirements are still unknown, the design effort is focused on including flexibility and versatility to an as large extent as possible. This is one of the reasons to why the "novel design concept" is presented as part of the solution for the design since this concept will make it possible to adopt the cells to future known and unknown modes of processes and operations. The flexibility and versatility is also adopted for the shipment of waste where the interfaces are developed in such a fashion that they can accommodate a large range of shipment containers.

7. References

[1] P. Garrec *et al*., "Evaluation Tests of the Telerobotic System MT200-TAO in Areava- NC/NL Hague Hot Cells", 2nd Joint Emergency Preparedness and Response & Robotics and Remote Systems Topical Meeting, 2008, Albuquerque

[2] http://en.wikipedia.org/wiki/Augmented_reality

[3] R. Linander, U. Odén, "Status update on the ESS Target systems development", ICANSXXI, 2014, Mito, Japan

[4] ADR-S: European Agreement concerning the International Carriage of Dangerous Goods by Road (Swedish version). MSBFS 2011:1

3-3. Integrated Interface

This is a blank page.

3.3.1

Thermal Hydraulic and Thermo-Mechanical Design of the Proton Beam Window for ESS

J Wolters[1, 4], M Butzek[1], B Laatsch[1], Y Beßler[1], G Natour[1], P Nilsson[2] and P Sabbagh[3]
[1] Forschungszentrum Juelich GmbH, 52425 Juelich, Germany
[2] European Spallation Source ESS, Lund, Sweden
[3] DAES Development of Advanced Engineering Solutions, Geneva, Switzerland

E-mail: j.wolters@fz-juelich.de

Abstract. The proton beam window for the European Spallation Source ESS will separate the 1 bar monolith helium atmosphere and the accelerator vacuum. In medium power spallation sources like ISIS, SINQ or the SNS source in Oak Ridge, cylindrical or spherical double walled water cooled windows are used, but during the design of the beam window for the spallation source SNS it became obvious, that this concept is already pushed to its limits at a beam power of 1.4 MW. A novel design concept called pan-pipe design was proposed for the ESS-PBW, which is optimized for high coolant pressures – as helium is the designated coolant for the PBW at ESS - and the typical pressure difference of 1 bar over the window. In the present study the detailed thermo-mechanical design of the PBW made of aluminium is shown. The main focus of the investigations was set on fatigue loading due to mechanical and cyclic thermal loads and on an optimized flexible interface between the PBW and its massive frame.

1. Introduction

The ESS proton beam window will separate the 1 bar monolith helium atmosphere and the accelerator vacuum. In 2003 a novel design concept called pan-pipe design was proposed for the PBW for higher beam powers [1]. This design was optimized for high coolant pressures and the typical pressure difference of 1 bar over the window. Due to the interim stop of the ESS-project in 2003 only very rough investigations were shown in [1], which were now adapted to the current ESS conditions – e.g. helium as designated coolant medium and new proton beam parameters - and further particularized for this report.

This report concentrates on thermo-mechanical stresses and fatigue due to normal operation conditions. Off-normal loads were only considered with respect to the thermal layout so far (cp. chapter 3). In a next step all possible load cases - including faulty conditions - and their impact on the life-time of the PBW have to be investigated in detail.

[4] To whom any correspondence should be addressed.

2. Pan Pipe Design

The pan-pipe design is shown in Figure 1. Basic drivers for the design of the beam window are

- cooling: window material is subjected to volumetric energy deposition by the proton beam and by scattered neutrons from the surroundings and the target
- mechanical strength: mechanical loads imposed on the window material are the coolant pressure and the pressure difference between the helium atmosphere and the accelerator vacuum
- radiation damage: basically driving the life time and thus the handling frequency
- defocusing: proton beam will be scattered by the window material

Al6061-T6 [2] was chosen as the preferred material for the window because of its low density, which guaranties a good transmissibility for protons and a moderate heat deposition, and its good mechanical properties. On the other hand this choice limits the maximum temperature to approximately 100 °C, because at higher temperatures (>130 °C) the material will lose its tempered state in a long term and consequently its strength.

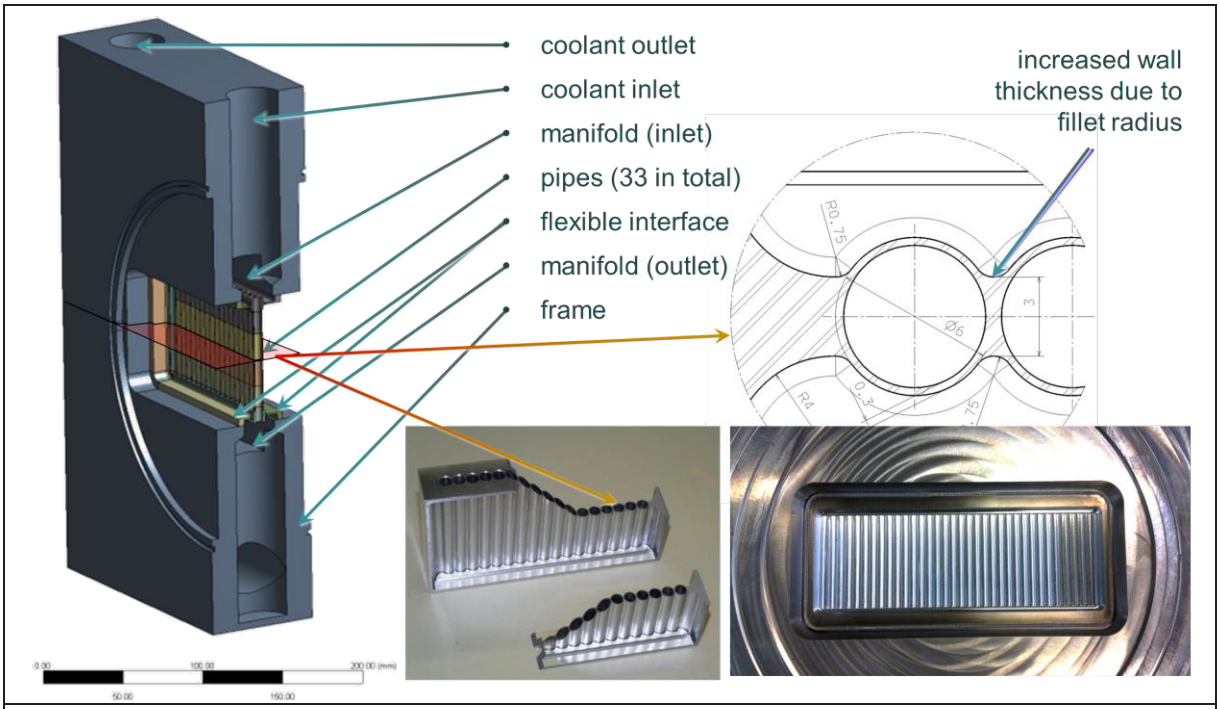

Figure 1. Pan-pipe design: The window itself consists of 33 pipes, each 6mm in diameter, and a flexible interface to the massive aluminium frame. At present manufacturing and welding tests are carried out at Forschungszentrum Jülich GmbH, ZEA-1 (bottom right figures)

The current design focuses on minimizing the wall thickness to be cooled by using an array of small pipes – 33 in total - connected to each other. The single pipes with an outer diameter of 6 mm and a wall thickness of only 0.3 mm are suitable to resist the high coolant pressure of 10 bar, that will lead to circumference stress in the pipe walls, and the pressure difference of 1 bar between the monolith helium atmosphere and the accelerator vacuum, that will lead to bending stresses in the PBW. The clamping of the PBW in its massive frame is flexible in vertical direction to allow the pipes to thermally expand in longitudinal direction. Moreover the tilting effect at both ends of the pipes due to the deflection of the PBW is compensated by the flexible clamping. Thus the stresses in the PBW within the beam footprint could be reduced significantly and the zone of maximum thermo-mechanical

stressing could be transferred to the flexible interface. This is important since radiation damage will degrade ductility and fatigue resistivity of the material within the beam– which is still a point that has to be investigated carefully in the near future.

The flexible interface of the PBW is built into a massive aluminum block containing the cooling connections (cp. Figure 1). The central borehole in the massive aluminum frame is the helium inlet and the helium will leave the configuration through the two boreholes on the side. In order to distribute the helium flow to all single pipes and to collect it again after having passed the window, manifolds are foreseen above and below the PBW.

Manufacturing of the window will be performed by machining the outer contour of the pipes from a solid block of aluminum, followed by drilling holes of a diameter of 5.4 mm leaving a wall thickness of 0.3 mm. Thus there is no need for using joining techniques like brazing or welding in the zone suffering most from proton beam radiation. Figure 1 shows a first proof-of-manufacturing window from the year 2003 to analyse to tolerances regarding the wall thickness and a current test weld of a prototypic window in its massive frame.

3. Thermal layout

In order to determine thermal stresses for the whole PBW configuration a detailed CFD (Computational Fluid Dynamics) model was set up in ANSYS CFX [3], which includes all relevant solid parts as well as the coolant passages of the configuration. The thermal-hydraulic calculations on the PBW were performed for the reference mass flow rate of 0.2 kg/s, a helium inlet temperature of 20 °C and a parabolic heat deposition profile (cp. Figure 2, left side). The peak value of the applied time-averaged heat deposition profile is 0.5 kW/cm³, which is a conservative value for the nominal beam. The half width of the beam footprint is 80 mm and the half height is 30 mm [4]. Outside the beam footprint a heat deposition distribution which decreases with the distance to the beam axis to the second power and which results in a maximum power density of about 1 W/cm³ in the massive frame of the PBW is considered (cp. Figure 2, right side). The power density during the pulse is determined by the time averaged values scaled by 1/f/tpulse = 1/14 s^{-1}/2.86 ms ≅ 25, while in between the pulses no thermal load is considered.

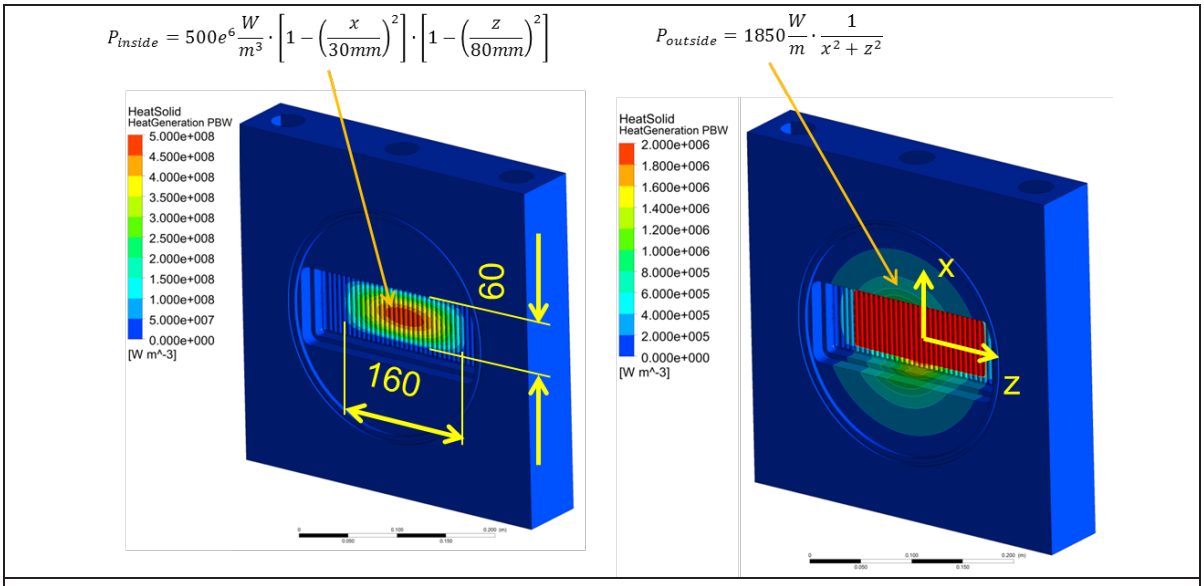

Figure 2. Time averaged heat deposition profiles within (left) and outside of beam footprint (right)

Turbulence is modelled by using the kω-SST model [5]. For aluminum constant material properties according to [6] were used, while for helium pressure and temperature dependent values according to the formulas given in [7] and [8] were used.

The results of the thermal hydraulic calculation with respect to the coolant flow and the temperatures in the PBW are shown in Figure 3, left hand side. The maximum temperature after a pulse is about 65 °C for nominal loading conditions. The temperature increment in the centre of the beam window due to the pulsed operation is about 14 °C. For off-normal conditions, which are given by a slightly focused beam footprint of 140 mm x 50 mm and a maximum beam shift of 6 mm [4], the maximum temperature can go up to 80 °C (not shown in Figure 3).

In case of a beam trip it takes only about half a second till the structural material of the PBW is cooled down to coolant temperature again (cp. Figure 3, right hand side). Thus even for short beam trips (< 1 s) a full beam trip stress cycle has to be considered in the fatigue analysis.

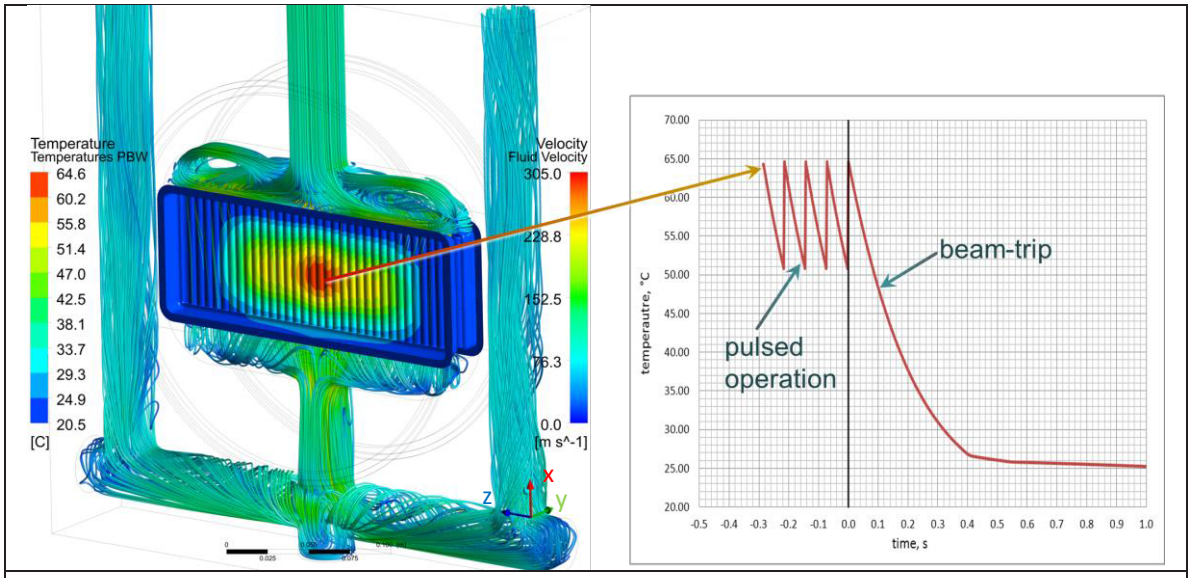

Figure 3. Results of thermal-hydraulic calculation

4. Thermo-mechanical layout

The thermo-mechanical simulations were performed with ANSYS Workbench [9], using the imported fluid pressure and temperature distribution from the CFD calculation. Moreover the pressure difference of 1 bar over the window was applied to the mechanical model.

The clamping of the massive frame of the PBW is considered by simplified boundary conditions. On the one hand the surfaces on the sides of the massive frame are fixed in x- and y-direction and are not allowed to rotate about the z-axis, while they can still deform. This is realized by so called ‘remote displacements’ with a ‘deformable’ behaviour. These boundary conditions simulate the lateral guidance of the frame. Moreover for both sealing grooves of the frame rotation about the x-axis was suppressed and a rigid behaviour was used for the corresponding ‘remote displacements’, in order to consider the stiffness of the connected flanges. More precise boundary conditions will be investigated later on, when the detailed design of the frame and its surrounding is fixed. Anyway, the expected impact on the results for the PWB is small.

With respect to the applied temperatures three different cases were investigated, which are necessary to assess the fatigue limit:

- thermal state prior to a pulse,
- thermal state after a pulse and
- uniform coolant temperature after a beam trip.

The single pipes of the PBW are well designed to withstand the coolant pressure of 10 bar and the bending due to the pressure difference of 1 bar between the helium atmosphere in the monolith and the accelerator vacuum, what can easily be shown by analytical formulas for bending and pressurized pipes. The main optimization task was to design the flexible interface between the single pipes and the stiff frame, which is on the one hand flexible enough to reduce local stresses due to the clamping of the pipes and to compensate the thermal expansion of the PBW and which is on the other hand stiff enough to bear the mechanical loads. Moreover the design mustn't be too complex in order to guarantee easy manufacturing. In Figure 4 deformations for the PBW and its flexible interface are shown just due to the pressure loads (left side) and due to the additional thermal expansion of the PBW after a pulse (right side). An amplification factor due to the short-time heating up of the PBW during the pulse is not considered and can be neglected since the period time of the first eigenmode at 3800 Hz is one order of magnitude shorter than the pulse time.

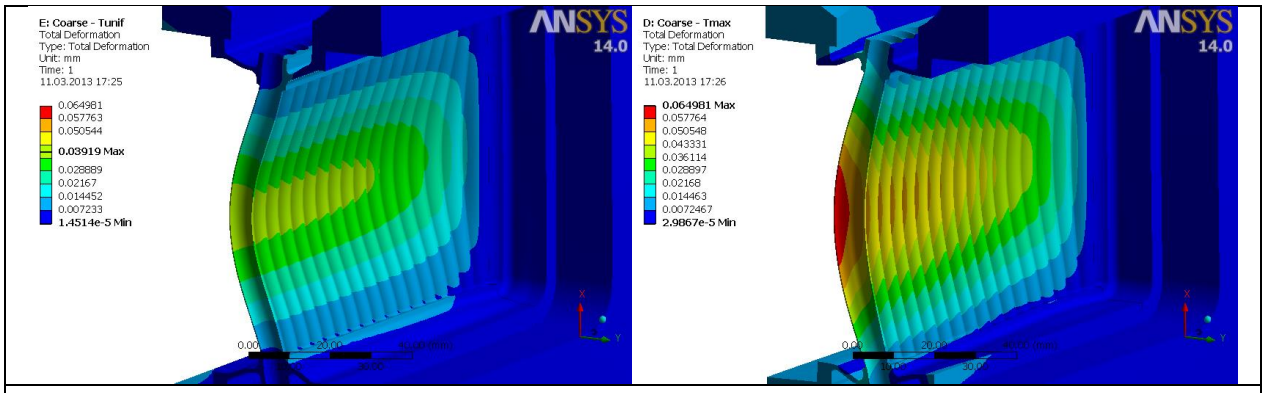

Figure 4. Deflection of the PBW; left side: just due to pressure loads; right side: due to thermal and pressure loads

In Figure 5 the stress distribution (equivalent stress) is shown for the global model – again just due to pressure loads (left side) and due to the additional thermal expansion of the PBW after a pulse (right side). It is obvious that within the single pipes of the PBW the primary stresses due to the pressure are far below the allowable stress of $S_m = 87$ MPa [10], while due to the thermal loads and the resulting lateral thermal expansion the single pipes will be additionally stresses by an ovalization. This will lead to stresses in the pipe walls of about 65 MPa (Figure 5, right side). But even this value is far below the allowable primary membrane and even more below the allowable membrane plus bending stress of $1.5\ S_m = 130.5$ MPa [10].

The maximum stress will occur in the flexible interface between the window and its massive frame. Here a refined sub-model was used to precisely resolve notch stresses for the following fatigue analysis. The maximum stress in the flexible interface arises if the maximum temperature after a pulse is applied. Again, the maximum value of 98 MPa in Point A (shown in Figure 6) is even below the allowable primary membrane plus bending stress. Without thermal loads Point B is highly stressed due to the deflection of the PBW and the resulting tilting in the flexible interface. Here the maximum stress is less than 86 MPa. It is also obvious that for those two points the stress state will change

significantly with the thermal load. As a consequence these two points are of special interest for the fatigue analysis, particularly because the dominant stress component in y-direction is a tensile stress.

For point C of the flexible interface significant cyclic stresses will also occur for pulsed operation and beam trips, but here the dominant stress component is pressure which is less critical with respect to a complete failure due to crack initiation.

For point D the calculated equivalent stress is in the range of the maximum bending stress of the flexible interface, but here the stress state does not depend so much on the thermal load. Therefore this point is non-critical with respect to fatigue.

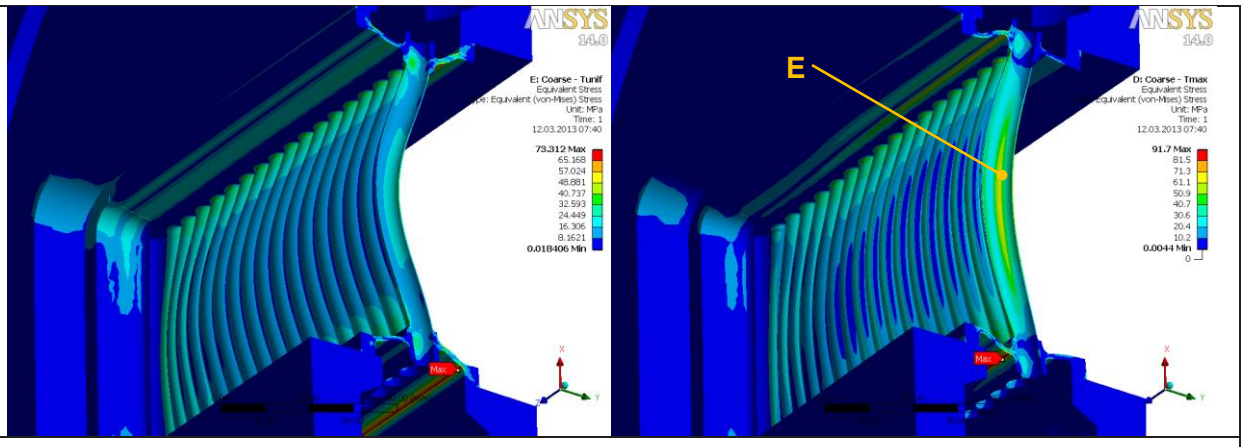

Figure 5. Stresses (equivalent) in the PBW; left side: just due to pressure loads; right side: due to thermal and pressure loads

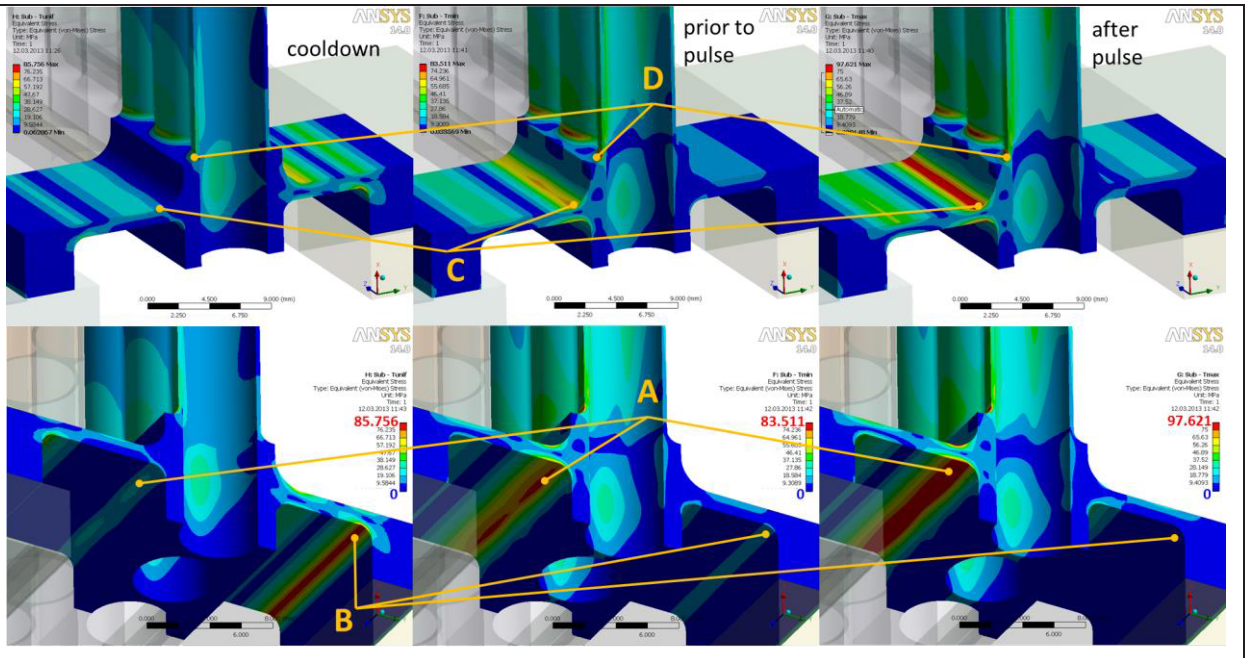

Figure 6. Local stresses (equivalent) for the refined sub-model

For the fatigue analysis two load cycles are considered. Regarding the pulsed operation the two stress states prior to a pulse and after a pulse are compared and corresponding mean stresses and stress amplitudes were determined. For beam trips the stress states after a pulse and after cool-down are compared.

With respect to the pulsed operation 242 days of operation per year have to be considered [11], which results in about $3 \cdot 10^8$ stress cycles if the PBW is replaced only once a year - according to [11] this is the final goal, while changing the PBW twice a year is the current specification. The number of expected beam trips per year is about 29000 according to [11].

The fatigue analysis is based on the FKM design rule [6] using a safety factor of 1.6 for the components endurance strength. The results are shown in Table 1. In general the degree of utilization for the flexible interface is larger for the considered 29000 beam trips than for the pulsed operation. The maximum degree of utilization occurs for point B (cp. Figure 6) and is 27.4 % due to the pulsed operation and 51.5 % due to beam trips. The sum of both values is well below 100 %.

For point E (cp. Figure 5) the resulting degree of utilization is 42.5% and therefore much lower than for the flexible interface. But one has to take into account, that this point is located within the beam footprint and is exposed to a higher radiation damage, which is up to now not considered in the analysis.

Table 1. Resulting degree of utilization with respect to fatigue according to the FKM design rules

	Point	A	B	C	D	E
degree of utilization [%]	pulsed operation	25.6	27.4	19.5	5.9	21.6
	beam trips	45.3	51.5	45.9	16.8	20.9
	total	70.9	78.9	65.4	22.7	42.5

5. Summary & Outlook

The ESS proton beam window was designed to withstand thermal loads due to a 5 MW proton beam and mechanical loads due to the necessary coolant pressure and the pressure difference over the window of 1 bar. In the present report it was shown, that the foreseen helium cooling at 10 bar pressure using a mass flow rate of 0.2 kg/s is sufficient to keep the aluminum temperature well below the maximum design temperature of 100 °C for normal and even for off-normal beam conditions.

The thermo-mechanical analyses have shown that the flexible interface between the PBW and its massive frame is well designed to compensate thermal strains in the thin-walled pipes of the PBW. Due to the flexible interface the maximum stress within the thin pipes of the PBW could be reduced to a maximum value of about 65 MPa for normal beam conditions. The stresses in the flexible interface are higher, but this region is not directly hit by the proton beam and moreover the wall thickness here is considerably higher than the thickness of the pipes of the PBW. All stresses are well below the allowable stresses.

With respect to fatigue the analysis were made according to the FKM design rules. The most relevant zones are located in the flexible interface. Here the maximum total degree of utilization is about 80 %, considering one year of operation. Less critical are the thin-walled pipes of the PBW. Here the total degree of utilization is about 43 %, not considering a possible radiation induced decrease of the endurance strength here.

At present manufacturing and welding tests are carried out for the PBW and its frame at the Central Institute for Engineering, Electronics and Analytics in Jülich. In these tests welding parameters are optimized to get a vacuum-tight connection between the PBW and its massive frame and to improve the quality of this connection.

For the next step with respect to the PBW design a thin coating of the PBW, which will be used for beam-diagnostics, has to be specified and considered in the calculations. Moreover faulty conditions have to be investigated in order to assess measures that are needed to safely handle such conditions. Here the most important aspects are how quick faulty conditions have to be detected and how fast the beam has to be switched off to prevent the PBW from complete failure.

Once the design of the PBW and its frame is completed, the calculations have to be adapted and finally the fatigue analysis has to be carried out according to MCC-MR, considering radiation damage of the material.

6. References

[1] M. Butzek, T. Kulessa and J. Wolters, *Proton Beam Window for High Current Densities,* ESS-Report No. ESS 03-147-T, 2003.

[2] S. Peggs and R. Kreier, *ESS Technical Design Report, Release 1.0 (under active development),* November 28, 2012.

[3] ANSYS., Inc, *ANSYS CFX 14.0,* Southpointe, 275 Technology Drive, Canonsburg, PA 15317, November 2011.

[4] P. Nilsson, *Proton Beam Window Loads,* Lund: ESS AB, 2012.

[5] F. R. Menter, *Two-Equation Eddy-Viscosity Turbulence Models for Engineering Applications,* AIAA Journal, vol. 32, no 8., pp.1598-1605, August 1994.

[6] Forschungskuratorium Maschinenbau, *FKM-Richtlinie: Rechnerischer Festigkeitsnachweis für Maschinenbauteile,* Frankfurt am Main: VDMA Verlag GmbH, 1998.

[7] KTA, *Sicherheitstechnische Regel des KTA, KTA 3102.1, Auslegung der Reaktorkerne von gasgekühlten Hochtemperaturreaktoren, Teil 1: Berechnung der Helium-Stoffwerte,* BAnz., Juni 1978.

[8] Helge Petersen, Danish Atomic Energy Commission, Research Establishment Riso, *The Properties of Helium: Density, Specific Heats, Viscosity, and Thermal Conductivity at Pressures from 1 to 100 bar and from Room Temperature to about 1800 K,* Riso Report, September 1970.

[9] ANSYS Inc., *ANSYS Workbench 14.0,* November 2011.

[10] AFCEN, *RCC-MRx code (draft), Section III - Tome 1 - Subsection B: Class N1Rx Reactor Components, its Auxiliary Systems and Supports,* December 2010.

[11] P. Sabbagh, *Cycle assumptions for fatigue analysis,* Lund, Sweden: European Spallation Source ESS AB, EDMS ID Number 1225592, 2012.

3-4. Accelerator and Beam Transport

This is a blank page.

3.4.1

J-PARC: The path to 1 MW at J-PARC, including 400 MeV linac improvement, RCS improvements and front-end upgrades

Kazami Yamamoto[1]
J-PARC Center, JAEA, Tokai, Ibaraki 319-1195, Japan.

E-mail: kazami@post.j-parc.jp

Abstract. An accelerator system of Japan Proton Accelerator Research Complex (J-PARC) operated since May 2008 for neutron experiments. The accelerator system consists Linac, Rapid Cycling synchrotron (RCS) and Main Ring. The original design of RCS injection energy is 400 MeV, but first operation was started by 181 MeV for budget reason. New acceleration cavities were installed in J-PARC linac summer shutdown of 2013, and user operation to Material and Life science Facility (MLF) by the injection energy of 400 MeV was started from February 2014. Owing to the beam commissioning of 400MeV injection energy, the amount of the beam loss was enough small and we established 300 kW continuous operation. In this paper, we report the present status and future plan of J-PARC linac and RCS.

1. Introduction

The Japan Proton Accelerator Research Complex (J-PARC) is facilities for the various physical experiments. The J-PARC facilities were constructed in the Tokai site of the Japan Atomic Energy Agency (JAEA). The accelerator complex consists of a 400 MeV linac, a 3 GeV Rapid-Cycling Synchrotron (RCS), and a Main Ring synchrotron (MR)[1]. RCS delivers 3 GeV, high power proton beam to the MLF, and MR delivers 30 GeV proton beams to Neutrino target and Hadron Experimental hall. The beam commissioning of the linac started in November 2006[2][3][4]. Construction of another accelerators and experimental facilities were continued afterwards, the RCS started to deliver proton beam to the MLF in May 2008[5]. The user operation for MLF started in December 2008[6], and the beam power was gradually increased. However, the great east earthquake caused many serious damages to all J-PARC facilities in March 2011. We completed the recovery work in only nine months and restarted user operation[7]. After the earthquake, we smoothly increased the output power and the user operation of 300 kW power was started at the end of 2012[12]. However, it was necessary to improve the linac and RCS to achieve more output power. Then, the acceleration energy of the linac was raised to 400MeV by installing a new acceleration cavity in the summer of 2013. The injection system of the RCS has also been increased simultaneously for 400MeV injection. In addition, the front end is replaced in the summer of 2014 to increase the beam current of 50 mA.

2. Linac energy upgrade in 2013

In order to increase the output power of RCS, the acceleration energy of the linac was increased from 181 MeV to 400 MeV at the first setout. This energy upgrade aims to mitigate the effect of the

space charge in RCS injection process and to reduce the beam loss. Therefore, the ACS (Annular-ring Coupled Structure) cavity was developed[9][10]. 25 ACS modules have been fabricated in total. 21 modules are used to acceleration, and rest 4 are used for debuncher. The ACS cavities were installed in the summer shutdown period of 2013[11]. Figure 1 shows the linac accelerator tunnel after installation of ACS cavities.

Figure 1. The linac accelerator tunnel after installation of ACS cavities.

Aftre installation of ACS cavities, we started the high-power conditioning of the ACS cavities. Figure 2 shows a typical conditioning history of ACS cavity. In the conditioning sequence, we put short pulse RF (50 us) up to 2 MW at first. After that we put longer pulse RF (600 us) up to 2MW. The average conditioning time for one ACS cavity is 149h. The detail conditioning sequence is written in the reference[12].

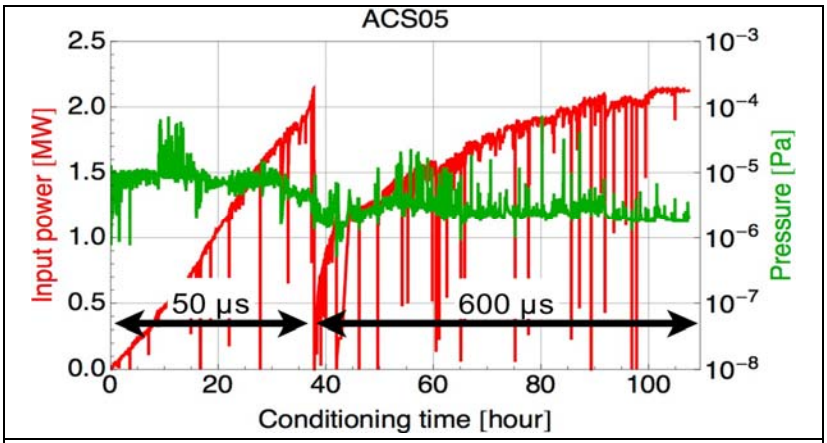

Figure 2. Typical conditioning history of ACS cavity.

A beam commissioning with new ACS cavities are carried out from December 2013 to January 2014. After the commissioning, we achieved acceleration energy of 400 MeV on January 17[13]. Then we started user operation at the acceleration energy of 400MeV, but we need more study time in order to clear next issues. The first issue is a halo formation in the ACS section. This halo brings about the

beam loss in the RCS. Proper matching is needed by help of new additional longitudinal monitors. The other issue is higher radioactivity at some points of ACS section.

3. Accelerator improvements in summer shutdown 2014

In summer shutdown period of 2014, we improved many accelerator components of linac and RCS. Here we introduce some major improvements.

3.1. Linac

The most important improvement is replacement of the front-end system for higher peak current. Figure 3 shows a test bench of new front end system.

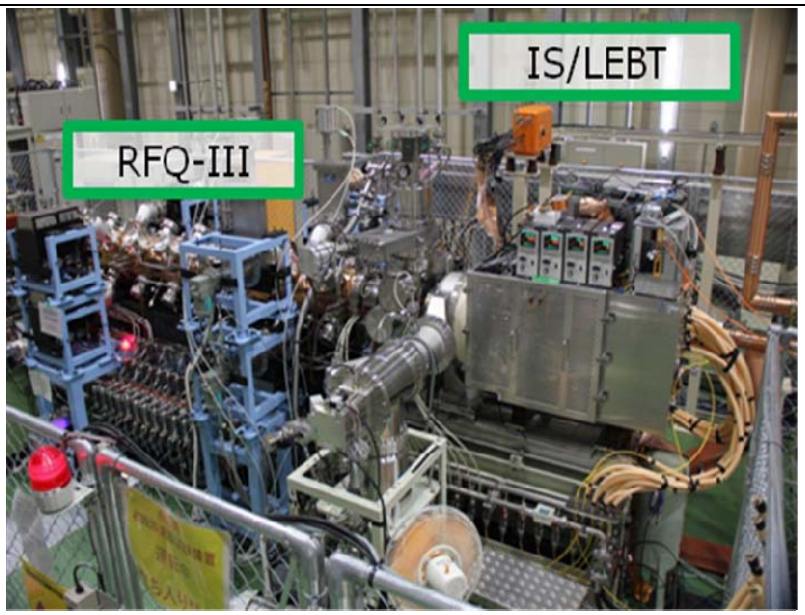

Figure 3. Test bench of the new front end.

The front-end system consists of new ion source, RFQ-III and some parts of the MEBT1. The old ion source used a filament to produce the ion plasma and it did not need Cs. On the other hand, new system adopts the Cs seeded RF-driven system[14]. RFQ-III is optimized for the beam current of 50 mA[15].

The rf-driven H^- ion source and RFQ-III were tested in a test bench, which was constructed in the J-PARC linac building. We checked various parameters of the test bench[16], and we tried long-term continuous operation of this system[17]. Figure 4 shows a test result of long-term operation. Finally, we achieved 683 hrs. (about 1 month) continuous operation. However, discharge of the RFQ frequently occurred during long-term operation test. Thus we decided to install additional pump in actual beam line and keep conditioning as possible.

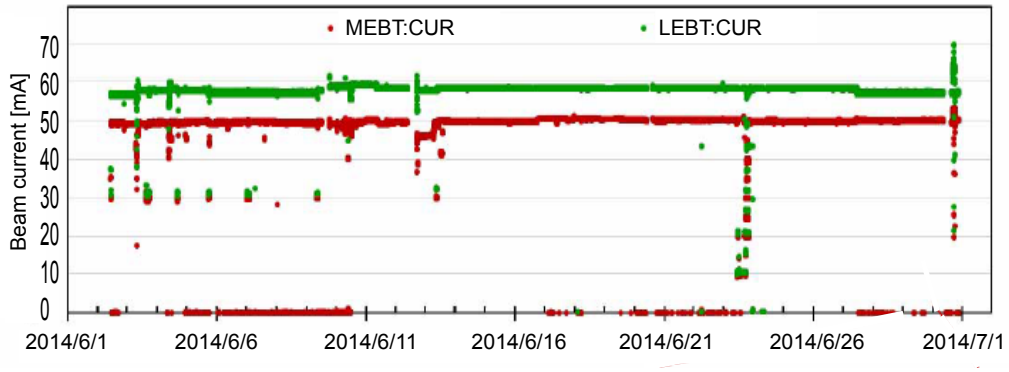

Figure 4. Result of the long-term operation test.

From the results of the first 400MeV beam commissioning, the linac beam had much halo than the lower acceleration energy(181 MeV) operation. In order to improve this condition, we need a beam monitor which can measure the longitudinal shape of the beam. Bunch Shape Monitor (BSM) was installed once for this purpose, but it was replaced due to its high outgas rate[13][18]. Therefore we bake BSM to improve its vacuum property and will install it again in summer 2014.

3.2. RCS

In RCS, a malfunction occurred to the power supply of the injection bump magnet that had been reinforced for 400MeV injection. The flattop region of the shift bump current had a slope due to the defect of the power supply system. This induced the beam orbit shift during injection. Figure 5 shows the magnetic field pattern defect of the shift bump magnet, and the orbit shift due to the defect is shown in figure 6.

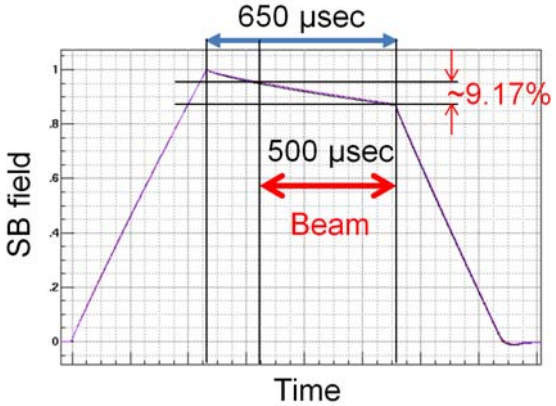

Figure 5. The magnetic field pattern of the shift bump magnet. When it's normal, the magnetic field during injection period has to be flat. However, it has a slope and decreases 9.17 % during injection period.

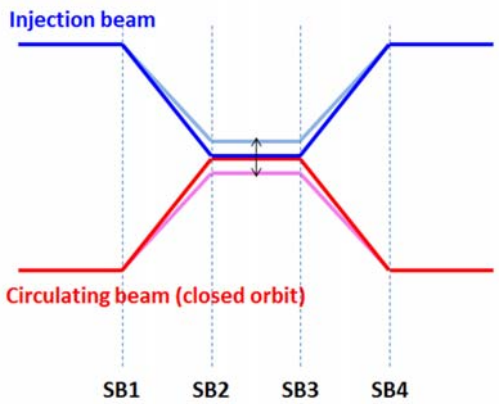

Figure 6. Orbit shift due to the defect of the shift bump field. Four shift bump magnets are excited the one power supply, and these magnetic fields make the injection and circulating orbit merge. Due to the slope of the magnetic field pattern, the injection and circulating beam are separated each other.

So far, we compensated this orbit shift by the other magnets(PBH1-4,PSTR1-2). Figure 7 shows the current waveforms of the injection magnets for compensation, and the injection orbit before and after correction are sown in figure 8.

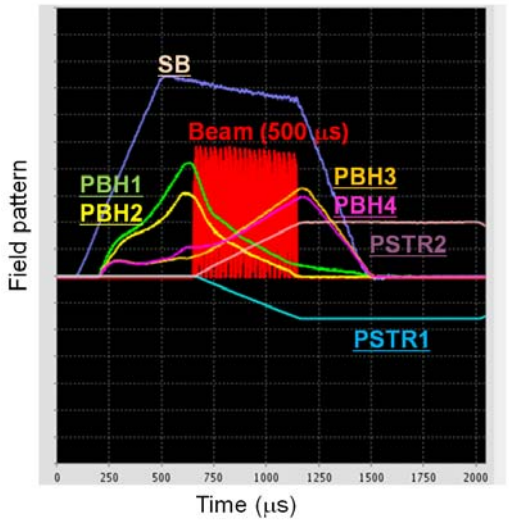

Figure 7 The current waveforms of the injection magnets for orbit correction.

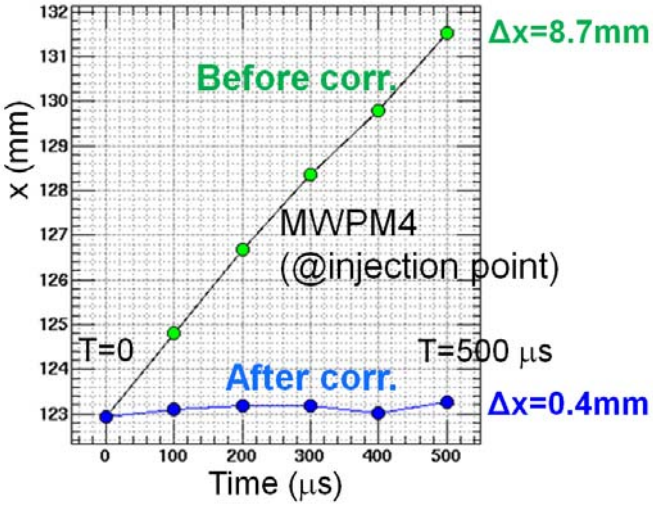

Figure 8 The injection orbit before and after correction.

We also improved the halo scraper system of Linac - 3 GeV RCS Bema Transport (L3BT) line. Previous results[19] showed the scraper system was able to remove the halo of injection beam, and the beam loss in the RCS was reduced. However, the frame of old scraper is too small and the radiation shield of the dump is not enough for continuous operation. We renovated the halo scraper of L3BT line and the dump line for scraped beam.

4. Conclusions and future plan

To achieve the 1 MW output power, the improvements of J-PARC linac and RCS were carried out. As a result, the linac energy was successfully upgraded to 400 MeV with the new ACS system. So far, achieved beam power in user operation is 300 kW for MLF users. The new front-end system will operate to increase the peak current from 30 mA to 50 mA, and the RCS will try to high power demonstration of 1 MW-equivalent beam in Autumn 2014. After that, if possible, we will gradually increase a delivered beam power from 300 kW. Finally, we plan to deliver the design beam power of 1 MW by middle of 2015. But there are some issues to achieve stable 1 MW operation. In the linac, we need to reduce the beam halo and decrease beam loss at ACS section. In the RCS, a countermeasure of the activation at the charge-exchange foil chamber is required. We will clear these issues by the beam commissioning and hardware improvements.

5. References

[1] 2003 *Technical design report of J-PARC* (*KEK Report* 2002-13) (*JAERI-Tech* 2003-44) ed Y Yamazaki
[2] Naito F 2007 Present status of J-PARC *Proc. APAC2007* (Indore, India) MOXMA01
[3] Ikegami M 2008 Progress in the Beam Commissioning of J-PARC Linac and its Upgrade Path *Proc. LINAC08* (Victoria, Canada) MO201
[4] Hasegawa K, Asano H, Chishiro E, Hori T, Ito T, Kobayashi T, Kondo Y, Namekawa Y, Oguri H, Ohkoshi K, Suzuki H, Ueno A, Yamazaki M, Anami S, Fang Z, Fukui Y, Ikegami K,

Kawamura M, Naito F, Nanmo K, Tanaka H and Yamaguchi S 2008 Operating experience of the J-PARC linac *Proc. LINAC08* (Victoria, BC) MOP004
[5] Hotchi H 2008 Status of J-PARC commissioning *Proc. 42nd ICFA advanced beam dynamics workshop HB2008* (Nashville, TN) OPL02
[6] Kinsho M 2009 Status of the J-PARC 3 GeV RCS *Proc. PAC09* (Vancouver, Canada) TU6PFP065
[7] Yamamoto K 2012 J-PARC recovery status *Proc. 52nd ICFA advanced beam dynamics workshop HB2012* (Beijing) MOI1A02
[8] Koseki T and Hasegawa K 2014 Present status of J-PARC -after the shutdown due to the radioactive material leak accident- *Proc. IPAC14* (Dresden, Germany) THPME061
[9] Ao H and Yamazaki Y 2012 *Phys. Rev. ST Accel. Beams* **15** 011001
[10] Ao H, Ueno A, Hirano K, Asano H, Morishita T,Hasegawa K and Yamazaki Y 2012 *Phys. Rev. ST Accel. Beams* **15** 051005
[11] Hasegawa K 2014 Commissioning of energy upgraded linac of J-PARC *Proc. LINAC14* (Geneve) TUO2C06
[12] Ao H, Tamura J, Nemoto Y, Ito T, Ouchi N, Fang Z, Futatsukawa K, Nammo K, Sugimura T and Asano H 2014 High power conditioning of annular-ring coupled structures for the J-PARC linac *Proc. LINAC14* (Geneve) THPOL07
[13] Maruta T, Futatsukawa K, Liu Y, Miyao T, Miura A, Sako H and Ikegami M 2014 Recent progress of beam commissioning at J-PARC linac *Proc. LINAC14* (Geneve) TUO2C06
[14] Ueno A, Koizumi I, Ohkoshi K, Ikegami K, Takagi A, Yamazaki S and Oguri H 2014 *Rev. Sci. Instrum.* **85** 02B133
[15] Kondo Y, Hasegawa K, Morishita T and Robert A J 2012 *Phys. Rev. ST Accel. Beams* **15** 080101
[16] Kondo Y, Morishita T, Yamazaki S, Hori T, Sawabe Y and Takagi A 2014 Beam test of a new RFQ for the J-PARC linac *Proc. LINAC14* (Geneve) MOPP091
[17] Morishita T, Kondo Y, Hori T, Yamazaki S, Hasegawa K, Hirano K, Oguri H, Takagi A, Sugimura T and Naito F 2014 High-power test results of the RFQ III in J-PARC linac *Proc. LINAC14* (Geneve) TUPP095
[18] Miura A, Oguri H, Ouchi N, Tamura J, Feschenko A V, Mirzojan A N, Futatsukawa K, Miyao T, Maruta T and Ikegami M 2013 Bunch length measurement of 181 MeV beam in J-PARC linac *Proc. IPAC13* (Shanghai) MOPME027
[19] Okabe K, Yamamoto K, Yoshimoto M and Kinsho M 2014 Transverse H- beam halo scraper system in the J-PARC L3BT *Proc. IPAC14* (Dresden, Germany) MOPRI108

3.4.2

ESS: The current beam design and target interface

M. Lindroos, M. Eshraqi
European Spallation Source, ESS, Lund, Sweden

Abstract. The ESS top level parameters of 5 MW, 3 ms pulse length and 14 Hz repetition rate are given by user requirements. The choice of 2 GeV, 62.5 mA and 2.87 ms pulse length were at laboratory level and were largely technology driven, e.g. the desire to keep beam current sufficiently low to avoid severe space charge issues resulting in the need of parallel front ends. After technology choices had been made, the final set of requirements resulting in the ESS 2013 lattice design were derived in an iterative process with cost and beam dynamics issues being the two main driving parameters. In large, cost was pushed to a minimum with emittance growth along the linac being used as a quality indicator. The beam is finally transported from the end of the last accelerating element to the target through a dogleg and is rastered over the target surface. We will in this paper review the ESS accelerator design process and will discuss the latest results mainly on the optics of the linac.

1. Introduction

The European Spallation Source, already under construction in Lund, Sweden, has been financed to be a facility with the single purpose of providing spallation neutrons to users and therefore the design parameters have been heavily affected by the requirements dictated by neutron users. These parameters, the high level requirements, are the unprecedented power of 5 MW, a beam pulse of $\sim$ 3 ms and a repetition rate of 14 Hz. The choice of final beam energy of 2.0 GeV and 62.5 mA of beam current are however technology and cost driven. For example a higher beam energy increases the cost of the linac [1] and increasing the beam current strengthens the space-charge non-linear forces that could lead to increased halo growth and higher chance of beam loss. The selection of a reasonable beam energy and current which keeps the linac costs limited while the risk of beam losses is still manageable is discussed in detail in [1].

The ESS linac accelerates 62.5 mA of protons up to 2 GeV in a sequence of normal conducting and superconducting accelerating structures and eventually paints a tungsten target with this beam where a high flux of neutrons will be generated in a neutron rich target material at the same pulse rate as the proton beam. The proton pulses are 2.86 ms long with a repetition rate of 14 Hz − corresponding to a duty cycle of 4%. These parameters are high level parameters which affect the design and geometry of the instruments and the neutron guides.

Hands-on maintenance and machine protection set limits of 1 W/m and 0.1 W/dm respectively, on beam losses and have been a concern in every high power linac. In the ESS case a loss at such a level is in the order of 10^{-7} with respect to the total beam power. Therefore it is very important to design the accelerator, specially for high power accelerators, such that it does not excite particles to beam halo.

At a frequency of 352.21 MHz a 62.5 mA beam has $\sim$ 1.1×10^9 protons per bunch. From $\sim$ 200 MeV onward the acceleration is done at twice the frequency of the front end, 704.42 MHz,

to improve the energy efficiency of the linac. The frequencies, transition energies and structures are schematically shown in figure 1.

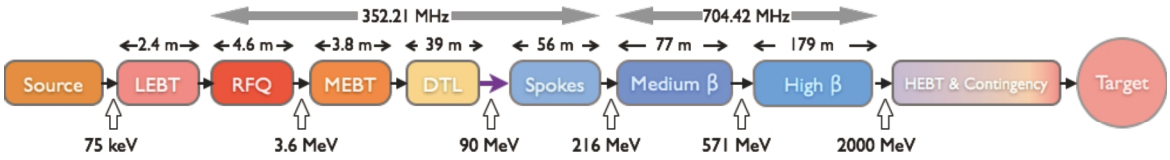

Figure 1: Block layout of the ESS baseline linac 2013, OptimusPlus (not to scale). Warm colored boxes represent the normal conducting components and cold color boxes the superconducting sections.

2. Architecture

2.1. Ion Source and LEBT

The high intensity beam of protons is produced by a Microwave Discharge Ion Source, MDIS. The beam pulse generated by the proton source is up to 3 ms long with an energy of 75 keV and a proton intensity exceeding 80 mA at the source exit. These type of ion sources have a high reliability just shy of 100% and a long mean time between failures, MTBF. The high reliability of these sources has already been demonstrated in similar ion sources [2]. The source is followed by the Low Energy Beam Transport, LEBT, which is composed of two magnetic solenoids that match the beam to the downstream RFQ, a chopper system that removes low quality head and tail of the beam, an iris that is used to generate different (lower) beam currents, and a set of beam diagnostics that measures the beam before it is injected to the linac.

2.2. RFQ

The four-vane RFQ as the first rf accelerating structure in the ESS linac, accelerates, focuses, and bunches the continuous 75 keV beam to 3.62 MeV within 4.6 m [3]. The output energy of the RFQ has increased in this layout from 3 MeV to 3.62 MeV in a process of optimizing all the transition energies in the linac. The beam current at the exit of the RFQ under nominal operation modes should be 62.5 mA, which taking into account the nominal transmission of 98%, the input beam should be at least 64 mA. The rf frequency of the RFQ and hence the bunches is 352.21 MHz. The peak electric fields on the vane surface has been limited to a Kilpatrick value of 1.6.

2.3. MEBT

A medium energy beam transport between the RFQ and the DTL transports and matches the beam out of the former structure to the latter one, provides means to collimate the beam, measures the beam's transverse and longitudinal profile and chops off the remaining low quality bunches which couldn't have been cleaned out by the LEBT chopper. The MEBT is composed of 11 quadrupoles, three buncher cavities, a chopper with its correspondent dump system, 3 sets of 4 independent collimating plates and beam diagnostics.

2.4. DTL

The drift tube linac brings the beam energy to 89.6 MeV in five tanks [4]. Each tank is fed by a 2.8 MW klystron, having left a 30% margin for LLRF, tuning and waveguide losses, 2.2 MW

of power is delivered to the cavity via two rf windows, almost 50% of which is transferred to the beam. Higher input energy to the DTL resulted in longer input cells with several positive consequences; longer cells could house bigger quadrupoles reducing their magnetic gradient for the same integrated gradient, have longer gaps reducing the field at the flat of the drift tube due to magnets and also rf, and enhances the effective shunt impedance, ZTT. The transverse focusing is still provided by permanent magnet quadrupoles, PMQs, that are housed in every other drift tube. Three corrector dipoles per plane per tank are correcting the beam center. The constraints present in a DTL required an optimization process on where to put these corrector dipoles.

2.5. Spoke Section

The DTL is the last normal conducting structure, and right after it comes the Low Energy Differential Pumping section, LEDP, that is used to create the required vacuum quality at the transition to superconducting cavities. The spoke cavities are used to accelerate the beam from 89.6 MeV to 216 MeV. One of the reasons for choosing spoke cavities instead of the conventional normalconducting structures in this energy range is their relatively large transverse aperture and tune-ability for different phase and energy beams. These 352.21 MHz double-spoke cavities with an optimum β of 0.50 are housed in pairs in 13 cryomodules, and are separated by spoke warm units, SWU. Every SWU is composed of a pair of quadrupoles each being equipped with a single plane corrector and a beam position monitor, and a central slot allocated to beam diagnostics [5].

2.6. Elliptical Sections

The rf frequency doubles to 704.42 MHz at the beginning of the next structure, the medium-β elliptical cavities. There are two families of elliptical cavities accelerating the beam from the spoke output energy to 571 MeV using 36 medium-β cavities and further to 2.0 GeV by 84 high-β cavities. In both sections four cavities are housed in cryomodules of identical length. Having different geometric βs of 0.67 and 0.86 respectively, the medium-β cavities are given an extra cell (6-cell) with respect to high-β cavities (5-cell) to have almost the same length. This has been done to achieve the same period length in the medium and high-β sections, making them swap-able in case the required gradient in medium-β is not achieved. There are identical elliptical warm units, EWUs, before each cryomodule. These EWUs have the same functionality as SWUs, with bigger apertures, and longer quadrupoles. To have the same flexibility at the spoke to medium-β transition the period lengths in elliptical section is chosen to be exactly twice that of the spoke section [5].

2.7. HEBT

The same periodicity, in transverse plane, is maintained for 15 periods after the high-β section in the high energy beam transport, HEBT, for contingency purposes. After this contingency area, there is one more EWU which is followed by a vertical dipole with a bending angle of 4° that also works as a switch magnet between the beam dump and the target. The beam going to the target is bent downward to horizontal plane using a second vertical dipole after 6 periods of longer doublet focused sections that are adjusted to create an achromat dogleg. This beam is transported to the target using a set of quadrupoles and 8 raster magnets that paint the target surface in horizontal and vertical directions at different frequencies [6]. To reduce the beam center movement on target due to energy jitter the phase advance between the second dipole and the target surface is set to be a multiple of 180°. A fixed collimator may intercept beam halo, protecting edges of the target, and also stops the back scattered neutrons from target. When the beam is directed to the 12.5 kW beam dump (The first dipole switch off) the beam is magnified on to the dump entrance face using three quadrupoles.

2.7.1. Raster system The beam density on the surface of the target is desired to be as uniform as possible to achieve the lowest peak density. One can either use a non-linear magnetic system to achieve this goal (very distribution dependent) or paint the area with the beam. The ESS HEBT uses a fast horizontal-vertical sweeping system, dubbed raster system, to achieve this goal. The raster system is composed of four dithering dipole magnets per plane which sweeps the beam on the target surface within the 2.86 ms pulse, shaping a rectangle of 180×60 mm^2 (H×V) with almost a uniform density within the footprint that drops to zero at the same rate as the initial beam out of linac does [7]. These magnets are driven by two triangular waveform currents with frequencies of up to 40 kHz.

3. Beam dynamics

3.1. Design Criteria

In the latest design one of the main goals was to keep the cost of the accelerator at the budget, a linac that had a lower final energy, but higher current to keep the power constant. Increased beam current would have increased the effect of space-charge and therefore a study was performed to lower the effect of space-charge without increasing the cost [8]. Following this paper [8], the relative tune spread ($\zeta = 1 - \sigma/\sigma_0$), where σ and σ_0 are the phase advances with and without current respectively, is kept below 0.6 (limiting the number of mismatch resonances to only two) while the current is increased by 25%, see Fig. 2.

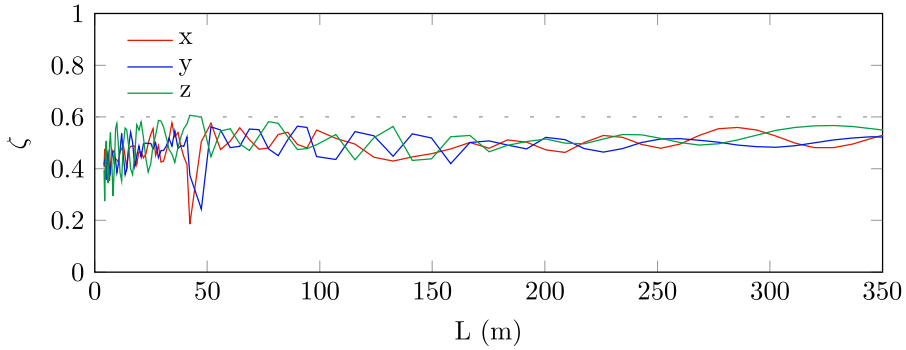

Figure 2: Relative tune spread along the linac, the dotted line marks the 0.6 limit.

The ESS linac will accelerate beam currents from 6.5 mA to 62.5 mA, therefore a smooth and monotonic variation of the phase advance per meter not only improves the matching, it also shortens the tuning time for different beam currents. On top of this, the structures are matched by smoothing the phase-advance variation at transitions to assure a good beam quality throughout the accelerator, even with different beam currents. The transverse phase advance per period is limited to 87° to reduce the percentage of the beam that due to their phase otherwise would have had a phase advance exceeding 90° per period.

To improve the acceleration efficiency, the longitudinal phase advance per period is limited throughout the linac to85°, a limit which is reached only in the medium β section. On top of the transverse aperture, the longitudinal acceptance has also been kept large not to cause longitudinal losses which eventually result in transverse losses.

Tracking a beam of 100,000 macro-particles with a gaussian distribution in 4D and truncated at $4 \times \sigma$ from the RFQ input to the target shows the beam behavior under perfect settings. This tracking is performed using the code TraceWin [9]. The envelopes stay confined well within the aperture and no significant emittance growth is observed in the linac, see figure 3. The halo values stay also confined with this design, removing the need for a collimation system.

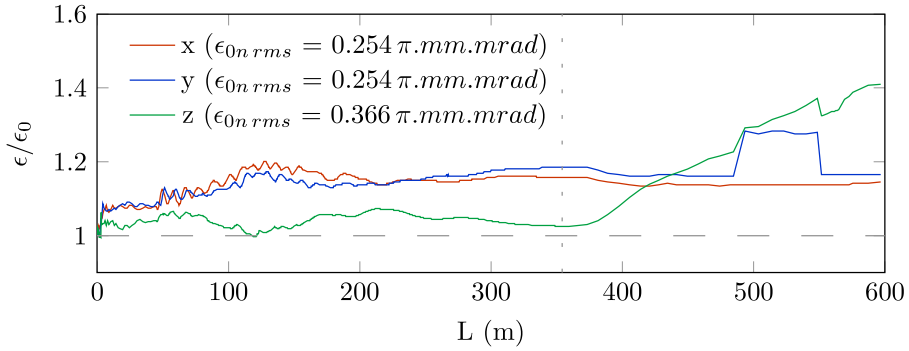

Figure 3: RMS emittance growth with respect to input beam along the linac and HEBT. Vertical dotted line shows the end of linac/start of HEBT.

4. Summary

The ESS linac is designed through a collaboration with several institutes and universities. Even with a reasonably high beam current an integrated and careful design of the linac beam dynamics assures that the beam quality along the linac is not degraded and losses are avoided. The high quality beam is swept on the neutron production target surface to create a uniform beam using a set of high frequency dipole magnets.

[1] D. McGinnis, "New Design Approaches for High Intensity Superconducting Linacs - the New ESS Linac Design", *in proceedings of* IPAC 2014, Dresden, Germany.
[2] L. Celona et al., Rev. Sci. Instrum. 75, 5 (2004).
[3] A. Ponton, "Note on the ESS RFQ Design Update", ESS Technical Report, 2014.
[4] R. D. Prisco, *et.al.*, "ESS DTL Status: Redesign and optimizations", *in proceedings of* IPAC 2014, Dresden, Germany.
[5] M. Eshraqi, "Beam physics design of the Optimus+ SC linac", eval.esss.lu.se/DocDB/0003/000309/003/OptimusPlus.pdf.
[6] H. D. Thomsen, S. P. Møller, "The ESS High Energy Beam Transport after the 2013 Design Update", *in proceedings of* IPAC 2014, Dresden, Germany.
[7] H. D. Thomsen, S. P. Møller, "The Design of the Fast Raster System for the European Spallation Source", *in proceedings of* IPAC 2014, Dresden, Germany.
[8] M. Eshraqi, J,-M, Lagniel, "On the choice of linac parameters for minimal beam losses", IPAC2013.
[9] R. Duperrier, N. Pichoff and D. Uriot, Proc. International Conf. on Computational Science, Amsterdam, The Netherlands, 2002.

3.4.3

Cyclotron-based high power neutron sources at PSI - operating experience and future outlook

D. Reggiani, D. Kiselev, T. Reiss, M. Seidel, R. Sobbia, V. Talanov and M. Wohlmuther

Paul Scherrer Institut, CH-5232 Villigen-PSI, Switzerland

E-mail: davide.reggiani@psi.ch

Abstract. The 1.4 MW PSI High Intensity Proton Accelerator (HIPA) operates concurrently two spallation sources, the continuous beam SINQ and the macro pulsed Ultra Cold Neutron (UCN) source. The paper discusses aspects related to beam operation, diagnostics and losses. Moreover, an outlook on the SINQ proton beam line upgrade projects currently under study like a beam flattening system as well as the design of a muon extraction channel are presented.

1. Introduction

The PSI high intensity proton accelerator (HIPA) generates a continuous wave (50.6 MHz frequency) 590 MeV, 1.4 MW beam [1]. A schematic of the accelerator complex is shown in Fig. 1. Protons are first brought to 870 keV by a Cockcroft-Walton generator and then transferred through a LEBT-section to the 72 MeV injector cyclotron. The medium energy beam is transferred to the 590 MeV ring cyclotron. High beam intensity can be achieved by limiting the extraction losses within the low 10^{-4} range, therefore preventing unsustainable machine activation. The 1.4 MW beam is first transported to a 5 mm thick meson production graphite target (M) where about 1% of the beam is lost. A second 40 mm thick graphite target (E) is mounted some 18 m downstream. About 8% of the beam is lost on the target itself while an additional 21% of it is absorbed by a collimator system that reshapes the highly divergent beam and protects accelerator components from activation and unnecessary beam load. The remaining beam is eventually transported to the SINQ neutron spallation source where it is completely stopped and absorbed. In case of a SINQ technical stop, the HIPA facility can still run at about 1 MW beam power (75% of the nominal intensity) due to a beam dump installed downstream of target E. A total of seven muon or pion secondary beam lines are located at the meson production targets M and E while SINQ provides neutrons for seventeen beam lines. In 2011 the ultra cold neutron (UCN) source was brought into routine operation at HIPA [2, 3]. This second spallation source runs concurrently to SINQ and is driven by macro pulses of the full 1.4 MW proton beam kicked into the UCN beam line with a typical duty cycle of about 1%. The switchover of a megawatt class beam between two beam lines is a unique feature of the PSI high intensity proton accelerator facility.

During the forty years of operation, the beam current of the PSI proton accelerator has been constantly increased from 0.1 to 2.4 mA. The aim for the next years is a further stepwise intensity upgrade that should bring the machine towards the 3.0 mA (1.8 MW) limit. However, some modifications in the transport of the high power beam are a prerequisite for reaching this

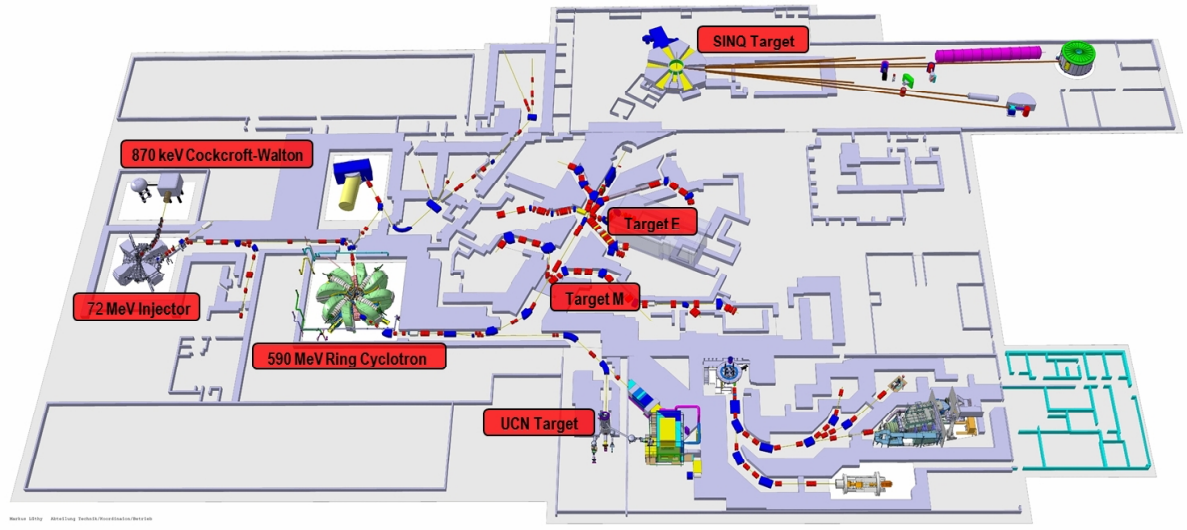

Figure 1. Overview of the PSI high intensity accelerator facility.

goal. One critical issue is the reduction of the beam losses downstream of target E, in particular on the collimator C2. Moreover, an additional increase of the beam current should be combined with a beam flattening system that would create a more uniform temperature distribution in the SINQ target. Another idea that was proposed recently is the possibility of extracting surface muons backscattered off the SINQ target and to guide them into a dedicated beam line. A two-year feasibility study is currently ongoing which should answer the question of the technical practicability.

2. Beam extraction

Extraction losses are usually the limiting factor of a high power cyclotron. At PSI, at the nominal beam intensity of 2.2 mA, the extraction losses are typically kept below 500 nA, which corresponds to the remarkable efficiency of 99.98%. Extraction losses result from the scattering of halo particles in the electrostatic deflector placed between the orbits of the last two turns. This effect can be minimized by providing a large orbit separation as well as by limiting the size of the beam deflector. Both these methods are applied at the PSI ring cyclotron. In an isochronous cyclotron the orbit separation is due to two different effects. The most obvious one is the acceleration term that causes a radius increment per turn given by:

$$\frac{dR}{dn_t} = \frac{R}{\gamma(\gamma^2-1)}\frac{U_t}{m_0c^2}$$

where U_t is the energy gain per turn, R the orbit radius and γ the relativistic factor. A large turn separation can therefore be obtained by building a large radius machine and by furnishing it with a powerful RF-system. In this way a large U_t or, respectively, a small number of turns N_t can be achieved. On the other hand, the relativistic term $\gamma(\gamma^2-1)$ disfavors the radius increment as the energy increases, thus limiting the maximum energy of a cyclotron accelerator to roughly 1 GeV. The extraction parameters of the PSI ring cyclotron are $R = 4460$ mm, $U_t \approx 3$ MeV, $\gamma = 1.63$. Plugged into the above equation, these figures give a radius increment between the last two turns of about 6 mm. This value can be substantially increased by exploiting the betatron motion of the beam around the ideal orbit. In fact, by carefully choosing the injection parameters, the phase of the horizontal betatron oscillation can be tuned in a way that at the location of the extraction deflector three turns overlap while the very last one gets a maximum

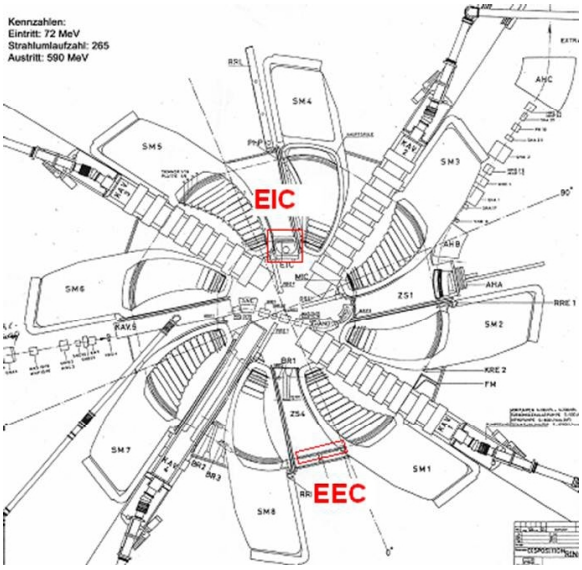

Figure 2. Drawing of the PSI 590 MeV ring cyclotron. The injection (EIC) and extraction (EEC) electrostatic elements are highlighted in red.

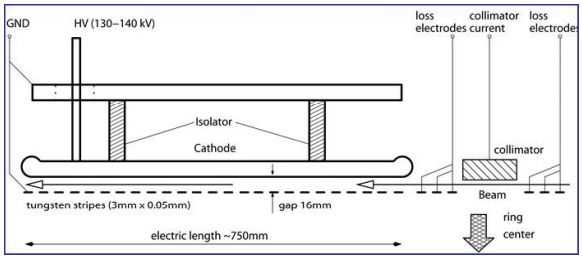

Figure 3. Principle of the electrostatic extraction channel EEC.

radial separation. In this way the gap between the last two turns can be raised from 6 to 18 mm at the PSI ring cyclotron.

A drawing of the ring cyclotron with the electrostatic injection and extraction elements is shown in Fig. 2. The extraction line consists of the electrostatic extraction channel (EEC) followed by the two sector magnets SM1 and SM2 (with the focusing element FM in between) and the magnetic transport line composed of the magnetic septum AHA and the AHB bend. The electrostatic element EEC is composed of a series of 50 μm thick tungsten stripes set to ground potential and placed in-between the last two turns of the ring cyclotron (Fig. 3). Thanks to this very thin structure, beam losses due to scattering are minimized. The cathode is located outside of the last turn and operates at a potential of -145 kV. The high voltage gap is 16 mm broad with an effective length of 920 mm. The total deflecting angle is $\theta_{beam} = 8.2$ mrad.

3. Beam transport to the SINQ target

After being extracted from the ring cyclotron, the beam is guided to the meson production targets M and E and eventually to the SINQ spallation source. Figure 4 represents the horizontal (x) and vertical (y) beam envelopes over the 116 m long transport channel. Light blue elements represent bending magnets while the red ones are quandrupoles. Collimator apertures are depicted as black arrows. Green areas represent the target regions where significant amounts of beam are lost. Away from targets, the average loss rate is as low as 1 nA/m (0.6 W/m). Figure 4 was obtained by putting together beam envelope fits of the three beam line sections ring extraction to target M, target M to target E and from target E to SINQ. Such fits are routinely performed at PSI employing the beam profiles measured by over fifty horizontal and vertical beam profile monitors and fitting the 2σ beam widths by means of the TRANSPORT computer code [5]. At the location of the meson production targets M and E, the 2σ beam widths are of the order of 1.5 mm and 2.5 mm in the horizontal and vertical plane respectively. Considering a Gaussian beam distribution, this translates into a peak beam power density of almost 200 kW/mm^2. Target M absorbs about 1% of the beam without a significant change

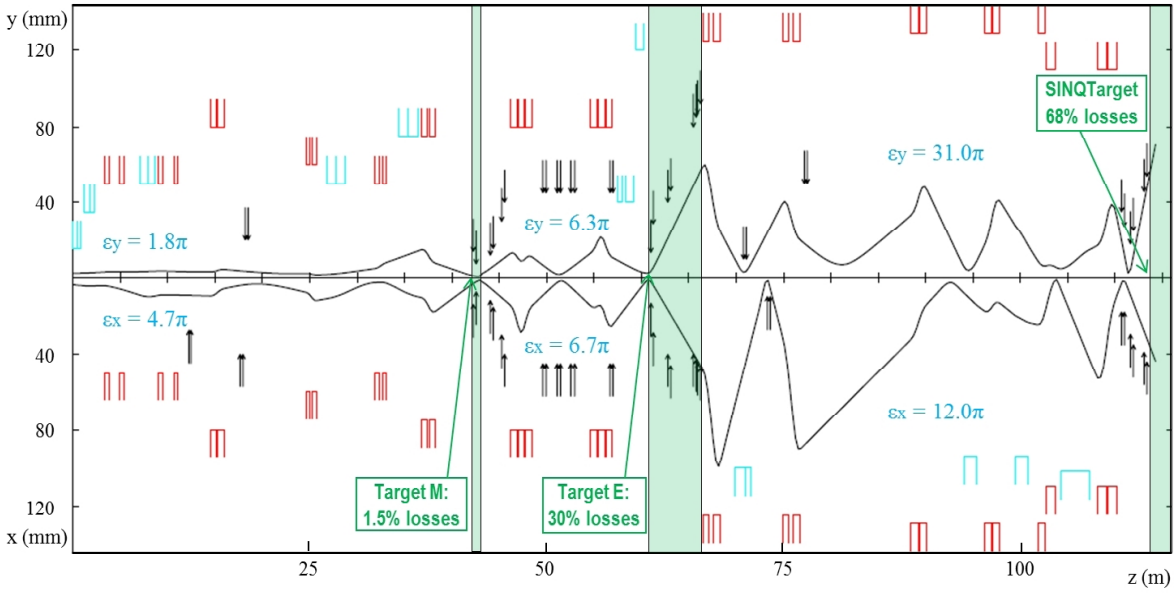

Figure 4. Horizontal and vertical beam envelopes along the PSI high intensity transport line starting from the ring extraction. Beam emittances (2σ) are expressed in unit of mm·mrad and refer to the non-dispersive component.

of the beam energy. The target is composed of a 5 mm thick graphite wheel rotating at a frequency of 1 Hz and shielded against beam misalignment by a Densimet® collimator. The beam transport between target M and target E in handled through a dispersion free beam line section composed of two quadrupole triplets. Two copper collimators are installed 1 m and 2 m downstream of target M respectively in order to shield the beam line components from large angle scattered protons. Between the two triplets and inside the last quadrupole, the vacuum pipe is furnished with four built-in 316L-steel collimators, each of them protecting a beam profile monitor from uncontrolled beam loss. Up to target E, the proton beam transport line is equipped with over 30 beam position monitors (BPMs). These diagnostic devices are integrated in an automatic beam position control system making use of the BPMs signals in order to control a similar number of steering magnets. Furthermore, the beam position and tilt in front of target E can be adjusted by means of a bump formed by three bending magnets. The design of the meson production target E is similar to the one of target M, but the thickness of the rotating wheel is 8 times larger (40 mm). This causes beam energy degradation from 590 to 575 MeV. Beam absorption and losses are also significant. Around 8% of the beam is absorbed by the target material, while about 21% is cut away by a group of four oxigen free copper (OHFC) collimators (Fig. 5) or lost in the local shielding. This collimation system, installed between target E and the first magnetic element, can be subdivided into two subsystems: the first two collimators (C0-C1) shield the beam line from large angle scattered beam particles, while the second pair (C2-C3) reshapes the proton beam leaving the target E region in order to match the geometric acceptance of the SINQ beam line. A pair of vertical and horizontal movable slits located 5 and 7 m downstream of C3 respectively capture halo particles originating from scattering off C2-C3. The C2-C3 water cooled collimator system is located 4.7 m downstream of target E. Each collimator is 30 cm long, has an elliptical cross section and a segmented structure made of teeth whose thickness grows along the radial as well as the longitudinal direction. In the present configuration, the collimators' elliptical aperture diverges along the beam direction in order to follow the increasing beam envelope. The collimator system was originally designed to withstand

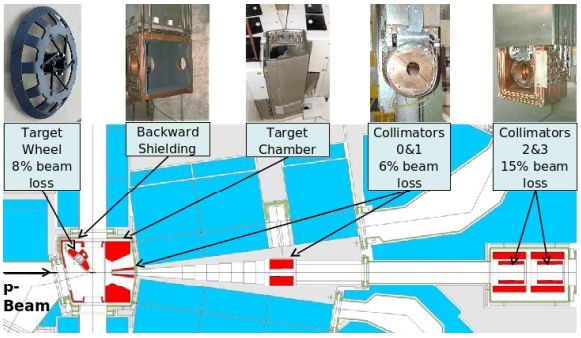

Figure 5. Horizontal cut through the target E region at the proton beam plane.

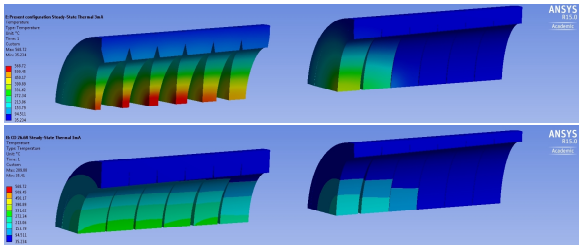

Figure 6. ANSYS simulation of the temperature distribution (same scale) in the collimators C2 (left) and C3 for the current (top) and the proposed new design (bottom).

2 mA (1.2 MW) beam current. ANSYS [4] simulations showed that, at 3.0 mA, C2 would reach a peak temperature of 570 °C in case of an aligned beam (Fig. 6). This value is well beyond the accepted safety limit of 405°C, corresponding to 50% of the melting temperature of copper. For this reason, a simulation based optimization of the collimator design was started [5, 6] and accomplished in 2014 [5, 7]. Turtle [8] beam line simulations have shown that a 12.5% widening of the collimator system aperture would be compatible with the beam line acceptance and would not have any negative impact on the loss rate on the beam line components located downstream of C3. Moreover, the shielded region located directly downstream of the collimators would profit from the decreased scattering rate and the overall beam line transmission would raise by about 4%. A slight re-tuning of the beam optics would allow to keep the beam footprint at the SINQ target window almost unaltered. This outcome represents the starting point for the optimization of the collimator geometry performed by means of ANSYS. The proposed new design exhibits a 12.5% wider opening at the downstream end of C3, thicker teeth (C2) and a convergent-divergent (C2-C3) aperture scheme. The results are a much more uniform temperature distribution and a peak temperature at 3.0 mA of only 290 °C in case of aligned beam (Fig. 6) and 386 °C considering a 1 mrad beam tilt.
Up to target E the bending plane is horizontal. However, SINQ has a vertical bending plane. After leaving the target E region, the beam reaches the dipole magnet AHL that deflects the protons downwards, 11 m below the level of target E. Three other bends then turn the beam upwards in order to reach the SINQ target from below. The last quadrupole doublet defocuses the beam such that at the target entrance the beam footprint presents an elliptical cross section with $2\sigma_x = 44$ mm and $2\sigma_y = 58$ mm. Three copper collimators installed immediately before the end of the beam line shield the rim of the target entrance window and, at the same time, prevent activation of the beam line components from back scattered neutrons. A review of the SINQ target can be found in [9].

4. The UCN beam line

Since August 2011, the UCN spallation source is operated at the PSI-HIPA complex. The concurrent operation of UCN and SINQ is made possible by a pulsing system that switches the entire 1.4 MW beam between the SINQ and UCN beam lines with a duty cycle of 1%. The typical pulse length is 6 s, with a maximum allowed duration of 8 s. During the UCN pulse, neutrons arising from the target are first thermalized in liquid D_2O and then cooled down to UCN in a deuterium crystal kept at 5 K. The generated ultra-cold neutrons are stored in a tank and eventually guided to the experiments. A drawing of the UCN beam line is presented in Fig. 7. The heart of the beam switching system is a small, air-cooled, fast kicker magnet installed about 12 m downstream of the ring extraction point. The 6 mrad tilt given by the kicker produces

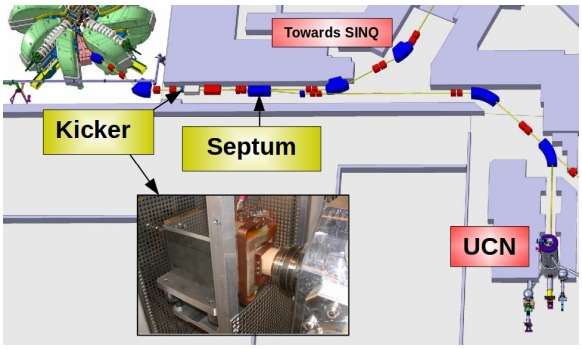

Figure 7. Drawing of the UCN beam line along with a picture of the kicker magnet.

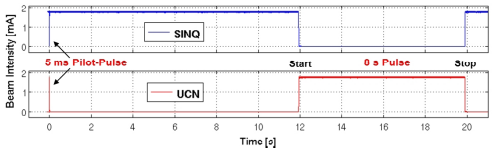

Figure 8. The first 8 s long megawatt UCN beam pulse produced in December 2011.

a 40 mm horizontal displacement seven meters downstream, thus allowing the beam to enter a magnetic septum getting diverted into the UCN beam line. During the transition, the beam is absorbed by a tungsten collimator installed at the upstream end of the septum. In order to limit activation, the switchover time has to be kept as short as possible. For this reason, the timing of the kicker power supply has been tuned such that the first 85% of the beam angular deflection is reached within 1 ms. Under these conditions, considering a UCN operation of one pulse every 200 s without interruptions over one year, calculations have shown that, after 15 days decay time, the collimator dose rate does not exceed 65 mSv/h at a distance of 3 cm from its surface. Nevertheless, instantaneous losses on the collimator are too large for the machine protection system. Hence, in order to prevent beam trips, the interlock thresholds of several beam loss monitors are substantially raised during 3 ms at the beginning of each kick. The actual UCN transport line begins at the location of the septum and guides the beam over 46 m towards the UCN source. Ten meters upstream of the target, the beam is blown up by a quadrupole magnet and then collimated so that at the target entrance it gets a circular footprint with a 4σ diameter of 160 mm. The kicking scheme includes at least one 7 ms short pilot pulse before each several seconds long UCN production pulse. This procedure was implemented in order to check that the proton beam is well centered already at the start of the production pulse. During the pilot pulse, the beam position is measured by 14 BPMs and 4 harp monitors. If the beam displacement exceeds the tolerance level, a centering step is performed and a new pilot pulse is kicked into the UCN beam line. The commissioning of the UCN started in 2008 and lasted three years. During this time the UCN source was not yet ready, therefore the beam line was developed and tested by employing a small beam dump installed for this purpose downstream of the last bending magnet. In December 2010, the first 8 s long megawatt beam pulse was produced (Fig. 8).

5. Simulation of a beam flattening system for SINQ

The spallation region of the SINQ target is composed of a rod bundle with over 30 rows of zircaloy tubes filled with lead, actively cooled by D_2O. The highly inhomogeneous Gaussian proton beam causes thermomechanical stresses that could lead, on the long term, to damage the target structure. This is a critical issue for the beam current upgrade program. In the SINQ beam line, the employment of non-linear magnetic elements, like octupoles, to fold beam fringes is ruled out because of the strong influence of such elements on the footprint shape. Additionally, octupole fields generate sharply peaked beam edges that would cause large activation of the three SINQ collimators. On top of that, due to lack of space, these elements could not be installed without a major reshuffle of the proton beam line. A relatively simple way of flattening the

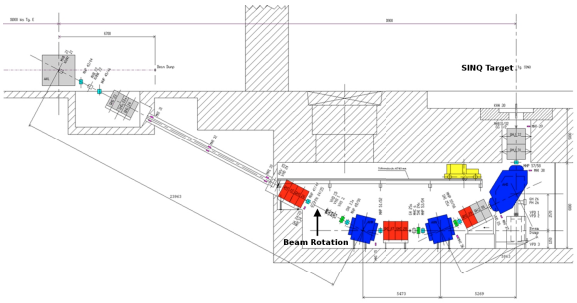

Figure 9. Layout of the SINQ beam line with the possible location of a beam rotation system, indicated by an arrow.

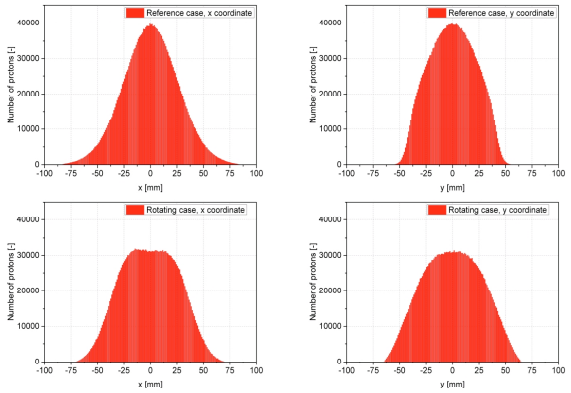

Figure 10. Turtle simulation of proton beam transverse distributions at the SINQ target entrance window with present optics (top) and applying a beam rotation system (bottom).

beam distribution could be accomplished by means of a beam rotation system [10]. The space needed for the installation of the two small dipoles would be available some 24 m upstream of the SINQ target entrance window (Fig. 9). Beam optics simulations were carried out with the goal of getting an efficient beam flattening with reasonable losses at the SINQ collimators. The resulting beam distribution (shown in Fig. 10 along with the present one) exhibits a 50% reduction of the peak current density (from 36.5 to 17.7 μA/cm^2). The energy deposition in the SINQ target and the effect of the beam rotation on the neutron flux were simulated with the Monte Carlo code MCNPX [11]. In order to start with a realistic source, the proton beam distributions generated by means of Turtle were used as input for MCNPX. The comparison of the peak energy deposition in the central rods over the target length for the present and the rotating beam (Fig. 11) shows the benefits of the beam rotation. Furthermore, a significant decline in the neutron production was ruled out. Nevertheless, due to the rotation of the proton beam, a time dependent oscillation of the neutron fluxes from the cold source has to be expected.

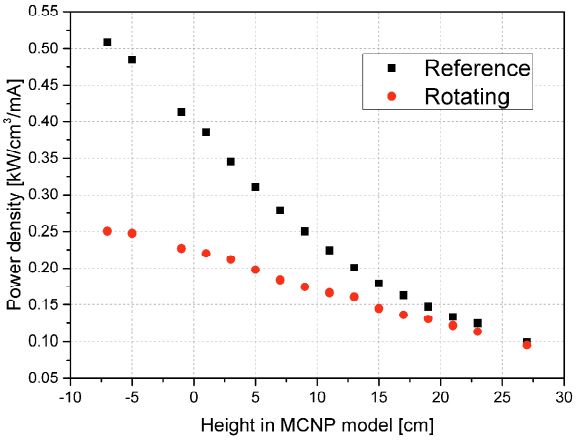

Figure 11. Peak energy deposition in the central rods along the target.

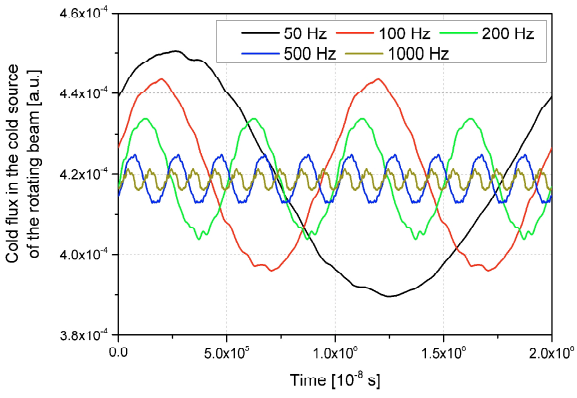

Figure 12. The time-dependent cold neutron flux in the cold D_2 source with different rotation frequencies.

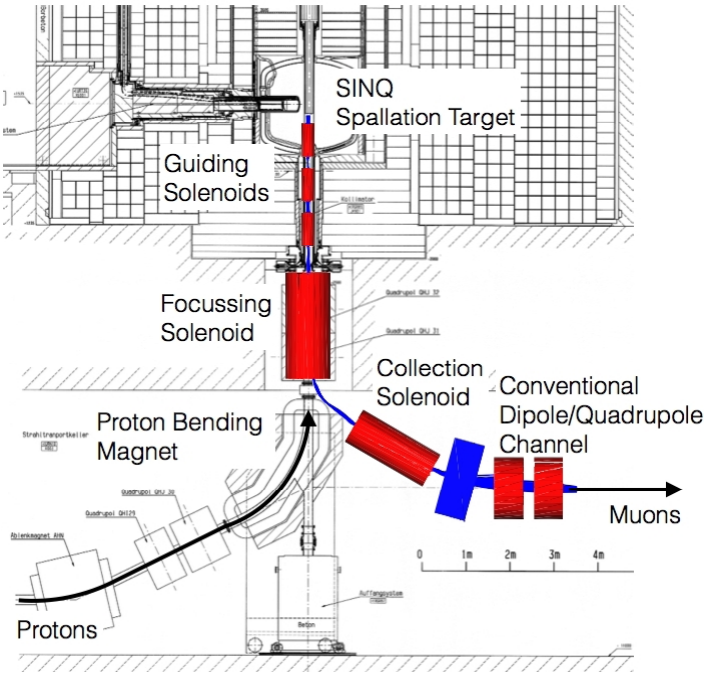

Figure 13. Schematics of the SINQ surface muons extraction concept. 28 MeV/c momentum backscattered muons are guided and focusses along the proton beam line by means of solenoid magnets before being deflected into a dedicated beam line through the fringing field of the last dipole magnet of the proton beam.

This modulation was simulated for different rotation frequencies (Fig. 12). In order to limit the cold neutron flux modulation to less than 2%, a rotation frequency on the order of 1000 Hz is required.

6. Study of surface muons extraction from SINQ

High rate muon beams are highly demanded tools both in applied and fundamental research. Solid state physicists exploit the so-called muon spin resonance (μSR) technique in order to probe the microscopic properties of novel materials. In particle physics, the search for lepton number violating processes, measurements of the muon decay properties as well as studies of muonic atoms decay are carried out by means of precision experiments relying on the availability of intense muon beams. At the PSI-HIPA facility muon rates of up to $4 \cdot 10^8$ μ/s are currently available at the target E secondary beam lines. Simulations have shown that this already remarkable figure could be substantially increased if one could collect the muons coming from the decay of pions produced in the neutron spallation target of the SINQ facility and stopped in its beam entrance window. A schematic showing the working principle of this concept is given in Fig. 13. Potentially, muon rates on the order of 10^{10} μ/s could be achieved in this way. The feasibility of this project is being assessed by a two year study currently carried out at PSI. Results are expected by mid 2015.

7. Conclusion

The PSI-HIPA 1.4 MW proton machine is a very well established facility and, after four decades, still at the forefront of the intensity frontier. Room for a stepwise improvement up to 1.8 MW is available and requires optimization of crucial aspects like extraction losses, beam collimation after target E as well as beam energy deposition on the SINQ target. An improved design of the target E collimator system was recently proposed and the manufacturing should be carried out within the next two years. The preliminary design of a beam rotation system for the SINQ spallation source at PSI was presented. Results showed that the beam rotation would bring substantial benefits in terms of distribution of the energy deposition in the SINQ target without affecting the neutron spectrum and yield. In order to limit the amplitude modulation of the

neutron flux, a rotation frequency in the order of 1 kHz is required. Another interesting idea currently under investigation is the possibility of exploiting the SINQ target as a high intensity source of surface muons.

References

[1] M. Seidel et al., "Production of a 1.3 MW proton beam at PSI" IPAC10, Kyoto, Japan, May 23-28, 2010.

[2] D. Reggiani et al., "A macro-pulsed 1.2 MW beam for the PSI ultra-cold neutron source", PAC09, Vancouver, Canada, May, 4-9, 2009.

[3] B. Lauss, "Ultracold neutron production at the second spallation target of the Paul Scherrer Institute", Proceedings of the ESS Science Symposium on Neutron Particle Physics at Long Pulse Spallation Sources 2013, Physics Procedia, Volume 51, pp 98101 (2014).

[4] ANSYS, Inc., http://www.ansys.com/

[5] D. Reggiani et al., "Beam Transport Optimization Studies of the PSI MW-Class Proton Channel", IPAC14, Dresden, Germany, June 15-19, 2014.

[6] Y. Lee et al., "New Design of a Collimator System at the PSI Proton Accelerator", HB2010, Morschach, Switzerland, September 27 - October 1, 2010.

[7] R. Sobbia et al., "PSI Technical memorandum", in progress.

[8] U. Rohrer, "Graphic Transport/Turtle Framework", http://aea.web.psi.ch/Urs_Rohrer/MyWeb

[9] W. Wagner, "PSIs experience with high-power target design and operation", 3rd High-Power Target Workshop, Bad Zurzach, Switzerland, September 10-14, 2007.

[10] D. Reggiani et al., "Simulation of a beam rotation system for the SINQ spallation source at PSI" IPAC'13, Shanghai, China, May 12-17, 2013.

[11] D.B. Pelowitz (ed.), "MCNPX User's Manual Version 2.7.0", Los Alamos National Laboratory Report, LA-CP-11-00438, April 2011.

3.4.4

Temporal Characteristics of the ESS Proton and Neutron Pulses

T J Shea[1], E Pitcher[1], A Takibayev[1], K Andersen[1], L Celona[2], P Henry[1], F Mezei[1,3], H D Thomsen[4] and L Zanini[1]

[1] European Spallation Source, P.O Box 176, SE-221 00 Lund, Sweden
[2] INFN-LNS, Via S. Sofia 62, 95123 Catania, CT Italy
[3] Hungarian Academy of Sciences, Wigner RCF, Budapest, Hungary
[4] Institute for Physics and Astronomy, ISA, Aarhus University, DK-8000 Aarhus, Denmark

E-mail: thomas.shea@esss.se

Abstract. The European Spallation Source will deliver 2.86 millisecond neutron pulses to neutron scattering instruments. The temporal character of these long neutron pulses depends on a number of factors such as the thermal neutron lifetimes in the moderator and reflector, and temporal fluctuations and trends in the proton current over the duration of the beam pulse. In addition, the proton beam delivery system produces an acceptable size on the target by transversely rastering a centimeter size beamlet during the time of each beam pulse. Since the moderator coupling depends on the proton beam position, this technique can lead to time-dependent neutron intensity. All of these factors affect the temporal structure of the neutrons delivered to the instruments in a wavelength-dependent manner. Simulation results will be presented, and the impact on instrument performance will be discussed.

1. Introduction

The ESS neutron instrument suite is being designed to accommodate pulses 2.86 ms long, arriving at a repetition rate of 14 Hz [1]. With this long pulse length, the temporal characteristics of the proton pulse can impact the structure of the moderated neutron pulse. Although the moderation process filters features with time constants of less than tens of μs, strong effects or those with long timescales can still impact the neutron pulse shape. Within the pulse, the two primary contributors to neutron intensity fluctuations are expected to be: 1) the fluctuating proton current on the target, and 2) the varying position of the proton beam as it is scanned across the target. Assessment of these effects may allow development of mitigation or correction techniques well in time for commencement of the ESS neutron science program.

2. Contributors to neutron intensity fluctuations

To deliver 5 MW on target, the ESS accelerator extracts pulses from a proton ion source, accelerates and transports them with low loss, finally producing 2.86 ms pulses of 2 GeV protons with a peak current of 62.5 mA. The beam delivery system then expands the millimeter-scale beam to transverse dimensions of about a centimeter, and scans it rapidly across the face of the target. Neutron intensity depends upon the proton beam current, energy, and position. The design of the accelerator allows an output energy variation of $\pm 1.5\%$ and the time structure of this variation depends upon RF control performance that is not yet known. Therefore, only the

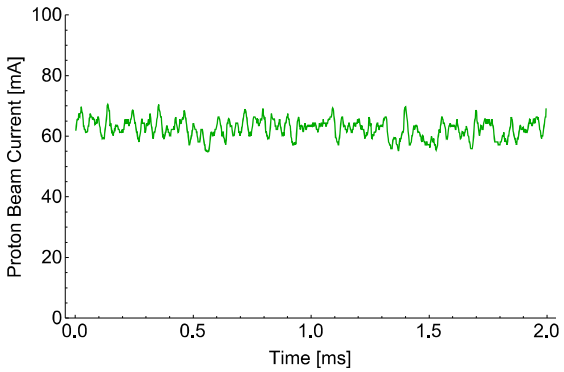

(a) Proton current waveform

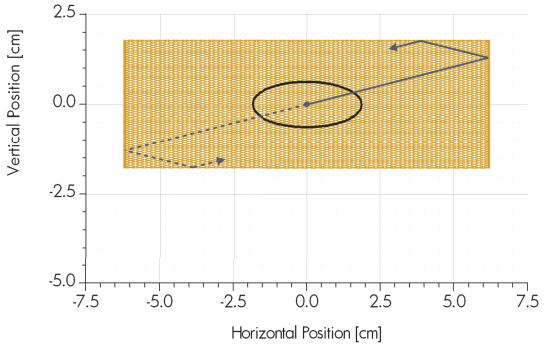

(b) The raster pattern showing about 10 μs of the direct (solid) and inverted (dashed) scans .

Figure 1: Two primary contributors to neutron intensity fluctuations

effects of proton beam current and position have been assessed. They are expected to be the dominate contributors to variations in neutron intensity, but others will be considered as the ESS design progresses.

2.1. Proton current variation

The accelerator requirements specify an output current that remains within a ±3.5% window after averaging over any 200 μs interval. Although the low energy sections could exhibit some small variations in beam loss within the pulse, the higher energy sections must achieve a total loss far below 1%. Therefore, variations in ion source current are expected to be the dominant source of current fluctuations in the pulse that reaches the target.

Although the ESS ion source is not yet available, tests with a similar source have already been performed. In pulsed mode, test results from December of 2013 exhibit current fluctuations of about 3% RMS within the pulse. To simulate a worst case pulse waveform, a representative pulse has been scaled such that it barely meets the requirements. This results in a 62.5 mA pulse that reaches the maximum allowable current variation and contains the time structure typical of an ESS-type ion source. Figure 1a depicts 2 μs of this beam current waveform.

2.2. Raster scanning

Hands-on maintenance of the accelerator mandates extremely low beam loss. To achieve this, the accelerator preserves a low emittance and small transverse beam size. Because the target cannot sustain the resulting power density, a beam delivery system moderately expands the small beam from the linac to a beamlet of RMS dimensions 15.9 mm vertically and 5.3 mm horizontally as depicted by the ellipse in figure 1b. Then, during the pulse, a raster magnet system scans the expanded beam across the target with triangular waveforms of 39.55 kHz horizontally and 29.05 kHz vertically. The maximum horizontal deflection is ±63 mm and the maximum vertical deflection is ±18 mm. Figure 1b shows the resulting raster pattern. Reference [2] provides more detail about the beam delivery system while reference [3] presents the design considerations and preliminary results that stimulated the present study.

3. Neutronics simulations

3.1. Model

The moderator-reflector assembly proposed for ESS is based on the innovative concept of low-dimensional neutron moderators [4]. Figure 2 shows the geometry adopted for the present study.

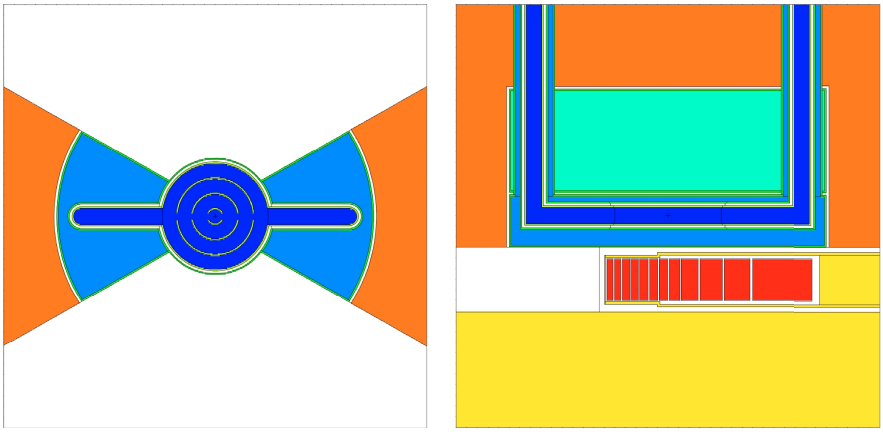

(a) Top view cross section through moderator

(b) Side view cross section through center of target and moderator assembly

Figure 2: Geometry of target, moderator and reflector assembly as modeled in MCNPX. Color legend: blue is liquid hydrogen, light blue is water, green is beryllium (+10% vol. water), red is Tungsten. The beam comes from the left.

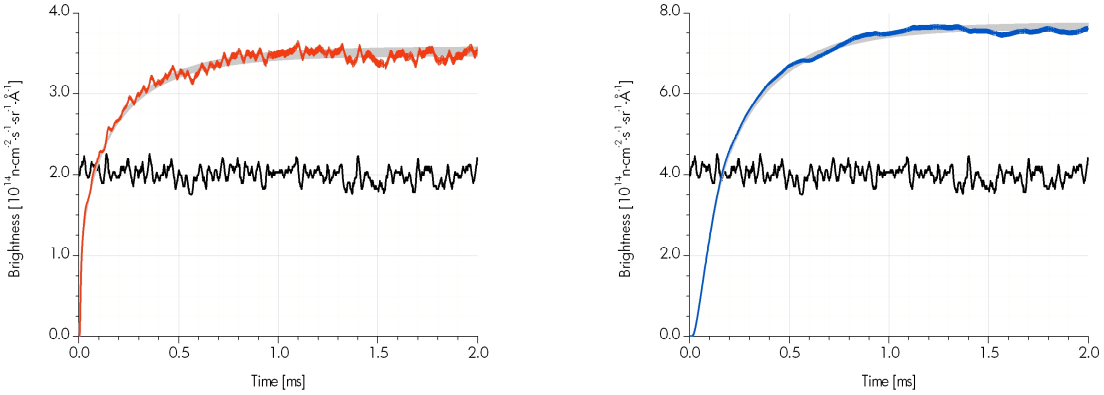

(a) 0.8 Å neutron pulse produced by thermal moderator: grey line from ideal proton pulse, red line from worst case proton pulse (black line, not to scale)

(b) 2.5 Å neutron pulse produced by cold moderator: grey line from ideal proton pulse, blue line from worst case proton pulse (black line, not to scale)

Figure 3: Neutron pulses resulting from beam on target without raster scanning

It consists of a flat, liquid para-hydrogen disk (cold moderator) within a water jacket featuring extended wings (thermal moderator). A beryllium reflector caps the moderator assembly.

Simulations have been performed using the MCNPX Version 2.6.0 particle transport code coupled with the ENDF-B/VII.0 and JENDL-4.0 nuclear data libraries [5–7]. In all cases, a time step of 300 ns was used.

3.2. Effect of proton current variations

To isolate the impact of proton current fluctuations, one series of simulations used a beam with a fixed location on target and the current waveform shown in figure 1a. Figure 3 shows the resulting neutron pulse intensity versus time from both the thermal and the cold moderators. For reference, the pulse produced by a proton beam of ideal square temporal profile is also

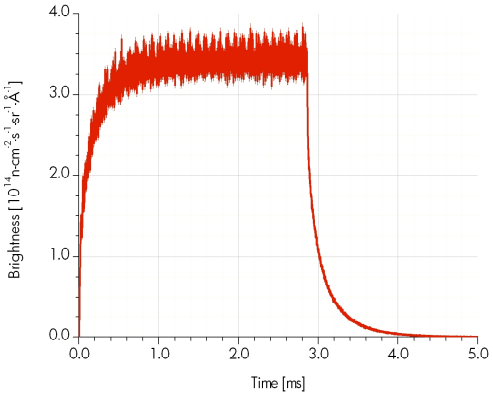

(a) 0.8 Å neutron pulse produced by thermal moderator from a single rastered pulse.

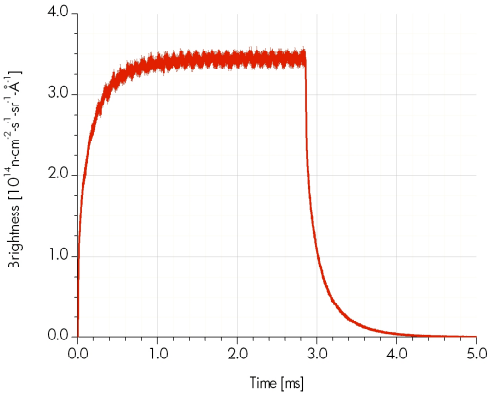

(b) 0.8 Å neutron pulse produced by thermal moderator averaged over 2 rastered pulses: direct and inverted.

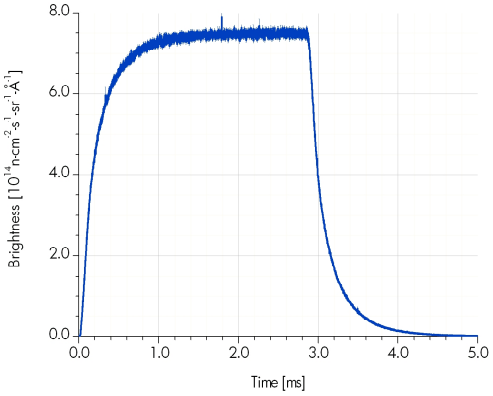

(c) 2.5 Å neutron pulse produced by cold moderator from a single rastered pulse.

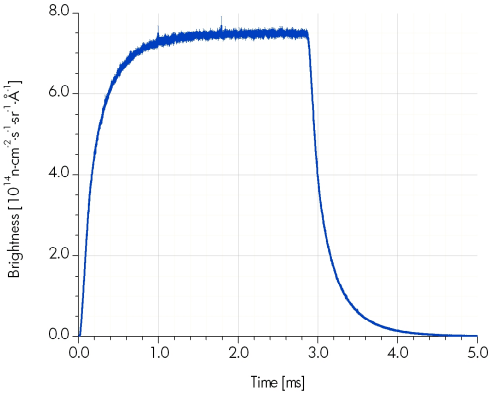

(d) 2.5 Å neutron pulse produced by cold moderator averaged over 2 rastered pulses: direct and inverted.

Figure 4: Neutron pulses produced by a rastered proton beam

shown. The effect of proton current fluctuations is smoothed in case of cold neutron pulse, while the thermal neutron pulse roughly follows the temporal profile of the incoming proton beam.

3.3. Effect of raster scanning

Earlier studies demonstrated the impact of raster scanning on neutron pulse shape [3], so a simple mitigation was developed and simulated for this study. Two pulses have been simulated based on the parameters described in section 2.2. The pulses differ only in the sign of the deflection waveforms and referred to as "direct" and "inverted" in figure 1b. The mitigation concept relies on producing a 14 Hz stream of alternating direct and inverted pulses, and then averaging over two subsequent pulses to produce a measurement nearly devoid of rastering induced fluctuations.

Figures 4 and 5 summarize the simulation results for an ideal proton pulse containing no current fluctuations. Single neutron pulses produced by this rastered proton pulse are shown in figure 4a (thermal moderator response) and figure 4c (cold moderator response). The fact that neutron pulses produced by the cold moderator do not exhibit large fluctuations can be explained by the specific properties of para-hydrogen: cold neutrons are extracted from the whole depth

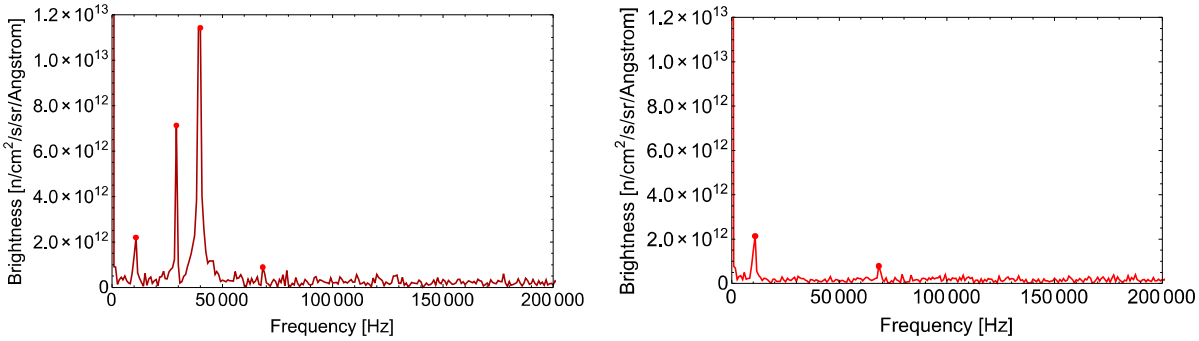

(a) From single neutron pulse.

(b) From average over direct and inverted pulse.

Figure 5: Amplitude spectra of neutron intensity fluctuations induced by raster scanning the proton beam (0.8 Å neutron pulses from the thermal moderator)

of the moderating material which itself covers all positions of the proton beamlet. Meanwhile, neutron intensity fluctuations are large from the thermal moderator because thermal neutrons are extracted mostly from the water surface. Referring to the averages over two subsequent pulses as shown in figures 4b and 4d, the mitigation concept appears successful with fluctuations noticeably reduced, particularly in the case of the thermal pulse.

Although the averaging technique significantly suppresses the raster induced modulation, some residual remains above the computational noise. Given the well defined frequencies of the the horizontal and vertical raster scanning systems, spectral analysis can help to illuminate the situation. Figures 5a and 5b show the amplitude spectra of the direct and averaged thermal neutron pulses respectively. As expected, averaging over two pulses virtually suppresses the fluctuations at the rastering frequencies. Lines at the coupling frequencies (sum and difference of the rastering frequencies) are still present, but In the time domain, these result in $< 1\%$ RMS and $< 3\%$ peak-to-peak fluctuations. Table 1 summarizes the fluctuation amplitudes for the primary frequency components of the cases that were simulated.

4. Discussion

The majority of ESS neutron instruments under development use a combination of choppers and the instrument total flight path length to tailor the neutron pulse and the available wavelength band to the desired characteristics. Preferably, wavelength dependent variations in the source neutron pulse and intra-pulse fluctuations should be minimized and inter-pulse characteristics should be as reproducible as possible. The raster induced characteristics are programmable and reproducible, but a portion of the proton current variations will fluctuate from pulse to pulse. For most measurements the data normalization is performed using beam monitor information covering many neutron pulses. In the limited number of cases where single pulse measurements are required to follow kinetics, it is usual to replace the low efficiency beam monitors with high efficiency monitors and these would then allow the fluctuations to be corrected in the normalized data. Also, the beam transport though the neutron guides smooths out fluctuations of the incident neutron pulse. Most other experiments can utilize the two pulse averaging technique, and in this case, the effects of rastering are smaller that those due to the proton current variations. For experiments that allow even longer acquisition times for each measurement point, the remaining harmonics can be suppressed by modulating the raster parameters with a pseudorandom pattern. Averaging each pulse pair would suppress the fundamental lines, and averaging over more pairs would further reduce effect of rastering, pulse-to-pulse current and energy fluctuations, and other random variations of proton pulse characteristics.

Table 1: Fluctuation amplitude within neutron pulse, tabulated separately for each component

	RMS [%]	peak-to-peak [%]
Due to ion source fluctuations:		
2.5 Å	0.8	2.8
0.8 Å	1.7	8.0
Due to rastering, single pulse:		
2.5 Å, total	0.9	8.7
0.8 Å, total	4.2	20.7
0.8 Å, DC to 12 kHz	0.6	2.6
0.8 Å, 30 kHz	1.5	4.9
0.8 Å, 40 kHz	3.7	10.9
Due to rastering, 2 pulse average:		
2.5 Å, total	0.7	5.2
0.8 Å, total	1.1	6.8
0.8 Å, DC to 12 kHz	0.6	2.6
0.8 Å, 30 kHz	0.09	0.4
0.8 Å, 40 kHz	0.05	0.2

References

[1] Peggs S *et al.* 2013 European Spallation Source technical design report Tech. Rep. ESS-2013-001 European Spallation Source Lund, Sweden

[2] Thomsen H D and Møller S P 2014 The ESS high energy beam transport after the 2013 design update *Proceedings of IPAC2014* WEPRO073 (Dresden)

[3] Shea T J, Pitcher E J, Andersen K, Bentley P, Henry P, Sabbagh P and Takibayev A 2013 Design considerations for the ESS accelerator-to-target region *Proceedings of PAC2013* MOPMA04 (Pasadena)

[4] Mezei F, Zanini L, Takibayev A, Batkov K, Klinkby E, Pitcher E and Schönfeldt T 2014 *Journal of Neutron Research* 101–105

[5] Pelowitz D B (ed) 2008 *MCNPX User's Manual Version 2.6.0* LA-CP-07-1473 (Los Alamos National Laboratory)

[6] Chadwick M, Obložinskỳ P, Herman M, Greene N, McKnight R, Smith D, Young P, MacFarlane R, Hale G, Frankle S *et al.* 2006 *Nuclear data sheets* **107** 2931–3060

[7] Shibata K, Iwamoto O, Nakagawa T, Iwamoto N, Ichihara A, Kunieda S, Chiba S, Furutaka K, Otuka N, Ohasawa T *et al.* 2011 *Journal of Nuclear Science and Technology* **48** 1–30

3.4.5

Instrumentation and machine protection strategy for the ESS target station

T J Shea[1], L Coney[1], R Linander[1], A Jansson[1], E Pitcher[1], A Nordt[1], C Thomas[1], H D Thomsen[2]

[1] European Spallation Source, P.O Box 176, SE-221 00 Lund, Sweden
[2] Institute for Physics and Astronomy, ISA, Aarhus University, DK-8000 Aarhus, Denmark

E-mail: thomas.shea@esss.se

Abstract. The European Spallation Source (ESS) linear accelerator will deliver a 5 MW, low-emittance 2 GeV proton beam directly to the target station at a rate of 14 Hz. The target is composed of helium-cooled plates of tungsten housed within a rotating wheel 2.5 meters in diameter. To limit power density, a transport line expands the proton beam to centimeter scale and rasters the expanded beam across the target surface. This technique produces a reasonably uniform current density that allows a service life of five years for the rotating tungsten target and six months for the upstream Proton Beam Window. Conversely, the low emittance of the beam allows an errant spot size small enough to damage target station components within a single 2.86 ms pulse. A suite of instrumentation systems located within the target monolith and further upstream in the transport line will detect errant conditions in both the beam and target. Instrumentation dedicated to monitoring target properties such as helium coolant flow, target balance and motion will be located on the downstream side of the target away from the incoming proton beam. Proton beam density, position, current, and halo properties will be monitored upstream of the target. Precise synchronization of the beam pulse and target rotation will also be done using beam arrival measurements. Detection of errant conditions will trigger the suppression of beam production via the Beam Interlock System within the ESS Machine Protection System. This paper will introduce the primary causes of damaging beam properties and describe the measurement techniques that will detect them on a time scale sufficiently fast to mitigate component damage.

1. Introduction

The ESS facility will integrate a 5 MW target station with a proton linear accelerator that produces 2.86 ms long pulses of 2 GeV protons. At full power, each pulse has a peak current of 62.5 mA and occurs at a repetition rate of 14 Hz. Beam transport from the accelerator to the target is depicted in figure 1. Upon inspection, the two distinct regions become apparent: the accelerator region upstream of the beam waist (marked CO in the figure 1), and the target region downstream of the waist. They are separated by a 2 m thick neutron shield wall that surrounds the beam waist and isolates the accelerator from the target. The two regions also have two unique rulebooks. In the accelerator, the design is driven by the requirement to accelerate and transport the beam with a loss of less than 1 W/m. This low loss requires a very low emittance beam inside of a relatively large aperture, and results in low activation that allows hands-on maintenance. Downstream, the target station must absorb both this primary beam and also the unmoderated spallation products. This requires a dramatically expanded beam

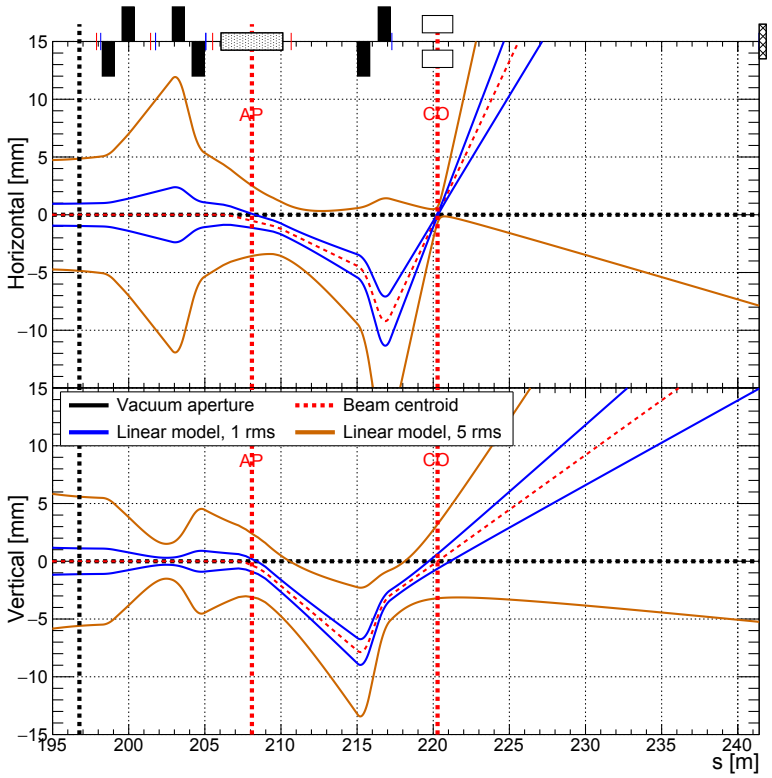

Figure 1: The transverse beam sizes along the beam delivery line from the accelerator to the target (far right edge of plot) at maximum raster amplitudes. The location and polarity of 6 DC quadrupoles are represented by black boxes.

passing through the target monolith's relatively tight shielded aperture. Here, maintenance is performed by remote handling.

The accelerator-to-target (A2T) line on the left side of figure 1 acts as the beam delivery system, transforming the small, bright proton beam from the ESS linac into a beam acceptable for the target components. Table 1 lists the nominal parameters of the beam at the target and at the Proton Beam Window located about 4 m upstream of the target. Within the target station, cooling systems and features like the rotating target wheel allow it to accept the full 5 MW beam. To achieve a neutron production run of several months between major maintenance periods, the beam delivery and target systems must all function correctly. With many target components operating near their engineering limits, instrumentation must detect target system malfunctions and errant beam conditions before damage occurs, and the machine protection system must promptly suppress proton beam production.

2. Beam Delivery

The A2T line must meet several requirements:

- Match the linac beam to the macroscopic beam size required at the target.
- Keep the beam edges contained while defocusing the beam at the target.
- Reduce the local time-averaged beam intensity at the Proton Beam Window and target.
- Facilitate a Neutron Shield Wall (NSW) that allows efficient transmission of the primary beam yet presents a narrow aperture to the neutrons backstreaming from the target. All magnets should preferably be located upstream of this wall.

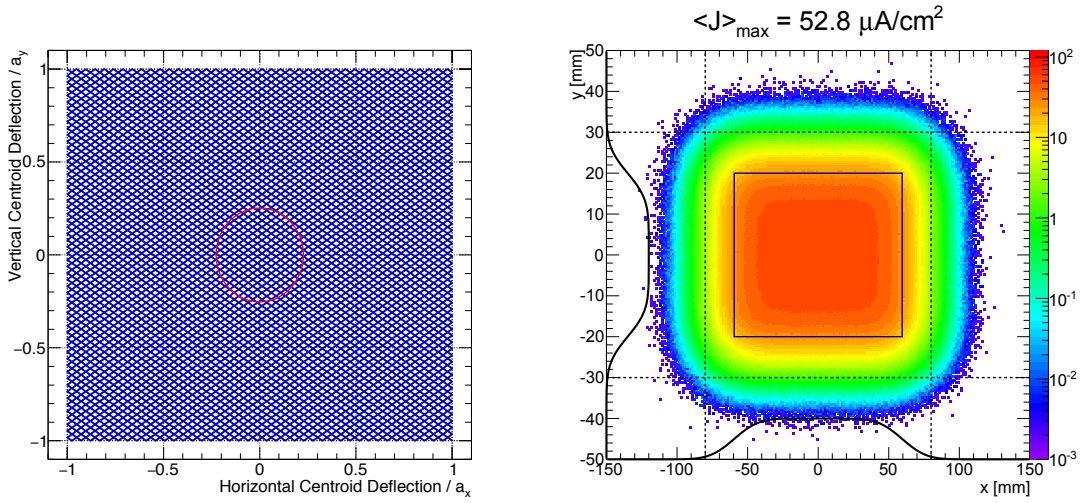

(a) A Lissajous-pattern generated by triangle waveforms with a frequency ratio of 113/83. For comparison, the beamlet relative RMS sizes at the target are illustrated by a red ellipse.

(b) The intensity distribution is scaled to represent the peak current density, normalized to 2.5 mA average current. The blue rectangle illustrates the outline of the raster pattern. The dashed lines indicate the footprint containing 99.0% of the beam.

Figure 2: Simulated raster pattern and consequent intensity distribution at the target following a full cycle of the Lissajous-pattern with the beam parameters in Table 1.

The requirements above are met by a transverse beam raster system that relies on a combination of DC and fast AC magnetic elements to moderately expand the linac beam and sweep it rapidly across the target.

2.1. The AC Optics

As described in [1, 2], the ESS will incorporate a raster system that sweeps the accelerator beamlet in a transverse pattern across the target surface. This technique lowers the time-averaged beam intensity while containing the beam within a defined rectangular footprint. A 2D mesh of interwoven sweep trajectories is generated through a Lissajous-like pattern. Such a pattern is defined by a frequency ratio f_x/f_y and phase ϕ_{xy} of two non-harmonic triangular sweep waveforms. The waveforms are applied to two sets of AC raster scanning magnets (RSMs) operating in the two transverse directions. By choosing very non-harmonic raster frequencies, e.g. $f_x/f_y = 113/83$, the patterns can reach almost limitless complexity, cf. figure 2a. The resulting sweep pattern will of course be convoluted with the beamlet profile. The uniformity of the resulting distribution will depend on the spacing between the respective sweeps relative to the beamlet size. A fine mesh would also to a large extent smear the beam profile, thus leaving the effective distribution more insensitive to the details of the beamlet profile.

To introduce the necessary oscillating beam displacements near the target, the raster system is foreseen to consist of 8 colinear raster scanning magnets (RSMs), two sets of 4 acting in the respective transverse planes. The RSMs in a set should ideally be synchronized and share the same field amplitude, but each of the 4 in a set are independent modules, thus eliminating some single points of failure. To avoid the need for active cooling of magnets and power supplies, the raster system is foreseen to be operated at a duty cycle of only 5%, appropriately more than the 4% beam pulse duty cycle (2.86 ms at 14 Hz).

Table 1: Beam parameters, horizontal (H) and vertical (V), at the Proton Beam Window (PBW) and the target

Parameter	Unit	Location	H	V
RMS beam size	mm	CO	0.14	0.64
	mm	PBW	10.7	4.10
	mm	target	13.5	5.05
Max. displacement	mm	PBW	47.1	15.8
(rastering)	mm	target	59.5	20.0
f_w	kHz	—	39.55	29.05
Avg. current density	μA/cm^2	PBW	84	
	μA/cm^2	target	53	
Footprint: 99.0%	mm	target	160	60
99.9%	mm	target	180	64

2.2. The DC Optics

To facilitate a small-aperture Neutron Shield Wall (NSW), the DC optics provides more than the means to set the size of the beamlet that is rastered across the target. By design, the AC displacements neutralize at a crossover point (CO) between the final magnetic elements and the target. By also setting a very small beam size at the CO, this is an ideal location for the NSW. This scheme requires a minimum of 6 DC quadrupoles. The location of the DC quadrupoles and 8 RSMs can be inspected in figure 1.

The final quadrupole doublet, downstream of the RSMs, neutralizes the raster displacements at the CO by imposing a transverse phase advance of 180° between the common raster magnet action point (AP) and the CO. Assuming the nominal optics, the CO thus becomes a pivot point of the oscillating raster motion. The first 4 quadrupoles of the A2T constitute a matching section that provides a minimum beam size at the CO while setting the $\simeq$ cm^2 beamlet size on the target. Assuming the parameters of table 1, a simulation of the intensity distribution at the target following each 2.86 ms beam pulse is shown in figure 2b. The distribution contains a relatively large uniform central region and respects the marked footprint, enclosing $\geq 99.0\%$ of the beam.

A snapshot of the beam optics, while the raster actions are at maximum amplitudes, is visible in figure 1. It is quite clear that the displacements are considerable compared to the 1-RMS beam sizes, especially downstream of the CO. Apart from providing the CO condition, the final quadrupole doublet also magnifies the angular deflection in the horizontal plane, thus balancing the amplitude setpoint of the RSMs acting in the two directions despite the $\simeq 3:1$ amplitude ratio required, cf. table 1.

3. Instrumentation

Three classes of instrumentation will be deployed to detect errant conditions:

(i) Beam delivery system instrumentation.

(ii) Target system instrumentation

(iii) Proton beam instrumentation

Subsection 3.1 briefly describes the instrumentation that will monitor the beam delivery magnets. In subsections 3.2 and 3.3, target and proton beam instrumentation receive a more detailed treatment. All of these systems can interface to the machine protection system (described in Section 4) in order to suppress beam production upon detection of errant conditions.

3.1. Beam Delivery System Instrumentation

Instrumentation will monitor the AC and DC magnet systems that determine the beam delivery optics. Being critical components, each raster scanning magnet will contain a Bdot loop which will directly monitor the derivative of the triangular magnetic field waveform. Under nominal conditions, the observed signal is a square waveform that occurs during the entire 2.86 ms duration of the beam pulse. Each of the raster magnets will be monitored independently. The current and voltage of the DC magnet circuits will be monitored and a window comparator will be used to detect deviation from the nominal set points. The monitored and interlocked magnets include all eight raster scanning magnets, the six quadrupoles, and four 2D dipole correctors.

3.2. Target System Instrumentation

The ESS target is a volume of tungsten contained in a wheel-like steel structure, cf. figure 3, that is rotating to spread the heat deposition and radiation damage. It is continuously cooled by pressurized helium circulated through a long shaft. On top of the shaft there is a drive and bearing unit that rotates the target wheel synchronized with the impinging pulsed proton beam. The integrity and lifetime of the target wheel as well as sufficient reliability and availability of the drive and bearing system depends on maintaining the operating conditions within specified ranges. Pressure and temperature surges, vibrations, deficient cooling flow, and misalignment may lead to failure or unavailability of the system. Therefore, extensive instrumentation will be deployed to monitor the performance and condition of the wheel and give relevant input to the machine protection system. Additional instrumentation will monitor other major components within the target station and with moderate response time, could detect the impact of persistent errant beams.

3.2.1. Target wheel rotation and helium coolant flow The two most important parameters to assure are the stable and precise rotation of the wheel and a sufficient mass flow of the helium coolant. Failure to maintain these conditions may lead to overheating of the wheel with subsequent structural damage or lifetime reduction.

The rotation of the wheel, nominally 25.5 RPM, will be monitored by instrumentation located on the target drive unit. Rotary encoders and magneto resistive sensors are envisaged to be mounted on the motor unit and the target wheel shaft. Other means of measuring the wheel rotation, if redundancy is required, may utilize the optical path to the target wheel disc that the target monitoring plug provides. This target monitoring plug is located downstream of the wheel.

The nominal mass flow of the helium coolant is set to 3 kg/s with an inlet temperature of approximately 40 degrees celsius. The cooling system will be equipped with several sensors for monitoring the helium flow rate, inlet and outlet temperature, pressure level and other important process parameters. Some of those measurement points will be dedicated to machine protection.

3.2.2. Condition monitoring of the target wheel unit In order to achieve expected availability and reliability for the target wheel unit, it is essential to understand condition of the system and its individual parts. Early indications when operating parameters begin to divert from their nominal values are needed for good planning of preventive maintenance. Flow rate, pressure and temperature measurements in the primary target cooling system will be monitored and recorded

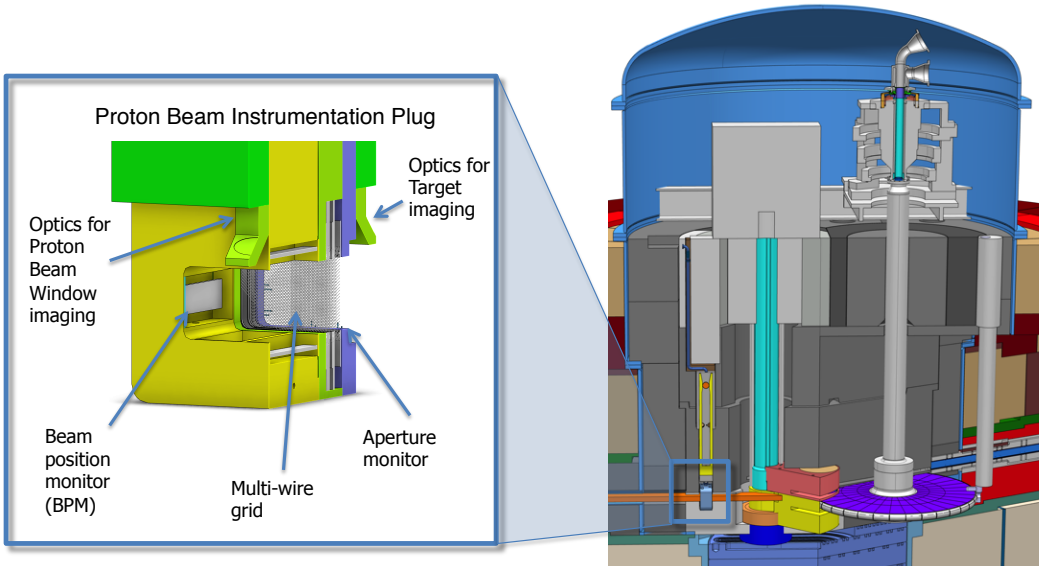

Figure 3: Conceptual rendering of the target monolith. Incoming proton beam (orange) from the left passes though the Proton Beam Window (not shown), then through the proton beam instrumentation plug (gray) and between the upper and lower moderator plugs (brown and yellow) before reaching the target wheel (purple). The wheel shaft (gray) extends approximately 5 m up to the drive and bearing unit, which also contains the pipe connections to the target primary cooling system. The target monitoring plug (gray) is located downstream of the target wheel. The inset on the left depicts the devices contained in the proton beam instrumentation plug.

in order to discover deviations from nominal operating conditions. That system is also proposed to contain a radioisotope sampling for early detection of unexpected release of volatile isotopes that could indicate damage of the spallation material.

The target wheel unit will, in addition to sensors measuring the rotation, be equipped with vibration and balance monitors as well as conventional motor and bearing condition monitors. For example, it is important to keep track of the degradation trends of bearings in order to plan for replacement at the right time.

The target monitoring plug, located downstream of the target wheel, will provide the possibility to use techniques like Laser Doppler Vibrometer, infrared temperature measurement and visible imaging for detection of vibrations, wobbling, mechanical misalignment, deformations, and thermal hotspots.

3.3. Proton Beam Instrumentation

In the target monolith and upstream, a suite of instrumentation will characterize the proton beam delivered to the target. This suite is based on concepts presented in [4]. The measurements will include the beam current, beamlet position, beam current density distribution, and the beam halo approaching the aperture.

3.3.1. Beam Current Monitors The beam current will be measured in A2T by two redundant Beam Current Monitor (BCM) systems based on the AC Current Transformers [3]. After digital filtering, these devices will provide a time resolution of about 1 μs and an amplitude precision of about 1 mA. In the context of target protection, these systems provide several indirect functions. The BCM data helps to verify that the peak current and the average power

are within the operating envelope approved for the target station. Imaging and grid systems normalize their data to BCM measurements so that intensity and fluence on target components can be accurately determined. Finally, the BCM provides pulse time-of-arrival information to support synchronization of the rotating target wheel.

3.3.2. Target Beam Position Monitor In addition to several traditional beam position monitors (BPM) in the A2T line, a BPM in the target monolith will monitor the beamlet position as it moves transversely during the pulse. The speed of this transverse motion exceeds 10 mm/μs and the position monitor must measure with a precision of a few mm. Therefore, the sample rate will exceed 1 MSa/s.

The beamline device will consist of electrodes as well as radiation tolerant coaxial cables and feedthroughs that bring the 352 MHz signals to the exterior of the monolith, where the signals will be processed. As depicted by figure 3, this electrode resides within the proton beam instrumentation plug. The aperture exceeds 200 mm horizontally, and thus considerable design effort will have to be expended to optimize performance. In particular, the signal to noise ratio at the 352 MHz bunching frequency will have to be high enough to ensure millimeter resolution over an approximate 1 MHz bandwidth, even with bunches that have lengthened during their >200 m drift from the linac.

The BPM electronics will first measure the position of the beamlet versus time within the pulse. To provide the interlock function, these measurements can be compared to reference waveforms. With further processing and an assumed beamlet size, an estimated map of the current density or other figures of merit can be synthesized and directly compared with the target requirements. The system will detect errant conditions within the pulse.

3.3.3. Imaging Systems Two imaging systems will measure the 2D current density distribution at the Proton Beam Window and at the surface of the target wheel. They will measure variations of the peak density to a precision of about 10% with a spatial resolution of about 1 mm. Position of the centroid will also be determined with a precision of about 1 mm. To achieve this performance, the systems will average over an entire pulse.

Figure 3 shows the location of the first mirrors, with one looking upstream at the Proton Beam Window and one looking downstream at the target. The primary components of the reflective optical systems reside within the proton beam instrumentation plug. The images are transported to the top of the monolith and then out to an area hospitable to cameras and other electronics. The source of these images is light produced as the protons pass through luminescent coatings on the window and target. Although it possesses a luminescent lifetime of a few ms, a coating of thermal-sprayed alumina doped with Chromium meets the requirement to measure individual pulses. Other technologies will be explored with the goal of providing intra-pulse measurements.

3.3.4. Grid System The grid system will consist of one multiwire grid assembly located in the target monolith. Two locations are under consideration: in the Proton Beam Window assembly and in the proton beam instrumentation plug. In the first location, the grid assembly would be located in vacuum just upstream of the window, while in the second location, depicted in figure 3, the grid assembly will be immersed in Helium at about atmospheric pressure. The device will measure the horizontal and vertical projections of the beam current density such that changes of 20 percent with respect to nominal peak density can be accurately determined. The grid's wire spacing is driven by the spatial resolution requirement of a few mm in either dimension, leading to a density of about a few wires per cm. The system will be interfaced to the beam interlock system so that beam can be interrupted within the pulse if the current density exceeds a programmable threshold. The goal is to make this determination in less than 100 μs.

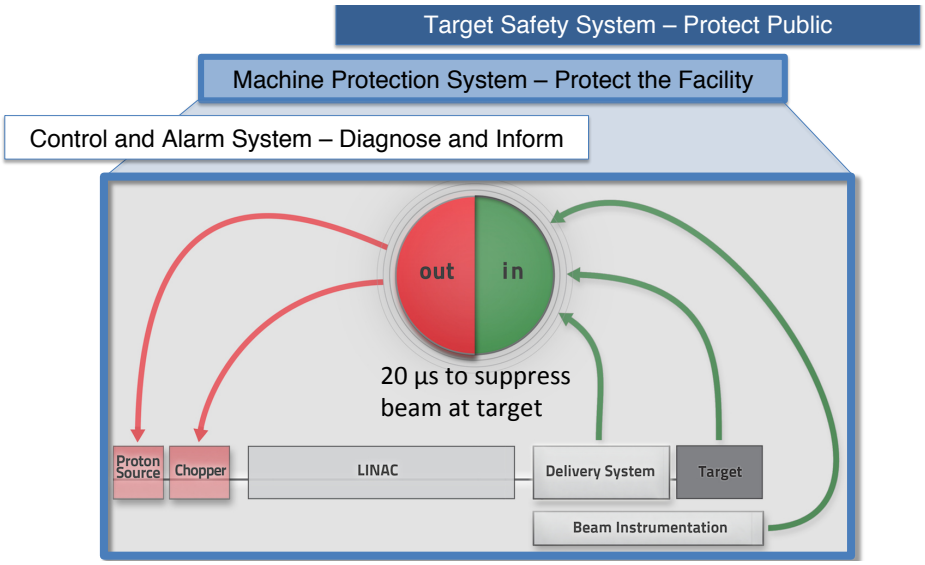

Figure 4: Overview of of the Machine Protection System

3.3.5. Aperture Monitors Aperture monitors consist of fixed sensors surrounding the apertures of the Proton Beam Window and the proton beam instrumentation plug. In addition, moveable sensors will reside close to the upstream aperture of the neutron shield wall. The fixed units in the monolith will ensure that less than 0.1% of the total beam current resides outside the defined footprint. Sensors on the moveable unit will be set far outside of the beam core, but close enough to detect the result of deviations from nominal DC optics.

The baseline concept for the sensor is a thermocouple array that can detect errant conditions after many pulses. To achieve faster response, a complementary technique that measures current induced by the charged particle shower will also be deployed. At the shield wall, the background should be low enough to enable the additional method of direct shower detection. Measurements within the pulse should be achievable.

4. Machine Protection System

Figure 4 shows the three layers of protection applied to the ESS target station. At the lowest integrity level, the control system provides a rich set of diagnostic data to operators. A subset of this data can trigger alarms, in many cases allowing operators to make corrections before the machine protection system trips. At the top of the figure, the target safety system provides the highest integrity level but only interrupts beam production under the most dire circumstances for the purpose of protecting the public. The machine protection system occupies the middle layer, providing an integrity level consistent with its mission of protecting hardware components for the purpose of achieving the availability goals of the ESS facility [5].

The lower portion of figure 4 shows the signal flow of the beam interlock system as it relates to target protection. Here, signals from the three types of instrumentation described above (green in the figure) reach back to two devices (red in the figure) to suppress beam production. After the errant condition is detected near the target station, the signal propagates though the interlock system, first interrupting the beam pulse with the transverse chopper at 3.5 MeV, and also stopping the rest of the pulse with slower devices upstream. About 4 μs of beam remains in the accelerator and this is still delivered to the target area. The total time from detection to the last proton arriving at the target is under 20 μs. The errant conditions that can cause this to occur are described in the next section.

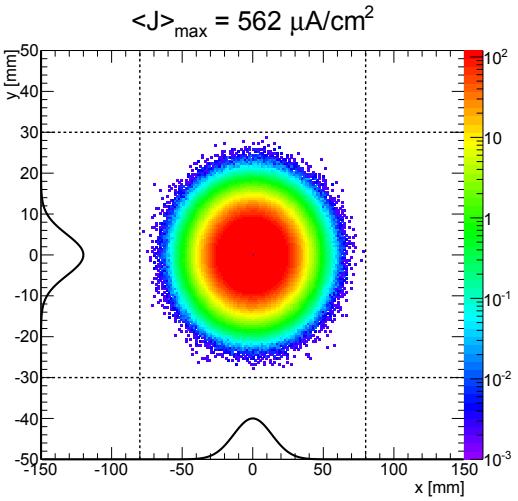

(a) Full raster system failure: unrastered beamlet.

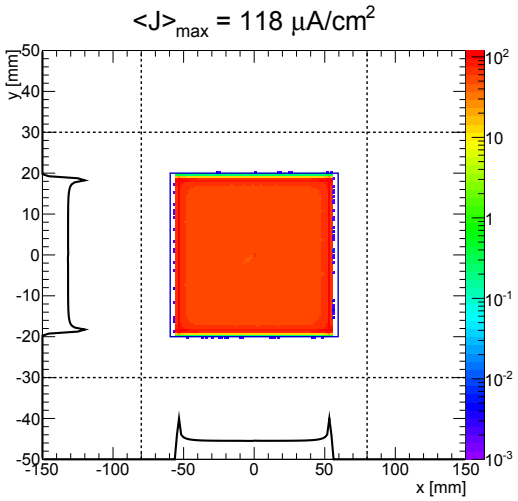

(b) Beamlet size decrease: a RMS size of 0.3 mm is assumed in both transverse directions.

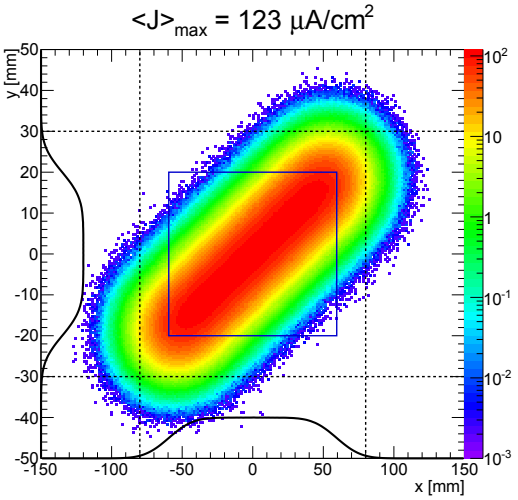

(c) Raster pattern reduction: $f_x/f_y = 1$.

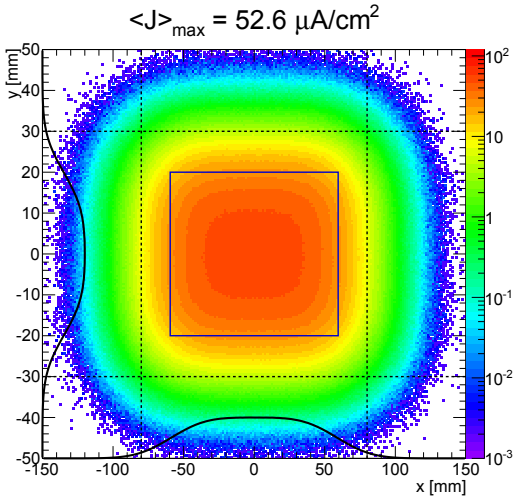

(d) Beamlet size increase: a 50% increase in RMS sizes is assumed.

Figure 5: Simulation results similar to Fig. 2b but including beam delivery system failures that result in errant beam conditions.

5. Errant Conditions

Before permitting beam on target, the instrumentation described in Sections 3.1 and 3.2 must collectively indicate that the beam delivery system and the target station are ready for the intended operational mode. This mode defines the allowed equipment state and the envelope of beam parameters, from the very restrictive set that may be used for low power verification up to the full pulse length, peak current, and repetition rate of 5 MW operations. During operations, this instrumentation suite can interrupt production upon detection of an equipment state inconsistent with the operational mode.

Having described the intended operation of the A2T line, it is evident that several conditions need to be met in order to deliver the nominal beam to the target. Any upstream quadrupole failing to deliver the intended integrated gradient will affect the beamlet size on the target. Due

Table 2: Events leading to errant beam conditions, with methods to detect the condition within the pulse (Intra-Pulse) and after averaging over one or more pulses (Avg.)

Event	Cause	Unmitigated Effect	Detection
RSM full failure, ×1	Power supply failure, misconfiguration	$J_{\max}$ increases by ×1.33	Intra-pulse: BPM, grid, Bdot; Avg: imaging
RSM full failure, ×8	As above, RSM and beam pulse synchronization	$J_{\max}$ increases by ×10	As above, but BCM with Bdot
Beam on target is displaced	DC correctors, misaligned input beam, misconfiguration	Beam losses along the monolith beam duct	Intra-pulse: BPM, aperture; Avg: imaging, target
Beamlet size on target too small	Quadrupole failure (power supply, misconfiguration)	Intensity edges and peaks in beam distribution, $\simeq \times 2$	Intra-pulse: grid, aperture(NSW); Avg: imaging
Final quad. doublet failure	Power supply failure, misconfiguration	Beamlet misfocused, raster ampl. changes	Intra-pulse: BPMs, grid, aperture; Avg: target, imaging
Beam energy deficiency	RF errors or cavity trips	As above, vertical displacement	As above
Raster pattern reduction	Misconfiguration	Intensity increase: footprint not exploited	Intra-pulse: BPM, grid; Avg: imaging

to the raster approach, the time-averaged beam distribution is fairly insensitive to such a change. Contrarily, if the final doublet is not performing as intended, the beam centroids will oscillate at the CO and the beamlet size and raster pattern will be affected at the target. These cases, and the examples that follow should first be detected by beam delivery instrumentation. Should this fail, the beam instrumentation will detect the result of the delivery system problem (errant beam parameters), and if that fails, then a subset of target instrumentation might detect the result of the persisting errant beam (usually power deposition where it should not be). Figure 5 shows a few examples of how the time-averaged beam distribution responds to failures to provide the proper beamlet and raster system parameters. Table 2 contains a list of selected failure events and how they will be detected, both within the pulse (Intra-pulse) and after averaging over one or more pulses (Avg.).

Compared to the unrastered beamlet, the raster system reduces the time-averaged peak current density by more than an order of magnitude. A complete raster system failure, shown in figure 5a, is thus believed to be the most detrimental single error. Since the RSM system and beam are pulsed, this failure could originate not only from configuration or hardware issues in the RSM system, but also from a desynchronization of the pulsed beam and RSM system. Total failure would first be detected by the Bdot probes alone. Bdot signals combined with BCM readings would catch the desynchronization case. In the target station, the BPM and grid would detect the unrastered beam within the pulse, while the imaging systems would detect the density increase after the pulse completes. In this example, as in most, the target instrumentation would probably not play a role unless the condition persisted long enough to cause damage.

The rastered distribution could benefit (in terms of reduced peak intensity and sharper edge)

from reducing the beamlet dimensions. This would however increase the static beamlet power density, which might damage the Proton Beam Window or the target wheel within one pulse in case of full failure of all 8 RSMs. Figure 5b shows the result of delivering the smallest beamlet size realistically producible. With the smaller beamlet dimensions, high-intensity edges and corner peaks become severely pronounced as a result of the finite raster waveform bandwidth, *i.e.* turning time. As long as the RSM system is operational, the local intensity would increase by a factor $\simeq 2$. It is unlikely to minimize the beamlet dimensions on target without simultaneously increasing the beam size considerably in the upstream quadrupoles. Therefore, movable aperture monitors should be able to detect such an error. In addition, the grid and the imaging systems could directly observe any significant local density increases.

The complex Lissajous-like raster pattern is easily generated by maintaining a close-to-irrational ratio of raster frequencies. This pattern can be severely reduced in complexity if f_x/f_y unintentionally changes and approaches an integer. Figure 5c depicts the worst case where $f_x/f_y = 1$, possibly due to a configuration error, resulting in a single diagonal raster line. Again, the failure leads to a local intensity increase by a factor $\simeq 2$. Since a configuration error is the most likely cause, the delivery system instrumentation would not catch the issue, and detection would depend upon the collection of beam instrumentation devices that observed example 5a.

In the final failure mode example, shown in figure 5d, the beamlet dimensions are 50% larger than the respective nominal values. The peak intensity of the rastered distribution is not affected significantly, but the beam spreads outside the nominal footprint regions. During the pulse, the aperture monitors would provide the most sensitivity to this condition, followed by the grid. The imaging systems may detect it after a single pulse, and much later, the target instrumentation may detect elevated temperatures in some components near the aperture.

6. Outlook

As the design of the ESS target station and A2T transport line proceeds, development of the machine protection strategy will continue in parallel. A number of events that could cause errant beams have already been considered and this has informed the design of the relevant instrumentation systems. Many more cases remain to be analyzed, including some more insidious than those presented here, and this analysis will result in further refinement of the instrumentation suite. Although the harsh environment of the target station presents a major challenge to the design of reliable instrumentation, the planned redundant and diverse systems should provide appropriate inputs to the beam interlock system, and therefore help to achieve the performance goals of the ESS facility.

References

[1] Thomsen H D Holm A Møller S P *et al.* 2013 A linear beam raster system for the European Spallation Source? *Proc. International Particle Accelerator Conference* (Shanghai)

[2] Thomsen H D and Møller S P 2014 The ESS high energy beam transport after the 2013 design update *Proc. International Particle Accelerator Conference* (Dresden)

[3] Hassanzadegan H Jansson A Thomas C Legat U Strnisa K Crisp J and Werner M 2014 Design, implementation and preliminary test results of the ESS beam current monitor system *Proc. International Particle Accelerator Conference* (Dresden)

[4] Shea T Böhme C Cheymol B Gallimore S Hassanzadegan H Pitcher E and Thomsen H D 2013 Proton beam measurement strategy for the 5 MW European Spallation Source Target *Proc. International Beam Instrumentation Conference* (Oxford)

[5] Nordt A Apollonio A and Schmidt R 2014 Overview on the design of the machine protection system for ESS *Proc. International Particle Accelerator Conference* (Dresden)

3.4.6

Beam flattening system based on nonlinear optics for high-intensity spallation neutron source

Shin-ichiro Meigo, Motoki Ohi, Kiyomi Ikezaki and Atsushi Akutsu

J-PARC Center, Japan Atomic Energy Agency, Tokai, Ibaraki 319-1195, Japan

E-mail: meigo.shinichiro @jaea.go.jp

Hiroshi Fujimori

J-PARC Center, High Energy Accelerator Research Organization (KEK), Tsukuba, Ibaraki 305-0801, Japan

Abstract. The Japan Spallation Neutron Source of the Japanese Proton Accelerator Research Complex generates a high-power proton beam (up to 1 MW) for collision with a mercury target. With increasing beam power, the target damage becomes increasingly serious. For the high-power short-pulse spallation neutron source, the damage inflicted by the proton beam on the target vessel containing a liquid metal target such as mercury is proportional to the fourth power of the peak intensity of the proton beam. Reducing the peak current density at the target is vital for constant beam operation. To this end, we developed nonlinear beam optics based on octupole magnets. However, to obtain a completely flat beam distribution, higher-order magnets are required. We found that a significantly flat beam distribution can be obtained by reducing the magnetic field of the octupole magnet. Calculations indicate that, by introducing octupole magnets, the peak current density can be reduced by 30%.

1. Introduction

The Japan Proton Accelerator Research Complex (J-PARC) [1] (shown in Fig. 1) now includes a MW-class pulsed neutron source that was installed in the Materials and Life Science Experimental Facility (MLF) of the Japan Spallation Neutron Source (JSNS) [2] and the Muon Science Facility [3]. Since 2008, this source has produced a high-power proton beam of 300 kW. To produce a neutron source, a 3 GeV proton beam collides with a mercury target, and to produce a muon source, the 3 GeV proton beam collides with a 20-mm-thick carbon graphite target. To efficiently use the proton beam for particle production, both targets are aligned in a cascade scheme, with the graphite target placed 33 m upstream of the neutron target. For both sources, the 3 GeV proton beam is delivered from a rapid cycling synchrotron (RCS) to the targets by the 3NBT (3 GeV RCS to Neutron facility Beam Transport) [4-6]. Before injection into the RCS, the proton beam is accelerated up to 0.4 GeV by a LINAC. The beam is accumulated in two short bunches and accelerated up to 3 GeV in the RCS. The extracted 3 GeV proton beam, with a 150 ns bunch width and a spacing of 600 ns, is transferred to the muon production target and the spallation neutron source.
Recently, pitting damage became evident in the mercury target container [7], and the extent of the damage is proportional to the fourth power of the peak current density of the proton beam [8]. After

operating the beam at high power, significant pitting damage was observed at the spent mercury target vessel at JSNS and at the Spallation Neutron Source in Oak Ridge National Laboratory [9, 10]. Using linear optics (i.e., quadrupole magnets) for beam transport, the peak current density can be reduced by expanding the beam at the target. However, beam expansion increases heat in the vicinity of the target, where shielding and the neutron reflector are located. Therefore, the peak current density is limited by the heat induced in the vicinity of the target. At the JSNS, the minimum peak current density is expected to be 9 μA/cm^2, which gives a thermal energy density at the target of 14 J/cc/pulse [11]. Because the pitting damage goes as the fourth power of the peak density, scanning the beam with a deflecting magnetic field will not mitigate the pitting damage.
To reduce the peak current density while conserving the integrated beam current, the beam profile should be flat. To obtain a flat beam profile, beam rastering, which uses pulsed magnets to create a flat time-averaged profile at the target, is a possible method. However, rastering does not help mitigate pitting damage to the target vessel. For a uniformly shaped beam, pitting damage per pulse to the target vessel is given by D1 in the following equation:

$$D_1 = \int (C/S_1)^4 \, dt, \tag{1}$$

where S1, C, and t are the beam cross-sectional area at the target, the beam charge per pulse, and the irradiation time, respectively. For beam rastering, pitting damage is described by

$$D_2 = \int (C/S_2)^4 \, P \, dt, \tag{2}$$

where S_2 and P are the beam cross-sectional area for rastering and the beam-position probability, respectively. To obtain a flat time-averaged beam profile over S_1, P is given by

$$P = S_2/S_1. \tag{3}$$

Using Eq. (2), pitting damage for beam rastering can be described by

$$D_2 = \int (C/S_2)^4 \, S_2/S_1 \, dt = D_1 (S_1/S_2)^3. \tag{4}$$

With beam rastering, damage D_2 is proportional to the third power of the ratio of the total beam cross-sectional area to the beam cross-sectional area of each pulse. Therefore, beam rastering cannot sufficiently mitigate pitting damage at the mercury target vessel.
In this paper, we describe a system of nonlinear beam optics and discuss the side effects involved with such a system, such as misalignment of the beam at the target. To reduce the peak current density, we developed a beam-flattening system based on nonlinear beam optics.

2. Design of nonlinear beam optics

The 3 GeV proton beam extracted from the RCS is well described by a simple Gaussian [6]. With ordinary (i.e., linear) beam optics, the beam shape remains a Gaussian at all positions along the beam path. Using nonlinear optics, the beam particles located at the beam periphery are deflected toward the beam center, which flattens the beam distribution. To obtain a flat distribution in both the horizontal and vertical directions, two octupole magnets are required. These octupole magnets can be placed anywhere upstream of the target except where the phase advance between the magnets and the mercury target is an integer multiple of π. Because the targets have been irradiated by the proton beam for 5 years, the radiation dose around the targets is too high to place a magnet there. Therefore, the two octupole magnets (OCT1, OCT2) were placed upstream of the muon target, as shown in Fig. 2.

2.1. Octupole Magnetic Field

Starting with a beam that has a Gaussian distribution in transverse phase space, the multipole magnetic fields are given by [12]

$$K'_{2n} = \frac{(n-2)!}{(n/2-1)!}\frac{(-1)^{n/2}}{(2\varepsilon\beta)^{n/2-1}}\frac{1}{\beta\tan\varphi} \qquad (n = 4, 6, 8, \cdots) \tag{5}$$

to obtain a flat beam distribution at the target. In Eq. (5), K'_{2n} is the integrated strength of the 2n-pole multipole magnet, with the magnet assumed to be a thin lens for simplicity. The quantity ε is the root mean square (rms) of the transverse emittance (π mm mrad), β is the beta function (m) at the octupole magnet, and ϕ is the phase advance between the octupole magnet and the target. Using Eq. (5), the required octupole magnetic field is

$$K'_8 = (\varepsilon\beta^2\tan\varphi)^{-1}. \tag{6}$$

In Eq. (5), magnetic field orders greater than octupole are required to obtain a completely flat distribution. Without a dodecapole magnetic field in Eq. (5), the beam distribution is not flat but is peaked at the edge of the beam [12, 13]. Note that such edge peaks can be easily eliminated at low-energy accelerator facilities using a beam collimator. For a high-power, medium-energy accelerator facility such as the JSNS, the edge peak cannot be easily eliminated. The principle of beam flattening systems is to bend the beam from the edge of the beam toward the center using high-order magnetic fields. At the center of the target, the peak intensity of the beam does not change significantly upon using high-order magnetic fields. Bending the beam toward the center of the beam with high-order magnetic fields causes the beam intensity to increase in the tail part of the beam. Therefore, the intensity of the edge peak can be reduced by decreasing the strength of the high-order magnetic fields, although the edge shape blurs.

We now consider the case in which the beam has a uniform distribution in transverse phase space. For this, the octupole field required is [14]

$$K''_8 = \cos^3\varphi/12\varepsilon\beta^2\sin\varphi, \tag{7}$$

where K''_8 is the octupole field required to obtain a beam with uniform distribution in phase space. In Eq. (7), the distribution in real space cannot be completely flat but, by averaging Eqs. (6) and (7), is expected to evolve into a flat distribution with the edge peak suppressed:

$$K_8 = (K'_8 + K''_8)/2. \tag{8}$$

Using the octupole magnetic field K_8 given by Eq. (8), a flat beam distribution can be obtained, as shown in Fig. 3. Although the distribution shown in Fig. 3 is not completely flat and the edge is not sharper than that obtained by Eq. (5), the edge peak can still be well suppressed.

3. Beam Flattening System at JSNS

The beam optics for an entire beam transport line is shown in Fig. 4, which shows the beta and dispersion functions from the RCS to the mercury target. To achieve a flat beam distribution, the octupole field must be proportional to the inverse square of the beta functions described in Eqs. (2) and (3). Because of the high momentum of the present beam, a large octupole field is difficult to attain. To obtain a flat beam distribution with an octupole magnet having a realistic K, the beam width at the octupole magnet is expanded to a large β value. The physical aperture of the quadrupole magnets was fixed at 300 mm; therefore, we set the physical aperture of the octupole magnets to 300 mm. For linear beam optics, the admittance of the beam is designed to be 324 π mm mrad, which is given by the beam collimator placed at the RCS. A recent study of the RCS [15] shows that the transverse emittance will be reduced to as little as 250 π mm mrad. Therefore, the beam admittance at the octupole magnet must be 250 π mm mrad and β is set to 200 m at the octupole magnets.

3.1. Octupole magnets

Based on the optics design, the two pieces of the octupole magnet shown in Fig. 5 were fabricated. The design magnetic field gradient is 800 T/m^3 and the magnet has a bore diameter of 0.3 m and is 0.6 m long in the direction of the pole. We used a Hall probe to measure the magnetic field gradient and confirmed that the magnetic field was consistent with the design value. During actual beam operation, beam centering at the octupole is important. To center the beam, a beam position monitor (BPM) was installed in each magnet. The octupole magnets were installed in the beam transport system in the autumn of 2013. With the octupole magnets excited, the beam profile was measured in front of the mercury target.

4. Result and discussion

4.1. Calculation of beam profile

To calculate the beam profile at the neutron source, we used the DECAY-TURTLE [16] code revised by the Paul Scherrer Institute (PSI) [17]. With the modification implemented by the PSI, beam transport calculations include octupole magnetic fields and beam scattering from the carbon target.

4.2. Comparison with experimental results

Figure 6 shows preliminary results of the measured beam profile with (black) and without (cyan) excitation of the octupole magnets. These results for the beam profile were obtained by a multiwire profile monitor (MWPM) placed at the proton beam window, 1.8 m upstream of the mercury target. For simplicity, the muon production target was placed outside the beam. The results of the calculation with and without excitation of the octupole magnets are also shown in Fig. 6 (lines). The calculation results are consistent with the experiment results both with and without excitation of the octupole magnets. Figure 6 also compares the profile with the muon target and the octupole field. We observed that the calculated beam distribution is more Gaussian than the measured beam distribution, which might be due to an excessive prediction of the scattering effect in the calculation. By accounting for this phenomenon, the calculation should provide a conservative peak density.

4.3. Effect of misaligned magnets

In actual beam operation, a misaligned magnet causes beam divergence. A survey has shown that the floor of the beamline facility settled unevenly after an earthquake and the water table underlying the tunnel shifted; therefore, we cannot avoid beam divergence. In this section, we discuss the effect of misalignment on the beam profile based on the beam optics shown in Fig. 4. To simplify the calculation, the beam profile is calculated without beam scattering at the muon target.
To identify the alignment tolerance of the octupole magnet, the beam profile at the target is calculated with the beam position offset at the octupole magnet. Without shifting the beam at the octupole magnet, the beam distribution is flat. For a horizontal offset of 2 mm in the beam position at the octupole magnet, the beam shape has a peak at the beam edge where the intensity increases by approximately 8%, as shown in Fig. 7. At the mercury target, the peak at the edge causes greater damage than the peak at the center. The maximum increase in intensity at the edge is considered to be

approximately 4%. Therefore, the allowable beam shift at the octupole magnet is approximately 1 mm. To adjust the beam position at the octupole magnet, BPMs will be installed. By installing BPMs and additional steering magnets, the beam position can be statically centered at the octupole magnets. In each beam shot, a fluctuation in horizontal position occurs because of the instability of the kicker magnet at the RCS. However, the instability for each shot is less than 1 mm so that the edge peak does not cause difficulties.
To calculate the tilting tolerance of the octupole magnet, we considered the case of 0.5 mrad. We observed that the tilting error does not influence the beam shape. Because the precision of the angular position of the octupole magnet is less than 0.2 mrad, tilt misalignment is not a problem. Downstream of the octupole magnets, six pieces of the quadrupole magnets were positioned around the muon production target. To obtain the required accuracy for the position of the downstream magnets, beam profiles were calculated for the quadrupole magnets with the beam offset. We found that misalignment of the quadrupole magnets caused the beam position to oscillate because of betatron oscillation. Thus, misalignment of the quadrupole magnets does not influence the beam shape, and the flat beam distribution at the target is preserved. Because the beam position at the target can be adjusted easily using the steering magnets, misalignment of the quadrupole magnets downstream of the octupole magnets is not an issue for beam flattening.

4.4. Effect of beam scattering at muon production target

To minimize the peak density and obtain a flat beam distribution at the neutron production target, we studied the effect of beam scattering from the muon target. For the octupole magnets in use, the beam distribution in horizontal phase space, before it penetrates the carbon target (for muon production), is shown in Fig. 8. We observed that the octupole magnetic field generates an arm-shaped distribution in phase space. The beam particles in the arm region play an important role in beam flattening at the mercury target. Figure 9 shows the beam distribution after it passes the carbon target. The beam divergence, which is plotted on the vertical axis of Fig. 9, is widely spread by the scattering so that the beam distribution becomes similar to a Gaussian. To maintain a flat distribution, this increase in beam divergence due to scattering should be suppressed. Therefore, to obtain a flat distribution, the beam should be focused at the muon production target to increase the beam divergence at the target.

5. Conclusion

To reduce the peak current density of the beam at the target, we developed a beam transport system that uses nonlinear beam optics (i.e., octupole magnets). The results of calculations show that the beam can be flattened using optics with a large beta function at the octupole magnets and by ensuring an appropriate phase advance between the octupole magnets and the mercury target. Furthermore, we studied how magnet misalignment affects the beam profile. With the beam offset at the octupole magnet, the beam density becomes large at the target edge. The acceptable offset of the beam at the octupole magnet is approximately 1 mm, which is a feasible precision for the present beam operation. The results of simulations show that the alignment error of quadrupole magnets located downstream of the octupole magnets does not influence the shape of the beam at the target. To reduce a severe increase in the beam emittance because of the scattering from the muon production target, the beam is focused at the muon production target to obtain a large beam divergence. Calculations that consider beam scattering from the muon production target indicate that the peak current density can be reduced by approximately 30% from the peak density without the nonlinear beam optics.
Octupole magnets have already been installed in the proton transport line, and the calculated beam profile is consistent with the beam profile obtained with octupole magnets in place. Note that the

present nonlinear optics system represents the first attempt to install such a system in a MW-class hadron accelerator.

References

[1] The Joint Project Team of JAERI and KEK, JAERI-Tech 99-56, 1999.
[2] Y. Ikeda, Nucl. Instrum. Meth. A600, (2009) 1.
[3] Y. Miyake, et al., Physica B 404 (2009) 957.
[4] S. Meigo, et al., Nucl. Instrum. Meth. A562, (2006) 569.
[5] S. Sakamoto, et al., Nucl. Instrum. Meth. A562, (2006) 638.
[6] S. Meigo, et al., Nucl. Instrum. Meth. A600, (2009) 41.
[7] M. Futakawa, et al., J. Nucl. Sci. Technol. 40 (2004) 895.
[8] M. Futakawa, et al., J. Nucl. Mater. 343 (2005) 70.
[9] T. Naoe, et al., J. Nucl. Mater. 450 (2014) 123.
[10] D. A. McClintock, et al., J. Nucl. Mater., 431 (2012) 147.
[11] S. Meigo, et al., MOPEB066, IPAC10 (2010)
[12] Y. Yuri, et al., Phys Rev ST Accel. Beams 10, 10401 (2007).
[13] N. Tsoupas, et al., Nucl Sci. and Eng. 126 71 (1997).
[14] F. Meot and T. Aniel, Nucl. Instrum. Meth. A 379, 196 (1996).
[15] H. Hotchi, et al., THPPP080, IPAC12 (2012)
[16] K.L. Brown, Ch. Iselin and D.C. Carey: Decay Turtle, CERN 74-2 (1974)
[17] PSI Graphic Turtle Framework by U. Rohrer based on a CERN-SLAC-FERMILAB version

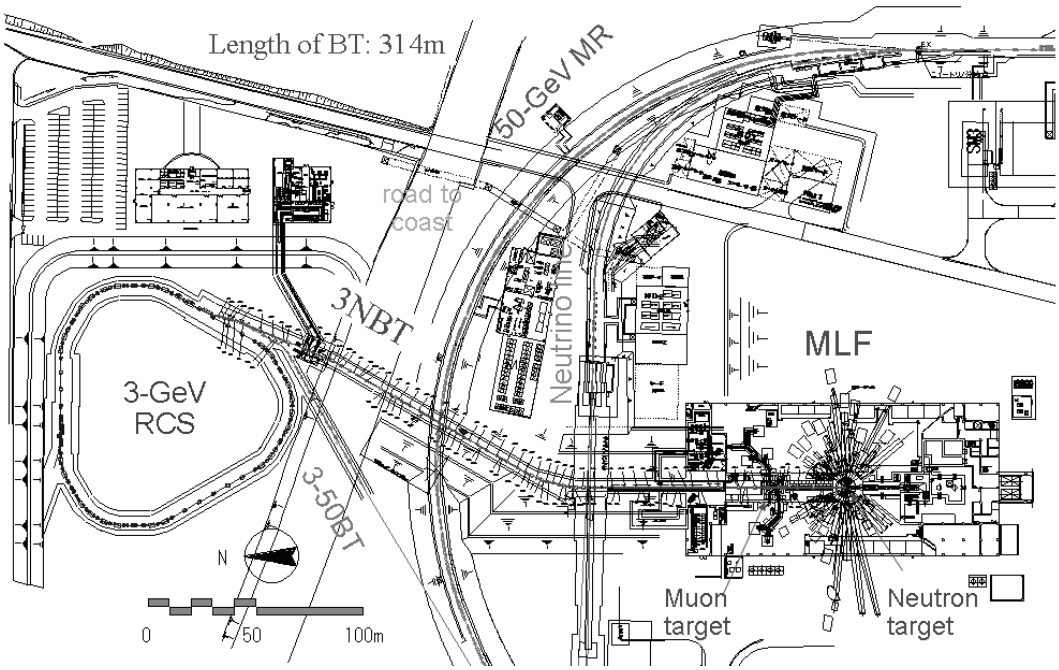

Figure 1: Plan of rapid cycling synchrotron (RCS) at the Materials and Life Science Experimental Facility at J-PARC.

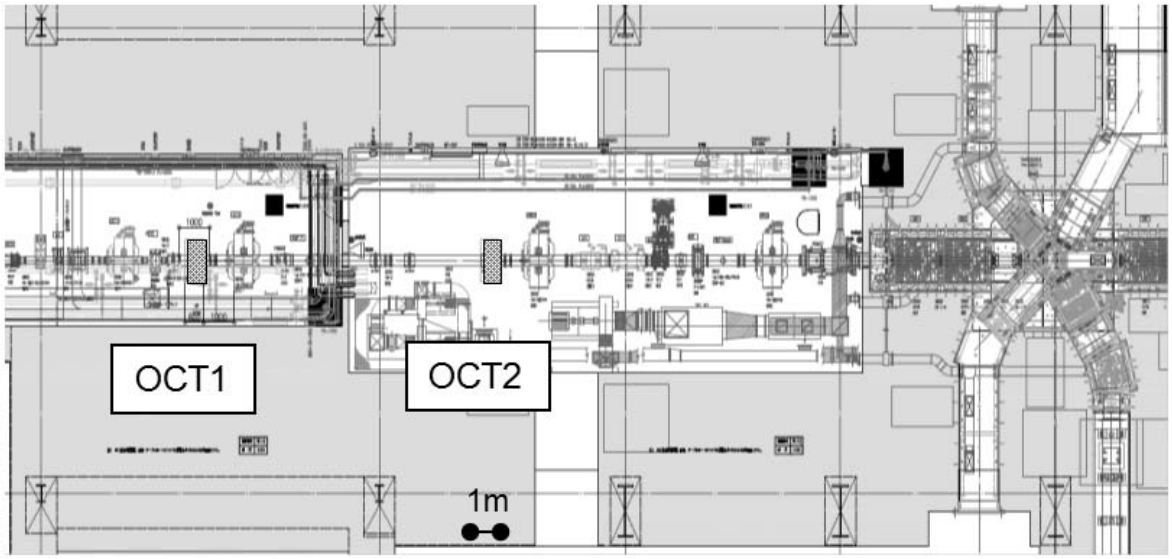

Figure 2: Plan of octupole magnets for beam expander system, which is to be placed upstream of muon production target

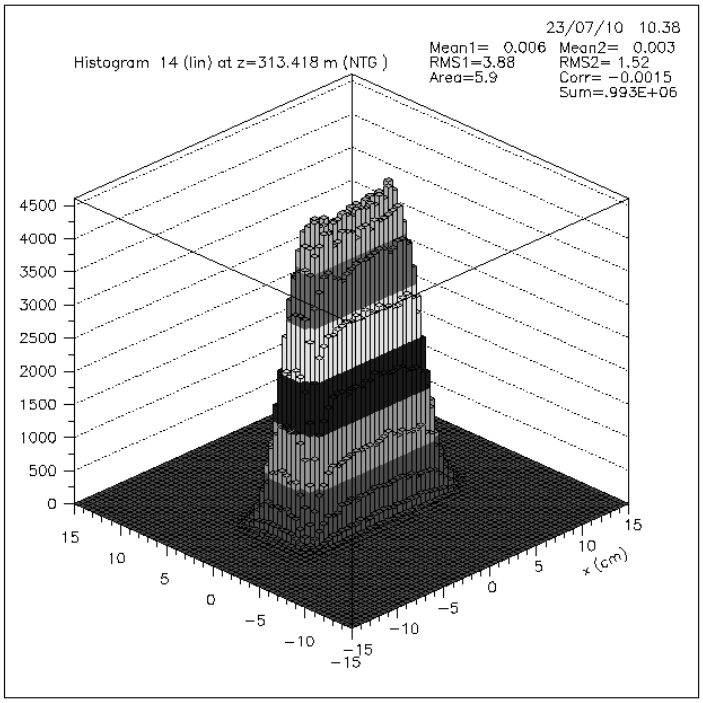

Figure 3: Flat beam distribution at the mercury target expanded by octupole magnets. Beam scattering from the muon production target is ignored.

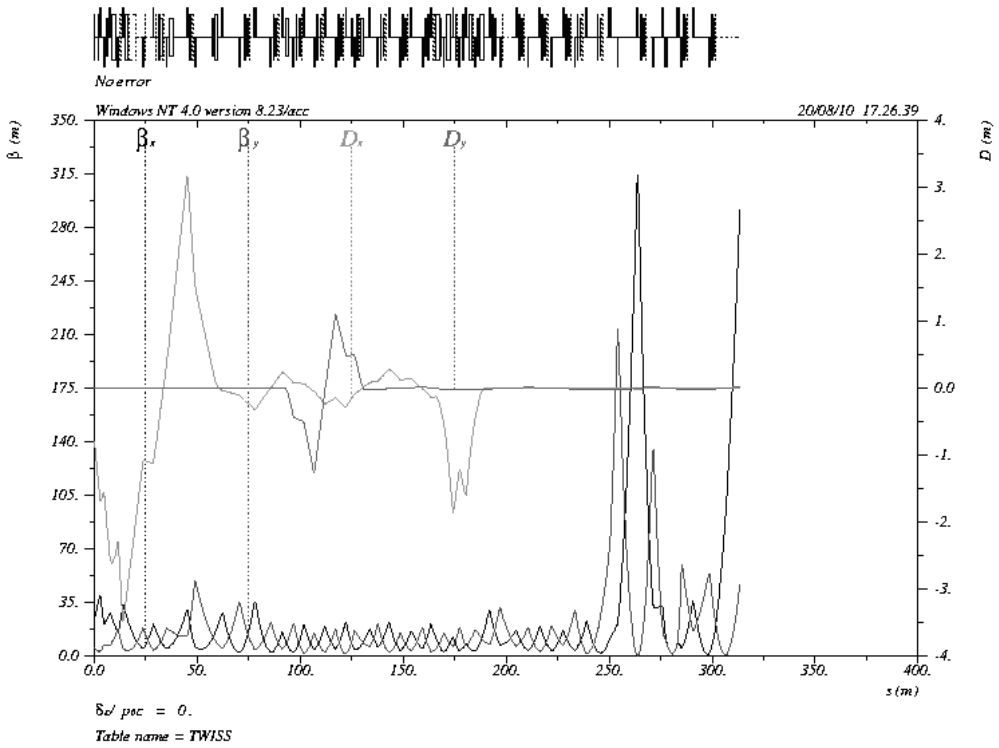

Figure 4: Beam optics and beta function for beam expander consisting of octupole magnets.

Figure 5: Fabricated octupole magnet with magnetic field gradient of 800 T/m^3.

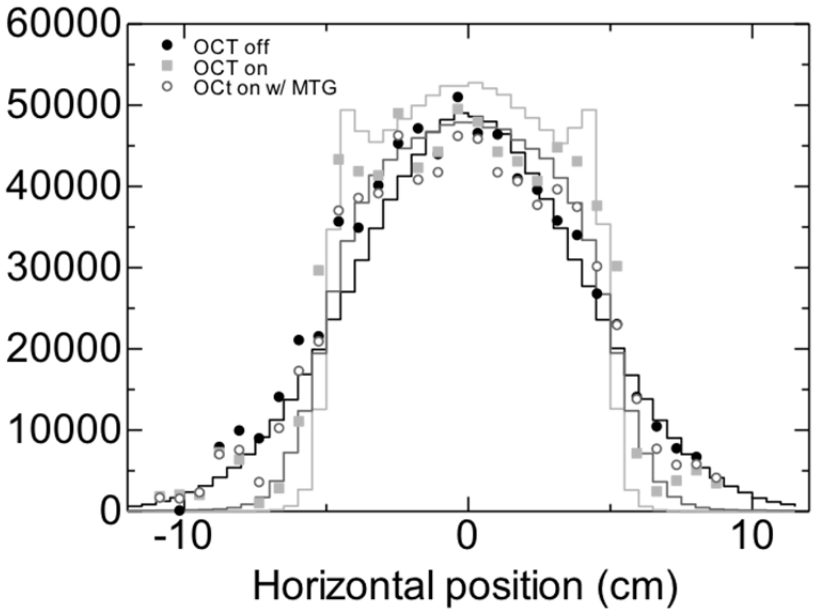

(a)

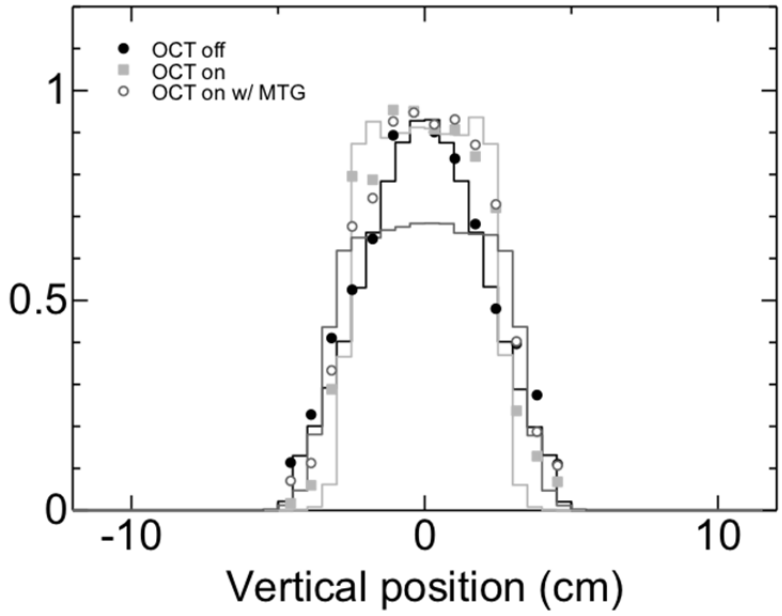

(b)

Figure 6: Beam profile in (a) horizontal and (b) vertical directions obtained by the MWPM (dots) compared with calculation by DECAY-TURTLE (lines) without octupole magnet excitation (black), with octupole magnet excitation (cyan), and with octupole magnet excitation and irradiation of muon production target (red).

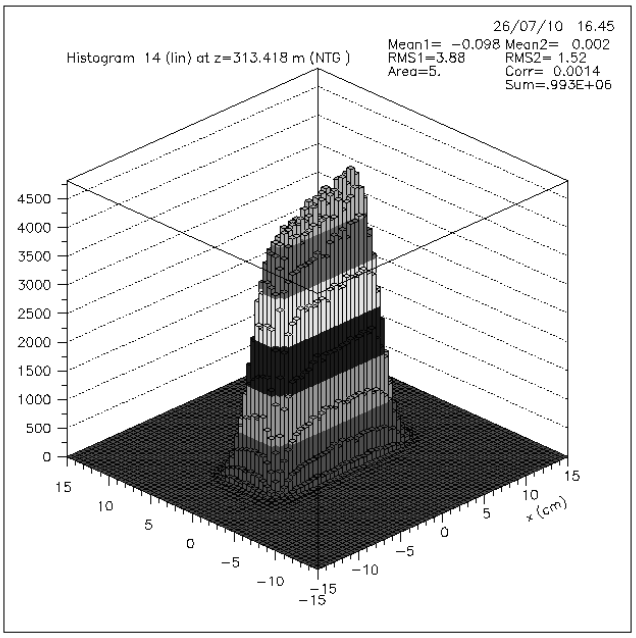

(a)

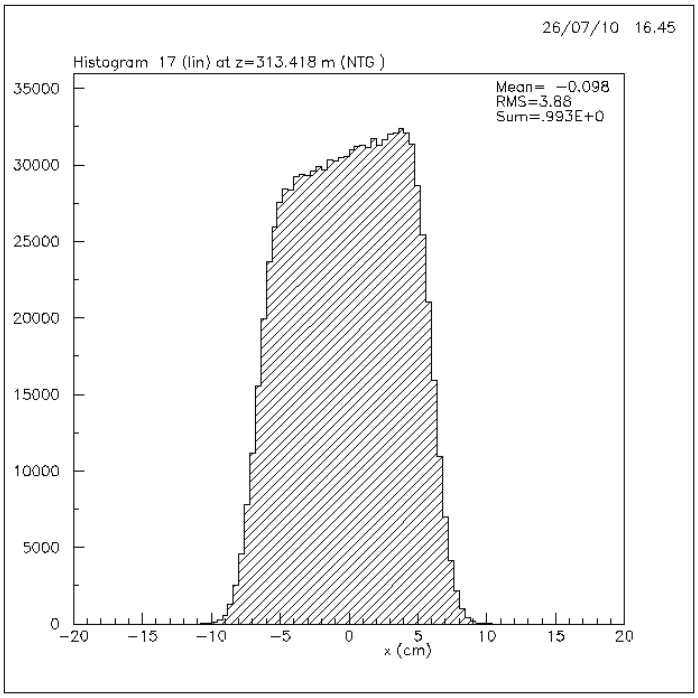

(b)

Figure 7: Horizontal beam profile at mercury target for 2 mm horizontal beam offset at octupole magnet (OCT2). (a) Vertical beam profile, (b) horizontal beam profile.

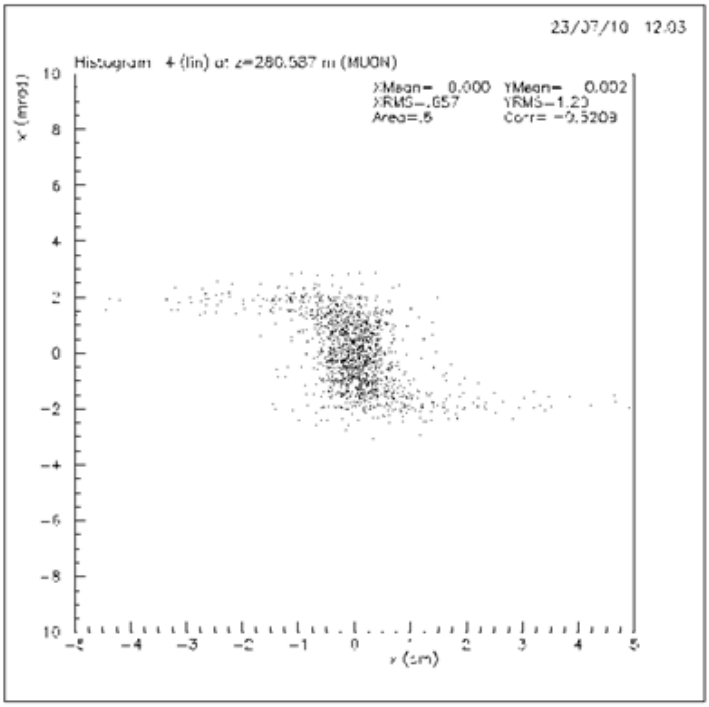

Figure 8: Transverse phase space distribution in horizontal direction for beam injected into muon production target.

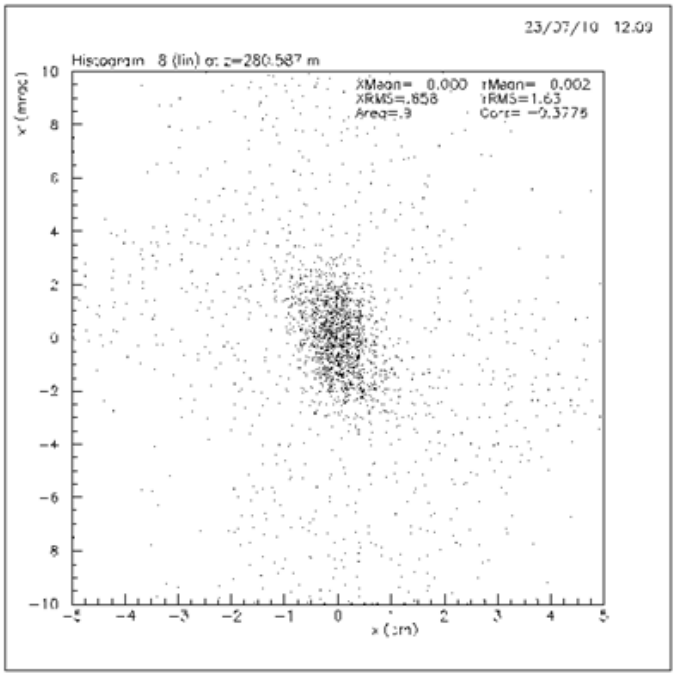

Figure 9: Transverse phase space distribution in horizontal direction for beam scattered from muon production target

3-5. Neutron Instruments

This is a blank page.

3.5.1

LoKI - A Broad Band High Flux SANS Instrument for the ESS

A J Jackson[1], K Kanaki[1], C I Lopez[1], C Zendler[1], E Nilsson[1], G Nagy[2], N Cherkashyna[1], A Sandström[1], T Nielsen[1], A Pettersson[1], S A Pullen[1], P M Bentley[1], T Gahl[1], R Hall-Wilton[1], I Sutton[1], K H Andersen[1]

[1] European Spallation Source, PO Box 176, Lund 221 00, Sweden
[2] Laboratory for Neutron Scattering and Imaging, Paul Scherrer Institute, 5232 Villigen PSI, Switzerland

E-mail: andrew.jackson@esss.se

Abstract. The European Spallation Source (ESS) will be a long pulse 5MW spallation neutron source built in Lund, Sweden. It is expected that 7 out of a final suite of 22 instruments will enter commissioning in 2019/2020, with the remainder coming online by 2025. LoKI is a SANS beamline designed primarily with the needs of the soft matter, bio-science and materials science communities in mind. The trend in all of these fields is towards complexity and heterogeneity. These factors are manifested both spatially and temporally and so high flux, small beam sizes and a wide simultaneous Q range are required. We are thus constructing a 10 m + 10 m SANS instrument with the sample position 22.5 m from the source. Using the full ESS pulse length of 2.86 ms and two pairs of choppers, this provides a wavelength band of 7 Å at 14 Hz or 17.5 Å at 7 Hz whilst maintaining reasonable resolution. The resolution can be enhanced by generating four shorter sub-frames with an optional series of additional choppers. Combining this configuration with variable beam collimation and multiple banks of detectors covering a large solid angle, maximal use is made of the flux available from the ESS source and measurements with over 3 orders of magnitude in simultaneous Q range are possible.

1. Introduction

The European Spallation Source (ESS), currently under construction in Lund, Sweden, aspires to be the world's leading facility for research using neutrons, with unprecedented source brightness and intensity [1]. The ESS will be a long pulse spallation neutron source with a pulse length of 2.86 ms and a repetition rate of 14 Hz [1]. A total of 22 instruments or beamlines will be operational or in commissioning by the end of 2025 with 7 entering commissioning in 2019/2020. Since 2011, the ESS has been managing the development of instrument concepts by university groups and research institutions across Europe, and by in-house scientists based in Lund. The choice of instruments is through an ongoing process of annual proposal calls and review by expert panels. The proposal for LoKI [2] was submitted in October 2012 and approved for construction in October 2013. Here we outline the conceptual design of the instrument with some reference to possible technical solutions.

2. Scientific Goals

Small angle neutron scattering is a technique that is applied across a spectrum of scientific disciplines, with users from chemistry, physics, biology, materials science, engineering and geoscience. LoKI is designed primarily with the needs of the soft matter, biophysics and materials science communities in mind and the trend in all of these fields is towards complexity and heterogeneity.

Complexity manifests itself in the study of multi-component systems studied as a function of multiple environmental conditions (e.g. pressure, temperature, shear, magnetic field) simultaneously. In order to be able to examine the possible parameter space, a combination of faster measurements, measurements on smaller sample volumes, and measurements with a good signal-to-noise ratio is required.

Heterogeneity is seen both spatially and temporally. Spatial heterogeneity is manifested as different structure at different length scales, from the nanometre scale to the millimetre scale. This can be driven by applied stimuli such as shear and flow [3], electrical or magnetic fields, or by intrinsic structural features of the material. Examples of the former are shear banding in surfactant systems [4] and the flow re-orientation of polymers. Examples of the latter are nano-composite materials, multi-component gels [5, 6, 7], and porosity in rocks [8, 9, 10, 11]. To address this spatial heterogeneity requires a wide Q range to examine the sub-micrometre length scales and small beams to examine the heterogeneity on the millimetre scale. Furthermore, since these heterogeneities are often driven by non-equilibrium conditions, the accessible Q range must be measured simultaneously.

Temporal heterogeneity is seen in the form of stimulus-response experiments (e.g. shear relaxation), in the kinetics of formation of materials when the components of the material are mixed (e.g. mixed micelle formation)[12, 13] and in the growth of biomolecule aggregates such as fibrils. In order to examine these systems with sufficient time resolution a high neutron flux is required and a wide simultaneous Q range is needed.

Not only are the systems of interest becoming more complex and heterogeneous, but they are also becoming smaller in volume. Examples of this are the small amounts of protein complexes that can be purified and deuterated, thin film systems such as organic photovoltaics, and biomimetic or polymer membranes. In these cases it is vital that the instrumental background be as low as possible in order to discern the small scattering signal obtained.

The ability to reach Q values above the typical 0.8 to 1.0 Å^{-1} opens up significant areas of new science when combined with wide-angle scattering studies and the rapidly advancing fields of materials simulation. The study of, for example, ionic liquids and their ordering in the presence of solutes calls for the combination of SANS, wide-angle scattering and atomistic or coarse-grained molecular dynamics simulations. The analysis techniques used in biological solution scattering, such as ab-initio shape reconstruction, require data out to high Q as do studies of nano-composite materials where the size of the particles or domains may be only a few nanometres.

Non-equilibrium studies often use complex sample environments and require strong integration of the sample environment with the neutron measurement in order to tie sample conditions tightly to the measured scattering. Space is also required for the use of in-situ complementary measurement techniques, for example light or x-ray scattering, or UV spectroscopy simultaneously with the neutron scattering measurement. LoKI has a flexible sample area that can be easily re-tooled for different experiments through the use of interchangeable sample environment platforms.

Consultation with the user community and advice from expert panels lead to the development of top level requirements that encapsulate the scientific needs discussed above:

- The instrument shall allow data to be collected to a Qmin of < 0.001 Å^{-1}.
- The instrument shall allow data to be collected to a Qmax of > 2 Å^{-1}.

- The instrument shall allow data to be collected simultaneously over a continuous Q range with Qmax/Qmin > 1000.
- The instrument shall match the size of the neutron beam to the size of the sample.
- The instrument should allow the Q resolution (dQ/Q) to be optimised for the experiment.
- The instrument should be capable of providing a Q resolution < 10% dQ/Q over the whole Q range.
- The instrument should allow data collection from samples < 8 mm^3 volume
- The instrument should maximise the signal-to-background (S/B) ratio of the small angle scattering.

3. Instrument Overview

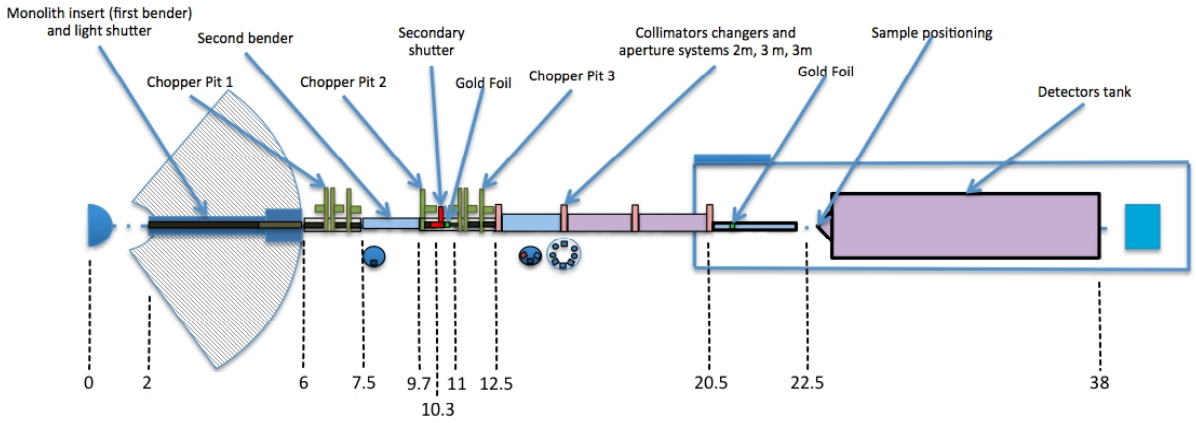

Figure 1. Layout of the LoKI instrument.

The instrument begins at 2 m from the source with a 4 m long bender to close line-of-sight by the 6 m position. The first chopper pit houses the bandwidth selection chopper pair at 6.5 m and the first resolution enhancement chopper at 7 m. A second 2.1 m long bender closes line-of-sight a second time between the first and second chopper pits. The second chopper pit houses the second resolution enhancement chopper at 10 m from the source. There is then a straight guide to the third chopper pit which houses the frame-overlap chopper pair at 11.5 m and the final resolution enhancement chopper at 12 m. The variable collimation begins at 12.5 m with the first aperture wheel, followed by: a 2 m long guide changer drum; the second aperture wheel at 14.5 m; a 3 m long guide changer drum; the third aperture wheel at 17.5 m; a 3 m long guide changer drum; and the final aperture wheel at 20.5 m. There is then a variable length evacuated flight tube between the final aperture wheel and the sample aperture, with the sample position at 22.5 m from the source. The detector system, for which there are two options, is then mounted following the sample. The two options for detector geometry are (Figure 5): (1) a "window frame" arrangement of three detector banks; and (2) a "barrel" arrangement where the detector vessel is lined with detector banks running parallel to the beam axis and a high-resolution rear detector is placed perpendicular to the beam axis for the lowest angles. In both cases the rear detector is moveable along the beam axis. The sample position and detector system are housed in the instrument cave which is constructed of steel "cans" filled with borated wax.

The instrument design has initially been optimised to make use of the recently conceived "pancake" moderator that the ESS is planning to use [14, 15]. This moderator produces a cold spectrum and has a viewable face of 3 cm high × 12 cm wide.

4. Optics

4.1. Line-of-sight

In order to minimise background and avoid the prompt spike of high energy neutrons produced when the proton beam hits the target, the instrument is designed to have the start of the collimation two times out of line-of-sight of the source. One times line-of-sight closure is achieved when no point at the exit of a section of the instrument has a direct line-of-sight to the start of that section. The first line-of-sight closure is designed as being at the outer wall of the target monolith, at 6 m from the source. The second line-of-sight closure takes this point as its start and is closed at the second chopper pit.

Several guide geometry options have been considered in developing the concept for the neutron optics. Monte Carlo simulations using Vitess [16] were used to assess the relative performance of the different options. Horizontal and vertical bends, both s-bends and continuous curves, were considered and the guide dimension in the direction of the bend was allowed to vary to minimise the curvature and potentially increase the transmission whilst maintaining line-of-sight closure. An additional requirement was that the guide be straight within the chopper pits and thus the lengths of the two benders were fixed at 4 m and 2.1 m respectively.

The result was that a horizontal s-bend was the most favourable, having a first bender, 4 m in length, 2.5 cm wide × 3 cm high with a radius of 66.0 m and a second bender, 2.1 m in length, 2.5 cm wide × 3 cm high with a radius of 36.8 m. Thus the guide is asymmetric in shape from the start of the optics at 2 m until the end of the second chopper pit. The guide then expands from 2.5 cm × 3 cm to 3 cm × 3 cm between the second chopper pit and the start of the collimation. All of the guides in the collimation section are 3 cm × 3 cm.

4.2. Collimation

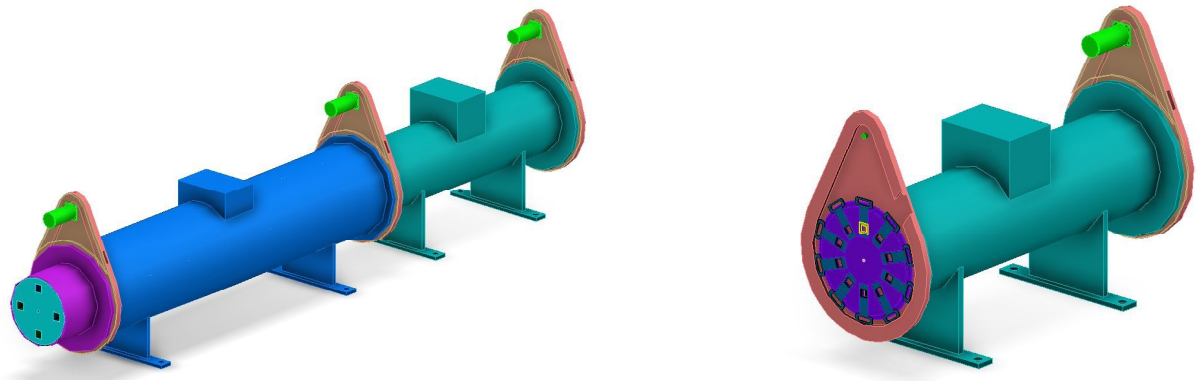

(a) (b)

Figure 2. The variable collimation system consisting of Collimation Drums (Figure 2a (section shown)) and Aperture Wheels (Figure 2b (shown connected to collimation drum)).

The variable collimation section provides for source-to-sample distances of 2 m, 5 m, 8 m and 10 m. The three longest distances can be matched with a corresponding sample-to-detector distance through moving the rear detector. The collimation system consists of three drums (Figure 2a) that allow for switching between guide and an empty tube lined with neutron absorbing material. A spare empty tube is provided for future upgrades and a blocked position is provided as a means of blocking the neutron beam if the secondary shutter is inoperable. At the ends of each collimation section are aperture wheels (Figure 2b) that provide 10 possible

aperture choices to allow the collimation to be tuned to the sample size and resolution required by the experiment.

5. Chopper System

5.1. Bandwidth Selection

Wavelength selection and frame overlap prevention is performed using two double-disc choppers. The first chopper, located at 6.5 m from the source, has two co-rotating discs, each with a 120° opening. This provides for an adjustable chopper aperture through variation of the phasing between the two discs. The second chopper, located at 11.5 m from the source, is identical to the first and provides the frame overlap suppression.

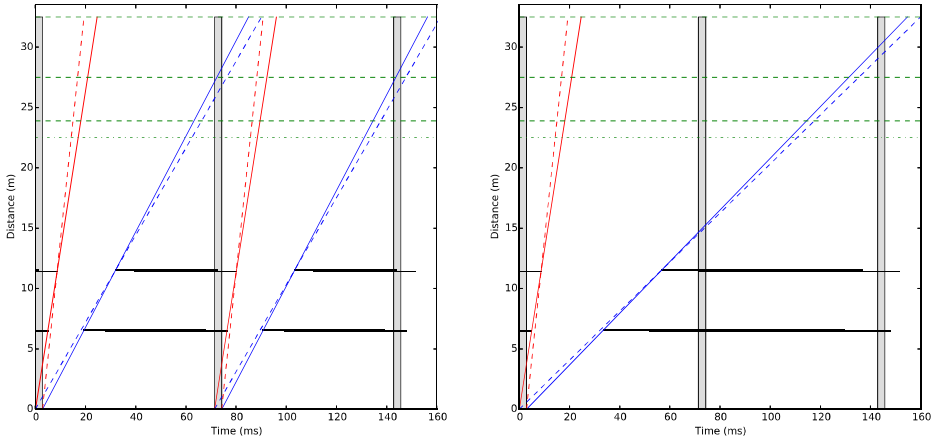

(a) (b)

Figure 3. Time-distance diagrams for Mode 1 (14Hz) (Figure 3a) and Mode 2 (7 Hz) (Figure 3b). Detector positions for a window-frame type layout are indicated with long dashes. Short dashes show the sample position.

LoKI provides two modes of operation offering different wavelength bands and hence different Q ranges. Mode 1 has the choppers running at 14 Hz. To access the wavelength band from 3 Å to 10 Å (2.0 Å to 11.0 Å with penumbra), an open time of 14.5 ms is required as seen in Figure 3a. The timing of the chopper with respect to the source can be adjusted such that a different range of wavelength is selected, for instance moving the whole band to longer wavelength. This allows the scientist to select for lower Q values whilst still using every pulse from the source. Such operation will also improve the wavelength resolution, as longer wavelengths will be used.

Mode 2 has the choppers running at 7 Hz. This allows access to the wavelength band from 3 Å to 18.5 Å (2.0 Å to 19.5 Å with penumbra), using every other source pulse as shown in Figure 3b. In order to achieve this range whilst still completely filling the frame the open time of the choppers must be adjusted, by changing the phasing of the discs, to be longer than twice that of 14 Hz operation.

5.2. Resolution Enhancement

The instrumental resolution dQ/Q is limited by the time-of-flight resolution of the shortest wavelengths that contribute to a given Q bin. In the default operation mode, dT is fixed at the pulse length of 2.86 ms. At the shortest detector distance, using 2 Å neutrons, this gives a dT/T of 27%. This value adds in quadrature with the other components of the resolution [17],

but will dominate the resolution at high Q. LoKI will enable two approaches to enhancement of Q resolution.

The first of these is through the use of neutron event recording, which identifies the time of arrival of each neutron at the detector. LoKI, along with all ESS instruments, will allow the scientist to determine the data binning scheme post experiment and it will be possible to exclude short wavelength neutrons from the data reduction and do so selectively as a function of Q. This is valuable for materials such as block-copolymer blends where there are strong peaks in the data that require high resolution but the inter-peak scattering is of lower intensity and so requires more neutron counts but can make use of lower resolution. In particular there is a need to have good Q resolution at high Q, for example in studies of fibres, liquid crystals or multi-lamellar systems such as lipid or surfactant vesicles. The ability to make use of longer wavelength, higher time resolution, neutrons at high angles will be key to being able to make use of post-measurement resolution tuning. This also demands a large solid angle of detectors and detectors at high angles.

The second approach is to employ a system of choppers to reduce the virtual length of the source pulse for the case of shorter wavelength neutrons [18]. This allows for approximately a threefold improvement in the resolution of the short wavelength frames. Whilst the integrated flux on sample is reduced using this method compared to using the full pulse at all wavelengths, it is equivalent to a flux increase at a given resolution obtained by rejecting short wavelengths in the data reduction using the method above. This frame multiplication method is therefore of most use when resolution enhancement over the whole Q range is required, rather than selective enhancement, for example in the case of solving the structures of biological macromolecules in solution.

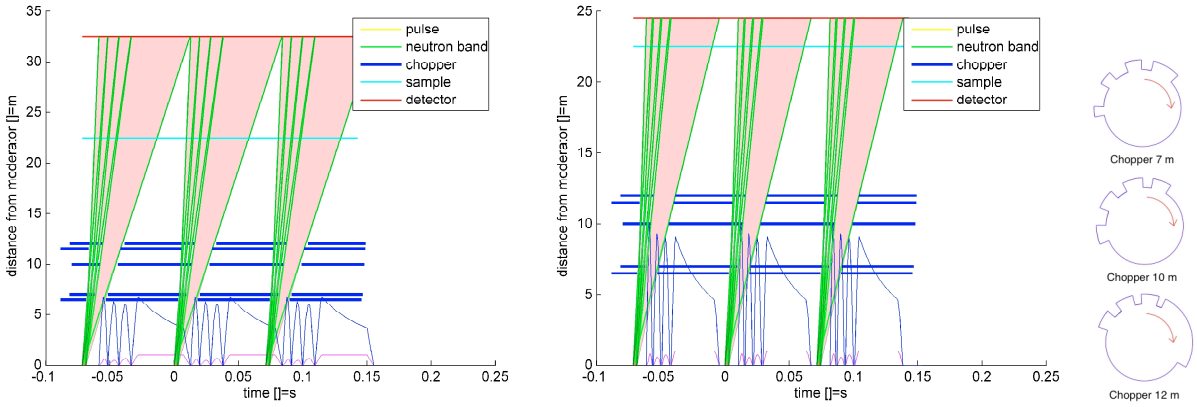

(a) (b) (c)

Figure 4. Time-distance diagrams with resolution enhancement choppers in place. Figure 4a shows the effect of the choppers with 10 m collimation. Figure 4b shows their effect with 2 m collimation. Figure 4c shows the chopper disc arrangement that produces the frame multiplication.

6. Detectors

The traditional approach of using ^{3}He detectors is no longer a viable option for ESS instruments, owing to the limited availability of ^{3}He, its high cost [19, 20, 21] and that some detector requirements cannot be fulfilled using this technology [22]. Thus an alternative neutron technology solution based on ^{10}B is introduced for this application. Boron carbide ($^{10}B_4C$)

thin-film detectors are currently being developed by several groups worldwide and are proven to be a reliable and promising replacement for ^{3}He detectors ([23, 24, 25, 26, 27, 28]).

6.1. Window Frame

The window frame detector geometry option consists of a series of three detector panels with holes in centre of the first two. In this way a large solid angle can be covered simultaneously. These detector banks are placed within a large vacuum vessel, and the sizes of the panels are designed to minimise the size of that vessel whilst still meeting the requirements for scattering angle coverage. Thus, the front and middle panel are 2.0 m × 2.0 m and the rear detector is 0.5 m x 0.5 m. Square holes are left in the centre of the front and middle panels to allow full illumination of the detectors behind. The front, middle and rear detectors have resolutions of 15 mm, 8 mm and 3 mm respectively.

The panels will utilise ^{10}B coated detection planes placed at an inclined angle in either a BAND (Boron Array Neutron Detector) or Multi-Blade [29] arrangement. The preferred BAND design makes use of boron coated alumina lamellae, a GEM system for signal multiplication and a padded anode for event location.

6.2. Barrel

The barrel detector geometry option has been described elsewhere [30, 31] and consists of ^{10}B coated panels lying parallel to the beam direction around the outside of an evacuated or gas filled tube. This geometry maximises the path length of neutrons through the boron conversion layer, whilst keeping it thin enough to allow escape of the conversion products. The inclined geometry allows the wire pitch to be 10 mm along the whole length of the tube whilst maintaining adequate angular resolution.

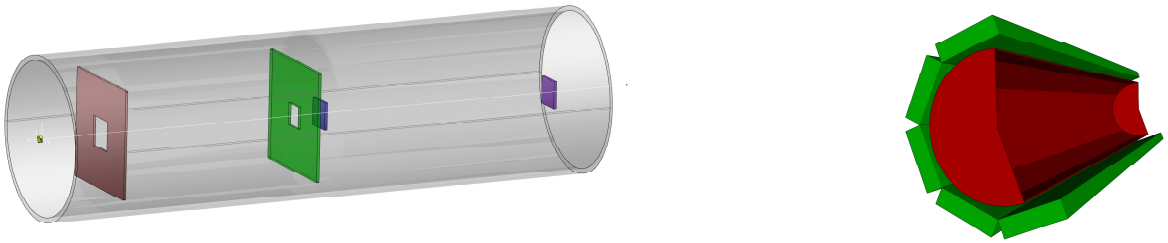

(a) (b)

Figure 5. Possible detector geometry configurations for LoKI, as they appear in the instrument proposal. Figure 5a shows the "window-frame" geometry inside a vacuum tank, while Figure 5b depicts the "barrel" geometry.

7. Performance

Monte Carlo simulations using McStas [32, 33] have been performed with the window-frame detector geometry. Using circular apertures and setting the source aperture to be twice the diameter of the sample aperture the flux at sample can be obtained and some values are shown in Table 1. In terms of flux on sample, LoKI will provide more than an order of magnitude increase over existing instruments and deliver a wide simultaneous Q range as shown in Figure 6.

8. Conclusion

Our initial work indicates that a world-leading SANS instrument can be built at the ESS making maximum use of the new moderator geometry. The instrument design will be completed in 2015/2016 and the instrument will enter hot commissioning with neutrons in 2019/2020.

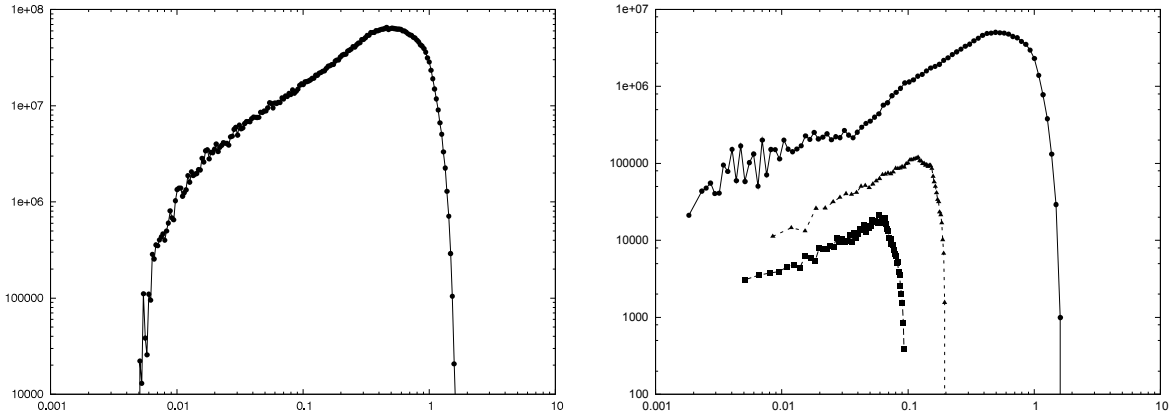

(a) (b)

Figure 6. Simulated elastic scattering from water at 2 m (Figure 6a) and 10 m (Figure 6b) collimation lengths with 20 mm diameter source and 10 mm diameter sample apertures (●) compared with simulation of 10 m (■) and 5 m (▲) collimation settings on D22.

Table 1. Flux at sample from Monte Carlo simulations as a function of collimation.

L1 (m)	A_1 diam (mm)	A_2 diam (mm)	Flux (n/s/cm^2)
2	20	10	1.4×10^9
5	20	10	2.5×10^8
10	20	10	1.1×10^8
2	10	5	1.1×10^8
5	10	5	3.0×10^7
10	10	5	6.4×10^6

References

[1] Peggs S *et al.* 2013 *ESS Technical Design Report* ESS-2013-001 (Lund, Sweden: European Spallation Source, ESS AB)

[2] Jackson A and Kanaki K 2013 URL `http://dx.doi.org/10.5281/zenodo.13302`

[3] Eberle A P R and Porcar L 2012 *Current Opinion in Solid State & Materials Science* **17** 33–43

[4] Helgeson M E, Vasquez P A, Kaler E W and Wagner N J 2009 *Journal of Rheology* **53** 727–756

[5] Waters D J, Engberg K, Parke-Houben R, Ta C N, Jackson A J, Toney M F and Frank C W 2011 *Macromolecules* **44** 5776–5787

[6] Tominaga T, Tirumala V R, Lee S, Lin E K, Gong J P and Wu W l 2008 *Journal of Physical Chemistry B* **112** 3903–3909

[7] Tirumala V R, Tominaga T, Lee S, Butler P D, Lin E K, Gong J P and Wu W l 2008 *Journal of Physical Chemistry B* **112** 8024–8031

[8] Wang H W, Anovitz L M, Burg A, Cole D R, Allard L F, Jackson A J, Stack A G and Rother G 2013 *Geochimica et Cosmochimica Acta* **121** 339–362

[9] Anovitz L M, Cole D R, Rother G, Allard L F, Jackson A J and Littrell K C 2013 *Geochimica et Cosmochimica Acta* **102** 280–305

[10] Sakurovs R, He L, Melnichenko Y B, Radlinski A P, Blach T, Lemmel H and Mildner D F R 2012 *International Journal of Coal Geology* **100** 51–64

[11] Clarkson C R, Solano N, Bustin R M, Bustin A M M, Chalmers G R L, He L, Melnichenko Y B, ski A P R and Blach T P 2012 *Fuel*

[12] Bressel K, Muthig M, Prevost S, Grillo I and Gradzielski M 2010 *Colloid and Polymer Science* **288** 827–840

[13] Hoffmann I, Heunemann P, Prevost S, Schweins R, Wagner N J and Gradzielski M 2011 *Langmuir* **27** 4386–4396
[14] Batkov K, Takibayev A, Zanini L and Mezei F 2013 *Nuclear Instruments & Methods in Physics Research Section a-Accelerators Spectrometers Detectors and Associated Equipment*
[15] Mezei F, Zanini L, Takibayev A, Batkov K, Klinkby E, Pitcher E and Schönfeldt T 2014 *Journal of Neutron Research* **17** 101–105
[16] Zsigmond G, Lieutenant K and Mezei F 2002 *Neutron News* **13** 11–14
[17] Mildner D F R and Carpenter J M 1984 *Journal of Applied Crystallography* **17** 249–256
[18] Kynde S, Hewitt Klenø K, Nagy G, Mortensen K, Lefmann K, Kohlbrecher J and Arleth L 2014 *Nuclear Instruments & Methods A* **764** 133–141
[19] Persons T M and Aloise G 2011 Tech. Rep. GAO-11-753 US Government Accountability Office Washington DC, USA
[20] Shea D and Morgan D 2010 Tech. Rep. R41419 Congressional Research Service Washington DC, USA
[21] Cho A 2009 *Science* **326** 778–779
[22] Kirstein O *et al.* 2014 PoS (Vertex2014) 029 arXiv:1411.6194 [physics.ins-det]
[23] Andersen K *et al.* 2012 ArXiv:1209.0566 [physics.ins-det]
[24] Zeitelhack K 2012 *Neutron News* **23** 10–13
[25] Bigault T, Birch J, Buffet J C, Correa J, Hall-Wilton R, Hultman L, Höglund C, Guérard B, Khapalov A, Piscatelli F and van Esch P 2012 *Neutron News* **23** 20–25
[26] Correa J 2012 Ph.D. thesis University of Zaragoza Spain
[27] Stefanescu I, Abdullahi Y, Birch J, Defendi I, Hall-Wilton R, Höglund C, Hultman L, Seiler D and Zeitelhack K 2013 *Nuclear Instruments and Methods A* **727** 109–125
[28] Höglund C *et al.* 2012 *J. Appl. Phys* **111** 104908
[29] Piscatelli F *et al.* 2014 *J. Instrum.* **9** P03007
[30] Kanaki K, Jackson A J, Hall-Wilton R, Piscitelli F, Kirstein O and Andersen K H 2013 *Journal of Applied Crystallography* **46** 1031–1037
[31] Kanaki K, Jackson A, Hall-Wilton R, Piscitelli F, Kirstein O and Andersen K H 2013 *Journal of Applied Crystallography* **46** 1528
[32] Lefmann K and Nielsen K 1999 *Neutron News* **10** 20
[33] Willendrup P, Farhi E and Lefmann K 2004 *Physica B* **350** 735

3.5.2

Investigation of timing and positioning of T_0 choppers at long pulse neutron sources

N. Violini, J. Voigt and T. Brückel

Jülich Centre for Neutron Science, JCNS, Forschungszentrum Jülich GmbH, Leo Brandt Strasse, D-52425 Jülich, Germany

E-mail: n.violini@fz-juelich.de

Abstract. We examine the prerequisites for the operation of T_0 choppers at a long pulse spallation source using the parameters of the European Spallation Source (ESS). We discuss the constraints imposed to the chopper position and the operation parameters by the long pulse nature and the low repetition rate of the ESS. For an instrument having a moderator-to-detector distance $L_D = 155$ m with a double elliptic neutron guide shape we analyze possible solutions for chopper rotational frequencies of 7 and 28 Hz, that are acceptable for a cold instrument, while for a bi-spectral or a thermal instrument the lower frequency requires the chopper to be placed at a large distance from the moderator.

1. Introduction

At spallation neutron sources a proton beam is injected into the neutron production target causing the emission of high-energy particles that can hardly be shielded, as the energy, e.g. for fast neutrons, is limited by the proton beam energy to several GeV. The high-energy particles, which can leave the monolith shielding, are potentially scattered and/or moderated within the instruments beam-lines. This source of background has to be kept as low as possible, since the key figure describing the performance of any neutron instrument is the signal to noise ratio. Several measures are currently in use at existing facilities and various options exist to assure that the experimental area is out of the direct line-of-sight of the neutron source. Geometrically the line-of-sight can be avoided by curved neutron guides[1] also including more involved design such as the *Selene* concept [2]. In time the use of T_0 choppers mitigates the intensity of high energy neutrons by blocking off the beam-line around the time of neutron production. It consists of a rotor with blades that block the beam-line and the rotor is synchronized with the injection of the proton beam and therefore with the emission of the prompt neutron pulse. The use of T_0 choppers is a common practice at spallation sources [3, 4]. T_0 choppers rotating at comparably high frequencies of 100 Hz are in use at the Japan Proton Accelerator Research Complex (J-PARC), where the tests performed on High Resolution Chopper Spectrometer (HRC) [5] show a reduction of two orders of magnitude in the background noise detected for monochromatic beams of energy above 100 meV [6].

The long pulse of the ESS requires different design parameters and also further technical development. The crucial difference between short and long pulse spallation sources is the interaction time of the proton beam with the target: the short pulse requires a fully opaque

chopper only for μs, while in the long pulse this time amount to several ms, which is a substantial fraction of the periodicity of the source.

Here we describe how the long pulse nature and the low repetition rate (14 Hz) of the ESS affect the layout of T_0 choppers, but we do not cover any aspects of the engineering design of a T_0 chopper and we especially keep the search for appropriate materials and thickness open. Our considerations apply to the different layouts that are used today, with a rotation axis parallel to the main neutron flight direction. We assume that the choppers are symmetric with respect to the rotation axis, i.e. they close the neutron beam twice during a full revolution.

2. Timing and positioning

We describe in figure 1 the absorption of a T_0 chopper as a function of time with respect to the pulse structure at the ESS, assuming that the chopper is placed at a distance L_{ST_0} from the moderator surface. First, the T_0 chopper has to confirm that the neutron beam is fully closed when high-energy particles are produced. We assume that this time range is given by the ESS neutron pulse length of τ_s =2.86 ms plus an additional arbitrary time after the pulse τ_{ag}, referred to as after glow, therefore having $T_0 = \tau_s + \tau_{ag}$. Furthermore the chopper reduces

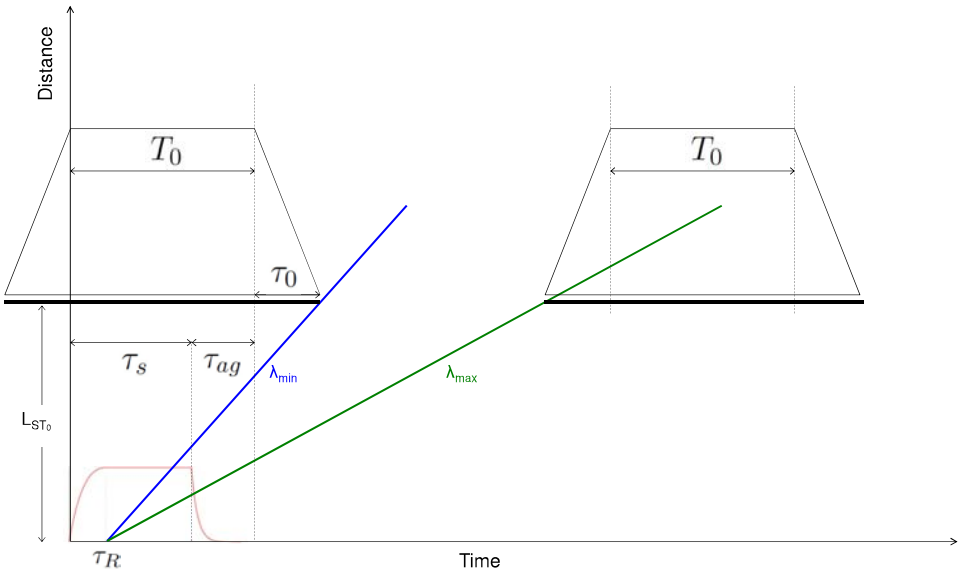

Figure 1. Schematic representation of the T_0 chopper time operation within a tof-diagram snapshot taken from the moderator to the chopper position L_{ST_0}. τ_0 is the opening and closing time, T_0 is the time interval in which the chopper is fully closed. Thus the horizontal black lines represent the chopper closing. The ESS pulse shape as a function of time is also represented (red curve). The blue and the green lines represent neutrons starting from the moderator at the rise time τ_R, with the desired minimal and maximal wavelength $\lambda_{\min}$ and $\lambda_{\max}$ respectively.

the transmission during the additional time necessary for the hammer to be removed from the neutron guide cross section

$$\tau_0 = \frac{2\arctan\frac{w}{2R}}{2\pi f} = \frac{\alpha}{2\pi f}, \tag{1}$$

where f is the chopper rotational frequency, w is the guide width and α the angular width of the neutron guide at the chopper position. The latter depends basically on the radius of the chopper blade and the guide cross section at the position of the chopper The radius R in

equation (1) is taken from the bottom of the neutron window to the axle of the chopper. The width of the chopper hammer has to be larger than the guide width in order to allow complete closing. Therefore the reduced transmission might be relevant for complex guide designs with variable cross section along the neutron flight path.

As a consequence of the long neutron pulse structure, the total angular width of the hammer, which is given by

$$\beta = T_0 \times 2\pi f + \alpha, \tag{2}$$

increases linearly with the frequency, as can be seen from table 1.

As it is seen in figure 1, fixing the position of the T_0 chopper reduces the transmission for any wavelength shorter than

$$\lambda_{\min} = \frac{h}{m_n} \frac{T_0 + \tau_0 - \tau_R}{L_{ST_0}}, \tag{3}$$

which depends on the starting time at the moderator of the neutrons reaching the chopper when it is fully open. When the chopper closes again, it determines the upper limit of the wavelength band, which is transmitted without gaps due to the chopper operation,

$$\lambda_{\max} = \frac{h}{m_n} \frac{(2f)^{-1} - \tau_0 - \tau_R}{L_{ST_0}}, \tag{4}$$

where it is assumed that the chopper closes the beam twice during a full revolution. However, the repetition rate of the T_0 chopper has to fulfill the more relaxed condition to be an integer multiple of the source frequency to block the background from every source pulse. The resolution defining chopper system selects the neutrons released during a portion of the pulse, whose length depends on the required energy resolution. For a chopper system as proposed in [7] the effective extraction time $\tau_R \pm \tau_{\text{eff}}/2$ can be centered at any time during the neutron pulse, independent of the incoming wavelength. In particular it can be moved towards the end of the pulse to maximize $\lambda_{\min}$ giving $\tau_R = \tau_s - \tau_{\text{eff}}/2$. The requested effective pulse length τ_{eff} constraints the position of the T_0 chopper L_{ST_0}, depending on the minimum wavelength required,

$$L_{ST_0}^{\min} = \frac{h}{m_n} \frac{T_0 + \tau_0 - (\tau_s - \tau_{\text{eff}})}{\lambda_{min}}, \tag{5}$$

while the upper limit for the position depends also on the requested bandwidth $\Delta\lambda$:

$$L_{ST_0}^{\max} = \frac{h}{m_n} \frac{(2f)^{-1} - \tau_0 - (\tau_R + \tau_{\text{eff}})}{\lambda_{\min} + \Delta\lambda}. \tag{6}$$

In figure 2 we present potential positions for the T_0 chopper to transmit at least the natural bandwidth ($\Delta\lambda = 1.88$Å) of a 155 m long instrument, which is a typical length for the long ESS instruments, as a function of the lowest wavelength λ_{min} to be transmitted for different chopper frequencies. The panel *b*) represents the neutron guide width assumed for the calculation of

Table 1. Hammer width of the T_0 chopper calculated from equation (2) for different rotational frequencies commensurate with the ESS source frequency. The neutron guide cross section used for the calculation is $8.5 \times 8.5\text{cm}^2$.

Frequency (Hz)	7	14	28	56
β (deg.)	29.57	36.78	51.19	80.02

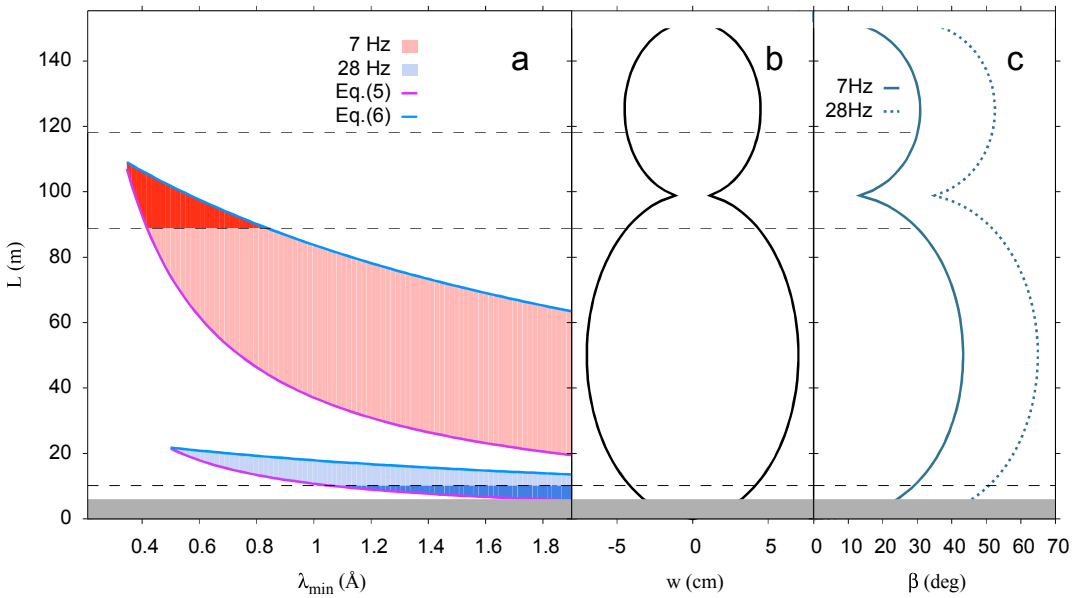

Figure 2. Possible positions for different frequencies of the T_0 chopper if the usable wavelength band starts at $\lambda_{\min}$ and extends over the natural bandwidth (here 1.88 Å for a total instrument length of 155m). The lower limit is defined by equation (5), the upper limit is set by the equation (6). The dark red and dark blue areas represent the regions where the guide width is smaller than 8.5cm. The pulse can be used for an effective pulse length $\tau_{\text{eff}} = 500\mu$s from the end of the pulse for the lower limit and from the beginning of the plateau at the upper limit, respectively. The grey area represents the inaccessible area within the monolith.

the hammer size according to equation (2) that is shown in panel *c*). The double elliptic shape results in a smaller guide width close to the focal points of the ellipses than compared to the width in the ellipse center, which is manifest in the T_0 chopper hammer width shown in panel *c)*. In order to limit the size of the hammer to a reasonable value, we emphasized with darker color the regions where the guide is smaller than 8.5cm, a value that is similar to the one assumed in [6]. Therefore two working conditions for the chopper are identified: it can be operated in the region across the connection of the two ellipses with a rotational frequency of 7 Hz or close to the start of the first ellipse for $f = 28$ Hz. The latter is valid for an instrument using neutrons with $\lambda > 1.1$ Å, which is sufficient for any cold instrument, while any instrument using thermal to epithermal neutrons needs a larger distance to make use of short wavelength neutrons. One could envision a T_0 chopper at this position as the second line-of-sight breaker, once the line-of-sight is first broken by a curved or kinked guide section upstream the chopper position. In this case the T_0 chopper has to block the fast particles emitted from the first impact point, therefore its thickness might be reduced as compared to a chopper in the primary fast particle spectrum.

Making use of acceptance diagrams in figure 3, the transmission properties of the T_0 chopper are analyzed for the two situations, assuming the position of the chopper is close to the upper limit expressed by equation 6:

- When the chopper is placed close to the moderator, as shown in the bottom panel, the lower bandwidth limit is quite high and a higher frequency is needed to keep τ_0 short or alternatively one might employ a set of two counter-rotating T_0 choppers in series [7]. On

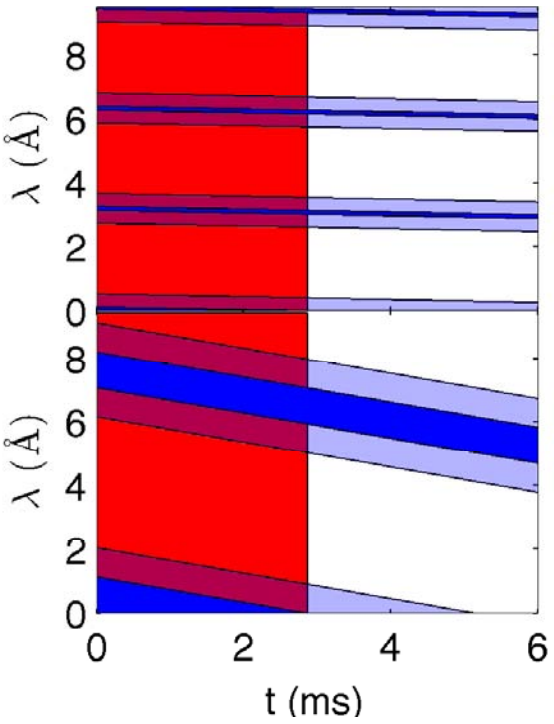

Figure 3. Acceptance diagrams for T_0 choppers spinning at different frequencies (top: 7 Hz, bottom: 28 Hz) and placed at different positions (top: $L_{ST_0} = 90$ m, bottom: $L_{ST_0} = 10$ m). The red areas indicates when the T_0 chopper transmits the neutrons originating from the source pulse, neglecting the after glow. The light blue area indicates regions where the chopper is opening and closing, in the dark blue regions the chopper is completely opaque. The T_0 chopper is fully closed for 2.86 ms. The chopper hammer size is calculated according to table 1. The repetition rate is twice the chopper frequency.

the other hand the transmitted bandwidth is twice wider than the natural bandwidth of an instrument with total length $L_D = 155$ m. An increase of the bandwidth by skipping a pulse can always be realized for this layout.

- Placing the chopper at a larger distance, as shown in the top panel, the lower wavelength limit is reduced for a lower frequency, despite the longer τ_0. The natural bandwidth starting from a lower limit of 0.7 Å is transmitted continuously, while higher order bands are separated by a wavelength gap that depends on the chopper position and speed. The gap in the spectrum is narrower, but the transmitted bandwidth is also reduced. Hence the choice of the T_0 chopper position can limit the opportunities for pulse skipping.

3. Conclusions

We discussed analytic considerations related to the use of T_0 choppers at a long pulse spallation source using ESS parameters. Due to the long pulse structure the T_0 chopper constraints the lower limit of the neutron wavelength spectrum. As the T_0 chopper and the source pulse act also as a band filter, the transmitted band must be at least as wide as the requested instrument band. We discussed in detail possible solutions for chopper frequencies of 7 and 28 Hz. Depending on the neutron wavelength band of interest these options are both acceptable for a cold instrument. For a bi-spectral or a thermal instrument, which uses neutron wavelengths down to 0.7Å the lower frequency requires the chopper to be placed at a large distance from the moderator. Considering the constraints and uncertainties attached to the T_0 chopper layout, additional means to prevent the effect on the instrument performance must be pursuit. Here we mention to avoid the direct line-of-sight sufficiently by the neutron guide layout, possibly for rather long instruments, or having the instrument so compact that the neutrons are always analyzed before the next source pulse begins. Our results show that the T_0 chopper design for a long pulse spallation source is a complex task and has severe implications for the instrument operation, not to mention the complexity of the engineering and radiological design. In particular the wavelength limits and gaps in the spectrum have to be considered to retain a large flexibility in

terms of usable neutron wavelength. We hope that the present contribution can be of use for instrument designers, which need to use T_0 choppers in their instrument.

3.1. Acknowledgments
Authors acknowledge funding by BMBF (Bundesministerium für Bildung und Forschung) through the collaborative project 05E10CJ1.

4. References

[1] Maier-Leibnitz H and Springer T 1963 *Reactor Sci. Technol.* **17** 217.
[2] Stahn J, Panzner T, Filges U, Marcelot C and Böni P 2011 *Nucl. Instr. and Meth. in Phys. Res.* A **634** S12-S16
[3] Jones T.J.L., Davidson I, Boland B.C., Bowden Z.A., Taylor A.D., *Proceedings of the 9th Meeting of the International Collaboration on Advanced Neutron Sources, Swiss Institute for Nuclear Research* 1987, p.529 (ISBN3-907998-01-4)
[4] McQueeney R.J. and Robinson R.A. 2003 *Neutron News* **14** 36
[5] Itoh S, Yokoo T, Satoh S, Yano S, Kawana D, Suzuki J and Sato T 2011 *Nucl. Instr. and Meth. in Phys. Res.* A **631** 9097
[6] Itoh S, Ueno K, Ohkubo R, Sagehashi H, Funahashi Y and Yokoo T 2012 *Nucl. Instr. and Meth. in Phys. Res.* A **661** 86-92
[7] Voigt J, Violini N and Brückel T 2014 *Nucl. Instr. and Meth. in Phys. Res.* A **741** 26-32

3.5.3

HFM-EXED - the high field facility for neutron scattering at HZB

Oleksandr Prokhnenko[1], Maciej Bartkowiak[1], Wolf-Dieter Stein[1], Norbert Stuesser[1], Hans-Juergen Bleif[1], Michael Fromme[1], Karel Prokes[1], Peter Smeibidl[1], Mark Bird[2], and Bella Lake[1]

[1]Helmholtz-Zentrum Berlin für Materialien und Energie, Lise-Meitner-Campus, Hahn-Meitner-Platz 1, 14109 Berlin, Germany

[2]National High Magnetic Field Laboratory, Florida State University, Tallahassee, Florida 32310, USA

E-mail: prokhnenko@helmholtz-berlin.de

Abstract.

Helmholtz-Zentrum Berlin is launching a high magnetic field facility for neutron scattering. Its two main components are the High Field Magnet, a 26 T hybrid magnet built specially for neutron scattering applications, and a dedicated Extreme Environment Diffractometer. The magnet is now in the final stage of commissioning and will be installed at the instrument in the near future. The neutron instrument itself has been in operation (without the magnet) for some time as a general purpose time-of-flight diffractometer. As the magnet will be permanently installed on EXED, the instrument capabilities have been expanded to include small angle scattering (Low-Q) and direct time-of-flight Spectroscopy. The elastic modes of operation have already been implemented whereas the inelastic one is under construction. In this paper we give an overview of the HFM-EXED facility with the main emphasis on its neutron scattering part.

1. Introduction

In order to gain a thorough understanding of the properties of modern functional materials, diverse characterization techniques must be employed. Among them is the material response to external perturbations such as temperature, pressure or magnetic field. In this respect, the combination of a microscopic probe such as neutrons and non-ambient sample environment conditions contributes considerably to the understanding of the physics and chemistry of new materials, and their functionality. Even more crucially, neutron scattering serves as one of the tools to unravel the details of fundamental physical phenomena and thus plays a significant role in understanding the laws of nature in general. Very often such investigations are performed under extremely non-ambient conditions. For instance, magnetic fields in the range of 30 T have led to the discovery of unexpected phenomena of fundamental importance, such as the Quantum Hall Effect and the Fractional Quantum Hall Effect [1, 2].

While different characterization techniques (e.g. measurements of static bulk properties, optical spectroscopy, nuclear magnetic resonance and electron spin resonance) benefit from the availability of magnetic fields of the order of tens of teslas, and up to one hundred tesla in pulsed regime, the existing neutron facilities do not have the capacity to access fields of a comparable

magnitude. This is an obvious drawback as the microscopic details of magnetic correlations in time and space can be uncovered only by means of neutron scattering.

The Helmholtz-Zentrum Berlin (HZB) has always stayed in the forefront of the neutron scattering under extreme conditions. It still holds the world record of 17.4 T DC field combined with neutron experiments at its BERII research reactor. Now, an ambitious project of extending this range significantly beyond 26 T is close to completion. The High Field Magnet (HFM) and a dedicated Extreme Environment Diffractometer (EXED) are two counterparts of the new high magnetic field facility for neutron scattering. With HFM-EXED, the HZB ensures its leading position in researching the most topical issues in physics, chemistry, and material science. These include unconventional superconductors, heavy Fermions, quantum and molecular magnets, low-dimensional systems, frustrated and topological systems, multifunctional materials and others. In this contribution we describe briefly the HFM and focus on the neutron-scattering capabilities of the facility.

2. High Field Magnet

The HFM is a "first of its kind" hybrid magnet system that is capable of producing fields above 26 T, making it by far the strongest DC field available for neutron scattering experiments worldwide. It has been built in collaboration with the National High Magnetic Field Laboratory (Tallahassee, Florida). The magnet is designed as a series connected hybrid system. With the aid of resistive insert coils, which are mounted in the room-temperature bore of a superconducting solenoid, fields between 26 and 32 T can be obtained for the cooling power of the resistive coil 4–8 MW [3]. In the initial stage of its operation the HFM will use 4 MW power, producing fields of about 26 T. To operate the hybrid system a complex technical infrastructure is required. It includes a 20 kA power supply for both coils connected in the series, a helium refrigerator for cooling the superconducting coil and a water cooling system for the resistive coil. The commissioning of the magnet, which is now close to completion, shows good results and the achieved B_{max} of about 26.3 T is in perfect agreement with the expectations.

The scattering space of the magnet is rather simple as shown in Fig. 1a. It is a solenoid with 30° conical openings at both ends, envisaged for neutron scattering, and a 50 mm room-temperature bore. The neutrons enter the magnet through one of the cones and their scattering is limited by the angular dimensions of both cones. In other words, only forward and backward scattering directions are accessible. Rotation of the magnet around its vertical axis allows to achieve a scattering angle as high as 2θ=30° (150° in backscattering), however, the vertical acceptance approaches zero for $2\theta \rightarrow 2\theta_{max}$.

In order to perform experiments at low temperatures, a special ^{3}He/^{4}He cryostat which is inserted into one of the magnet cones has been developed and is currently being tested. The cryostat should allow experiments with temperatures down to 0.5 K, with sample cross-section up to ≈13×13 mm^2. The details of the magnet and its sample cryostat are presented in a separate contribution of this meeting.

3. Extreme Environment Diffractometer

In order to compensate for the angular limitations imposed by the magnet, EXED uses a polychromatic (time-of-flight (TOF)) technique. A sketch of the instrument is given in Fig. 1b and details of the instrument design can be found in Refs. [4, 5]. Access to a wide neutron-wavelength band is achieved by means of a multispectral extraction system [6]. This system feeds neutrons from the thermal and cold moderators into the same neutron guide. The supermirror guide itself is essentially straight (100×60 mm^2 cross section) with a kink designed to remove neutrons with $\lambda < 0.7$ Å. The last 7.5 m of the guide are elliptically converging down to 50×30 mm^2, focusing the beam onto the sample located about 75 m from the neutron source. This focusing section is displayed in Fig. 2a. The m-values of the supermirrors vary across the

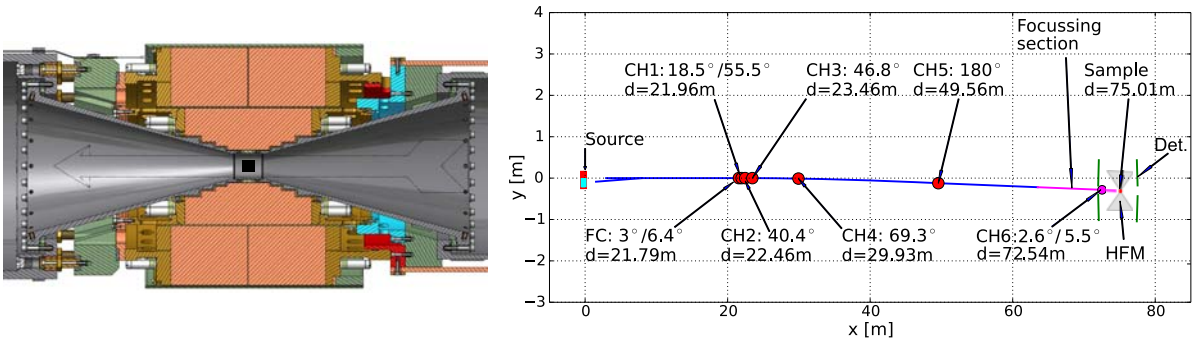

a) b)

Figure 1. a) Scattering geometry of the HFM. The picture shows the magnet cross section with the room temperature bore and the sample (black square), the magnet cones for neutron scattering access and the resistive coils. b) Schematic layout of EXED. The neutron source is composed of thermal (red) and cold (cyan) moderators. The bi-spectral extraction system feeds the thermal and cold neutrons into a single guide (blue solid line); the choppers FC, CH1-CH5 (red dots) constitute the currently existing chopper system. Angular sizes of their windows together with the distances from the source are also given. After the implementation of the inelastic mode (see below in the text), there will be a new focusing guide (magenta solid line) and a monochromatising double-disc chopper CH6 (magenta dot). The detector positions are indicated by green solid lines, and the magnet coils are outlined in gray.

guide reaching $m = 3$ for the extraction and focusing sections, while $m = 1.5$ for the straight parts [4, 5]. The resulting neutron spectrum is illustrated in Fig. 2b. It has a maximum around 3 Å, a cutoff at 0.7 Å and a shoulder below 2 Å. The latter two represent the effect of the kink and the thermal source contribution, respectively.

The instrument chopper system is complex. EXED is equipped with a Fermi chopper (FC), a double disc (CH1) and four single disc (CH2-CH5) choppers (Fig. 1b) [4, 5]. The first two are pulse generating choppers for high or medium/low resolution applications, respectively. They can provide a primary time resolution covering about 3 orders of magnitude (from μs to ms range). The other four choppers ensure there is no frame-overlap and define the wavelength band. Since the effective frequency of the whole chopper system is variable from 5 up to 120 Hz, the instrument operation becomes very flexible, ranging from a broad wavelength band (up to 14.4 Å) down to a short one (0.6 Å).

The entire instrument sample area is built out of nonmagnetic materials. There are four detector banks which are positioned in a way reflecting the geometry of the magnet: two in forward and two in backward scattering direction. Each detector bank is equipped with 48 position sensitive ^{3}He detector tubes with 1/2"-diameter. The effective length of the tubes is 0.9 m with 1% position resolution, resulting in 19200 detector pixels. Each of them produces a dataset of intensity vs. time.

The data acquisition system on EXED is event-recording-based, with precise timing and integration of external trigger sources. The external signals come from the choppers, the beam monitor in front of the sample and (optionally) the sample environment, containing information e.g. about the current sample temperature or magnetic field. The processing of the data is a two-step process. In the first step, a specially developed eGraph software identifies the opening time of the first chopper and, based on that, calculates TOF using the neutron detection time. After that it selects the appropriate neutron events and bins them in TOF and position coordinates and, finally, allows visualizing the data. In the second step, the software package Mantid is used

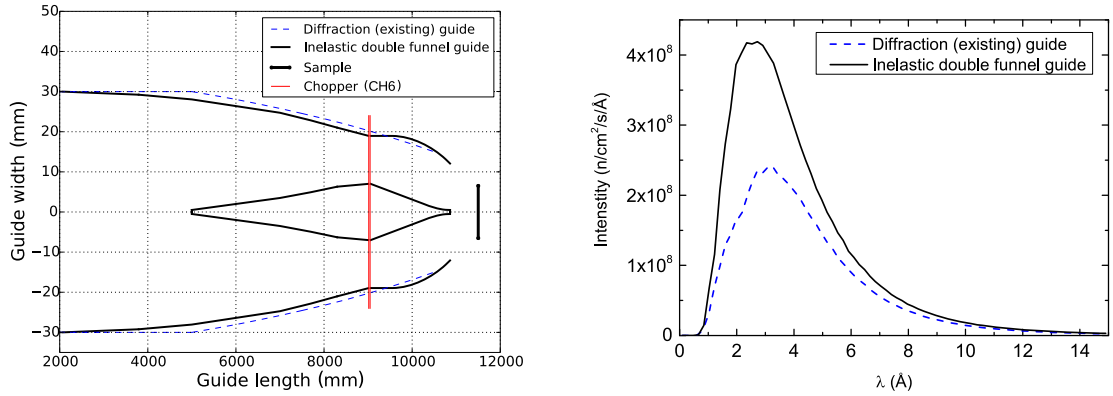

Figure 2. a) Geometries (in the horizontal plane) of the existing diffraction guide and the new double funnel guide. The position and size of the sample are indicated by a vertical black line. The position of the monochromatising CH6 in the inelastic guide is marked by a vertical red line. b) Neutron wavelength spectra at the sample position as simulated using VITESS neutron ray-tracing software package [7]. The plot compares the data obtained using the diffraction guide (dashed blue line) with the one expected for the double funnel guide.

for further data manipulation, reduction and analysis [8].

For a limited period of time EXED was available for internal and external users as a general-purpose TOF diffractometer combined with standard HZB sample environment. With the HFM installation, it will be transformed into a high field facility for neutron scattering. A special feature of this facility will be its multi-purpose operation. Indeed, because of the magnet size and complex operational infrastructure, the HFM cannot be transferred to other instruments like the standard superconducting magnets. As a result, to match the scientific case, the functionality of EXED has been extended. The existing Diffraction mode of operation is complemented by small angle (Low-Q) and Spectroscopy modes.

4. Modes of HFM-EXED operation

In this section we briefly describe the foreseen modes of EXED operation. They include the Diffraction and the Low-Q, both already implemented, as well as the Spectroscopy, which is currently under construction.

4.1. Diffraction

Since EXED had been designed as a diffractometer, the Diffraction is the most natural mode of the HFM-EXED operation. In this regime, HFM-EXED offers a broad range of applications ranging from high resolution to medium and low resolution (high flux) powder and single crystal diffraction in high magnetic fields. Some examples of powder diffraction experiments, performed on EXED during its initial operation, can be found in Refs. [9, 10, 11, 12]. One has to stress the high flexibility of the Diffraction mode as a general feature of a chopper instrument. It allows almost continuous relaxation of resolution (resulting in a corresponding flux gain) and selection of the wavelength band as requested by the experiment. This is extremely important as the HFM does not offer much flexibility in the secondary instrument. The main characteristics of the Diffraction mode are collected in Table 1.

Table 1. The main characteristics of HFM-EXED facility

Parameter	Diffraction	Low-Q	Spectroscopy
Wavelength range	0.7 - 15 Å	4 - 18 Å	1.8 - 7 Å
Angular range	5° - 30°, 150° - 170°	$< 10°$	$< 30°$
Q-range	$0.1 < Q < 12$ Å^{-1}	$Q \gtrsim 0.01$ Å^{-1}	$Q < 1.8$ Å^{-1}
Resolution	$\Delta Q/Q > 10^{-3}$	$\Delta Q/Q < 0.1$	$\Delta E/E \gtrsim 10^{-2}$

From the experimental point of view, the magnet angular constraints are not a serious issue for randomly oriented powders or single crystals isotropic with respect to the magnetic field direction. The TOF method combined with the 15° magnet rotation enables gapless coverage of momentum transfer Q-range from about 0.1 up to 12 Å^{-1}. A proper combination of the field orientation and the choice of wavelength range allows bringing reflections of interest into forward- or backscattering banks. The former are important for the observation of magnetic scattering while the latter are mainly used for the nuclear scattering. For anisotropic systems, however, the magnet angular constraints become an issue as the field orientation along a given crystallographic direction is then the main defining factor for the accessible range in the reciprocal space. It turns out that in the forward scattering banks the accessible scattering range will be mainly perpendicular to the field, while in the backscattering it is along the field (see Fig. 3 and explanations below).

As the restricted geometry of the instrument implies the importance of careful experiment planning, a software tool, EXEQ (EXED (E,q)-range calculator), has been created to assist the users of HFM-EXED in finding the optimal sample orientation [13]. The software uses pre-defined information about the neutron wavelength spectrum, detector geometry and positions and obstacles limiting the scattering angle. The user input defines the sample unit cell, sample orientation, instrument wavelength band and the desired wavelength resolution. The main output of EXEQ are the reciprocal space coverage maps as shown in Fig. 3. They illustrate the extent of the reciprocal space, in the units of sample Miller indices (h, k, l), that can be accessed using the given set of instrument parameters. The intensity reflects the actual instrument spectrum, multiplied by the duty cycle of the chopper system at the current resolution and bandwidth settings.

4.2. Low-Q

In order to enable the investigation of matter in the nanoscale range, such as the vortex state in type-II superconductors as a function of external magnetic fields, a special Low-Q setup had been built ($Q_{min} \approx 10^{-2}$ Å^{-1}). It comprises a pin-hole collimation section with variable apertures which replaces the last 5.5 m of the focusing guide. Two EXED detector banks are positioned at 6 m away from the sample and cover an in-plane angular range of about 2θ = -4.5–1.5° and 2.5–8.5°. A He-filled detector chamber in front of the detectors is used to suppress air scattering. The entire chopper system can run at a low frequency (5-10 Hz) as the wavelength resolution requirements in small angle scattering experiments may be relaxed. The wavelength band is typically centered at $\lambda > 4$ Å. The main characteristics of the Low-Q mode are given in Table 1.

The Low-Q mode was commissioned using a silver behenate powder sample, and flux-line lattice measurements on a Nb single crystal. Both confirm its feasibility and are in a good agreement with published data [14, 15].

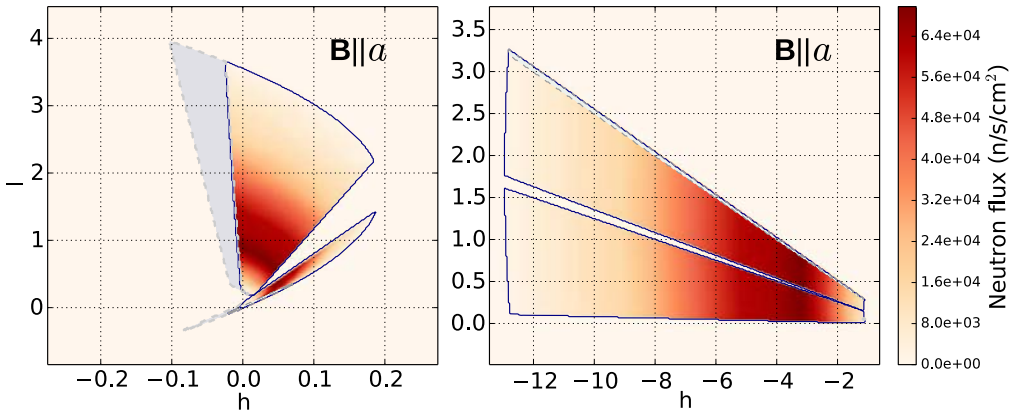

Figure 3. The instrument Q-coverage in Diffraction mode. The $(h0l)$-map is calculated with EXEQ for an "artificial" sample aligned with its a-axis parallel to the field and the c-axis perpendicular to the field in the equatorial plane, with the magnet rotated by 14° with respect to the incident beam. The wavelength band was set to 0.7–7.9 Å and the wavelength resolution to $\delta\lambda/\lambda$=0.1%. The detector panels located in forward (backward) scattering direction are grouped in the left (right) plot. The coverage of each detector panel is delimited by a blue solid contour line. The gray areas with a dashed-line contour in each plot correspond to the part of a detector panel that is shadowed by either the magnet cone, beam stop or guide housing.

4.3. Spectroscopy

The Spectroscopy mode will add a very important component to the scientific portfolio of HFM-EXED: It will allow studying dynamics of materials with magnetic degrees of freedom in high magnetic fields. For the purpose of performing inelastic experiments, EXED will operate as a direct TOF spectrometer. Here, a pulsed monochromatic neutron beam impinges onto the sample and TOF is used to analyze the change in the energy of the scattered neutrons. This is the most efficient way of performing inelastic experiments when taking into account the geometry and constraints of the magnet. Limited sample size inside the HFM and weak inelastic scattering cross sections imply the necessity to optimize for signal strength and low background conditions. The former will be achieved by enhancing the flux at the sample using a novel focusing guide, while the latter will be provided by means of a shielded and evacuated detector chamber. Below we briefly describe four main components of the Spectroscopy mode: i) an evacuated detector chamber for forward scattering with a built-in ii) ^{3}He detector array, and iii) a new focusing guide section that accommodates iv) a monochromatising double disc chopper.

The detector chamber will be connected directly to the forward-scattering cone of the magnet, and rotated together with the magnet. The chamber rotation will be limited to -2°...+15°. The inner side of the chamber will be shielded with Cadmium-absorber, and the outer one will be covered with polyethylene and Boron-absorber. After evacuation, the chamber will provide almost window-free flight path from the sample to the detector. The latter is based on the IN5 (ILL) multi-tube design and being built in collaboration with the ILL (Grenoble). The detector modules with 0.75"-diameter position-sensitive tubes will cover the entire available 30° angle in- and out-of-plane at 4.5 m away from the sample.

A distinct feature of the design of inelastic mode is the rather slow (120-240 Hz) monochromatising chopper (CH6 in Fig 1b) supported by conventional ceramic ball bearings and positioned relatively far from the sample, at 2.45 m. These are the consequences of high

stray magnetic fields close to the sample. As a result of the chopper speed limitations, it became necessary to reduce the size of the chopper window significantly. While the energy resolution is defined by the opening times of the first and last chopper and the corresponding chopper distances to the detector, the neutron flux depends also on the neutron transport system [16]. Therefore, the shape of the guide has been adjusted to the chopper windows and the sample size. For this we use a double funnel guide concept, first implemented at LET spectrometer at ISIS [17, 18]. Contrary to the LET design, however, the EXED guide does not expand after the chopper position, but is even further compressed because of the sample size limitations. As a result, the m values for the new guide reach 4.5. The new guide is visualized in Fig. 2a. In comparison with the existing diffraction guide the new guide provides over 60% integral intensity gain as can be derived from Fig. 2b.

The overall performance of the Spectrometer has been simulated using VITESS neutron ray-tracing software package and will be published elsewhere [7, 19]. Some results of the simulations including energy resolution and corresponding neutron flux for 5 Å wavelength (incident energy 3.3 meV) are summarized in Table 2. For comparison, the table comprises the relevant measured data from the ILL, FRM-II and NIST reactor-based disc chopper spectrometers.

After completion, the Spectroscopy mode will enable energy-resolved measurements over a limited Q-range (<1.8 Å^{-1}) with an energy resolution of a few percent and incident energy below 25 meV (Table 1). Planning of inelastic experiments, which is even more crucial than that of the elastic ones, will be covered by the inelastic version of EXEQ. It is being prepared and will be released in a due time.

Table 2. The expected performance of EXED Spectroscopy mode compared to existing neutron TOF spectrometers. The EXED data are simulated for 5 Å wavelength. The remaining data are the resolution and flux of the IN5 (ILL), TOFTOF (FRM-II) and DCS (NIST) spectrometers, measured with the same wavelength. Two different values of flux and energy resolution in case of TOFTOF, DCS and EXED correspond to their low and high resolution modes defined by use of different chopper windows.

Instrument name	Instrument setting	Flux (n/s/cm^2)	Energy resolution (μeV)
EXED	High flux	2.03×10^5	170
	High resolution	1.29×10^4	58
IN5 (ILL) [20]		6.83×10^5	100
TOFTOF (FRM-II) [21]	High flux	1×10^5	102
	High resolution	8×10^3	52
DCS (NIST) [22, 23]	High flux	2.6×10^4	115
	High resolution	6.7×10^3	55

5. Conclusions

HFM-EXED is a unique facility for neutron scattering in high magnetic fields. It will be the only instrument in the world where elastic (Diffraction and Low-Q) and inelastic neutron scattering experiments can be combined with steady-state magnetic fields as high as 26 T. The main characteristics of HFM-EXED operation modes are summarized in Table 1. The facility is open for accepting user proposals. The first experiments will start with the elastic modes and will be complemented by the inelastic one in the near future.

References

[1] K. v. Klitzing, G. Dorda, and M. Pepper, *Phys. Rev. Lett.* **45** (1980) 494
[2] D. C. Tsui, H. L. Stormer, and A. C. Gossard, *Phys. Rev. Lett.* **48** (1982) 1559
[3] P. Smeibidl, A.D. Tennant, H. Ehmler, M. Bird, *J. Low Temp. Phys.* **159** (2010) 402–405
[4] J. Peters, K. Lieutenant, D. Clemens, F. Mezei, *Z. Kristallogr. Suppl.* **23** (2006) 189–194
[5] K. Lieutenant, J. Peters, F. Mezei, *J. Neutron Res.* **14** (2006) 147–165
[6] F. Mezei, M. Russina, Patent Amtl. Aktz. 102 03 591.1 (Germany), and Patent Number US 7030397 B2 (USA)
[7] G. Zsigmond, K. Lieutenant, F. Mezei, *Neutron News* **13** (2002) 11–14; K. Lieutenant, C. Zendler, S. Manoshin, M. Fromme, A. Houben, D. Nekrassov, *J. Neutron Res.* **17** (2014) 45–51; VITESS http://www.helmholtz-berlin.de/vitess
[8] Mantid (2013): http://dx.doi.org/10.5286/SOFTWARE/MANTID
[9] I. O. Troyanchuk, D. Karpinsky, V. Efimov, V. Sikolenko, O. Prokhnenko and M. Bartkowiak, *J. Phys.: Condens. Matter* **26** (2014) 396002
[10] L. Gondek, K. Kozlak, J. Czub, J. Przewoznik, A. Kupczak, W. Sikora, A. Hoser, O. Prokhnenko, N. Tsapatsaris, *Acta Materialia* **81** (2014) 161172
[11] A. K. Bera B. Lake W.-D. Stein and S. Zander, *Phys. Rev.* B **89** (2014) 094402
[12] K. Prokes, J. A. Mydosh, O. Prokhnenko, W.-D. Stein, S. Landsgesell, W. Hermes, R. Feyerherm, and R. Pöttgen, *Phys. Rev.* B **87** (2013) 094421
[13] EXEQ http://www.helmholtz-berlin.de/pubbin/exeq.pl
[14] U. Keiderling, R. Gilles R, and A. Wiedenmann, *J. Appl. Cryst.* **32** (1999) 456–463
[15] A. Pautrat, A. Brulet, Ch. Simon, and P. Mathieu, *Phys. Rev.* B **85** (2012) 184504
[16] R. Lechner, *KEK* **23** (1991) 717–732
[17] R. Bewley, *Nucl. Instr. Meth.* A **492** (2002) 97-104.
[18] R. I. Bewley, J. W. Taylor, S. M. Bennington, *Nucl. Instr. Meth.* A **637** (2011) 128–134
[19] M. Bartkowiak, N. Stuesser, and O. Prokhnenko, *in preparation*
[20] IN5 http://www.ill.eu/instruments-support/instruments-groups/instruments/in5/
[21] T. Unruh, J. Neuhaus, and W. Petry, *Nucl. Instr. Meth.* A **580** (2007) 1414–1422
[22] DCS http://www.ncnr.nist.gov/instruments/dcs/dcs_perf.html
[23] J. R. D. Copley and J. C. Cook, *Chemical Physics* **292** (2003) 477485

3.5.4

The new single-crystal neutron Laue diffractometer in Berlin

G. N. Iles[1] **and S. Schorr**[1,2]

[1] Department Crystallography, Helmholtz-Zentrum Berlin, Hahn-Meitner Platz 1, 14109 Berlin, Germany

[2] Freie Universität Berlin, Institute of Geological Sciences, Malteserstr. 74-100, 12449 Berlin, Germany

Email: gail.iles@helmholtz-berlin.de

Abstract. We have recently completed construction of a thermal neutron Laue diffractometer in the experimental hall of the BER-II reactor at HZB in Berlin. The Fast Acquisition Laue Camera for Neutrons (FALCON) receives a direct stream of neutrons with a low gamma radiation count. Whilst other neutron sources report that guides containing multiple instruments interfere with the intensity and quality of the neutron beam reaching end positions, FALCON will benefit from a beam that does not pass through any objects upstream. A uniquely-designed shutter and beam definer deliver a highly focused neutron beam to the instrument with <1° divergence. The instrument comprises two scintillator plate detectors coupled to four iCCD cameras each. The neutron beam passes through the detector units enabling one detector to be placed in the backscattering position and the second detector in the transmission position. The image-intensified CCDs are capable of obtaining 20-bit digitization Laue images in under ten seconds and variable sample table and detector positions allow a full range of sample environments to be utilised. Simulations using McStas and the HZB in-house software, VITESS, show the expected resolution of our diffractometer. FALCON is currently in the commissioning phase and should be available to users in 2015.

1. Introduction

The neutron instrument suite at the Helmholtz-Zentrum Berlin had never included a Laue diffractometer, however, as of 2014, the Fast Acquisition Laue Camera for Neutrons (FALCON) has completed its construction phase. In this paper we describe the design process and decisions taken to produce the instrument and present some simulations of expected performance. Neutron Laue diffraction is commonly thought of as only being useful for the orientation of single-crystal samples. However, as has been shown by instruments at reactor sources such as VIVALDI [1], LADI [2] and KOALA [3] and at pulsed sources such as SXD [4] and SENJU [5], a wealth of science has been performed using this method.

Using the method of Laue diffraction a measurement of a large area of reciprocal space can be captured in a single image. The resulting Bragg reflections can be analysed to generate information about the structure of a sample through a phase change, for example, or to show additional reflections arising from the magnetic lattice. In particular, the studies of protein crystallography [6, 7] benefit greatly from analysis of Laue diffraction data, whilst the flux and intensity requirements for high-pressure studies using restricted-view high-pressure cells also benefit from the Laue method [8, 9].

The 'white' beam necessary for the Laue technique allows samples of a very small size (relative to those normally required for neutron scattering measurements) to be measured whereby crystals typically 1mm^3 in size are sufficient for high-quality data to be obtained.

2. Instrument Concept

The FALCON project was to be realized within three years and using a budget of just 300,000€. This small budget immediately affected the choice of detectors – arguably the most critical component of the instrument – and therefore the option of ^{3}He detectors was disregarded. Photonic Science had already supplied reliable and effective scintillator detectors to ILL for instruments such as Orient Express[10] and CYCLOPS [11]. Similar instruments for the orienting of crystals are used at other neutron sources, with JOEY [12] being open for user service.

Our intention is to perform hard condensed matter studies using FALCON; for example to investigate structural phase changes of perovskites under high pressure, and so we opted for a thermal beam profile with a peak at ~1.4Å. The Laue instrument was then planned for construction in the experimental hall of the BER-II reactor where instruments have a typically short beam path to the reactor core. Many of the high-pressure cells in use within the neutron scattering community have a narrow entrance hole for neutrons to enter, such as the Paris-Edinburgh cell [13], and so we wanted to ensure as high a flux as possible.

As a Laue instrument uses a polychromatic beam, such instruments must be built at the end of a beamtube or guide. Typically, such an instrument does not have sole use of such a beamtube, and as has been shown by measurements on the H22 guide at the ILL [14] monochromators from other instruments severely hamper the quality of the beam profile arriving at the end position. It is possible to use the neutron beam that has passed through a monochromator further upstream, however, this guarantees that the wavelength associated with that monochromator will be excluded from the polychromatic beam profile and would result in the loss of sets of Bragg reflections from the Laue pattern.

At HZB the instrument suite is being down-sized due to the imminent closure of the reactor in 2019. Therefore we were able to choose a beamtube for FALCON formerly housing two monochromator-style instruments which have been subsequently decommissioned. With both monochromators out of the beam, and an exit port just 8m from the reactor core, we have a high-flux neutron beam at the sample.

2.1. Beam profile

In order to provide a suitable beam profile for high-pressure studies, we utilised the pinhole principle. An 8m beamtube with height 90mm has a divergence of 0.64°, however, this must be collimated to provide a safe working beam of approximately 10mm in diameter. In order to match the divergence of the beamtube, we designed a well-shielded beam collimator that would simultaneously deliver a pinhole beam to the sample, and provide a shutter mechanism for opening and closing the beam. Further details of the mechanism have been reported elsewhere [15].

The exit hole using our in-house designed collimator is 16mm in diameter. This beam then travels through 5cm of air and through the centre of the first detector, impacting the sample approximately 50cm downstream diverging slightly due to the 20mm exit hole in the detector box. Simulations with VITESS [16] show a beam profile at the sample consistent with a thermal profile and is illustrated in figure 1.

Such a beam profile at the sample ensures that we can maintain our expected resolution of ~200μm whilst operating in 2x2 binning mode. This mode is most often used as it provides a good signal-noise ratio.

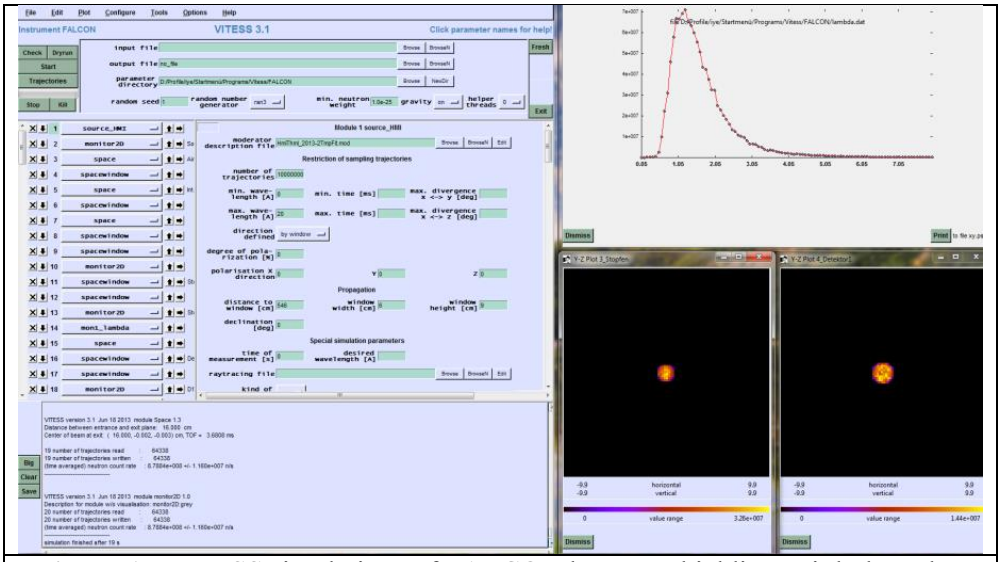

Figure 1. VITESS simulations of FALCON beam at shielding exit hole and at backscattering detector exit hole.

2.2. Detectors

Essential for the Laue technique is to have a detector to collect backscattering reflections as these are the strongest and most easily treatable reflections. Neutron image plate detectors such as VIVALDI and KOALA consist of almost 360° detector plates along the vertical axis whilst SXD and SENJU have a configuration of several small detectors placed in a spherical arrangement around the sample to capture as many reflections as possible. With our limited budget we opted for two scintillator plates; one to be fixed in the backscattering position, with another free to rotate about ω. In this way, a full map of reciprocal space can be generated with a few 'snapshots' at pre-determined positions around the sample.

Photonic Science [17] provided us with two detector boxes containing a 40x40cm scintillator plate of 6Li:ZnS:Ag coupled to four image-intensified CCDs (iCCD) each. In order to preserve the integrated chips within the cameras, each camera is placed at 90° with respect to the incoming beam. A mirror then placed at 45° to the beam direction, directs the created photons towards the image intensifier in order to protect the cameras from further degradation.

In keeping with the direct geometry of the instrument, the detector boxes designed by Photonic Science incorporate a steel tube which passes through the exact centre of the box to transport the neutrons directly to the sample. This then appears as a black hole in the centre of a FALCON image [18].

3. KOALA Data

During beamtime at the OPAL reactor operated by ANSTO, we measured Cu_2ZnSnS_4 samples [19] to investigate the site defects in these solar cell absorber materials [20]. Data from Laue diffractometer image plates has a resolution of ~100μm showing clear and distinguishable Bragg reflections, as shown in figure 2.

Whilst the scientific findings of this experiment are reported elsewhere [21], this data serves as a reference dataset for the commissioning of FALCON. The exact same samples measured using KOALA will be measured on FALCON, and in this manner we can calibrate our detectors and geometry algorithms correctly.

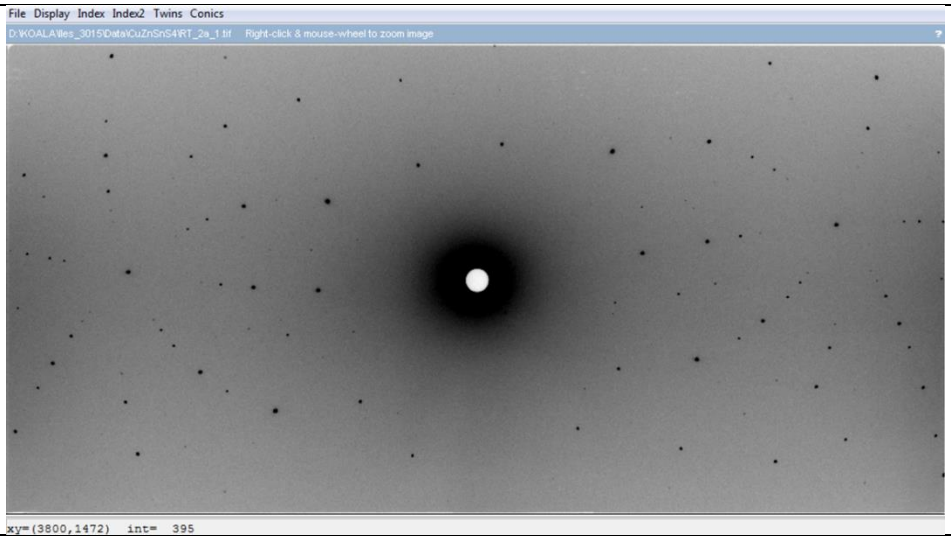

Figure 2. Example of Laue data obtained using KOALA (ANSTO) on a single-crystal sample of Cu_2ZnSnS_4.

4. Simulation results

The European Spallation Source (ESS) [22] is currently in the design phase and therefore extensive use is made of the simulation programme McStas, a monte carlo ray-tracing software for simulating neutron beams and scattering of particles through interactions [23]. One of the particularly useful features of this programme is a library of software for simulating existing neutron instruments at neutron sources around the world. With a minimum of experience a researcher can use McStas to simulate the results of a neutron scattering event with a sample of their choice on any instrument. To this end we have generated the code for simulating FALCON in McStas.

4.1 McStas simulations

Incorporating all the elements of the instrument, including the correct dimensions of the upstream elements e.g. shutter, collimators, FALCON has been simulated using McStas as illustrated in figure 3.

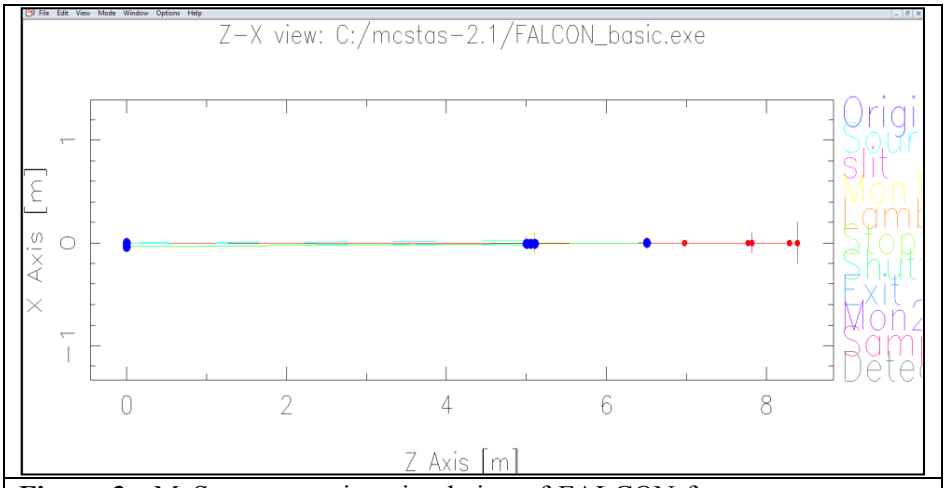

Figure 3. McStas ray-tracing simulation of FALCON from reactor core to sample.

In order to perform a simulation using the FALCON code, one must first download the McStas software, and then select FALCON within the drop-down menu as shown in figure 4.

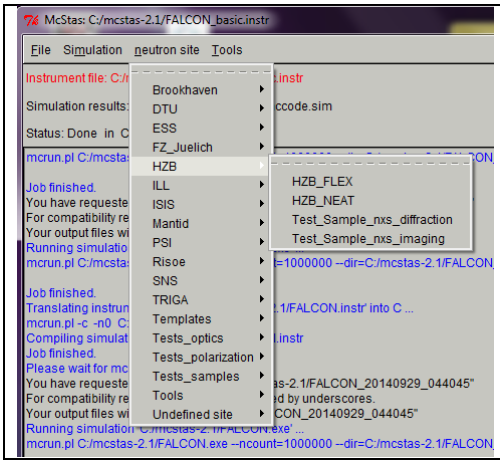

Figure 4. McStas drop-down menu showing location of FALCON simulation code.

5. Conclusion

Construction of FALCON is complete and in 2015 this Laue diffractometer will enter the commissioning phase. Simulations of the beam profile have been performed using VITESS whilst the instrument code for simulating neutron scattering from a given sample has been generated in McStas. FALCON will enter user service once commissioning is complete.

References

[1] Wilkinson C, Cowan JA, Myles DAA, Cipriani F and McIntyre GJ 2002 *Neutron News* **13** 37-41

[2] Blakeley MP, Teixeira SCM, Petit-Haertlein I, Hazemann I, Mitschler A, Härtlein M, Howard E and Podjarny AD 2010 *Acta Cryst. D* **66** 1198-1205

[3] Edwards AJ 2011 *Aus. J. Chem*. **64**(7) 869-872
Piltz R *Acta Cryst.* 2011 **A67** C155

[4] Keen DA, Gutmann MJ and Wilson CC 2006 *J. Appl. Cryst·* **39** 714-722

[5] Tamura I, Oikawa K, Kawasaki T, Ohhara T, Kaneko K, Kiyanagi R, Kimura H, Takahashi M, Kiyotani T, Arai M, Noda Y and Ohshima K 2012 *J. Phys.: Conf. Ser.* **340** 012040

[6] Fisher SJ, Blakeley MP, Cianci M, McSweeney S and Helliwell JR 2012 *Acta Cryst. D* **68** 800-809

[7] Blakeley MP and Fisher SJ 2013 *Encyclopedia of Biophysics* 1353-1361

[8] McIntyre GJ, Mélési L, Guthrie M, Tulk CA, Xu J and Parise JB 2005 *J. Phys.: Condens. Matter* **17** S3017

[9] Bull CL, Johnson MW, Hamidov H, Komatsu K, Guthrie M, Gutmann MJ, Loveday JS and Nelmes RJ 2014 *J. Appl. Cryst.* **47** 974–983

[10] Ouladdiaf B, Archer J, McIntyre GJ, Hewat AW, Brau D and York S 2006 *Physica B* **385–386** 1052–1054

[11] Ouladdiaf B, Archer J, Allibon JR, Decarpenterie P, Lemée-Cailleau M-H, Rodríguez-Carvajal J, Hewat AW, York S, Brau D and McIntyre GJ 2011 *J. Appl. Cryst.* **44** 392-397

[12] http://www.ansto.gov.au/ResearchHub/Bragg/Facilities/Instruments/Joey/index.htm

[13] Besson JM, Nelmes RJ, Hamel G, Loveday J.S, Weill G and Hull S 1992 *Physica B* **180–181** 907

[14] https://www.ill.eu/html/instruments-support/computing-for-science/virtual-instexp/virtual-instruments-and-experiments/ill-instrument-simulations/ill7curvedguide/
[15] Iles GN and Schorr S 2014 *Neutron News* **25** 2
[16] Lieutenant K, Zsigmond G, Manoshin S, Fromme M, Bordallo HN, Champion JDM, Peters J and Mezei F 2004 *(SPIE proceedings series ; 5536)* **ISBN 0-8194-5474-5** 134-145
[17] http://www.photonic-science.com/
[18] Iles GN and Schorr S 2015 *Physical Procedia*
[19] Iles GN, Gurieva G, Levcenco S and Schorr S 2013 *ANSTO Experimental report* Extension of the phase diagram of kesterite materials for solar cell technology **3015**
[20] Schorr S 2011 *Sol En Mat Sol Cells* **95** 1482-1488
[21] Iles GN, Schorr S, Pilz R, Reehuis M (to be published)
[22] http://europeanspallationsource.se/
[23] Willendrup P, Filges U, Keller L, Farhi E and Lefmann K 2006 *Physica B* **386** 1032

3.5.5

Construction of the energy-resolved neutron imaging system "RADEN" in J-PARC MLF

T. Shinohara[1], T. Kai[1], K. Oikawa[1], M. Segawa[1], M. Harada[1], T. Nakatani[1], M. Ooi[1], M. Arai[1], H. Sato[2], T. Kamiyama[2], H. Yokota[3], T. Sera[4], K. Mochiki[5], Y. Kiyanagi[6]

[1]J-PARC Center, Japan Atomic Energy Agency, Tokai 319-1195, Japan
[2]Faculty of Engineering, Hokkaido University, Sapporo 060-8628, Japan
[3]Center for Advanced Photonics, RIKEN, Wako 351-0198, Japan
[4]Faculty of Engineering, Kyushu University, Fukuoka 819-0395, Japan
[5]Faculty of Engineering, Tokyo City University, Tokyo 319-1195, Japan
[6]Graduate School of Engineering, Nagoya University, Nagoya 464-8603, Japan

E-mail: takenao.shinohara@j-parc.jp

Abstract. Construction of the Energy-Resolved Neutron Imaging System (RADEN) has started in 2012 at the beam line of BL22 in the Materials & Life Science Experimental Facility (MLF) of J-PARC. This is the first instrument dedicated to the pulsed neutron imaging experiments in the world. The primary purpose of this instrument is to perform the energy-resolved neutron imaging experiments effectively utilizing the pulsed neutron nature. Therefore, this instrument is designed to cover a broad energy range at the same time: not only cold neutrons up to 8.8 Å with a good wavelength resolution of 0.20% but also high energy neutrons with the energy of several tens keV. In addition, this instrument is intended to perform a state-of-the-art neutron radiography and tomography experiments in Japan. Hence, the maximum beam size of 300 mm square, and the highest L/D value of 7500 are provided.

1. Introduction

Neutron imaging is a very fundamental technique to visualize the internal structure of objects, and is regarded as an indispensable non-destructive inspection especially in the field of industry. Recently, a new neutron imaging technique, which utilizes neutron energy dependent transmission, called "energy-resolved neutron imaging", becomes a very attractive technique because of its capability not only to visualize but also to quantify the physical or chemical quantities with spatial resolution [1]. Therefore, this technique is expected to provide a chance for the neutron imaging to develop into a new scientific method, which is not a simple inspection of intra-structure of objects but a characterization of many properties inside objects with spatial resolution. Owing to recent developments, several imaging techniques regarding it are performed, i.e. Bragg edge imaging for crystallographic information [2], resonance absorption imaging for elemental composition and thermal information [3], and polarized neutron imaging for magnetic field information [4]. Conducting these imaging experiments, usage of the pulsed neutron beam brings several advantages due to its pulsed nature compared to those using monochromatic neutron beam from continuous sources. For example, at first, it is possible to measure the energy dependent phenomena efficiently by means of Time-of-Flight (TOF) method. Second, energy or wavelength resolution is intrinsically fine in the case of using

the short-pulsed neutron source, which is better than 1 %. Then, wide energy range neutrons from epithermal to cold neutrons are available simultaneously. So far, the low intensity of pulsed neutron beam from the low-power spallation neutron sources has set a limitation to the application of this imaging technique. However the construction of MW-class spallation neutron sources at J-PARC and SNS makes a change of such situation.

In Japan, technical developments of the pulsed neutron imaging have been intensively done using small accelerator driven neutron source at Hokkaido University (HUNS) and the pulsed neutron facility (Materials and Life science experimental Facility, MLF) in J-PARC. And also, in the Japanese pulsed neutron imaging project, a new beam line dedicated to the pulsed neutron imaging, named "RADEN" has proposed so as to make the pulsed neutron imaging technique operational phase, and its construction has started from 2012 at the beam line of BL22 of MLF. The main purpose of this instrument is, of course, fully performing the energy-resolved neutron imaging experiments by effectively utilizing the pulsed neutron's nature as a pioneering facility for the pulsed neutron imaging. In addition, it also has a role for the state-of-the-art neutron imaging instrument in Japan with sufficient neutron flux, selectable L/D values up to several thousands, and monochromatic neutron imaging capability, which has a comparable performance with those at world's several tens MW-class reactor sources. In this paper, we report the final design of the instrument and discuss the expected performance.

2. Beam line design

At first, we mention the requirements for the instrument, which has been discussed as the initial stage of the instrument design in our previous report [5, 6]. The necessary performance for each energy-resolved neutron imaging technique was considered in terms of the wavelength resolution and the wavelength/energy coverage. On the other hand, concerning the conventional neutron radiography and tomography experiments, another aspect, such as available beam flux, size and L/D value, which is directly coupled with the accessible spatial resolution, becomes important. Then, the minimum wavelength resolution of 0.2% and high energy neutrons with the energy of up to several tens of keV were settled based on the requirements from Bragg-edge and resonance absorption imaging techniques. In addition, because availability of longer wavelength neutrons is preferable to conduct experiments using neutron's optical properties, wavelength range was expanded into around 9 Å within the first frame. These requirements is achieved by viewing a decoupled moderator which possesses balanced performance of the pulse width and the neutron intensity as well among three types of hydrogen moderators of J-PARC MLF, and by setting two sample positions. At the near sample position located at the distance of 18 m from the source, a high time averaged beam flux less than 9.8 x 10^7 n/sec/cm^2 and coverage of a broad wavelength range are expected, while a large beam size up to 300 mm square and fine wavelength resolution of 0.2% are done at the far sample position of 23 m.

The resulting beam line layout of RADEN is shown in Figure 1 and the expected parameters are summarized in Table 1.

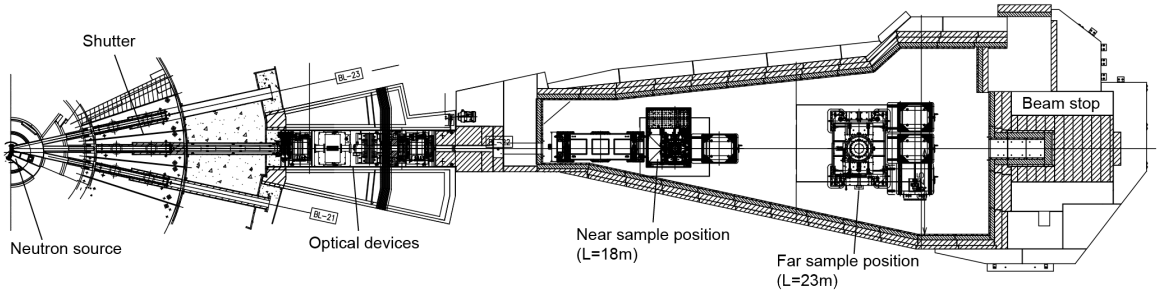

Figure 1. Layout of RADEN instrument.

Table 1. Basic parameters of RADEN.

Beam line	BL22	
Moderator type	Supercritical hydrogen decoupled moderator	
Sample position	18 m	23 m
Beam Size	< 221 x 221 mm^2	< 300 x 300 mm^2
L/D ratio	180 ~ 5000	230 ~ 7500
Wavelength resolution (cold)	0.26%	0.20%
Energy resolution (epithermal)	1.6%	1.2%
Longest wavelength (first frame)	8.8 Å	6.9 Å

2.1 Shielding design

At first, the shielding is one of the essential components of this instrument. To conduct neutron imaging experiments, handling large objects and arranging the experimental setup freely are quite important. Therefore, designing the shielding as thin as possible is quite important to secure a wide experimental area. However, as RADEN utilizes most biggest beam and sample size in the MLF and high-energy neutrons, massive shield is necessary to attenuate radiation outside of the shielding efficiently. To design and optimize the shielding structure, we have performed dose rate calculation and evaluated its performance using PHITS code [7] (Figure 2). As the results, the shielding wall was decided to consist of 4 layers, i.e., boron included mortar, polyethylene, steel and concrete from the inside. Moreover, because the neutron imaging detectors are put in the direct beam line, scattered neutrons and radiated gamma ray from the beam stop directly irradiate detectors from the rear and cause a huge background. To suppress such background, the beam stop was placed as far as possible from the detector position. Two heavy doors, which are driven electrically, are used to intercept the radiation at the gateway, while most of the instruments adopt a labyrinth structure with a light door without any shielding performance. This is because accessibility to the experimental area takes precedence for RADEN.

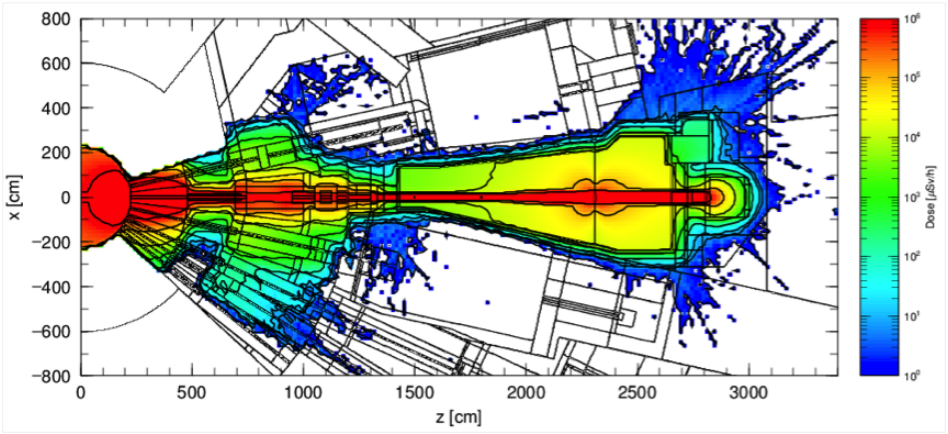

Figure 2. Typical calculation result of the dose rate using PHITS code. The sum of neutron and gamma ray doses is shown.

2.2 Optical devices

In the upstream of the experimental area, several optical devices are installed as shown in Figure 3. The optical devices of RADEN are divided into two groups. One is beam collimation and shaping device group and another is energy selection device one. The former group is composed of a shutter, rotary collimators and slits. In addition, this beam line is equipped with a light shutter, named blocker,

to suppress undesired sample activation. To make the beam size at the sample position enlarged, an aperture is needed to be placed as close as possible to the source. Then, the existing heavy shutter was replaced into new one with three collimator insertion devices, whose hole sizes are 100 mm x 100 mm, 50 mm- ϕ and 26 mm-ϕ. Using these collimators, beam size ranging from 100 x 100 mm^2 to 300 x 300 mm^2 will be achieved at the far sample position (23 m away from the neutron source), and the smallest L/D value producing highest neutron flux is provided. Inside the preposition shield, two rotary collimators with 4 aperture slots are installed (Figure 4 (a)). The front rotary collimator is used to make higher L/D value for high spatial resolution experiments by small apertures, and the rear one is to limit the beam size as adequate to the object size. Because RADEN uses high energy neutrons with the energy of over keV, these collimators are made of thick steel and polyethylene and have an artifice to reduce neutron reflection at the inner wall of them.

The latter optics group is composed of filters, a double disk low-speed chopper and a T0 chopper (Figure 4 (b), (c)). Five kinds of filters, that is, Bi (25 mm, 25mm, 50 mm), Pb (25 mm, 50 mm), Cd (1 mm), acrylic resin (5 mm), and borosilicate glass (2 mm), are placed in front of the first rotary collimator. Bi and Pb filters are used for gamma ray attenuation especially in the case of resonance absorption imaging experiment, at which the T0 chopper is stopped to access high energy range. Cd filter is also used in resonance absorption experiments to cut off thermal and cold neutrons. The acrylic resin and the borosilicate glass are for neutron intensity attenuation. The double disk chopper, which can be operated in 25 Hz and 12.5 Hz, defines the available wavelength range in one frame. Changing the opening angle by adjusting the delay of each disk properly enable us to suit the bandwidth at different sample position. The quasi-monochromatic neutron beam with the wavelength resolution of around 10% can be served when the opening angle is adjusted to smallest value. The T0 chopper is installed to eliminate the prompt neutron pulse and flush gamma ray produced at the instance of neutron generation. This chopper has one heavy hammer made of Inconel alloy, which rotates synchronized with the accelerator, and the hammer only comes in the beam at T = 0. By means of the T0 chopper, the neutron background caused by the fast neutrons decreases effectively.

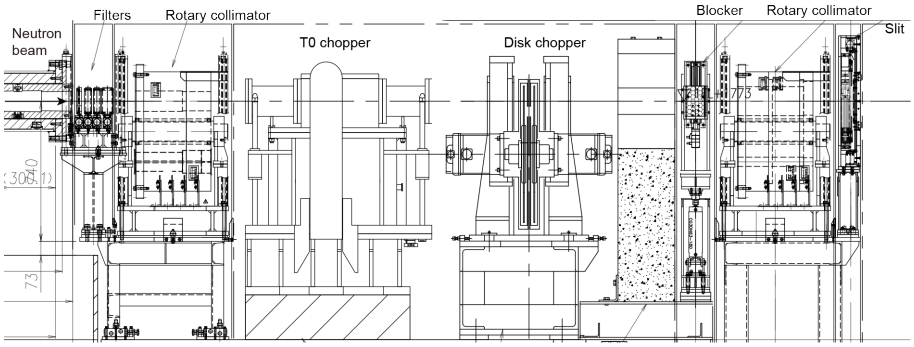

Figure 3. Arrangement of optical devices for beam shaping inside the preposition shield.

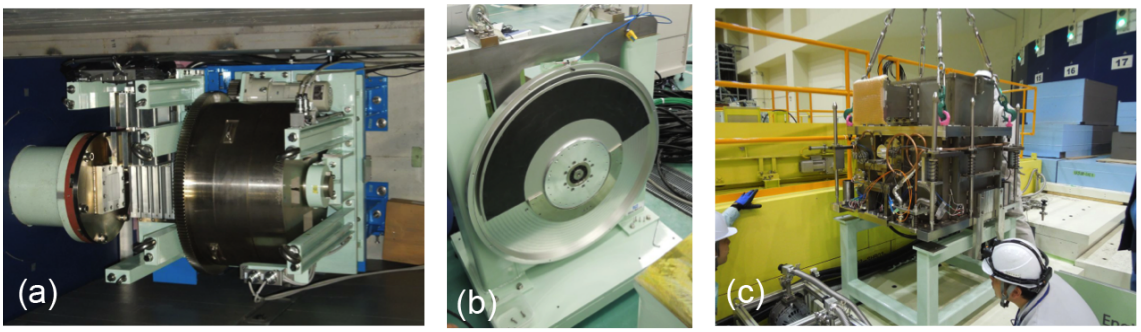

Figure 4. Photographs of some optical devices. (a) Rotary collimator, (b) Disk chopper, and (c) T0 chopper.

2.3 Sample environment

Inside the measurement area, there installed some stages for sample mounting and detector. And also, exchangers for optional equipment are settled (Figure 5). Three sample stages are prepared for mounting and positioning the sample, and their topmost movable axis are rotational considering the computerized tomography experiment. Basic specifications of each sample stages are shown in table 2. They are remotely controlled from outside of the shielding using the device control software. The top table of each stage conforms to the MLF standard for sample environment so as to mount various devices such as a cryostat, an electromagnet, a furnace, and so on. Especially the large sample stage placed at the distance of 23 m from the neutron source is designed to equip with mechanical test devices developed at the engineering materials diffractometer TAKUMI [8] for Bragg edge imaging experiments.

The medium sample stage sits on the optical bench located at the near sample position. When the medium sample stage is removed, optical tables for the polarized neutron experiment or other experiments using special devices can be slide into the beam position by an automated exchanger. The small rotation stage for CT measurements is available by putting on the top of those sample stages. Flight tubes, which are filled with He gas and inner walls are covered with neutron absorber, are placed in the gap of beam line to suppress the possible neutron beam attenuation due to the air scattering. In front of the near sample position, there is a lift to exchange the flight tube and the equipment for the polarization analysis. With this lift, we can easily switch the setup from the unpolarized neutron beam to the polarized one.

Optionally RADEN is equipped with the apparatuses for neutron diffraction measurements composed of ^{3}He position sensitive detector tubes and a soller collimator complementary to the Bragg edge imaging and for gamma ray detector to support precise analysis of the resonance absorption.

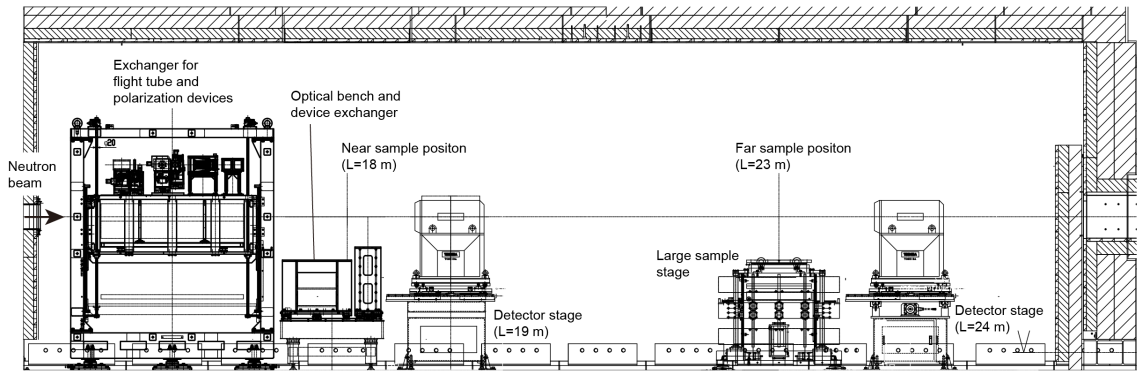

Figure 5. Arrangement of stages and exchangers in the measurement area.

Table 2. Specifications of sample stages.

Stage	Position	Movable axis			Max. load	Table size
		θ	X, Y, Z	R_X, R_Y		
Large	L=23m	±173°	±300 mm	-	1.0 ton	700 mm-ϕ / 750 mm x 750 mm
Medium	L=18m	±175°	±100 mm	±5 °	600 kg	300 mm-ϕ / 700 mm-ϕ
Small	Portable	360°	-	±5 °	10 kg	150 mm-ϕ

2.4 Detectors

To conduct the energy resolved neutron imaging using pulsed neutrons, precise TOF information is essential and the neutron detectors required to have fine time resolution. The counting type imaging

detector is promising owing to their sub micro second time resolution while their spatial resolution is relatively course. Then, we selected three candidates, that is, μNID detector [9], GEM detector [10] and pixel detector composed of pieces of small Li glass scintillators and a multi-anode photo multiplier. On the other hand, regarding the conventional neutron imaging fine spatial resolution is desirable. Hence, a cooled CCD camera system with a ^{6}LiF/ZnS scintillator screen and a CMOS camera combined with neutron image intensifier are prepared together with the counting type detectors.

3. Conclusion

We have been constructing the energy-resolved neutron imaging system RADEN from 2012 at the beam line of BL22 in J-PARC MLF. Because this is designed to utilize the good nature of the short-pulsed neutron beam, every energy-resolved neutron imaging experiment becomes possible with fine energy resolution. And also it has an important role as the state-of-the-art neutron radiography and tomography instrument in Japan. It was designed to satisfy the requirements from both of these imaging techniques and several devices have been installed. In Nov. 2014, the first neutron beam was delivered to this beam line and the commissioning study started after that. We are going to start user programs from 2015.

Acknowledgement

This work was partially supported by Grant-in-Aid for Scientific Research (S) 23226018 from Japan Society for the Promotion of Science.

References

[1] Kiyanagi Y, Sato H, Kamiyama T, Shinohara T, 2012 *J. Phys.: Conf. Ser.* **340** 012010.
[2] Sato H, Takada O, Iwase K, Kamiyama T, Kiyanagi Y, 2010 *J. Phys.: Conf. Ser.* **251** 012070.
[3] Kaneko K, Kamiyama T, Kiyanagi Y, Sakuma T, Ikeda S, 1999 *J. Phys. Chem. Solids* **60** 1499.
[4] Shinohara T, Sakai K, Ohi M, Kai T, Harada M, Oikawa K, Maekawa F, Suzuki J, Oku T, Takata S, Aizawa K, Arai M, Kiyanagi Y, 2011 *Nucl. Inst. Meth. Phys. Res.* **A 651** 121.
[5] Kiyanagi Y, Kamiyama T, Sato H, Shinohara T, Kai T, Aizawa K, Arai M, Harada M, Sakai K, Oikawa K, Ohi M, Maekawa F, Sakai T, Matsubayashi M, Segawa M, Kureta M, 2011 *Nucl. Inst. Meth. Phys. Res.* **A 651** 16.
[6] Kiyanagi Y, Shinohara T, Kai T, Kamiyama T, Sato H, Kino K, Aizawa K, Arai M, Harada M, Sakai K, Oikawa K, Ooi M, Maekawa F, Iikura H, Sakai T, Matsubayashi M, Segawa M, Kureta M, 2013 *Physics Proc.* **43** 92.
[7] Sato T, Niita K, Matsuda N, Hashimoto S, Iwamoto Y, Noda S, Ogawa T, Iwase H, Nakashima H, Fukahori T, Okumura K, Kai T, Chiba S, Furuta T, Sihver L, 2013 *J. Nucl. Sci. Technol.* **50** 913.
[8] Harjo S, Moriai A, Torii S, Suzuki H, Suzuya K, Morii Y, Arai M, Tomota Y, Akita K, Akiniwa Y 2006 *Mater. Sci. Forum* **524-525** 199.
[9] Parker J D, Hattori K, Fujioka H, Harada M, Iwaki S, Kabuki S, Kishimoto Y, Kubo H, Kurosawa S, Miuchi K, Nagae T, Nishimura H, Oku T, Sawano T, Shinohara T, Suzuki J, Takada A, Tanimori T, Ueno K, 2013 *Nucl. Inst. Meth. Phys. Res.* **A 697** 23.
[10] Shoji M, Uno S, Uchida T, Murakami T, Sekimoto M, Koike T, Nakano E, Yamamoto K, Hoshi Y, Nagashima F, 2012 *J. Inst.* **7** C05003.

3.5.6

Instrument Developments and Neutron Brillouin Scattering Experiments on HRC

Shinichi Itoh[1], Tetsuya Yokoo[1], Takatsugu Masuda[2], Hideki Yoshizawa[2], Minoru Soda[2], Yoichi Ikeda[2], Soshi Ibuka[1], Toshio Asami[2], Ryosuke Sugiura[2], Daichi Kawana[2], Tomoko Shinozaki[2], and Yoshiaki Ihata[3]

[1]Neutron Science Division, Institute of Materials Structure Science, High Energy Accelerator Research Organization, Tsukuba, Ibaraki 305-0801, Japan
[2]Neutron Science Laboratory, The Institute for Solid State Physics, The University of Tokyo, Tokai, Ibaraki 319-1106, Japan
[3]Technology Development Section, Materials and Life Science Experimental Facility, J-PARC Center, Tokai, Ibaraki 319-1195, Japan

E-mail: shinichi.itoh@kek.jp

Abstract. To study condensed-matter dynamics over a wide energy-momentum space with high resolutions, the High Resolution Chopper Spectrometer (HRC) was installed at BL12 in MLF/J-PARC. In the previous ICANS meeting, we reported the performance of the HRC after the initial construction. Since then, we made further developments on the instrumentation. In particular, neutron Brillouin scattering (NBS) experiments became feasible by reducing the background noise at low scattering angles.

1. Introduction

The High Resolution Chopper Spectrometer (HRC) was installed at the BL12 beam port in the Materials and Life Science Experimental Facility (MLF), the Japan Proton Accelerator Research Complex (J-PARC), in order to study dynamics in condensed matters with high-resolutions and relatively high-energy neutrons [1, 2, 3]. A schematic layout of the HRC is illustrated in Fig. 1. The HRC faces the decoupled moderator which emits neutrons with sharp pulses. The sample is mounted at $L_1 = 15$ m from the moderator. On the primary flight path from the neutron source to the sample, some devices are mounted to control the incident neutron beam: a supermirror guide tube to increase the neutron flux, a T0 chopper to eliminate background noise originated by the initial burst of high energy neutrons, a Fermi chopper to monochromatize the incident beam and to control the resolution and the neutron flux, and an incident beam collimator system to reduce background noise due to unwanted scattering. An array of position sensitive detectors (PSDs) is located at $L_2 = 4$ m from the sample covering the scattering angles between $\phi = 3^\circ$ and 42° horizontally and $\pm 20^\circ$ vertically for conventional experiments. Another array of PSDs is located at $L_2 = 5.2$ m down to $\phi = 0.5^\circ$ for neutron Brillouin scattering (NBS) experiments. We confirmed that, under limited conditions, the neutron intensity and the energy resolution were in good agreement with the design values [1]. We here describe further instrument developments as well as success in the NBS experiments.

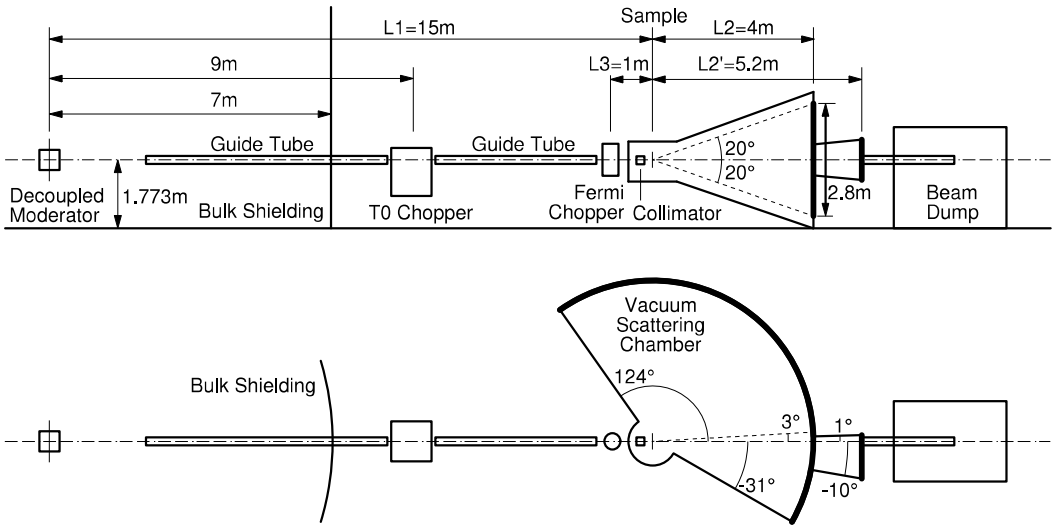

Figure 1. Schematic layout of the HRC, a side view (upper) and a top view (lower). Thick lines indicate PSDs to be mounted.

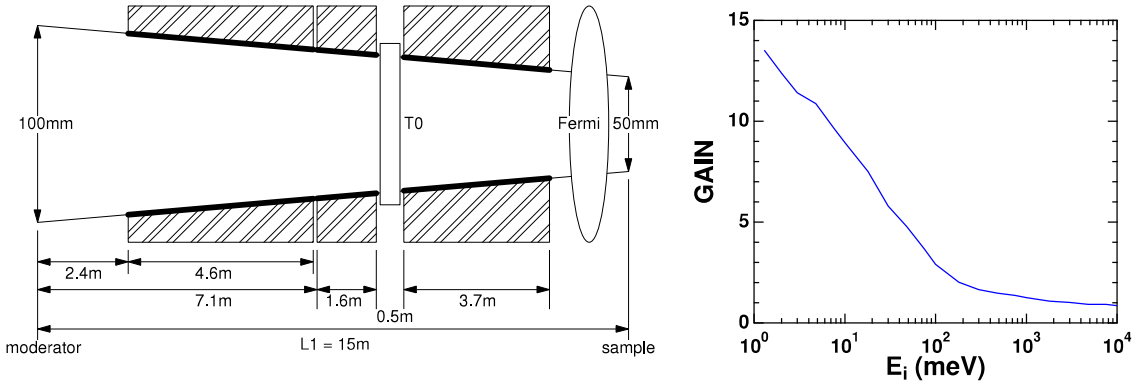

Figure 2. Scehmatic layout of the supermirror guide tube (thick lines) in the primary flight path (left), and observed gain of the supermirror guide system on the HRC in comparison with the previous setup where only the upstream section of 4.6 m was installed (right).

2. Instrument Developments

Since the above initial construction, we have continuously improved the HRC at many points as described below. In particular, by the installation of the collimator system to reduce background, the NBS experiments have been feasible on HRC.

2.1. Supermirror Guide Tube

On the primary flight path of $L_1 = 15$ m, the supermirror guide tube was initially installed only in the shutter and the biological-shielding sections of 4.6 m, and the collimator tube was in the downstream section of 5.3 m, in the initial construction. After that, the collimator tube was replaced by a supermirror guide tube of 5.3 m [4]. By this installation, we obtained a great intensity gain, as shown in Fig. 2.

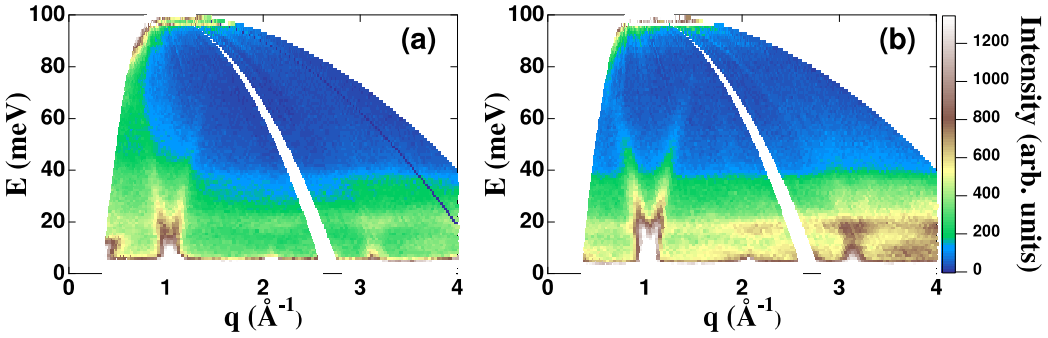

Figure 3. Excitation spectrum from $CsVCl_3$ measured with $E_i = 102$ meV, without a collimator system and an initial guide tube system (a), and with the 2.3° collimator and the full guide tube system (b). The intensities are normalized by the number of protons incident to the neutron production target. The noise at low-q has been greatly reduced by the 2.3° collimator, also the neutron flux has been increased by the installation of the guide tube.

2.2. Collimator System

A Soller collimator system composed of slits of vertical sheets of Cd with a thickness of 0.1 mm was installed just upstream of the sample. We can automatically select one of the two collimators with the collimation of 2.3° or 0.6° [4].

Since there was a huge background noise at low angles, as shown in Fig. 3 (left), a measurement with an empty can was required. Figure 3 shows excitation spectra in a one-dimensional antiferromanget, $CsVCl_3$, measured at 20 K. By using the 2.3° collimator, the background at low angles was greatly reduced and a spectrum from the sample can be obtained without an empty scan, as shown in Fig. 3 (left).

In the lower angle region, PSDs are installed down to $\phi = 0.5°$. These low angle detectors as well as sub-eV incident neutrons enable the NBS experiments on the HRC [5]. Figure 4 shows observed spectra from an empty can at $\phi = 0.64°$ with the incident neutron energy of $E_i = 102$ meV. A spread of the direct beam at the energy transfer of $E = 0$ meV and a spurious peak at $E = 5$ meV were observed with the collimator with the 0.6° collimation. The direct beam spread was eliminated and the spurious peak was reduced by using the collimator with the 0.3° collimation. The spurious peak at $E = 5$ meV, originating from a reflection of the direct beam at a position near the PSDs, could be successfully eliminated by masking the position with a cadmium plate. Finally, based on these developments, 2.3° and 0.3° collimators were replaced by 1.5° and 0.2° collimators, respectively.

2.3. Computational Environment

An experimental control environment was developed to combine the measurements of neutron counts with the control of devices such as choppers, temperature controllers, goniometers, vacuum system, and so on, as shown in Fig. 5 [4]. The HRC Control Platform was developed and installed on the computer named DAQ-OP (DAQ operator). The HRC Device Control Software controls the devices as well as the DAQ middleware (DAQ MW) via the Control LAN through the Platform. The HRC Experiment Control Software executes a sequence composing begin/end of measurements and controls of devices. At present, almost all the devices on the HRC can be controlled through this platform and these operations can be connected with the data acquisition (begin/end of measurements). In order to optimize the computing environment, the composition of the computers was improved.

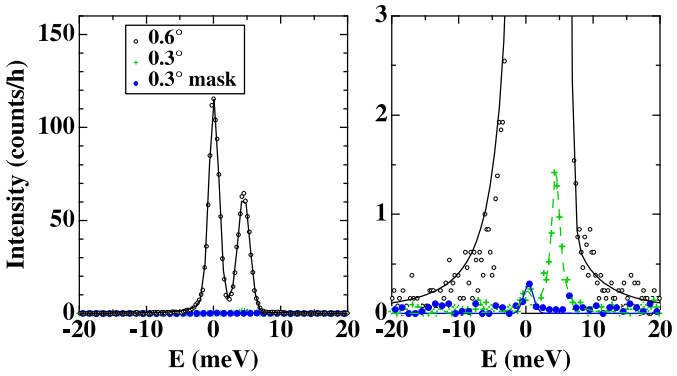

Figure 4. Background noise at $\phi = 0.64°$ for the 0.6°, the 0.3° collimators, and the 0.3° collimator with a cadmium mask at the position of the direct beam hit. The same data are plotted in both figures with different scales in the vertical axes. The lines are guides to the eye.

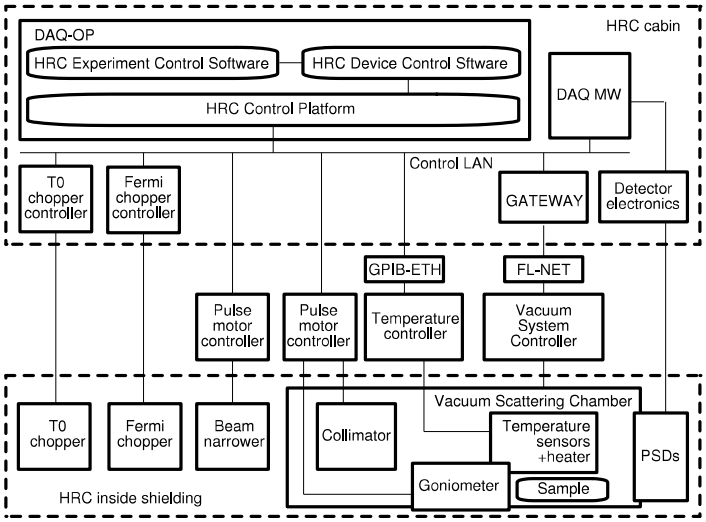

Figure 5. Experimental control environment on the HRC. GPIB-ETH represents a GPIB/Ethernet converter. The vacuum system is accessible through a Gateway server and an FL-net interface. The incident neutron beam is controlled by the T0 chopper, the Fermi chopper, the narrower, and the collimator. The sample environments such as the temperature and the crystal angle are controlled.

We also developed the software to analyze single crystal sample data as well as powder sample data. The analyzed data can be transformed to the standard Mslice format for a convenience of users. Also, the process for the alignment of the sample crystal became very easy. The excitation spectra in the three-dimensional system on the four-dimensional energy-momentum space can be also measured by rotating the crystal axis of the sample, and visualized.

2.4. Other Developments

Initially, we installed two Fermi chopper: one is a so-called sloppy chopper for high intensities and the other is optimized for $E_i = 200$ meV at 600 Hz with the optimum condition. Therefore,

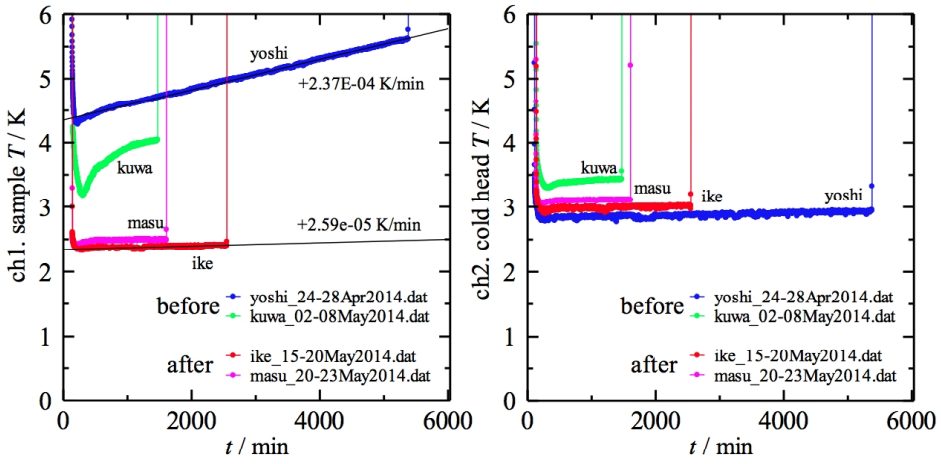

Figure 6. Temperature variations at the sample can (left) and the cold head of the refrigerator (right) before and after the improvement of the radiation shielding on the GM-type refrigerator.

the optimum condition, where the chopper open time is equivalent to the pulse width, was realized in the energy range of $E_i = 10 - 200$ meV. At present, we installed a Fermi chopper optimized for $E_i = 500$ meV at 600 Hz, and then the energy range for the optimum resolution of $\Delta E/E_i = 2.5$ - 3% was extended up to $E_i = 500$ meV [4].

In the initial construction, the sample area was separated from the vacuum scattering area near PSDs with a thin Al foil in the vacuum scattering chamber, and the sample area was evacuated by a small TMP (turbo molecular pump) to achieve a high vacuum for cooling down the sample. The TMP was replaced by a cryopump with a pumping speed of 28 m^3/s and the Al foil was removed. A gate valve with a diameter of 750 mm was also mounted between the cryopump and the chamber. A cryopump system is now used for evacuating the vacuum scattering chamber encompassing the sample and the flight path of the scattered neutrons. After installing this system, the regeneration process of the cryopump, which is the process to release absorbed molecules, was optimized and a frequency of the evacuation without the regeneration was greatly reduced.

For conventional experiments, 128 pieces of 2.8 m PSDs, which are mounted into two detector banks, covers $\phi = 3 - 42°$ at present. 64 pieces of 2.8m PSDs are mounted on each detector bank panel of 1.5 m × 3 m with a vacuum flange, and two panels with PSDs are hold on the vacuum scattering chamber. To remove the panel from the vacuum chamber, it was necessary to remove the shielding block above the vacuum scattering chamber first, and then, remove the panel by using a crane installed at the experimental hall. At present, we mounted a rail on the vacuum chamber body just above each panel, and the panel can be removed from the chamber along the rail by using a hand chain hoist. By using this mechanism, we replaced the damaged PSDs by new ones in a much easier procedure without removing the shielding.

We have a variety of sample environments: a GM type refrigerator, a ^{3}He sorption pumping type refrigerator, a ^{3}He circulation type refrigerator, and a cryomagnet. The GM-type refrigerator is conventionally used to cool the sample down to 4 K stably. This refrigerator shows a good cooling performance by improving the radiation shielding, which is made of thin Al foil and contacts to the cold head. The sample temperature down to 2.5 K and the heat-up rate of 26 μK/min on the sample have been confirmed, as shown in Fig. 6. A temperature sensor with a fine calibration is used at the sample, and that with a rough calibration is at the cold head. This may cause the higher temperature indication at the cold head for the best case indicated

by "*ike*" and "*masu*". Also, the lowest temperatures of 0.3 K and 0.6 K were confirmed for the ^{3}He sorption pumping type refrigerator and the ^{3}He circulation type refrigerator, respectively.

A cryomagnet to apply the magnetic field up to 14 T to the sample down to 0.3 K was introduced. We performed the commissioning at the Guide Hall of JRR-3M, and confirmed that it was successfully operated with the maximum magnetic field of 14 T at the lowest temperature of 0.3 K. Then we moved the cryomagnet to the HRC, and examined the maximum magnetic field in the actual setup of the experiments. We confirmed the maximum magnetic field of 10 T on the HRC without any damage to devices at around the sample area.

3. Neutron Brillouin Scattering Experiments

On the HRC, the NBS experiments became feasible by reducing the background noise at low scattering angles down to $\phi = 0.5°$. NBS is the most promising way to observe excitations in the forward direction from powders, polycrystals, or liquids. Owing to the kinematical constraints of neutron spectroscopy, E_i in the sub-eV region is necessary for measuring scattering in the meV range of E near to (000), and with a high energy resolution of $\Delta E/E_i$, further, the scattered neutrons need to be detected at very low ϕ. Low angle detectors are essential to access the present energy momentum space. In fact, the region above the dashed line in Fig. 7, which is the envelope of scan loci for $\phi = 5°$ with respect to E_i, can never be accessed using a conventional spectrometer with the lowest scattering angle of $\phi = 5°$, for instance.

3.1. Feasibility of NBS on HRC

First, NBS experiment was performed on the HRC to observe spin waves in a polycrystalline sample of a cubic perovskite, $La_{0.8}Sr_{0.2}MnO_3$, (Curie temperature: $T_C = 316$ K). Magnetic properties of this material are well elucidated and it has been already reported that spin waves were measured by using a single crystal sample. Figure 7 (a) shows the dispersion relation of spin waves in $La_{0.8}Sr_{0.2}MnO_3$ measured with $E_i = 102$ meV, where $\Delta E/E_i = 2\%$. The observed dispersion relations at 245 K was well fitted to $E = DQ^2$, where Q is the scattering vector. The D value was obtained to be 88 ± 2 meVÅ^2 at 245 K. This value is in good agreement with the results ($D = 89$ meVÅ^2 at 250 K) obtained by the previous experiments using a single crystal [8, 9]. Therefore, the feasibility of NBS experiments on the HRC was demonstrated [5, 6, 7].

3.2. Spin dynamics in metallic ferromagnet $SrRuO_3$

Spin waves in a polycrystalline ferromagnet $SrRuO_3$ ($T_C \sim 160$ K) were measured, because a large single crystal suitable for inelastic neutron scattering experiments has not yet been synthesized. This material has recently become attractive because of an enhanced anomalous Hall effect due to the robust spin-orbit coupling of the Ru 4d orbital [10]. The measurement was performed at 7 K with $E_i = 102$ meV, and well-defined spin wave peaks were observed. As shown in Fig. 7 (a), the dispersion relation of spin waves in $SrRuO_3$ was well fitted to $E(Q) = E_g + DQ^2$ with an apparent energy gap E_g [6]. Also, the temperature (T) dependence of D and E_g was investigated. We found that $D(T)$ was almost independent of T up to T_C, and $E_g(T)$ could be related to the anomalous Hall conductivity. These results might suggest the intermediate electron correlation in $SrRuO_3$ as well as the vital role of magnetic monopoles in momentum-space as a source of strong Berry curvature originating from the spin-orbit interaction [11].

3.3. Spin waves in permanent magnet $Nd_2Fe_{14}{}^{11}B$

$Nd_2Fe_{14}B$ is a well-known song permanent magnet with $T_C = 580$ K and the saturation magnetization of 1.6 T. At room temperature, all spins are aligned along the c*-axis. Below 130 K the system exhibits a spin reorientation. Because the unit cell includes four chemical formulae of $Nd_2Fe_{14}B$ in a tetragonal lattice, spin-wave branches are expected to be complicated. In a

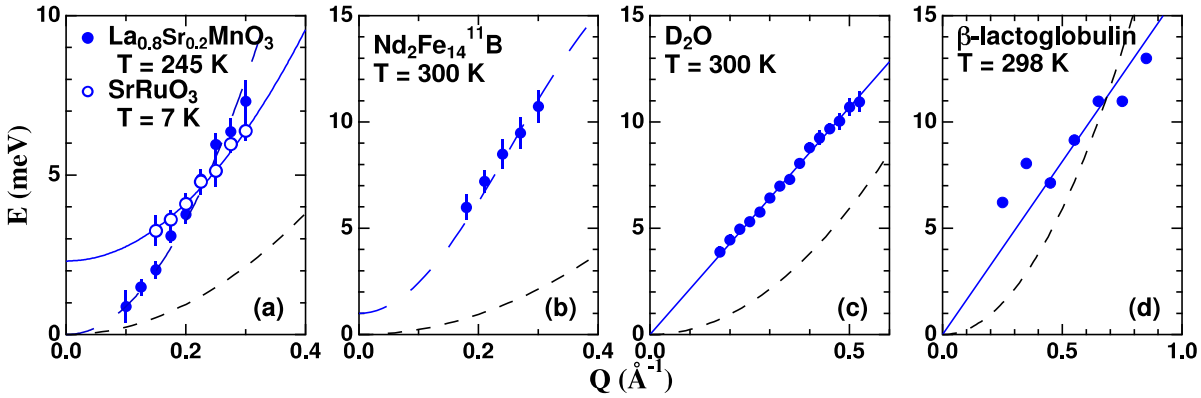

Figure 7. Dispersion relations obtained by the NBS on the HRC: spin waves in $La_{0.8}S_{r0.2}MnO_3$, $SrRuO_3$ (a) and in $Nd_2Fe_{14}{}^{11}B$ (b), phononic excitations in D_2O (c) and in β-lactoglobulin (d). The solid lines are fitted curves. The dashed lines are the dispersion relations reported previously. The region above the dotted black line in each figure, which is the envelope of scan loci for the scattering angle of 5° (the lowest angle for a conventional spectrometer) with respect to E_i, can never be accessed using a conventional spectrometer.

previous inelastic neutron scattering experiment using a single-crystalline sample of $Nd_2Fe_{14}{}^{11}B$, a spin-wave branch was detected only along the c*-axis around (002) at 6 and 295 K [12]. We performed NBS experiments in a $Nd_2Fe_{14}{}^{11}B$ polycrystalline sample at 6 and 300 K with E_i = 257 meV and ΔE = 5.7 meV [7, 13]. The observed spin-wave peaks at 300 K were well fitted to Gaussian scattering functions with widths determined from the resolution, and the peak positions were determined in Fig. 7 (b). The observed peak positions were on the dispersion curve along the c*-axis reported in the previous experiment using a single crystal [12]. No magnetic peaks were observed at 6 K, this result is also consistent with the reported dispersion at 6 K.

3.4. Phononic excitations in liquid D_2O

Phononic excitations in a liquid D_2O were measured at 300 K with E_i = 102 meV and ΔE = 2.0 meV [7]. The observed spectra showed broad excitation peaks and a resolution-limited elastic peak. The excitation peaks were fitted with a damped harmonic oscillator scattering function convoluted with the instrumental resolution width multiplied by a temperature factor and the peak positions $E(Q)$ were determined. The present analysis was identical to that for the previous inelastic neutron scattering experiment [14]. As shown in Fig. 7 (c), the Q dependence of the observed peak positions down to Q = 0.02 Å^{-1} was well fitted to $E(Q) = cQ$ with c = 21.4 ± 0.2 meV, which is equivalent to c = 3250 ± 30 m/s. The observed sound velocity c was in good agreement with that for the fast sound observed in the previous experiment with E_i = 80 meV and ΔE = 4.8 meV down to Q = 0.035 Å^{-1} [14].

3.5. Collective dynamics of hydrated β-lactoglobulin

Protein hydration plays a fundamental role in protein behavior: water-protein interactions affect protein folding, maintain structural integrity, mediate molecular recognition, and accelerate enzymatic catalysis. Many scattering measurements, both elastic and inelastic, and many molecular dynamics simulations, have been performed to investigate the relation between protein dynamics and that of the surrounding solvent molecules. Single particle dynamics of proteins and

hydrated water have been investigated using incoherent scattering from hydrogen in hydrated protein powder. On the other hand, the investigation of collective dynamics of proteins and hydrated water using coherent scattering is relatively scarce, although it contains important information of structure and dynamics. First, we performed NBS experiment of pure D_2O at room temperature on the HRC, as mentioned above. The fast sound mode due to the collective dynamics of water was detected. Next, hydrated β-lactoglobulin powder was measured at 180 - 298 K. The inelastic neutron scattering spectra show well-defined acoustic excitations that change in excitation energy with Q in the low Q region. The obtained dispersion relation is shown in Fig. 7 (d) and the high-frequency sound velocity was almost independent of the temperature and was 2460 $\pm$ 110 m/s at 298 K [15].

4. Summary

Since the initial construction, we have continuously improved the HRC at many points. We believe that the HRC shows the best performance based on the present technology. In particular, by the installation of the collimator system to reduce background, NBS experiments have been feasible on the HRC. The NBS is the promising way to observed coherent excitations in powder, polycrystalline, noncrystalline and liquid systems. In the current research in material science, most of the newly synthesized materials are chemically and structurally complicated such that large single crystals are not always possible to be synthesized. NBS experiments on the HRC bring about new opportunities to such material development.

Acknowledgments

This neutron scattering experiments were approved by the Neutron Scattering Program Advisory Committee of the Institute of Materials Structure Science, High Energy Accelerator Research Organization (Proposal Nos. 2012S01, 2013S01 and 2014S01). The NBS experiments were conducted in collaboration with Y. Endoh, M. Fujita, Y. Kaneko, Y. Tokura, K. Ono, K. Saito, N. Inami, and K. Yoshida.

References

[1] Itoh S, Yokoo T, Satoh S, Yano S, Kawana D, Suzuki J and Sato S J 2011 *Nucl. Instr. Meth. Phys. Res.* A **631** 90
[2] Yano S, Itoh S, Satoh S, Yokoo T, Kawana D and Sato T J 2011 *Nucl. Instr. Meth. Phys. Res.* A **654** 421
[3] Itoh S, Yokoo T, Kawana D, Yano S, Satoh S, Sato T J, Masuda T, Yoshizawa H 2012 *Proc. 20th Meeting of the International Collaboration on Advanced Neutron (ICANS-XX)* (Centro Atomico Bariloche) p 416
[4] Itoh S, Yokoo T, Kawana D, Yoshizawa H, Masuda T, Soda M, Sato T J, Satoh S, Sakaguchi M and Muto S 2013 *J. Phys. Soc. Jpn.* **82** SA033
[5] Itoh S, Yokoo T, Kawana D and Endoh Y 2013 *J. Phys. Soc. Jpn.* **82** SA034
[6] Itoh S, Endoh Y, Yokoo T, Kawana D, Kaneko Y, Tokura Y and Fujita M 2013 *J. Phys. Soc. Jpn.* **82** 043001
[7] Itoh S, Yokoo T, Kawana D, Kaneko Y, Tokura Y, Fujita M, Yoshida K, Saito K, Inami N, Takeichi Y, Ono K, Endoh Y 2014 *J. Phys.: Conf. Series* **502** 012043
[8] Endoh Y and Hirota K 1997 *J. Phys. Soc. Jpn.* **66** 2264
[9] Moussa F, Hennion M, Kober-Lehouelleur P, Reznik D, Petit S, Moudden H, Ivanov A, Mukovskii Y M, Privezentsev R and Albenque-Rullier F 2007 *Phys. Rev. B* **76** 064403
[10] Fang Z, Nagaosa N, Takahashi K S, Asamitsu A, Mathieu R, Ogasawara T, Yamada H, Kawasaki M, Tokura Y and Terakura K 2003 *Science* **302** 92
[11] Itoh S, Endoh Y, Yokoo T, Park J-G, Kaneko Y, Tokura Y, Nagaosa N 2014 *unpublished*
[12] Mayer H M, Steiner M, Stüßer N, Weinfurter H, Kakurai K, Doner B, Lindgård P A, Clausen K N, Hock S, Rodewald W 1991 *J. Magn. Magn. Matter.* **97** 210
[13] Ono K, Inami N, Saito K, Takeichi Y, Yano M, Shoji T, Manabe A, Kato A, Kaneko Y, Kawana D, Yokoo T and Itoh S 2014 *J. Appl. Phys.* **115** 17A714
[14] Teixeira J, Bellissent-Funel M C, Chen S H, Dorner B 1985 *Phys. Rev. Lett.* **54** 2681
[15] Yoshida K, Yamaguchi T, Kawana D, Yokoo T and Itoh S 2014 *MLF Annual Report 2013* (J-PARC Center) *in press*

3.5.7

Recent status of a cold neutron disk chopper spectrometer, AMATERAS

Kenji Nakajima[1], Seiko Ohira-Kawamura[1], Tatsuya Kikuchi[1], Yukinobu Kawakita[1], Yasuhiro Inamura[1], Ryoichi Kajimoto[1], Mitsutaka Nakamura[1], Kazuhiko Soyama[1], Masahide Harada[1], Kenichi Oikawa[1], Shinichi Takata[1], Hiromichi Tanaka[1], Takaaki Iwahashi[1], Wataru Kambara[1], Yasuhiro Yamauchi[1], Kazuhiro Aoyama[1] and Masatoshi Arai[1]

[1]Materials & Life Science Division, J-PARC Center, Japan.

E-mail: kenji.nakajima@j-parc.jp

Abstract. Recent issues of a cold-neutron disk-chopper spectrometer AMATERAS are reported. Five years have been passed since we had the first neutron beam on AMATERAS. The user program is running steadily since after the visiting of the first user in 2009. In parallel to that, machine studies and commissioning works to improve spectrometer performance have been continuously done. Effort has been done on fixing the beam-transport problem, which causes the serious intensity loss at the sample position. After replacing 8.6 m section of super mirror and re-doing the mirror alignment, a part of intensity has been recovered, while still some of problems are remained. We also spent effort on reducing background caused by several sources. Study on the background sources and implementation of countermeasures are progress.

1. Introduction

AMATERAS (Figs. 1 and 2) is a cold-neutron multi disk-chopper spectrometer at Materials and Life Science Experimental Facility (MLF) at J-PARC. By using a pulse shaping chopper and owing to the high peak intensity from a coupled moderator source at MLF, AMATERAS is designed to realize high intensity and fine and flexible energy resolution measurements in quasielastic and inelastic neutron scattering experiments from cold to thermal neutron energy region [1, 2]. The spectrometer has had the first neutron beam in May 2009 and had the first user in December 2009. In parallel to the user program, machine study and technical works to maintain and to improve spectrometer performance have been continuously done. Since the last ICANS meeting held in 2012, replacement of a defected parts (a disk of one of high-speed disk choppers, a gas-leaked detector tube and other electronic parts in DAQ system), upgrading and improving of spectrometer components,

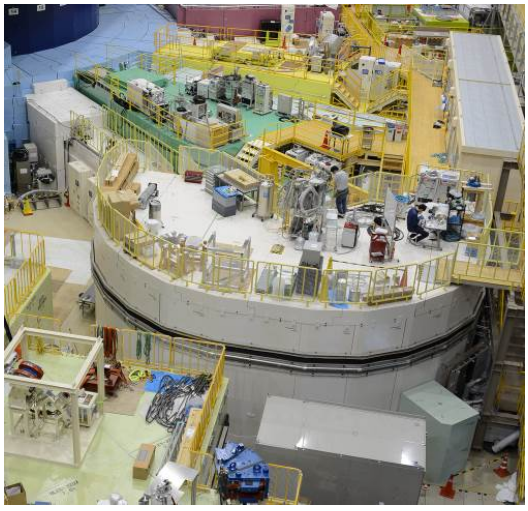

Figure 1. Recent photo of AMATERAS.

development of data analysis method and commissioning of N_2 beam monitors, newly introduced sample environments (an oscillating radial collimator, a furnace, cryostats, a 7T cryomagnet (one of MLF common accessories) and so on) have been done. Especially, we have done refurbishment of the beam transport section to solve an issue of a serious intensity loss at the sample position. Also, there is progress in the work of reduction of background, which is caused by several sources in the case of AMATERAS.

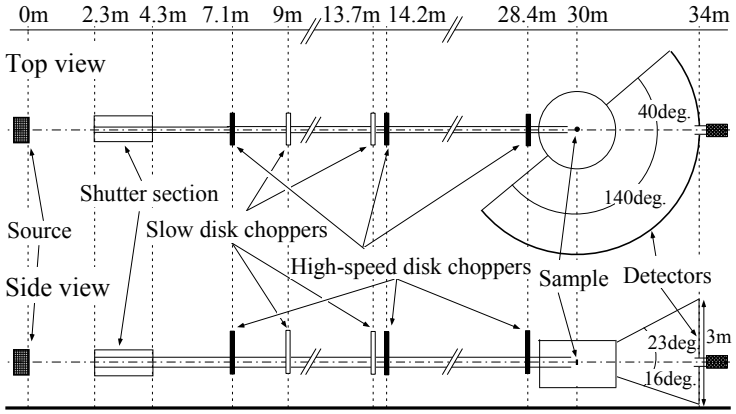

Figure 2. Schematic view of AMATERAS. Cited from Ref. [3].

2. Refurbishment of the beam transport

2.1. Overview of AMATERAS beam transport and its issues

The beam transport of AMATERAS is described in Fig. 3 [2]. The beam transport consists from *m*=3.0 and 3.8 super mirrors. The horizontal geometry has curved section (R = 2,000 m) between 7.2 m and 26.8 m from the source [1, 2, 4].

The vertical geometry is combination a straight section, an elliptical section, and a transition section between the straight and elliptical parts [1, 2, 3, 5]. Actually, the beam transport is combination consists of 28 tubes of straight and linear-tapered super mirror guides (Fig. 4 (a)). One or two tubes (each length is 0.35 ~ 2.0 m, typically 1.0 m) are set in a stainless steel vacuum jacket (Fig. 4 (b)). After aligning each tube in jackets by using push pins and adjusting screws, all jackets were set into supporting flames (Fig. 4 (c)), which have adjusting mechanisms for the jackets. The jackets were connected with formed

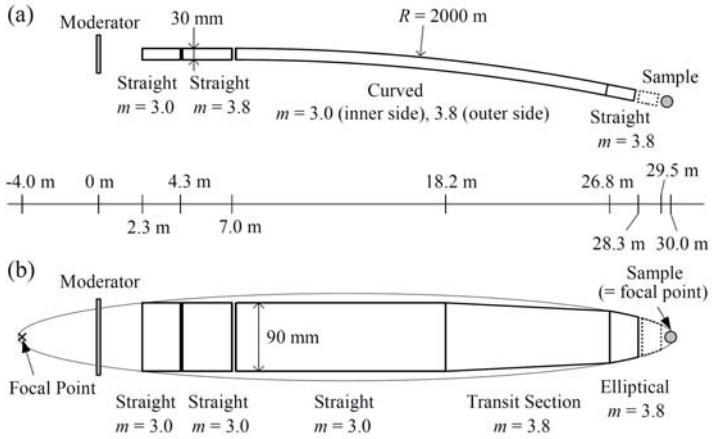

Figure 3. Schematic view of beam transport of AMATERAS (horizontal (*upper panel*) and vertical (*lower panel*) geometries). Cited from Ref. [2].

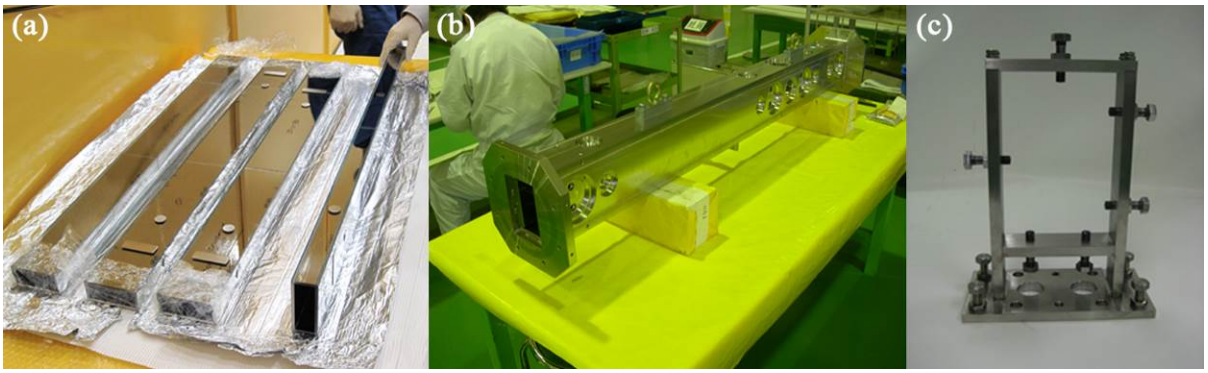

Figure 4. (a) Super mirror guides, (b) a guide jacket and (c) a support flame of AMATERAS.

bellows after alignment (Fig. 5).

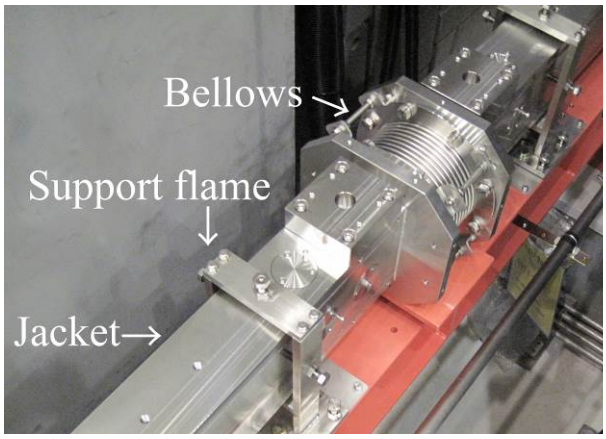

Figure 5. A connection between two jackets.

In very early stage of the spectrometer commissioning, we realized that the neutron flux at the sample position is less than the expected value estimated from Monte-Carlo (MC) simulation [2]. There are three possibilities of sources of this problem, i) problems in the mirror aliment, ii) problems in the performance of super mirrors and/or iii) problems in our Monte-Carlo simulations. Soon after realizing poor performance of the intensity, we inspected the alignment of mirrors at a part (9.4 m ~ 13.4 m from the source) of the beam transport and found one of vacuum jackets rotated unexpectedly in the horizontal plane. Also, degrees of rolling of sections were deviated from values which were recorded in the installation. These evidences indicated that the mirrors were moved from original positions.

Another plausible source of the intensity loss was performance of super mirrors. In 2012, we were reported that borofloat-glass substrate super mirrors used in AMATERAS could have poor performance. In the AMATERAS's case, because of poor pre-treatment of glass surface, the reflectivity could be less than 40%, which was expected more than 80% in the specification document. AMATERAS uses suspected mirrors in the sections at 18.2 m and after from the source. Unfortunately, we did not inspect these parts of mirrors, because time schedule of construction was too tight when we installed them. To examine this possibility, we replaced 1.3 m section of tubes at the most downstream position, which we can easily access to, with well characterized mirrors (m=3.6, reflectivity is 65% or more). We found the intensity gain of about intensity gain of 5% which is small at the long wave length region and is large at the short wave length region. That observation is consistent if the original mirror of the reflectivity was 40%.

2.2. Refurbishment of AMATERAS beam transport

From the evidences described in 2.1, we decided to carry out a major refurbishment of the beam transport of AMATERAS. The refurbishment plan contained i) replacement of all borofloat glass super mirrors and ii) re-alignment of all beam transport at downstream of a biological shielding. Also, iii) we remade the supporting flames increasing thickness of steel plates to make them firmer, and replaced formed bellows between jackets with more soft welding bellows to reduce the tension between jackets. These are counter measure against unexpected moving of mirrors.

We purchased new mirrors in JFY 2012 from Mirrotron Ltd. Fabrication of new support flames and bellows were done consequently. Replacement and re-alignment of mirrors were carried out in long shut down period of J-PARC in 2013. In July 2013, we removed the top and side of beam line shielding. Alignment of the beam line using new mirrors, new support flames

Figure 6. Re-alignment work at AMATERAS.

and new bellows was done in November 2013 (Fig. 6, 7). After the refurbishment, positions of vacuum jackets were measuring by using a laser tracker and were recorded.

2.3. Results and remaining problems

After the large refurbishment, in February 2014, we checked the neutron flux at the sample position by measuring incoherent scattering from vanadium and by measuring inelastic and quasielastic scatterings from several samples, which were measured on AMATERAS before. We observed substantial increase of the intensity. At long wavelength region, intensity after refurbishment was 20% higher than that of before and, at higher energy region, it became almost twice (Fig. 8). The absolute intensity at the sample position, however, is still lower than the MC simulation results, which may imply that we should more seriously consider the 3rd possibility, i.e. the validity of our MC simulation calculations done before the construction. Another remaining problem is that we found the drop of the intensity very recently. We are afraid that jackets or mirrors in them may be moving. We are watching the intensity change of AMATERA carefully and are planning to open the beam line shielding in the next shut down to check the alignment.

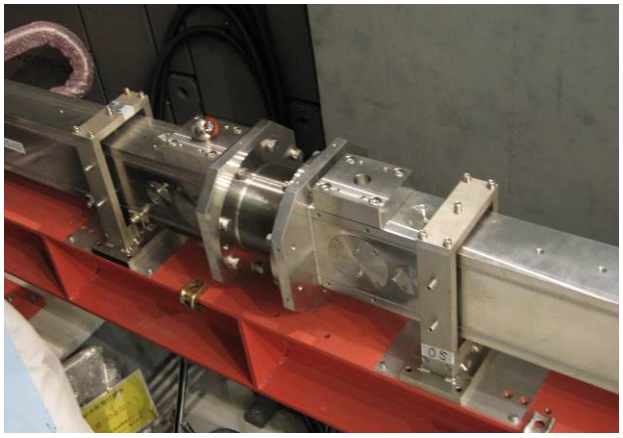

Figure 7. A photo of the same part shown in Fig. 5 taken from the opposite side after the refurbishment. One can see that designs of support flames and a bellows have been changed.

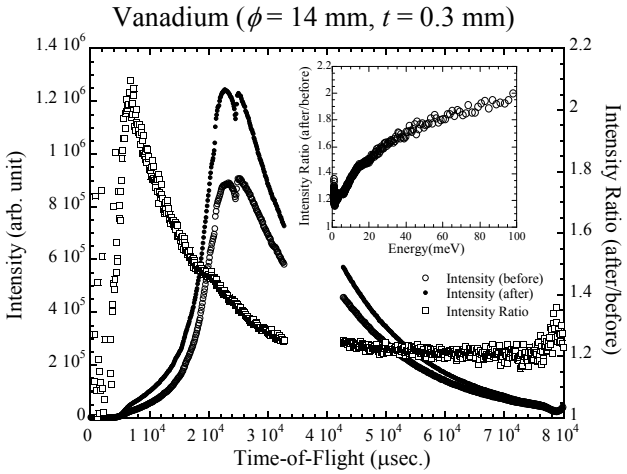

Figure 8. Scattering intensity from vanadium cylinder (ϕ = 14 mm, t = 0.3 mm) before/after the refurbishment of the beam transport. Intensity ratios are also shown.

3. Backgroun issues

3.1. Background at AMATERAS

Background (noise) is always critical to inelastic spectrometers. Reducing background is one of the highest priority issues of me as it is in the case of usual spectrometers. To minimize the background, AMATERAS i) employs a curved section in the beam transport to eliminate γ-ray and fast neutrons from the source, ii) void of inside of the beam line shielding is minimized by putting concreate blocks, steel plates and

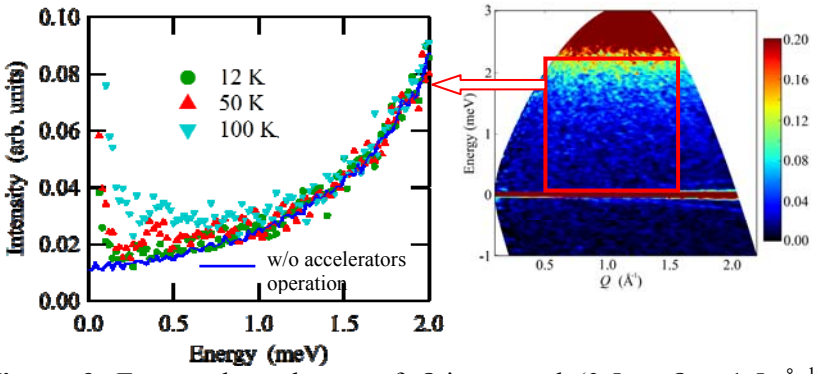

Figure 9. Energy dependences of Q-integrated ($0.5 < Q < 1.5$ Å^{-1}) intensities from magnetic powder sample. Results at three different temperatures are shown together with the data measured when J-PARC accelerators were stopped (solid line).

polytrimethylene blocks, iii) the inside of the shielding of the hatch which accommodates a scattering chamber is covered with B_4C contained (25wt%) precast concrete (t = 35 mm) and iv) the inside of the scattering chamber is covered with Cd plates (t = 0.5 mm). As results of these efforts, current background level (except that from samples) in the experiments on AMATERAS is 30 Count $h^{-1}PSD^{-1}m^{-1}$, which is time independent. One of examples is shown in Fig. 9. We are also suffered from another type background. It happens within short time range and simultaneously illuminates all pixels of detectors. As results, flat and Q-independent false inelastic signals are observed (Fig. 10).

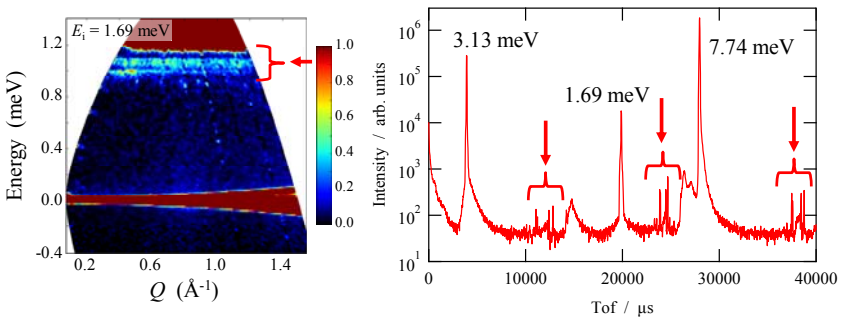

Figure 10. False signals observed at AMATERAS. Q-independent signals around 1.0 meV in the left panel is resulted from short-time signals (backgrounds) indicated by arrows in the right panel.

3.2. Time-independent background

One can see in Fig. 9 that the time-independent background counts at AMATERAS do not depend on whether the accelerators are in operation or not. The evidence implies origins of these counts are suspected to be electric noise of DAQ system and/or from environment radiations. By increasing the lower-level discrimination (LLD) (Fig. 11) or decreasing applying high-voltage (HV), we confirmed that the time-independent background. However, we are cautious about changing DAQ parameters, since changing the LLD higher than the optimized level causes decrease of the counter efficiency and decreasing HV causes decrease of the counting rate. About the environmental radiation background, most of parts come from the floor under the scattering chamber (Fig. 11(b)). As a series of tests, we put polytrimethylene and boracic acid bags under the scattering chamber. We found boron contain material is effective to reduce the background. Therefore, now we are preparing B_4C tiles to cover the floor of under the scattering chamber.

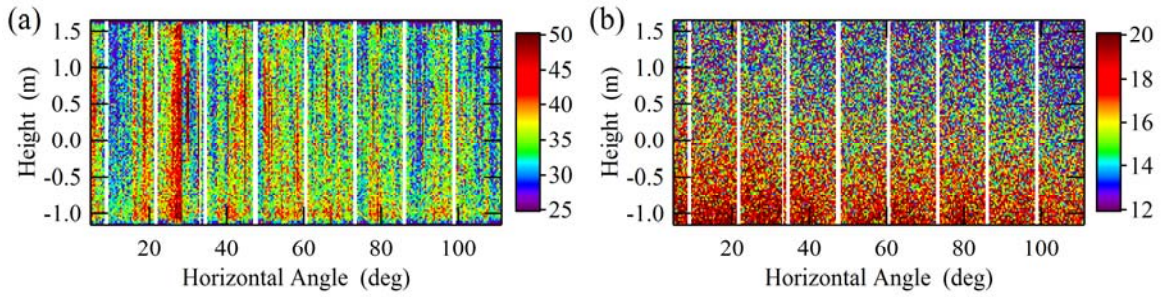

Figure 11. Intensity maps processed using (a) normal LLD and (b) 195% higher LLD. Measurement was done when J-PARC accelerators were stopped. The scale is counts/hour.

3.3. Short-time background

About short-time background, by analysing time-of-flight and flight path length we spotted the source of false signals. We converted the observed times of false signals into the flight path lengths from the source. These positions correspond to the position of a Cd window, B_4C beam narrowers and the sample position. We suspect that neutrons arrived at these positions emit γ-ray, which travels speed of light and causes noise to ^{3}He counters. There are so many Cd plates and B_4C near and around AMATERAS beam line. We are planning to replace those which possibly have direct neutron beam with other materials, for example, ^{6}Li.

4. Summary

A cold-neutron disk-chopper spectrometer AMATERAS is running steadily since its starting operation in 2009. We are continuously working on improving and upgrading the spectrometer. Recently, we have been worked on improving the beam-transport performance and reducing background, which need our further efforts.

Although there are remaining items to be improved, the user program on AMATERAS is running successfully since after the visiting of the first user in December, 2009. Until June, 2014, 61 proposals have been carried out, which have resulted more than 20 papers, 5 theses and nearly a hundred of presentations at scientific meetings. Among of them, unique data analysis methods fully utilize unique futures of AMATERAS were developed [6]. Recently two press releases were issued on studies on biology [7] and magnetism [8]. In December 2014, AMATERAS had an interim assessment by neutron instruments review committee of MLF, J-PARC, which all instruments at MLF are obliged to have after 5 years their operations. AMATERAS had positive assessment, and committee recommended continuing AMATERAS project for next 5 years.

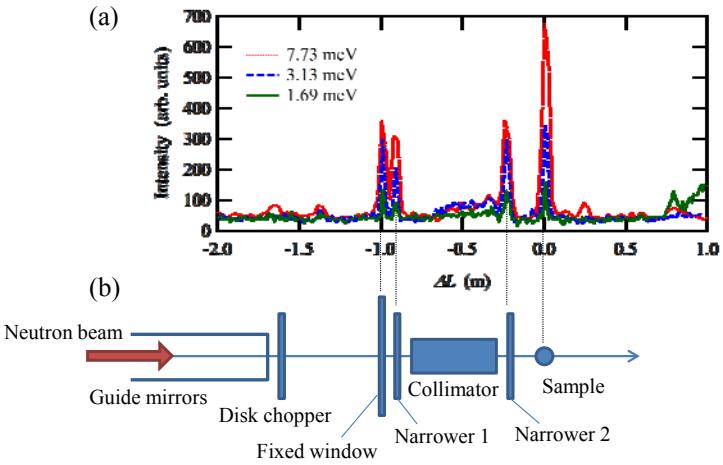

Figure 12. Time-of-flights of false signals are converted into the flight distances (ΔL = (flight path length from the source) -30 m)

We are continuing to spend effort to improve performance of AMATERAS to produce further scientific results from this spectrometer.

[1] Nakajima K *et al*. 2007 Cold-Neutron Disk-Chopper Spectrometer at J-PARC 2007, *J. Neutron Res*. **15** 13.

[2] Nakajima K *et al*. 2011 AMATERAS : A Cold-Neutron Disk Chopper Spectrometer *J. Phys. Soc. Jpn.* **80** SB028.

[3] Nakajima K, Ohira-Kawamura S, Kikuchi T, Kajimoto R, Takahashi N, Nakamura M, Soyama K and Osakabe T 2015 Beam-transport optimization for cold-neutron spectrometer *EPJ Web of Conf.* **83** 03011.

[4] Kajimoto R, Nakajima K, Nakamura M, Osakabe T, Sato T J and Arai M 2008 Curved neutron guide of the cold neutron disk-chopper spectrometer at J-PARC *J. Neutron Res.* **16** 81.

[5] Kajimoto R, Nakamura M, Osakabe T, Sato T J, Nakajima K and Arai M 2006 Study of Converging Neutron Guides for the Cold Neutron Double-Chopper Spectrometer at J-PARC *Physica B* **385-386** 1236.

[6] For example, Kikuchi T *et al.* 2013 Mode-distribution analysis of quasielastic neutron scattering and application to liquid water *Phys. Rev. E* **87** 062314.

[7] Soda M *et al*. 2014 Spin nematic interaction in multiferroic compound $Ba_2CoGe_2O_7$ *Phys. Rev. Lett*. **112** 127205.

[8] Nakagawa H et al. 2014 Local Dynamics Coupled to Hydration Water Determines DNA-sequence Dependent Deformability *Phys. Rev. E* 022723.

3.5.8

TOF studies of multiple Bragg reflections in cylindrically bent perfect crystals at small pulsed neutron source

P Mikula[1] **and M Furusaka**[2]
[1]Nuclear Physics Institute ASCR, v.v.i., 25068 Řež, Czech Republic
[2]Faculty of Engineering, Hokkaido University, Sapporo, Hokkaido, 060-8628, Japan

E-mail: mikula@ujf.cas.cz

Abstract. It is well known that multiple Bragg reflections (MBR) realized in a bent-perfect crystal (BPC) slab can provide a monochromatic beam of excellent resolution parameters. The sets of different lattice planes participated in MBR effects that are mutually in dispersive diffraction geometry behave differently in comparison with the case of perfect nondeformed or mosaic crystals. Due to the elastic bending – homogeneous deformation - the kinematical approach can be applied in this MBR process. The homogeneous elastic deformation can enormously strengthen the MBR effects which can be then investigated even at small pulsed neutron sources. In this way, by using neutron diffraction and the TOF method carried out at the Hokkaido Linac neutron source many strong MBR reflections accompanying forbidden Si(222) of Si(002) ones can be observed. The advantage of the TOF method consists in the fact that not only primary MBR reflections related to the basic forbidden reflections could be observed but also their non-negligible higher orders which could be easily separated in the time-of-flight spectra.

1. Introduction

Using a conception of the reciprocal lattice space, MBR effects occur whenever two or more reciprocal lattice vectors lie on the surface of Ewald sphere simultaneously [1-4]. It means that a primary crystal lattice represented by a scattering vector $\mathbf{g}_1$ is oriented with respect to the incident beam in such a way that more than one set of planes are simultaneously operative for a given wavelength (see figure 1). One of them may be described as an operative secondary reflection represented by a scattering vector $\mathbf{g}_2$. In fact there can be several secondary reflections. However, it follows from the crystal symmetry that when a secondary reflection fulfils the Bragg condition simultaneously with the primary one, there exists automatically the tertiary reflection represented by $\boldsymbol{g}_3 = \boldsymbol{g}_1 - \boldsymbol{g}_2$ (see figure 2), which is co-operative with the secondary one. The vector sum $\mathbf{g}_2+\mathbf{g}_3$ then represents a double diffracted beam which has the same direction as the one that could have been reflected by the particular primary set of planes represented by the scattering vector $\mathbf{g}_1$ ($\mathbf{g}_1= \mathbf{g}_2+\mathbf{g}_3$). Thus, the MBR effects can result in a so called *Aufhellung* when reducing the intensity of a strong primary reflection or *Umweganregung* when increasing the intensity of a weak primary reflection. In the extreme case of the *Umweganregung* a positive diffraction intensity simulation of forbidden primary reflection can appear. Since the Renninger's first observation of the MBR-peaks many theoretical and experimental investigations of the generally n-beam cases mostly related to X-ray diffraction have been published (see e.g. [4]; in this book many related references can be found).

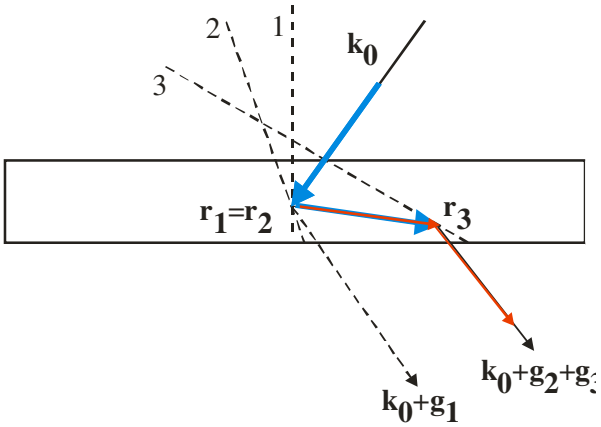

Figure 1. Schematic diagram of a two-step multiple Bragg reflection simulating a primary reflection. The numbers 1,2 and 3 represent the primary, secondary and tertiary reflection planes, respectively.

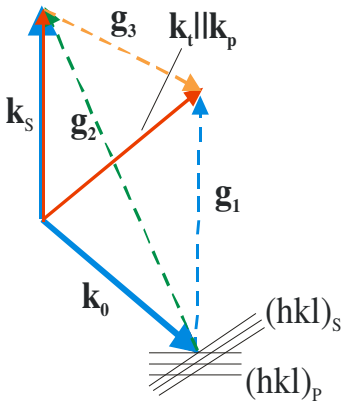

Figure 2. Schematic diagram of a two-step multiple Bragg reflection simulating a primary reflection in reciprocal space.

Concerning neutrons, relatively small MR-effects were observed in mosaic crystals [5-9]. Contrary to X-rays, in the case of perfect single crystals the flux of thermal neutrons at present neutron sources is usually not sufficient for the observation of such small dynamical diffraction effects. However, the situation is quite different in the case of neutron diffraction by elastically deformed perfect crystals [10-17]. In the related papers there is described an observation of a large strengthening of the MBR intensity of the monochromatic beam by ultrasonic vibrations and later by cylindrical bending. In this paper we show that the strenthening of the MBR effects by cylindrical bending is so strong that the effects can be effectively studied by the TOF method even at Linac based small neutron source (Hokkaido University, Sapporo).

2. Experimental details

For bringing more reciprocal lattice points on the Ewald sphere and the investigation of multiple reflection effects two methods are usually used:

a. Method of azimuthal rotation of the crystal lattice around the scattering vector of the primary reflection for a fixed neutron (X-ray) wavelength (e.g. [16,17]).

b. Method of θ–$2\theta_D$ scan in the white beam for a fixed azimuthal angle (e.g. [14,15]). θ is the Bragg angle related to the primary reflection and $2\theta_D$ is the scattering angle at which a point detector is set.

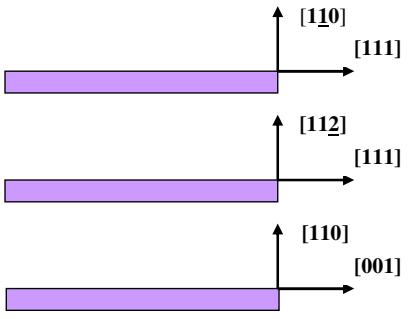

Figure 3. Three Si slabs of different cut were used in the experimental TOF investigation of chosen MBR effects.

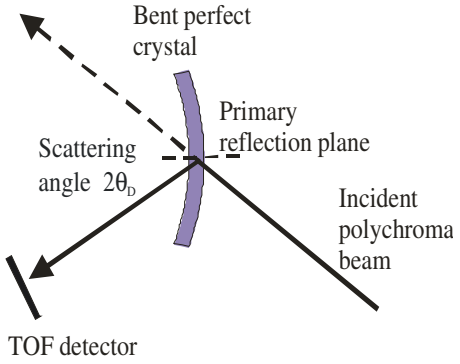

Figure 4. Schematic drawing of the experimental setting.

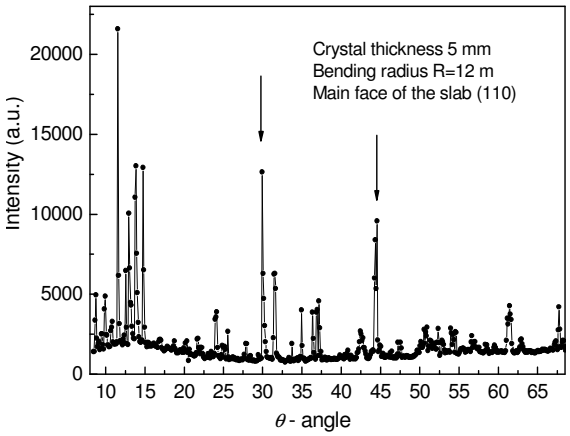

Figure 5. Part of the θ–$2\theta_D$ scan carried out by meas of the crystal slab with the largest face parallel to (1$\underline{1}$0) and set for (222) reflections.

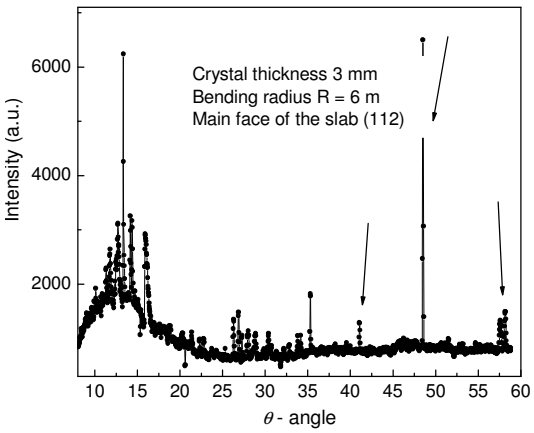

Figure 6. Part of the θ–$2\theta_D$ scan carried by means of the crystal slab with the largest face parallel to (11$\underline{2}$) and set for (222) reflections.

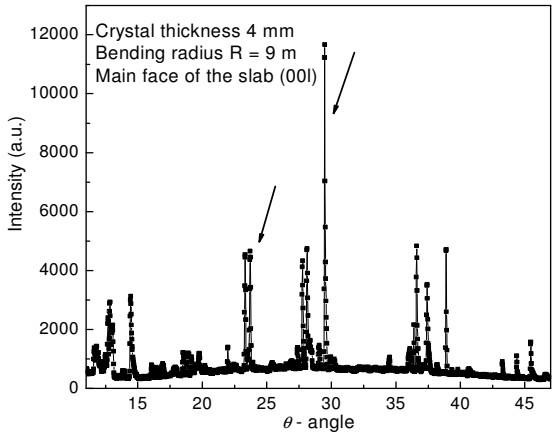

Figure 7. Part of the θ–$2\theta_D$ scan carried out by means of the crystal slab with the largest face parallel to (110) and set for (002) reflections.

However, if the polychromatic incident beam is impinging on the crystal which fulfils a MBR-condition for some primary reflection and the neutron wavelength λ, the related MBR-effect can be overlapped by the ones related to higher orders of λ/n (n is integer). It should be pointed out that the higher orders could be either allowed higher orders of primary reflections or higher orders of MBR-effects. For example, if the Si(222) crystal (forbidden reflection) is set in the Bragg reflection and also some other reciprocal points are on the Ewald sphere together with the <222> one (which is one of our experimental cases), the obtained possible neutron diffraction signal may consist of individual contributions coming from the allowed reflections Si(111), Si(333), Si(444) etc. as well as from MBR-effects accompanying Si(111), Si(222), Si(333), Si(444), etc. The symmetric transmission geometry has appeared to be the easiest diffraction geometry for MBR studies in the elastically deformed (cylindrically bent) perfect crystals where mutual orientation of the scattrering vector $\boldsymbol{g}$ with respect to the deformation vector $\boldsymbol{u}$ plays an enormous role in the reflectivity properties of the deformed crystal. According to e.g. ref. 18 and 19 the integrated reflectivity of a deformed crystal is a function of the scalar product $(\boldsymbol{g}\cdot\boldsymbol{u})$ which may be zero for both forbidden and its higher order reflections, i.e. $(\boldsymbol{g_1}\cdot\boldsymbol{u})=0$, $((\boldsymbol{g_1}/n)\cdot\boldsymbol{u}))=0$. It means that the corresponding integrated reflectivities are independent of the deformation represented by the displacement of atoms $\boldsymbol{u}$ [20,21]. This is also valid for our chosen case of the cylindrical bending and symmetric transmission geometry. On the other hand $(\boldsymbol{g_2}\cdot\boldsymbol{u}) = -(\boldsymbol{g_3}\cdot\boldsymbol{u})$ need not be zero and the deformation can bring about a large increase of the MBR-effect keeping the integrated reflectivity related to the primary reflection and higher order primary reflections constant at the value of the perfect

crystal. Therefore, for the investigation of the MBR- effects by the TOF method three Si slabs of different cut but all set in the symmetric transmission diffraction geometry were used (see figures 3 and 4). Several rather strong MBR effects already known from the earlier diffraction measurements carried out by the θ–$2\theta_D$ scanning in the white beam for a fixed azimuthal angle ϕ=0° have been chosen for these TOF studies. Parts of the related θ–$2\theta_D$ scans taken from ref. [14,15] where the chosen MBR effects for the TOF measurements are marked by arrows are shown in figures 5-7.

3. TOF experimental results

For indexing of the MBR-effects accompanying allowed or forbidden reflections we refer to the calculation procedures introduced e.g. in the papers [17,22,23]. Figures 8-10 show the calculated parts of the azimuth-Bragg angle relationships for the basic 222 and 002 primary reflections of the diamond structure and the chosen experimental points related to the MBR peaks labeled by arrows (see figures 5-7) are marked by circles. The indexes of individual lines in figures 8-10 correspond to the secondary reflections which can bring about the MBR effect

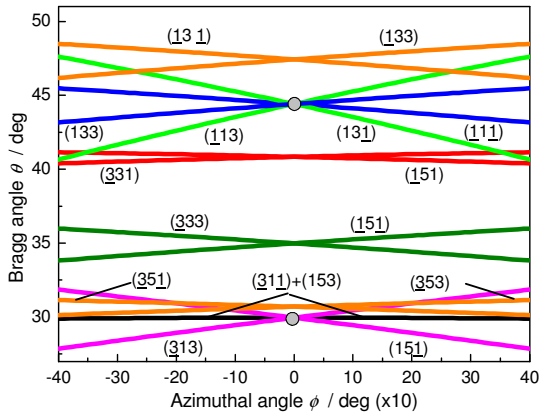

Figure 8. Part of the azimuth–Bragg angle relationships for the 222 primary reflections of the diamond structure for the slab having the main face parallel to (1$\underline{1}$0) planes.

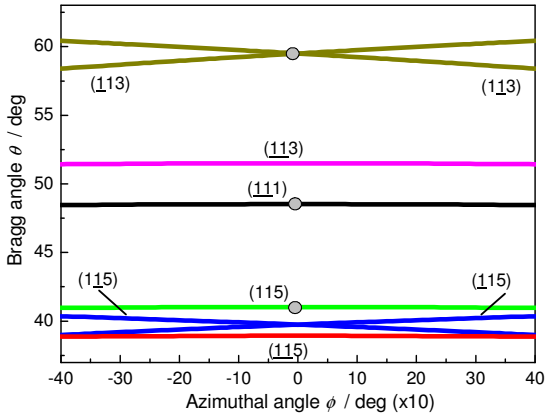

Figure 9. Part of the azimuth–Bragg angle relationships for the 222 primary reflections of the diamond structure for the slab having the main face parallel to (11$\underline{2}$) planes.

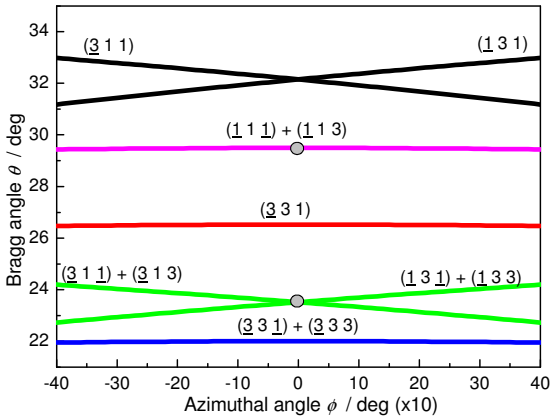

Figure 10. Part of the azimuth–Bragg angle relationships for the 002 primary reflections of the diamond structure for the slab having the main face parallel to (1$\underline{1}$0) planes.

with respect to the chosen primary reflection. The cooperative tertiary reflection can be simply calculated from the substraction of the indexes of the primary and secondary reflections as (h_p-h_s, k_p-k_s, l_p-l_s)=(h_t,k_t,l_t) (see figure 2).

The TOF experimental investigations were carried out on the linac based small accelerator cold neutron source at the Hokkaido University in Sapporo. By using the performance schematically shown in figure 4 and the flight path of about 7 m the TOF spectra were collected at the marked points (see figures 5-10) related to three chosen Si slabs of different cut. The following figures 11-17 display the obtained TOF spectra. In principle, in the case of the first two crystal slabs one could

expect to see Si(111) reflections as well as the related possible MBR effects. As no such reflections were observed, for a better visibility of other effects at shorter neutron wavelengths only parts of the spectra ending at the channel number 600 (from possible 1024) are displayed. Moreover, it is known that the shorter neutron wavelength the higher the density of reciprocal points in the reciprocal space. Consequently, also the number of pairs of secondary/tertiary reflections increases.

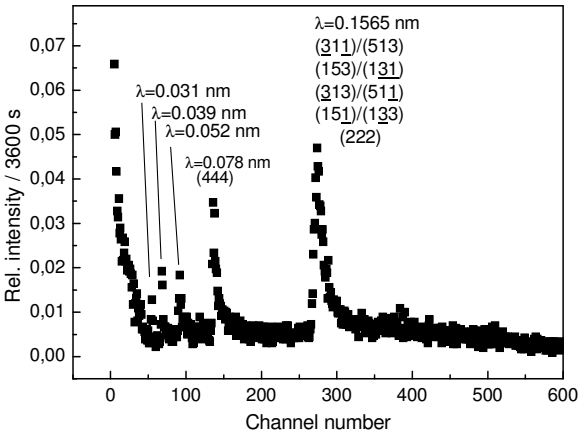

Figure 11. TOF spectrum taken with the bent crystal slab (R=8 m) of the thickness of 3.7 mm set for forbidden Si(222) reflection at θ=30° (see figures 5 and 8).

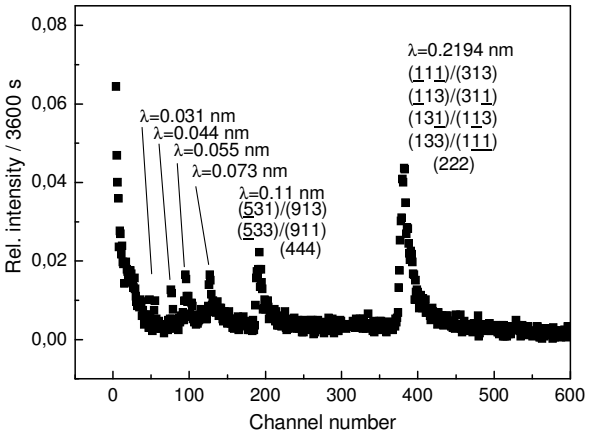

Figure 12. TOF spectrum taken with the bent crystal slab (R=8 m) of the thickness of 3.7 mm set for forbidden Si(222) reflection at θ=44.4° (see figures 5 and 8).

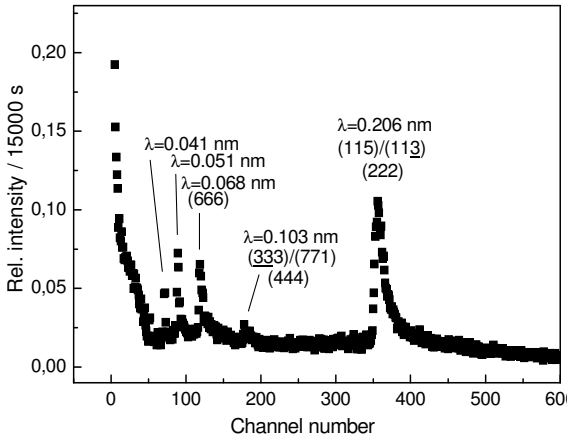

Figure 13. TOF spectrum taken with the bent crystal slab (R=10 m) of the thickness of 4.1 mm set for forbidden Si(222) reflection at θ=41° (see figures 6 and 9).

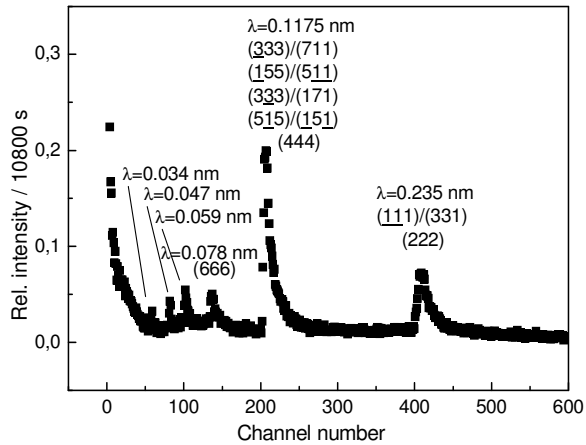

Figure 14. TOF spectrum taken with the bent crystal slab (R=10 m) of the thickness of 4.1 mm set for forbidden Si(222) reflection at θ=48.5° (see figures 6 and 9).

Therefore, in the present case, indexing of higher order MBR-effects was not calculated but only the expected neutron wavelengths (λ/n) are marked. The inspection of the figures 11-17 reveals the following effects. In all cases of figures 11-15 the forbidden Si(222) reflection is simulated by strong MBR effects and also accompanied by higher order MBR effects. However, the second order MBR effect is very weak in figure 13 and it is missing in figure 15. As the Si(444) reflection is allowed, it also means that its contribution due to the symmetric transmission geometry is very small which

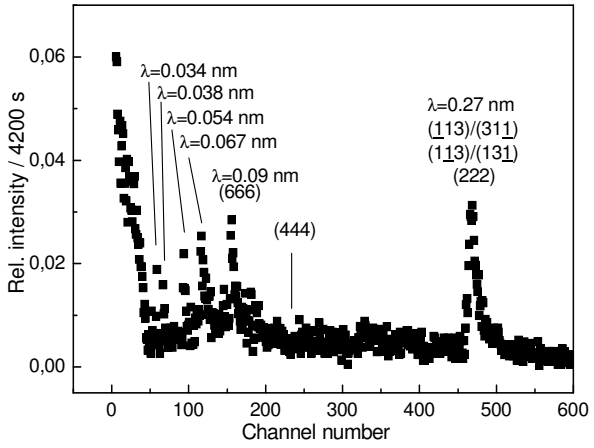

Figure 15. TOF spectrum taken with the bent crystal slab (R=10 m) of the thickness of 4.1 mm set for forbidden Si(222) reflection at θ=59.5° (see figures 6 and 9).

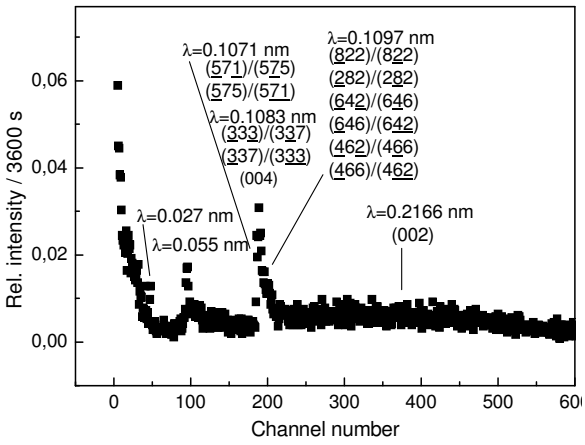

Figure 16. TOF spectrum taken with the bent crystal slab (R=10 m) of the thickness of 4.1 mm set for forbidden Si(002) reflection at θ=23.5° (see figures 7 and 10).

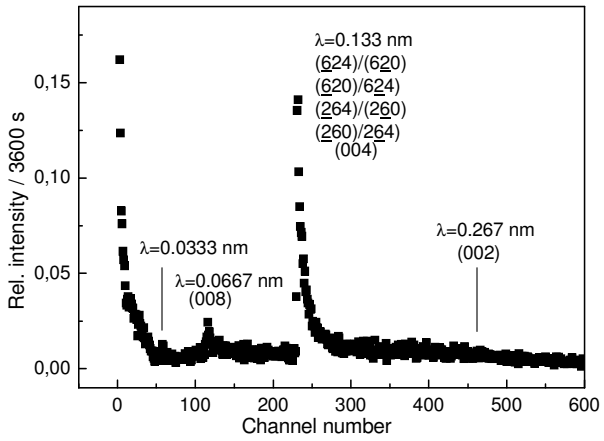

Figure 17. TOF spectrum taken with the bent crystal slab (R=10 m) of the thickness of 4.1 mm set for forbidden Si(002) reflection at θ=29.5° (see figures 7 and 10).

corresponds to a perfect nondeformed crystal (see the text in the former paragraph). On the other hand in the case of searching the MBR effect with respect to the forbidden Si(002) reflection, none was observed. But second orders MBR effects accompanying allowed Si(004) reflection are very strong.

4. Summary

On the basis of the obtained experimental results it can be stated that the MBR-effects could be considerably strengthened by elastic deformation and can be investigated by the TOF method even at small accelerator based neutron sources. TOF spectra allow us to distinguish contributions of higher orders from the first order. Thanks to homogeneous elastic deformation of the perfect single crystal the double diffraction process can be simply assumed as a diffraction by a bicrystal system consisting of two different (deformed) single crystals mutually in the dispersive setting. As has been already tested at the steady state sources, the double diffracted beam is highly monochromatic and highly collimated. The double diffracted beam may have the cross-section of several square centimetres. Strong MBR effects can be used e.g. in high resolution neutron diffractometry, in neutron radiography, for precise determination of the neutron wavelength an thus for a possible spectroscopic characterisation of neutron sources. On the other hand, MBR effects can bring about severe limitations in precise structural investigations, namely when elastically deformed crystals are used as samples.

Acknowledgements

Bragg diffraction optics investigations are in the Czech Republic supported by GACR project no. 14-36566G, by the ESS project LM2010011: 'Contribution to Partnership in Large Research Infrastructure of Pan-European Importance' as well as by the project of EU-FP7-NMI3 II: "Integrated Infrastructure Initiative for Neutron Scattering and Muon Spectroscopy", 2009-2015.

References

[1] Ewald P P 1937 *Z. Kristallogr*. **A97** 1.
[2] Renninger M 1960 *Z. Kristallogr*. **113** 99.
[3] Pinsker Z G 1978 *Dynamical Scattering of X-rays in Crystals*. Berlin: Springer-Verlag.
[4] Chang S H 1984 *Multiple Diffraction of X-rays in Crystals*, Springer Verlag, Berlin; 1987 Moscow, Mir (Russian translation).
[5] Moon R and Shull C G 1964 *Acta Cryst*. **17** 805.
[6] Kuich G and Rauch H 1965 *Acta Phys. Austriaca* **20** 7.
[7] Kuich G and Rauch H 1967 *Nukleonik* **9** 139.
[8] Thomson P and Grimes N V 1977 *J. Appl. Cryst.* **10** 369.
[9] Seong B S, Shin E, Lee C H, Em V T and Shim H S 2001 *J. Neutron Res.* **9** 363.
[10] Mikula, P., Michalec, R.T., Vrána, M. and Vávra, J 1979 *Acta Cryst*. **A 35** 962.
[11] Mikula P, Vrána M, Michalec R T, Kulda J and Vávra J 1980 *Phys. Stat. Sol.(a)* **460** 549.
[12] Vrána M, Mikula P, Michalec R T, Kulda J and Vávra J 1981 *Acta Cryst*. A**37** 459.
[13] Mikula P, Kulda J, Vrána M, Michalec R T. and Vávra J 1982 *Nucl. Instrum. Methods* **197** 563.
[14] Mikula P, Vrána M and Wagner V 2004 *Physica B* **350** e667.
[15[Mikula P, Vrána M and Wagner V 2006 *Z. Kristallogr. Suppl*. **23** 205.
[16] Mikula P, Vrána M, Šaroun J, Seong B S, Em V and Moon M K 2011 *Nucl. Instrum. Methods in Phys. Res.* A, **634** S108.
[17] Mikula P, Vrána M, Šaroun J, Em V, Davydov V and Seong B S 2012 *J. Appl. Cryst.* **45** 98.
[18] Kulda J and Mikula P 1985 *Phys. Stat. Sol. (a)* **92** 95.
[19] Takagi S 1969 *J. Phys. Soc. Japan* **26** 1239.
[20] Mikula P, Kulda J, Vrána M and Chalupa B 1984 *J. Appl. Cryst*. **17** 189.
[21] Alexandrov Yu A, Eichhorn F, Kulda J, Lukáš P, Machekhina T A, Michalec R, Mikula P, Sedláková L N and Vrána M 1988 *Physica B* **151** 108.
[22] Cole H, Chambers F W and Dun H M 1962 *Acta Cryst.* **15** 138.
[23] Kotwitz D A 1968 *Acta Cryst*. **A24** 117.

3.5.9

Recent progress in the chopper spectrometer 4SEASONS at J-PARC

R Kajimoto[1], M Nakamura[1], Y Inamura[1], K Kamazawa[2], K Ikeuchi[2], K Iida[2], M Ishikado[2], K Nakajima[1], S Ohira-Kawamura[1], T Nakatani[1], W Kambara[1], H Tanaka[1], Y Yamauchi[1], K Aoyama[1], T Hosoya[1], K Kiriyama[2], K Aizawa[1] and M Arai[1]

[1] Materials and Life Science Division, J-PARC Center, Japan Atomic Energy Agency, Tokai, Ibaraki 319-1195, Japan

[2] Research Center for Neutron Science and Technology, Comprehensive Research Organization for Science and Society (CROSS), Tokai, Ibaraki, 319-1106, Japan

E-mail: ryoichi.kajimoto@j-parc.jp

Abstract. 4SEASONS is a thermal neutron chopper spectrometer operated in the Materials and Life Science Experimental Facility at the Japan Proton Accelerator Research Complex. This instrument has been available to users since 2009, and was declared a public beamline in 2011. On the other hand, the instrument continues to be upgraded by installation of more detectors, development of new choppers, and further attempts to decrease the background scattering. In this article, we review how these progresses have improved the instrument performance and present some results of machine investigations.

1. Introduction

4SEASONS (aka *SIKI* in Japanese) is one of the four chopper spectrometers in the Materials and Life Science Experimental Facility (MLF) at the Japan Proton Accelerator Research Complex (J-PARC). The instrument is designed for measurements of dynamics in the 10^0–10^2 meV energy range with relaxed resolution and high flux [1, 2]. 4SEASONS was originally developed to investigate high critical-temperature (high-T_c) oxide superconductors, and the first inelastic scattering experiment was performed in 2009. Since 2011, 4SEASONS has been classified as a public beamline, and its use has extended to a wider range of studies including chemistry and industry, although studies of superconductors and related materials still comprise the largest proportion of experimental proposals.

A detailed understanding of the instrument's performance is being actively sought, and the instrument continues to be upgraded [3–9]. In this article, we review the recent studies on the performance and the upgrading works of this instrument.

2. Specifications and upgrades of 4SEASONS

2.1. Basic specifications

First, we briefly describe the specifications of the instrument [2]. A schematic of 4SEASONS is presented in Fig. 1. 4SEASONS is installed in the BL01 beamline, whose neutron source is the coupled moderator of supercritical hydrogen [10]. Neutrons are transported through a straight

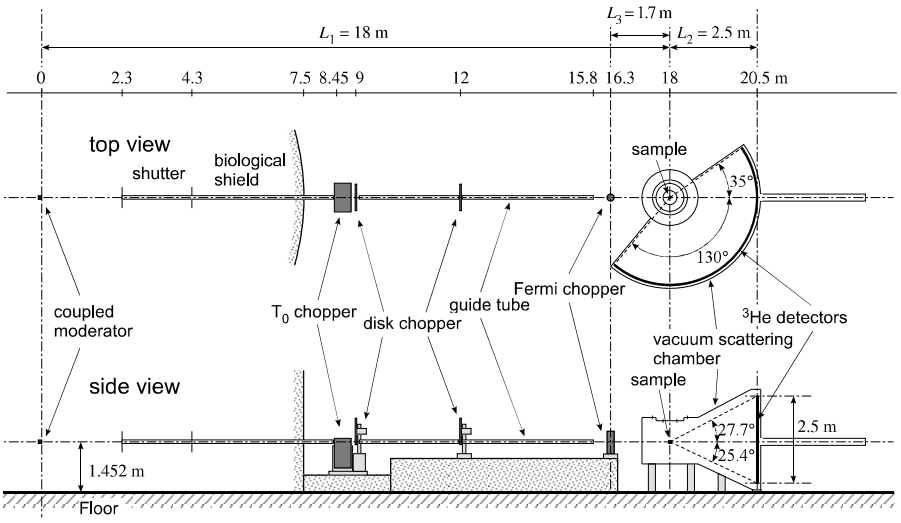

Figure 1. Schematic view of 4SEASONS [2].

neutron guide tube coated with supermirrors, which is installed between 2.3 m downstream from the moderator and 2.2 m upstream from the sample. The cross section of the guide tube gradually decreases with increasing distance from the moderator, focusing neutrons on the sample at $L_1 = 18$ m from the moderator. The m value of the supermirror (ratio of the critical angle to that of the Ni mirror) varies from 3.2 to 4 as a function of the distance [2, 11]. The ∼10–500 meV incident neutrons are monochromated by a fast-rotating Fermi chopper positioned at $L_3 = 1.7$ m upstream from the sample. By taking advantage of the fact that the chopper rotates considerably faster than the repetition rate of the neutron source [12, 13], 4SEASONS can simultaneously perform measurements at multiple incident energies (Multi-E_i measurements) [14]. In addition to the Fermi chopper, there is a T_0 chopper for suppressing fast neutrons and two disk choppers for band definition. The neutrons scattered from the sample are detected over time by the detectors placed $L_2 = 2.5$ m from the sample. The time-of-flight data are acquired by the data acquisition system based on the event-recording [15]. These data are converted to the dynamical structure factor by the software package Utsusemi, which provides a flexible data analysis environment ranging from primitive histogramming of the time-of-flight data to slice-and-cut of single crystal data in the four-dimensional momentum-energy space [3, 16].

2.2. Detectors

4SEASONS is equipped with ^{3}He position-sensitive detectors (PSDs), each having a diameter of 19 mm and length of 2.5 m, cylindrically arranged around the sample (See Fig. 5). The detector bank can be installed with 352 PSD pieces, covering horizontal angles from −35.3° to +130.5° relative to the direct beam. Until recently, however, the angular coverage by the PSDs was only −35.3° to +54.5°. Although such limited range of the scattering angle does not preclude magnetic excitation measurements, it evidently restricts the research targets of the instrument. Unfortunately, the recent ^{3}He crisis prevents us from completely filling the detector bank in the near future. Nevertheless, we are trying to extend the detector coverage as best we can, and PSDs are newly added to the instrument each year. Currently, the maximum horizontal scattering angle is 84.0° (as at the end of fiscal 2014), and is expected to reach 90° in fiscal 2015. The extended detector coverage has already benefited measurements of phonons or atomic vibrations in strongly correlated electron systems and industrial materials.

The PSDs are installed in a vacuum environment; namely, on the posterior wall of the vacuum

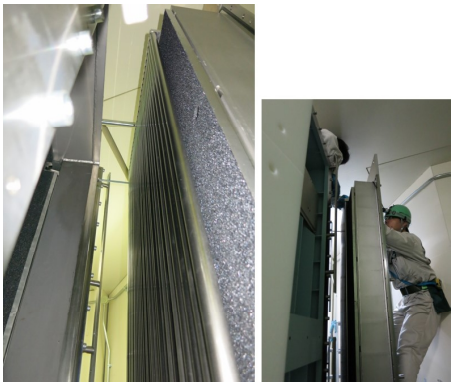

Figure 2. MLF technical staff installing PSDs on one of the detector panels of 4SEASONS.

scattering chamber. This wall, which constitutes the detector bank of 4SEASONS, comprises 11 panels, each of which can hold 32 PSD pieces. Each panel was originally designed to be detached from the vacuum scattering chamber by an overhead crane in the experimental hall. For PSD installation, we had to remove a detector panel from the shielding house using the crane, and lay it upon the floor. However, this proved to be a troublesome task, particularly when frequently installing a small number of PSDs. Recently, we developed a compact jig that slides and fixes one of the detector panels inside the shielding house, which significantly eases the task of installing and uninstalling PSDs. In Fig. 2, MLF staff members use this jig to install PSDs.

2.3. Fermi chopper

The Fermi chopper of 4SEASONS is uniquely characterized by its straight slits. This Fermi chopper allows neutron transmission at every π rotations of the chopper, increasing the number of available E_is in the Multi-E_i measurements [14]. Because straight slits incur greater transmission losses than curved slits, we adopted a wide (sloppy) slits to compensate the extra loss. Each slit is 2 mm wide and 100 mm deep (the width and depth dimensions are dented by w and D, respectively). With this geometry and a rotating frequency f of 600 Hz, the opening time of the Fermi chopper $\Delta t_\mathrm{ch} = w/(2\pi D f)$ equals the pulse width of the moderator Δt_m at $E_\mathrm{i} = 500$ meV [2].

Our straight-slit chopper adopts the same depth dimension as traditional curved-slit choppers ($D = 100$ mm). This dimension is not exactly optimized for the Multi-E_i measurements, because it is too deep to transmit low energy neutrons (energies typically below $\sim$10 meV). Thus, we developed a new Fermi chopper with much shorter slits ($D = 20$ mm). To maintain the spatial divergence w/D of the original chopper, each slit of the new chopper is 0.4 mm wide.

The performance of the new Fermi chopper was estimated in Monte Carlo simulations using the simulation package McStas [17, 18]. Figure 3 compares the calculated energy resolution and neutron flux between the current long-slit chopper and the new short-slit chopper. As the parameter w/D is identical, the energy resolutions of both choppers nearly coincide. On the other hand, the short-slit chopper permits considerably higher neutron flux than the long-slit chopper, particularly at low energies. These results suggest that the new chopper will significantly enhance the performance of 4SEASONS by adopting the new chopper. The new chopper has already been manufactured and delivered to MLF, and will soon be tested with the neutron beam soon.

2.4. Effect of the guide tube on energy resolution

Energy resolution is an essential indicator of instrument performance, and must be correctly estimated to optimize the experimental conditions and improve the chopper design. While

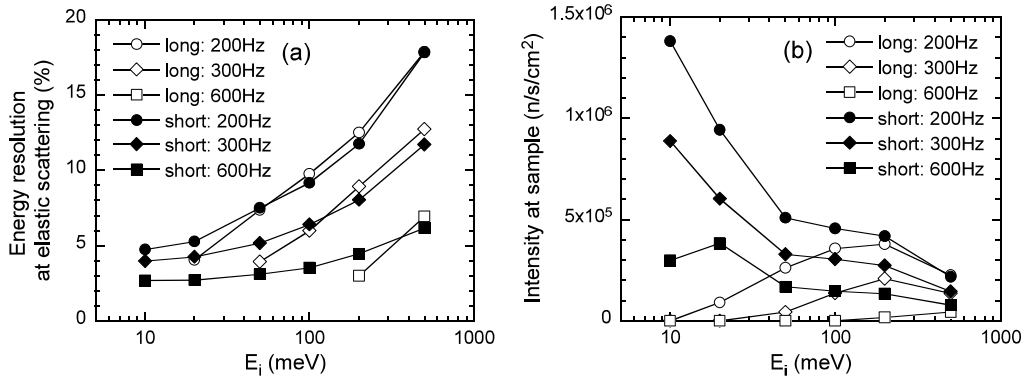

Figure 3. Energy resolution and neutron flux obtained by Monte Carlo simulations of the long-slit chopper (open symbols) and the short-slit chopper (closed symbols) at $f = 200$, 300, and 600 Hz [19]. (a) Energy resolution at the elastic scattering; (b) Neutron flux on a $(2\times2)\,\mathrm{cm}^2$ sample, assuming 1 MW proton beam power.

estimating the energy resolution of a Fermi chopper spectrometer, we must consider the angular divergence of the neutron beam [20]. Beam divergence effects are particularly important if the spectrometer has a neutron guide tube, as does 4SEASONS.

The energy resolution of a chopper spectrometer relative to the incident energy E_i at the energy transfer $\hbar\omega$ is given by the well-known formula [20]

$$\frac{\Delta\hbar\omega}{E_\mathrm{i}} = 2\sqrt{\left\{\frac{\Delta t_\mathrm{ch}}{t_\mathrm{ch}}\left[1+\frac{L_1}{L_2}\left(1-\frac{\hbar\omega}{E_\mathrm{i}}\right)^{\frac{3}{2}}\right]\right\}^2+\left\{\frac{\Delta t_\mathrm{m}}{t_\mathrm{ch}}\left[1+\frac{L_3}{L_2}\left(1-\frac{\hbar\omega}{E_\mathrm{i}}\right)^{\frac{3}{2}}\right]\right\}^2+\left[\frac{\Delta L_2}{L_2}\left(1-\frac{\hbar\omega}{E_\mathrm{i}}\right)\right]^2}, \quad (1)$$

where the path length uncertainty ΔL_2 results from the sample and detector sizes, and t_ch is the neutron time-of-flight from the moderator to the Fermi chopper. For a Fermi chopper with finite depth D, Δt_ch is effectively increased by the angular divergence of the incident neutrons $\Delta\phi_\mathrm{i}$, and becomes [20]

$$\Delta t_\mathrm{ch} = \frac{w}{2\pi D f}p(u). \quad (2)$$

Here $p(u)$ represents the increase in Δt_ch by the angular divergence, and is given by

$$p(u) = \begin{cases} 0 < u < 0.8: & p(u) = 1 + u/4, \\ 0.8 < u < 2: & p(u) = 2 + u - (4u - u^2)^{1/2}, \\ 2 < u: & p(u) = u, \end{cases} \quad (3)$$

where the parameter u is the ratio of $\Delta\phi_\mathrm{i}$ to the angular collimation, defined by the geometry of the slits w/D:

$$u = \Delta\phi_\mathrm{i}/(w/D). \quad (4)$$

In the absence of a guide tube, the $\Delta\phi_\mathrm{i}$ of the chopper spectrometer is constant and determined by the geometry of the instrument [20]. However, in 4SEASONS, neutrons are reflected off the supermirror-coated guide tube; therefore, the $\Delta\phi_\mathrm{i}$ depends on E_i. Specifically, we have

$$\Delta\phi_\mathrm{i} \sim 2\theta_\mathrm{c} \propto E_\mathrm{i}^{-1/2}, \quad (5)$$

where θ_c is the critical reflection angle of the supermirror. Assuming that $\Delta\phi_\mathrm{i}$ is determined by the θ_c of the supermirror at the end of the guide tube, as described in Ref. 5, we can

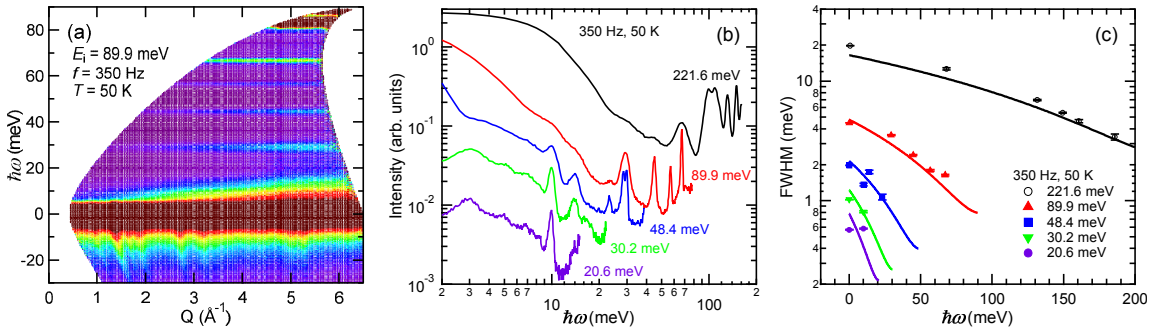

Figure 4. (a) Neutron scattering intensity map of $C_4H_2I_2S$ at $T = 50\,\mathrm{K}$ with $E_\mathrm{i} = 89.9\,\mathrm{meV}$ and $f = 350\,\mathrm{Hz}$. Several non-dispersive modes are clearly observed at $\hbar\omega = 29.3(1)$, 44.8(1), 56.8(1), and 67.0(1) meV, which originate from rotational and vibrational energy modes [21, 22]. (b) Neutron scattering intensities as functions of $\hbar\omega$ at various E_i with $f = 350\,\mathrm{Hz}$, obtained by slicing the neutron scattering intensity maps along the $\hbar\omega$ direction. Data are offset along the vertical axis for clarity. (c) Measured energy resolutions as functions of $\hbar\omega$ at various E_i with $f = 350\,\mathrm{Hz}$, deduced from the FWHMs of the peaks observed in the energy spectra in (b). Solid lines are the energy resolutions for each E_i calculated by Eq. (1), accounting for the angular divergence of the neutron beam [7].

reproduce the observed energy resolution under both elastic and inelastic scattering conditions (see Fig. 4) [2, 7].

The E_i dependence of $\Delta\phi_\mathrm{i}$ significantly influences the optimal energy resolution in a Multi-E_i experiment. If the experimental conditions are optimized, Δt_ch will be comparable to Δt_m in Eq. (1). Δt_m decreases as E_i increases, becoming proportional to $E_\mathrm{i}^{-1/2}$ in the slowing-down region of the moderator ($E_\mathrm{i} \gtrsim 20\,\mathrm{meV}$). Therefore, we cannot optimize the energy resolution at all E_i's in the Multi-E_i measurement, if Δt_ch is independent of E_i, as naively expected for a Fermi chopper rotating at a fixed speed. However, according to Eqs. (2)–(5), Δt_ch and Δt_m are both proportional to $E_\mathrm{i}^{-1/2}$ when w/D is considerably smaller than $\Delta\phi_\mathrm{i}$. Therefore, the energy resolution can be optimized at most of the E_i's by appropriately choosing the rotating frequency of the chopper [5]. On the basis of these considerations, we are developing a new Fermi chopper that optimizes the energy resolution over a wide range of E_i in the Multi-E_i measurements [5, 23, 24].

3. Background scattering problems

3.1. Vanes in the vacuum scattering chamber

As stated in § 2.2, the detectors of 4SEASONS are housed on the detector bank in the vacuum scattering chamber, which constitutes the posterior wall of the chamber. Recently, the gaps between the neighboring detector panels were installed with vertical vanes made of B_4C resin [Fig. 5(a)]. Located parallel to the scattered beam path, these vanes prevent cross-talk of neutrons between the detectors in the chamber. Each vane is 20 mm thick and 530 mm long, where the length is oriented along the beam path. These vane dimensions do not create shadows on the detectors.

To evaluate the effect of the vanes on the background scattering, we measured the inelastic scattering of a test sample that produces weak magnetic excitation signals. Figures 6(a) and 6(b) show the inelastic scattering intensities of a single crystal of $La_{1.92}Sr_{0.18}CuO_4$ at $\sim$5 K before and after vane installation. The data are cross-cut at $\hbar\omega = 125 \pm 15\,\mathrm{meV}$ and presented on the (H, K) plane in the reciprocal lattice. As the (H, K) plane was arranged perpendicular to the

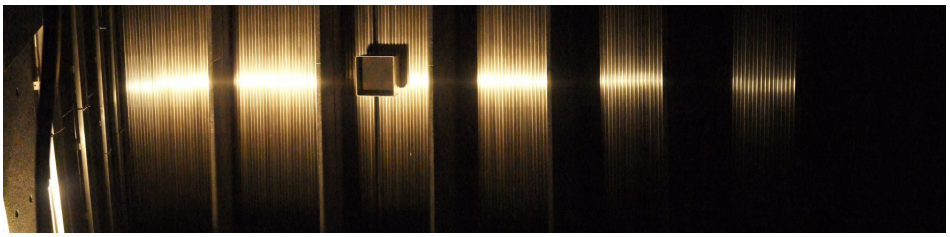

Figure 5. ^{3}He detector tubes and B_4C resin absorbing vanes, installed inside the vacuum scattering chamber of 4SEASONS [4]. The square block is the beam stop, also made of B_4C resin.

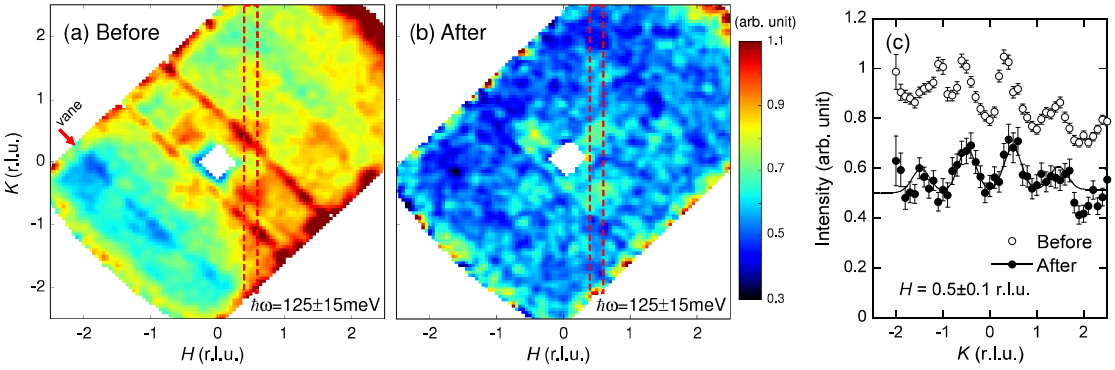

Figure 6. (a) and (b) Intensity maps of the inelastic scattering spectra, measured from a single crystal of $La_{0.82}Sr_{0.18}CuO_4$ at $\sim$5 K with $E_i = 204$ meV before and after the installation of the vanes, respectively [4]. The data are cross-cut at $\hbar\omega = 125 \pm 15$ meV and projected onto the (H, K) plane. The power of the proton beam and the measurement time of the data are 220 kW and 23 h, respectively, in (a), and 120 kW and 8 h, respectively, in (b). The difference in the utilized neutron fluxes is normalized by the proton beam currents. (c) Slices of the data in (a) (open symbols) and (b) (closed symbols) at $H = 0.5 \pm 0.1$. The sliced regions are enclosed by red dotted lines in (a) and (b). Solid line in (c) fits the closed symbols to four Gaussians multiplied by the magnetic form factor for Cu $3d_{x^2-y^2}$ [25].

incident beam, the observed data reflect the geometry of the detector bank. When measuring the data in Fig. 6(a), we had already installed one B_4C vane in a gap between two detector panels; the position of this vane is indicated by the arrow in Fig. 6(a). Although magnetic excitation signals are visible at $(\pm 0.5, \pm 0.5)$ in Fig. 6(a), the entire detector bank (except for the area to the left of the vane) is severely contaminated by the high background. Furthermore, several streaks appear at the positions corresponding to the gaps between the detector panels. These streaks are attributed to neutrons that were scattered by the gaps and subsequently hit the adjacent detectors. In contrast, the vane installation considerably reduces the background over the entire detector bank, and the unwanted streaks completely vanish.

The data in Figs. 6(a) and 6(b) were sliced along the K direction at $H = 0.5 \pm 0.1$, and the slices are presented in Fig. 6(c). The vane installation reduced the background intensity by approximately 40% [cf. closed and open symbols in Fig. 6(c)]. Although the background intensity was not diminished by the vane installation, they should now reflect the intrinsic background introduced by the multi-phonons in the large (96 g) sample. Because of difference in beam power and measurement time, the neutron flux of the data in Fig. 6(b) [and the closed symbols in Fig. 6(c)] is approximately 1/6th that of the data in Fig. 6(a) [and the open symbols

Figure 7. MLF technical staff installing the radial collimator on 4SEASONS.

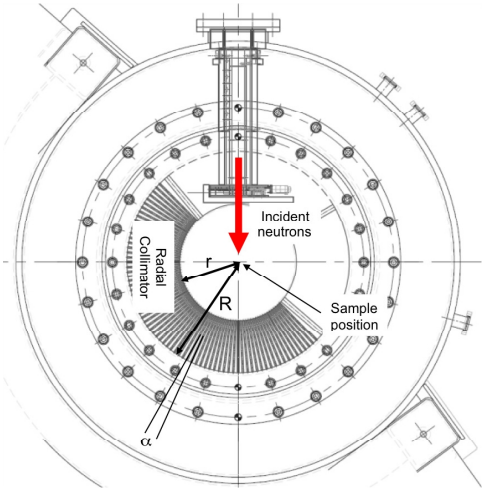

Figure 8. Schematic of a part of the 4SEASONS vacuum scattering chamber installed with the radial collimator. r, R, and α indicate the inner radius, outer radius, and angular separation of the collimator blades, respectively [9].

in Fig. 6(c)]. This reduced neutron flux worsens the statistics of the former data. Nevertheless, the signal-to-noise ratio is sufficiently improved to reveal clear peaks at $K = \pm 0.5$ in Fig. 6(c). Even weaker peaks, whose intensities are reduced by the Q (momentum transfer) dependence of the magnetic form factor, are observable at $K = \pm 1.5$. On the other hand, in the absence of the vanes, the data are contaminated by the high background and the streaks observed in Fig. 6(a), yielding an incorrect excitation profile [see open symbols in Fig. 6(c)].

3.2. Radial collimator

To minimize scattering from the sample environment such as the cryostat or sample can, we have developed a radial collimator [9], an assembly of vertical absorbing blades that radially encloses the sample (Fig. 7). Each blade is an aluminum plate of thickness 100 μm coated on both surfaces with a 25 μm-thick cadmium plating (i.e. the total thickness is 150 μm). By choosing cadmium as the absorbing material, we ensure that the blade contains no hydrogenous materials, and is therefore free of neutron scattering by hydrogen atoms [9]. Figure 8 illustrates the top view of the vacuum scattering chamber of 4SEASONS installed with the radial collimator. The radial collimator is attached to the 800 mm flange of the vacuum scattering chamber, and provides an aperture of the 400 mm flange used by the standard sample environmental devices of MLF. The collimator comprises 72 vertical blades covering a horizontal angular range of -45° to $+135^\circ$. The inner radius r and outer radius R of the collimator are 210 mm and 400 mm, respectively. The angular separation α between the blades is 2.5°. From these dimensions, the diameter of the visible sample d [26] is estimated as $\alpha \cdot rR/(R-r) = 19.3$ mm.

To evaluate the performance of the radial collimator, we compared the elastic neutron scattering profiles in the presence and absence of the collimator. Figure 9 plots the elastic scattering profiles of an 8.5-mm-diameter rod of vitreous silica (v-SiO_2) inserted in a top-loading cryostat. The inner wall of the cryostat is an aluminum cylinder with a 100 mm diameter. In the absence of the radial collimator, the aluminum wall gives rise to strong peaks at certain Q positions (indicated by arrows in Fig. 9). Broad peaks from the non-crystalline SiO_2 are also observed. With the radial collimator installed, the aluminum peaks are significantly

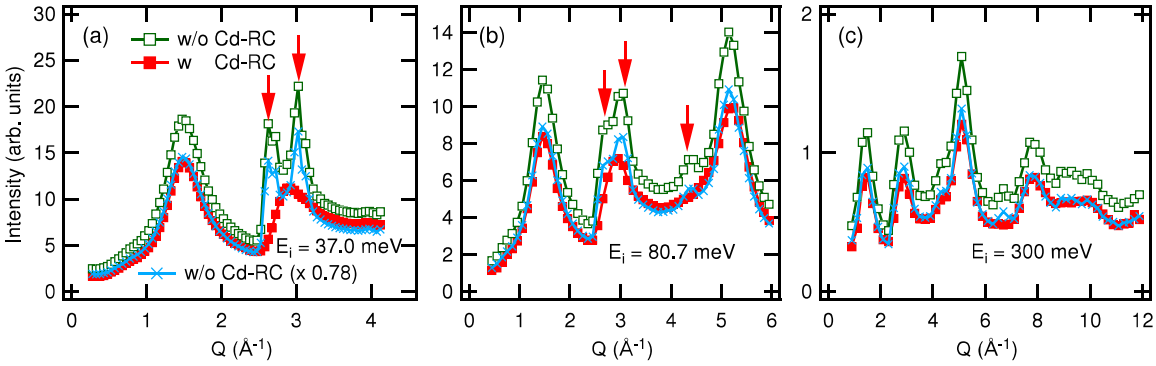

Figure 9. Q dependences of elastic structure factor for v-SiO_2, measured with (solid squares) and without (open squares) the radial collimator with (a) $E_i = 37.0$ meV, (b) 80.7 meV, and (c) 300 meV. Crosses show the intensity of the data without the radial collimator multiplied by 0.78.

attenuated, demonstrating the effectiveness of the radial collimator in suppressing scattering from the sample environment. On the other hand, the radial collimator reduces the intensity of data to approximately 78% that of data collected without the collimator. Given that the size of the sample (8.5 mm) is considerably less than the visible sample size ($d = 19.3$ mm), this transmission is too low . We speculate that intensity might be lost by slight distortion of the cadmium blades. Although this problem is ongoing, the radial collimator has been already used in several measurements. It proved particularly useful in phonon measurements, where the target inelastic scattering signals are often superimposed by aluminum phonons.

3.3. Delayed neutron background

Another major cause of background in instruments such as 4SEASONS, which utilize straight beamlines at spallation neutron sources, is high-energy neutrons that reach the secondary spectrometer directly from the source. Most of these high-energy neutrons are produced when the proton beam hits the neutron target at the time-of-flight $t \equiv 0$ (T_0), and are detected shortly afterward. Such high-energy neutrons are usually suppressed by a T_0 chopper with a thick metal blade [27]. 4SEASONS is equipped with a T_0 chopper with a 300-mm-thick Inconel hammer, which successfully suppresses this class of high-energy neutrons [2, 28]. However, we recently revealed another type of background caused by very fast neutrons that are continuously emitted from the source and transported along the beamline [8]. Although these neutrons are influenced by the Fermi chopper, their ultra-high energies cannot be suppressed by the Fermi chopper. Consequently, the background at the detector oscillates synchronously with the rotational period of the Fermi chopper (see dashed lines in the time-distance plot of Fig. 10). This background is likely sourced by delayed neutrons produced through the β^- decay of nuclides included in the spallation products in the mercury target of MLF [29].

Figure 11 shows a typical time spectrum of the delayed-neutron background. Under the conditions of these data, the incident neutrons that would reach the detector at $t \gtrsim 22\,000\,\mu$s are discriminated by the band choppers, and are further impeded by the long slits of the Fermi chopper. Therefore, no elastic-scattering peak appears in this time region. However, a finite and constant intensity exists [indicated by the dashed line in Fig. 11(a)]. This intensity sharply decreases at $t \sim 40\,000\,\mu$s, when the beamline is blocked by the hammer of the T_0 chopper rotating at 25 Hz. Closer inspection of the time spectrum reveals a temporal oscillation of the background [Fig. 11(b)], which can be decomposed into two oscillations; one with sharp strong peaks [dashed lines in Fig. 11(b)], the other with broader and weaker peaks [dash-dotted lines in Fig. 11(b)]. The sharper and broader peaks coincide with the times of opening the Fermi

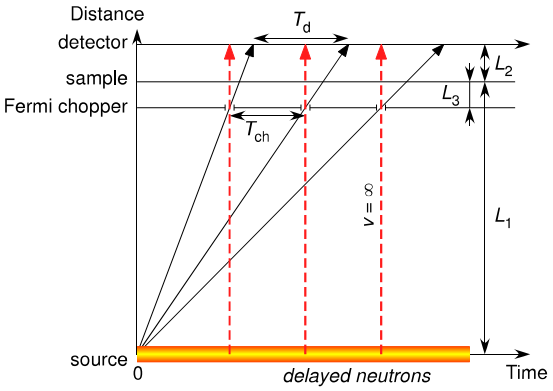

Figure 10. Time-distance diagram of chopper spectrometer [8]. Solid and dashed lines indicate elastic scattering and delayed neutrons, respectively, that pass through the Fermi-chopper opening, which has a period of T_{ch}. Note that T_{ch} is different from the period of the elastic scattering at the detector T_d.

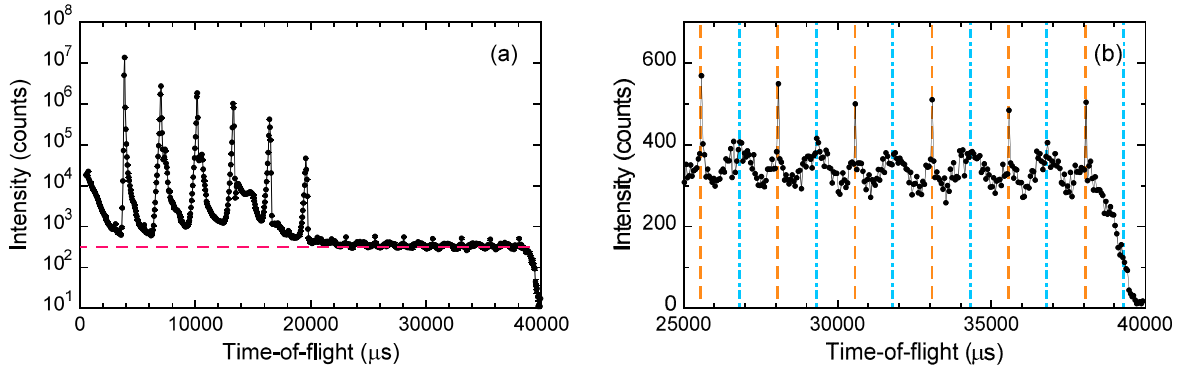

Figure 11. (a) Time spectrum of a single crystal of $La_2CoO_{4.24}$ measured at 6 K for 1.5 d at a proton-beam power of 290 kW [8]. The sharp peaks represent elastic scattering of neutrons with incident energies (in order of increasing time) $E_i = 149$, 45.1, 21.4, 12.5, 8.2, and 5.8 meV. The tails on each elastic-scattering peak manifest from inelastic scattering from the sample. The dashed line indicates the background discussed in the text. (b) Magnified view of panel (a) in the range $20\,000\,\mu s \leq t \leq 40\,000\,\mu s$. Dashed and dash-dotted lines indicate the times of opening the Fermi chopper and rotating it by $\pi/2$, respectively.

chopper and rotating it by $\pi/2$, respectively.

A similar oscillating background was observed by a chopper spectrometer at the ISIS facility of the Rutherford Appleton Laboratory, when the facility used uranium as the neutron target [30]. In this case, the oscillating background originated from delayed neutrons continuously emitted from the fissionable target material. Our observations indicate that, even in facilities using non-fissionable targets, an inelastic-scattering instrument should be carefully designed to offset the delayed neutron effects.

4. Summary

We have reviewed recent progress in the upgrade and performance evaluation studies of the chopper spectrometer 4SEASONS. The increased detector coverage, development of a new Fermi chopper, and successful suppression of background scattering should significantly improve the instrument's performance. To further develop the instrument components such as the Fermi chopper, we require a deeper understanding of the basic performance of the instrument, such as its energy resolution. On the other hand, the recently recognized problem of delayed neutron background might constrain the performance, and requires drastic countermeasures.

Acknowledgments
We thank S. Ji, J. Suzuki, and M. Harada for valuable discussions. We also thank M. Fujita for providing the single crystal of $La_{1.82}Sr_{0.18}CuO_4$ and for valuable discussions. We greatly acknowledge technical support by M. Sawabe, A. Kamiya, K. Inoue, T. Futagami, M. Kobayashi, A. Kishi, and K. Satou. Experiments on 4SEASONS were performed under the approvals of J-PARC and CROSS (proposal nos. 2012B0125, 2012I0001, 2012I0101, 2013I0001, and 2013I0101). The construction of 4SEASONS was supported by KAKENHI (no. 17001001).

References

[1] Kajimoto R *et al.* 2007 *J. Neutron Res.* **15** 5
[2] Kajimoto R *et al.* 2011 *J. Phys. Soc. Jpn.* **80** SB025
[3] Inamura Y, Nakatani T, Suzuki J and Otomo T 2013 *J. Phys. Soc. Jpn.* **82** SA031
[4] Kajimoto R *et al.* 2013 *J. Phys. Soc. Jpn.* **82** SA032
[5] Ikeuchi K, Nakamura M, Kajimoto R and Arai M 2013 *J. Phys. Soc. Jpn.* **82** SA038
[6] Kajimoto R, Nakamura M, Nakajima K and Fujita M 2013 *Nucl. Instrum. Methods Phys. Res.* A **729** 365
[7] Iida K, Ikeuchi K, Ishikado M, Suzuki J, Kajimoto R, Nakamura M, Inamura Y and Arai M 2014 *JPS Conf. Proc.* **1** 014016
[8] Kajimoto R, Nakamura M, Inamura Y, Kamazawa K, Ikeuchi K, Iida K, Ishikado M, Nakajima K, Harada M and Arai M *JPS Conf. Proc.* to be published
[9] Nakamura M *et al. JPS Conf. Proc.* to be published
[10] Maekawa F *et al.* 2010 *Nucl. Instrum. Methods Phys. Res.* A **620** 159
[11] Kajimoto R, Nakajima K, Nakamura M, Soyama K, Yokoo T, Oikawa K and Arai M 2009 *Nucl. Instrum. Methods Phys. Res.* A **600** 185
[12] Mezei F 1997 *J. Neutron Res.* **6** 3
[13] Mezei F, Russina M and Schorr S 2000 *Physica* B **276-278** 128
[14] Nakamura M, Kajimoto R, Inamura Y, Mizuno F, Fujita M, Yokoo T and Arai M 2009 *J. Phys. Soc. Jpn.* **78** 093002
[15] Nakatani T *et al.* 2009 *Proc. 12th Int. Conf. on Accelerator and Large Experimental Physics Control Systems* (Kobe) p 676
[16] Inamura Y, Nakajima K, Kajimoto R, Nakatani T, Arai M, Otomo T, Suzuki J, So J Y and Park J G 2010 *Proc. the 19th Meeting on Int. Collaboration of Advanced Neutron Sources* (Grindelwald) IP117
[17] Lefmann K and Nielsen K 1999 *Neutron News* **10** 20
[18] Willendrup P, Farhi E and Lefmann K 2004 *Physica B* **350** 735
[19] Nakamura M and Kajimoto R 2014 *JPS Conf. Proc.* **1** 014018
[20] Windsor C G 1981 *Pulsed Neutron Scattering* (London: Taylor & Francis Ltd.)
[21] Granroth G E, Kolesnikov A I, Sherline T E, Clancy J P, Ross K A, Ruff J P C, Gaulin B D and Nagler S E 2010 *J. Phys.: Conf. Ser.* **251** 012058
[22] Abernathy D L, Stone M B, Loguillo M J, Lucas M S, Delaire O, Tang X, Lin J Y Y and Fultz B 2012 *Rev. Sci. Instrum* **83** 015114
[23] Nakamura M *et al.* 2014 *Nucl. Instrum. Methods Phys. Res.* A **737** 142
[24] Nakamura M *et al.* 2015 *Proc. the 21nd Meeting on Int. Collaboration of Advanced Neutron Sources* (Mito) this issue

[25] Shamoto S, Sato M, Tranquada J M, Sternlieb B J and Shirane G 1993 *Phys. Rev.* B **48** 13817

[26] Copley J R D and Cook J C 1994 *Nucl. Instrum. Methods Phys. Res.* A **345** 313

[27] Jones T J L, Davidson I, Boland B C, Bowden Z A and Taylor A D 1987 *Proc. the 9th Meeting on Int. Collaboration of Advanced Neutron Sources* (Villingen) p 529

[28] Kajimoto R *et al.* 2010 *Proc. the 19th Meeting on Int. Collaboration of Advanced Neutron Sources* (Grindelwald) IP122

[29] Harada M private communication

[30] Arai M, Taylor A D, Bennington S M, Bowden Z A, Osborn R, Kohgi M, Ohoyama K and Nakane T 1991 *Proc. the 11th Meeting on Int. Collaboration of Advanced Neutron Sources* (Tsukuba) p 644

3.5.10

Progress on POLANO spectrometer for polarized neutron experiment

Tetsuya Yokoo[1,2], Kenji Ohoyama[3], Shinichi Itoh[1,2], Kazuaki Iwasa[3], Naokatsu Kaneko[1,2], Manabu Ohkawara[3], Seiji Tasaki[4], Takashi Ino[1,2], Kaoru Taketani[1,2], Kazuya Aizawa[2], Takayuki Oku[2], Hiroyuki Kimura[3] and Taku J Sato[3]

[1]High Energy Accelerator Research Organization (KEK), Tsukuba, Ibaraki 305-0801, Japan
[2]J-PARC Center, Tokai, Ibaraki 319-1195, Japan
[3]Tohoku University, Sendai, Miyagi 980-8577, Japan
[4]Kyoto University, Kyoto 606-8501, Japan

E-mail: tetsuya.yokoo@kek.jp

Abstract. A joint project between KEK and Tohoku University was initiated with the aim of future construction of a polarized neutron spectrometer at the Materials and Life Science Experimental Facility (MLF), J-PARC and research program for functional magnetic materials in 2009. Our principal concept is to achieve higher-energy polarization analysis of inelastic scattering beyond a reactor-based neutron source. We target the energy range up to $\Delta E =$ 40 meV with using SEOP for polarizer and bender supermirror as an analyzer of $m = 5$ to 5.5 as the first step. In the second step, we focus on higher energy experiments (0 meV $< \Delta E <$ 100 meV) with a large change of its layout. The basic shield designing has been completed and shielding capability of radiation was assessed. Also, the designs of the beam transport section using $m = 4$ supermirror guide tubes are completed. In order to achieve a high flux polarized neutron experiment, we plan to adopt cross correlation method. R&D of the correlation chopper is now under way.

1. Introduction

The success of the chopper spectrometer MARI applied to materials science at the ISIS neutron facility [1], has highlighted the importance of the so-called chopper spectrometers to neutron beam line instruments. At the Japan Proton Accelerator Research Complex (J-PARC), the Materials and Life Science Experimental Facility (MLF) is a newly constructed world leading pulse neutron experimental facility, where three chopper-type spectrometers are now part of the research program. One of the remaining technical issues that should be realized in MLF is the use of a polarization neutron technique with a pulsed neutron beam. Although the polarized neutron technique has been developed and used for many years, the application of the time-of-flight (TOF) method has only been realized in recent years. In particular, with regard to the inelastic spectrometer, the polarized neutron technique finds limited practical use in wide scattering angle instruments. Some of elastic neutron instruments such as a small angle scattering instrument, a reflectometer, a single crystal diffractometer and an imaging instrument plan to use polarized neutron technique option but is not planned for the instruments dedicating the inelastic scattering yet. In the light of recent discoveries in material science, many of the

observed complex phenomena are largely due to the entangled physical degrees of freedom of spins, charges, orbitals, and even lattice vibration. In neutron scattering experiments, the varying dependence of momentum, energy, and temperature can be interpreted by these of degrees of freedoms. However, a unique, effective, and direct way to observe these properties separately is via the polarization analysis. Thus, the polarized neutron experiments are quite significant for material science particularly for research on magnetism, hydrogen materials, and strongly correlated electron systems with multiple physical degrees of freedom.

A joint project between the Institute of Materials Structure Science (IMSS), KEK and the Institute of Material Research (IMR) of Tohoku University under the aegis of KEK Inter-University Research Program was initiated with the aim of future construction of the forthcoming spectrometer which enables us the inelastic polarization analysis and research program for functional magnetic materials. The project has been launched in 2009 starting as an S-type project with financial support from the KENS neutron facility. After the budget was successfully sanctioned and obtained for the project, actual construction has begun in 2013.

Our principal concept is to achieve higher-energy polarization analysis of inelastic scattering beyond a reactor-based neutron source. The suite of inelastic spectrometers involving an inverted geometry spectrometer and a spin-echo instrument in MLF can cover a relatively wide area in momentum (Q) and energy (E) space with various Q and E resolutions. Slow dynamics in soft matter to electron band excitation are targeted in the wide dynamical range of 10^{-9} eV $\leq E \leq 2\times10^{0}$ eV. For detailed dynamical studies of advanced material science, polarization analysis is an inevitable technique in addition to the wide Q-E coverage. Hence, we propose a chopper-type polarized neutron spectrometer POLANO which enables us to carry out inelastic experiments with reasonable intensity for research of dynamical properties in materials.

2. Geometrical Condition

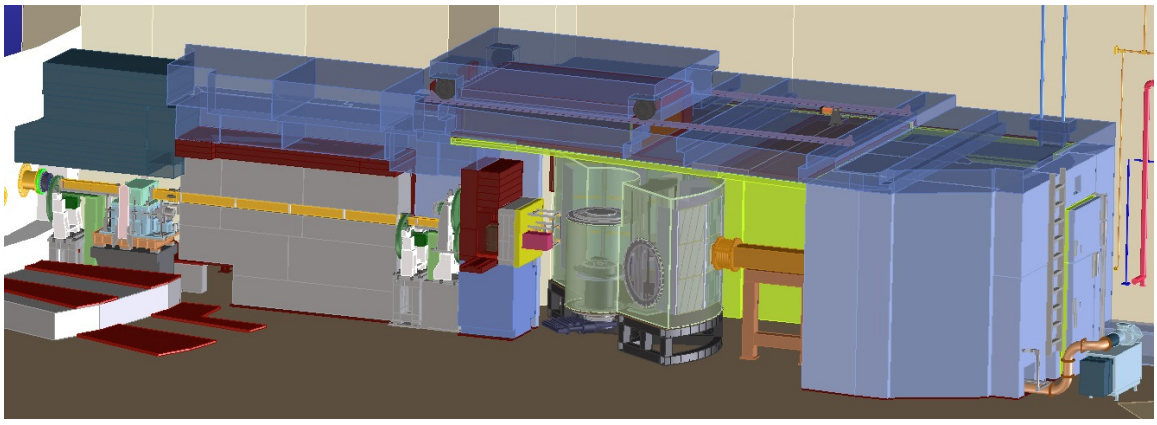

Figure 1. Schematic view of POLANO spectrometer

Schematic view of POLANO spectrometer is depicted in Fig. 1 and the instrumental parameters of POLANO were listed in Table 1 [2]-[4]. Some parameters were revised from Ref. [2]. E_i and k_i denote incident neutron energy and wave number of incident neutron, respectively in the table. The design features of POLANO are compactness with reasonably wide sample space design, higher neutron flux, higher neutron energy polarization up to 100∼150 meV, and medium resolution. The geometrical lengths were chosen as $L_1 = 17.5$ m (moderator-sample distance), $L_2 = 2.0$ m (sample-detector distance), and $L_3 = 1.85$ m (Fermi chopper-sample distance). We used a slightly shorter distance in L_2 from Ref. [2], but the energy and momentum resolution are not significantly affected.

Table 1. Basic instrumental parameters in POLANO

Parameters	
beam port	beam line 23 (BL23)
moderator	H_2 decoupled
L_1 (moderator-sample distance)	17.5 m
L_2 (sample-detector distance)	2.0 m
L_3 (Fermi chopper-sample distance)	1.85 m
energy resolution $\Delta E/E_i$	3∼5% at elastic position
momentum resolution $\Delta Q/k_i$	1∼2%
sample size	20 × 20 mm
detector angle (horizontal)	3° ∼120°
detector angle (vertical)	-7° ∼7°

3. Shielding

The shielding design was evaluated based on γ and neutron ray tracing by using the Monte Carlo PHITS code. Figure 2 shows an example of the calculated γ and neutron dose distribution about the designed beam line and main shielding. The POLANO is viewing a decoupled moderator that is one of three types of hydrogen moderators (coupled, decoupled and poisoned), and the view of the moderator is 10 cm square of cross section. A radiation dosage of less than 6.25 μSv/h of surface dose was achieved with concrete, steel and boric acid as shielding materials.

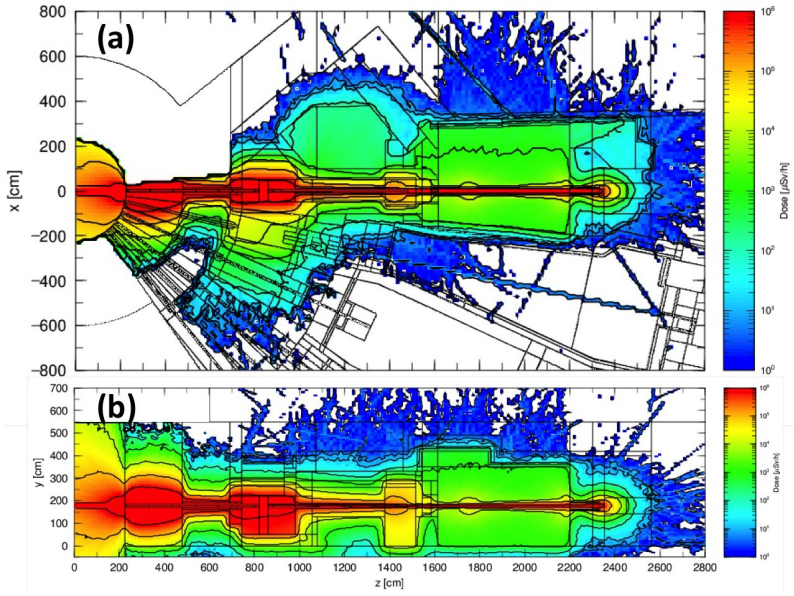

Figure 2. Typical calculated result of ray tracing Monte Carlo simulation. The sum of the γ-ray and neutron doses is mapped as a contour plot for both of top view (a) and side view (b). The neutron source is beam line BL23 viewing decoupled moderator of the MLF.

In certain parts of the shielding in the vicinity of the sample space, stainless steel was used as a non-magnetic material in order to make possible the conduction of high-magnetic field experiments. Two entrances are located at the back of the instrument and at the top of the shielding (roof) with personnel protection system (PPS) on each entrance. The PPS is the safety

inter lock system involving shutter controller, emergency stopping system and door controller. The top entrance hatch is massive concrete shielding of 26 ton is electronically controlled its opening and closing by sliding on the rail.

4. Beam Transport

The 23rd beam line, where POLANO is installed, is viewing decoupled moderator with a known pulse width of $\Delta t_m = a/\sqrt{E_i}$ with a=2.5 for decoupled moderator. After moderator neutrons are transported by $m = 4$ supermirror guide tubes optimized for 110∼120 meV neutron intensity [2, 3] with a McStas simulation [5, 6]. An elliptical guide optimized section by section (section length = 50 cm) can yield a neutron flux of 3.9×10^5 [n/(sec·meV·cm^2·MW)], which is almost comparable with a coupled moderator beam line at E ∼100 meV. The finally designed view of the guide tube is illustrated in Fig. 3. We tested several neutron energies to be optimized, namely, the range of 20-30 meV, 60-70 meV and 110-120 meV. Additionally, the evaluated neutron flux is plotted in Fig 4 as a function of neutron energy. Since the focusing guide

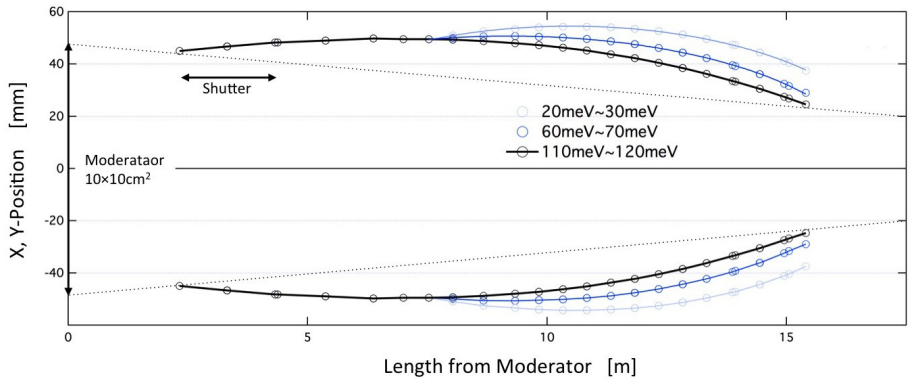

Figure 3. Evaluated guide tube cross section optimized for neutron energies 20-30 meV (light blue symbol), for 60-70 meV (blue symbol) and 110-120 meV (black symbol). Cited from Ref. [3]

tubes affect beam divergence, we estimate the beam profile as well. Figure 5 shows the intensity distribution at L = 16.435 m from the moderator, where a SEOP ^{3}He filter cell will be placed. The beam width at the ^{3}He filter has a full width of 8 cm at the bottom, and 4 cm at the half height. In the early stage, ^{3}He cells with a diameter of 5 cm will be used because the ^{3}He polarizing technique has already been established for 5 cm cells. Since cells with a diameter of 10 cm have now been developed, the beam exiting the polarizer will be almost fully polarized in the final stage.

Figure 6 depicts the neutron beam flux observed in an area of 2 × 2 cm^2 after the beam passed through a Fermi chopper rotating at frequencies at 200, 400 and 600 Hz. The dimensions of the Fermi chopper are rotor diameter D=80 mm, slit width d = 2 mm, and curvature radius r = 450 mm with a transmission efficiency of 0.8 as shown in Fig 7. Since POLANO is aimed at the incident neutron energy range up to E_i = 100 meV, the evaluated intensity and resolution below 100 meV are reasonable for the polarization analysis experiments. Further, to estimate the energy resolution, a vanadium cylinder with outer radius of 12.5 mm inner radius of 12 mm and height of 4 cm was set at the sample position. An energy resolution of 4∼5% can be obtained below 100 meV with the integrated intensity over 1×10^5 [1/s/cm^2] at the sample position for an accelerator power of 1 MW as shown in Fig. 6(b).

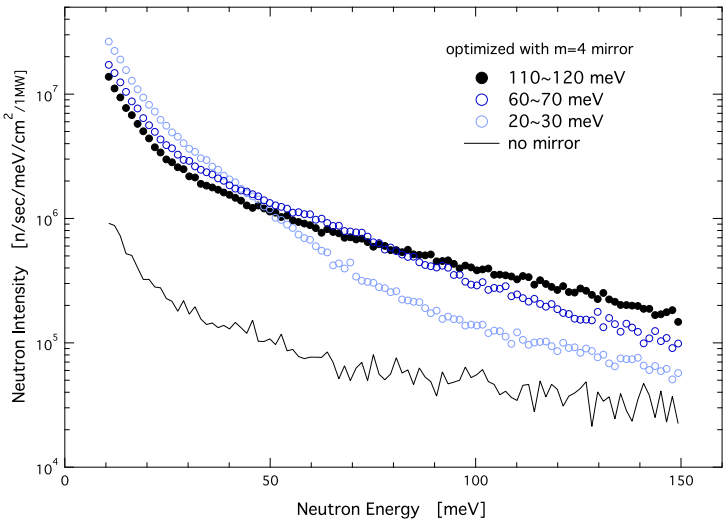

Figure 4. Simulated results of the effect of guide tubes by McStas. The m = 4 mirror is used to optimize for several neutron energies. 20-30 meV (light blue symbol), 60-70 meV (blue symbol) and 110-120 meV (black symbol) from Ref. [3].

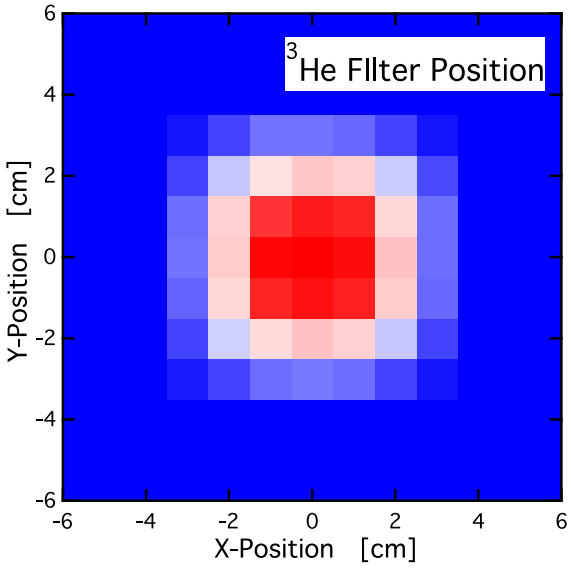

Figure 5. Neutron flux distribution at the ^{3}He SEOP cell position.

5. Mechanical Choppers

Below the exit of a biological shield, several types of choppers are placed. T0 chopper is the first chopper to eliminate fast and epithermal neutrons with a massive metal blade rotating with a maximum speed of 100 Hz. This is originally developed as a MLF standard [7]. The blade is made of Inconel X750, which is known for having high strength without using radiological elements with long lives such as cobalt. Though the weight of the blade is over 120 kg, at 100 Hz of rotating speed, less than ± 5 μs of jitter (phase control accuracy) was achieved.

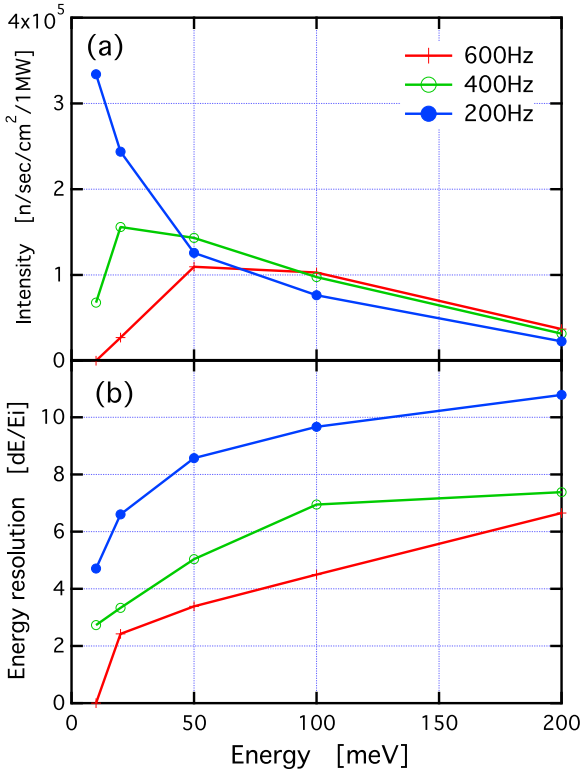

Figure 6. (a) Neutron intensity and (b) energy resolution estimation by McStas. monochromatized beam obtained by a Fermi chopper rotating at 200, 400, 600 Hz is used. Cited from Ref. [4].

In order to avoid the frame overlap of a 25 Hz proton (neutron) pulse in MLF, a slow rotating disk chopper will be installed in the beam line. Two disk choppers synchronized with neutron pulse are placed at $L = 7.5$ and 13.9 m. A Fermi chopper will be used for monochromatizing the incoming neutron energy. It is the same type of Fermi chopper developed for High Resolution Chopper spectrometer in MLF [8], which has a 600 Hz maximum speed with 0.3 μs jitter enabling high resolution and transmission experiments.

For more effective measurements, we adopt the cross correlation method that utilizes multiple wavelengths of neutrons for one inelastic measurement. Hence, we have intensity gains of a factor of ten or higher in principle. A special type of disk chopper (correlation chopper) is required to realize this correlation method. The disk diameter is ideally over 1000 mm with a rotational speed of 350 Hz. Additionally, 255 (2^N-1) open and close sequences are required to be on the disk [9]. These conditions are mechanically quite difficult to realize because the maximum stress evaluated is almost 4000 MPa at the edge of the rotating disk. Totally new designing of the disks is now under way with carbon fiber reinforced plastic (CFRP) materials to realize a mechanically rotating correlation chopper.

6. Vacuum chamber and detectors

A vacuum chamber is to be installed at the sample-detector section to avoid air scattering and to ensure evacuated insulation for the refrigerator. Figure 8 shows the design of the vacuum chamber. To ensure flexible use of the sample space, the chamber is designed to be detachable,

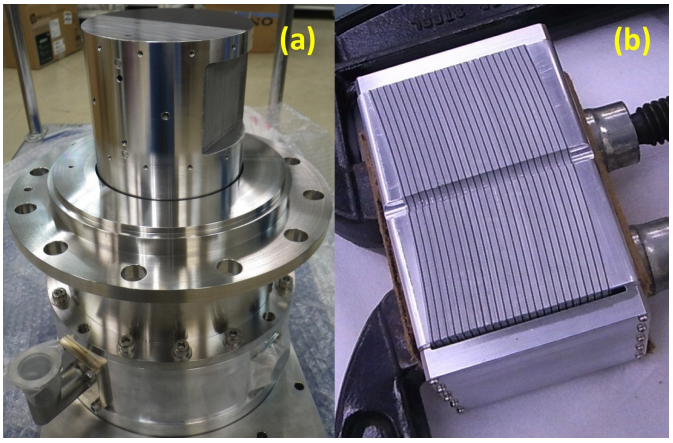

Figure 7. (a) The rotor of Fermi chopper installed in POLANO. (b) Slit package

and it is composed of three parts. The sample chamber is the first chamber, in which the sample is placed and the sample environments are set. The second is a connecting chamber that connects the sample chamber and scattering chamber. Both the sample and scattering chambers are sealed by thin (t=1.5/2.0 mm) aluminum windows, and the chambers are completely isolated from air. Certain magnetic devices such as the spin flipper (positioned after the sample) will be installed in this section. The third is the scattering chamber wherein the suite of analyzer mirror and detectors are placed. In addition, B_4C vanes and liners are planned to be installed in the chamber [4].

At the end of the scattering chamber, position sensitive detectors (PSDs) are to be installed on the inside of the chamber. For energy range of the POLANO, large pressure of ^{3}He gas is not required to achieve reasonable detector efficiency. Therefore, we adopted the use of a 10 atm gas pressure PSD with 600 mm effective length and 3/4 inches of diameter. An efficiency of about 70% is expected for 100 meV neutrons. The PSDs are arranged in three layers in the vacuum chamber. The horizontal scattering angle (detector angle) ranges from -30° to 130°, and the range is ±25° along the vertical direction. At first, only horizontal (center) layers are to be fully installed for polarization analysis experiments. The detectable vertical angle is ±8°.

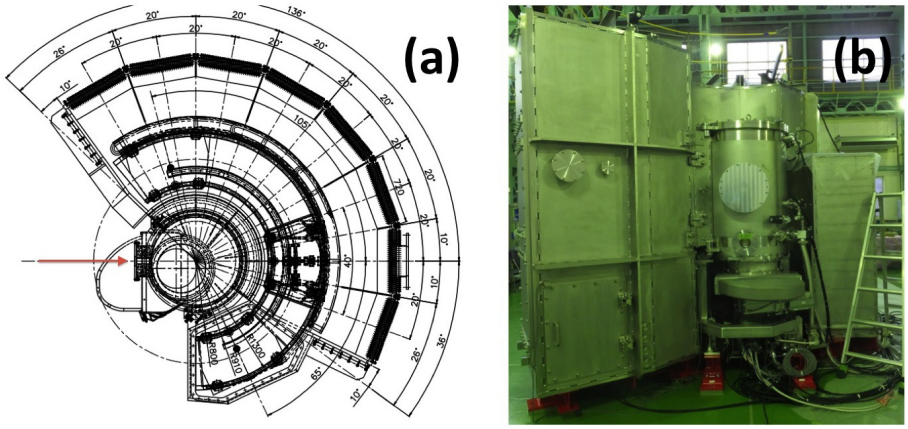

Figure 8. (a) Top view drawing of the vacuum chamber. Neutron beam is injected from lift along red arrow. (b) View of the manufactured vacuum chamber from the front.

7. Polarization Devices

The polarizer, analyzer, and other magnetic devices installed in the POLANO are currently under development [10, 11]. As the polarizer, a cylindrical ^{3}He spin filter (HeSF) based on the spin-exchange optical pumping (SEOP) technique will be used to polarize neutrons in the wide energy range. During the experiments, the HeSF is operated in the on-beam mode to maintain ^{3}He polarization. A HeSF with a diameter of 3 cm will be installed in the POLANO in the spring of 2015. HeSF systems with larger diameters (5 to7 cm) are now under development. We have already succeeded in preparing a GE180 cell with a diameter of 10 cm.

One of the serious technical issues affecting POLANO is the choice of a spin analyzer with a large solid angle. Since the technology concerning polarized ^{3}He in GE180 glass cells with "large solid angles" is not currently available in Japan, a phased approach needs to be adopted for the spin analyzer to be used in POLANO. In the first stage, a 5.5 Q_c supermirror bender analyzer with a covered scattering angle of about 18° will be installed on a rotatable stand around the sample because it is most practical in the thermal neutron range. The distance between the sample and the aperture of the supermirror will be 850 mm. The 5.5 Q_c supermirror can cover up to $E_f \sim 40$ meV, corresponding to an energy excitation range of 50 to 60 meV. This energy range is of great scientific interest, corresponding to phenomena such as spin-lattice couplings in multiferroic systems, geometrical spin frustration systems, and multipole orderings in rare earth compounds. On the other hand, since we have installed a focusing guide tube between the moderator and the Fermi chopper to obtain high flux at the sample position, it is necessary to ensure matching of the angular divergence of the focusing guide tubes and analyzer.

We also keep developing dynamic nuclear polarization (DNP) system. As neutron-proton scattering length of the triplet channel is much smaller than that of the singlet channel [12], the neutron beam transmitted through a polarized proton target gets polarized. A brute force way to polarize sufficient number of protons in the target is applying strong external magnetic field to it and cooling it down to low temperature. However, even if we cool it down to 1 K and apply external magnetic field of 5 T to it, the thermal equilibrium Boltzmann polarization of the protons is less than 1% and the target cannot be used as a practical neutron polarizer. To highly polarize proton spins, we can use the dynamic nuclear polarization (DNP) method. In the above mentioned situation, although the polarization of protons is less than 1%, that of unpaired-electrons is nearly equal to unity as the magnetic moment of electron is much larger than that of proton. To test the enhancement of the proton polarization by this method for several target materials that contain protons and unpaired-electrons and estimate their performance as neutron polarizers, we are preparing instruments for DNP of proton spins.

To cool a target down and apply external magnetic field to it, we use the cryostat that was used by Crabb [13]. The ^{4}He evaporation refrigerator can cool the target down to 1 K and the split coil superconducting magnet can apply the magnetic field of 5 T. To measure the enhancement of the proton polarization, we prepared instruments, which are used in studies of continuous wave nuclear magnetic resonance (CW NMR) spectroscopy. Our system uses a coil that acts as a transmitter of the radio wave that is irradiated to the target and a receiver of the radio wave generated by the target material. When the energy difference between the two proton spin states due to the static magnetic field is equal to the photon energy of the radio wave generated by the coil, the radio wave is absorbed and the amplitude of the reflected voltage from the coil decreases. As this signal depends on the polarization of the protons and the radio wave frequency [14], we can estimate the polarization enhancement by measuring the radio wave frequency dependence on the reflected voltages. To test the CW NMR system, we installed a Teflon sheet, which contains fluorine nucleus whose magnetic moment is 6% smaller than that of proton. We scanned the radio wave frequency over the range around the Larmor frequency of fluorine and observed a clear signal at the expected frequency as shown in Fig 9.

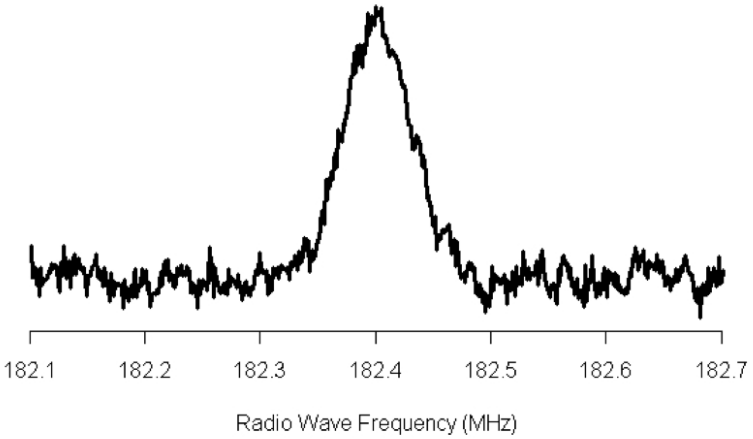

Figure 9. Observed NMR signal of Teflon sheets.

Acknowledgments

This work and POLANO project was approved by the Neutron Scattering Program Advisory Committee of IMSS, KEK (Proposal No. 2009S09 and No.2014S09). The authors TY and SI were partly supported by Grant-in-Aid for Scientific Research (C) (24540352) also TY was supported by Grant-in-Aid for Scientific Research (C) (26400376) from the Japanese Ministry of Education, Culture, Sports, Science and Technology (MEXT), Japan.

References

[1] Taylor A D, Arai M, Bennington S M, Bowden Z A, Osborn R, Andersen K, Stirling W G, Nakane T, Yamada K and Welz D 1991 *KEK Report (Proc. 11th Meet. Int. Collab. Advanced Neutron Sources, ICANS-XI)* **90-12** 705

[2] Yokoo T, Ohoyama K, Itoh S, Suzuki J, Iwasa K, Sato T J, Kira H, Sakaguchi Y, Ino T, Oku T, Tomiyasu K, Matsuura M, Hiraka H, Fujita M, Kimura H, Sato T, Suzuki J, Takeda M, Kaneko K, Hino M and Muto S 2013 *J. Phys. Soc. Jpn.* **82** SA035

[3] Yokoo T, Ohoyama K, Itoh S, Suzuki J, Nanbu M, Kaneko N, Iwasa K, Sato T J, Kimura H and Ohkawara M 2014 *J. Phys. Conf. Series* **502** 012043

[4] Yokoo T, Ohoyama K, Itoh S, Iwasa K, Kaneko N, Suzuki J, Ohkawara M, Aizawa K, Tasaki S, Ino T, Taketani K, Ishimoto S, Takeda M, Oku T, Kira H, Hayashi K, Kimura H and Sato T J 2015 *EPJ Web of Conferences* **83** 03018

[5] Lefmann K and Nielsen K 1999 *Neutron News* **10/3** 20

[6] Willendrup P, Farhi E and Lefmann K 2004 *Physica B* **350** 735

[7] Itoh S, Ueno K, Ohkubo R, Sagehashi H, Funahashi Y and Yokoo T 2011 *Nuclear Instruments and Methods in Physics Research A* **654** 527

[8] Itoh S, Ueno K and Yokoo T 2012 *Nuclear Instruments and Methods in Physics Research A* **661** 58

[9] Rosenkranz S and Osborn R 2008 *Pramana Journal of Physics* **71** 705

[10] Ohoyama K, Yokoo T, Itoh S, Suzuki J, Iwasa K, Sato T J, Kira H, Sakaguchi Y, Ino T, Oku T, Tomiyasu K, Matsuura M, Hiraka H, Fujita M, Kimura H, Sato T, Suzuki J, Shimizu H M, Arima T, Takeda M, Kaneko K, Hino M, Muto S, Nojiri H, Lee C H, Park J G and Choi S 2013 *Journal of Physical Society of Japan* **82** SA036

[11] Ohoyama K, Yokoo T, Itoh S, Ino T, Ohkawara M, Oku T, Tasaki S, Iwasa K, Sato T J, Ishimoto S, Taketani K, Kira H, Sakaguch Y, Nanbu M, Hiraka H, Shimizu H M, Takeda M, Hino M, Hayashi K, Kenzelmann M, Fliges U and Hautle P 2014 *Journal of Physics Conference Series* **502** 012051

[12] Bethe H A and Morrison P 1956 *Elementary Nuclear Theory (Wiley)*

[13] Crabb D G, Higley C B, Krisch A D, Raymond R S, Roser T, Stewart J A and Court G R 1990 *Phys. Rev. Lett.* **64** 2627

[14] Abragam A 1961 *The Principles of Nuclear Magnetism (Oxford University Press)*

3.5.11

MAGIC chopper: basic concept and experimental evaluation

M. Nakamura[1], K. Ikeuchi[2], R. Kajimoto[1], W. Kambara[1], Th. Krist[3], T. Shinohara[1], M. Arai[1], K. Iida[2], K. Kamazawa[2], Y. Inamura[1] and M. Ishikado[2]

[1] Materials and Life Science Division, J-PARC Center, Japan Atomic Energy Agency, Tokai, Ibaraki 319-1195, Japan
[2] Research Center for Neutron Science and Technology, Comprehensive Research Organization for Science and Society, Tokai, Ibaraki 319-1106, Japan
[3] Helmholtz Zentrum Berlin for Materials and Energy, Hahn-Meitner-Platz 1, 14109 Berlin, Germany

E-mail: mitsutaka.nakamura@j-parc.jp

Abstract. The efficiency of inelastic neutron scattering measurement by a chopper spectrometer can be markedly improved by utilizing multiple incident energies (Multi-E_i method). However, in conventional chopper system, the optimization of experimental condition for all the incident energies is absolutely impossible. We have proposed and developed a new Fermi chopper with supermirror-coated slitpackage, so-called MAGIC chopper, in order to overcome the problem. The nearly full optimization of experimental condition for Multi-E_i method using a prototype of MAGIC chopper has been experimentally demonstrated.

1. Introduction

Inelastic neutron scattering (INS) measurements by chopper spectrometers at pulsed spallation neutron sources have greatly contributed to the development of materials science. There, a sample is irradiated by incident neutron beam monochromated by a mechanical chopper, and the momentum transfer (Q) and energy transfer (E) in the sample are detected by time-of-flight (TOF) technique. A high incident energy (E_i) measurement provides us the dynamical properties in a wide Q-E range, while a low E_i measurement more precise information on dynamical properties although the coverage of Q-E range becomes narrow. Chopper spectrometers should remain to be flagship instruments in the new generation pulsed neutron sources such as Japan Proton Accelerator Research Complex (J-PARC). However, an INS measurement has a drawback in measurement efficiency. Due to the faint signal of inelastic process, long measurement time and a large amount of sample have been needed to acquire a good-quality INS data. This situation prevented us from carrying out INS measurements under various experimental conditions within a limited beam time, and has been an impediment to progress in materials science.

Conventional INS measurements by a chopper spectrometer at a pulsed neutron source utilize single monochromatic incident beam. On the other hand, several E_i beams are delivered to the sample within 1-frame of a period of the pulsed source, because the rotating frequency of monochromating chopper is usually much higher than the frequency of the pulsed source. In other words, a single E_i experiment has wasted the other incident neutrons and yielded a long

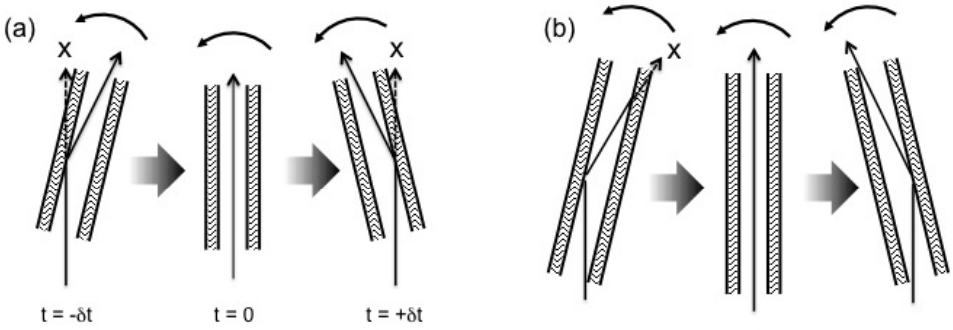

Figure 1. Schematic illustration of (a) MAGIC chopper concept and (b) the relation between the rotating slits and the reflected neutrons.

dead-time on a TOF measurement. If we can utilize the multiple E_{i}'s inherently selected by the chopper, the efficiency of an INS measurement should be significantly improved [1, 2, 3, 4]. Previously, we succeeded in demonstrating that multiple two-dimensional maps of a dynamical structure factor in Q-E space are simultaneously obtained by one measurement using the Fermi chopper spectrometer 4SEASONS [5] which is installed at BL01 of the Materials and Life Science Experimental Facility (MLF) in J-PARC. We refer to this technique used in J-PARC as Multi-E_{i} method. This technique has been already in widespread use at J-PARC [6, 7, 8]. However, it must be noted that the Multi-E_{i} method in a conventional chopper spectrometer involves a crucial problem. Usually, the chopper opening time Δt_{ch} is tuned to the pulse width emitted from moderator Δt_{m}, because the relation of $\Delta t_{\mathrm{m}} \approx \Delta t_{\mathrm{ch}}$ is an optimized condition for INS measurement by a chopper spectrometer. The Δt_{m} depends on neutron energy and the Δt_{ch} of a conventional chopper keeps constant at all times, and so the Multi-E_{i} method using a conventional chopper cannot realize the optimized experimental condition for each of incident energies. The lower incident energy measurement in Multi-E_{i} method realizes better energy resolution at the expense of intensity. The pulse peak intensity of neutron source in J-PARC reach a maximum at a relatively low-energy region ($\sim$ 10 meV), and thus the lower energy measurement in Multi-E_{i} method should be highly significant even if the intensity is sacrificed. However, the higher incident energy measurement in Multi-E_{i} method often causes a worthless result due to the worse energy resolution.

In order to overcome the optimization problem in Multi-E_{i} method, we proposed a new Fermi chopper with supermirror-coated straight slits (MAGIC chopper). We have developed a prototype of MAGIC chopper, and carried out the transmittance experiment on pulsed neutron beam at J-PARC. This paper describes the basic concept [9] and the experimentally-confirmed performance [10] of a rotating supermirror-coated slit package. The feasibility of high efficient INS measurement with MAGIC chopper is also discussed.

2. Basic concept of MAGIC chopper

2.1. Energy dependent chopper opening time

Supermirror has characteristic features associated with neutron wavelength. That is, larger critical angle is allowed for the incidence of neutron with longer wavelength. With the aid of supermirror on the surface of the transmitters we can make efficient use of neutrons with the MAGIC chopper which were doomed to be unavailable with a conventional chopper as shown in Fig. 1(a). The block arrows in Fig. 1 denote the evolution of time. The effective chopper

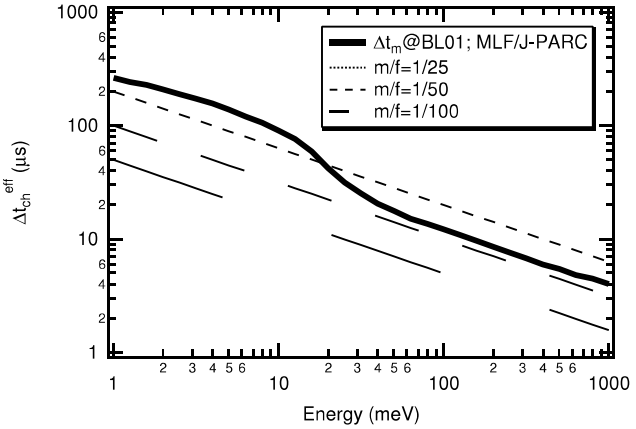

Figure 2. Energy dependent chopper opening time $\Delta t_{\rm ch}^{\rm eff}$ for several m/f cases.

opening time $2\delta t$ depicted in Fig. 1(a) can be written as

$$2\delta t = \Delta t_{\rm ch}^{\rm eff} = 2 \times \frac{1.73 m \lambda_{\rm i}}{2\pi f} \times 10^3 (\mu{\rm s}), \tag{1}$$

where m is the m-value of the supermirror, f (Hz) the chopper frequency, and the term $1.73 m\lambda_{\rm i}$ (mrad) corresponds to the critical angle for incident neutron $\lambda_{\rm i}$ (Å). This equation means that the chopper opening time can be effectively extended for longer neutron wavelength. From the expression of Eq. (1) the ratio m/f is an important parameter to adjust the behavior of $\Delta t_{\rm ch}^{\rm eff}$. It should be noted that the rotating slits with the finite depth block the reflected neutrons in case that the reflection direction is opposite to the rotation direction. The relation between the rotating slits and the reflected neutrons are shown in Fig. 1(b). The practical case of this effect will be described in Sec. 4. Figure 2 shows the energy dependencies of $\Delta t_{\rm ch}^{\rm eff}$ for several m/f cases. The data of energy dependent $\Delta t_{\rm m}$ for 4SEASONS, which is downloaded from the web page [11], is also included in the figure for comparison. Let us stress that the *energy dependent* $\Delta t_{\rm ch}$ can be realized by MAGIC chopper.

For high energy neutrons, the angular divergence defined by the chopper geometry should determine the chopper opening time. Consider a rotating single slit of width w (mm), depth D (mm), and frequency f (Hz). The chopper opening time originated in the slit divergence is

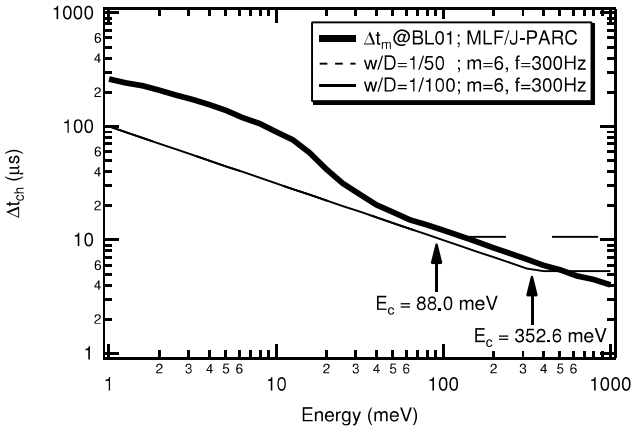

Figure 3. Energy dependent chopper opening time for two different w/D cases. In this figure we assume $m = 6$ and f=300 Hz.

given by

$$\Delta t_{\rm ch}^{\rm div} = \frac{w}{2\pi D f} \times 10^6 [\mu{\rm s}]. \tag{2}$$

Thus, we can estimate the crossover wavelength $\lambda_{\rm c}$ from the condition of $\Delta t_{\rm ch}^{\rm eff} = \Delta t_{\rm ch}^{\rm div}$,

$$\lambda_{\rm c} = \frac{1000}{3.46m} \cdot \frac{w}{D} [\text{Å}]. \tag{3}$$

As seen in Eq. (3) the ratio w/D is a parameter to define the crossover wavelength (energy). The energy dependent chopper opening times $\Delta t_{\rm ch}$ for two different chopper divergences (w/D = 1/50 and 1/100) are represented in Fig. 3. We assumed the condition of $m = 6$ and f = 300 Hz in this figure. Under the condition of $m = 6$, the ratio $w/D = 1/50$ (20 mrad) yields $\lambda_{\rm c}$ = 0.96 Å($E_{\rm c}$ = 88 meV), and $w/D = 1/100$ (10 mrad) gives $\lambda_{\rm c}$ = 0.48 Å($E_{\rm c}$ = 352.6 meV). It is obvious that the smaller angular collimation shifts the crossover energy towards higher energy region.

2.2. Nearly constant energy resolution

For a chopper spectrometer, the energy resolution at elastic position can be expressed as

$$\frac{\Delta E}{E_{\rm i}} = \left[\left\{ 2\frac{\Delta t_{\rm ch}}{t_{\rm c}} \left(1 + \frac{L_1}{L_2} \right) \right\}^2 + \left\{ 2\frac{\Delta t_m}{t_{\rm c}} \left(1 + \frac{L_3}{L_2} \right) \right\}^2 \right]^{1/2}, \tag{4}$$

where $E_{\rm i}$ is the incident energy of neutrons, $\Delta t_{\rm ch}$ the chopper opening time, $\Delta t_{\rm m}$ the pulse width at the moderator, $t_{\rm c}$ the traveling time of incident neutron from moderator to monochromating chopper, L_1 the distance from moderator to sample, L_2 the distance from sample to detector, and L_3 the distance from monochromating chopper to sample.

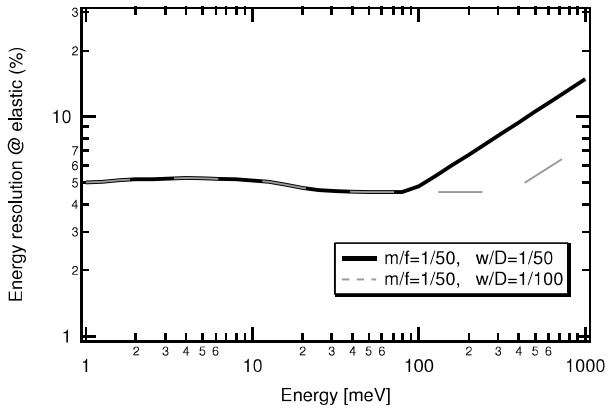

Figure 4. Calculated energy resolutions at elastic position for several chopper configurations.

According to the instrumental parameter of 4SEASONS, L_1 = 18 m, L_2 = 2.5 m, and L_3 = 1.8 m[14]. By substituting the energy dependent chopper opening time into $\Delta t_{\rm ch}$ in Eq. (4), we can estimate the energy resolution of 4SEASONS equipped with MAGIC chopper. Calculated energy resolutions for several cases are shown in Fig. 4. In case of the $m/f = 1/50$ and $w/D = 1/100$ configuration, the energy resolution becomes almost constant ($\sim 5\%$) in the wide range of incident energy 1 − 300 meV. This is a consequence of the energy dependence

of effective chopper opening time, that is $\Delta t_{\rm ch} \propto 1.73 m\lambda_{\rm i} \propto E_{\rm i}^{-1/2}$. Therefore, all the energy dependent terms in Eq. (4) are cancelled out since $t_{\rm c}$ is proportional to $E_{\rm i}^{-1/2}$ and $\Delta t_{\rm m}$ follows a $E_{\rm i}^{-1/2}$ variation in a wide energy range.

3. Experimental evaluation

3.1. Slit package

Two types of slit packages, one with and the other without neutron supermirrors, were prepared in order to investigate the characteristic properties of a supermirror-coated slit package. The slit package without neutron supermirrors was composed of alternating Si and ^{10}B layers. The Si wafers, of thickness 150 μm, transmit neutrons, whereas the ^{10}B, of thickness $\sim$15 μm, is a strong absorber. In the case of the slit package with neutron supermirrors, both sides of the Si wafers were coated with Ni/Ti supermirrors with $m = 3$. The slit packages were fixed by a holder as shown in Fig. 5. Unnecessary transmitting neutrons resulting from the shorter depth of a slit package (17 mm) than the width of the beam window (30 mm), can be shielded by the Cd plates, of thickness 0.5 mm, which are inserted at the both lateral sides of a slit package.

3.2. Rotation testing machine

We have developed a rotation testing machine in-house to investigate the performance of rotating slit packages. A holder containing a slit package was inserted in a rotor body made of aluminum. Balance adjustment of rotor-body and holder complex was made by a balancing machine. Figure 6 shows a photograph of the rotation testing machine. The rotation was driven by a servomotor with mechanical bearings, and it was synchronized with a trigger signal at the repetition rate of the pulsed neutron source. The rotor body and holder complex were rotated by the rotation testing machine, and the maximum rotation frequency was designed to be 150 Hz.

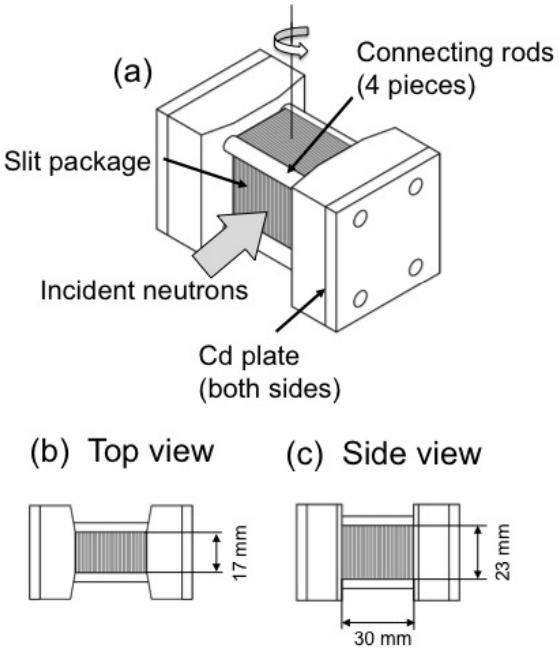

Figure 5. Schematic drawings of a slit package; (a) diagrammatic perspective view, (b) top view and (c) side view.

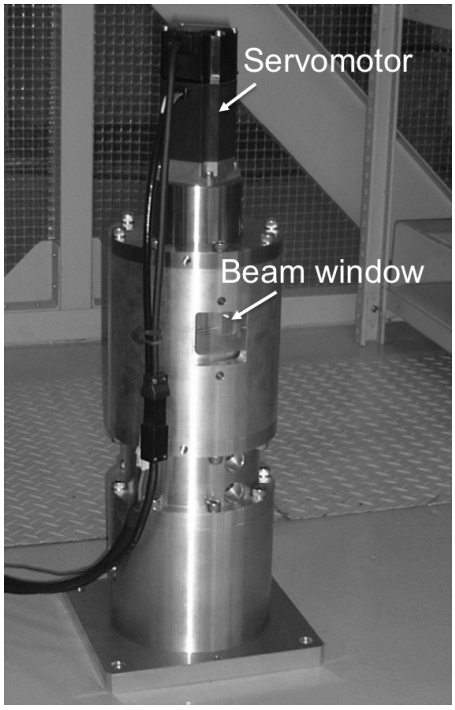

Figure 6. Photograph of a rotation testing machine.

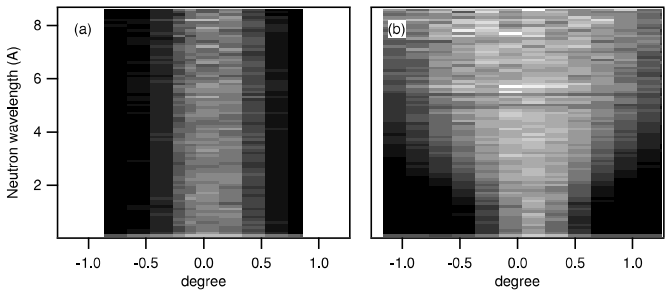

Figure 7. Two-dimensional maps of rocking curve measurement for slit packages (a) without and (b) with neutron supermirrors ($m = 3$).

3.3. Transmittance experiment

Neutron transmittance experiments were carried out on NOBORU (BL10 of MLF) which is designed to study neutronic performance of the spallation neutron source system of J-PARC and to provide a test beam port to promote research and development on innovative neutron devices [12, 13]. In this study, we performed two kinds of transmittance experiments to evaluate the performance of slit packages with and without neutron supermirrors.

One of the experiments performed was the rocking curve experiment. This experiment was performed to study the *static* properties of the slit packages. In the experiment, a pulsed white neutron beam was delivered to the slit package, which was placed on a goniometer located 13,400 mm from the neutron moderator. The band definition chopper was used for frame overlap suppression. The transmitted beam was detected at a ^{3}He neutron beam monitor made by LND, Inc. which was situated 13,700 mm from the neutron moderator. The size of the incident beam was 20 mm $\times$ 20 mm at the center of the slit package.

The other experiment was the synchronous rotation experiment. In this experiment, the rotation was synchronized with the repetition rate of the pulsed neutron source to elucidate the *dynamic* properties of the slit packages. The rotation testing machine incorporating the slit package was located 13,400 mm from the neutron moderator. The rotation frequency was 100 Hz for the two different slit packages, with and without neutron supermirrors; the phase delay was identical for each measurement. The size of the incident white beam size was 10 mm $\times$ 10 mm at the center of the slit package. The transmitted neutrons were detected by a two-dimensional neutron detector, which consisted of a position sensitive photomultiplier tube with a ZnS(Ag)/^{6}LiF scintillator on the surface. Information about the position and the arrival time of the neutron was recorded for each event. The detector surface was located 13,880 mm from the neutron moderator.

4. Results and discussions

Two dimensional maps of rocking curve measurements are given in Fig. 7. Collected TOF data are converted to the neutron wavelength dependent data by the following relation,

$$\lambda = 3.956 \times \frac{t}{L}(\text{Å}), \tag{5}$$

where t (μs) is the TOF at the detector, and L (mm) the distance from moderator to detector. The width of the time (wavelength) bin was 346 μs (0.1 Å). Figure 8 shows the one dimensional plots of rocking curve measurement for various incident wavelength regions, where the intensity was averaged over a certain range of incident wavelength. Transmitted neutron intensity in Fig. 8 are normalized by the direct beam intensity, obtained by removing the slit package from the path of neutron beam.

As expected, the peak width for the supermirror-coated slit package grew wider in direct proportion to the wavelength. This is due to the fact that a larger critical angle is allowed for

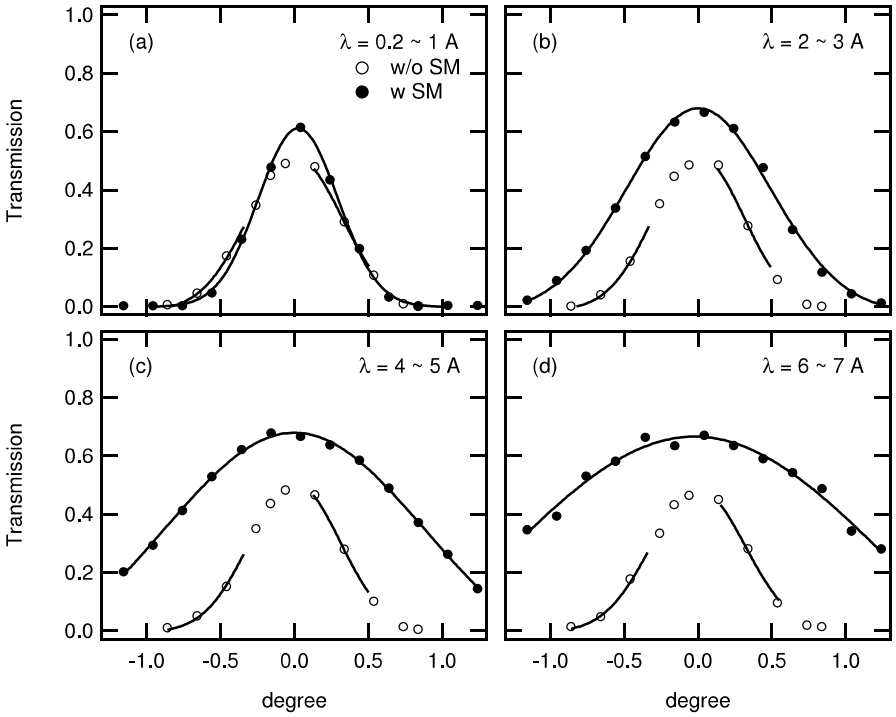

Figure 8. One dimensional plots of rocking curve measurement for slit packages with and without neutron supermirrors ($m = 3$). The intensity was averaged over a certain range of incident wavelength and normalized by the direct beam intensity measurement. Various ranges of incident wavelength are shown in the figures.

the longer wavelength neutrons. On the other hand, the peak height for the supermirror-coated slit package was found to be greater than that for the slit package without neutron supermirrors. This was an unexpected finding. The neutron supermirrors in the slit packages play an important role not only in the extension of effective chopper opening time, but also in the focusing of the divergent neutron beams.

Next, we discuss the synchronous rotation experiment. Figure 9 shows the TOF spectra of transmitted neutrons, both with and without supermirrors; the rotation frequency was 100 Hz, and the phase delay was identical for both slit packages. Intensities given in Fig. 9 are normalized by the direct beam intensity measurement. In the case of 100 Hz rotation without neutron supermirrors, we can observe several peaks at every ~ 5179 μs, which corresponds to one-half of the rotation period at the detector position, i.e., $1/100 \times 1/2 \times 13,880/13,400 \times 10^6 \mu$s. There was little difference between the two slit packages in the shorter TOF region (higher energy region). However, the differences were clear in the lower-energy region where for the slit package with the neutron supermirror, the intensity distribution widened and shifted toward the longer TOF side, unlike the case of the slit package without neutron supermirrors. The increase in the peak height for the supermirror-coated slit package was also confirmed in the synchronous rotation experiment. The intensity distribution in the supermirror-coated slit package can be explained by the relation between the rotation direction of slit package and the reflection direction of the neutrons shown in Fig.1(b). In the longer-TOF region depicted on the right-hand side of Fig. 1(b), the slits move in the same direction as the reflected neutron. In other words, the

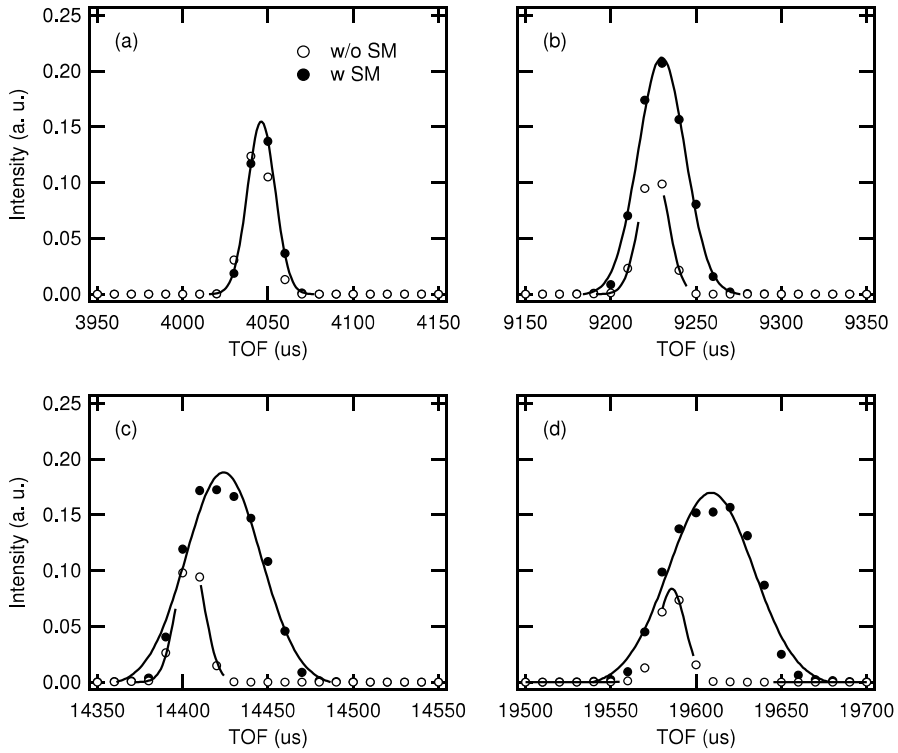

Figure 9. The TOF spectra of transmitted neutrons from rotating slit packages with and without neutron supermirrors ($m = 3$). The rotation frequency is 100 Hz for both the cases.

rotating slits provide a passage to the reflected neutrons. On the other hand, in the shorter-TOF region illustrated on the left-hand side of Fig. 1(b), the rotating slits block the reflected neutrons because the reflection direction is opposite to the rotation direction.

The width of the pulse transmitted by a rotating slit package, $\Delta t_{\rm ch}$, can be estimated from the observed pulse width at a detector, $\Delta t_{\rm d}$, as shown in Fig. 9,

$$\Delta t_{\rm ch} = \Delta t_{\rm d} \times (13,400/13,880), \tag{6}$$

where 13,400 mm is the distance from moderator to slit package, and 13,880 mm is the distance from moderator to the detector. Two pulse widths transmitted by the slit packages with and without neutron supermirrors are plotted in Fig. 10. The pulse width of supermirror-coated slit package decreases with neutron energy. This feature is exactly the essential characteristic of MAGIC chopper. The calculated result for $m = 3$ and $f = 100$ Hz in Eq. (1) is also plotted in Fig. 10. These experimental results are in good agreement with the calculated result.

Let us consider the energy resolution under the assumption that the supermirror-coated slit package used in this study is installed in the Fermi chopper spectrometer 4SEASONS at J-PARC. By substituting the pulse width transmitted by the supermirror-coated slit package into $\Delta t_{\rm ch}$ in Eq. (4), we can estimate the energy resolution of 4SEASONS equipped with the supermirror-coated slit package. As shown in Fig. 11, the energy resolution becomes almost constant ($\sim 5\%$) in the wide range of incident energy, which is also consistent with our prediction.

The energy dependence of the intensity gain of the supermirror-coated slit package is shown in Fig. 12. The integrated intensities of a supermirror-coated slit package are divided by that

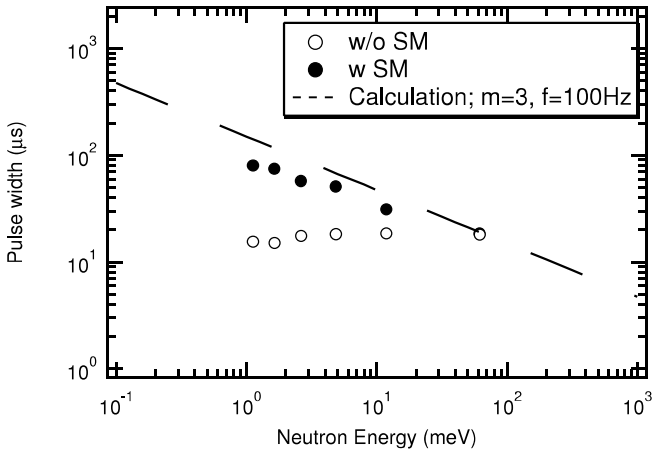

Figure 10. Energy dependence of pulse widths in the case of rotating slit packages with and without neutron supermirrors ($m = 3$). The rotation frequency is 100 Hz for both the cases. The calculated result from Eq. (1) is also plotted.

of the slit package without neutron supermirrors. The gain factor at around 1 meV reaches approximately 20. Until now, the Fermi chopper has never been intended for monochromating such slow neutrons due to the finite depth of slit package. This study demonstrated that a supermirror-coated slit package can monochromate the slow neutrons with high transmission, which confirm that an instrument with the MAGIC chopper can provide superior performance over the wide energy range from cold to epithermal neutron energies.

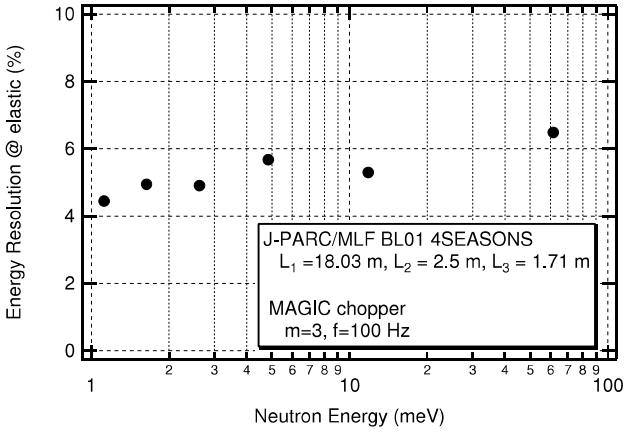

Figure 11. Estimated energy resolution at the elastic position for the Fermi chopper spectrometer 4SEASONS containing the supermirror-coated slit package described in this paper.

5. Conclusion

We proposed to apply a supermirror-coated slit package to monochromating chopper (MAGIC chopper) in order to optimize the experimental conditions for each of incident energies in INS experiment on pulsed neutron source. It is found that a rotating supermirror-coated slit package increases the effective chopper opening time in a lower energy region, which confirms that the MAGIC chopper can overcome the difficulty in the optimization problem of INS experiment with Multi-E_i method. Furthermore, the intensity gain obtained by a supermirror-coated slit package is found to reach 20 at $E \sim 1$ meV. This study experimentally proved that the MAGIC chopper can significantly improve the measurement efficiency of INS experiment by a chopper spectrometer, and thus contribute to open up a new field of materials science.

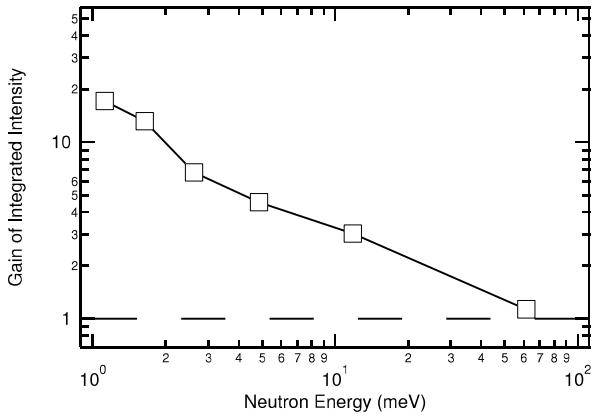

Figure 12. Integrated intensity gain for the supermirror-coated slit package ($m = 3$). The rotation frequency is 100 Hz. All values in the figure are normalized by the integrated intensities for a rotating slit package without neutron supermirrors.

Acknowledgement

This work was supported by a Grant-in-Aid for Specially Promoted Research (No. 17001001) from the Ministry of Education, Culture, Sports, Science and Technology, Japan, and a Grant in-Aid for Scientific Research (C) (No. 20612016) from the Japan Society for the Promotion of Science. The experiment on NOBORU was conducted under Project No. 2009A0083.

References

[1] Mezei F 1997 *J. Neutron Research* **6** 3
[2] Mezei F, Russina M, Schorr S 2000 Physica B **276-278** 128
[3] Nakamura M, Nakajima K, Kajimoto R, Arai M 2007 *J. Neutron Research* **15** 31
[4] Russina M and Mezei F 2009 *Nucl. Instrum. Methods Phys. Res.* A **604** 629
[5] Nakamura M, Kajimoto R, Inamura Y, Mizuno F, Fujita M, Yokoo T, Arai M 2009 *J. Phys. Soc. Jpn.* **78** 093002
[6] Iida K, Kofu M, Katayama N, Lee J, Kajimoto R, Inamura Y, Nakamura M, Arai M, Yoshida Y, Fujita M, Yamada K, Lee S H 2011 *Phys. Rev.* B **84** 060402(R)
[7] Kajimoto R, Nakajima K, Ohira-Kawamura S, Kakurai K, Arai M, Hokazono T, Oozono S, Okuda T 2010 *J. Phys. Soc. Jpn.* **79** 123705
[8] Ishikado M, Nagai Y, Kodama K, Kajimoto R, Nakamura M, Inamura Y, Wakimoto S, Nakamura H, Machida M, Suzuki K, Usui H, Kuroki K, Iyo A, Eisaki E, Arai M and Shamoto S 2011 *Phys. Rev.* B **84** 144517
[9] Nakamura M, Arai M, Kajimoto R, Yokoo T, Nakajima K and Krist Th 2008 *J. Neutron Research* **16** 87
[10] Nakamura M, Kambara W, Krist Th, Shinohara T, Ikeuchi K, Arai M, Kajimoto R, Nakajima K, Tanaka H, Suzuki J, Harada M, Oikawa K and Maekawa F 2014 *Nucl. Instrum. Methods Phys. Res.* A **737** 142
[11] http://j-parc.jp/researcher/MatLife/en/instrumentation/ns3.html
[12] Oikawa K, Maekawa F, Harada M, Kai T, Meigo S, Kasugai Y, Ooi M, Sakai K, Teshigawara M, Hasegawa S, Futakawa M, Ikeda Y, Watanabe N 2008 *Nucl. Instrum. Methods Phys. Res.* A **589** 310
[13] Maekawa F, Oikawa K, Harada M, Kai T, Meigo S, Kasugai Y, Ooi M, Sakai K, Teshigawara M, Hasegawa S, Ikeda Y, Watanabe N 2009 *Nucl. Instrum. Methods Phys. Res.* A **600** 335
[14] Kajimoto R, Nakamura M, Inamura Y, Mizuno F, Nakajima K, Ohira-Kawamura S, Yokoo T, Nakatani T, Maruyama R, Soyama K, Shibata K, Suzuya K, Sato S, Aizawa K, Arai M, Wakimoto S, Ishikado M, Shamoto S, Fujita M, Hiraka H, Ohoyama K, Yamada K, Lee D H 2011 *J. Phys. Soc. Jpn.* **80** SB025

3.5.12

Preliminary study of SANS with focusing mirrors at CPHS

Huarui Wu[1], **Xuewu Wang**[1*], **Dazhi Liu**[2]

[1] Department of Engineering Physics, Tsinghua University
[2] Nuclear Reactor Laboratory, Massachusetts Institute of Technology

E-mail: * wangxuewu@tsinghua.edu.cn

Abstract. Axisymmetric grazing-incidence neutron focusing optics were proposed by researchers from MIT recently. We adapted these focusing mirrors to the design of SANS instruments at Compact Pulsed Hadron Sources (CPHS) which confront challenges of extremely low neutron flux. In this paper, we demonstrated one of a kind focusing mirrors: PP mirrors which consist of two coaxial paraboloids. We analyzed its geometry and we also showed the results of the ray-tracing simulations to demonstrate the performances of PP mirrors and prove that the focusing mirrors can lead to dramatic improvements for the SANS instruments based on compact neutron sources. Furthermore, different optimizations according to the desired particular improvements were discussed.

1. Introduction

The traditional Small-Angle Neutron Scattering (SANS) instruments use a collimation system which limits the size and the divergence of neutron beam[1]. Applying this traditional design to compact neutron sources would make it harder to achieve the flux we need. Therefore its significant to develop a new SANS design method especially for CPHS which is a low-energy accelerator-driver neutron source under construction in Tsinghua University[2]. Many of the techniques for focusing neutrons have been adapted from devices that have been developed for focusing X-rays[3].Inspired by the axisymmetric Wolter-type mirrors which are commonly utilized in X-ray astronomy and microscopy, the MIT group have been doing a great job to apply the idea to neutron focusing mirrors which mainly include paraboloid-paraboloid and ellipsoid-hyperboloid mirrors[1][4][5][6]. The geometrical optics of paraboloids show that neutrons emitted from the focus of a paraboloid could be reflected to be parallel and a parallel beam could be focused to the focus. Two paraboloids can be jointed up to reflect neutrons from one focus to the other as a SANS instrument implement. In this paper, we analyzed the geometry of PP mirrors to study the impact of mirrors position and radius on Q range and sample size and use a ray-tracing software package, McStas[7][8], to study the improvements of neutron flux compared with the typical SANS design[9] for CPHS when equipped with single-layer PP mirrors.

2. Geometrical analysis

The schematic layout of a SANS instrument equipped with PP mirrors is shown in Figure 1. PP mirrors consist of two parts, the left part and the right part are a section of a Paraboloid respectively. We define the Z position of the intersection which is Z_i in Figure 1 as the position

of axisymmetric PP mirrors and we use the radius of the intersection R_i to represent the radius of mirrors.

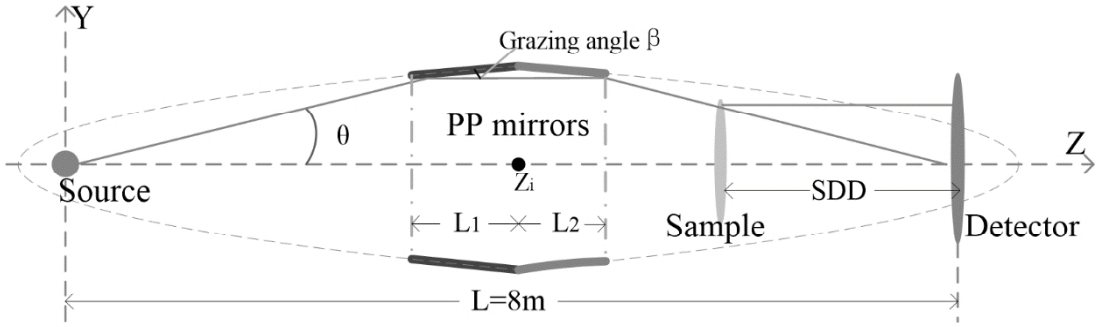

Figure 1. Schematic layout of a SANS instrument with PP mirrors. L denotes the distance from source to detector. L_1 is the length of left part and L_2 is the length of right part. SDD denotes the distance from sample position to detector position. θ is the angle between incident rays and optical axis Z while β is the grazing angle between the rays and mirrors.

Set L_1=0.6m and neutron source is monochromatic whose wavelength is 5 $\mathring{A}$. When Z_i and L_1 is determined, the magnification M of the optical system and L_2 are also determined:

$$M = \frac{L - Z_i}{Z_i} = \frac{L_2}{L_1} \tag{1}$$

The instrument equipped with PP mirrors is such a optical system in which the source represents the object and the spot in detector is the image. The radius of image R_{spot} is decided by M and source radius R_{source}, $R_{\text{spot}} = M \times R_{\text{source}}$. Many SANS experiments require reaching the smallest possible $Q(Q_{\min})$ which is one of the key performances of SANS instruments. We derived mathematical expressions for $Q_{\min}$ in our new system:

$$Q_{\min} = \frac{2\pi}{\lambda} \frac{M R_{\text{source}}}{\text{SDD}} \tag{2}$$

L_1, R_i and Z_i practically determine the mirrors ability to focus neutrons. The neutron flux increases as the increasing of R_i and thus we want to enlarge the mirrors as possible as we can. But R_i is limited by neutrons total reflection. Neutrons reflect twice in PP mirrors and only when both the reflections are total reflections can neutrons focus on the detector plane, thus the grazing angles should be smaller than the critical grazing angle which is satisfied by $\beta_c = 0.099\lambda$ in Ni mirrors. We derived mathematical expressions for grazing angle β_1 in left mirror and grazing angle β_2 in right mirror when neutrons are emitted from neutron source (0,0) and reflect in (Z_{10}, Y_{10}) firstly:

$$\beta_1 = \arctan\left(\frac{1}{\sqrt{1 + \frac{2Z_{10}}{p_1}}}\right) \tag{3}$$

$$\beta_2 = \arctan\left(\frac{1}{\sqrt{1 + \frac{2Z_{10}}{p_2}\frac{L - Z_i}{Z_i}}}\right) \tag{4}$$

Parameters p_1 and p_2 are determined by Z_i and R_i: $p_1 = -Z_i + \left(Z_i^2 + R_i^2\right)^{1/2}$, $p_2 = Z_i - L + \left[(Z_i - L)^2 + R_i^2\right]^{1/2}$. When $Z_i > L/2$, we proved that $\beta_2 > \beta_1$ which means R_i is determined by $(\beta_2)\text{max} < \beta_c = 0.495°$ and β_2 increases as Z_{10} decreases.

Moreover, sample size is a particular factor we need to consider about. In most of the SANS experiments, sample size is less than 1cm×1cm. In our new system, radius of sample is determined by R_i, Z_i and SDD: $R_{\text{sample}} \approx R_i \times \text{SDD}/(L - Z_i)$. Table 1 displays five schemes for the design of instruments with PP mirrors on the premise of sample radius less than 2cm.

Table 1. In order to set the sample radius less than 2cm, we adjusted SDD and this makes Q_{min} larger than the smallest we can achieve. Obviously, Q_{min} is smallest when we put sample on the end of PP mirrors but that would make sample as large as mirrors. I(PP)/I(No) means the ratio of the flux with PP mirrors to that without mirrors which we call traditional design and I(PP)/I(No) is calculated through simulations. The traditional configuration[9]: the source radius $R_{\text{source}} = 1.4$cm, the sampler aperture radius R_{sample}=0.5cm, SDD=5m, L=8m.

Scheme Number	M	Z_i (m)	Z_{start} (m)	Z_{end} (m)	R_i (cm)	SDD (m)	R_{sample} (cm)	Q_{min} ($10^{-3}\mathring{A}^{-1}$)	I(PP) /I(No)
1	1	4.00	3.40	4.60	6.43	1.00	1.89	17.6	3.8
2	1/2	5.30	4.70	5.60	4.44	1.00	1.85	8.8	3.5
3	1/3	6.00	5.40	6.20	3.31	1.00	1.84	5.8	1.1
4	1/4	6.40	5.80	6.55	2.65	1.00	1.83	4.4	0.54
5	1/5	6.60	6.00	6.73	2.32	1.00	1.83	3.7	0.34

According to Table 1, PP mirrors with smaller M can improve Q_{min} better but gain worse neutron intensity. SDD has no effect on intensity but has a significant impact on R_{sample}, Q_{min} and geometrical resolution. The larger SDD, the smaller sample and the better geometrical resolution we can achieve: $\Delta Q_{\text{geo}} = 4\pi M \times R_{\text{source}}/(\lambda \times SDD)$.

3. Ray-tracing simulations

We used McStas to study some key problems existing in single-layer PP mirrors. In our simulations, source radius is set to be 2.0cm. We put a source slit right after the source and the default radius is 1.4 cm. To compare with the new designs, the traditional configuration ($R_{\text{source}} = 1.4$cm, $R_{\text{sample}} = 0.5$cm, SDD=3m) was simulated. Table 1 shows the intensity ratio between instruments with PP mirrors and the traditional instruments. Its obvious that a smaller Z_i and a larger R_i could result in a higher intensity according to not only simulations but also solid angle analysis.

Table 2. Optimized R_i in different schemes

Scheme	1	2	3	4	5
M	1	1/2	1/3	1/4	1/5
Optimized R_i(cm)	5.1	4.1	3.1	2.4	2.1
I(PP)/I(No)	14.1	3.3	1.3	0.60	0.41

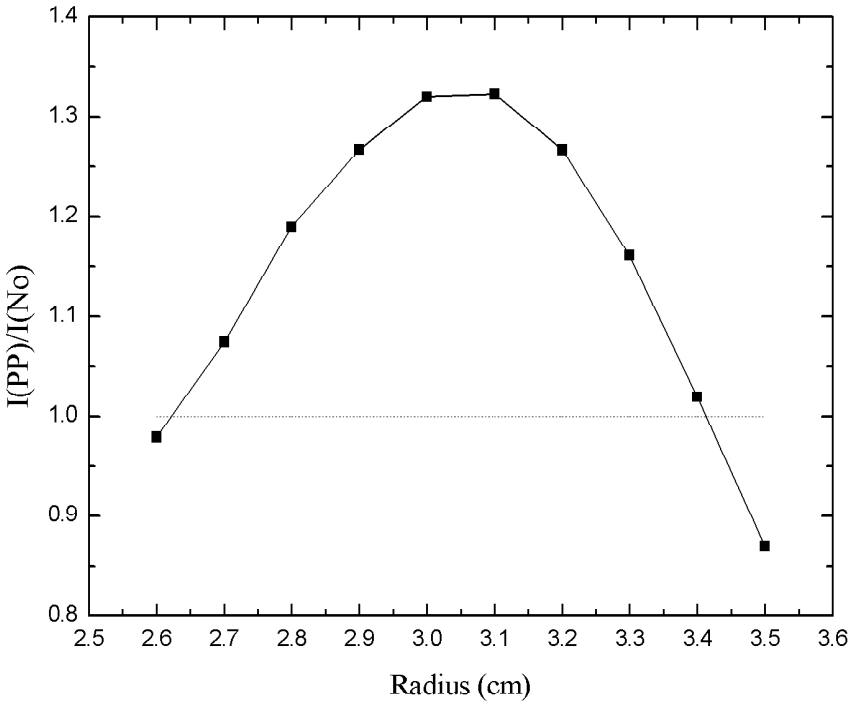

Figure 2. Intensity ratio as a function of radius of PP mirrors in scheme 2 where $M = 1/3$, SDD=1.0m.

R_i in Table 1 was calculated on the basis of point source assumption. Actually neutron source is an areal source which would cause neutrons emitted from the edge of the source may not be focused to the focal by means of two successive total reflections, so we need to adjust R_i to achieve higher intensity. Figure 2 shows the optimized R_i is smaller than that in Table 1 because of the areal sources effect. The intensity increases over 30% when R_i is set to 3.1cm compared with $Ri = 3.3$cm in Table 1. Table 2 displays the adjusted R_i of schemes from 1 to 5 in Table 1 and the adjusted ones can also decrease radius of samples.

Figure 3 demonstrates how the length of left part Paraboloid affect the neutron intensity. The results show a linear relationship between the length and intensity, and the slop increases as the M increases. The slopes of lines when M is 1, 1/2 and 1/3 are 21.87times/m, 5.25times/m and 2.20times/m respectively. So enlarge mirrors length in larger M configuration can gain neutron intensity economically. But when we want to increase neutron intensity through extending mirrors length, we should also consider if there is enough space to extend and the condition of fabrication.

Figure 4 displays the linear relationship between the neutron intensity and source radius. The slopes of lines when M is 1 and 1/3 are 9.72times/cm and 1.12times/cm respectively. According to formula (2), $Q_{\min}$ increases as R_{source} increases and decreases as M decreases. It is concluded that $Q_{\min}$ doesnt change when R_{source} increases by 2 times and M decrease by half. Comparing configuration A with $M = 1$ and $R_{\text{source}} = 1.4$cm and configuration B with $M = 1/2$ and $R_{\text{source}} = 2.8$cm, we find that the neutron intensity ratio of configuration A is more than 2 times than that of configuration B which tells us that a larger M and smaller R_{source} can bring better

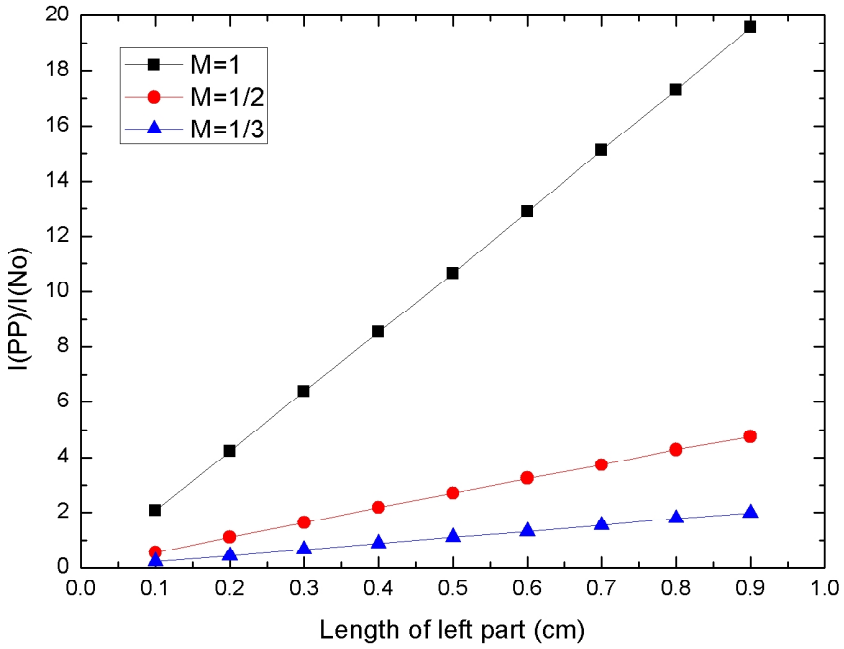

Figure 3. Neutron intensity ratio vs length of left part.

intensity and better ΔQ when we keep $Q_{\min}$ constant, but configuration A causes larger sample than other with smaller M.

4. Dissussion

The SANS instruments with different PP mirrors show different performances. The most important performances are $Q_{\min}$, ΔQ, neutron intensity and sample size is a parameter which must be considered in our new design based on focusing mirrors. Our research shows that its impossible to gain better performances in every aspects for PP mirrors but we can set the new instruments to behave very well in some particular performances to meet our needs.

For CPHS which is eagerly to increase flux, we can set M and R_i a larger value, for example, $M = 1$ and $R_i = 5.1$cm, this configuration could increase the flux by a factor of 14. But it is hard to achieve a smaller $Q_{\min}$ and a smaller sample in the same time. If we make SDD=3m, we can get a smaller $Q_{\min}$ than that in traditional design but also a very larger sample. A possible way to decrease the sample size is to employ a ring sample because the illuminating area of sample is a ring. Figure 5 displays the area of ring sample in different schemes. Setting SDD less than 1.3m can keep the area of ring sample smaller than traditional sample area. However, sample area is still more than 3 times larger than that in traditional design. And if SDD is set to less than 1.3m then $Q_{\min}$ would be nearly 2 times larger than that in traditional design. A better $Q_{\min}$ and a smaller sample size are incompatible but PP mirrors can be optional to meet different needs.

It is a great advantage for experiments using larger samples to gain much higher flux with smaller $Q_{\min}$ when M and SDD are larger and PP mirrors are nested. Nested multilayer mirrors increase the collection area by the placement of co-axial mirrors one inside another, as routinely

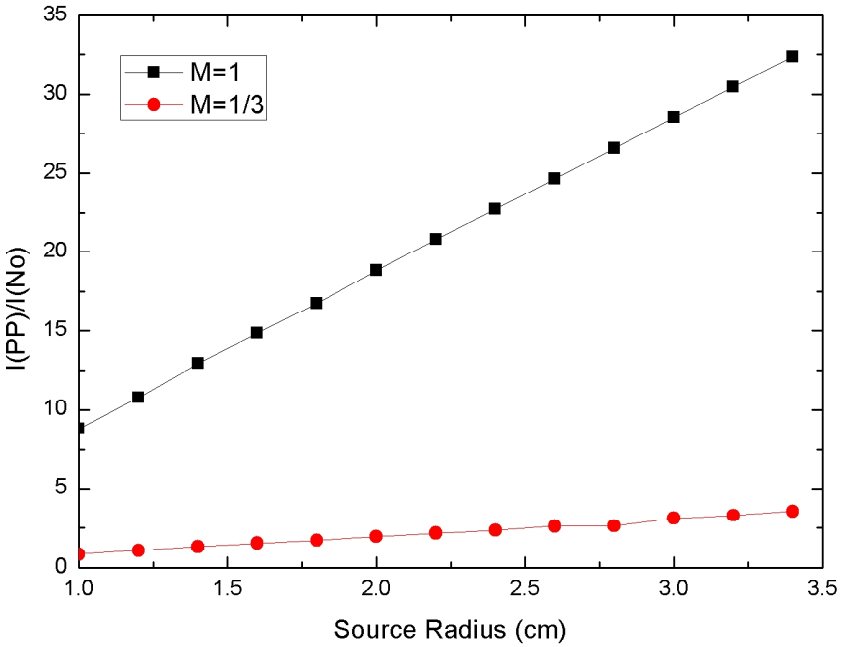

Figure 4. Neutron intensity ratio vs source radius.

done in X-ray astronomy[4]. It is estimated that a four-layer PP mirrors could increase flux by a factor of 50.[1] The construction of such a SANS instrument at CPHS specially aim at those experiments easy to employ larger sample.

Otherwise, the design with PP mirrors can also apply to improve $Q_{\min}$ when flux is not so important. When $M = 1/5$ and SDD $= 1.3$, $Q_{\min}$ can be decrease 2.5 times. In this case, we need a high-resolution detector and we are planning to choose MCPs to complete it.

Also, a balanced design is available when we use nested mirrors with $M = 1$, SDD=2, and R_i less than 4cm or other settings. When we adopt nested mirror into our design, higher neutron intensity is easy to achieve so that we can have better choice to improve other performances.

5. Conclusion

We demonstrate a design with focusing PP mirrors based on CPHS both in geometrical calculations and McStas simulations. SANS instruments with PP mirrors can be improved in flux and $Q_{\min}$ which is very important to SANS experiments. With larger samples, it is easy to increase neutron flux by a factor of 50. PP mirrors can also help us to extend $Q_{\min}$. These transformative improvements have great potential to change the traditional design economically and put many research into a higher stage.

PP mirrors can be used in neutron image, too. We still have much work to optimize it and its fabrications is still worth studying. We are aiming to construct the first SANS instrument equipped with such focusing mirrors and make CPHS perform better function.

[1] The radius of four layers are 5.8, 5.1, 4.6 and 4.0 respectively.

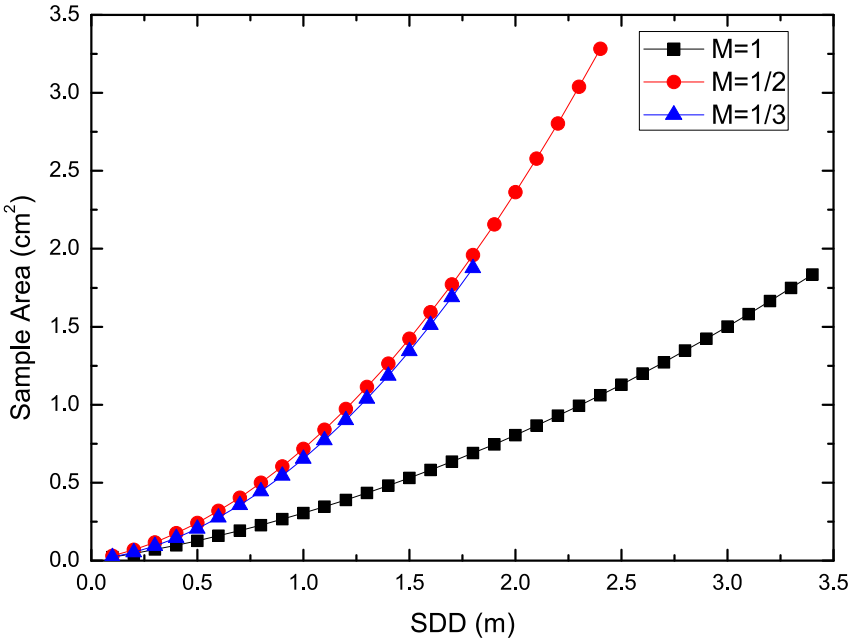

Figure 5. Relations between sample area and SDD when samples are made into rings.

6. Acknowledgement

We are grateful to Dr.Boris Khaykovich of Massachusetts Institute of Technology. This work was supported by the National Natural Science Foundation of China (No. 11322548).

References

[1] Liu D, Gubarev M V, Resta G, Ramsey B D, Moncton D E and Khaykovich B 2012 *Nuclear Instruments and Methods in Physics Research Section A: Accelerators, Spectrometers, Detectors and Associated Equipment* **686** 145–150
[2] Wei J, Bai Y, Cai J, Chen H, Cheng C, Du Q, Du T, Feng Z, Gong H, Guan X *et al.* 2010 *IPAC* **10** 633
[3] Mildner D and Gubarev M 2011 *Nuclear Instruments and Methods in Physics Research Section A: Accelerators, Spectrometers, Detectors and Associated Equipment* **634** S7–S11
[4] Khaykovich B, Gubarev M, Bagdasarova Y, Ramsey B and Moncton D 2011 *Nuclear Instruments and Methods in Physics Research Section A: Accelerators, Spectrometers, Detectors and Associated Equipment* **631** 98–104
[5] Liu D, Khaykovich B, Gubarev M V, Robertson J L, Crow L, Ramsey B D and Moncton D E 2013 *Nature communications* **4**
[6] Liu D, Hussey D, Gubarev M, Ramsey B, Jacobson D, Arif M, Moncton D E and Khaykovich B 2013 *Applied Physics Letters* **102** 183508
[7] Lefmann K and Nielsen K 1999 *Neutron news* **10** 20–23
[8] Willendrup P, Farhi E and Lefmann K 2004 *Physica B: Condensed Matter* **350** E735–E737
[9] Huang T, Gong H, Shao B, Wang D, Zhang X, Zhang K, Wei J, Wang X, Guan X, Loong C K *et al.* 2012 *Nuclear Instruments and Methods in Physics Research Section A: Accelerators, Spectrometers, Detectors and Associated Equipment* **669** 14–18

3.5.13

Band neutron chopper: a solution for large beams and limited space

Alexander Ioffe[1, 3], Peter Stronciwilk[2]

[1]Jülich Centre for Neutron Science, Forschungszentrum Jülich GmbH
Outstation at MLZ, Lichtenbergstr. 1, 85747 Garching, Germany

[2]Central Institute for Engineering, Electronics and Analytics, Engineering and Technology (ZEA-1), Forschungszentrum Jülich GmbH, Wilhelm-Johnen-Straße 52428 Jülich, Germany

E-mail: a.ioffe@fz-juelich.de

Abstract. With existing neutron choppers, the width of produced neutron pulses is coupled with the size of the rapidly rotating parts: the higher the linear speed at the chopper periphery, the shorter the produced neutron pulses. Indeed, choppers with a large diameter are in fact necessary. However, serious problems may occur when chopper disks are installed close to the neutron source (target) as this may result in a conflict with the shielding of neighbouring beams.

Here we describe a new type of chopper that is free from such limitations. It employs a circular band made of a flexible material transparent for neutrons and coated with a neutron absorber for exception of a few small parts serving as neutron windows. The band is driven by a motor with a controllable rotation frequency, allowing for the control of the linear speed of the band; indeed the neutron pulse width is decoupled from the source repetition rate. This kind of flexibility, which allows for the *in-situ* adjustment of the chopper parameters, cannot be provided by disk or Fermi choppers.

Moreover, an increase of the beam height does not influence the chopper construction, whereas for disk choppers, an increase in the diameter of the disk is necessary. Thanks to this flexibility and the arbitrary length of the band, the position of the motor and related electronic components also becomes arbitrary, so that they can be placed away from the neutron guide, in the "radiation-free" area. This prolongs their lifetime and offers an easy access to them during the source operation.

1. Introduction

Traditional neutron choppers are rotating disks coated with a neutron absorbing material fully absorbing neutrons. Neutron beam can only penetrate the disk through narrow stripes (neutron windows) that are either free from the absorbing coating or cuts in the disk body.

The frequency of the produced neutron pulses f_{pulse} is defined by the rotation frequency of the disk f_{disk} and the number of neutron windows on it:

[1] To whom any correspondence should be addressed.

$$f_{pulse} = nf_{disk} \tag{1}$$

When used at pulsed neutron sources, disk choppers provide the time shaping of neutron pulses by moving a small chopper disk window of size S_w across the beam of the size S_{beam} with a high speed $v_{chopper}$. The width of the neutron pulse (FWHM) is given

$$\tau = \frac{\sqrt{S_{beam}^2 + S_w^2}}{v_{chopper}} \tag{2}$$

where $v_{chopper} = 2\pi f_{disk} R$ is the linear speed at the peripheree of the chopper disk of radius R, so that

$$\tau = \frac{\sqrt{S_{beam}^2 + S_w^2}}{2\pi f_{disk} R} \tag{3}$$

For the pulse shaping choppers, the rotation frequency of the chopper disk is equal to the repetition frequency of the pulsed source and the only free parameter to tune τ is the chopper radius R. Therefore, to achieve small τ at low repetition rates, e.g. for 10-15 Hz, R should be rather large. Indeed, the duration of the neutron pulses produced by a disk chopper is coupled with its size: the shorter should be the neutron pulse, the higher should be the linear speed at the chopper periphery and the larger should be the size of the disk. Moreover, the required size of choppers can be even larger in the case if they should be used to interrupt the beams propagating in the neutron guides of a large cross-section, particularly around the centre of elliptic focusing neutron guides, where the cross-section of those can approach 30cm.

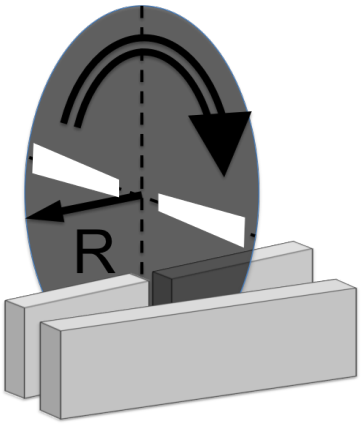

Fig. 1. Positioning of a large chopper disk in a neutron guide system and a possible place conflict

However, a possible size of chopper disks is limited. Beside mechanical constrains that may be imposed on large disks, serious problems may arise when chopper disks should be installed so close to the target, that they may conflict with neighbouring beams (Fig. 1). For example, for the 5.5° beam separation thought for the ESS, the distance between neutron beams at the face of the biological shielding (6m from the target) is only 56cm. This does not only impose a limit on the chopper size, but also causes serious problems with an access to choppers during the operation of the source without interruptions of the operation of the neighboring instruments.

Therefore, there is a serious problem in the use of pulse shaping choppers to be placed close to the target. Another problem related to the use of the disk choppers is that the chopper motors and related electronics will be positioned rather close to the neutron beam at the beginning of neutron tract, where they can be heavily irradiated by high-energy gammas and fast neutrons, that may significantly reduce their lifetime.

Here we are suggesting principally a different kind of neutron chopper that doesn't employ the rotating disk and therefore is free from limitations discussed above.

2. Band neutron chopper

In the suggested neutron chopper a flexible band coated by a neutron absorbing material is used instead of the disk. The band forms the closed ring that is moved across the neutron beam (Fig. 2). A few places on the band are not coated with the absorbing layer and are functioning as neutron windows. This band is moving across the neutron beam (e.g. across the neutron guide) blocking the neuron beam all the time beside short time intervals when the neutron beam is crossed by a neutron window – this is how the chopping of the neutron beam is achieved.

In more details, the ring can be made for example of thin carbon fibre film (about 0.5mm), which is flexible in horizontal direction and transparent for neutrons (similar fibres, however even much thicker, are used in commercial disk choppers produced by ASTRIUM). The surface of the band is both side coated by a thin polymer film containing a strong neutron absorbing material (e.g. made of ^{10}B or Gd with the thickness of a few mm; alternatively, the neutron absorbing material can be embedded in the band), so that the band is completely opaque for the neutron beam. A few places on the band are not coated with absorbing layer and are functioning as neutron windows.

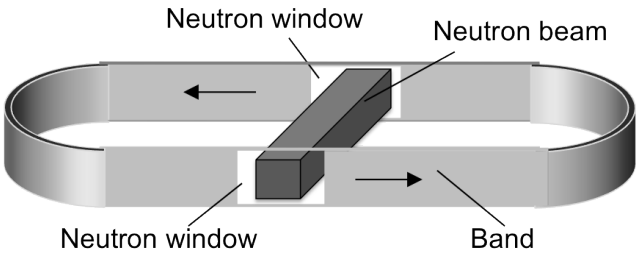

Fig. 2. Principle of band neutron chopper

To provide short neutron pulses with reduced speed of the band, two neutron windows on two bands moving in opposite directions are used, so that each of them is blocking a half of the width of the neutron beam (Fig.3).

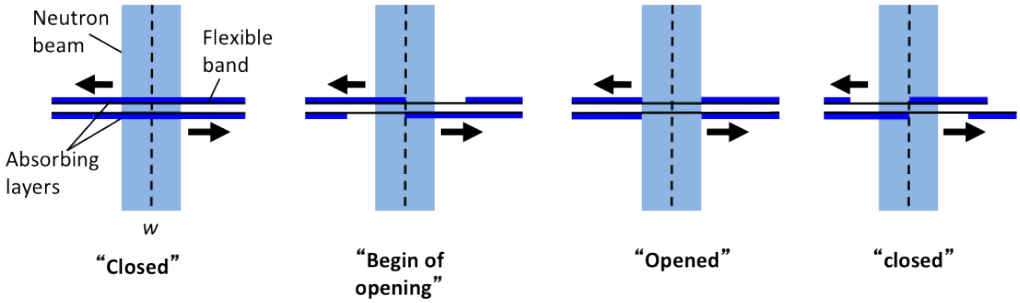

Fig. 3. The use of two oppositely moving bands for interruption of neutron beams

The opening time for the each half of the beam is given as w/v_{band}, where w is the width of the neutron beam and v_{band} is the speed of the band. If the width of neutron windows is equal to the beam width, then the closing time is equal to the opening time, so that the full width of the neutron pulse is $\Delta\tau = w/v_{band}$ (Fig. 4).

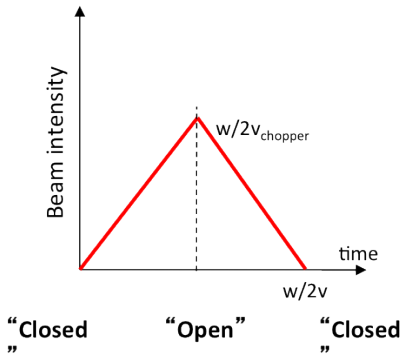

Fig. 4. Time diagram of neutron pulse

The band is driven by a motor (Fig. 5) and guided into the break in the neutron guide by a set of rollers. There are two different operation modes: (i) with a constant rotating speed; or (ii) with controlled and reversible rotating speed (e.g. DC-motor). In the mode (i) the distance l between neutron windows and speed of the band should be equal to the repetion time between neutron pulses

$$T = l / v_{band} \tag{4}$$

In the mode (ii), one can regulate the the band speed, e.g. to reduce the band speed to $v_{band}^{(1)}$ during the "closed" phase of the chopper, thus increasing T (see Eq.(3)), and then to increase the band speed (up to maximal) just before neutron windows enter the neutron beam to get a necessary pulse width

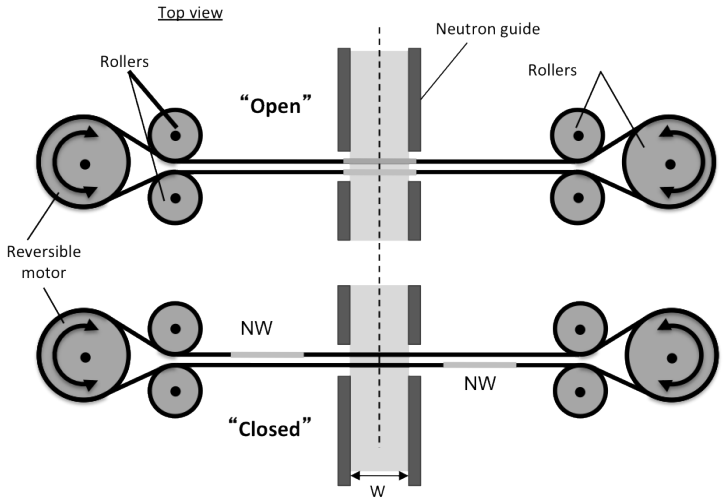

Fig. 5. The neutron band chopper: closed band is used for moving "sub-bands" with the same speed but in oppposite directions.

$\tau = w/v_{band}^{(2)}$ (Fig. 6). Thus, the neutron pulse width $\Delta\tau$ is decoupled from the period T of neutron pulses (or from the repetition rate of a pulsed source). Such a flexibility allowing for the "on-line" adjustment of chopper parameters can not principally be provided neither by disk nor Fermi choppers.

Another big advantage of the band chopper is that thanks to the flexibility and an arbitrary length of the band, the position of the motor and electronic components also becomes arbitrary, so that they can be placed at a practically arbitrary distance from the neutron beam in a "radiation-free" area (Fig. 6).

This has twofold positive consequences: first, the lifetime of motor and electronic components will be prolonged as they will not be heavily irradiated and, second, this will allow for the avoidance of the service or replacement of the failing parts of neutron choppers placed in areas with a very high

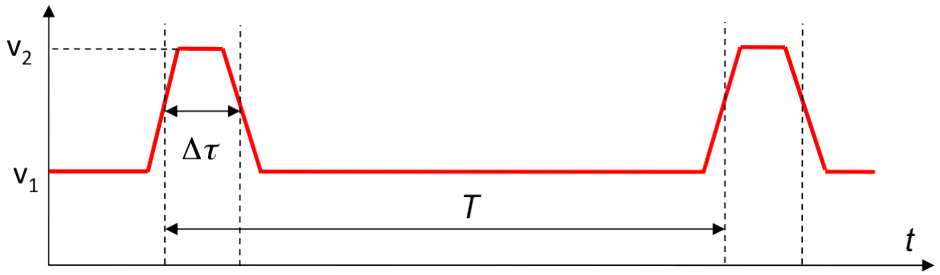

Fig. 6. Time diagram for band chopper with adjustable speed v_{band}.

radioactive level. The latter becomes especially critical for a neutron facility in the case of "a high density" of neutron beams (e.g. separated by 5^0, as planned at the ESS) and a large number of choppers simultaneously used at many instruments. Even a small failure rate, say 1% per cycle, will result in the failure of two choppers from all installed at 22 instruments means an average failure of one chopper each two cycles. If heavy shutters are used, access to a failed chopper will require the closing of shutters for at least two or even four instruments. However, in the case of the use of light shutters that only block thermal/cold neutrons, the forbidden for the access area around such a beam will be spread over much more instruments. Indeed, the access to the failed component will require the shut down of a large number of instruments or even the source as a whole – neither of these approaches is hardly an alternative to leave the failed instrument unusable for the whole operation cycle.

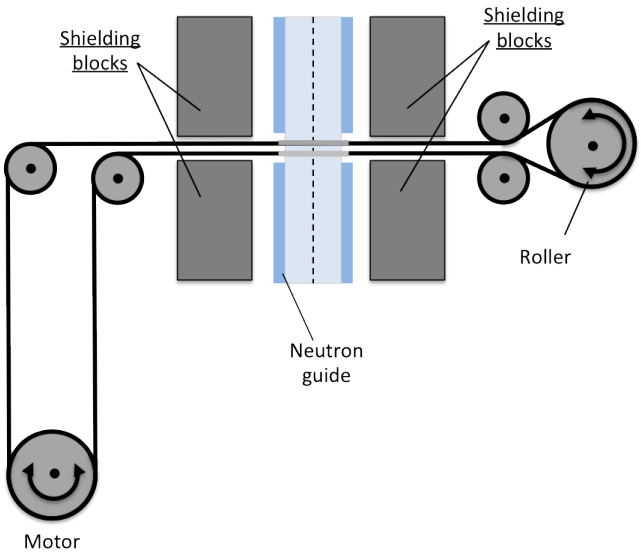

Fig. 7. Neutron band chopper with remotely positioned motor (and electronic components)

Possible operation modes of the band chopper are shown in Fig. 8. If the band is moving with a constant speed in one direction (Fig. 8a), then the operation is similar to one for standard disk choppers, however the discussed above flexibility of the positioning of the motor makes it attractive in the case of taught space conditions. If the band is moving in one direction, however with a variable speed (Fig. 8b), the

pulse width and repetition rate are decoupled. The same can be achieved by the oscillatory motion of the band in opposite directions (Fig. 8c).

3. Conclusions

In this article we describe a new kind of neutron chopper – the band chopper. For the interruption of a neutron beam a flexible band coated with a sufficiently strong neutron absorber is used. In contrast to the currently used disk choppers, the linear speed of the band is not coupled with the chopper radius that should be rather large for slow rotation frequencies required for low repetition rate pulsed sources: the size of chopper disks may be limited because of the place conflict with neighbouring neutron guides.

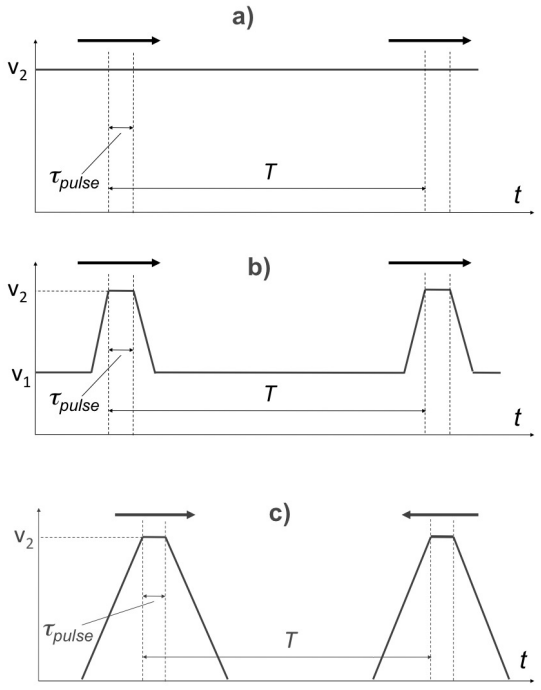

Fig. 8. Possible operation modes of the band chopper.

Moreover, because of the flexibility and an arbitrary length of the band, motor and related electronic components can be positioned in a “radiation-free” area outside of the biological shielding of the neutron beams. This will both prolong the lifetime of electronic components and allow for their service or exchange even during the operation of the source: the problem that becomes critical in the case of a dense neutron beams’ arrangement, when access to failed components will require the shut down of a significant number of neighboring instruments.

From the engineering point of view, an advantage of the band chopper is that all mechanical components can be standardized, so that the choppers for different neutron beams will differ only by the band (height and size/position of neutron windows).

4. References

[1] Linander R, et al., “ESS target station-an overview of the monolith layout and design”, *11th Int. Topical Meeting on Nuclear Applications of Accelerators, Bruges, 2013,* http://accapp13.org/sites/default/files/WEOTA03.pdf

3.5.14

Current status of a TOF-Laue single crystal neutron diffractometer SENJU

T Ohhara[1], R Kiyanagi[1], A Nakao[2], T Hanashima[2], K Munakata[2], T Moyoshi[2], T Kuroda[2], K Kaneko[1], I Tamura[1], K Oikawa[1], T Kawasaki[1], Y Yamauchi[1] and S O Kawamura[1]

[1]J-PARC Center, JAEA, Tokai, Ibaraki 319-1195, Japan.
[2]CROSS, Tokai, Ibaraki 319-1106, Japan

E-mail: takashi.ohhara@j-parc.jp

Abstract. A TOF-Laue single crystal neutron diffractometer at the BL18 of MLF/J-PARC, SENJU, was designed for precise crystal and magnetic structure analyses under extreme environments such as low-temperature, high-pressure and high-magnetic field. On-beam test measurements of 4K cryostat, high-pressure cell and vertical-field superconducting magnet were carried out to evaluate the background from each device. All devices worked as planned and single crystal neutron diffraction measurements under extreme conditions on SENJU were successfully achieved.

1. Introduction

SENJU is a time-of-flight (TOF) Laue single crystal neutron diffractometer which was launched in March 2012 at the BL18 of MLF/J-PARC. SENJU was designed for crystal and magnetic structure analyses of inorganic/organic crystalline materials with small single crystal less than 1.0 mm^3 in volume [1,2]. To achieve the purpose, SENJU has 37 scintillation area detectors [3] to measure many Bragg reflections simultaneously as shown in figure 1 and use relatively short wavelength incident neutron (λ > 0.4 Å) to cover wide range of reciprocal space. SENJU was also designed for measurement under extreme conditions such as low-temperature, high-pressure and high-magnetic field [1,2]. Single crystal neutron diffraction measurement under extreme condition is an important analytical technique in the field of materials science because this technique is one of the best way to obtain the precise crystal and magnetic structures of many materials which shows interesting properties such as magnetism, superconductivity or ferroelectricity under various extreme conditions. Many single crystal diffractometers which have wide area detectors, for example, SXD [4] at ISIS, VIVALDI [5] and CYCLOPS [6] at ILL, KOALA [7] at ANSTO have a flange at the top of the sample chamber to accept various types of sample environment devices. SENJU also has a vacuum sample chamber with the MLF standard size flange to accept various types of sample environment devices which are developed and used in MLF to achieve various types of extreme conditions.

Some test measurements in the commissioning phase showed that 0.4~4.4 Å wavelength incident neutrons are available as the 1st frame and 4.6~8.8 Å as the 2nd frame, estimated neutron intensity at the sample position with 1MW accelerator power is 0.6 x 10^6 $n \cdot s^{-1} \cdot mm^{-2}$ in the standard mode and 1.3 x 10^6 $n \cdot s^{-1} \cdot mm^{-2}$ in the focused mode (with a insertion focusing guide). In addition, the measurements with empty vacuum sample chamber showed that the background is 1/1000 lower than the neutron

scattering from a ϕ5 mm V-Ni null alloy [2]. Figure 2 shows a typical diffraction image at SENJU, a TOF Laue neutron diffraction image of a ϕ2 mm size ruby single crystal.
After the initial commissioning of SENJU, commissioning and test measurements of three sample environment devices, 4K cryostat with 2-axes goniometer, piston cylinder type high-pressure cell and vertical-field superconducting magnet were conducted to check the operation and to evaluate the background from the devices and S/N ratio of diffraction spots when a sample crystal was mounted on the devices. This paper describes the results of commissioning and on-beam test measurements of those sample devices.

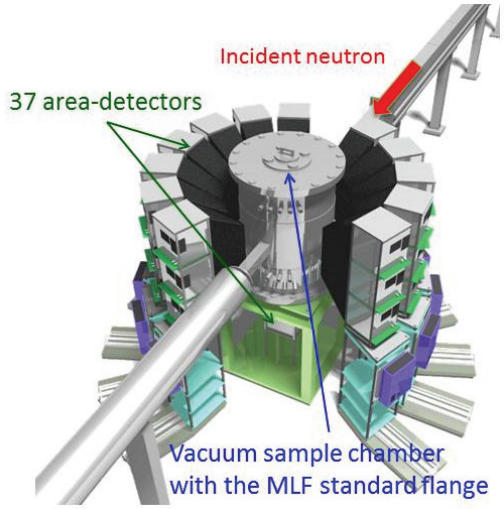

Figure 1. Schematic view of SENJU.

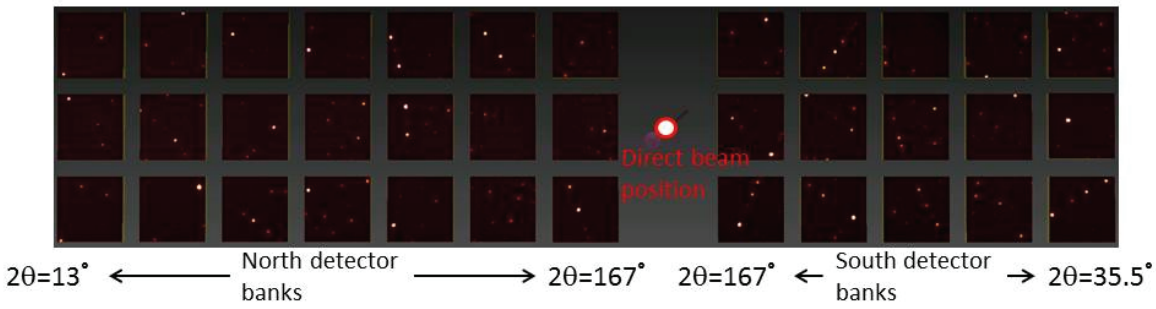

Figure 2. A typical diffraction image at SENJU, a TOF Laue neutron diffraction image of a ϕ2 mm size ruby single crystal.

2. Commissioning and on-beam test measurements of sample devices

2.1. 4K cryostat with 2-axes goniometer

4K cryostat is one of the most important sample environment devices for diffraction measurements of materials science. In usual low temperature experiment with 4-circle single crystal neutron diffractometer, a cryostat is mounted on a large goniometer equipped with ω, χ and ϕ axes to rotate the sample crystal to access to arbitrary points in the reciprocal space. However, because SENJU has no space to set a large goniometer at the sample position, we developed a new piezo-based low temperature 2-axes fixed-χ goniometer system [8]. Figure 3 shows the photograph of the goniometer at the cold-head of a closed-cycle cryostat. This goniometer has two piezo rotating devices (ω, ϕ) and a fixed-χ arm to change the crystal orientation under vacuum and low temperature condition. Because of the poor thermal conductivity of the piezo rotators, additional copper mesh wires were attached between the cold-head and the χ arm, and the χ arm and the sample holder (XY-stage) as heat paths.

The result of a cooling test showed that the lowest temperature at the sample position was 3.8 K and the cooling time from room temperature to the lowest was 4.5 hours as shown in figure 4. Two piezo rotators, attocube systems AG ANR240/RES for the ω axis and ANR220v/RES for the ϕ axis, stably work even in the lowest temperature. An on-beam test measurement of this cryostat showed that there was no additional background from the cryostat except weak powder diffractions from two cylindrical radiation shields in the vacuum chamber in which four 5 μm thickness Al foils are on the direct beam path.

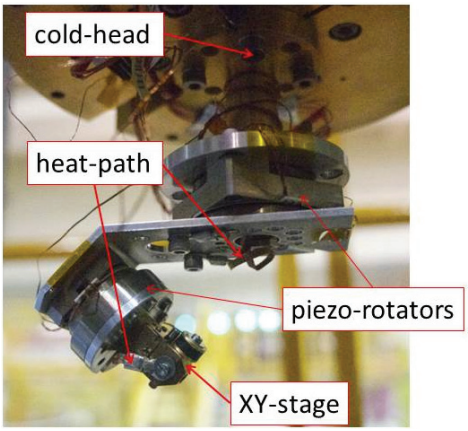

Figure 3. Photograph of the 2-axes goniometer at the cold-head of the cryostat.

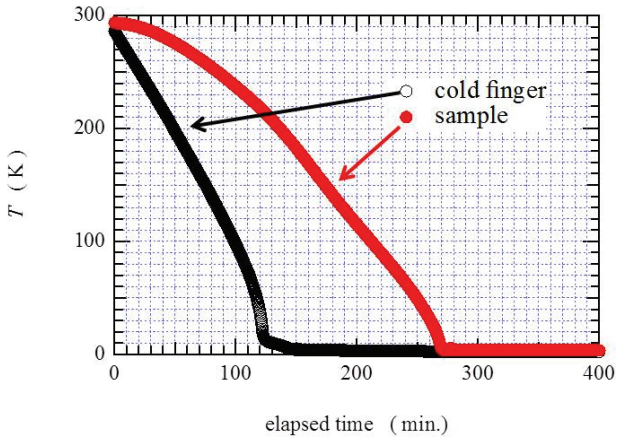

Figure 4. Cooling curves of the 4 K cryostat of SENJU. Red dots show the temperature change of the sample position.

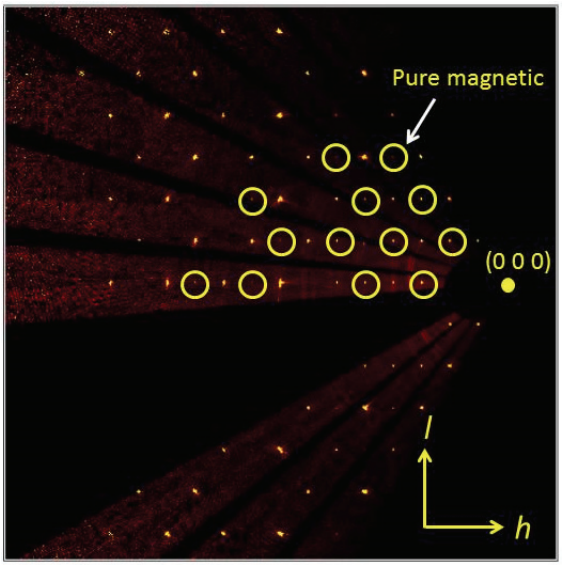

Figure 5. *(h0l)* plane of the diffraction from MnF_2 at 4.3 K. Yellow circles indicate pure magnetic reflections.

To confirm the performance of the cryostat, we carried out a structure analysis of the low-temperature phase of a MnF_2 single crystal, which shows paramagnetic – antiferromagnetic phase transition at 75 K [9]. The reported space group is $P4_2/mmm$ and cell parameters are a = b = 4.87 Å and c = 3.30 Å. 2 x 2 x 2 mm MnF_2 single crystal was mounted on the XY-stage at the top of the goniometer and temperature of the cold-head was set to 4.0 K. Finally, the temperature gauge at the XY-stage in the figure 3 indicated 4.3 K. In the diffraction measurement, neutron exposure time was 10 hours. Figure 5 shows an observed diffraction image of the reciprocal space, (h0l) plane. Many pure magnetic reflections of the antiferromagnetic phase (white circles) were observed. Powder pattern from the

cryostat is very weak comparing to the Bragg peaks from the sample crystal. In this measurement, 2048 reflections including 51 pure magnetic reflections ($I > 3\sigma(I)$) were observed. After the refinement of the 14 structure parameters including magnetic structure parameters, final R value was 5.28% ($I > 3\sigma(I)$) and obtained magnetic moment of Mn was $\mu(Mn) = 4.7(1)\ \mu_B$. Those were acceptable values. This result indicates that the cryostat has enough cooling capacity and the neutron scattering from the cryostat rarely disturbs the structure analysis.

2.2. High-pressure piston-cylinder cell

Varying pressure is sometimes very important to explore new properties of a functional material. A compact piston-cylinder type high-pressure cell, which has an ideal geometry because the apparatus has a wide opening accessible direction for incoming and scattered neutrons, made from copper-beryllium alloy (< 2 GPa) was tested on SENJU. A taurine single crystal with 1.5 x 1.5 x 1.5 mm size was enclosed in the pressure cell together with deuterated glycerol and pressurized up to 1 GPa. Accelerator power was 300 kW and the exposure time was 6 hours. Even through the intensity of neutrons scattered from the pressure cell was relatively high, many distinct Bragg reflections from the taurine crystal were observed as shown in figure 6. The result shows that this piston-cylinder cell can be used as one of the high-pressure environments of SENJU.

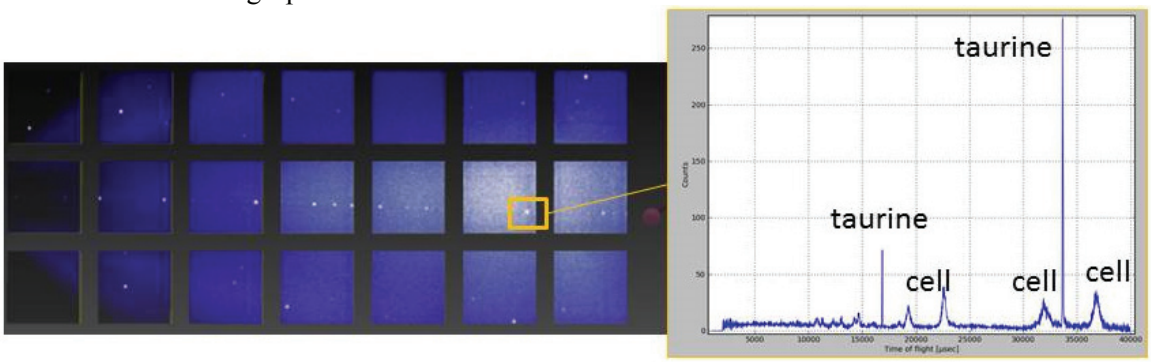

Figure 6. A neutron Laue image and a TOF profile of the taurine crystal in the piston-cylinder type high-pressure cell measured at SENJU.

2.3. Vertical-field superconducting magnet

Magnetic field is an important sample environment in researches of magnetism. To realise a neutron scattering experiment in magnetic field, a vertical-field magnet was developed as a MLF standard sample environment device. The first test of the magnet showed that the maximum magnetic field was 6.85 T and minimum temperature was 50 mK respectively. Then, the magnet was set in the vacuum chamber of SENJU without sample and exposed to neutron beam at room temperature to check the background from the magnet. Figure 7(a) shows a diffraction image of all detectors. Whereas the upper and the lower detectors were hidden by the magnet as expected, all the equatorial plane detectors and the bottom detector are available for diffraction measurement with the magnet. Figure 7(b) shows the 1st frame (0.4~4.4 Å) time-of-flight neutron spectrum of one of the highest angle detectors from the magnet. As expected, many Bragg peaks from the magnet were observed. On the other hand, as shown in figure 7(c), there is no Bragg peak from the magnet in the spectrum of the 2nd frame (4.4~8.8 Å), important wavelength region for measurements of magnetic reflections in the field of materials science.

A test measurement of the magnet with a sample crystal was also carried out. A single crystal of $CeCoGe_3$ [10] with 3.0 x 1.5 x 1.5 mm size was set in the magnet. Measurement temperature was 1.5 K, magnetic field was 0.5 T, accelerator power was 300 kW and neutron exposure time was 2.5 hours. The diffraction image and a TOF profile in figure 8 shows that Bragg peaks of the sample crystal were much higher than the peaks of Al from the magnet even in the 1st frame.

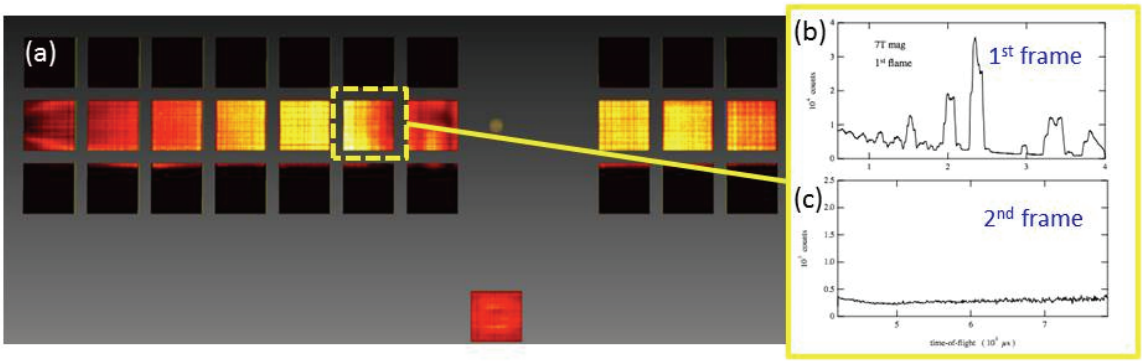

Figure 7. Neutron scattering from the magnet measured at SENJU. (a) Scattering image of the area detectors. (b) The 1st frame (0.4 – 4.4 Å) TOF profile of the detector enclosed by the dashed line. (c) The 2nd frame (4.6 – 8.8 Å) TOF profile of the detector enclosed by the dashed line.

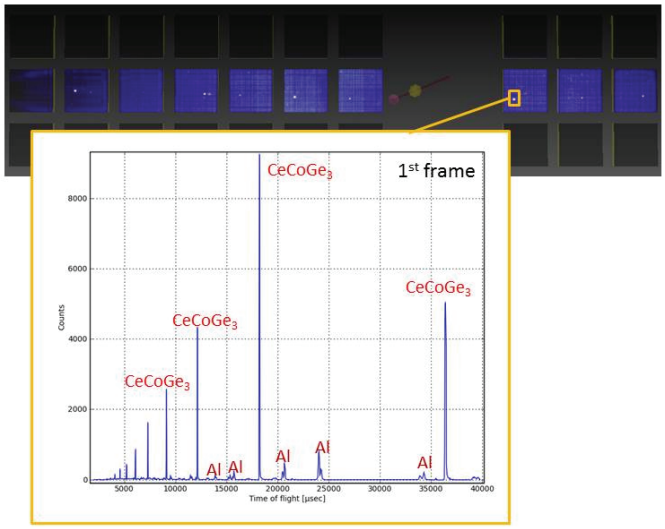

Figure 8. A neutron Laue image and a TOF profile of the $CeCoGe_3$ crystal in the magnet measured at SENJU.

3. Summary

Commissioning and on-beam test measurements of the devices at SENJU showed that the all three devices worked as planned on SENJU. The 4 K cryostat has enough cooling capacity and the powder pattern from the cryostat rarely disturbed the structure analysis. In cases of the magnet and high-pressure cell, powder patterns from the devices were observed but Bragg peaks from the samples were clearly observed. Those results indicate that the main purpose of SENJU, crystal and magnetic structure analyses of inorganic/organic crystalline materials under extreme conditions, was successfully achieved. The devices described in this paper are available for the general user program at SENJU. In near future, we will develop new collimators for the magnet and the high-pressure cell to reduce the powder patterns and improve the quality of diffraction data.

References

[1] Tamura I, Oikawa K, Kawasaki T, Ohhara T, Kaneko K, Kiyanagi R, Kimura H, Takahashi M, Kiyotani T, Arai M, Noda Y and Ohshima K 2012 *J. Phys. Conf. Ser.* **340** 012040

[2] Oikawa K, Kawasaki T, Ohhara T, Kiyanagi R, Kaneko K, Tamura I, Nakamura T, Harada M, Nakao A, Hanashima T, Munakata K, Kimura H, Noda Y, Takahashi M and Kiyotani T 2014 *JPS Conf. Proc.* **1** 014013

[3] Kawasaki T, Nakamura T, Toh K, Hosoya T, Oikawa K, Ohhara T, Kiyanagi R, Ebine M,

Birumachi A, Sakasai K, Soyama K and Katagiri M 2014 *Nucl. Instrum. Meth. Phys. Res.* A **735** 444
[4] Keen D A, Gutmann M J and Wilson C C 2006 *J. Appl. Cryst.* **39** 714
[5] Wilkinson C, Cowan J A Myles D A A, Cipriani F and McIntyre G J 2002 *Neutron News* **13** 37
[6] Ouladdiaf B, Archer J, Allibon J R, Decarpentrie P, Cailleau M H L, Carvajal J R, Hewat A W, York S, Brau D and McIntyre G J 2011 *J. Appl. Cryst.* **44** 392
[7] http://www.ansto.gov.au/ResearchHub/Bragg/Facilities/Instruments/Koala/
[8] Kaneko K, Munakata K, Dohi Y, Noda Y, Hanashima T, Sato K, Kawasaki T, Kiyanagi R, Nakao A, Ohhara T, Oikawa K and Tamura I 2013 *MLF Annual Report 2012* 43
[9] Erickson R A 1953 *Phys. Rev.* **90** 779

This is a blank page.

3-6. Devices

This is a blank page.

3.6.1

Development of an in-situ spin-exchange optical pumping ^{3}He neutron spin filter

Takayuki Oku[1], Hirotoshi Hayashida[2], Hiroshi Kira[2], Kenji Sakai[1], Kosuke Hiroi[1], Takenao Shinohara[1], Yoshifumi Sakaguchi[2], Takashi Ino[3], Manabu Ohkawara[4], Kenji Ohoyama[4], Lieh-Jeng Chang[5], Mitsutaka Nakamura[1], Jun-ichi Suzuki[2], Hirohiko M. Shimizu[6], Kazuya Aizawa[1], Masatoshi Arai[1], Yasuo Endoh[1], Kazuhisa Kakurai[1]

[1] JAEA, Tokai, Ibaraki 319-1195, Japan
[2] CROSS, Tokai, Ibaraki 319-1106, Japan
[3] KEK, Tsukuba, Ibaraki 305-0801, Japan
[4] Institute for Material Research, Tohoku University, Sendai, Miyagi 980-8577, Japan
[5] Department of Physics, National Cheng Kung University, Tainan 70101, Taiwan
[6] Nagoya Univ., Furocho, Chikusa, Nagoya 464-8602, Japan

E-mail: takayuki.oku@j-parc.jp

Abstract. In order to apply the ^{3}He neutron spin filter (NSF) to experiments at an intense pulsed neutron experimental facility such as the J-PARC, it is important to make the system stable, useful and easy to setup and operate, because the system is located inside a radiation shield for high energy gamma ray and neutrons. In this study, we have developed compact laser optics with a volume holographic grating (VHG) element for a spin-exchange optical pumping (SEOP) system, and composed an in-situ SEOP ^{3}He-NSF. The details of the setup and its performance are reported.

1. Introduction

We have been developing a ^{3}He neutron spin filter (NSF) for efficient utilization of pulsed neutrons, since the ^{3}He NSF is effective for neutrons in the wide energy range. The ^{3}He NSF is effective especially for neutrons with energy higher than several-tens-meV, and can cover a large solid angle and polarize neutrons without deflecting them from their original trajectory. In order to apply the ^{3}He NSF to experiments at a pulsed neutron experimental facility such as the J-PARC, it is important to make the system stable, useful and easy to setup and operate. In this study, we have developed an in-situ spin-exchange optical pumping (SEOP) ^{3}He-NSF with a spin flip function for the ^{3}He polarization based on the adiabatic fast passage (AFP) NMR.

2. A compact laser optics

We have developed compact laser optics with an air-cooled laser diode array (LDA). The output laser power of the air-cooled LDA is about 30 - 40 W, which is much lower than that of a water-cooled one. However, it is enough to polarize ^{3}He gas within a small-sized cell [1]. The laser spectrum of the LDA is broader than the absorption line width of Rb [2]. Thus, we employed a volume holographic grating (VHG) element to compose an external cavity laser (ECL) to sharpen the laser spectrum to

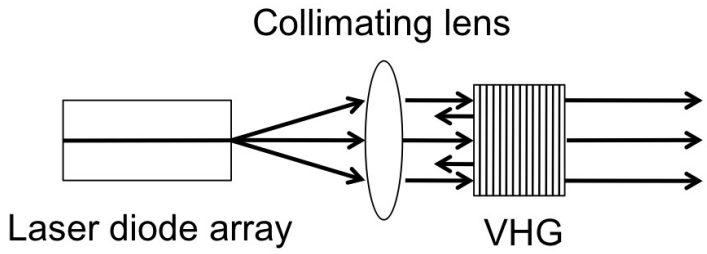

Figure 1. A schematic layout of the external cavity laser with a VHG element.

match it to the Rb absorption line [3] (Fig. 1). The developed laser optics are shown in Fig. 2. The LDA is cooled with a Peltier device and a fan (Fig. 2). Collimating and shaping lenses and a λ/4 wave plate were assembled in a box (Fig. 2). Therefore, the circularly polarized laser is extracted from the box. We have measured the final laser power, and it was found that the total laser power loss was 20 % in the setup.

The measured laser spectra with and without the feedback are shown in Fig. 3. The laser spectrum was narrowed to be a FWHM of 0.35 nm by the feedback, which is 16 % of the original spectrum width without the feedback (Fig. 3). The specification value of the spectrum width of the VHG element is 0.14 nm. The observed spectrum width obtained with the feedback was about 2.5 times that of the specification value of the VHG. This may be due to a mis-alignment of the optical components such as the so-called "smile" of the LDA (The "smile" is defined as the bending of the line of emitters of the LDA [4, 5]).

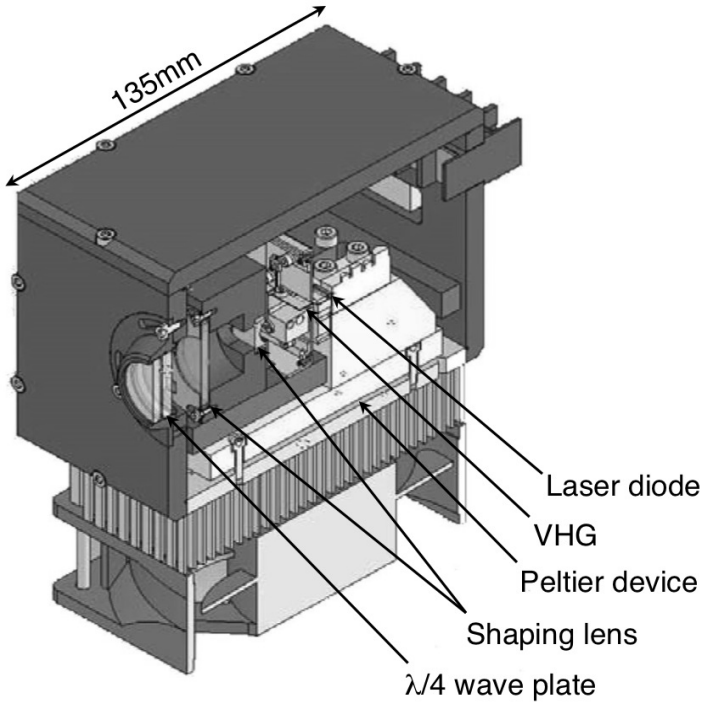

Figure 2. The cross sectional view of the developed laser optics.

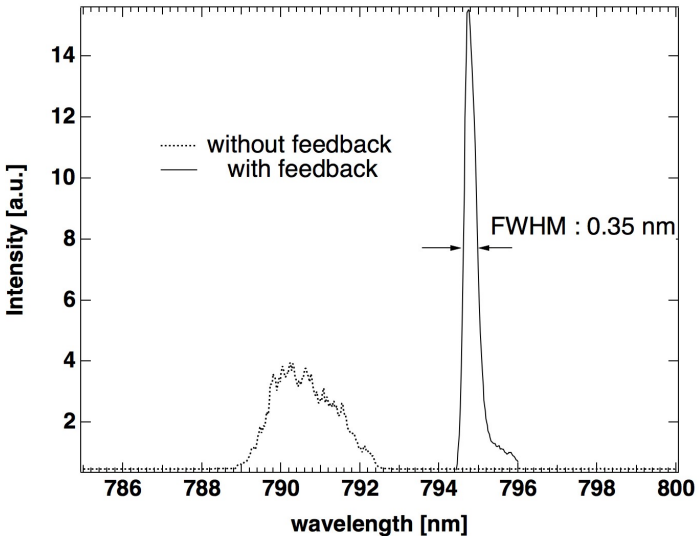

Figure 3. The measured laser spectra with and without feedback to narrow the spectrum.

3. An In-Situ SEOP ^{3}He NSF

We have composed a setup for the in-situ SEOP ^{3}He NSF with the developed laser optics (Fig. 4(a)). Our previous in-situ SEOP setup with the ECL in Littrow configuration is also shown in Fig. 4(b). The new setup has a simpler structure and is easier to set up and operate, because most of the optical components are integrated in the box for the developed laser optics (Figs. 2, 4(a)).

^{3}He gas with a gas quantity of 11 atm-cm is contained in a GE-180 glass cell with a size of 34 mmϕ x 52 mm-L. The cell is located in an Al-oven which is set inside the solenoid coil (Fig. 5). The oven is equipped with RF and pick-up coils for AFP-NMR (Fig. 5). The polarity of ^{3}He can be π-flipped by the AFP-NMR. The AFP-NMR signal is proportional to the polarization degree of ^{3}He, $P_{^3\mathrm{He}}$, which can be measured by it [6].

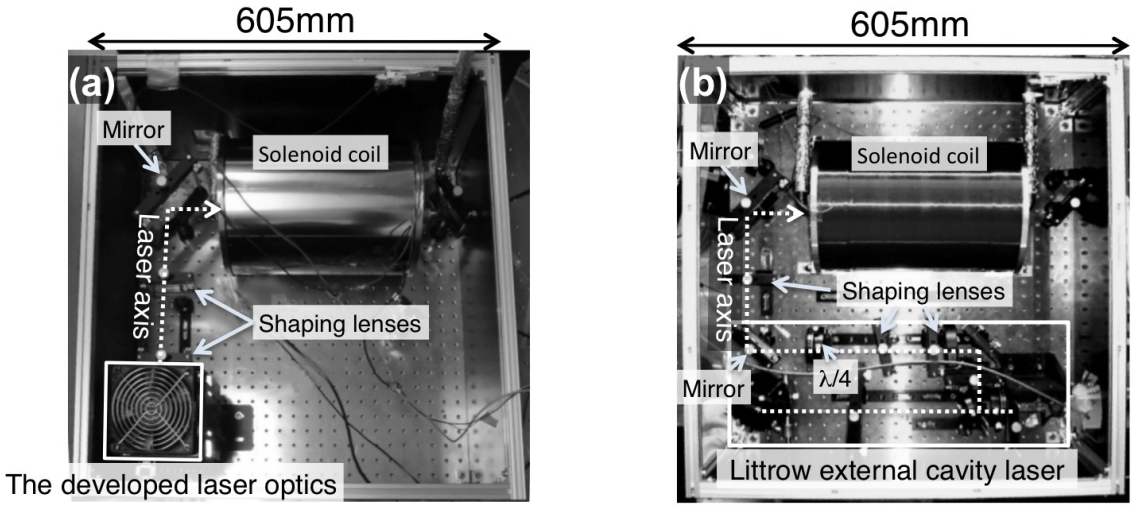

Figure 4. (a) The in-situ SEOP ^{3}He-NSF with the developed laser optics, and (b) the previous setup with the Littrow ECL.

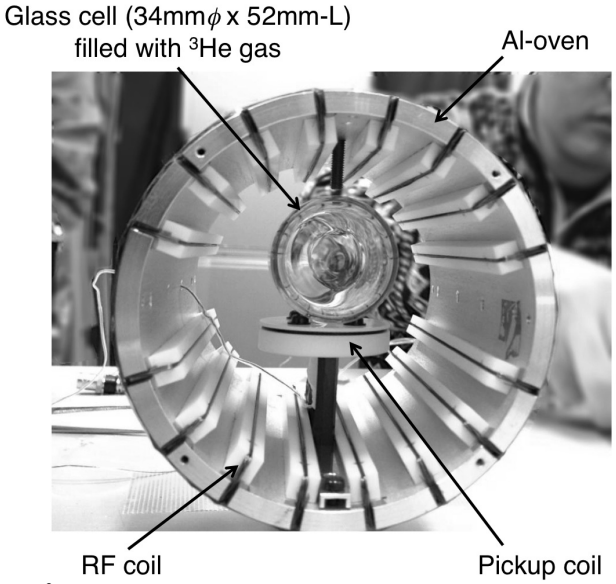

Figure 5. ^{3}He gas in a GE-180 glass cell is located in the Al-oven.

Fig. 6 shows the time evolution of the AFP-NMR signal after we start the laser irradiation to polarize ^{3}He spin. The polarization build-up time constant was 10 h, and we have achieved P_{3He} = 70% which is high enough for practical applications.

By flipping the polarity of the ^{3}He polarization, the polarity of the generated polarized neutron beam is alternated. Therefore, a flipping system for the ^{3}He spin functions as a neutron spin flipper. By the AFP-NMR, polarity of the ^{3}He polarization can be π-flipped. In the case of the in-situ SEOP ^{3}He-NSF, polarity of the circularly-polarized laser for the SEOP must be flipped to keep the absolute polarization of the ^{3}He spin. To change the polarity of the laser, a half-wavelength plate was installed. The rotation angle of the half-wavelength plate was optimized, and a polarization of 98% was obtained for the circularly-polarized laser. The ^{3}He polarization reached 70% and was confirmed to be stable for over a week.

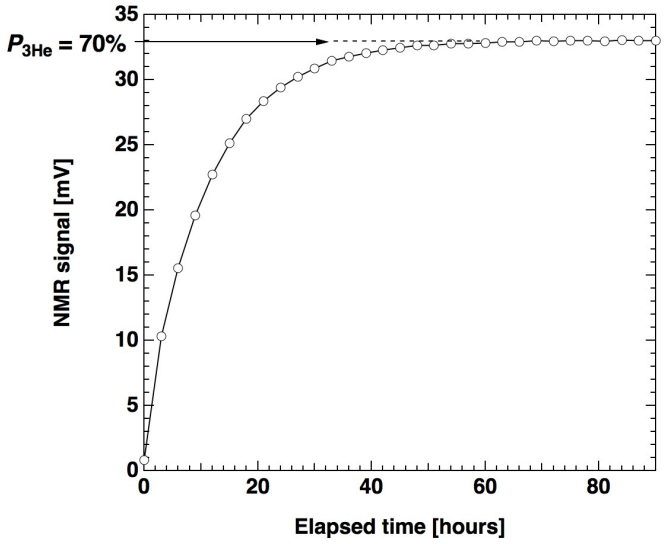

Figure 6. The time evolution of the NMR signal, which is proportional to P_{3He}, after the laser irradiation is started.

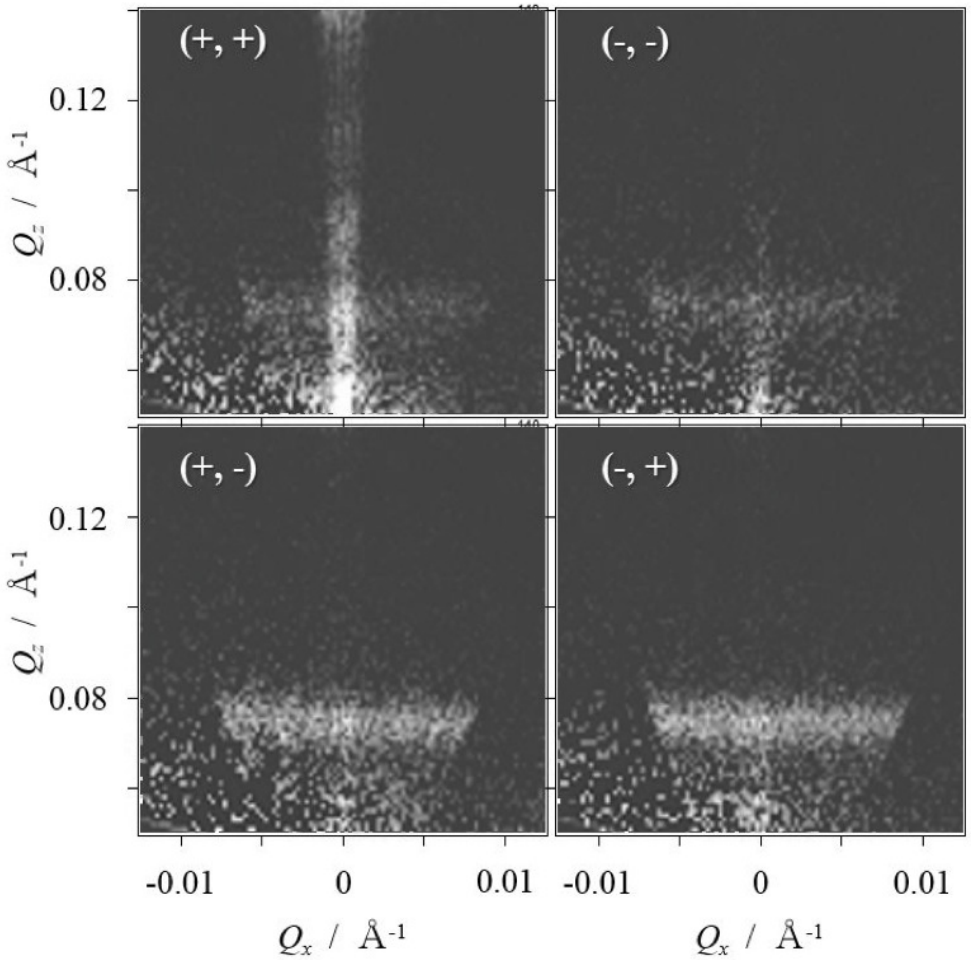

Figure 7. The obtained intensity distributions of the polarized neutron reflectivity from the Fe/Cr thin multi-layers.

4. Demonstration

A demonstration of the ^{3}He-NSF was performed at the neutron reflectometer SHARAKU (BL17) at J-PARC MLF. The in-situ SEOP ^{3}He-NSF was located at 1200 mm downstream of the sample, and used as a neutron spin analyzer. A 2d-PSD was placed after the ^{3}He-NSF. A guide coil was set between the sample and the ^{3}He-NSF for the adiabatic neutron spin transport. We performed polarized neutron reflection measurements from a Fe/Cr multilayered thin film with the giant magneto-resistance effect [7]. By flipping the spin polarity of incident and reflected neutrons, we measured intensity distributions of (+, +), (-, -), (+, -) and (-, +) reflectivities. The first sign in the pair indicates spin polarity of incident polarized neutrons and the second that of reflected ones. Figure 7 shows the reflectivity distributions measured with the applied field of 200 Oe. Off-specular reflections around Q_z=0.08Å^{-1} were clearly measured in the cases of (+, -) and (-, +). This indicates the existence of the antiferromagnetic correlations which align perpendicular to the applied field direction. The obtained data were well consistent with the results of Ref. [7].

5. Conclusion

We have developed compact laser optics with the VHG element for the in-situ SEOP ^{3}He NSF. We used an ECL to narrow the width of the laser spectrum to match it to the width of the Rb absorption line with a laser power loss of 20 %. We have composed the in-situ SEOP ^{3}He NSF with the developed laser optics and achieved the P_{3He} of 70 %. The AFP-NMR was integrated into the setup to control the polarity of ^{3}He spin and measure P_{3He}. The AFP-NMR and the half-wavelength plate for the the circularly-polarized laser were integrated into the setup to control the polarity of ^{3}He spin of the in-situ SEOP system. The spin flip function for the polarized neutrons were demonstrated by the polarization analysis experiment at the polarized neutron reflectometer SHARAKU (BL17).

Acknowledgments

This work was partially supported by the Quantum Beam Fundamentals Development Program, MEXT, and J-PARC center. We are grateful to Mr. Tanaka of Toyoko Kagaku Co. Ltd. and Mr. Kato of Feria Ltd. for their useful help and discussion in designing the laser optics.

References

[1] T.E. Chupp, et al.: Phys. Rev. C **36** (1987) 2244.
[2] D.R. Rich, et al.: Appl. Phys. Lett. **80** (2002) 2210.
[3] T.R. Gentile, et al.: J. Appl. Cryst., **33** (2000) 771.
[4] X. Liu, W. Zhao, H. Liu: "*Packaging of High Power Semiconductor Lasers*", Springer (2014)
[5] H. Kissel et al.: Proc. SPIE **8241**, 82410Q (2012).
[6] T.E. Chupp, et al.: Phys. Rev. C **36** (1987) 2244.
[7] M. Takeda, et. al., Physica B, **213&214** (1995) 248.

3.6.2

Reflection of slow neutrons from powder of nanorods

V K Ignatovich[1] and V V Nesvizhevsky[2]

[1] Joint Institute for Nuclear Research, 6 Joliot-Curie, Dubna 141980 Russia
[2] Institut Max von Laue - Paul Langevin, 71 avenue des Martyrs F-38042 Grenoble Cedex 9 France

E-mail: v.ignatovi@gmail.com, nesvizhevsky@ill.eu

Abstract. Two phenomena were recently observed: efficient diffuse reflection of very cold neutrons (VCN) from nano-structured matter for any angle of neutron incidence to the matter surface, and also quasi-specular reflection of cold neutrons (CN) from nano-structured matter for small angles of neutron incidence to the matter surface. In both cases, powder of diamond nanoparticles was used as nano-structured matter, and the measured reflection probabilities by far exceeded the values known for alternative reflectors. Both these phenomena are already used in neutron experiments and for building neutron sources. In the present theoretical work, we consider an option of further increasing the efficiency of nano-structured reflectors due to replacing spherical nanoparticles by nanorods. We showed that VCN albedo from powder of randomly oriented nanorods is lower than their albedo from powder of nanospheres of equal diameter. However albedo of VCN and quasi-specular reflection of CN from powder of long nanorods oriented parallel to the powder surface exceed those for powder of nanospheres of equal diameter.

1. Introduction

Efficient neutron reflectors are needed in experiments as well as for building neutron sources. For ultracold neutrons (UCN) [1-3] ($E < u \approx 10^{-7}$ eV), neutron optical potential of matter u is nearly the ideal reflector, which provides the probability of specular reflection close to unity, at any temperature of matter and at any incidence angle. Neutrons of higher energy E also can be totally specularly reflected from mirrors but only at small grazing angles, smaller than some critical angle $\theta_c \approx \sqrt{u/E}$ different for different materials. To increase the critical angle, say, n times, supermirrors M(n) are produced, which are multi-layers composed of bilayers of two substances with different optical potentials. The thickness of bilayers are gradually changing from one bilayer to the next one according to some law [4]. In this way the best mirror M(6.7) was produced in Japan [5]. It contains 4000 bilayers. Such a supermirror, which though provides almost 20% reflectivity at $\theta = \theta_c$, nevertheless gives not only specular, but also large fraction of nonspecular diffuse reflection. It happens because of large interlayer roughnesses appearing as a result of incommensurability of layer thicknesses and interatomic distances. It is possible to overcome this defect by using periodic chains of bilayers as reported in [6]. This algorithm had not yet been technologically realized.

Until recently, efficient reflectors of neutrons with the energy of up to $10^{-2(3)}$ eV had not been known. At the energy of $\sim 10^{-2}$ eV, neutron wavelength is comparable with inter-atomic distances thus effects of elastic diffraction and diffuse reflection in respectively ordered and

disordered matter appear. At even larger energies, inelastic processes, which provide moderation and reflection of neutrons in nuclear reactors [7], prevail.

Two phenomena were observed recently: efficient diffuse reflection of very cold neutrons (VCN) from nano-structured matter for any angle of neutron incidence to the matter surface, and also quasi-specular reflection of cold neutrons (CN) from nano-structured matter for small angles of neutron incidence to the matter surface [8-15]. In both cases, powder of diamond nanoparticles was used as nano-structured matter, and the measured reflection probabilities by far exceeded the values for known alternative reflectors. Both these phenomena are already used in neutron experiments and for building neutron sources. In the present theoretical work, we consider an option of further increasing the efficiency of nano-structured reflectors replacing spherical nanoparticles by nanorods. To be specific, we choose two values of neutron velocity: 1) 50 m/s, as nano-structured reflectors are very efficient at this neutron velocity, and 2) 450 m/s, as, on one hand, the efficiency of nano-structured reflectors made of nanospheres rapidly decreases at this neutron velocity and, on another hand, such reflectors are highly requested, for instance, for increasing UCN density in UCN sources based on superfluid helium [16, 17], used in particular for the GRANIT spectrometer [18], aiming at studies of/with quantum states of neutrons in gravitational and centrifugal potentials [19, 20], [21-23]. If optical potential of a nanorod material is much smaller than neutron kinetic energy and if neutron scattering cross section is much smaller than geometrical cross section of the nanorod then the amplitude of neutron scattering can be calculated in perturbation theory. These approximations are valid for all cases of interest in the present work. In this case, the amplitude $F(\boldsymbol{q},\boldsymbol{l})$ of neutron scattering at a nanorod with a radius ρ and a length $2a$ with an axis along the unit vector $\boldsymbol{l}$ equals:

$$F(\boldsymbol{q},\boldsymbol{l}) = N_0 b \int_V d^3r \exp(i\boldsymbol{q}\cdot\boldsymbol{r}) = N_0 b \int\limits_{-a}^{a} dz \int\limits_0^{\rho} \rho' d\rho' \int\limits_0^{2\pi} d\phi \exp(iq_l z + iq_\rho \rho' \cos\phi) =$$

$$\frac{4\pi N_0 b}{q_l} \sin(q_l a) \int\limits_0^{\rho} \rho' d\rho' J_0(q_\rho \rho') = u_0 a \rho^2 \mathrm{sinc(q_l a)} \frac{\mathrm{J_1(q_\rho \rho)}}{\mathrm{q_\rho \rho}}, \qquad (1)$$

where sinc(x)=sin(x)/x, $u_0 = 4\pi N_0 b$ is potential of neutron interaction with the nanorod matter divided by a factor $\hbar^2/2m$ (m is the neutron mass, $\hbar$ is the reduced Planck constant), N_0 is the number of atoms in the unit volume of the nanorod, b is the length of neutron coherent scattering on a nucleus of the nanorod matter, $\boldsymbol{q} = \boldsymbol{k}_0 - \boldsymbol{k}$ is the transferred momentum, $\boldsymbol{k}_0$, $\boldsymbol{k}$ are momenta of the neutron before and after scattering, $q_l = \boldsymbol{q}\cdot\boldsymbol{l}$, $q_\rho = \sqrt{\boldsymbol{q}^2 - q_l^2}$, $J_0(x)$ and $J_1(x)$ are Bessel functions; and we also used the following expressions:

$$J_0(x) = \int_0^{2\pi} \frac{d\phi}{2\pi} \exp(ix\cos\phi), \qquad \int_0^x x' dx' J_0(x') = x J_1(x).$$

In this work we consider neutron scattering on diamond nanorods. The potential of interaction of a neutron with a nanorod matter is always assumed to be equal to 300 neV, as it is for neutron scattering at crystal diamond. This approximation is valid in the first order for nanospheres [24] as well as for nanorods [25], because their densities are close to the density of bulk diamond, and their shells are not very thick [26, 27], [28]. However, more accurate but also more bulky descriptions will be required for concrete reflector realizations. The refection is understood here as albedo, i.e. the probability of neutron reflection integrated over all backward angles. We will calculate albedo following works [29-31], and will remind below briefly the calculation method.

2. Method of albedo calculation

First we will define notations. A neutron moving along a solid angle Ω with the polar axis along the internal normal to the matter surface is defined by the state vector $|\Omega\rangle$. An angular distribution $P(\Omega)$ will be characterized by the state vector:

$$|P\rangle = \int_{4\pi} P(\Omega) d\Omega |\Omega\rangle. \tag{2}$$

The norm of this state $N_P = \int_{4\pi} P(\Omega) d\Omega$ is calculated by means of multiplication of eq. (2) from the left by a meter

$$|m\rangle = \int_{4\pi} d\Omega |\Omega\rangle,$$

using a natural relation $\langle\Omega||\Omega'\rangle = \delta(\Omega - \Omega')$. In particular, isotropic distribution of incident and reflected neutrons corresponds to the state

$$|P_{\rm is}\rangle = \int_{2\pi} \frac{|\cos\theta|}{\pi} d\Omega |\Omega\rangle. \tag{3}$$

Its norm is unity.

A scatterer, which transforms a neutron state $|\Omega'\rangle$ to a state $|\Omega\rangle$ with a probability $w(\Omega \leftarrow \Omega')$, is described by means of an operator

$$\hat{\boldsymbol{W}} = \int_{4\pi} |\Omega\rangle w(\Omega \leftarrow \Omega') \langle\Omega'| d\Omega d\Omega'.$$

A neutron from a state (2) is scattered into the state:

$$|P'\rangle = \hat{\boldsymbol{W}}|P'\rangle = \int_{4\pi} |\Omega\rangle w(\Omega \leftarrow \Omega') P(\Omega') d\Omega d\Omega' = \int_{4\pi} P'(\Omega) |\Omega\rangle d\Omega,$$

where

$$P'(\Omega) = \int_{4\pi} w(\Omega \leftarrow \Omega') P(\Omega') d\Omega'.$$

In order to calculate albedo R_D from a layer of powder with a finite thickness D, one first calculates albedo R_∞ from an infinitely thick layer. For this purpose, one splits a layer of small thickness ξ from the infinite one; scattering on this layer is calculated using perturbation theory, and it is presented in a form of a reflection $\hat{\boldsymbol{\rho}}_\xi$ and a transmission $\hat{\boldsymbol{\tau}}_\xi$ operators. In order to find the operator $\hat{\boldsymbol{R}}_\infty$ of reflection from an infinitely thick layer for incident neutrons in a state $|\Omega_0\rangle$, one has to know their distribution $|X_\xi\rangle = \hat{\boldsymbol{X}}_\xi |\Omega_0\rangle$ behind the thin layer. For the operator $\hat{\boldsymbol{X}}_\xi$ one could write a self-consisting equation

$$\hat{\boldsymbol{X}}_\xi = \hat{\boldsymbol{\tau}}_\xi + \hat{\boldsymbol{\rho}}_\xi \hat{\boldsymbol{R}}_\infty \hat{\boldsymbol{X}}_\xi, \tag{4}$$

which shows that $\hat{\boldsymbol{X}}_\xi$ is constructed from the transmission through the layer $\hat{\boldsymbol{\tau}}_\xi$ and from the contribution of $\hat{\boldsymbol{X}}_\xi$ itself, because a neutron behind the layer ξ is reflected from the infinite layer then is reflected ones again from a layer ξ, and returned to the infinitely thick layer, where the state $|X_\xi\rangle$ is formed together with the part characterized by the transmission $\hat{\boldsymbol{\tau}}_\xi$.

If we know $\hat{\boldsymbol{X}}_\xi$, we can write an equation for $\hat{\boldsymbol{R}}_\infty$:

$$\hat{\boldsymbol{R}}_\infty = \hat{\boldsymbol{\rho}}_\xi + \hat{\boldsymbol{\tau}}_\xi \hat{\boldsymbol{R}}_\infty \hat{\boldsymbol{X}}_\xi. \tag{5}$$

From (4) it follows

$$\hat{\boldsymbol{X}}_\xi = \left(\hat{\boldsymbol{I}} - \hat{\boldsymbol{\rho}}_\xi \hat{\boldsymbol{R}}_\infty\right)^{-1} \hat{\boldsymbol{\tau}}_\xi, \tag{6}$$

where $\hat{\boldsymbol{I}} = \int_{4\pi} |\Omega\rangle\langle\Omega| d\Omega$ is a unit operator. Substituting of (6) into eq. (5) gives

$$\hat{\boldsymbol{R}}_\infty = \hat{\boldsymbol{\rho}}_\xi + \hat{\boldsymbol{\tau}}_\xi \hat{\boldsymbol{R}}_\infty \left(\hat{\boldsymbol{I}} - \hat{\boldsymbol{\rho}}_\xi \hat{\boldsymbol{R}}_\infty\right)^{-1} \hat{\boldsymbol{\tau}}_\xi. \tag{7}$$

Operators $\hat{\boldsymbol{\rho}}_\xi$ and $\hat{\boldsymbol{\tau}}_\xi$ are related to macroscopic scattering cross sections:

$$\hat{\boldsymbol{\rho}}_\xi = \xi \hat{\boldsymbol{\Sigma}}_b, \qquad \hat{\boldsymbol{\tau}}_\xi = \hat{\boldsymbol{I}} + \xi \hat{\boldsymbol{\Sigma}}_f - \xi \Sigma_t \hat{\boldsymbol{S}}, \tag{8}$$

where

$$\hat{\boldsymbol{\Sigma}}_b = \int\limits_{\boldsymbol{n}\cdot\Omega<0} d\Omega \int\limits_{\boldsymbol{n}\cdot\Omega'>0} |\Omega\rangle \Sigma_s(\Omega \leftarrow \Omega') \frac{d\Omega'}{\cos\theta'} \langle\Omega'| = \int\limits_{\boldsymbol{n}\cdot\Omega>0} d\Omega \int\limits_{\boldsymbol{n}\cdot\Omega'<0} |\Omega\rangle \Sigma_s(\Omega \leftarrow \Omega') \frac{d\Omega'}{\cos\theta'} \langle\Omega'| \tag{9}$$

the operator of back scattering from the left or from the right,

$$\hat{\boldsymbol{\Sigma}}_f = \int\limits_{\boldsymbol{n}\cdot\Omega>0} d\Omega \int\limits_{\boldsymbol{n}\cdot\Omega'>0} |\Omega\rangle \Sigma_s(\Omega \leftarrow \Omega') \frac{d\Omega'}{\cos\theta'} \langle\Omega'| = \int\limits_{\boldsymbol{n}\cdot\Omega<0} d\Omega \int\limits_{\boldsymbol{n}\cdot\Omega'<0} |\Omega\rangle \Sigma_s(\Omega \leftarrow \Omega') \frac{d\Omega'}{\cos\theta'} \langle\Omega'| \tag{10}$$

is the operator of forward scattering from the left or right, $\Sigma_s(\Omega \leftarrow \Omega')$ is the differential macroscopic scattering cross section, $\Sigma_t = \Sigma_s + \Sigma_a$ is the total macroscopic cross section, consisting of the integral scattering Σ_s and absorption Σ_a cross sections, and

$$\hat{\boldsymbol{S}} = \int\limits_{2\pi} |\Omega\rangle \frac{d\Omega}{\cos\theta} \langle\Omega| \tag{11}$$

is an operator, which takes into account that the number of scatterers along the neutron path increases with increasing of the incidence angle.

At small value of ξ eq. (7) can be linearized and reduced to

$$\hat{\boldsymbol{R}}_\infty \hat{\boldsymbol{\Sigma}}_b \hat{\boldsymbol{R}}_\infty + \left(\hat{\boldsymbol{\Sigma}}_f - \Sigma_t \hat{\boldsymbol{S}}\right) \hat{\boldsymbol{R}}_\infty + \hat{\boldsymbol{R}}_\infty \left(\hat{\boldsymbol{\Sigma}}_f - \Sigma_t \hat{\boldsymbol{S}}\right) + \hat{\boldsymbol{\Sigma}}_b = 0. \tag{12}$$

We suppose that the distribution of reflected neutrons is isotropic, and represent the solution of (12) in the form

$$\hat{\boldsymbol{R}}_\infty = R_\infty \int\limits_{\boldsymbol{n}\cdot\Omega<0} |\Omega\rangle \frac{|\cos\theta|}{\pi} d\Omega \int\limits_{\boldsymbol{n}\cdot\Omega'>0} d\Omega' \langle\Omega'| = R_\infty |P_{\rm is}\rangle\langle m|. \tag{13}$$

Substitute it in (12) and multiply (12) from the left by $\langle m|$ and from the right by $|P_{\rm is}\rangle$. Then we get

$$R_\infty^2 \Sigma_b + 2R_\infty(\Sigma_f - \Sigma_t) + \Sigma_b = 0, \tag{14}$$

where

$$\Sigma_b = \int\limits_{\boldsymbol{n}\cdot\Omega<0} d\Omega \int\limits_{\boldsymbol{n}\cdot\Omega'>0} \Sigma_s(\Omega \leftarrow \Omega') \frac{d\Omega'}{2\pi} = \int\limits_{\boldsymbol{n}\cdot\Omega>0} d\Omega \int\limits_{\boldsymbol{n}\cdot\Omega'<0} \Sigma_s(\Omega \leftarrow \Omega') \frac{d\Omega'}{2\pi}, \tag{15}$$

$$\Sigma_f = \int\limits_{\boldsymbol{n}\cdot\Omega>0} d\Omega \int\limits_{\boldsymbol{n}\cdot\Omega'>0} \Sigma_s(\Omega \leftarrow \Omega') \frac{d\Omega'}{2\pi} = \int\limits_{\boldsymbol{n}\cdot\Omega<0} d\Omega \int\limits_{\boldsymbol{n}\cdot\Omega'<0} \Sigma_s(\Omega \leftarrow \Omega') \frac{d\Omega'}{2\pi} \tag{16}$$

are macroscopic cross sections of backward and forward scattering. Since $\Sigma_t = \Sigma_s + \Sigma_a = \Sigma_b + \Sigma_f + \Sigma_a$, then solution of eq. (12) can be represented in the form

$$R_\infty = \frac{\sqrt{\Sigma_a + 2\Sigma_b} - \sqrt{\Sigma_a}}{\sqrt{\Sigma_a + 2\Sigma_b} + \sqrt{\Sigma_a}} = \frac{\sqrt{1 + 2\Sigma_b/\Sigma_a} - 1}{\sqrt{1 + 2\Sigma_b/\Sigma_a} + 1}. \tag{17}$$

In order to calculate albedo from a wall of a finite thickness, one has to know a law of attenuation of neutron intensity in the matter. It follows from eq. (6). After linearization of it at small ξ, substitution of (13) and multiplication from left by $\langle m|$ and from the right by $|P_{\rm is}\rangle$ one gets

$$\langle m|\hat{\boldsymbol{X}}_\xi|P_{\rm is}\rangle = 1 - \xi/L \approx \exp(-\xi/L),$$

where

$$1/L = 2\sqrt{\Sigma_a + 2\Sigma_b}\sqrt{\Sigma_a} = 2\Sigma_a\sqrt{1 + 2\Sigma_b/\Sigma_a}. \tag{18}$$

Thus $\hat{\boldsymbol{X}}_z$ at a depth z can be represented as

$$\hat{\boldsymbol{X}}_z = |P_{\rm is}\rangle \exp(-z/L)\langle m|. \tag{19}$$

For calculating reflection $\hat{\boldsymbol{R}}_D$ and transmission $\hat{\boldsymbol{T}}_D$ from/through a layer of a thickness D we use eq-s. (4), (5) splitting a layer of a finite thickness D from the semiinfinite one. The equations then look:

$$\hat{\boldsymbol{X}}_D = \hat{\boldsymbol{T}}_D + \hat{\boldsymbol{R}}_D\hat{\boldsymbol{R}}_\infty\hat{\boldsymbol{X}}_D, \qquad \hat{\boldsymbol{R}}_\infty = \hat{\boldsymbol{R}}_D + \hat{\boldsymbol{T}}_D\hat{\boldsymbol{R}}_\infty\hat{\boldsymbol{X}}_D. \tag{20}$$

They can be resolved with respect to $\hat{\boldsymbol{R}}_D$ and $\hat{\boldsymbol{T}}_D$ for known $\hat{\boldsymbol{X}}_D$ and $\hat{\boldsymbol{R}}_\infty$. Assuming $\hat{\boldsymbol{R}}_D = R_D|P_{\rm is}\rangle\langle m|$, we get

$$R_D = R_\infty \frac{1 - \exp(-2D/L)}{1 - R_\infty^2 \exp(-2D/L)}. \tag{21}$$

It follows from (17) and (18) that in order to calculate R_D, which will be named below as simply R, one has to get macroscopic cross sections Σ_b and Σ_a, which are averaged over angles differential cross sections.

3. Calculation of macroscopic cross sections

From the scattering amplitude (1), one could calculate a differential cross section

$$d\sigma(\boldsymbol{q},\boldsymbol{l})/d\Omega = |F(\boldsymbol{q},\boldsymbol{l})|^2 = |u_0|^2a^2\rho^4\mathrm{sinc}^2(\mathrm{q_l a})\left|\frac{\mathrm{J_1(q_\rho\rho)}}{\mathrm{q_\rho\rho}}\right|^2. \tag{22}$$

Consider an angular distribution of scattered neutrons. The polar axis is directed along the wave vector $\boldsymbol{k}_0$ of the incidence wave, and the axis is in the plane of vectors ($\boldsymbol{k}_0$, $\boldsymbol{l}$) perpendicular to $\boldsymbol{k}_0$. where $\boldsymbol{l}$ is a unit vector along the rod axis. Then $\boldsymbol{k}_0 \cdot \boldsymbol{l} = k\cos\theta_0$ and

$$q_l = \boldsymbol{q}\cdot\boldsymbol{l} = k(\cos\theta_0 - \cos\theta_0\cos\theta_0 - \sin\theta\sin\theta_0\cos\phi), \tag{23}$$

where θ, ϕ are the angles of the vector $\boldsymbol{k}$ of the scattered wave. Eq. (22) can be integrated over angle ϕ. Taking into account the symmetry of eq. (23), we get

$$\frac{d}{d\cos\theta}\sigma(\theta,\theta_0) = |u_0|^2a^2\rho^4\int_0^\pi 2d\phi\ \mathrm{sinc}^2(\mathrm{q_l a})\left|\frac{\mathrm{J_1(q_\rho\rho)}}{\mathrm{q_\rho\rho}}\right|^2. \tag{24}$$

After multiplication of the differential cross section (24) by a number of nanorods N_1 in the unit volume, we get the macroscopic differential scattering cross section Σ:

$$\Sigma(\theta,\theta_0) = N_1 \frac{d}{d\cos\theta}\sigma(\theta,\theta_0) = A\int_0^{\pi} 2d\phi\ \mathrm{sinc}^2(\mathrm{q_l a})\left|\frac{\mathrm{J_1(q_\rho \rho)}}{\mathrm{q_\rho \rho}}\right|^2, \tag{25}$$

where

$$A = \gamma|u_0|^2 a\rho^2/2\pi,$$

and the value $\gamma = N_1 V_1 = N_1 2\pi\rho^2 a$ characterizes a fraction of volume occupied by nanorod matter. In the following we will assume $\gamma = 0.1$. In order to describe precisely some concrete neutron nanorod reflectors we will need a more accurate model. The dimension of the coefficient A is 1/cm, and its value depends of nanorod parameters. In order to compare neutron cross sections for different nanorods, we introduce a convenient common dimensional coefficient

$$A_0 = \gamma|u_0|^2\rho_0^3/2\pi. \tag{26}$$

If nanorod radius is $\rho_0 = 10$ nm, then $A_0 = 3.4\ \mu m^{-1}$ (for diamond $1/\sqrt{u_0} = 8.27$ nm). The macroscopic cross section of neutron scattering (25) can be represented in the following form:

$$\Sigma(\theta,\theta_0) = 2A_0\frac{\overline{\rho}^3}{\beta}\int_0^{\pi} d\phi\ \mathrm{sinc}^2(\overline{\mathrm{q}}_\mathrm{l}\alpha)\left|\frac{\mathrm{J_1}(\overline{\mathrm{q}}_\rho\alpha\beta)}{\overline{\mathrm{q}}_\rho\alpha\beta}\right|^2, \tag{27}$$

with dimensionless parameters $\overline{q} = q/k$, $\alpha = ak$, $\beta = \rho/a$, $\overline{\rho} = \rho/\rho_0$. The macroscopic differential cross section $\Sigma(\theta,\theta_0)$ of scattering of a neutron on powder of nanorods, in units $2A_0\overline{\rho}^3/\beta$, is shown in Fig. 1 ($a = 1000$ nm) and in Fig. 2 ($a = 10$ nm), as a function of the neutron scattering angle θ provided the neutron incidence angle θ_0 equals 0, $\pi/4$ and $\pi/2$, the nanorod radius = 0=10 nm, and for the neutron velocity $v = 450$ m/s.

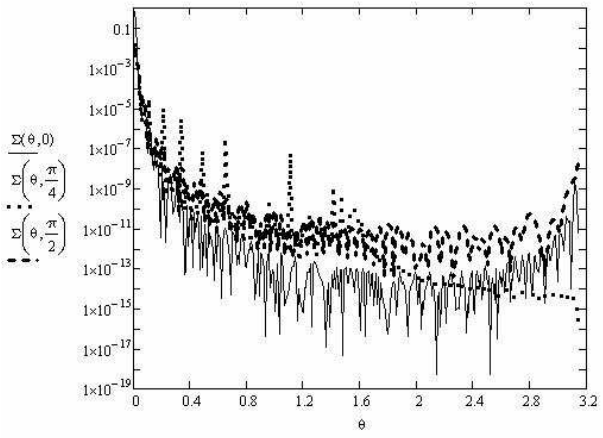

Figure 1. Dimensionless differential cross section $\Sigma(\theta,\theta_0)$ of the neutron scattering on nanorods as a function of the neutron scattering angle θ and the neutron incidence angle θ_0. The angles are measured relative to the nanorod axis, $v = 450$ m/s, $a = 1000$ nm.

Angles are given in radians. Cross sections of neutron scattering on nanorods with the half-length equals radius $a = \rho$ are approximately equal to the cross section of neutron scattering on spherical nanoparticles of equal radius, therefore we will use in the following for simplicity the same analytical expressions for qualitative comparison of results for long nanorods and

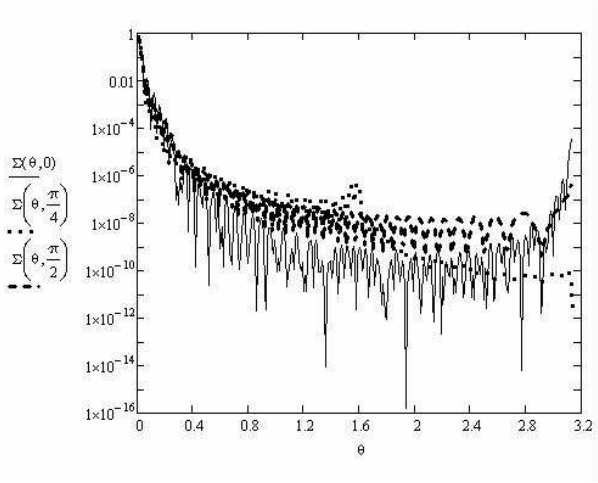

Figure 2. The same as in Fig. 1, but for the nanorod half-length of $a = \rho = 10$ nm.

for spherical nanoparticles. The average angle of neutron scattering on nanoparticles is equal approximately to the ratio of neutron wavelength to nanoparticle size. Thus, neutrons scatter on long nanorods to smaller angles (Fig. 1) then they scatter on short nanorods (Fig. 2). And the cross sections of neutron scattering to the zero angles are equal to each other as well as to $\pi/2$. It is interesting to note some increase of cross sections for backscattering, which is particularly visible for nanorods. It is useful to consider separately the cases of chaotic and ordered orientation of long nanorods in reflectors. In section 4 we consider the reflection of isotropic VCN flux from a reflector built of chaotically oriented nanorods; in section 5 we analyze the reflection of CN from a reflector built of nanorods with the axis parallel to the reflector surface while they are isotropically oriented over the azimuth angle.

4. Cross section of backward neutron scattering on chaotically oriented nanorods

To find scattering of neutrons on isotropically distributed nanorods one can average (22) over directions $\boldsymbol{l}$ for a given vector $\boldsymbol{q}$, which is chosen as a polar axis. In that case $\overline{q}_l = \overline{q}\cos\theta_l$ and $\overline{q}_\rho = \overline{q}\sin\theta_l$, and one should average (22) over angle θ_l of nanorod orientation. After averaging and multiplication by particle density N_1 we get in units $A_0\overline{\rho}^3/\beta$:

$$\langle d\Sigma_s(\boldsymbol{q},\boldsymbol{l},\alpha,\beta)/d\Omega\rangle = \int_0^1 dx\ \mathrm{sinc}^2(\mathrm{x}\overline{\mathrm{q}}\alpha)\left|\frac{\mathrm{J}_1(\sqrt{1-\mathrm{x}^2}\overline{\mathrm{q}}\alpha\beta)}{\sqrt{1-\mathrm{x}^2}\overline{\mathrm{q}}\alpha\beta}\right|^2. \tag{28}$$

In order to calculate the neutron albedo from powder of nanorods, we should know the cross section of backward scattering relative to the normal to the powder surface. We define the normal to surface to be the polar axis directed towards matter. Then the $\overline{q}$ for backward scattered neutrons is

$$\overline{q} = \sqrt{2(1+\cos\theta\cos\theta_0 - \sin\theta\sin\theta_0\cos\phi)}, \tag{29}$$

where θ and ϕ are the scattered neutron angles, and axis is in the incidence plane. We denote $y = \cos\theta\cos\theta_0 = \sin\theta\sin\theta_0\cos\phi$, integrate over $d\Omega = d\phi d\cos\theta$, average over directions θ_0 of incidence neutrons, and present this expression in the form

$$\Sigma_s(\alpha,\beta) = \int_{-1}^1 dy\delta(y-\cos\theta\cos\theta_0+\sin\theta\sin\theta_0\cos\phi)d\Omega d\cos\theta_0 S(y,\alpha,\beta), \tag{30}$$

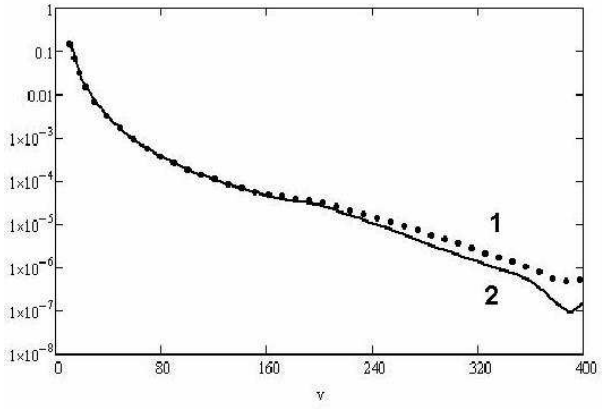

Figure 3. Dimensionless macroscopic cross section of neutron backward scattering $\Sigma_b(\alpha,\beta)/\beta$ on powder of long nanorods ($\Sigma bl(v)$) with the half-length of $a = 1000$ nm and on powder of short nanorods ($\Sigma bs(v)$) with the half-length of $a = 10$ nm. In both cases, the nanorod radius equals $\rho = 10$ nm.

where

$$S(y,\alpha,\beta) = \int_0^1 dx\ \mathrm{sinc}^2(\mathrm{x}\sqrt{2(1+\mathrm{y})}\alpha)\left|\frac{\mathrm{J}_1(\sqrt{1-\mathrm{x}^2}\sqrt{2(1+\mathrm{y})}\alpha\beta)}{\sqrt{1-\mathrm{x}^2}\sqrt{2(1+\mathrm{y})}\alpha\beta}\right|^2. \tag{31}$$

After integration of eq. (30) over $d\phi$ we get

$$\Sigma_b(\alpha,\beta) = \int_{-1}^1 dy I(y) S(y,\alpha,\beta), \tag{32}$$

where

$$I(y) = \int_0^1 d\cos\theta \int_0^1 d\cos\theta_0 \frac{\Theta(\sin^2\theta\sin^2\theta_0 > (\cos\theta\cos\theta_0 - y)^2)}{\sin^2\theta\sin^2\theta_0 - (\cos\theta\cos\theta_0 - y)^2}, \tag{33}$$

and Θ is the step-function, which is equal to 1 provided inequality in its argument, and is equal zero otherwise. Function I(y) is calculated in (A4). It is equal to

$$I(y) = \pi\Theta(y>0) - \arctan\left(\frac{\sqrt{1-y^2}}{y}\right). \tag{34}$$

Fig. 3 shows the dimensionless macroscopic cross section $\Sigma_b(\alpha,\beta)$ of neutron scattering as a function of its velocity v for powder of nanorods with the half-length $a = 1000$ nm, and $a = 10$ nm.

5. Absorption cross section

The total cross section is defined by the imaginary part of the forward scattering amplitude (1):

$$\Im(F(\boldsymbol{q},\boldsymbol{l}))_{q=0} = u_0'' a\rho^2/2 = N_0 k\sigma_l(k) a\rho^2/2, \tag{35}$$

and it actually describes absorption, as scattering in the perturbation theory is not included in this expression. The macroscopic cross section of absorption is equal:

$$\Sigma_a(k) = \frac{4\pi}{k} N_1 \Im(F(\boldsymbol{q},\boldsymbol{l}))_{q=0} = \frac{4\pi}{2k} N_1 N_0 k\sigma_l(k) a\rho^2 = \frac{\gamma u_0^2 \rho_0^3}{2\pi}\frac{k_T\sigma_l(k_T)}{2kbu_0\rho_0^3} = A_0\frac{C\overline{\rho}}{\alpha\beta}, \tag{36}$$

where

$$C = \frac{k_T \sigma_l(k_T)}{2bu_0\rho_0^2} = \frac{\sigma_l(k_T)}{2bk_T(u_0/k_T^2)\rho_0^2}. \tag{37}$$

T denotes the ambient temperature, $\rho_0 = 10$ nm, $b = 6.65$ fm, and $u_0/k_T^2 = E_c/E_T = 12 \times 10^{-6}$. In the following, we will consider two cases of particular interest:

(i) Nanoparticles at a so small temperature that neutron heating in powder can be neglected, and also neutron cooling would even increase albedo. Also hydrogen in powder is substituted by deuterium, and neutron absorption in deuterium can be neglected. It is the case of most efficient reflector, which could be built using the principle considered in the present article. In this case, absorption cross section is attributed to one carbon atom; it is equal $\sigma_l(kT) = 0.0035$ bn, and $C = C_0 = 6.28 \times 10^{-7}$.

(ii) Nanoparticles at the ambient temperature, with a realistic admixture of hydrogen. As nanopowder reflectors are most efficient for small neutron energy compared to the ambient temperature (energy), then inelastic neutron scattering is equivalent to neutron loss. And inelastic scattering is governed by a relatively small admixture of hydrogen in powder. As shown in [32], the minimum admixture of hydrogen atoms, which can be achieved by means of heating and degassing of powder, corresponds to the following composition $C_{12.4+0.2}H$, and the total cross section of neutron scattering on the atom of residual hydrogen at the ambient temperature, measured for neutrons with the wavelength of 4.4 Å, equals 108 ± 2 bn. In this case, the efficient cross section per one atom of the composition is $\sigma_l(kT) = 3.56$ bn. Thus the most pessimistic estimation gives $C = C_a = 5.2 \times 10^{-4}$. Neutron albedo from an infinitely thick layer of nanorods is equal [25-27] (17):

$$R_\infty(\alpha, \beta, \overline{\rho}, C) = \frac{\sqrt{1 + Q(\alpha, \beta, \overline{\rho}, C)} - 1}{\sqrt{1 + Q(\alpha, \beta, \overline{\rho}, C)} + 1}, \tag{38}$$

where

$$Q(\alpha, \beta, \overline{\rho}, C) = \frac{2\Sigma_b}{\Sigma_a} = \frac{2}{C}\Sigma_b(\alpha, \beta)\frac{\alpha\beta}{\overline{\rho}}. \tag{39}$$

Calculations of neutron albedo from an infinitely thick layer of nanorods, as a function of the velocity v of incidence neutrons for long ($a = 1000$ nm) and short ($a = 10$ nm) nanorods, show that neutron albedo from nano-structured powder for the neutron velocity of $v = 400$ m/s is significantly larger than the coefficient of neutron reflection 5×10^{-9} from continuous matter.

Besides the reflection from infinite matter, albedo is characterized also by the exponential attenuation in matter $\exp(-x/L)$, i.. by the attenuation length (18):

$$1/L = 2\sqrt{\Sigma_a + 2\Sigma_b}\sqrt{\Sigma_a} = 2\Sigma_a\sqrt{1 + Q(\alpha, \beta, \overline{\rho}, C)} = L_0^{-1}(C)\kappa^{-1}(\alpha, \beta, \overline{\rho}, C). \tag{40}$$

Substitution of (36) gives

$$L_0^{-1}(C) = 2CA_0, \qquad \kappa(\alpha, \beta, \overline{\rho}, C) = \frac{\alpha\beta}{\overline{\rho}\sqrt{1 + Q(\alpha, \beta, \overline{\rho}, C)}}. \tag{41}$$

Consider now the neutron reflection from a layer of nanopowder with a finite thickness d. Albedo from such a layer is defined by formula:

$$R(d, \alpha, \beta, \overline{\rho}, C) = R_\infty(\alpha, \beta, \overline{\rho}, C)\frac{1 - \exp(-2d/L(\alpha, \beta, \overline{\rho}, C))}{1 - R_\infty^2(\alpha, \beta, \overline{\rho}, C)\exp(-2d/L(\alpha, \beta, \overline{\rho}, C))}. \tag{42}$$

Fig. 4 shows dependence R(v) for the nanopowder thickness of $d = 3$ cm for long and short nanorods with the neutron loss coefficients C_0 and C_a. The figure shows that the neutron albedo from a sufficiently thin layer of nanoparticles is higher by 6-7 orders of magnitude than neutron reflection from continuous matter.

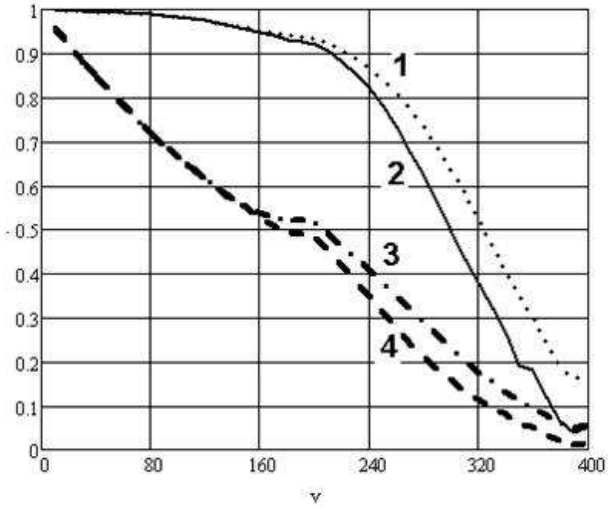

Figure 4. Albedo from powder of nanorods of length: 1, 3) $a = 10$ nm; 2, 4) $a = 1000$ nm; with absorption parameter C equal to 1. 2) C_0; 3, 4) C_a. In all cases, the nanorod radius equals $\rho = 10$ nm. It is seen that quasi spherical nanorods reflect better than long ones.

6. Axes of nanorods are oriented parallel to the interface

Now consider the case when nanorods are oriented parallel to the powder surface. We define the polar axis along the normal to the interface directed towards matter, and axis in the incidence plane then:

$$\overline{q}_l = \sin\theta_0 \cos\chi - \sin\theta\cos(\phi - \chi), \tag{43}$$

where χ is the azimuth angle of the nanorod orientation, and θ, ϕ are scattering angles. Then

$$\overline{q}_\rho = \sqrt{2(1 + \cos\theta\cos\theta_0 - \sin\theta\sin\theta_0\cos\phi) - (\sin\theta_0\cos\chi - \sin\theta\cos(\phi - \chi))^2}. \tag{44}$$

After averaging over nanorod orientation, integrating over backward scattering angles, and averaging over angular distribution of incident neutrons, we get

$$\Sigma_b(\alpha, \beta, \overline{\rho}) = \int_0^1 dx \int_0^1 dy \Sigma_{b,\theta}(x, y, \alpha, \beta, \overline{\rho}), \tag{45}$$

where

$$\Sigma_{b,\theta}(x, y, \alpha, \beta, \overline{\rho}) = \frac{\overline{\rho}^3}{\beta} \int_0^{2\pi} d\phi \int_0^{2\pi} \frac{d\chi}{2\pi} \mathrm{sinc}^2(\alpha \overline{\mathrm{q}}_\mathrm{l}(\mathrm{x}, \mathrm{y}, \alpha, \beta)) \left| \frac{\mathrm{J}_1(\alpha\beta\, \overline{\mathrm{q}}_\rho(\mathrm{x}, \mathrm{y}, \alpha, \beta))}{\alpha\beta\, \overline{\mathrm{q}}_\rho(\mathrm{x}, \mathrm{y}, \alpha, \beta)} \right|^2. \tag{46}$$

Numerical integration of (46) shows the macroscopic cross section of neutron backward scattering as a function of $x = \cos\theta$ for given values of $y = \cos\theta_0$. This dependence for long nanorods ($\beta = 0.01$) at $\overline{\rho} = 1$, the neutron velocity $v = 450$ m/s and two values of cosine of the incident angle $y = 0,3$ and $y = 0,8$ is shown in fig. 5. One can see the peaks in the vicinity of $\cos\theta = \cos\theta_0$, which correspond to quasi-specular reflection. For isotropic distribution of nanorods the quasi specular reflection will possibly appears only after introduction of an interference between the waves scattered on different grains.

Integration in (45) and substitution into albedo formulas gives the results shown in fig. 6. Here we show neutron albedo from a layer with the thickness of 3 cm as a function of the

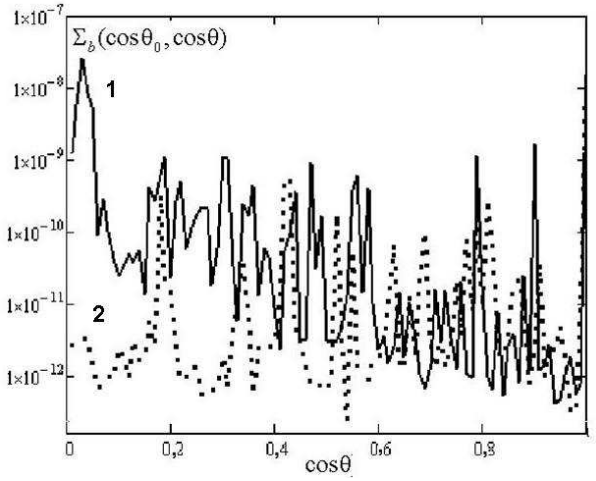

Figure 5. Dependence $\Sigma_{b\theta}(\cos\theta_0, \cos\theta, \alpha, \beta, \overline{\rho})$ on $\cos\theta$ at 1) $\cos\theta_0 = 0.3$; 2) $\cos\theta_0 = 0.8$ – for long nanorods: $\beta = 0.01$, $\rho = 10$ nm and for $v = 450$ m/s.

neutron speed v, m/s; the layer consists of long and short nanorods oriented along the interface but isotropically with respect to the azimuth around the interface normal. Albedo is calculated for small and large content of hydrogen. It is seen that albedo from long nanorods is higher than that from short quasi spherical ones. The results of calculations are in good agreement with the experimental observations for v in the range 50-150 m/s [11].

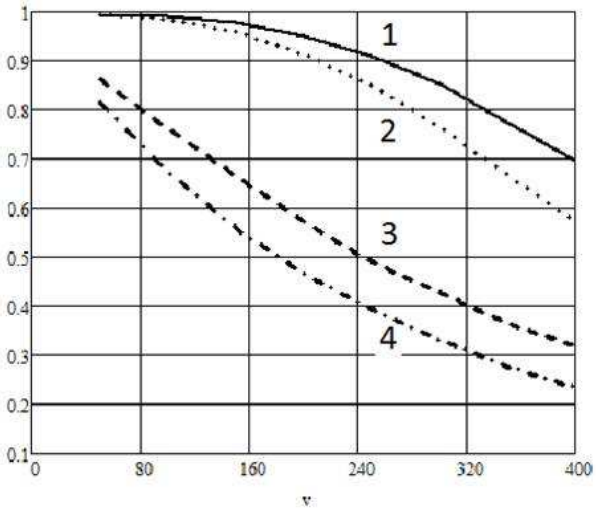

Figure 6. . Albedo $R_d(v)$ from powder layer of thickness $d = 3$ cm composed of: 1, 3) long ($a = 1000$ nm) and 2,4) short ($a = 10$ nm) nanorods with the radius $\rho = 10$ nm; for two loss coefficients 1, 2) $C = C_0 = 6.28 \times 10^{-7}$ and $C = C_a = 5.2 \times 10^{-4}$ as a function of neutron velocity v, m/s.

7. A problem of accounting for the real angular distribution

We have assumed above that albedo is calculated for the isotropic distribution of reflected and incident neutrons. How would change the results, if one does not keep these assumptions? In

order to answer this question, one has to solve eq. (12) in its general form. It is an extremely complex problem involving a non-linear integral equation. It can be simplified, provided a natural assumption that all functions depend only on cosines of incidence and reflected angles. Then the integral equation can be reduced by discretization to an algebraic matrix equation of the second order of the form

$$\hat{\boldsymbol{Z}}\hat{\boldsymbol{A}}\hat{\boldsymbol{Z}} + \hat{\boldsymbol{B}}\hat{\boldsymbol{Z}} + \hat{\boldsymbol{Z}}\hat{\boldsymbol{C}} + \hat{\boldsymbol{D}} = 0. \tag{47}$$

However solving such a quadratic matrix algebraic equation also is a complex problem. In fact, a quadratic matrix equation for the matrix $N \times N$ is equivalent in the general case to a polynomial equation with the power $2N^2$. And even, if one calculates numerically all its roots, there will stay a problem of choosing a proper set of roots. However it is possible to shed light on a role of scattering anisotropy by suggesting solution of eq. (12) not in the purely isotropic form (13), but as a combination of isotropic and specular distributions as shown in (47),

$$\hat{\boldsymbol{R}}_\infty = R_\infty \int_{\boldsymbol{n}\Omega<0} |\Omega\rangle \frac{|\cos\theta|}{\pi} d\Omega \int_{\boldsymbol{n}\Omega>0} d\Omega' \langle\Omega'| + \int_{\boldsymbol{n}\Omega<0} d\Omega |\Omega\rangle \boldsymbol{n}_{\Omega<0} f(\Omega) \langle\Omega| \boldsymbol{n}_{\Omega>0}, \tag{48}$$

where the specular part is presented by the diagonal term. This option will be considered in another work.

8. Conclusion

In the present theoretical work we considered a possibility to increase efficiency of nano-structured reflectors of slow neutrons by means of substituting spherical nanoparticles by nanorods. We show that albedo of VCN from powder of disordered nanorods is smaller than the albedo from powder of nanospheres. However, albedo of VCN and quasi-specular reflection of CN from powder of nanorods oriented parallel to the reflector surface exceed respective values for powder of nanospheres.

Acknowledgments
The authors are sincerely grateful for useful discussions and critics to our colleagues V A Artem'ev, E V Lychagin, A Yu Muzychka, and A V Strelkov.

Appendix A. Calculation of the integral (19)

Denote $\cos\theta = v$, $\cos\theta_0 = u$. Then integral (19) is presented in the form

$$I(y) = \int_0^1 du \int_0^1 dv \frac{\Theta(1 - u^2 - v^2 + u^2v^2 > y^2 - 2yuv)}{1 - u^2 - v^2 + u^2v^2 - y^2 + 2yuv} = \int_0^1 du I_1(u, y), \tag{A.1}$$

where integral $I_1(u, y)$, after variable substitution $x = (v - uy)/sqrt1 - u^2 sqrt1 - y^2$ is reduced to

$$I_1(u,y) = \int_{-x_1(u,y)}^{x_2(u,y)} dx \frac{\Theta(x^2 < 1)}{\sqrt{1-x^2}} = \frac{\pi}{2}\left(1 + \Theta\left(u > \sqrt{1-y^2}\right)\frac{|y|}{y}\right) + \\ + \arcsin(x_1(u,y))\Theta\left(u < \sqrt{1-y^2}\right). \tag{A.2}$$

Limits of integration in (2) are

$$x_1(u,y) = \frac{uy}{\sqrt{(1-u^2)(1-y^2)}}, \qquad x_2(u,y) = \frac{1-uy}{\sqrt{(1-u^2)(1-y^2)}}. \tag{A.3}$$

Modulus of these limits have to be smaller than unity, but $x_2(u,y) > 1$ for any values of u and y, therefore the upper limit, due to the inequality in the integral, has to be replaced by unity. The lower limit, $|x_1(u,y)| \leq 1$, only when $u \leq u_1(y) = \sqrt{1-y^2}$. If $u > u_1(y) = \sqrt{1-y^2}$, then modulus of the lower limit has to exceed unit and thus the lower limit should be replaced by -1 or +1, which depends on the sign of y. Accounting for all these conditions leads to (A2). Substitution of (2) into (1) and integration by parts of the term containing arcsin provides the final result:

$$I(y) = \int_0^1 du I_1(u,y) = \frac{\pi}{2}\left[1 + (1+\sqrt{1-y^2})\frac{y}{|y|}\right] + \sqrt{1-y^2})\frac{y}{|y|}\frac{\pi}{2} -$$
$$- \int_0^{\sqrt{1-y^2}} \frac{yudu}{(1-u^2)\sqrt{1-u^2-y^2}} = \pi\Theta(y>0) - \arctan\left(\frac{\sqrt{1-y^2}}{y}\right). \qquad \text{(A.4)}$$

References

[1] Luschikov V I, Pokotilovskiy Yu N, Strelkov A V et al 1969 Observation of ultracold neutrons *JETP Lett.* **9** 23

[2] Ignatovich V K 1990 *The Physics of Ultracold Neutrons* (Oxford, UK: Clarendon Press)

[3] Golub R, Richardson D J, and Lamoreux S K 1991 *Ultracold Neutrons* (Bristol: Higler)

[4] Mezei F 1976 Novel polarized neutron devices - supermirror and spin component amplifier *Commun. Phys.* **1** 81

[5] Maruyama R, Yamazaki D, Ebisawa T et al 2007 Development of neutron supermirrors with large critical angle, *Thin Solid Films* **515** 5704

[6] Carron I and Ignatovich V 2003 Algorithm for preparation of multilayer systems with high critical angle of total reflection *Phys. Rev.* A **67** 043610

[7] Amaldy E, and Fermi E 1936 On the absorption and the diffusion of slow neutrons, *Phys. Rev.* **50** 899

[8] Nesvizhevsky V V 2002 Interaction of neutrons with nanoparticles, *Phys. At. Nucl.* **65** 400

[9] Artem'ev V A 2006 Estimation of neutron reflection from nanodispersed materials, *At. Energy* **101** 901

[10] Nesvizhevsky V V, Lychagin E V, Muzychka A Yu et al 2008 The reflection of very cold neutrons from diamond powder nanoparticles, *Nucl. Instrum. Meth.* A **595** 631

[11] Lychagin E V, Muzychka A Yu, Nesvizhevsky V V et al 2009 Storage of very cold neutrons in a trap with nano-structured walls, *Phys. Lett.* B **679** 186

[12] Lychagin E V, Muzychka A Yu, Nesvizhevsky V V et al 2009 Coherent scattering of slow neutrons at nanoparticles in particle physics experiments, *Nucl. Instrum. Meth.* A **611** 302

[13] Nesvizhevsky V V, Cubitt R, Lychagin E V et al 2010 Application of diamond nanoparticles in low-energy neutron physics, *Materials* **3** 1768

[14] Cubitt R, Lychagin E V, Muzychka A Yu et al 2010 Quasi-specular reflection of cold neutrons from nano-dispersed media at above-critical angles, *Nucl. Instrum. Meth.* A **622** 182

[15] Nesvizhevsky V V 2011 Reflectors for VCN and applications of VCN *Rev. Mexicana Fiz.* **57** 1

[16] Golub R, and Pendlebury J M 1975 Super-thermal sources of ultra-cold neutrons, *Phys. Lett.* A **53** 133

[17] Schmidt-Wellenburg Ph, Andersen K N, Courtois P et al 2009 Ultra-cold neutron infrastructure for the gravitational spectrometer GRANIT, *Nucl. Instrum. Meth.* A **611** 267

[18] Baessler S, Beau M, Kreuz M et al 2011 The GRANIT spectrometer, *Comp. Rend. Phys.* **12** 707

[19] Luschikov V I, and Frank A I 1978 Quantum effects occuring when ultracold neutrons are stored on a plane, *JETP Lett.* **28** 559

[20] Nesvizhevsky V V, Boerner H G, Petukhov A K et al 2002 Quantum states of neutrons in the Earth's gravitational field, *Nature* **415** 297

[21] Nesvizhevsky V V, Voronin A Yu, Cubitt R et al 2010 Neutron whispering gallery, *Nature Phys.* **6** 114

[22] Nesvizhevsky V V 2010 Near-surface quantum states of neutrons in the gravitational and centrifugal potentials, *Physics-Uspekhi* **53** 645

[23] Nesvizhevsky V V 2012 Gravitational quantum states of neutrons and the new GRANIT spectrometer, *Mod. Phys. Lett.* A **27** 1230006

[24] de Carli P S, and Jamieson J C 1961 Formation of diamond by explosive shock, *Science* **133** 1821

[25] Irifune T, Kurio A, Sakamoto S et al 2003 Materials - ultrahard polycrystalline diamond from graphite, *Nature* **421** 599

[26] Aleksenskii A E, Baidakova M V, Vul' A Y et al 1999 The structure of diamond nanoclusters, *Phys. Solid State* **41** 668

[27] Dolmatov V Yu 2007 Detonation nanodiamonds: synthesis, structure, properties and applications, *Uspekhi Khimii* **76** 375
[28] Dubrovinskaia N, Dubrovinsky L, Crichtion W et al 2005 Aggregated diamond nanorods, the densest and least compressible form of carbon, *Appl. Phys. Lett.* **87** 083106
[29] Ignatovich V K, and Shabalin E P 2007 Algebraic method for calculating a neutron albedo, *Phys. At. Nucl.* **70** 265
[30] Ignatovich V K 2006 *Neutron optics* (M.: Nauka Fizmatlit)
[31] Utsuro M, and Ignatovich V 2010 *Handbook of neutron optics* (Berlin: Wiley-VCH)
[32] Krylov A R, Lychagin E V, Muzychka A Yu et al 2011 Study of bound hydrogen in powders of diamond nanoparticles, *Crystallography Rep.* **56** 102

3.6.3

Development of position-sensitive scintillation neutron detectors at J-PARC/MLF

Tatsuya Nakamura[1], Kentaro Toh[1], Kaoru Sakasai[1], Katsunori Honda[1], Kazuhiko Soyama[1], Masaki Katagiri[2]
[1]J-PARC Center, JAEA, Tokai, Ibaraki 319-1195, Japan
[2]Frontier Research Center for Applied Atomic Sciences, Ibaraki University, Tokai, Ibaraki 319-1195, Japan

E-mail: nakamura.tatsuya@jaea.go.jp

Abstract. Development of position-sensitive scintillator detectors at the J-PARC/MLF is briefly reviewed. This paper focuses on the detectors particularly using wavelength shifting fiber technology. Recent R&D works including a time-of-flight neutron imager and those for alternative to helium-3 gas detectors are also presented.

1. Introduction

Position-sensitive neutron detectors have been intensively developed for neutron scattering instruments for decades. Particularly those detectors with scintillation technology have been acknowledged indispensable for pulsed neutron diffraction instruments. Many of superior position-sensitive scintillation detectors have been developed at ISIS detector group. They have carefully tailored and optimized the detector performances depending on the purposes, providing the state-of-the-art detectors to their neutron instruments [1].

The development of position-sensitive scintillator detectors for J-PARC was initiated in the late '90s. An emerging WLS fiber technology seemed suitable at the time to design for detectors with various characteristics adjusted to the neutron scattering instruments in the MLF of the J-PARC. Although it had not yet convinced whether a WLS fiber technology could meet a high requirement in terms of gamma-ray insensitivity Dr. Katagiri took a decisive step to challenge in developing scintillator detectors using wavelength-shifting (WLS) fibers.

In this paper we briefly review the two-dimensional detectors developed using WLS fibers for neutron scattering instruments, iBIX and SENJU, in the J-PARC/MLF. In addition we introduce a progress in scintillator phosphor development. Finally recent works including the time-of-flight neutron imager and the detector for alternative to helium-3 gas detectors are presented.

2. Wavelength-shifting fiber based scintillation detector

2.1. iBIX detector

The iBIX is a single crystal diffractometer for biomolecular crystallographic study. The two-dimensional detector for iBIX (called iBIX detector, hereafter) was our first WLS-fiber-based scintillation detector developed in the J-PARC/MLF. The specifications required to the detector were quite challenge at the time. Bragg peak intensities on the detector in the instrument had been expected very low hence the detector had to have a high detection efficiency, more than 50% for thermal

neutrons whilst maintaining acceptable gamma-ray sensitivity to the order of 10^{-6}. The detector also had to be designed compact with modularity to enable multiple detectors tiled around the sample. Each detector should have the least neutron-insensitive area over the detector face to increase packing rate. Moreover a severe peak separation in space demanded a detector to have a spatial resolution of less than 1 mm. No such detector had been ever commercially available except paying unacceptably low detector efficiency.

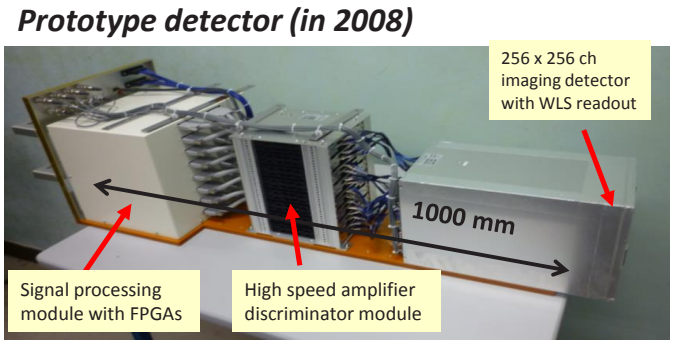

Figure 1. A prototype detector for iBIX instrument.

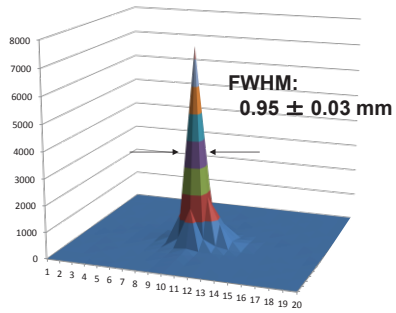

Figure 2. A collimated beam measured with the iBIX detector.

The WLS fibre technology has been intensively used in high energy physics experiments. There for gamma-ray or x-ray detection a single scintillator screen is usually sandwiched with WLS fibre ribbons from the top and bottom in favour of light collection. In order to make it suitable to neutron detection new detector head structure was introduced, where two ^{10}B-doped ZnS scintillator screens actually sandwich the crossed WLS fibres arrays [2]. By doing so a number of the scintillator screens became double ensuring a high neutron capture rate, thus for detection efficiency.

Figure 1 shows a prototype detector produced in 2008. The physical size is almost identical to the one installed in the iBIX. The detector has a neutron-sensitive area of 133 × 133 mm^2, making a filling factor to 69% over the detector face [3]. Each WLS fiber connects one of the pixels in a multi-anode PMT. Detector electronics: 256 × 2 channels of amplifier and discriminator cards and the signal processing module, are placed behind the detector head so that to make the detector compact and modular. The detector operates in a photon counting method.

The detector head is made with packed 1/2-mm diameter WLS fibre ribbons. This makes the detector pixel size small enough to measure precise structure of Bragg peaks. Figure 2 shows a measured beam profile when a neutron beam was collimated with 1-mm diameter incident to the detector. The detector measured the collimated beam 0.95±0.03 mm in full width at half maximum, reproduced the beam profile very well. This result indicated that the detector has a spatial resolution less than 1 mm and it is close to the pixel size of 0.5 mm. The achieved spatial resolution is nearly approaching to the “light spread limit”, which is calculated including light scattering within the scintillator and the fibre arrays [4].

2.2. SENJU detector

We have developed a two-dimensional detector that has larger area than the iBIX detector for SENJU in the J-PARC [5]. The SENJU is also a single crystal diffractometer that sees one of the poisoned moderators in the J-PARC/MLF. The SENJU required a large area and a large number of detector modules for scanning a wide range of reciprocal space in one measurement. The major differences from the iBIX detector are: a large neutron-detective area with a moderate spatial resolution, a count rate capability up to 50 kcps, and a tolerance to leakage magnetic field up to 200G. Figure 3 shows a schematic view of the neutron-detecting head. We have made following changes in the detector head:

add the air gap deliberately between the WLS fibres instead of packing to each other, spliced the WLS fiber to the clear fiber which is bent backward with a radius of 3 mm to minimize the dead area.

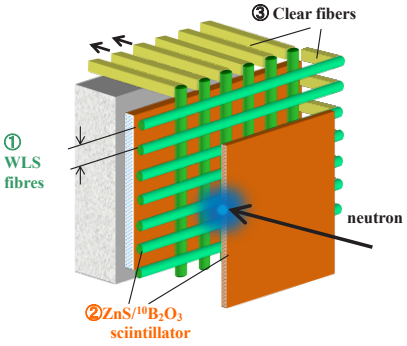

Figure 3. A schematic view of detecting head of SENJU detector.

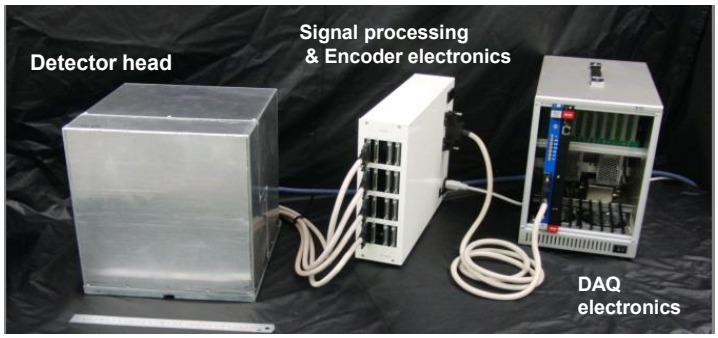

T. Nakamura, et al. NIM -A, 686(2012)64.

Figure 4. Detector system of SENJU [5].

The dual scintillator screens are maintained similar to the iBIX detector. With this design the detector becomes to have a large coverage at an affordable cost, high detection efficiency and minimized neutron-insensitive area.

Figure 4 shows detector system of SENJU(showing only one detector module). The detector module is designed to have a neutron-sensitive area of 256 × 256 mm^2 with a 4-mm spatial resolution. One signal processing & encoder electronics can handle four detector modules, which saves a lot with detector electronics. The neutron event data are recorded in list mode for post data processing.

2.3. R&D for Scintillator phosphor

We have developed the new ZnS phosphor intensively to decrease its afterglow to ensure a count rate capability of the detector. With the commercial ZnS scintillator the afterglow lasts for a few tens of

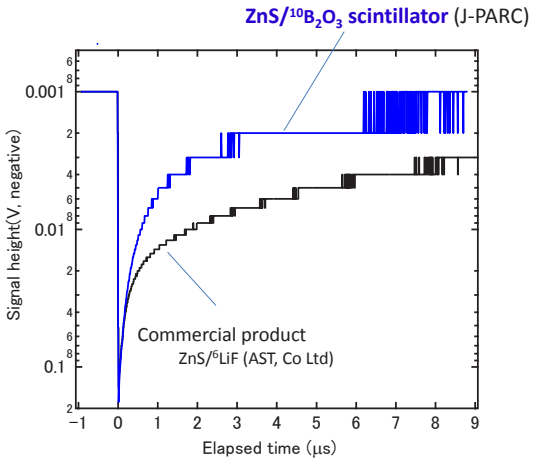

Figure 5. Comparison of the averaged waveforms of neutron-induced signals [6].

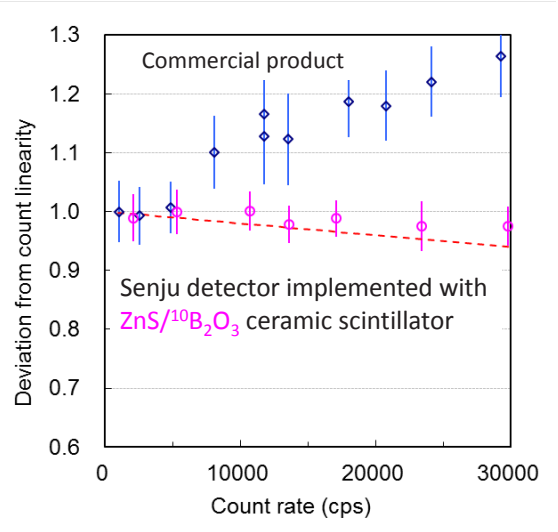

Figure 6. Normalized count rate of the SENJU detector implemented with a commercial product (ZnS/^{6}LiF) and the developed scintillator (ZnS/$^{10}B_2O_3$) [6].

microseconds, which kills a count rate capability of the detector significantly with our signal processing method.

Figure 5 shows averaged neutron-induced signal waveforms of the commercial products (ZnS/^{6}LiF produced by AST Co. Ltd) and our scintillator made with new ZnS phosphor (ZnS/$^{10}B_2O_3$) [6]. The both signals had similar primary decay time constant of ~60 ns, but our scintillator exhibited much lower afterglow than the commercial product (The afterglow decreased about one thirds compared to the commercial product.) Note that the averaged signal exhibited similar pulse height at the beginning part, indicating that the new scintillator would not decrease detector efficiency much with a proper signal processing although a total amount of detected photons became less compared to the commercial product.

Figure 6 shows the normalized count rates of the SENJU detector implemented with the commercial scintillator and the new ZnS/$^{10}B_2O_3$ scintillator screen. The count rate of the detector was divided by the count measured by a detector monitoring the incident neutrons (a ^{3}He detector with a detection efficiency of ~10^{-4} for thermal neutrons), with the resultant normalized ratio facilitating comparisons with the theoretical calculations. With the commercial scintillator the detector suffered a lot with multicounting at more than count rate of 5kcps, resulting in the significant deviation from the theory. It was clearly shown that the count rate follows nearly to the theoretical calculation up to 30 kcps with the new scintillator, extending our count rate capability by a factor six compared to the one with the commercial product.

2.4. Detectors installed in the beam lines

Figure 7 shows the photograph of the detectors in the iBIX. 30 detector modules have been installed in the detector banks by the end of 2013. Figure 8 shows a view of the SENJU at present. The detector banks have fully populated with the detector modules by the end of 2013. Total 37 detectors cover 30% of the solid angles around the sample [7].

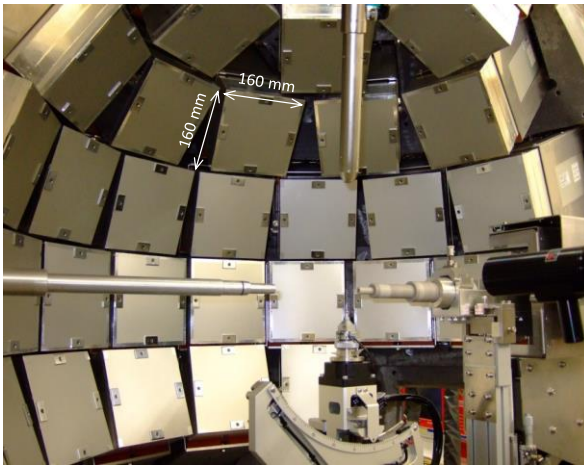

Figure 7. Photograph of the iBIX.

Figure 8. Photograph of the SENJU.

3. Time-of-flight neutron imager with WLS fiber technology

Apart from beam line detectors we have been working detector R&D that could be useful or may have some possibilities for future neutron scattering instruments. Development of a time-of-flight neutron imager is one of such activities. It has been acknowledged that neutron radiography or neutron tomography is a powerful non-destructive technique to visualize an object what is not seen with other radiations such as by x-rays. We tried to see a possibility of making such detector using WLS fibre technology. Particularly the detector that can meet the requirements both in a spatial resolution less

than 100 μm and low gamma-ray sensitivity is a challenge over the conventional detectors such as CCD, MSGD, ^{6}Li-loaded glass scintillator. So far neutron-sensitive micro-channel plate detector offers promising prospects in terms of a spatial resolution and count rate but it is hard to have a capability of rejecting gamma-ray to the level of 10^{-7} in principle.

Figure 9 shows a schematic view of a detector head of the proposed neutron time-of-flight imager [8]. The detector is comprised of a thin scintillator screen, a light image magnifier made of a fiber optic taper, and WLS fiber arrays. The idea is that the magnified neutron(light) image by a factor of 3.1 is measured with the light sensors with a fine pixel size. For this purpose the dedicated WLS fibers with a diameter of 100 μm were produced, which is the smallest ever made as a WLS fibre as far as we acknowledge. In combination with the proper image magnifier the effective size of the detector pixel becomes 34×34 μm^2.

Figure 10 shows a measured beam profile covered with a Cd mask on the detector face. The detector exhibited a spatial resolution of 68 μm in FWHM, which is the best achieved ever with this type of detector. The detector also exhibited a gamma-ray sensitivity of less than 10^{-7} thanks to the thin thickness of the ZnS screen and the less amounts of WLS fibers.

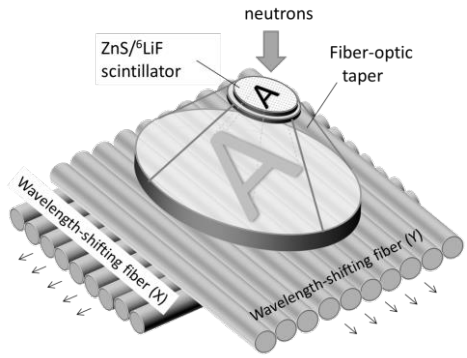

Figure 9. A schematic view of the WLS fiber detector with a sub 100-μm spatial resolution [8].

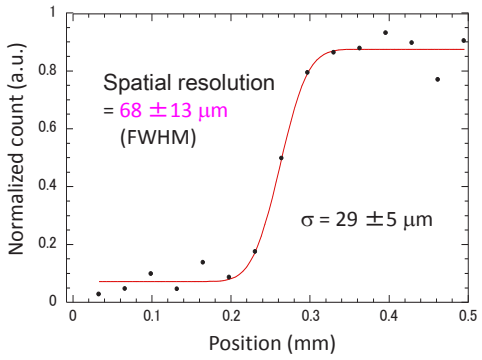

Figure 10. Fitting result to beam edge profile measured with Cd mask on the detector face [8].

4. Detectors as alternative to helium-3 gas based PSDs

Recent world-wide shortage of ^{3}He gas has accelerated the development of neutron detector technologies that could be alternative to conventional ^{3}He-gas-based detectors. We have been working on the scintillation neutron detectors that could be used for inelastic neutron scattering instruments in

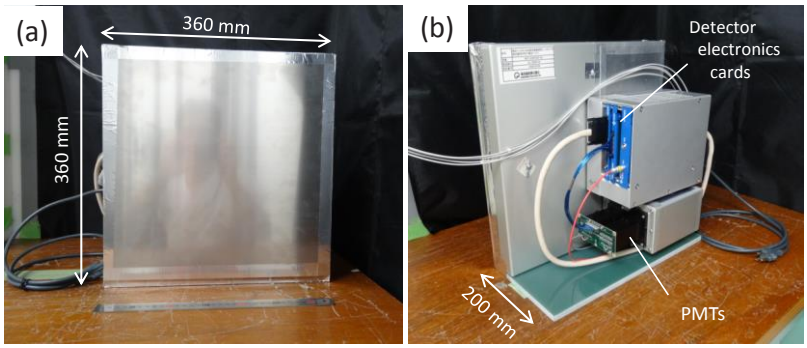

Figure 11. Photograph showing (a) front and (b) rear view of the prototype detector [9].

future under the frame work of international collaboration on neutron detectors. Two lines of development works are underway at the J-PARC/MLF. One is a SENJU type detector which is aimed at installing outside of a vacuum tank and the other is the scintillator WLS fibre coil detector called SFC detector which is aimed at installing inside a vacuum tank.

4.1. SENJU type detector

The SENJU type detector follows almost similar to the detector structure with the SENJU detector. A pitch of the WLS fibres is 5 mm, in contrast to 4 mm in the original detector, which increases the neutron-sensitive area of the detector by a factor of 1.56. The pixel size can be made larger (i.e. 20 × 20 mm^2) to decrease a number of electronics while keeping the size of detector pixel small enough for inelastic neutron scattering instruments. This can be done by reading out four WLS fibres as potting into one PMT channel which ensures reasonable light-collection efficiency with great flexibility in pixel size. Figure 11 shows a photograph of the prototype detector. The detector is designed to have a neutron-sensitive area of 320 × 320 mm^2. The detector is designed to be compact and light weighted with a physical size of 360 × 360 × 200 mm^3. The weight of the detector is 11.6 kg. All of the detector electronics—including PMTs, the amplifier/discriminator card, the high-voltage card and the signal processing/encoder card—are made dedicated for this detector and installed behind the neutron-detecting head.

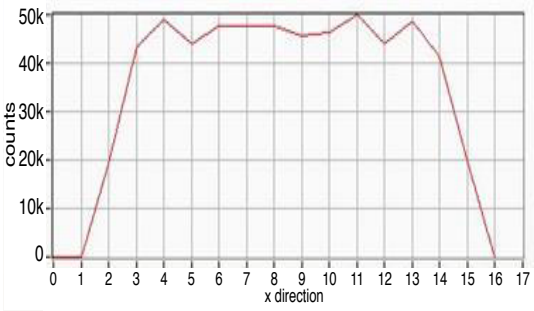

Figure 12. Count projection measured with a prototype detector.

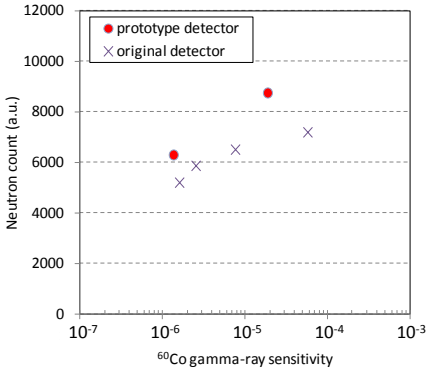

Figure 13. Neutron count versus ^{60}Co gamma-ray sensitivity [9].

Figure 12 shows count projection along x-direction. The count uniformity was evaluated as about 15% (SD) by Gaussian fitting, which would be acceptable for most neutron-scattering experiments (the scintillator screens that have a size of 256 × 256 mm^2 are temporarily implemented at present). Figure 13 shows the detector metrics, with the neutron count (detection efficiency) plotted versus the ^{60}Co gamma-ray sensitivity. The data measured with the original detector are included for comparison. At the ^{60}Co gamma-ray sensitivity of 10^{-6} (the normal operating condition), the prototype detector exhibited 20% larger neutron counts than the original detector, with a calibrated detection efficiency of about 40% for thermal neutrons. Increasing the area of the detector would be the future task together with lowering the intrinsic background rate.

4.2. Scintillator WLS fiber coil detector

The idea of the scintillator WLS fiber coil detector is to make the detector element with a rolled WLS fibre coil sandwiched with the rolled cylindrical scintillator screens[10]. With these elements the detector can be made tubular shape and long that would make it much easy to be installed in the vacuum tank. Since the incidence neutron experiences four layers of scintillation screens the detector has a potential to have high detection efficiency, which is similar to that of the 6-bar 1-inch diameter

^{3}He gas PSD. Moreover the detector is pixelated, so the detector can operate at much higher global count rate per tube than the conventional ^{3}He gas PSD.

Figure 14 shows the demonstrator detector that has 64-elements and a 1-inch diameter ^{3}He gas-based PSD for comparison. The element size of the SFC detector is made 22 × 20 mm to fit in the 1-inch diameter Aluminium tube (although the present diameter of the demonstrator detector tube is 30 mm due to a ready availability). Clear fibres from each coil elements penetrate through the tube centre to the multianode-PMTs which are placed at one end of the tube. At present the detector exhibited detection efficiency of 35-45% for thermal neutrons with an acceptable gamma sensitivity and multicount rate. This can be improved by optimizing the fiber coil structure and minimizing the light loss at the splicing parts between the WLS and clear fiber.

Figure 15 shows normalized beam profiles with a Cd mask measured using the ^{252}Cf source. A cylindrical piece of rolled Cd with a thickness of 0.7 mm and a length of 225 mm covered the left, centre and right areas of the detector. The detector reproduced the profile of the masked beam very well: the detector measured the masked area as ~220 mm (10.5 pixels) at full width at half maximum for all the masked positions, demonstrating the capability of the one-dimensional position sensitivity of the detector.

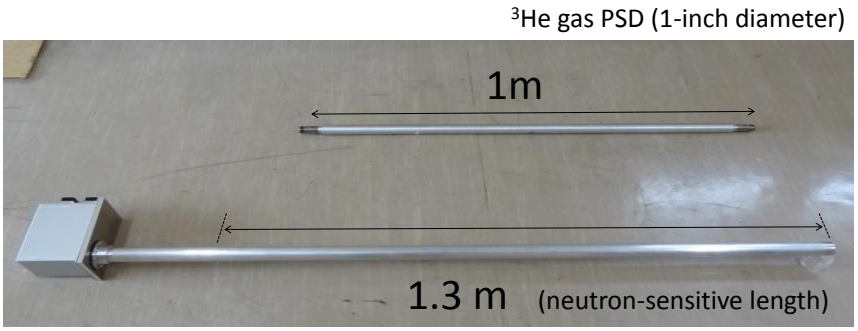

Figure 14. Photograph of a 64-element SFC detector (1-inch diameter ^{3}He gas PSD is also shown as reference) [10].

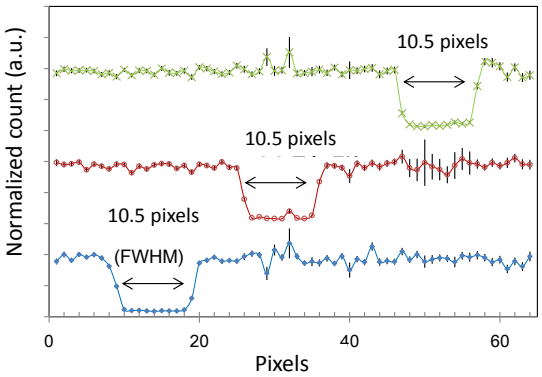

Figure 15. Normalized beam profiles with a Cd mask measured using the ^{252}Cf source [10].

5. Summary

We have intensively developed position-sensitive scintillation neutron detectors by using WLS fiber technology. The WLS fiber technologies add great flexibility to detector designs and the detector

structure has been optimized for iBIX and SENJU. New scintillator material that can improve a count rate capability of the detector has been developed and its feasibility demonstrated. Further detector development for alternative to ^{3}He gas PSDs will continue for future.

6. References

[1] ISIS facility: http://www.isis.stfc.ac.uk/
[2] Katagiri M, et al. 2004 *Nucl. Instr. & Meth*. A **529** 313
[3] Hosoya T, et al. 2009 *Nucl. Instr. & Meth*. A **600** 217
[4] Nakamura T, et al. 2014 *J. of Instr*. **Vol 9** C11020
[5] Nakamura T, et al. 2012 *Nucl. Instr. & Meth*. A **686** 64
[6] Nakamura T, et al. 2014 *J. of Phys. Conf. ser*. **528** 012043
[7] Kawasaki T, et al. 2014 *Nucl. Instr. & Meth*. A **735** 444
[8] Nakamura T, et al. 2014 *Nucl. Instr. & Meth*. A **737** 176
[9] Nakamura T, et al. 2014 *J. of Phys. Conf. ser*. **528** 012042
[10] Nakamura T, et al. 2014 *Nucl. Instr. & Meth*. A **741** 42

3.6.4

^{3}He-free triple GEM thermal neutron detectors

A. Pietropaolo[1,2], G. Claps[1], F. Murtas[3], L. Quintieri[4], G. Celentano[1], A. Vannozzi[1],A. Santoni[1] R. Riedel[5]

1 ENEA Frascati Research Center, via E. Fermi 45, 00044 Frascati (Roma), Italy
2 MIFP, Mediterranean Institute of Fundamental Physics - Via Appia Nuova 31, 00040 Marino (Rome), Italy
3 CERN, CH-1211 Geneva 23, Switzerland
4 ENEA Casaccia Research Center, via Anguillarese 301, 00123 S. Maria di Galeria (Rome), Italy
5 Oak Ridge National Laboratory - 2008 MS-6466, Oak Ridge, TN 37831-6466, USA

***Corresponding author**: antonino.pietropaolo@enea.it

Abstract. A novel type of thermal neutron detector based on the gas electron multiplier (GEM) technology is presented in the framework of the research and development activity on the ^{3}He replacement for neutron detection. The device relies on a series of boron-coated alumina sheets placed perpendicularly to the incident neutron beam direction. The detector, named side-on GEM (S-GEM), was tested (in a prototypal version) on beam at the TRIGA reactor of the ENEA-Casaccia Research Centre (Italy), ISIS spallation neutron source (UK) and at the High Flux Isotope Reactor at the Oak Ridge National Laboratory (US) to assess its performance. The obtained results demonstrate the effectiveness of the proposed detector configuration to achieve a good spatial resolution and, in the perspective, higher thermal neutron efficiency, comparable to ^{3}He tubes typically used for diagnostic in nuclear reactors. The main issues to be addressed to reach the goal, mostly related to boron coating procedures and characterization, are also pointed out.

1. Introduction

The global shortage of ^{3}He for neutron detection purposes triggered an intense and interesting research and development activity worldwide to find out effective solutions. Different approaches have been proposed so far such as the use of boron or lithium fluoride loaded detectors [1–6]. Although reactions producing charged particles in the final state are widely investigated, also thermal neutron radiative capture has been recently used [5,7,8]. In this paper, a particular gaseous detector, namely the gas electron multiplier (GEM) [9], is described. In particular, a triple GEM device [10,11] was equipped with a sequence of alumina sheets, coated by boron films on both wide surfaces, acting as neutron–charged-particle converters. The detector window is made on the frames of the GEM foils, so that the neutron beam can impinge laterally (that is, perpendicularly to the wider surface) onto the detector rather than frontally, as typically happens in other applications [12,13]. The device, conceived and assembled at the Istituto Nazionale di Fisica Nucleare (INFN-Laboratori Nazionali di Frascati) and named as side-on GEM (S-GEM) [14], was tested at the TRIGA reactor (ENEA-Casaccia Research

Centre, Italy), ISIS spallation source (UK) and High Flux Isotope Reactor (HFIR) (Oak Ridge National Laboratory, US) [15,16]. Previously to experimental tests, a series of Monte Carlo simulations, thoroughly described and discussed in Ref. [14] were performed using two different codes for a thorough description of the physics underlying the detector's operation and as a mandatory validation step for other simulations of more complex detector's architectures that should lead to define a more efficient device.

2. Experimental setups and measurements

The S-GEM detector structure is shown in figures 1 and 2.

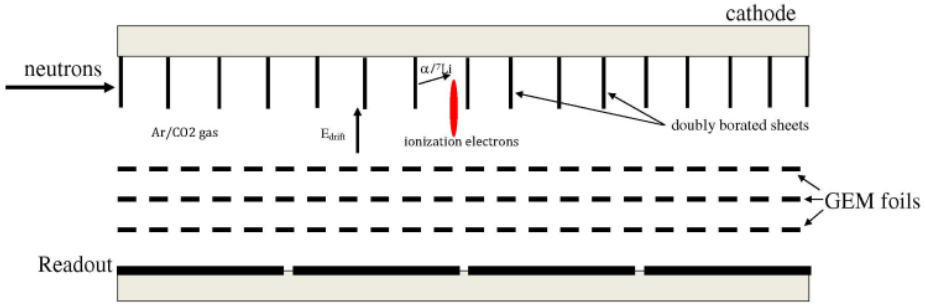

Figure 1: *Schematic of a S-GEM detector*

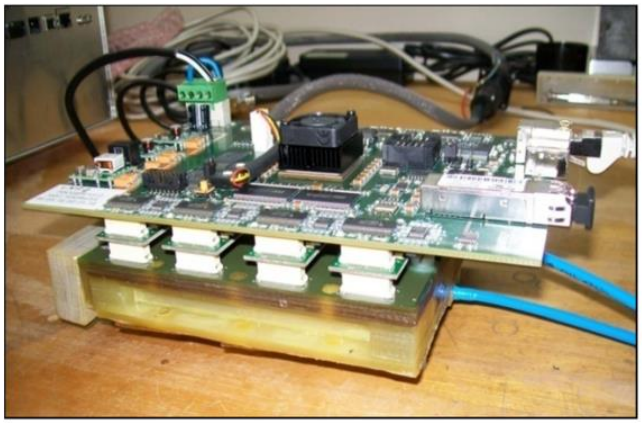

Figure 2: *Picture of an assembled S-GEM*

In the S-GEM configuration, the neutron beam impinges perpendicularly to the wider alumina sheets, that is parallel (rather than perpendicular) to the cathode contrarily to the typical configuration applied in almost all GEM-based detectors applications. When a neutron is absorbed in the ^{10}B layer, an alpha particle and a ^{7}Li ion are produced following the reactions $n+^{10}B \rightarrow ^{4}He+^{7}Li$ (Q=2.8 MeV, BR=7%) or $n+^{10}B \rightarrow ^{4}He+^{7}Li+\gamma$(478 keV) (Q=2.3 MeV, BR=93%). The secondary ions ionize the Ar/CO_2 gas mixture (70%/30%) in the drift region of the detector thus producing electrons that, moving under the influence of the electric field in this region, reach the three GEM foils. In this region they are further proportionally multiplied in cascade, inducing a detectable signal in the pad-based readout. The first S-GEM prototype designed was made of two sets of five 40x10x1 mm^3 glass sheets arranged in the same detector: a borated set and not borated one in order to check, under localized irradiation, the difference between the two sets (the reader is referred to Ref [14] for more details). The readout was composed of 128 pads 3x6 mm^2 organized in a matrix of 16x8. ^{10}B coating was obtained by means of electron beam evaporation techniques. Located on the external side, there is the readout electronics consisting of a set of eight CARIOCA chip cards and a FPGA mother board, the details being described in ref. [12].

The upgraded version of the S-GEM was made with the readout pads arrangement chosen in such a way to achieve a better spatial resolution along the beam direction. The cathode is an aluminium plate, that on the internal side facing the gas mounts 16 borated alumina sheets in half of the active volume of the drift region and one borated alumina sheet on the other half side. Each sheet is 50 mm long, 10 mm high and 400 μm thick while the drift region is 12 mm high, so that the sheets do not touch the first GEM foil. A 10×1 cm^2 area 0.5 mm thickness of epoxy glass window was obtained on the lateral side of the drift region and parallel to the borated sheets.
Both the detectors film depositions were carried out at the ENEA-Frascati Research Centre (Italy) using a vacuum chamber equipped with a multi-crucible Thermionics 3 kW electron beam system with 4 kV of electron acceleration voltage and 750 mA of maximum current. Boron tablets of 0.5 inches diameter were used as source for evaporation using boron metal powder enriched in ^{10}B (isotopic ^{10}B > 97 at%, Eagle Picher Technologies, LLc). Five glass substrates were disposed side by side on a rotating sample holder in such a way that both surfaces could be subsequently exposed to the evaporation source and substrates could be completely coated during the same coating process. Film growth rate was monitored by a quartz crystal controller and fixed at 0.2–0.3 nm/s by tuning the electron beam current. The distance between the evaporation source and sample holder was 12.5 cm. In this configuration, the film thickness uniformity over the whole deposition area 40x50 mm^2 is greater than 90%. Each surface was coated with 300 nm ^{10}B film. Although the optimized thickness may be in the order of about 1 μm, this thickness was chosen to achieve a low intrinsic efficiency for a single sheet, as the detector was to be used on the direct neutron beam in a condition similar to a beam monitor. Films as thick as 680 nm were successfully deposited on a single surface exhibiting good adherence and stability against aging (no delamination occurred within 2–3 months).

2.1 TRIGA measurements

The first prototype S-GEM with glass sheets was tested at the TRIGA reactor operating at the ENEA-Casaccia Research Centre (Italy) [17]. The reactor can be operated at different powers, from a few Watt to 1 MW, with a neutron flux of about 2x10^6 n/cm^2/s (at the maximum power) featuring a Maxwellian spectrum peaked 25 meV and a FWHM of about 70 meV, as shown in figure 3.

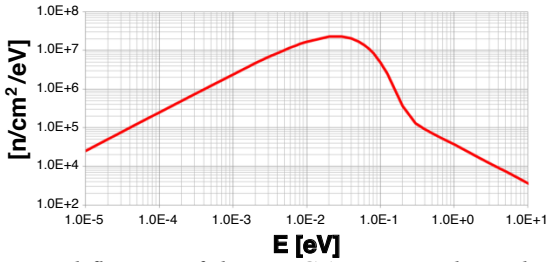

Figure 3: *Neutrons spectral fluence of the TRIGA reactor along the thermal extraction line*

By running at different powers (and thus at different neutron fluxes) the detector response was investigated in terms of detector's count rate as a function of the incident neutron rate from the beam line. Figure 4 shows S-GEM counts and reactor power (from a few Watt to 1 MW) as a function of time and the correlation between the S-GEM count rate and the neutrons rate provided by the reactor along the extraction port chosen for the measurements. A good linearity over 6 orders of magnitude is found and the slope of the fitting line, that provides an estimation of the detection efficiency, results to be 4.8(5)%.

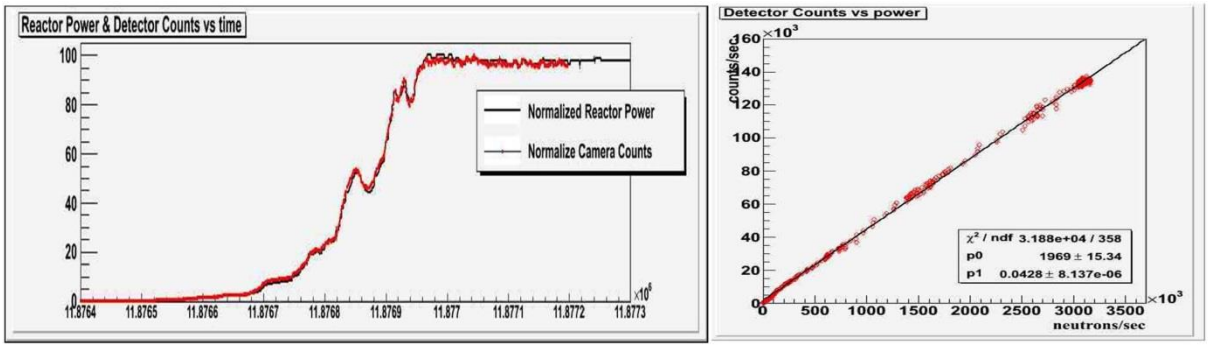

Figure 4: *(left) Normalized S-GEM counts (red) and TRIGA power (black) as a function of time; (right) S-GEM counts vs neutron rate (correlation plot). The linear fit provides detector's efficiency.*

2.2 ISIS measurements

The same detector tested at the TRIGA reactor was also tested at the ISIS spallation neutron source [18] at the Rutherford Appleton Laboratory (UK) using the ROTAX beam line [19]. This instrument is a neutron diffractometer, mostly used for magnetic neutron scattering and cultural heritages studies using neutron diffraction [20,21]. At present, it is used as a test beam line for detector development [22,23]. ROTAX is downstream of the PRISMA beam line and it is in the line of view of a solid methane moderator at T~95 K. The primary flight path (from moderator to the sample position) is $L_0 \approx 15$ m. A T0 chopper blocks the beam when the protons hit the target thus blocking out a large component of the fast neutrons and gammas, while the use of the neutron guides in the front end of the PRISMA beam line ensures an enhanced thermal neutron intensity at the sample position. The neutron spectrum is peaked at about 10 meV and features a high energy tail up to multi-MeV energies [24]. The measurement was performed by placing the S-GEM in the incident neutron beam at a distance of about 16 m from the moderator and recording neutron counts by using a time window of 1 ms and delaying it with respect to the ISIS clock in steps of 1 ms from 0 to 19 ms (i.e. the whole time frame of ISIS beam lines). The detector was biased at a voltage of about 870 V, that is at a gain to ensure an almost complete rejection of the gamma background (see figure 5 and refer to Ref. [11]), composed of different contributions and always occurring in a neutron beam line and [25,26].

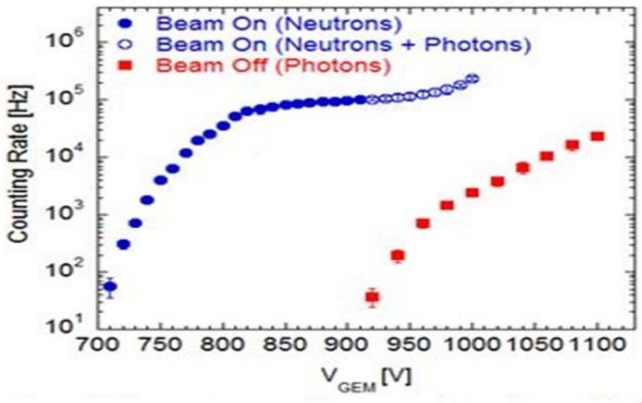

Figure 5: *S-GEM counting rate as a function of total GEM bias for different irradiation conditions*

The detector results insensitive to the 478 keV gamma rays coming from the radiative thermal neutron capture in boron. The reconstructed time spectrum (corresponding to the incident neutron spectrum in the time-of-flight domain) is shown in Fig. 6 and compared to the same spectrum measured by the ROTAX incident neutron beam monitor (a Li-glass scintillation detector) operating with the standard

Data Acquisition Electronics used at ISIS. The two spectra were normalized with respect to the peak at 6 ms of the S-GEM spectrum for a more clear shape comparison. The two trends are very similar and show a peak at about 6 ms and then a rapid falling edge starting at 2 ms. The peak at 6 ms is the peak of the Maxwell–Boltzmann component of the neutron spectrum induced by the effect of the moderator while the rapid decrease below 2 ms is due to the combined effect of the T0 chopper operating on ROTAX, and used to cut away from the beam the high-energy neutrons components and the gamma flash from the target, and the decreasing efficiency of the monitor and S_GEM with increasing neutron velocity (both ^{6}Li and ^{10}B absorption cross section decrease as 1/v, v being the neutron velocity).

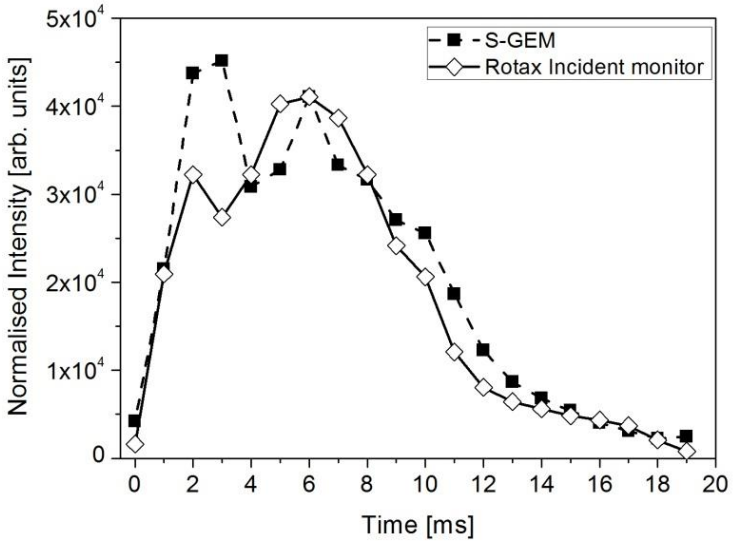

Figure 6: *Comparison between the time of flight neutron spectrum recorded by the Li-glass neutron beam monitor of ROTAX and that recorded by the S-GEM (see text for details).*

Another measurement was performed on ROTAX by placing two close spaced (about 5 mm distance) cadmium sheets, 1 mm thickness and about 10x1 cm^2 area. The two sheets were placed in front of the entrance window of the S-GEM in such a way to intercept the incident neutron beam and absorb thermal neutrons impinging onto the Cd surface. Indeed, 1 mm natural Cd provides a very high (close to 100%) absorption efficiency for neutrons with energy up to about 400 meV (cadmium cut-off). Figure 7 shows the 2D intensity plots and the corresponding contour plots relative to the measurements with and without the cadmium sheets in front of the S-GEM. In the right panel, counts are registered in the region between the two absorbing Cd sheets. It is to be stressed that in both cases shown in Fig. 7, the signals from gamma-rays (both environmental as well as from neutron radiative capture in ^{10}B and Cd) do not contribute thanks to the high rejection capability of the detector at the used operational bias. This further measurement is a clear demonstration that the S-GEM detector is sensitive to thermal neutron with a spatial resolution related to the pad's dimension.

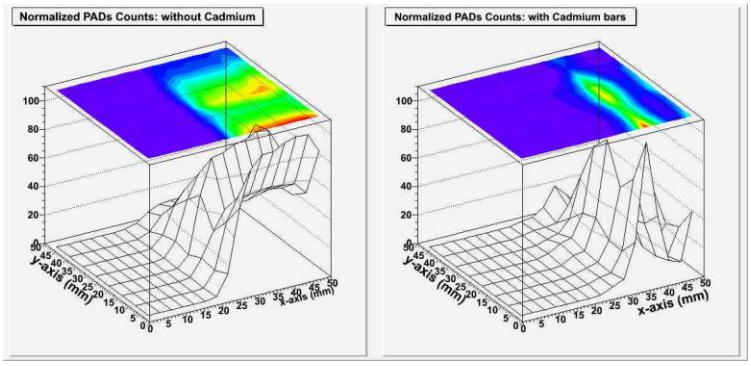

Figure 7: *2D Intensity profiles recorded through the S-GEM, obtained by using two cadmium sheets in front of the detector*

2.3 HFIR measurements

The S-GEM detector mounting 16 borated alumina sheets was characterized at the CG1A beam line at the HFIR facility, a nuclear research reactor located at Oak Ridge National Laboratory (ORNL, Oak Ridge, Tennessee, US). HFIR operates at 85 MW power and is one of the highest-flux reactor-based sources of neutrons for condensed-matter research in the United States. CG1A is a detector test station providing 4.2 Å neutrons at an estimated flux of 2×10^6 n cm^{-2}. The neutron beam used for the measurements extended on an irradiation area of 5×5 cm^2 and had an angular divergence lower than one degree, making it extremely useful to characterize resolution, uniformity, distortion and performance with a high neutron flux. The HFIR neutron spectrum, shown in figure 8, features a Maxwell-Boltzmann distribution peaked at λ= 4.23 Å (E ~ 4.57 meV) with a Full Width at Half-Maximum (FWHM) of about 0.11 Å.

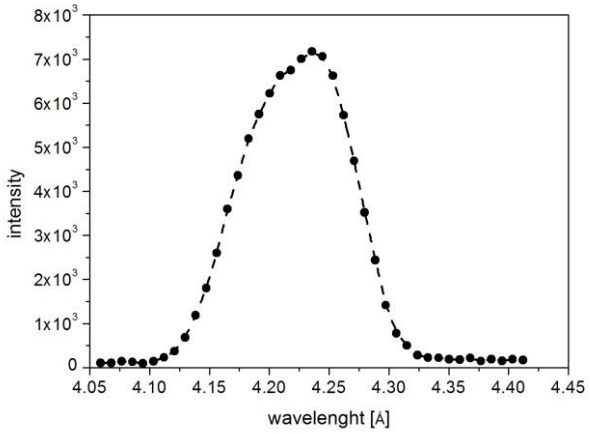

Figure 8: *HFIR neutron spectrum as a function of wavelength.*

This spectrum is measured using the time-of-flight analysis. This is accomplished by using a pinhole neutron chopper operating at about 100 Hz and a ^{3}He detector approximately 1.5 m from the chopper. The main goals of the experimental tests were to evaluate linearity and accuracy in beam positioning and to measure the detector efficiency. For beam intensity tests, the experimental set-up is sketched in figure 9.

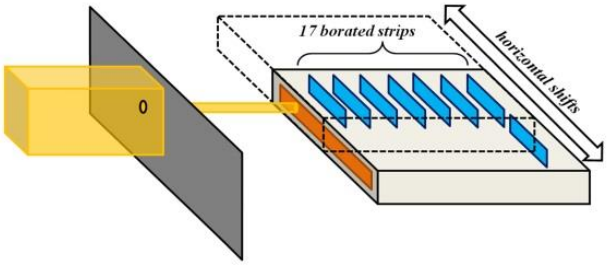

Figure 9: *Schematic of the experimental setup for the S-GEM measurements at HFIR reactor*

A 2 mm thick borated aluminium mask was placed at a distance of about 2m from the source to provide an almost complete absorption of about 99.7% neutrons over the whole spectrum shown in fig. 8. The mask features a 2.5 mm diameter hole to provide a collimated beam for positioning tests described below. Beyond the screen there was the S-GEM detector mounted on a mobile support so that it could be displaced along the horizontal direction parallel to the window. During the beam positioning tests the detector was moved in steps of 10 mm (with an accuracy of better than 10 μm) scanning in such a way the whole window by the small-hole beam. Then, to make efficiency measurements, an ^{3}He tube (1 cm in diameter and 30 cm long with 10 bar pressure) was placed in front of the S-GEM detector providing an efficiency close to 1 at the neutron spectrum peak. During the S-GEM measurements the ^{3}He detector was moved away, while during the measurements with the ^{3}He tube the GEM detector was not recorded. The S-GEM measurements were performed in two different positions with respect to the beam passing through the mask hole, in order to irradiate the 16-sheets region and the single-sheet one. To evaluate the overall background sensitivity of both ^{3}He and GEM detectors, the measurements were done also with the mask hole closed. The S-GEM was operated with a biasing voltage of 870V, corresponding to a gain of about 180, that allows an effective lowering of the gamma sensitivity as already shown in other experimental tests [11,14]. The ^{3}He tube used a PDT model 20A preamplifier and was biased at about 1200 V. The TTL output of the PDT preamplifier is input into an ORTEC 974 counter and the count rate is the average value over a 100 s counting time. The efficiency of the ^{3}He tube has been verified using a second ^{3}He tube operating under similar conditions with a different PZT amplifier. Dead time loss is not significant in the ^{3}He detector below 1E+4 counts s^{-1}. During the detector position scan, a sequence of 3D beam profiles like those shown in figure 10(a) was measured. The 2D beam profile [figure 10(b)] was obtained by summing all the counts on the four pads along the X-axis. A Gaussian function was used to fit these profiles: their central value provides a measure of the beam positions. Figure 10(c) shows the intensity profiles along the X-direction (neutron beam axis) for the four pads rows. The S-GEM detector worked using an internal trigger and registered the number of counts over a time window of 1 s after each trigger.

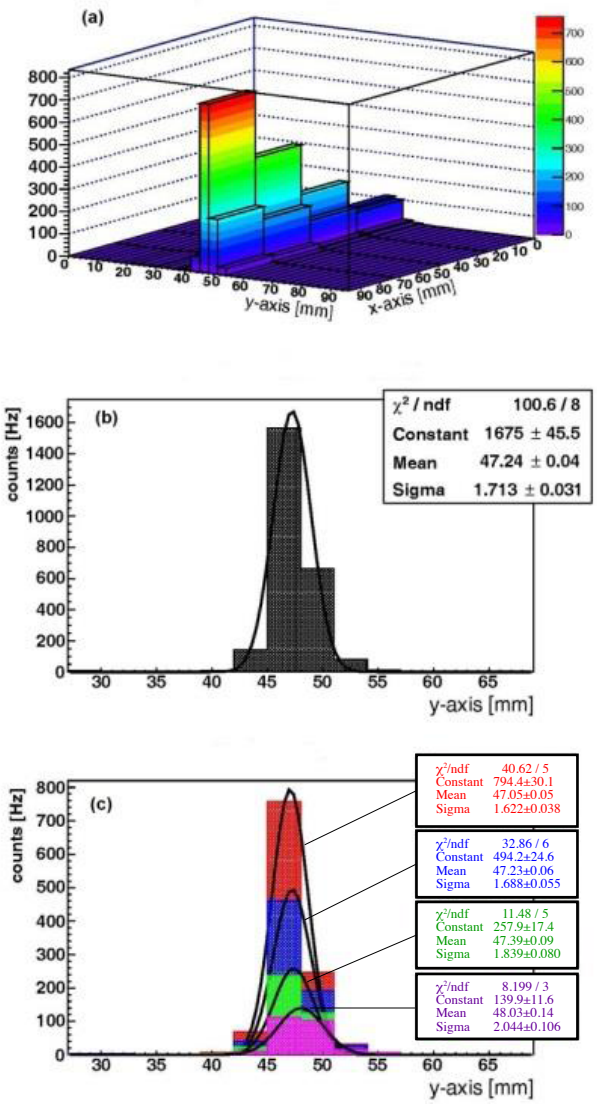

Figure 10: *(a) 3D beam profiles measured during the detector position scan over the active window; (b) a beam profile on the Y section, obtained summing all the counts on the pads along X-direction; (c) beam profiles obtained on the 32 Y pads on each of the four pads sectors along the X direction.*

The Gaussian fit shows an increase in the FWHM of the beam profile, along the neutron flight path inside the detector, of about 25% between the first and the last pads sector. This is most likely due to a small divergence of the beam. A position resolution of 770±80 μm is found [27]. In figure 11, the 3D plots represent the cumulative counts distribution on each pad obtained by summing the counts for each trigger. Analysing these distributions, it is possible to calculate the mean of the counts number and its uncertainty for the two beam configurations.

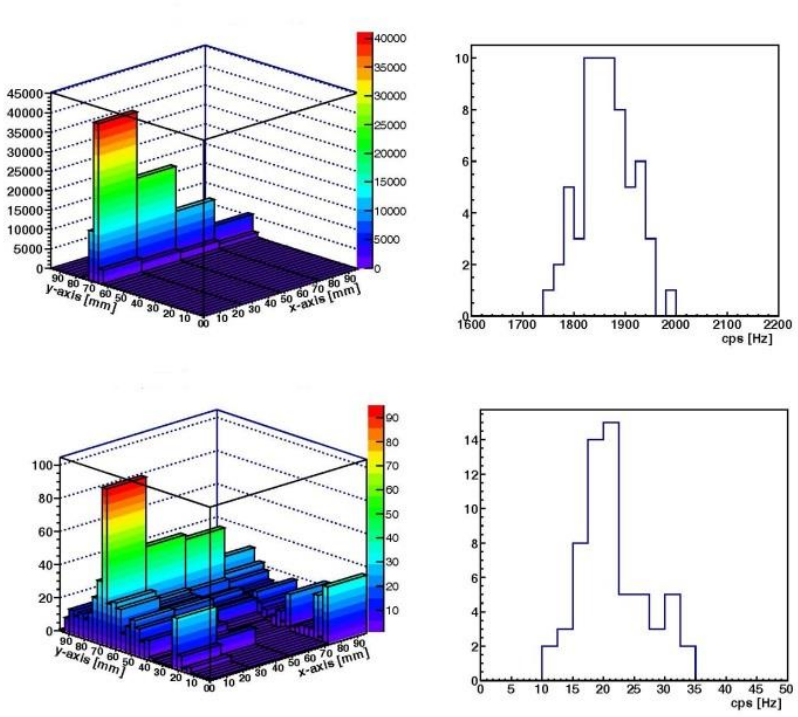

Figure 11: *(upper panel) 3D plot of the total counts distribution in the S-GEM in the open pencil beam configuration and histogram of the total counts distribution in the S-GEM, obtained summing over the whole set of acquisition triggers of the measurement. (Lower panel) the same kind of plots of the the upper panel but for the closed pencil beam configuration, i.e. background measurements.*

Table 1 reports the calculated values of the efficiency S/B ratio for S-GEM and ^{3}He tube. The background counts in the S-GEM are mostly due to environmental neutrons (almost an isotropic components and a directional one due to neutron beam, passing through the mask) as the gamma sensitivity at the chosen operation bias is almost null. The higher background sensitivity of the ^{3}He tube, as compared to the S-GEM, is primarily due to the incomplete shielding of 30 cm long tube to background neutrons. The absolute S-GEM efficiency was calculated as

$$\varepsilon_{\text{S-GEM}} = \frac{(C_{\text{GEM}} - C_{\text{GEM-BCKG}})/CS}{(C_{^3\text{He}} \cdot C_{^3\text{He-BCKG}})/\varepsilon_{^3\text{He}}} \quad (1)$$

In relation (1), C_{GEM} and $C_{\text{GEM-BCKG}}$ are the overall counts and the background counts in the S-GEM, respectively, while $C_{^3\text{He}}$ and $C_{^3\text{He-BCKG}}$ are the same quantities for the ^{3}He tube; $\varepsilon_{^3\text{He}}$ is the ^{3}He tube absolute efficiency (99%) and CS is the cluster size. This last value is a statistical parameter taking into account the possibility for a neutron to fire more than one single pad in the S-GEM detector. Estimation of cluster size has been obtained carrying out measurements with small integration times (< 20 μs) and very low intensity beams. The estimated value at 870 V is CS=1.34 ± 0.02. The evaluated absolute efficiency at 5.1 meV of the S-GEM on the 16-sheets region is 31% ± 1%, while for the single-sheet region it is found to be (2.8 ± 0.5)%.

Table 1: Signal and background counts for S-GEM and ^{3}He tube detectors and measured values of signal-to-background ratio and efficiency, the efficiency of ^{3}He tube being known by measurements performed previously

	S-GEM	**^{3}He Tube**
Overall mean counts [s^{-1}]	1863	6011
Background mean counts [s^{-1}]	21	1586
Signal/Background	87.7	2.8
Efficiency [%]	31	99
Single sheet efficiency [%]	2.8	

3. Conclusions and perspectives

A new configuration of a GEM-based neutron detector named Side-on GEM (S-GEM) was tested and characterized on beam at the TRIGA reactor (ENEA Casaccia), ISIS spallation neutron source (Rutherford Appleton Laboratory, UK) and the HFIR reactor (Oak Ridge National Laboratory, US), respectively. Two different prototypes were tested: a first detector made of a series of glass sheets borated on both sides, the ^{10}B layer being 300 nm, and filled by Ar/CO2 mixture, a second one with 16 alumina sheets borated with 1 μm ^{10}B. The tests at the TRIGA reactor provided a first experimental determination of the detector efficiency and of its dynamic range in the present configuration, over an extended interval of neutron flux. The experimental tests at ISIS showed the effectiveness of the S-GEM in detecting thermal neutrons, producing the main features of the neutron spectrum in a comparable way with respect to the standard neutron beam monitor used on the beam line. The HFIR tests have shown an improved efficiency and improved spatial resolution thanks to an optimized pads layout, also pointing out important issues to be addressed on boron deposition. In perspective, the devices can be made more efficient by a controlled deposition procedure and new tests are envisaged both on the reactors and time of flight neutron sources.

References

[1] Kouzes R. T., Ely J. H., Lintereur A. T., Siciliano E. R. and Woodring M. L., PNNL Report, No. 19050 (2009).
[2] Lintereur A., Conlin K., Ely J., Erikson L., Kouzes, R., Siciliano E., Stromswold D. and Woodring M., Nucl. Instrum. Methods A **652** (2011), 347.
[3] Klein M. and Schmidt C. J., Nucl. Instrum. Methods A **628** (2011) 9.
[4] Tremsin A. S., Feller W. B. and Downing R. G., Nucl. Instrum. Methods A **539** (2005), 278.
[5] Festa G., Pietropaolo A., Grazzi F., Barzagli E.,Scherillo A. and Schooneveld E. M., Nucl. Instrum. Methods A **654** (2011),373.
[6] Barbagallo M., Cosentino L., Greco G., Guardo, ., Montereali R. M., Pappalardo A., Scirè C., Scirè S., Vincenti M. A. and Finocchiaro P., Nucl. Instrum. Methods A **652** (2011), 355.
[7] Festa G., Pietropaolo A., Reali E., Grazzi F. and Schooneveld E. M., Meas. Sci. Technol., 21 (2010) 035901.
[8] Pietropaolo A. et al., in prepration.
[9] Sauli F., Nucl. Instrum. Methods A, 386 (1997) 531.
[10] Murtas F., Buonomo B., Corradi G., Mazzitelli, G., Pistilli M., Poli Lener M., Tagnani D. and Valente P.,Nucl. Instrum.Methods A, 617 (2010) 237.
[11] Murtas F., Croci G., Pietropaolo A., Claps G.,Frost C. D., Perelli Cippo E., Raspino D., Rebai M., Rhodes N. J., Schooneveld E. M., Tardocchi M. and Gorini G., JINST, 7 (2012) P07021.

[12] Bonivento W., Jarron P., Moraes D., Riegel W. and Dos Santos F., Nucl. Instrum. Methods A, 491 (2002) 233.
[13] Guedes G. P., Breskin A., Chechik R., Vartsky D., Bar D., Barbosa A. F. and Marinho P. R. B., Nucl. Instrum. Methods A, 513 (2003) 473.
[14] Pietropaolo A., Murtas F., Claps G., Quintieri L., Raspino D., Celentano G., Vannozzi A. and Frasciello O., Nucl. Instrum. Methods A, 729 (2013) 117.
[15] HFIR website: http://neutrons.ornl.gov/facilities/ HFIR/.
[16] Berry K. D., Bailey K. M., Beal J., Diawara Y., Funk L., Hicks J. S., Jones A. B., Littrell K. C., Pingali S. V., Summers P. R., Urban V. S., Vandergriff D. H., Johnson N. H. and Bradley B. J., Nucl. Instrum. Methods A, 693 (2012) 179
[17] ISIS web site: ⟨www.isis.stfc.ac.uk⟩.
[18] Tietze H., Schmidt W., Geick R., Physica B **156–157** (1989) 550 ⟨http://www.isis.stfc.ac.uk/instruments/rotax⟩.
[19] Kockelmann W., Kirfel A., Physica B 350 (2004) e581.
[20] Filabozzi A., Andreani C., De Pascale M.P.,. Gorini G, Pietropaolo A., Perelli Cippo E., Senesi R., Tardocchi M., Kockelmann W., Journal of Neutron Research **14** (2006), 55.
[21] Pietropaolo A., Andreani C., Rebai M., Giacomelli L., Gorini G., Perelli Cippo E., Tardocchi M., Fazzi A., Verona Rinati G., Verona C., Marinelli M., Milani E., Frost C.D., Schooneveld E.M., Europhys. Lett. **92** (2010), 68003.
[22] Pietropaolo A., Andreani C., Rebai M., Giacomelli L., Gorini G., Perelli Cippo E., Tardocchi M., Fazzi A., Verona Rinati G., Verona C., Marinelli M., Milani E., Frost C.D., Schooneveld E.M.,Europhys. Lett.**94** (2011), 62001.
[23] Bedogni R., Esposito A., Andreani C., Senesi R., De Pascale M.P., Picozza P., Pietropaolo A., Gorini G.,. Frost C.D, Ansell S., Nucl. Instr. Meth. A **612** (2009) 143.
[24] Smirnov A.N., Pietropaolo A., Prokofiev A.V., Rodionova E.E., Frost C.D., Ansell S., Schooneveld E.M., Gorini G., Nucl. Instr. Meth. A **687** (2012), 14.
[25] Pietropaolo A., Tardocchi M., Schooneveld E.M., Senesi R., Nucl. Instr. Meth. A **568** (2006), 826.
[26] Pietropaolo A., Perelli Cippo E., Gorini G., Tardocchi M., Schooneveld E.M., Andreani C., Senesi R., Nucl. Instr. Meth. A **608** (2009), 121.
[27] Claps G., Murtas F., Pietropaolo A., Celentano G., Vannozzi A., Santoni A.,. Quintieri L and Riedel R. A., Europhys. Lett. **105** (2014), 22002.

3.6.5

Development and future prospects of wavelength shifting fibre detectors at ISIS

G. Jeff Sykora[1], Erik M. Schooneveld[1] and Nigel J. Rhodes[1]
[1]Instrumentation Division, STFC, ISIS Facility, Rutherford Appleton Laboratory, Harwell Oxford, United Kingdom

E-mail: Jeff.sykora@stfc.ac.uk

Abstract. Recent advances in WLSF detector technology at ISIS are presented here. Cost reduction strategies, such as a transition from single anode to multi-anode PMTs and optically isolated scintillator elements to continuous scintillator sheets, will be discussed. Advantages and current disadvantages of WLSF detector technology will also be discussed. Thermal neutron detection efficiencies of approximately 65% with corresponding gamma sensitivities on the order of 10^{-7} are shown. Pixel to pixel variation of less than ±6% has been achieved for linear and 2D position sensitive detectors. These properties make WLSF detectors viable for a variety of applications at ISIS.

1. Introduction

Scintillation detectors using ZnS:Ag/^{6}LiF are currently used in a number of facilities such as J-PARC [1], [2], SNS [3] and ISIS. At the ISIS pulsed neutron and muon scattering facility, these scintillation detectors have been employed for more than two decades and service approximately half of the instruments [4]. The current generation of ZnS:Ag/^{6}LiF detectors on ISIS are optically coupled to photomultiplier tubes (PMT) with clear optical fibres [4]. New instruments will, however, require larger area or finer resolution detectors which render clear optical fibres obsolete due to high costs and manufacturing difficulties. J-PARC and SNS have ZnS:Ag/^{6}LiF detectors operational that are using wavelength shifting fibre (WLSF) instead of clear optical fibres and are considerably cheaper to produce with reduced manufacturing complications. ISIS is therefore also developing WLSF based ZnS:Ag/^{6}LiF detectors.

ISIS, along with other facilities, is developing WLSF detector technology to suit a variety of instruments. IMAT is the first ISIS instrument planning on using WLSF detectors on a large scale [5]. Modifications to the IMAT detector design have made WLSF detectors useful for a broad range of neutron scattering applications including current reflectometers and future single crystal diffractometers.

Details of neutron scattering applications at ISIS suitable to WLSF detector technology are described below. Developments in WLSF detector technology for a broad range of applications are discussed in terms of instrument specifications.

2. Detector requirements for new and upgraded instruments

ZnS:Ag/^{6}LiF scintillator detectors on ISIS have generally serviced low rate (<5 kHz local peak rate) powder diffractometers, like ENGIN-X, POLARIS, GEM, HRPD and PEARL. Some of these powder diffractometers will soon be due for upgrades which will include larger area coverage. Reflectometers

like CRISP and SURF on TS1 operate with clear fibre coupled scintillator limiting the position resolution of the detector to 1.2mm and are thus due for upgraded detectors.

New instruments like IMAT, which is currently under construction, and LMX, which is proposed for a future phase of TS2, are good candidates for WLSF detectors because of their unique requirements. Future prospects of WLSF detectors on ISIS also include large inelastic spectrometers. These spectrometers are usually equipped with ^{3}He detectors, but ^{3}He has become rare and expensive [6], [7]. Instruments suited to WLSF detectors and their detector requirements are described below.

2.1 IMAT

IMAT is an imaging and diffraction instrument for materials science utilizing a new technique called tomography driven diffraction [8]. The diffraction detector suite will include the ability for strain and texture analysis. In order for the instrument to operate efficiently, there must be high angular coverage with detector pixilation for texture analysis. Diffraction banks are proposed to cover a total of 18m^2 with detector banks at 2theta positions of 20, 45, 90, 125 and 155 degrees. The secondary flight path of the 90 degree bank will be 2 m [5]. The detector array will require 2 dimensional positioning to facilitate texture analysis. Each detector will consist of pixels 4mm x 100mm with minimal dead space to provide d-spacing resolution $\Delta d/d = 0.7\%$ at 90 degrees. The detector will need to cope with approximately 10 kHz local peak rate.

2.2 Linear reflectometers – CRISP

CRISP was the first neutron reflectometer on ISIS and is designed to study interfacial phenomena with the ability to perform polarized neutron reflectometry [9], [10]. Currently, a clear optical fibre coded ZnS:Ag detector with 260mm linear coverage is used to detect off-specular reflections. Clear optical fibre coupling limits the position resolution of the detector to 1.2mm and is reported to limit the rate capability of the instrument. Future experiments will likely require 0.5mm linear position resolution with a factor of 10 improvement in the current count rate capability of 1.5kHz per detector pixel. Off-specular reflectivity also requires elimination of ghosting artefacts which exist in the current detector.

2.3 2D reflectometers – Surf, Inter, PolRef and OffSpec

The current suite of reflectometers is operated with linear position sensitive detectors (PolRef, OffSpec and Inter) similar to that on CRISP described above. Surf utilizes a small 2D clear fibre coupled ZnS:Ag/^{6}LiF detector [11]. In some cases, users need to have horizontal as well as vertical position sensitivity which requires rotation of the detector by 90 degrees and a second data set. 2D detectors would greatly simplify the process as well as add to the scientific merit of some experiments. The 2D detectors would be required to maintain similar 1.2mm position resolution. As with a linear reflectometer detector, count rate improvements of over a factor of 10 are desired while maintaining a high degree of pixel to pixel uniformity.

2.4 LMX

LMX is a proposed high flux single crystal diffractometer which will be used for large molecular crystallography [12]. Single crystal diffraction requires 2 dimensional detectors. Small proposed secondary flight paths between 0.25m – 0.75m require the detector to have a maximum position resolution of 1mm x 1mm (0.5mm x 0.5mm is preferable) and be insensitive to parallax errors.

2.5 Inelastic spectrometers

Current inelastic neutron spectrometers like LET on TS-2 cover large areas (up to 40m^2) and use resistive wire ^{3}He tubes [13]. Due to very limited supply of ^{3}He, the amount of ^{3}He required for such detectors is now too large to be considered in future inelastic spectrometers. Detector requirements for future inelastic spectrometers would be similar to LET, i.e. a coarse 2 dimensional position resolution

(20mm x 20mm) with neutron detection efficiency better than 80% at 1.8Å, low intrinsic background and insensitivity to gamma (around 10^{-7}).

3. Wavelength shifting fibre detector variations

Wavelength shifting fibre coupled ZnS:Ag/^{6}LiF detectors offer significant advantages in cost savings, ease of assembly and are ideally suited to provide fine position resolution requirements. Development has been focused on maintaining high detection efficiencies and reliability. These detectors are described below.

3.1 Linear Position Sensitive Detectors – Diffractometers and reflectometers

Two styles of linear WLSF detectors have been developed, one has complete optical isolation (called the isolated linear detector) and another is a low-cost solution without optical isolation (called the continuous linear detector). Photographs of the two detector types are shown in Figure 1. The isolated linear detector was developed as a solution to general powder diffractometers with the guarantee of complete optical isolation in the scintillator-fibre head. Constraining the light to a single detector pixel prevents misplacement of neutron events (known as ghosts) and multi-counts due to light spread across the detector.

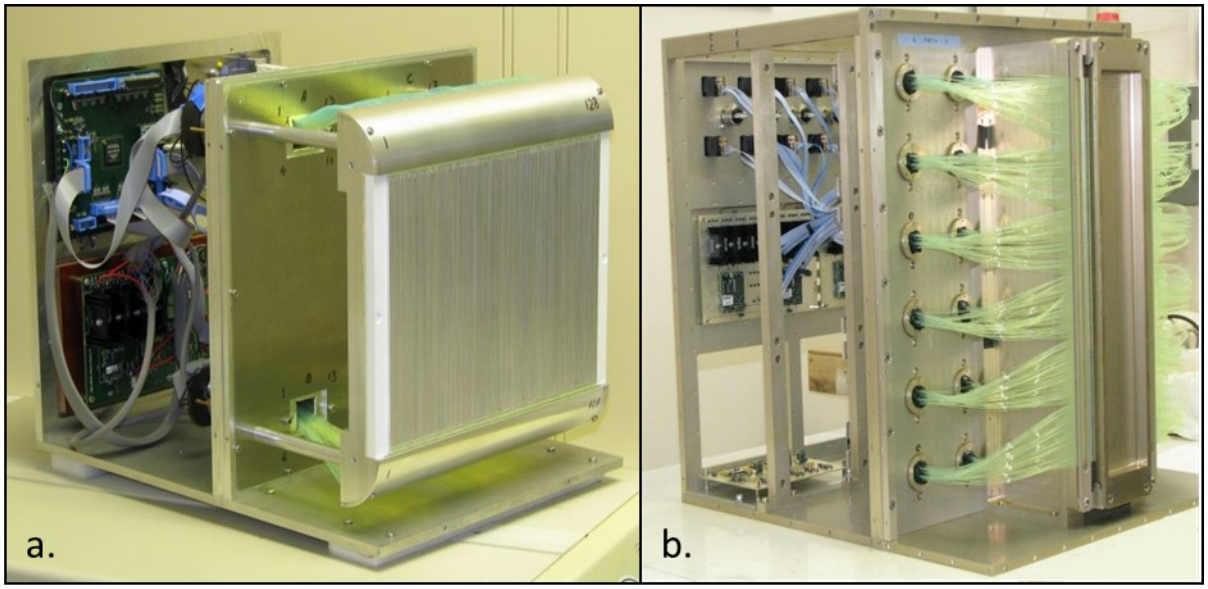

Figure 1. Photographs of the isolated linear detector (a.) and the continuous linear detector (b.).

The isolated linear detector was constructed with 2 mm wide and 200 mm long pixels. Each pixel consisted of two 1mm diameter wavelength shifting fibres sandwiched between two 0.46 mm thick ZnS:Ag/^{6}LiF scintillator (AST [14] 2:1 scintillator) strips and wrapped in thin aluminium foil. Two scintillator strips were used to increase neutron absorption efficiency compared to a single sheet. A dual coincidence fibre code was used to eliminate PMT noise events and decrease the number of PMTs used to read out the detector. The fibres were coded such that four scintillator elements were viewed by a single pixel of a Hamamatsu H8711 16 channel multi-anode PMT (MA-PMT). A Photograph of the detector is shown in figure 1a. Figure 2 shows the neutron detection efficiency of the isolated linear detector as a function of wavelength compared to that of a 6 bar ^{3}He detector measured at Reactor Institute Delft (RID). The isolated linear detector was 65% efficient at 1.8Å, has 2mm position resolution, 16 kHz maximum local count rate capability and $3x10^{-7}$ gamma sensitivity. A detailed study of the isolated linear detector at RID can be found elsewhere [15].

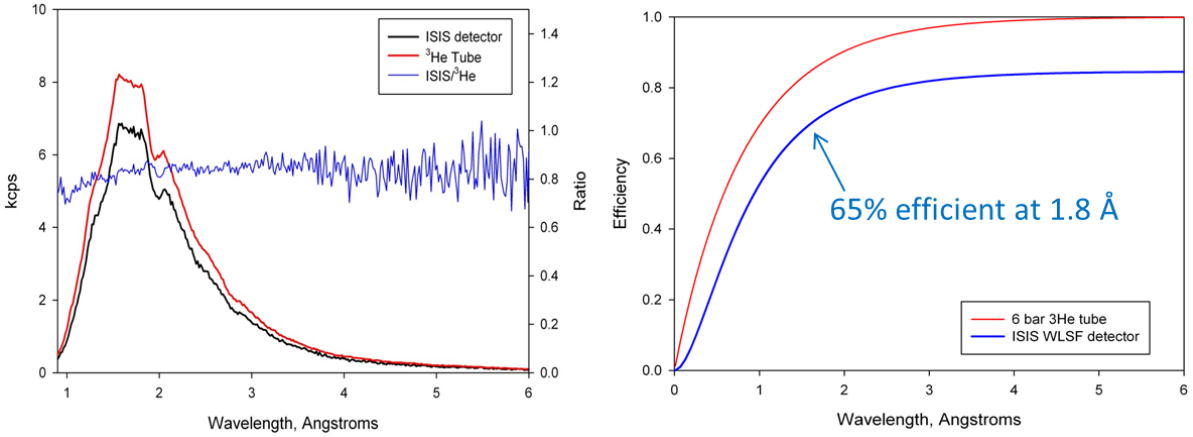

Figure 2. (Left) Time-of-flight neutron spectra as detected by a 6 bar, 25.4mm ^{3}He tube (red line) and isolated linear detector (black line) and the ratio between the two (blue line). (Right) Calculated efficiency as a function of wavelength for the ^{3}He tube and the isolated linear detector.

An isolated detector is relatively difficult to assemble due to cutting the scintillator and wrapping individual scintillator elements. It is also practically impossible to build a detector with less than 2mm position resolution with the optically isolated pixel concept. Constructing a detector with single, continuous, sheets of ZnS:Ag/^{6}LiF solves these issues.

The continuous linear detector (pictured in figure 1b) was constructed to suit the CRISP reflectometer needs. The detector consisted of parallel rows of 768 fibres that were 0.5mm in diameter. The fibres were sandwiched between two single sheets of 406mm x 66mm x 0.46mm AST 2:1 scintillator which were placed so their inside surfaces were in contact with the fibres. Fibres were coded into 24, 16-channel, MA-PMTs. Every other pixel of the PMT was used (called the active PMT pixel) to eliminate cross-talk between PMT channels. Each active PMT pixel was coupled to one end of 8 fibres. A dual coincidence fibre code was optimized to minimize the possibility of ghosting and optimize global count rate capability.

Ghosting occurs as a result of scintillation light from one neutron overlapping in time with afterglow of another neutron interacting in a different location in the detector. Despite limiting ghosting with the chosen fibre code, light spread in the scintillator-fibre head increases the chances of ghosting. A signal processing algorithm was developed to eliminate ghosting artefacts. The algorithm resulted in at least a factor of 10 reduction in ghosts with only a 15% decrease in neutron detection efficiency (from 65% to 56% at 1.8Å). Details of the ghost reduction algorithm are beyond the scope of this paper. Position resolution was determined to be 0.7mm which considerably better than the 1.2mm position resolution of the detectors used on CRISP. It is believed that light spread coupled with a simple position determination algorithm broadens the peaks beyond the fibre pitch.

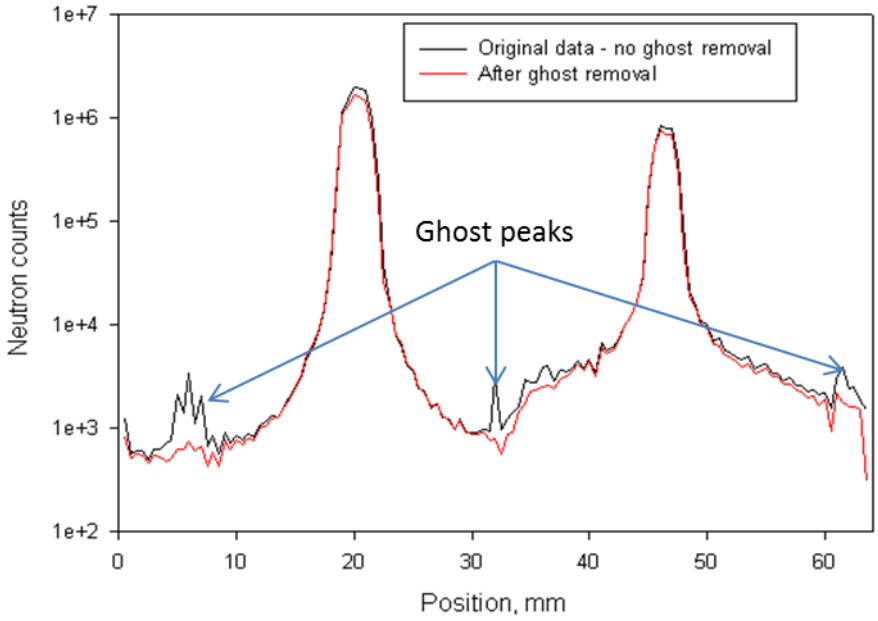

Figure 3. Position spectrum of the continuous linear detector measured on the CRISP beamline with a super mirror sample depicting results of the ghost removal processing algorithm.

3.2 IMAT detector options

IMAT requires 4mm resolution in 2 theta and coarse 100mm resolution in the azimuthal direction. Rectangular pixel sizes needed for IMAT led to three possible geometries as shown in Figure 4. In the first geometry, WLS fibres were divided by reflective slats defining the pixel dimensions to be 4mm x 100mm. Reflective slats were used to prevent excessive light spread. Two continuous sheets of 0.46mm thick AST 2:1 scintillator were fixed in contact with the slats. A small amount of scintillation light is still able to spread into the adjacent pixel because of light scattering in the scintillator (called scintillator cross-talk). This effect was minor and was eliminated by a cross-talk reduction algorithm in the electronics. In this solution, the fibres were sharply bent at 2.5mm radius to allow stacking in the (coarse) azimuthal direction with minimum dead space. Two fibres were spaced evenly in each detector pixel to decrease the number of fibres and therefore decrease the amount of labour needed to produce the detector. Spacing of the fibres resulted in less light collection but maintained overall neutron detection efficiency at the operating discriminator level (200mV). The black curve in figure 5 shows the normalized count-rate of this solution as a function of discrimination level.

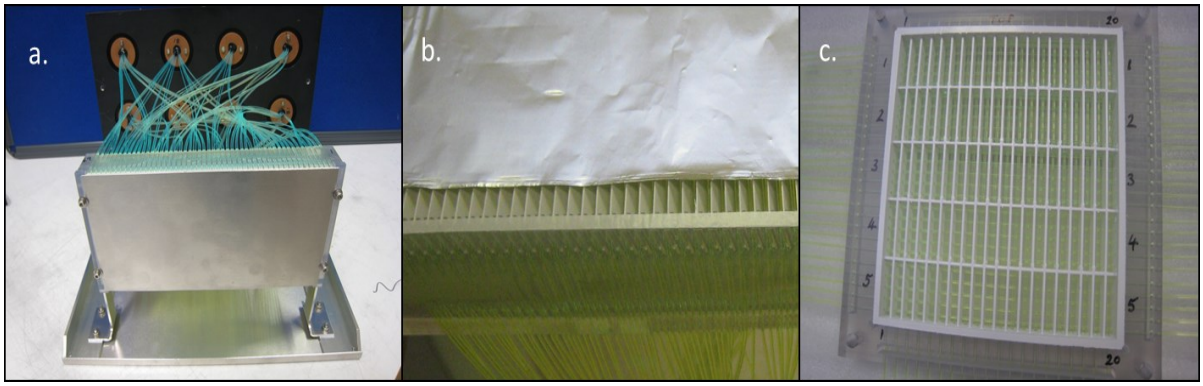

Figure 4. Photographs of the IMAT detector options. (a.) Is a continuous flat scintillator sheet with 2.5mm bend radius fibres, (b.) is a zoomed in photo of the venetian scintillators and (c.) is the fibre support grid for the crossed-fibre detector.

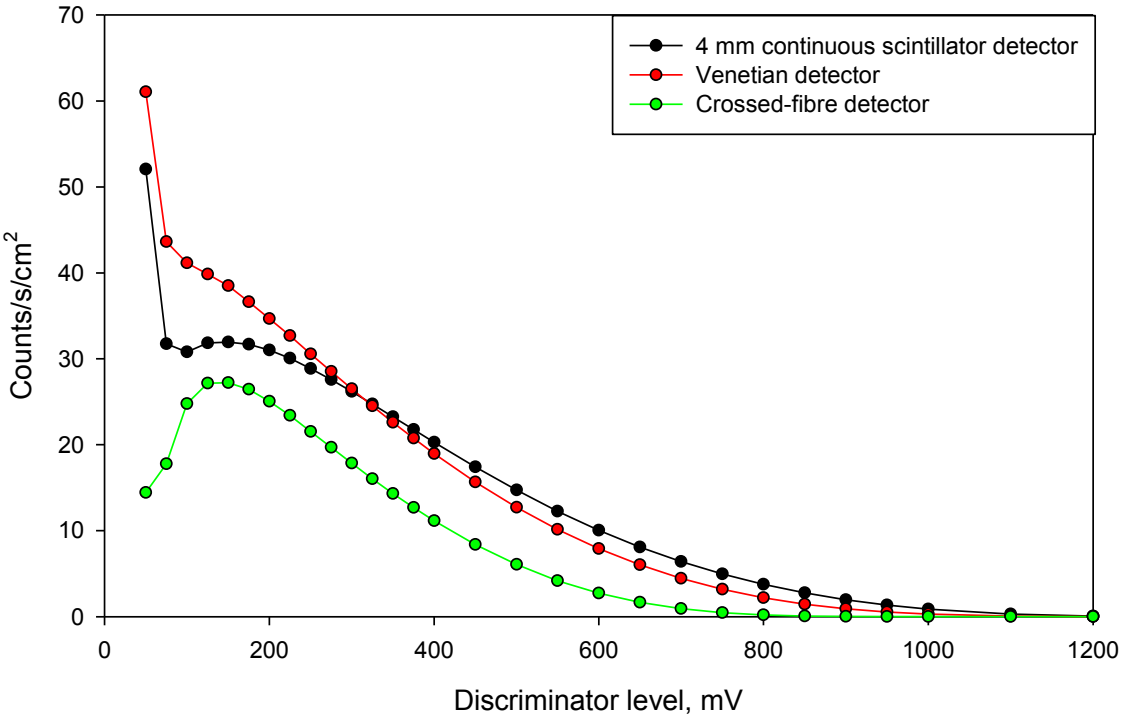

Figure 5. Plot of the area and time normalized counts as a function of discriminator level for the three IMAT detector options, measured with a ^{241}AmBe source. This plot shows the relative efficiencies and light collection of each detector.

The second solution (pictured in Figure 4b) again used a linear array of sharply bent fibres but has scintillators that are individually cut and angled at 72 degrees relative to the neutron's angle of incidence (called a Venetian geometry). The Venetian geometry was chosen to increase the neutron absorption efficiency by virtue of longer path lengths of the neutron through the scintillator. Each scintillator had a reflector attached to the back of it and the entire active area was covered in Aluminium foil to prevent light spread into adjacent detector pixels. The overall pixel size was 4mm x 100mm. The fibres were coded into 38mm single anode PMTs. As in the continuous scintillator detector, the linear detectors are stacked to provide azimuthal position sensitivity.

Figure 6 is a plot of the efficiency as a function of wavelength for the Venetian geometry relative to the flat geometry detector. There is a 15% increase in efficiency at 1.8Å which is attributed to the increased path length in the scintillator. There is as much as a 40% increase in efficiency at long wavelengths which is a result of the ability of light to escape the scintillator and efficiently collected by the fibres. Long wavelength neutrons are absorbed at the surface of the scintillator resulting in scintillation occurring at the surface. In the flat geometry, scintillation light is scattered through the bulk of the opaque scintillator. These events have the least amount of light collected and are the most difficult to detect. In the Venetian geometry, low energy neutrons are absorbed at the surface nearest the fibres making those events the brightest and thus easiest to detect.

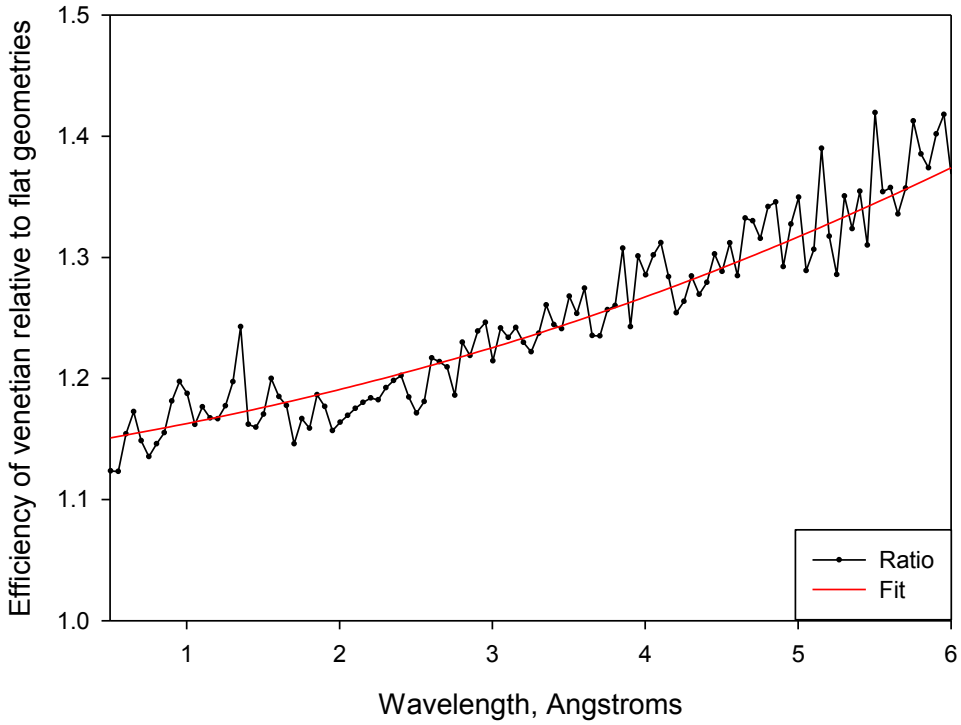

Figure 6. Relative efficiency of the Venetian geometry compared to the continuous flat scintillator detector option for IMAT.

The third solution is a 2-dimensional crossed fibre detector pictured in Figure 4c. The 2theta plane is coded into 4mm pixels and the azimuthal direction is coarsely coded into 20mm pixels making a single pixel 4mm x 20mm. The crossed-fibre support was constructed such that each detector pixel was optically isolated by a thin wall coated with reflective paint. Two continuous sheets of 0.46mm thick AST 2:1 scintillator were placed on the top and bottom of the fibre support. Fibres were coded into 16-channel MA-PMTs. Different pixel sizes can be obtained by either different fibre coding or re-binning the data to make larger pixels. 4-fold fibre coding coincidence was used in order to reduce the number of PMTs needed.

As seen in Figure 5, the crossed-fibre approach suffers from reduced efficiency due to 4 fold coincidence. Efficiency is reduced by approximately 30%. This reduction in efficiency is likely a convolution of effects from the 4-fold coincidence and optical cross-talk in the MA-PMTs. When the PMTs in each plane of fibres were summed to simulate 2-fold coincidence, the efficiency is the same as isolated linear detector (or approximately 65% at 1.8Å). This demonstrates that neutrons are being absorbed, but not detected with 4-fold coincidence.

3.3 2D fine resolution – reflectometers and LMX

A unique 3-layer crossed-fibre detector (pictured in figure 7) was developed as a solution to suit the needs of single crystal diffractometers and reflectometers. 1mm diameter WLS fibres were placed on a 1mm pitch. Top and bottom layers contained 60ppm of dye allowing partial transmission of light to the middle layer. The middle layer was highly absorbing, with a dye content of 300ppm. Top and bottom layers were read out separately and provide horizontal position information while the middle layer provides vertical position information. 3 fibre layers allowed for scintillators to be placed on both the top and bottom of the fibre support system while helping to reduce light spread in the scintillator-fibre cavity.

Fibre ends were coded in 4-fold coincidence into six 16 channel MA-PMTs. 4-fold coincidence coding allowed for 16384 pixels (128x128 pixels) to be readout by 96 PMT channels with 8 fibre ends coupled to each PMT pixel. In the first instance, only one quadrant of the detector could be read out due to limitations on the number of available electronics channels. No fundamental problems prevent readout of the entire detector.

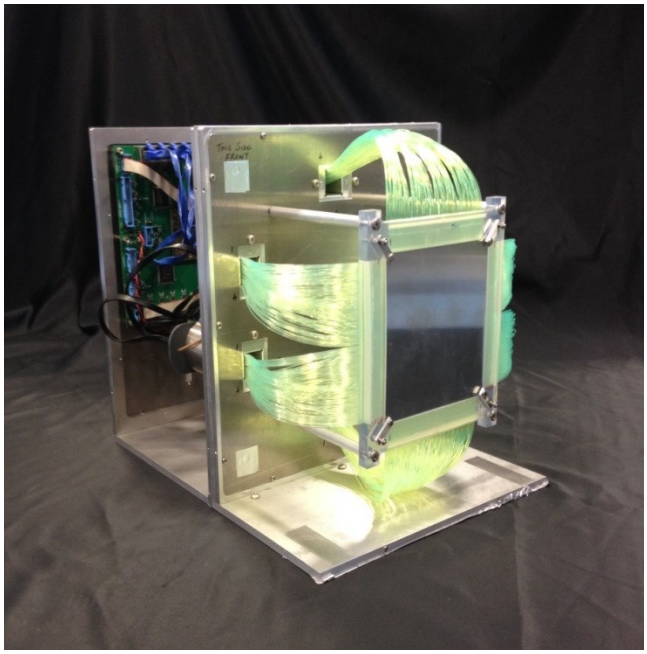

Figure 7. Photograph of the 2D fine resolution detector concept.

4-fold coincidence coding reduced the efficiency of the detector from the nominal 65% at 1.8Å to approximately 40%, as in the IMAT crossed-fibre detector. Light spread from the scintillator to the second layer of fibres also complicates positioning algorithms causing events to be rejected. Signal processing and position reconstruction algorithms are currently under development to improve event recognition and increase efficiency.

An image of the position reconstruction of a Cd mask as well as the position resolution are shown in Figure 8. Full-width at half maximum gives the position resolution to be 1.2mm. Light spread in the scintillator likely causes a small ambiguity in positioning causing slight broadening beyond the 1mm fibre pitch. 1.2 mm spatial resolution is sufficient for an instrument like LMX. Resolution could be further improved by using smaller diameter fibres and more sophisticated positioning algorithms.

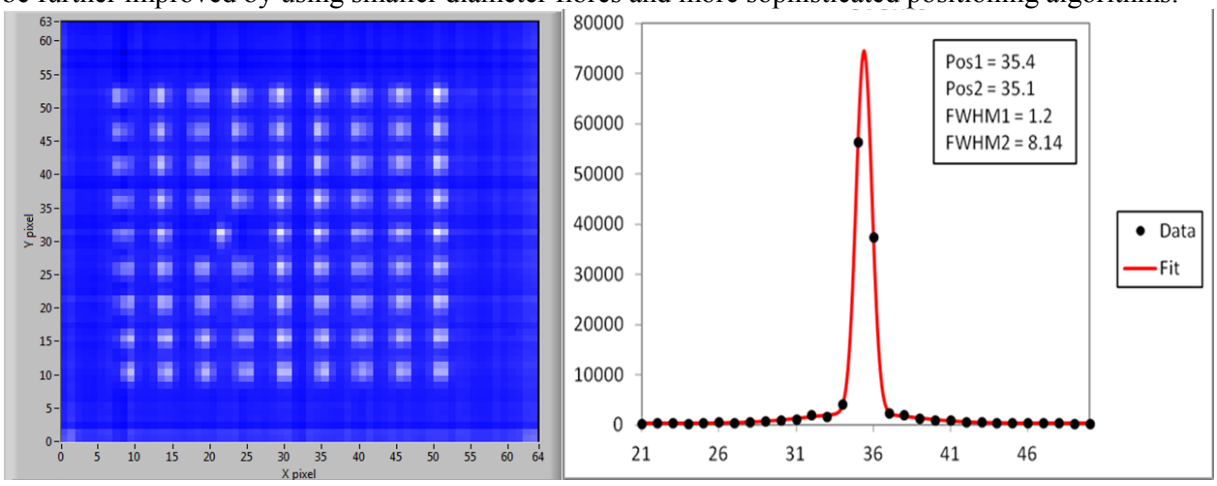

Figure 8. (Left) 2D position reconstruction of a Cd mask on top of the detector and (right) Gaussian fit of the counts in the middle layer of the detector behind a mask of 0.7mm diameter showing position resolution of 1.2mm.

3.4 2D coarse resolution – inelastic spectrometers

A coarse 2D detector, shown in Figure 9, was built with pixel sizes similar to that of resistive wire ^{3}He tubes. An optically isolating, plastic fibre support grid was printed with 20mm x 20mm pixels arranged in an 8x8 array (160mm x 160mm overall active area). The fibre grid had guide holes on a

5mm pitch. The WLS fibres were placed in the grid in orthogonal planes to provide 2D position information. Two continuous sheets of 0.46mm thick 2:1 AST ZnS:Ag/^{6}LiF scintillators on aluminium backing plates were placed directly on the grid facing the fibres. Fibres in each row and column of detector pixels were coupled to separate pixels on a MA-PMT providing a 2 fold coincidence for every detector pixel. 64 pixels were read out by a single 16 channel MA-PMT.

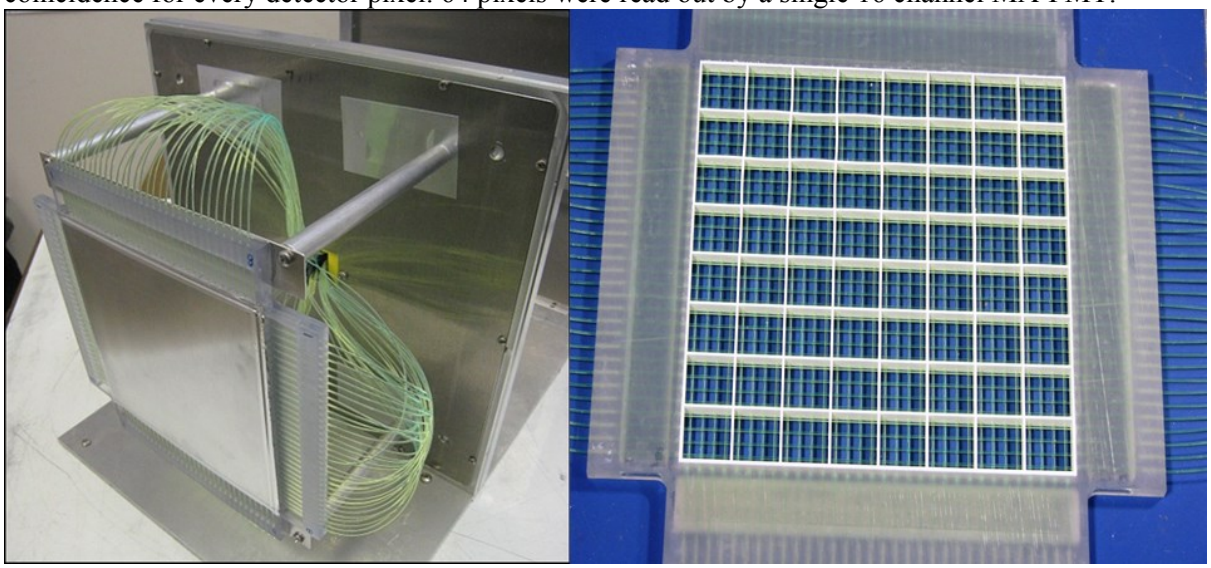

Figure 9. Photographs of the 2D coarse resolution concept and fibre support grid.

Neutron detection efficiency of the 2-fold coarse resolution 2D detector was 65% at 1.8Å, the same as the theoretically expected detection efficiency, despite having a large fibre pitch. Figure 10 shows the efficiency and light collection of the coarse 2D detector relative to the isolated linear detector. Light collection is lower than the isolated linear detector due to the large fibre pitch. Reduced counts for the detector with a standard position reconstruction algorithm (black curve) at low discriminator values are a result of light cross-talk, mainly on the MA-PMT. The red curve in figure 10 demonstrates that light cross-talk is eliminated by a cross-talk reduction algorithm in signal processing.

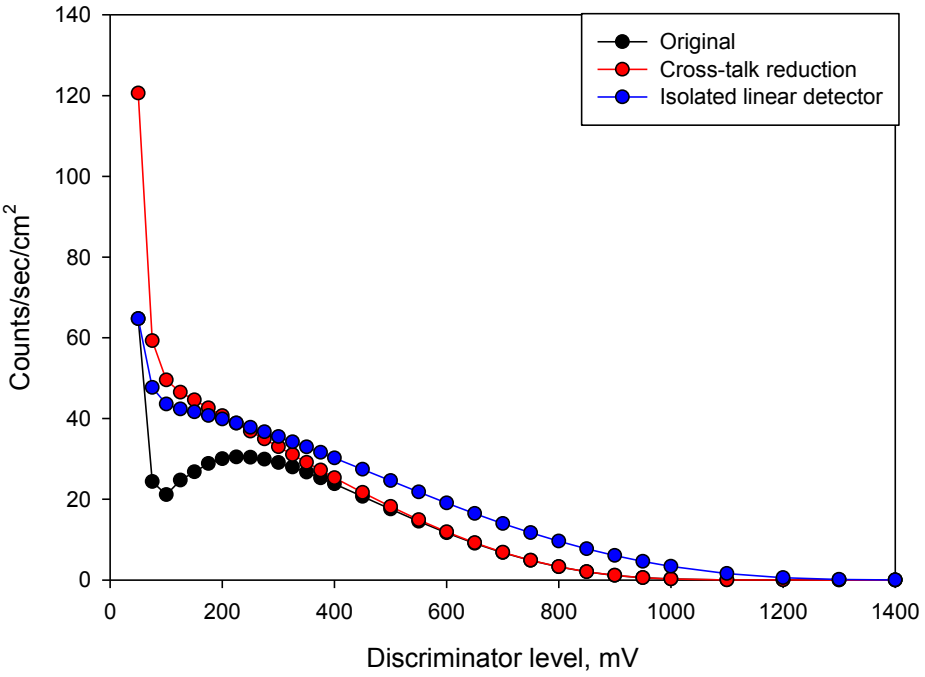

Figure 10. Plot of the area and time normalised counts as a function of discriminator level for the coarse 2D detector showing light collection and efficiency compared to the isolated linear detector measured with a ^{241}AmBe source.

One problem with the current coarse 2D detector is the inherent sensitivity to background radiation. Currently, ^{3}He detectors have background count rates of approximately 0.1 counts per hour per cm^{2}, whereas the (2-fold coincidence) scintillator detector is approximately a factor of 30 worse than that. In general, 4-fold coincidence detectors have a lower background rate than 2-fold coincidence detectors. The sensitivity to background radiation of the coarse 2D detector therefore might be improved by using a 4-fold coincidence read out, provided that acceptable detection efficiency can be achieved.

4. Conclusions

Current WLSF detectors have shown exceptional performance in terms of efficiency, position resolution and gamma sensitivity. There are now WLSF detector options for general powder diffraction, the IMAT 90 degree bank, 1D and 2D reflectometry, single crystal diffraction and inelastic spectroscopy. There are still challenges to overcome in order to take full advantage of some instruments. Reflectometers could be more effective if the rate capability of the detectors was increased. The background of WLSF detectors needs to be reduced for inelastic spectroscopy. Research and development is ongoing to address these issues. Despite these challenges, wavelength shifting fibre detector technology is versatile and ideally suited to many applications.

5. Acknowledgements

The authors would like to thank the ISIS neutron detector group for their support, particularly Brian Holland for his invaluable contribution to detector assembly. A portion of the ^{3}He replacement detector work was funded by the NMI3-II Grant Agreement no. 283883.

Appendix A. Evaluation procedures

All detectors undergo the same initial evaluation procedure to ascertain relative thermal neutron detection efficiency, pixel to pixel uniformity and light collection capability. After initial evaluation has been performed, detector requirement specific tests are performed on a beam line at ISIS. Beam line tests are performed to verify position resolution, rate capability, ghosting, wavelength dependent neutron detection efficiency and uniformity.

Initial evaluations are performed by irradiating the detector with neutrons from a water moderated ^{241}AmBe source. Moderated ^{241}AmBe is a broad spectrum neutron source with median energy at 25meV and a significant, but undetermined, contribution of fast neutrons. Every detector was placed approximately 30cm from the face of the moderator such that the main flux was perpendicular to the face of the detector. It has been established that at this position, using a 200mV discrimination level, a count-rate of 40 counts/sec/cm^{2} for a detector with two continuous sheets of 0.46mm thick 2:1 AST ZnS:Ag/^{6}LiF scintillators corresponds to a detection efficiency of 65% for 1.8Å neutrons.

The ALF and CRISP instruments on ISIS were used to evaluate wavelength dependent efficiency, position resolution, rate capability and ghosting. EMMA is a new instrument on ISIS and was used to investigate positioning accuracy of the detector. ALF is a general purpose TOF instrument used for crystal alignment and detector testing. ALF views the 95K methane moderator and has a wavelength range of 0.6Å – 5.2 Å. Detectors can be placed either in the beam or in scattering. The CRISP TOF reflectometer [9], [10] was operated in un-polarized mode with a wavelength range of 0.5Å to 12Å with the T-Zero chopper running at 25 Hz. Beam slits on CRISP allowed for easy control of the beam size and flux on the detector. EMMA is the new equipment, materials and mechanics analyzer built in place of the previously decommissioned HET chopper spectrometer. EMMA has a dedicated detector testing blockhouse with the option of operating as a chopper spectrometer. EMMA views the room temperature water moderator providing wavelength range from 0.2Å to 3Å.

All detectors were purpose built to address different needs and as such were subject to different test conditions. Specific test conditions were not described in detail because more details will be elaborated on in future publications.

References

[1] Y. Ikeda 2009, "J-PARC status update," *Nucl. Instr. Meth. Phys. Res. A,* **600**, 1-4

[2] T. Nakamura, T. Kawasaki, T. Hosoya, K. Toh, K. Oikawa, K. Sakasai, M. Ebine, A. Birumachi, K. Soyama and M. Katagiri 2012, "A large-area two-dimensional scintillator detector with a wavelength-shifting fibre readout for a time-of-flight single-crystal neutron diffractometer," *Nucl. Instr. Meth. Phys. Res. A,* **686**, 64-70

[3] M. L. Crow, J. P. Hodges and R. F. Cooper 2004, "Shifting scintillator prototype large pixel wavelength-shifting fiber detector for the POWGEN3 poweder diffractometer," *Nucl. Instr. Meth. Phys. Res. A,,* **529**, 287-292

[4] N. J. Rhodes, E. M. Schooneveld and R. S. Eccleston 2004, "Current status and future directions of position sensitive neutron detectors at ISIS," *Nucl. Instr. Meth. Phys. Res. A,* **529**, 243-248

[5] W. Kockelmann, S. Zhang, J. Kelleher, J. Nightingale, G. Burca and J. James 2013, "IMAT – a new imaging and diffraction instrument at ISIS," *Physics Pocedia,* **43**, 100-110

[6] D. A. Shea and D. Morgan 2010, "The Helium-3 Shortage: Supply, Demand and Options for Congress," CRS Report for Congress

[7] R. T. Kouzes, A. T. Lintereur and E. R. Siciliano 2014, "Progress in alternative neutron detection to address the helium-3 shortage," *Nucl. Instr. Meth. Phys. Res. A,* **784**, 172-175

[8] G. Burca, J. James, W. Kockelmann, M. Fitzpatrick, S. Zhang, J. Hovind and R. van Langh 2011 "A new bridge technique for neutron tomography and diffraction measurements," *Nucl. Instr. Meth. Phys. Res. A,***651**, 229-235

[9] J. Penfold, R. C. Ward and W. G. Williams 1987, *Journal of Physics E: Sci. Inst.* 20, 1411 .

[10] R. Felici, J. Penfold, R. C. Ward and W. Williams 1988, *Applied Physics A: Solids and Surfactants,* **45**, 169

[11] D. G. Bucknall, J. . Penfold, J. R. P. Wbster, A. Zarbakhsh, R. M. Richardson, A. Rennie, J. S. Higgins, R. A. L. Jones, R. K. Tomas, S. Roser and E. Dickinson 1995, "SURF - a second generation neutron reflectometer," in *Proceedings of the meetings ICANS-XIII and ESS-PM4*, Villigen

[12] D. Keen 2007, "LMX - A diffractometer for large molecular crystallogrophy draft proposal,"

[13] R. I. Bewley, J. W. Taylor and S. M. Bennington 2011, "LET, a cold neutron multi-disk chopper spectrometer at ISIS," *Nucl. Instr. Meth. Phys. Res. A,* **637**, 128-134

[14] Applied Scintillation Technologies Ltd, [Online]. Available: http://www.appscintech.com/.

[15] G. J. Sykora, E. M. Schooneveld, N. J. Rhodes and L. Van Eijck 2012, "Gamma Sensitivity of a ZnS:Ag(6-LiF) Wavelength Shifting Fibre Detector in Mixed Neutron-gamma Fields," in *IEEE Nuclear Science Symposium and Medical Imaging*,.

3.6.6

Development of a New Exclusive Function with a Center-of-Gravity Calculation for the 2012 Model ^{6}Li Time Analyzer Neutron Detector System

Setsuo Satoh[1]
High Energy Accelerator Research Organization (KEK), Oho 1-1, Tsukuba, Ibaraki 305-0801, Japan.

E-mail: setsuo.satoh@kek.jp

Abstract. A 2012 model ^{6}Li time analyzer neutron detector (LiTA12) system has been developed as a high-count-rate neutron detector. An exclusive function with a center-of-gravity calculation, which not only prevents over-counting due to cross-talk, but also obtains fine position resolution, has been included in this version. This device can detect neutrons with a 3 mm position resolution in a detection area of 49 × 49 mm^2, and is arranged as a 16 × 16 matrix with a detection efficiency of approximately 40% of that of a ^{3}He detector. A maximum count rate of 50 million counts per second (Mcps) was obtained. In addition, the center-of-gravity pixel size obtained is 0.4 mm, although the actual pixel size is 3 mm.

1. Introduction

Neutron scattering experiments are indispensable for the structural analysis of various condensed matter and in the development of advanced materials. Therefore, large-scale experimental facilities where these experiments can be performed are being constructed globally. However, the efficiency of existing neutron detectors is sub-optimal owing to the difficulties involved in direct neutron detection. A ^{3}He gas detector, which is the most frequently used apparatus, is also the best neutron detector available; however, it has a low count rate and low position resolution. A neutron scintillator detector is one of the solutions for overcoming these drawbacks.

A data acquisition (DAQ) group at the Neutron Science Laboratory (KENS) in the High-Energy Accelerator Research Organization (KEK) has developed various other types of detector systems. This group was established to develop DAQ electronics and software for experimental spectrometers used at the Materials and Life Science Experimental Facility (MLF) in the Japan Proton Accelerator Research Complex (J-PARC). For instance, this group developed the neutron encode-module with network (NEUNET) system [1] for ^{3}He gas detectors, which is the de-facto standard in J-PARC/MLF. This system is used in more than half of the experimental spectrometers at this facility and can control thousands of ^{3}He gas detectors.

The same group also developed a ^{6}Li time analyzer (LiTA) system [2] as a high-count-rate and high-efficiency detector, which is still used in a small number of experimental spectrometers. However, the LiTA system is large and unstable. Therefore, a 2012 model LiTA (LiTA12) system [3, 4] has been developed. This report outlines the improvements to this system, and presents a newly added exclusive

[1] To whom any correspondence should be addressed.

function with a center-of-gravity calculation that not only prevents cross-talk between pixels, but also obtains fine position resolution. Although the real pixel size is 3 mm, the obtained center-of-gravity pixel size is 0.4 mm.

2. LiTA12 system

2.1. Basic design specifications

The LiTA12 system has a high-count-rate function and an exclusive function. The high-count-rate function is usually used in high-intensity neutron environments in the histogram mode. The exclusive function prevents multi-counting of cross-talk, allowing use as a no-cut scintillator, and generates event data to calculate the center-of-gravity.

The LiTA12 system consists of a LiTA detector, an amplifier, and four LiTA12 Versa Module Europa (VME) modules. Figure 1 shows the main components of the LiTA12 system with a no-cut scintillator detector for the exclusive function. The LiTA detector uses the multi-anode-type photo-multiplier tube (MA-PMT, Hamamatsu Photonics K.K.: H9500 series), which has a 49 × 49 mm^2 detection area, arranged as a 16 × 16 matrix of a two-dimensional (2D) detector with a 3.04-mm pitch. For the high-count-rate function, 256 pixelated ^{6}Li glass scintillators, 2.1 × 2.1 × 1 mm^3 in size, corresponding to each anode, are used. With respect to the exclusive function, a no-cut scintillator of dimensions 50 × 50 mm^2 is used, which is installed on the MA-PMT, as shown in Figure 1. The amplifier consists of eight 32-channel boards, and it amplifies the signals of the 256-pixel data.

The LiTA12-VME has four LiTA12-ADC boards with 16 analog-to-digital converters (ADCs), and each module can convert 64 pixels to digital data. Therefore, 256 pixel data is converted by four LiTA12-VME modules.

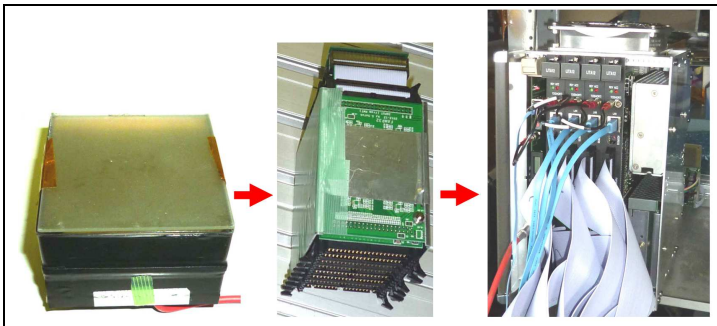

Figure 1. Block diagram of the LiTA12 system with a no-cut scintillator detector for the exclusive function.

2.2. High-count-rate function

The high-count-rate function is used in high-intensity neutron environments. It is easy to acquire a high count rate with simple composition for every pixel, provided that there is no cross-talk between pixels. Figure 2 shows a block diagram of the high-count-rate function process.

Each ADC board controls large high-speed storage in the histogram mode, and is capable of accumulating complete histogram data for every pixel. In order to access the large storage at high speed, the board has two static RAMs that can be accessed independently. Because first-in, first-out (FIFO) memories are equipped with several data flow joints, the data are accumulated without loss.

The histogram mode creates two types of histograms: a time-analyzing histogram, and a pulse-height-analyzing histogram. The time-analyzing histogram has 16,384 channels for each pixel in the memory IC, and the time resolution of the histogram can be set from 40 ns to 1.3 ms with a step of 20 ns. The pulse-height-analyzing histogram has 512 channels for each pixel in the internal memory of the field-

programmable gate array (FPGA) on the board. The VME module controls the Gbit-SiTCP in order to read data from the ADC boards and write it to an external PC at any time [5].
In this function, neutrons with 3 mm position resolution can be detected in a detection area of 49 × 49 mm^2, and it is arranged as a 16 × 16 matrix with an efficiency of approximately 40% of that of a ^3He detector; a maximum count rate of up to 50 million counts per second (Mcps) was obtained.

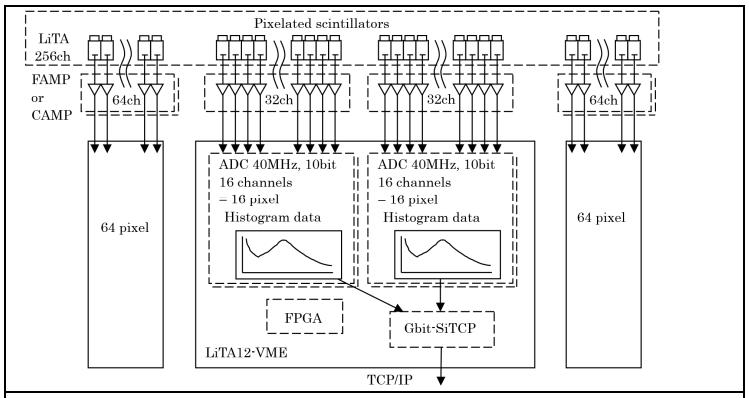

Figure 2. Block diagram of the high-count-rate function.

2.3. Exclusive functions
The exclusive function with the center-of-gravity calculation has been integrated by changing the FPGA program without changing the hardware. Because it is difficult to perform the center-of-gravity calculation in the FPGA, it is calculated by the control-PC in event mode.
All neutrons are obtained by comparing a cluster of adjacent pixels. For each comparison period, the signal strength of all pixels is compared to that of the adjacent pixels. When the signal strength of all pixel is greater than those of all adjacent pixels, the cluster is regarded as the neutron data, and the data from the largest pixel and the eight adjacent pixels are sent to the PC as event data. Figure 3 illustrates a principle of the exclusive function.
In order to compare every pixel to the adjacent pixels, the pixel data must be allocated to the actual 2D pixel arrangement of the MA-PMT. Because the detector requires four VME modules, they must be connected to each other by extended cables. Therefore, the VME module collects pixel data from the four ADC boards and the two neighboring VME modules contain pixels adjacent to the edge pixels of this module.

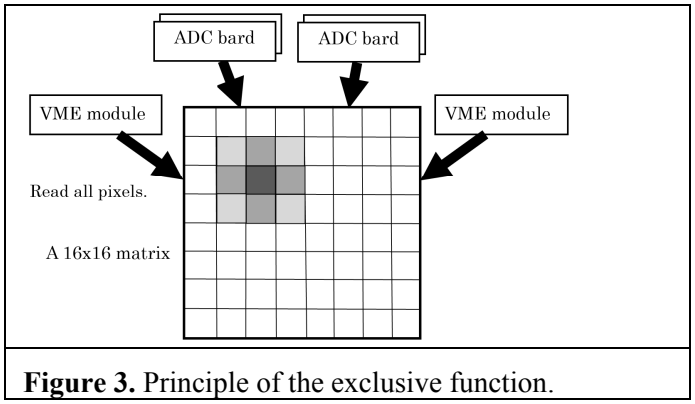

Figure 3. Principle of the exclusive function.

2.4. Event mode
The high-count-rate and exclusive functions generate event data in the event mode without a change of hardware. The event data, which are basically 64 bits, allow off-line analyses. The high-count-rate

function and the exclusive function without the center-of-gravity calculation consist of a header (8 bits), a time-of-flight (TOF) (24 bits), a pixel number (14 bits), a pulse height (10 bits), and reserved bits (8 bits). The exclusive function with the center-of-gravity calculation consists of two headers (16 bits), a TOF (24 bits), a pixel number (6 bits), nine pulse height data (81 bits), and a reserved bit (1 bit), which is sent as two event data.

3. Experimental data

3.1. Exclusive functions with the center-of-gravity calculation

The exclusive function with the center-of-gravity calculation was tested at BL16 at MLF in J-PARC. Figure 4 shows the data of the function. Figure 4(a) is a "KENS" character of Cd on the front of the ^{6}Li glass scintillator detector with dimensions of 50 × 50 ×1.0 mm^{3}; (b) is a 2D graph as a 16 × 16 pixel (real data size, 3 mm), and it is difficult to read the characters; (c) is a 2D graph as a 128 × 128 pixel with the center-of-gravity calculation (eight times position-resolution, 0.4 mm), and the characters are easy to read, but there is a significant amount of noise; (d) is a 2D graph as a 128 × 128 pixel with the center-of-gravity calculation that is compensated by the data without the Cd character, and the characters are visible with high accuracy. Shadows of two tapes that include hydrogen are seen. In addition, because a maximum count rate of up to approximately 3 Mcps was obtained, the count rate achieved by the exclusive function with the center-of-gravity is suitably high.

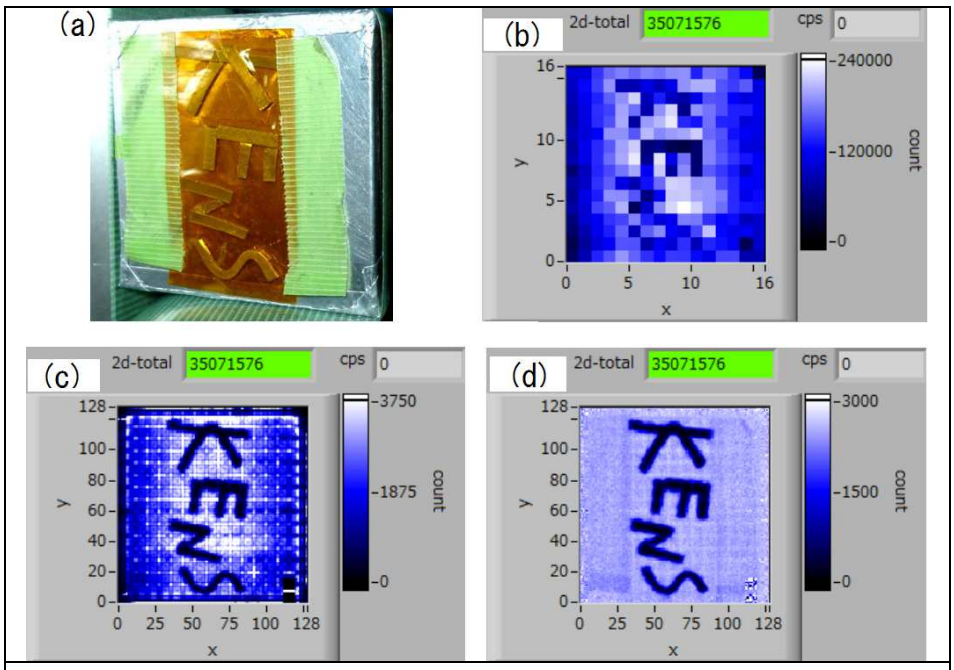

Figure 4. (a) Cd "KENS" character, (b) 2D graphs as a 16 × 16 pixel, (c) those as a 128 × 128 pixel, (d) those as a 128 × 128 pixel compensated by the data without the Cd character.

4. Conclusion

In this study, a new exclusive function was developed with a center-of-gravity calculation for the LiTA12 system, which obtains fine position resolution compared to the actual position resolution. Although the real pixel size is 3 mm, the obtained center-of-gravity pixel size is 0.4 mm. This new function is useful for high position-resolution experiments involving a high-intensity neutron source, such as those performed at J-PARC.

5. Acknowledgments
I would like to thank Dr. N. Yamada, who permitted the use of the BL16 beam-line at MLF in J-PARC. It helped prove for the first time that the exclusive function with the center-of-gravity calculation works well for a neutron beam.
The LiTA12 system was funded by the Neutron Scattering Program Advisory Committee of IMSS, KEK (Proposal No.2009S11).

6. References
[1] Satoh S, et al. 2009 Development of a readout system employing high-speed network for J-PARC in *Nucl. Instrum. Methods Phys. Res. A* **103** 600. http://www.sciencedirect.com/science/article/pii/S0168900208016720.
[2] Satoh S 2003-2006 Development of Readout System for Neutron Scintillator Detectors in KENS REPORT XV, p. 369.
[3] Satoh S 2013 Development of a 2012 model for the ^{6}Li time analyzer detector system, to be published in *Physics Procedia, 4th International Meeting of Union for Compact Accelerator-driven Neutron Sources (UCANS-IV),* September 2013, Hokkaido University.
[4] S. Satoh 2014 Development of a New Exclusive Function for a 2012 model for the ^{6}Li time analyzer detector system, to be published in *JPSJ, 2nd International Meeting of J-PARC Symposium (J-PARC Symposium 2014)*, July 2014, Tsukuba Epocal.
[5] Uchida T 2008 Hardware-Based TCP Processor for Gigabit Ethernet, *IEEE Trans. Nuc. Sci.* **55** 1631.

3.6.7

Development of Ce:LiCAF Scintillator System for High Precision Nuclear Data Measurement Using Short Pulsed X-Band Electron Linac Based Neutron Source

D. Matsuyama[1], Y. Kusumawati[1], K. Tagi[1], T. Fujiwara[1] and M. Uesaka[1]

[1] The University of Tokyo

matsuyama.daiki@nuclear.jp

Abstract. We are developing a new neutron source at Tokai campus of University of Tokyo. In order to measure high precision nuclear data using this system, the neutron detector should have a large neutron cross section and fast decaying time. An inorganic scintillator Ce:LiCAF has a great characteristic in time resolution. However, an electron Linac emits intense gamma-rays, and this is an important issue for precise neutron measurement. There are two methods of discriminating between neutrons and gamma-rays. The first is the method using a difference of the spatial range of secondary particles. The ranges of the secondary particles of neutron are shorter than that of gamma-rays. The calculated results of Geant4 show the crystal thickness must be less than 5 mm for discrimination. However, the crystal size should be larger than 1 mm x 1 mm to keep reasonable signal-to-noise ratio. The improvement of discrimination due to the change of the size is confirmed by experiment. The other is the method which uses a difference of the light decaying time. The rising time of the signal of gamma-rays is shorter than that of neutrons. By using two shaping amplifiers having different time constants, the signal of gamma-rays can be eliminated.

1. Introduction

A short pulsed X-Band electron Linac based neutron source has been under development as an incoming neutron source of a research reactor Yayoi in Tokai campus. After the decommissioning of the Yayoi reactor, we have decided to install the Linac in the core space of the reactor. Schematic drawing of allocation of the Linac to the Yayoi area is shown in Figure 1[1]. Because of the compactness of the X-Band Linac, we can move it in the reactor. Accelerated electron collides with the neutron target, and because of the generation of the bremsstrahlung X-ray, photon neutron reaction is occurred. Generated neutron are irradiated with the measurement sample and detected by the neutron detector. High precision nuclear data can be obtained by this new neutron source. In order to measure high precision nuclear data, the neutron detector should have a large neutron reaction cross section and fast decay time. ^{10}B or ^{3}He gaseous detector has a large neutron reaction cross section and low gamma-ray sensitivity, but due to the slow rise time of those detectors, they are not able to be used in high precision Time of Flight (TOF) measurement. On the other hand, inorganic neutron scintillators have a great characteristic in timing resolution. Especially, the light decay time of

inorganic scintillator Ce:LiCAF is about 40 ns, and that is superior to other neutron scintillators [2]. However, an electron Linac driven neutron source emits intense gamma-ray, and gamma-ray sensitivity of inorganic scintillators would be an issue for precise neutron measurement.

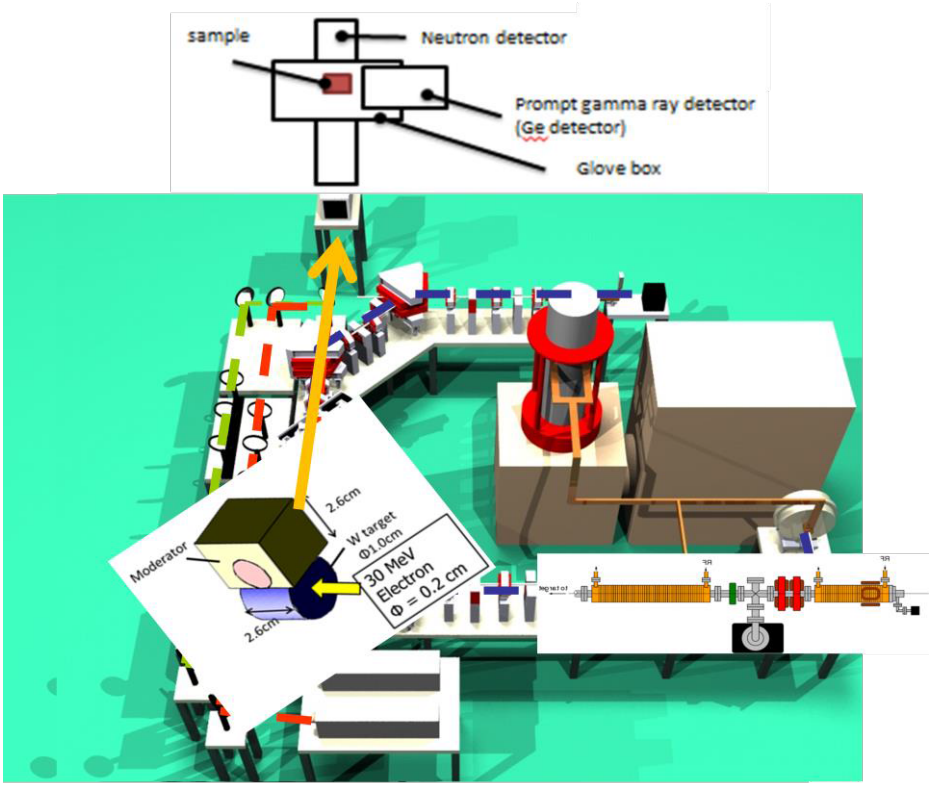

Figure 1. Allocation of the Linac to Yayoi area (from Reference 1)

2. Discriminating between neutron and gamma-ray

There are two methods of discriminating between neutron and gamma-ray. One is a method using the difference of the range of the secondary particles. When Ce:LiCAF crystal is irradiated with neutron, ^{6}Li absorb neutron and emits charged particles, such as alpha-particle and triton. These secondary particles are absorbed in the crystal and they excite the crystal and emit photons. When it is irradiated with gamma-ray, the secondary particle would be electrons. The range of alpha-particle and triton are 10 μm orders of magnitude, however, that of electron is 1 mm order [3]. Therefore, by controlling the Ce:LiCAF crystal size that alpha-particle and triton will be absorbed but electron will be not, the discrimination ability will be improved.

The other is a method which uses the difference of the light decay time of scintillator. The rise time of the signal caused by neutron is slower than that of the signal caused by gamma-ray [4]. A signal whose rise time is slow will be attenuated more than a fast signal by electronic circuits that have small time constant. Therefore, when two electronic circuits are prepared and one has a small time constant and the other has a big one, the signal caused by neutron is only counted by selecting the signal which has small pulse height in small time constant electronic circuit and big in big time constant electronic circuit. A signal caused by gamma-ray is big in two electronic circuits.

3. Change of the size of the scintillator

Using Geant4 Monte Carlo simulation code, energy deposition of neutron and gamma-ray in the Ce:LiCAF are calculated. Figure 2 shows the result that the size of square measure of the crystal is fixed at 10 mm × 10 mm and the thickness is changed from 0.5mm to 20mm. When the thickness of the crystal is changed from 0.5 mm to 5 mm, the detection rate of neutron is changed in proportion to the thickness. In the range of the 5-20 mm thickness, which of gamma-ray is also changed in proportion to the thickness, but in the range of 1-5 mm thickness, the detection rate is extremely decreased, from 1.55×10^{-2} to 1.35×10^{-4}. Figure 3 shows the result that the thickness of the crystal is fixed at 2 mm and the size of square measure is changed from 2 mm × 2 mm to 20 mm × 20 mm. The change of the detection rate of neutron is only 36%, from 1.22×10^{-3} to 1.57×10^{-3}, but 20 mm × 20 mm crystal detect gamma-ray about four times as much as 2 mm × 2 mm crystal, from 6.00×10^{-4} to 2.64×10^{-3}. So if the sizes of crystal become small, the number of the gamma-ray signal in neutron signal become small, but if the size of square measure become small, the number of irradiating neutron become small, and measuring time become long. In order to keep the measuring time short, and discriminate gamma-ray, the size of square measure should be large, and the thickness should be smaller than 5 mm. The simulation result was confirmed by neutron/gamma-ray measurement experiment by pulse height analysis using Multi Channel Analyzer. Figure 4 shows the result of the experiment that 2 mm × 2 mm × 2 mm crystal and 10 mm× 10 mm × 2 mm crystal is irradiated by neutron and gamma-ray. Radiation sources of neutron and gamma-ray are ^{60}Co and ^{252}Cf.The γ-ray signal level of 2 × 2 mm crystal is lower than that of 10 × 10 mm crystal, so the small crystal has a better discriminating characteristic, and this result agrees with the result of numerical simulation.

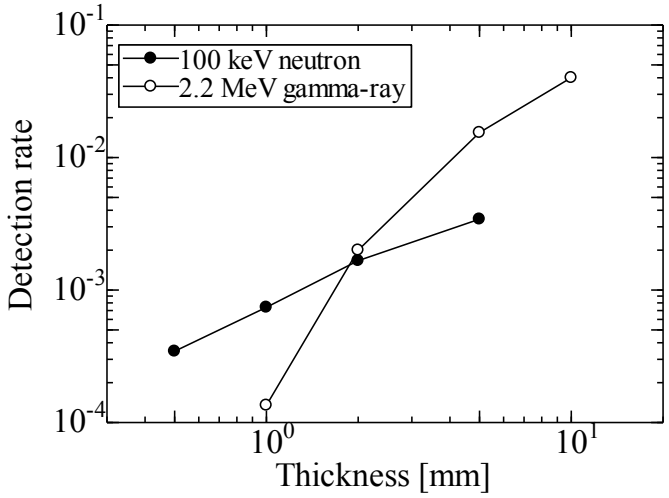

Figure 2. Change of detection rate following the change of the thickness of crystal

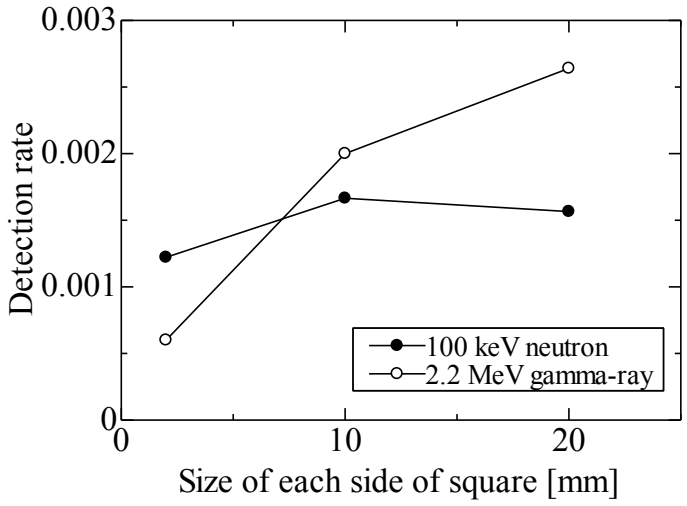

Figure 3. Change of detection rate following

the change of the size of the crystal

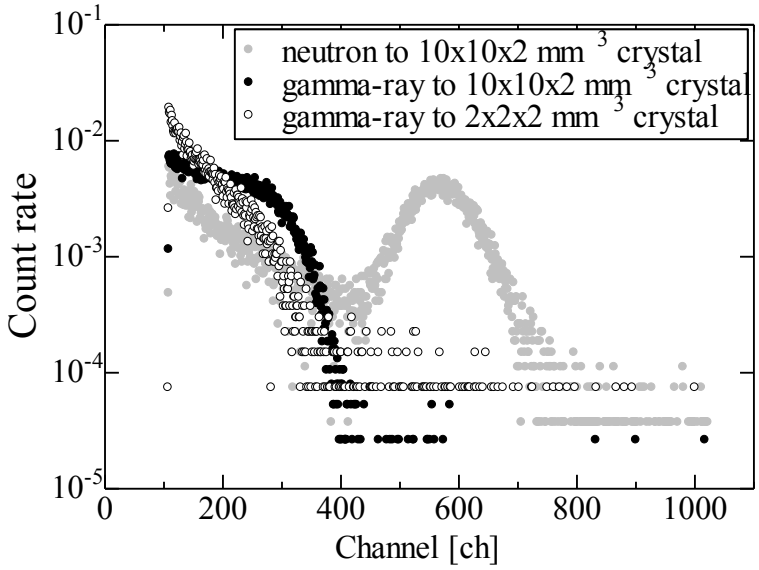

Figure 4. Change of gamma-ray signal level following the

square measure of crystal

4. Change of the time constant of the electronic circuit

The rise time of the signals which are caused by neutron and gamma-ray were obtained by measurement experiment, the former is about 300 ns, and the latter is about 450 ns. In order to use the

difference of these rise times and discriminate them, an electronic circuit which has a small time constant and attenuates the neutron signal more intensely than gamma-ray signal is needed. Figure 5 shows the principle of the discriminating electronic circuit. If input signal is gamma-ray signal, the signal is large in both small time constant circuit and large time constant circuit, but NOT circuit is connected to the big time constant circuit, so AND circuit outputs negative signal. If input signal is neutron signal, the signal become small in small time constant circuit and the signal cannot exceed the threshold of the comparator, so NOT circuit outputs a signal and AND circuit outputs too. Finally, only neutron signal is counted.

To realize this system, the small time constant electronic circuit must attenuate the neutron signal more extremely than the gamma-ray signal. Using 5 ns time constant electron circuit, neutron signal become about 12% smaller than gamma-ray signal.

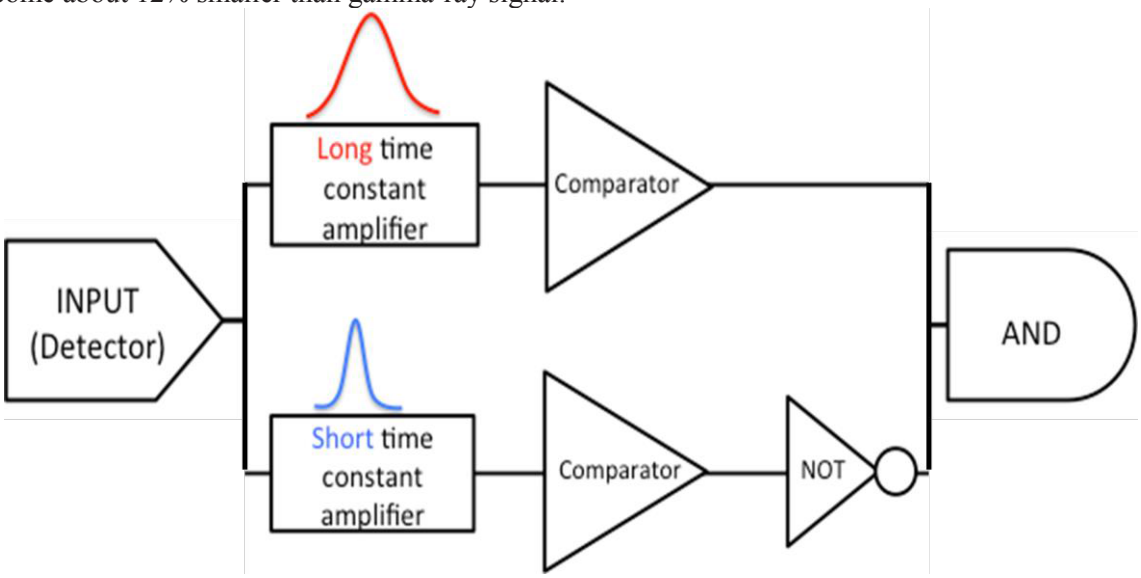

Figure 5. Composition of the discriminating electronic circuit

5. Conclusion

The neutron gamma discrimination method with the inorganic scintillator Ce:LiCAF is researched for high precision nuclear data measurement. In order to discriminate neutron and gamma-ray, the crystal size should be small. As a result of the numerical simulation, when the crystal thickness is shrunken from 1 mm to 0.5 mm, about 85 % of gamma-ray effect is eliminated. In order to get the same result, the crystal size must be shrunken from 20 mm x 20 mm to 2 mm x 2mm (83 % gamma-ray effect is eliminated), however, then the number of irradiated neutron is decreased to 1/100, so the measurement time become longer. So crystal thickness should be shrunken for the discrimination and it should be less than 5 mm.

Discrimination method using the difference of the rising time of each signal is researched. As the result of simulation, using two electron circuits that have large and small time constants, each signal level of neutron and gamma-ray is changed selectively. However, using the electron circuit that have a much smaller time constant than the rising time, the change of signal level is only 12 %. It is needed to research more suitable time constant and the composition of the electron circuit to achieve larger change of signal level. Using these methods, we plan to obtain precise nuclear data by X-Band electron Linac based neutron source at Tokai campus.

Reference

[1] M.Uesaka, K.Tagi, D.Matsuyama, T.Fujiwara, K.Dobashi, M.Yamamoto, H.Harada, "Compact Short-Pulsed Electron Linac Based Neutron Sources for Precise Nuclear Material Analysis", Proceedings of the International Symposium, Nuclear Physics and Gamma-Ray Sources for Nuclear Security and Nonproliferation, Ricotti,Tokai-mura,Japan, 28-30 January 2014, World Scientific, p74

[2] T. Fujiwara, H. Takahashi, T. Yanagida, et al., "Study on Ce:LiCAF scintillator for ^{3}He alternative detector", Neutron News Volume23 Number4, pp.31-34(2012)

[3] GLENN F. KNOLL, "Radiation Detection and Measurement THIRD EDITION", trans. Itsuro Kimura and Eiji Sakai, 2001

[4] Kenichi Watanabe, Yoshiyuki Kondo, Atsushi Yamazaki, et al., "Neutron-Gamma Discrimination in a Ce:LiCAlF6 Scintillator Based on Pulse Shape Discrimination Using Digital Signal Proccessing", IEEE Nuclear Science Symposium Conference Record NP1.M-217, pp.436-439(2011)

This is a blank page.

3-7. Sample Environments

This is a blank page.

3.7.1

Neutron scattering in very high magnetic fields with the new hybrid magnet at Helmholtz Centre Berlin

P Smeibidl[1], M Bird[2], H Ehmler[1], O Prokhnenko[1] and B Lake[1]

[1]Helmholtz Zentrum Berlin (HZB), Hahn-Meitner Pl. 1, D-14109 Berlin, Germany
[2]National High Magnetic Field Laboratory (NHMFL), Tallahassee, FL 32310, USA

peter.smeibidl@helmholtz-berlin.de

Abstract. At HZB a dedicated facility for neutron scattering at extreme magnetic fields and low temperatures is close to completion, the new High Field Magnet (HFM) on the Extreme Environment Diffractometer (EXED). To open up higher fields to neutron research HZB follows a new approach with completely different magnet technology. The aim is the construction of a multi purpose instrument which offers diffraction experiments as well as small angle neutron scattering and inelastic scattering. It is projected according to the special geometric constraints of analysing samples in a high field magnet. The potential scientific impact of the HFM-EXED facility is extraordinarily high. Key scientific questions, from unraveling competing interactions in high-T_C superconductors to the chirality of the molecules of life, are eagerly awaiting answers by using the combination of high magnetic fields and neutron scattering.

1. Introduction

Research in high magnetic fields in connection with elastic and inelastic neutron scattering provides a unique experimental tool to further improve our understanding of matter, and paves the way for the discovery of entirely new phenomena, and, subsequently, to the development of future technologies in general. However, to combine both techniques is challenging. Geometrical limitations imposed on the system due to the necessity to have sufficient angular access for the incoming and scattered neutron beam together with budgetary, energy, technological, and other practical constraints (such as the duty cycle and lifetime of pulse-field coils) usually lead to much lower maximum field strengths of magnets used for neutron research as compared to magnets used in specialized high-field facilities.

Up to now, technology that is based on superconducting coils such as Nb_3Sn led to portable magnet units limited to about 17 T capable of being used at different diffraction and/or scattering instruments that in turn can be optimized for a particular type of neutron diffraction/scattering technique. Any further increase of the magnetic field requires a significant modification of the technology. Besides the possibility of using high-temperature superconductor coils (high Tc's) such as YBCO tapes the only two other technologies are resistive magnets or pulsed magnets. While, at reactor sources, the latter can utilize only a negligible fraction of the neutrons that are available in the experiment, the former magnets require an enormous investment in infrastructure, especially in power and cooling systems. These enormous needs for electrical power can be reduced by a combination of a resistive insert with superconducting outsert leading, however, to an even higher degree of overall complexity. This way of producing higher magnetic fields has been selected at HZB. The resulting unique series-connected

hybrid horizontal magnet with medium-wide angular access for scattered beams, is very heavy and not transferable to another instrument. Yet, a whole spectrum of scientific problems is expected to be tackled with such a magnet. This is enabled by the multipurpose neutron scattering instrument EXED on which the magnet will be situated that combines diffraction, inelastic scattering, and medium-small angle diffraction techniques.

2. Description of the facility

HZB, in collaboration with the National High Magnetic Field Laboratory, Tallahassee, FL, USA, is currently finalizing a project that combines a dedicated neutron scattering instrument (EXED) with a horizontal solenoid magnet with tapered cones (HFM) [1].

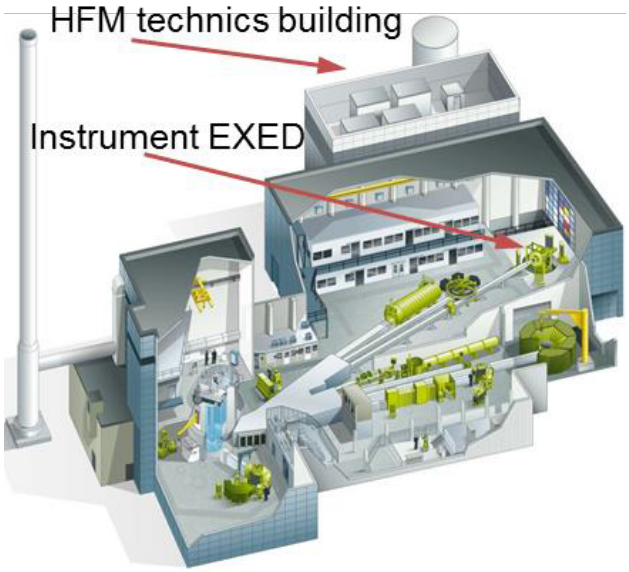

Figure 1. Neutron scattering facilities at HZB with hybrid magnet on instrument EXED

The magnet utilizes series-connected hybrid (resistive insert and superconducting outsert) technology and is capable of producing 25-31 T, depending on the power supplied to the resistive coils which can be between 4.0 and 8.0 MW.

2.1. Extreme environment diffractometer EXED

The EXED instrument is currently a time-of-flight (TOF) instrument optimized for medium-SANS and diffraction under restricted geometrical conditions. An upgrade to increase its signal-to-noise ratio and to implement inelastic scattering capabilities is planned. This unique experimental setup will play a major role in high-field neutron diffraction and spectroscopy. It will also strengthen the leading position of HZB in magnetic field neutron scattering as it will offer by far the highest steady magnetic field for neutron research.

EXED is optimized for conducting powder and single-crystal experiments in restricted angular environments such as under the conditions of HFM, which has 30° neutron access in forward and backward scattering. Until the installation of the magnet, EXED complements HZB's diffraction-instrument suite by providing measurement characteristics typical for pulsed instruments e.g. high resolution in backscattering ($\Delta d/d \geq 10^{-3}$) and large dynamic range (0.4 - >100 Å). Variable wavelength resolution and wavelength band combined with 4 moveable detector banks make the instrument very flexible and continuously adjustable to the requirements of a particular problem. In its current configuration the instrument has no angular restrictions and is used with all types of standard sample environment available at HZB as well as user equipment.

As the design of HFM was further clarified it became clear that the EXED instrument has to cope with the complexity of the whole magnet project that comprises an extended infrastructure. This led to plans for an upgrade of EXED. In addition to improving the diffraction performance (signal-to-noise ratio and full angular coverage), it is especially important to complement the instrument portfolio by inelastic capabilities in the form of a direct time-of-flight (TOF) spectrometer. The upgrade will include four main components:

- an evacuated detector chamber for forward scattering with built-in
- ^{3}He detector array covering 30° in- and out- of plane and positioned 4.5 m away from the sample, and
- a new focusing guide section that accommodates
- a monochromating chopper assembly.

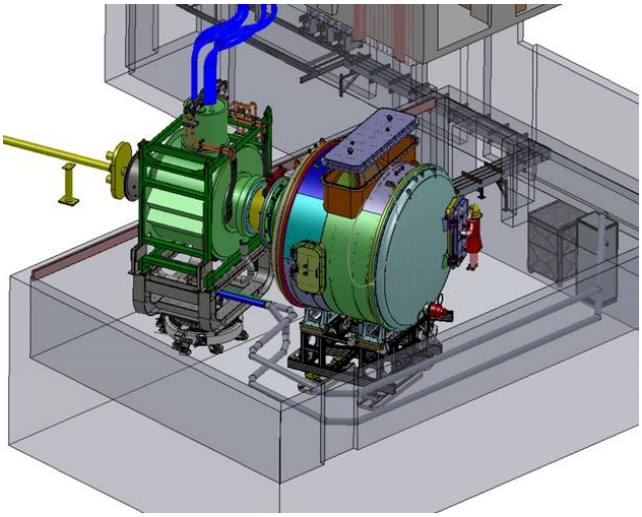

Figure 2. Hybrid magnet and new detector chamber

Limited sample size inside HFM and weak inelastic scattering cross sections imply the need for optimization for signal strength and low background conditions. The former is achieved by enhancing the flux at the sample using a novel focusing guide while the latter is provided by means of a shielded and evacuated detector chamber. After completion, the upgraded EXED will enable energy-resolved measurements over a limited Q-range < 3.25/λ (Å^{-1}) in addition to the existing elastic capabilities.

It is foreseen that all magnet and infrastructure tests will be finalized during the second half of 2014. At the end of this period, the magnet will be installed at the EXED instrument and instrument commissioning will be performed. According to current plans, the first friendly-user experiments could be performed in the second quarter of 2015.

The first experiments will use only the diffraction and small-angle capabilities of EXED. The INS option upgrade is in the phase of preparation and should be implemented in 2015/2016, so that the first INS user experiments could be performed in 2016.

2.2. Hybrid magnet

The new hybrid magnet, a 'first of its kind system' with horizontal field orientation, designed and constructed in collaboration with NHMFL, will not only allow for novel experiments, it will be at the forefront of development in magnet technology for neutron scattering experiments. With a set consisting of a superconducting cable-in-conduit coil and different resistive coils of conical shape at both ends of the system, maximum fields between 25 T - 31 T will be possible with cooling power between 4 MW - 8 MW for the resistive part.

A sectional view of the magnet system is pictured in Fig. 3. The primary technical parameters are provided in Table 1.

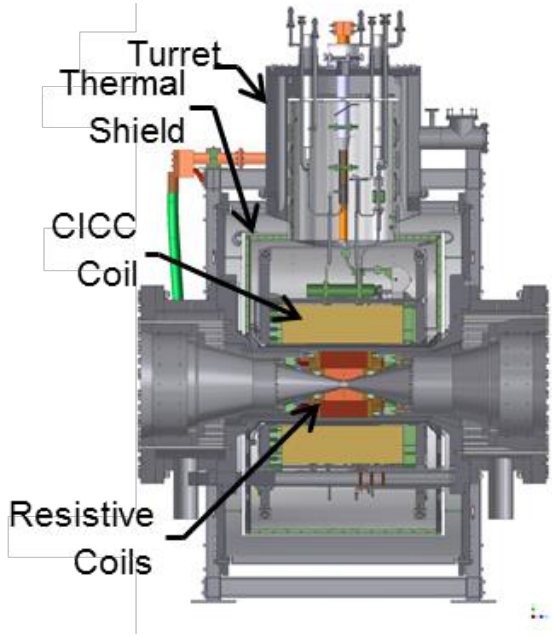

Figure 3. Hybrid magnet system

Table 1. Magnet specification data

Hybrid Magnet Operating Parameters	
Central field	26 T
Power resistive coil	4 MW / 8 MW
B resist. 4 MW / 8 MW	 13 T / 18 T
B supercond.	13 T
Warm bore (center)	50 mm
Scattering angle	30°
Operating current	20 kA
Ramp time	30 min
System height	~ 5 m
Total weight	~ 25 t
Cold mass	~ 6 t

The resistive coils in the center have a conically shaped inner diameter to conform to the bore. It is series connected to a single superconducting coil with Nb_3Sn CICC conductor. The entire magnet system has the bore horizontal so it can align with the neutron beam axis. In addition, the magnet system will sit on an instrument table so it can rotate +/- 15° for exposure of samples to the neutron beam.

All cryogenic and electrical utilities port through an upper “turret” for interface with the technical utilities. The thermal shields are cooled via the helium refrigerator at nominally 40 K.

A large part of the functional requirements of the cryostat stem from the electromagnetic interactions between the superconducting and resistive coils. Features are designed to accommodate potential axial and radial misalignments and axially offsetting fault forces created from a fast shut down of the resistive coils.

For the first project phase a continuous ^{3}He cryostat combined with a closed cycle precooling cryostat is planned for sample cooling. The sample cryostat is a separate independent unit which has to be inserted into the magnet cone.

Another option is to remove the inner coil altogether and keep just the superconducting outsert, which would provide a field of 13T over a large warm bore of almost 0.5m diameter at almost zero electrical cost. This feature of the magnet is truly unique. No other magnet has such a large available space. It should be mentioned that the large warm bore of HFM would allow complex sample environments. Usually only 1 or 2 sample environments are used together during any particular measurement e.g. temperature and magnetic field. Here the large available space allows magnetic fields of 13T to be used simultaneously with temperature, pressure, electric field, laser light, etc. Of particular importance are Paris-Edinburgh pressure cells. The higher pressure cells are too bulky to be placed inside available magnets preventing the combination of field with pressures above ~2.5GPa.

Uniquely this magnet is able to accommodate the larger Paris Edinburgh cells allowing pressures of up to 30 GPa with 13T magnetic fields at low or high temperatures.

Another task of the project HFM-EXED, is the design, construction, and installation of the technical infrastructure for safe and reliable operation of the magnet system during user service. The construction, installation, commissioning and test activities of the building for the three big infrastructure components needed for magnet operation, high-pressure water cooling for the resistive coil, 4 K helium cooling of the superconducting coil and 20 kA power supply were complete by end 2013.

The installations of a control system for the operation of the magnet along with the technical infrastructure and the neutron instrument EXED were finished.

3. Magnet system assembly

The system assembly was an international achievement with the cold mass being completed at the NHMFL in the USA, cryostat to cold mass interfaces made at Criotec Impianti in Italy, and final assembly at the HZB in Germany.

Fabrication of the superconducting cable-in-conduit coil and cold-mass assembly was completed at the National High Magnetic Field Laboratory. The cold mass then was transported to Criotec Impianti in Italy where Paschen and leak tests were conducted as part of acceptance qualifications and the major components of the cryostat were assembled around it. Subsequently, the coil with cryostat was transported to the "magnet assembly and test hall" at the HZB for the final assembly. After rotation to have the magnet axis horizontal, the remaining assembly tasks including all cryogenic and electrical utilities were completed.

Figure 4. Cold mass

Figure 5. Assembly of vacuum container around cold mass

Figure 6. Rotation of magnet to orient magnet axis horizontal

The fabrication of the resistive coil was completed at NHMFL in January 2014. The installation in the room temperature bore of the magnet cryostat was completed by end May 2014 as the last step of system installation.

4. Magnet commissioning and test

After completion of the last assembly task the system was connected to all infrastructure facilities and to the data acquisition and control systems and the testing was started with the resistive coil alone.

All operating data (coil stress and cooling performance) were in agreement with our expectations. On June 23 the full field of 13.1 T at 20 kA and 4 MW was attained for the first time.

The next step was the connection of the superconducting coil to the He refrigerator via the flexible transfer lines and the cool down of the 6 t cold mass to 4 K. The base temperature was reached on August 8. Since then the full hybrid system commissioning was performed. At first a complete check of all interfaces and data acquisition systems of the central control system was executed. The checks of the system safety include the interlocks of all peripheral systems for the operation of the power supply and the adjustment and fine tuning of the coil protection systems for the resistive and superconducting coils. With increasing system current the performance data have to be verified and for each limit overrun of operating data the emergency shutdown procedures have to be tested. The impact on the operation of all system components for the magnet and the technical infrastructure needs to be checked.

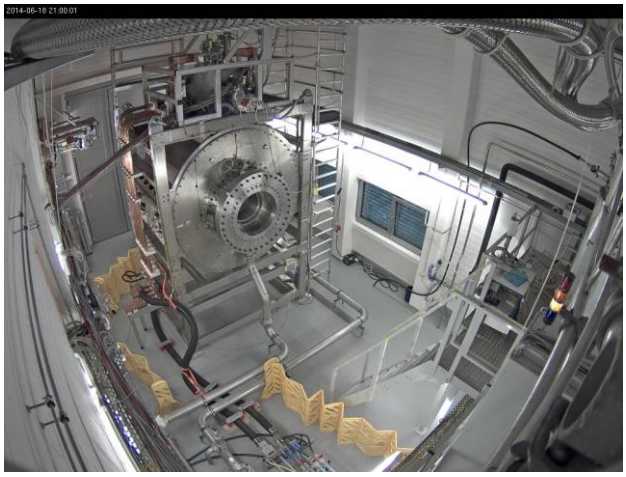

Figure 7. Series-connected hybrid magnet under test

On 16 October 2014 the full field of the hybrid system of 26.28 T at the maximum design current of 20 kA was reached for the first time. The system operates stable within the calculated operational parameters.

To conclude, the HFM-EXED facility is a unique combination of a hybrid magnet dedicated to and optimised for neutron scattering offering the highest static magnetic fields for neutron science in the world. The field is much higher than those available elsewhere and will remain so for years.

References

[1] Bird M D, Adkins T, Bole S T, Cantrell K R, Dixon I R, Gavrilin A V, Lu J, Painter T A, Walsh R P, Weijers H W, Xu T, Zhai Y 2009 *IEEE Trans. Appl. Supercond.***19** 1612-16

3.7.2

Cryogenic Loading Devices for Materials Science & Engineering Studies at J-PARC

Stefanus Harjo[1], Kazuya Aizawa[1], Takuro Kawasaki[1], Tatsushi Nakamoto[2] Tsutomu Hemmi[3] and Takaaki Iwahashi[1]

[1] J-PARC Center, JAEA, Tokai, Ibaraki 319-1195, Japan.
[2] Cryogenics Science Center, KEK, Tsukuba, Ibaraki 305-0801, Japan
[3] Fusion Research Development Directorate, JAEA, Naka, Ibaraki 319-1106, Japan

E-mail: stefanus.harjo@j-parc.jp

Abstract. TAKUMI, the engineering materials diffractometer in the MLF of J-PARC, has developed two unique SE devices working with functions of low temperature, load and strain: a 100 K cooling system for loading experiment and a cryogenic loading machine. The 100 K cooling system for loading experiment is a compact vacuum chamber equipped with loading specimen jigs, and can mount the standard loading machine of TAKUMI. The specimen jigs can be set in a temperature range of 77 K to 473 K by controlling the liquid nitrogen flow and heater power. The industrial superconducting materials society, however, requires a loading machine working at a superconducting temperature such below 10 K. The cryogenic loading machine has been developed for this purpose. This machine is designed to able to cool down sample area together with the load frame, and a 4 K GM cooler is chosen as the core of cooling system. This machine can be used for tensile test at temperatures down to 7 K and at loads up to 50 kN.

1. Introduction

TAKUMI [1] is a time of flight (TOF) neutron diffractometer in the MLF of J-PARC [2], which is dedicated for engineering sciences. TAKUMI covers evaluation of strains or stresses inside engineering components, evaluation of microstructural evolutions during deformations and/or thermal processes, during manufacturing and/or during service, crystallographic investigation of small regions in engineering materials, and texture analysis. In the commissioning, the performances of TAKUMI were confirmed as follows. The best resolution $\Delta d/d$ of 0.17% was achieved by collimating the incident beam (high resolution mode) [3]. The d-range at a single frame bandwidth, i.e. standard operation, was 0.05 nm – 0.27 nm [3]. This range is the optimum range for engineering materials like steels, aluminum alloys, and so on. The neutron incident flux measured using the Au foil at the sample position was the same with that simulated using the McStas [4] with TAKUMI optics configuration. The neutron incident fluxes (simulated at 1 MW operation) at the sample position for the high intensity and high resolution modes are 4.8×10^7 cm^2 s^{-1} and 2.2×10^7 cm^2 s^{-1}, respectively. TAKUMI adopts an event data recording method, which enables data reduction during or after the measurement with manipulating detector position, TOF binning, collection time, and so on [5]. Figure 1 shows the current situation of TAKUMI.

To make TAKUMI productive in basic engineering sciences and applications, development of various sample environment (SE) devices is an important issue. TAKUMI has developed many various SE devices and opened them to support the user programs. The SE devices and its specifications are listed in Table 1. Many of them have been already used in various experiments producing many publications.

[1] To whom any correspondence should be addressed.

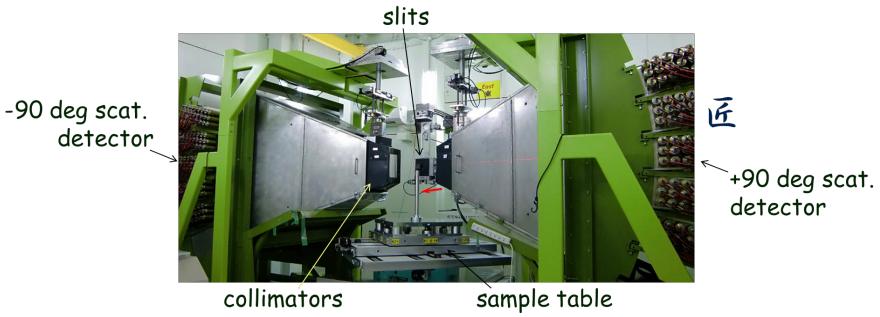

Figure 1. Current situation of TAKUMI.

Table 1. Sample environment devices in TAKUMI

	Specifications	Status	Publication examples used each SE
Radial collimators	Gauge widths: 5 mm, 2 mm, 1 mm Pair per each	Ready	[6], [7]
Standard loading machine	Gear-type Ten. 50 kN, Comp. 30 kN Load, displ. or strain control	Ready	[8], [9]
Furnace system for high temp loading	Added to standard loading machine Halogen lamp furnace Temperature up to 1273 K Vacuum or inert gas	Ready	[10]
100 K cooling system for loading experiment	Added to standard loading machine Liquid nitrogen flow + heater Temp range: 80 K – 473 K	Ready	[11]
Cryogenic loading machine	Gear-type with GM cooler Temperature down to 6 K Tension 50 kN Load, displ. or strain control	Ready	[12]
Fatigue machine	Hydraulic driving Tension-compression up to 50 kN Repetition up to 30 Hz	Under commissioning	
High temp. loading machine for small specimen	Gear-type Tension-compression up to 25 kN Temperature up to 873 K Inert gas	Under commissioning	
Dilatometer	Halogen lamp furnace Temperature up to 1273 K Vacuum or inert gas	Ready	[13], [14]
Eulerian cradle	Texture measurement or 3-axial stress measurement	Ready	[15]
Gandolfi camera	Powder diffractions of textured samples	Ready	[16]

These SE devices make TAKUMI not only as the neutron engineering diffractometer with high accuracy and high efficiency, but also covering a wide application area. A new SE device, so-called thermec-mastor, that was developed in a collaboration with the Elements Strategy Initiative for Structure Materials (ESISM) at Kyoto University, is also under commissioning. This SE device enables a rapid heating, a rapid cooling and a rapid deformation under vacuum or inert gas condition,

i.e., a simulation of thermo-mechanical treatment. This device will be also opened for general users when it is ready. In the present report, the designs of the 100 K cooling system for loading experiment and cryogenic loading machine, and the research examples used these devices will be briefly introduced.

2. 100 K cooling system for loading

Studies on the mechanisms of strengthening behaviors and/or functions of engineering materials are not enough only at room temperature (RT). Deformation studies at low and high temperatures give us much useful information to understand the basic properties of materials, and also to confirm the stabilities at conditions in uses. In TAKUMI, the deformation studies at high temperatures up to 1273 K can be conducted using the standard loading machine combined with a furnace system, but deformation studies at temperatures close to 273 K need a different type of device. Moreover, many engineering materials are used or show their functions mainly in a temperature range of 100 K - 423 K. There are many types of cooling systems for providing low temperatures, which apply the liquid nitrogen, the liquid helium or the Gifford-McMahon (GM) cooler. TAKUMI paid attention on a cooling system for high-pressure studies [17], because this system was able to cool down the sample temperature quickly and the time needed to change the sample was relatively short. This system applied the liquid nitrogen flow to cool anvils in a Paris-Edinburgh high-pressure cell.

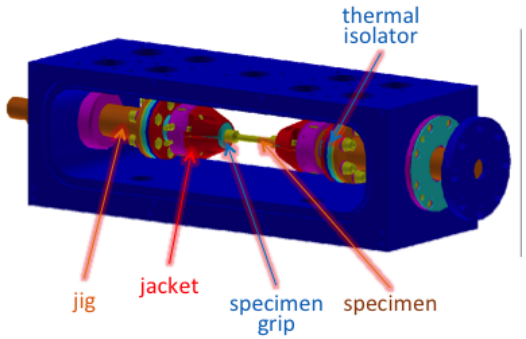

Figure 2. Illustration of 100 K cooling chamber for loading experiment.

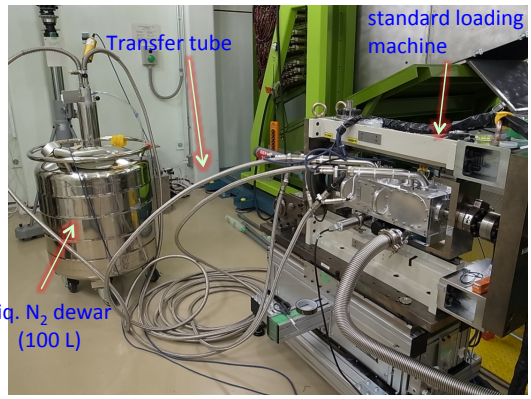

Figure 3. The 100 K cooling system for loading experiment mounted the standard loading machine.

Figure 2 shows the design of compact vacuum chamber for low temperature loading experiment. The jigs can mount the standard loading machine. Thermal isolators are put in between the jigs and grips to shut off the heat input from the outside. The grips are covered by jackets for cooling and heating. The jackets are connected to the liquid nitrogen dewar using transfer tubes, and also to the diaphragm pumps using pipes via the gas-flow controllers. The pipes between the chambers and controllers are equipped with heaters to vaporize the liquid nitrogen. Resistant heaters are also put in the jacket to control the temperature and to heat the specimen above RT. The gas-flow controllers and the power of resistant heaters are further controlled using single loop controllers (SDC35, Azbil Corp.). The temperature controls are done on the jacket, while the temperatures in the specimen are only monitored. The temperatures in the jackets can be controlled from 77 K to 473 K. The procedure of changing specimen is simple (less than 3.6 ks) and time needed to reach the coolest temperature is short (less than 3.6 ks).

As the first trial using this system, transformation-induced plasticity (TRIP) behavior in commercial JIS-SUS304 steel was investigated. Tensile loading experiments were conducted at three different temperatures, 295 K, 213 K and 113 K. The tensile tests were conducted in a step-load controlling manner with 300 s holding in the elastic region, and in a continuous manner (without any pause) with a constant crosshead speed at an initial strain rate of about $1.0\times10^{-5}s^{-1}$ in the plastic region. Meanwhile, the neutron diffraction measurement was performed continuously without any pause during tensile test. Figure 4 shows the nominal stress strain curves of SUS304 obtained from tensile loading tests at different temperatures. The tensile strength increases with the decreasing of loading test temperature. In loading tests at low temperatures (213 or 113 K), the tensile stresses decrease or are kept constant at

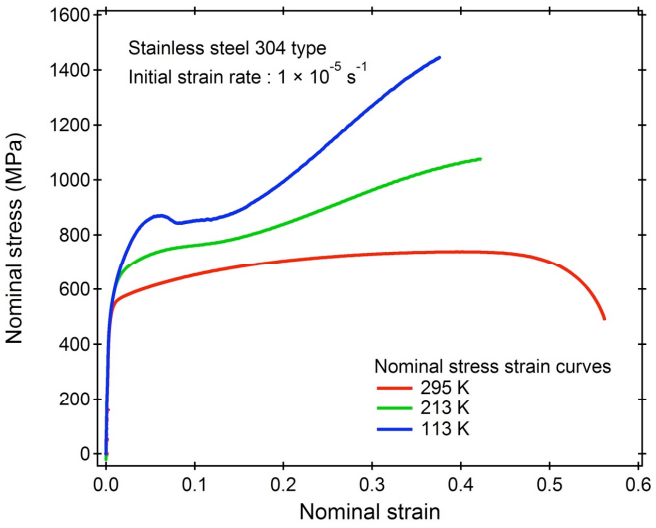

Figure 4. Nominal stress strain curves of SUS304 obtained at different temperatures.

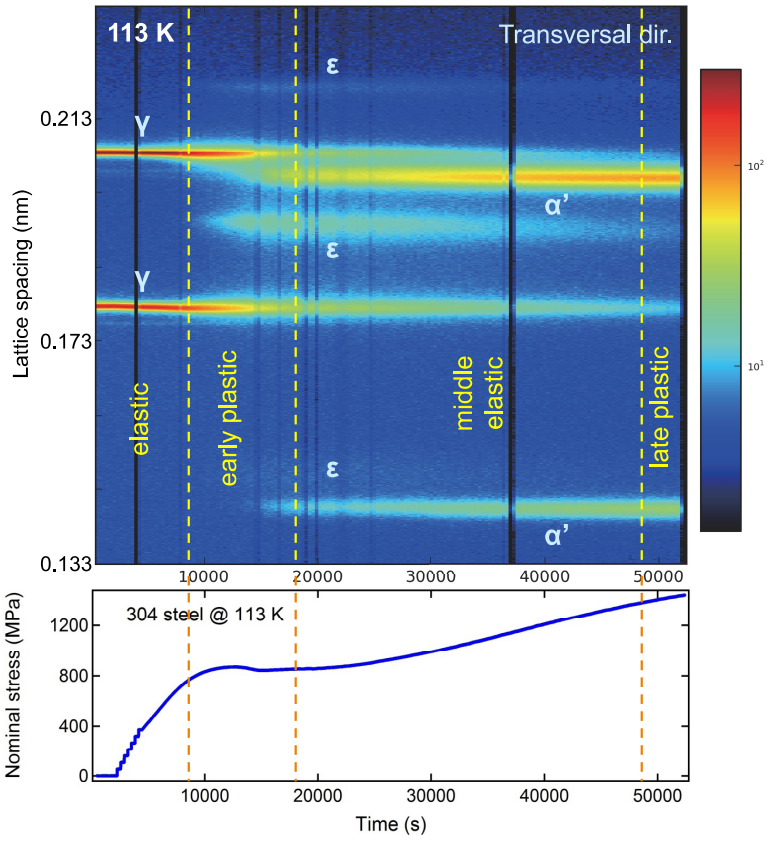

Figure 5. 2-D diffraction patterns of SUS304 at 113 K in the transversal direction.

early stage of plastic deformation. The tensile stress in loading test at 113 K drops at nominal strain of about 0.06, is kept almost constant a while (showing dynamic softening [11,18]), then increases again at nominal strain of about 0.12 with a very large increasing rate. Figure 5 shows 2-D diffraction patterns as functions of lattice spacing and time in the tensile test of SUS304 at 113 K. The TRIP phenomenon starts at the onset of plastic deformation with occurrence of ε phase, and is accompanied by the dynamic softening. The formation of α' phase appears at further stage of deformation, and is followed by the large work hardening.

3. Cryogenic loading machine

Engineering studies of industrial superconducting composites using neutron diffraction need deformation tests at temperatures much lower than 100 K, because the expression of superconductivity mostly requires ultra-low temperatures. The presence of strains in the superconducting phases in industrial superconducting materials like Nb_3Sn composites is well known to affect the superconducting properties [19], and therefore to understand the internal strains is very important, particularly under its use conditions (less than 10 K). To answer this requirement, the cryogenic loading machine was developed in TAKUMI. ENGIN-X at ISIS has developed a cryogenic chamber for in situ neutron diffraction measurements during deformation tests at low temperatures [20]. The lowest temperature that can be realized by this device was about 30 K, though two GM coolers were used. This device was used by mounting on the standard loading machine of ENGIN-X, which is similar to the 100 K cooling system for loading experiment, described above. Therefore, a different design should be developed to achieve temperatures below 10 K.

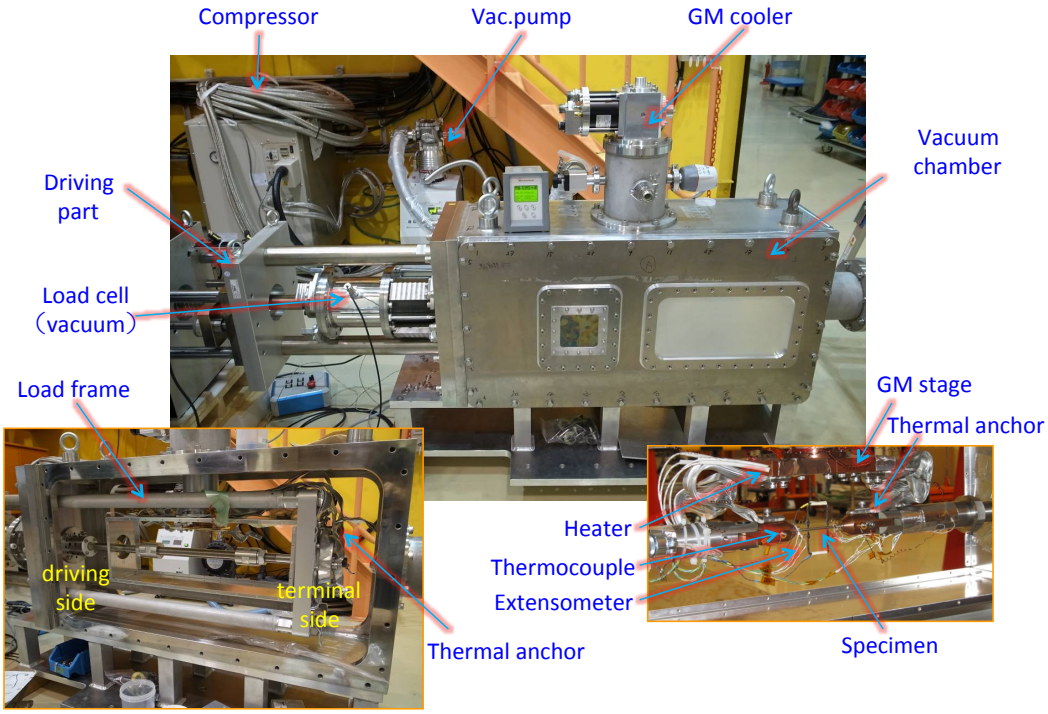

Figure 6. Cryogenic loading machine developed at TAKUMI.

The principle of designing a cryogenic system having a very low achieving temperature, is to maximize the coefficient of performance. It can be changed thinking as minimizing the temperature difference between the high temperature and low temperature sides to minimize the heat input. A design that includes the loading frame to be evacuated and cooled, was decided to be manufactured after a heat calculation. Figure 6 shows the current situation of cryogenic loading machine. It is shown that, a GM cooler is applied in this system. The GM cooler (SRDK-415D-W71C, Sumitomo Heavy Industries, Ltd.), which has two stages of cooling cycles, is used. The GM stage of 4.2 K (1.5 W) is used to cool the sample area, and the GM stage of 50 K (35 W) to cool the load frame. The loading jig mounts a driving part located outside of the chamber that works up to 50 kN. A load cell with vacuum specification is put in between the loading jig and driving part.

To confirm the cooling performance, a specimen of SUS304 was set in the system and a cooling test at the maximum power of the GM cooler was performed. The neutron diffraction measurement was conducted at the same time. Figure 7 shows the temperature change with respect to the time. The grips achieve 15 K within the first 9 ks. The temperatures are then gradually decreased for the next 28.8 ks, where the lowest temperature is 7 K. The diffraction patterns were analysed using Z-Rietveld software [21] to refine the lattice constants (a). The thermal strains during cooling were subsequently calculated using the expression $(a - a_0)/a_0$, where a_0 represents the lattice constant at RT and at un-deformed state.

The coefficients of thermal expansion estimated from the thermal strains were similar to that reported in [22]. The in situ neutron diffraction during tensile test in the elastic region at 7 K was subsequently performed, and the lattice strains were found to be the same with those measured by the extensometer put on the specimen [13]. The temperature range of 7 K – 200 K (at the grips) can be controlled in this system.

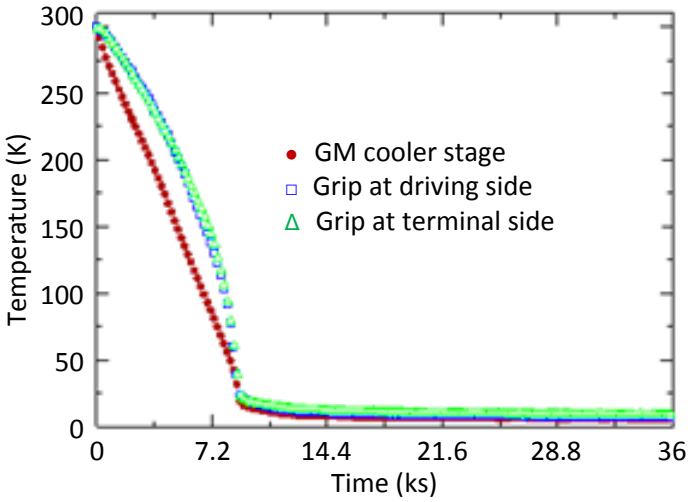

Figure 7. The cooling performance of the cryogenic loading machine; the temperature change as a function of time.

Figure 8 shows the lattice strains in Nb_3Sn phase measured from in situ neutron diffraction measurements during tensile tests of Rutherford Nb_3Sn cables at RT and at about 10 K (low temperature: LT). Lattice strains were analysed in different (hkl). The lattice strains in as-reacted (AR) Nb_3Sn Rutherford cable for the axial (longitudinal) direction at RT (RT) and at un-deformed state (so-called thermal strain), is compressive. The values of thermal strains become larger by cooling to LT, but the lattice strain responses to the applied stress are similar regardless of the temperature. Meanwhile, the lattice strains in the Rutherford Nb_3Sn cable after a pre-bend treatment (PB) for the axial direction at RT and at un-deformed state, are relaxed to be close to zero. The changes of thermal strains due to cooling to LT in PB cable are small, and the lattice strain responses are also smaller than those in AR cables. The smaller thermal strains and smaller lattice strain responses to the applied stress are expected to improve the superconducting properties of the Rutherford Nb_3Sn cable during its use in magnet applications.

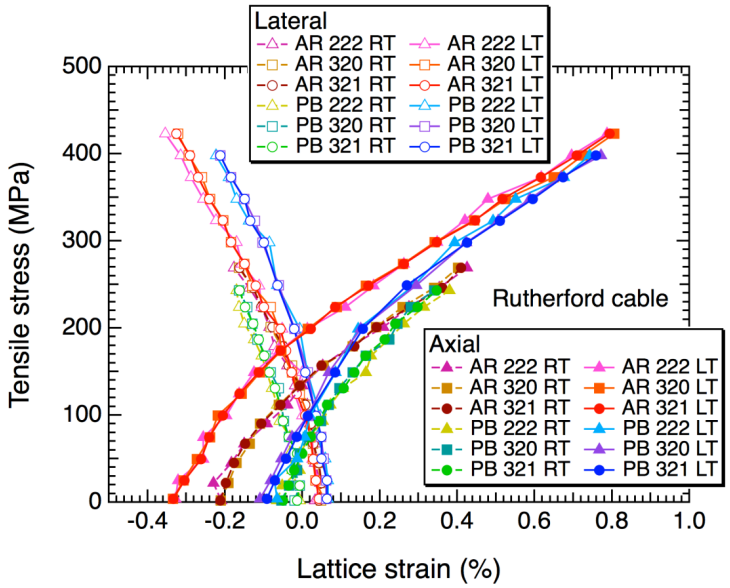

Figure 8. Lattice strains measured during tensile deformation of Rutherford Nb_3Sn cables. Lattice strains were analysed in different (hkl).
AR: As-Reacted, PB: Pre-Bent treatment, RT: RT, LT: low temperature about 10 K

4. Summary

TAKUMI is a neutron engineering diffractometer with high accuracy and high efficiency. Various kinds of sample environment devices are very important to cover wide engineering sciences. Two different types of cryogenic loading devices that cover different temperature ranges have been developed. (i) 100 K low temperature system for loading experiment: uses liquid nitrogen flow; only the sample area is cooled; the temperature range is 77 K – 473 K (in the specimen grips or the jackets); the procedure of changing specimen is simple; and the time needed to reach the coolest temperature is short (less than 3.6 ks). (ii) Cryogenic loading machine: uses GM cooler; the load frame is also evacuated and cooled; and the temperature range is 7 K – 200 K (at the specimen grips). Both devices are ready to be used to support user programs at TAKUMI.

5. References

[1] Harjo S, Moriai A, Torii S, Suzuki H, Suzuya K, Morii Y, Arai M, Tomota Y, Akita K and Akiniwa Y 2006 *Mater. Sci. Forum* **524-525** 199
[2] Ikeda Y 2005 *J. Nucl. Mater.* **343** 7
[3] Harjo S, Ito T, Aizawa K, Arima H, Abe J, Moriai A, Iwahashi T and Kamiyama T 2011 *Mater. Sci. Forum* **681** 443
[4] Lefmann K and Nielsen K 1999 *Neutron News* **10** 20
[5] Ito T, Nakatani T, Harjo S, Arima H, Abe J, Aizawa K and Moriai A 2010 *Mater. Sci. Forum* **652** 238
[6] Suzuki H, Harjo S, Abe J, Xu P, Aizawa K, Akita K 2013 *Nucl. Instrum. Methods A* **715** 28
[7] Hemmi T, Harjo S, Nunoya Y, Kajitani H, Koizumi N, Aizawa K, Machiya S and Osamura K 2013 *Supercond. Sci. Technol.* **26** 084002
[8] Morooka S, Sato N, Ojima M, Harjo S, Adachi Y, Tomota Y and Umezawa O 2011 *IJAE* **2** 361
[9] Aizawa K, Gong W, Harjo S, Abe J, Iwahashi T and Kamiyama T 2013 *Mater. Trans.* **54** 1083
[10] Harjo S, Ito T, Gong W, Suzuki H and Aizawa K 2011 *CAMP-ISIJ* **24** 1121
[11] Harjo S, Kawasaki T, Gong W, Aizawa K and Iwahashi T *JPS Conf. Proc.* accepted
[12] Yamaguchi T, Fukuda T, Kakeshita T, Harjo S and Nakamoto T 2014 *Appl. Phys. Lett.* **104** 231908
[13] Jin X, Nakamoto T, Harjo S, Hemmi T, Umeno T, Ogitsu T, Yamamoto A, Sugano M, Aizawa K, Abe J, Gong W and Iwahashi T 2013 *Rev. Sci. Instrum.* **84** 063106
[14] Osamura K, Machiya S, Tsuchiya Y, Suzuki H, Shobu T, Sato M, Harjo S, Miyashita K, Wadayama Y, Ochiai S and Nishimura A 2013 *Supercond. Sci. Technol.* **26** 094001
[15] Gong W, Aizawa K, Harjo S, Abe J, Iwahashi T and Kamiyama T 2013 *Mater. Trans.* **54** 974
[16] Xu P, Harjo S, Ito T, Gong W, Suzuki H, Akita K, Suzuki T, Tomota Y and Lutterotti L *JPS Conf. Proc.* accepted
[17] Gong W, Tomota Y, Harjo S, Su Y H and Aizawa K 2015 *Acta mater.* **85** 243
[18] Komatsu K, Moriyama M, Koizumi T, Nakayama K, Kagi H, Abe J and Harjo S 2013 *High Pressure Res.* **33** 208
[19] Ekin J W 1980 *Cryogenics* **20** 611
[20] Oliver E, Evans B, Chowdhury M, Major R, Kirichek O and Bowden Z 2008 *Meas. Sci. Technol.* **19** 034019
[21] Oishi R, Yonemura M, Nishimaki Y, Torii S, Hoshikawa A, Ishigaki T, Morishima T, Mori K and Kamiyama T 2009 *Nucl. Instrum. Methods A* **600** 94
[22] Collocott S J and White G K 1986 *Cryogenics* **26** 402

Acknowledgments

Authors wish to acknowledge staffs of the MLF of J-PARC for assistance or encouragement in these developments, Drs. S. Awaji, K. Takahashi of Tohoku University and X. Jin of RIKEN for valuable discussions. These works got partially financial supports from JSPS grants (KAKENHI No. 23109003, 26600146 and 26289264).

3.7.3

Concepts for Sample Positioning using Industrial Robots at ISIS

Matt North[1], Saurabh Kabra[1]
[1] STFC, ISIS, Rutherford Appleton Laboratory, UK

E-mail: matt.north@stfc.ac.uk, saurabh.kabra@stfc.ac.uk

Abstract. This paper offers a conceptual outline regarding the application of industrial robots for automated sample positioning activities at the ISIS Neutron & Muon source, located at the Rutherford Appleton Laboratory in the UK. Drivers for a change in the approach to traditional component positioning tasks are highlighted, from which the concept of applying an industrial robot platform for neutron camera positioning at the Imaging and Materials Science & Engineering (IMAT) instrument, automation of sample changes for top loading closed cycle refrigerators and the automation of sample changing and positioning for texture measurements on powder diffraction instruments is discussed.

1. Introduction

The ISIS neutron & muon source located at the Rutherford Appleton Laboratory in the UK. ISIS operates two targets stations, 30 beamline instruments with over 1800 domestic and international users per year. The facility comprises of a 70MeV LINAC feeding a dual harmonic proton accelerator, producing 200uA 800MeV protons to two independent targets. Proton extraction is such that TS1 operates at 40Hz and TS2 at 10Hz repetition rates, producing 128kW and 32kW respective target power.

ISIS has a total of 26 neutron and 4 muon instruments covering diffraction, spectroscopy, reflectometry and SANS techniques. On completion of the TS2 Phase-II construction project an additional four instruments will increase the SANS and reflectometry instrument suite with ZOOM[1] and LARMOR[2] whilst adding neutron chip irradiation with CHIPIR[3] and neutron imaging with IMAT[4].

2. Triggers for future development of sample positioning and manipulation systems

2.1. Increasing Experimental Throughput

Regardless of the measurement technique, a gain in neutron flux and associated reduction in measurement period is the primary driver for automating sample changes and sample positioning, to remove or reduce preparatory bottlenecks, reduce strain on human resource or streamline instrument operation.

ISIS target station one target is currently moving towards a future target and moderator upgrade which is estimated to increase the neutron flux by an average gain factor 3.4 across the instrument suite. [5] Coupling a source upgrade with beamline equipment upgrades such as the addition of

modern neutron guides enables instruments to see potential neutron flux gain increases by an order of magnitude. [6]

A range of sample changers are currently used at ISIS to enable automation of sample changing tasks on select beamlines on both the first and second target stations. Typically diffraction and small angle neutron scattering measurements have the capacity for the highest experimental throughput with measurements durations as low as 15 minutes. Reflectometry measurements can be similar in period but experimental throughput is restricted by the sample alignment process. Spectrometry measurements require much greater periods to get useful data, for simple experiments where sample signature data is the primary requirement, such as with express access, the minimum measurement durations is around five hours.

The GEM[7] and POLARIS[8] high intensity diffraction beamlines at the first target station use a 20 position carousel sample changer, shown in figure 1, for automated measurements at room temperature, at atmospheric pressure, with samples contained in standard vanadium cans. Currently measurement durations are as low as 30 minutes, providing automated sample changes over a minimum 10 hour period. Looking to the future with higher neutron fluxes, both GEM and POLARIS will experience measurement durations in the 10 minute range at which point the current capacity of the existing sample changer limits its value and a new type of sample changer must to be developed to meet this high throughput future.

Figure 1: 20 Position Carousel Sample Changer

2.2. Beamline Access Routes

Express access to instruments is an important part of the range of ISIS access routes enabling a comparably simple route for users to quantify the value in neutron techniques. [9] ISIS is exploring the value and practicalities of a range of facility access models. In this context if there is significant growth in express access this could erode the value of existing sample changers to a level where changer capacity will not cover automation through an express period.

2.3. Widening Technical Capabilities

Measurements at cryogenic temperatures and texture measurements are two types of measurement that currently have the potential for associated short measurement durations but are not currently catered for by the existing set of sample changers at ISIS. Texture measurements can be completed in the carousel style sample changer if the changer is lifted out of the instrument and rotated, however this methodology deviates from automated instrument operation.

3. Industrial Robots vs. Traditional Sample Positioners

Traditionally the solution to sample positioning has been the in house development of bespoke motion systems. This methodology produces systems that vary significantly with little scope for shared deployment across beamlines. Consequentially development costs and commissioning times are amplified and varying levels of support and maintenance are required. As previously described the inflexibility of the traditional sample changer model means that step changes in beamline neutronic performance, such as instrument or source upgrades requires settling with non-optimal operation or complete redesigns.

With this in mind a major advantage of applying an industrial robot system is the flexibility of motion and subsequent increased scope in motion solutions that can be delivered. Hardware costs can be up to an order of magnitude lower in comparison to in house designs. Industrial robot system operation is also reliable with mean time between failure rates generally around 80,000 hours with low associated maintenance frequencies. [10]

Figures 2 and 3 show two common types of industrial robot. SCARA robots are commonly used for high throughput pick and place whereas the 6 axis robotic arms are used where a greater degree of flexibility is required for component or tool positioning tasks. Repeatability of the robot end effector is a key factor of a robot system and repeatability in the order of 100μm is not uncommon with many off the shelf systems. Positional accuracy is not so easily defined and is dependent on many factors including robot pose, payload weight, end effector working volume, joint paths, operating environment, robot manufacturing quality and the kinematic model referenced by the robot controller. For these reasons robot manufacturers do not freely quote positional accuracies which can be as high as 15mm in some cases. [11]

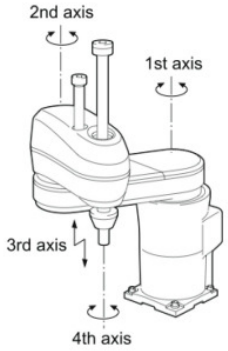

Figure 2: SCARA Robot Schematic

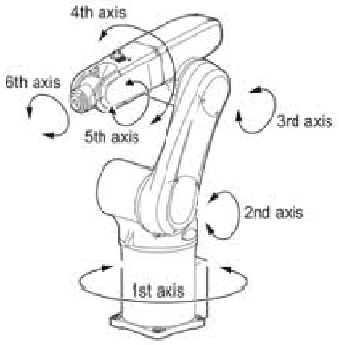

Figure 3: 6 Axis Robot Arm Schematic

Improving the kinematic model of a robot provides a generic approach to improving positional accuracy of industrial robots. Many robot manufacturers can provide an absolute robot which is shipped with a calibrated kinematic model specific to the robot arm. The calibration process utilises a laser tracker system to plot the errors between the standard kinematic model and the robot end effector over a number of points through the working volume. The kinematic model is then adjusted to take account of the difference. The level of improvement in positional accuracy provided by robot calibration is not standard across the board but can increase absolute positional accuracy in the 120μm region for a robot working in a restricted $0.4m^3$ volume with a 1.3kg payload. [12]

4. Conceptual Applications for Industrial Robotics at ISIS

4.1. Camera Positioning System

IMAT (Imaging and Materials Science & Engineering) is a neutron imaging and diffraction instrument for materials science, materials processing and engineering being constructed as part of the ISIS

second target station phase-II project. The special features of the instrument will be energy-selective neutron imaging and the combination of neutron imaging and neutron diffraction. It is expected that IMAT will start operating in September 2015. [4]
Neutron imaging measurements on IMAT will require different neutron cameras to be positioned accurately beyond the sample. Imaging requirements define the automation of neutron camera selection and positioning. Integrating this requirement on an instrument with wide detector coverage, as shown in figure 4, dictates the need for imaging equipment to be completely removed from the sample area. These needs could not be adequately met through traditional positioning systems.

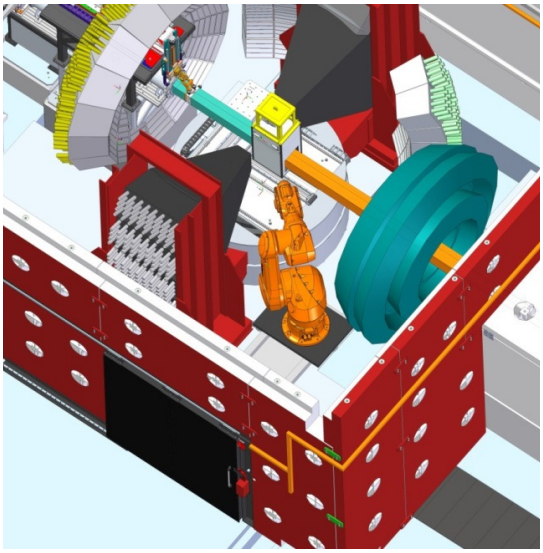

Figure 4: 3D representation of the IMAT blockhouse

A 6 axis robot arm provides the level of kinematic flexibility required to meet the motion requirements, however to ensure a high quality of measurement there is a requirement for the robot arm to hold a neutron camera with positional stability better than 40µm for periods up to an hour. The working volume constraints require the robot arm to hold pose, reaching out in the order of 2m from the base with up to a 70kg payload. A feasibility study was performed showing that, without application specific robot calibration or positional tracking feedback, typical repeatability with a 70kg load was in the order of 70µm with drift in the order of 10µm to 150µm over a 30 minute period. [12] This drift envelope can be significantly reduced to sub 10µm by employing a peripheral laser tracking device as a positional sensor to enable closed loop control of the robot end effector.

4.2. Cryogenic Sample Changer

A similar approach to automated sample changes on x-ray diffraction beamlines can be adapted to neutron sources; applying an industrial robot to move samples between a precooled sample rack and a closed cycle refrigerator (CCR). A novel approach has been developed to position vanadium cans in a CCR without the need to use the traditional method of mounting sample and associated thermometry wiring on sample stick mechanics. The addition of baffles and thermometry to the sample can and the inclusion of a positioning seat in the CCR insert are the only modifications required. Figure 5 shows vanadium can including thermometry contact PCB and baffles. Figure 6 shows the fixed sample seat ready for mounting in a CCR insert complete with sprung contacts to complete the temperature sensing circuit.

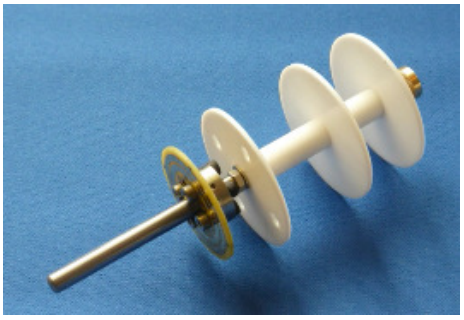

Figure 5: Sample Can with Integrated Baffles

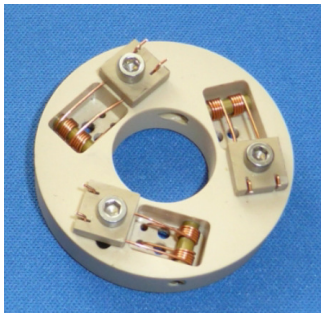

Figure 6: Insert seat showing sprung contacts

By ensuring that the sample can baffle dimensions are similar in diameter to the CCR insert a controlled flow of gas through the insert produces enough pressure to move the vanadium can through the insert. Offline experimentation has proven that this method provides robust control of sample position and robust, repeatable connections have been made for sample thermometry as the can is seated in the operating position.

Sample precooling is an essential component of an automated cryogenic sample changer for high throughput experiments. In general precooling samples to liquid nitrogen temperature halves the total time to cool a sample to 4K. An important aspect of automating cold samples changes is to ensure that there is no ice deposition on the sample can or inside associated sample environment during the movement and positioning of the sample can.

For a CCR the greatest risk of ice deposition in the insert is during entry and egress of the sample into the insert volume. This is can be managed by isolating the insert volume from the outside environment via an automated gate valve and controlling the flow of exchange gas through the insert volume during a sample change. For the sample can the greatest risk of ice deposition is during the pick and place task between the precooled location and the CCR. By integrating pipework onto the robot arm end effector, adequate control of precooled gas flow across the sample during the pick and place task can ensure that the sample can is kept in a dry cold environment.

4.3. Ambient Sample Changer

The principles outlined in the cryogenic sample changer concept can be applied to provide improvements to the existing carousel sample changer used for powder diffraction by providing scope for increased sample capacity. Enabling operation in a vacuum environment; reducing background scatter. The capability to monitor sample temperature and the possibility to control sample temperature by filling the insert with cooled or heated exchange gas.

4.4. Automated Texture Measurements

6 axis articulated arms have the kinematic freedom, using the axis convention provided in figure 7, to move a sample through 360° in φ, χ and Ω. Both φ and Ω can be mapped to a single revolute axis; J1 and J6 respectively using the convention shown in figure 3. To ensure that χ is kept perpendicular to φ throughout the range of motion, χ is potentially a composite motion of axis J2 through to J5.

Controlling from a calibrated kinematic model of the robot can provide positional accuracy better than 500μm with rotational resolution of 1° from a single axis making a 6 axis arm an ideal candidate for texture measurements on powder samples where the neutron beam size is larger than the sample size.

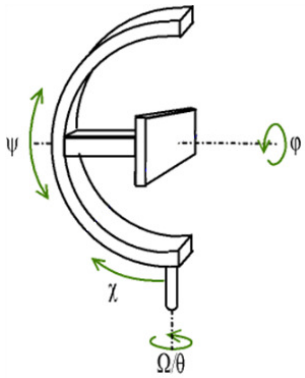

Figure 7: Eulerian Cradle Schematic

The operating environment required for texture measurements produces greater challenges. Mounting the sample to the end of a robot arm requires the robot to operate inside an evacuated volume in the instrument tank during a measurement. Robot operation in a vacuum is possible with minor modification to a robot arm to ensure that pressure differentials across robot joints are managed and heat from motor operation is dissipated into a peripheral heat sink. [12]

The physical constraints dictated by the working volume are a significant concern as the range of robot motion and pose required for a texture measurement may, if unconstrained, need an operating volume greater than the physical constraints of the instrument tank, posing a significant hazard to damaging the instrument, robot arm or sample can. DENSO produces one of the smallest 6 axis robot arms on the market with a radial reach of just 430mm [13] This small robot still exceeds the extents of most instrument tank working volumes at ISIS. Parasitic scattering and detector shadowing by the robot arm as it moves inside the working volume is also a concern, having a detrimental effect on the quality of the measurement.

Many robot manufacturers provide 3D environments as part of robotic motion design environments enabling the design to simulate control programs, mapping the path and pose of the robot arm and identifying potential collisions. Integrating 3D models of the instrument infrastructure into the 3D design environment provides a precise indication to the extent of the physical constraints posed by tank apertures and the position of the robot arm referenced to instrument detector positions allowing working volumes to be constrained and robot arm motion and position refined. Parasitic scatter can also be reduced by employing classic material shielding methods, with an emphasis on ensuring that the additional weight does not have detrimental impact on positional accuracies.

With respect to automating sample changes with texture measurements mounting the 6 axis arm in an evacuated volume has the major drawback of isolating the arm from the sample rack. The application of two robotic arms in cooperative motion is a viable solution with one robot performing a pick and place task outside of the instrument tank, passing the sample through an air lock to the second robot performing the sample positioning task in the instrument tank.

5. Challenges for Industrial Robot Application

As previously highlighted industrial robots currently have the capabilities to meet the positioning and working environment requirements of a range of applications at ISIS. To truly capitalise on the flexible, standardised, robust motion system that a 6 axis robot provides is to apply a standard robot platform to a range of applications. Taking sample changing as an example, there is a wide variety of in house designed sample changers at ISIS used for a particular type of sample can on a particular beamline. Amalgamating these to a single entity which has the flexibility to be deployed across many beamlines for many different types of samples and environments is a valuable goal. However, the greatest barrier to realising this is the variation in working volumes around the instrument sample areas.

Figure 8 highlights the diverse range of sample areas at ISIS. Deploying a standard robot cell at each of these locations is not trivial, it can be seen that there is a varying amount of area for deploying the robot system and it's peripheral components and the final position the robot arm must deliver the sample to ranges from deep wells as seen in WISH, to moderate heights on sample positioners, LARMOR.

One viable option is to design a standard robot cell which is incorporated with instrument specific mechanics defining the location of the robot arm and associated equipment. Using modern 'teach by hand' robot arms [14] in conjunction with mechanical reference dowels could provide a flexible and user friendly method for managing the variation in equipment position across the beamlines, with robot automated control tasks being defined as a standard and remaining unchanged at each location.

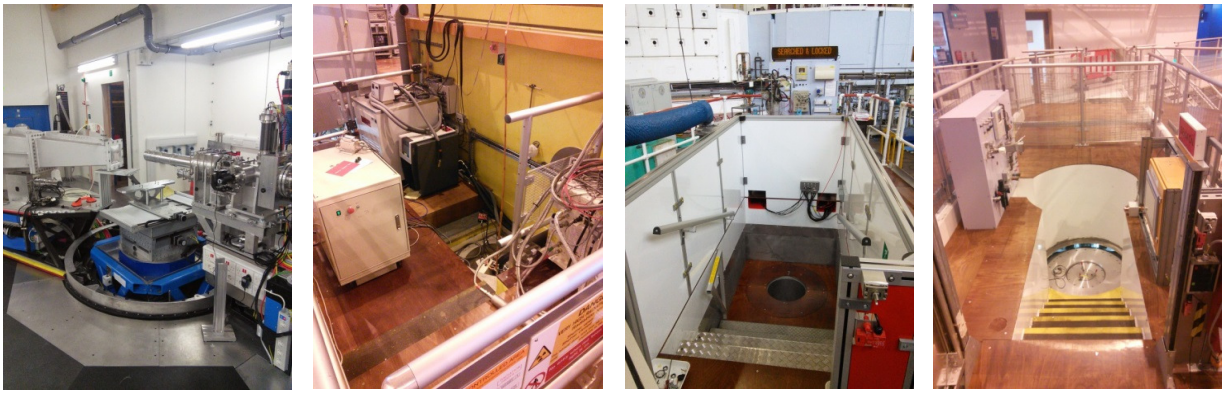

Figure 8: ISIS Instrument sample areas. From left to right: LARMOR, NIMROD, POLARIS, WISH.

6. CONCLUSIONS

It is clear that industrial robots can provide a low cost, reliable and flexible platform to develop solution to automate a variety of sample and beamline equipment positioning tasks. The series of revolute joins that makes up a robot provides essentially open loop control of the end effector which limits the robots positional accuracy, however there are well established methods to improve positional accuracies to the extent that they meet the requirements for sample changing and component positioning tasks.

The traditional methodology of designing one off sample changers and associated control systems in house for a specific beamlines is resource heavy, expensive and complicates operational support and equipment maintenance. Using a robotic arm as a generic standard to develop from is very attractive proposition; however the differing working environments found across beamlines makes this difficult in practical terms and further work is required to understand the management of these differences in detail.

7. ACKNOWLEDGEMENTS

Thanks to Dr Winfried Kockelmann, Jim Nightingale and Steve Cox for their information on the IMAT Camera Positioner project.

Thanks to Dr Oleg Kirichek information and images relating to the cryogenic sample changer concept.

8. REFERENCES

[1] http://www.isis.stfc.ac.uk/instruments/Zoom/
[2] http://www.isis.stfc.ac.uk/instruments/Larmor/

[3] http://www.isis.stfc.ac.uk/instruments/Chipir/
[4] http://www.isis.stfc.ac.uk/Instruments/Imat/
[5] Skoro G, and Ansell S, 2014 Neutronics modelling for the ISIS TS-1 upgrade, Proceedings of ICANS XXI: International Collaboration on Advanced Neutron Sources.
[6] Fernandez Castanon J, 2013 'Monte-Carlo simulations for the development of TOSCA's guide at ISIS.' Report: RAL Technical Reports RAL-TR-2013-002.
[7] http://www.isis.stfc.ac.uk/instruments/gem/gem2467.html
[8] http://www.isis.stfc.ac.uk/instruments/polaris/polaris4643.html
[9] http://www.isis.stfc.ac.uk/user-office/isis-access-mechanisms15082.pdf
[10] 'Special Report: Robotics - ABB Group' (2005) ISSN: 1013-3119
[11] Fixel P, 2006. Absolute Accuracy Marketing Presentation, ABB Automation Technologies.
[12] Communication with robot manufacturers, August 2014 through to October 2014.
[13] http://www.densorobotics-europe.com/en/product/vp-5243g
[14] 'Your new robot colleague – coming out of its cage.' http://www.universal-robots.com/GB/Universal_Robots/News.aspx?Action=1&NewsId=808&PID=18758

3.7.4

Present status of sample environment at J-PARC MLF

Tomokazu Aso[1], Yasuhiro Yamauchi[1], Yoshifumi Sakaguchi[2], Koji Munakata[2], Motoyuki Ishikado[2], Seiko Ohira-Kawamura[1], Tetsuya Yokoo[3], Masao Watanabe[1], Shinichi Takata[1],Takanori Hattori[1], Wataru Kambara[1], Takayuki Oku[1], Yukinobu Kawakita[1] and Kazuya Aizawa[1]
[1]J-PARC Center, JAEA, Tokai, Ibaraki 319-1195, Japan.
[2]CROSS TOKAI, Tokai, Ibaraki 319-1106, Japan.
[3]KEK, Tsukuba, Ibaraki 305-0801, Japan

Abstract. In Materials and Life Science Experimental Facility (MLF) of J-PARC, a Sample Environment (SE) team has been officially organized in a newly established section, Technology Development Section, with succeeding the previous ad hoc SE team. We, the SE team, are proceeding with the SE standardization in MLF, and working on operation of so-called beamline (BL)-common SE equipment. We currently have a vertical-field superconducting cryomagnet, a ^{3}He-^{4}He dilution refrigerator insert, a top-loading ^{4}He cryostat and a high-temperature furnace as the BL-common SE equipment. In order to maintain them and to prepare for users' experiments, two SE areas are equipped in the experimental halls, though their spaces are still not enough. Much larger workshop for long-time commissioning, a sample synthesis room and sample characterization rooms will be soon prepared in a new building under construction. We also contribute to safety improvement as the members of the MLF equipment safety committee.

1. Introduction

Sample environment (SE) is one of indispensable components to perform the neutron scattering experiment. Various environments, such as high and low temperatures, magnetic field and high pressure, are required by users depending on their research fields. Japanese neutron facilities have had a culture that each instrument individually prepares its SE equipment, where instrument scientists are responsible not only for their instruments but for SE and researchers operate the equipment for their experiment. However, such environments should be supported by facility-wide activities. In the Materials and Life Science Experimental Facility (MLF) in Japan Proton Accelerator Research Complex (J-PARC), the original SE team was organized as "SE task" in 2004, which is about four years before the first neutron beam of MLF. Members of this task were scientists working at MLF, and had discussed the strategy in our facility and standardization of SE based on their experience of neutron experiments as a user or instrument scientist. This team was reorganized as the "SE team" in 2009, almost concomitantly with an opening of the user program. Then two engineers joined, and had discussed a guideline of the SE

[1] 2-4 Shirakata-Shirane, Tokai-mura, Naka-gun, Ibaraki 319-1195, Japan
E-mail: aso.tomokazu@jaea.go.jp

standardization of SE, taking over the previous SE task, and the support system in SE. This SE team was a so-called interim team, and each member had another responsibility, though it was an advantage that the members could respond to users' requests immediately. As shown in Fig. 1, the number of proposals and users are increasing year by year. Then the variety of the required SE should also increase. Therefore, it is necessary to respond users' requests effectively and to establish the user support system.

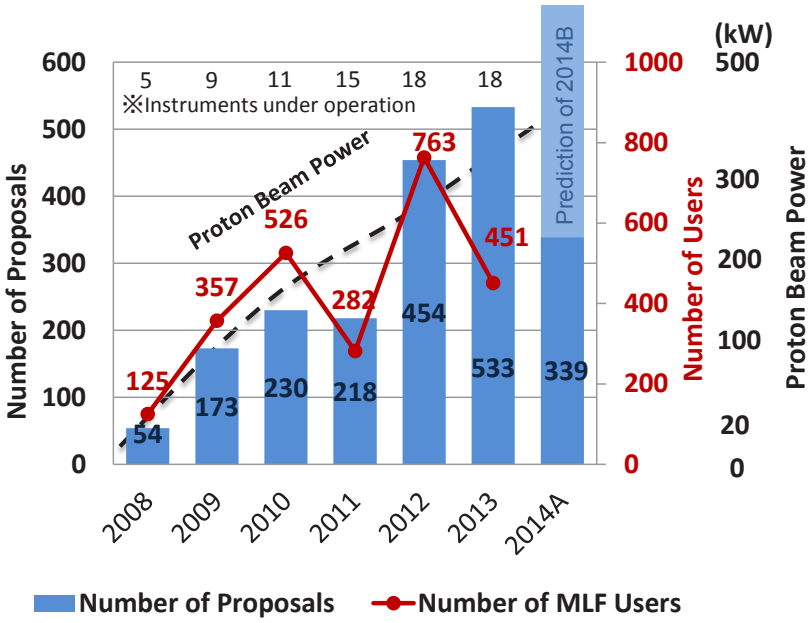

Figure 1. Number of proposals and users in MLF.

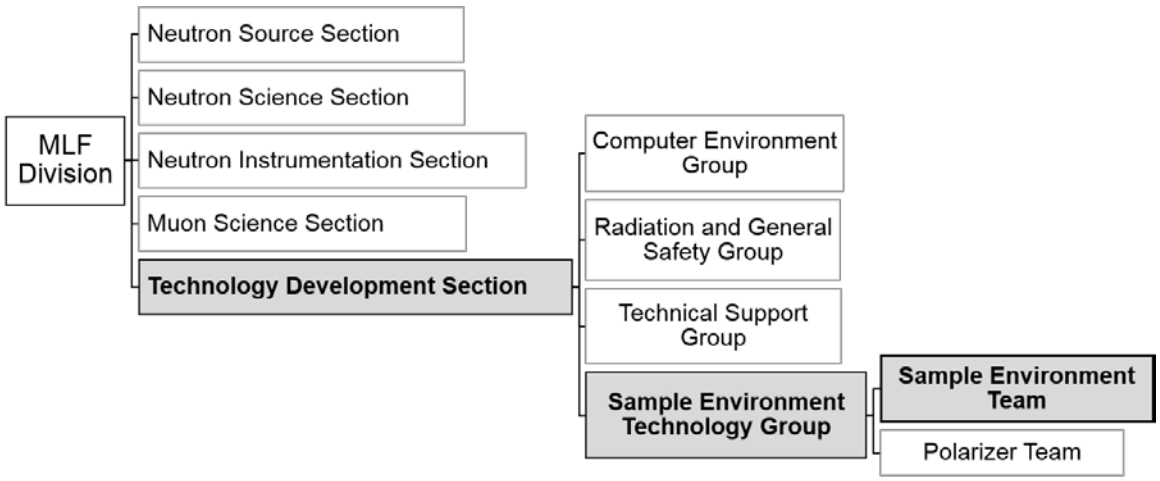

Figure 2. Organization of the MLF division.

In April 2013, the Materials and Life Science Division at J-PARC Center has established a new section, Technology Development Section, for the purpose of technical support of common equipment and development, operation and maintenance of common devices. The Technology Development

Section have four groups, Computer Environment Group, Radiation Safety Group, Technical Support Group and Sample Environment Technology Group as shown in Fig. 2. Then the SE team was officially organized in the Sample Environment Technology Group. The newly organized SE team consists of staff members from JAEA, KEK and CROSS so as to be able to support any beamlines (BL's) across the boundaries of institutes, no matter if it is a public BL or not. The new SE team aims to manage the overall SE in MLF, which is the first attempt in Japanese neutron scattering experimental facilities. Here we can take comprehensively safety measures on the whole equipment in MLF. In this team, we aim to establish a proper system composed of several professional sub-groups such as cryogenics and magnets, high temperature, high pressure, soft matter, and so on.

2. SE equipment

2.1 Standardization of SE in MLF

As mentioned above, we aim to prepare the SE equipment which is used commonly at each BL. Then we need to consider some compatibility among the instruments. We have discussed standardization of SE in MLF to provide a so-called "SE protocol", on the basis of the experience in practical experiments and by investigating the situation of other facilities, since the original SE team was organized. Each BL is enabled to use such BL-common SE equipment by referring to this guideline for designing the instrument. This results in sharing of technology, reducing costs and efficiency of experiments.

Table 1. Representative items in the SE protocol.

Items	Specification, Type, etc.
Dimensions for a vacuum scattering chamber	- Flange size: 200φ, 400φ and 800φ in accordance with JIS - 1000φ as an option flange. - Flange to beam center: 600 mm
PCD and size of bolts on a goniometer	- PCD: 650 mm (large equipment) / 260 mm (small equipment) - Size of the bolts: M12 (large equipment) / M10 (small equipment) - Goniometer to beam center: 350 mm (large equipment) / 210 mm (small equipment)
Standard closed-cycle refrigerator	- Cold head: RDK-415D (Sumitomo) - Compressor: F-50L (water-cooled)
Temperature controllers and censors	- Controllers: LakeShore 340 and 350 - Censor (T > 1.5 K, under zero magnetic field): Si diode censor - Censor (T > 1.5 K, under magnetic field): Cernox censor
Sample cells	- Bottom of the cold tail to beam center: 50mm - Dimensions at attachment: M4 x 8 screws, PCD 44 mm position - Dimensions at attachment (room temperature, 1 atm): M6 x 1 screw for powder samples
Pulse motor controller	PM16C-04XD(L) (16ch, Tsujicon)

The representative items in this protocol are listed in Table 1. For the instruments having a vacuum scattering chamber, such as the total diffractometer and chopper spectrometer, were recommended to refer to the standard dimensions of the flange shown in Table 1. An optional flange of 1000φ is expected to be used for additional devices such as a radial collimator and polarizer. A symmetric line including two bolts should be located on the neutron beam. For the instruments having a goniometer, such as the small-angle scattering instrument, PCD and size of the bolts to set the SE equipment on the goniometer are standardized for two kinds of equipment, large and small ones, as shown Table 1. Cryomagnets and some cryostats and furnaces are classified in the large equipment, while other compact systems are

classified in the small equipment. The instruments can use any BL-common SE equipment designed based on these two kinds of dimensions by preparing an appropriate adapter. The standard closed-cycle refrigerator (CCR) is available for the measurement at temperatures above ~4 K. Some instruments have a top-loading type of this CCR, and other have a bottom-loading type. The insert of the top-loading type CCR is not standardized at present. The recommended compressor, F-50, is a water-cooling type. The SE team possesses not only its spare but air-cooling type compressors (CSA-71A), so that one can carry out test operation of the CCR even in the period when the cooling water is not supplied. The standard temperature controller has been decided to be LakeShore 340. However, we currently recommend LakeShore 350 as a new standard because manufacturing LakeShore 340 has already been stopped. Dimension around the sample cell is standardized by entirely referring to that at the Research Reactor JRR-3, since some users relatively use the reactor (JRR-3) and spallation source (MLF). To control the rotary stage on the SE equipment, the SE team recommends to introduce a pulse motor controller listed in Table 1 (Tsujicon), which can be controlled on a software for data taking. Note that we have also discussed other items such as coupling for cooling water and helium recovery lines and data logger

Table 2. Typical SE equipment prepared by each BL.

BL	SE equipment
BL01	4K top-loading cryostat, high-temp. insert
BL02	Top-loading cryofurnace
BL03	Gas-flow cryostat
BL04	Auto sample changer
BL08	4K cryostat, 1K cryostat, 10K top-loading cryostat, V-furnace, Auto sample changer
BL09	10-700K top-loading hot stage, 4K top-loading cryostat, 1000K furnace, Auto sample changer for installing V-Ni holder, Auto sample changer for in-situ measurement, Storage battery cell
BL10	Goniometer (5-axes)
BL11	Multi-anvil press (500 t x 6 axes), Paris Edinburgh press (200 t), Palm cubic press (100 t), Low-temperature press (100 t)
BL12	4K cryostat, 6K cryostat, ^{3}He cryostat, 14T vertical-field magnet
BL14	4K bottom-loading cryostat, Top-loading cryofurnace
BL15	Auto sample changer, Loading machine, 10T vertical-field magnet, 4T horizontal-field magnet Laser furnace, 4K bottom-loading cryostat, Air core electromagnet,
BL16	Auto sample changer, High-temperature cell, Low-temperature cell, Humidity controlled cell
BL17	Electromagnet, 4K cryocooler
BL18	4K cryostat, 2-axis goniometer, 1-axis goniometer, High-pressure cell
BL19	Loading machine, Furnace system for high temperature loading, Dilatometer, Cryogenic loading machine, Eurelian cradle, Gandolfi goniometer + heater, Fatigue machine, High temperature loading machine for small sample, 100K cooling chamber for loading experiment
BL20	Auto sample changer, 30 sample changer, V-furnace, Atmosphere furnace, Cryofurnace with sample changer, Goniometer
BL21	Auto sample changer, in-situ meas, V foil heater, Cryofurnace, Impedance measurement system, Temperature-controlled sample changer, 2 dimensional element spectroscopy system

2.2 SE equipment

In MLF, some SE equipment, which is dedicated for an instrument, strongly required by users or used frequently as a standard one, has been managed and operated by the instrument staff at each BL. Representative SE equipment prepared at BL's is shown in Table 2. Some of them are designed based on the SE protocol, in order to enable us to use them even at another instrument. On the other hand, the SE team has introduced and managed the BL-common SE equipment, which may not be frequently used but is necessary. At present, we possess four pieces of the BL-common SE equipment, which are in operation or under commissioning: a vertical-field superconducting cryomagnet, a ^{3}He-^{4}He dilution refrigerator insert, a top-loading-type ^{4}He cryostat and a high-temperature furnace with an Nb heater. We have managed them and support their operation during users' experiments. Note that we plan to introduce other equipment in response to users' demands in the future.

Figure 3. BL-common SE equipment managed by the SE team. (a) Vertical-field superconducting cryomagnet, (b) ^{3}He-^{4}He dilution refrigerator insert, (c) top-loading-type ^{4}He cryostat and (d) High-temperature furnace with a Nb heater.

Figure 3(a) shows the vertical-field superconducting cryomagnet (Scientific Magnetics). This equipment has an asymmetric-coil pair so that it can be used even in the polarized neutron experiment, and its maximum magnetic field is 7 T. The magnet coils are coated with B_4C, which is a neutron

absorber. The magnet was designed supposing that an open angle in the vertical direction is ±10º for 20 mm of the sample height. In the horizontal direction, the magnet has 30º of a blind angle for pipes and wires, the direction of which was determined by investigating the detector positions at most instruments. The system has a liquid helium bath without any re-condense system. The sample stick is rotated approximately 180º, and is cooled down to 1.5 K. This cryomagnet can be set both on a vacuum scattering chamber with the 800φ flange and on a goniometer. As the system has aluminum windows, it is suitable for the single-crystal diffractometers, chopper spectrometer, small-angle neutron scattering (SANS) instrument etc. rather than the powder diffractometer. On-beam commissioning works have been carried out at cold-neutron disk-chopper spectrometer, AMATERAS (BL14), polarized neutron reflectometer, SHARAKU (BL17) and extreme environment single crystal neutron diffractometer, SENJU (BL18) [1].

Other than the conventional sample stick, a ^{3}He-^{4}He dilution refrigerator insert (Taiyo-Nippon Sanso co.), shown in Fig. 3(b), can be also set into the cryomagnet. The lowest temperature is below 100 mK, and we have achieved 50 mK with no sample during the first test operation. The inner diameter of the sample space is 40 mm, and the distance from the bottom surface of the cold head to the beam center is 40 mm, which is shorter than the standard value in MLF. This insert is currently under commissioning. In order to use this dilution refrigerator insert in the measurement under zero magnetic field, we have prepared a top-loading-type ^{4}He cryostat, which was manufactured by Suzuki Shokan co. (Fig. 3(c)). This cryostat is a wet system having liquid helium and nitrogen baths, and has a rotary stage of the insert. Temperature range is from 2K to the room temperature. As the system also has aluminum tails and windows as well as the cryomagnet. The system has a 400φ flange to be set on the vacuum scattering chamber, and also can be set onto a goniometer as the small-size equipment. This equipment is still under commissioning.

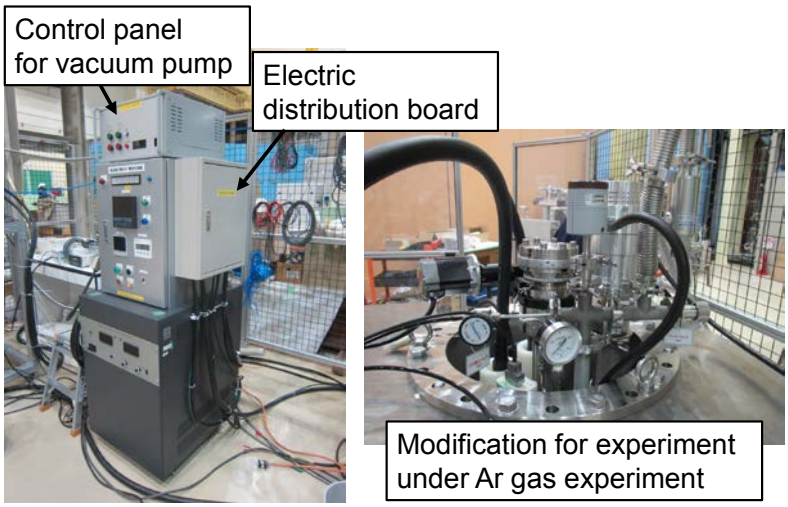

Figure 4. High-temperature furnace after the improvements.

Figure 3(d) shows a high-temperature furnace with a niobium heater, manufactured by AS Scientific Products. The maximum operating temperature is 1600 ºC in a vacuum and 1300 ºC in an argon gas. The sample stick can be rotated. The heater part and surrounding radiation shields are made of niobium, which is known to make up few background due to incoherent scattering. Therefore, this furnace is mainly used at quasielastic and inelastic scattering instruments. However, the elastic scattering from many niobium foils on the direct beam causes serious background in the nonzero region of energy transfer because the flight paths for neutrons scattered at a niobium foils are slightly shorter

or longer than that for neutrons scattered at the sample. Thus, an oscillating radial collimator have been developed by some instruments to be used together with the furnace [2]. This equipment is now in operation and has ever been used for the experiments at AMATERAS (BL14) and small and wide angle neutron scattering instrument, TAIKAN (BL15). We note that some improvements have been made by the SE team, as shown in Fig. 4. A control panel for vacuum pumps and an electric distribution board were installed for users' convenience and safety. A gas inlet line was equipped in order to conduct a high-temperature experiment under argon atmosphere. Taking into account the heating up of the outer case of the furnace, we decided on a rule that an experiment under argon atmosphere must be performed below 1300 ºC.

3. Infrastructure for SE

It is essential to keep the infrastructure, which is a so-called "SE area", to prepare the SE equipment for users' experiments and to maintain its performance inside or near the experimental hall. There was no such an area when the MLF started operation. We prepared the SE areas in the 1st and 2nd experimental halls in MLF in a few recent years (Fig.5). Although the experimental hall was already occupied by instruments and their cabins, we could prepare the SE area with a space of ~30 m^2 in the 1st experimental hall. On the other hand, there was less space in the 2nd experimental hall. We can use a space of ~20 m^2 as the SE area in the 2nd experimental hall for the duration of the beam operation, while its area is reduced to half so that the rest area is used for other purposes for the construction works during the shutdown period. Utilities such as the power supply, cooling water line, compressed air line, helium gas recovery line and the exhaust line have been introduced in both SE areas, and then we started the commissioning and maintenance of the SE equipment, repair and replacement of parts, and so on. Taking into account that the number of the SE equipment increases in near future, the current SE areas in the experimental halls are definitely insufficient. Thus we need to discuss a solution to expand the area, though there is no available space inside the both experimental halls.

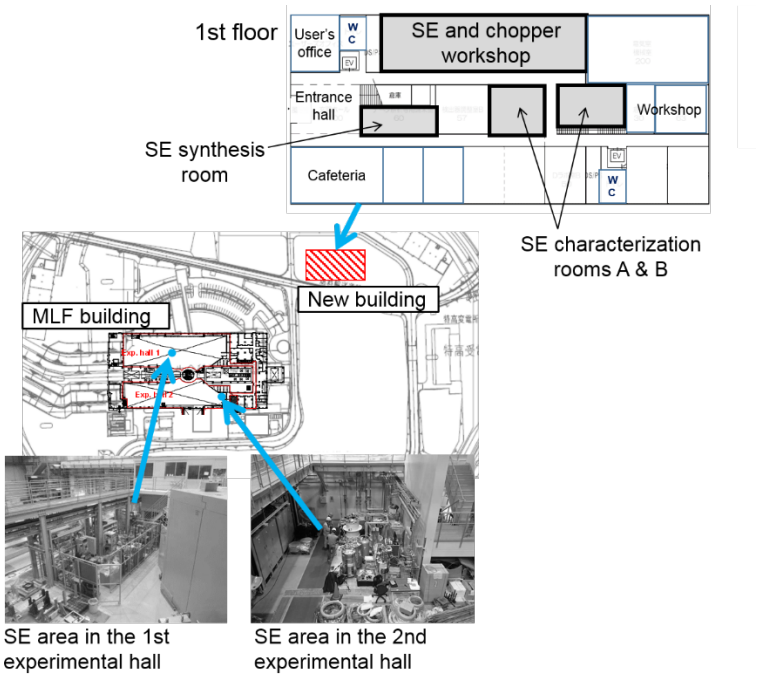

Figure 5. Working areas related to SE in the MLF building and the new building.

A new building for the MLF user support, which is being constructed near the MLF building, is about to be completed in the end of March 2015. This building is used for the things related to the user

support, such as sample preparation, data analysis, development and maintenance of devices, and so on. As far as SE is concerned, it is planned to prepare an SE and chopper workshop, which is dedicated for maintenance of the SE equipment and choppers, a sample synthesis room, sample characterization rooms for various research field and a chemical laboratory on the first floor, as shown in Fig. 5. In the SE and chopper workshop, long-term commissioning and maintenance of the SE equipment will be carried out. In addition, the development of the new SE equipment will also be conducted here. This room is shared with the chopper development group, which works on development and commissioning of choppers. In the sample synthesis room, users can prepare the samples before bringing them into MLF. In the characterization rooms, various measurements, such as structure analysis and magnetic susceptibility, specific-heat and adsorption measurements, can be performed before the experiment.

4. Safety

Figure 6 shows the safety examination system for users' equipment and devices in MLF. Some of us (W.K., T.O., Y.S. and K.A.) are the regular members and one of us (Y.Y.) is a cooperative member of the MLF equipment safety committee, and we contribute to the improvement on the safety environment at MLF. This system is also applied for the SE equipment and devices, including those prepared by the BL groups. The safety examination is conducted by the committee, and the equipment is allowed to be used at MLF, on the basis of the result.

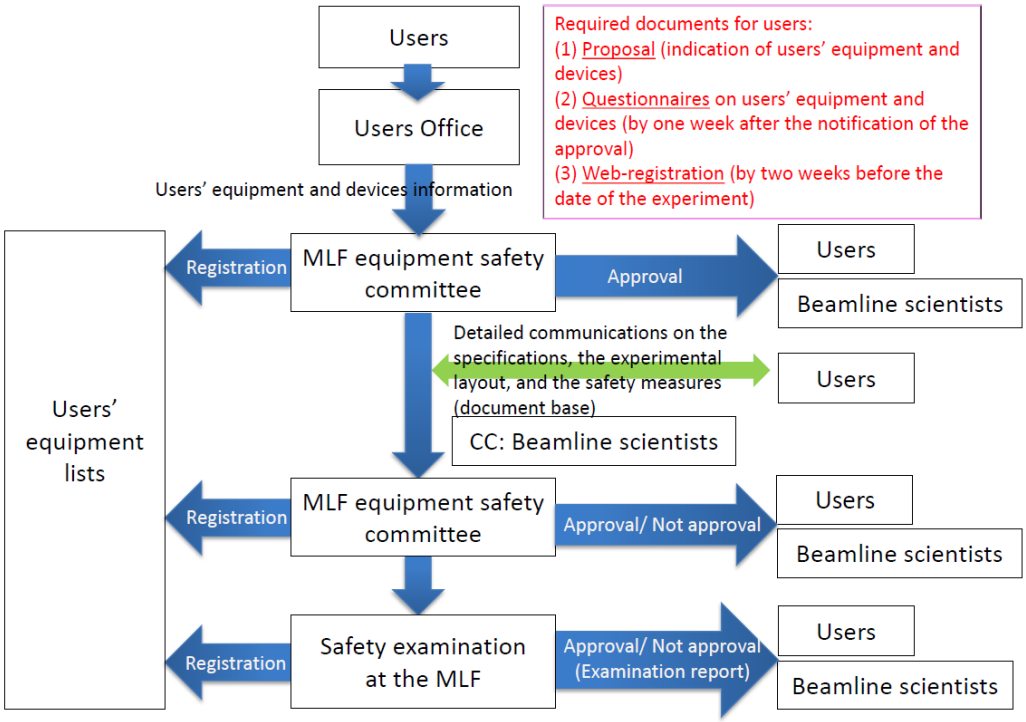

Figure 6. Safety examination system for users' equipment and devices at the MLF

The SE team contributes to the improvement on safety related to the SE equipment at MLF. Here we show the safety measures on the top-loading-type cryostat we took as an example. The top-loading-type cryostat generally contains a risk caused by inappropriate setting of a sample stick. Namely, the air could be inhaled inside the sample space continuously from a small leakage at the O-ring to be condensed there, when the sample stick is cooled down. As the result, the sample stick may be ejected

suddenly when changing the sample, due to rapid evaporation of the accidentally condensed air. In fact, MLF has ever experienced this incident during a user's experiment. Responding to this problem, we have taken the following steps to prevent such incidents, and have strongly recommended each BL that possesses a top-loading cryostat irrespective of whether the system is wet or dry to take these safety measures.

The safety measures taken on the top-loading cryostat at MLF are displayed in Fig. 7. Firstly, we modified the sample stick to have an open end and added a relief valve on the tube just below the top flange so that the excess pressure is released through the end hole, the relief valve on the center stick and the original relief valve on the cryostat even when the bottom baffle of the sample space is sealed by an ice block. As a further step, we applied "D-cuts" to the baffles to prevent for a baffle to be sealed entirely by ice. In addition, especially for the inserts with no hollow tubes such as dilution refrigerator, a short detachable stainless wire is necessarily connected to the cryostat and its insert when the insert is pulled up for the sample exchange, to avoid ejection of the insert. It is also recommended to adopt the O-ring with a center ring to place the O-ring surely.

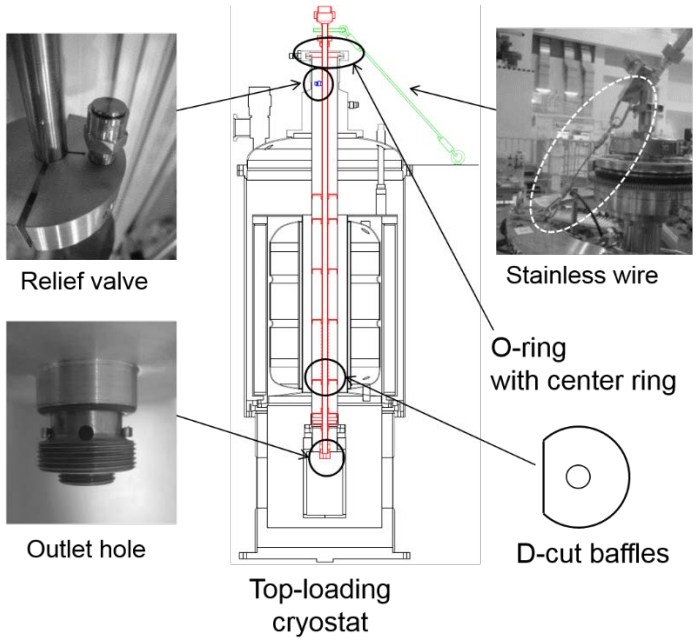

Figure 7. The recommended safety measures for top-loading cryostat.

5. Summary

The SE team has been officially organized in the Technology Development Section newly established in MLF. We are working on management and operation of BL-common SE equipment and development of SE devices. The SE team has discussed standardization of SE in MLF since the previous SE team was organized, based on our experience in practical experiments and by investigating the situation of other facilities. This guideline is recommended to be referred by each instrument. We have prepared some pieces of the versatile BL-common SE equipment, which are a vertical-field superconducting cryomagnet, dilution refrigerator insert, ^{4}He cryostat and high-temperature furnace. They are now in operation or under commissioning. The SE areas were prepared in the 1st and 2nd experimental halls, and have been used for short-term commissioning on the SE equipment and preparation of it for users' experiments. We will also equip more areas related to SE, such as the SE workshop and sample preparation room, in the new building for user support. Furthermore, some of us

contribute to the improvement on safety environment in MLF as the members of the MLF equipment safety committee. Then we take comprehensively safety measures even on the user's carry-in devices and BL-dedicated SE equipment in MLF. We note that we have just started preparation of some new environments as follows. Responding to users' request, we have just started preparing high pressure system, aiming to finally develop low-temperature and high-pressure environment for inelastic neutron scattering. We are also planning to generalize the pulsed magnet system for neutron scattering, which H. Nojiri and co-workers have developed at Spallation Neutron Source (SNS) in Oak Ridge National Laboratory and MLF [3], by cooperating with them, in order to introduce it for the general users.

References

[1] Ohhara T, Kiyanagi R, Kaneko K, Tamura I, Nakao A, Hanashima T, Munakata K, Moyoshi T, Kuroda T, Oikawa K, Kawasaki T, Yamauchi Y and Ohira-Kawamura S *JPS Conf. Proc.* in press.
[2] Nakamura M, Kawakita Y, Kambara W, Aoyama K, Kajimoto R, Nakajima K, Ohira-Kawamura S, Ikeuchi K, Kikuchi T, Inamura Y, Iida K, Kamazawa K and Ishikado M *JPS Conf. Proc.* in press.
[3] Nojiri H, Yoshii S, Yasui M, Okada K, Matsuda M, Jung J-S, Kimura T, Santodonato L, Granroth G E, Ross K A, Carlo J P and Gaulin B D 2011 *Phys. Rev. Lett.* **106** 237202; Ohoyama K, Lee S, Yoshii S, Narumi Y, Morioka T, Nojiri H, Jeon G S, Cheong S-W and Park J-G 2011 *J. Phys. Soc. Jpn.* **80** 125001.

This is a blank page.

3-8. Shielding

This is a blank page.

3.8.1

Development of helium vessel in CSNS

Li Lin[12], Wei He[12], Haibiao Zheng[12], Tianjiao Liang[23], Jianfei Tong[12]

1China Spallation Neutron Source (CSNS), Institute of High Energy Physics (IHEP), Chinese Academy of Sciences (CAS)， Dongguan 523803, China
2Dongguan Neutron Science Center (DNSC), Dongguan 523808, China
3Institute of Physics, CAS, Beijing 100190, China

linli@ihep.ac.cn

Abstract. Helium vessel is one of important equipments in target station of CSNS, which maintains an inert environment （helium at a slight positive pressure）around the moderators, provides credited confinement functions, and provides access ports for the proton beam, 20 neutron beams and the target. Helium vessel components should be designed to last more than 40 full power years. Water cooling has been arranged in sections of helium vessel to remove the heat deposited by a 500kW beam. This paper describes the thermal analysis and thermal-solid coupling analysis which is performed to optimize structural design.

1. Introduction

CSNS is designed to accelerate proton beam pulses to 1.6GeV kinetic energy at 25Hz repetition rate, striking a solid metal target to produce spallation neutrons. The accelerator is designed to deliver a beam power of 100KW with the upgrade capability to 500kW by raising the linac output energy and increasing the beam intensity. Figure 1 shows a pictorial view of CSNS.

Figure 1. Pictorial view of CSNS

2. Overview

The functions of helium vessel system are to maintain an inert environment (helium at a slight positive pressure) around the moderators, provide a locating surface and structural support for target and proton beam window assembly, support the reflector plug, provide containment in the event of a failure of the target, moderators and reflector plug, and provide access for cooling water to reflector plug and moderators and access for liquid hydrogen line to moderators.

2.1 Design requirements

Helium vessel system components should be for 500kW beam power based on a proton beam energy of 1.6GeV and an average beam current on target of 312.5 uA. Non-replaceable components should have a design basis lifetime of 40 years, while replaceable components should be designed for maximum life within engineering and budget constraints. The mean design requirements are following.

- Inert atmosphere: Vessel should provides an inert atmosphere in the event of a hydrogen leak from the moderatos and containment of activated cooling water in the event of a water leak from the target or the reflector.
- Structural: Helium vessel system should be designed to carry the combined stresses due to coolant pressure, dead-weight loads, thermal effects, and seismic events.
- Thermohydraulic: The cooling water system must remove the heat deposited by a 500kW beam.
- Mechanical: The vessel should provide access ports for proton beam, neutron beams and target. The vessel should provide feedthrough ports for the reflector and moderators piping and connections for vessel utilities. The vessel upper head should allow for replacement of the reflector plugs.
- Remote maintenance: The vessel and neutron beam window should facilitate the use of remote handling equipments used to service the neutron beam window and reflector plugs.
- Seismic: All components should be designed such that the safety functions are maintained during a seismic event up to the 7 degree seismic intensity.
- Instrument and control: Systems will procure the sensors required to measure pressure, temperature and flow, and will provide mounts and taps as required for each instrument at locations throughout the system.
- Decommissioning: System should be designed for disassembly and decommissioning.
- Materials: Material for all structural components should be 316L & 304L austenitic stainless steel.
- Design standard: Vessel should be designed and fabricated according to China national standard JB4732-1995 (The Steel Pressure Vessel-Design by Analysis code).

2.2 Lay out

Helium vessel system (shown in Figure 2) is a vertical cylindrical geometry. It provides access for installing and removing the reflector assemblies vertically through the core vessel top opening, and for installing the target through horizontal ports in the core vessel. The whole system includes the core vessel, the support skirt, the outer reflector, and utility piping inside the core vessel (i.e., vacuum, helium, cooling piping).

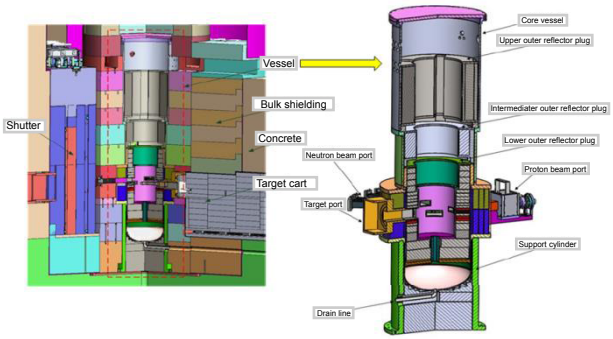

Figure 2. Helium vessel system layout

3. Detail design

3.1 The core vessel

As shown in Figure 3, the core vessel is made up of three components, the chimney assembly, the center section and the lower vessel that are welded together.

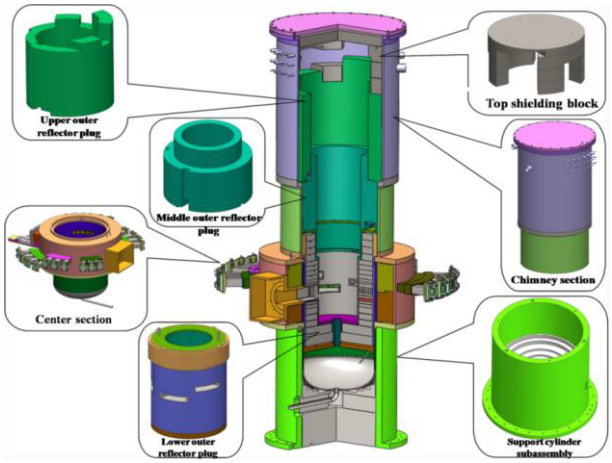

Figure 3. Helium vessel main parts

The chimney is a S30403 step-shaped cylinder structure with a nominal diameter of 2100/2280 mm and a height of 4350 mm. The nominal wall thickness is 50 mm.

The center section is jacket structure with a nominal diameter of 2900 mm and a height of 1400 mm. The nominal wall thickness is 50 mm. The jacket encloses the water-cooled shielding with holes machined for cooling water. The center section contains the proton beam interface, the target interface, and the neutron beam lines. The center section shown in Figure 4.

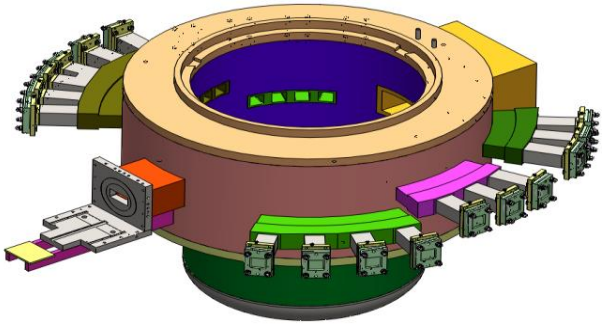

Figure 4. Lower core vessel

Proton beam window (PBW) separates the helium or rough vacuum environment inside the vessel from the high vacuum inside the proton beam line. The proton beam window will be replaced periodically because of accumulated material damage caused by proton fluence. To facilitate replacement of this intensely heated and irradiated structure, pneumatic (inert gas) seals and a vertical assembly and removal path are incorporated into the design. To minimize scattering losses, the window will be located outside the lower vessel, approximately 1890 mm from the center. The window will be located within a housing which also contains the proton beam diagnostics as shown in Figure 5. The sealing surfaces are inside the housing attached to the core vessel. The shelf, flange, and rectangular tube extension should be cooled by light water because of the heat generated by scatter from PBW. The cooling passage is produced by drill and plug. Small shelf is extended from the box for remote vacuum seal clamp to RTBT tube. The housing will support 5 tons load from PBW assembly.

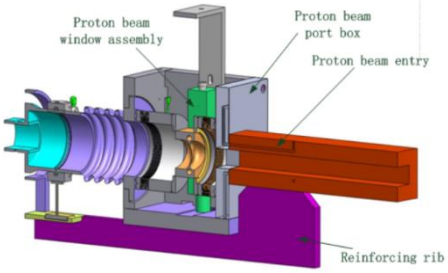

Figure 5. Proton beam port

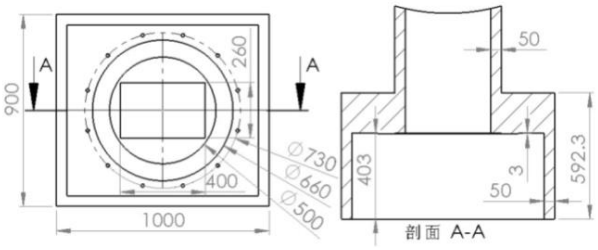

Figure 6. Target box

Target will be inserted into a target box are showed Figure 6. Inside surface of the box provides a mating surface for target inflatable seal, required surface roughness of Ra 0.2um.

Helium vessel has 20 neutron beam lines, eleven above the target, eight below the target and high energy neutron beam. The neutron beam slots which view the decouple moderators will be lined with decoupler material which is cadmium with thickness of 1mm. Neutron beam port windows with seals will be bolted to the flanges shown in Figure 7. These windows have the shape of a convex spherical surface (thickness 1.5mm, Al 6061). Double racetrack seals made of close-wound helical spring and aluminum jacket are used for seal. These windows are expected to have a long lifetime based on the experience of existing spallation facilities. So the design of the neutron beam windows will facilitate the remote handling.

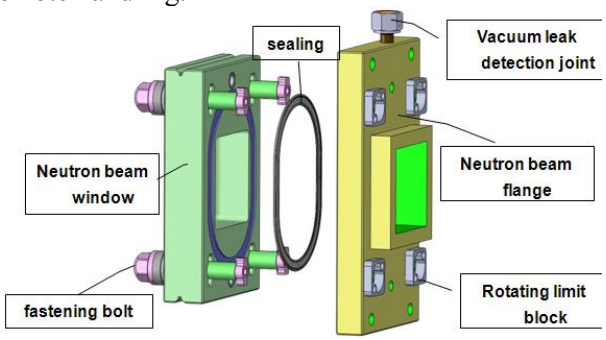

Figure 7. Neutron beam window

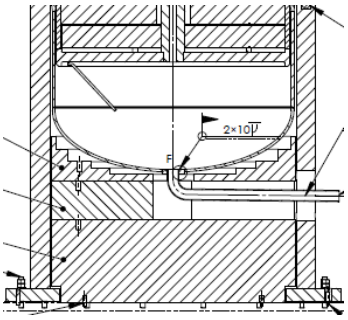

Figure 8. Drain line

The lower vessel is composed of lower cylinder and ellipse head. The collection volume attached to the lower vessel is designed to contain any water that might spill into the core vessel in the event of a failure of the target or reflector.

The drain line is allowed to remove any liquids spilled into the helium vessel. As shown in Figure 8, the drain line terminates in drain tank designed to accommodate the maximum feasible spillage of cooling water inventory. The drain line is a DN80 single wall pipe sloped down to the drain tank (hydraulic slope 2%), which is welded to core vessel when assembly. Ultrasonic and penetrant inspection must be performed after welding on site. Procurement initiated on the drain line so that section embedded in concrete will be available during building construction.

3.2 Support skirt

The support skirt with a nominal wall thickness of 150mm supports the core vessel and all vessel internal components independently from the external shielding, shown in Figure 9. The support skirt is tied into the foundation mat by studs threaded into the base plate embedded in the concrete. These studs bear shear and overturning moment created in a seismic event. A stainless steel layer is built on the upper surface of the support skirt by surfacing welding in order to prevent the interface between support skirt made of carbon steel and vessel made of stainless steel from corrosion.

Figure 9. Support skirt roundness correction

3.3 The outer reflector

The outer reflector plugs consist of top shielding, upper outer reflector plug, middle outer reflector plug and lower outer reflector plug. As shown in Figure 10, the outer reflector plugs with steps to prevent radiation streaming surrounds the inner plug.

The lower outer plug must be cooled with light water, while the other outer plugs do not need. The lower outer plug made of stainless steel is contained within the lower 1870mm-diameter core vessel and slots are cut for the neutron beam lines, the proton beam and the target assembly. The neutron beam slots will be lined with decoupler material similar to which in the inner plugs. Neutron decouplers, which can keep the pulse width short, are made from 1mm thick cadmium. The size of the proton beam hole will be close to that of the nominal beam profile so that, in off-normal cases, stray proton beam energy would be absorbed in this plug rather than in the moderators. A supply line within the plug will bring the light water to the bottom, and the return flow to the top will cool the stainless shielding. The weight of the outer plug assembly is 31 tones. It will be supported on a ring resting on the base of the lower core vessel.

The intermediate and upper outer plugs surround the inner plug and slots are cut for the reflector and moderator piping (cooling, helium and vacuum). The intermediate and upper outer plugs are made of carbon steel with aluminum coating (thickness ≥150 μm). The upper outer plug relies on conduction to the actively cooled components. To minimize the number of remote connectors of piping, the intermediate and upper outer plugs extend 3960 mm above the target center and all connections are located above the plugs.

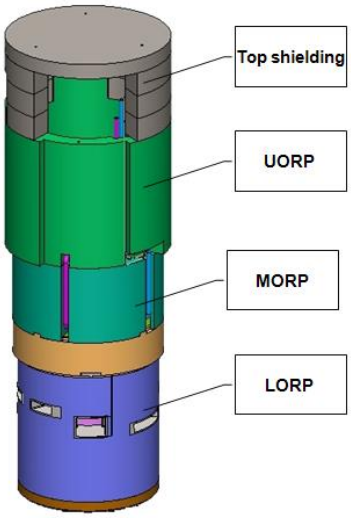

Figure 10. Outer reflector

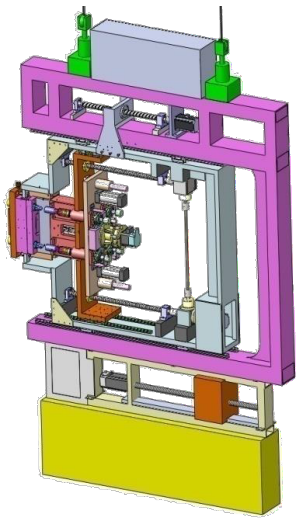

Figure 11. Remote handling device for neutron beam window

3.4 Remote handling device for neutron beam window

The neutron beam windows provide the pressure boundary at the inlets of the neutron beam ports. Studs in the helium vessel flanges and remotely installed nuts secure the window to the vessel flanges and provide the necessary sealing force. The windows are expected to have a long lifetime based on the experience of existing spallation facilities. However, design of the neutron beam windows should facilitate the remote replacement of this irradiated structure because of accumulated material damage caused by neutron fluence. As shown in Figure 11, remote handling device contains two components: bodies supporting frames and elevating section which includes hanger, window handling system and balancing system. Maintain operation will be performed in the gap between bulk shield interstitial blocks.

4. Analysis calculation

4.1 Thermal calculation

In order to study thermal deposition and power-density distribution of helium vessel, the model of target-moderators-reflectors-core vessel was built by MCNPX, and then calculates thermal deposition and power-density distribution of components in helium vessel. The thermal deposition of core vessel contains: lower outer reflector plug, center section of helium vessel and some passive-cooling shielding. Table 1 shows the thermal deposition of helium vessel and inner components.

Table 1. Helium vessel thermal deposition

Components	Heat deposition (500kW)	Cooling mode
Lower outer reflector plug	53kW	Water-cooling
Center section of helium vessel	12kW	Water-cooling
Middle and upper outer reflector	179.4W	Passive cooling
Passive-cooling Shielding	203.1W	Passive cooling
Total	65.04kW	

The maximum temperature below 64℃ present to target port tube due to high heat deposition at 500kW, Figure 12 shows the temperature distribution of center section and lower outer reflector plug after water-cooling as input data of thermal-solid coupling analysis. As a whole, the temperature was well-distributed and difference in temperature was less than 20℃, the temperature near proton beam port should be lower due to proton beam cooling structure.

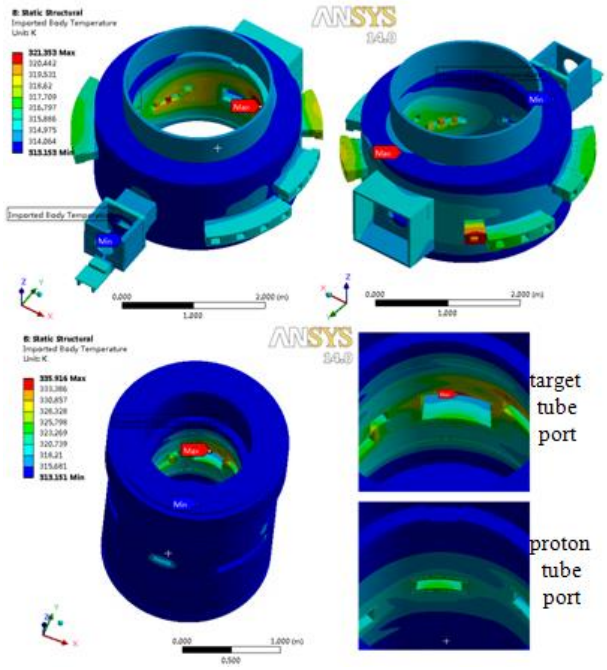

Figure 12. Temperature distribution of center section and lower outer reflector plug after water-cooling

4.2 Structure strength analysis

FEA analysis was performed using the helium vessel model compromise of shell and solid elements imposed appropriate loading according to different working conditions. Analysis criterion were as follows:

- The temperature has been predicted to reach a maximum of 65℃.
- The allowable design stress intensity for all forms of S30403 is 118MPa for any temperature less than 150℃ (JB4732-95).
- The allowable design stress intensity of Al6061T6 is 68MPa for any temperature less than 100℃ (JB4734-2002).
- The maximum displacement less than 2mm.

For integral model three different calculation conditions were considered, such as working condition, design condition and maintenance condition. There were four calculation conditions of lower outer reflector plug, such as working condition, design condition, maintenance condition and cooling failure condition.

4.2.1 Vessel working conditions structure strength analysis

Shows Integral model working conditions stress & deflection, for example, FEA analysis was initially performed using the full model of the vessel. Applied loads include:

- 0.0025 MPa internal overpressure
- 0.4 MPa pressure in the water jacket
- Gravity loads of all internal shielding and equipment
- 100 kN inflatable seal force in target port
- 50 kN inflatable seal force in proton beam port
- 5 Tons gravity load on proton beam port

Restraint: support skirt bottom plane full restraint, shown in Figure 13.

Conclusions: Figure 13 shows the maximum stress intensity appears on upper support plate groove for lower outer reflector plug alignment block, the maximum stress intensity is 47.854MPa. The maximum displacement is 0.264 mm in proton beam port. With the proper corner radius to reduce stress concentration at this location, the vessel satisfies the requirements of the allowable design stress intensity by the pressure vessel code. Vessel deflections are small.

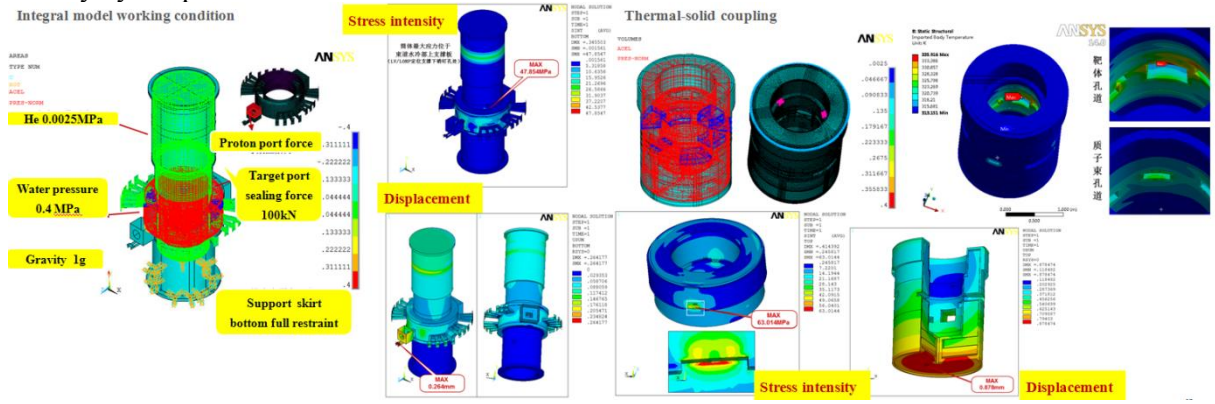

Figure 13. Vessel working condition FEA model

Figure 14. Lower outer reflector plug FEA model

4.2.2 LOPP working conditions thermal-solid coupling analysis

FEA analysis was initially performed using the model of lower outer reflector plug. Applied loads include:

- 0.0025MPa internal overpressure
- 0.5MPa pressure in the water jacket
- Gravity loads of all internal shielding and equipment
- shielding equivalent pressure 0.153&11.313MPa
- the temperature distribution of water-cooling, MAX temperature 62.916℃

Restraint: lower outer reflector plug alignment block groove side toroidal restraint and groove plane axial restraint, shown in Figure 14.

Conclusions: Figure 14 shows the maximum stress intensity appears on upper support plate groove for lower outer reflector plug alignment block, the maximum stress intensity is 63.014MPa. The maximum displacement is 0.878 mm in proton beam port. With the proper corner radius to reduce stress concentration at this location, the vessel satisfies the requirements of the allowable design stress intensity by the pressure vessel code. Vessel deflections are small.

4.3 Anti seismic calculation

CSNS located in Dong guan City, Guangdong Province where seismic fortification intensity is level 6. The helium vessel is defined as important facility, seismic fortification intensity of helium vessel is level 7. The seismic load will be represented by a 0.2G lateral acceleration (single direction, not vibrating). The purpose of this study is to document the stresses and deflections associated with a seismic event, FEA analysis was initially performed using the full model of the vessel. Applied loads include:

- 0.1MPa internal overpressure
- 0.6MPa pressure in the water jacket
- Gravity loads of all internal shielding and equipment
- 100kN inflatable seal force in target port
- 50kN inflatable seal force in proton beam port
- 5Tons gravity load on proton beam port
- 0.2g horizontal acceleration (along target direction)

Restraint: Support skirt bottom plane full restraint, shown in Figure 15.

Conclusions: Figure 15 shows the maximum stress intensity is 68.508MPa which appears on support skirt pin contact. The maximum displacement is 0.988mm at center of lid.

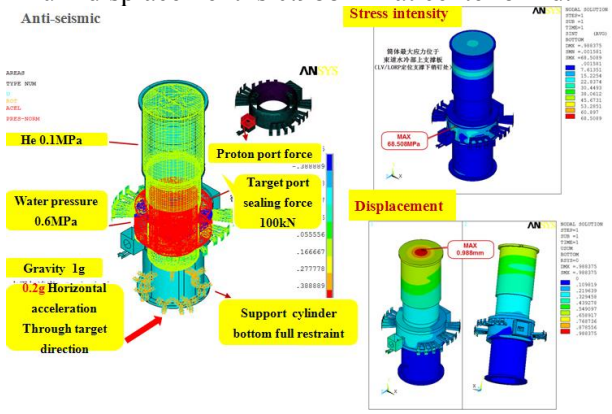

Figure 15. Vessel anti-seismic FEA model

5. Manufacture and installing

5.1 Manufacture progress

The helium vessel manufacturing process review was held in Nanjing on January 2013. The review content included manufacturing process scheme, quality plan and production schedule. The detailed engineering drawings of helium vessel were formally issued on January 2013, and formal processing was started.

5.1.1 Center section

Cylinder and the lower flange were assembled, fixed support in the cylinder upper opening, and welded after the cylinder rolling, welding, and roundness correction. The wall and end-face of the outer and inner cylinder were machined by vertical lathe, based on the lower flange surface, adjusting cylinder to coincide with the center of the turntable of CNC facing boring lathe, and then indexing to determining the location of the fan-shaped and square-shaped hole, boring the holes. Assembling and welding the tube blocks, shielding block, the upper flange, etc. Assembling error of all tubes are measured and adjusted to the allowable range. Welding deformation is the main factor causing manufacturing errors of all tubes. To reduce the welding deformation, fixing support, taking anti-deformation to ensure the correct position of each tube. Real-time monitoring the deformations and adjusting the welding sequence, lowering welding input and interpass temperature during the manufacturing process. Finishing the protons and the target tubes connecting flange, polishing to the requirement with

the lower flange surface as the reference plane, Figure 16 & 17 shows center section is under assembling and welding.

Figure 16. Center section assembling

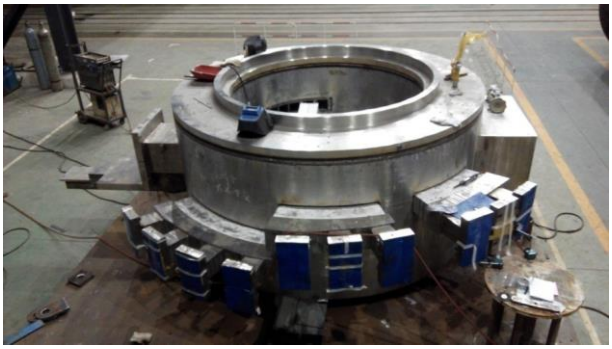

Figure 17. Center section welding

The neutron beam tube block consist of upper & lower plates and interval block, reserving machining allowance on the upper and lower plate thickness, the side face of outside plate, the interval block processed; sandwiching cadmium plate between those plates and stainless steel plate, and then bolting; assembling the plates, and inserting the square (114 × 114) mandrel to correct position of each plate, bolting and welding, plug welding thread sink hole on the interval block. Machining tube profile, positioning face and positioning stepped square hole with inner hole as reference. Inserting the square mandrel (H8/e8 fits) to assembling and welding the branch tube and confluence tube; taking anti-deformation measures to reduce welding deformation, finally finishing the flange face to the requirement.

5.1.2chimney section

Chimney section cylinder has been rolled, welded, roundness correction, vibration aging was proceeded, and then boring pipe openings according to piping layout design. Figure 18 shows Chimney section in assembling.

Figure 18. Chimney section welding

5.1.3 LORP

Cylinder and the lower flange are assembled, fixed support in the cylinder upper opening, and welded after the inside and outside cylinders rolling, welding, roundness correction. The wall and end-face of the outer & inner cylinder are machined by vertical lathe. Assembling and welding partially cooling plate, and the lower flange, fixing support in the cylinder upper opening to prevent deformation. Based on the lower flange face, adjusting cylinder to coincides with the center of the turntable of CNC facing boring lathe, and then indexing to determining the location of the fan-shaped and square-shaped hole,

boring the holes. Assembling and welding the tubes, cooling plates, the upper flange, etc. Fixing support, taking anti-deformation measures to ensure the correct position of each tube. Finishing the outer wall of the cylinder, positioning groove and end face by vertical lathe.

5.2 Installation of support skirt

Before installation of support skirt, installation error of the base plate was reinspected. Use pins in the base plate to positioning the support skirt. Use four screws in the foundation ring of the support skirt to adjust the upper surface elevation of the support skirt to 1.1m (error is less than 0.5mm), All installation and adjustment were monitored by laser tracker. Installing inner shielding block in the support cylinder, then welding drain line. Figure 19 shows support skirt after installation.

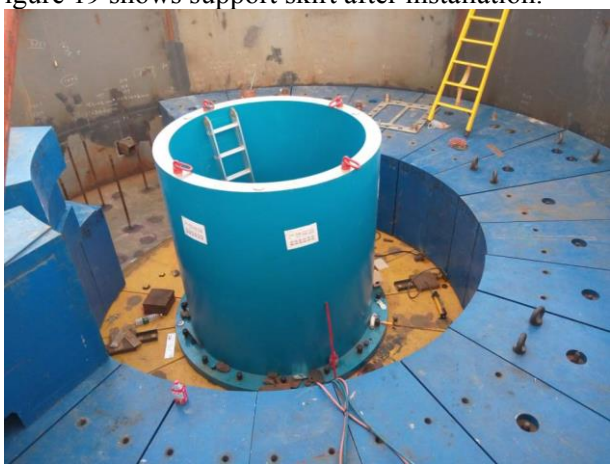

Figure19. Support skirt installment

5.3 Acceptance Testing Requirement

After completion of installation and prior to commissioning with the proton beam, a series of tests shall be performed on the Vessel Systems to insure and demonstrate their readiness for operation. The following tests shall be performed as part of acceptance testing:

- Demonstrate leak tightness of assembled water piping;
- Demonstrate leak tightness of the core vessel pressure boundary for both vacuum and helium environments;
- Demonstrate ability to install the proton beam window using remote handling equipment;
- Demonstrate ability to make and break pipe and structural joints required for maintenance of equipment;
- Demonstrate that the coolant flow through the vessel is within design parameters;
- Demonstrate ability of inflatable seal to seal against the proton beam window box fitting;
- Demonstrate ability of inflatable seal to seal against target assembly;
- Demonstrate ability to install the neutron beam window using remote handling equipment; and
- Demonstrate functionality of core vessel drain system.

6. Conclusion

- The design of helium vessel was reasonable, and met physical requirements.
- The machining and welding quality are under control in fabrication procedure.
- The progress of helium vessel meet the requirements of construction schedule
- The manufacture of helium vessel will be completed in the end of 2014.

References

[1] *Spallation Neutron Source Core Vessel Final Analysis Reports*
[2] *Technical Design Report of Spallation Neutron Source Facility in J-PARC*
[3] *Physical Design and Technical Development of CSNS Target Station and Instruments*

3.8.2

Overcoming High Energy Backgrounds at Pulsed Spallation Sources

Nataliia Cherkashyna[1], Richard J Hall-Wilton[1,2], Douglas D DiJulio[1], Anton Khaplanov[1], Dorothea Pfeiffer[1,3], Julius Scherzinger[1,4], Carsten P Cooper-Jensen[1,5], Kevin G Fissum[1,4], Stuart Ansell[6], Erik B Iverson[7], Georg Ehlers[8], Franz X Gallmeier[8], Tobias Panzner[9], Emmanouela Rantsiou[9], Kalliopi Kanaki[1], Uwe Filges[9], Thomas Kittelmann[1], Maddi Extegarai[1], Valentina Santoro[1], Oliver Kirstein[1,10] and Phillip M Bentley[1,5]

1 European Spallation Source ESS AB, SE-221 00 Lund, Sweden
2 Mid-Sweden University, SE-851 70 Sundsvall, Sweden
3 CERN, CH-1211 Geneva 23, Switzerland
4 Division of Nuclear Physics, Lund University, SE-221 00 Lund, Sweden
5 Department of Physics and Astronomy, Uppsala University, 751 05 Uppsala, Sweden
6 ISIS, Rutherford Appleton Laboratories, Harwell Oxford, Didcot OX11 0Q, United Kingdom
7 Instrument and Source Division, ORNL, Oak Ridge, TN-37831, USA
8 Quantum Condensed Matter Division, ORNL, Oak Ridge TN-37831, USA
9 Paul Scherrer Institute, 5232 Villigen PSI, Switzerland
10 The University of Newcastle, Callaghan NSW 2308, Australia

E-mail: nataliia.cherkashyna@esss.se

Abstract. Instrument backgrounds at neutron scattering facilities directly affect the quality and the efficiency of the scientific measurements that users perform. Part of the background at pulsed spallation neutron sources is caused by, and time-correlated with, the emission of high energy particles when the proton beam strikes the spallation target. This prompt pulse ultimately produces a signal, which can be highly problematic for a subset of instruments and measurements due to the time-correlated properties, and different to that from reactor sources. Measurements of this background have been made at both SNS (ORNL, Oak Ridge, TN, USA) and SINQ (PSI, Villigen, Switzerland). The background levels were generally found to be low compared to natural background. However, very low intensities of high-energy particles have been found to be detrimental to instrument performance in some conditions. Given that instrument performance is typically characterised by S/N, improvements in backgrounds can both improve instrument performance whilst at the same time delivering significant cost savings. A systematic holistic approach is suggested in this contribution to increase the effectiveness of this. Instrument performance should subsequently benefit.

1. Introduction

In this contribution during ICANS XXI, the results of both simulation studies and experimental surveys trying to verify shielding at a basic level were shown, relating to the consideration of future instrument shielding at European Spallation Source (ESS) which is currently under construction in Lund, Sweden [1]. In the spirit of ICANS, this writeup will not concentrate

on the state of detailed simulations or surveys themselves, as these are better written up in individual journal contributions when complete, but rather try and give a perspective on how these important studies might fit together, and to give a few philosophical musings on what might be the most effective way to do it. It should be noted that these musings should not be taken as unique, but rather fit into a field of approaches, some of which were also shown at ICANS [2]. Shielding is very much topical!

In contrast, neutron optics and transport has made great strides during the 90's and 00's — advances in neutron optics [3] being instrumental in this. Very roughly speaking this is about transporting maximal brilliance transfer of the desired phase space of neutrons to the sample position. Coupled with this development, and with the coincident rise [4] and democratisation [5] of computing power, are the now ubiquitous [6] and user-friendly ray-tracing programs such as McStas [7–9] and Vitess [10–12] which use Monte Carlo techniques [13] to simulate the thermal and cold neutron transport to have a huge effect on instrument design. These techniques have become so ingrained, that no proposed instrument design is believed without having been *"verified"* using one of these simulations to evaluate ideal performance.

Simply put, these programs are idealistic calculations to optimise phase space transport of neutrons from source to sample and beyond; this is effectively optimisation of the signal at the sample. However, most existing instruments performance is better characterised by a figure of merit related to some function of signal-to-noise (S/N) performance. Often the limiting factor at the floor of the noise is the instrumental background. As such, background calculations are now an essential part in the optimisation process, that needs to be done in harmony with the cold/thermal neutron simulation programs. As will be seen below, it is also not given that signal optimisation is the same as signal-to-background (S/B) optimisation.

2. Shielding of Backgrounds

Shielding is often seen as a *"necessary evil"* for the budget of the instrument; needed for radiological protection purposes, licensing and safety. For spallation sources it adds up to a very significant fraction of the instrument budget [14–16]. Indeed, more can be spent on shielding than on neutron optics, which is intriguing given how much Monte-Carlo time is often dedicated to the optimisation of the guide shape in preference to the optimisation of the shielding. This is especially true when adding up the effort and cost of fixing poor experimental backgrounds during instrument operational phases over the lifetime of the facility. Considering shielding only in the safety context neglects the most important role that shielding has to play in an instrument's performance: maximising the S/B ratio.

Shielding is also typically considered locally at a static point - i.e. in this position what amount of shielding is needed for the present particle fluences. This neglects the synergies from a holistic approach to its design for an instrument: *i.e.* rather than taking the radiation field as given and absolute for an particular instrument design and post-mortem design the shielding around it; instead the goal should be to try to engineer this radiation field to make it minimal at the points which are key for instrument performance — normally the detectors and sample position — and mould the radiation field to allow the quantity ($\propto$ cost) of shielding to be globally reduced.

In terms of materials utilised, only four are typically considered in neutron scattering:

(i) Concrete. This is taken as a *"light hydrogen containing"* cheap material, primarily to bulk to shield gammas and to moderate fast neutrons. Whilst it is just about the cheapest material [1], surprisingly it is not ideal at either of the other two tasks, and the hydrogen content of concrete is not so great. Impurities in the concrete also activate readily if the concrete is allowed to be inadvertently illuminated by strong neutron beams.

[1] Except water and earth which are much under-utilised.

(ii) Steel. This is taken as a *"heavy, dense"* cheap material to slow and stop fast and high energy neutrons [17]. Stainless steels activate to the point of being a hazard, whereas mild steels exhibit regions of neutron transparency in the resonant energy range of 100s keV to around 1 MeV.

(iii) Plastic. This is a light material that is used to slow fast neutrons (< 20 MeV).

(iv) A boron-containing substance. This is to *"mop up"* thermal and cold neutrons. Typical applications are plates of boron carbide, or plastics made with boric acid that combine absorbing and moderating properties.

Perception of cost and a fear of activation issues leads to the exclusion of many other attractive materials being considered.

Lastly, shielding is a multidisciplinary problem: a variety of solutions have been found for several applications. It is therefore apt to ask whether any parts of the solutions found in other disciplines have a lesson for neutron scattering?

3. Background Sources

One of the most striking pictures illustrating the differences in backgrounds between reactor and spallation sources can be seen from comparing the frequently shown neutron source energy distributions. This is shown in figure 1. The difference is significant, with a much longer tail from spallation sources towards higher energies; almost up to the incident beam energy of the proton. However, how does this make a difference to the background level?

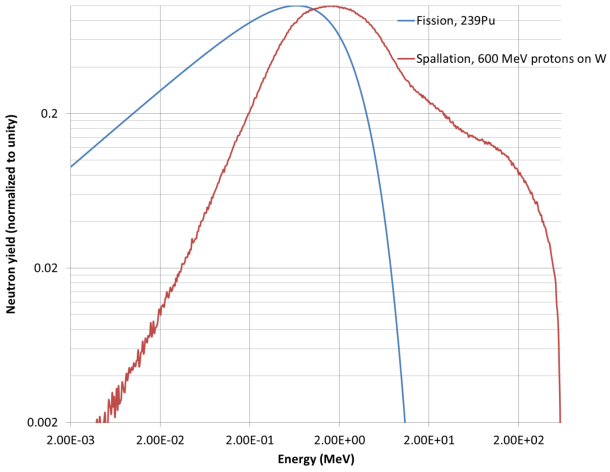

Figure 1. Neutron emission spectrum from fission compared to spallation, after Shetty [18].

It should be noted that of course spallation sources are not new: therefore measurements of background at existing sources are important to understand these effects - and just as importantly how they propagate down to instruments - these cascades are important as it is the background at the instrument that is most important.

To understand these cascades, it is important to review and understand what can happen to these background particles.

A prime candidate mechanism in the prompt pulse is the phenomenon of particle showers. These are the cascades of secondary particles produced by high energy particle interactions with dense matter. There are two different mechanisms of particle showers: electromagnetic and hadronic [19]. As shown in figure 2, electromagnetic shower is more localised in a material, while hadronic shower is more spatially extended. Electromagnetic showers are caused by photons

and electrons. Electrons create many events in matter by ionisation and bremsstrahlung, and photons are able to penetrate quite far through material before they lose energy. The second type, hadronic showers, is caused by hadronic particles (baryons and mesons: protons, neutrons, pions, kaons, etc) that are made of quarks - and strong nuclear forces are involved into those interactions. The hadronic showers are characterised by ionisation and interactions between incident particles and nuclei of the material. Hadronic showers are complex, as many reactions take place and many different particles are produced, and it is essential to use sophisticated modelling packages such as Geant4 [20] to understand hadronic showers.

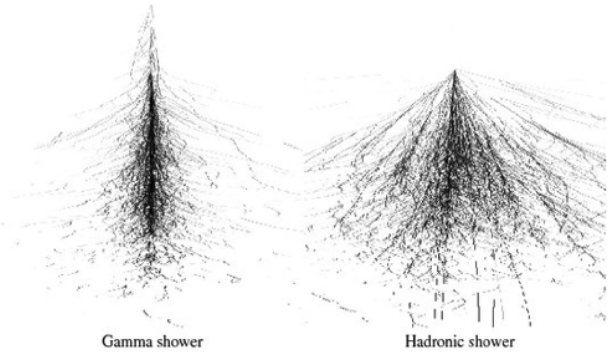

Figure 2. The different character of electromagnetic(gamma) and hadronic showers [19].

Some of the interactions of note can be summarised as follows:

(i) High energy gamma photons ($\sim$ 10 $-$ 50 MeV) readily liberate neutrons via GDR photonuclear processes [21].

(ii) Inelastic scattering of high energy (100s MeV and GeV) neutrons in shielding produces secondary hadrons (mostly neutrons).

(iii) Fast neutrons are readily scattered through gaps, light materials, down guide tubes and pipework. The scattering "reflectivity" of most materials to fast neutrons is between 40 and 60 %.

(iv) The mean free path, and the tenth value (amount of shielding to reduce the fast neutron flux by a factor of ten) can be quite large at spallation source energies. Typically, 1 metre of concrete is needed to attenuate a GeV neutron flux by a factor of 10. Where reactors may be able to shield with a few tens of cm of material, at higher energies these thicknesses can prove to be insufficient with dramatic results, since these in turn can be readily reflected (point iii), generate secondary neutrons 10s–100s of metres from the escape point and potentially inside other instruments (point ii) after they have escaped.

Point i, and particularly point ii above, generate showers that produce neutrons. The primary and secondary neutrons can travel large distances, and lose energy in the instrument shielding, generating more secondaries in the process. Because the count rates can be quite low, and because the primaries are of such high energy compared to thermal neutron energies, it is not straightforward to measure the primary radiation intensity with most thermal neutron detectors, making it difficult to identify the primary source. Once the neutrons lose enough energy into the keV – 1 MeV region, the resonances in steel make steel shielding far less effective. Where the primaries are escaping seems to vary from facility to facility, so it is important to consider potential accelerator, accelerator-to-target, target, beamline sources. Moreover, the beamline

contributions can be from optics shimming/collimation/ "horse-collars", chopper pits, shielding stacking, conduits, and beamstops.

Point iii above means that care has to be taken in evaluating gaps in the shielding, and how the beamline is laid out. Ensuring that primary energetic neutrons escape into bulk shielding, both around the beamlines and in the beamstops, whilst preventing secondary propagation to the instruments is critical. This can be in the form of "get lost" tube concepts for beamstops, and carefully designed pockets of empty space or low density material around the neutron guides between the heavy collimator blocks.

Hence, *effective 'line of sight'* differs for fast and thermal neutrons and for gammas. The transport of all three species varies significant for different materials. Even if line of sight is blocked to the source for visible photons, fast neutrons can scatter through the neutron guide glass and vacuum system easily, and can propagate further down the curved guide, particularly if secondary neutrons are emitted. It is important to over-engineer the line of sight criterion. Therefore *'line of sight'* becomes a much more *mushy* and malleable criterion than a simple geometrical definition.

4. Background Simulation

The ray-tracing programs McStas [7–9] and VITESS [10–12] are frequently-used Monte Carlo [22] techniques to simulate the thermal and cold neutron transport. They do not however also simulate instrument backgrounds from fast neutrons or gammas. They must therefore be combined with additional simulations dedicated to modelling these backgrounds.

The steps needed to optimise shielding are as follows:

(i) Simulation of phase space of interest - i.e. McStas/VITESS simulation of thermal/cold neutrons. This simulation can partially simulate some background effects, such as multiply-scattered neutrons or neutrons scattered in ancillary equipment near the sample or detectors.

(ii) Background simulation using specialised high energy/nuclear tools.

(iii) Normalise these appropriately and sum these to give the S/B for the instrument — typically the best estimator for a figure of merit for instrument performance.

(iv) Ensure that the critical parts of this simulation are validated. In particular ensure that the simulation results themselves are both sensible (back of envelope) and cross validated with a second method.

Background simulations might involve MCNPX, which is a general-purpose Monte Carlo code that can be used for neutron, photon, electron, or coupled neutron/photon/electron transport [23,24]. Equally it could use Geant4, which is a C++ toolkit for creating simulations of the passage of particles through matter and electromagnetic fields, and has areas of application such as high energy, nuclear and accelerator physics [20], including the detector response to this background. Another alternative could be PHITS — a general purpose Monte Carlo particle transport code written in FORTRAN. This code deals with the transport of all types if particles within the wide energy range up to 100s of GeV. Several nuclear reaction models and nuclear data libraries are available [25].

Another simulation tool is CombLayer [26], which provides a means of rapidly producing complex MCNPX geometries, that depend on a long list of ranged variables, whilst at the same time optimising the MCNPX input to run quickly. It is also intended to help with placement of tallies, maintaining consistent materials and some variance reduction.

Geant4 is used to perform the simulations within the frame of instrument background studies and detector physics at ESS. That toolkit is a well-known main simulation engine for high energy physics applications. Different materials were investigated in order to understand their shielding properties against high energy particles. The toolkit includes different physics models and

processes (electromagnetic, hadronic, optical), tracking, hits, large set of geometrical features, wide energy range.

The physics list recommended for shielding applications in the energy range of interest is QGSP BERT HP, it is chosen for the shielding studies performed recently. This is the set of physical processes which describe the interaction of particles with dense matter [20]. The abbreviation means the following: QGS is for quark-gluon string model, P means precompound, BERT means that Bertini intra-nuclear cascade model is used [27], and HP states that high precision neutron tracking model is also included [28].

For ESS, to ensure that such studies are done in a consistent and rigorous fashion, using known processes, a framework based around Geant4 has been setup precisely for these shielding, detector and instrument design studies [29,30]. Of particular note is that this includes additions to Geant4 to ensure that the processes relevant to thermal neutron scattering are implemented and much better described by the simulation [31,32].

As part of the validation process, the best strategy is to measure and understand observed backgrounds at extant running spallation sources. Here it is important to have an open honest dialogue, to be able to learn lessons from existing sources. An extensive measurement program has been carried out; as the results this far show it is impressive how good the shielding is in general.

The radiation protection adage *"distance, shielding, time"* has applications also to background reduction. The following 2 sections deal with aspects on the "distance" and "shielding" parts of this adage. Utilising the third, "time", is viable for a reactor source, however for a pulsed spallation source, it is difficult to utilise this for background minimisation, when the source pulse defines so much about the temporal features in the background. Combined with time-of-flight and the distances on the instrument, it defines the background time characteristics. This often leads to a prompt pulse effect, making sensitive measurements not possible during this time period, or requiring that measurements use flight times less than the repetition period of the source. Such deadtimes are less tenable for a long pulse spallation source, such as ESS, necessitating a greater reduction in background levels.

5. Geometrical Effects

Simple geometrical effects on the radiation fields may be highly important. It is important to remember how these scale:

- Point sources, such as the sample, beam stop, or a deformity. The radiation field scales as $1/r^2$ with distance.
- Beamlines. The radiation field scales as $1/r$ with distance.
- Surfaces, such as the monolith wall or loss along a large area of guide wall. To first order the radiation field does not scale with distance; it scales slowly based upon boundary conditions of the surface illuminated and attenuation.

Understanding and engineering such geometries can be used to either reduce the amount of material needed, or to concentrate losses in particular locations to reduce shielding needs elsewhere.

Another type of structure is the *"get-lost tube"* as mentioned previously, which transports the unused neutrons after the sample away from the detectors, before dealing with them in an appropriately designed beamstop system. This has proven to be highly useful for background reduction of neutrons backscattered around the detectors, after passing through the sample.

There is a prescription that the sample should be out of line of sight. But as already formulated earlier: *What does line of sight mean? What is the effective line of sight?* Even more importantly - is line of sight the same for different particle species?

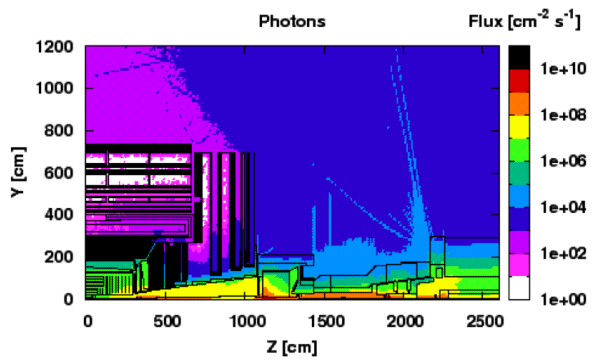

Figure 3. Simulated photon flux in 7TeV centre-of-mass pp collisions at nominal luminosity shown for a quadrant of the CMS [35] experiment at the LHC [36], CERN. The simulation uses the FLUKA code [37]. The coordinate system is shown relative to the interaction point for the pp collisions. From [38].

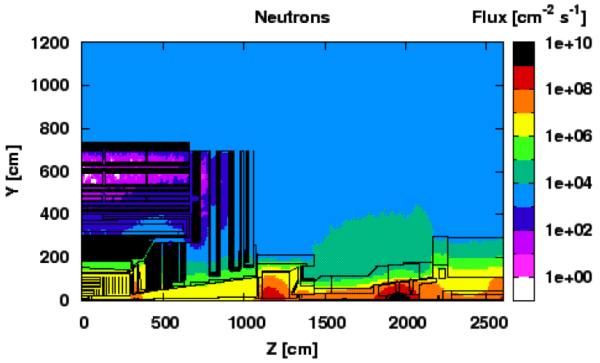

Figure 4. Same as for figure 3 but showing neutrons fluxes in the CMS experiment. From [38]

This concept can be adapted also to try and reduce background from line of sight losses; by optically removing the signal neutrons from the line of sight, and letting high energy gammas and fast neutrons go straight into a controlled loss area. By geometrically directing these background particles to known loss points, scatter and albedo from these losses downstream towards the sample position can be vastly reduced. In many ways such a geometry for dealing with different energy and particle species is very much analogous to a synchrotron, where one particle type (eg electrons) is bent around the ring, whilst the light produced in this curve is produced in a straight line form the bending point, and off-momentum electrons take a different (typically tighter) orbit, and so can be cleaned by specific collimination on the inner side of the ring. All three particle types take a different physical flight path.

When a straight beamline is necessary, it might even be optimal to allow the background to pass through unhindered. Low pressure gaseous detectors, for example, can be quite insensitive to fast and epithermal neutrons and gammas [33, 34]; danger arises when material budgets increase, moderating the neutrons and increasing the interaction probability of gammas. This would require specific selection of materials to minimise particular materials, in particular hydrogen containing ones - and local shielding against thermal neutrons around the detectors. An analogy to this possible approach can also be found in typical high energy physics experiments, such as those at the LHC. Here the radiation source is point-like — and the most sensitive detector volumes are very close to the source and on the exterior. To reduce both background levels and dose to sensitive electronics, the material budget is carefully engineered to produce a well-understood and manageable radiation flux in all detector components. An example from the CMS experiment is shown in figures 3 and 4, showing that sensitive components close in can have fluxes many orders of magnitude below those further out. A similar concept may help instruments requiring straight beamlines.

It is also the case that for the highest energy particles, there may be a shower. This may mean that a loss point close to, eg, an instrument cave, a too-thin collimator or a T_0 chopper could easily increase rather than decrease the background. It is therefore important to define well for what location the background is to be minimised, and design for that location the best background possible. Typically this means removing loss locations as far from this sensitive location as possible. This can be simply summarised as *"choosing the loss point"* for undesired

particles.

6. Material

As mentioned in section 2, the traditional choice has been to converge on iron and concrete as shielding materials; typically this is seen as only a civil engineering task. Often this choice is dictated by the standard concrete block which exists at the facility. With a green-field site, a greater degree of flexibility exists, and should be investigated whether a less brute force approach can be applied.

Additionally hydrogen-containing substances are very useful as they moderate fast neutrons. However, close to guides they may be detrimental, as moderated neutrons scattered back into the guide may give background effects with a long-tailed time structure, and they are also rather transparent to the high energy neutrons because of the low density. Care should be taken in their placement after the first set of choppers so that they are behind a barrier layer of rich boron material or other good thermal absorber, preventing moderated neutrons from escaping back out and further lengthening the tail of the pulse. Another risk with hydrogenous materials that must be mitigated is the hazard of fire. It is important at a green field site to consider plastics and waxes early so that the building systems can cope with the potential fire load.

The ESS is now concentrating effort into the shielding properties of numerous different materials, such as specialised concrete, laminated materials, tungsten and copper-based solutions [39]. The last ones include, for example, copper guides [40], or copper alloys such as brass. Copper has been demonstrated at high energy physics labs in multiple roles. It has superior shielding properties compared to iron and mild steels, due to the resonances in the total neutron cross section. This is shown in figures 5 and 6. On the figure the simulated energy

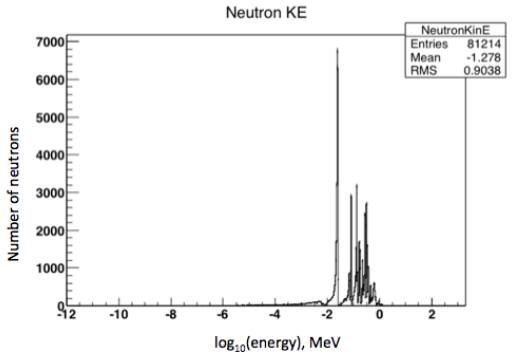

Figure 5. Energy spectrum of spallation neutrons attenuated by the 50 cm block of iron. Number of neutrons as a function of energy is shown.

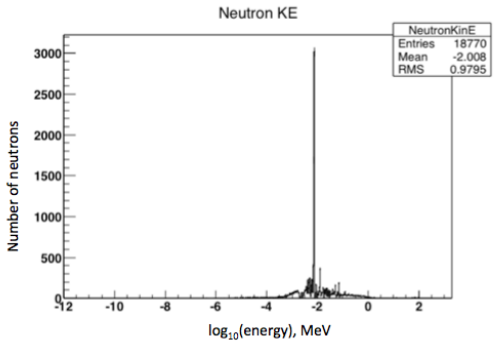

Figure 6. Energy spectrum of spallation neutrons attenuated by the 50 cm block of copper. Number of neutrons as a function of energy is shown.

spectra of neutrons that came through the 50 cm blocks of those two materials are shown; spectrum used for the simulation was the ESS spallation spectrum.

Copper-based solutions deep inside key shielding areas are consequently seen to be attractive avenue of further research in reaching our background goals. The aim is to use most appropriate and efficient dense material in the areas where moderating of the fast neutrons is essential for background suppression; shapes and volumes of shielding materials are also under investigation. A global cost-benefit study of materials and material combinations for key parts of the instrument shielding and guide bunker is well underway at ESS.

The integration of the neutron optics with the shielding strategy is crucial for a synergistic, high performance system. Neutron guides are typically made of glass and surrounded at some distance by a vacuum tube: these are easy streaming paths for energetic neutrons as observed on CNCS at Spallation Neutron Source (ORNL). Therefore, using copper close to guide, or as guide substrate to ensure that fast neutrons are slowed and stopped in as little material as possible is a very promising shielding option. On the other hand, the glass guides are excellent escape or "get lost" points if they are purposely designed with the right bulk shielding geometry behind them, and interspersed periodically with denser materials.

Recently copper was used in bags as a trial *"bricolaged"* shielding improvement at CNCS (shown in figure 7), and this brought a reduction in the prompt pulse background by 25%, shown in figure 8.

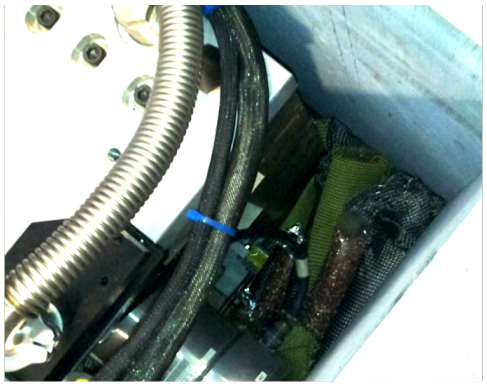

Figure 7. Bags with copper as an additional shielding at CNCS

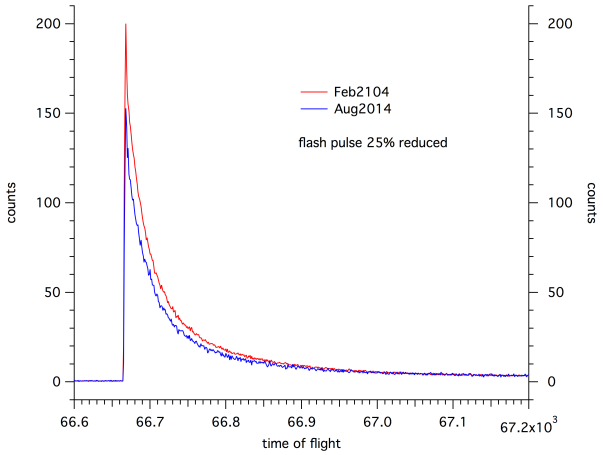

Figure 8. Background reduction on CNCS achieved by adding copper in a few key places on the beamline.

These early tests are very promising, and further reductions are anticipated with more work. This highlights the great progress that the SNS team members are making in addressing instrument backgrounds of this kind, which — despite being highly complex issues — do not necessarily have to involve very expensive solutions if the choice of materials and their locations can be identified. It should also be contrasted with the effort needed to increase the efficiency of modern, optimised guide sytstems by 25%.

One more topic to discuss is the activation. Activation is an important issue in the choice of material, as neutrons activate material easily. This is important to reduce decommissioning costs, and allow access to locations for maintenance. Here both the desired material and its impurities should be considered. Steel is in principle good in that aspect, however there are many cases where unforeseeable impurities have created extreme activation problems on relatively moderate doses [41, 42]. Copper has a reputation for activating greatly; however studies [43] for the CMS experiment at the LHC showed that over a longer time frame, as the daughter products were short lived, the activation can be lower than other materials - even lower than aluminium after several months for the CMS radiation field. Indeed, whilst the shielding performance of copper at high energy is comparable to stainless steel, the activation of copper is far superior to stainless steel. It is vital to verify this result with actual simulations for the expected ESS neutron spectra and radiation field.

Here, the non-functional requirements on manual access and maintenance targets are needed, in combination with extensive simulation of activation and lifetime, taking particular note of

measured impurity levels to produce a known predictable result. Doing so avoids much heartache later.

7. Summary

We have presented a summary of the efforts currently underway in a collaboration between several laboratories, to address issues in neutron instrument performance. What remains a priority for the immediate future is a combined, holistic approach involving all of these facets.

Working on the shielding will have a significant effect on the instrument performance; and is a larger potential source of gain in instrument performance nowadays than optimised optics, which is frequently around — or beyond — 80% designed brilliance transfer for modern concepts and technology. Further brilliance transfer gains will become increasingly expensive with smaller returns in performance, however by more advanced shielding, it is possible to both reduce costs and to reduce backgrounds. Reduced backgrounds directly improves instrument performance, as the figure of merit for most instrument design is most closely correlated to functions of S/B. For many instrument categories, it is possible to imagine an order of magnitude improvement to existing designs. This is in fact a design goal for the instruments at the ESS.

At first glance, such a strategy might seem to indicate increased total costs, but this is not the case. An effective system design, placing the materials in the right places, reduces the total volume of material required and actually reduces the total system cost. This allows greater investment in other parts of the instrument, such as custom sample environment, and more expensive and reliable mechanical devices that translate into less maintenance and downtime to repair faults. These enhance instrument productivity and performance in slightly less tangible or less directly-visible ways as raw neutron flux gains have in the past, but are significant in the long term and should not be underestimated.

We have described how the pulsed background is comprised of a complex admixture of fast, epithermal and thermal neutrons and gammas. Therefore, to achieve the desired performance gains, a holistic, horizontal and combined approach to the shielding appears to be most sensible, cutting across both optics and shielding for a new source such as ESS — and is in fact the strategy for the Neutron Optics and Shielding group [44], taking inspiration from the Paul Scherrer Institute in Switzerland. But more than this, closely linking the work with the Detector design and Chopper interface management is absolutely essential. It also cuts across the design of the instrument suite as a whole, and the way that the integration projects are run at the facility level. It is not just about "radiation-protection" in fact it is far beyond it; though radiation safety and personal protection are paramount, typically, the levels of sensitivity of the instrument are at least an order of magnitude beyond these requirements. This is because the peak, pulsed background levels are so high compared to the time-averaged background levels that, by achieving prompt-pulse background objectives at pulsed spallation sources, the safety objectives should be already exceeded.

All of these aspects take time, patience, thought and above all validation in depth.

Significant synergy now exists between the spallation sources on this topic, and it is to the benefit of the entire community to exploit this collaboration.

References

[1] Peggs S *et al.* 2013 ESS TDR Tech. rep. Lund, Sweden: European Spallation Source, ESS AB
[2] ICANS XXI Mito, Japan 2014 *Abstracts S-01 — S-07, session 9, shielding*
[3] For an overview see Bentley P M, Cooper-Jensen C P and Andersen K H High intensity neutron beamlines 2013 *Reviews of Accelerator Science and Technology 6* 259–274
[4] Moore G E Cramming more components onto integrated circuits 1965 *Electronics Magazine* 4
[5] Lyons D Linux rules supercomputers 2005 *Forbes March 15*
[6] Weiser M The computer for the 21st century 1991 *Reproduced in: ACM SIGMOBILE Mobile Computing and Communications Review 1999* **3**

[7] Lefmann K and Nielsen K 1999 *Neutron News* **10**
[8] Willendrup P, Farhi E and Lefmann K 2004 *Physica B* **350**
[9] URL `http://www.mcstas.org/about/`
[10] Wechsler D, Zsigmond G, Streffer F and Mezei F VITESS: Virtual instrumentation tool for pulsed and continuous sources 2000 *Neutron News* **11** 25
[11] Zsigmond G, Lieutenant K and Mezeia F Monte Carlo simulations of neutron scattering instruments by VITESS: Virtual instrumentation tool for ESS 2002 *Neutron News* **13** 4
[12] URL `http://www.helmholtz-berlin.de/forschung/oe/em/transport-phenomena/projekte/vitess/index_en.html`
[13] Metropolis N and Ulam S The Monte Carlo Method 1949 *Journal of the American Statistical Association (American Statistical Association)* **44** 335341
[14] Jackson A and Kanaki K URL `http://dx.doi.org/10.5281/zenodo.13302`
[15] Jackson A *et al.* LoKI - A Broad Band High Flux SANS Instrument for the ESS 2014 *ICANS XXI Mito, Japan* **Abstract NI01**
[16] URL `http://europeanspallationsource.se/macromolecular-diffractometer-0`
[17] Muhrer G, Bevilacqua R and Pitcher E 2014 *How much carbon in steel is really needed?* Abstract S-07 ICANS XXI Mito, Japan
[18] Shetty N V 2013 *Study of Particle Transport in a High Power Spallation Target for an Accelerator-Driven Transmutation System* Ph.D. thesis Faculty of Georesources and Materials Engineering, RWTH Aachen University
[19] Gaudio G, Livan M and Wigmans R 2009 Proceedings of the international school of physics "enrico fermi"
[20] Agostinelli S 2003 *Nucl. Instum. and Methods in Phys. Res. A* **506** 250–303
[21] Baldwin G C and Klaiber G S Photo-fission in heavy elements 1947 *Phys Rev* **71** 3–10
[22] Lux I and Koblinger L 1991 Monte Carlo Particle Transport Methods: Neutron and Photon Calculation Tech. rep. Boca Raton: CRC Press
[23] McKinney G W *et al.* Mcnpx overview 2006 *Proceedings of the 2006 HSSW, FNAL, IL*
[24] URL `https://mcnp.lanl.gov/`
[25] URL `http://phits.jaea.go.jp/`
[26] URL `https://github.com/SAnsell/CombLayer/`
[27] Heikkinen A 2005 Implementing the bertini intra-nuclear-cascade in the geant4 hadronic framework, the monte carlo method: Versatility unbounded in a dynamic computing world Tech. rep. Chattanooga, Tennessee
[28] Speckmayer P Impact of the choice of physics list on geant4 simulations of hadronic showers in tungsten 2010 *CERN LCD-Note-2010- 002* URL `http://cds.cern.ch/record/1443829`
[29] Kittelmann T, Stefanescu I, Kanaki K, Boin M, Hall-Wilton R and Zeitelhack K Geant4 based simulations for novel neutron detector development 2013 *20th International Conference on Computing in High Energy and Nuclear Physics (CHEP)*
[30] Kittelmann T *et al.* Geant4 based simulations for novel neutron detector development 2013 *abstract NPO2-138, IEEE NSS* (Seoul)
[31] Kittelmann T and Boin M Polycrystalline neutron scattering for geant4: NXSG4 2015 *in press J. Computer Physics Communications*
[32] Cai X X *et al.* Preliminary assessment of geant4 hp models and cross section libraries by reactor criticality benchmark calculations 2013 *abstract N45-2, IEEE NSS* (Seoul)
[33] Khaplanov A *et al.* In-beam test of the boron-10 multi-grid neutron detector at the in6 time-of-flight spectrometer at the ill 2014 *J. Phys.: Conf.* **528**
[34] Khaplanov A *et al.* Investigation of gamma-ray sensitivity of neutron detectors based on thin converter films 2013 *JINST 8* **P10025**
[35] CMS The cms experiment at the cern lhc 2008 *JINST 3 S08004* **doi:10.1088/1748-0221/3/08/S08004**
[36] Evans L and Bryant P The lhc machine 2008 *JINST 3 S08001* **doi:10.1088/1748-0221/3/08/S08001**
[37] Fermilab 2006 *The FLUKA code: description and benchmarking, Proceedings of the Hadronic Shower Simulation Workshop* vol 31-49 (AIP Conference Proceeding)
[38] Müller S 2011 *The Beam Condition Monitor 2 and the Radiation Environment of the CMS Detector at the LHC* Ph.D. thesis Karlsruhe
[39] Cherkashyna N *et al.* High energy particle background at neutron spallation sources and possible solutions 2014 *J. Phys.: Conf.* **Ser.528:012013**
[40] *Developed in collaboration between ESS and Swiss Neutronics. Article in preparation*
[41] Gregoire O and Ladriere J Activation of stainless steel with high energy neutrons 2001 *Journal of Nuclear Materials* **298** 309
[42] Kojima S *et al.* Determination of radionuclides induced by fast neutrons from the jco criticality accident in tokai-mura, japan for estimating neutron doses 2001 *J. Radiation Research* **42** (Suppl): S45–S53

[43] Huhtinen M 1996 *The radiation environment at the CMS experiment at the LHC* Ph.D. thesis Helsinki U. of Tech.
[44] URL `http://europeanspallationsource.se/neutron-technologies`

3-9. Data Acquisition and Analysis

This is a blank page.

3.9.1

Data acquisition and device control software framework in MLF, J-PARC

Takeshi Nakatani[1], Yasuhiro Inamura[1], Takayoshi Ito[2] and Toshiya Otomo[3]

[1] Materials and Life Science Division, J-PARC Center, Japan Atomic Energy Agency, Tokai, Ibaraki 319-1195, Japan
[2] Research Center for Neutron Science and Technology, Comprehensive Research Organization for Science and Society (CROSS), Tokai, Ibaraki, 319-1106, Japan
[3] Institute of Materials Structure Science（IMSS), KEK, Oho, Tsukuba, Ibaraki 305-0801 Japan

E-mail: takeshi.nakatani@j-parc.jp

Abstract. We have developed the standard software framework unified data acquisition and device control at the beginning of the Materials and Life Science Experimental Facility (MLF) in the Japan Proton Accelerator Research Complex (J-PARC). The software framework called "IROHA" is introduced and used in several instruments at MLF from 2008. In use of the software framework for five years, several improvement points as follows were suggested to IROHA. They are 1) separation of device control and instrument management (i.e., the roles of device control are operation, monitor and logging of devices, the roles of instrument management are logging of measurement, authorization and certification), 2) interface of experimental database for measurement information and 3) platform-independent user interface. In this article, we describe the details of the new software framework "IROHA2".

1. Introduction

Many kinds of the experimental instruments are operated in Materials and Life science experimental Facility (MLF), Japan Proton Accelerator Research Complex (J-PARC) to get scientific research results in the neutron and muon science. The instruments are composed of many devices, which are the data acquisition system (DAQ), the devices of the beam transportation and the sample environment, etc. A lot of users have done various kinds of experiments by using the instrument control system. We have developed the flexible and scalable software framework unified DAQ and device control while construction of the day-one instruments in MLF [1]. The software framework, named "IROHA", has been introduced and used in the several instruments in MLF.

After the operation of IROHA for several years, some improvements are suggested as follow. Because the software components of IROHA were tightly coupled, all components, not only software but also hardware, in the instrument had to operate correctly. If one component was broken, we had to stop the system, remove the trouble component and restart the system. In addition, because the software components were not provided the individual user interface, it was necessary that all components operate even if we wanted to control only one device.

The various information of measurement is produced by the experiments in MLF. We have developed MLF experimental database (MLF EXP-DB) to manage such measurement information [2]. To

manage this information efficiently, it is necessary to formalize the information. The role expected of IROHA is to connect between the measurement information and MLF EXP-DB.
Recently, people properly use some kinds of information apparatus according to a situation. In this case, even if the apparatus is different, a user interface is suitable to be similar i.e., platform-independent. Thus, it is preferable to be platform-independent in the user interface of the instrument control system in MLF.
In 2013, we started to plan the upgrade of IROHA to achieve higher user-friendliness, availability, flexibility and scalability. We have discussed and designed the improvement points in IROHA. The points of upgrade are as follows.

1) Software functions which are proper role-sharing between device control and instrument management
2) Interface between measurement information and MLF EXP-DB
3) Platform-independent user interface

In this article, we describe the detail of the new standard control software framework for the instrument in MLF, named "IROHA2".

2. Architecture

The software of the instrument control system in MLF is composed of three layers which are the user interface layer, the management server layer and the control server layer including DAQ Middleware [3] (shown in Figure 1). The layer of the user interface is the front end of the instrument control system. The layer of the management server is the management of measurements with the configuration of the instrument. The layer of the control servers is each device control. We have adopted the client-server model between the layers. The communication protocol between the layers is the exchange of messages formatted XML over HTTP. Because the layers communicate with HTTP, each layer is easily able to be distributed in the network. We have been able to control DAQ and devices with the single user interface while load balancing. Thus, we can construct the instrument control system with flexibility and scalability. The scope of the control software framework IROHA2" in the instrument control system is the management server and the control servers without DAQ Middleware.

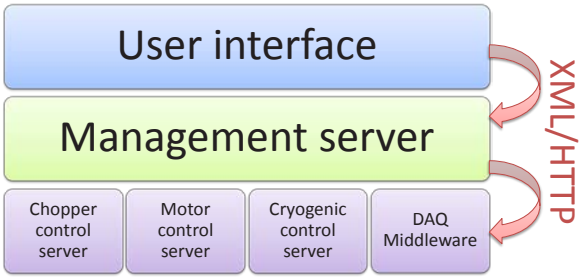

Figure 1. The software architecture of the instrument control system in MLF.

3. Upgrade points of IROHA2

3.1. Role sharing of device control and instrument management

When we designed IROHA2, we redefined the roles of each software component. The roles in the management server layer are the measurement management, which are measurement run control and logging of measurements with the configuration of the instrument, authorization and certification of users. The roles in the control server layer are each device control, such as operation, monitoring and logging of the device. In IROHA2, we defined the software of the

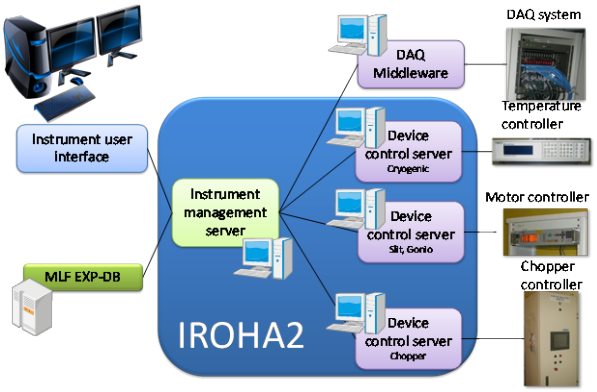

Figure 2. The deployment diagram of IROHA2.

management server layer the instrument management server and the control server layer the device control server (shown in Figure 2). The instrument management server is the single process in the instrument control system and the device control servers exist device by device. Each software component is able to run independently and connect each other on demand. We can change the configuration of the instrument control system as needed; the devices are able to attached or detached without stopping the system.

3.2. Interface between measurement information and MLF EXP-DB

We have defined one of the roles of the instrument management server the interface between the users' experimental data and MLF EXP-DB. The instrument management server performs the communication between MLF EXP-DB and IROHA2. In the measurement, the instrument management server collects and records the experimental meta-data, which includes the DAQ and devices' conditions and the information of the user, the proposal and the samples. We have named the experimental meta-data "Run Information". Run Information is generated by the instrument management server in every measurement. MLF EXP-DB automatically searches, registers and catalogues the Run Information linking the experimental raw data. By using this information, MLF EXP-DB can recognize which sample is measured, who obtains the experimental data in which proposal.

3.3. Platform-independent user interface

A web interface is one of the most popular user interfaces in the world. Nowadays, the equipment accessing to web is not only the computer but also the mobile device, such as the tablet terminal and the smart phone. Previously, the web contents were necessary to be designed according to each equipment respectively, but recently, the single web content designed with so-called "Responsive Web" is available for use from any equipment. Therefore, we have adopted the web user interface designed with Responsive Web as the platform-independent user interface of IROHA2 to realize user-friendly interface. The user interfaces of the device control servers and the instrument management server are shown in Figure 3. We can maintain the devices, configure the instrument control system and run control of measurements on a web browser.

(a) (b)

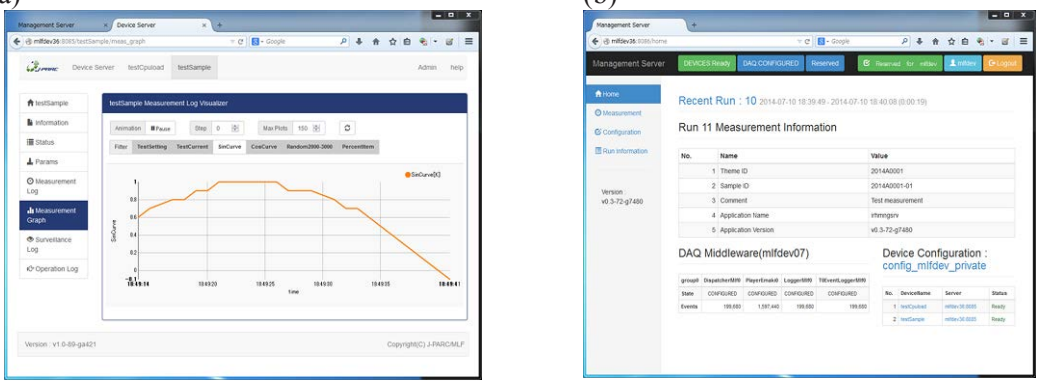

Figure 3. The Screenshots of the device control server (a) and the instrument management server (b).

4. Implementation

The implementation of IROHA2 is shown in Figure 4. As mentioned before, IROHA2 has been adopted the client-server model with XML/HTTP. To implement this model, we introduce Bottle [4] with Python. Python is one of the most popular script languages in the programming languages. In the neutron science community, Python is the most familiar script language. Python has the default module processing XML file. The web framework, Bottle, is one of the simple web frameworks for Python. Because Bottle can be used as a single file module, we have been able to easily implement the client-server model with XML/HTTP written in Python with Bottle.

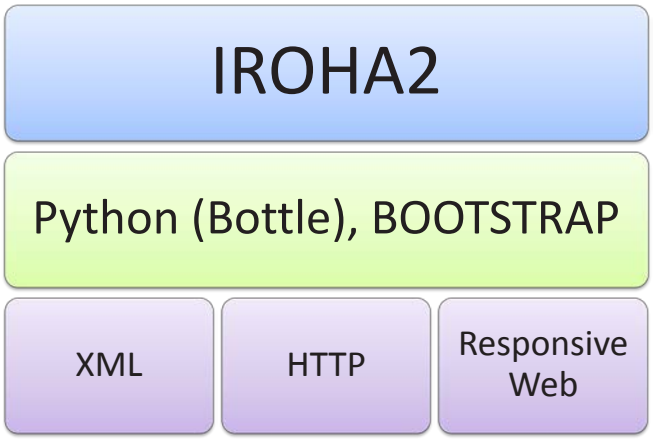

Figure 4. The implementation of IROHA2.

A web interface is primitively written in HTML. However, it is difficult to make the platform-independent web interface with HTML from scratch. We have adopted BOOTSTRAP [5] to realize the platform-independent web interface designed "Responsive Web". BOOTSTRAP is one of the most popular frameworks for Responsive Web. We have made the user interface of the device control servers and the instrument management server by BOOTSTRAP.

5. Conclusion and Future plan

We have upgraded our control software framework (IROHA2) which is user-friend, available, flexible and scalable. By using IROHA2, we will be easily able to do experiments, configure the instrument control system and maintain the devices in the instruments on a web browser. We will develop automatic measurement software called the sequence management server and introduce it into IROHA2. When the software will have developed, we will introduce IROHA2 into the instrument control system in MLF.

Acknowledgments

We wish to acknowledge valuable discussion and suggestion with the MLF computing environment team.

References

[1] T. Nakatani, Y. Inamura, T. Ito, S. Harjo, R. Kajimoto, M. Arai, T. Ohhara, H. Nakagawa, T. Aoyagi, T. Otomo, J. Suzuki, T. Morishima, S. Muto, R. Kadono, S. Torii, Y. Yasu, T. Hosoya and M. Yonemura: Proceedings of ICALEPCS2009 673-675.

[2] T. Nakatani, Y. Inamura, T. Ito, K. Moriyama and T. Otomo: JPS Conf. Proc. 1, 014010 (2014)

[3] K. Nakayoshi, Y. Yasu, E. Inoue, H. Sendai, M. Tanaka, S. Satoh, S. Muto, J. Suzuki, T. Otomo, T. Nakatani, T. Ito, Y. Inamura, M. Yonemura, T. Hosoya and T. Uchida: Nuclear. Inst. Meth. Phys. Res., A 623, 537 (2010).

[4] http://bottlepy.org/.

[5] http://getbootstrap.com/.

3.9.2

Hardware Aspects, Modularity and Integration of an Event Mode Data Acquisition and Instrument Control for the European Spallation Source (ESS)

T Gahl[1,5], M Hagen[1], R Hall-Wilton[1,2], S Kolya[1], M Koennecke[3], M Rescic[1], T H Rod[1], I Sutton[1], G Trahern[1] and O Kirstein[1,4]

[1] European Spallation Source, PO Box 176, SE-22100 Lund, Sweden
[2] Mid-Sweden University, SE-85170 Sundsvall, Sweden
[3] Laboratory for Neutron Scattering and Imaging, Paul Scherrer Institut, CH-5232 Villigen PSI, Switzerland
[4] University of Newcastle, Callaghan, Australia

E-mail: thomas.gahl@esss.se

Abstract. The European Spallation Source (ESS) in Lund, Sweden is just entering the construction phase with 3 neutron instruments having started in its design concept phase in 2014. As a collaboration of 17 European countries the majority of hardware devices for neutron instrumentation will be provided in-kind. This presents numerous technical and organisational challenges for the construction and the integration of the instruments into the facility wide infrastructure; notably the EPICS control network with standardised hardware interfaces and the facilities absolute timing system. Additionally the new generation of pulsed source requires a new complexity and flexibility of instrumentation to fully exploit its opportunities. In this contribution we present a strategy for the modularity of the instrument hardware with well-defined standardized functionality and control & data interfaces integrating into EPICS and the facilities timing system. It allows for in-kind contribution of dedicated modules for each instrument (horizontal approach) as well as of whole instruments (vertical approach). Key point of the strategy is the time stamping of all readings from the instruments control electronics extending the event mode data acquisition from neutron events to all metadata. This gives the control software the flexibility necessary to adapt the functionality of the instruments to the demands of each single experiment. We present the advantages of that approach for operation and diagnostics and discuss additional hardware requirements necessary.

1. Introduction

The European Spallation Source (ESS) is designed as a long pulse neutron source with the maximum overall flux as its main objective. Integrated flux levels will be much higher than existing facilities and the geographical layout will comprise instruments of 160m and longer spanning over 3 instruments halls. At the same time the instruments for these kinds of sources need to be more flexible and complex with up to 20 choppers along the beam line. All this presents operational challenges that are best addressed with a good mixture of techniques from existing neutron facilities and other disciplines like x-ray experiments, fundamental physics or industrial applications. Advanced grounding concepts, high rate data acquisition, flexible experimental setup, advanced remote diagnostics tools, pre-emptive maintenance are a few keywords for that.

[5] To whom any correspondence should be addressed.

At the same time the ESS project represents also an organisational challenge with most of the instruments hardware provided in-kind by the 17 European partner countries. Integration of these contributions either as single instruments components or complete instruments into the ESS infrastructure is only possible with a flexible and modular instrument control system. This also supports clear definitions of functionalities and interfaces of the modules. We will present our ideas of such a system addressing technical, operational and organisational challenges of the future ESS.

2. ESS control infrastructure

2.1. EPICS control system (ICS)

ESS will use EPICS as a global control system for instruments, machine (accelerator, target), central infrastructure and part of conventional facilities. It acts as a horizontal device layer for data exchange between the different parts of the facility although for instrument control and operation the main signal flow will be vertically between the instruments hardware below and the user interfaces on top of the layer (figure 1). All ESS hardware links to the EPICS layer by means of standardised input/output systems (control boxes). The Integrated Controls System Division (ICS) will provide control boxes, EPICS network and hardware driver all over the facility. This ensures a high degree of standardisation and synergy within ESS.

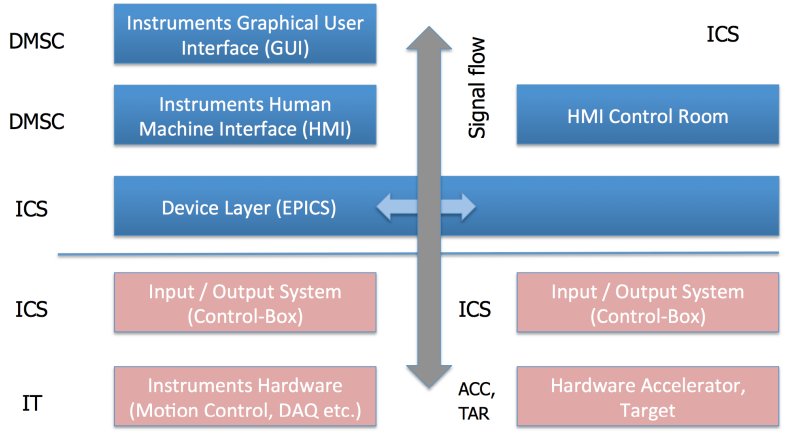

Figure 1. ESS facility wide control system layers (blue: software, rose: hardware).

2.2. User interface (DMSC)

All user interface scripts/GUIs as part of the software layers on top of EPICS are provided by the Data Management and Software Centre (DMSC). The entire control loop of the experiment including scientific calculations, coordinate transformations, sequencing, local experiment monitoring, and all user interface is handled within this layers. This includes data acquisition and data reduction for monitoring purposes as well. The DMSC software interfaces to EPICS and for large data volumes directly with the instruments hardware.

It should be noted that nothing is configured locally 'on the instrument'. This makes the DMSC interface the only access for the instruments users; there is nothing like a local monitoring at the instrument. The only local systems are for expert diagnostics and commissioning. The instrument cannot perform normally (even in a limited fashion) without DMSC supervision.

2.3. Timing network and signals (ICS)

ESS is using a centralised absolute timing system that is provided by ICS [1]. A generator is distributing the clock of a master oscillator and the absolute facility time to a number of timing receivers through a dedicated optical fibre network. A transport layer solution presented by Micro Research Finland [2] is envisaged as technical solution. Per default a timing receiver is present in every control box and thus makes the functionality available to all hardware connected to EPICS. Delay times in the network are compensated in steps of 11.357ns (equals 2.4m fibre length) once the exact position of the receiver and thus the length of the fibre are fixed.

Timestamps are global, across the entire facility, although the resolution of the time stamp used can be optimised in each instance; the highest resolution is 11.357ns. Coordinated synchronous strobes are available at the timing receiver interface (figure 2) to facilitate coordinated synchronous control across instrument subsystems. So, for example, instrument run control can be coordinated to any required precision. Signals include 88.0525Mhz master clock, custom clocks in fractions of the master, 14Hz master pulse, and any custom pulses in multiples and fractions of 14 Hz; all synchronised with jitter requirements as low as 1ns and possibly delayed to the master pulse in multiples of 113,57ns.

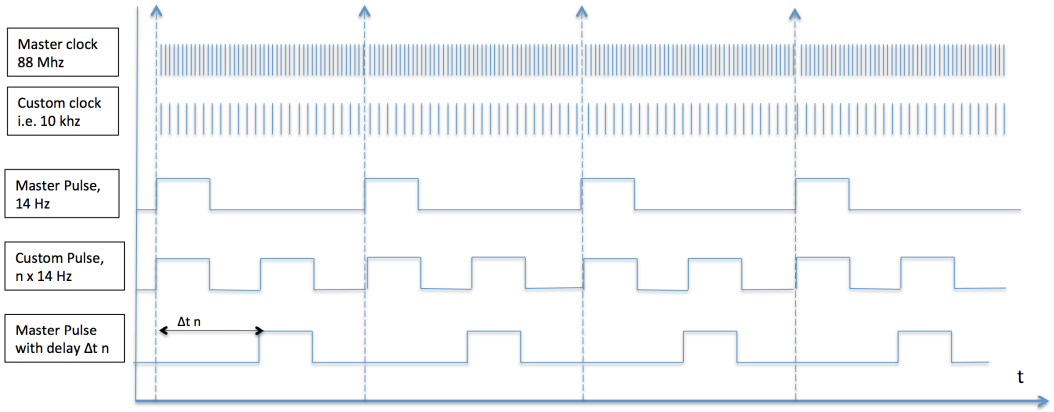

Figure 2. Set of synchronous strobe signals available at the timing receiver interface.

3. Instrument control and readout concept

3.1. Modular concept

The control and readout model that has been envisaged for ESS instruments is modular, where an instrument is made up from a number of independent subsystems ("modules") that do not interact with each other, but only centrally through the EPICS and DMSC interfaces. Each module simply takes care of it's own responsibilities, collecting data (which can be neutron or meta data) or controlling some physical configuration of the instrument (motion control, chopper speed and phase, magnets, etc.) or often both. These systems present the data in the natural form for the module – data is time-stamped, but the significance of the timing cannot be realised until the data is combined at the DMSC. Similarly, detector data is formatted in the natural units of the detector (channel number etc.) rather than physical units (e.g. position) so that the local readout systems do not have to change when an instrument is reconfigured.

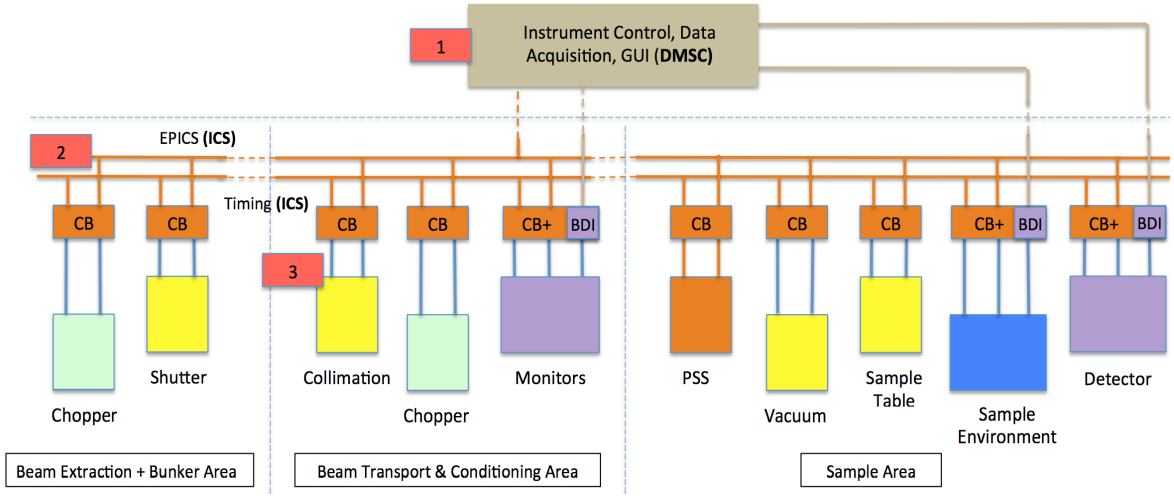

Figure 3. Topology of the modular instrument control concept for a 160m long Neutron Scattering Instrument at ESS. (CB = Control Box, BDI = Bulk Data Interface).

3.2. Topology (figure 3)
Backbone of the ESS instrument control is the EPICS and Timing network of the ICS with the control boxes as interface points (orange). Physically there will be one EPICS subnet per instrument with connectivity to the whole facility. All instruments subsystems (different colours according to functionality) link to these boxes and could be clustered in electrically isolated groups following the geographical layout of the instrument in the different instrument halls. The user interface of the DMSC (brown) is connecting to the EPICS layer via a data gateway. Modules with larger volumes of data like detector electronics or fast sample environment require a dedicated link to a DMSC aggregator node called a bulk data interface (BDI, violet, figure 3). The red boxes #1 to 3 indicate engineering user interfaces on the different layers for diagnostics purposes.

3.3. Design principles
Every control process that can be done (or has to be done) locally in one of the modules will be done locally, every signal that needs to be related to data from other modules has to be time stamped and sent to the DMSC user interface. That gives clear functionalities and clear interfaces for single modules, easy to specify and to bring in as in-kind contributions or from external suppliers. All modules are linked together by the instrument control/data acquisition software of the DMSC (via the EPICS layer); it's a crucial part of the instrument and will be tailored to the needs of each instrument. It gives the flexibility necessary to adapt the same hardware to each of the ESS instruments and to future instrument upgrades: the hardware is done once and prepared for all future (hi-level) functionalities.

However care must be taken about the latency in collecting the data from all modules together to allow the formation of a full 'frame' of neutron data being presented to the user for monitoring purposes. We will address this by introducing a maximum tolerated 'latency budget' as a design requirement for the whole instrument control system.

4. Module interfaces and functionalities

Each control module basically has two or three interface types to the upper device layers: Timing, command interface and – if necessary- an interface for larger volumes of data (figure 4).

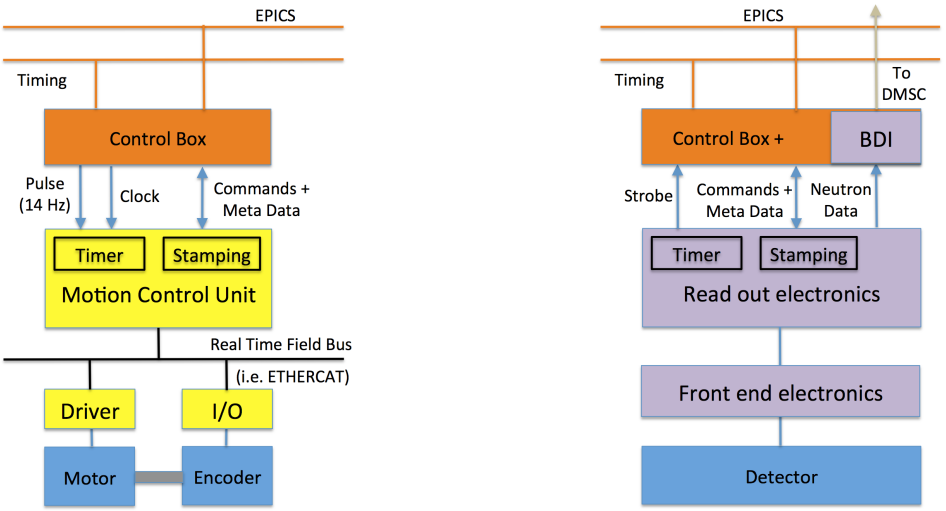

Figure 4. Interfaces and time stamping functionality for a motion control module (left) and a detector electronics module (right).

4.1. Command and meta data interface
The command interface connects through the control box to the EPICS network and is able to transfer smaller volumes of instruments metadata through this channel as well. This data is bridged via gateway to the DMSC user interface 'off instrument'. Currently the data rate is limited to about 1kB/s but improvements of data rates in later versions of EPICS (version 4) will be considered. Physically this command/meta data connection is mostly a serial interface like RS232 or Ethernet with latencies between 20 and 100 ms.

4.2. Time stamping
Following the modular control concept described in section 3 it is mandatory to timestamp all instruments data. This could easily be done by the timing receiver in the control box but is limited in precision by the latency of the connection between the modular control unit and the control box. For higher precision it is necessary to transfer the absolute time information from the control box to the control electronics of the module (or transfer the whole timing receiver). In figure 4 we describe two ideas of synchronising internal timing clocks in control modules with the absolute time of the timing receiver. Either a pulse from the control box is synchronising a timer in the control unit (motion control, left) or a strobe is sent from the control module to the control box and time stamped there (detector electronics, right). In both cases the absolute time of the event is sent to the module via the command interface where it can be related to the internal time of the module. Within the control module the absolute time information can be transferred further by means of real time field busses (e.g. ETHERCAT).

4.3. Detector readout and bulk data interface (BDI)
The readout electronics for detectors will be based on FPGAs that will perform data collection and transmission, and necessary (i.e. unavoidable) data reduction or matching. Although ESS has a high flux, the data rates are small compared to particle physics or radio astronomy and we are not too constrained by bandwidth concerns. We anticipate operating the BDI links at 10Gb/sec, but 40Gb/sec links are already readily available and affordable. To generalise, we expect to include basic background suppression in firmware, and cross data flagging to ensure all relevant data is output, but processing such as cluster centroid finding or time based data matching would be performed in software.

5. Advanced use cases in neutron instrumentation

5.1. Taking neutron data on the fly
Extending the event mode data acquisition from neutron data to motor positions is addressing the requirements for a ‘scanning on the fly‘ in the most flexible way. Neutron data can be related to freely configurable motor position ranges; a binning that might be adapted after the experiment according to analytical or statistical needs. Even higher grades of automation are possible with this setup where the speed of an instrument movement is determined on the fly by the count rate and the desired statistics. At the same time the sampling rate of the motor position data is determined by the wanted precision in space and the given speed. Introducing synchronised movements with non-linear relations between axes even makes something like fully automated constant energy scans with neutron data on the fly feasible.

5.2. Stroboscopic mode in sample environment
Once the time stamping procedure is implemented in the instruments subsystems no further hardware development is necessary to introduce new time relation between neutron data and processes running on the instrument (e.g. in sample environment). Software development can be done ‘off instrument‘ and it is easier to experiment with alternative processing schemes in parallel. At the same time processes can be synchronised to the 14Hz proton pulse if required by the scope of the experiment. Stroboscopic experiments are easy to set up as the properties of the process and the neutron data depend on exact the same time structure and therefor could be easily related.

5.3. Flexible chopper veto
Time stamping the TDC signal of all choppers allows for a flexible handling of the veto condition for data acquisition. Per default all experimental data is acquired and grouped/sorted in different quality classes according the value of the corresponding TDC signal. The user can decide after the experiment which ‘quality‘ of data he includes in his experimental analysis. This might save usable data that otherwise would be lost due to strict veto conditions.

5.4. Diagnostics of beam transport and chopper systems
Advanced diagnostics is a key requirement of ESS instrumentation. We envisage placing a neutron beam monitor behind each chopper group to monitor the neutron flux. By time stamping the monitor events the level and the time structure of the neutron flux at the different positions of the beam line can be related to the time structure of the corresponding choppers TDC signals. Results can be

presented on an ‘oscilloscope style‘ diagnostics screen or on a time-distant diagram like figure 5. At the same time the properties of the beam transport system can be analysed and monitored by comparing the neutron flux at the corresponding opening times of the choppers (as indicated in figure 5 for the brown 2.5 - 3.97Å range).

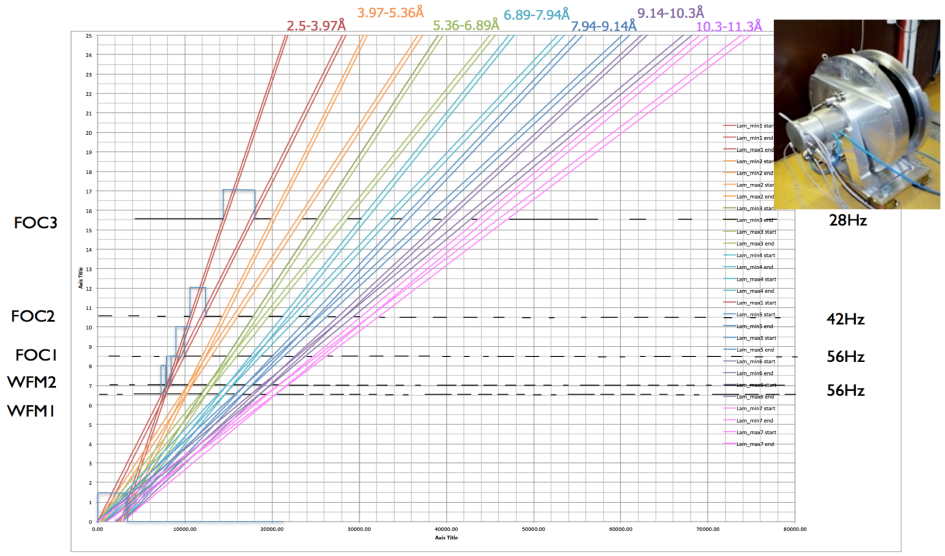

Figure 5. Time-distance (x-y) diagram of a wave frame multiplication chopper unit.

6. Conclusion

With the proposed modular instrument control concept we address the demanding challenges for ESS instrumentation. Instrument subsystems are simpler - easier to specify and easier to maintain. With clear defined functionalities and interfaces they are easy to bring in as in-kind contributions or from external suppliers. The proposed concept fits exactly in the topology of the ESS wide control infrastructure thus profiting from standardisation and maximising synergies within the whole ESS project.

In some cases the concept of an extended event mode data acquisition represents additional hardware requirements e.g. for time stamping or data transfer. Data rate and latency requirements have to be addresses carefully in the design phase. But once the hardware is standardised and in place the subsystems are prepared for the majority of the future functional and operational upgrades. The functionality of the whole system depends solely on the DMSC user interface software that might start with simple standard applications, introducing gradually more demanding functionalities in future upgrades.

Already now the concept is supporting advanced use cases for experiments and diagnostics like on-the-fly scans, stroboscopic data acquisition or advanced neutron beam diagnostics. A lot more will follow in the future once the ESS has started commissioning and user operation.

Acknowledgments

We would like to thank our colleagues and collaborators in and outside ESS for the lively and fruitful discussions and the contribution of ideas and possible solutions with a special mention of ISIS, PSI, JCNS and CERN.

References

[1] Peggs S et al. 2013 *ESS Technical Design Report ESS-2013-001* (Lund, Sweden: European Spallation Source ESS AB)
[2] Pietarinen J 2008 *MRF Timing System* Timing workshop CERN (http://www.mrf.fi/pdf/presentations/MRF.CERN.Feb2008.pdf)
[3] Koennecke M, 2012 *Data Acquisition System Design for ESS* (Villigen: Paul Scherrer Institute)
[4] Rod T H et al. 2012 *Instrument Control at ESS: Analysis and Strategy* (Copenhagen: Niels Bohr

3.9.3

Neutron diffraction imaging at NOVA (J-PARC), HRPD, RESA, and TNRF (JRR-3)

Shin-ichi Shamoto[1], Tadashi Imaki[2], Hidetoshi Oshita[3,4], Takeshi Nakatani[3], Katsuaki Kodama[1], Naokatsu Kaneko[3,4], Hiroshi Suzuki[1], Hiroshi Iikura[1], Atsushi Moriai[1], Masahito Matsubayashi[1], Naoki Igawa[1], Kenji Yamaguchi[1], Kenji Masuko[2], Kensaku Sakamoto[2], Kentaro Suzuya[3], Toshiya Otomo[3,4]

[1]QuBS, Japan Atomic Energy Agency, Tokai, Ibaraki, 319-1195, Japan,

[2]Information Technology System's Management and Operating Office, Center for Computational Science & e-Systems, Tokai, Ibaraki, 319-1195, Japan,

[3]J-PARC Center, Japan Atomic Energy Agency, Tokai, Ibaraki, 319-1195, Japan,

[4]Institute of Materials Structure Science, High Energy Accelerator Research Organization (KEK), Tsukuba, Ibaraki, 305-0801, Japan

E-mail: shamoto.shinichi@jaea.go.jp

Abstract. Neutron diffraction imaging for a SUS430 plate (ϕ=25.0 mm, t=7.4 mm) embedded in a copper block sample (ϕ=50.0 mm and t=20.0 mm) has been tested at the high-intensity total diffractometer NOVA in J-PARC, the High-Resolution Powder Diffractometer HRPD and the diffractometer for Residual Stress Analysis RESA in JRR-3. The results are also compared with that measured at the Thermal Neutron Radiography Facility TNRF in JRR-3.

1. Introduction

The radiography is a technique to visualize inside of a material by radioactive ray transmission variation nondestructively. In the case of large metallic alloys such as bronze sculptures [1,2], a white neutron beam is very powerful because of the high transmittance and the high total flux. On the other hand, by using a monochromatic neutron beam, refraction contrast and ultra-small angle scattering property can be imaged, although the neutron flux is strongly reduced [3, 4]. Neutron phase imaging is a very sensitive method due to the refractive index contrast of a material. Polarized neutron imaging enables us to observe distribution of magnetic flux or magnetization of a material [5]. Neutron diffraction measurement is also a very powerful tool to observe crystal structure, lattice strain, phase ratio in a mixed sample, and so on. Its imaging can be a powerful tool to observe crystal structure distribution in a material. Energy-dispersive Bragg-edge imaging is one of the neutron diffraction imaging methods [2]. The other is a simple neutron diffraction imaging. As for x-ray diffraction imaging, heterogeneous materials were studied in a voxel size of 2.3×2.3×1.6 μm [6]. This small volume is achieved due to high intensity x-ray beam at synchrotron radiation facility (ESRF). In comparison with the synchrotron x-ray beam, neutron beam is still much weaker, but has a high

transmission capability. In addition, diffraction intensity of the highest intensity total diffractometer NOVA (BL-21) at the Materials and Life Science Facility (MLF) in J-PARC increases year by year [7]. We have checked the feasibility of diffraction imaging at various diffractometers, HRPD and RESA, at a continuous neutron source reactor, JRR-3 by measuring a test sample, a copper block with a SUS430 plate, in addition to at NOVA in J-PARC/MLF.

2. Experimental methods

The test sample composed of three pieces, as shown in Fig. 1. It was a copper block with a cylindrical cavity where a SUS430 plate was inserted. Copper atom has 11.81 barn in the total neutron cross section, while SUS430 with about 83 at% iron and about 17 % chromium has about 12.8 barn [8].

Neutron radiography was carried out at the Thermal Neutron Radiography Facility (TNRF) installed at 7R beam port in JRR-3 in Japan, where the average neutron flux was about 1.5 x 10^8 n/cm^2/sec. A radiography photo was taken for 4 sec. Neutron diffraction measurements were carried out at the Diffractometer for the Residual Stress Analysis (RESA) at T2-1 and the High Resolution Powder Diffractometer (HRPD) at 1G in JRR-3. The neutron fluxes for both diffractometers were about 1 x 10^5 n/cm^2/sec. The incident neutron wave lengths were 0.2073 nm and 0.1823 nm for RESA and HRPD, respectively. At the RESA, the sample was measured by $\Delta 2\theta$=0.1 deg. step with silts of W2 x H15 mm^2 before and after the sample for 100 and 220 sec at each step on copper and SUS430, respectively. At the HRPD, the sample was measured by 64 ^{3}He detectors with $\Delta 2\theta$=0.05 deg. step for 130 sec with a slit of W4 x H10 mm^2 only before the sample. The collimation was Open (35')-40'-Sample-6'.

Neutron diffraction imaging of the test sample was performed with 3x3 mm^2 resolution for about 4 days at high-intensity total diffractometer NOVA in J-PARC at 205-280 kW. The pulse peak neutron flux at the sample position of NOVA was about 1.0 x 10^7 n/cm^2/sec at 300 kW. For this measurement, the test sample is set on an aluminum rod fixed by a male screw of M4 on another copper bottom cap. So the aluminum rod has a female screw to fix it. A goniometer with 4 remote (*x, y, θ, RX*) and 1 manual (*RZ*) axes made by Meysho Kiko Co. was set at NOVA. Each measurement was carried out based on the neutron beam monitor count of NOVA (4.7M counts ~ 30 sec at 300 kW). Three natural sintered B_4C slits with 5 mm thickness were used to cut direct neutron beam to the sample, while the spectrometer slits were fully open. First one had a 20x20 mm^2 square hole. Second one narrowed the beam down to 3 mm vertically. Third one narrowed it down to 3 mm horizontally. The sample table on a goniometer was shifted horizontally and vertically by each 3 mm in 57x33 mm^2 (maximum 100x100 mm^2) normal to the beam. The sample table is rotated by 10 degrees step. Minimum scattered neutron transmission in this sample is 0.08% at λ=1.805 Å. Here we ignored this large neutron absorption in all cases for comparison. Diffraction data were taken only from left side of 90 degree banks (2θ=72~108 degrees) to the moderator of NOVA. In this configuration, Debye-Sherrer ring of a sample is covered by about 20%. In other words, diffracted intensity in the area is integrated, regardless of the crystallinity of the irradiated sample. Time in time of flight diffraction patterns was converted to *d*-value. Diffraction intensities in a specified *d*-range were mapped in an image as a photo by our original program "Neudift" [9], after subtracting the background automatically in addition to a simple absorption correction. The obtained photos were enlarged by MicroAVS.

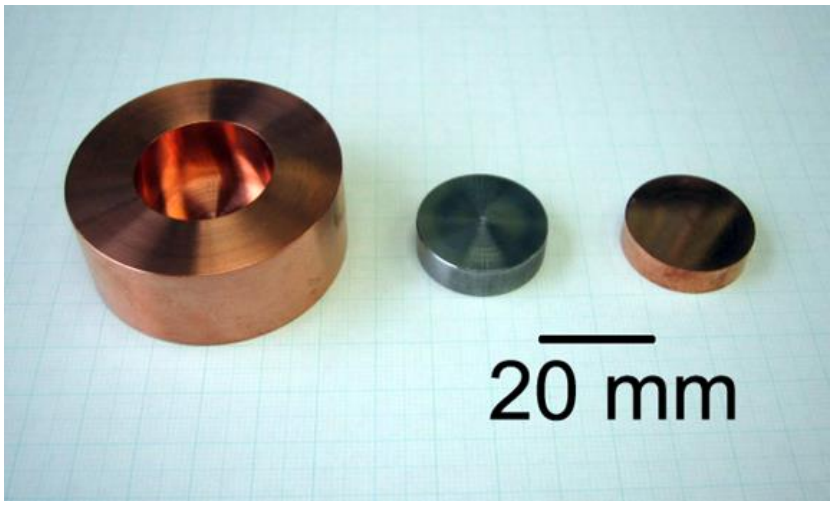

Figure 1. Used test sample pieces. From left, a copper block (ϕ=50.0 mm, t=20.0 mm) with a cylindrical cavity (ϕ=25.1 mm, d=14.5 mm), where a SUS430 plate (ϕ=25.0 mm, t=7.4 mm) was inserted, and capped by a copper plate (ϕ=25.0 mm, t=6.5 mm).

3. Results and Discussion

Figure 2 shows a side view of the test sample by neutron radiography measured at TNRF. The material difference between copper and SUS430 cannot be distinguished in the side view by the attenuation contrast regardless of the thickness. The opening gap with 0.6 mm width is weakly visible. This kind of difficulty can be overcome by using a diffraction technique, which is very sensitive to the structure. For example, copper has a face-centered cubic (FCC) structure with a lattice parameter of 3.6149 Å, while SUS430 has a body-centered cubic (BCC) structure with a=2.803 Å. Because of this structural difference, they were easily detected by the neutron diffraction patterns measured at HRPD, as shown in Fig. 3. Depending on the scattering area determined by incident and final neutron beams, the diffraction pattern changed drastically. At the reactor source, the neutron flux at the sample position is reduced by 3 orders of magnitudes, since only monochromatic neutron beam is used for the neutron diffraction. In this sense, the measuring time for the diffraction imaging may be increased by 3 orders of magnitudes.

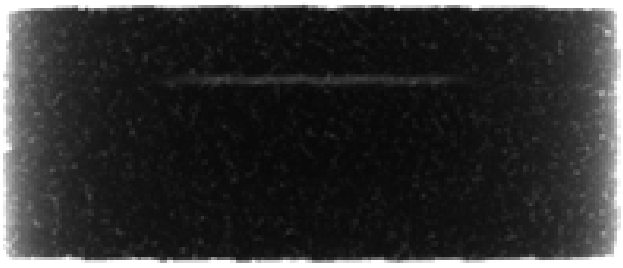

Figure 2. Radiography image for the packed sample of 3 pieces in Figure 1.

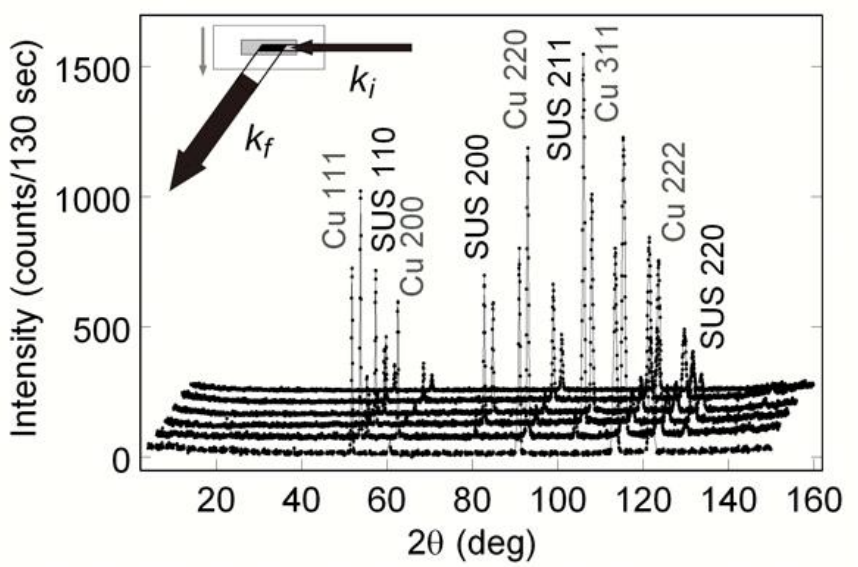

Figure 3. Neutron diffraction patterns of the test sample measured at HRPD from 1.5 mm to 21.5 mm by 4 mm step sliding along the gray axis in the inset. The diffraction pattern is shifted by 2 degrees and 50 counts each with increasing the sliding. Inset: Incident and final neutron wavevectors, k_i and k_f, are shown by black arrows with beam widths relative to the sample size. Positional scanning was carried out by sliding the black parallelogram scattering volume along the gray axis.

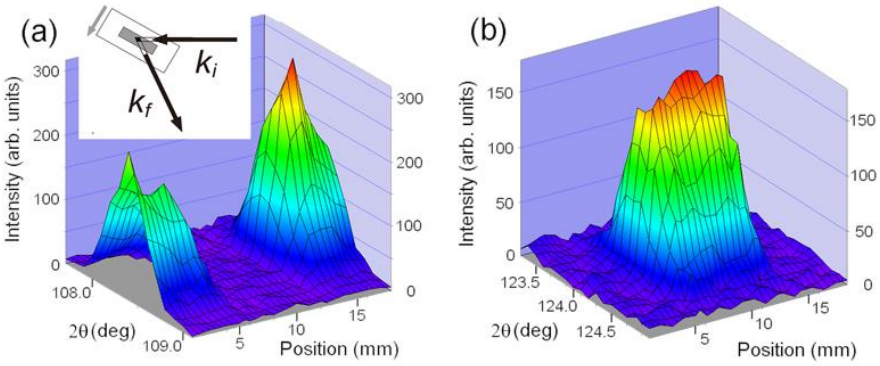

Figure 4. 3-dimentional neutron positional diffraction patterns of the test sample measured at RESA. The diffraction area was scanned by 0.5 or 1 mm step from 1 to 18 mm along the gray axis in the inset of (a). (a) 220 reflection for the FCC copper block. (b) 211 reflection for the BCC SUS430 plate. Inset: Incident and final neutron wavevectors, k_i and k_f, are shown by black arrows with beam widths relative to the sample size. Positional scanning was carried out by sliding the black parallelogram scattering volume along the gray axis.

Based on these results, we performed line structure scanning at RESA with narrow slits, which restricted the gauge volume as shown in the inset of Fig. 4(a). Two reflections of 220 for FCC copper and 211 for BCC SUS430 were measured at this diffractometer. The former reflection appeared at 2θ=108.4 degrees, while the latter peak was at 2θ=124.2 degrees as shown in Fig. 4. Since their

diffraction peaks have similar 2θ angles, the observed gauge volumes are the almost same to each other. The intensity weakly varies due to the possible large grain sizes of two materials. As shown in Fig. 4, the diffraction imaging clearly exhibited the positions of two materials, which contrasts to the photo in Fig. 2.

Figure 5 shows the side view of SUS430 plate in the copper block obtained by using high-intensity total diffractometer NOVA in J-PARC/MLF. The copper block and the aluminium rod weakly appear in the figure. Neutron absorption effect is corrected by a simple linear equation as a function of path length in the sample along x, which is normal to the direct beam direction z. This approximation corresponds to a limit of small absorption coefficient along x, but neglects the path along the incident beam. Event recording data were converted to d-dependent diffraction intensity table with an interval of Δd=0.01 Å. Integrated Bragg peak intensity at each pixel was obtained by simple summation of the intensities in the range of Δd=0.05 Å after subtracting both neighboring sides of diffraction intensities with the width of Δd=0.02 Å as a background. This intensity estimation method produces negative values on both sides of a positive peak due to the concave curve, which were regarded to be zero. Once 2D diffraction imaging is achieved, the tomography may be achieved with a set of various rotated data by using an existing tomography program.

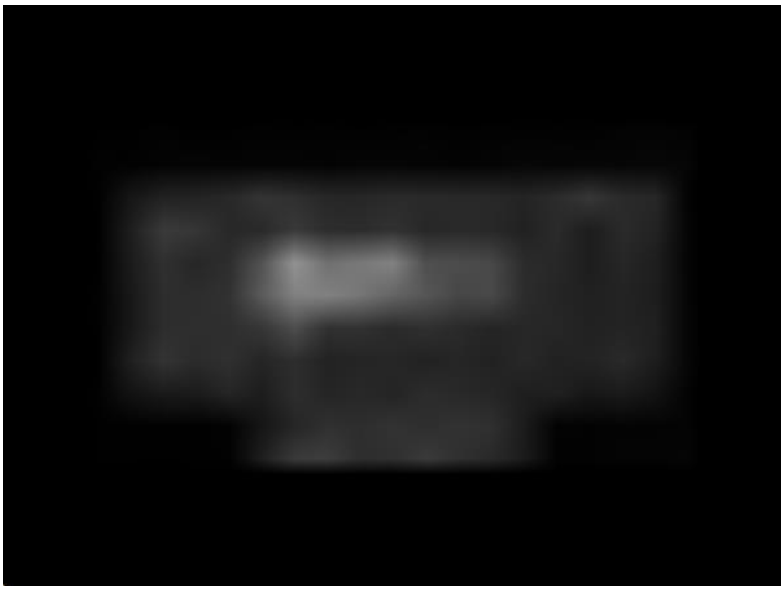

Figure 5. Neutron diffraction image of d~1.15 Å peak, corresponding to 211 reflection of the BCC SUS430 measured at NOVA.

Let us discuss the measuring efficiencies of diffraction imaging at various diffractometers. If we use slits with W x H before and T x H after the sample at the scattering angle 2θ, the measuring gauge volume V_g is $WHT/\sin 2\theta$. Here, we will define one Pixel Imaging Efficiency, PIE, which is defined simply to be Bragg peak intensity integrated by θ-2θ scan (counts/sec)/measuring time (sec)/gauge volume (mm^3).

In the experiment of RESA as shown in Fig. 4, V_g is 60-63 mm^3 depending on the scattering angle 2θ. Maximum integrated intensity of 220 reflection peak for the copper block with V_g of 63.2 mm^3 was 1448.1 counts/100 sec, while that of 211 reflection intensity for the SUS430 with V_g of 60.0 mm^3 was 1003.0 counts/100 sec. The background intensity was about 6-9 counts/100 sec. PIEs of RESA for copper 220 and SUS430 211 reflection peaks were 0.229 and 0.167, respectively.

As for the HRPD case with T=15 mm, maximum integrated intensity of 220 reflection peak for the copper block was 10426.2 counts/130 sec for V_g of 600.1 mm^3, while that of 211 reflection peak for the SUS430 was 4138.3 counts/130 sec for V_g of 613.4 mm^3. PIEs of HRPD for copper 220 and SUS430 211 reflection peaks were 0.134 and 0.052, respectively. The background intensity was about 23-39 counts/130 sec.

In the case of NOVA at J-PARC/MLF, maximum integrated intensity of 220 reflection peak for the copper block was 11646.8 counts/30 sec for V_g of 450 mm^3, while that of 211 reflection peak of the SUS430 was 772.3 counts/30 sec for V_g of 225 mm^3. PIEs of NOVA for copper 220 and SUS430 211 reflection peaks were 0.863 and 0.114, respectively. Under the long gauge volume conditions, these PIEs have large disadvantage of nearly one order of magnitude even in the former case in comparison with other diffractometers. Especially, in the latter case, the PIE value is strongly reduced due to the horizontal sample geometry. The background intensity was 30-44 counts/30 sec in these measurements.

As a result, all PIEs for these three diffractometers are comparable to each other for one measuring point at a d-value, although NOVA has several times higher efficiency than others. It should be noted that the multi-detector and time-of-flight instrument such as NOVA gives us a diffraction pattern in a wide Q-range all at once. This can further extend additional efficiency of wide-Q range measurement, resulting in an important merit even in comparison with that of high-intensity synchrotron x-ray diffractometers.

For a diffractomer monochromated by highly ordered pyrolytic graphite, the incident neutron flux is strongly reduced from the white neutron beam. Alternative way to get high intensity would be to use broad neutron spectrum at the sacrifice of the Q-resolution in the diffraction measurement to specialize the diffractometer for the diffraction imaging.

Here, we showed the efficiency of neutron diffraction imaging at various diffractometers. By using multi-detector system, the efficiency for a wide-Q range measurement can be dramatically improved even at the same diffractometer. Neutron lens can also increase the efficiency. In addition to the reciprocal space measurement, we may measure the atomic pair distribution function (PDF), in other word, real space measurement analysis, in the small area, which enables us to study phase separation, decomposition of amorphous or inhomogeneous liquid materials, for example.

Anyway, these nondestructive analyses would be very helpful for studying the inside of industrial materials with many phases. Among the various quantum beams, the neutron is a unique beam for the high penetration and the high sensitivity for light elements and magnetic moments. Intense pulse neutron sources such as J-PARC/MLF may provide us a chance to explore new type of imaging fields. In our previous study, crystal structures in an ammonite fossil were studied as an example by the neutron diffraction imaging method at NOVA in J-PARC [10].

4. Summary

The measuring efficiencies of diffraction imaging at various diffractometers are studied by using a simple test sample. Obtained efficiencies were comparable to each other for one measuring point. But time-of-flight measurement can multiply the efficiency significantly due to the time-of-flight method with a wide Q-range. Existing diffractometers such as RESA can be used for this scanning down to the sub-mm resolution. In order to reduce the diffraction volume, multi-detectors, neutron optics, and special monochromator with low Q-resolution are to be equipped. In addition, high intensity neutron source is inevitable. Possible new fields to be explored by this diffraction imaging were also discussed.

Acknowledgments

The authors would like to thank Drs. H. Matsue, T. Taguchi, A. Hoshikawa, Y. Ishii, M. Kureta, M. Segawa, and S. Iikubo for their help and fruitful discussions. This work was benefited from the use of following instruments, NOVA at J-PARC (Proposals 2012B0172, 2013B0099), RESA, HRPD, and TNRF at JRR-3.

References

[1] E. H. Lehmann, Neutron News, **17**-1, 22 (2006).
[2] "Neutron Imaging and Applications: A Reference for the Imaging Community" (Springer, 2009): Ian S. Anderson, Robert L. McGreevy and Hassina Z. Bilheux.
[3] W. Treimer, M. Strobl, A. Hilger, C. Seifert, and U. Feye-Treimer, Appl. Phys. Lett. **83**, 398 (2003).
[4] M. Strobl, W. Treimer, and A. Hilger, Appl. Phys. Lett., **85**, 19 (2004).
[5] N. Kardjilov, I. Manke, M. Strobl, A. Hilger, W. Treimer, M. Meissner, T. Krist and J. Banhart, Nature Phys. **4** (2008) 399.
[6] P. Bleuet, E. Welcomme, E. Dooryhee, J. Susini, J.-L. Hodeau and P. Walter, Nature Mat. **7** (2008) 468.
[7] H. Ohshita, T. Otomo, S. Uno, K. Ikeda, T. Uchida, N. Kaneko, T. Koike, M. Shoji, K. Suzuya, T. Seya and M. Tsubota, Nucl. Instrum. Methods Phys. Res. Sect. A **672** (2012) 75.
[8] Albert-Jose Dianoux, and Gerry Lander, *Neutron Data Booklet* (Institute Laue-Langevin, Grenoble, 2002).
[9] Diffraction intensity mapping program "Neudift" ver. 1 is developed by one of the authors, Mr. Tadashi Imaki, for conversion of diffraction data sets to a photo.
[10] Shin-ichi Shamoto, Katsuaki Kodama, Tadashi Imaki, Takeshi Nakatani, Hidetoshi Oshita, Naokatsu Kaneko, Kenji Masuko, Kensaku Sakamoto, Kenji Yamaguchi, Kentaro Suzuya, Toshiya Otomo, JPS Conf. Proc. 1, 014011 (2014)

3.9.4

Automation of neutron spectrometry experiments using network technologies

V K Ignatovich[1], I M Salamatin[1] K M Salamatin[2] and A E Senner[2]

[1] FLNP JINR, 6 Joliot-Curie, Dubna, Moscow reg., 141980 Russia

[2] International University "Dubna", 17 University, Dubna, Moscow reg., 141980 Russia

E-mail: v.ignatovi@gmail.com

Abstract. Standardized means of experiments description and of operations sequence control, which do not require editing system components, when experiment is changed, are proposed.

1. Introduction

A new structure of distributed software for experiments automation system (EAS) for series of research works in neutron spectrometry was developed. Every particular experiment contains a list of data recording conditions, and a method of data recording and processing. Upon completion of the experimental data analysis a new research plan with change of experimental procedures usually occurs. As a rule the new experiment requires hardware and software changes. Modification of each EAS, as was mentioned in [1], requires a work of a team of several programmers for about 6 months. The known ideologist of the Code Gear of the Borland Software firm David Intersymon notes that such a long development time is associated with the lack of an adequate strategy for code reuse of existing programs [2]. Therefore, to shorten the new experiments preparation time one must be able to use existing software components. A goal of this paper is to show some methods, which help to make unified components and to use existing components without their modification when experiment conditions are changed. The main question when creating a unified program is how to link individual components without their modification at such changes.

2. Linking components in software of EAS

At usual static linking the needed information (such as network addresses of interacting components and information about interfaces) is somehow fixed before the start of the EAS. The static linking is robust and allows faster execution of interaction and communication between system components. However a failure of one of the components during the EAS operation in this case leads as a rule to loss of efficiency of the entire system, and even small changes in the experimental procedure require modification of several components. The static linking significantly complicates the reuse of components in EAS without their modification. This defect is absent in dynamical linking, because necessary information to ensure the interoperability of components is produced during the EAS operation itself. Therefore the dynamical linking for EAS development has the advantage in the case of systems with frequently variable functions.

The dynamical linking uses network technologies, and the most popular of them were analyzed in [3,4]. As a result of this analysis a special version of a mediator program DiCME (Distributed Components Messaging Environment) for dynamical linking of components was developed. The mediator DiCME provides basic technological support for EAS software and has the following key features:

(i) automatic search and linking of components;
(ii) asynchronous mechanism for remote execution of procedures;
(iii) transmission of information to multiple processes simultaneously;
(iv) processing of all interactions of components of EAS with the same means;
(v) independence of the access to the components procedures upon the network address of the computer.

3. Possibilities of the components unification

If the experimental procedure requires new equipment not provided in advance, it becomes necessary to change the composition of the components used and to edit the sequence of operations in the experiment. There are two traditional methods of an experiment control:

(i) usage of a fixed group of procedures written in a programming language, where each procedure implements a specific method of the experiment, and required parameters are set via a dialog box, or are obtained from a data file;
(ii) usage of an interpreter in EAS composition and preparing an experiment control program (script) in the form of a list of calls of external routines, and values of the parameters.

In both methods, in fact, the program of the operations sequence control in the experiment includes a list of procedures calls, which results in a rigid components coupling. Practice shows that error rate in written scripts can reach 70%, and the adjustment of EAS software, which uses scripts and configuration files can take up to two days [5]. Substantial simplification was proposed in [6,7], but these studies do not solve the general problem of scripts - the problem of components linking. To solve the problem of unification and to develop a dynamical method of components linking, when the experimental technique changes, an analysis of the functional composition and of characteristics of the EAS software components was made. Based on this analysis the following features were found [8]:

- dynamical linking of components for remote procedures execution is necessary only for the main functions: management of conditions for registration, conversion and archiving of experimental data;
- the result of a remote procedure must contain 1) a mandatory shutdown signal, addressed to the caller (the experiment managing program or the user interface) and 2) detailed information (list of registered data, description of the managed object state, a diagnostic message , etc.) addressable to auxiliary functions;
- implementation of auxiliary functions (data visualization, feedback, etc.) requires a special method for connecting components, taking into account the spontaneous nature of requests for such operations and the independence of the basic functions (in normal conditions) upon the results of operations of the auxiliary functions.

Having in mind these features, it is proposed in the given paper to exclude the procedure calls from the experiment description and to separate the experiment managing tool from the description of the experimental procedure. The proposed method of the experiment management is as follows:

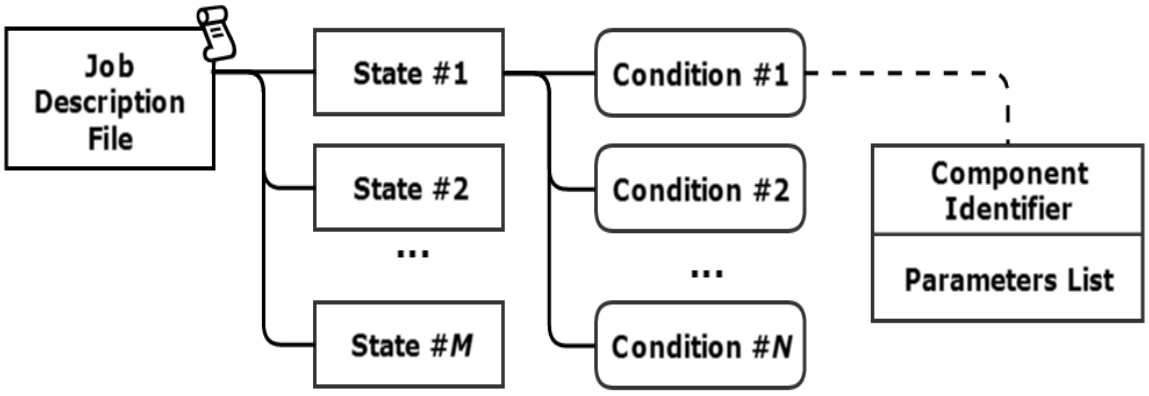

Figure 1. The structure of the PSJ file for an experiment

- experiment managing program completes two abstract processes (conditions formation and data registration) and by default assumes that the data registration goes after the formation of the conditions. The program dictates the conditions for the data registration in an experiment description file;
- specification of these abstract processes (for example, the composition of the components used) is performed dynamically using the file with conditions of data registration created by a subsystem of experiment description.

4. The subsystem of the experiment description

To describe the methodology and compose experiment description file information about the devices and components working with them (devices passports) is required. Detection system and the data input controller for the spectrometer are fixed. A set of components performing data input, conversion and archiving, are usually combined into a data acquisition (DAQ) subsystem, and call of this subsystem can be performed by default after the formation of the data registration conditions. Subsystem describing experimental procedure includes a database (DB) and two interactive programs: 1) the one used by programmers for producing passports of devices and components, managing the data registration conditions; 2) and the other one, PSJ (Preparation of Single Job), used by experimenters.

4.1. The program for devices passports

compilation creates and stores in the DB the documentation: devices description in the JSON format. Documentation includes: the name of the controller and a list of devices connected to it; the type of the component working with the controller, its unique identifier (GUID), used for addressing component, and descriptions of parameters. Parameters composition (application protocol) is defined by the component developer.

4.2. The PSJ program

uses the list of available devices (and components) from the database. From this database, the user selects in a dialogue the desired components in his experiment and makes a list of devices that in the process of the experiment will determine the data registration conditions. For each device in the list one can specify a list of consecutive values of the used control parameter. The result of this work is PSJ-file with a table describing the desired states in the experiment hardware system. In each state, a data exposition is performed. The structure of the PSJ file for an experiment is shown in Fig.1.

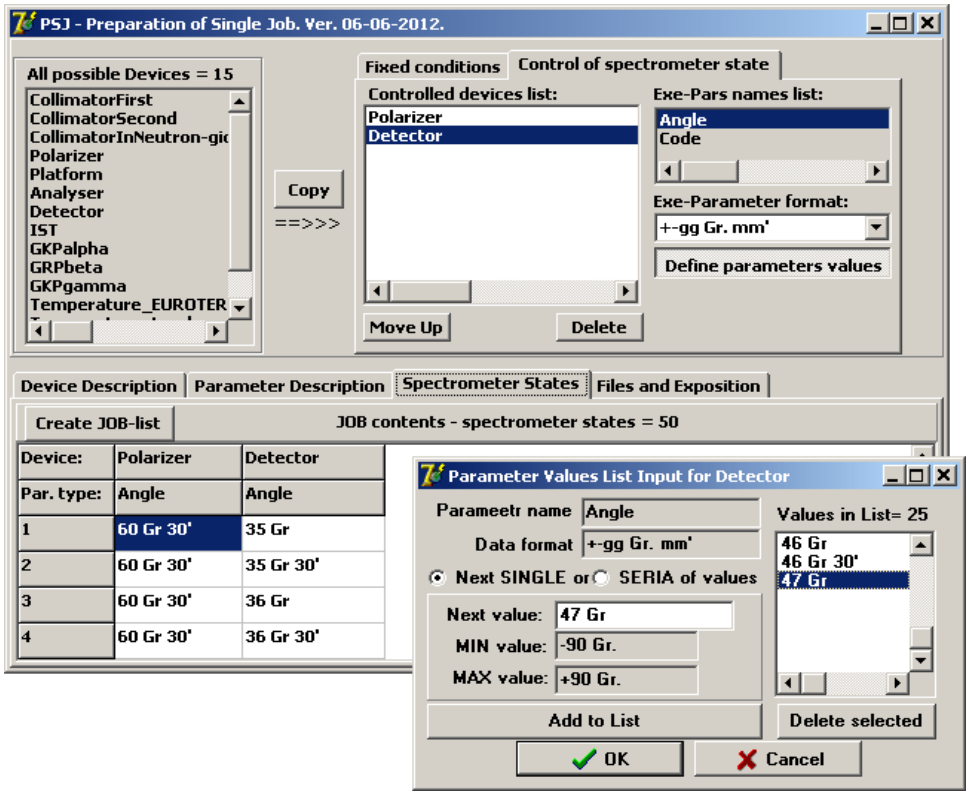

Figure 2. The user interface for PSJ file preparation

A distinctive feature of the method proposed in this paper from those used in other systems is that the PSJ program produces a list of data registration conditions instead of the actions described in the form of a procedure calls list in a script file or hard-coded procedures. Description of the experimental technique uses only experimenter's terminology: names of the spectrometer components, angular positions, etc. The program automatically composes PSJ file with components identifiers (GUID) in the JSON format. A user interface of the job preparing program is shown in Fig.2.

5. An experiment management with a mediator DiCME and PSJ files

Fig.3 shows the interaction of the experiment management program (EMP) and mediator DiCME in basic operations of the EAS software. The PSJ file comes to the EMP entry. EMP selects the consecutive description of the system state (list of the data registration conditions) and sends a description of each condition to the mediator DiCME. Description of the condition carries information about the component (GUID) sufficient for its search and linking to EMP, and also a list of parameters. DiCME finds the needed component and passes to it a message describing the condition containing the list of parameters. EMP functions as a dispatcher of the components used. The choice and call of needed procedures that implements the required data registration conditions is performed in the components that drive the hardware, based on the interpretation of the referred to them conditions descriptions. For example, to manage the position of the polarizer condition description in JSON format looks as follows:

device:"polarizer", parameter:"angle", value: "30 grad"

Each component, which receives a message from EMP should return to EMP signal (DONE/ ERROR) of the operation completion. After receiving of such signals from all the devices listed

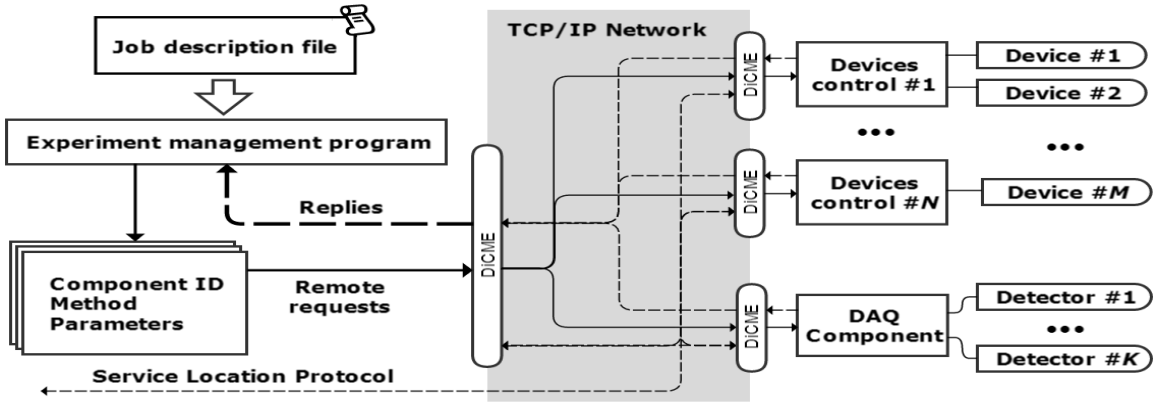

Figure 3. Scheme of interaction of EMP and mediator DiCME in implementing the basic tasks of the EAS

in the description of the desired EAS state, the EMP starts DAQ subsystem. Completion signal of the data acquisition allows the EMP to switch to processing of the next state in the job description file. Using dynamic linking method [4], contrary to the CORBA etc. technologies, one does not need preparatory dialogue between the components to configure remote execution procedure. The described linking method does not limit the development of the experimental procedure, and its changes do not affect the EMP and inter-component communication mediator DiCME, because the EMP and DiCME are transparent to the parameters lists.

The most significant features of auxiliary operations are as follows:

- spontaneous nature of information about events and the ability to postpone its treatment;
- a necessity to transmit information to multiple processes, the composition of which, generally speaking, is not known to the source of information and can be changed by EAS user during the EAS software working.

To link the auxiliary components a version of the "subscription" algorithm is used. In this algorithm the component-consumer once declares interest in a particular type of information. Then a special component (Event Manager, a part of DiCME) caters for all "signed" with the the interested information, when it appears. A schematic diagram of a mediator DiCME serving auxiliary operations in EAS is shown in Fig.4.

As a result, the implementation of auxiliary operations through DiCME allows a user to dynamically arrange the system with the necessary auxiliary functions simply by running on any computer of local network of the desired component.

6. Experiment management program

The method of constructing a unified EMP and the assignment to the experiment is described above in detail. The practice of precise measurements requires some additions. Fig.5 shows a diagram of the management program in the high precision measurements. The diagram shows that many hours of exposure in each state ("States control cycle" in fig. 5) of the experimental setup is divided ("Statistics accumulation cycle" in fig. 5) into several (usually identical) shorter runs, the results of which can be summed. Due to this, comparison of the data in separate files, obtained under same conditions, permits to detect possible drift of background, of detector efficiency and other effects, and filter out incorrect data.

This EMP protocols the job: program remembers the last command, the number of the last completed state of the system (executed jobs line), and some other data, and uses it to

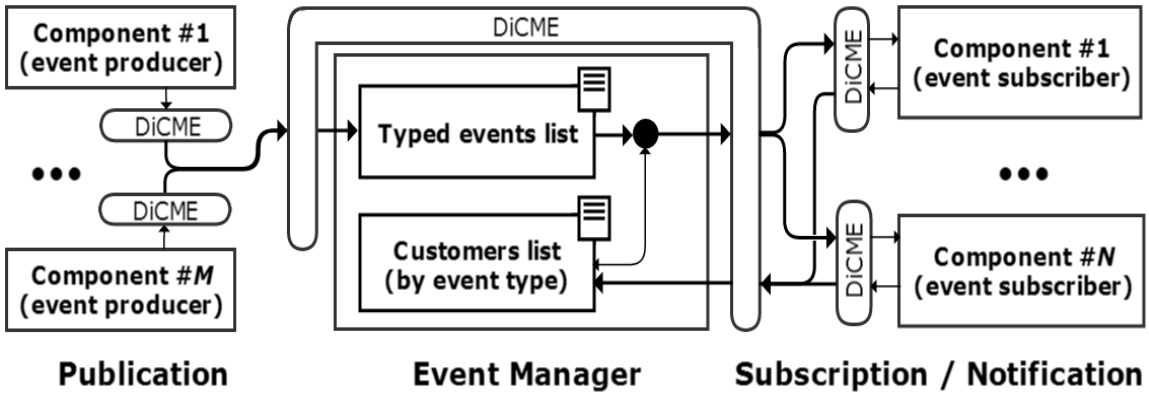

Figure 4. Scheme of the event manager and mediator DiCME serving auxiliary operations.

automatically generate file names. This means that at failures it is possible to restart the system. After restart it will continue to work starting with the last unfinished state. Local menu provides several debug modes.

7. Key findings

The subsystem which describes the experimental technique forms the information base for components dynamic linking algorithms, for specifying the functional composition of the processes performed by the experiment management program, and for automatic integration of components into the EAS software. This subsystem significantly reduces the software adjustment for a new experiment and facilitates the work of the experimenter, which is a key element, because it made possible to transfer the EAS software to experimenters themselves to manipulate it, when the experiment is changed. Model of EMP performing two abstract processes (formation of data registration conditions and data registration), is appropriate for different experiments and in other systems. Proposed EAS software is a problem-oriented distributed software package of applied programs, including managing components for the package (means of interoperability of components and experiment management program) and the standardized application components. Subsystem of experimental technique descriptions provides a language for package management. The proposed structure can be used in other areas

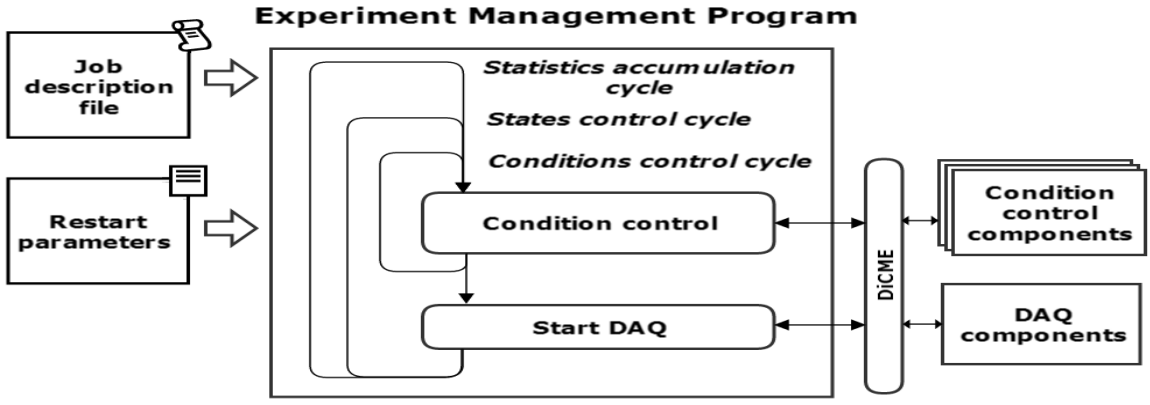

Figure 5. Scheme of the experiment management program for long measurements.

of human activity, for example, for technology processes automation. The approach presented here was applied to the development of EAS software for spectrometers used in experiments on neutron sources IBR-2 and IREN at JINR [9-11].

References

[1] Levis P, Cooper G, Trouw F et al 2010 Data Acquisition and Instrument Control at the Lujan Center: An Update *NOBUGS2010, Preliminary Agendas NOBUGS34*

[2] Taft D 2008 What we expect from the year 2027-th *PC Week/RE* n 8 (614) 11-17 (in Russian)

[3] Salamatin K M 2013 The choice of technology for constructing component system for automation of experiments in the field of neutron spectrometry *Commun. JINR P13-2013-72, Dubna* (in Russian)

[4] Salamatin K M 2014 DiCME - distributed components messaging environment for automation of experiments for low energy physics *Software Engineering* n 3, 3-11 (in Russian)

[5] Konnecke K, Hauser N, Franceshcini F et al 2008 *Treepath Based Instrument Control NOBUGS2008* n 132

[6] Nakatani T, Inamura Y, Ito T et al 2010 Present status of the computing environment for the experimental instruments in J-PARC/MLF *NOBUGS2010, Preliminary Agendas NOBUGS40*

[7] Clarke M, Nakatani T, Inamura Y et al 2010 Making life easier for scientists: developing an Experiment Scheduler for the MLF *NOBUGS2010, Posters NOBUGS2010*

[8] Salamatin I M, Salamatin K M 2014 Network technologies in software systems for neutron spectrometry automation *Applied Informatics* 3(55) 5-25 (in Russian); Development of components-based EAS for low energy physics through the use of network technologies *Commun. JINR P13-2013-74, Dubna* (in Russian)

[9] Tsulaia M I, Salamatin I M, Sirotin A P et al 2013 The Kolkhida Setup Upgrade *Proc. ISINN-21 (Alushta, Ukraine, May 20-25, 2013), Dubna E3-2013-40* (Dubna: JINR) 77

[10] Kuznetsov V L, Kuznetsova E V, Sedyshev P V 2013 Investigation of Possibilities for the Measurement of Parity Violation in Neutron Diffraction at the IBR-2M Reactor *Proc. of Internat. Seminar ISINN-20 (Dubna, May 27-29, 2012) Dubna E3-2013-22* (Dubna: JINR) 66-68

[11] Shvetsov V N, Alpatov S V, Astakhova N V et al 2012 8-input system for neutron-nuclear research by the method of time-of-flight *Instruments and Experimental Techniques* **55** 561-568

3.9.5

$^{6}Li/^{7}Li$ and $^{14}N/^{15}N$ isotopic substitution experiments using NOVA spectrometer at J-PARC

Yasuo Kameda*[1], Takuya Miyazaki[1], Yuko Amo[1], Takeshi Usuki[1] and Toshiya Otomo[2]
[1]Department of Material and Biological Chemistry, Faculty of Science, Yamagata University, Yamagata 990-8560, Japan
[2]Institute of Material Structure Science, KEK, Tsukuba, Ibaraki 305-0801, Japan

E-mail: kameda@sci.kj.yamagata-u.ac.jp

Abstract. Neutron scattering measurements have been carried out for $^{6}Li/^{7}Li$ and $^{14}N/^{15}N$ isotopically substituted aqueous $^{*}Li^{*}NO_3$ solutions in D_2O using the high intensity total scattering spectrometer NOVA installed in J-PARC. In the present study, concentration of the solute was extended to the very dilute region at 1 mol% $LiNO_3$, and information on the hydration structure of Li^+ and NO_3^- was successfully deduced. In the aqueous 1 mol% $LiNO_3$ solution, it has been found that Li^+ is surrounded by 6.0 ± 0.2 water molecules with the nearest neighbour $Li^{+}\cdots O$ distance of 2.00 ± 0.02 Å. The hydration number of NO_3^- in aqueous 1 mol% $LiNO_3$ solution is determined to be 6 ± 2 with the intermolecular distance between N atom and the nearest neighbour D (D_2O) atom of 3.0 ± 0.1 Å. Concentration dependence of hydration parameters for these ions is discussed.

1. Introduction

Isotopic substitution method is one of the most promising applications in the structural investigations of non-crystalline materials using neutron total scattering experiments. The environmental structure around isotopically substituted atom can be extracted by taking subtraction of scattering cross sections observed for samples with different isotopic compositions [1]. A drawback of this technique might be the difficulty in obtaining sufficient S/N ratio of subtracted intensity data. In order to keep favourable statistical accuracy in the subtracted intensity, the use of high intensity incident neutron beam is indispensable.

In the present paper, we report results of neutron scattering measurements on $^{6}Li/^{7}Li$ and $^{14}N/^{15}N$ substituted aqueous $^{*}Li^{*}NO_3$ solutions in D_2O using the NOVA spectrometer installed in J-PARC. In the present study, concentration of the solute was extended to the very dilute region at 1 mol% $LiNO_3$ and information on the hydration structure of Li^+ and NO_3^- was successfully deduced. In the present analysis, the re-normalization procedure for the observed scattering cross sections was applied employing the least squares fitting analysis of intramolecular interference terms for D_2O and NO_3^- in order to confirm the absolute amplitude of observed difference function.

*To whom any correspondence should be addressed.

2. Experimental and Data Analysis

^{6}Li- and ^{7}Li-enriched lithium nitrate was prepared by reacting $^{6}Li_2CO_3$ (95.6% ^{6}Li) and $^{7}LiOH{\cdot}H_2O$ (99.94% ^{7}Li) with slightly excess amount of concentrated $H^{14}NO_3$ (99.6% ^{14}N, natural abundance) and $H^{15}NO_3$ (88.9% ^{15}N) aqueous solutions. The dehydration of the product solution was achieved by heating at 180 ºC under vacuum more than a day. The weighted amount of enriched anhydrous $^{*}Li^{*}NO_3$ was dissolved into D_2O (99.9 % D, Aldrich Chemical Co.) to prepare 1, 5 and 10 mol% $^{*}Li^{*}NO_3$ solutions with different ^{6}Li/^{7}Li and ^{14}N/^{15}N isotopic compositions. Average coherent scattering lengths of Li and N atoms in sample solutions used in this study are summarized in Table 1. The sample solution was introduced into a thin-walled cylindrical vanadium cell (6.0 mm in inner diameter and 0.1 mm in thickness) and sealed by an Indium-seal.

Table 1. Average coherent scattering lengths of Li and N atoms.

Sample	$b_{Li}/10^{-12}$cm	$b_{N}/10^{-12}$cm
$(^{6}Li^{14}NO_3)_{0.1}(D_2O)_{0.9}$	0.182	0.936
$(^{7}Li^{14}NO_3)_{0.1}(D_2O)_{0.9}$	-0.222	0.936
$(^{7}Li^{15}NO_3)_{0.1}(D_2O)_{0.9}$	-0.222	0.677
$(^{6}Li^{14}NO_3)_{0.05}(D_2O)_{0.95}$	0.182	0.936
$(^{7}Li^{14}NO_3)_{0.05}(D_2O)_{0.95}$	-0.222	0.936
$(^{7}Li^{15}NO_3)_{0.05}(D_2O)_{0.95}$	-0.222	0.677
$(^{6}Li^{14}NO_3)_{0.01}(D_2O)_{0.99}$	0.182	0.936
$(^{7}Li^{14}NO_3)_{0.01}(D_2O)_{0.99}$	-0.222	0.936
$(^{7}Li^{15}NO_3)_{0.01}(D_2O)_{0.99}$	-0.222	0.677

Neutron diffraction measurements were carried out at 25 ºC using the NOVA spectrometer [2] installed at BL21 of the MLF pulsed neutron source in the J-PARC, Tokai, Japan. Incident proton beam power of proton accelerator was 160 kW in measurements for 5 and 10 mol% $^{*}Li^{*}NO_3$ solutions, and 220 kW for 1 mol% $^{*}Li^{*}NO_3$ solutions, respectively. Scattered neutrons (neutron wave band of $0.1 \leq \lambda \leq 8.7$ Å) were detected by ca. 900 of 20 atm ^{3}He position sensitive proportional counters (1/2 inch ϕ, 800 mm in active length with 5 mm in positional resolution) installed at 20º (13.1 – 27.9º), 45º (33.6 – 54.9º), 90º (72.7 – 107.4º) and back scattering (136.5 – 169.0º) detector banks. Data accumulation time was ca. 4 h for each sample. Measurements were made in advance for 6 mm ϕ vanadium rod, empty cell and instrumental background.

Observed scattering intensities for the sample were corrected for instrumental background, absorption of sample and cell [3], multiple [4] and incoherent scatterings. The coherent scattering lengths, scattering and absorption cross sections for the constituent nuclei were referred to those tabulated by Sears [5]. The wavelength dependence of the total cross sections for H and D nuclei was estimated from the observed total cross sections for H_2O and D_2O, respectively [6]. The inelasticity correction for the observed self-scattering term was applied by the use of the observed self-scattering intensities from the liquid null-H_2O [7].

The first-order difference function $\Delta_X(Q)$, X = Li and N, is derived from the numerical difference between scattering cross sections observed for two solutions that are identical except for the scattering lengths of Li or N atoms [1]. The $\Delta_X(Q)$ normalized for a stoichiometric unit, $(^{*}Li^{*}NO_3)_x(D_2O)_{1-x}$, can be written as a linear combination of partial structure factors, $a_{Xj}(Q)$, involving contributions from the X-j pair:

$$\Delta_X(Q) = \Sigma A_{Xj}[a_{Xj}(Q) - 1]. \quad (1)$$

The weighting of the structure factor can be written as $A_{Xj} = 2c_Xc_j\Delta b_Xb_j$ (for j ≠ X) and $A_{Xj} = c_X^2(b_X^2 - b_{X'}^2)$ (for j = X), where c_j and b_j denote the number in the stoichiometric unit and the coherent scattering length of j atom, respectively. Since the weighting factors, A_{XO} and A_{XD} are much

larger than others in the present experimental condition, the observed $\Delta_X(Q)$ is dominated by the short-range X-D_2O interaction. The observed $\Delta_X(Q)$ from forward angle detector pixels located at $13.1 \leq 2\theta \leq 54.9^o$ agree well within the statistical uncertainties, they were combined at the Q-interval of 0.1 Å^{-1} and used for subsequent analyses. The distribution function around X atom, $G_X(r)$, is obtained from the Fourier transform of $\Delta_X(Q)$:

$$G_X(r) = 1 + (\Sigma A_{Xj})^{-1}(2\pi^2\rho r)^{-1}\int_0^{Q_{max}} Q\Delta_X(Q)\sin(Qr)\,dQ$$
$$= [\Sigma A_{Xj}\, g_{Xj}(r)]\,(\Sigma A_{Xj})^{-1}, \quad (2)$$

where, ρ denotes the number density of the sample. The upper limit of the integral was set to be 20 Å^{-1} in the present study.

Structural parameters concerning the hydration shell of X were obtained through the least squares fitting procedure applying the following model function [8-10]:

$$\Delta_X^{model}(Q) = \Sigma\, 2c_X n_{X\alpha} b_\alpha \Delta b_X \exp(-l_{X\alpha}^2 Q^2/2)\sin(Qr_{X\alpha})/(Qr_{X\alpha})$$
$$+ 4\pi\rho\,(\Sigma A_{Xj})\exp(-l_0^2 Q^2/2)[Qr_0\cos(Qr_0) - \sin(Qr_0)]Q^{-3} + \gamma, \quad (3)$$

where, $n_{Li\alpha}$ is the coordination number of α atom around X. Sort-range parameters $l_{X\alpha}$ and $r_{X\alpha}$ denote the root-mean-square amplitude and internuclear distance of the X···α pair, respectively. The long-range parameter, r_0, means the distance beyond which the continuous distribution of atoms around X can be assumed. The parameter, l_0, describes the sharpness of the boundary at r_0. A constant, γ, was introduced to adjust the center of the interference oscillation, which is effective for improving the fit. Structural parameters $n_{X\alpha}$, $l_{X\alpha}$, $r_{X\alpha}$, l_0, r_0 and γ are determined from the least squares fit to the observed $\Delta_X(Q)$. The fitting procedure was performed in the range of $0.1 \leq Q \leq 20.0$ Å^{-1} with the SALS program [11], assuming that the statistical uncertainties distribute uniformly. In the least squares fitting calculation, the Marquardt method was employed. The dynamical bi-weight method was used for weight adjustment of the observed data [11].

In order to check reliability of the data correction and normalization procedures employed in the present study, the least squares fitting analysis was first carried out for the observed total interference term before taking the first-order difference. Since intermolecular interference term diminishes much faster than intramolecular one with increasing Q-value, interference amplitude observed in sufficiently high-Q region can be regarded as the intramolecular interference contribution. In the present analysis, the theoretical intramolecular interference term, $i^{intra}(Q)$, was evaluated by the sum of intramolecular interference terms for D_2O, $i_{D_2O}{}^{intra}(Q)$, and NO_3^-, $i_{NO_3^-}{}^{intra}(Q)$, molecules as follows:

$$i^{intra}(Q) = \beta[(1-x)\, i_{D_2O}{}^{intra}(Q) + x\, i_{NO_3^-}{}^{intra}(Q)], \quad (4)$$

where

$$i_{D_2O}{}^{intra}(Q) = 4b_O b_D \exp(-l_{OD}^2 Q^2/2)\sin(Qr_{OD})/(Qr_{OD})$$
$$+ 2b_D^2 \exp(-l_{DD}^2 Q^2/2)\sin(Qr_{DD})/(Qr_{DD}), \quad (5)$$

and

$$i_{NO_3^-}{}^{intra}(Q) = 6\, b_N b_O \exp(-l_{NO}^2 Q^2/2)\sin(Qr_{NO})/(Qr_{NO})$$
$$+ 6b_O^2 \exp(-l_{OO}^2 Q^2/2)\sin(Qr_{OO})/(Qr_{OO}). \quad (6)$$

β denotes the overall renormalization factor which indicates appropriateness of the data correction and normalization procedures employed. In the fitting procedure, intramolecular parameters for D_2O molecule, l_{OD}, r_{OD}, l_{DD} and r_{DD}, as well as the factor β were treated as independent parameters. Since contribution from the intramolecular interference term for NO_3^- should be relatively small, intramolecular parameters for NO_3^- were fixed to the literature values (l_{NO} = 0.045 Å, r_{NO} = 1.252 Å, l_{OO} = 0.065 Å, and r_{OO} = 2.169 Å) [12-14]. The least squares fitting analysis was performed in the range of $10 \leq Q \leq 40$ Å^{-1} with the SALS program [11].

3. Results and Discussion

Before evaluation of the first-order difference function, the least squares fitting analysis was carried out for the observed total interference function to check the absolute interference amplitude of each sample solution using equation (4). To avoid large inelasticity effect on the observed scattering intensity, scattering cross sections obtained from forward angle detector banks (13.1 – 54.9º) were combined at the Q-interval of 0.1 Å^{-1} and used for the least squares fitting analysis. A satisfactory fit was obtained in the range of $10 \leq Q \leq 40$ Å^{-1}. The value of renormalization factor, β, for each solution is very close to the unity within the experimental uncertainties (β = 0.96(2) – 1.01(3)), implying that data correction and normalization procedures have been adequately carried out in the present study and the absolute value of the difference function should be reliable. The present value of intramolecular O-D distance within D_2O (r_{OD} = 0.970 - 0.976 Å) is somewhat slightly small when compared with that reported for pure liquid water (0.983(8) Å [15], 0.983(5) Å [16], 0.987(5) Å [17]). The present values of r.m.s. amplitudes for the intramolecular O-D and D-D interactions (l_{OD} = 0.058 - 0.061 Å and l_{DD} = 0.117 – 0.14 Å) are in good agreement with those for pure liquid water (l_{OD} = 0.067(8) Å and l_{DD} = 0.12(4) Å [16]).

The first order difference function, $\Delta_{Li}(Q)$, observed for 1, 5 and 10 mol% $Li^{14}NO_3$ solutions is represented in Figure. 1. The distribution function around Li^+, $G_{Li}(r)$, was obtained from the Fourier transform of the observed $\Delta_{Li}(Q)$ as depicted in Figure. 2.

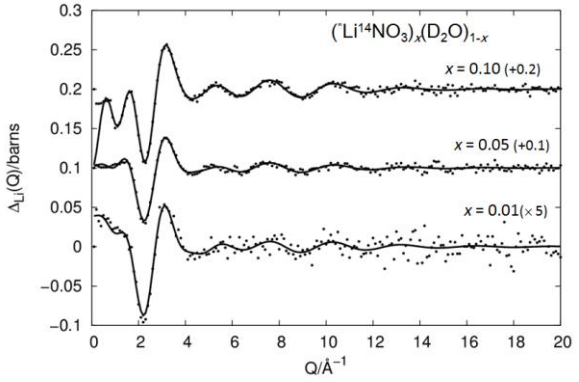

Figure 1. First-order difference function, $\Delta_{Li}(Q)$, observed for 1, 5 and 10 mol% $^*Li^{14}NO_3$ heavy water solutions (dots). The best fit of the calculated $\Delta_{Li}(Q)$ is indicated by a solid line.

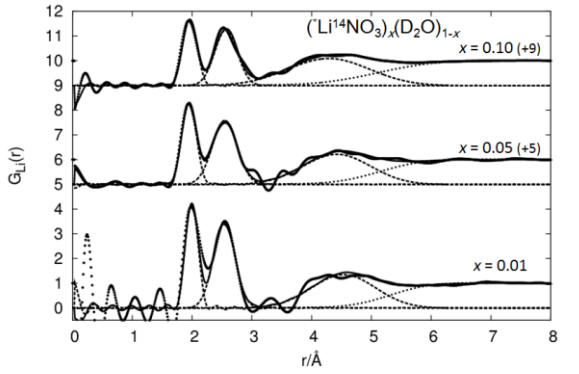

Figure 2. Distribution function around Li^+, $G_{Li}(r)$, observed for 1, 5 and 10 mol% $^*Li^{14}NO_3$ heavy water solutions (dots). The Fourier transform of the best fit of calculated $\Delta_{Li}(Q)$ is indicated by a solid line. Short- and long-range contributions are denoted by a broken- and dotted lines, respectively.

Dominant short range peaks appearing at around 2 and 2.6 Å in the present $G_{Li}(r)$, are assigned to the nearest neighbour $Li^{+}\cdots O$ and $Li^{+}\cdots D$ interactions, respectively [18-24]. In the fitting procedure, the structural parameter, n_{LiD}, was fixed to $2n_{LiO}$ during the present least squares fitting procedure. The second coordination sphere of Li^{+} was treated as a single interaction with the coherent neutron scattering length in equation (3), b_{α}, being $b_O + 2b_D$. The long-range random distribution of atoms was taken into account in the analysis, which is important to improve the fit in the low-Q region. As described in Figure. 1, the observed $\Delta_{Li}(Q)$ for each solution is satisfactorily reproduced by the calculated model function in the whole Q-range observed. Final results of independent parameters are listed in Table 2.

Table 2. Results of the least-squares refinement of the observed $\Delta_{Li}(Q)$[a].

x	interaction	i···j	r_{ij}/Å	l_{ij}/Å	n_{ij}
0.1	$Li^{+}\cdots D_2O$(I)	$Li^{+}\cdots O$	1.969(8)	0.117(9)	4.12(6)
		$Li^{+}\cdots D$	2.58(1)	0.187(7)	[6.24][b]
	$Li^{+}\cdots D_2O$(II)	$Li^{+}\cdots D_2O$	4.4(1)	0.68(2)	14(4)
			r_0/Å	l_0/Å	
	Long-range		5.2(3)	0.8(3)	
0.05	$Li^{+}\cdots D_2O$(I)	$Li^{+}\cdots O$	1.957(4)	0.113(5)	5.18(3)
		$Li^{+}\cdots D$	2.564(5)	0.204(4)	[10.36][b]
	$Li^{+}\cdots D_2O$(II)	$Li^{+}\cdots D_2O$	4.5(1)	0.563(9)	14(5)
			r_0/Å	l_0/Å	
	Long-range		5.2(4)	0.6(4)	
0.01	$Li^{+}\cdots D_2O$(I)	$Li^{+}\cdots O$	2.00(2)	0.10(3)	6.0(2)
		$Li^{+}\cdots D$	2.55(4)	0.18(2)	[12.0][b]
	$Li^{+}\cdots D_2O$(II)	$Li^{+}\cdots D_2O$	4.6(5)	0.54(4)	15(3)
			r_0/Å	l_0/Å	
	Long-range		5.4(2)	0.5(1)	

[a] Estimated standard deviations are given in parentheses.

[b] Fixed at the value $2n_{LiO}$.

The present value of r_{LiO}, for 5 and 10 mol% $LiNO_3$ solutions is in good agreement with that obtained in previous neutron diffraction studies [18-22], while, the value, r_{LiO} = 2.00(2) Å determined for 1 mol% $LiNO_3$ solution is slightly larger than those obtained for more concentrated solutions. The present values of the nearest neighbor $Li^{+}\cdots D$ distance, 2.55(4), 2.564(5) and 2.58(1) Å observed for 1, 5 and 10 mol% $LiNO_3$ solutions agree well with those reported previously [18-22]. The present results of n_{LiO} for $LiNO_3$ solutions indicate that the concentration dependence of the hydration number of Li^{+} is actually present. Previous neutron diffraction studies for aqueous LiCl [18,19] and LiBr [20] solutions suggested that hydration number of Li^{+} varies with solute concentration.

Difference functions, $\Delta_N(Q)$, observed for 1, 5 and 10 mol% $^7Li^*NO_3$ solutions are indicated in Figure 3. Interference features extended to higher-Q region are clearly observed. The distribution functions around N atom within NO_3^- are depicted in Figure 4. Dominant first peak located at r = 1.25 Å is obviously assigned to intramolecular N-O interaction within the NO_3^-. A broad peak appearing at $r \sim 3$ Å is attributable to the nearest neighbour $N\cdots D_1$ (D_2O) interaction, which has been found for concentrated aqueous $NaNO_3$ solution [13]. The nearest neighbour $N\cdots O$ (D_2O) and $N\cdots D_2$ (D_2O) interactions are certainly involved in the r-range $r = 3 \sim 4$ Å in the present $G_N(r)$ functions.

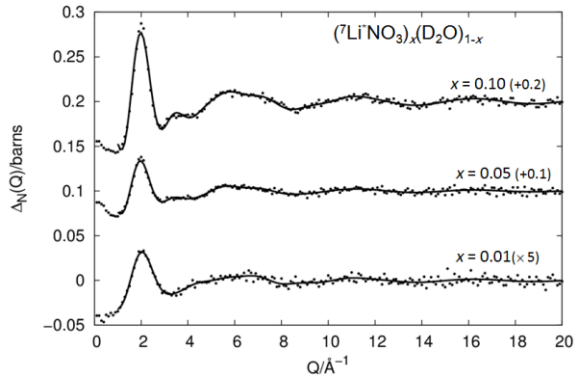

Figure 3. First-order difference function, $\Delta_N(Q)$, observed for 1, 5 and 10 mol% $^7Li^*NO_3$ heavy water solutions (dots). The best fit of the calculated $\Delta_N(Q)$ is indicated by a solid line.

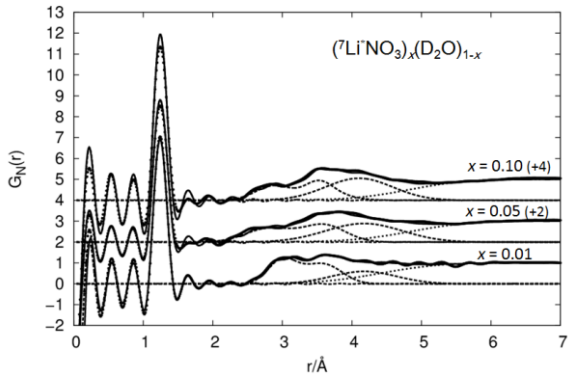

Figure 4. Distribution function around N atom, $G_N(r)$, observed for 1, 5 and 10 mol% $^7Li^*NO_3$ heavy water solutions (dots). The Fourier transform of the best fit $\Delta_N(Q)$ is indicated by a solid line. Short- and long-range contributions are denoted by a broken- and dotted lines, respectively.

Hydration parameters of NO_3^- were determined through the least squares fitting analysis of the observed $\Delta_N(Q)$. In the fitting procedure, the intramolecular N-O, the intermolecular first nearest neighbour N···D_2O(I) and the second nearest neighbour N···D_2O(II) interactions were taken into account for short-range interactions. In the fitting procedure, intramolecular parameter n_{NO} was fixed to 3 considering the intramolecular structure of NO_3^-. For the first nearest neighbour N···D_2O(I) interaction, structural parameters r_{NO}, l_{NO} and a bond angle ∠N-O···D_{w1} were treated as independent parameters. The second nearest neighbour N···D_2O(II) interaction was treated as a single interaction with the coherent scattering length b_α, being $b_O + 2b_D$. The long-range random distribution of atoms was involved in the model function. The refinement for the observed $\Delta_N(Q)$ was carried out in the range with $1.0 \le Q \le 20.0$ Å^{-1}.

Table 3. Results of the least-squares refinement of the observed $\Delta_N(Q)$[a].

x	interaction	i···j	r_{ij}/Å	l_{ij}/Å	n_{ij}
0.1	Intramolecular	N-O	1.254(1)	0.050(1)	[3.0][b]
	N···D_2O(I)	N···D_{w1}	2.90(2)	0.261(2)	4.4(3)
		∠N-O···D_{w1}	136.9(2)°		
	N···D_2O(II)	N···D_2O	4.16(2)	0.48(2)	8.8(5)
			r_0/Å	l_0/Å	
	Long-range		4.92(2)	0.64(2)	
0.05	Intramolecular	N-O	1.253(1)	0.070(1)	[3.0][b]
	N···D_2O(I)	N···D_{w1}	2.85(4)	0.329(3)	5.2(7)
		∠N-O···D_{w1}	142(4)°		
	N···D_2O(II)	N···D_2O	4.25(2)	0.55(5)	9(1)
			r_0/Å	l_0/Å	
	Long-range		4.95(4)	0.55(4)	
0.01	Intramolecular	N-O	1.250(1)	0.054(1)	[3.0][b]
	N···D_2O(I)	N···D_{w1}	3.0(1)	0.198(2)	6(2)
		∠N-O···D_{w1}	129(11)°		
	N···D_2O(II)	N···D_2O	4.2(3)	0.5(3)	6(3)
			r_0/Å	l_0/Å	
	Long-range		4.5(1)	0.68(9)	

[a] Estimated standard deviations are given in parentheses.
[b] Fixed.

The present value of intramolecular N-O distance agrees well with that observed in aqueous $NaNO_3$ solution [13] and molten $LiNO_3$ [12]. The nearest neighbour $N\cdots D_{w1}$ distance was obtained to be 3.0(1), 2.85(4) and 2.90(2) Å for 1, 5 and 10 mol% $LiNO_3$ solutions. These values agree well with the value 2.8 Å reported for aqueous 10 mol% $NaNO_3$ solution [13]. The hydration number of NO_3^- is found to change from 4.4 in the 10 mol% $LiNO_3$ solution to 6 in the 1 mol% $LiNO_3$ solution.

Acknowledgements

The authors would like to thank the instrumental staff members of the NOVA spectrometer for their help during the course of neutron diffraction measurement and transformation of the scattering data. The neutron scattering experiment was approved by the Neutron Scattering Program Advisory Committee of IMSS, KEK (Proposal No. 2009S06). This work was partially supported by Grant-in-Aid for Scientific Research (C) (No. 26390110) from the Ministry of Education, Culture, Sports, Science and Technology, Japan.

References

[1] Enderby J E and Neulson G W 1979 *Water, A Comprehensive Treatise* vol 6 (Plenum press, New York and London) p 1
[2] Otomo T, Suzuya K, Misawa M, Kaneko N, Ohshita H, Fukunaga T, Itoh K, Mori K, Sugiyama M, Kameda Y, Yamaguchi T, Yoshida K, Kawakita Y, Maruyama K, Shamoto S, Takeda S, Saitoh S, Muto S, Suzuki J, Ino I, Shimizu H, Kamiyama T, Ikeda S, Yasu Y, Nakayoshi K, Senda H, Uno S and Tanaka M 2011 *MLF Annual Report 2009, J-PARC* 10-05, p 62
[3] Paalman H H and Pings C J 1962 *J. Appl. Phys.* **33** 2635
[4] Blech I A and Averbach B L 1965 *Phys. Rev.* **137** A1113
[5] Sears V F 1992 *Neutron News* **3** 26
[6] Granada J R, Gillette V H and Mayer R E 1987 *Phys. Rev. A* **36** 5594
[7] Kameda Y, Sasaki M, Usuki T, Otomo T, Itoh K, Suzuya K, Fukunaga T 2003 *J. Neutron Research* **11** 153
[8] Narten A H, Danford M D and Levy H A 1967 *Discuss. Faraday Soc*. **43** 97
[9] Caminiti R, Cucca P, Monduzzi M and Saba G 1984 *J. Chem. Phys*. **81** 543
[10] Ohtaki H, Fukushima N 1992 *J. Solution Chem*. **21** 23
[11] Nakagawa T and Oyanagi Y 1980 *Program system SALS for nonlinear least-squares fitting in experimental sciences −from Recent Developments in Statistical Inference and Data Analysis* (North-Holland, Amsterdam)
[12] Kameda Y, Kotani S and Ichikawa K 1992 *Mol. Phys*. **75** 1
[13] Kameda Y, Saitoh H and Uemura O 1993 *Bull. Chem. Soc. Jpn.* **66** 1919
[14] Kameda Y, Sugawara K, Usuki T and Uemura O 1998 *Bull. Chem. Soc. Jpn.* **71** 2769
[15] Powles J G 1981 *Mol. Phys.* **42** 757
[16] Kameda Y and Uemura O 1992 *Bull. Chem. Soc. Jpn*. **65** 2021
[17] Zeidler A, Salmon P S, Fischer H E, Neuefeind J C, Simonson J M, Lemmel H, Rauch H and Markland T 2011 *Phys. Rev. Lett*. **107** 145501-1
[18] Newsome J R, Neilson G W and Enderby J E 1980 *J. Phys. C: Solid State Phys.* **13** L923
[19] Howell I and Neilson G W 1996 *J. Phys.: Condens. Matter* **8** 4455
[20] Kameda Y, Suzuki S, Ebata H, Usuki T and Uemura O 1997 *Bull. Chem. Soc. Jpn*. **70** 42
[21] Kameda Y, Mochiduki K, Imano M, Naganuma H, Sasaki M, Amo Y and Usuki T 2005 *J. Mol. Liq*. **119** 159
[22] Kameda Y and Uemura O 1993 *Bull. Chem. Soc. Jpn.* **66** 384
[23] Yamagami M, Yamaguchi T, Wakita H and Misawa M 1994 *J. Chem. Phys.* **100** 3122
[24] Yamaguchi T, Ohzono H, Yamagami M, Yamanaka K, Yoshida K and Wakita H 2010 *J. Mol. Liq*. **153** 2

3.9.6

Abstract programming interface for MCTAL files

Nicolò Borghi, Konstantin Batkov

European Spallation Source, Tunavägen 24, 223 63, Lund, Sweden

E-mail: konstantin.batkov@esss.se

Abstract. MCNPX allows to save its calculation results in the MCTAL files and plot them by means of the MCPLOT utility. We have developed an implementation of abstract programming interface (API) to read MCTAL files. This API allows to extract data from the MCTAL files for further analysis and, if necessary, save it in any desired format. As an example, a converter from MCTAL to ROOT format is presented.

1. Introduction

The current work aims to provide a convenient mechanism to extract data from the MCNPX [1] output files in the MCTAL format. This mechanism is implemented as an abstract programming interface (API) developed in the Python language. It provides a set of classes to read MCTAL files and extract data from them in a fully automatic way. This possibility is essential for extensive MCNPX calculations, where one needs to analyse results of numerous runs.

The API manual and examples can be found on the project home page:
https://code.google.com/p/mc-tools

Interfacing with the mctal API does not require complex coding. It is as simple as importing the module, making an instance of the MCTAL class and calling the `Read()` method to get a list of all the tallies in the mctal file:

```
from mctal import MCTAL
m = MCTAL(mctalFileName)
tallies = m.Read() # get list of tallies from a mctal file
for f in tallies:
    ... # do your analysis here
```

2. ROOT converter

From our point of view, a big inconvenience of the standard MCPLOT utility is lack of ability to analyse data.

The ROOT framework [2, 3] developed at CERN is a tool to perform statistical data analysis. We use it in our everyday studies, therefore as an example of application of this API, we have developed a converter from the MCTAL format into the ROOT format.

```
[kbat@jasper ]$ mctal2root -h
usage: mctal2root [-h] [-v] mctal_file [root_file]

A mctal to ROOT conversion script.

positional arguments:
 mctal_file     the name of the mctal file to be converted
 root_file      the name of the output ROOT file

optional arguments:
 -h, --help     show this help message and exit
 -v, --verbose  explain what is being done
```

3. An example

Let's convert a MCTAL file into the ROOT format:

```
[kbat@jasper ]$ mctal2root mctal
  ROOT file saved to: mctal.root
[kbat@jasper ]$ ls -l mctal*
-rw-r----- 1 kbat 126510  mctal
-rw-r----- 1 kbat  21893  mctal.root
```

Note the size difference due to ASCII to binary conversion and the ROOT internal compression.

The ROOT file contains 4 objects which correspond to the MCNPX tallies:

```
[kbat@jasper ]$ root mctal.root
root [1] .ls
TFile**         mctal.root
 TFile*         mctal.root
  KEY: THnSparseT<TArrayF>      f6;1
  KEY: THnSparseT<TArrayF>      f15;1
  KEY: THnSparseT<TArrayF>      f25;1
  KEY: THnSparseT<TArrayF>      f35;1
```

Repeating the MCTAL file structure, the ROOT data is saved as a 8-dimensional histogram THnSparse:

```
root [1] f5->Print("a")
THnSparseT<TArrayF> (*0x2eb0250): "f5" ""
  8 dimensions, 1.0054e+06 entries in 1005402 filled bins
    axis 0 "f": 1 bins (0..1), variable bin sizes
    axis 1 "d": 1 bins (0..1), variable bin sizes
    axis 2 "u": 1 bins (0..50006), variable bin sizes
    axis 3 "s": 1 bins (0..1), variable bin sizes
    axis 4 "m": 1 bins (0..1), variable bin sizes
    axis 5 "c": 1 bins (0..1), variable bin sizes
    axis 6 "e": 201 bins (0..3000), variable bin sizes
    axis 7 "t": 5002 bins (0..1e+37), variable bin sizes
```

This histogram can be analysed and visualised by making use of standard ROOT techniques. For instance, let's plot the time spectrum:

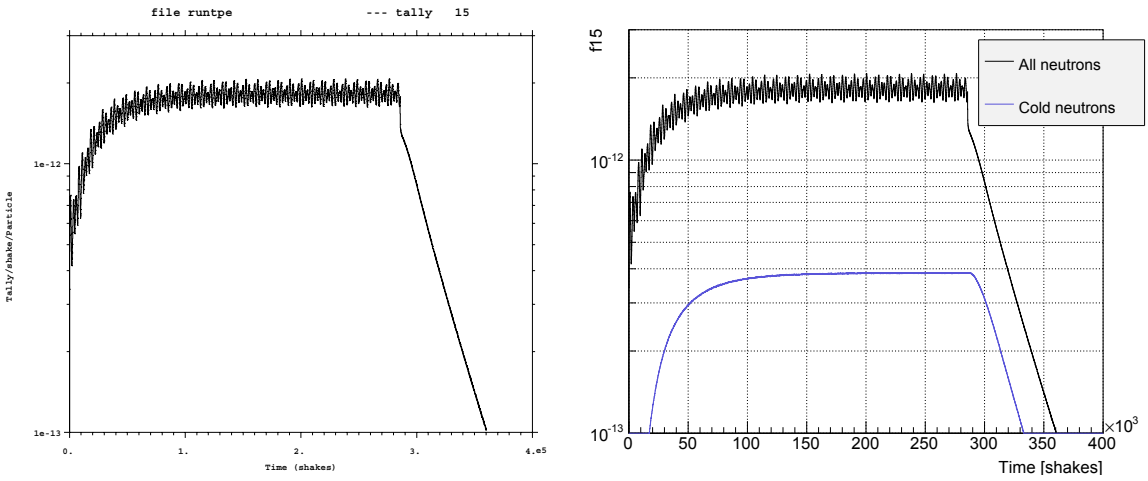

Figure 1. Examples of a histogram depicted with `mcplot` (left) and `ROOT` (right)

```
root [2] TH1 *h = f5->Projection(7) // axis 7 corresponds to
                                    // time
root [2] h->Scale(1, "width")       // divide the bins by their
                                    // width
root [3] h->Draw()                  // draw the histogram
```

The resulting distribution is shown in black in the right pad of Fig. 1.

Let's plot the time spectrum for the cold neutrons only (energy below 5 meV):

```
f15->GetAxis(6)->SetRangeUser(0, 5E-9) // select the energy range
TH1 *hc = f15->Projection(7)
hc->SetLineColor(kBlue)                // set the histogram color
hc->Scale(1, "width")
hc->Draw("hist,same")                  // draw at the same pad
```

The resulting spectrum is shown in blue in the right pad of Fig. 1.

`ROOT` allows to perform any kind of data analysis with these objects. Refer to the http://root.cern.ch website for details.

4. Supported and unsupported features

The code has been extensively used during last year by several persons, and we currently believe that is can handle all `mctal` records except the following ones:

- `KCODE` data;
- Tallies with perturbation records (produced by the `pert` card).

These features are not implemented just because the authors never use them, but if necessary they can be supported by the code in the future.

5. Conclusions

- We have developed an API to provide a convenient access to the information stored in the `MCTAL` files.
- Based on this API we have developed a tool to convert the `MCTAL` files into the `ROOT` file format.
- These tools simplify the visualisation and analysis of the results obtained with `MCNPX`.

6. See also

The `MCTAL` API and the `ROOT` converter are the parts of a larger project called `mc-tools`: https://code.google.com/p/mc-tools. This project includes several other Monte Carlo tools listed below:

- Converter of `wssa` files into the `ROOT` format;
- Converter of `ANGEL` files (standard `PHITS` output) into the `ROOT` format;
- A tool to animate 3D geometry in `PHITS`.

Acknowledgments

We thank Troels Schönfeldt, Esben Klinkby, Riccardo Bevilaqua and Furutaka Kazuyoshi for their discussions and contribution in the project.

References

[1] LANL Los Alamos, New Mexico, USA *MCNP5/MCNPX manual*
[2] Brun R and Rademakers F 1996 ROOT — an object oriented data analysis framework *Proceedings AIHENP'96 Workshop* (Lausanne, Switzerland) see also http://root.cern.ch.
[3] Brun R and Rademakers F 1997 *Nucl. Instrum. Methods Phys. Res., Sect. A* **389** 81–86

3.9.7

Neutron Diffraction Study of Piezoelectric Material under Cyclic Electric Field using Event Recording Technique

T. Kawasaki [1], T. Ito[2], Y. Inamura[1], T. Nakatani[1], S. Harjo[1], W. Gong[1], T. Iwahashi[1] and K. Aizawa[1]

[1]J-PARC Center, JAEA, Tokai, Ibaraki 319-1195, Japan.
[2]CROSS, Tokai, Ibaraki 319-1106, Japan

E-mail: takuro.kawasaki@j-parc.jp

Abstract. The stroboscopic data reduction technique for pulsed neutron diffraction was used in order to investigate the behaviours of the crystal lattice and the ferroelectric domains of the piezoelectric material in the multilayer-type piezoelectric actuator under a cyclic electric field. The division of neutron intensity data based on the condition of external fields recorded as event data can be performed by this technique. The peak shift and the intensity variations depending on the strength of the field were successfully observed in the divided diffraction patterns. The microscopic deformation estimated from the lattice strain and the domain switching agreed with the macroscopic behaviour of the actuator. The usefulness of the technique for the study of responses of materials to cyclic electric fields was demonstrated.

1. Introduction

Recently, time-resolved *in-situ* measurement is attracting great interest in order to observe transient phenomena of materials under external fields. Event-recording system of Materials and Life science experimental facility (MLF) at J-PARC has an advantage for time-resolved measurements, because of "event" characteristic of the data. For this purpose, new techniques for the measurement and the data reduction were developed and tried to adopt for the evaluation of the steel during the deformation [1].

Here, the responses of the crystal structure and the crystal lattice of piezoelectric materials to a cyclic electric field were chosen as the target to be investigated using this technique. Since piezoelectric materials are used in a variety of devices including sensor, actuator and the others, they are one of the important materials to be investigated. Generally, the performance of the materials is expressed by the parameter which shows the macroscopic deformation called piezoelectric *d* parameter. On the other hand, piezoelectric effect originates from the microscopic phenomena that are lattice strains, domain switching and ionic displacements. To understand the macroscopic characteristics of the material, the microscopic characteristics should be investigated in detail. The responses of these characteristics to the applied electric fields and mechanical stresses of lead zirconate titanate (PZT)-based and other types of piezoelectric ceramics or single crystals were evaluated using *in-situ* neutron and X-ray diffraction experiments [2, 3, 4].

In this study, the first trial of application of the event-recoding technique to the neutron diffraction experiment in MLF to investigate the behaviour of the material under the electric field was performed. The microscopic responses of the PZT-based piezoelectric material in a multilayer-type actuator under

driving by a cyclic electric field were investigated using the engineering neutron diffractometer TAKUMI at BL19 of MLF at J-PARC. The obtained data were reduced to the field-condition-resolved (time-resolved) diffraction patterns with the specific field conditions. The lattice strain and the domain characteristics of the material in each condition are investigated.

2. Experimental

A commercially obtained multilayer piezoelectric actuator (PSt150, Piezomechanik GmbH) shown in figure 1 was used as the sample for the neutron diffraction measurement. The schismatic drawing of the experiment is shown in the figure 2. The sample was mounted horizontally on the sample stage of TAKUMI with the axial (layer stacking) direction to be 45° to the incident neutron beam. The neutron diffraction intensities in the directions of parallel and perpendicular to the applied electric field were measured simultaneously by ±90° detector banks. The gauge volume for the measurement was restricted to be 2×2×8 mm^3 by the beam slit and the radial collimators. High-resolution mode that has the resolution $\Delta d/d$ of 0.2 % was used for the measurement.

The sinusoidal wave signal with the frequency of 0.5 Hz from a function generator (33210A, Agilent Technologies Inc.) was amplified to the voltage of 0 ~ 130 V by a high-voltage amplifier (HEPOT-5B20, MATSUSADA Precision Inc.) and applied to the sample. The signal applying to the sample during the measurement was recorded as event data by a TrigNET [5] module and DAQ-middleware [6] together with neutron diffraction intensity and T_0 event which is a sync signal with generation of a neutron pulse. A TrigNET module has two types of analog-to-digital converter (ADC) inputs, high-speed and low-speed. Here, a low-speed ADC input was used for recording the signal. In the experiment, the diffraction intensity was collected in 12 hours, and the accelerator power of J-PARC was 300 kW.

Referring to the signal event data, collected neutron event data, which has the information about the detected position on the detectors and the time-of-flight from the neutron source, was divided by the voltage condition of every 10 V in the range from 0 V to 130 V and converted to the diffraction patterns using the software Utsusemi [7] and Emaki [8] developed based on Manyo-library [9]. Note that very flexible data reduction based on various analog or digital signals and time can be done by using these module and software after the measurement. Further, the condition window for the data division can be set freely. The diffraction patterns were analysed using the software Z-Rietveld [10] in order to refine the peak positions, the lattice parameters and the integrated intensities of the peaks.

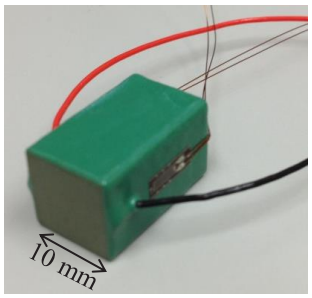

Figure 1. A multilayer piezoelectric actuator. A strain gauge is stuck on the side of the actuator in order to measure the macroscopic strain.

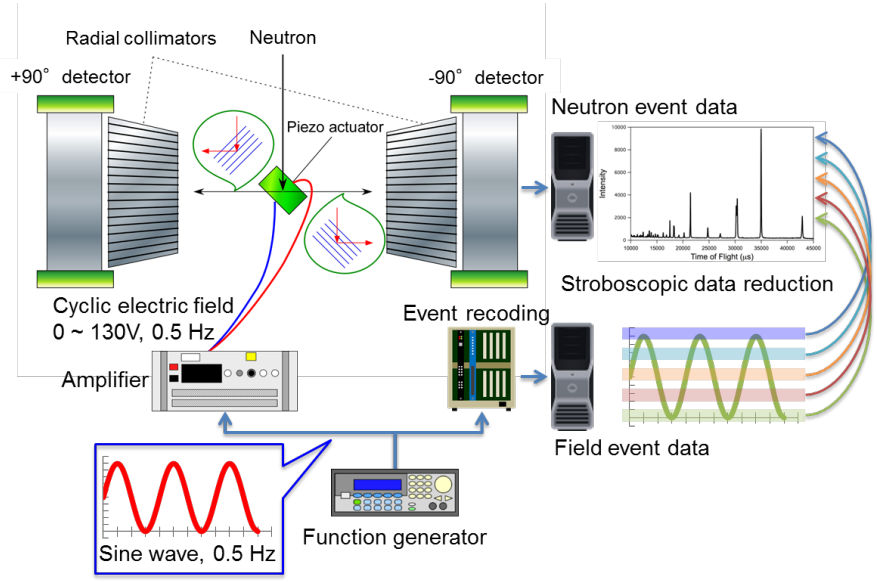

Figure 2. The schismatic drawing of the experimental setting.

3. Results and Discussions

All of diffraction peaks in the diffraction pattern without the field were characterized by the tetragonal unit cell with the space group of P4mm and the lattice parameters were refined to be a = 4.0251(1) Å and c = 4.0481(1) Å. These are close to the parameters of PZT that has a perovskite-type crystal structure. Figure 3 shows the peak profiles of 111, 200 and 002 reflections measured at axial direction of the actuator. The gradual peak shift and intensity variation depending on the electric field can be seen. The shift of 111 peak on the larger d side means an increasing of the lattice spacing by the applied electric field, and is a so-called inverse-piezoelectric effect. The decreasing of the intensity of 200 reflection and opposite variation in that of 002 reflection indicate the increase of the domains of which c-axis lies to the direction of the applied field. Both of these phenomena cause macroscopic elongation in this direction, and are agree with the nature of the actuator well. Thus the evolution of diffraction patterns is consistent with the macroscopic nature such as strain and electric field.

The electric field dependence of the lattice spacing of (111), (200) and (002) planes are shown in figure 4 (a). Although all the spacing increases with the rise of the field, there is crystal orientation dependence in the inclination. The deformation in [111] direction was larger than other directions, and its value was 0.09% at the field of 125 V in the present sample. The integrated intensities of 200 and 002 reflections in the axial direction at the various fields were obtained and the ratio of these two reflections was plotted in figure 4 (b). The ratio of I_{002}/I_{200} increased from 1.4 to 3.1 with the rise of the field by 90° domain switching. The deformation caused by this switching in the axial direction at 125 V is estimated from the variation of the volume fractions of the a-axis and the c-axis domains and the lattice parameters to be 0.09%. The macroscopic deformation of the actuator measured by a strain gauge was about 0.1 % at 125 V. The actuator consists of a polycrystalline material and includes various orientations of crystal grains. Because the behaviors of both the lattice strain and the domain switching have crystal orientation dependence, the contribution

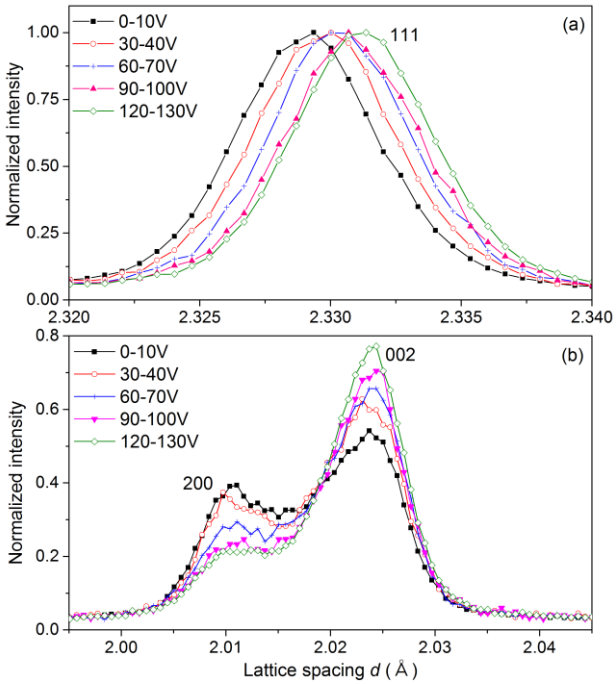

Figure 3. The diffraction peak profiles of (a) 111, (b) 200 and 002 reflections in the axial direction.

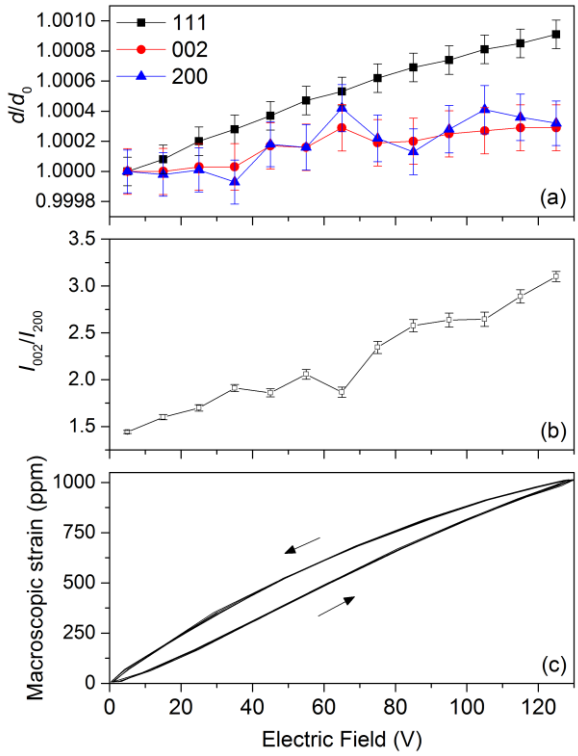

Figure 4. The electric field dependencies of (a) the strain in [111], [200] and [002] directions, (b) the intensity ratio of I_{002}/I_{200} and (c) the macroscopic strain.

of the microscopic deformation to the macroscopic one would be evaluated more precisely by adopting multi-peak analyses.
The measurement and the data reduction techniques which are used in the present study select and summed up the neutron events in the particular condition. Therefore, faster phenomena can be also observed if it has cyclic nature. On the other hand, the present data reduction is dividing data based on only the strength of the electric field, and it isn't classified whether the field is rising or declining. Because the hysteresis loop was found in the electric field-strain curve shown in figure 4 (c), the state of the materials may be different in these two situations. The data reduction based on the more complex condition should be done as the next step.

4. Summary

The behaviours of the lattice and the domain in the piezoelectric material under the electric field were investigated using event recording technique developed for time-resolved neutron diffraction experiment in MLF. Neutron diffraction intensities from the piezoelectric actuator were collected together with the waveform signal of the applied electric field as event data. The measurement and the data reduction were successfully finished and the stroboscopic diffraction patterns based on the strength of the field were obtained. The microscopic deformation which was estimated from the lattice strain and the domain switching of the material agreed with the macroscopic strain of the actuator. Further development of the measurement and the data handling techniques is in progress in order to analyse the behaviour more precisely. The extensive study of responses of materials to dynamical external fields is expected by applying the technique to neutron scattering experiments for various dielectric materials, ionic conductors and other materials which reply to an electric field.

Acknowledgement

This study was supported by JSPS KAKENHI Grant Number 26790071, and the experiment was performed under the approval of J-PARC center (Proposal No. 20140162).

References

[1] T. Ito, S. Harjo, Y. Inamura, T. Nakatani, T. Kawasaki, J. Abe, and K. Aizawa, *Materials Science Forum*, **783-786** (2014) 2071.
[2] M. K. Durbin, E. W. Jacobs, J. C. Hicks and S. –E. Park, *Appl. Phys. Lett.* **74** (1999) 2848.
[3] J. E. Daniels, T. R. Finlayson, A. J. Studer, M. Hoffman and J. L. Jones, *J. Appl. Phys.* **101** (2007) 094104.
[4] A. Pramanick, A. D. Prewitt, M. A. Cottrell, W. Lee, A. J. Studer, K. An, C. R. Hubbard and J. L. Jones, *Appl. Phys.* A**99** (2010) 557.
[5] T. Seya, S. Muto and S. Satoh, *MLF Annual Report*, (2010) 102.
[6] K. Nakayoshi, Y. Yasu, E. Inoue, H. Sendai, M. Tanaka, S. Satoh, S. Muto, N. Kaneko, T. Otomo, T. Nakatani, and T. Uchida, *Nucl. Instrum. Methods Phys. Res*., Sect. A**600** (2009) 173.
[7] Y. Inamura, T. Nakatani, J. Suzuki and T. Otomo, J. Phys. Soc. Jpn. **82** (2013) SA031.
[8] T. Ito, T. Nakatani, S. Harjo, H. Arima, J. Abe, K. Aizawa and A. Moriai, *Materials Science Forum*, **652** (2010) 238.
[9] J. Suzuki, T. Nakatani, T. Ohhara, Y. Inamura, M. Yonemura, T. Morishima, T. Aoyagi, A. Manabe and T. Otomo, *Nucl. Instrum. Methods Phys. Res.*, Sect. A**600** (2009) 123.
[10] R. Oishi, M. Yonemura, Y. Nishimaki, S. Torii, A. Hoshikawa, T. Ishigaki, T. Morishima, K. Mori and T. Kamiyama, *Nucl. Instrum. Methods Phys. Res.*, Sect. A**600** (2009) 94.

This is a blank page.

3-10. New Moderator Concept and Compact Source

This is a blank page.

3.10.1

Status report on the Low Energy Neutron Source — 2014

David V. Baxter[1], F. Li, S. R. Parnell, R. Pynn, T. Rinckel, and T. Wang
Center for Exploration of Energy and Matter, and Department of Physics
Indiana University, 2401 N. Milo Sampson Ln, Bloomington, IN 47405, USA.

E-mail: baxterd@indiana.edu

Abstract. LENS produced its first neutrons almost 10 years ago and has now entered a steady state of operations with particular focus on the educational and instrumentation innovation aspects of its mission. Key elements in the facility's success over the last decade have been the alignment of its mission with the objectives of a number of major neutron sources and its ability to educate and train students in ways that are difficult to implement at major facilities. In this paper, we summarise some of the recently installed improvements to the facility, describe some recent scientific activities, and look back at some of its significant accomplishments over the last 10 years.

1. Introduction

LENS is a Compact Accelerator-driven Neutron Source (CANS) based on (p,nX)Be reactions involving a 13 MeV proton beam and a 1.1mm thick beryllium target. It normally operates at a beam power of 3 to 4 kW with a 20 Hz repetition rate, but the repetition rate and pulse width can be varied to suit particular experiments [1,2]. The facility operates on the campus of Indiana University and is supported by a portion of the indirect funds generated by research grants associated with the facility. Therefore, it does not serve as a traditional user facility, but rather concentrates on providing unique educational and instrumentation innovation opportunities while also facilitating materials research. The facility has three conventional neutron instruments (SANS, SESAME, and a neutron radiography/tomography station), a developmental beam line used for studies of moderator performance and testing novel detector ideas (the Moderator Imaging Station, or MIS), and a station for irradiating electronics with fast neutrons (Neutron Radiation Effects Facility, or NREF). Over the last decade, 10 students have received their PhD for work associated with LENS (some during construction and some using the neutron beams at the facility) and seven more are currently pursuing their PhD, 10 post-doctoral fellows have worked with LENS, and another 10 undergraduate students have conducted research at the facility.

The facility ran for an average of roughly 1500 hr/yr over the past couple of years. Something under 10% of this time was devoted to operation of the fast-neutron target station. Roughly 25% of the operation time on the cold-neutron target station is devoted to experiments on the performance of novel moderator designs (in collaboration with researchers from SNS, LANL, ESS and ISIS) and the remaining time devoted to normal operations for research with the SANS, SESAME and MIS

[1] To whom any correspondence should be addressed.

instruments. In the upcoming years, we expect to see an expansion of operations on the fast-neutron target as we will ramp up both our radiation effects and radiography activities.

The floor plan of the facility is shown in figure 1. The facility's two target stations are the circular features at the end of the proton beamlines leading away from the accelerator (which appears at the lower left in figure 1). The upper target station houses a 1-cm thick solid methane moderator operating at 6K and feeds the SANS, SESAME and MIS instruments with cold neutrons [2]. The lower target station in figure 1 feeds the radiography instrument and a station for irradiating electronics with neutrons at a rate of up to $2x10^{10}$n/(cm^2·s) (1 MeV equivalent flux for small samples right next to the target). This second target station has a room-temperature polyethylene moderator that may be covered with Cd (to allow a difference measurement that is sensitive to only thermal neutrons), or removed completely (to study the effects of fast neutrons).

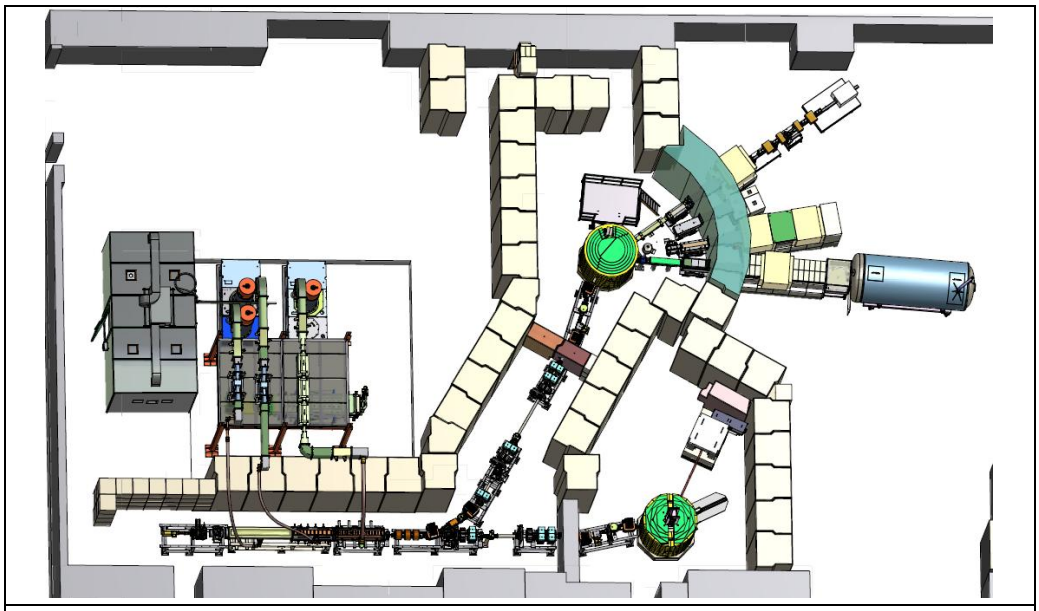

Figure 1. Floor plan of the LENS facility in 2014. Recent additions to the facility include improvements to the DUT assembly, and upgrades to the radiography facility (both on the lower, fast neutron, target station) and the installation of an in-situ polarized ^{3}He analyser and new detector on the SEAME instrument on the (upper) cold neutron target station.

2. Recent facility activities

Over the last two years, we have introduced some improvements to a number of the instruments at LENS. The SESAME (Spin-Echo Scattering Angle Measurement) instrument was fitted with an on-line pumped ^{3}He polarization analyser and an array of 16 linear position sensitive detectors to replace the supermirror analyser and multi-PMT position-sensitive detector that were previously used on this instrument. We have discovered that the complicated correlation between neutron phase space and polarization analysing power of the supermirror analysers causes issues with the interpretation of SESAME data, so installation of the ^{3}He analyser was a major step forward for this instrument [3]. The instrument has also supported the development of several generations of magnetic Wollaston prisms, which are presently used to effect the spin encoding at the heart of the instrument's operation. This included a novel water-cooled triangular prism design with only two layers of Al wire in the beam path for each prism, in order to maximize the transmission of the devices. We also discovered

that the polarization loss in these wire-wound devices is very sensitive to the precise geometry of neighbouring sheets (in particular, it was important that the individual wires in the current sheets that define the common hypotenuse of neighbouring triangular coils shown in figure 2 interdigitate rather than lining up directly each other to reduce polarization losses [4]).

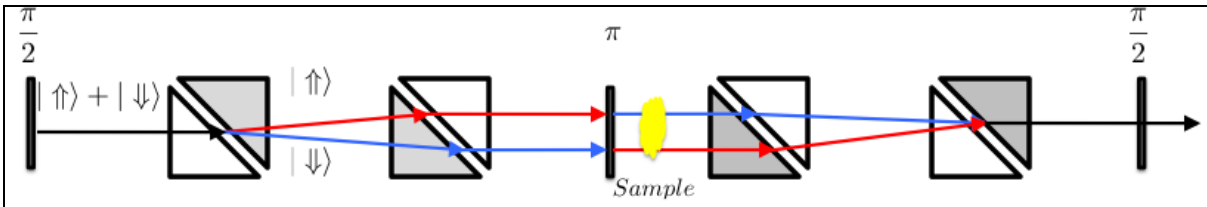

Figure 2. This schematic shows the basic operation of the SESAME instrument in SESANS mode. The triangular regions are magnetic prisms (grey for fields in the positive z direction, and white in the negative z direction). Each pair of triangles forms a magnetic Wollaston prism. The instrument starts with a $\pi/2$ flip to place the neutron spin in the x-y plane, and the prisms act as birefringent media for the up and down components of the neutron spin. These components are separated spatially by the first pair of Wollaston prisms (through refraction at the common hypotenuse of each triangle pair), and recombined by the second pair. Any difference in the integrated scattering length density of the sample over the length defined by this separation distance will show up as a change in the neutron polarization when measured at the end of the instrument [3,4,5].

The Neutron Radiation Effects Facility was modified two years ago in order to increase the size of the electronics boards that can be irradiated by providing vertical access to the target area for the Device Under Test (DUT) through a dumb-waiter system. We are presently adding new diagnostics to provide better real-time monitoring of the dose delivered to the parts as well. As a part of this more recent project, we are also upgrading the radiography facility to enhance its fast-neutron imaging capability by providing line-of-sight to the target from the imaging instrument's fluorescent screen. In the coming years, we anticipate an increase in the activity for both the irradiation and radiography stations at LENS through increased interactions with a regional base of users with interests in these areas. We note that the current standards for radiation effects testing specifically mention use of reactors which may no longer available for such testing within a decade or less [6], so this could be another area where small sources such as LENS could have a significant impact.

3. Operational Experience

Over the last several years, the performance of our RF system has improved considerably [7]. Three years ago we completed the transition from legacy switch tubes in our klystron control circuitry to modern Y-847B tubes from CPI. Prior to this change, the RF systems would typically trip several times per week (up to a few times per day). Even after the installation of the new switch tubes, the system continued to trip more often than we would like, but most recently our RF reliability has steadily increased to the point where it is no longer a significant issue (it is now common to go several days or even a week without RF trips interfering with operation). In addition to the installation of the new tubes, key elements of this transition have been the decision to run the high-voltage tanks with heaters to raise the oil temperature to about 35°C, and the slight re-working of some of the connections in those tanks. Collaborations with the RF group at Los Alamos have proved most helpful in addressing these issues.

For reasons that we do not yet understand, target lifetime has become a major operational issue within the last year. When we changed target design to the current 1.2 mm thick circular target from our

original 4mm thick rectangular version in 2010 [8], we initially found it necessary to change targets only after the target's O-rings providing the seal between the target cooling system and the vacuum failed due to accumulated radiation damage. This typically resulted in a routine where we would change an intact target at something like 80 to 100 kW-days of accumulated beam. More recently, although the target design itself has not changed, the targets themselves have started to exhibit cracking after accumulate beam of from 1 to 70 kW-days of operation, and in typical operation these cracks have most often been the feature that limits the time between target exchanges. This is a continuing problem, and our present thinking is that it will have to be address by going over to a composite target design similar to that developed for the Riken Accelerator-driven Neutron Source (RANS) [9]. In this design, the Be target material is backed by a layer of Vanadium or Niobium, which acts as a sink for the protons.

4. Research Activities

The majority of the research conducted at LENS over the last few years has been associated with the development of new neutron instrumentation. The relative ease with which the LENS TMR may be reconfigured has led to the development of a program in experimental neutronics that has been active for more than six years. The most recent projects in this area have included several experiments investigating the convoluted moderator concept originally put forward by Stuart Ansell of ISIS [10], and most recently an experiment on a single-crystal reflector/filter. In this same general area, we have measured the neutron total cross section of a number of potential neutronic materials (methane, D_2O etc.), and have demonstrated that our SANS instrument, with suitable small and temporary modifications, can be used to measure neutron transmission in samples from below 0.1meV to above 1eV with a single accelerator setting (typically 10Hz with a 0.15ms pulse width). Our neutronics experiments have been conducted in collaboration with researchers from the SNS, ESS, ISIS and LANSCE neutron facilities, and this activity demonstrates the important role that CANS facilities are able to play in supporting the international scattering facilities. Over the last two years we have also conducted a number of experiments to provide preliminary data on samples to be measured later at one of the major facilities, which is another example of synergistic interactions among these two different types of facilities [11].

Our SANS instrument has recently provided published data on micelle structures [12] and several more SANS studies are in preparation at this time. We see this activity increasing over the next two years. As discussed above, changes to the analyser and detector have been crucial to bringing the SESAME instrument into useful service, and we have now demonstrated measurements at spin-echo lengths up to 1 micron with this instrument [3,4,5]. Even with its earlier detector and analyser, however, the SESAME instrument has provided the polarized neutron optical bench that was crucial to the second major instrumentation development program at our facility. In constructing the SESAME instrument, several refinements have been made to the devices through which the neutron spatial position or momentum can be encoded in the neutron spin state. This started with the development of novel coil winding patterns in conventional magnetic prisms in order to minimize the material seen by neutrons as they pass through the instrument [4], but it has also included increased current capacity (to extend the instrument's range) and the development of novel techniques for alignment of such instruments [5].

Over the last several years, the SESAME instrument has supported the development of a number of devices for manipulating neutron spins using magnetic fields confined to precise geometries using high-Tc superconducting YBCO films deposited on sapphire substrates as Meissner screens [13]. One of the key challenges in developing spin-echo instrumentation is minimizing the impact of Larmor aberrations on the final spin state of the neutrons as they pass through the instrument. The use of symmetry in the design of the instrument can cancel many of these aberrations, but the use of

Meissner screens to precisely define the magnetic field geometry helps to minimize the aberrations associated with each element. Another advantage of these YBCO on sapphire films is that they introduce negligible absorption or small angle scattering, and this maximizes the transmission of the neutron beam through the devices [14]. The high transition temperature of the films allows us to use inexpensive cryocoolers and relatively straight-forward cryogenic engineering in the design of the devices. By using YBCO tapes to produce the magnetic fields, we have been able to construct a simple device for Spherical Neutron Polarimetry. [15]. A number of other similar spin-manipulation devices have also been developed on this instrument, and these are discussed in more detail in other publications [13-17]. We have also found that the design of these components is aided enormously through the use of modern magnetic field simulation codes, provided the code is equipped to handle superconducting components.

5. Conclusions

Over the last ten years, LENS has demonstrated the traditional role of small university-based neutron facilities (education, instrumentation development and materials research) can be fulfilled with an accelerator-based source design. We have demonstrated a number of novel neutronic concepts and established important research programs in neutronics and novel instrumentation. We look forward to continuing these activities into the coming decade.

6. Acknowledgements

LENS was constructed with support from the National Science Foundation (NSF) through grants DMR-0220560 and 0320627, the Department of Defence and the State of Indiana, and it is operated with support from Indiana University. Neutronics research and the development of the SESAME instrument and its conventional magnetic devices has been supported by the DOE's Office of Basic Energy Science through grant DE-SC0009584 and a number of subcontracts from Oak Ridge and Los Alamos National Labs. The development of the Meissner based spin manipulation devices has been supported by the NSF through grant DMR0956741.

7. References

[1] Baxter D V, Cameron J M, Derenchuk V P, Lavelle C M, Leuschner M B, Meyer H O, Nann H, and Snow W M, 2005, "Status of the Low Energy Neutron Source at Indiana University," *Nucl. Instr. Meth.* **B 241** 209-212.

[2] Lavelle C M, Baxter, D V, Lone, M A, Nann, H, Cameron J M, Derenchuk V P, Kaiser H, Leuschner M B, Lozowski W, Meyer H O, Pynn R, Remmes N, Rinckel T, Snow W M and Sokol P E, 2007, "Neutronic design and measured performance of the Low Energy Neutron Source target moderator reflector system," *Nucl. Instr. Meth*., **B 261**, 956-959.

[3] Parnell S R, Washington A, Li K, Yan Y, Stonaha P, Li F, Wang T, Walsh A, Chen W, Parnel A J, Fairclough P, Baxter D V, Snow W M and Pynn R, 2015, "Spin Echo Small Angle Neutron Scattering (SESANS) using a continuously pumped ^{3}He neutron polarization analyser," submitted to *Rev. Sci. Instr*.

[4] Stonaha P, 2013, "Studies of porous anodic alumina using spin echo scattering angle measurement", PhD thesis, Indiana University, Bloomington, IN.

[5] Washington A L, 2013, "Investigating hard sphere interactions through spin echo scattering angle measurement," PhD Thesis, Indiana University, Bloomington, IN.

[6] ASTM standard E720, 2005, "Standard guide for selection and use of neutron sensors for determining neutron spectra employed in radiation-hardness testing of electronics," ASTM Intl, 100 Barr Harbor Dr, PO Box C700, West Conshohocken PA.

[7] Rinckel T, Baxter D V, Doskow J, Kaiser H, Pynn R, Sokol P E, 2012, "LENS operating experience," *Phys. Proc*. **26**, 161-167.

[8] Rinckel T, Baxter D V, Doskow J, Sokol P E, Todd T, 2012, "Target Performance at the Low Energy Neutron Source," *Phys. Proc*. **26**, 168-177.

[9] Y. Yamagata, personal communication.

[10] Iverson E B, Baxter D V, Muhrer G, Ansell S. Dalgliesh R, Gallmeier F X, Kaiser H and Lu W, 2014, "Enhancing neutron beam production with a convoluted moderator," *Nucl. Instr. Meth.,* **A762**, 31-41.

[11] Yan C, et al., 2013, "Photophysics and morphology of a polyfluorene donor-acceptor triblock copolymer for solar cells, *J. Polymer Sci*, **51**, 1705-18

[12] Das N C, Cao H, Warren G T, Gladden JR and Sokol P E, 2012, "Shape and size of highly concentrated micelles in CTAG/NaSaI solutions by Small Angle Neutron Scattering (SANS)," *Langmuir*, **28,** 11962-968.

[13] Wang T, Li F, Parnell S R, , Hamilton W A, Kaiser H, Washington A L, Baxter D V and Pynn R, 2014 "Neutron spin manipulation devices using YBCO filsm", J. Phys. Conf. Ser., 528, 012024.

[14] Parnell S R, Kaiser H, Washington A L, Li F, Wang T, Baxter D V, and Pynn R, 2013, "Design of a cryogen free cyro-flipper using a high Tc YBCO film," *Phys. Proc.* **42**, 125-29.

[15] Li F, Parnell S R, Hamilton W A, Maranville B B , Wang T, Semerad R., Baxter D V, Cremer J T and Pynn , 2014, "Superconducting magnetic Wollaston prism for neutron spin encoding," *Rev. Sci. Instr.*, **85**, 053303.

[16] Parnell S R, Kaiser H, Washington A L, Li F, Wang T, Baxter D V and Pynn R, 2013, "Performance of a polarized neutron cryo-flipper using a high-Tc YBCO film, *Nucl Instr. Meth*., **A722**, 20-23.

[17] Wang T, Parnell S R, Li F, Washington A L, Hamilton W A, Baxter D V and Pynn R, 2015 "Compact spherical neutron polarimeter using high-Tc superconducting YBCO films", unpublished.

3.10.2

Fundamental physics possibilities at the European Spallation Source

Esben Klinkby[1,2], Konstantin Batkov[1], Ferenc Mezei[1], Eric Pitcher[1], Troels Schönfeldt[1,2], Alan Takibayev[1] and Luca Zanini[1]

1) European Spallation Source ESS AB, Box 176, S-221 00 Lund, Sweden
2) DTU Nutech, Technical University of Denmark, DTU Risø Campus, Frederiksborgvej 399, DK-4000 Roskilde, Denmark

E-mail: esbe@dtu.dk

Abstract. The construction of the European Spallation has recently started in Lund, Sweden. In addition to the neutron scattering instruments the ESS is designed to serve, the construction of a new spallation source opens up new possibilities for fundamental physics experiments. In this paper some of the possibilities for in-pile experiments are discussed, i.e. experiments that impacts the target-moderator-reflector systems and that can best be constructed if they are considered already in the design phase of a new facility. The main focus of the work reported here is put on possible changes to the baseline target-moderator-reflector design that would allow for ultra cold neutron production and extraction. For completeness, the paper also discuss possible discovery physics experiments that are presently being studied in the framework of ESS. In parallel to the topics discussed here, work is ongoing investigating the scientific potential for in-beam fundamental physics experiments at the ESS.

1. Introduction

In this paper several possibilities for fundamental physics at the ESS are discussed. First, and in greatest detail, the concept of a through-going beam-tube is discussed (Section 2). The impact on existing cold/thermal beam-lines is quantified and the heat-load of a candidate ultra cold neutron (UCN) moderator placed in the through-going tube is calculated. Aiming at providing an overview of ongoing efforts, other novel ideas for UCN moderators are briefly presented in Section 3: A voluminous liquid D_2 moderator, an in-pile solid D_2 as well a satellite methane moderator.
Finally in Section 4 the possibilities of discovery physics at the ESS are discussed, in particular the searches for neutron-anti-neutron oscillations and dark photons.

2. Through-going tube

The possibilities for installing a UCN moderator at the ESS strongly depend on the layout of the target-moderator-reflector. In figure 1 the central parts of the target-moderator-reflector are shown according to the baseline design of the Technical Design Report [1]. In this scenario, voluminous para-hydrogen moderators (two cylinders of 16 cm diameter, 13 cm high) are situated on each side of the target, and thus close to the spallation hot-spot. The introduction of a UCN moderator would have to stay clear of the two existing moderators - for example by placing it in a through-going tube underneath the lower para-hydrogen moderator. As the main focus of

the ESS facility is that of providing cold and thermal neutrons, it is essential when evaluating possible changes to the baseline design to monitor the performance impact on the cold/thermal neutrons available at the instrument beam-lines. Therefore, a study was carried out monitoring the flux available for UCN moderation versus the impact on neutron flux in the cold/thermal beam-lines - for different vertical positions of the through-going tube.

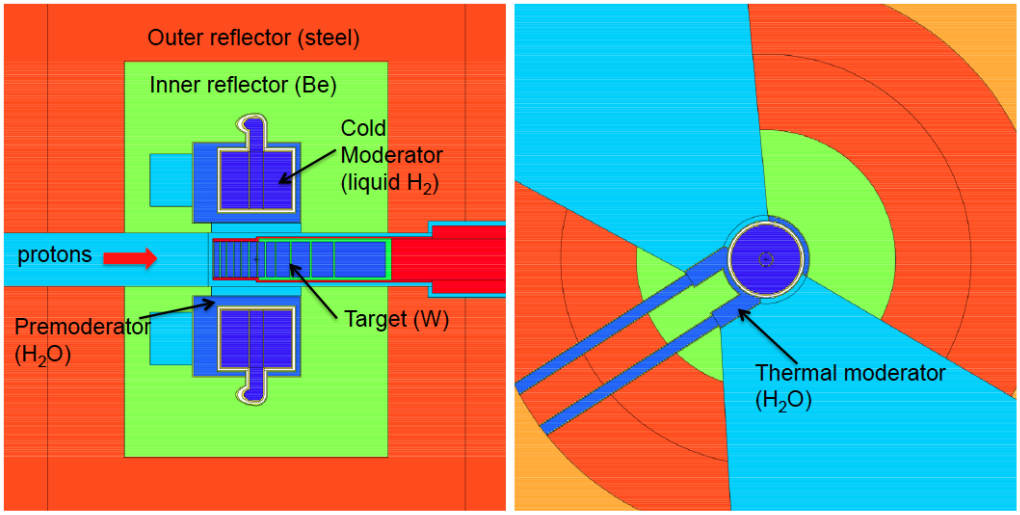

Figure 1. Vertical (left) and horizontal (right) cross section of the target-moderator-reflector geometry in the Technical Design Report [1].

2.1. Simulation setup

Based on the baseline MCNPX[2, 3] model used for the neutronics calculations of the ESS Technical Design Report (TDR)[1], a 25 cm×25 cm tube is defined. To best avoid the dominantly forward directed high energy shower particles from the proton beam impacting the target wheel, while obtaining maximal thermal flux, the tube is centered around and parallel to the x-axis (ie. perpendicular to the proton beam). The tube is centered at $z = 0$ while the y coordinate (the 'depth' under the proton beam) is left free and various possibilities are studied: $y \in [-47.5; -62.5]$ cm (central in tube)[1]. Figure 2 shows an example in which the void volume (the UCN through-going tube) replaces parts of the beryllium inner reflector (red), but more severely impacts the outer reflector (orange).

To measure the possible impact on cold/thermal beam lines, eight representative point detectors are placed in the beam-ports at the boundary of the Target-Moderator-Reflector(TMR) plug, corresponding to the blue stars on the lower right insert of figure 2.

2.2. Results

Comparing flux ratios between modified (i.e. including UCN tube) and baseline design, in the three energy bins (cold, intermediate and thermal) show that regardless of the position of through-going tube, the upper beam-lines are unaffected.

[1] The coordinate system used at the ESS is right-handed, with the protons travelling along the z-axis, impacting the target in the origin. The y-axis is positive upwards (i.e. opposite gravity).

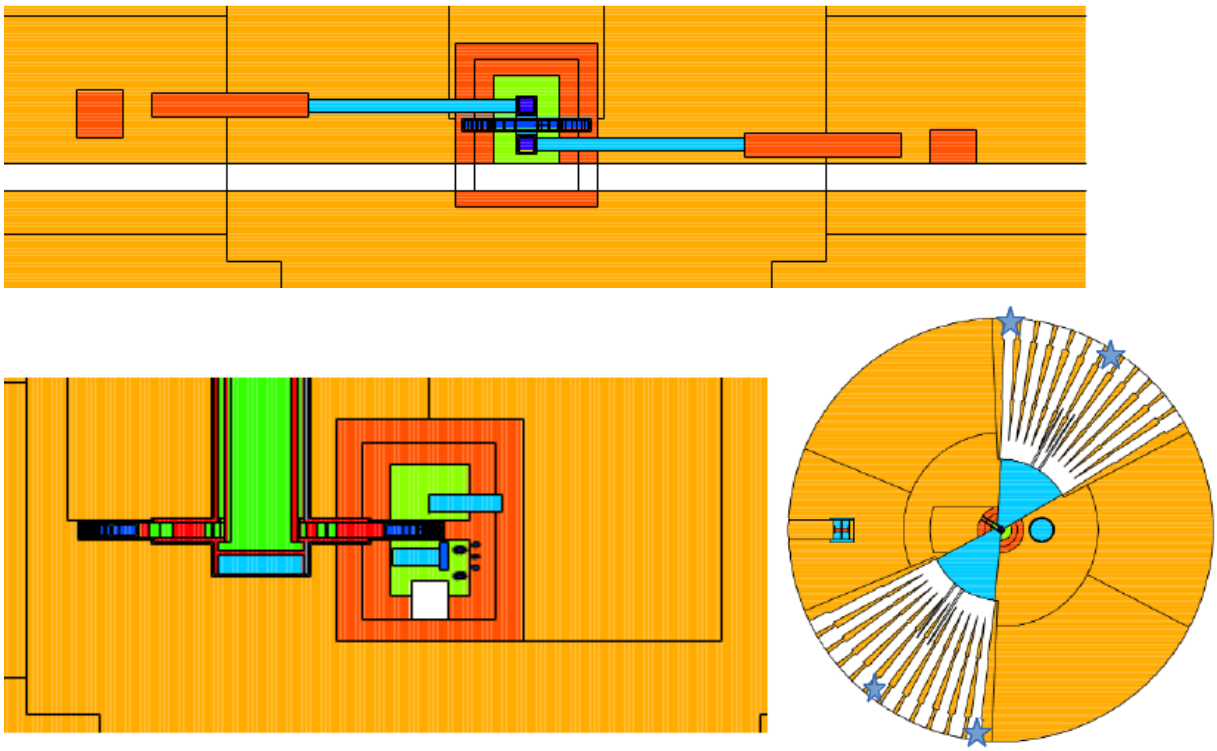

Figure 2. Geometry of the target, moderator and reflector showing the UCN through-going tube (white areas in upper and lower left-hand inserts) placed at y = -47.5 cm (central), corresponding to the topmost of the studied geometries. The blue stars in the lower right-hand insert shows the position of the lower point detectors. Note that the xz-plane (lower right-hand insert) is cut at y = -18 cm, wherefore the UCN tube is not visible.

Table 1. Flux and heat-load at different y-positions (central) of the through-going tube.

y position [cm]	Flux [n/s/cm^2]	Heat-load [W/cm^3]
-47.5	2.4 $\times 10^{13}$	0.20
-55.0	1.3 $\times 10^{13}$	0.11
-62.5	2.9 $\times 10^{12}$	0.06

Furthermore, the impact does not fluctuate significantly between the four lower tally positions: Therefore the response of all lower tallies are collapsed to one average for each position of the through-going tube.

Finally, the relation between the impact in terms of relative decrease in available cold/thermal flux at the cold/thermal instruments versus the (central) flux available for UCN production is shown in figure 3. It can be concluded that in the baseline configuration of the ESS TMR, a through-going tube can be introduced with insignificant impact on the cold/thermal beam-lines. In the through-going tube a flux of up to 2 $\times 10^{13}$ n/cm^2/s can be reached. The results are summarised in table 1, along with the heat-load results based on inserting a dummy 16cm $\times$16cm $\times$16cm para-hydrogen central in the tube.

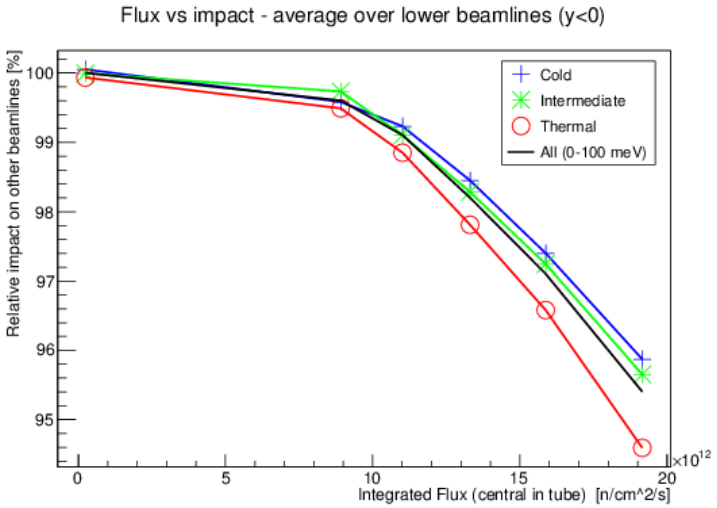

Figure 3. Relation between cold, intermediate and thermal flux in the lower cold/thermal beam-lines versus the flux available for UCN, central in the through-going tube. The black curve shows the average between the cold, intermediate and thermal curves. Each point corresponds to a specific vertical position of the through-going tube.

Table 2. Heat-load on cryogenic ^{4}He and integrated cold/intermediate/thermal flux for the ESS implementation of Golub's UCN design discussed in the text, and shown in figure 4. The results are obtained from a MCNPX simulation - the relative statistical uncertainties are ~0.1%.

Heat-load [mW/cm^3]	Flux [0-5]meV [n/cm^2/s]	Flux [5-20]meV [n/cm^2/s]	Flux [20-100]meV [n/cm^2/s]
2.5	3.8×10^{12}	9.0×10^{12}	1.8×10^{12}

2.3. ^{4}He UCN moderator according to Golub's design

Taking into account Carnot efficiency of cooling at cryogenic temperatures as would be required for a UCN moderator, the heat-loads of table 1 are problematic. Inspired from work of Golub and collaborators [4] that faced similar difficulties, the design shown in figure 4 is considered. Here, bismuth's ability to shield against gammas and filter neutrons is exploited. The corresponding heat-load and flux in the cryogenic volume is shown in table 2.

In [5] Golub and co-authors provide a scheme, for calculating maximum UCN production in a ^{4}He moderator, given an incoming cold/thermal spectrum and integrated flux. Inserting the values of table 2 and the observed spectrum, one arrives at a total maximal UCN production rate in 30 cm $\times$ 30 cm $\times$ 30 cm ^{4}He to be $1.5\cdot10^8$ UCN/s. It should be stressed that this is the maximum production rate, and it does not take into account any of the challenges confronted when attempting to store, extract or handle the UCN's. In addition, the design discussed here does not allow for two cold/thermal moderators at ESS is therefore not a viable option for ESS. Once the layout of the cold and thermal moderators have been decided, the study of the possibility to add a UCN moderator, will need to be revisited.

3. Other ideas for UCN moderators

3.1. Voluminous D_2 moderator

To facilitate experiments depending on the total number of neutrons in a sizable beam, the option of a voluminous D_2 moderator, in a large cross-section extraction guide is discussed and

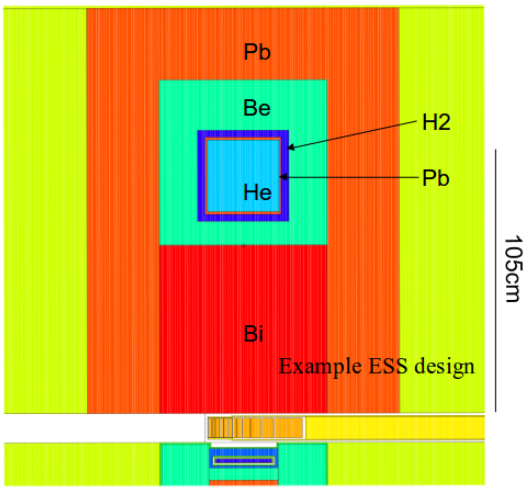

Figure 4. Possible design of an in-pile ^{4}He moderator at ESS - inspired from Golub [4].

its neutronic performance has been investigated. Under the assumption, that the scattering instruments at the ESS are served by a single moderator above the target, the performance of a 25 cm×25 cm×20.6 cm rectangular D_2 moderator placed in a through-going beam-tube under the target has been studied. The results of this feasibility study show that at least 3-4 times cold neutron beam intensity could be accomplished with respect to what would be available from a TDR configuration (figure 1). For details, the reader is referred to [6].

3.2. Satellite ^{4}He moderator

In figure 5(left) the ^{4}*He satellite* is sketched as suggested by E. Lychagin and collaborators.

The basic idea is to move the UCN moderator to a distance where the heating is manageable. When this is combined with the exclusive use of low neutron capture materials, a very high UCN density can be achieved even at a significant distance to the spallation target . The viewed surface of the cold (or thermal) moderator, and thus the size of the moderator, is a limiting parameter. For more details see [7].

3.3. D_2 pump

In this design, proposed by V. Nesvizhevsky, some of the characteristics of the 2 GeV long pulse proton driver at the ESS are exploited. An ultra-cold (few K) solid deuterium moderator (∼1 cm thick) is installed close to the spallation target, and is fed by a large liquid deuterium moderator.

During the duration of the pulse: 2.5 ms, the UCN will move ∼ 0.5 cm (at ∼ 4 m/s), thus filling the *halo* in front of the D_2. During the time between pulses, a membrane slowly push the UCN back away from the D_2, after which it rapidly moves back to the D_2, ready for the next pulse. The configuration is sketched in figure 5(right) - for details see [8].

4. Potential for discovery physics at ESS

The lack of discoveries at accelerators exploring the high energy frontier strengthens the motivation search of new physics elsewhere. The unprecedented proton beam power of 5 MW expected at the ESS pose unique possibilities to search for new physics, including the searches for $n\bar{n}$ oscillations and Dark Photons briefly discussed below.

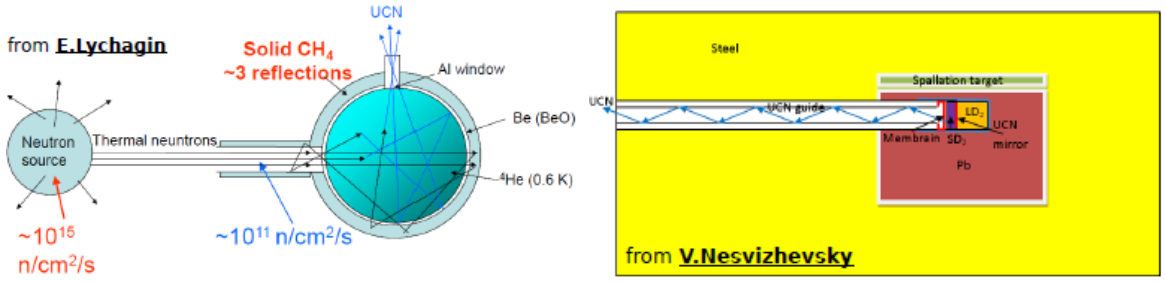

Figure 5. Sketches of the Satellite ^{4}He moderator (left) and D_2 pump (right) as referred to in the text.

4.1. Search for $n\bar{n}$ oscillations

Deviations from baryon number conservation have not been observed, but yet the Universe consists of baryons rather than anti-baryons. It is an intriguing question, to explain how the asymmetry came to be. Also, to explain that neutrinos are light, interactions with lepton number violation with ΔL=2 are needed. If quarks and leptons are unified at some scale, $\Delta L = 2 \Leftrightarrow \Delta B = 2$, ie. $n\bar{n}$ oscillations could then be a consequence of GUT theories for neutrino masses. If neutrons can oscillate to anti-neutrons, the probability would be proportional to the flight time squared, so an experiment to search for $n\bar{n}$ oscillations would aim for highest possible flight time, which would require an intense cold neutrons beam and good vacuum. To observe the anti-neutrons, and annihilation target (film) is needed and it should be surrounded by detectors in a magnetic field to track the produced charged pions and calorimeters to perform energy measurement of the neutron pions. By this approach the invariant mass of the annihilating particle can be reconstructed offline and background can be severely suppressed. Since this would be a discovery type of experiment background suppression is essential since any presence of background at all would reduce the sensitivity. The present limit: $\tau > 0.87 \times 10^8$ s was set by ILL experiment [9], using an approach according to lines ideas suggested here. However, partly due to the fact that the the experiment was built at an existing facility it suffered from a number of constraints - some of which can be avoided by planning the experiment while the facility is being designed. Presently an $n\bar{n}$ collaboration being formed with the intention to propose a $n\bar{n}$ experiment at ESS. Initial calculations suggest that the sensitivity could be at least two orders of magnitude better that what was reached at the ILL experiment.

4.2. Search for Dark Photons

The expectation that ESS will set a world record in beam power makes it an excellent place to look for new physics that couples to Standard Model particles, but is suppressed, and therefore escaped detection at colliders due to a low production rate. Examples include dark matter candidates such as dark photons [11] - particles coupling (slightly) to photons in the presence of matter. If such particles would exist they could possibly be produced in the harsh radiation environment of the ESS target. Once produced, they could escape through the shielding. By placing a calorimeter along the proton beam direction downstream from the target (on the backside of the shielding) one could search for dark photons converted back to photons in (or immediately before) the calorimeter. Such particles would appear as a excess of events (a peak) in the observed spectrum, corresponding to the given dark photon mass. Dark photons has been searched for using similar approaches in the past - the present limits are based on samples up to 10^{19} protons on target are shown in figure 6.

At ESS 10^{23} protons on target is expected yearly - a feasibility study investigating the ESS sensitivity for dark photon search is foreseen.

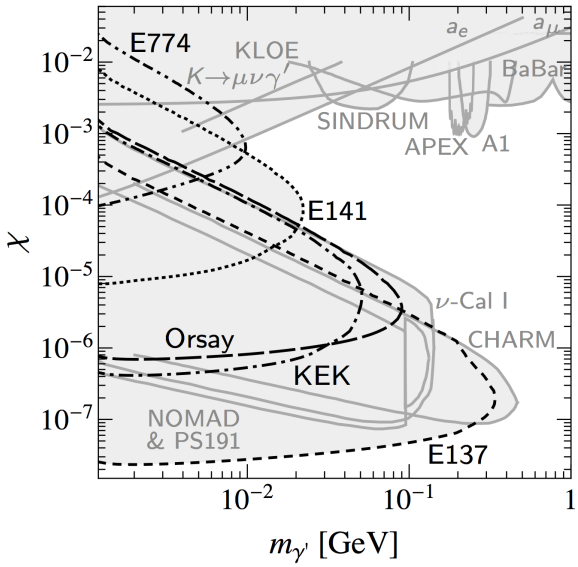

Figure 6. Present limits of of dark photon searches in the parameter space of the coupling strength, χ and dark photon mass $m_{\gamma'}$. The figure is due to S. Andreas [10].

5. Acknowledgements

This work has received financial support from CRISP - the Cluster of Research Infrastructures for Synergies in Physics. CRISP is co-funded by the partners and the European Commission under the 7th Framework Programme Grant Agreement 283745.

References

[1] Peggs S (editor) 2013 ESS Technical Design Report, *ESS-doc-274*
[2] Waters L S, McKinney G W, Durkee, J W, Fensin M L and Hendricks J S and others 2007. The MCNPX Monte Carlo radiation transport code. *AIP Conf.Proc.* **896**, 81-90
[3] X-5 Monte Carlo Team 1987, MCNP – A General Monte Carlo N-Particle Transport Code, Version 5, *LA-UR-03-1987*
[4] Golub R, *et al.* 1981 *Ultra-Cold Neutrons at the SNQ Spallation Source*, *TUM-E21/SNQ-UCN/81-4*
[5] Golub R, Richardson D J and Lamoreaux, S K 1991 *Ultra-Cold Neutrons* ISBN 9780750301152
[6] Klinkby E, Batkov K, Mezei F, Schönfeldt T, Takibayev A and Zanini L 2014 Voluminous D2 source for intense cold neutron beam production at the ESS. arXiv:1401.6003
[7] Lychagin E V, Muzychka A Y, Nekhaev G V, Nesvizhevsky V V, Sharapov E I and Strelkov A V 2014, UCN source at an external beam of thermal neutrons, *Advances in High Energy Physics* to be published
[8] Nesvizhevsky V V 2014 An option of "UCN pump" for ESS. arXiv:1405.7495
[9] Baldo-Ceolin M, Benetti P, Bitter T, Bobisut F, Calligarich E and others 1994 A New experimental limit on neutron - anti-neutron oscillations. *Z.Phys* **C63**, 409-416
[10] Andreas S, Light Weakly Interacting Particles: Constraints and Connection to Dark Matter. Ph.D. Thesis (Hamburg U.). 2013. *DESY-THESIS-2013-024*
[11] Particle Data Group Collaboration (K.A. Olive (Minnesota U.) 2014 *et al.*) 2014 Review of Particle Physics *Chin.Phys* **C38** 090001

3.10.3

Benchmark experiments on "entry-grooves" in moderator / reflector material

K. Thomsen, P. Ponya, T. Reiss and P. Vontobel

Paul Scherrer Institut, 5232 Villigen PSI, Switzerland

knud.thomsen@psi.ch

Abstract. Some influence of the surface structure on the coupling of neutrons with moderating material is well established, e.g. reentrant holes or –grooves are employed at different facilities to enhance the flux of neutrons emanating from moderators. For increasing performance, hitherto emphasis and effort has mainly been focused on amplifying useful neutron flux by optimizing the output-side of moderators. Recent preliminary numerical studies have indicated that similar structuring as established for boosting the flux at the output-side of a moderator might also be beneficial at the input-side by first letting the neutrons better enter the moderator volume. Experiments will be reported on a series of measurements illuminating several cubes of polyethylene with surface structuring in the thermal neutron beam of the NEUTRA facility at PSI, SINQ. With the new dual-detector set-up at NEUTRA, both the transmission through, as well as the reflection from the cube can be measured for different alignments and orientations. Demonstrating good agreement between calculations and measurements while verifying the above predictions for this mock-up geometry can be taken as a starting point for investigating more representative conditions. Whether significant improvements over simple-shaped moderator geometries can be achieved in realistic settings needs to be scrutinized by taking all relevant boundary conditions into consideration.

1. Introduction

Neutrons in spallation sources are set free with energies much higher than suitable for using them as probes in diverse instruments. Their energy has to be reduced, i.e. they are thermalized or cooled to even lower energies by means of moderators. There is a long tradition in optimizing these moderators, because it is of interest for any instrument to obtain a maximum signal-to-noise ratio for any given input power. Thus, it is proven and well established at many sources that certain geometrical structures enhance the neutron output from moderators. Still, the efficiencies of the diverse stages between the spallation reaction and the collection of appropriately moderated neutrons leaving the moderators are disappointingly low.

The simple idea proposed recently was that anything, which enhances the coupling of a neutron field on the output side of a moderator, might also be helpful when employed on its input-side.

Very preliminary simulations indicated some effects of structures like grooves or holes; they can improve the filling of the moderator material to start with and thus subsequently boost the neutron flux out of that material. Details and references are given in reference [1]. This paper further investigates these ideas. Recently, benchmark experiments on toy-geometries have been begun, work is still ongoing. First results of measurements at PSI´s NEUTRA radiography station at the spallation neutron source SINQ have been obtained and are reported here.

2. Experimental set-up

2.1. The NEUTRA facility

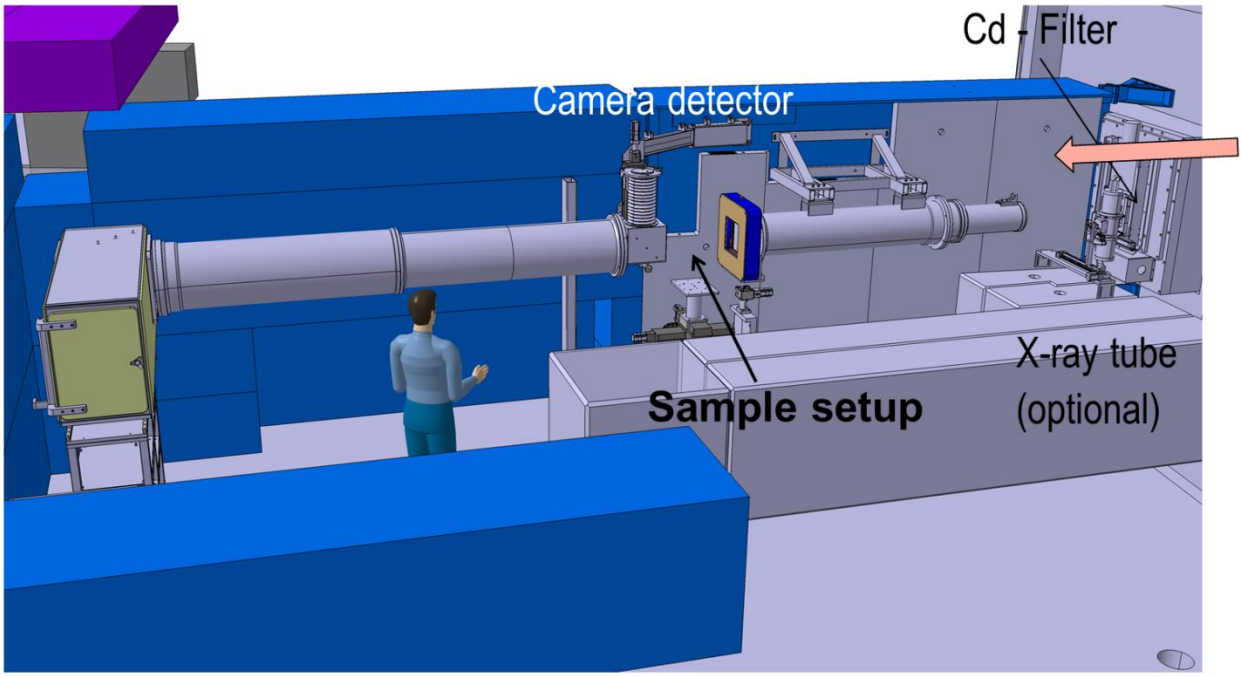

Figure 1. The NEUTRA radiography station at PSI´s SINQ spallation neutron source, http://www.psi.ch/sinq/neutra.

The radiography station NEUTRA (see figure 1) usually works with thermal neutrons (see figure 4). It features a high degree of flexibility concerning possible experimental set-ups [2]. For the measurements on the mock-up moderator specimens the middle position has been used, marked "Sample setup" in figure 1. There, an almost parallel beam of thermal neutrons was available, and detectors for thermal neutrons based on ^{6}Li doped ZnS have been used. Both, image acquisition with CCD cameras and imaging plates have been employed. Exposure times were 5-6 seconds and 60 seconds for experiments with thermal and "fast" input, respectively.

2.2. Specimens and configurations

Standard neutron radiographs with the detector behind the samples as well as images perpendicular to the neutron beam, i.e., sideways at 90^{o}, with the detector area aligned parallel to the incoming neutron beam, have been taken for many different configurations.

Specimens consisted of diversely structured Polyethylene (POLY) cubes with a side-length of 2 cm and distinguished by diverse structures (see figure 2). These (surface) features included six evenly distributed grooves extending over a third of the extension of a cube, 20 drillings of the same depth on a side and a through-hole of 5 mm diameter. For comparison, full cubes were also included in the sample 'towers'. In order to be able to separate them in the images, the different POLY cubes were separated by layers of POLY containing the strong neutron absorber material boron carbide.

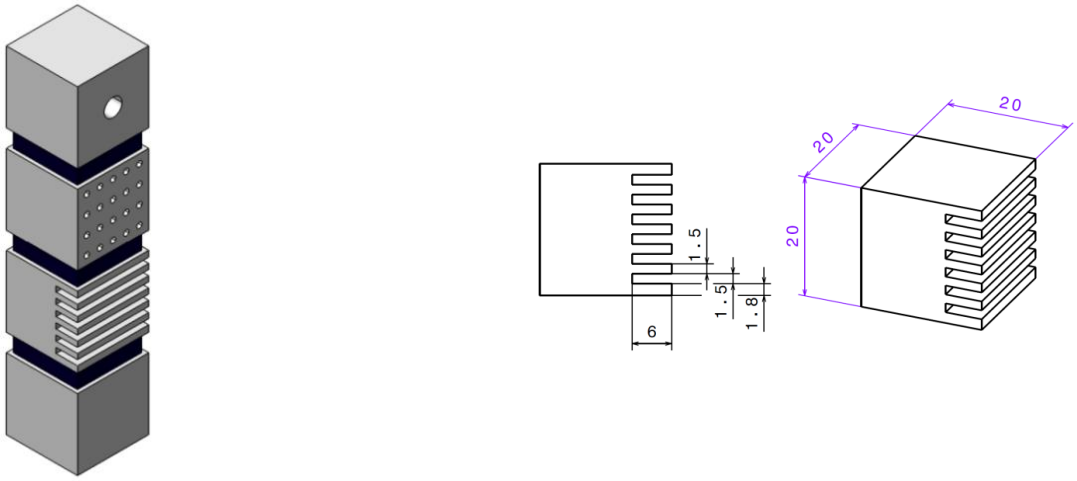

Figure 2. Example of specimen with differently structured POLY cubes of 20 mm side length, separated by neutron absorbing material.

Various specimens were rather uniformly illuminated by the incoming neutron beam as indicated by the arrow on the right hand side in figure 1. Many radiographs have been taken with two towers present at the same time. Side-ways measurements were taken with only one specimen present at a time (see figure 3).

Figure 3. Examples for configurations with two (left) and one (right) specimen. In standard radiography set-ups (left) the detector (scintillator and CCD camera) is behind the samples and the neutrons illuminate the two columns simultaneously. With the detector sideways (right) only one column could be investigated at a time. Some of the measurements with one column included detectors both behind and on the side. The single column (right) is mirrored in the detector behind it and in an imaging plate at the side. From these optical reflections by plane surfaces an assessment concerning the alignment (e.g. tilt) of the columns can be drawn.

2.3. Spectra

Both, thermal and epi-thermal neutrons have been employed. The latter have been obtained by closing a light instrumental shutter containing layers of cadmium and boron carbide to filter out the dominant thermal fraction of the neutron beam. Thus, some "fast" contribution remained. In an attempt to coarsely characterize the achievable fast flux, numerical simulations with MCNPX were performed (see figure 4).

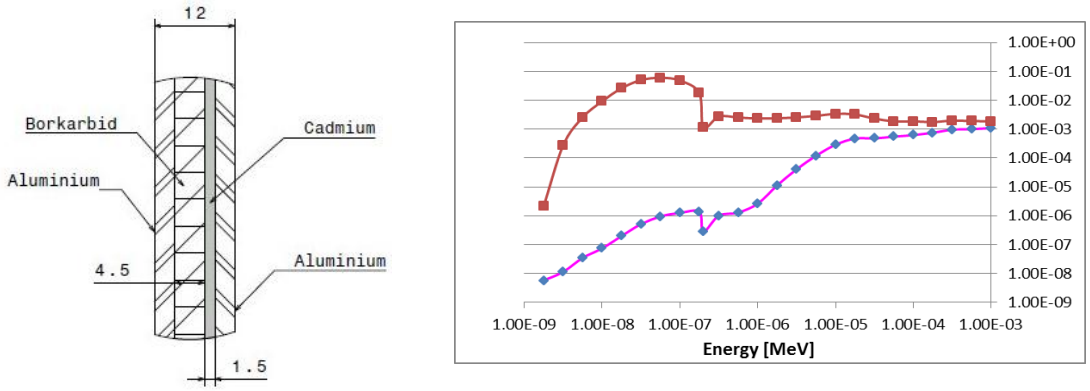

Figure 4. A "fast" neutron beam has been obtained by letting the standard thermal beam arriving from the left hand side pass through a light shutter (left). Extending the measured thermal part of the spectrum by an 1/E contribution, the effect of the shutter has been simulated (right). The thermal fraction in the remaining flux was found to be suppressed by several orders of magnitude.

Whereas a high intensity neutron-flux of about 1.2 10^7 n/cm^2/sec was available for experiments with the original thermal neutron beam, the signal was low for the set-up with "fast" neutrons. With standard thermal input, signal-to-noise was more than satisfactory for exposure times of 5 or 6 seconds. On the other hand, with the "fast" input, 60 seconds of exposure were necessary, and even then contributions of several sources of noise marred the obtained pictures. Dark current in the CCD detectors was suppressed by cooling. Additionally, it was attempted to calibrate the measurements and take care of fixed pattern noise stemming from the granulation of the used scintillator plates during image analysis and evaluation.

3. Results

During several experimental campaigns a large number of measurements have been performed, both, with thermal and with "fast" neutrons´ input, in diverse set-ups. Initial radiographs were recorded with two specimens present at the same time. The underlying assumption, i.e., that they would not "disturb" each other, was proven wrong immediately.

3.1. Measurements in standard radiography mode

Comparing images obtained in standard radiography alignment for thermal versus "fast" input neutrons, general similarities and some differences can be noted. All results reported here have been obtained in the "NEAR" condition, i.e., with a distance between columns and detectors of about 5 mm. More results recorded for larger distances up to 6 cm ("FAR") have been taken but not yet analyzed.

As a general remark, the here presented images were enhanced for best visibility, numerical values and profiles are as measured and normalized making use of the full depth (16 bit) resolution of the measured data. All plots are with arbitrary, relative units.

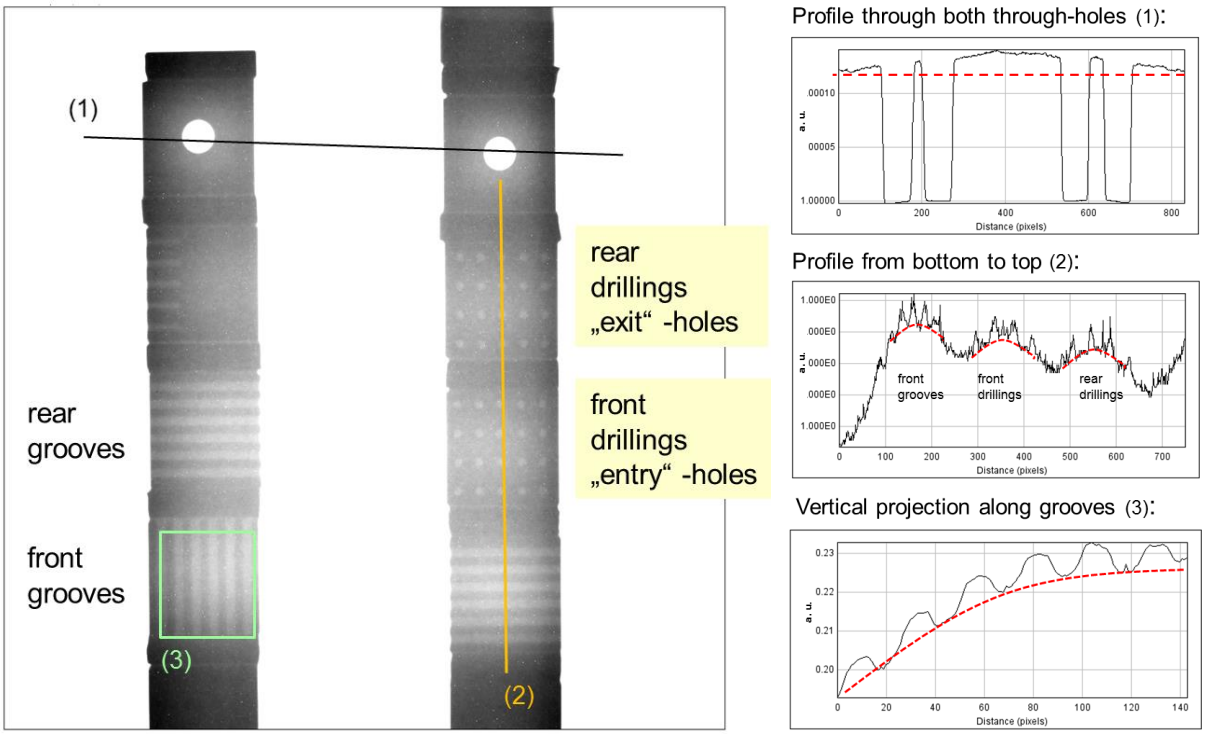

Figure 5. Radiography with thermal neutron beam (left); profiles along the specified lines and over an area, respectively, are given (right). Red dotted lines do not indicate any modelling, they are just meant to guide the eye. Most prominent, large amounts of scattering are visible: in the center between the two columns higher levels are detected than towards the rims at the sides (profiles 1 and 3). The modulation in the image thus is not just produced by "simple" attenuation. Comparing full cubes with grooved ones, it is found that the reduction of scattering material due to the grooves by 15 % results in an observed enhancement of the throughput by more than 50 %. Features at the front yield rather similar effects for the through-going neutrons as the same features at the rear side. For each individual cube, more neutrons come from the center than from the periphery (profile 2).

It seems important to note that a strong background is observed with one or two POLY-towers in the beam. This diffuse background leads to a global "curvature" of the measured overall neutron distribution and is especially visible in the case of two specimens. This unstructured background adds to all detected more local features; the "empty" field between two specimens actually shows the highest measured neutron intensity. Here, it is only hypothesised that the diffuse component stems from the overlay of neutrons scattered from the individual cubes with the distribution of the re-emitted neutrons from the sides of the cubes following a Lambert law. This can nicely explain the local curvature seen for single cubes with a prominent peaking of the scattered intensity in the center of the surface facing the detector.
From this it becomes clear that the obtained images cannot simply be interpreted as attenuation-based radiographs. There is strong scattering and a Lambert-Beer law is not applicable in this conditions.

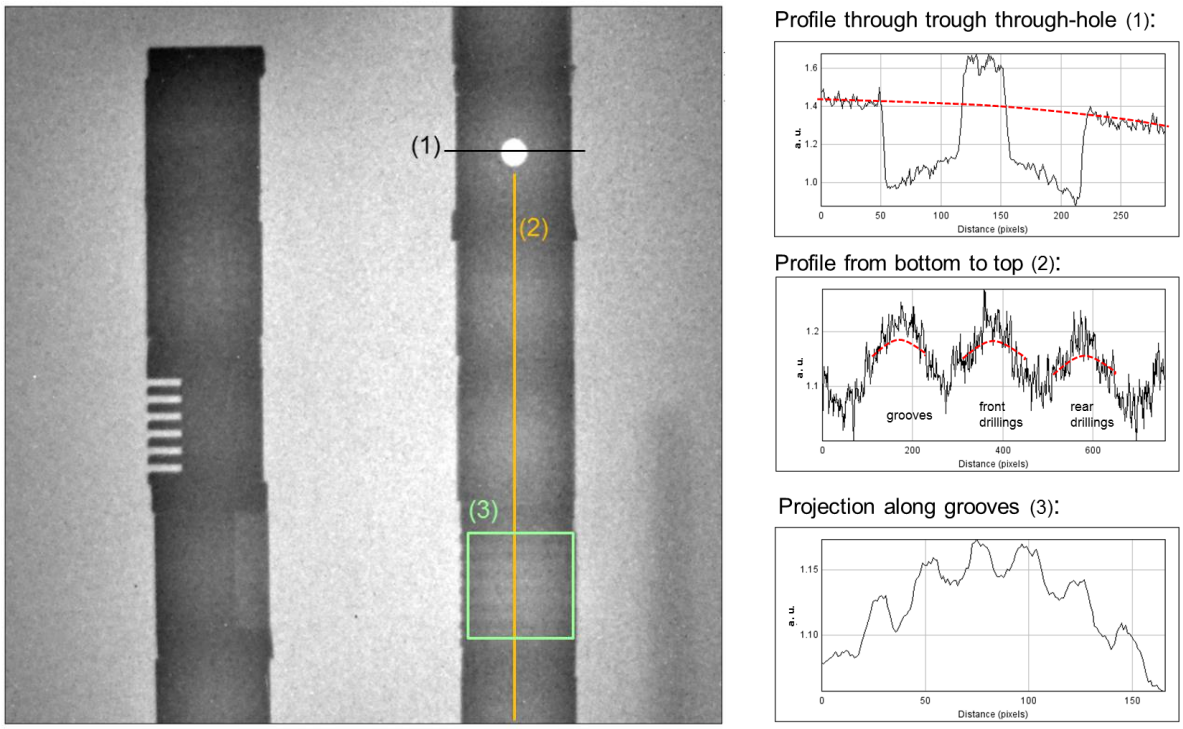

Figure 6. Radiography with "fast" neutron beam (left); profiles along the specified lines and over an area, respectively, are given (right). Compared to the configuration of figure 5, the left hand column had been turned by 90°. Although the signal-to-noise is worse, the findings are similar to the ones obtained with the thermal neutron beam (figure 5). Scattering is clearly observed; the image is brighter between the specimens than along the sides (the shadow on the far right has been produced by a thin strip of gadolinium for tests). A peculiar observation is resulting from the through-hole close to the top of the right column (profile 1): this hole obviously works as an "entry-hole" and also as an "exit-hole" with the total effect of boosting the thermal flux behind it to a higher value than in the empty field in the center of the image.

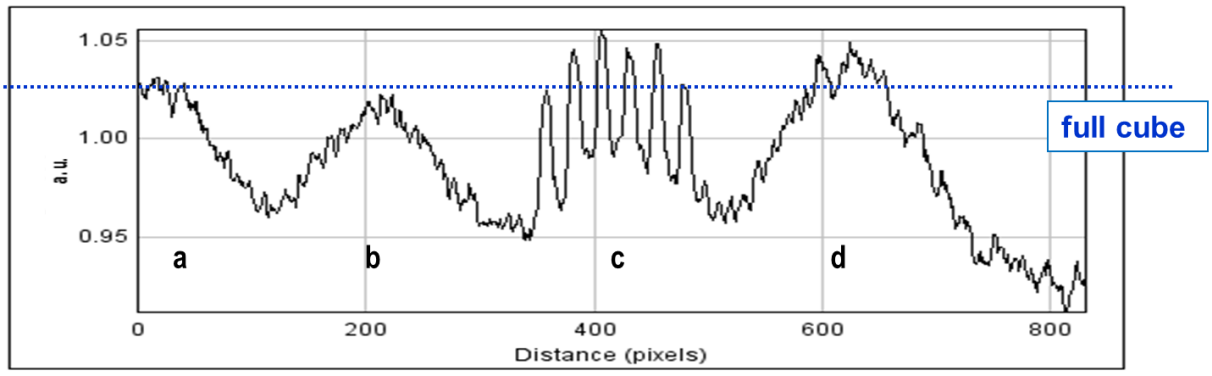

Figure 7. Radiography with "fast" neutrons; further analysis of the image presented in figure 6. Analysis of a profile over an area extending along the center of the left hand column hints at effects attributable to the structuring; from left to right (bottom to top in figure 6): full cube's reference response (a) indicated also by the dotted line; vertical grooves facing to the other column and "depleted" thermal flux passing through (b); horizontal grooves facing to the side and "depleted" thermal flux passing through (c); drillings facing the "fast" incoming neutron beam (i.e., "entry holes") leading to an enhancement of thermalized neutrons leaving from the rear side of that cube (d).

3.2. Sideways measurements

In an incremental stepwise approach, given first hints concerning the effectiveness of the implemented structures obtained in standard radiography alignment, more measurements have been performed looking especially for neutrons scattered 90° to the side with respect to the incoming neutron beam.

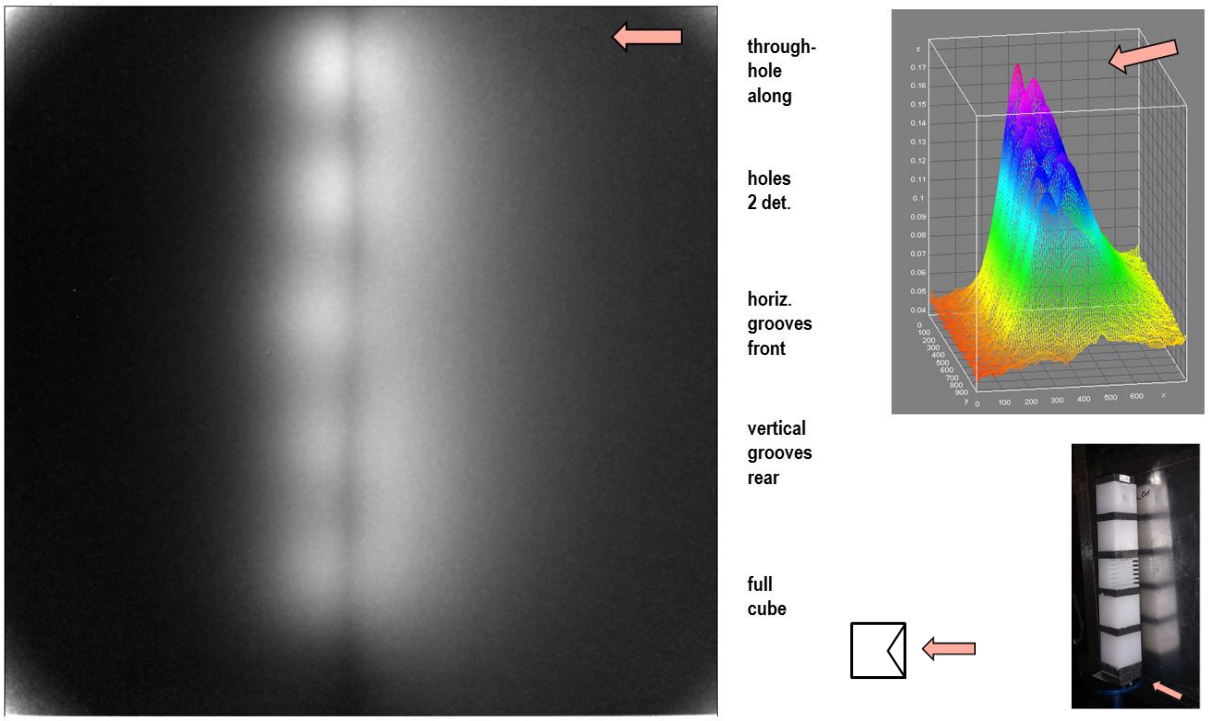

Figure 8. Sideways image for thermal neutrons' input (left); 3-D visualisation and set-up (right). The red arrows indicate the direction of the incident neutron beam. Some inadvertent "leaning" of the sample-column is documented in the photograph. The bright corners of the image are an artefact caused by the normalization procedure. The dominant fraction of the neutrons impinging on the sample is "diffusely scattered back" (especially visible in the 3-D plot). A well-distinct line of low intensity is observed between backscattered flux and neutrons emanating at 90° from the individual cubes. More sideways' intensity is measured at the position of the cube with input-grooves (middle) than for the full cube (bottom).

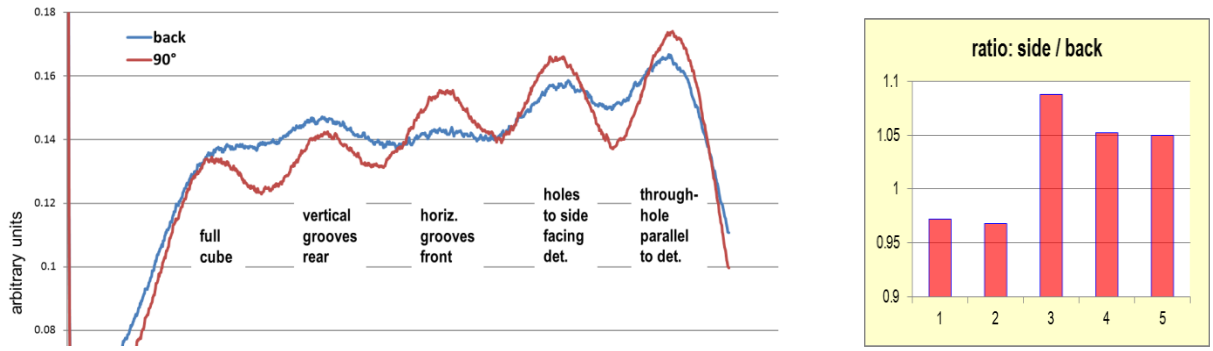

Figure 9. Sideways scattering for thermal neutrons' input; further analysis of the image in figure 8. Profiles along the column show significant differences between "reflected" neutrons and flux leaving the cubes at 90° sideways; the structuring of the cubes does have an impact (left). In order to compensate for the "leaning" of the

sample, ratios between “reflected” and “scattered” fractions are plotted for the individual cubes (right). Most noticeable is that the maximum effect is found for grooves on the front facing towards the incoming beam (middle position “3” in this orientation of the specimen). Grooves on the opposite rear side reduce the fraction scattered at 90° to the side (2), whereas drillings on the side facing the detector (4) and a through-hole running along the incoming beam (5) augment it. Scattering from the full cubes (1) here looks very similar to the neighbouring sample with rear grooves (2).

For direct comparison, more results obtained with the same specimen as in figures 8 and 9 are reported next; figures 10 and 11 show images obtained in almost identical conditions, but with the specimen turned by 180° and with better alignment of the tower, i.e. straight and not “leaning”.

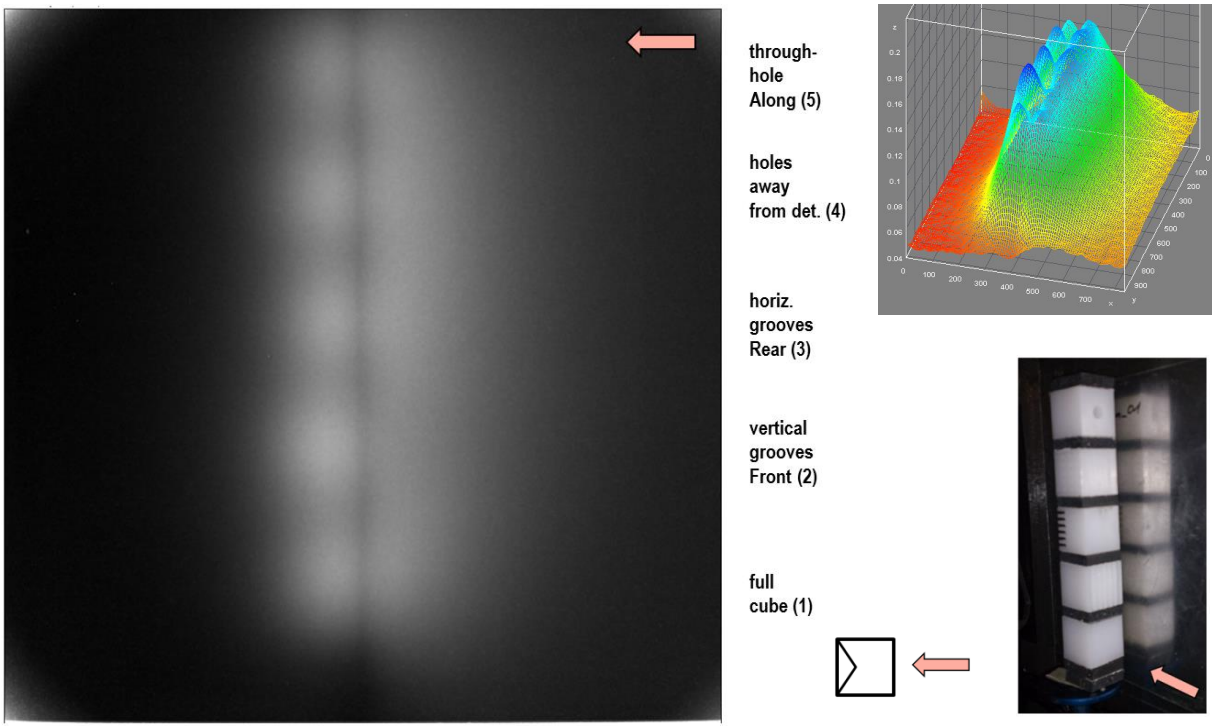

Figure 10. Sideways image for thermal neutrons’ input (left); 3-D visualisation and set-up (right). The principal findings are the same as in figure 8 above with the same sample turned 180°, i.e., front and rear sides were exchanged and here, the drillings pointed away from the detector; straight alignment of the column with respect to the detector plane. The most important difference is that by turning the column the positions of cubes with grooves facing the incoming beam or the opposite rear side have been swapped and the ratios of the scattered fractions changed accordingly as seen in figure 11. Scattering to the side at 90° from the cube featuring entry grooves (2) is stronger than from the full cube below (1).

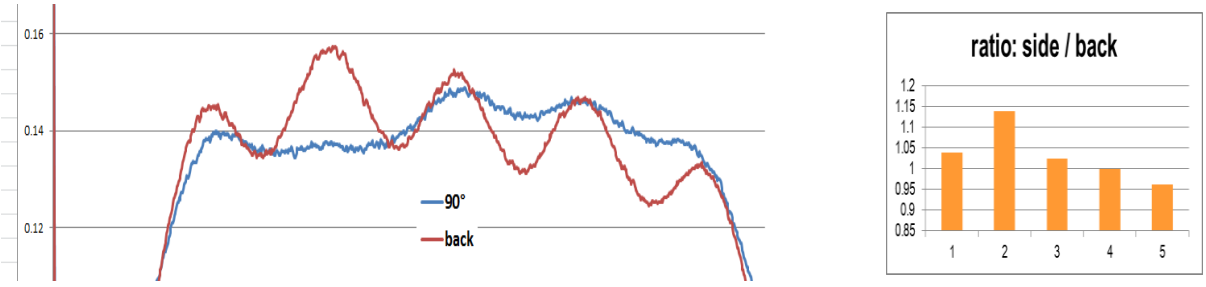

Figure 11. Sideways scattering for thermal neutrons’ input; further analysis of the image in figure 10. Most neutrons are scattered 90° to the side from the cube now pointing with grooves towards the incoming neutron beam, i.e., with entry-holes, and the “directly reflected flux” there is reduced correspondingly (2).

With strongly reduced flux to start with and resulting difficulties with respect to the achievable signal-to-noise ratio, measurements with a "fast" neutrons' input proved more difficult than with thermal input. Nevertheless, sideways images could be taken with imaging plates and also with the CCD camera set-up pivoted 90° to the side. For the configurations with identical input and sample-conditions but different detectors, the obtained results were qualitatively identical. For their "nicer" appearance, here, two experiments employing an imaging plate are presented in figures 12 and 13.

The striking difference between images obtained with thermal and "fast" input, respectively, is the lack of a detected fraction, which is "directly reflected back" from the entry surface of the cubes. Given the almost exclusive sensitivity of the detectors for thermal neutrons, this matches perfectly with expectations, as only multiple scattered and thus moderated neutrons give a signal.

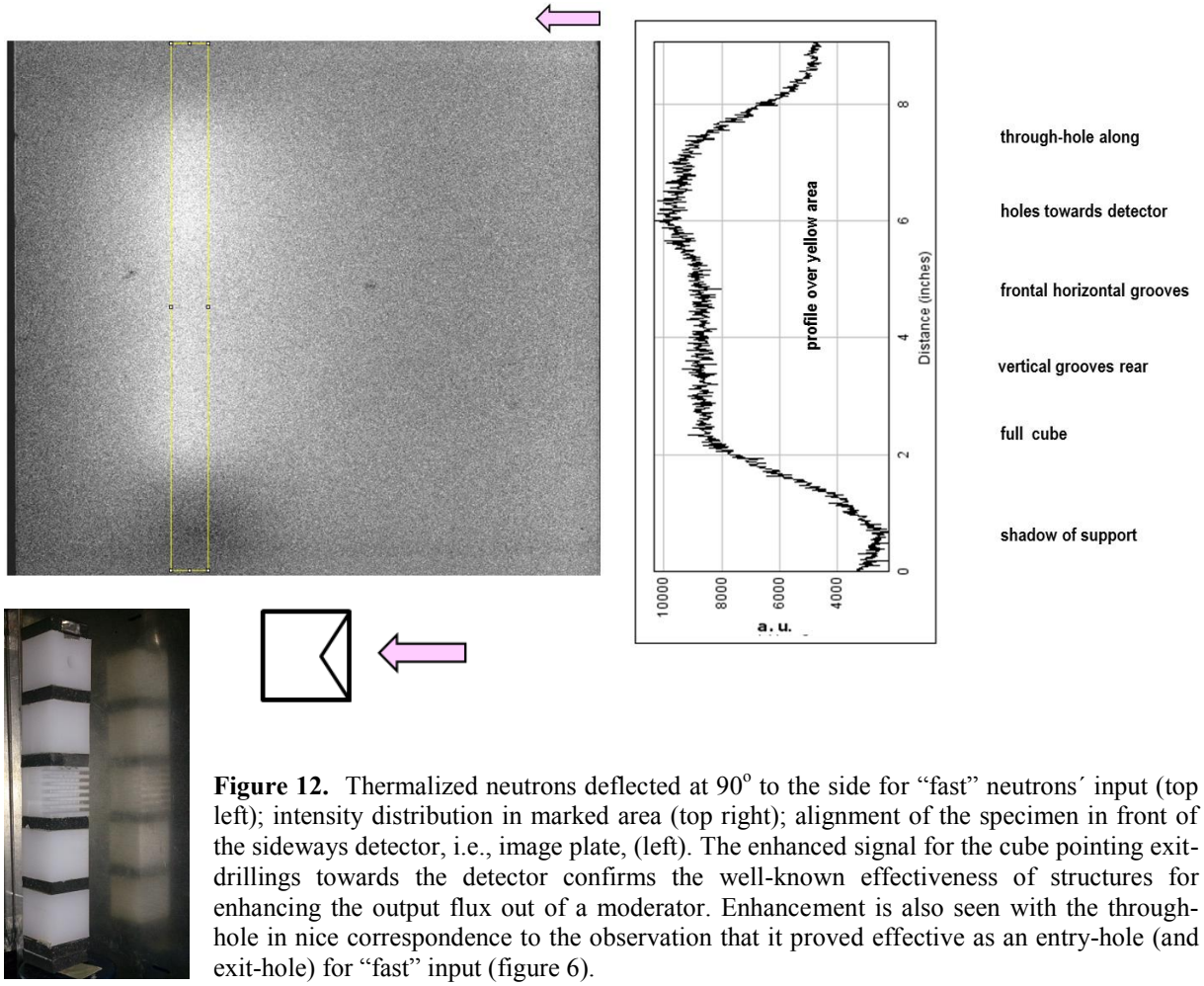

Figure 12. Thermalized neutrons deflected at 90° to the side for "fast" neutrons´ input (top left); intensity distribution in marked area (top right); alignment of the specimen in front of the sideways detector, i.e., image plate, (left). The enhanced signal for the cube pointing exit-drillings towards the detector confirms the well-known effectiveness of structures for enhancing the output flux out of a moderator. Enhancement is also seen with the through-hole in nice correspondence to the observation that it proved effective as an entry-hole (and exit-hole) for "fast" input (figure 6).

Rotating the specimen of figure 12 by 90° in clockwise direction turned the exit-drillings into entry-drillings; results are shown in figure 13. Noticeably, the peak in the detected flux 90° to the side stayed at the same position on the detector. Some more effects of the diversely structured cubes are discussed below in the caption of figure 13.

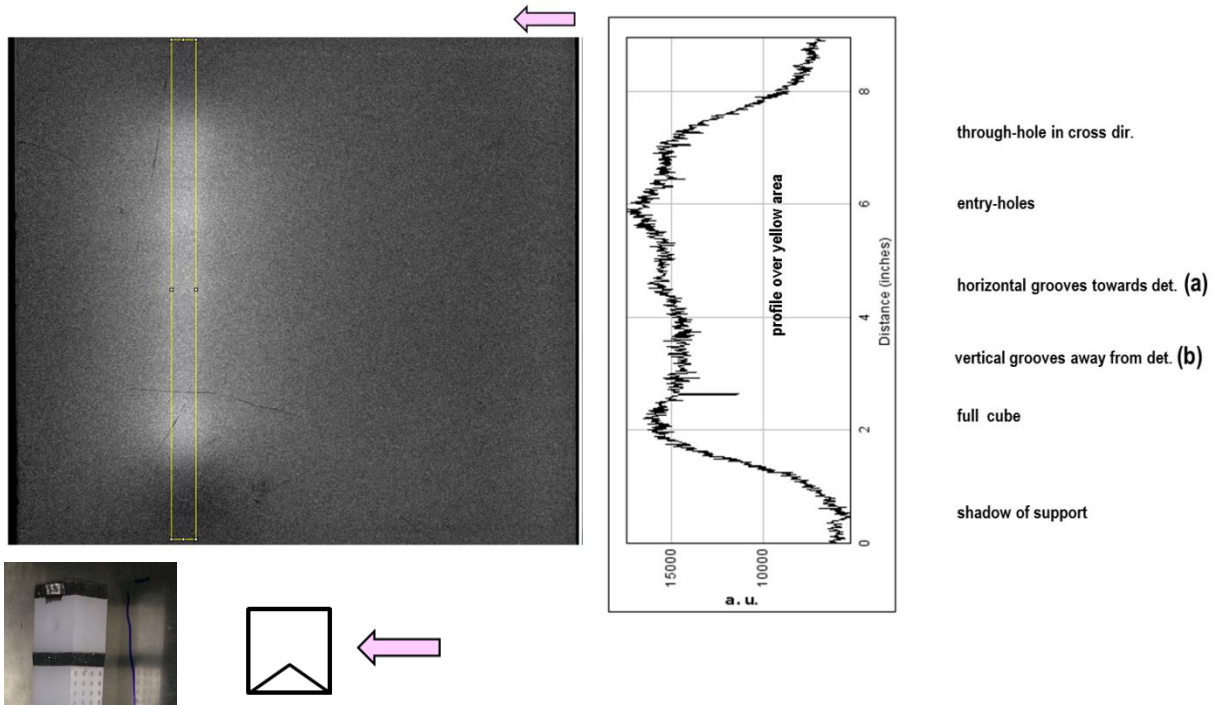

Figure 13. Thermalized neutrons deflected 90° to the side for "fast" neutrons´ input (top left); intensity distribution in marked area (top right); alignment of the specimen in front of the sideways detector, i.e., image plate, (left). The same specimen as in figure 12, just rotated by 90°. Entry-holes enhance the flux to the side. Comparing entry-grooves (a) to exit-grooves (b), the former boost the scattered / moderated fraction to the side whereas the latter reduces it, i.e. grooves are directing the emanating neutrons according to expectations, which means "draining" away from the detector when facing in the opposite direction. In this setting, the through-hole shows a small effect as exit-hole.

3.3. Preliminary Simulations

In parallel to the measurements, simulations were carried out with MCNPX in an attempt to reproduce the experimental findings. To start with, a full cube and one with grooves facing the incident neutron flux has been investigated. Both, radiography and sideways detectors have been simulated, and the responses to thermal as well as "fast" neutron beams were calculated.

Just the same as with the experiments, work is still in progress, and the results of the simulations as available right now have to be considered preliminary. Nevertheless, similarities and differences have already been found between the simulations and measurements and are reported in figures 14 and 15 below.

Results so far are only available for local features; in particular, no global effects like the measured extended diffuse background in the "empty" field have been investigated.

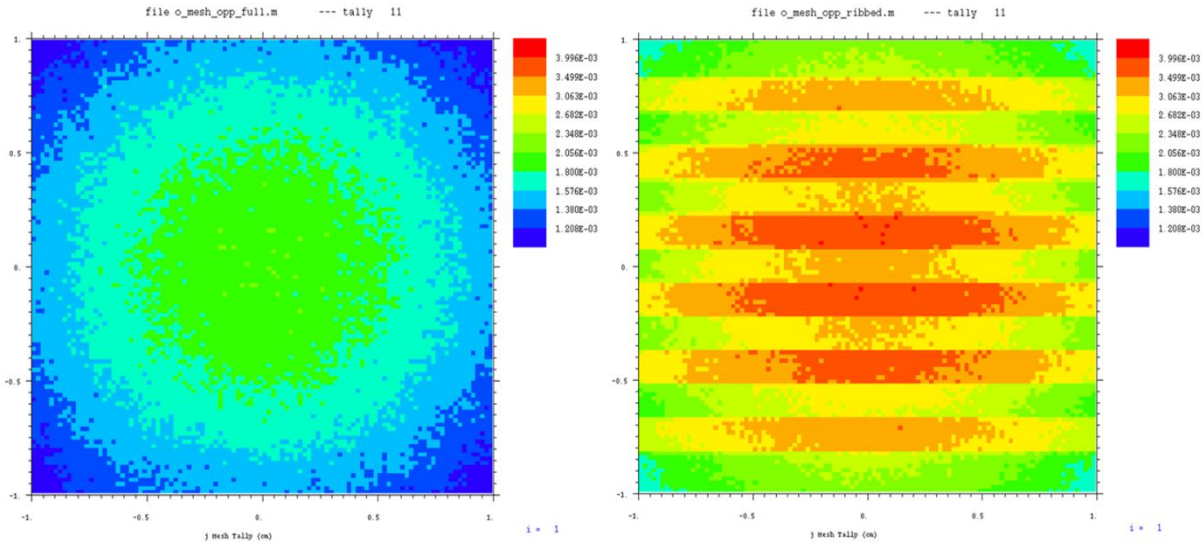

Figure 14. Radiography with thermal neutron beam, simulation results for a full cube (left) and for a cube whose grooves are facing the incoming beam, i.e. entry-grooves (right). The plots are on the same color-coded scale. An enhancement of the output flux is clearly visible for a cube with entry grooves (15% less material) compared to a full cube; the obtained ratio of 1.54 for the integrated values matches perfectly with the experimental results, compare figure 5.

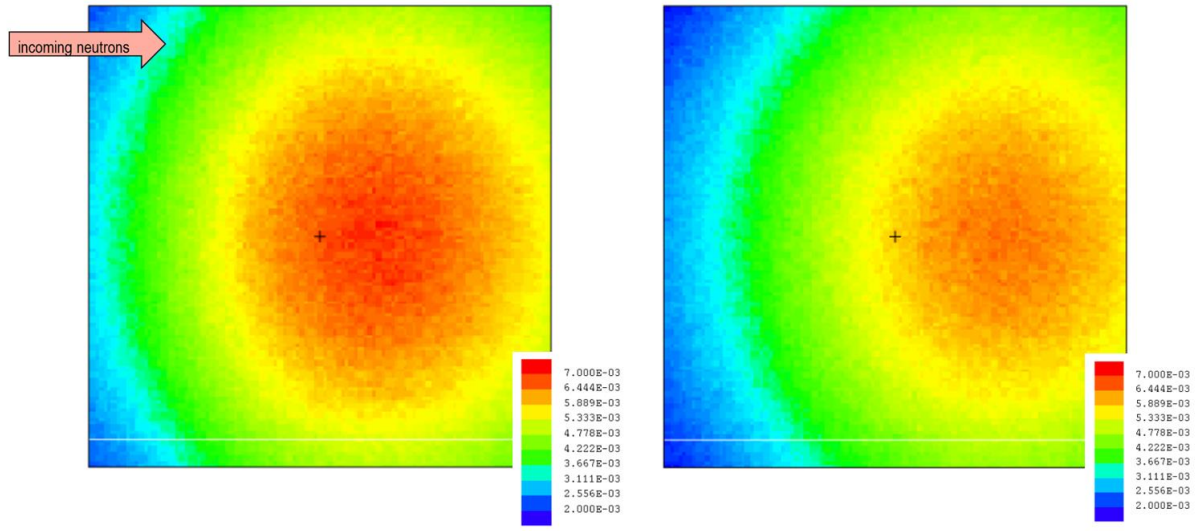

Figure 15. Simulation results with a sideways detector employing thermal neutrons' input, for a full cube (left) and for a cube with entry-grooves (right); plots are on the same scale. A clear shift of the detected flux in forward direction is found for both samples; this could explain the dark line described in figures 8 and 10; additional, more detailed simulations are required.
Simulations indicate a higher total flux 90^{o} to the side for a full cube (left) compared to the one with entry grooves (right); this doesn't match with the measured data which indicate the opposite (see figures 10 and 11).

One hypothesis currently is that differences in the observed scatterd distributions for different input neutron beams might be linked to the conditions employing thermal neutrons, which actually always contained some contamination by "fast" neutrons.

4. Discussion and Preliminary Conclusions

This is work in progress. Not all the measured data have been analyzed yet, and more are to come. The same holds true for the simulations. Nevertheless, it seems safe to claim that evidence for an enhanced coupling of a neutron field to moderator material due to structuring has been found, both, for the input *into* as for the output *out of* the moderator. Quite generally, effects for „entry-“ and „exit-“ holes appear to be rather similar. Some differences for thermal compared to “fast” neutrons seem to exist.

When analyzing different measurements, which involved similar set-ups and, in particular, when contrasting images recorded with the CCD cameras with data obtained by imaging plates, it can be concluded that error bars were sufficiently low not to demolish the principal findings reported here. For these first mock-up experiments the aim was to obtain some qualitative results and understanding, - enough to continue the effort with refined methods in order to complete the picture and derive quantitative results.

It goes without saying that more work is still needed before it is clear how the here presented results can efficiently be used in the design of real moderators; this does not appear to be trivial [3]. One principled obstacle in realistic geometries might result from the observed similarity in the effects of input- and output- structures; what works as an entry-hole, also works as an exit-hole. With neutrons arriving from a target, an entry-hole might not only enhance the filling but at the same time also boost the draining of neutrons in this same direction, i.e., the effects observable at the intended output surfaces of a moderator might largely cancel.

4.1. Next Steps

As of the writing of this paper (September 2014), in addition to continued work on already recorded data, more measurements and simulations are planned. It might, for example, be interesting to measure “reflected” / moderated neutrons for “fast” input with a detector, which is dedicated sensitive to epi-thermal neutrons. Conversely and somehow complimentary to the investigations with thermal and “fast” input spectra, the scattering from diversely structured specimens for cold input neutrons could give interesting data points.

Collaborations with partners for some further scrutiny of the reported effects would be most welcome, and opportunities for discussion are used as they arise at ICANS XXI and during a specialized conference on neutron radiography immediately thereafter [4].

Acknowledgments
Strong support by, amongst others, C. Franklyn, G. Heidenreich, A. Kalt, E. Lehmann, M. Magán, M. Morgano, and F. Sordo is gratefully acknowledged.

References

[1] K. Thomsen, Conceptual Proposal for Compound Moderators with Preferential Emission Directions, *Physics Procedia*, in print.
[2] E. H. Lehmann, P. Vontobel and L. Wiezel, Prpoerties of the Radiography Facility NEUTRA at SINQ and its Potential for use as European Reference Facility, *Nondestructive Testing and Evaluation* 16, 191-202, 2001.
[3] M. Magán and F. Sordo, private communication, 2013.
[4] K. Thomsen, P. Ponya, T. Reiss and P. Vontobel, Influence of Surface Structures on the Coupling of Neutrons with Moderating Material, World Conference on Neutron Radiography, WCNR-10, Grindelwald, October 2014.

3.10.4

Control system of filling of chamber for cryogenic moderator of IBR-2 research reactor

A. Bogdzel, A. Verhoglyadov, V. Zhuravlev, S. Kulikov, F. Levchanovsky, E. Litvinenko, A. Petrenko, A. Sirotin, A. Churakov, E. Shabalin
Joint Institute for Nuclear Research, Dubna, Russia

E-mail: verhoglyadov_al@mail.ru

Abstract. High-performance cold neutron moderator for the IBR-2 reactor is manufactured at the Frank Laboratory of Neuron Physics and operates in normal mode at present. Material for cold moderator is mixture of mesitylene and m-xylene in the form of solid beads with diameter of about 3-4mm. These beads are replaced in the moderator's chamber periodically. Uniformity of chamber volume filling is one of the problems of moderator operation. Observation of filling process is realized by acquisition of 2D images of moderator on two coordinate PSD by the method of "camera-obscura". Ready-built monitoring system allows controlling the level of working medium in chamber of moderator, to measure neutron spectra and to control of warming and drain of used mesitylene. At the present time monitoring system is installed at 8th channel of IBR-2 reactor, it detects 12- times gain of 6-10Å neutron flux with using of new moderator. Also absence of appreciable spectrum degradation was observed.

1. Introduction

The unique system of cryogenic neutron moderators is being installed on research pulsed reactor IBR-2 at the Joint Institute for Nuclear Research in Dubna at present time [1,2]. Slow, «cold» neutrons with wavelength higher than 0.2-0.3 nm is necessary instrument for research of new complicated nanostructures by the methods of neutron scattering, including organic materials and biological objects. Original design of new of new cryogenic moderator on solid mesitylene with its high parameters will provide the leadership of research reactor IBR-2 between worlds pulsed neutron sources.

High-performance cold neutron moderator for the IBR-2 reactor operates in normal mode at present. Material for cold moderator is mixture of mesitylene and m-xylene in the form of solid beads with diameter of about 3-4mm. These beads are replaced in the moderator's chamber periodically. Uniformity of chamber volume filling is one of the problems of moderator operation. Observation of filling process is realized by acquisition of 2D images of moderator on two coordinate PSD by the method of "camera-obscura".

2. Observation system of CM chamber

In the process of operation of cryogenic moderator a number of tasks related to the control of the moderator chamber occur:

1. Receive two-dimensional images of the loaded mesitylene to control the filling of the chamber.
2. Measure the neutron spectrum from the moderator at different temperature of the working medium. Record the change of neutron spectrum within the cycle of the reactor (degradation of the spectrum).

3. Control the process of annealing and drain of the working medium after the cycle of the reactor. Control the level of mesitylene and neutron spectrum.

Two-dimensional image of the surface of a moderator is formed on a position-sensitive detector when thermal and cold neutrons from the moderator pass through a small (about Ø0.5 mm) horizontal slit in cadmium diaphragm [3]. Fig. 1 presents simplified scheme of experiment of control system of cold moderator filling with using the method of "camera-obscura". Two-dimensional image of moderator's surface is formed on position-sensitive detector by transmission of thermal and cold neutrons through small (about Ø0,5mm) horizontal slit in cadmium diaphragm. Obtained image gives reverse one-dimensional distribution of neutron flux on the surface of moderator in vertical direction. The image is averaged out in horizontal direction. Scale of image is determined by distances between PSD, diaphragm and moderator. The distances A and B on the Fig.2 are realistic and images come out smaller than actual size of moderator (reduction k=A/B≈0,295). The shield of PSD and collimators of borated polyethylene (brown color on figure) are used for reduction of background. Vacuum volume occupies most part of neutrons' trajectory and decreases neutron losses in the air.

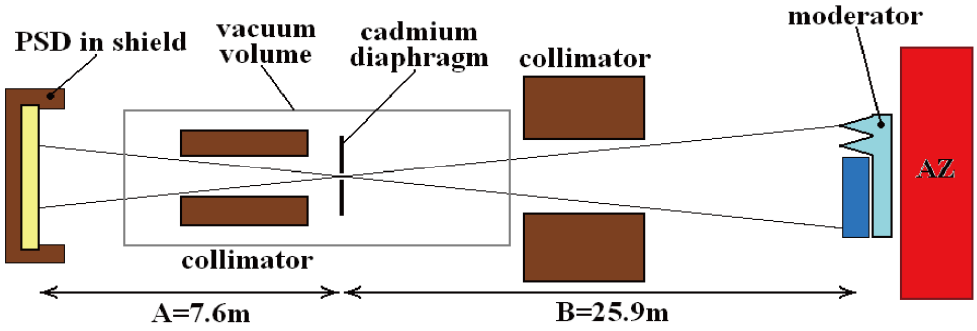

Figure 1. Layout of the experiment with a gap on 8th channel of IBR-2.

Neutron spectrum is measured by time-of-flight method.

Equipment is installed at 8th channel of IBR-2 reactor, which axis is orthogonal to the face plane of moderator. Position-sensitive detector [4] has a working area of 180x180mm. It is placed so that the centre of the detector is on the horizontal axis of spectrometer (Fig 2).

Figure 2. PSD in shield is installed on 8th channel.

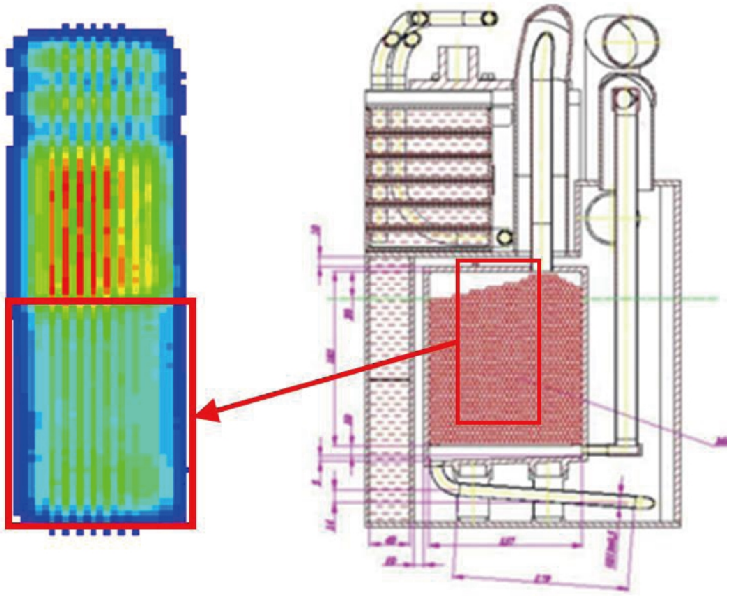

Figure 3. Correspondence between image and moderator chamber. Rectangle shows the working medium of the moderator. The image is obtained with neutrons $\lambda = 0.7$Å and higher.

The electronic block of data acquisition consists of discriminator, high voltage unit, block of delays and power supply, installed in a rack. Signal from rack together with signals of reactor starts are transmitted to the PC where they are processed by software DeLiDAQ [5].

3. Results

The obtained two-dimensional image for thermal neutrons is shown in Fig. 3. The figure shows the correspondence between image and real moderator chamber.

On Fig. 3 one can clearly see the level of mesithylene in the chamber.

2D images and spectra of new cryogenic moderator were obtained in experiments on the beam. The gain of cold neutron flux and decrease of thermal neutron flux were determined for temperature of mesitylene equal 30K and 100K.

Control system for chamber of cryogenic moderator with method of “camera-obscura” is created and operates in normal mode on IBR-2 at present.

The first results of operation of cold moderator are described in [6]. Neutron spectra of cryogenic moderator were measured at different temperatures of mesithylene (Fig. 4). Addition of cold moderator to the water premoderator gives gain-factor of cold neutrons of about 13. 2D images of moderator’s working substance were obtained, it allowed to control of filling and draining of chamber.

4. Conclusion

The system of control and measuring equipment, designed for cryogenic moderator IBR-2 reactor, satisfies all the requirements and is simple to use. All control subsystems are combined in two personal computers, so all information about the state of the system is displayed and saved. Access to the system of measuring instruments is organized via network. The first working cycles of moderator confirmed the reliability and stable operation of the whole control system.

2D images and spectra of new cryogenic moderator were obtained in experiments on the beam. The gain of cold neutron flux and decrease of thermal neutron flux were determined for temperature of mesitylene equal 30K and 100K.

Control system for chamber of cryogenic moderator with method of “camera-obscura” is created and operates in normal mode on IBR-2 at present.

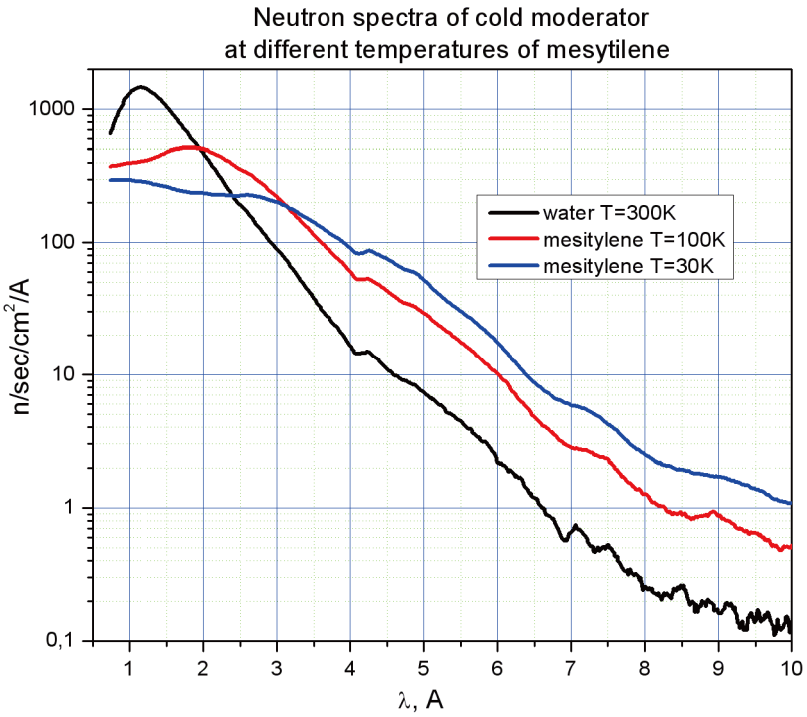

Figure 4. Neutron spectra obtained from the surface of the cryogenic moderator.

The main results, obtained by using of system:

- neutron spectra of cryogenic moderator
- gain-factor of cold neutrons is about 10-12
- 2D images of moderator's chamber
- control of filling and draining of chamber.

Acknowledgements

The authors acknowledge the assistance of the following people who have contributed to this work: Yu. V. Nikitenko.

References

[1] S. Kulikov, E. Shabalin. Complex of neutron moderators for the IBR-2M reactor. In: Proceedings of 17th Meeting of the International Collaboration on Advanced Neutron Sources, ICANS-XVII. April 25-29, 2005. Santa Fe, New Mexico.

[2] E.P. Shabalin et al., Pelletized Cold Neutron Moderators for the IBR-2M reactor. In: Proc. of the 6th International Workshop on UCN&CN Physics and Sources, S.- Petersburg-Moscow, 1-7 July 2007: http://cns.pnpi.spb.ru/ucn/articles/Shabalin.pdf.

[3] Janos Fuzi. Direct measurement of cold neutron moderator spectra. Nuclear Instruments and Methods in Physics Research A 586 (2008) 41-45.

[4] A. V. Belushkin, A. A. Bogdzel, V. V. Zhuravlev, S. A. Kutuzov, F. V. Levchanovski, E. I. Litvinenko, Li Yong Jai, Ts. Ts. Panteleev, V. I. Prikhod'ko, A. N. Chernikov, A.V. Churakov, et al. Development of gas-filled position-sensitive detectors of thermal neutrons at the Frank Laboratory of Neutron Physics of the Joint Institute for Nuclear Research. Physics of the Solid State, ISSN:1063-7834, eISSN:1090-6460, 52, 5, 1025- 1028, 2010.

[5] F.V. Levchanovsky, E.I. Litvinenko, A.S. Nikiforov, B. Gebauer, Ch. Schulz, Th. Wilpert. Software modules of DAQ PCI board (DeLiDAQ) for position-sensitive MWPC detectors with delay line readout. Nucl. Nuclear Instruments and Methods A 569 (2006) 900-904.

[6] V. Ananiev, A. Belyakov, M. Bulavin, E. Kulagin, S. Kulikov, K. Mukhin, T. Petukhova, A. Sirotin, D. Shabalin, E. Shabalin, V. Shirokov, A. Verhoglyadov. The world's first pelletized cold neutron moderator at a neutron scattering facility. Nuclear Instruments and Methods in Physics Research B 320 (2014) 70-74.

3-11. Safety and Operation for High Power Facilities

This is a blank page.

3.11.1

Safety Measures for the Operation of the Materials and Life Science Experimental Facility (MLF) of J-PARC - Restart of MLF Operation from the Radioactive Material Leak Incident at the Hadron Experimental Facility-

Yoshimi Kasugai

Radiation Safety Section, J-PARC Center

kasugai.yoshimi@jaea.go.jp

Abstract. The radioactive material leak incident at the Hadron Experimental Facility (HD) in J-PARC on May 23, 2013, is briefly introduced. After the incident, the framework of safety management and emergency response in J-PARC was reconstructed. As one of the main items of the change, introduction of an "Alert" status is described. In addition the resuming process of the operation of the Materials and Life Science Experimental Facility (MLF) is mentioned.

1. Introduction

On May 23, 2013, a radioactivity leak incident occurred at the Hadron Experimental Facility (HD). [1] The incident caused internal exposures of users and staff, and radioactive release to the environment outside the site boundary. In addition, reporting the incident to the authorities concerned was delayed significantly, although the event should have been reported to the relevant authorities because of deviation from legal regulation. We, J-PARC, were criticized seriously and lost public trust. For the reasons, we had to stop the operation of all J-PARC facilities[1], including the Materials and Life Science Experimental Facility (MLF), indefinitely just after the reporting on the incident.

For resume of the operation, the relevant authorities urged us to confirm the soundness of facilities in terms of radioactivity confinement and to reform the safety organization to enable quick and adequate response to abnormal incidents. The results of confirmation and the reformation plan were to be reviewed by an external expert panel organized for review of the incident. In addition, for recover of the public trust, briefing sessions for neighborhood inhabitant of J-PARC were held several times. After having tough days for 8 months, the beam operation for the MLF user program could start on February 17, 2014.[2]

In this report, we briefly describe the HD incident and the resuming process of the MLF operation. In addition, the design concept of the radiation safety measures of MLF, which is requested to explain at the external expert panel, is described.

[1] The "all J-PARC" includes the accelerator, the Materials and Life Science Experimental Facility (MLF), the Hadron Experimental Facility (HD) and the Neutrino Experimental Facility (NU). The accelerator consists of a 400 MeV Linac, a 3 GeV Synchrotron and a 50 GeV Synchrotron for protons.

[2] The beam operation of NU also started on May 26, 2014. As for HD, since reformation of the ventilation system and the whole target system were required, the beam operation will be started later.

The outline of the HD incident is described in the next section, and how we reconstructed safety policy for resuming the J-PARC beam operation is shown in section 3. In section 4, the design concept of radiation protection measures in MLF are presented.

2. Outline of the incident of the Hadron Experimental Facility

In HD, beams of secondary particles such as K and π mesons were produced by bombarding a gold target with 30 GeV protons provided from the 50 GeV Synchrotron (MR).[3] The proton beam was provided by the slow extraction[4] method: in the normal operation 3×10^{13} protons are slowly extracted over 2 sec.

The user operation was going well until just before noon on May 23, 2013. At 11:55 a.m., an abnormally-short proton beam of 5 ms duration was bombarded to the hadron target because of a malfunction of the slow beam extraction system. At the incident, 2×10^{13} protons which are 2/3 of normal case were suddenly extracted in 5 ms. On that occasion, the gold target was partially melted owing to very high instantaneous heat input, although the beam operation to HD was stopped by interlock system.[5] Consequently, radioactive materials generated and accumulated in the gold target were released to the experimental hall of HD because the target was not hermetically shielded and confinement capability of primary proton beam line was not sufficient. For the radioactive contamination of HD hall, the gamma-ray radiation monitors in the experimental hall showed an increase to ~4 μSv/h at a maximum, and the staff and users in the experimental hall inhaled the airborne radioactivity.[6]

In this stage, the radiation monitors in the hall showed that radioactive products originated from the hadron target were entirely spread to the hall. However, the data and information were not collected and analyzed properly, and nobody recognized what was really happening until the late afternoon.

Furthermore, ventilation fans[7] equipped on the walls of the hadron hall were turned on to validate the monitor values, and the radioactive products in the hall were released to the environment outside of the radiation controlled area.

The Regulation Law of Japan requested us to report incidents on radiation matters such as radioactivity leakage to the environment and unexpected exposures of radiation workers, etc. In the J-PARC, the incident was not considered to report at the primary stage because the radioactivity leakage was considered only within the radiation controlled area.

On the next day of May 24, some of the experimenters who worked at the hadron hall at the time of the incident were inspected with a whole body counter for internal exposure. As the results, it was found that they received significant internal exposure up to 1.7 mSv. In addition, the Nuclear Fuel Engineering Laboratories of JAEA, which locates next to the J-PARC site, inquired on increase of radiation levels in their monitoring posts at the time of ventilation fan operation. The data log of the area monitors of J-PARC also proved to indicate leak of radioactivity to outside of the controlled area of HD. On the basis of these facts, J-PARC sent reporting to the relevant authorities on this incident at 10 p.m. on May 24; one and half days had passed since the primary incident occurred on May 23. Due to the considerable delay of reporting, the public trust to J-PARC was degraded seriously.

---

[3] The 50-GeV synchrotron was being operated with acceleration energy of 30 GeV at the incident.

[4] On the other hand, the proton beam was provided to NU by the fast extraction.

[5] The J-PARC interlock system consists of MPS (Machine Protection System) and PPS (Personnel Protection System). On the incident, the MPS stop the beam operation with alerting to proton beam loss and overvoltage of the electrical power supply for the extraction magnet system.

[6] The total number of personnel working in the radiation controlled area of HD during the incident was 102. As a result of the measurements with a whole-body counter, it was found that 34 personnel received detectable internal exposure in the range of 0.1-1.7 mSv.

[7] The “ventilation fun” is just a fan without filtering function for radioactive material. Ventilation system with filtering function had not been equipped in the hadron hall because this area was assigned as an uncontaminated controlled area.

Just after the reporting, the beam operation of all J-PARC facilities, including MLF, stopped indefinitely.

3. Reconstruction of J-PARC safety organization and the MLF management

After the incident, the minister of MEXT (Ministry of Education, Culture, Sports, Science and Technology) requested us to inspect the soundness of facilities in terms of radioactivity confinement and to reform the safety organization to respond to abnormal incidents quickly and adequately. We made serious effort to confirm the radiation safety of all facilities other than HD, and to establish a new system for emergency response to an abnormal incident.

The problem of the HD incident was 1) occurrence of the incident, and 2) improper emergency response to the incident. The aim of the reformation of the safety organization was to eliminate the problems. Three issues, a) unclear responsibility and command line, b) insufficient review capability for possible risks, and c) unclear criterion for judgement and actions, were traced to essential ones for suppression of recurrence of similar incidents. The J-PARC safety organization was reformed on the concept. In addition, cultivation of safety culture and drills for emergency situation was also important to support the organization. Various activities and drills were conducted for the purposes.

The result of inspection for the radioactivity confinement of the MLF is described in the next section. In this section, the new emergency-response system is presented in the following.

Before the HD incident, J-PARC had only one status for response to a serious accident, called “Emergency status”. We learned from the HD incident that we should have an intermediate status to respond to incident which may be abnormal but is not an apparent accident. In such situation, we learned that the important is systematic actions to collect and analyse the information. We introduced such one and call it as “Alert status”. The conceptual drawing of the structure of three kinds of risk-management statuses, “Normal”, “Alert” and “Emergency” is shown in Fig. 1.

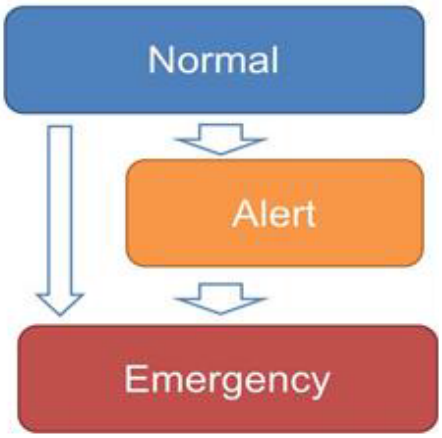

Figure 1. The conceptual structure of the new risk management system of J-PARC.

The normal status is one for normal cases and/or minor troubles which can be solved by actions within a division or a section. In the normal status, a shift leader[8] makes a decision to transition to the “Alert” status when the specified incidents related to the interlock system for personnel protection or the radiation monitors and so on.

If the high risk or rare interlock arises and radiation behaves abnormally, the situation needs systematic actions over sections and divisions to know what is happening. In the “Alert” status, the

[8] Shift teams, consisting of a shift leader and shift staff, are present at the central control room and the MLF control room during the beam operation.

facility manager or its deputy manager declares the situation, and they are responsible for collecting information and analysis of the incident together with the facility staff.

If they find that the incident is developing or may develop to a real accident, he declares transition to the "Emergency" status. In some cases such as fire or an undoubtable real accident, the shift leader has to make direct transition from "Normal" to "Emergency" status. In the emergency status, the emergency head quarter is set up at the Tokai site to report immediately to the relevant authorities and the neighboring local governments.

The new framework of the emergency response was reviewed at the external panel and explained at the briefing sessions for neighbourhood inhabitant.

In order to put into practice the policy change and to introduce that to the facility management, all operation-and-user manuals were fully revised. In addition, emergency drills were conducted several times on the basis of new safety framework in MLF.[9] The first drill was carried out on September 13, and the second one was done on November 15, 2013.[10] All MLF staff, including CROSS[11] and users, participated in the drill. The outline of the drill scenario was as follows:

- Radioactive gas products are detected during the beam operation by the radioactivity monitors in the hot cell where the circulation system of mercury which contain a huge amount of radioactivity has been installed,
- Declaration of transition to "Alert" status by a shift leader,
- Collecting and analysis of radiation monitoring data and other information under the direction of the facility manager of MLF,
- Recognizing the mercury leak from the mercury circulation system,
- Declaration of transition to "Emergency" status by the MLF manager,
- User evacuation and the radiological survey of their bodies,
- Taking measures to stop the mercury leakage,
- Reporting to the proper authorities.

The drills were accomplished without major problems, and all staff could understand the new system through the drills. We could restart, with confidence, the user operation of MLF on February 17, 2014.

4. Safety measures of MLF

Finally, in this section, we describe the radioactivity-confinement capability of MLF, which is what we explain to the relevant authorities and the external expert panel after the HD incident to show the soundness of MLF for safety.

The schematic drawing of the multilayer system for radioactivity confinement of MLF is shown in Fig. 2. The mercury target has a double wall structure: the mercury container is covered by the safety hull which has channels of primary cooling water. Then even if the mercury container is ruptured because of the pressure wave generated by proton beam impingement, radioactive mercury spills can be contained in the target vessel.[12] In addition, the helium vessel and the confinement of the neutron-target station also work as barriers for radioactive products release.

---

[9] Prior to the emergency drills, the education on the new emergency-response framework was conducted for all staff.

[10] The second drill on November 23 was positioned as one of the final tests for restart of MLF operation. Therefore the performance was inspected by the surrounding local government.

[11] "CROSS" is the Comprehensive Research Organization for Science and Society, which was established to promote the public access to the neutron beam facility.

[12] The leak monitors of resistance wires are set in the intermediate layer in order to detect the leaked mercury. The leak monitors are connected to the interlock system. In addition, the radioactive materials in the intermediate layer are always monitored by the radioactivity monitoring system: the detail of the monitoring system was presented in the ICANS-XIX held on March 8-12, 2010. See the reference in the following: Y. Kasugai, K. Ohtsu and T. Kai, "Monitoring System of Mercury Target Failure Using Radioactivity Measurement", Proceedings of ICANS-XIX (2010).

Therefore we could clearly respond to the question on radioactivity confinement as follows: MLF has an inherent safety system for preventing release of radioactivity generated in the targets even in abnormal incidents. The targets have been set in a multilayer structure with confinement capability of radioactivity.

On the other hand, the mercury circulation located on the hot cell is a single-barrier system: the piping wall of the mercury circulation system is just of a single barrier. We presume that there is very low possibility for leakage from the piping on the basis of the data on corrosion between flowing mercury and stainless steel as the piping material. Nevertheless radioactive materials in the hot cell are always monitored during the proton-beam operation in order to detect a small leakage of radioactivity and to take measures to stop leakage as soon as possible if the leak of radioactivity is detected. Even if the leakage occurs in the hot cell by any chance, the hot cell can be isolated from the external environment by stopping the ventilation and closing the air valves equipped in the ventilation duct.

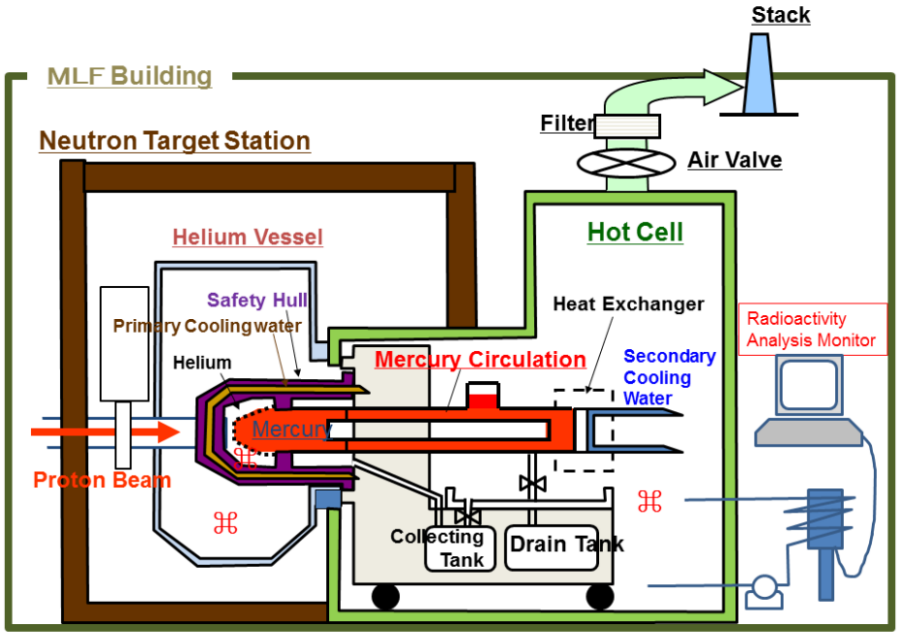

Figure 2. Schematic drawing of the multilayer system for radioactivity confinement of the neutron target at MLF. The leakage of the radioactive materials originated from the mercury for neutron production is monitored at the helium layer in the mercury target, the helium vessel and in the hot cell. (The monitoring positions are shown with ⌘ in the figure.)

5. Summary

The HD incident on May 23, 2013 and the reconstruction of the J-PARC safety management system were reviewed, and the radioactivity-confinement capability of MLF was explained.

After the incident, all J-PARC staff and users began to carry the safety card shown in Fig. 3 with them. We always keep the slogan “Science with Safety” in mind.

Figure 3. J-PARC Safety card. On the back side of the card, the emergency- call numbers and the map on the evacuation assembly spot are given.

References

[1] The detailed information on the HD incident can be found on the J-PARC web site. The address of the Japanese page is http://j-parc/jp/index.html and that of the English page is http://j-para.jp/index-e.html

3.11.2

J-PARC cryogenic hydrogen system improvement for stable long-lasting operation

Hideki Tatsumoto[1], Kiichi Ohtsu[1], Tomokazu Aso[1], Yoshihiko Kawakami[1]

J-PARC Center, JAEA, Tokai, Ibaraki 319-1195, Japan.

E-mail: tatumoto@post.j-parc.jp

Abstract. The J-PARC cryogenic hydrogen system provides cryogenic hydrogen at a supercritical pressure of 1.5 MPa, whose temperature is less than 20 K, to three moderators so as to produce pulsed cold neutron beam with superior neutronic performance. The nuclear heating is estimated to be 3.75 kW at the moderators for a 1-MW proton beam operation. The heat load added to the hydrogen system is removed through a heat exchanger by a helium refrigerator with a refrigeration power of 6.45 kW at 16.5 K. Although the proton beam power has gradually increased up to 300 kW since April 2008, long-lasting stable operation of the helium refrigerator had never been conducted because of the performance degradation of the heat exchanger until 2010. It was clarified that the performance degradation was caused by impurities such as moisture and nitrogen adsorbed on an activated charcoal located downstream of the compressor. In 2011, we prepared a purification system, which consisted of a cryogenic adsorber, a dryer filled with zeolite and a heater for regeneration, and impurity detectors. As a result, long-lasting stable operation has been successfully achieved for 95 days.

1. Introduction

At the J-PARC spallation neutron source, high-energy MeV-order neutrons generated from a mercury target are reduced to an appropriate energy level (meV order) in three types of hydrogen moderators (i.e., coupled, decoupled, and poisoned). Fig. 1 shows a schematic of the J-PARC cryogenic hydrogen system, which provides supercritical cryogenic hydrogen to the moderators at a supercritical pressure of 1.5 MPa and temperature of 18 K and removes 3.8 kW of nuclear heating for the 1-MW proton beam operation [1]. The temperature rise is estimated to be 2.4 K at a circulation flow rate of 0.19 kg/s. It is cooled by a helium refrigerator with a refrigeration power of 6.45 kW at 15.6 K [2]. There was a concern that a slight temperature rise would lead to a large pressure increase in the hydrogen loop because the supercritical hydrogen behaves as an incompressible fluid. We prepared a heater for thermal compensation and an accumulator, with a bellows structure, for volume control so as to mitigate the pressure fluctuation (caused by turning the proton beam on and off) below the allowable pressure of 0.1 MPa [3]. An ortho–para hydrogen converter was prepared to provide para-hydrogen concentration of more than 99% to the moderators [4].

The cryogenic hydrogen system has been operated since May 2008 [1] when the proton beam power was 40 kW. The proton beam power gradually increased up to 120 kW until 2010. However, we had a problem of unstable helium refrigerator operation caused by impurities. Long-lasting stable operation of the helium refrigerator has never been conducted because of the performance degradation of the heat exchanger. We prepared a purification system, which consisted of a cryogenic adsorber, a

dryer filled with zeolite and a heater for regeneration, and impurity detectors, to effectively remove the impurities in the helium refrigerator.

In this paper, we describe the problem of the unstable helium refrigerator operation and the purification system introduced to mitigate the problem.

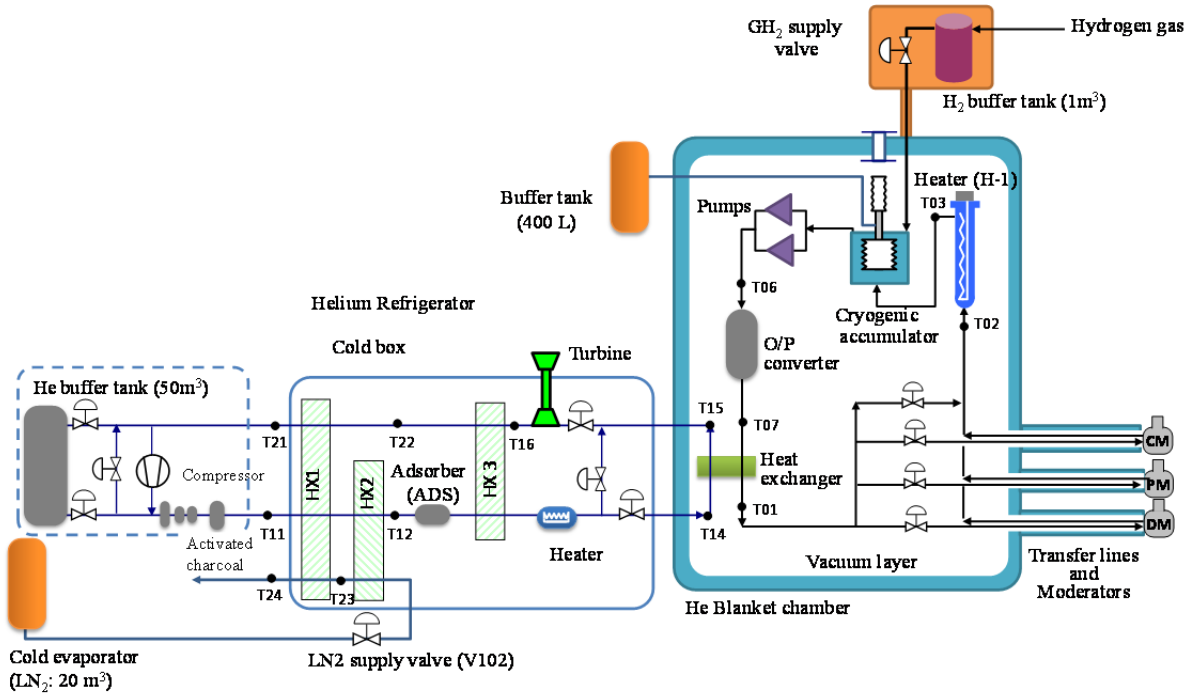

Figure 1. Schematic of the J-PARC cryogenic hydrogen system.

2. Helium refrigerator

An oil-lubricated screw compressor compresses helium with a mass flow rate of 290 g/s from 0.3 to 1.68 MPa. The rated shaft power is 690 kW. The high-pressure stream enters the cold box with a mass flow rate of 275 g/s and is cooled to approximately 80 K through the plate-fin heat exchangers (HXs) HX1 and HX2, where liquid nitrogen is used for precooling. The liquid nitrogen consumption is estimated to be 22 g/s. The feed gas passed through HX1 and HX2 is routed to an 80 K adsorber (ADS), filled with activated charcoals, where the trace amounts of nitrogen are mainly removed. The high-pressure helium temperature passing through HX3 is controlled at 17 K by an 8-kW heater. We had confirmed through a commissioning process, which was performed within a week, that the helium refrigerator met our requirements.

3. Unstable helium refrigerator operations

3.1. Helium refrigerator operation from 2008 to 2009

We tried to operate the cryogenic hydrogen system for more than two weeks for the first time in October 2009 (RUN #27), when the proton beam power was 40 kW. Fig. 2 shows the temperature behavior at the cold end of a heat exchanger in the high-pressure helium stream. The helium refrigerator was operated without liquid nitrogen precooling because the nuclear heating was only 150 W for the 40-kW proton beam power. Although the initial temperature was maintained at approximately 150 K, it gradually increased. After 18 operating days, the temperatures rapidly increased to 170 K.

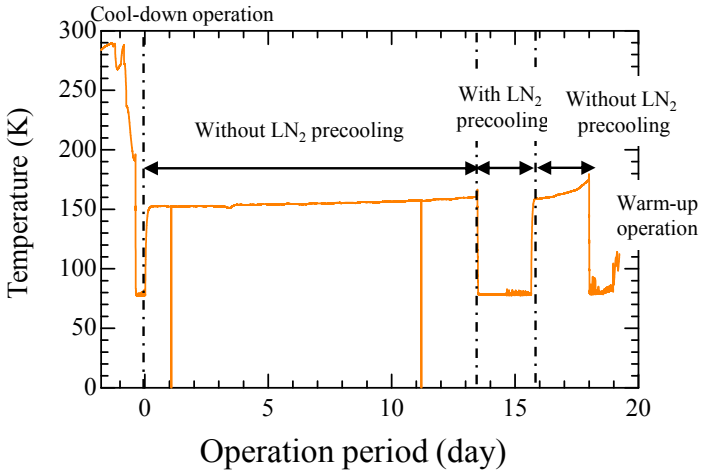

Figure 2. Temperature behavior at the cold end of a heat exchanger in the high-pressure stream.

Fig. 3 shows the pressure difference between the warm end of HX1 and the outlet of ADS. As the operation time increased, the pressure difference became higher. It was assumed that some impurities were accumulating on the surface of HX, and the heat exchange efficiency was deteriorating.

After warming up the helium refrigerator by supplying helium to the cold box, we measured dew points in the helium refrigerator. There was moisture with a dew point was –30 °C in HXs of the high-pressure helium stream, although the dew point before the operation was reduced to –70°C by a purification operation using ADS.

To conduct stable operation of the helium refrigerator, we tried to purge the moisture existing in HXs using a dry nitrogen gas with a dew point lower than –96 °C and reduced the dew point below –76 °C. Most of the nitrogen in HXs was evacuated, and the residual was reduced below 1.7 ppm using a cryogenic adsorber. Fig. 4 shows the temperature and pressure difference behaviors in RUN#28 after purification, when the proton beam power was 120 kW. The helium refrigerator was successfully operated for 43 days without any problem for the first time, although there was a temperature rise of a few Kelvin.

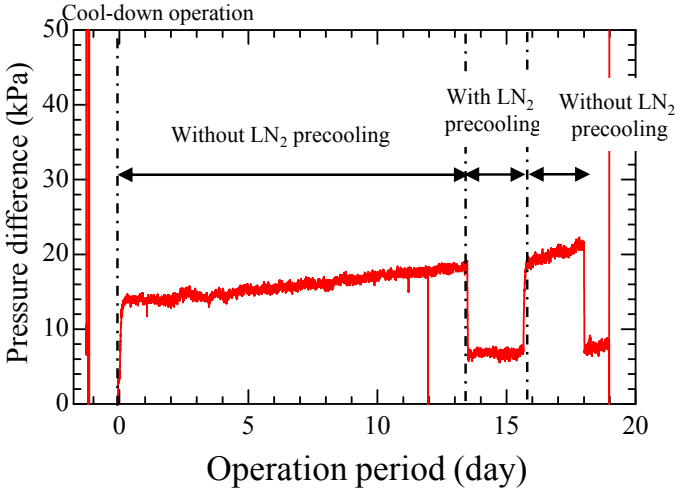

Figure 3. Pressure difference between HXs and ADS in the high-pressure stream.

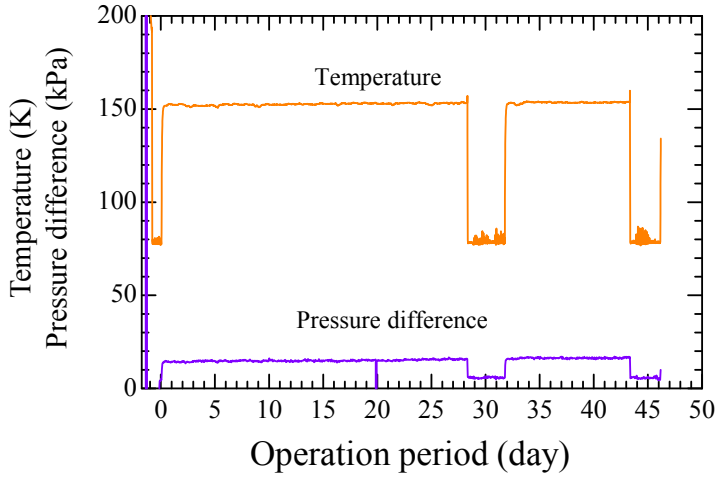

Figure 4. Temperature and pressure difference in RUN#28 after purification.

3.2. Helium refrigerator operation in 2010

For the first time, we exchanged the activated charcoal in the summer outage of 2010. The activated charcoal vessel is located downstream of the compressor and the packing weight is 350 kg. After the replacement, we evacuated the activated charcoal vessel below a few Pascal and performed a purification operation using the cryogenic adsorber for one week. We confirmed that the dew point in the helium stream was reduced to 1.8 ppm, which was lower than that for RUN#27.

Fig. 5 shows the behaviors of the helium refrigerator operated in October 2010 when the proton beam power was 120 kW. After the cool-down operation, we stopped using the liquid nitrogen precooling. The pressure difference through HXs gradually increased, and a rapid temperature rise appeared at the cold end of HXs after three days. We tried to cool the helium stream at HXs by providing liquid nitrogen because the continued operation of our cryogenic system was required. Although the pressure drop and temperature were temporarily reduced, the pressure drop continued to increase; the temperature was 20 K higher than that for normal operation and remained unstable. After nine days, the pressure difference increased to 120 kPa. As shown in Fig. 5(b), the helium temperature of the high-pressure stream at the cold end of HX2 and the nitrogen temperature at the warm end of HX2 rapidly increased up to 220 K, while the temperatures of the nitrogen and the low-pressure helium stream were reduced below 0 °C at the warm end of HX1. We considered that the rapid deterioration of the heat exchange capability of HX1 could be caused by the extraordinary deposition of impurities such as moisture on the surface of HX. Eventually, the pressure difference exceeded 500 kPa. We stopped the helium refrigerator operation for its protection and warmed it up by supplying helium gas into the vacuum chamber up to 30 kPa.

After the temperature of HXs increased to room temperature, we measured the dew point of the high-pressure helium stream in HX1 and HX2. A dew point of –20 °C was detected, although it was reduced below –72 °C, which was lower than that for the operation in 2009, before the cool-down operation. On the other hand, a dew point of –40 °C was detected in ADS. There was no moisture that had an unfavorable impact on the helium refrigerator operation except in HXs and ADS. Accordingly, it is assumed that the moisture desorbed from the activated charcoal would generate unstable helium refrigerator operation. Moisture in the high-pressure helium stream would be adsorbed on the surface of HX, whose temperature is normally maintained below 0 °C, by passing through HXs during the cryogenic operation. The purified helium stream results in promoting the desorption of moisture from the activated charcoal. We considered that this phenomenon was continuously repeated because large amounts of moisture would be adsorbed on the activated charcoal.

To resume the helium refrigerator operation, we needed to regenerate the activated charcoal using a hot dry nitrogen gas, which should be maintained below 100 °C because of the allowable temperatures

of the seal material and a filter in the activated charcoal vessel. We prepared a temporary heater to increase the temperature of the purge nitrogen gas.

Fig. 6 shows the regeneration operation of the activated charcoal, which was performed with a dry hot nitrogen gas with a supply temperature of approximately 90 °C and a dew point of –96 °C. The activated charcoal vessel was covered with a lagging material. The dew point was measured at the outlet of the activated charcoal. It took five days for the charcoal temperature to increase to 90 °C at a flow rate of 30 Nm^3/h, although the outlet temperature increased only to 72 °C. During the

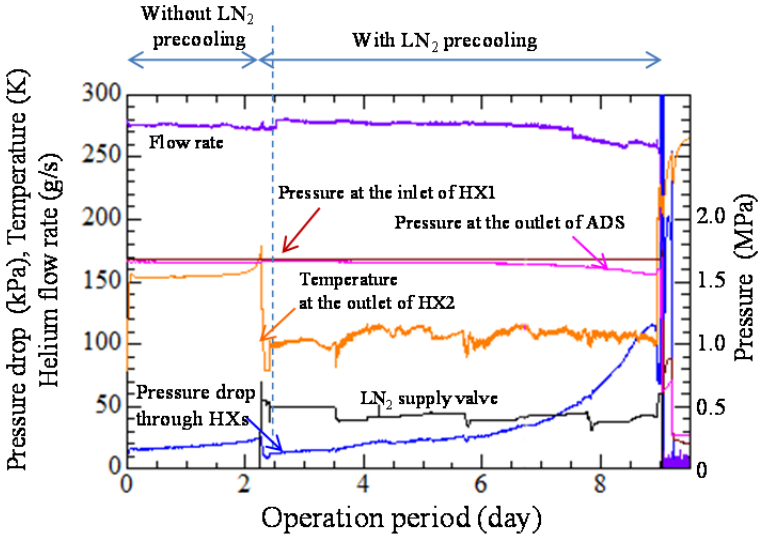

(a) Behaviors of the helium refrigerator over an entire run period.

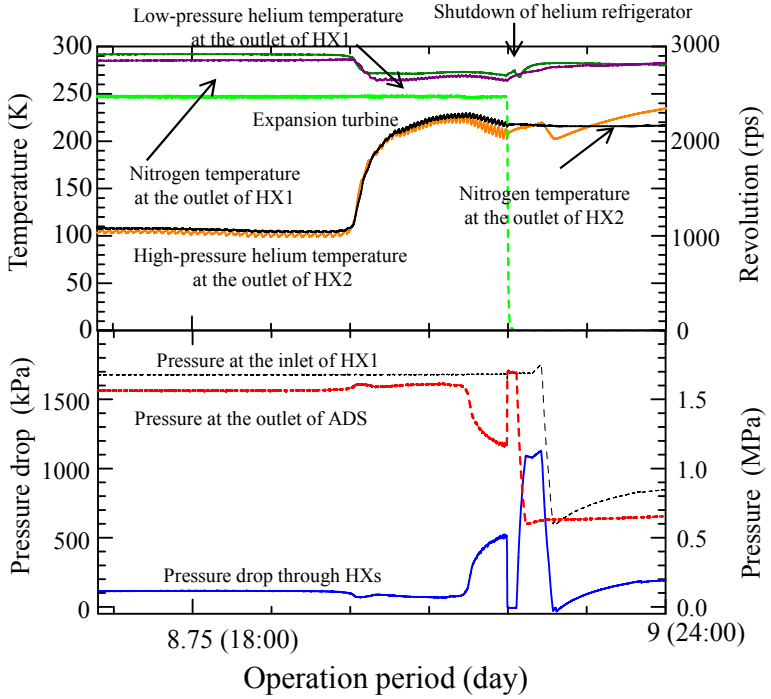

(b) Behaviors of temperature, pressure, and pressure difference at an anomalous occurrence.

Figure 5. Unstable operation of the helium refrigerator in October 2010.

regeneration, the purge nitrogen flowed upward with the effect of natural convection. With the increase in the activated charcoal temperature, the dew point temporarily increased from –68 °C to –50 °C during the early stage. Subsequently, it gradually decreased to –62 °C in 19 days. Furthermore, the dew point can be reduced to -74.5°C, with a decrease in the temperature from 90 °C to 10 °C. Most of the nitrogen in the activated charcoal vessel was removed by evacuating it three times, and the residual nitrogen was eventually removed using a cryogenic adsorber.

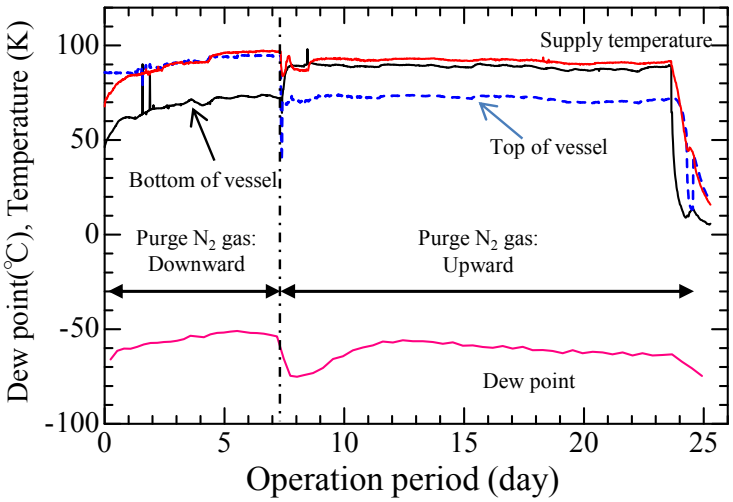

Figure 6. Regeneration operation of the activated charcoal in 2010.

On the other hand, ADS was also filled with activated charcoal and its packing weight was 26 kg. The moisture in ADS was removed by a dry nitrogen gas. The dew point can be reduced to –64 °C by purging ADS for one week.

Fig.7 shows the temperature at the cold end of HXs in the high-pressure helium stream and the pressure difference through HXs and ADS during cryogenic operation after the regeneration. Although it appears that the pressure drop through HXs increased slightly, the temperature at the cold end of HX was maintained nearly constant for one month. We could perform a stable one-month operation of the helium refrigerator.

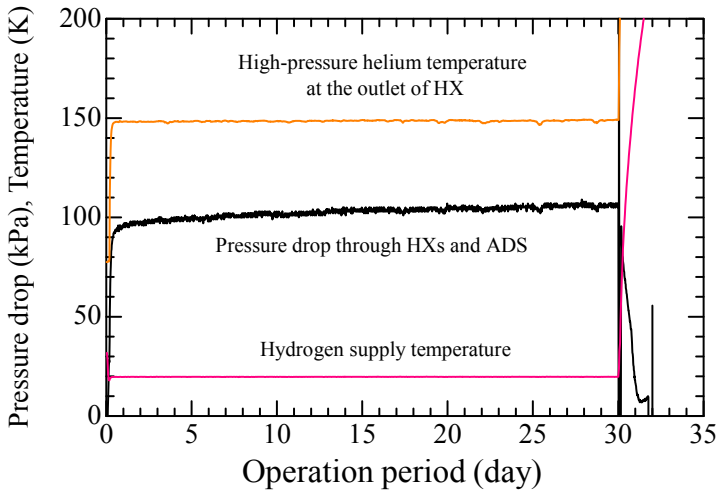

Figure 7. Temperature at HXs and pressure difference through HXs and ADS after the regeneration in 2010.

However, the pressure drop was considerably larger than the usual value, which was approximately 15 kPa. Before the cool-down operation, there was seat leakage through a turbine bypass valve (V103). Powders of the activated charcoal that came from ADS were found at the seat and the shaft of the valve. Furthermore, at the expansion turbine start-up, the expansion ratio became larger than the normal value, as shown in Fig.8. It was found in the summer of 2011 that the powders also existed at the filter at the inlet of the turbine. Therefore, we replaced damaged ADS with a new one. Fig. 9 shows the photograph of ADS that was removed from the cold box. It was found that the abnormal pressure difference, as shown in Fig. 8, was due to the powder of the activated charcoal that became trapped in the filter of ADS.

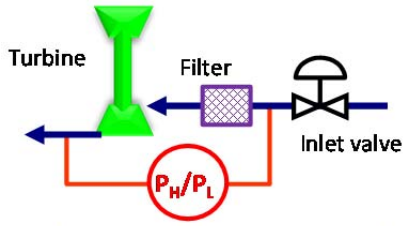

(a) Schematic of the expansion turbine unit.

(b) Photograph of the turbine inlet valve.

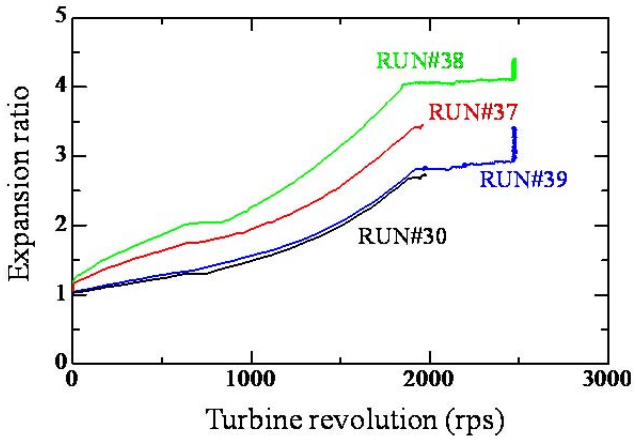

(c) Comparison of expansion ratio for each operation.

Figure 8. Expansion ratio of the turbine at the start-up.

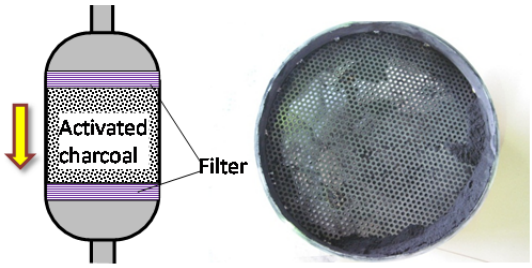

(a) Schematic of ADS.

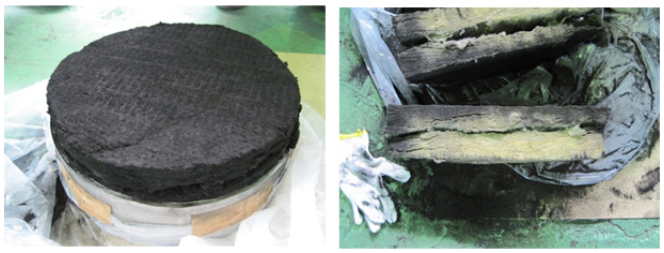

(b) Photographs of the powderized activated charcoal in ADS.

Figure 9. Damaged ADS of the helium refrigerator.

4. Improvement of the helium refrigerator

4.1. Purification system

Fig. 10 shows the purification system, which consists of a dryer, a cryogenic adsorber, a heater and gas analyzers. We prepared it to realize the stable operation of the helium refrigerator by removing impurities such as moisture and nitrogen. The dryer, which has a volume of 0.064 m^3 and is filled with zeolite, mainly removes moisture. The operating pressure is 1.58 MPa, which corresponds to the discharge pressure of the compressor. It was designed to be continuously operated at a flow rate of 100 Nm^3/h for 48 h under the following dew point conditions: –20 °C at the dryer inlet and below –70 °C at its outlet. After the purification operation, the dryer needs to be regenerated using a dry hot nitrogen

gas with a flow rate of 100 Nm^3/h and a temperature of 150 °C for a few hours. The dryer is evacuated below 10 Pa to reduce the nitrogen concentration below 20 ppm. Empirically, we confirmed that three cycles of evacuation reduced the nitrogen concentration in it below 20 ppm. It takes approximately 12 h to finish the regeneration process.

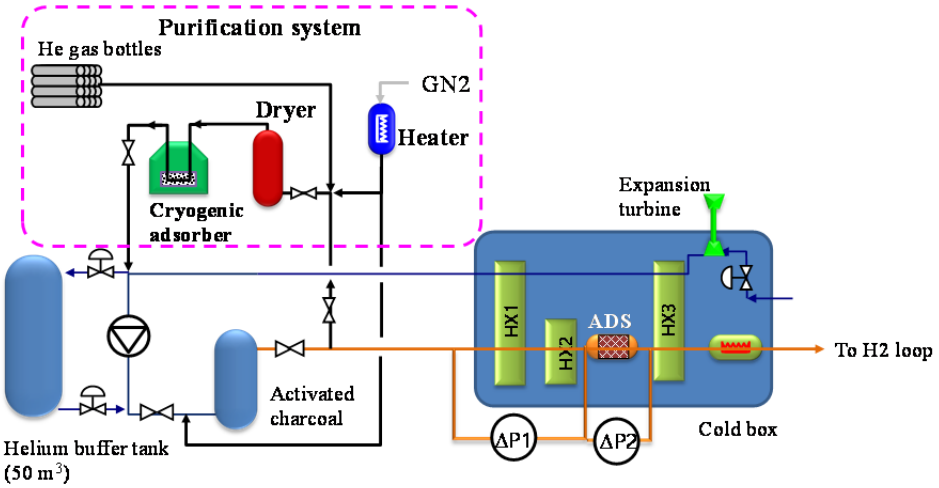

Figure 10. Schematic of the purification system.

A cryogenic adsorber, which is "MODEL HE" manufactured by Linde Cryogenics, was prepared to mainly remove the nitrogen component in the helium stream. Activated charcoal is used and cooled by liquid nitrogen. The allowable flow rate is 100 Nm^3/h. We always measure the nitrogen concentration at the outlet of the cryogenic adsorber using gas chromatography to confirm its performance degradation. We have empirically confirmed that the nitrogen concentration is always maintained below a measurable limit, even if the inlet nitrogen concentration is approximately 100 ppm after the regeneration of the dryer.

A 5-kW heater was prepared to effectively regenerate the dryer and the activated charcoal for the compressor using dry hot nitrogen gas from a cold evaporator with a volume of 20 m^3.

Furthermore, differential pressure transmitters are installed at HX1 and HX2 in the high-pressure helium stream and ADS to continuously monitor for an abnormal pressure difference increase through HXs and ADS.

4.2. Regeneration of the activated charcoal

We exchanged the activated charcoal in the summer maintenance of 2013 when the operating temperature limit of the filter and seal materials in the charcoal vessel was increased to 150 °C for the efficiency of the regeneration operation. Fig. 11 shows the behaviors of a dew point and temperature of the activated charcoal during the regeneration operation. Unlike that in 2010, the flow rate of the dry nitrogen gas passing through the charcoal vessel can increase to 100 Nm^3/h and the temperature required for the regeneration can also increase to more than 100 °C. The initial dew point was –83 °C at the outlet of the charcoal vessel. Although the dew point temporarily increased to –28 °C with the increase in the regeneration temperature, it gradually decreased to –61 °C within 17 days. Furthermore, with the decrease in the charcoal temperature down to 50 °C, the dew point decreased to –93 °C. We confirmed that the regeneration had been operated effectively and the period of the regeneration can be shortened by 30% compared with that in 2010.

4.3. Purification operation

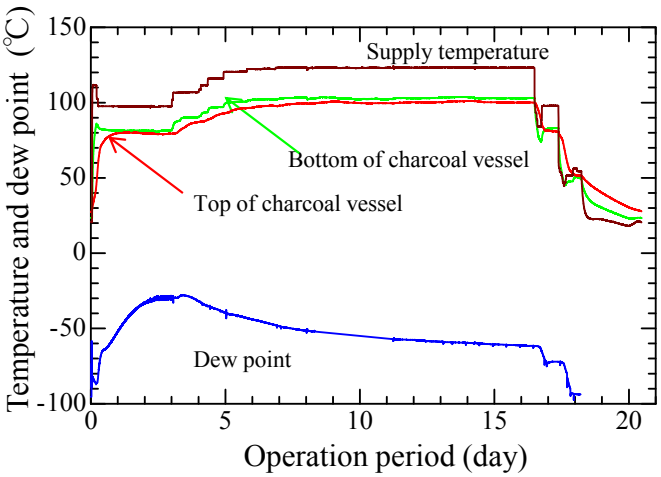

Figure 11. Behavior of a dew point and temperature of the activated charcoal during the regeneration operation.

The helium stream passes through the dryer and the cryogenic adsorber at a flow rate of 4.9 g/s (100 Nm^3/h), which corresponds to 5% of the main stream. Fig.12 provides one example of moisture and nitrogen in the helium stream during the purification operation. The dryer was regenerated using hot dry nitrogen gas every 48 h, even without performance deterioration. The cryogenic adsorber is regenerated when an increasing trend in the amount of nitrogen appears. The adsorber vessel is warmed to room temperature using warmed nitrogen gas and is evacuated below 10 Pa. We confirmed that the nitrogen and moisture can be reduced below 0.1 ppm and –85 °C within one week, although this depends on initial concentrations.

The complement of helium gas is supplied to the suction side of the compressor at 0.2 MPa, passing through the dryer and the cryogenic adsorber. We use helium gas bottles with a “four nines” grade. We confirmed that the nitrogen concentration is always maintained at the outlet of the cryogenic adsorber below measureable limits by gas chromatography.

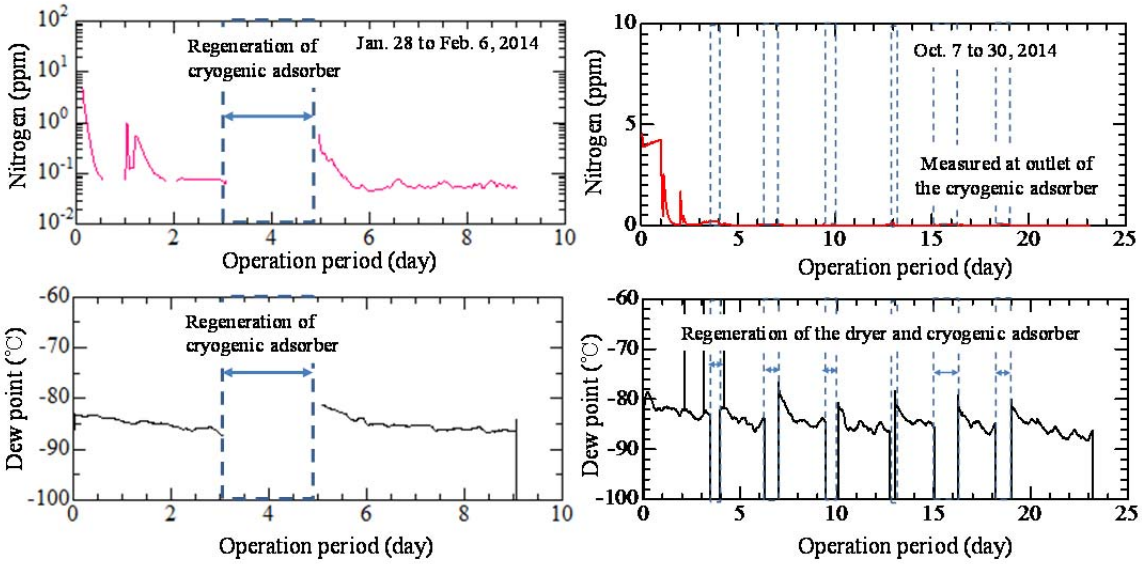

(a) January 28 to February 6, 2014. (b) October 7 to 30, 2014.

Figure 12. Purification operation.

4.4. Stable operation of the helium refrigerator

Fig. 13 shows the behaviors of temperature and pressure difference around HXs during cryogenic operation. The helium flow rate through the cold box is 273 g/s. The initial concentrations of moisture and nitrogen were reduced below 1.0 ppm, which corresponds to the dew point of –76 °C and 0.2 ppm,

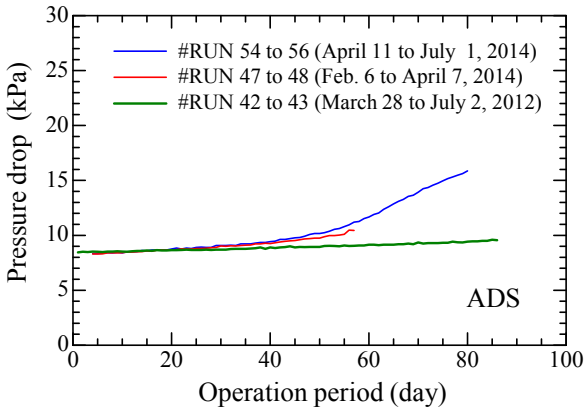

(a) Pressure drop through ADS.

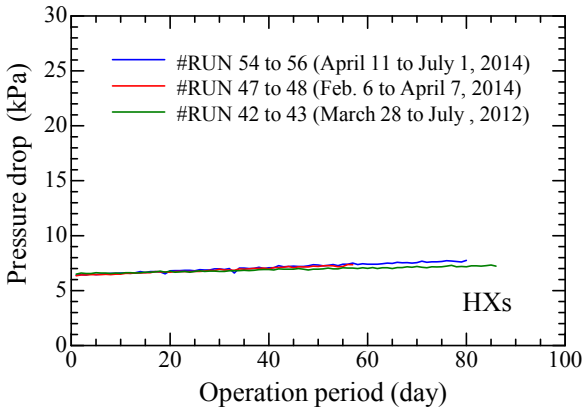

(b) Pressure drop through HXs.

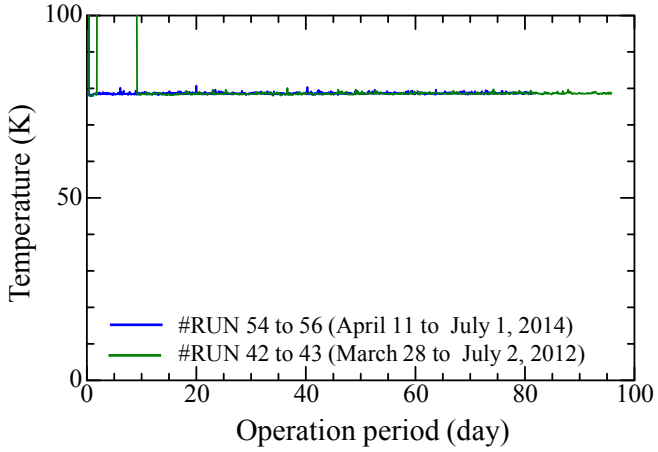

(c) Temperature at the cold end of HX in the high-pressure helium stream.

Figure 13. Behaviors of temperature and pressure drops during cryogenic operation.

respectively, by the purification operation. Although the increase in the pressure drop through ADS becomes larger compared with that for HX, they are approximately 7.5 kPa at a maximum for 80 days of operation. Fig. 14 shows the desorbed impurities in ADS during the warm-up process of the helium refrigerator. We take a sample of the gas from ADS at 0.6 MPa at each temperature. A remarkable desorption of nitrogen appears in the vicinity of 120 K. The desorbed nitrogen increases to 626 ppm in ADS at room temperature. The increase in the pressure drop through ADS is assumed to be mainly due to nitrogen adsorbed on ADS. On the other hand, the increases in pressure difference of HXs are lower than 1.35 kPa for 80 days of operation, and they are considerably smaller than those for the operation until 2010. Fig. 15 shows the impurities desorbed from the surface of HX during the warm-up operation. It appears that nitrogen, oxygen, and hydrogen have relatively little impact on the increase in the pressure drop of HX. However, the dew point rapidly becomes lower above 280 K. We stopped the measurement of the dew point because it exceeded –20 °C. It was found that the moisture is mainly adsorbed on the surface of HXs. The temperature downstream of HX can be maintained at approximately 78 K. The slight fluctuation is affected by the behavior of the liquid nitrogen supply valve. The impurity can be reduced effectively by introducing the purification system and we can

conduct a stable three-month long-lasting operation of the helium refrigerator without any problem. In future, we will attempt a more long-lasting operation of the helium refrigerator toward the achievement of a stable 1-MW proton beam operation.

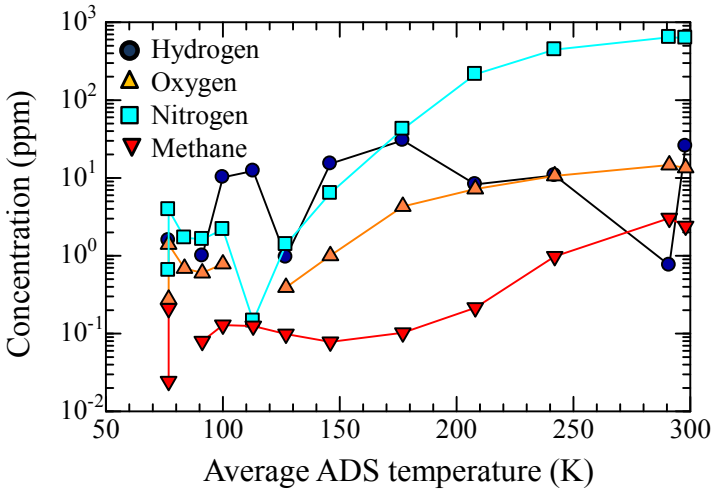

Figure 14. Desorbed impurities in ADS during the warm-up process.

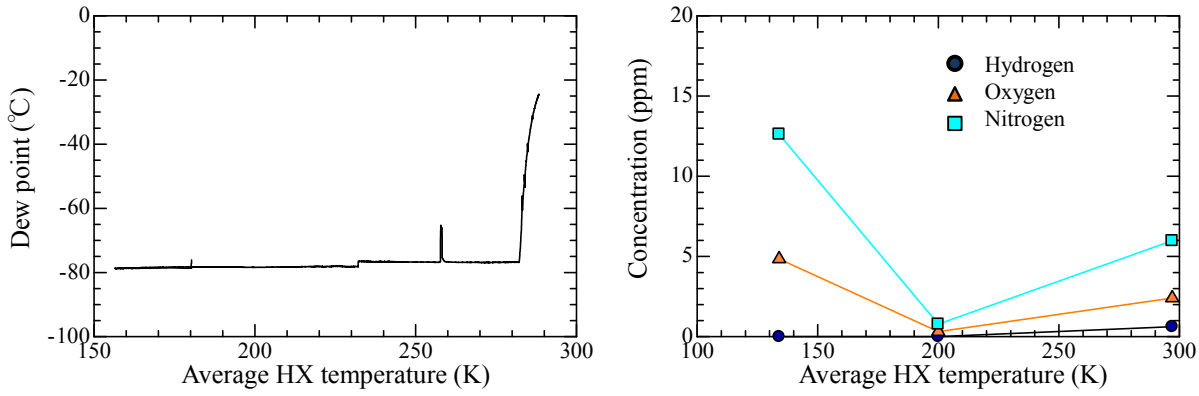

(a) Moisture (b) H_2, O_2 and N_2

Figure 15. Impurities desorbed from the surface of HX during the warm-up operation.

5. Conclusions

It had been impossible to conduct stable long-lasting operation of the helium refrigerator until 2010. We found that the cause of instability was mainly due to moisture that adsorbed on the surface of the activated charcoal downstream of the compressor.

A purification system, which consisted of a dryer, a cryogenic adsorber and a heater for regeneration, was installed in 2011. We have established a method for purifying the helium refrigerator. We successfully performed a three-month long-lasting stable operation of the helium refrigerator without any problems.

Acknowledgments
The authors thank Mr. Uehara, Mr. Sakurayama, and the operator team for the J-PARC cryogenic hydrogen system for supporting the helium refrigerator operation.

References

[1] Tatsumoto H, Aso T, Ohtsu K, Uehara T, Sakurayama H, Kawakami Y, Kato T and Futakawa M, *Advances in Cryogenic Engineering* 55A, Melville, New York, 2010, pp.297-304.
[2] Tatsumoto H, Aso T, Kato T, Ohtsu K, Hasegawa S, Maekawa F and Futakawa M, *Procof ICEC 22 and ICMC 2008* Korea 2008 pp. 711-716.
[3] Tatsumoto H, Aso T, Ohtsu K, Uehara T, Sakurayama H, Kawakami Y, Kato T and Futakawa M *Adv. in Cryo. Eng.* 57A 2012 pp.368-375
[4] Tatsumoto H, Ohtsu K, Aso T, Kawakami Y and Teshigawara M *Adv. in Cryo. Eng.* 59A 2014

3.11.3

Development of the Personnel Safety System for the ESS

Garry Trahern, Stuart Birch, Paul Wright, Annika Nordt, Linda Coney

European Spallation Source, P.O. Box 176, 221 00 Lund, SE

E-mail: garry.trahern@esss.se

Abstract. The 5 MW European Spallation Source (ESS), scheduled to begin operations in 2019, will be the brightest source of spallation neutrons as yet built. High-energy neutrons are produced when the 2 GeV proton beam from the ~600 m long linear accelerator interacts with a rotating tungsten target wheel contained within the target monolith. These fast neutrons are slowed down by the target moderators and reflector systems to suitable energies for experiments and then delivered to over 20 different instruments through beam ports. At such a facility, safe operations is of utmost importance, and, as such, requires the implementation of several layers of control and safety systems. At the ESS, a comprehensive control system will be implemented throughout the facility, including the accelerator, target, and neutron-scattering instruments. This integrated control system (ICS) will bring together all segments of the machine into a unified structure. The Personnel Safety System (PSS) is one of the core systems of ICS, along with the Machine Protection System (MPS) and timing system. The PSS is an active safety system that protects workers from radiation, both prompt and residual, stemming from operation of the proton accelerator. Protection is achieved by controlling access to restricted areas, interrupting beam operation upon the detection of non-nominal conditions, and generating alarms via area radiation monitors being interlocked to the proton beam source. The system is segmented to facilitate configuration control, support multiple operational modes, and address the specific needs of the accelerator, target, and instrument areas. This paper will describe the development of the PSS, including the definition of requirements, functional specification for each segment, and evaluation of interfaces with other ESS systems.

1. Integrated Control System Scope

The Integrated Control System (ICS) at ESS is the control system to monitor and control the proton Accelerator, Target Station Systems, Neutron Instruments and Conventional Facility infrastructures. ICS will be based on the EPICS control system framework. While the ICS itself is not a safety critical system, the ICS organization is also responsible for delivering to the facility not only the personnel safety systems (PSS) but also systems related to oxygen deficiency hazards (ODH) and area radiation monitoring interlocked to the beam (ARM), and these systems will be safety qualified.

To understand why ICS has been selected to develop the PSS at ESS some context for the decision is required. ESS is a green field laboratory whose purpose is neutron spallation based material research. The ESS, an accelerator driven neutron source with an average proton beam power of 5 MW is currently under construction in Lund, Sweden and is aiming to be the world's brightest neutron source by the end of the decade. First spallation neutrons should be available in late 2019. An organization being built literally from the ground up such as ESS cannot have the Environmental, Safety and Health (ESH) personnel in place from early on, providing either the technical requirements for personnel safety relative to prompt radiation or the technical means to implement a design to meet

such requirements. The ICS organization, on the other hand, will provide integrated control systems for the whole facility, and will have the technical means to implement systems ensuring safe access as well as providing the processes necessary to enforce safe practices during entry to the technical facilities such as the accelerator tunnel, target station systems and neutron instruments. Controls organizations such as at SNS, Oak Ridge Laboratory/USA have previously had this same responsibility so there is precedence for the ICS organization at ESS to provide the personnel safety systems. However, there are areas related to personnel and public safety for which ICS should not be responsible, and so a scope definition for ICS personnel safety systems is required.

The budget and schedule to deliver that scope will be proposed to ESS management in early 2015. A team is being hired composed of four engineers and technicians and ICS expects to have completed this recruitment by early 2015. Then the work of designing, manufacturing, installing and commissioning the PSS at ESS will proceed as quickly as possible given that these systems need to be in place very early during ESS installation and commissioning phases as well as at various test stands to be built on site.

2. Scope and Requirements for the Personnel Safety System

The scope of the personnel safety systems for ICS has been identified and approved and will cover the following systems:

- Accelerator personnel safety system.
- Accelerator oxygen depletion system.
- Accelerator radiation monitoring system.
- Accelerator Test Stand personnel safety system.
- Target personnel safety system.
- Target radiation monitoring system.
- Target maintenance cell personnel safety system.
- Neutron Instrument (LOKI) personnel safety system.
- Neutron Instrument (ODIN) personnel safety system.
- Neutron Instrument (NMX) personnel safety system.
- As soon as the initial design of new neutron instruments begins a new personnel safety system will be required. In total there will be 22 neutron instruments.

From the above list there are three critical areas within the facility, which will protect personnel from exposure to prompt radiation arising from operations of the proton accelerator and to protect from oxygen deficiency hazards and finally to generate beam inter-locked alarms from radiation that might exist in restricted technical areas of the facility.

3. PSS (Personnel Safety System related to access)

The ESS Personnel Safety System (PSS) will be designed, manufactured, installed and commissioned in accordance with IEC 61508 [1].

IEC 61508 is an international standard concerned with functional safety achieved by safety related systems that are primarily implemented in Electrical / Electronic and/or Programmable Electronic technologies (E/E/PE). The PSS is an example of this and falls within the scope of IEC 61508. This standard provides an overall safety lifecycle structure for functional safety systems as detailed in figure 1.

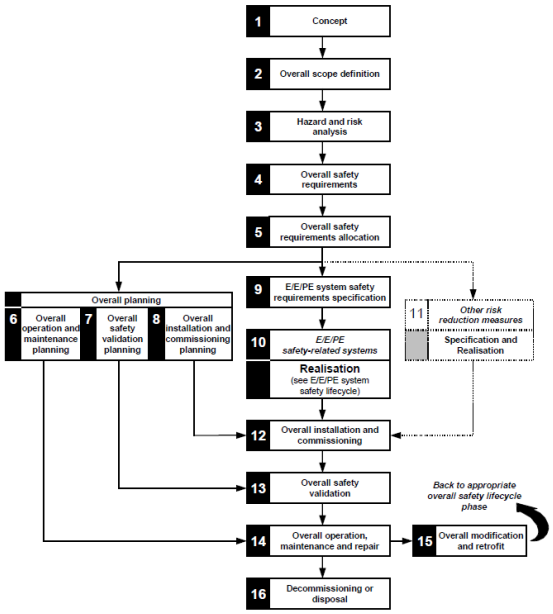

Figure 1. IEC 61508 Safety Lifecycle

To be able to complete the overall safety requirements, a Hazard and Risk Analysis must be undertaken for the ESS Accelerator, Target station and subsequent Neutron Instruments. This will be completed in conjunction with the personnel who are aware of all the hazards within each part of the facility.

A decision can then be made on the risks that the PSS will have to reduce, and a safety requirements allocation can be formulated.

To be able to calculate the safety integrity level (SIL) that the PSS will be designed to, all other risk reduction methods must be understood. Their level of risk reduction to the overall safety system can then be calculated. These external risk reduction methods could include but are not limited to:

- Human factors.
- Radiation shielding.
- External non-electrical signs.
- Training.

A detailed quantitative risk analysis using appropriate methods will be carried out, and this will enable the calculation of SIL's for each part of the PSS. The system will then be designed to the appropriate SIL.

The PSS is also governed by the Stral Sakerhets Myndigheten (SSM) (The Swedish Radiation Safety Authority) rules on ionizing radiation and will also operate within the ESS safety framework. The maximum tolerable risk level will be 10^{-6} or at H4 level in the SSM terminology.

The PSS design for the accelerator is in its infancy. Here are the basic principles of the system. The PSS system will be designed using Safety PLC's, Safety relays and also using a trapped key philosophy. The Safety PLC and hardware manufacturer has not yet been appointed.

The function of the ESS PSS is to prevent personnel remaining in or entering the Accelerator, Target or Neutron instruments when hazardous conditions exist. This will be achieved by means of physical searches supervised by a safety controller, access controlled by mechanical interlocks and the facility to request an ESS beam trip or exit the associated areas in the event that a potentially

hazardous situation arises. Accordingly, the PSS will be made up of 3 major sub-systems, which are described in more detail for the accelerator in the following:

Sub-System 1 (Safety Controller + I/O): A Safety Controller will monitor and control all safety related devices in and associated with the ESS Accelerator. The Safety Controller will facilitate and monitor the status of the accelerator search sequences. These searches ensure that no personnel remained in the areas of the accelerator tunnel or in other associated PSS controlled areas under search; and when complete the safety controller will release the trapped keys on the corresponding doors to allow locking of these doors. The Safety Controller will also monitor the safety devices and trigger a stop of beam operation if hazardous conditions exist and the access gates to the accelerator are opened. The Safety Controller will also provide information on system status and other visual/audio status indications. The Safety Controller will interface with the system via I/O Safety Modules.

Sub-System 2 (Trapped Key Units): A variety of trapped key devices will ensure that if hazardous conditions exist the gates which provide access into the PSS controlled areas and any protective removable shielding cannot be unlocked and various key-controlled permits cannot be issued.

Sub-System 3 (ESS Beam Trip): The system will provide a means for either authorised workers working in the tunnel or Sub-System 1 to request an ESS Beam Trip at any time. A permit is to be continuously issued from the PSS during normal operating conditions. Removing this permit constitutes requesting an ESS Beam Trip. An ESS Beam Trip will be requested if a Beam Off Button (BOB) is pressed or the Safety Controller issues an ESS Beam Trip signal.

There will be two main access entrances into the accelerator tunnel. Entrance 1 is at the front end near to the proton source. This will be the main access. Entrance 2 will be at the transition between the high beta elliptical cavities and the HEBT (see figure 3). Personnel will enter a PSS controlled area via an entry station. Each entry station will have two gates to ensure that personnel only enter the area when conditions are safe (a third door is provided for emergency egress only). A diagram of an entry station is shown in Figure 2. A swipe card system will be installed to ensure only authorised and fully trained staff can enter the tunnel.

A Public address system will also announce the status of the PSS system to personnel whilst in the tunnel.

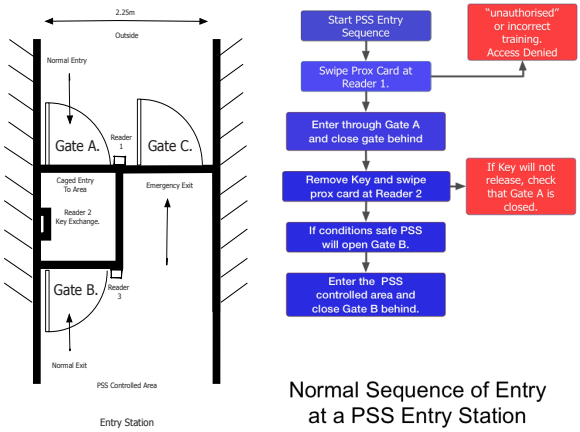

Figure 2. Entry Station

The accelerator will be divided into seven separate zones see figure 3 for the accelerator tunnel zones:

Table 1. Accelerator Tunnel Zones

Zone	Equipment in each zone	Zone Length (metres)
1	Proton source and low energy beam transport (LEBT), Radio frequency quadrupole (RFQ) and Medium energy beam transport (MEBT).	30
2	Drift tube linac (DTL).	23
3	Spoke Resonators	55
4	Medium energy Beta cavities	77
5	High energy Beta cavities	179
6	High energy beam transport (HEBT)	139
7	Accelerator to Target (A2T)	100

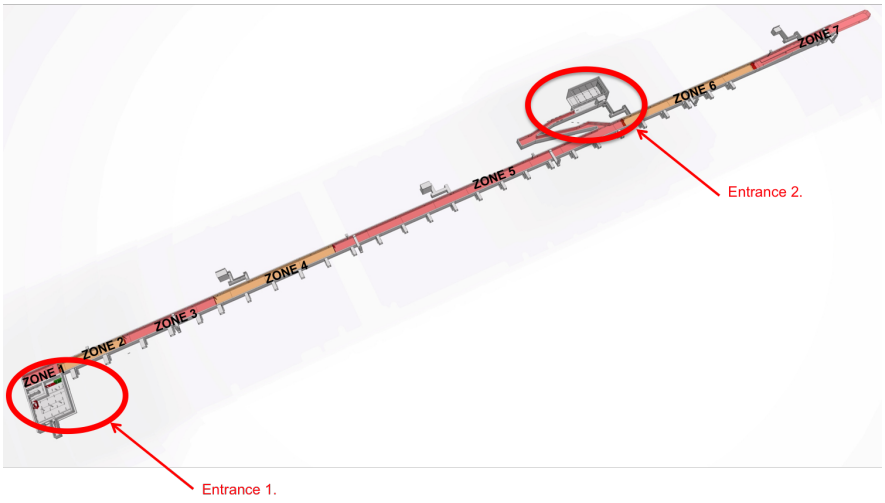

Figure 3. Accelerator Entrances and Tunnel Zones

A fenced gate will separate each of the seven zones allowing for independent search areas. Zones 1 to 4 will be searched from Entrance 1, and Zone's 5, 6 and 7 will be searched from Entrance 2. This will produce the most efficient way to service and search the tunnel.

Search and beam off stations will be placed between 10 and 20 metres apart along the full length of the tunnel.

4. Oxygen Deficiency Hazard (ODH)

The ESS will use superconducting technology for the majority of the LINAC sections in the accelerator. The cryogenic system will have a total inventory of approximately 2,000 kg of liquid helium in the accelerator tunnel at a temperature of 2 K. Such a large amount of helium inventory in the 600 m long tunnel could create a serious hazard to personnel in the event of a release. In order to mitigate these hazards a risk analysis will be performed to identify protective features including fixed alarms, emergency exhaust fans and special work control procedures for certain operations. The risk analysis will be part of the design lifecycle for a permanent mitigation system that will be designated the Oxygen Deficiency Hazard (ODH) system. While several systems will be required for the facility the following only addresses the system provided for the accelerator tunnel.

4.**1** *Design Lifecycle*

The ODH system will be provided by the Protection Systems group in ICS that is also responsible for the PSS. While both systems will be designated as safety critical systems there is a basic difference between the ODH system and the PSS. The PSS can terminate beam operation and RF production to totally eliminate the hazard arising from prompt radiation; the ODH system can only detect and mitigate the hazardous condition by alarming personnel and/or triggering a ventilation system. In this sense the ODH system is similar to fire and gas detection systems found in industry. The design lifecycle is similar to that used by the PSS, but the results of the risk assessment are used to identify mitigation strategies.

The results of the unmitigated risk assessment will be used to define work control processes, personnel protective equipment requirements and the ODH system risk reduction requirements including safety functions and reliability. When the design is complete, a mitigated risk assessment will be performed to ensure that risk reduction targets have been met, and the risks from the cryogenic systems are acceptable.

Excellent work has been performed at CERN, the European Organization for Nuclear Research, Geneva/Switzerland, in this area, and ESS intends to use their work as a basis for the analysis that will be performed at ESS.

4.2 *Tunnel ODH System*

Certain features are planned for the ODH system for the tunnel. Three basic functions are planned:

- Detection
- Area alarms
- Passive or active ventilation

The ODH system will be controlled by a logic solver that will tie together these functions and also provide information to operator displays.

4.2.1 *Detection*. Releases of inert gases are normally detected by monitoring the oxygen level inside the enclosure. A normal oxygen level is 20.9% by volume. Levels below 19.5% generally require a response, but physiological effects on healthy persons are minimal at oxygen concentrations above 18% (near sea level).

Oxygen concentration can be detected via several different methods but measurements can be perturbed by the presence of helium in the gas mixture. Electrochemical cells have typically been used but special sensors are required when helium is present in the gas mixture. When using this type of

sensor the instrument output is based on the partial pressure of oxygen. The indicated oxygen level can vary based on atmospheric pressure and humidity. As the normal alarm setpoint of 19.5% oxygen is very close to the normal value of 20.9% changes in atmospheric conditions as well as instrument drift can result in false alarms.

Ionizing radiation inside the accelerator enclosure will damage electronic components. Since oxygen detection devices generally have electronics associated with the sensor unit this precludes the use of in-situ oxygen sensors in the tunnel. One solution would consist of a remotely mounted sensor/ electronics package with a flow pump to extract an air sample from the tunnel.

A system under investigation is an oxygen deficiency monitor as manufactured by Oxigraf Inc.[2] The sensor uses laser diode technology to monitor oxygen levels that is not affected by helium or atmospheric conditions and does not require periodic replacement. The unit can be supplied with a high flow sample pump that can obtain a sample measure in 15 to 20 seconds using 30 m of sample tubing. Each unit can be used to sample four different locations.

An important question concerning the sensor placement is the required speed of response. In addition to flow sampling lag discussed above there will be a delay in the response of the system based on the location of the sensor versus the location of the release. Wider sensor spacing will result in slower response times since on average it will take longer for the helium to migrate from the release point to the nearest sensor.

4.2.2 *Area Alarms*. The ODH system will provide audio/ visual evacuation alarms similar to a fire alarm system. These alarms will be used to evacuate workers from the accelerator tunnel in the event of a release. The visual alarms will use a unique color and will be provided along the entire length of the tunnel. The locations of the visual alarms will be coordinated with PSS HMI panels. Visual alarms will also be provided at each tunnel entrance to warn workers that an ODH condition exists inside the tunnel. A “system OK” light will also be provided at each entrance so workers can determine if the ODH system is operating properly prior to entry.

The tunnel audible alarm inside the tunnel will be provided by the PSS/ ODH public address system. The alerting tone provided by the loudspeaker system will be unique to the ODH system.

4.2.3 *Passive or Active Ventilation*. Conventional Facilities (CF) will provide a smoke removal system consisting of five exhaust fans with a capacity of 5 m^3/s each. Each fan is tied to a duct leading down to the tunnel ceiling. A smoke curtain is installed in the tunnel at the entrance of each duct to restrict smoke migration from one area to another. Automatic dampers will be installed on the tunnel ceiling to prevent air from being exhausted from the tunnel when the proton beam is operating.

The ODH system will be designed to directly control the ceiling mounted dampers independently of the CF control system. As the smoke removal fans will not have backdraft dampers helium can be passively vented outside the tunnel in the event of a release. The ODH system will monitor the damper positions both open and closed and (in conjunction with the PSS) will not allow entry into the tunnel unless the dampers are open.

Depending on the results from the risk analysis, the ODH may also directly control the smoke exhaust and makeup air fans to provide active ventilation of the tunnel during a helium release.

4.2.4 *Logic Solver*. The ODH system will use a safety PLC based logic solver separate from other systems such as the PSS. The logic solver will monitor the status of each oxygen monitor, activate alarms and activate the exhaust fans and dampers. The logic solver will use distributed input/ output devices communicating with the PLC via the PSS safety Ethernet network. The logic solver will be integrated with EPICS via a secure firewall to allow remote status display and archiving of system data.

5. Area Radiation Monitoring (ARM)

There will be radiation monitors placed in appropriate positions through the accelerator klystron gallery (actual positions still to be determined)/not in the tunnel as well???. These devices will constantly monitor and record radiation levels and will trigger a stop of beam operation if excessive levels are measured and pre-defined thresholds are exceeded. Figure 4 shows the approximate radiation monitor positions. These will mainly be located at the entrance to the-stubs in the Klystron Gallery and at the Accelerator tunnel main entrances and emergency exits.

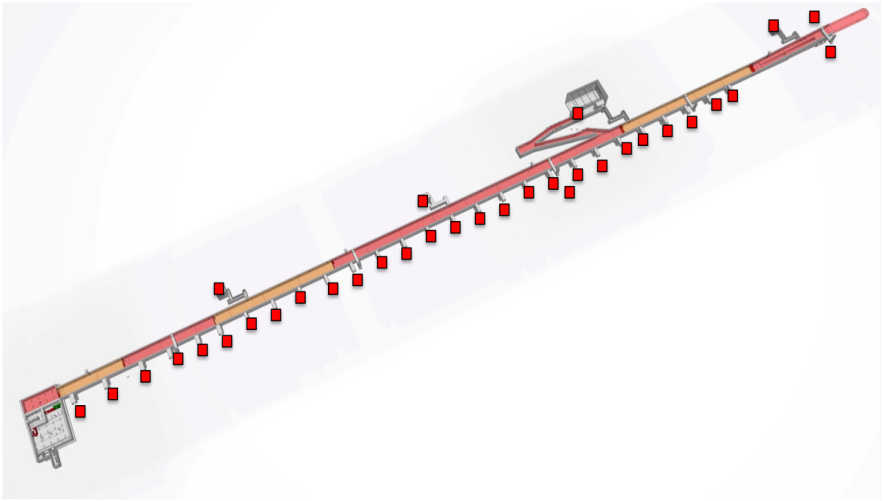

Figure 4 Approximate radiation monitor positions

6. Conclusions

It should be noted that the scope and strategy for each of the ESS Personnel Safety Systems have now been outlined and approved, and whilst the design is in the very early stages the philosophy will remain the same even if the overall design changes.

References

[1] IEC 61508, parts 1-7: 2010, *Functional safety of electrical / electronic / programmable electronic safety-related systems,* Switzerland: Geneva, International Electrochemical Commission, 2010.
[2] Oxigraf, Inc., 1170 Terra Bella Ave. Mountain View, CA 94043.

3.11.4

Progress of the General Control System for the Materials and Life Science Experimental Facility in J-PARC

Kenji Sakai, Motoki Ooi, Akihiko Watanabe, Tetsuya Kai, Yuko Kato, Shin-ichiro Meigo, and Hiroshi Takada

J-PARC Center, Tokai, Ibaraki, Japan

E-mail: kenji.sakai@j-parc.jp

Abstract. For safe and stable beam operation, the general control system (GCS) of the Materials and Life Science Experimental Facility (MLF) comprises several subsystems, such as an integral control, interlock, server, network, and timing distribution systems. Since the first beam injection in 2008, GCS has operated stably without any serious troubles, even with annual upgrades to the target devices for ramping up beam power and annual incremental upgrades of the user systems. In recent years, however, it has been significantly improved with regard to sustainable long-term operation and maintenance. The monitor and operation system of GCS has been upgraded by changing its framework software to improve its potential flexibility for maintenance. The interlock system was also modified in accordance with a re-examination of the Japan Proton Accelerator Research Complex (J-PARC) risk management system. This study reports the recent progress of GCS.

1. Introduction

The Materials and Life Science Experimental Facility (MLF) at the Japan Proton Accelerator Research Complex (J-PARC) generates pulsed muon and neutron beams by injecting highly intense proton beams supplied from accelerators through the 3-GeV proton beam transport line (3NBT) into graphite and mercury targets. Then, it supplies the muon and neutron beams to many user instruments placed in two experimental halls of MLF [1]. For safely and efficiently supplying muon and neutron beams, a general control system (GCS) operates within MLF. GCS comprises several integrated subsystems, such as a controller for the muon and neutron targets, interlock systems for safe operations, and shared servers for administering operational data [2, 3, 4]. It is an independent system that controls the target stations, including a mercury target and neutron moderators with supercritical hydrogen. Although GCS is an independent system, it works closely with the control systems of the accelerators and other facilities in J-PARC.

After the construction of most of GCS subsystems was completed, commissioning for operation and control of the entire MLF proceeded stepwise in June, 2007. During a short period before the first beam injection, the trial operations, performance tests, and improvements of GCS subsystems were executed under restricted conditions. Since the first proton beam injection in May, 2008, GCS has been operated safely and stably without any serious troubles. In recent years, however, it has been significantly improved with regard to sustainable long-term operation and maintenance. This study provides an overview of the recent progress of GCS for MLF in J-PARC.

2. Overview of GCS in MLF

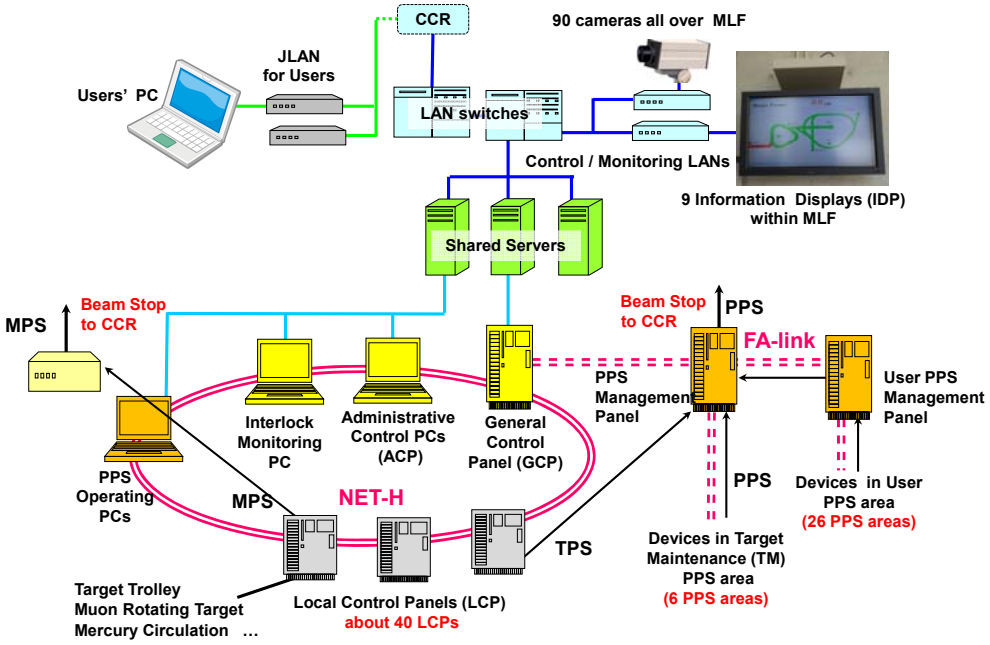

Figure 1. Outline of GCS within MLF in J-PARC.

Fig. 1 shows an outline of GCS within MLF. It comprises several subsystems, such as integral control and interlock systems, shared servers, network systems, and a timing distribution system [2, 5]. GCS administers three kinds of interlock systems related to beam stop, called the machine, target, and personnel protection systems (MPS, TPS, and PPS). The integral control and interlock systems comprise personal computers (PCs) and programmable logic controllers (PLCs), such as administrative control PCs (ACP), the general control panel (GCP), PPS management panel (PPS-MP), and local control panels (LCPs). These systems are connected through duplicate optical networks for PLC linking, called the NET-H and FA-link, and duplicate metal cables. They operate the instruments in the entire MLF, such as the target trolley, muon rotating target, and mercury circulation systems, by the ACP and GCP through the NET-H and approximately 40 LCPs. Moreover, they safely administer many instruments and high radiation areas, work closely with the interlock systems of the accelerators and other facilities through the Central Control Room (CCR) of J-PARC, stop beam injections if necessary, and maintain safety in MLF in emergencies. The shared servers comprise server PCs for purposes such as web distribution (WD), data storage (DS), and monitoring cameras. They acquire, arrange, store, display, and distribute over 7000 operational data items. Operations for GCS are executed by a monitor and operation (MO) system comprising an ACP, PPS operating PC (PPS-PC), interlock monitoring PC (IM-PC), DS server, WD server, and others, in a MLF control room (MLF-CR) located on the third floor of MLF.

Network systems of GCS comprise a control LAN (C-LAN) and monitoring LAN (M-LAN). The C-LAN is a duplicate Ethernet system for controlling the accelerator and facilities within J-PARC administered through CCR. M-LAN is used to control approximately 90 monitoring cameras in MLF using a camera server. In addition, J-PARC has a network system for general users (JLAN). C-LAN is connected to JLAN extending from CCR and goes through a firewall. The WD server distributes operational information, such as operational status, beam power, and beam trend, to users through nine information displays (IDPs) connected to C-LAN, and users' PCs connected to JLAN in the form of a Web browser.

3. Recent progress of GCS in MLF

After the construction of most of GCS subsystems was completed, commissioning for operation and control of the entire MLF proceeded stepwise in June, 2007. Fig. 2 shows the time series of commissioning on operation and control of the MLF. Since the first beam injection in 2008, GCS has been operated as expected without any serious troubles, even with annual upgrades to the target systems for ramping up the proton beam power and annual incremental upgrades to the user apparatus. It also worked in accordance with its safety design when the Great East Japan Earthquake (GEJE) occurred in March, 2011 [5, 6]. In recent years, however, it has been significantly improved with regard to sustainable long-term operation and maintenance. The MO system of GCS has been upgraded by changing its framework software to improve its potential flexibility in its maintenance [7, 8]. Moreover, the risk management system for J-PARC was re-examined because of an incident that caused radioactive material leakage at J-PARC Hadron Experimental Facility in May 2013, where an "Alert" status for examining signs of an abnormal situation was added between the "Normal" and "Emergency" statuses. Consequently, the interlock systems of GCS were also improved.

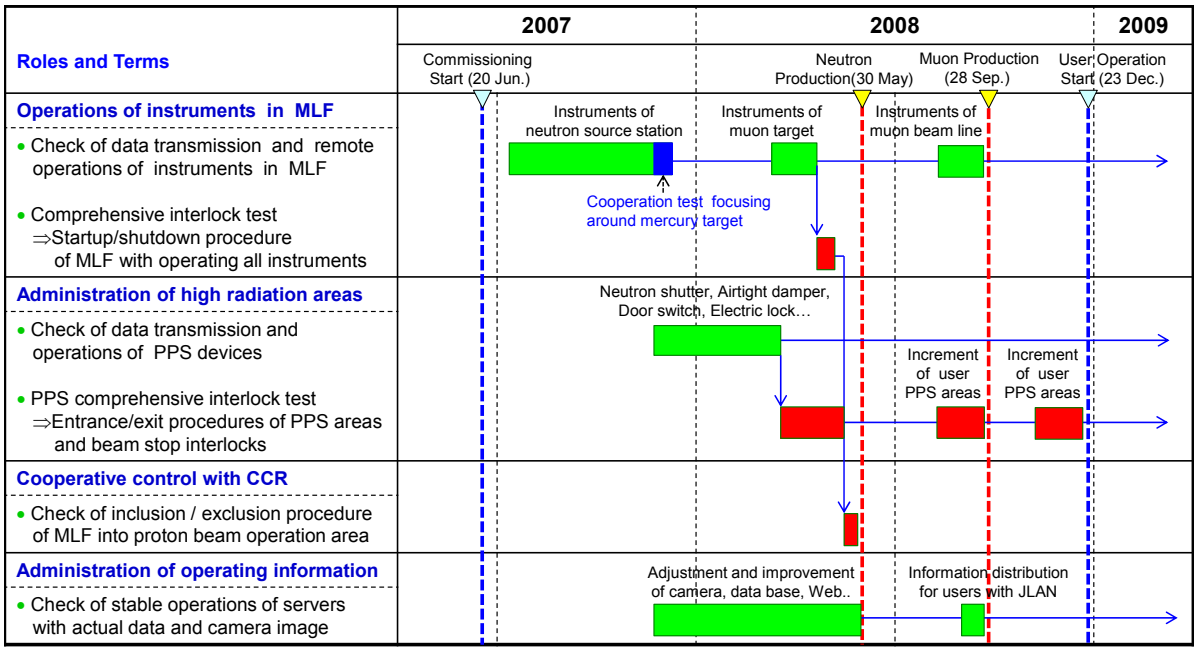

Figure 2. Time series of commissioning on operation and control of the whole MLF.

3.1. Interlock system

Fig. 3 represents the structure of the interlock systems within GCS as of November, 2014. The interlock systems, comprising MPS, TPS, and PPS, play an important role in ensuring the safety of personnel and machines [5]. MPS is a system for preventing trouble in important machines due to unusual irradiations by prohibiting proton beam injections. In Fig. 3, seven LCPs, which have sensors for detecting MPS events, are connected to an MPS controller through metal cables. If MPS sensors detect unusual events, MPS signals are collected in each LCP and transmitted to the MPS controller. The MPS controller transmits two kinds of beam-stop signals, called "MLF Inhibit" and "MLF MPS" to CCR. It transmits "MLF Inhibit" signal at first after receiving MPS signals. Then, proton beam injections into MLF are stopped by changing the distribution patterns (which are generated by a scheduled timing system of J-PARC) of the proton beam pulses from the accelerators to each facility. If the beam pulse is detected during transmission of the "MLF Inhibit" signal, the "MLF MPS" signal

for terminating the accelerator operation is transmitted to CCR. Then, the radio-frequency power to the linear accelerator (LINAC) is terminated and beam shutters between the ion-source and RFQ (a type of LINAC) are closed.

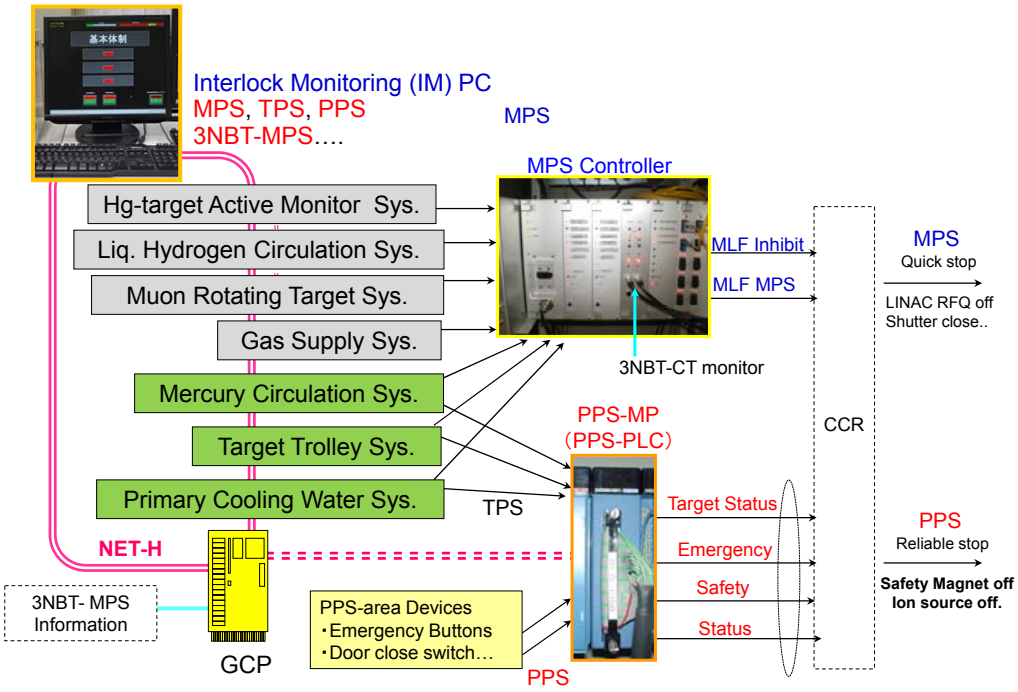

Figure 3. Structure of the interlock systems within GCS.

PPS is a system for preventing exposure of personnel to high radiation. In MLF, there are two kinds of PPS areas, called the target maintenance (TM) and user PPS areas in Fig. 1. In six TM PPS areas, PPS devices, such as door controllers, electric door locks, and door limit switches (LS), are controlled by PPS-MP. In 20 neutron and 6 muon user PPS areas, user PPS devices such as beam stopper (BS) controllers for operating neutron shutters or muon blockers are administered by user PPS-MP. PPS also terminates the proton beam to protect personnel from high radiation during proton beam injections. The exclusive PLC in PPS-MP transmits four kinds of signals, called "Target Status," "Safety," "Emergency," and "Status," to CCR for permitting or prohibiting proton beam injections. Since the beam stop by PPS requires higher reliability than MPS, not only the beam shutter close but also the ion-source termination are included in this procedure.

TPS is a system for preventing problems related to the mercury target from becoming serious when the beam stop operation executed by MPS fails. Since the beam stop by TPS is required to have the same reliability as PPS, TPS signals are transmitted to CCR as the "Target Status" after collecting in PPS-MP. Then, the beam is terminated by executing the PPS beam stop procedure. In Fig. 3, three LCPs for the target trolley, mercury circulation, and primary water circulation systems transmit TPS signals.

IM-PC collects and monitors detailed information about the 128 MPS, 10 TPS, and PPS items through the PLC links in a lump. It deals with the information about the MPS of the 3NBT, which directly influences the beam operation of MLF, and displays the status related to the risk management system. If MPS or TPS events related to mercury leakage are detected, IM-PC and IDPs display the "Alert" status, and the MPS controller transmits "MLF MPS" for terminating accelerator operation independently of the "MLF Inhibit" transmission.

3.2. Upgrade of monitor and operation systems

In Fig. 1, the current MO system, which comprises ACP, PPS-PC, servers, and other components, was designed on the basis of the iFIX- Supervisory Control and Data Acquisition (SCADA) and iHistorian software systems for framework and data storage. Furthermore, it has functioned as expected. However, the downside was its costly maintenance because of its poor flexibility on the operating system (OS) and software versions. To improve the maintenance flexibility of GCS, we planned a significant upgrade of the MO system [7, 8]. According to the plan, we considered the schematic of the upgraded MO system in 2012, on the basis of the condition of the current functions, so as to control all LCPs, and acquire, store, and distribute operational data in a suitable data format. Fig. 4 outlines the schematic of the upgraded MO system. In Fig. 4, the following components of the MO system were adopted: experimental physics and industrial control system (EPICS) as framework software, an OPC server as a data input/output module, control system studio (CSS) as a user interface window, postgre SQL for the DS server, and web OPI for the WD server. Furthermore, we manufactured the prototypes of the upgraded MO system and evaluated its actual performance with true data, such as data transmission speed from the PLCs, control functions from the user interface windows, storage capability of the DS, and long-term reliability. After confirming that it works properly, as designed, we built two full-scale upgraded MO systems in 2013. One is the MO system, which controls the devices for the target stations by using more than 130 operation screens and acquires operational data for about 7000 items every second. The other system administers PPS devices using seven screens and acquires data for about 1400 items. They have been operated in parallel with the current systems during beam operation and maintenance for over half a year, and have been debugged, unlike the current systems, which were replaced in 2014.

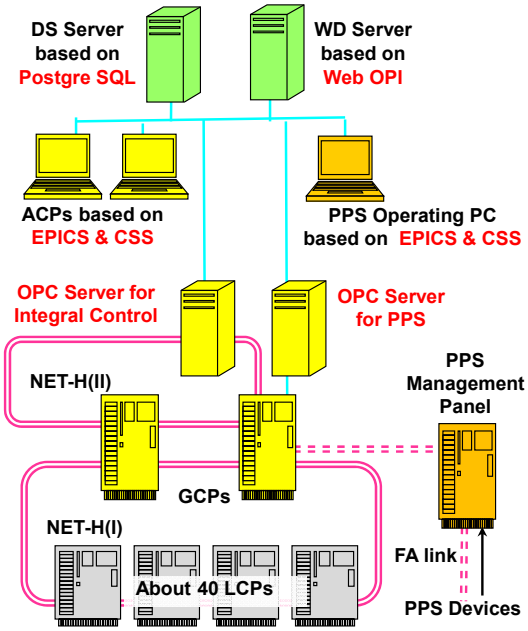

Figure 4. Structure of the upgraded MO systems.

3.3. Safety design in emergency

GCS is designed with regard to safety for various emergencies on the basis of the failsafe concept [5]. In Fig. 1, the main components, such as GCP and PPS-MP, optical networks, and metal cables are duplicated, and if the devices or cable relating to proton beam injections fail or disconnect, the beam stop signals are transmitted to CCR. In a loss of external power supplies, the control functions of GCS are maintained by uninterruptible power sources (UPSs) and back-up generators; almost all instruments relating to the target stations are automatically shut down according to their interlock sequences in emergencies and operational data continue to be stored in the DS server every 5 s. If the power supplies for PPS devices around PPS areas are lost, entrance into the area is prohibited by mechanically locking the door (although exit from the area is always enabled). In addition, the storage function for the data of PPS devices every second has been designed for quickly comprehending the actual PPS status.

On the day of the GEJE, the beam operation of MLF was stopped in the morning and the target stations were on standby for the restart of the beam operation in the evening [6]. In MLF, strong quakes were detected by the liquid-level and pressure sensors in many circulation systems after about

90 s, and the external power supplies were lost after about 150 s. The control function of GCS was kept active by the back-up generators until manual shutdown for about 3 h. Immediately after the power loss, the beam stop signals on "Target Status" were transmitted by the shutdown of the mercury and primary water circulation systems. All doors of TM areas were mechanically locked. These results substantiated the validity of its safety design for emergency accidents [5, 6].

4. Summary

This study explained the outline of GCS for MLF and provided an overview of its recent progress with a focus on the MO system, interlock systems, and safety design in an emergency. The MO system of GCS was upgraded by changing its framework software to improve its potential flexibility for maintenance. The interlock systems were modified based on a re-examination of the J-PARC risk management system. With regard to sustainable long-term operation and maintenance, exchange and upgrade of various instruments in GCS such as client PCs, servers, PLCs, batteries, and the monitoring camera system should be executed carefully at an appropriate time while maintaining its safe and stable operation. In fact, the power supplies and batteries within the control panels and PLCs have been exchanged stepwise since 2013, a full-scale upgrade of the network systems of GCS was started in 2014, and the monitoring camera system will be materially upgraded in a few years.

Acknowledgments

The authors are grateful to the members of the Neutron Source Section and the staff of J-PARC Center for their useful help and suggestions.

References

[1] Ikeda Y 2005, *J. Nucl. Materials* **343** 7
[2] Sakai K, Ooi M, T. Kai, Kinoshita H, Kawasaki S, Watanabe A, Kaminaga M and Futakawa M 2009, *Nucl. Instr. Meth. A* **600** 75
[3] Ooi M, Kai T, Kinoshita H, Sakai K, Kaminaga M, and Futakawa M 2009, *Nucl. Instr. Meth. A* **600** 120
[4] Kai T, Sakai K, Nakatani T, Takada H, Oikawa K, Shimomura K, Higemoto W, Kinoshita H, Ooi M and Kaminaga M 2009, *Nucl. Instr. Meth. A* **600** 176
[5] Sakai K, Kai T, Ooi M, Watanabe A, Nakatani T, Higemoto W, Meigo S, Sakamoto S, Takada H and Futakawa M 2014, *Progress in Nuclear Science and Technology Vol.* **4** 264
[6] Sakai K, Futakawa M, Takada H, Sakamoto S, Maekawa F, Kinoshita H, Seki M, Haga K, Kogawa H, Wakui T, Naoe T, Kasugai Y, Tatsumoto H, Aso T, Hasegawa S, Oikawa K, M. Ooi, A. Watanabe, Teshigawara M, Meigo S, Ikezaki K, Akutsu A and Harada M 2012 *Proc. of ICANS-XX, Bariloche, Río Negro, Argentina, March 4–9, 2012* 113
[7] Sakai K, Ooi M, and Watanabe A 2013 *MLF Annual Report 2012* 75
[8] Ooi M, Sakai K, Watanabe A, Akutsu A, Meigo S and Takada H 2013, *Proc. of ICALEPCS-2013, San Francisco, CA, USA* MOPPC017

3.11.5

Development of the target safety system for the ESS target station

Linda R Coney[1] and Atefeh Sadeghzadeh
European Spallation Source, P.O. Box 176, 221 00 Lund, SE.

E-mail: linda.coney@esss.se

Abstract. The European Spallation source (ESS) will be a 5 MW neutron spallation research facility where an energetic proton beam incident upon a helium-cooled tungsten target is converted to neutron beams. The liquid hydrogen moderator, water moderator, and reflector systems within the target monolith slow down the high-energy neutrons, produced through the spallation process, to cold and thermal neutrons suitable for use by experiments. Several layers of control, protection, and safety systems will be implemented in order to ensure safe operation of this advanced facility. The Target Safety System (TSS) is dedicated to the nuclear safety functions of protecting the public from exposure to unsafe levels of radiation and preventing the release of radioactive material beyond permissible limits. It is a safety-rated monitoring and control system subject to the highest reliability demands in ESS operation. In the event of an abnormal situation, the TSS guarantees that the target station operates within the design domain. It is likely that the TSS will trigger and control internal and external mitigation functions including termination of proton beam production. This paper will describe the development of the TSS, including the definition of requirements utilizing hazard analyses of all target station systems, evaluation of interfaces with accelerator and control systems, and development of the design logic.

1. Introduction

The European Spallation Source (ESS) will be a 5 MW high-power, long-pulse neutron spallation research facility. The ESS linear accelerator produces an energetic proton beam at a repetition rate of 14 Hz. A series of raster magnets ultimately directs the beam onto a helium-cooled rotating tungsten target located in the ESS target monolith, thereby producing high-energy neutrons through the spallation process. Several high-level ESS beam and target parameters are given in table 1. The liquid hydrogen moderator, water moderator, and reflector systems within the monolith surround the neutron production area of the target and convert these high-energy neutrons into cold and thermal neutrons suitable for use by experiments. Several layers of control, protection, and safety systems, including the Target Safety System (TSS), will be implemented in order to ensure safe operation of this advanced facility.

1.1. Target Station

The target monolith[1] is designed to convert protons from the accelerator into neutrons of the appropriate energy spectrum for use in experiments while providing sufficient shielding to contain radioactive by-products produced in the target and to reduce neutron background in the experimental hall. The monolith houses the rotating tungsten target along with several plugs containing the moderators and reflectors, proton beam instrumentation, target monitoring equipment, and the proton beam window which separates the vacuum environment of the accelerator from the helium environment in the monolith. Beam guides within the neutron beam extraction lines transport intense thermal and cold neutron beams from the target to each neutron-scattering instrument in the

[1] To whom any correspondence should be addressed.

experimental hall. Figure 1 shows a cross section of the target monolith with the location of these systems and plugs identified.

Table 1. High-level parameters for the ESS beam and target.

Beam Parameter	Value	Target Parameter	Value
Average Beam Power	5 MW	Target material	Tungsten
Macro-pulse length	2.86 ms	Target wheel size	2.5 m diameter
Proton kinetic energy	2 GeV	Rotation rate	25.5 rpm
Pulse repetition rate	14 Hz	Estimated lifetime	5-10 years

The 2.5 m diameter target wheel within the monolith consists of 33 helium gas-cooled sectors of tungsten. Proton beam pulses from the accelerator are synchronized with the rotation of the target, with each sector receiving a rastered beam pulse every 2.4 seconds. The odd number of sectors prevents the beam from inadvertently passing through the helium cooling channels in the event that a desynchronized beam pulse impacts the target between sectors. The tungsten target transforms the incoming protons into fast neutrons through spallation, while also producing heat, radioactive isotopes and prompt radiation. The estimated operational lifetime of a full target assembly is 5 years.

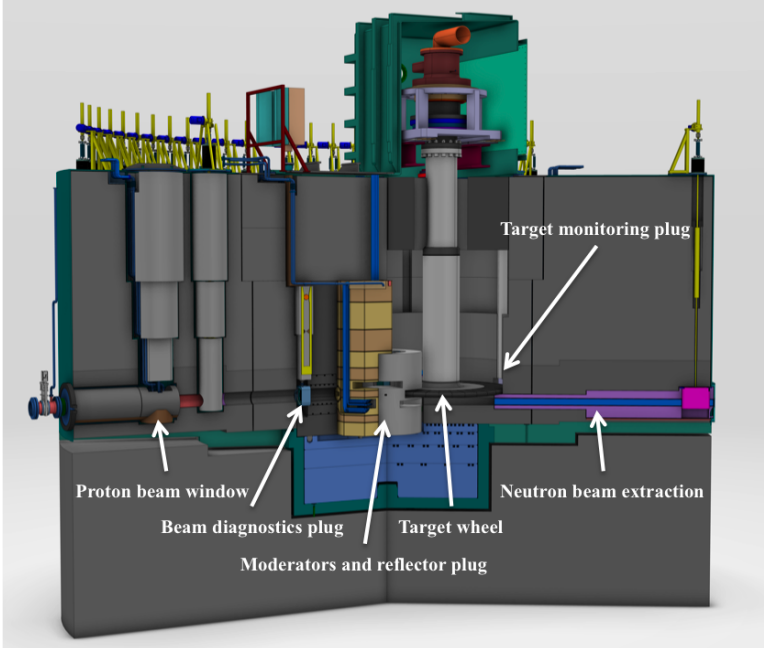

Figure 1. Cross section view of the ESS target station monolith showing the layout of important components including the target wheel, moderator and reflector plug, instrumentation plugs and neutron beam extraction lines. In this view, the proton beam enters the monolith from the left.

The moderator-reflector assembly surrounds the upstream portion of the target and converts the fast neutrons into cold and thermal neutrons. During this process, absorption of neutrons by target structures produces radioactive waste. The cold moderators in the monolith contain liquid hydrogen and have an estimated operational lifetime of 2-5 years. It is anticipated that it will be necessary to replace the moderator assembly more often than the target assembly.

Surrounding the target, moderator-reflector plug, and all target components is approximately 7000 tons of steel radiation shielding designed to contain the highly penetrating gamma and fast neutron radiation created in the target. This is complemented by additional concrete shielding to absorb

thermal and cold neutrons. In total, the target monolith is a 10 m high and 11 m diameter cylinder located in the ESS target building.

1.2. Target Station Building

The target monolith is housed within the target building as shown in figure 2. In addition to the monolith, equipment necessary for target component operation including fluid systems, filtering systems, and cooling systems is located in utility rooms. The active cells area, used for handling, processing, and storage of activated target components, is also located within the target building. Target components, including the wheel assembly and moderator-reflector plug, will be removed from the monolith and brought by crane to the processing cell through the high bay. There the equipment will be disassembled using remote handling techniques in preparation for local storage in the adjacent maintenance cell until such time as the material is ready for transport off site.

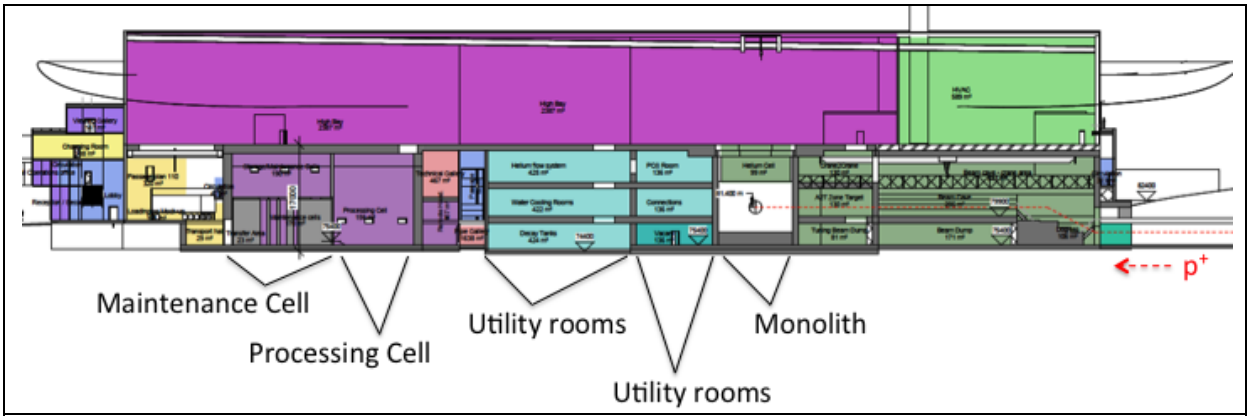

Figure 2. Side view of the ESS target building monolith showing the location of target station equipment including the target monolith, utility rooms housing equipment necessary for target component operation, and the high bay running the length of the building. The active cells area for handling of radioactive target components includes the processing cell, maintenance cell, and remote handling galleries. In this view, the proton beam enters the target area from the right, either continuing at accelerator level to the beam dump or stepping up to monolith level to the target wheel.

Additionally, figure 2 shows that there are two paths available for the proton beam into the target building. The beam can either continue to the beam dump, located at the same elevation as the accelerator, for beam studies or it can be raised to target level and continue to the monolith for neutron production. Ventilation systems for all areas are also housed in several locations within the building.

Putting the entire facility in context, the ESS is being designed and built in Lund, Sweden. This is a region with approximately 100,000 inhabitants. Additionally, there will be 450 – 500 ESS employees and roughly 3000 users per year involved with nuclear spallation experiments. All target station systems and the inventory of radioactive material must be taken into consideration from a safety perspective to assess possible risks and to evaluate the potential need for safety-related controls.

2. Target Safety System

The Target Safety System (TSS) is dedicated to the nuclear safety functions of protecting the public and workers from exposure to unsafe levels of radiation and preventing the release of radioactive material beyond permissible limits. It is a safety-rated monitoring and control system subject to the highest reliability demands in ESS operation. In the event of an abnormal situation, the TSS guarantees that the target station will operate within the design domain. It is likely that the TSS will trigger and control internal and external mitigation functions including termination of proton beam production. The TSS is subject to the highest reliability and quality assurance demands for any control system at the ESS, and will be separate from all other control systems. As a safety-credited system, the Target Safety System is an essential component of the licensing process for the ESS.

2.1. TSS context

The TSS operates independently alongside other control systems within the target station: the normal monitoring and process control, the Machine Protection System (MPS), and the Personnel Safety

System (PSS) [2]. At the ESS, all non-safety monitoring and process control for equipment throughout the facility will be integrated into one unified control system by the Integrated Control System (ICS) division. A standardized control framework, EPICS (Experimental Physics and Industrial Control System) [3], has been chosen for this system. EPICS has been used at many large-scale scientific projects world-wide and provides an excellent basis for platform standardization, device integration, and control development. The EPICS system provides control services for several modes of operations, monitoring and controls archiving, and data logging for target station equipment.

The remaining control systems at the ESS, and specifically, within the target station, have specialized scope and requirements for increasing levels of reliability and quality assurance as shown in figure 3. The MPS is designed to protect equipment from damage due to malfunction or errant beam loss, thereby protecting the investment in the facility and optimizing machine performance. The PSS is a safety system designed to protect personnel from radiological hazards primarily by controlling access to restricted areas. The TSS will limit the transfer of radioactive contamination to the public, workers, and the environment and does not depend on elements of any other controls system to perform its safety functions. Additionally, the TSS is the only controls system within the ESS that does not fall under the responsibility of the ICS division.

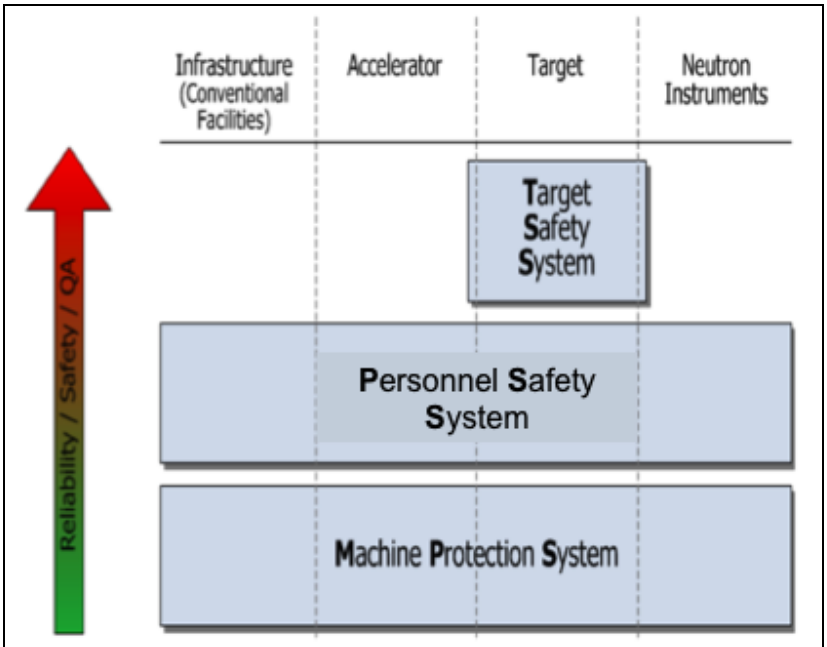

Figure 3. Representation of the main safety controls systems (Target Safety System and Personnel Safety System) and damage prevention controls system (Machine Protection System) showing scope of involvement and respective requirements for reliability.

The MPS is a machine protection system designed to optimize operational efficiency, facility availability, and machine reliability. This system will stop the proton beam in the event of equipment failures, prevent damage to elements in the accelerator and target, and provide tools for failure tracing throughout the machine. As such, it is not a safety-classified system; however, the MPS does contribute to the layered approach to safety by triggering alarms and actions, such as performing an emergency shutdown of the beam, when target station systems are detected to be operating outside of permitted ranges. The MPS has the capability to shut down the proton beam very quickly (~10 μs) and will have a high level of reliability. In contrast to the TSS, which has no requirement on post-trigger machine availability, operation of the facility must be possible in the event of any MPS action.

The PSS is a safety-classified system designed to protect personnel against unnecessary exposure to hazards from the machine, including but not exclusive to radioactivity and electromagnetic radiation. PSS systems will be installed throughout the ESS and will control access to restricted areas within the accelerator, target station, and instruments. PSS systems will be concerned with access control, radiation monitoring, oxygen deficiency monitoring, and alarm systems. Protection from radiation

generated by the beams will be achieved by shutting down the proton beam upon detection of unacceptable conditions. The PSS will monitor doors, locks, and other access points to ensure they remain closed during ESS operations. Entrance to and egress from radiation-controlled areas will be managed by the PSS according to classifications defined according to different operational modes of the facility.

2.2. TSS requirements

As shown in figure 3, the TSS is the safety system subject to the highest reliability requirements within the ESS controls system domain. The TSS guarantees that the target systems operate within the design domain, and it will bring the target station into a safe state from a nuclear safety perspective in the event of an abnormal event. This will reduce the risk of harm to workers, the public, and the environment. Requirements for TSS monitoring and actions are currently being analysed. It is anticipated that the TSS will need to be able to perform an emergency shutdown of the proton beam. However, actions are not necessarily restricted to beam shutdown.

Preliminary top-level design and test requirements for the TSS have been identified and include the following:

- Single failure criterion,
- Fail-safe principle,
- Emergency power supply coverage for TSS equipment,
- Qualified for extreme operating conditions, including seismic classification for a subset of TSS functions,
- Physical separation and fire protection,
- Pre-operational testing, and
- Periodic testing of TSS equipment.

In more detail, there must be no single point of failure vulnerability within the TSS system. This implies the use of layers of redundancy, independence, and diversity along with physical separation adapted to different potential aggressors. For each hazardous scenario identified during the hazard analysis process, the safe state for the target station must be clearly identified. TSS actions will default to this safe state and actuator commands will be 'de-energize to trip' rather than the reverse. For example, in the event of a loss of power, TSS actuators will default to the safe position. The nature of the emergency power supply coverage for the TSS has yet to be determined. This will depend on the time-scale for TSS continued monitoring and actions within all identified hazard scenarios. Additionally, in contrast to the MPS, there is no post-trip machine availability requirement for the TSS. It is anticipated that a detailed analysis of any scenario involving an action by the TSS would be necessary prior to a facility restart.

Applying the top-level requirements allows the development of initial design concepts for the TSS system. There will be two independent shutdown mechanisms to stop the proton beam. Shutdown of the beam will be accomplished using both the ion source and RFQ (radio-frequency quadrupole) in the front end of the accelerator. The TSS will have direct access to these elements. Priority will be given to the TSS over the PSS and/or MPS for control of the shutdown mechanisms in the event that these systems also choose to achieve proton beam shutdown using the same accelerator components. The TSS design is based on using highly reliable safety-rated PLCs (programmable logic controller). There will be two separate TSS rooms in the target building housing redundant, independent PLC systems. There will be independent paths to each beam shut-off system: one through the accelerator tunnel and another through the klystron gallery. The TSS rooms have been identified in the ESS conventional facilities plan, and details of the cable paths from each room to both beam shutdown locations are being developed. The TSS will be separate from other non-safety controls systems and equipment, and will require independent cable-trays, UPSs (uninterruptable power supplies), and sensors.

The overarching philosophy for TSS design development enables the satisfying of safety requirements and the protection of workers and the public with a system that is as simple as possible in order to achieve a very high level of reliability. At this time, the shutdown of the proton beam is the only specific action identified as a requirement for the TSS. However, additional target-specific monitoring and controls actions may be required within systems such as the He cooling for the target

wheel, wheel motion, and ventilation for target areas. Detailed requirements for TSS monitoring and actions are currently being determined using the Hazard Analysis process.

3. Hazard Analyses

Hazard analyses are being performed on all target station systems. This tool is used to understand potential hazardous scenarios within the ESS target station and to define necessary mitigations. Initially, a qualitative hazard analysis is done for each system under evaluation. This produces design recommendations for the target station systems and study recommendations to allow for the quantitative evaluation of hazardous scenario consequences. When analysed from a radiation safety perspective, mitigations may include requirements for active controls system intervention. In this way, inputs and outputs for the TSS are identified, TSS requirements are defined, and the TSS logic design and architecture can be developed.

Information from relevant studies and modifications to component design is then fed back into a quantitative hazard analysis where a more rigorous analysis can be performed. Given that most target station systems are in the preliminary design phase, this iterative process is necessary and accommodates evolutions in design and the implementation of recommendations from earlier safety analysis.

3.1. Hazard analysis procedure

There are many steps required in the hazard analysis procedure. First, the system under analysis is defined. This may include the production of drawings or schematics as well as a written description of the system including assumptions made for the purpose of the analysis. This also includes the definition of boundaries to the system under analysis and the description of relevant interfaces. In this way, the hazard analyses can be broken down into smaller; more easily understood systems. Next, hazards relevant to the system under study are identified. These include but are not limited to radioactivity, stored energy, explosion, impact such as a load drop, and hazards from the proton beam. The effects of rare events including earthquakes, fire, and an airplane crash are also evaluated.

Next, for each target station system, initiating events and top events are identified. Top events are instances of faults within the system that could produce a hazardous situation. Initiating events are actions, incidents, or occurrences leading to a given top event. For example, a top event could be the leak of air from the processing cell to the galleries. Possible initiating events could include the removal of a through-wall manipulator, a seal failure, loss of power to the ventilation system, or the erroneous opening of an access point. For each system, there are likely to be multiple top events identified during the hazard analysis. In order to understand the potential impact of each top event, the consequences without mitigation are described.

Once the consequences are understood, an unmitigated risk ranking is assigned to each top event. This is determined as a function of the probability that the top event will occur and the severity of the unmitigated consequences in the event of an occurrence. Figure 4 shows the grid used to determine the risk rankings. Probability of occurrence ranges from H1 to H4 with the probability decreasing by at least one order of magnitude for each level. For the qualitative analysis, the selected probability is largely based on expert engineering knowledge for similar systems. The severity is determined based on the consequences and differs when performing the analysis from a radiation safety perspective compared to other hazards. Table 2 shows the radiation exposure limits for both workers and the public as defined in the ESS General Safety Objectives (GSO) and the limits required by the Swedish radiation authority (SSM). Limits are listed for each category of event from H1-H4. If different initiating events have different probabilities to occur, the risk ranking for each is evaluated separately. If they are of the same order of magnitude, grouping of events can be done.

As shown in figure 4, some risk rankings are unacceptable and, therefore, require mitigation. Others indicate a recommendation for the reduction of the risk, while the low probability-low severity events are tolerable as is and do not require risk reduction. For those events not in the tolerable category, the next step in the hazard analysis is to identify applicable mitigations for each top event. These could be in the form of design changes or recommendations designed to reduce the probability of occurrence or the severity of the resulting consequences. Associated triggers for active safety system intervention can also be included as a mitigating factor to reduce the probability of occurrence. In this way, requirements for TSS monitoring and actions are identified. Once mitigation factors are identified, the risk ranking is reassessed, taking into consideration the effect of the mitigations on probability and/or severity of occurrence of the top event. If the risk ranking still does not fall into the tolerable range during this re-evaluation, then further mitigation is likely to be necessary.

Probability			
H1 (Normal Operation)	Risk reduction recommended	Unacceptable	Unacceptable
H2 (Incidents)	Risk reduction recommended	Unacceptable	Unacceptable
H3 (Unexpected events)	Tolerable	Risk reduction recommended	Unacceptable
H4 (Design basis Accident)	Tolerable	Tolerable	Risk reduction recommended
Severity	Minor Damage	Moderate damage	Major damage
	Non-radiation: mild symptoms, no remaining injury	Non-radiation: requires medical care, could give remaining injury	Non-radiation: possibility of death
	Radiation: no increased radiation exposure, typically 0-1 containment barriers impaired	Radiation: significant uncertainty regarding outcome, but not expecting increased radiation exposure. Typically 1-2 containment barriers impaired	Radiation: increased radiation exposure. Typically 2-3 containment barriers impaired.

Figure 4. Categories used for determining the risk ranking for top events during the hazard analysis process. Probability of occurrence categories range from H1-H4 in decreasing probability.

Table 2. Radiation exposure limits as defined in the ESS safety objectives and those required by the Swedish radiation authority (SSM) for different categories of events.

	From the ESS General Safety Objectives		From SSM
Event likelihood	Worker Limit (Effective dose)	Public Limit (Effective dose)	Public limit
Normal operation – H1	10 mSv/year	0.05 mSv/year	0.1 mSv
Incidents – H2 10^{-2} < Probability	20 mSv/event	0.5 mSv/occurrence	1 mSv
Unanticipated events – H3 10^{-4} < Probability < 10^{-2}	50 mSv/event	5 mSv/occurrence	10 mSv
Design basis accident – H4 10^{-6} < Probability < 10^{-4}	50 mSv/event	20 mSv/occurrence	100 mSv

3.2. Hazard analyses status

A comprehensive hazard analysis is being done on the ESS target station. Monolith systems under evaluation during this process include the cold moderator, water moderator, reflector, monolith, proton beam window, and target system. For each of these, the relevant primary fluid systems are also evaluated. In this case, the target system is defined as the wheel, the drive, and the target helium cooling system. Those parts of the target station that are not located within the monolith are also evaluated in order to develop a comprehensive safety case. These include the ventilation systems for different parts of the target building, intermediate cooling systems, the beam dump, active cells, remote handling, and an analysis focused specifically on proton beam-induced events.

The initial qualitative hazard analysis has been done for the following systems: water moderator, cold moderator, reflector, and target system. Analysis is in progress for the active cells and ventilation systems with remote handling and beam events next in the queue. The proton beam window (PBW), redesigned monolith, active liquid and gaseous storage, and beam dump systems hazard analyses will

follow. The first systems involved in the qualitative analysis will soon be revisited with a quantitative hazard analysis, incorporating design recommendations and results from the initial studies. Documentation will be formalized and updated, events will be grouped as appropriate, and TSS requirements will be finalized and logic refined. The preliminary design review of the TSS logic is planned for 2015 with the critical design review of the TSS system in 2016. Manufacturing, installation, and commissioning will follow with the goal of producing the first beam on target in 2019.

4. Interfaces

As part of the development of the TSS, interfaces with systems both internal and external to the target station must be evaluated and defined. Interfaces with target station systems are determined by the hazard analysis process and may include sensors, actuators, and data monitoring and tracking. As it is necessary for the TSS to shut down the proton beam, there are naturally interfaces with the ion source and RFQ in the front end of the accelerator. The TSS group is collaborating with the accelerator group to define the interfaces and to optimize the beam shutdown mechanisms. Other potential interfaces between the TSS and the accelerator are under evaluation. These could include components such as the bending magnets that determine whether beam is sent to the target or the beam dump.

One of the most urgent interfaces that must be clearly defined is that between the TSS and conventional facilities. Construction on the ESS has begun recently, and time is short to identify interfaces that impact building design and construction. Requirements for the TSS rooms including cooling needs, intended occupancy, fire prevention, and security access have been defined. Additionally, the effort to identify the optimal TSS cable paths from the target building rooms to the accelerator front end and cable requirements has intensified.

Finally, all interfaces between target systems and ICS systems are being defined. Figure 5 shows a preliminary overview cartoon representation of these interfaces. As part of this process, interfaces between the TSS and other controls systems including the MPS and PSS are being evaluated. The TSS will have independent components such as PLCs, sensors, actuators, cables, cable trays, and will not have inputs from other controls systems. However, it is possible that the TSS will send a signal verifying that it is functional to the target MPS for incorporation into the beam permit system. The TSS may also send data into EPICS via the ICS control box, thereby enabling the use of the archiving tool. Evaluation of these potential interfaces and determination of possible methods for execution while maintaining the high reliability level required for the TSS is on-going. No interfaces between the TSS and PSS are foreseen at this time.

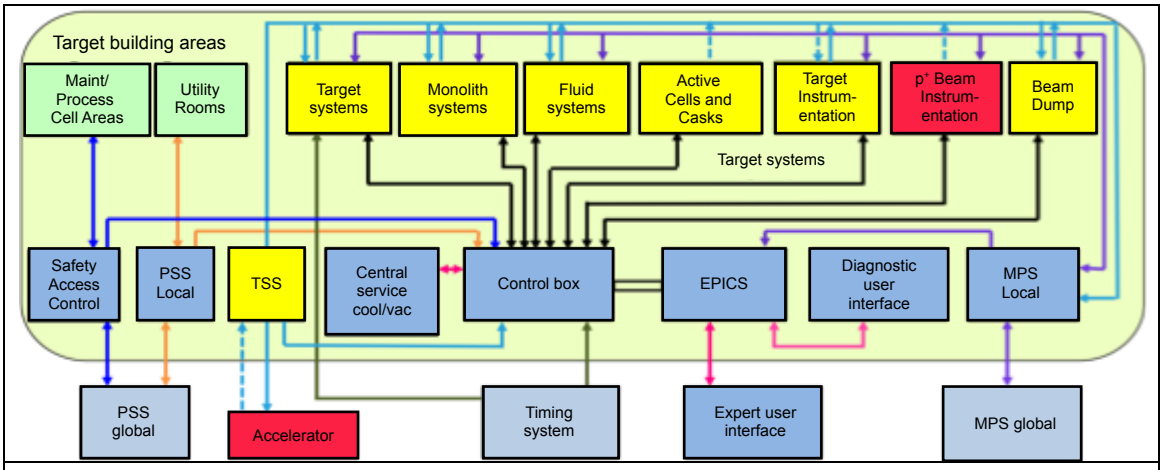

Figure 5. Overview of interfaces between systems within the target station and building and ICS controls systems including standard operations controls within EPICS, MPS, and PSS.

5. Conclusion

The process to derive the set of Target Safety System controls has been developed and is well under way. The TSS purpose within the global safety plan is understood as is the division of scope between

it and the other controls systems at the ESS. Qualitative hazard analyses are being executed in order to derive target station system design requirements, identify necessary studies, and determine initial TSS requirements. Further quantitative analyses will be used to refine these requirements, define the TSS logic, and build up a description of the TSS architecture where complexity will be minimized in order to meet the requirement for a very high level of reliability. Simultaneously, collaboration continues between the target, accelerator, safety, conventional facilities, and ICS groups to ensure that proper interface definitions exist for the TSS and to prepare for these interfaces as soon as possible. The final Target Safety System design is planned for 2016 with the underlying goal to protect the public from exposure to unsafe levels of radiation and prevent the release of radioactive material beyond permissible limits.

References

[1] Peggs S 2013 *ESS Technical Design Report – chapter 3 Target Station* Available on: http://eval.esss.lu.se/DocDB/0002/000274/013/TDR_online_ver_ch3.pdf
[2] Trahern G, Birch S, Wright P, Nordt A and Coney L 2014 Development of the personnel safety system for the ESS, SO-04-1185874 these proceedings.
[3] EPICS website with comprehensive information available at: http://www.epics.org.

3.11.6

Management of the radioactive waste and emissions within the European Spallation Source facility

Daniela Ene
ESS-AB, Lund, Tunavagen 24, Sweden.

E-mail: daniela.ene@ess.se

Abstract. The European Spallation Source (ESS) is the European common effort in designing and building a next generation large-scale user facility for studies of the structure and dynamics of materials. The schematic layout of the ESS facility is based on a linear driver (linac) directing proton pulses (5 MW of 2 GeV) of 2.86 ms length at 14 Hz onto a tungsten target where neutrons are produced via spallation reactions. Furthermore the neutrons will be moderated to thermal and cold energies by water and liquid hydrogen. These thermal and cold neutrons will be transported by 22 beamlines to the scattering instruments, mainly used for neutron scattering research. This paper reports the status of the waste management plan of the ESS facility and the radiological consequences of the discharge of the radioactive gaseous waste into the environment. Estimations of types and quantities of waste that the ESS project will generate at different stages: commission, operation, and decommissioning were derived using: i) Monte Carlo calculations ii) scaling the activity from the operational experience of the existing spallation sources. Associated waste treatment/conditioning options and final disposal route were further analyzed in order to define the waste type and packet descriptions in agreement with Swedish regulations and policy. Particular attention was devoted to the highly activated components of the target station and its surroundings. First estimates of the radioactive waste water to be produced during ESS operations and solutions for its handling will be provided. An overview of the different aspects of the tritium management in ESS facility will be given. Finally, the source term for atmospheric releases and the radiological assessment of the dose to the critical group will be reported.

Introduction

The development of the waste management plan is an iterative process based on the actual status of the project and consultations with the organizations involved in waste treatment, conditioning, transport and disposal, as well as with the regulator. This paper provides a preliminary waste management plan based on the actual status of the European Spallation Source (ESS) project [1]. The main goals of the ESS waste management plan are: i) to establish the major objectives of the waste management process, ii) to provide estimates of the total ESS waste volumes to be generated, iii) to identify and categorize the waste streams from the ESS facility according to what the different treatment lines can handle and to suitable disposal facilities, iv) to identify, discuss and analyse the management of problematic waste; v) to define the main elements of the management of the radioactivity on ESS site, vi) to define the treatment/conditioning options appropriate for the waste streams and where they will be performed; vii) to define the waste disposal options and assess the disposal volumes needed.

1 Radioactive waste

1.1 Radioactive waste streams and amounts

All radioactive waste from ESS will be handled and disposed of within the Swedish system for management of radioactive waste. The waste classification system used within this work is in accordance with Swedish policy and practice that define the following waste classes: i) free release material; ii) very low level waste (VLLW); iii) SFR-waste: short-lived low- and intermediate level waste (SL-ILW); iv) SFL-waste: long-lived low-and intermediate level waste (LL-ILW); v) Heat generating waste. Swedish regulatory guidelines [2] were used to classify ESS waste based on clearance index approach. The derivation of the waste amounts was based on Monte Carlo calculations for high activated replaceable components during operation and decommissioning or on experience feedback from other similar facilities. As a first estimate, about **25,000 tons of waste** is expected to be sent for final disposal from operation and decommissioning. This figure does not consider VLLW that may be clearable during the lifetime of the facility or after its final shut-down.

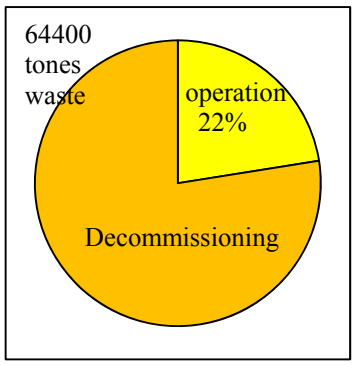

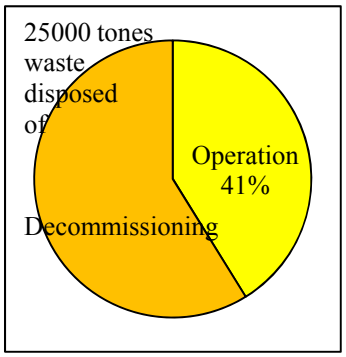

Figure 1. Mass repartition between operation and decommissioning waste: generated waste (left) and waste to be disposed of (right).

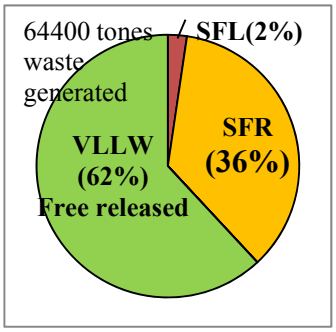

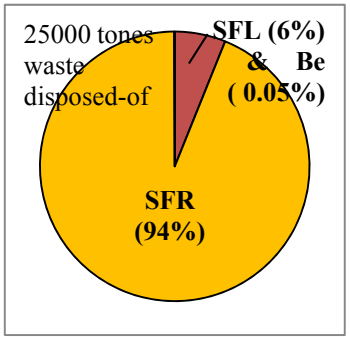

Figure 2. Mass repartition between categories considering both operation and decommissioning waste: generated waste (left) and waste to be disposed of (right).

The figure 1 shows that the major part of the waste will come from decommissioning (about 78%) from the waste generated and (about 59%) of the waste to be disposed of. The difference represents the amount of waste to be free released on site.
As shown in the figure 2 the main part of the radioactive waste (about 62%) may be classified as VLLW and further cleared and as SFR waste, without requiring deep final disposal. The reported values are estimations subjected to evolutions and regular updates. Special consideration was given to waste such: beryllium, tritiated water, spent-ion exchange resins, etc.

1.2 Waste treatment and conditioning options
A concept for optimized radwaste management of the ESS facility was further developed based on experience and lessons learned from nuclear facilities in operation and during decommissioning projects in Sweden. The principle flow chart for different ESS waste streams from the waste generated to disposal, underlying this concept, is shown in figure 3.

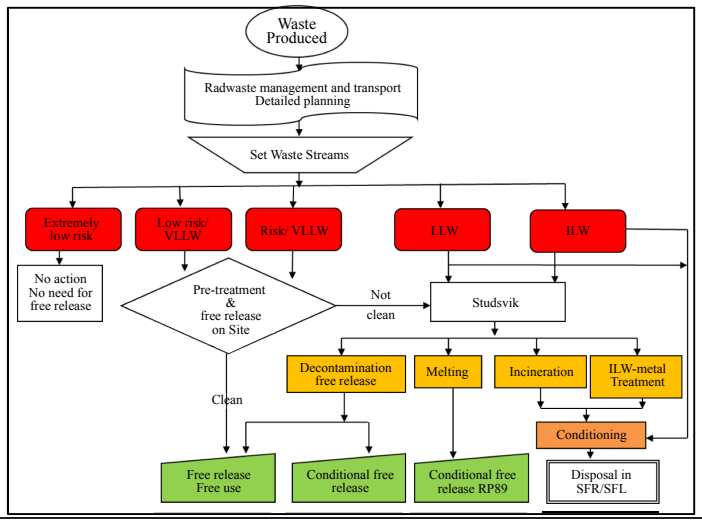

Figure 3. Flow chart for radwaste logistics at the ESS facility during operation.

As is shown in the figure the waste streams were divided into risk-based categories. Treatment/conditioning solutions compatible with the existing experience (where available) in the waste Swedish system were proposed for the identified waste streams. Majority of waste that will not be free released on site will be sent for treatment/conditioning in Studsvik company. In the reference scenario it is considered that spent ion exchange resins and tritiated water arising during the operation of the purification system of the target will be conditioned on-site before shipment. The details of what conditioning processes will be used are still subject to studies.
Careful attention should be given to the ESS waste packages assigned as ILW/SFL type waste because the waste acceptance criteria for SFL disposal facility are not yet assessed. The treatment and conditioning of this type of waste may be performed in Studsvik according to two potential options: i) segmentation and conditioning or ii) melting ILW/encasing ILW in molten LLW. Both potential options mentioned above require an initial investment (cost and time) either for upgrading of an existing facility (the hot cell or the pond) or for commissioning of a new facility (optimized pond or a ILW melting device) in Studsvik. Other potential variant is to use ductile cast iron containers designed to meet requirements for on-site storage, transport and disposal. ESS will work closely with Studsvik and Swedish disposal operator, SKB, to agree on suitable packages.
The final state of ESS VLLW waste could be free release. In Sweden the clearance concept was recently adopted [2] and a code of practice for clearance procedures was developed [3].

This guideline will be used by ESS to create the routines/instructions for the waste free release, in agreement with Swedish regulations.
As requested by Swedish law in the frame of the ESS waste management plan the Best Available Technique (BAT) is being used to determine the optimum logistics for the waste [4]. In this respect emphasis was driven towards evaluation of the pros and contras of the options and finding the optimum solution for handling of the high activated components of the facility.
According with Swedish waste management system practice [5] each waste that is transported to final disposal shall be described in a waste type description (WTD) document**.** In this respect the data about the optimized waste streams and their treatment/conditioning will later be used to prepare the WTD reports for further submittal to the authority for approval.

1.3 Waste disposal. Assessment of disposal volumes needed.
Based on the assessment undertaken here a rough estimation of the waste volumes to be disposed of in Swedish disposal system has been made. Comparing the estimated values with the capacity of existing and planned repositories in Sweden it was found that the ESS waste will take up to 15 % of the disposal volume for the Swedish radioactive waste management system. Additionally collaboration work with SKB is underway to identify indicator nuclides in order to provide input necessary to include ESS waste in the design and safety assessment and make complementary licensing for planned disposal facilities.

1.4 Onsite management of radioactive waste.
An overview of the waste management on the ESS site is also given with emphasis upon the characterization of generated waste and traceability of the waste during the whole process—from the dismantling of the components to the final disposal is an important step in waste management.
ESS intends to use three complementary radiological characterization methods: i) radiation detection, ii) direct Monte Carlo calculations and iii) matrix method [6].
Waste storage options: hot cell and interim storage facility for radioactive materials are analyzed in terms of their capacity requirements and the preliminary data relevant for the waste streams planning. In addition, the design principles and good practices that will be followed to minimize the activity and the volume of radioactive waste generated from ESS facility operation and maintenance

2 Emissions and radiological impacts

The evaluation of the environmental impact of ESS during the design phase, as well as during the operation of the facility is a mandatory request of Swedish Nuclear Authority. Therefore the radiological consequences from potential radioactive waste discharges arising from ESS were also assess. These discharges are in form of gaseous discharges to the atmosphere from a stack, aqueous discharges to public sewer and migration of contaminant with the groundwater. Only airborne releases are presented in this section.

2.1 Source term estimates.
The source term for atmospheric releases can be separated into two distinct release operations:

- On-line emissions, and
- Emissions resulting from processing.

2.1.1 Online emissions
The continuously venting of the air from the tunnel during operation may be assumed also mainly for releasing of the moisture and heat. The ventilation system within the linac tunnel was defined in [7]. The table 1 shows the source term derived based on calculations performed in [8] where 1 Watt/m beam loss was assumed. The effectiveness of the HEPA filters to be used within the tunnel was taken from [9].

Table 1. Source term for airborne release from online operations: contribution from the linac tunnel.

Nuclide	$T_{1/2}$(s)	Chemical form		Production** in the tunnel (Bq/year)	Source Term (Bq/year) r=5/h
C-11	1.22E+03	CO, CO_2	gas	8.92E+10	8.93E+10
N-13	5.98E+02	*NO_2*	*gas*	8.80E+10	8.81E+10
O-15	1.22E+02	O_2	gas	4.92E+10	4.93E+10
Be-7*	4.60E+06	BeO_2	aerosol	2.51E+10	7.56E+06
H-3	3.89E+08	H_2O	vapor	1.87E+09	1.87E+09
Ar41	6.58E+03	Ar	*gas*	1.51E+09	1.51E+09
P-32*	1.23E+06	PO_2	aerosol	4.25E+08	1.28E+05
P-33*	2.19E+06	PO_2	aerosol	9.51E+08	2.86E+05
S-35*	7.54E+06	SO_2	aerosol	2.67E+08	8.01E+04

* Effectiveness of the HEPA filter of 99.97%
** Total volume of the tunnel is 11550 m^3

On-line emissions through the stack into the atmosphere from the target station are supposed to be negligible. This assumption is based on the fact that helium cooling loop of the target is a closed circuit. The amount of volatiles removed from the loop depends on their fractional release from the tungsten target, which in turn depends sensitively on the target operating temperature and accumulated damages. As a conservative assumption for the purpose of assessing environmental impact, in [10] it was assumed that all of the volatiles produced in the target are readily released into the helium coolant. Using further a conservative assumption of 2% per day leakage rate from the pipes of the loop, the release to the environment is given in the table 2.

Table 2. Source term arising from leakage to the environment by the primary helium coolant loop.

Nuclide	Activity in He loop (Bq)	Source Term (Bq/year)
H-3	2.00E+11	8.32E+11
I-125	9.00E+10	3.74E+8*

• A filter effect with (99.9%) was considered for ^{125}I leaked from the He loo

2.1.2 Processing emissions

The main contributions to atmospheric releases arising from processing operations are provided in the table 3. The first two rows show data from on-site cementation of tritiated contaminated water.

This water is a result of the purification loop in the primary target helium and may be generated directly from activated cooling water systems.

The remaining items in the table are resulting from target dismantling. The ^{125}I and ^{148}Gd releases are included for reference, despite low release rates.

Finally, hot cell operations that will cut the target shaft will necessarily generate small releases of activated steel as aerosols, along with small amounts of aggregated and activated tungsten dust. The amounts of airborne particulates are estimated by the following conservative assumptions: 0.1% of the stainless steel in the shaft is cut, and 0.1% of the cut material has a size distribution allowing transport as suspended particles.

These particles will pass through 99.9% efficient HEPA filtration; therefore a release factor of 1E-09 on the shroud is possible, though unlikely. As resulted from table 2 tritium is a big contributor to release and radionuclide inventory at the facility.

Table 3. Source term for airborne release from processing operations.

Nuclide	Chemical form	Activity (Bq)	Release Fraction	Source Term
^{3}H	H20, gas	6.00E+14	1%	6.00E+12 Bq/y
^{125}I	HI, HIO3	1.00E+08	1%	1.00E+06 Bq/y
^{3}H	gas	Wheel:6E14	4.E-5 to 0.1%	2E+9 to 6E+11 Bq/5y
^{181}W	Dust/aerosol	Wheel:10E15	4.00E-08	5.00E+07 Bq/5y
^{179}Ta	Dust/aerosol	Wheel:8E15	4.00E-08	3.00E+07 Bq/5y
^{148}Gd	Dust/aerosol	Wheel:8E11	4.00E-08	3.00E+04 Bq/5y

2.2 Effective dose assessment

2.2.1 Dispersion and deposition

The dispersion was derived applying the standard Gaussian dispersion formula [11]. The main parameters and assumptions used are given in [10]. In this study an overall deposition velocity of about 5 mm s^{-1} to outdoor horizontal surfaces was used. The long-term deposition factor on the ground is then simply estimated multiplying the dispersion value with that velocity. The calculated dispersion and deposition parameter for the ESS reference release point and ESS critical groups are listed in table 4. In the table HL stands for a hypothetical presence reference population group identified just at the border of the land owned by ESS located in the most frequent wind direction.

Table 4. Topological relations and calculated dispersion and deposition factors for the ESS reference release point.

Air release point	Västra Odarslöv farm / HL				Östra Torn farm			
	Distance (m)	Azimuth (°)*	χ (s m^{-3})	ζ (m^{-2})	Distance (m)	Azimuth (°)[1]	χ (s m^{-3})	ζ (m^{-2})
TS edge H = 45 m	660	180/ 90 (HL)	2E-5 (= 50 m, σ_z = 30 m)	1E-7	330	180	5E-6 (σ_y = 30 m, σ_z = 20 m)	2.5E-8

* Degrees from North

2.2.2 Dose calculation

The radio-ecological models, describing the transport, dispersion and accumulation of radioactivity in various environmental matrices, were further combined with radiological models transforming an external exposure or an intake of radioactivity into the effective dose. The methodology that was applied to estimate ingestion dose is based on the ECOSYS model that is implemented in ARGOS system. Essentially, the outcome of the NKS PARDNOR project [12] implemented recently in ECOSYS system was heavily used for the present estimates. The following exposure pathways were assessed for the three age groups of the ESS critical groups:

- External dose from the contaminated plume during its passage
- External dose from deposition of airborne contaminants on surfaces
- External dose from deposition of airborne contaminants on humans
- Internal exposure due to inhalation of radioactive air (direct from the plume and resuspension);
- Internal exposure due to ingestion of radionuclides in: green vegetable, root vegetable, fruits, meat, leaver and milk from caw, sheep, pork and chicken, milk products.

The parameters and assumptions used in calculations are provided in [10].

The table 5 and table 6 give the estimated annual doses break downed by radionuclide and pathway for the local population group living in Vastra Oderslov (the ESS agriculture critical group) and for HL.

Table 5. Annual dose contributions (Sv/y) from release of radionuclides to air during normal operation at a hypothetical reference person placed within the prevalent wind direction (wind blows towards RP during 20% of the year)

Nuclide	Activity*$_{outlet}$ (Bq y^{-1})	Tritium (adult)	Inhalation (1y)	(15 y)	(adult)	External plume	deposition	skin	Total Reference person
H-3	**7.43E+12**	**4.09E-07**							**4.09E-07**
Be-7	1.00E+07		**2.30E-13**	6.79E-14	5.48E-14	5.80E-14	1.02E-11	3.40E-13	1.08E-11
C-11	2.60E+12					2.80E-07			***2.80E-07***
N-13	2.70E+12					2.60E-07			***2.60E-07***
O-15	1.50E+12					5.40E-08			***5.40E-08***
Ar-41	4.10E+10					6.20E-09			6.20E-09
I-125	**3.74E+08**		**8.28E-10**	2.58E-10	1.84E-10	5.28E-13	5.92E-11	2.72E-12	8.90E-10
Total		**3.64E-06**	**4.16E-11**	1.30E-11	9.23E-12	**6.00E-07**	1.32E-11	4.76E-13	**1.01E-06**

Table 6. Annual dose contributions (Sv/y) from routine release of radionuclides to air during normal operation at Vastra Oderslov farm (agriculture group).

Nuclide	Activity*$_{outlet}$ (Bq y^{-1})	Tritium (adult)	Ingestion (1 y)	(15 y)	(adult)	Inhalation (1y)	(15 y)	(adult)	External plume	deposition	skin	Total Reference person
H-3	**7.43E+12**	**4.09E-07**										**4.09E-07**
Be-7	1.00E+07		**2.50E-11**	6.73E-12	5.38E-12	**2.30E-13**	6.79E-14	5.48E-14	2.90E-14	5.10E-12	1.70E-13	3.10E-11
C-11	2.60E+12								1.40E-07			1.40E-07
N-13	2.70E+12								1.30E-07			1.30E-07
O-15	1.50E+12								2.70E-08			2.70E-08
Ar-41	4.10E+10								3.10E-09			3.10E-09
I-125	**3.74E+08**		**9.06E-08**	3.50E-08	2.38E-08	**8.28E-10**	2.58E-10	1.84E-10	2.64E-13	5.92E-11	2.72E-12	9.14E-08
P-32	6.90E+05		**6.56E-06**	8.97E-07	5.59E-07							6.56E-06
P-33	1.10E+06		**1.54E-06**	2.20E-07	1.21E-07							1.54E-06
S-35	2.00E+05		**2.20E-06**	4.00E-07	1.52E-07							2.20E-06
Total		3.64E-06	**1.03E-05**	**1.52E-06**	**8.33E-07**	**4.16E-11**	**1.30E-11**	**9.23E-12**	**3.00E-07**	**8.06E-12**	**3.06E-13**	1.11E-05

3. Conclusion

One of the main outcomes of this report is the descriptions provided on all waste types and the waste management considered. The waste amounts reported here are based upon the baseline design of the facility [1] whose design now enters a more refined stage. The operation/maintenance plans of the facility shall be developed and optimized as well. Therefore the current data are estimations subjected to evolutions and regular updates.

Additionally, this work concludes that all the annual doses to exposed groups as a result of airborne discharges into the environment are a small fraction from 50 μSV y^{-1} ESS limit for members of the public

References

[1] S. Peggs 2013 ESS Technical Design Report http:www.esss.se
[2] SSMFS2011:2 2011 Radiation Safety regulations free release of materials, facilities, buildings and land for activities involving ionizing radiation (in Swedish)
[3] SKB-R11-15 2011 Nuclear industry practice for clearance of materials, rooms and buildings, and land. Tutorial (in Swedish)
[4] Ene, D 2012 Proposal for approach to be used for determining ^{3}H release reduction, Technical Report ESS-0001921
[5] Almqvist, L. 2009 Waste Manual - low and intermediate level waste, version 2.0, Dokument ID 1195328, SKB (in Swedish)
[6] Magistris, M., 2007 *Nucl. Instr. Meth. Phys. Res. B* 626, 182
[7] Engman I 2014 Preliminary design Accelerator building G01 HVAC systems Technical specification Technical report ESS-0007674
[8] Ene D. 2011 *Progress Nucl. Sc. Tech.* 2 382
[9] SSMFS 2008:15 2008 The Swedish Radiation Safety Authority's Regulations concerning Emergency Preparedness at Certain Nuclear Facilities
[10] Ene D 2012 Environmental Impact Analysis Technical report ESSS-0001898
[11] Clarke R.H. 1979 *A model for short and medium range dispersion of radionuclides released to the atmosphere* NRPB-R91 (Harwell, Oxon, UK)
[12] Nielsen, S.P., Andersson, K.G. 2011 *PardNor - PARameters for ingestion Dose models for NORdic areas* NKS-232 (ISBN 978-87-7893-304)

This is a blank page.

Agenda

This is a blank page.

PROGRAM (Oral)

Sep. 29 (Mon) Hall A

Session Integrated Interface (plenary)

Chair: Masatoshi Arai

Organisational interfaces: Past experience and some lessons learned
Roger Pynn (Indiana Univ.)

Neutron moderators, beam extraction and delivery to sample
Feri Mezei (ESS)

Five years of the ISIS second target station from ideas to operational instruments
Sean Langridge (RAL)

Optimisation of the ESS instrument suite for pancake moderators
Ken Andersen (ESS)

Instruments - Advanced modeling of neutron scattering data at SNS and SNS-TS2 approach on moderator - instruments interfaces
Garrett Granroth (ORNL)

Experiences on integrated interface at J-PARC/MLF
Hiroshi Takada (J-PARC)

Session Prominently Progressed Facilities (Plenary)

Chair: Jack Carpenter

ISIS: past, present and future
Robert McGreevy (RAL)

Modernized IBR-2 reactor and first experiments at its neutron beams
Sasha Belushkin (JINR)

The ORNL Spallation Neutron Source (SNS): Status report and future plans
Kevin Jones (ORNL)

Progress of J-PARC/MLF
Masatoshi Arai (J-PARC)

Session Strategies for Next Steps at Facilities (Plenary)

Chair: Hesheng Chen

As for upgrade of PSI
Christian Ruegg (PSI)

ISIS Target Station 1 upgrade project
Matt Fletcher (RAL)

Plans for the Second Target Station at the Oak Ridge National Laboratory Spallation Neutron Source

Ken Herwig (ORNL)

From LANSCE to MaRIE: An experimental facility concept revolutionizing materials in extremes research
John L. Erickson (LANL)

Plan of ADS in J-PARC
Toshinobu Sasa (J-PARC)

Preliminary plan of STS in J-PARC
Masatoshi Futakawa (J-PARC)

Session Reflectometry, SANS

Chair: Robert McGreevy

LoKI- A broad band high flux SANS instrument for the ESS
Andrew Jackson (ESS)

Status of the small and wide angle neutron scattering instrument TAIKAN of J-PARC
Jun-ichi Suzuki (CROSS)

VERITAS, a vertical reflectometer for long pulse neutron sources
Stefan Mattauch (JCNS)

Polarized neutron reflectometry with the interface pulsed neutron source at J-PARC
Masayasu Takeda (J-PARC)

Pulsed source SANS efforts in China
Julian Tao (CSNS)

Session Integrated interface (Evening panel discussion)

Moderator: Roger Pynn

Feri Mezei (ESS), Sean Langridge (RAL), Ken Andersen (ESS), Thomas Proffen (ORNL), Dimitri Argyriou (ESS), Robert McGreevy (RAL), Ken Herwig (ORNL), Masatoshi Arai (J-PARC)

Sep. 29 (Mon) Room 8

Session Safety & Operation for High Power Facilities

Chair: Eric Pitcher

Radioactive material leak accident at the Hadron Experimental Facility and safety measures for operation of the Materials and Life Science Experimental Facility of J-PARC
Yoshimi Kasugai (J-PARC)

Improvements to Lujan Neutron Scattering Center operations plan and sample management system

Charles T. Kelsey (LANL)

Improvement of the J-PARC cryogenic hydrogen system aimed at long-lasting stable operation
Hideki Tatsumoto (J-PARC)

Development of the personnel safety system for the ESS
Garry Traherm (ESS)

Progress of general control system for Materials and Life Science Experimental Facility in J-PARC
Kenji Sakai (J-PARC)

Development of the target safety system for the ESS target station
Linda Coney (ESS)

Management of the radioactive waste and emissions within the European Spallation Source facility
Daniela Ene (ESS)

Sep. 29 (Mon) Room 10

Session Target

Chair: John Hains

Co-chair: Masatoshi Futakawa, Rolando Granada, Bertrand Blau

Implementation of pitting mitigation for the JSNS Hg target
Masatoshi Futakawa (J-PARC)

Operational experience and plans for SNS Hg target
John Galambos (ORNL)

Progress of the ESS monolith design and engineering solutions for target and moderator systems
Rikard Linander (ESS)

Thermal hydraulic design of double-walled mercury target vessel
Katsuhiro Haga (J-PARC)

Post-irradiation examination of the MEGAPIE target
Yong Dai (PSI)

Target station upgrade at LANSCE
Michal Mocko (LANL)

Sep. 30 (Tue) Hall A

Gunter Bauer Memorial

Chair: Masatoshi Arai

Speaker: Jack Carpenter (ANL)

Session Advances in Coming Facilities (Plenary)
Chair: Mark Bourke

European Spallation Source construction update
Jim Yeck (ESS)

As for advances in CSNS
Hesheng Chen (CSNS)

Session Spectroscopy

Chair: Robert McGreevy
Co-chair: Ken Andersen, Kenji Nakajima, Alexander Ioffe

Overview of spectrometers at Materials and Life Science Experimental Facility, J-PARC
Kenji Nakajima (J-PARC)

VOR: A wide bandwidth chopper spectrometer at the ESS to explore uncharted scientific areas.
Pascale Deen (ESS)

T-REX: A time-of-flight reciprocal space explorer for the future ESS source
Nicolo Violini (FZJ)

High throughput inelastic neutron scattering, from fiction to reality
Timmy Ramirez-Cuesta (ORNL)

Session Polarization

Chair: Robert McGreevy
Co-chair: Ken Andersen, Kenji Nakajima, Alexander Ioffe

Polarization at pulsed neutron sources
Alexander Ioffe (FZJ)

MEOP, SEOP and the deployment of polarised neutron capabilities at ANSTO
Wai Tung Hal Lee (ANSTO)

Development of compact laser optics for an in-situ spin-exchange optical pumping ^{3}He neutron spin filter
Takayuki Oku (J-PARC)

Spin manipulation components using high-Tc superconducting materials
David Baxter (LENS)

Sep. 30 (Tue) Room 8

Session Accelerator and Beam Transport #1

Chair: Ken Herwig

Co-Chair: Michikazu Kinsho

J-PARC: The path to 1 MW at J-PARC, including 400 MeV linac improvement, RCS improvements, and plans for frontend upgrades
Kazami Yamamoto (J-PARC)

SNS: Recent advances in power to routine 1.3 - 1.4 MW operation and future plans
John Galambos (ONRL/SNS)

ESS: The current ESS beam design and target interface
Matts Lindroos (ESS)

Session Accelerator and Beam Transport #2

Chair: Ken Herwig
Co-Chair: Michikazu Kinsho

Cyclotron-based high power neutron sources - operating experience and future outlook
Davide Reggiani (PSI)

The path to 2.8 MW operation for the SNS accelerator
John Galambos (ORNL/SNS)

Accelerator upgrades for the ISIS facility
John Thomason (STFC/RAL/ISIS)

Temporal characteristics of the ESS proton and neutron pulses
Tom Shea (ESS)

Instrumentation and machine protection strategy for the ESS target station
Tom Shea (ESS)

X/S-band electron linac based neutron sources for advanced nuclear science & technology & education
Misturu Uesaka (Univ. of Tokyo)

Development of beam shaping system based on non-linear optics at JSNS
Shin-ichiro Meigo (J-PARC)

Recent progress of beam commissioning in the J-PARC 3-GeV rapid cycling synchrotron
Hiroyuki Harada (J-PARC)

Localization of the beam loss caused by the foil scattering for high-intensity routine operation in the J-PARC 3-GeV rapid cycling synchrotron
Shinichi Kato (Tohoku Univ.)

Sep. 30 (Tue) Room 10

Session Utilities and Remote Handling

Chair: John Hains
Co-chair: Masatoshi Futakawa, Rolando Granada, Bertrand Blau

SINQ utilities and remote handling system: 17 years of operational experience
Bertrand Blau (PSI)

Operational experience on utilities and remote handling on ISIS (more than two decades of experience)
David Haynes (ISIS)

The ESS target station hot cell facility and associated logistics
Magnus Gohran (ESS)

Operational experience on utilities and remote handling on J-PARC
Hidetaka Kinoshita (J-PARC)

Session Shielding

Chair: Gunter Muhrer
Co-chair: Yoshiaki Kiyanagi

PHITS code and its application to the JSNS shielding
Koji Niita (RIST)

Shielding design of Mo-99 production facility
Michal Mocko (LANL)

Shielding design at SNS
Franz Gallmeier (ORNL)

Development of helium vessel in CSNS
Li Lin (CSNS)

Shielding design of RIKEN accelerator-driven neutron source (RANS)
Sheng Wang (RIKEN)

High-energy backgrounds at pulsed neutron sources
Nataliia Cherkashyna (ESS)

How much carbon in steel is really needed?
Gunter Muhrer (ESS)

Oct. 1 (Wed) Hall A

Session Blue Sky Session (Panel discussion)

Chair: Andrew Taylor

Dimitri Argyriou (ESS), Jack Carpenter (ANL), Roger Pynn (Indiana Univ.), Henrik Rönnow (ETH), Ferenc Mezei (ESS), Masatoshi Arai (J-PARC), Andrew Taylor (RAL)

Session New Moderator Concept and Compact Source #1 (Plenary)

Chair: Dave Baxter
Co-chair: Michihiro Furusaka

Compact accelerator driven neutron source
Kiyanagi Yoshiaki (Nagoya Univ.)

The pelletized cold neutron moderator at the IBR-2 reactor - The first experience of exploitation
Sergey Kulikov (JINR)

Low-dimensional high brightness hydrogen moderators
Alan Takibayev (ESS)

Oct. 2 (Thu) Hall A

Session Moderator

Chair: John Hains
Co-chair: Masatoshi Futakawa, Rolando Granada, Bertrand Blau

Moderator performance characterization, operational experience, and plans at JSNS
Makoto Teshigawara (J-PARC)

SNS Second Target Station moderator studies
Franz Gallmeier (ORNL)

Moderator configuration choice for ESS
Konstantin Batkov (ESS)

Moderator optimization studies for ESS
Konstantin Batkov (ESS)

Using SSW and ROOT to study advanced brightness features for the ESS
Troels Schonfeldt (ESS)

Characterization and benchmarking of the neutron flux at the SINQ thermal beam lines for the SINQ upgrade project
Vadim Talanov (PSI)

Neutronics modelling for the ISIS TS1 upgrade
Goran P. Skoro (ISIS)

CombLayer: A fast parametric MCNP(X) model contructor
Stuart Ansell (ISIS)

ISIS Target Station 2 reflector modifications
Stephen D. Gallimore (STFC-RAL-ISIS)

Development of moderators and reflectors for CSNS

Wenting Du (CSNS)

The pelletized cold neutron moderator at the IBR-2 reactor, The first experience of exploitation
Sergey Kulikov (JINR)

Technological system for controlling and monitoring operation of the cryogenic moderator at the IBR-2M reactor
Maxim Victorovich Bulavin (JINR)

CAB models for water: New scattering kernels for the interaction of thermal neutrons with water
J. Rolando Granada (Argentine Atomic Energy Commission)

A new method in assisting moderator study at SNS
Wei Lu (ORNL)

Session Diffraction and Imaging

Chair: Robert McGreevy
Co-chair: Ken Andersen, Kenji Nakajima, Alexander Ioffe

Beamline for European Materials Engineering Research
Jochen Fenske (HZB)

HFM-EXED - The high field facility for neutron scattering at HZB
Oleksandr Prokhnenko (HZB)

The new single-crystal neutron Laue diffractometer in Berlin
Gail Iles (HZB)

ODIN - The future imaging instrument at ESS
Markus Strobl (ESS)

The first energy-resolved neutron imaging system in the world - “RADEN” at J-PARC MLF
Takenao Shinohara (J-PARC)

Oct. 2 (Thu) Room 8

Session Data Acquisition and Analysis #1

Chair: Toshiya Otomo
Co-chair: Mark Hagen

Data acquisition for the Spallation Neutron Source
Steven M. Hartman (ORNL)

Developments in data acquisition, reduction and analysis at the SNS
Garret Granroth (SNS)

Architecture of data analysis and management software at CSNS

J.R. Zhang (CSNS)

Data acquisition and device control software framework in MLF, J-PARC
Takeshi Nakatani (J-PARC)

Hardware aspects, modularity and integration of an event mode data acquisition and instrument control for the European Spallation Source ESS AB
T. Gahl (ESS)

Session Data Acquisition and Analysis #2

Chair: Toshiya Otomo
Co-chair: Mark Hagen

Transformation of S(Q,E) to G(r,t) with MEM
Tatsuya Kikuchi (J-PARC)

The center for accelerating materials modeling from SNS data
Stuart Campbell (SNS)

Session New Moderator Concept and Compact Source

Chair: Dave Baxter
Co-chair: Michihiro Furusaka

Combined neutron moderator for the IBR-2 reactor, Project of moderator with continuous change of pellets in the chamber on the basis of the combined moderator, Refrigerator 1200 Watt 10K for neutron moderators, Technical devise and support for moderators
Konstantin Alexandrovich Mukhin (JINR)

An update on the LENS facility for 2014
David V. Baxter (LENS)

Fundamental physics possibilities at the European Spallation Source
Esben Bryndt Klinkby (ESS)

Novel approach of thermal and fast neutron imaging and data analysis at RANS - RIKEN accelerator-driven compact neutron source-
Yoshie Otake (RIKEN)

Session New Moderator Concept and Compact Source (Night session)

Chair: Dave Baxter
Co-chair: Michihiro Furusaka

Convoluted moderators for enhanced slow neutron beam production
Erik B. Iverson (ORNL)

Benchmark experiment on "entrygrooves" in moderator / reflector material
Knud Thomsen (PSI)

Triphenylmethane as a new moderator material
Thomas Huegle (LANL)

Oct. 2 (Thu) Room 9

Session Sample Environments #1

Chair: Zoe Bowden
Co-chair: Kazuya Aizawa

Pulsed high magnetic fields for pulsed neutron sources - Recent progress and applications -
Yasuo Narumi (Tohoku Univ.)

Impact of the cryogen free revolution on operation of ISIS facility
Oleg Kirichek (ISIS, STFC)

Neutron scattering in very high magnetic fields - The new hybrid magnet at Helmholtz Centre Berlin
Peter G Smeibidl (HZB)

10kbar hydrogen intersifier system
Christopher Michael Goodway (ISIS, STFC)

Session Sample Environments #2

Chair: Zoe Bowden
Co-chair: Kazuya Aizawa

Cryogenic loading devices for materials science & engineering studies at J-PARC
Stefanus Harjo (J-PARC)

Concepts for sample manipulation & automation using robotics at ISIS
Matt Rechard North (STFC)

High-pressure and high-temperature neutron experiments using 6-axis multi-anvil press, ATSUHIME
Asami Sano-Furukawa (J-PARC)

Oct. 2 (Thu) Room 10

Session Neutron Optics #1

Chair: Nigel Rhodes
Co-chair: Kazuhiko Soyama

Development of focusing suppermirrors by means of ion beam sputtering and ultra-precise figuring techniques
Dai Yamazaki (J-PARC)

Conceptual design of a reflective focusing system for a small angle neutron scattering instrument
Damian Martin Rodriguez (ESS)

Development of a large multiple segment elliptical neutron focusing mirror

using metal substrate
Shin Takeda (Hokkaido Univ.)

Session Neutron Optics #2

Chair: Nigel Rhodes
Co-chair:Kazuhiko Soyama

Neutron optics at BL06 beam line for spin echo (VIN ROSE)
Masahiro Hino (Kyoto Univ.)

Development of general guide concepts for the European Spallation Source
Carolin Zendler (ESS)

Reflection of slow neutrons from powder of nanorods
Vladimir Ignatovich (JINR)

Session Devices

Chair: Nigel Rhodes
Co-chair: Kazuhiko Soyama

Detector development within the international collaboration on neutron detectors
Nigel Rhodes (RAL)

Development of position-sensitive scintillator neutron detectors at the J-PARC/MLF
Tatsuya Nakamura (J-PARC)

Performance of boron lined straw tubes for large area neutron detectors
Davide Raspino (RAL)

High quality $^{10}B_4C$ coatings for detection of cold neutrons
Gregor Jacek Nowak (HZG)

^{3}He-free triple GEM thermal neutron detector
Antonino Pietropaolo (ENEA)

Development and future prospects of wavelength shifting fibre detectors at ISIS
Garrett Jeff Sykora (RAL)

Development of Ce:LiCAF scintillator system for high precision nuclear data measurement using short pulsed X-band electron linac based neutron source
Daiki Matsuyama (Tokyo Univ.)

Fast neutron imaging system for nondestructive inspection of large-scale concrete structure
Yoshichika Seki (RIKEN)

A vision for detectors for the European Spallation Source ESS AB

Richard J Hall-Wilton (ESS)

Oct. 3 (Fri) Hall A

Workshop Conclusion

Closing Session

Poster Session

Facility Session

Three years of operational experience with the high intensity ultracold neutron source at PSI
Bertrand Blau (PSI)

Comparison of observed and calculated ISIS TS1 neutronic response
Robert Bewley (ISIS)

New Sorgentina Fusion Source (NSFS) - Experimental facility supporting materials research
Patrizio Console Camprini (ENEA Brasimone Research Centre)

Benchmarking the neutronic performance of the cold neutron source at Australia's OPAL reactor
Weijian Lu (ANSTO)

Target and Moderator Development

Pressure wave reduction due to gas microbubbles injection in mercury target of J-PARC
Hiroyuki Kogawa (J-PARC)

In-situ structure integrity evaluation for high-power spallation neutron source using a laser Doppler method
Tao Wan (J-PARC)

Very high-cycle fatigue behavior in mercury target vessel for high-power pulsed spallation neutron source
Xiong Zhihong (Ibaraki Univ.)

Status update on the ESS target systems development
Rikard Linander (ESS)

An investigation into the suitability of additive manufacture techniques for neutron moderator vessels
Stephen D. Gallimore (STFC-RAL-ISIS)

The mockup of the decoupled & poisoned hydrogen moderator in CSNS
Chunming Hu (CSNS)

Brightness measurement of the cold neutron source at SINQ, PSI
Tibor Reiss (PSI)

Development of a small accelerator based cold neutron source
Chris Franklyn (Necsa)

Measurements of neutron beam performance at the Spallation Neutron Source
Erik Iverson (ORNL)

Water helium mixture for use in neutron sources as premoderator, coolant and leak detection at the same time
Yannick Bessler (FZJ)

Welding processes of high-strength aluminum alloys for using in cold sources
Yannick Bessler (FZJ)

Engineering perspective of the ESS moderator and reflector systems
Rikard Linander (ESS)

Progress of the Au-In-Cd alloy decoupler development in JSNS
Motoki Ooi (JAEA)

Very high-cycle fatigue behavior in mercury target vessel for high-power pulsed spallation neutron source
Takashi Naoe (J-PARC)

Progress on the design of the target station for the European Spallation Source
Eric J. Pitcher (ESS)

Alternative target designs for power upgrade of the TS1 target at the ISIS neutron facility
Cristian Bungau (Univ. of Huddersfield)

Integrated Interface

Fast neutron applications at ESS
Alberto Milocco (Univ. of Milano-Bicocca)

Thermal hydraulic and thermo-mechanical design of the proton beam window for ESS
Jorg Wolters (FZJ)

Accelerator and Beam Transport

Plasma window study for gas target
Kun Zhu (Peking Univ.)

Challenges for next generation accelerator-based neutron sources
Kevin W. Jones (ORNL)

Neutron Instruments

Chopper system and neutron optics of the beamline for European Materials Engineering Research (BEER) at ESS
Mustapha Rouijaa (Helmholtz-Zentrum Geesthacht)

Polarized ^{3}He development at SNS
Xin Tong (ORNL)

SIMRES - A simulation tool for development of neutron scattering instruments at reactor and spallation sources
Jan Saroun (Nuclear Physics Institute ASCR)

Towards the high-sensitive detection of hydrogen based on the proton polarization technique in neutron protein crystallography
Ichiro Tanaka (Ibaraki Univ.)

Overview of the McStas monte carlo ray-tracing instrument simulation project
Peter K Willendrup (DTU Physics)

Instrument developments and neutron Brillouin scattering experiments on HRC
Shinichi Itoh (KEK)

Recent status of a cold neutron disk chopper spectrometer AMATERAS
Kenji Nakajima (J-PARC)

Development of polarized and focused neutron beam at the small and wide angle neutron scattering instrument TAIKAN
Kazuki Ohishi (CROSS)

TOF studies of multiple Bragg reflections in cylindrically bent prefect crystals at small pulsed neutron source
Pavol Mikula (Nuclear Physics Institute of the ASCR, v.v.i.)

General purpose powder diffractometer at CSNS
Le Kang (IHEP)

High resolution SESANS with time gradient magnetic fields spectrometer: Feasibility study for the implementation at long pulsed neutron sources
Raul V. Erhan (IFIN-HH)

Multitask approach for neutron beam lines at spallation neutron sources
Antonino Pietropaolo (Consiglio Nazionale delle Ricerche-Istituto dei Sistemi Complessi)

Monte Carlo simulations for the EPSILON and SKAT long flight path diffractometers at the IBR-2 pulsed neutron source

Raul Victor Erhan (JINR, Dubna)

Recent progress in the chopper spectrometer 4SEASONS at J-PARC
Ryoichi Kajimoto (J-PARC)

Present status of BL19 TAKUMI at J-PARC
Stefanus Harjo (J-PARC)

Concept of multi-purpose extreme conditions instrument for the ESS
Oleksandr Prokhnenko (Helmholtz-Zentrum Berlin)

Progress on POLANO spectrometer for polarized neutron experiment
Tetsuya Yokoo (KEK)

MAGIC chopper: theory, simulation, and experimental evaluation
Mitsutaka Nakamura (J-PARC)

Design of neutron guide system for high-flux reactor PIK
Peter Konik (Petersburg Nuclear Physics Institute)

Development of a medium and small angle neutron scattering instrument iANS optimized for compact accelerator driven neutron source
Toshinori Ishida (Hokkaido Univ.)

Magnetic shield design of in-situ SEOP polarized ^{3}He neutron spin filter for high magnetic field sample environment accessories at J-PARC
Hiroshi Kira (CROSS)

Neutron diffractometer encompassing protein crystals with large unit cell volume at J-PARC
Kazuo Kurihara (JAEA)

Using Fermi choppers for spallation source based chopper spectrometers
Jorg J Voigt (Forschungszentrum Julich)

Current status of the small and wide angle neutron scattering instrument TAIKAN at J-PARC
Shin-ichi Takata (J-PARC)

Design of the new SANS instruments on CPHS
Huarui Wu (Tsinghua Univ.)

The time-of-flight ultra-small-angle neutron scattering (TOF-USANS) instrument at SNS: Commissioning started in August 2014
Jack Carpenter (ANL)

Band chopper: a solution for large beams and limited space
Alexander Ioffe (Juelich Centre for Neutron Science)

Thermal neutron tomography and transmission spectroscopy at RIKEN accelerator-driven compact neutron source
Masako Yamada (RIKEN)

Multi pulse-shaped incident energy band measurements on the TOF type near backscattering spectrometer DNA in J-PARC
Kaoru Shibata (J-PARC)

Current status of a TOF-Laue single crystal neutron diffractometer SENJU
Takashi Ohhara (J-PARC)

Applications of new neutron beam monitor (nGEM)
Hidetoshi Ohshita (KEK)

A radial collimator for a time-of-flight neutron spectrometer
Jennifer Lynn Niedziela (ORNL)

Devices

Development of a flexible neutron supermirror sheet and its application
Masahiro Hino (Kyoto Univ.)

Development of an in-situ SEOP ^{3}He neutron spin filter for magnetic imaging techniques at J-PARC
Hirotoshi Hayashida (CROSS)

A neutron imaging detector based on the muPIC micro-pixel chamber and its application to magnetic imaging with polarized, pulsed neutrons at J-PARC
Joseph D Parker (CROSS)

Research on a metallic-ellipsoidal mirror for focusing neutron beams
Jiang Guo (RIKEN)

Development of a 2012 model for the ^{6}Li time analyzer (LiTA12) detector system
Setsuo Satoh (KEK)

Development of various shielding devices to suppress background in J-PARC
Wataru Kambara (J-PARC)

The estimation of the crystallinity on the silicon wafer surface which was coating Gd thin film on the backside, by the double crystal X-ray diffraction method
Kaoru Shibata (J-PARC)

Sample Environments

Recent progress in sample environment at CSNS
Haitao Hu (Chinese Academy of Sciences)

Light irradiation experiments at J-PARC - Installation and demonstration
Yoshifumi Sakaguchi (CROSS)

Present status of sample environment at J-PARC MLF
Tomokazu Aso (J-PARC)

In-situ scattering experiment under high pressure hydrogen gas by high-intensity total diffractometer, NOVA
Kazutaka Ikeda (KEK)

Shielding

A study of the neutron backgrounds at SINQ
Douglas David DiJulio (ESS)

Data Acquisition and Analysis

Mantid data reduction and visualization at SNS and HFIR
Peter F Peterson (ORNL)

Neutron diffraction imaging at NOVA (J-PARC) and HRPD, RESA, and TNRF (JRR-3)
Shinichi Shamoto (JAEA)

Automation of neutron spectrometry experiments using network technologies
Vladimir K. Ignatovich (FLNP JINR)

^{6}Li/^{7}Li and ^{14}N/^{15}N isotopic substitution experiments using NOVA spectrometer at J-PARC
Yasuo Kameda (Yamagata Univ.)

Abstract programming interface for MCTAL files
Nicolo Borghi (ESS)

Neutron diffraction study of piezoelectric material under cyclic electric field using event recording technique
Takuro Kawasaki (JAEA)

The data management and software centre for the ESS
Mark Edward Hagen (ESS)

Z-MEM & Z-3D, maximum entropy method and visualization software for electron/nuclear density distribution in Z-Code
Yoshihisa Ishikawa (J-PARC, IMSS, KEK)

Monte Carlo simulation of the resolution ellipsoid for the SEQUOIA spectrometer
Garrett E. Granroth (ORNL)

Web monitor and prototype analysis at the SNS
Garrett E. Granroth (ORNL)

New Moderator Concept and Compact Source

Control system of filling of chamber for cryogenic moderator of IBR-2 research reactor
Alexandr Evgenyevich Verhoglyadov (JINR)

Design on target and moderator of X-band compact electron linac neutron source for short pulsed neutrons
Kazuhiro Tagi (Tokyo Univ.)

Approximate S(a,b) program for H_2 containing MOFs and other confined systems
Stuart Ansell (RAL)

Safety & Operation for High Power Facilities

Neutron guide activation and handling for the European Spallation Source
Zsofia Kokai (ESS)

Studies of magnet activation due to beam losses and back-scattered neutrons
Cristian Bungau (Univ. of Huddersfield)

List of Attendees

This is a blank page.

Index	Given Name	Middle	Family Name	Affiliation	E-mail Address
A	Kazuya		Aizawa	J-PARC Center, Japan Atomic Energy Agency (JAEA)	aizawa.kazuya@jaea.go.jp
	Ken		Andersen	European Spallation Source, (ESS)	ken.andersen@esss.se
	Stuart		Ansell	ISIS, Rutherford Appleton Laboratory (RAL)	stuart.ansell@stfc.ac.uk
	Masatoshi		Arai	J-PARC Center, Japan Atomic Energy Agency (JAEA)	masaarai@hotmail.co.jp
	Junko		Arai		
	Dimitri	N.	Argyriou	European Spallation Source, (ESS)	dimitri.argyriou@esss.se
	Tomokazu		Aso	J-PARC Center, Japan Atomic Energy Agency (JAEA)	aso.tomokazu@jaea.go.jp
B	Konstantin		Batkov	European Spallation Source, (ESS)	kbat.amarysjtb@lizardie.com
	David	V.	Baxter	Indiana University	baxterd@indiana.edu
	Alexander	V.	Belushkin	Frank Laboratory of Neutron Physics, JINR	belushk@nf.jinr.ru
	Djelloul		Benzaid	KHEMIS MILIANA UNIVERSITY	benzaidhd@yahoo.com
	Yannick		Bessler	Forschungszentrum Juelich	y.bessler@fz-juelich.de
	Robert		Bewley	ISIS, Rutherford Appleton Laboratory (RAL)	robert.bewley@stfc.ac.uk
	Bertrand		Blau	Paul Scherrer Institut (PSI)	bertrand.blau@psi.ch
	Mark	A.	Bourke	Los Alamos National Laboratory (LANL)	bourke@lanl.gov
	Zoe	A.	Bowden	ISIS, Rutherford Appleton Laboratory (RAL)	zoe.bowden@stfc.ac.uk
	Thomas		Brueckel	Forschungszentrum Juelich	t.brueckel@fz-juelich.de
	Maxim	V.	Bulavin	Joint institute for nuclear research	bulavin85@inbox.ru
	Cristian		Bungau	University of Huddersfield	C.Bungau@hud.ac.uk
	Michael		Butzek	Forschungszentrum Juelich	m.butzek@fz-juelich.de
C	Stuart	I.	Campbell	Oak Ridge National Laboratory (ORNL)	campbellsi@ornl.gov
	John	M.	Carpenter	Argonne National Laboratory (ANL), Oak Ridge National Laboratory (ORNL)	rdcarp2@yahoo.com
	Rhonda	D.	Carpenter		
	Nataliia		Cherkashyna	European Spallation Source, (ESS)	nataliia.cherkashyna@esss.se
	Seiko		Ohira－Kawamura	J-PARC Center, Japan Atomic Energy Agency (JAEA)	seiko.kawamura@j-parc.jp
	Linda	R.	Coney	European Spallation Source, (ESS)	linda.coney@esss.se
	Robert		Connatser	European Spallation Source, (ESS)	robert.connatser@esss.se
	Lisa		Connatser		
D	Yong		Dai	Paul Scherrer Institut (PSI)	yong.dai@psi.ch
	Wanpei		Dai-Liu		
	Pascale		Deen	European Spallation Source, (ESS)	pascale.deen@esss.se
	Douglas	D.	DiJulio	European Spallation Source, (ESS)	douglas.dijulio@esss.se
	Wenting		Du	China Spallation Neutron Source (CSNS), Institute of High Energy Physics	duwt@ihep.ac.cn
E	Shinichiro		Ejiri	TAIYO NIPPON SANSO CORPORATION	
	Daniela	A.	Ene	European Spallation Source, (ESS)	daniela.ene@esss.se
	Raul	V.	Erhan	Horia Hulubei National Institute for R&D in Physics and Nuclear Engineering	raul.erhan@gmail.com
	John	L.	Erickson	Los Alamos National Lab (LANL)	jerickson@lanl.gov
	Pamela	A.	Erickson		
	Mohammad		Eshraqi	European Spallation Source, (ESS)	mohammad.eshraqi@esss.se
F	Maksym		Fainberg		
	Jochen		Fenske	Helmholtz-Zentrum Geesthacht	jochen.fenske@hzg.de
	Matt		Fletcher	ISIS, Rutherford Appleton Laboratory (RAL)	matt.fletcher@stfc.ac.uk
	Chris		Franklyn	South African Nuclear Energy Corporation	cbfranklyn@gmail.com
	Norihisa		Fujioka	SEIKO EG&G	norihisa.fujioka@sii.co.jp
	Kentaro		Fukuda	Tokuyama Corporation	
	Ramona		Furiani		
	Michihiro		Furusaka	Hokkaido University	
	Masatoshi		Futakawa	J-PARC Center, Japan Atomic Energy Agency (JAEA)	futakawa.masatoshi@jaea.go.jp
G	Thomas		Gahl	European Spallation Source, (ESS)	thomas.gahl@esss.se
	John		Galambos	Oak Ridge National Laboratory (ORNL)	jdg@ornl.gov
	Stephen	D.	Gallimore	ISIS, Rutherford Appleton Laboratory (RAL)	stephen.gallimore@stfc.ac.uk
	Franz	X.	Gallmeier	Oak Ridge National Laboratory (ORNL)	gallmeierfz@ornl.gov

Index	Given Name	Middle	Family Name	Affiliation	E-mail Address
	Magnus		Gohran	European Spallation Source, (ESS)	magnus.gohran@esss.se
	Christopher	M.	Goodway	ISIS Facility, STFC, Rutherford Appleton Laboratory	Chris.Goodway@stfc.ac.uk
	J.	R.	Granada	Argentine Atomic Energy Commission	granada@cnea.gov.ar
	Garrett	E.	Granroth	Oak Ridge National Laboratory (ORNL)	granrothge@ornl.gov
	Jiang		Guo	RIKEN	jiang.guo@riken.jp
H	Katsuhiro		Haga	J-PARC Center, Japan Atomic Energy Agency (JAEA)	haga.katsuhiro@jaea.go.jp
	Mark	E.	Hagen	European Spallation Source, (ESS)	mark.hagen@esss.se
	John	R.	Haines	European Spallation Source, (ESS)	john.haines@esss.se
	Richard	J.	Hall-Wilton	European Spallation Source, (ESS)	richard.hall-wilton@esss.se
	Takayasu		Hanashima	Comprehensive Research Organization for Science and Society (CROSS)	taka.hana8740@gmail.com
	Hiroyuki		Harada	J-PARC Center, Japan Atomic Energy Agency (JAEA)	hharada@post.j-parc.jp
	Stefanus		Harjo	J-PARC Center, Japan Atomic Energy Agency (JAEA)	stefanus.harjo@j-parc.jp
	Steven	M.	Hartman	Oak Ridge National Laboratory (ORNL)	hartmansm@ornl.gov
	Kazutaka		Hayashi	Mitsubishi Electric	
	Hirotoshi		Hayashida	Comprehensive Research Organization for Science and Society (CROSS)	h_hayashida@cross.or.jp
	David	J.	Haynes	ISIS, Rutherford Appleton Laboratory (RAL)	david.haynes@stfc.ac.uk
	Kenneth	W.	Herwig	Oak Ridge National Laboratory (ORNL)	herwigkw@ornl.gov
	Noriyuki		Hikida	Toshiba Electron Tubes & Devices Co.,Ltd.	noriyuki.hikida@toshiba.co.jp
	Masahiro		Hino	Research Reactor Institute, Kyoto University	hino@rri.kyoto-u.ac.jp
	Fujio		Hiraga	Hokkaido University	hiraga@eng.hokudai.ac.jp
	Takuya		Hosobata	RIKEN	takuya.hosobata@riken.jp
	Chunming		Hu	China Spallation Neutron Source (CSNS), Institute of High Energy Physics	hucm@ihep.ac.cn
	Haitao		Hu	China Spallation Neutron Source (CSNS), Institute of High Energy Physics	huht@ihep.ac.cn
	Thomas		Huegle	Los Alamos NAtional Laboratory	huegle@lanl.gov
I	Vladimir	K.	Ignatovich	FLNP JINR	v.ignatovi@gmail.com
	Kazuki		Iida	Comprehensive Research Organization for Science and Society (CROSS)	k_iida@cross.or.jp
	Yuki		Iinuma		
	Kazutaka		Ikeda	J-PARC Center, High Energy Accelerator Research Organization (KEK)	kikeda@post.j-parc.jp
	Gail	N.	Iles	Helmholtz-Zentrum Berlin	gail.iles@helmholtz-berlin.de
	Yoji		Inui	Tokuyama Corporation	
	Alexander		Ioffe	Forschungszentrum Juelich	a.ioffe@fz-juelich.de
	Svetlana		Ioffe		
	Toshinori		Ishida	Hokkaido University	rinkyo.ishida@eng.hokudai.ac.jp
	Motoyuki		Ishikado	Comprehensive Research Organization for Science and Society (CROSS)	m_ishikado@cross.or.jp
	Yoshihisa		Ishikawa	European Spallation Source, (ESS)	yoshihisa.ishikawa@j-parc.jp
	Shinichi		Itoh	J-PARC Center, High Energy Accelerator Research Organization (KEK)	shinichi.itoh@kek.jp
	Erik	B.	Iverson	Oak Ridge National Laboratory (ORNL)	iversoneb@ornl.gov
	Yoshihisa		Iwashita	Kyoto University	iwashita@kyticr.kuicr.kyoto-u.ac.jp
J	Andrew	J	Jackson	European Spallation Source, (ESS)	andrew.jackson@esss.se
	Kevin	W.	Jones	Oak Ridge National Laboratory (ORNL)	joneskw@ornl.gov
	Cindi		Jones		
K	Ryoichi		Kajimoto	J-PARC Center, Japan Atomic Energy Agency (JAEA)	ryoichi.kajimoto@j-parc.jp
	Kazuhisa		Kakurai	Quantum Beam Science Center (QuBS), Japan Atomic Energy Agency (JAEA)	kakurai.kazuhisa@jaea.go.jp
	Kazuya		Kamazawa	Comprehensive Research Organization for Science and Society (CROSS)	k_kamazawa@cross.or.jp
	Wataru		Kambara	J-PARC Center, Japan Atomic Energy Agency (JAEA)	kambara.wataru@jaea.go.jp
	Yasuo		Kameda	Yamagata University	kameda@sci.kj.yamagata-u.ac.jp
	Sayaka		Kameda		
	Saulius		Kaminskas	Oak Ridge National Laboratory (ORNL)	kaminskass@ornl.gov

Index	Given Name	Middle	Family Name	Affiliation	E-mail Address
	Laura		Kaminskas		
	Hiroshi		Kanasaki	TOSHIBA ELECTRON TUBES & DEVICES CO., LTD	
	Koji		Kaneko	Quantum Beam Science Center (QuBS), Japan Atomic Energy Agency (JAEA)	
	Le		Kang	Institute of High Energy Physics, Chinese Academy of Science	kangl@ihep.ac.cn
	Yoshimi		Kasugai	J-PARC Center, Japan Atomic Energy Agency (JAEA)	kasugai.yoshimi@jaea.go.jp
	Shinichi		Kato	Graduate School of Sience,Tohoku University	skato@post.j-parc.jp
	Yukinobu		Kawakita	J-PARC Center, Japan Atomic Energy Agency (JAEA)	yukinobu.kawakita@j-parc.jp
	Takuro		Kawasaki	J-PARC Center, Japan Atomic Energy Agency (JAEA)	takuro.kawasaki@j-parc.jp
	Lana	D.	Kelsey		
	Mary-Margaret	E.	Kelsey		
	Charles	T.	Kelsey IV	Los Alamos National Laboratory (LANL)	ckelsey@lanl.gov
	Tatsuya		Kikuchi	J-PARC Center, Japan Atomic Energy Agency (JAEA)	
	Hidetaka		Kinoshita	J-PARC Center, Japan Atomic Energy Agency (JAEA)	kinoshita.hidetaka@jaea.go.jp
	Michikazu		Kinsho	J-PARC Center, Japan Atomic Energy Agency (JAEA)	kinsho.michikazu@jaea.go.jp
	Hiroshi		Kira	Comprehensive Research Organization for Science and Society (CROSS)	h_kira@cross.or.jp
	Oleg		Kirichek	ISIS, Rutherford Appleton Laboratory (RAL)	oleg.kirichek@stfc.ac.uk
	Koji		Kiriyama	Comprehensive Research Organization for Science and Society (CROSS)	k_kiriyama@cross.or.jp
	Oliver		Kirstein	European Spallation Source, (ESS)	oliver.kirstein@esss.se
	Yoshiaki		Kiyanagi	Nagoya University	kiyanagi@phi.phys.nagoya-u.ac.jp
	Esben	B.	Klinkby	Technical University of Denmark & European Spallation Source	esbe@dtu.dk
	Hiroyuki		Kogawa	J-PARC Center, Japan Atomic Energy Agency (JAEA)	kogawa.hiroyuki@jaea.go.jp
	Zsofia		Kokai	European Spallation Source, (ESS)	zsofia.kokai@esss.se
	Hideto		Komazuka	GE Energy Japan	hideto.komazuka@ge.com
	Peter		Konik	Petersburg Nuclear Physics Institute	104pet104@gmail.com
	Sergey		Kulikov	Joint Institute for Nuclear Research	ksa@nf.jinr.ru
	Takayuki		Kumakura	ONO SOKKI CO.,LTD	
	Kazuo		Kurihara	Quantum Beam Science Center (QuBS), Japan Atomic Energy Agency (JAEA)	kurihara.kazuo@jaea.go.jp
L	Sean		Langridge	ISIS, Rutherford Appleton Laboratory (RAL)	sean.langridge@stfc.ac.uk
	Wai Tung		Lee	Australian Nuclear Science and Technology Organisation	wtl@ansto.gov.au
	Li		Lin	Institute of High Energy Physics, Chinese Academy of Sciences	linli@ihep.ac.cn
	Rikard		Linander	European Spallation Source, (ESS)	rikard.linander@esss.se
	Mats	A.	Lindroos	European Spallation Source, (ESS)	mats.lindroos@esss.se
	Wei		Lu	Oak Ridge National Laboratory (ORNL)	luw2@ornl.gov
	Weijian		Lu	Australian Nuclear Science and Technology Organisation (ANSTO)	wjl@ansto.gov.au
	Daniel		Lyngh	European Spallation Source, (ESS)	daniel.lyngh@esss.se
M	Damian		Martin Rodriguez	European Spallation Source, (ESS)	damian.rodriguez@esss.se
	Masako		Yamada	RIKEN	yamadamasako@riken.jp
	Daiki		Matsuyama	the University of Tokyo	matsuyama.daiki@nuclear.jp
	Stefan		Mattauch	Forschungszentrum Juelich	s.mattauch@fz-juelich.de
	Robert	L.	McGreevy	ISIS, Rutherford Appleton Laboratory (RAL)	robert.mcgreevy@stfc.ac.uk
	Shin-ichiro		Meigo	J-PARC Center, Japan Atomic Energy Agency (JAEA)	meigo.shinichiro@jaea.go.jp
	Ferenc		Mezei	European Spallation Source, (ESS)	ferenc.mezei@esss.se
	Pavol		Mikula	Nuclear Physics Institute ASCR	mikula@ujf.cas.cz
	Alberto		Milocco	University of Milano-Bicocca	alberto.milocco@mib.infn.it
	Noboru		Miyata	Comprehensive Research Organization for Science and Society (CROSS)	n_miyata@cross.or.jp
	Manabu		Mochizuki	SUGA ZOUKEI KOGYO Co. Ltd.	
	Michal		Mocko	Los Alamos National Laboratory (LANL)	mmocko@lanl.gov
	Guenter		Muhrer	European Spallation Source, (ESS)	gunter.muhrer@esss.se

Index	Given Name	Middle	Family Name	Affiliation	E-mail Address
	Konstantin	A.	Mukhin	Joint Institute for Nuclear Research	kostik001@mail.ru
	Koji		Munakata	Comprehensive Research Organization for Science and Society (CROSS)	
N	Hiroaki		Nakagawa	Kyoritsu Electric Corporation	
	Kenji		Nakajima	J-PARC Center, Japan Atomic Energy Agency (JAEA)	kenji.nakajima@j-parc.jp
	Mitsutaka		Nakamura	J-PARC Center, Japan Atomic Energy Agency (JAEA)	mitsutaka.nakamura@j-parc.jp
	Tatsuya		Nakamura	J-PARC Center, Japan Atomic Energy Agency (JAEA)	nakamura.tatsuya@jaea.go.jp
	Ichiro		Nakamura		
	Noriaki		Nakao	Shimizu Corporation	
	Takeshi		Nakatani	J-PARC Center, Japan Atomic Energy Agency (JAEA)	takeshi.nakatani@j-parc.jp
	Takashi		Naoe	J-PARC Center, Japan Atomic Energy Agency (JAEA)	naoe.takashi@jaea.go.jp
	Yasuo		Narumi	Institute for Materials Research, Tohoku University	narumi@imr.tohoku.ac.jp
	Kenji		Naruse	Bee Beans Technologies Co.,Ltd.	
	Jennifer	L.	Niedziela	Oak Ridge National Laboratory (ORNL)	niedzielajl@ornl.gov
	Koji		Niita	Research Organization for Information Science and Technology	niita@rist.or.jp
	Hiroyuki		Nojiri	Institute for Materials Research, Tohoku University	
	Matt	R.	North	ISIS, Rutherford Appleton Laboratory (RAL)	matt.north@stfc.ac.uk
	Gregor	J.	Nowak	Helmholtz-Zentrum Geesthacht	Gregor.Nowak@hzg.de
O	Ulf	K.	Oden	European Spallation Source, (ESS)	ulf.oden@esss.se
	Takashi		Ohhara	J-PARC Center, Japan Atomic Energy Agency (JAEA)	takashi.ohhara@j-parc.jp
	Kazuki		Ohishi	Comprehensive Research Organization for Science and Society (CROSS)	k_ohishi@cross.or.jp
	Hidetoshi		Ohshita	J-PARC Center, High Energy Accelerator Research Organization (KEK)	ohshita@post.kek.jp
	Takayuki		Oku	J-PARC Center, Japan Atomic Energy Agency (JAEA)	takayuki.oku@j-parc.jp
	Natsuki		Okuda	Visible Information Center, Inc.	
	Motoki		Ooi	J-PARC Center, Japan Atomic Energy Agency (JAEA)	ohi.motoki@jaea.go.jp
	Yoshie		Otake	RIKEN	yotake@riken.jp
P	Joseph	D.	Parker	Comprehensive Research Organization for Science and Society (CROSS)	j_parker@cross.or.jp
	Peter	F.	Peterson	Oak Ridge National Laboratory (ORNL)	petersonpf@ornl.gov
	Antonino		Pietropaolo	ENEA Frascati Research Centre-Nuclear Technologies Laboratory	antonino.pietropaolo@enea.it
	Eric	J.	Pitcher	European Spallation Source, (ESS)	eric.pitcher@esss.se
	Daniel	E.	Pooley	ISIS, Rutherford Appleton Laboratory (RAL)	daniel.pooley@stfc.ac.uk
	Oleksandr		Prokhnenko	Helmholtz-Zentrum Berlin	prokhnenko@helmholtz-berlin.de
	Roger		Pynn	Indiana University	rpynn@indiana.edu
R	AJ (Timmy)		Ramirez-Cuesta	Group Leader Chemical Spectroscopy	ramirezcueaj@ornl.gov
	Davide		Raspino	ISIS, Rutherford Appleton Laboratory (RAL)	davide.raspino@stfc.ac.uk
	Davide		Reggiani	Paul Scherrer Institut (PSI)	davide.reggiani@psi.ch
	Tibor		Reiss	Paul Scherrer Institut (PSI)	tibor.reiss@psi.ch
	Nigel	J.	Rhodes	ISIS, Rutherford Appleton Laboratory (RAL)	nigel.rhodes@stfc.ac.uk
	Thomas	H.	Rod	European Spallation Source, (ESS)	thomas.rod@esss.se
	HENRIK	M.	Ronnow	EPFL-LQM, RIKEN-CEMS & ISSP	
	Mustapha		Rouijaa	Helmholtz-Zentrum Geesthacht	mustapha.rouijaa@hzg.de
	Christian		Rueegg	Paul Scherrer Institute (PSI) and University of Geneva	christian.rueegg@psi.ch
S	Yoshifumi		Sakaguchi	Comprehensive Research Organization for Science and Society (CROSS)	y_sakaguchi@cross.or.jp
	Kenji		Sakai	J-PARC Center, Japan Atomic Energy Agency (JAEA)	kenji.sakai@j-parc.jp
	Kaoru		Sakasai	J-PARC Center, Japan Atomic Energy Agency (JAEA)	sakasai.kaoru@jaea.go.jp
	Asami		Sano-Furukawa	Quantum Beam Science Center (QuBS), Japan Atomic Energy Agency (JAEA)	sano.asami@jaea.go.jp
	Jan		Saroun	Nuclear Physics Institute ASCR	saroun@ujf.cas.cz
	Toshinobu		Sasa	J-PARC Center, Japan Atomic Energy Agency (JAEA)	sasa.toshinobu@jaea.go.jp
	Setsuo		Satoh	J-PARC Center, High Energy Accelerator Research Organization (KEK)	setsuo.satoh@kek.jp
	Masaru		Sawahata	KANTOGIKEN CO.LTD	

Index	Given Name	Middle	Family Name	Affiliation	E-mail Address
	Toshihiro		Sawahata	Metal Technology Co. Ltd.	
	Christian		Scheffzuek	KIT Karlsruhe	christian.scheffzuek@kit.edu
	Troels		Schonfeldt	European Spallation Source, (ESS) & DTU Nutech	trsch@dtu.dk
	Yoshichika		Seki	RIKEN	yseki@riken.jp
	Hideki		Seto	J-PARC Center, High Energy Accelerator Research Organization (KEK)	hideki.seto@kek.jp
	Shinichi		Shamoto	Quantum Beam Science Center (QuBS), Japan Atomic Energy Agency (JAEA)	shamoto.shinichi@jaea.go.jp
	Thomas	J.	Shea	European Spallation Source, (ESS)	thomas.shea@esss.se
	Kaoru		Shibata	J-PARC Center, Japan Atomic Energy Agency (JAEA)	shibata.kaoru@jaea.go.jp
	Takenao		Shinohara	J-PARC Center, Japan Atomic Energy Agency (JAEA)	takenao.shinohara@j-parc.jp
	Goran	P.	Skoro	ISIS, Rutherford Appleton Laboratory (RAL)	goran.skoro@stfc.ac.uk
	Peter	G.	Smeibidl	Helmholtz Centre Berlin	peter.smeibidl@helmholtz-berlin.de
	Raffaello		Sobbia	Paul Scherrer Institut (PSI)	raffaello.sobbia@psi.ch
	Kazuhiko		Soyama	J-PARC Center, Japan Atomic Energy Agency (JAEA)	
	Markus		Strobl	European Spallation Source, (ESS)	markus.strobl@esss.se
	Hiroyuki		Sugiyama	Hamamatsu Photonics	hsugi@etd.hpk.co.jp
	Jun-ichi		Suzuki	Comprehensive Research Organization for Science and Society (CROSS)	j_suzuki@cross.or.jp
	Garrett	J.	Sykora	ISIS, Rutherford Appleton Laboratory (RAL)	jeff.sykora@stfc.ac.uk
T	Kazuhiro		Tagi	Faculty of Engineering, Tokyo University	tagi@nuclear.jp
	Hiroshi		Takada	J-PARC Center, Japan Atomic Energy Agency (JAEA)	hiroshi.takada@j-parc.jp
	Shin-ichi		Takata	J-PARC Center, Japan Atomic Energy Agency (JAEA)	shinichi.takata@j-parc.jp
	Masayasu		Takeda	Quantum Beam Science Center (QuBS), Japan Atomic Energy Agency (JAEA)	takeda.masayasu@jaea.go.jp
	Shin		Takeda	Hokkaido University	s-takeda@eng.hokudai.ac.jp
	Alan		Takibayev	European Spallation Source, (ESS)	alan.takibayev@esss.se
	Vadim		Talanov	Paul Scherrer Institut (PSI)	Vadim.Talanov@psi.ch
	Ichiro		Tanaka	Ibaraki University	i.tanaka@mx.ibaraki.ac.jp
	Julian		Tao	China Spallation Neutron Source (CSNS), Institute of High Energy Physics	taoj@ihep.ac.cn
	Cindy		Tao		
	Hideki		Tatsumoto	J-PARC Center, Japan Atomic Energy Agency (JAEA)	tatumoto@post.j-parc.jp
	Andrew		Taylor	Science and Technology Facilities Council	sue.carter@stfc.ac.uk
	Jonathan	W.	Taylor	DMSC - ESS	jon.taylor@stfc.ac.uk
	Makoto		Teshigawara	J-PARC Center, Japan Atomic Energy Agency (JAEA)	teshigawara.makoto@jaea.go.jp
	John		Thomason	ISIS, Rutherford Appleton Laboratory (RAL)	john.thomason@stfc.ac.uk
	Knud		Thomsen	Paul Scherrer Institut (PSI)	knud.thomsen@psi.ch
	Katsuaki		Tomoyori	Quantum Beam Science Center (QuBS), Japan Atomic Energy Agency (JAEA)	tomoyori.katsuaki@jaea.go.jp
	Katsuaki		Tomoyori	J-PARC Center, Japan Atomic Energy Agency (JAEA)	tomoyori.katsuaki@jaea.go.jp
	Xin		Tong	Oak Ridge National Laboratory (ORNL)	tongx@ornl.gov
	Garry		Trahern	European Spallation Source, (ESS)	garry.trahern@esss.se
U	Mitsuru		Uesaka	University of Tokyo, Nuclear Professional School	uesaka@nuclear.jp
V	Alexandr	E.	Verhoglyadov	Joint Institute for Nuclear Research	verhoglyadov_al@mail.ru
	Christian	J.	Vettier	European Spallation Source, (ESS)	christian.vettier@esss.se
	Marie	C.	Vettier		
	Maria	G.	Vidal de Ramirez		
	Nicolo		Violini	Forschungszentrum Juelich	n.violini@fz-juelich.de
	Jorg	J.	Voigt	Forschungszentrum Juelich	j.voigt@fz-juelich.de
W	Tao		Wan	J-PARC Center, Japan Atomic Energy Agency (JAEA)	wan.tao@jaea.go.jp
	Sheng		Wang	Neutron BeamTechnology Team, RIKEN Institute	swang@riken.jp
	Masao		Watanabe	J-PARC Center, Japan Atomic Energy Agency (JAEA)	
	Patrik		Westman Carlsson	European Spallation Source, (ESS)	patrik.carlsson@esss.se
	Peter	K.	Willendrup	DTU Physics	pkwi@fysik.dtu.dk
	Jorg		Wolters	Forschungszentrum Juelich	j.wolters@fz-juelich.de

Index	Given Name	Middle	Family Name	Affiliation	E-mail Address
	Huarui		Wu	Tsinghua University	wuhuarui1992@gmail.com
	ZhiHong		Xiong	Graduate School of Science and Engineering, Ibaraki University	xiong.zhihong@jaea.go.jp
Y	Masanori		Yamada	NIKI GLASS CO., LTD	
	Yutaka		Yamagata	RIKEN	
	Kazami		Yamamoto	J-PARC Center, Japan Atomic Energy Agency (JAEA)	kazami@post.j-parc.jp
	Dai		Yamazaki	J-PARC Center, Japan Atomic Energy Agency (JAEA)	dai.yamazaki@j-parc.jp
	Yigang		Yang	Tsinghua Unviersity	yangyigang@mail.tsinghua.edu.cn
	Janes	H.	Yeck	European Spallation Source, (ESS)	james.yeck@esss.se
	Hideaki		Yokomizo	Comprehensive Research Organization for Science and Society (CROSS)	h_yokomizo@cross.or.jp
	Tetsuya		Yokoo	J-PARC Center, High Energy Accelerator Research Organization (KEK)	tetsuya.yokoo@kek.jp
	Masao		Yonemura	J-PARC Center, High Energy Accelerator Research Organization (KEK)	yone@post.kek.jp
	Osamu		Yushiro	Toshiba Electron Tubes & Devices Co., Ltd	osamu.yushiro@toshiba.co.jp
Z	Luca		Zanini	European Spallation Source, (ESS)	luca.zanini@esss.se
	Carolin		Zendler	European Spallation Source, (ESS)	carolin.zendler@esss.se
	Junrong		Zhang	China Spallation Neutron Source (CSNS), Institute of High Energy Physics	jrzhang@ihep.ac.cn
	Shuoyuan		Zhang	Comprehensive Research Organization for Science and Society (CROSS)	
	Shaoying		Zhang		
	Kun		Zhu	Peking University, GE Energy	zhukun@pku.edu.cn

Author Index

This is a blank page.

Author Index

This is a blank page.

Editorial Notes

This is a blank page.

Editorial Notes

There are many things that I'd like to mention about the meeting. I bring up especially, excursion and banquet. This ICANS meeting returned to Japan again after 14 years. J-PARC hosted this meeting in Mito. We focused on this area's traditional events exposed to Japanese local culture. It was a beach seining and a Japanese drum. We also conducted BBQ just after beach seining so as to eat the caught fish while it was fresh. The beach seining is a typical traditional seine fishing method, which was conducted for over roughly 300 years at this area. Recently, it declined due to the development of off-shore fisheries. Currently, it is sometimes conducted as experiencing fishing exposed to traditional culture.

We were most worried about typhoon. As you know, Japan is visited by many typhoons the autumn season. It was gambling. Every day, I checked the forecast. Though the typhoon came to Japan the day before excursion, the typhoon's course just went astray fortunately. However, fisherman could not decide to do the beach seining due to the high wave caused by typhoon until right before and I did not know what was going to happen for a while, because it started to rain hardly as we approached the coast.

It was very impressive that so many seagulls gathered around seining, the sunlight was leaked through a rift in the clouds and a rainbow was seen for a moment. It was first experience even for me. Finally, one small-truckload of fish (mainly sardines, only five salmons) was caught. Fisherman was surprised at getting so many fishes in this season. He thought that it was due to typhoon, resulting in affecting the migration of fish. Fried fresh-sardine was served however the demand far outran the supply.

Anyway, the excursion ended a great success. If next chance, what do we try?

regards,
teshi

The ICANS-XXI was very well attended with over 200 participants. The weather was almost nice, and we could have a huge catch of fishes in the beach seine in the excursion symbolizing rich nature of Ibaraki prefecture. Thus, the collaboration meeting was completed abundantly in

scientific and technical discussions, weather and foods. Our task was to prepare the proceedings, which is appropriate for the successful meeting. About 80 articles were submitted for the proceedings. Then, we could edit substantial proceedings for it. Finally, it's an honor for us to join the editing talk for the proceedings of the great collaboration meeting ICANS-XXI.

T. O.

国際単位系（SI）

表１．SI 基本単位

基本量	SI 基本単位	
	名称	記号
長さ	メートル	m
質量	キログラム	kg
時間	秒	s
電流	アンペア	A
熱力学温度	ケルビン	K
物質量	モル	mol
光度	カンデラ	cd

表２．基本単位を用いて表されるSI組立単位の例

組立量	SI 組立単位	
	名称	記号
面積	平方メートル	m^2
体積	立方メートル	m^3
速さ，速度	メートル毎秒	m/s
加速度	メートル毎秒毎秒	m/s^2
波数	毎メートル	m^{-1}
密度，質量密度	キログラム毎立方メートル	kg/m^3
面積密度	キログラム毎平方メートル	kg/m^2
比体積	立方メートル毎キログラム	m^3/kg
電流密度	アンペア毎平方メートル	A/m^2
磁界の強さ	アンペア毎メートル	A/m
量濃度(a)，濃度	モル毎立方メートル	mol/m^3
質量濃度	キログラム毎立方メートル	kg/m^3
輝度	カンデラ毎平方メートル	cd/m^2
屈折率(b)	（数字の） 1	1
比透磁率(b)	（数字の） 1	1

(a) 量濃度（amount concentration）は臨床化学の分野では物質濃度（substance concentration）ともよばれる。
(b) これらは無次元量あるいは次元１をもつ量であるが、そのことを表す単位記号である数字の１は通常は表記しない。

表３．固有の名称と記号で表されるSI組立単位

組立量	SI 組立単位			
	名称	記号	他のSI単位による表し方	SI基本単位による表し方
平面角	ラジアン(b)	rad	1(b)	m/m
立体角	ステラジアン(b)	sr(c)	1(b)	m^2/m^2
周波数	ヘルツ(d)	Hz		s^{-1}
力	ニュートン	N		m kg s^{-2}
圧力，応力	パスカル	Pa	N/m^2	m^{-1} kg s^{-2}
エネルギー，仕事，熱量	ジュール	J	N m	m^2 kg s^{-2}
仕事率，工率，放射束	ワット	W	J/s	m^2 kg s^{-3}
電荷，電気量	クーロン	C		s A
電位差（電圧），起電力	ボルト	V	W/A	m^2 kg s^{-3} A^{-1}
静電容量	ファラド	F	C/V	m^{-2} kg^{-1} s^4 A^2
電気抵抗	オーム	Ω	V/A	m^2 kg s^{-3} A^{-2}
コンダクタンス	ジーメンス	S	A/V	m^{-2} kg^{-1} s^3 A^2
磁束	ウエーバ	Wb	Vs	m^2 kg s^{-2} A^{-1}
磁束密度	テスラ	T	Wb/m^2	kg s^{-2} A^{-1}
インダクタンス	ヘンリー	H	Wb/A	m^2 kg s^{-2} A^{-2}
セルシウス温度	セルシウス度(e)	℃		K
光束	ルーメン	lm	cd sr(c)	cd
照度	ルクス	lx	lm/m^2	m^{-2} cd
放射性核種の放射能(f)	ベクレル(d)	Bq		s^{-1}
吸収線量，比エネルギー分与，カーマ	グレイ	Gy	J/kg	m^2 s^{-2}
線量当量，周辺線量当量，方向性線量当量，個人線量当量	シーベルト(g)	Sv	J/kg	m^2 s^{-2}
酸素活性	カタール	kat		s^{-1} mol

(a)SI接頭語は固有の名称と記号を持つ組立単位と組み合わせても使用できる。しかし接頭語を付した単位はもはやコヒーレントではない。
(b)ラジアンとステラジアンは数字の１に対する単位の特別な名称で、量についての情報をつたえるために使われる。実際には、使用する時には記号radおよびsrが用いられるが、習慣として組立単位としての記号である数字の１は明示されない。
(c)測光学ではステラジアンという名称と記号srを単位の表し方の中に、そのまま維持している。
(d)ヘルツは周期現象についてのみ、ベクレルは放射性核種の統計的過程についてのみ使用される。
(e)セルシウス度はケルビンの特別な名称で、セルシウス温度を表すために使用される。セルシウス度とケルビンの単位の大きさは同一である。したがって、温度差や温度間隔を表す数値はどちらの単位で表しても同じである。
(f)放射性核種の放射能（activity referred to a radionuclide）は、しばしば誤った用語で"radioactivity"と記される。
(g)単位シーベルト（PV,2002,70,205）についてはCIPM勧告2（CI-2002）を参照。

表４．単位の中に固有の名称と記号を含むSI組立単位の例

組立量	SI 組立単位		
	名称	記号	SI 基本単位による表し方
粘度	パスカル秒	Pa s	m^{-1} kg s^{-1}
力のモーメント	ニュートンメートル	N m	m^2 kg s^{-2}
表面張力	ニュートン毎メートル	N/m	kg s^{-2}
角速度	ラジアン毎秒	rad/s	m m^{-1} s^{-1}=s^{-1}
角加速度	ラジアン毎秒毎秒	rad/s^2	m m^{-1} s^{-2}=s^{-2}
熱流密度，放射照度	ワット毎平方メートル	W/m^2	kg s^{-3}
熱容量，エントロピー	ジュール毎ケルビン	J/K	m^2 kg s^{-2} K^{-1}
比熱容量，比エントロピー	ジュール毎キログラム毎ケルビン	J/(kg K)	m^2 s^{-2} K^{-1}
比エネルギー	ジュール毎キログラム	J/kg	m^2 s^{-2}
熱伝導率	ワット毎メートル毎ケルビン	W/(m K)	m kg s^{-3} K^{-1}
体積エネルギー	ジュール毎立方メートル	J/m^3	m^{-1} kg s^{-2}
電界の強さ	ボルト毎メートル	V/m	m kg s^{-3} A^{-1}
電荷密度	クーロン毎立方メートル	C/m^3	m^{-3} s A
表面電荷	クーロン毎平方メートル	C/m^2	m^{-2} s A
電束密度，電気変位	クーロン毎平方メートル	C/m^2	m^{-2} s A
誘電率	ファラド毎メートル	F/m	m^{-3} kg^{-1} s^4 A^2
透磁率	ヘンリー毎メートル	H/m	m kg s^{-2} A^{-2}
モルエネルギー	ジュール毎モル	J/mol	m^2 kg s^{-2} mol^{-1}
モルエントロピー，モル熱容量	ジュール毎モル毎ケルビン	J/(mol K)	m^2 kg s^{-2} K^{-1} mol^{-1}
照射線量（X線及びγ線）	クーロン毎キログラム	C/kg	kg^{-1} s A
吸収線量率	グレイ毎秒	Gy/s	m^2 s^{-3}
放射強度	ワット毎ステラジアン	W/sr	m^4 m^{-2} kg s^{-3}=m^2 kg s^{-3}
放射輝度	ワット毎平方メートル毎ステラジアン	$W/(m^2$ sr)	m^2 m^{-2} kg s^{-3}=kg s^{-3}
酵素活性濃度	カタール毎立方メートル	kat/m^3	m^{-3} s^{-1} mol

表５．SI 接頭語

乗数	名称	記号	乗数	名称	記号
10^{24}	ヨタ	Y	10^{-1}	デシ	d
10^{21}	ゼタ	Z	10^{-2}	センチ	c
10^{18}	エクサ	E	10^{-3}	ミリ	m
10^{15}	ペタ	P	10^{-6}	マイクロ	μ
10^{12}	テラ	T	10^{-9}	ナノ	n
10^9	ギガ	G	10^{-12}	ピコ	p
10^6	メガ	M	10^{-15}	フェムト	f
10^3	キロ	k	10^{-18}	アト	a
10^2	ヘクト	h	10^{-21}	ゼプト	z
10^1	デカ	da	10^{-24}	ヨクト	y

表６．SIに属さないが、SIと併用される単位

名称	記号	SI 単位による値
分	min	1 min=60 s
時	h	1 h =60 min=3600 s
日	d	1 d=24 h=86 400 s
度	°	1°=(π/180) rad
分	’	1’=(1/60)°=(π/10 800) rad
秒	”	1”=(1/60)’=(π/648 000) rad
ヘクタール	ha	1 ha=1 hm^2=10^4m^2
リットル	L, l	1 L=1 l=1 dm^3=10^3cm^3=$10^{-3}m^3$
トン	t	1 t=10^3 kg

表７．SIに属さないが、SIと併用される単位で、SI単位で表される数値が実験的に得られるもの

名称	記号	SI 単位で表される数値
電子ボルト	eV	1 eV=1.602 176 53(14)×10^{-19}J
ダルトン	Da	1 Da=1.660 538 86(28)×10^{-27}kg
統一原子質量単位	u	1 u=1 Da
天文単位	ua	1 ua=1.495 978 706 91(6)×10^{11}m

表８．SIに属さないが、SIと併用されるその他の単位

名称	記号	SI 単位で表される数値
バール	bar	1 bar=0.1MPa=100 kPa=10^5Pa
水銀柱ミリメートル	mmHg	1 mmHg≈133.322Pa
オングストローム	Å	1 Å=0.1nm=100pm=10^{-10}m
海里	M	1 M=1852m
バーン	b	1 b=100fm^2=(10^{-12}cm)^2=$10^{-28}m^2$
ノット	kn	1 kn=(1852/3600)m/s
ネーパ	Np	SI単位との数値的な関係は、対数量の定義に依存。
ベル	B	
デシベル	dB	

表９．固有の名称をもつCGS組立単位

名称	記号	SI 単位で表される数値
エルグ	erg	1 erg=10^{-7} J
ダイン	dyn	1 dyn=10^{-5}N
ポアズ	P	1 P=1 dyn s cm^{-2}=0.1Pa s
ストークス	St	1 St =$1cm^2$ s^{-1}=$10^{-4}m^2$ s^{-1}
スチルブ	sb	1 sb =1cd cm^{-2}=10^4cd m^{-2}
フォト	ph	1 ph=1cd sr cm^{-2} =10^4lx
ガル	Gal	1 Gal =1cm s^{-2}=$10^{-2}ms^{-2}$
マクスウエル	Mx	1 Mx = 1G cm^2=10^{-8}Wb
ガウス	G	1 G =1Mx cm^{-2} =10^{-4}T
エルステッド(a)	Oe	1 Oe ≙ (1000/4π)A m^{-1}

(a) ３元系のCGS単位系とSIでは直接比較できないため、等号「 ≙ 」は対応関係を示すものである。

表10．SIに属さないその他の単位の例

名称	記号	SI 単位で表される数値
キュリー	Ci	1 Ci=3.7×10^{10}Bq
レントゲン	R	1 R = 2.58×10^{-4}C/kg
ラド	rad	1 rad=1cGy=10^{-2}Gy
レム	rem	1 rem=1 cSv=10^{-2}Sv
ガンマ	γ	1 γ=1 nT=10^{-9}T
フェルミ		1 フェルミ=1 fm=10^{-15}m
メートル系カラット		1 メートル系カラット= 0.2 g = 2×10^{-4}kg
トル	Torr	1 Torr = (101 325/760) Pa
標準大気圧	atm	1 atm = 101 325 Pa
カロリー	cal	1 cal=4.1858J（「15℃」カロリー），4.1868J（「IT」カロリー），4.184J（「熱化学」カロリー）
ミクロン	μ	1 μ =1μm=10^{-6}m

（第8版，2006年）